

DYF ~~G Pratt~~

C#3

C#3

FEB 1 1993

AGARD-CP-91-71

AGARD-CP-91-71

0.3

# AGARD

ADVANCED RESEARCH AND DEVELOPMENT

AN INTERNATIONAL ORGANIZATION OF NATIONAL RESEARCH ESTABLISHMENTS

AGARD CONFERENCE PRE-PRINT No. 91

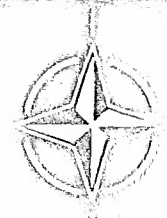
on

## Inlets and Nozzles for Aerospace Engines

PROPERTY OF U.S. AIR FORCE  
AEDC MODEL 7  
F40800-01-0-0004

CONFERENCE REPORTS  
NEW COPY

OF THE ATLANTIC TREATY ORGANIZATION



**DISTRIBUTION AND AVAILABILITY  
ON BACK COVER**  
PROPERTY OF U.S. AIR FORCE  
AEDC TECHNICAL LIBRARY  
ARNOLD AFB, TN 37389

TL  
500  
N584  
no. 91  
c. 3

AGARD-CP-91-71

NORTH ATLANTIC TREATY ORGANIZATION  
ADVISORY GROUP FOR AEROSPACE RESEARCH AND DEVELOPMENT  
ORGANISATION DU TRAITE DE L'ATLANTIQUE NORD  
Group Consultatif Pour la Recherche et le Développement Aérospatial

INLETS AND NOZZLES FOR AEROSPACE ENGINES

Papers presented at the 38th Meeting of the AGARD Propulsion  
and Energetics Panel held at the Park Hotel, Sandefjord, Norway, 13-17 September 1971.

## THE MISSION OF AGARD

The mission of AGARD is to bring together the leading personalities of the NATO nations in the fields of science and technology relating to aerospace for the following purposes:

- Recommending effective ways for the member nations to use their research and development capabilities for the common benefit of the NATO community;
- Providing scientific and technical advice and assistance to the North Atlantic Military Committee in the field of aerospace research and development;
- Continuously stimulating advances in the aerospace sciences relevant to strengthening the common defence posture;
- Improving the co-operation among member nations in aerospace research and development;
- Exchanging of scientific and technical information;
- Providing assistance to member nations for the purpose of increasing their scientific and technical potential;
- Rendering scientific and technical assistance, as requested, to other NATO bodies and to member nations in connection with research and development problems in the aerospace field.

The highest authority within AGARD is the National Delegates Board consisting of officially appointed senior representatives from each Member Nation. The mission of AGARD is carried out through the Panels which are composed of experts appointed by the National Delegates, the Consultant and Exchange Program and the Aerospace Applications Studies Program. The results of AGARD work are reported to the Member Nations and the NATO Authorities through the AGARD series of publications of which this is one.

Participation in AGARD activities is by invitation only and is normally limited to citizens of the NATO nations.

The material in this publication has been reproduced directly from copy supplied by AGARD or the author.

Published December 1971

533.697



*Printed by Technical Editing and Reproduction Ltd  
Harford House, 7-9 Charlotte St, London. W1P 1HD*

#### AGARD PROPULSION AND ENERGETICS PANEL OFFICERS

CHAIRMAN: Professor I.Glassman, Princeton University, New Jersey, USA.  
DEPUTY CHAIRMAN: Mr F.Jaarsma, National Aerospace Laboratory, Amsterdam, Netherlands.

#### PROGRAM COMMITTEE FOR 38TH MEETING

Mr N.F.Rekos, National Aeronautics and Space Administration, Washington DC, USA. (Chairman)  
Professor C.Casci, Politecnico di Milano, Milan, Italy.  
Professor A.E.Fuhs, Naval Postgraduate School, Monterey, California, USA.  
Mr R.J.Lane, Rolls-Royce (1971) Ltd., Bristol Engine Division Filton, UK.  
Professor O.Lutz, Deutsche Forschungs- und Versuchsanstalt für Luft- und Raumfahrt E.V., Brunswick, Germany.  
Mr R.J.Mowill, A/S Kongsberg Våpenfabrikk, Kongsberg, Norway.  
Mr J.Suruge, Office National d'Etudes et de Recherches Aérospatiales, Châtillon-sous-Bagneux, France.

#### HOST NATION COORDINATOR FOR 38TH MEETING

Mr S.E.Høst, Norwegian Defence Research Establishment, Kjeller, Norway.

#### PANEL EXECUTIVE

Dr R.P.Hagerty, AGARD, Neuilly-sur-Seine, France.

The Propulsion and Energetics Panel wishes to express its thanks to the hosts — the Norwegian National Delegates to AGARD — for the invitation to hold the meeting in Sandefjord and for the provision of the necessary facilities and personnel to make the meeting possible.

PAPERS 12, 13, 15, 17, 18, 19, 20, ETC  
LISTED ON MISSING FOLLOWING PAGE VI  
ARE IN THE DOCUMENT IN NUMERICAL  
SEQUENCE.

CONTENTS

	Page
PROPULSION AND ENERGETICS PANEL OFFICERS & PROGRAM COMMITTEE	iii
PREFACE BY THE PROGRAM COMMITTEE CHAIRMAN	iv
"INLETS AND NOZZLES FOR AEROSPACE ENGINES"	Reference
<u>SESSION I. ENGINE-AIRPLANE INTERFERENCE REPRESENTATION IN WIND TUNNEL TESTING</u>	
REVIEW OF THE CONCLUSIONS OF THE AD HOC COMMITTEE ON ENGINE AIRPLANE INTERFERENCE AND WALL CORRECTIONS IN TRANSONIC WIND TUNNEL TESTS by A.Ferri	1
INLETS-AIRPLANE TESTING IN TRANSONIC WIND TUNNELS by F.Jaarsma	2
NOZZLE AND EXHAUST TESTING IN TRANSONIC FLIGHT REGIME by A.E.Fuhs	3
<u>SESSION II. ENGINE-AIRPLANE INTERFERENCE REPRESENTATION IN WIND TUNNEL TESTING (Continued)</u>	
PROBLEMES DE MESURE SUR MAQUETTE DE LA POUSSEE D'UN ARRIERE - CORPS D'AVION SUPERSONIQUE - TUYERES DE REFERENCE par B.Masure	4
MOYENS ET EXEMPLES D'ESSAIS AU C.E.Pr par J.C.Ripoll et J.B.Cocheteux	5
MEASUREMENT FULL-SCALE OF PROPELLING NOZZLE PERFORMANCE IN AN ALTITUDE TEST FACILITY by J.C.Ascough	6
INLET-ENGINE-NOZZLE WIND TUNNEL TEST TECHNIQUES by D.N.Bowditch	7
WIND TUNNEL INVESTIGATIONS OF A SUPERSONIC AIR INTAKE WITH VARIOUS AUXILIARY INTAKES AT LOW SPEEDS by H.Eibl and R.Friedrichs	35
<u>SESSION III. THRUST VECTORING AND CONTROL</u>	
WIND TUNNEL TESTING OF V/STOL ENGINE MODELS - SOME OBSERVED FLOW INTERACTION AND TUNNEL EFFECTS by R.A.Tyler and R.G.Williamson	8
VECTORED THRUST IN AIR COMBAT by C.R.James, Jr	9
AERODYNAMICS OF THRUST REVERSER DESIGN by W.J.Lewis and H.Prechter	10
INFLUENCE DE QUELQUES PARAMETRES CARACTERISTIQUES SUR LES PERFORMANCES DES EJECTEURS par J.M.Hardy	11
RAPID MIXING NOZZLES FOR V/STOL APPLICATIONS by C.M.Chesters	14

SESSION VIII. SUBSONIC AND TRANSONIC AEROPROPULSION

FLOW ANALYSIS IN AXISYMMETRIC SUBSONIC INLETS OF SMALL GAS TURBINES by P.M.Gallet	16
THE ANALYSIS OF A SUBSONIC AXISYMMETRIC INLET FOR COMPRESSOR MATCHING by R.E.Stanley	29
ON THE APPLICATION OF A TIME-DEPENDENT TECHNIQUE IN TRANSONIC DOUBLE FLOW NOZZLE SOLUTIONS by C.Osnaghi and E.Macchi	27
ETUDE THEORIQUE ET EXPERIMENTALE DE LA CO-EXISTENCE DE DEUX FLUX DANS UN CANAL DE SECTION CONSTANTE par J.Paulon	31
APPENDIX A: DISCUSSIONS	A1
APPENDIX B: PANEL PUBLICATIONS IN RECENT YEARS	B1

REVIEW OF THE CONCLUSIONS OF THE AGARD AD HOC COMMITTEE

ON ENGINE AIRPLANE INTERFERENCE AND WALL CORRECTIONS IN TRANSONIC WIND TUNNEL TESTS

Antonio Ferri<sup>†</sup>  
Director, Aerospace Laboratory  
Astor Professor of Aerospace Sciences  
New York University  
Bronx, New York 10453

Recent developments of high performance airplanes have generated requirements for the prediction of the aerodynamic performance of airplane designs with high accuracy, certainly better than that which is presently possible with available experimental techniques. As a result, a critical review of present methods for prediction of performances from model and component experimental data is taking place. In many NATO nations the development of better experimental techniques is in progress; such activities are carried on at a national level. Special attention is given to the transonic range at low lift or high L/D where small difference in flow produces large differences in performance. For this reason, the Director of the AGARD, supported by the National Delegates, has initiated an Ad Hoc Committee activity for the purpose of generating a direct exchange of information and technical opinions, and of stimulating joint programs in this field. The topics considered by the Ad Hoc Committee are related to two specific problems in transonic tests: (1) correct representation in wind tunnel tests of the interaction between engine flow and airplane characteristics; (2) wall interference at high lift.

The Committee consisted of specialists from different nations nominated by the National Delegates. The Ad Hoc Committee has performed this task and has prepared a set of recommendations included in this report that now should be followed up by existing permanent committees. The purpose of my presentation is to review briefly some of the recommendations related to engine interference and outline areas where additional activities are required. The operation of the Committee has been organized as follows:

The Committee prepared a questionnaire which was sent to selected organizations interested in this problem in each country. The objective of the questionnaire was to obtain consistent and comparable sets of information on the approaches used to simulate engine interference and to evaluate the effects of incomplete simulation of wind tunnel tests and on the type of corrections used for evaluating wall interference, especially at high lift. In addition, justification was requested on the lack of correction when corrections were not performed, and on the wind tunnel turbulence and its effect on the results.

The results of the different contributions were summarized by members of the Committee and presented in an organized form to a meeting of Specialists. Such summaries have been published by the AGARD and are available. At this meeting, only one representative of each organization that replied to the questionnaire was invited; no observers were present. The main part of the meeting was devoted to the discussion and preparation of the recommendations. All of the activities were initiated and concluded during the period of one year.

The Propulsion and Energetic Panel plans to continue such type of activities in the field of engine airplane interference with the help of the Fluid Dynamics Panel, and has asked me to outline a possible follow-up program. My plan is to continue activities in the field of engine airplane integration problems outlined by the Ad Hoc Committee and to propose a meeting for next year, organized along the same line of operation. I will discuss some of the topics now, where in my opinion a joint effort could be justified in order to obtain your suggestions and comments before fixing the program.

The problems to be investigated can be divided into two separate groups:

- 1) Prediction of flight characteristics of the inlet and nozzle design from an engine performance point of view.
- 2) Determination of the interaction between the engine power plants and the airplane and efforts of such interaction on airplane performances.

An optimization of installation needs a good compromise between the two requirements. The most important topics related to the first group discussed by the panel are inlet characteristics, nozzle characteristics and definition of engine thrust for a given nozzle design.

Usually in the design and investigation of inlet performances, only the front part of the airplane is considered to be important and approximately represented in the tests. Usually the inlet in the inlet tests does not feed an engine; therefore, the exhaust areas of the duct is much larger than the exhaust area of the actual engine, and thus the rear part of the model is quite different from the actual airplane design. Figure 1 is a typical model used for these kind of tests. In some cases, the characteristics of the flow downstream can affect substantially the flow entering the inlet and the flow field in the region of the boundary layer scoops or boundary layer bleeds. The Committee recommended that this possibility be clearly recognized and that in each inlet tested in transonic flow some effort should be devoted to ascertain that the downstream effects, however small, are correctly represented. The results of this investigation should be attached to any report describing the experimental results. The Committee feels that such problems can be solved more easily for engine installations attached to the fuselage, while it is more difficult for the podded engine installation because the exhaust of the engine affects all of the flow field (Figs. 2-3). Attempts are often made to test the inlet at lower entering mass flow and then corrections are introduced to extrapolate performances to the correct mass flow. Such corrections are inaccurate at

<sup>†</sup>Chairman, AGARD Ad Hoc Committee on Engine Airplane Interference and Wall Corrections in Transonic Wind Tunnel Tests

transonic flow, because of the possibility of discontinuous variation of the flow due to small changes of inlet mass flow. Here methods to add energy to the inlet flow are required.

The approach of engine simulators developed recently appear interesting. However, it is not clear that the present activities are completely satisfactory, because some of the engine simulations do not represent correctly the scaling parameters that define the mixing characteristics downstream of the engine. In some of the simulations, only the bypass flow is ingested while the mass of the main engine is not ingested by the simulator inlet; therefore, the inlet conditions are not simulated. Differences in mass flow between 15 and 25% are accepted. Figure 3 indicates a comparison between a simulator used in one of the tests and the actual engine installation. The difference can be important in the region of the inlet. The difference can and should be eliminated by passing more air across the fan; therefore, by passing the correct mass flow through the inlet, an attempt should be made to improve the conditions in the rear. My intention is to consider this problem as one of the problems to be investigated in the next phase of the work. An actual simulator design is shown in Fig. 4.

Usually, boundary layer scoops and airplane shapes in front of the inlet are scaled geometrically in the tests. Sometimes the geometry of the scoop is changed in such a way that the inlet is free from ingesting low energy boundary layer. This is obtained by increasing the size of the boundary layer scoop. The problem of correct aerodynamic representation of the airplane configuration when tested at Reynolds numbers different from flight is an important problem that exists for all airplane components. Such problems have not been considered carefully up until now. While the problem of Reynolds number simulation for the complete configuration requires large facilities, the problem of better simulation of local conditions can be achieved in present facilities. For example, the airplane shape should be changed to take into account different displacement thicknesses in order to have the correct pressure distribution; additional tests should be made in order to obtain boundary layer scoop drag and inlet performances especially at transonic speed when shock waves are found. Special attention should be given to the simulation of induced fields due to the fuselage in the front of the inlet. Present methods for evaluating scoop, bleed drag, and spillage drag do not take into account differences in Reynolds numbers and are neither standard or satisfactory. In addition, the approach used is seldom defined in the report. The Committee felt that the AGARD should take the initiative to try to define acceptable standards for the performance of such tests. This is the second topic that I consider for future work.

One of the important quantities to be measured in the inlet is the mass flow. Usually the mass flow is obtained through flow meters that are calibrated with high accuracy before the tests under uniform stagnation conditions. In inlet tests, the stagnation conditions often are not uniform because the model temperature is different from the stagnation temperature of the tunnel and a large amount of distortion exists ahead of the flow meter. The required accuracy of the order of 1 - 0.5% cannot be insured unless more complex calibrations are performed.

The dynamic characteristics of the inlet are important; however, scaling criteria are not available and therefore reduced scale measurements are not completely satisfactory. Additional work is especially required in order to analyze more accurately the interaction between inlet and engine at the interface for bypass engines. Here the one-dimensional type of analysis does not apply.

In relation to the nozzle design, several shortcomings have been pointed out by the Committee. First, the nozzle characteristics as a function of geometry are usually obtained from separate tests where the engine flow is not simulated and without correct representation of distortion of stagnation conditions or correct representation of the external flow. Usually, engine performances are measured using a converging nozzle. These characteristics are used to obtain performances of the engine using a different nozzle by correcting the measured engine performance on the basis of the difference of performances between the new nozzle and the nozzle used in the tests. In the engine tests, the external flow is not simulated; however, in a converging nozzle, the performance of the nozzle is affected by the distribution of the stagnation condition of the internal flow and by the external conditions of the flow because these conditions affect the shape of the sonic line (Fig. 7). The characteristics of the nozzles are measured in facilities using cold air and having uniform stagnation conditions where the external flow is often simulated. Then the data for the engines are corrected using the measured nozzle characteristics and by assuming average properties of the engine flow upstream of the nozzle. This method used for the determination of performances is approximate and can introduce errors of one or two percent for flows having large gradients of stagnation properties. In Figs. 8, 9, and 10, results of an analysis are presented that clarify the sources of such error. A nozzle configuration has been analyzed having a given mass flow, and constant average stagnation conditions, discharging in a converging and slightly diverging nozzle. In one case uniform conditions  $p_{01}$  and  $T_{01}$  are assumed to exist at the entrance of the nozzle, while in other cases a distribution either of stagnation temperature, or stagnation pressure, or both, are assumed to exist. The assumed distribution is shown in Fig. 8. The average conditions are the same in all cases. The sonic line shape and the Mach number at the throat are shown in Figs. 9 and 10. The throat area has been adjusted slightly in each case to have the mass flow constant. Loss of total impulse occurs because of the presence of viscosity and heat conduction when gradients are present. The losses are largest when stagnation pressure and temperature are variable and are of the order of 2.5% of the total temperature of the jet. The corresponding loss in thrust is much larger than this value.

The performances of actual nozzles for different flight conditions are often obtained from cold tests. For many flight conditions, separation occurs either inside or outside of the nozzle. The separated flow region is not represented correctly by cold tests because the separation depends strongly on the mixing between the external and internal flows. The mixing is controlled by the ratio between velocity and density of the internal and external flows that are not simulated in cold tests; therefore, the extrapolation of such data to flight conditions can introduce errors.

Figures 11 and 12 show a typical installation used frequently for investigating the interaction between internal and external flows. The inlets in the case, shown in Fig 12, are not represented, but are substituted by a faired surface and the air is carried through the support in the fuselage. All boundary conditions that influence the region of separation, such as pressure distribution, boundary layers, etc., are not simulated in such tests. The problem is more complex in many present engine installations where

bypass or cooling air is injected in the nozzle. Such air usually has stagnation conditions that are different from the stagnation conditions of the external and engine flows, (Fig. 13). The mixing of these flows depends on the actual stagnation conditions of the different flows, and the drag of the nozzle or drag of the external part of the airplane is influenced by these quantities. However, these quantities are not usually simulated correctly in the present testing techniques, even when engine simulators are used. The drag of the rear part of the airplane at transonic speed can be 30 to 40% of the total drag of the airplane for a two engine configuration. Such a quantity cannot be obtained accurately from wind tunnel test methods used at the present-time.

When podded engines are investigated, the flow from the engines affect the aerodynamics of the airplane. Even where simulators are used and the inlet mass flow is correctly represented, the flow displacement produced by the engine flow is usually not accurately represented. This lack of correct representation can introduce in some cases differences in the local flow field. A correct representation of the mixing downstream of the engine requires that the stagnation conditions of the engine jet are correctly represented; otherwise, the mixing of the two streams produces different displacement thickness. Figure 14 indicates the variation of streamtube area due to mixing at constant pressure for different jet conditions, and different engines discharging in a single nozzle. When the interference between the engine and wing is important, such interference can be evaluated only by means of much more sophisticated experimental techniques. No indication of the importance of such effects is available, and the importance depends on the configuration. As a conclusion, the Committee felt that the tests, either of components or of the complete model, as performed up until now do not represent the best possible effort. Many factors introduce errors in the results. Reynolds numbers, support interference, aeroelastic effects on the model, tunnel calibration, and wall interaction are very important parameters. However, additional parameters that are also very important are accurate determination of inlet performance actual engine thrust with a given nozzle, nozzle performance and accurate representation of engine airplane interference. The present requirements of very accurate predictions are above the possibilities of present experimental techniques. Therefore, a concentrated effort to improve accuracy of present experimental methods is justified, and the present situation, where more accurate results are requested, without giving the experimental groups the possibility of improving experimental techniques should be changed.

The introduction of the engine simulators appears very promising for better determination of installed engine performances and engine airframe interference; however, it complicates substantially the experimental techniques. In addition, sufficient effort has been devoted to obtaining satisfactory simulation. An additional shortcoming in all of these problems is that many of the problems are not openly recognized by the users of the data, and the experimental methods are not standardized.

The Propulsion and Energetics Panel of the AGARD will try to organize an effort to outline some of the possible efforts required to try to overcome some of these difficulties.

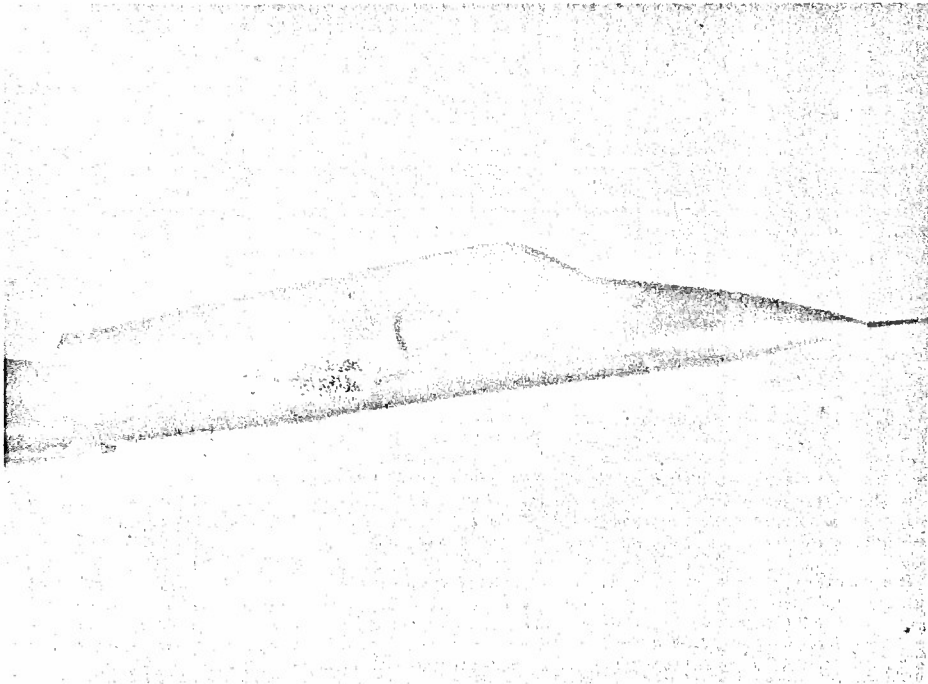


FIG.1 TYPICAL INLET TEST MODEL

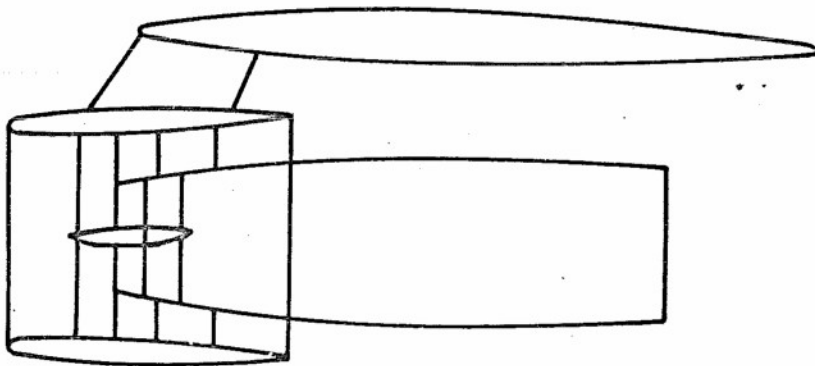


FIG.2 TURBOFAN UNDER A WING

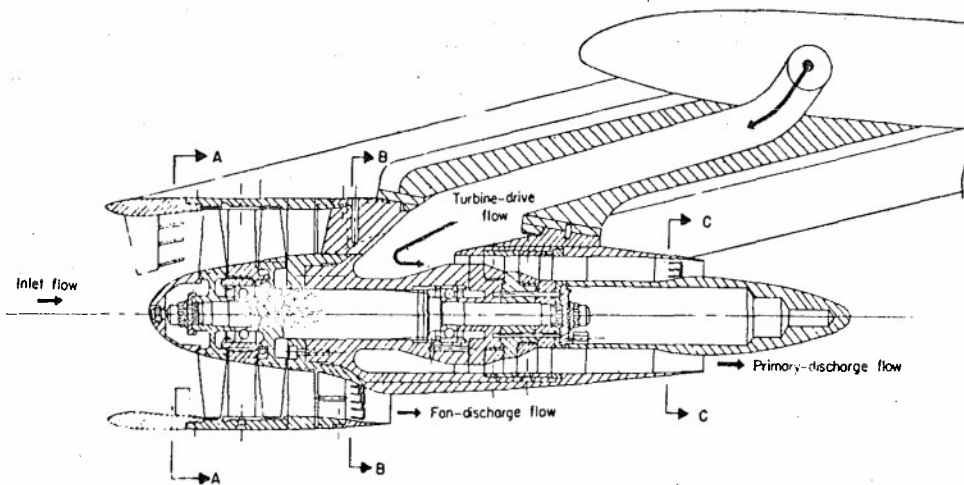


FIG.3 TYPICAL TURBOFAN SIMULATOR DESIGN

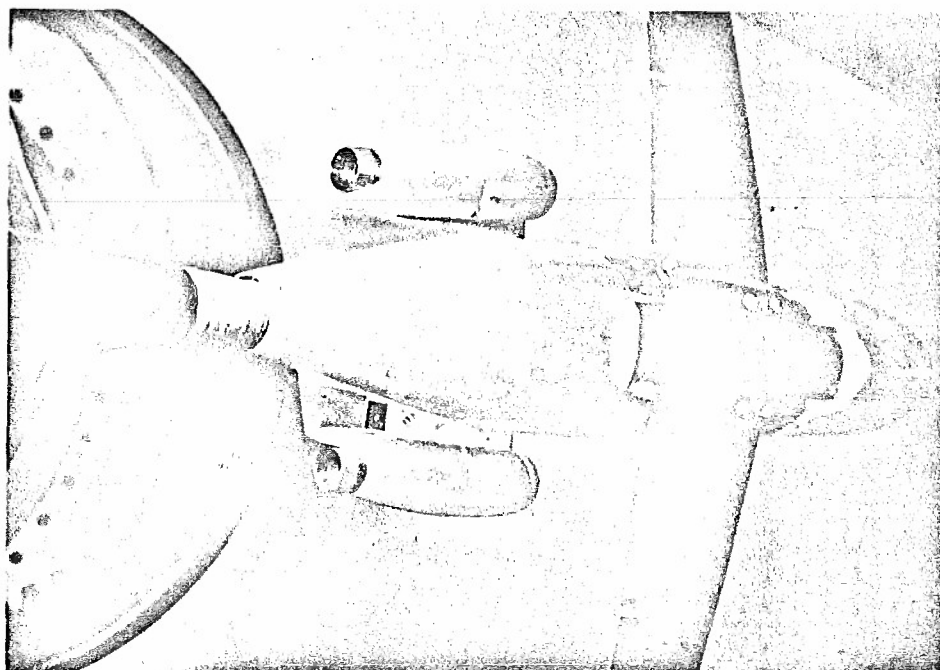


FIG.4 TURBOFAN INSTALLATION TEST

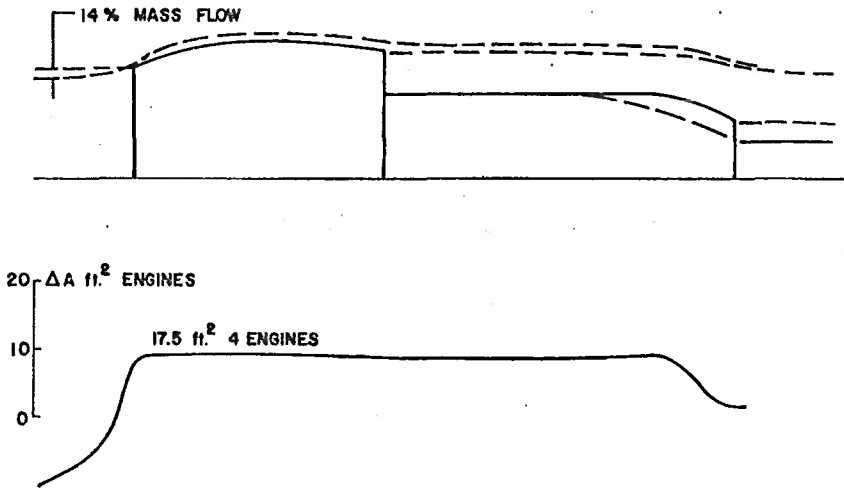


FIG.5 STREAMTUBE OF TYPICAL SIMULATOR

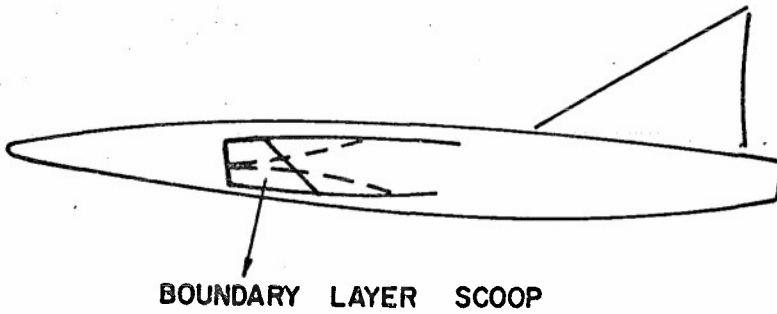


FIG.6 BOUNDARY LAYER SCOOP AIRPLANE INTERACTION

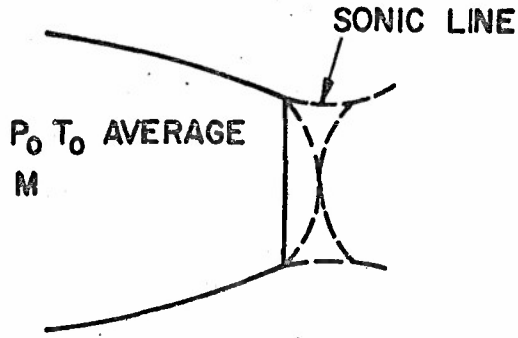


FIG.7 SONIC LINE IN CONVERGING NOZZLE

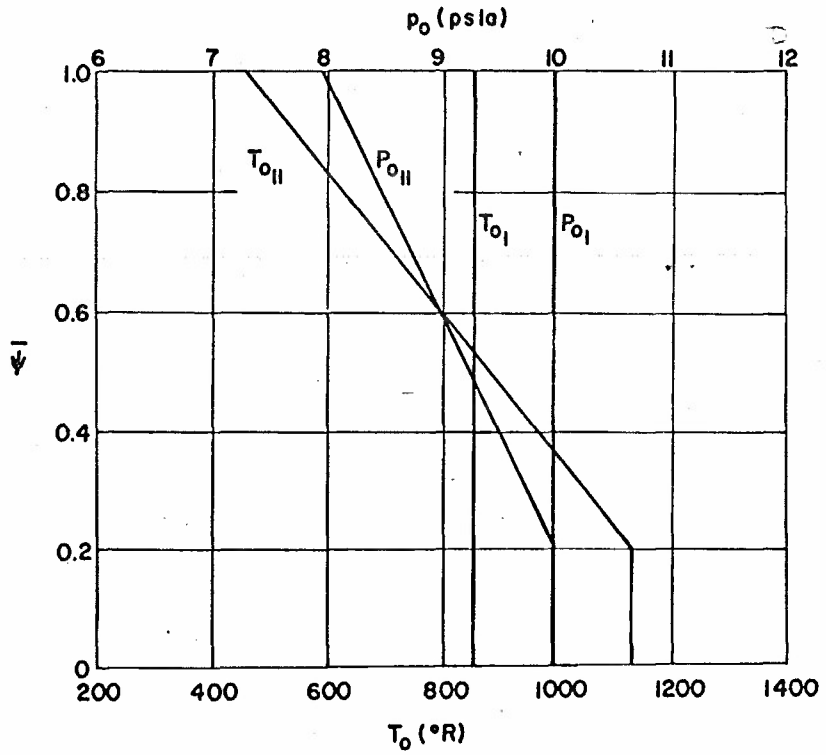
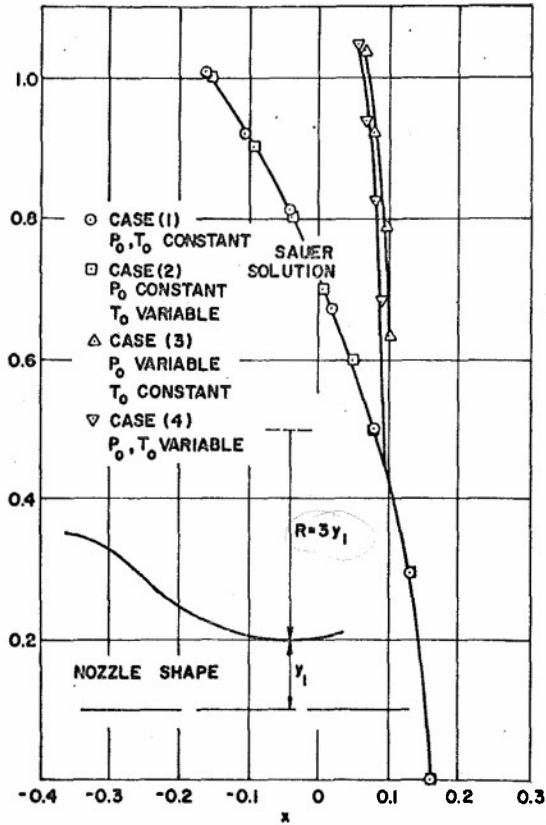
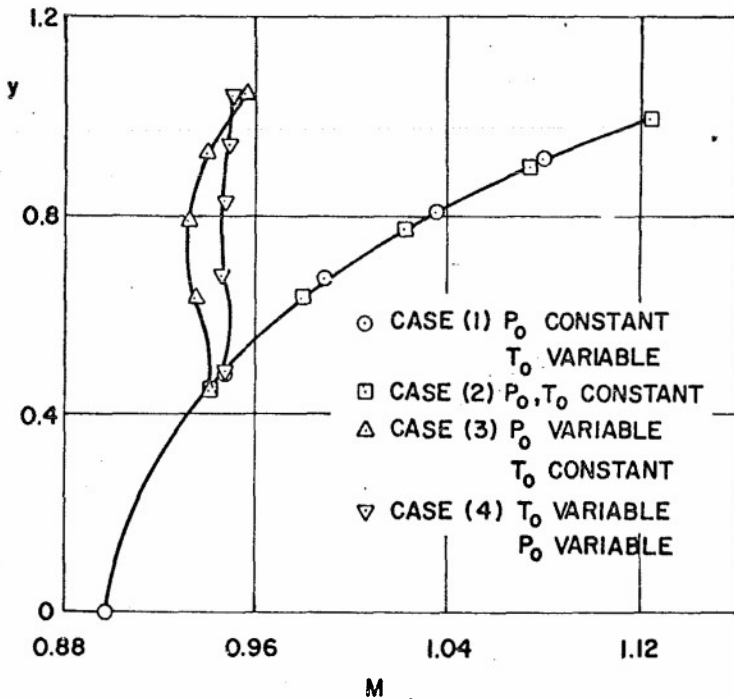


FIG.8 STAGNATION CONDITIONS AS FUNCTIONS OF MASS FLOW



*How about these solutions made?*

FIG.9 SONIC LINE SHAPES



*same question!*

FIG.10 THROAT MACH NUMBER DISTRIBUTIONS

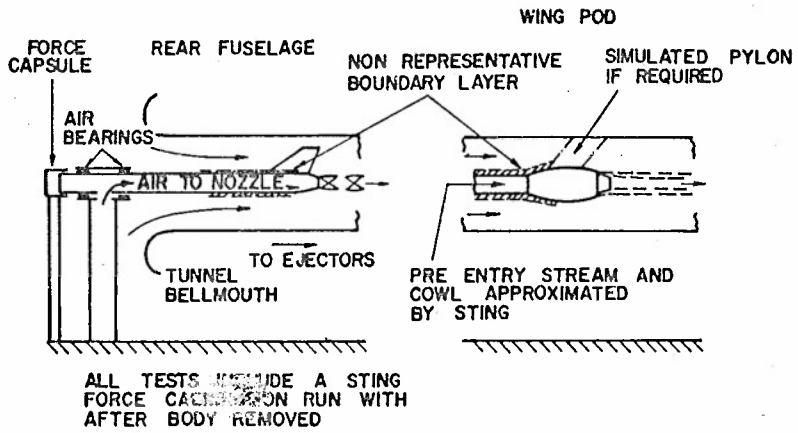


FIG.11 NOZZLE TEST RIG WITH EXTERNAL FLOW

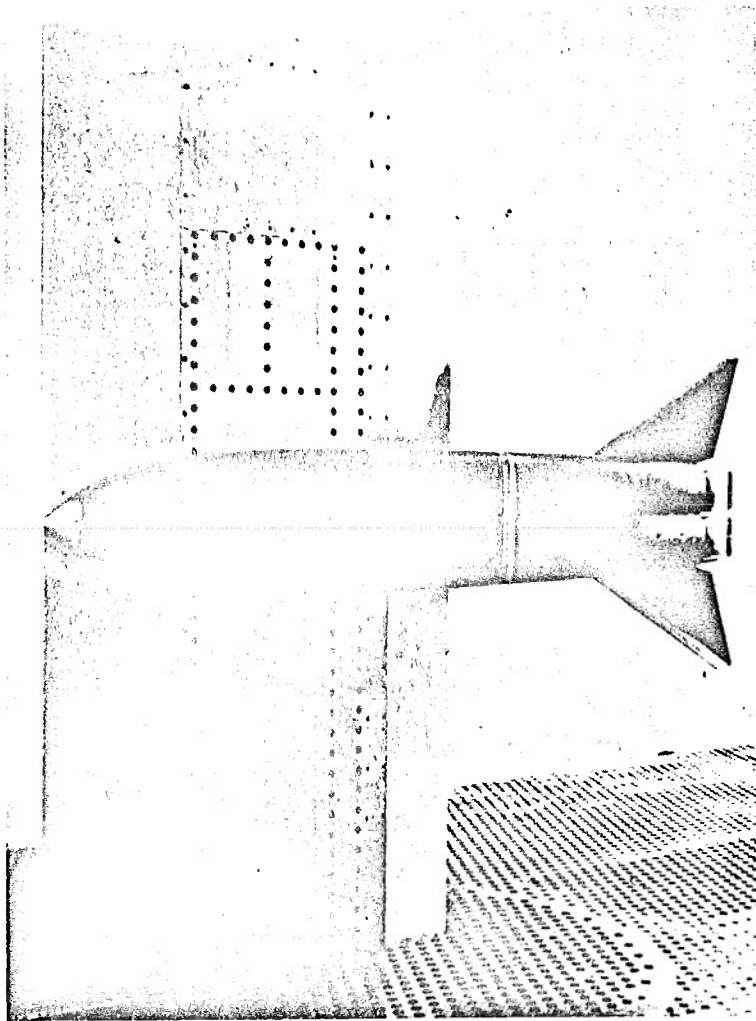


FIG.12 RIG MOUNTED ON TRANSONIC TUNNEL MODEL CART

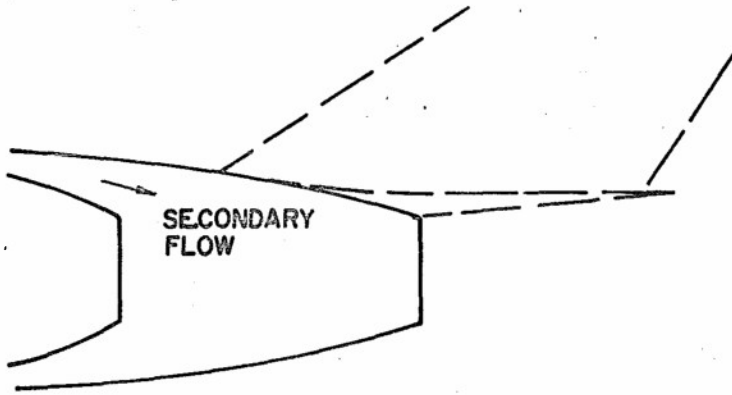


FIG.13 SCHEMATIC OF INTERNAL EXTERNAL FLOW INTERACTION

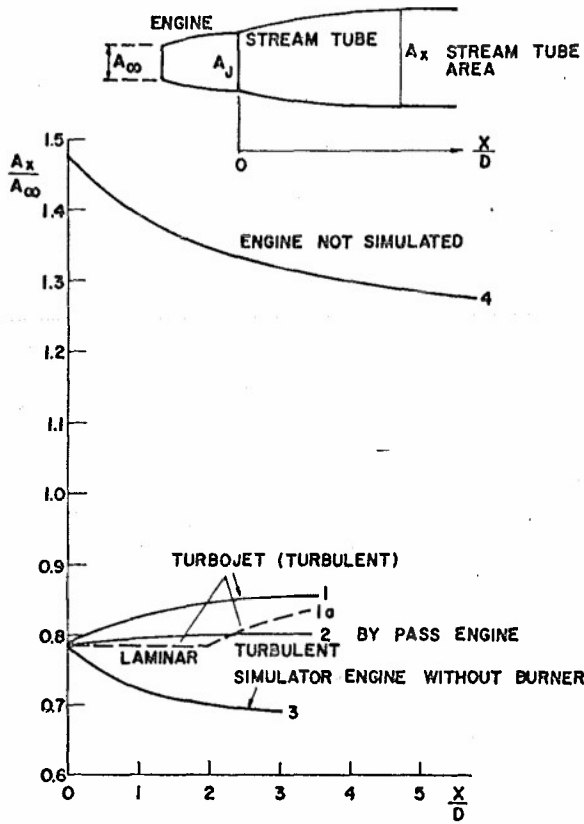


FIG.14 VARIATION OF JET ENGINE STREAM TUBE DUE TO MIXING

## INLETS-AIRPLANE TESTING IN TRANSONIC WIND TUNNELS

by

P. JAARSMA

NATIONAL AEROSPACE LABORATORY NLR  
AMSTERDAM  
THE NETHERLANDS.

## SUMMARY

In this paper the results and recommendations on inlet testing in transonic wind tunnels, as obtained from the AGARD Ad Hoc Study on "Engine-Airplane Interference in Transonic Tests" are discussed in more detail. Special attention will be directed towards mass flow measurements, external drag determination, boundary layer representation for diverters and bleeds, and unsteady flow phenomena in inlets.

## INTRODUCTION

In April 1970 an Ad Hoc Committee was initiated by the Director of ACARD and supported by the National Delegates Board, under leadership of Prof. A. Ferri, for the purpose of studying the general problem of performance predictions of aircraft from wind tunnel data and engine specifications, particularly at transonic speeds. The object was to review the various techniques as used in the ACARD countries and, if possible, to make recommendations for further studies.

In the spring of 1970 a questionnaire was distributed among aeronautical laboratories operating transonic wind tunnels, aircraft manufacturers, engine companies, and airplane operators. The questionnaire contained specific questions regarding inlets, engine thrust and exhausts and generally asked for information on test procedures, techniques, applied corrections, obtained and required accuracies and, if available, comparison between wind tunnel data and free flight data. The response to the questionnaire was very good; all leading aviation companies, establishments and agencies in the ACARD countries cooperated in the study. In September 1970 a specialists meeting was held discussing the advantages and limitations of the various techniques and procedures, observing missing or weak links and recommending further work. The conclusions and recommendations are written by Prof. A. Ferri, the Ad Hoc Study Group chairman, and the technical informations as gathered from this study has been reported by the present author (1). This paper is a summary of the information as obtained on inlet testing in wind tunnels in the transonic speed regime.

The development of high performance aircraft requires the prediction of aerodynamic performances with such high precision, which is above what is currently possible with available technique. This is especially true for the transonic flight regime, which is of importance for transports and fighters, the former for economic cruise reasons, the latter for ferry and combat missions.

Since the exerted net thrust by the engine as felt by the airframe is of primary importance in the analysis of the engine airframe integration, most emphasis has been given to the thrust and drag components as obtained from wind tunnel measurements and engine test bench data. Fig. 1 illustrates a schematic representation of an highly integrated airframe installation. The various drag terms due to engine installation are defined below. These definitions are not standard however and are not used in a similar manner by each group. Fig. 2 shows the usual bookkeeping procedures for combining all test results to provide compatible thrust and drag performance predictions. In general four models in the thrust minus drag counting are used: (a) the aeroforce model with a reference mass flow through the inlet, (b) the sting effects model, for corrections on the data of the aeroforce model due to the support system, (c) the inlet drag model or propulsion model yielding data on corrections due to the interference between the internal inlet flow and the external flow, and data on inlet performance, and (d) the jet effects model yielding corrections on the afterbody aerodynamics and nozzle performance in the external flow field. This summary will concern only the models (a) and (c); the latter being rather obvious, the former for reasons of correcting the aeroforce data due to the internal flow.

## AEROFORCE MODELS

For aeroforce models of almost all jet powered aircraft the inlet mass flow is usually completely or almost completely simulated. The basic force coefficients (lift, drag, moments, etc.) are determined from such models when the measured data from pressure plotting or balance readings are corrected for the internal flow through the inlet. A clear statement regarding conditions when complete inlet mass flow duplication is required to minimize the uncertainties of wind tunnel aerodynamic data is not possible on the basis of past experience. Aircraft which cruise in the transonic speed regime require accurate accounting for inlet mass flow ratio since both aerodynamic and propulsion performance are sensitive to mass flow ratio operating conditions. Vehicles of the type which require a rapid acceleration through transonic Mach numbers are also affected by the direct and indirect effects of mass flow ratio, since aircraft thrust minus drag is usually a minimum at these conditions.

Two techniques exist for inlet mass flow simulation at transonic speeds namely, flow-through inlets or pods, and use of powered engine simulators. The former is the simplest and is generally used in the early stage of wind tunnel testing. In order to apply this technique three conditions must be met:

- adequate exit area
- low pressure at exit, preferably below ambient
- low total head losses in the internal duct.

Regulation of the inlet airflow below maximum can be accomplished by inserting restrictions in the duct. The advantage of this technique besides its simplicity is its consequent ease of measuring forces. The main disadvantage is the need for increased exit area compared to the real jet exhaust which must involve geometric distortion e.g. incorrect nacelle length or boattail angle or elimination of turbine afterbody in case of podded fans. For complete aircraft models such as with podded engine installations this increased exit area might be unacceptable and geometric scaled engine pod models are used in that case. The value of these pods is then not to simulate inlet flow, but to simulate an entire nacelle-pylon system. Effects of various pod and pylon contours and mounting positions on airplane stability and drag can be evaluated from increments obtained from flow-through pod-on models. Optimum configurations can then be investigated further with more refined techniques such as powered simulators or blown nacelles. Use of turbine driven fan jet simulators is a recent development, which extends the power-off simulation of the flow-through pod to include some effects of both primary and fan exhausts. It is practice now-a-days that this technique is applied in the final complete wind tunnel models.

The external drag is usually the most difficult problem of measurement. Fig. 3 poses the usual questions and dilemmas that the experimentalist encounters when planning a complete aeroforce aircraft model for wind tunnel testing with one of its objectives being the representation and measurement of the engine nacelle drag. The questions posed are of course only concerned with the inlets and the shape of the model; there are similar questions associated with the representation of the jet exhaust flow.

The external drag is defined as the sum of the longitudinal forces acting on the force boundaries of the pre-entry streamtube and those parts of the body and wing which are wetted by the external flow (but excluding any base area of the nacelles).

Drag coefficient of the full scale aircraft is then:

$$C_{D_{\text{aircraft}}} = C_{D_{\text{Bal}}} - C_{D_{\text{base}}} - C_{D_{\text{internal}}} - C_{D_{2f_{\text{external}}}} + C_{D_{f_{\text{external}}_{\text{aircraft}}}}$$

where  $C_{D_{Bal}}$  = drag coefficient of complete configuration (including nacelles) measured in the wind tunnel. This term will include corrections associated with the model support system e.g. forces due to model definition to permit rear sting mounting. This is done by testing a model with a correct rear fuselage shape mounted on a twin sting support.

$C_{D_{base}}$  = drag coefficient of any unrepresentative installation base

$C_{D_{2f, external}}$  = skin friction drag coefficient appropriate to all model surfaces wetted by external flow.

$C_{D_{f, external}}$  = external skin friction drag coefficient of the aircraft at full scale Reynolds number

$C_{D_{internal}}$  = standard internal drag coefficient

= - net standard thrust coefficient

$$= \frac{2A}{A_{en}} - \left\{ (P_e - P_{\infty}) + \rho_e V_e^2 \right\} \frac{A_e}{q_{\infty} A_{en}}$$

or

$$= \frac{1}{q_{\infty} A_{en}} \int_{A_e} P_e \left\{ \gamma M_e^2 \frac{V_{\infty}}{V_e} - (1 + \gamma M_e^2) \right\} dA + \frac{P_{\infty} A_e}{q_{\infty} A_{en}}$$

$$= \frac{1}{q_{\infty} A_{en}} \int_{A_e} P_e f_1(M_e) dA + \frac{2}{\gamma M_{\infty}^2} \frac{A_e}{A_{en}}$$

$$\text{where } f_1(M_e) = \gamma M_e^2 \frac{\left(\frac{V}{a}\right)_{\infty}^2}{\left(\frac{V}{a}\right)_e^2} - (1 + \gamma M_e^2)$$

Use of this function is very beneficial at supersonic speeds and choked exit conditions, especially if  $M_{\infty} \approx 2$ , than this function is about zero.

Hence, in general four measurements are necessary to determine external drag of a model with free flow through the engine ducts: (a) overall force measurement, (b) nacelle and body base pressure, (c) static pressure distribution in the internal flow at or close to its exit, and (d) pitot pressure distribution in the internal flow at or close to its exit. Fig. 4a and b illustrate two examples for exit flow surveys of aeroforce models showing both static and total pressure probes. Typical surveys contain some 30 to 120 pitot pressures and some 15 to 50 static pressures. In tests at transonic speeds it is necessary to measure internal flow by means of a few fixed pitot tubes supported from the duct walls at the same time as the base pressure and force measurements are made. These few pitot measurements are then used to assess the absolute level of pitot tube measurements taken when surveying the exit flow in a separate tunnel run.

#### SPECIAL INLET MODELS

Special inlet models are tested on a larger scale than aeroforce models which give first the inlet performance, and second refined corrections for the aircraft characteristics as determined from the aeroforce model for the complete envelope of the engine (e) operating regimes. Fig. 5 gives an example of such a bookkeeping procedure, particularly devoted to the inlet drag terms. In the connotation of this figure the  $\Delta D_{ref}$  value would be applied to the vehicle drag polar as obtained from the aeroforce model. Compatibility is maintained between external aerodynamic and propulsion forces by correcting the installed engine thrust,  $F_N$ , by the change in inlet drag from the basic inlet to the propulsion reference inlet,  $\Delta D_I$  (a similar correction is included for the nozzle afterbody,  $\Delta D_N$ ). The  $\Delta D_I$  correction consists of several incremental components which are mentioned in this figure.

In designing such an inlet model for wind tunnel testing, again several questions must be answered. The major questions are: a) the degree of airframe representation, wings? tail planes? Jet flow?, b) how should the fuselage and compression surface boundary layers be represented (diverter size and bleed), c) the degree of simulation of the bleed and bypass exit conditions, and d) what is the most appropriate model testing scheme.

Regarding the first questions, at transonic speeds the upstream airframe surfaces and to a great extent the downstream surfaces must be simulated at inlet tests in the wind tunnel. Usually a compromise must be made between what is practical and what is desirable. At least checks should be made that neglected surface, exhaust or system simulation does not influence the required results or can be accounted for by some other means. No standard rules are available which can give a priori an indication of the interference effects of downstream surfaces on the flow near the inlet, for measuring the inlet drag terms.

#### TECHNIQUES

The second important decision that must be made for the design of the special inlet drag model is whether the complete inlet model (i.e. inlet plus fuselage or wing) is mounted on a balance or only the inlet. Fig. 6 depicts an arrangement where the inlet alone is mounted on the balance. This leads to measurement of smaller forces, with those associated with the inlet being predominant. In addition the means of measuring the internal mass flow can be located wherever desired and whatever means necessary to ensure accurate measurement can be introduced (e.g. screens, venturi, multi tube rakes etc.) easily.

The disadvantages are: (a) the sealing problems at the junction between the metric and non-metric portions of the duct, (b) the accurate measurement of forces on parts of the fuselage on the balance that could change as inlet flow conditions change, (c) the difficulties of measuring momentum of the internal flow at the duct junction position where the flow may still be quite non-uniform, and (d) the general difficulties of interpreting forces measured on only part of a model. Changes of geometry which lead to changes of pressure on non-metric parts of the model can lead to spurious conclusions as to the efficiency of the geometric changes being studied. Inlet flow is discharged through an extended duct far enough downstream to avoid any influence on the inlet. Fig. 7 shows a solution to the same problem, where larger forces are measured by the balance as in fig. 6. This arrangement better includes the complete effect of inlet, bypass and bleed changes on the inlet + forebody performance as measured by the balance with the disadvantage of yielding less refined data. The metric line is provided along the cylindrical part of the model, where the external flow is almost uniform. The seal is rolled on itself if the metric part is translated, so that the reaction is constant. This sealing technique seems to be very satisfactory. Fig. 8 shows the method where the complete model is mounted on the balance, and only the unit used for traversing the internal flow for measurement of mass flow and momentum are non-metric. The forces being measured now include fairly large components (eg base, nose and canopy drag) which are not required. This had the effect of inhibiting the reproduction of other components on the model, such as wings, to reduce the overall loads and increase the sensitivity of the balance to the force components which are of interest. Thus the effect of, say, bypass door operation on the stability of the configuration has to be sacrificed. The model tends to become rather long if the flow measurement station is to be at a position where the flow is fairly uniform. To avoid difficulties due to shock reflections at low supersonic speeds with a long model, the rear half has to be made with constant cross sections; hence true geometrical representation may be lost. However, the sealing problems as in fig. 6 and 7 at the duct junction have disappeared and changes in geometry of the nacelles can be studied with the knowledge that their total effect is being measured. The base drag is measured by pitot tubes placed approximately 0.5 mm from the base. The base is shrouded to try to produce uniform base pressure under all conditions.

As seen in the complete model tests, the external drag is determined from three drag measurements:

$$D_{\text{external}} = D_{\text{balance}} - D_{\text{base}} - D_{\text{internal}}$$

The balance force,  $D_{\text{balance}}$ , needs to be corrected for the base drag,  $D_{\text{base}}$ , or by the sealing drag (both obtained by pressure plotting), and by the internal drag,  $D_{\text{int}}$ , is the difference between the freestream momentum minus the impulse at the measuring station or exit.

The installation drag of podded high bypass fan engine may be as high as 10% of the net engine thrust. This fact necessitates careful nacelle and pylon design for such configurations in order to minimize unfavourable interference effects. The goal of the inlet designer is to achieve a reduced pressure on the external inlet cowl such that the axial component of the integrated relative surface pressure results in a thrust force equal to the additive drag. For reversible inviscid flow complete additive drag cancellation would occur. To this end isolated inlet tests are performed to obtain optimum cowl design at all speeds encountered. As with integrated engine installations for these inlets it is possible to approach this problem, at least up to a given Mach number, by studying the force operating on the forebody cowl with an integrated balance, and by measuring the internal flow very precisely. Alternatively the forces can be obtained from pressure measurements on the forebody cowl and from boundary layer measurements for the skin friction. The advantage of this last combination is that a detailed description of the flow can be obtained. This description is necessary to optimize the shroud shape. Fig. 9 shows an experimental set up of this approach of an isolated inlet. The external drag consists of a term equal to the pressure integration along the dividing stream tube from upstream infinity to the external station on the shroud until the point where the external inlet drag is defined (hence containing additive drag minus shroud suction force), and of a term representing the external friction forces on the inlet shroud, which can be determined from the boundary layer rake measurements.

This technique has two practical difficulties:

1. The lip suction force is very strongly influenced by any error in determining the location of the stagnation line.
2. An accurate solution for the compressible equations of motion of the flow ahead of the inlet must be calculated before the additive drag can be determined and compared with the measured lip suction force. Both of these difficulties can be avoided if tests are carried out with an axial force measurement on inlet models. An arrangement which is proposed to use in a transonic wind tunnel is shown in figure 10 (3). After making the following definitions,

$$\text{Additive drag } D_{\text{add}} = \int_{A_{\infty}}^{A_1} (p - p_{\infty}) dA$$

$$\text{Suction thrust } T_{1s} = \int_{A_1}^{A_4} (p_{\infty} - p) dA - \int_{S_1}^{S_4} \tau dS$$

$$\text{External drag: } D_{\text{ext}} = D_{\text{add}} - T_{1s}$$

It can be shown that the external lip drag,  $D_{\text{ext}}$ , can be calculated from measured quantities on such a test arrangement as:

$$D_{\text{ext}} = \dot{m}_{\infty} (V_n - V_{\infty}) + A_n (p_n - p_s) + A_4 (p_c - p_{\infty}) + A_s (p_s - p_c) - H$$

This method faces again the sealing problem and cannot be used under installed conditions. If a pressure gradient exists along the external side of the sealing, a flow will result within the sealing gap, which will disturb the downstream boundary layer, hence influencing the upstream flow, particularly at transonic speeds.

#### MASS FLOW MEASUREMENTS

It is obvious that the inlet mass flow is a primary inlet variable and must be controlled and measured with extreme precision. For example a double ramp intake operating at  $M_{\infty} = 2.2$  an effective change of ramp of  $1^\circ$  results in a change of maximum inlet flow  $(\Delta A_{\infty}/A_{en})_{\text{max}}$  of 1% and a change of

additive drag coefficient  $\Delta C_{D_{add}}$  of 0,008. It is therefore generally agreed that if the external drag is

being determined from the difference of a drag balance measurement and the internal drag-as described in the previous section - the inlet mass flow should be measured at least within  $1/2$  %/o. With specially designed mass flow cells, measurement of mass flow to within 1 %/o certainty can be normal routine. If insufficient care is taken errors as large as 5 %/o may result. The least inaccuracy can be expected if the mass flow is computed from rake surveys in the internal duct only and can only be obtained if the distortions at the measuring station are small.

The higher accuracies are obtained if the measuring cell is calibrated against a standard. It is usual that the exit is formed by a sonic or near sonic exhaust with plug. The mass flow can then be written as a function of the discharge coefficient of the exhaust. What is important in quoting the stated accuracies of these coefficients are the numbers on the standard deviations and on the possible error of the mean. The former should be at least less than  $1/2$  %/o. The presence of noise could cause perturbations of the order of  $1/2$  %/o. By careful calibration the error of the mean of the discharge coefficient can be less than  $0,1$  %/o. However in inlet tests, usually the stagnation temperature distribution is not measured. When the model is at a different temperature as the stagnation temperature of the tunnel, and heat transfer takes place in the inlet duct, the stagnation temperature distribution should be measured in front of the flow meter in order to obtain the required accuracy. In addition in the calibration rigs the actual distortion of the stagnation pressure and temperature measured in the inlet should be represented. When possible, the distortion should be minimized in front of the flow meter. For example supercritical internal inlet flow will give distortions and therefore rapid deterioration in the accuracy of inlet flow and internal drag measurement and could lead to wrong conclusions regarding the external drag.

Fig. 11 shows a standard cell for measurement of the mass flow which is also used to measure engine face pressure recovery and flow distortions. This is a completely self contained piece of equipment which can be made in several sizes (2). Some results of calibration tests are also shown.

Fig. 12 shows an example of a rig used to calibrate these mass flow cells. At the present time a standard NGTE choked nozzle (whose discharge coefficient is known to  $\pm 1/4$  %/o) is being used to calibrate a large range of standard flow orifices. With the NGTE nozzle removed, these calibrated orifices are then used to calibrate the mass-flow measurement cells which are operated in a choked exit condition. A later development is the design of a new standard choked nozzle having very low throat curvature and laminar flow. This standard will rely on a calculated discharge coefficient which is (a) very close to unity and (b) will have very small error (4). This nozzle will be followed by an efficient diffuser so that it is hoped that it can be used directly to calibrate the cells, both of them operating choked.

The author wonders why air mass flow cell calibrations are not performed with rather direct means without the necessity for introducing corrections for discharge coefficients. Fig. 13 depicts such set-ups where the mass flow is deduced from the time filling a well-known volume (starting point the switch over of a three-way valve, and stopping point the rise or drop of pressure in the reference volume) or from the rate of rise or descent of a gascontainer. The volumes should typically be between 100 and 1000  $m^3$  for test cells for wind tunnel applications, and do not require large investments. The only uncertainties arise from time measurements, dimensions, and static pressure and temperature measurements; all quantities can be measured to a high degree of accuracy.

#### BLEED, BYPASS, DIVERTERS

The accurate determination of bleed/bypass and also of spillage drag effects in the transonic range of Mach numbers is an important requirement. It is at these speeds where bypass and spillage mass flows are the greatest and where effects on performance can be large.

Simulation of inlet bleed (including bypass) and spillage effects is accomplished with the inlet drag model. The bleed/bypass geometry is simulated on this model as accurately as possible. Adjacent surfaces such as wings, fuselage, etc., which could interact with the flow from the bleed/bypass exhaust systems must also be duplicated to scale on the inlet model. It is the practice during wind tunnel tests to duplicate a range of bleed/bypass mass flow ratios in combination with a range of operating inlet mass flow ratios. In this manner the proper drag increments can be assessed for a wide variety of matched inlet-engine operating conditions. It is not recommended that any external bleed should be incompletely represented.

The major correction from wind tunnel inlet model to full scale aircraft involves the boundary layer on the fuselage forebody. The problem on integrated airframe-engine configurations is the adequate scaling of the boundary layer thickness to the geometric scale of the model for the full range of flight conditions ( $M_\infty$ ) and attitudes ( $\alpha$  and  $\beta$ ). Corrections for the effect of boundary layer thickness on the inlet flow field are difficult to accomplish with accuracy. Improperly assessed forebody flow field effects have been the major reason for past propulsion deficiencies experienced during full scale flight. This is particularly true for boundary layer scoops or diverters since at the reduced Reynolds number of the wind tunnel model the ratio of the diverter height ( $h$ ) and the boundary layer thickness ( $\delta$ ) is smaller than at full scale if the former is scaled geometrically. In inlet design, a compromise is usually required between drag and the diverter performance. Such a compromise tends to select a solution where the outer part of the boundary layer enters the inlet, and it is this compromise that cannot usually adequately be obtained from wind tunnel tests. In general the parameter  $h/\delta$  is used which describes the proportion of boundary layer ingested by the intake. Though convenient, it is obvious that a parameter which is a ratio of the loss of momentum in the boundary layer air ingested to the momentum of the remaining "free stream" air entering the intake would be more appropriate. However, it is obvious that further thought and systematic experimentation is required to elucidate better simulation criteria for model and full scale representation than just identical  $h/\delta$  values. Whatever parameters do emerge (and in practice they may still amount to something similar to using identical values of  $h/\delta$ ) there remains the problem of how to achieve them physically. As illustrated in fig. 14 to obtain identical values of  $h/\delta$ , model and full scale, there are the following possibilities of geometrical changes to the model:

- (a) Move intakes bodily out from the sides of the fuselage.
- (b) Move wall of inlet adjacent to the fuselage side outwards keeping the rest of the intake identical.
- (c) Reduce body size adjacent to the inlets so that fineness ratio of the forward fuselage is increased.
- (d) Bleed some of the boundary layer from the fuselage forward of the position of the intakes.

The last of these alternatives would appear to be the best but has difficulties associated with force measurements, establishment of the correct profiles turbulent boundary layer before the inlet position is reached, etc.

Usually the pressure drag of the diverter  $\Delta C_{D, \text{div}}$  is determined based on the diverter frontal area, and this coefficient is then applied to the correct size diverters on the full scale aircraft.

Fig. 15 shows a typical inlet test arrangement with bleed and bypass to the external flow. The goal of this set-up is to measure the pressure recovery, and flow distortions at the engine face. For models determining the internal flow the scales should be as large as possible, preferably of the order of 1/6th for a average fighter aircraft.

In duplicating bleed systems in a model for internal flow quality measurements the goal is to maintain a viscous layer through the inlet which reacts to inlet pressure gradients similarly to full scale flight operation. It is advisable then to perform some theoretical analysis on the flight vehicle bleed system to determine plenum back pressures and then perform wind tunnel tests over a small range of back pressures near that value in order to be absolutely certain of acquiring representative data. In cases where wind tunnel test conditions do not match flight Re (Reynolds number based on boundary layer height), it may be necessary to make adjustments in the size of bleed holes (or slots) in order to remove the proper amount of flow.

#### EXTERNAL FLOW SIMULATION FOR INLET FLOW TESTS

Besides the problem of diverter and bleed representation in wind tunnels the simulation of the flow field in which an inlet is immersed can be also, an important and difficult task in transonic wind tunnel tests. If the inlet system is to operate only at high subsonic Mach numbers and/or is located reasonably well ahead of the regions where the flow fields are significantly affected by the proximity of the flight vehicle, isolated inlet tests are acceptable. An ultimate check-out is always necessary with the correct model flow field. When inlets are closely integrated with the flight vehicle and especially when these inlets are designed for moderate to high supersonic Mach number flight, the inlet flow field is mostly defined by the vehicle forebody shape and attitude, but can be affected tangibly by diverter shapes, near by stabilizer surfaces, nose booms, and external stores. If a large part of the airframe must be simulated in the wind tunnel for proper flow field duplication, losses must be accepted for the reduced scale, and hence reduced Reynolds number.

In simulating the external flow field at transonic Mach numbers, it is particularly important to reproduce viscous conditions, vortices and local flow angularities, local values of Mach number and total pressure also come into play as part of this simulation. The inlet may be rather sensitive to local flow angularities with flow separation (internal or external) resulting from high flow incidence angles with inlet boundary layer diverters, side plates, or cowls. Vortex formation from some of the possible upstream sources mentioned above may be shed into the region where an inlet is to be located and, consequently, should be defined during development wind tunnel tests. Also, in transonic inlet tests it is advisable to consider duplicating some disturbances downstream of the inlet, e.g., downstream portions of the wing when the inlet is shielded by the wing. In this context, the question arises also, does the actual engine exhaust influence the inlet flow field. Usually this question remains unanswered, but might be worthy of consideration in many instances.

Fig. 16 shows an example of the type of instrumentation which might be provided for such installations including boundary layer profile measurements, wing and fuselage static pressure surveys, and inviscid flow field measurements. The flow field measurements should be made with some type of cone probe arrangement with which local flow angularity, Mach number and total pressure can be determined.

Another testing technique to be explored is the use of small scale forebody tests to determine inlet flow fields. If a low blockage aerodynamic device can then be constructed which reproduces the flow field generated by the actual forebody, it would be possible to test the larger scale inlet in the correct flow field generated by this device. The questions to be answered in future investigations of this concept are whether the flow fields can be duplicated, whether varying aircraft angles-of-attack can be reproduced, and whether inlet installation in the simulated flow field has the same effect as its installation in the vicinity of the actual vehicle forebody.

#### INLET DISTORTIONS

For the inlet flow entering the engine four properties are of primary importance namely, the mass flow, the pressure recovery, the stationary distortions and the unsteady or dynamic distortions. Mass flow measurements have been discussed, whereas pressure recovery measurements usually do not generate many difficulties provided the pitot and static pressure data at the compressor face are sufficiently detailed. Also the static distortion determination should not present any problem (except for Reynolds number scaling) provided the data are consistent with the distortion requirements of the engine as defined by the engine manufacturer.

The recent advance of the turbofan engine cycle for application in high performance supersonic vehicles has required more detailed study for engine-interfaces dynamic-interactions. The engine might randomly surge after perhaps sometimes spent at a steady state condition which initially appeared to be acceptable to the engine. Indications at present are that the engine is insensitive to inflow dynamics in the lower transonic operation regime. However, during supersonic operation, starting at  $M_{\infty} \approx 1.1$ , the engine is susceptible to the dynamic distortions. Fig. 17 gives an example of the reduction in stall margin of a turbofan engine (where 10% loss in surge line  $\approx$  100% reduction in stall margin) versus the low frequency turbulence level, generated by various means. The lower diagram shows the percent loss in total flow for the same condition. In the first case a correlation can be found; in the latter correlation is completely lost. It is clear from these figures that more work is needed to establish better correlations which describe the influence of the dynamic distortion properties on the engine characteristics. Recent experience suggests that the initiation of surge can probably be linked to the steady state distortion index provided this information can be sampled quickly enough i.e. if the steady state distortion factor is exceeded while the compressor is rotating for one revolution then surge can be initiated (5). If this is true then the measuring problem in the wind tunnel reduces to dynamic measurement of pressures through the use of miniature high response pressure transducers.

However after the measurement in the wind tunnel the problem arises how to translate the wind tunnel data to full scale with the actual engine. The causes of the distortions can be numerous and probably mutual interference exists. Important factors in this phenomenon are turbulence caused by

by separations, turbulence level and frequency, acoustic characteristics of the main flow, compressor dynamics and acoustic characteristics. This means that Reynolds number, scale and engine characteristics are primary parameters. The dependence of scaling laws on these parameters is unknown (6).

#### CONCLUDING REMARKS

From the answers as obtained in the questionnaire and from the discussions between specialists held afterwards, it can be concluded that more effort on inlet performance predictions at transonic speeds is required, especially on the following subjects:

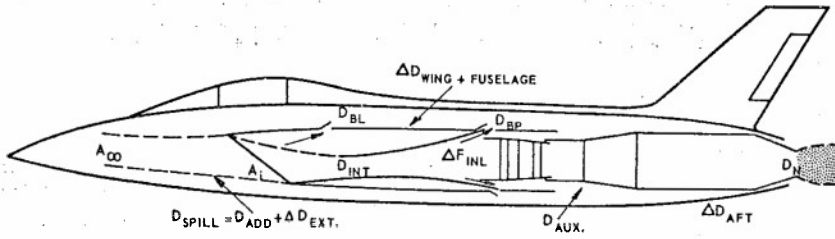
- 1e. Better criteria are needed under which conditions and to which extend the downstream geometry and systems (e.g. exhaust flow) should be represented in wind tunnel tests for external drag components (bleed, spillage, bypass, diverter) assessment;
- 2e. It should be very useful to define one or more standard inlet configurations for testing in the various test rigs for inlet drag component assessment in order to establish standards for the accuracy of data gathering and reduction for particular testing schemes and techniques.
- 3e. More knowledge should become available on the relationships between upstream distortions (pressure, temperature, unsteady, swirl) on the measuring accuracy of various techniques and test cells for inlet mass flow measurements; also a standard (or technique) should be formulated for mass flow test cell calibrations.
- 4e. Better techniques and criteria should come available how to represent the viscous and inviscid upstream flow field for performance testing of inlet systems (diverters, bleeds, bypass). What are the relevant parameters which should be kept constant.
- 5e. Criteria should come available how to represent the external flow in which the inlet is operating for measuring the internal performances of an inlet.
- 6e. More information is needed on the scaling laws for stationary and unsteady flow distortions at the compressor entrance plane, in combination with the engine dynamics and noise characteristics.

#### ACKNOWLEDGEMENTS

Some parts of this summary report has been directly reproduced from the survey report and hence from the contributions as supplied by various groups responding to the questionnaire. The author expresses his gratitude to those groups.

#### REFERENCES

1. A. Ferri  
F. Jaarsma and  
R. Monti                      Engine airplane Interference and Wall Corrections in Transonic Wind Tunnel Tests, AGARD Advisory Report AR-36, to be published.
2. E.L. Goldsmith              Variable Geometry Intakes at Supersonic Speeds - Some Techniques and some Test Results. AGARD CP. 34, Sept. 1968.
3. J.S. Holdhusen              Analysis and Demonstration Techniques for Installation Aerodynamics Effects on High Bypass Turbofans. AGARD CP.34, Sept. 1968.
4. J.E. Gresn                    A Design of Sonic Nozzle for the Precise Measurement of Mass Flow. Zeitschrift für Flugwissenschaften, 19(1971). Hsft 3, or RAE TR 70201.
5. F.W. Burcham and  
D.L. Hughes                    Analysis of In-Flight Pressure Fluctuations, Leading to Engine Compressor Surge in an F-111A Airplane for Mach numbers to 2.17. AIAA Paper 70-624.
6. G.S. Flourds and  
B. Brimelow                    Pressure Fluctuations Cause Compressor Instability, 69-9055, Air Force Aero Propulsion Laboratory, Airframe/Propulsion Compatibility Symposium, June 1969.



- $F_U$  = UNINSTALLED GROSS THRUST AS SPECIFIED BY ENGINE COMPANY WITH REFERENCE NOZZLE
- $F_i$  = INSTALLED GROSS THRUST =  $F_U + \Delta F_N - D_N + \Delta F_{INL}$ .
- $\Delta F_N$  = DIFFERENCE IN GROSS THRUST OF ACTUAL NOZZLE DIFFERENT FROM REFERENCE NOZZLE EXHAUSTING INTO QUIESCENT ATMOSPHERE.
- $D_N$  = DIFFERENCE IN GROSS THRUST OF ACTUAL NOZZLE EXHAUSTING INTO QUIESCENT ATMOSPHERE AND WITH EXTERNAL FLOW
- $\Delta F_{INL}$  = DIFFERENCE IN GROSS THRUST DUE TO INLET FLOW DISTORTIONS AND NOT COMPLETE PRESSURE RECOVERY
- $D_{SPILL}$  = SPILLAGE DRAG DUE TO  $A_\infty < A_i$  VS  $A_\infty = A_i$   
=  $D_{ADD} + \Delta D_{EXT}$
- $D_{ADD}$  = ADDITIVE OR PRE ENTRY DRAG (PRESSURE FORCES ACTING ON STREAMTUBE)
- $\Delta D_{EXT}$  = CHANGE IN INLET EXTERNAL DRAG, PRESSURE DRAG, WAVE DRAG, FRICTION DRAG (IDEALLY  $D_{ADD} - \Delta D_{EXT}$ )
- $D_{INT}$  = INTERNAL INLET DRAG
- $D_{BL}$  = CHANGE IN AIRPLANE DRAG WITH BOUNDARY LAYER BLEED VS NO BLEED
- $D_{BP}$  = CHANGE IN AIRPLANE DRAG WITH BY-PASS INSTALLED VS NO BY-PASS
- $\Delta D_{W+A}$  = CHANGE IN AIRPLANE DRAG (EXCEPT INLET) DUE TO  $A_\infty < A_i$  VS  $A_\infty = A_i$  OR  $A_\infty = A_{REF}$
- $D_{AUX}$  = CHANGE IN AIRPLANE DRAG DUE TO AUXILIARY AIRSYSTEM INSTALLED VS NO AUX. SYSTEM INSTALLED
- $\Delta D_{AFT}$  = CHANGE IN AIRPLANE DRAG DUE TO ACTUAL NOZZLE FLOW AND REFERENCE NOZZLE FLOW OR REFERENCE NOZZLE GEOMETRY
- $F_N$  = NET THRUST =  $F_i - \dot{M} V_\infty$  ( $\dot{M}$  = ENGINE MASS FLOW)

Fig.1 Schematic representation of various thrust and drag terms

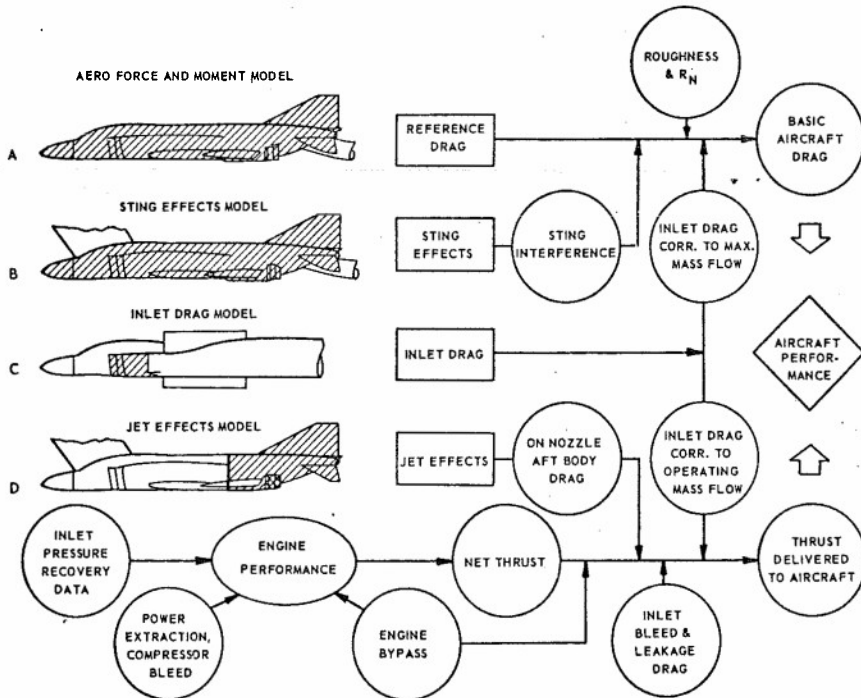


Fig.2 Thrust and drag accounting system

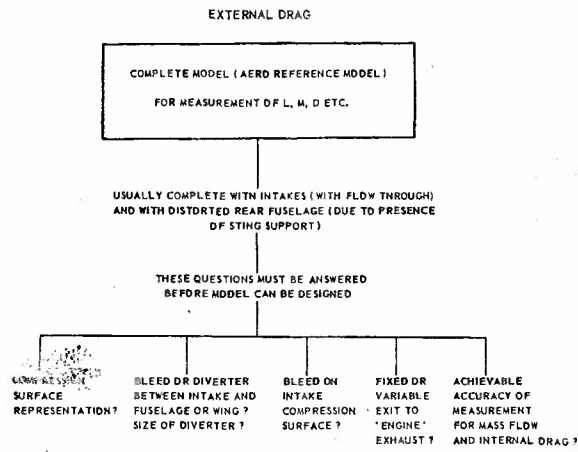


Fig.3 Problems of representation of air inlets on complete aircraft models

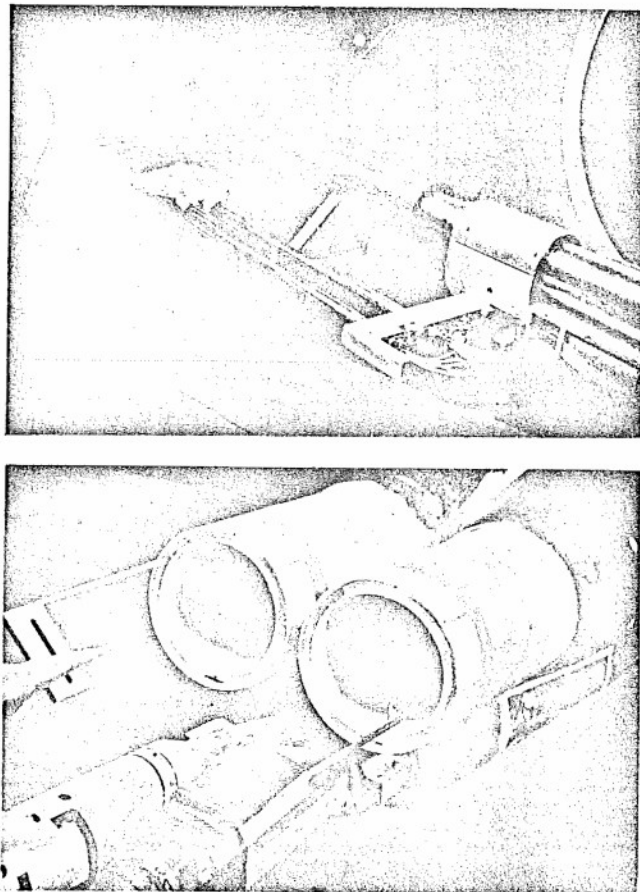
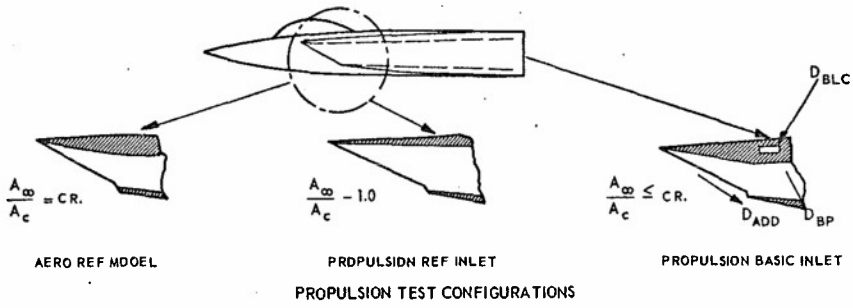


Fig.4 Examples of supersonic transport model installation in wind tunnels for exit flow survey



AERO FORCE MODEL

DRAG  $A/V = O_{AERO} MODEL - \Delta D_{REF}$   
 $\Delta O_{REF} = O_{AERO} REF - O_{PROP} REF$   
 $\Delta O_{REF}$  OBTAINED FROM PRDPULSION MODEL  
 $\Delta D_{REF}$  OBTAINED FOR RANGE OF  $\alpha$

PRDPULSION MODEL

$F_N = F_G - \Delta D_I$   
 $\Delta O_I = O_{PRDP} BASIC - D_{PROP} REF$   
 $= \Delta D_{I_{CR}} + \Delta O_{I_{ADD}} + \Delta O_{I_{BLC}} + \Delta O_{I_{BP}}$   
 $\Delta D_I$  OBTAINED FOR RANGE OF  $\alpha$

Fig.5 Inlet drag bookkeeping

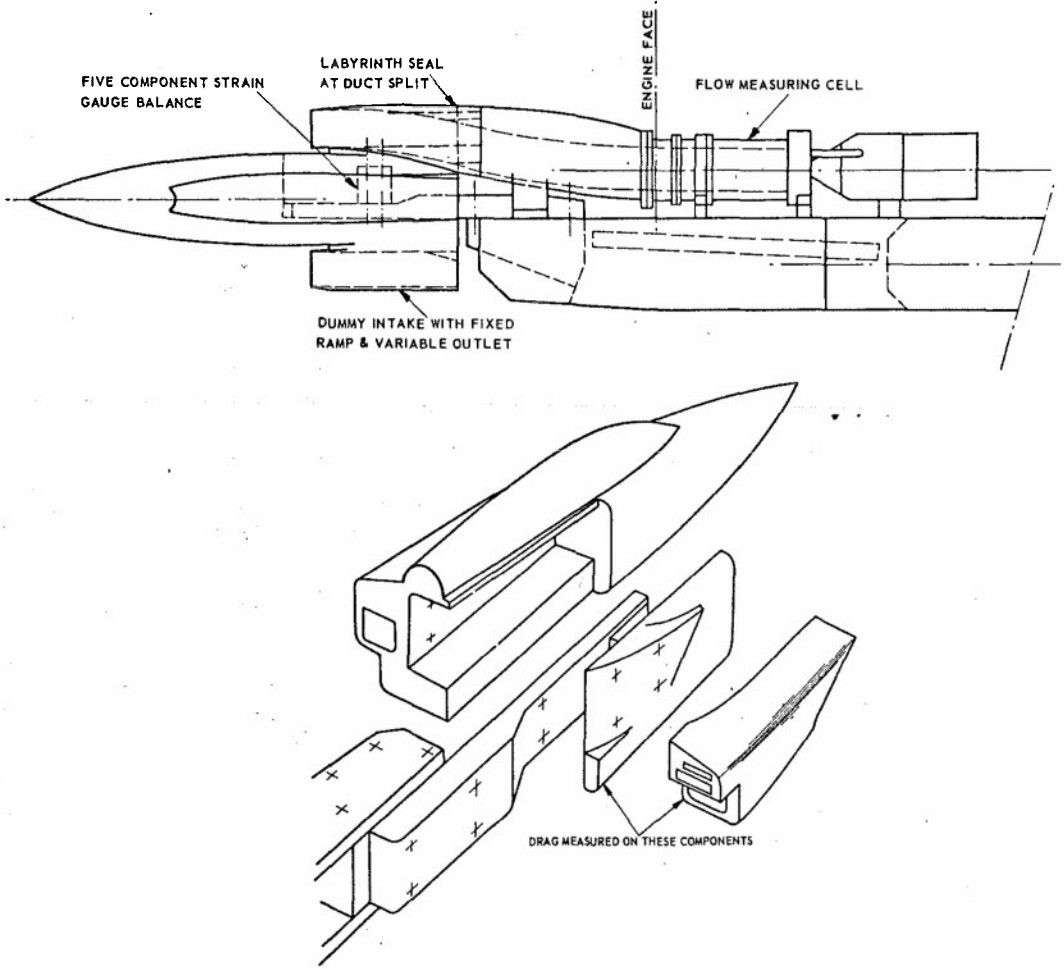


Fig.6 Inlet model with metro inlet only

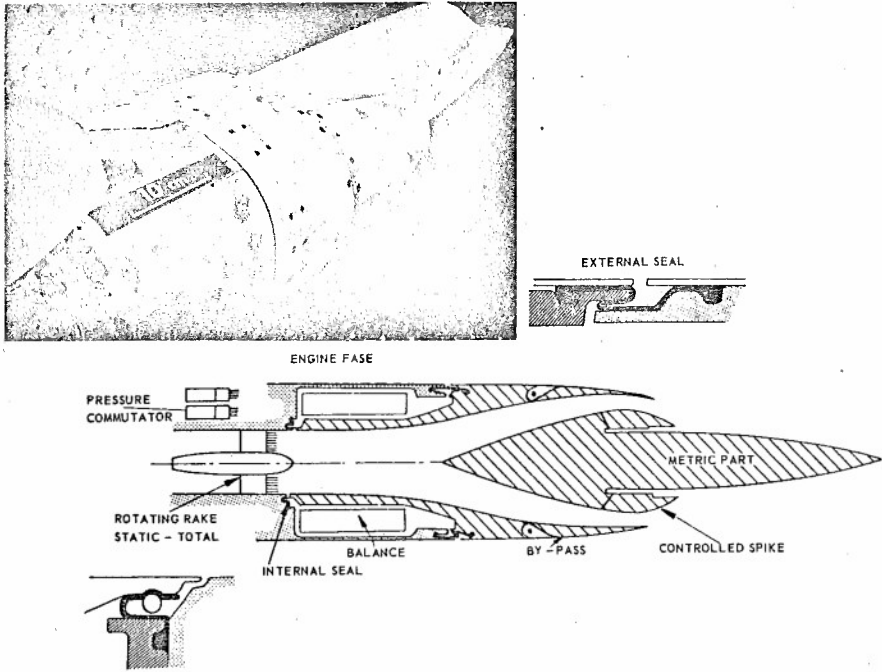


Fig.7 Inlet performance model with metric forebody and inlets

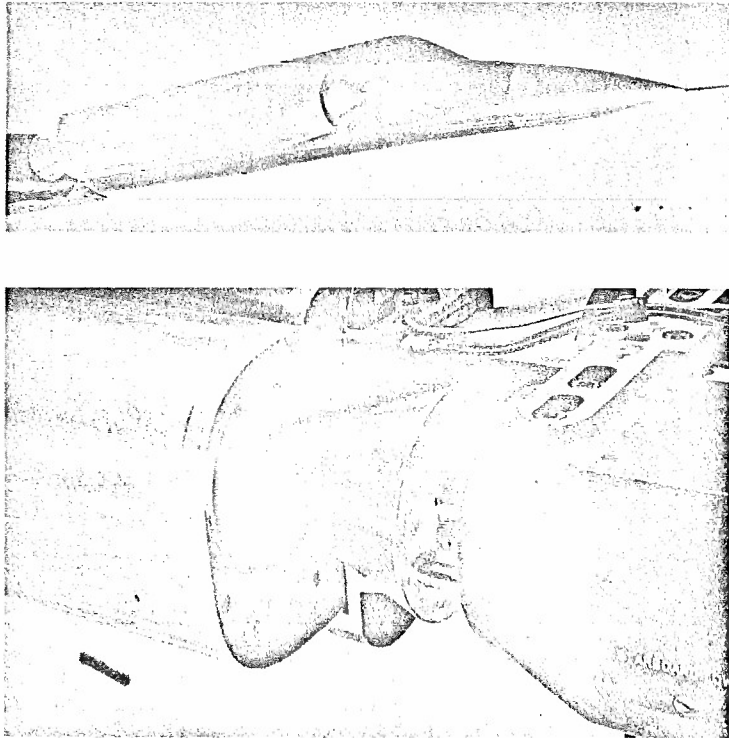


Fig.8 Partial model of strike-fighter for measurement of cowl, spillage and diverter drag

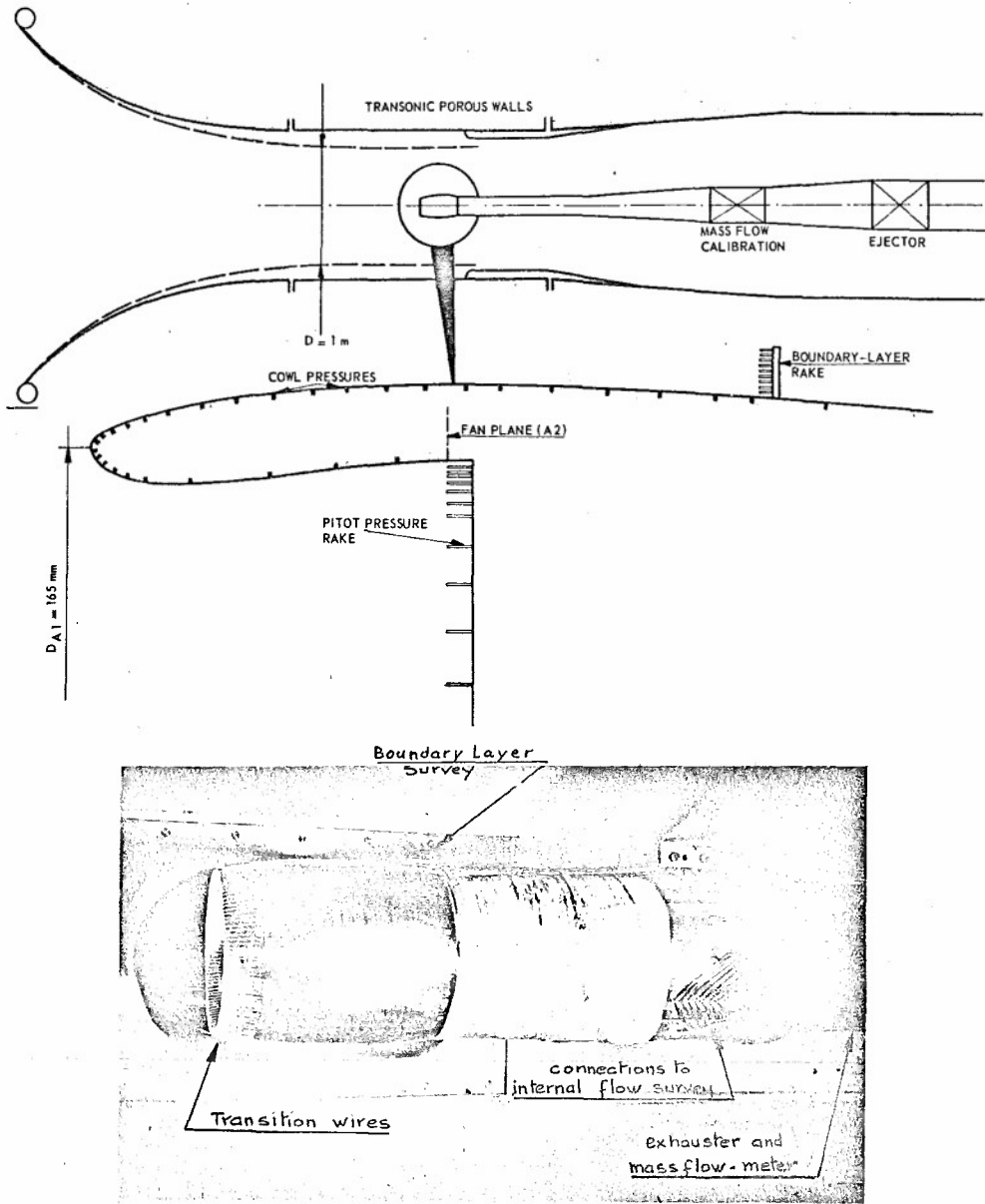


Fig.9 Isolated fan inlet tests with pressure survey

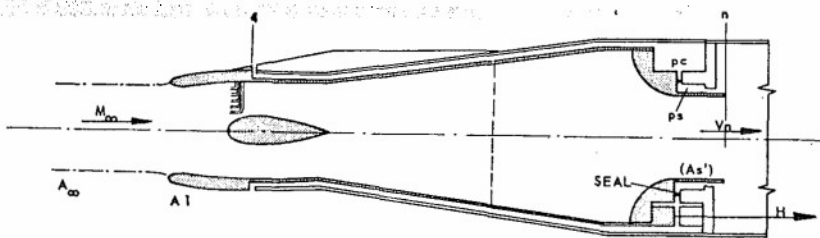


Fig.10 Isolated fan inlet tests with metric cowl

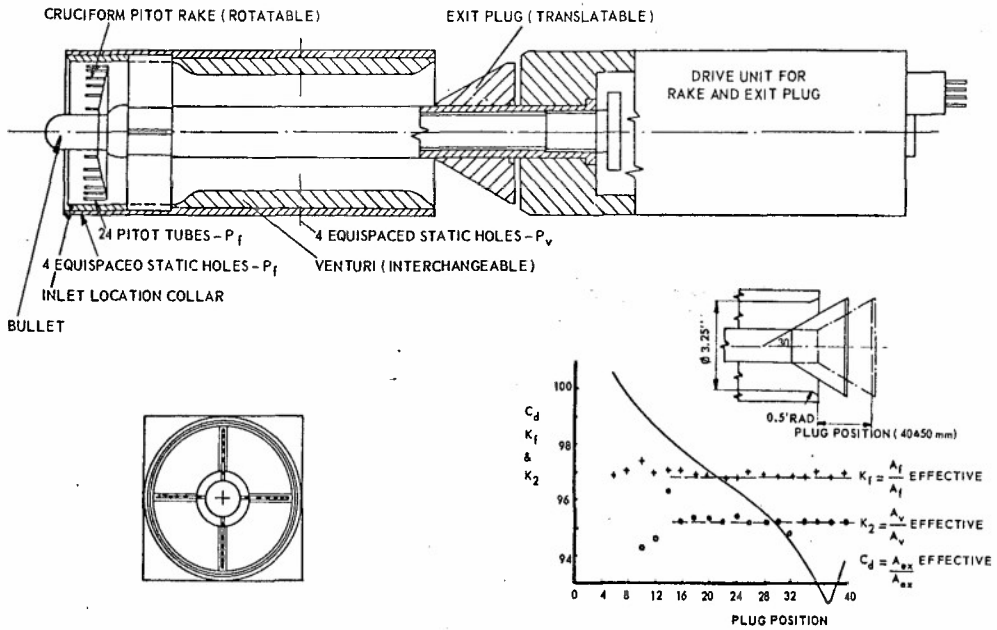


Fig. 11 Cell for measurement of engine face recovery, flow distortions and mass flow, including calibration data

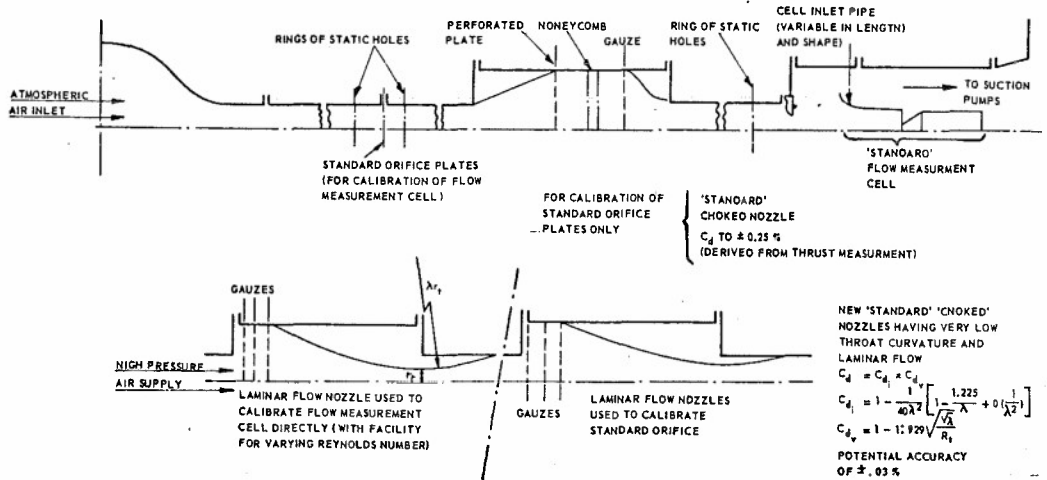


Fig. 12 Mass flow calibration tunnel

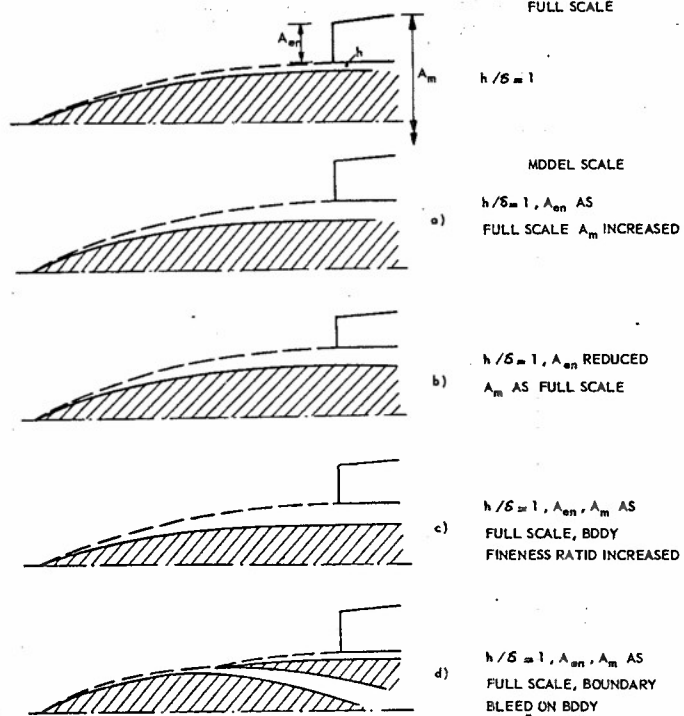


Fig.14 Possible geometry changes to inlet model retaining  $h/b$

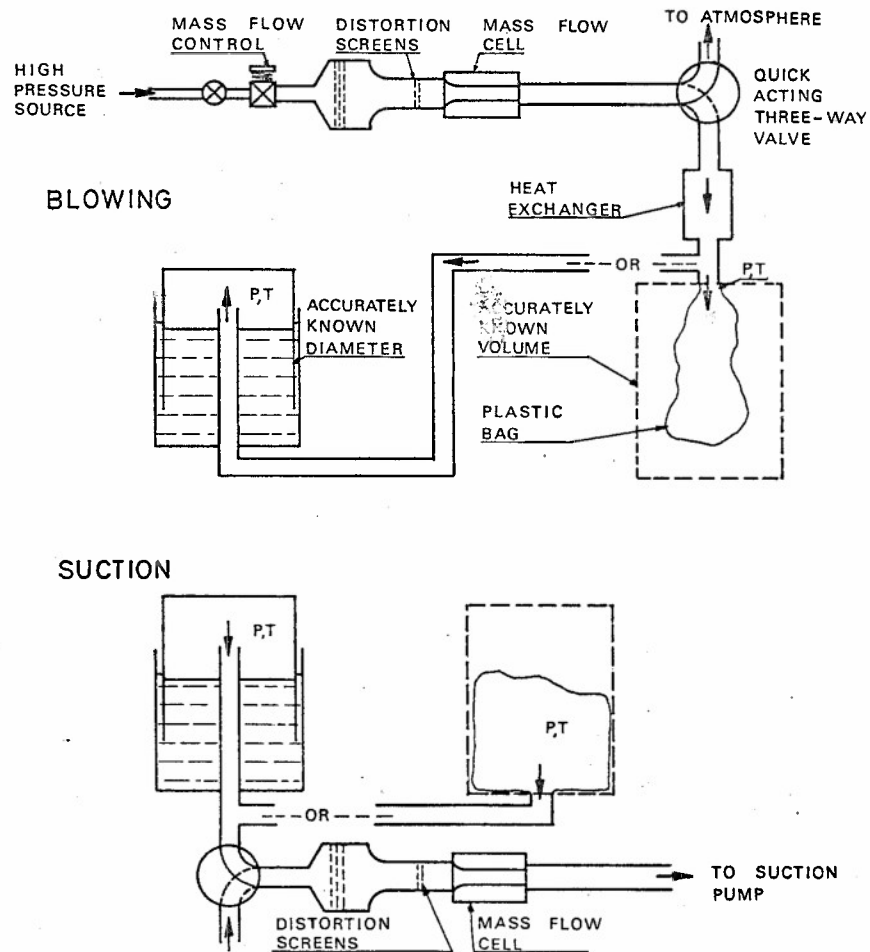


Fig.13 Possible mass flow cell calibration arrangements

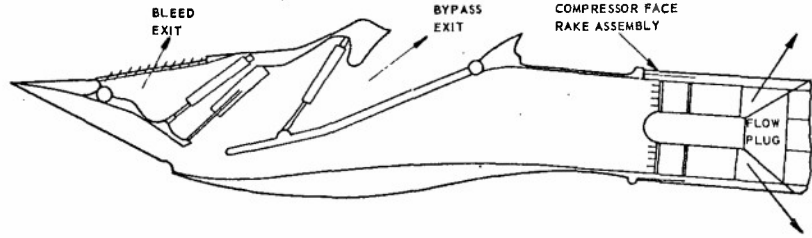


Fig.15 Typical inlet performance test arrangement with bleed and by pase to external flow

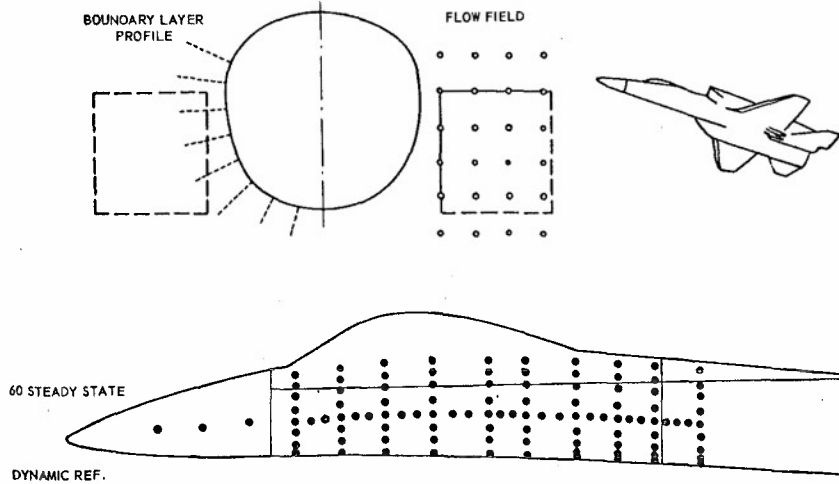


Fig.16 Example of external flow field survey

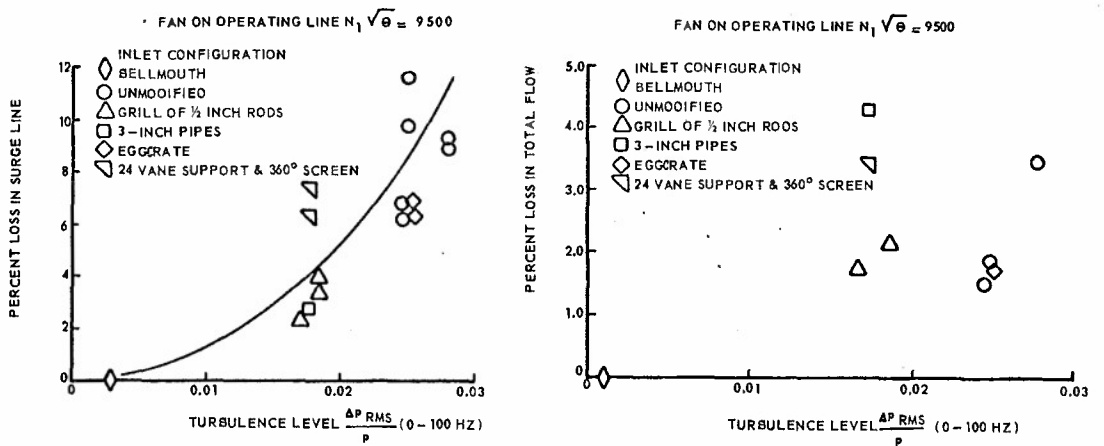


Fig.17 Surges line reduction and loss in flow VS turbulence level

## NOZZLE AND EXHAUST TESTING IN TRANSONIC FLIGHT REGIME

by

Dr. Allen E. Fuhs  
 Professor of Aeronautics  
 Naval Postgraduate School  
 Monterey, California, 93940  
 United States of America

## SUMMARY

This paper is a broad survey based on the AGARD ad hoc study on Engine Airframe Interference. In the early stages of development, wind tunnel tests of nozzles and exhausts are conducted both isolated and in models of the afterbody. Later, thrust measurements are made in test facilities at sea level and altitude conditions followed by flight tests. Drag of nozzle, boattail, etc., is determined as well as thrust. Simulation of exhausts by hot and cold gases, ejectors, and powered simulators is an important facet of testing. Unsteady aerodynamics of internal and external flow and aeroelastic phenomena need to be examined. These topics are discussed for both podded and buried engines. Major conclusions of the study related to exhausts and nozzles are given.

## LIST OF SYMBOLS

When one symbol is adjacent to a second symbol in parentheses, the first symbol is the one commonly used in the United States of America. The symbol in parentheses is the one used in Europe.

$A_e$	nozzle exit area, $ft^2$	$F_g, (X_g)$	gross thrust, $lb_f$ , (newton)
$A_j$	jet cross-sectional area, $ft^2$	$F_i, (X_{id})$	isentropic gross thrust; ideal gross thrust, $lb_f$ , (newton)
$A_p$	area at plane of probe traverse, $ft^2$	$F_m$	measured force during engine test, $lb_f$
$A_w$	wall area of a nozzle, $in^2$	$F_{net}$	net thrust, $lb_f$
$A_x$	jet cross-sectional area at station $x$ , $ft^2$	$h_e$	specific static enthalpy at nozzle exit, $BTU/lb_m$
$A_{in}, A_o$	inlet capture area, $ft^2$	$h_T$	specific stagnation enthalpy, $BTU/lb_m$
$A^*$	area at sonic conditions, $ft^2$	HP	horsepower
B	bypass ratio	m	mass flow ratio for an inlet which is the ratio of actual mass flow rate to mass flow rate with no spillage
$C_d, (C_D)$	discharge coefficient	$\dot{m}_a$	mass flow rate of air, $lb_m/sec$
$C_{Dadd}$	additive drag coefficient	$\dot{m}_c$	mass flow rate through the core of a turbofan, $lb_m/sec$
$C_{Dcowl}$	cowl drag coefficient	$\dot{m}_e$	mass flow rate in turbine exhaust of a simulator, $lb_m/sec$
$C_{Dspill}$	spillage drag coefficient	$\dot{m}_f$	mass flow rate of fuel; mass flow passing through the fan of a turbofan, $lb_m/sec$
$C_{F-D}$	thrust minus drag coefficient which is ratio of (F-D) to ideal thrust	$\dot{m}_j$	mass flow rate of simulator exhaust jet, $lb_m/sec$
$C_{FG}, (C_T)$	gross thrust coefficient	$\dot{m}_o, \dot{m}_\infty$	inlet mass flow rate, $lb_m/sec$
$C_p$	pressure coefficient; specific heat capacity at constant pressure, $BTU/lb_m^{OR}$	$\dot{m}_t$	mass flow rate through turbine, $lb_m/sec$
$C_{pbase}$	base pressure coefficient	$\dot{m}_o V_o, (X_r)$	ram drag, $lb_f$ , (newtons)
D	aircraft drag, $lb_f$ ; nozzle diameter, ft	M	Mach number
$D_a$	afterbody drag, $lb_f$	$M_a$	Mach number at engine-bellmouth flange
$D_b$	base drag, $lb_f$	$M_e$	exhaust Mach number
$D_E$	exhaust drag, $lb_f$	$M_{EXIT}$	Mach number at exit plane of a converging nozzle
$D_i$	nozzle internal drag, $lb_f$	$M_\infty$	freestream or flight Mach number
$D_I$	inlet drag, $lb_f$		
$D_n$	external nozzle drag, $lb_f$		
$D_{et}$	sting drag, $lb_f$		
F, (X)	net thrust, $lb_f$ , (newton)		

$N, (n)$	shaft angular speed, revolutions per minute, RPM	$V_i$	velocity due to ideal expansion, ft/sec
$NFR, (P)$	nozzle pressure ratio which is nozzle stagnation pressure divided by $p_e$	$V_\infty, U$	freestream velocity; flight velocity, ft/sec
$p$	static pressure, $lb_f/in^2$ , (newton/m <sup>2</sup> )	$X$	dimensionless axial distance measured from throat
$p_e$	static pressure at nozzle exit, $lb_f/in^2$	$y$	radial distance at exit plane of a converging nozzle, ft
$P_T, (P)$	stagnation pressure, $lb_f/in^2$ , (newton/m <sup>2</sup> )	$\alpha$	wave number for a wavy wall, 1/ft
$P_{Tj}$	jet stagnation pressure, $lb_f/ft^2$	$\beta$	fraction of turbine drive mass flow mixed with the jet mass flow
$P_w$	static pressure at wall, $lb_f/in^2$	$\gamma$	ratio of heat capacities
$P_\infty$	freestream static pressure, $lb_f/in^2$	$\gamma_j$	heat capacity ratio for gases in exhaust jet
$R$	gas constant for air, 1715 ft <sup>2</sup> /sec <sup>2</sup> °R	$\delta_j$	boundary layer thickness for internal nozzle flow, in
$Re$	Reynolds number	$\delta_\infty$	boundary layer thickness for external flow, in
$( )_R$	subscript to denote reference values for which drag and thrust increments are zero	$\epsilon$	amplitude of a wavy wall, ft
$( )_R$	subscript to denote reference values attained with the aeroforce model	$\theta$	ratio of actual temperature to standard temperature for corrected variables in turbomachinery; angle between exhaust velocity vector and axial component of velocity; when swirl is present angle between axial and radial components
$T$	static temperature, °R, (°K)	$\Lambda$	swirl angle measured from axial component to circumferential component
$T_a$	static air temperature at engine-bellmouth flange, °R	$\rho$	gas static density, $lb_m/ft^3$
$T_e$	static temperature at nozzle exit, °R	$T_c$	compressor stagnation temperature ratio
$T_T, (T_t)$	stagnation temperature, °R, (°K)	$T_r$	ram temperature ratio
$T_{Tj}$	jet stagnation temperature, °R	$T_t$	turbine stagnation temperature ratio equal to downstream divided by upstream stagnation temperature
$v_r, v_\theta, v_z$	radial, circumferential, and axial components of velocity, ft/sec		
$V_a$	velocity of air at engine-bellmouth flange, ft/sec		
$V_e$	axial component of exhaust velocity, ft/sec		

## INTRODUCTION

A vehicle has a mission to accomplish. The mission is basically defined in terms of range, payload, cruise Mach number, cruise altitude, and similar items. Vehicle studies indicate the best design approach to satisfy mission requirements. In regard to propulsion, results from the studies include installed thrust, specific fuel consumption, propulsion flexibility (ability to operate under widely varying conditions), and other facets.

The mission defines an operating map in terms of Mach number and altitude. Furthermore, key features from energy maneuverability may be included in the map. Additional operational aspects, such as remote site operation, multiple fuel operation, maintenance, etc., are part of mission and operational requirements. The vehicle design defines ranges of angle of attack, angle of yaw, engine acceleration and deceleration times, local Mach number at inlet, local exhaust pressure, and similar details. Engine specifications become more narrowly and precisely defined. For the propulsion engineer, these operational requirements translate into hot and cold day limits, distortion limits, blow-out limits, windmill-start limits, stability margins, requirements for peripheral equipment, age and foreign object damage (FOD) deterioration, engine life, continuity of thrust, etc.

To meet the engine specifications, the propulsion engineer has several choices: Use existing engines, modify an existing engine, or develop a new engine. If existing engines are screened for suitability, it is necessary to translate test cell data to installed values. The best match is sought between engine performance and engine specifications. An ability to predict installed performance based on uninstalled engine data is essential. The same is true when a new engine is being developed to match a mission.

Some of the difficulties of obtaining installed thrust from test cell results are illustrated in Figure 1. Inlet flow differs. Nozzle design and nozzle environment differ. There are secondary flows, and there may be tertiary flows.

Considering transonic flow, a qualitative graph which depicts the situation in regard to thrust and drag is given in Figure 2. The width of the band gives the uncertainty due to measurement inaccuracies.

#### MEASUREMENT OF ENGINE THRUST

The force which the propulsion system develops is the net thrust,  $F$ ; this is the force which overcomes aircraft external drag. Net thrust is related to gross thrust,  $F_g$ , by

$$F = F_g - \dot{m}_a V_\infty \quad (1)$$

where  $\dot{m}_a V_\infty$  is the ram drag. Obviously, to obtain net thrust, the mass flow rate of air,  $\dot{m}_a$ , must be measured accurately. Techniques include calibrated venturi and calibrated bellmouth for test cells and corrected engine speed,  $N/\sqrt{\theta}$ , for flight test. Additive drag, which does not appear in Eq (1), must be accounted for.

Gross thrust can be related to properties at nozzle exit plane

$$F_g = \int_{A_e} \rho_e V_e^2 dA + \int_{A_e} (p_e - p) dA \quad (2)$$

where  $V_e$  is the axial component of exit velocity. A gross thrust coefficient is used and is defined by

$$C_{FG} = F_g / F_i \quad (3)$$

where  $F_i$  is an ideal thrust. The gross thrust coefficient has several valuable characteristics. Size of the engine or nozzle is eliminated. Since the ideal thrust can be readily related to cycle analysis,  $C_{FG}$  provides a tie between cycle analysis and actual engine data. A scheme for predicting  $F_g$  when nozzle geometry changes can be based on  $C_{FG}$ .

The ideal thrust can be calculated from

$$F_i = (\dot{m}_a + \dot{m}_f) V_i \quad (4)$$

where  $\dot{m}_f$  is fuel mass flow rate and  $V_i$  is the ideal velocity at nozzle exit.  $V_i$  can be calculated from

$$V_i = \sqrt{2(h_T - h_e)} \quad (5)$$

where  $h_T$  is stagnation enthalpy and  $h_e$ , the static enthalpy at  $T_e$  and  $p_e = p$ . Equation (5) accounts for variable heat capacity during expansion. Equation (5) is a one-dimensional equation. Since  $h_T = h_T(p_T, T_T)$ , the values of  $p_T$  and  $T_T$  must represent the nozzle entrance values in some average sense. Herein lies a problem, i.e., how to define an average for  $p$ ,  $p_T$ ,  $T$ , and  $T_T$ . When there is a profile at the nozzle entrance, it is not possible to assign an average which satisfies all of the equations of motion.

There are several ways to measure  $F_g$ ; two of the techniques (load cell and exhaust survey) will be discussed here. Consider the test arrangement shown in Figure 3 which is an altitude test facility. Figure 4 is a sea level static test arrangement which is included here for comparison. The gross thrust is given by

$$F_g = F_m + \dot{m}_a V_a + (\text{corrections}) \quad (6)$$

where  $F_m$  is the force measured by the load cell, and  $\dot{m}_a V_a$  is the ram drag. A calibrated bellmouth can give  $\dot{m}_a$  with an accuracy of 1 per cent. The velocity is determined from

$$V_a = \sqrt{\frac{RT_a}{\gamma} M_a} \quad (7)$$

$$M_a = f\left(\frac{p_a}{p_{T_a}}\right)$$

The arrows identify the quantities which are measured within the bellmouth.

Corrections are made for forces due to a labyrinth seal at the bellmouth, for hook up of pipes, tubes, etc., and for induced flow external to the engine.

An alternate approach is to traverse the nozzle. Within current testing philosophy this is generally regarded as a secondary method. As shown in Figure 5 a rake is moved across the nozzle and measures  $p$ ,  $p_T$ , and  $T$ . From these data  $M$ ,  $V$ , and  $\rho$  are calculated at the plane of the probe. Static pressure ports are used to determine  $p_w$ . Gross thrust is given by

2. whereas slow angle??

$$F_g = \int_{A_P} \frac{\rho M^2 \gamma R T}{(1 + \tan^2 \theta + \tan^2 \Lambda)} dA + \int_{A_P} (p - p_\infty) dA + \int_{A_W} (p_W - p_\infty) dA - (\text{friction on } A_W) \quad (8)$$

If  $v_r$ ,  $v_\theta$ ,  $v_x$  are the radial, circumferential, and axial components of velocity respectively, then  $v_r = v \tan \theta$  and  $v_\theta = v \tan \Lambda$ . The first integral in Eq (8) is placed in the distinct form to emphasize that swirl angle  $\Lambda$  is important. *Theoretically or actually and when?*

By careful attention to experimental details it is possible to obtain agreement between  $F$  from Eq (8) and  $F$  from Eq (6) within 1 per cent. A large source of error for  $C_{FG}$  may be introduced by the method used to calculate  $F$ . Using a variety of plausible calculation procedures for  $F$ , it is possible to get a spread in  $C_{FG}$  of 3 to 4 per cent. One conclusion is that a consistent and intellectually appealing way is needed to relate cycle analysis to real engine data.

To obtain installed thrust the approach has been to use  $C_{FG}$  as a factor to scale gross thrust. Suppose you know  $C_{FG}$  for an engine using a converging nozzle. If a plug nozzle is used, then

$$F_{g\text{PLUG}} = \frac{C_{FG}(\text{PLUG, MODEL})}{C_{FG}(\text{CONV, MODEL})} F_{g\text{CONV}} \quad (9)$$

Sources of error following this procedure include influence of external flow, total temperature of jet, Reynolds number effects, swirl, leakage, profiles in the flow properties, and occurrence of turbulence and other unsteady phenomena. These errors and related details are discussed in later sections of this paper.

For a given  $p_T$  and  $T_T$ , gross thrust is not a function solely of nozzle geometry; i.e., for given  $p_T$  and  $T_T$ , a gross thrust value cannot be assigned to a nozzle geometry.  $F$  depends on both internal and external flow details. The magnitude of the influence of the external flow depends on nozzle type. Blow-in door ejector nozzles, plug nozzles, and, to a lesser degree, convergent nozzles are sensitive to the external flow. Converging diverging nozzles are almost insensitive to external flow.

Profiles of  $p_T$ ,  $T_T$ , or Mach number have a definite influence on gross thrust. There are engine types with pronounced profiles, e.g., turbofans with common discharge nozzle for both core and fan streams and turbojets with modulated afterburners. (A commonly used fix for afterburner combustion instability or screech is to distribute heat release so as to avoid antinodes in wave patterns.)

Equation (9) indicates use of model nozzle data to obtain prediction for full scale. This is valid provided profiles of internal flow properties between models and full scale are similar; otherwise, errors can be introduced.

To emphasize the significance of  $p_T$  and  $T_T$  profiles entering a converging nozzle, calculations were performed. The inputs to the calculations and some of the results are shown in Figure 6. The Mach number across the exit plane is shown. For Case 1, the Mach number is nearly the same as for uniform  $T_T$  based on an average  $T_T$ . For Case 2, the Mach number at exit is altered. Loss of thrust is 1.8 per cent for Case 1 and 2.5 per cent for Case 2.

The shape of the sonic line is shown in Figure 7. It is apparent that flow conditions at the exit change when the internal flow profiles change. This changes the integrand of the integrals in Eq (2). In addition, the sonic line shape changes with nozzle pressure ratio, which is stagnation pressure at nozzle entrance divided by ambient static pressure.

Engine tests are frequently conducted using a converging nozzle as the reference. Considering the sensitivity of gross thrust from convergent nozzles to nozzle pressure ratio, a converging diverging (CD) nozzle may be a better choice for a reference. Use of a CD nozzle does not, however, change the dependence on entrance profiles.

Figure 8 shows some typical data and illustrates the possible errors between various sources. Using average  $p_T$  and  $T_T$  along with a 1-D theory, the value of thrust coefficient is predicted. (See dash-dot curve.) When model test data are extrapolated to full scale, the result is shown in Figure 8 as a dashed curve. The solid curve and data points are for the actual nozzle.

Flow in the gas turbine is three dimensional. When accuracy of 1 per cent or 2 per cent is desired for thrust, three-dimensional aspects must be accounted for. For coarse work, engine performance stated in terms of quantities involving 1-D calculations, e.g.,  $F_g$ , is adequate. For refined work, engine performance should be given in terms of flow profiles at some station between the turbine exit and nozzle entrance. These profiles form the boundary conditions for a computer determined  $F_g$  or an experimental evaluation of  $F_g$  using model nozzles.

## EXHAUSTS

### Introduction

Once a given jet engine has been selected, the nozzle selection remains open. As shown in Figure 9, there is a wide variety of nozzle designs from which to choose. The aim of this section is to indicate how a prediction of installed thrust can be made based on wind tunnel data and engine test cell data. The techniques for estimating nozzle performance and jet interference will be discussed.

The transonic flight regime is a region where afterbody and nozzle drag is high. There are at least four operating conditions that must be thoroughly investigated: (1) transonic cruise,

(2) transonic acceleration, (3) transonic deceleration, and (4) high-g maneuvers. These four operating conditions have different nozzle pressure ratio, exhaust stagnation temperature, nozzle area ratio, heat capacity ratio, and aircraft angle of attack. Figure 10 shows the typical range for some of these variables.

Afterbody models are used to complete the necessary drag data. These models are in addition to the aeroforce model, which is a reproduction of the complete aircraft. Afterbody drag and nozzle drag may be 20 to 40 per cent of complete aircraft drag at transonic flight. A variety of bookkeeping procedures has been developed to define, identify, measure, diagnose, and correct forces of various components.

The trend in nozzle design has been to iris and plug nozzles. Development of fan engines has made cooling air available. Turbojets needed a flow of cooling air which could be obtained from ejector action of the primary jet. Early jet fighter aircraft placed heavy emphasis on ejector nozzles. For some supersonic aircraft, blow-in door ejector nozzles provide performance gains in transonic flight. Variable geometry nozzles are essential for multiple Mach number design points.

There is a wide number of variables related to nozzles and exhausts. Table I lists these variables. A particular nozzle problem can be stated or specified by taking one adjective for each variable from the right-hand column. When this is done, there are 62,208 different combinations, implying that number of nozzle configurations!

TABLE I. VARIABLES RELATED TO EXHAUSTS

Variable	Possible Values or Feature
Mainstream Mach Number	Subsonic - Transonic - Supersonic - Hypersonic
Jet Mach Number	Subsonic - Transonic - Supersonic - Hypersonic
Nozzle Pressure Ratio	Overexpanded - Optimum - Underexpanded
Direction of Jet	Parallel - Acute Angle - Normal
Number of Exit Ports	Single - Dual - Multiple
Spacing of Multiple Jets	Narrow - One Jet Diameter - Wide
Number of Nozzle Streams	Primary - Primary and Secondary - Primary, Secondary, and Tertiary
Geometry of Afterbody	Axisymmetric - Nonaxisymmetric
Shape of Afterbody	Blunt Base - Smooth Contour
Boundary Layer, Internal	Laminar - Turbulent
Boundary Layer, External	Laminar - Turbulent
Ratio $S^*$ to Jet Diameter	(Smooth Variation of This Parameter)
Sensitivity to External Flow	None - Influenced

An important aspect of nozzle and exhaust testing is the fidelity of jet simulation. Jet simulation will be discussed.

Test planning involves many considerations including the type of nozzle and type of installation. Extent of simulation, as mentioned previously, must be decided. Compromises are required by constraints of local facilities and program goals; decisions concerning compromises are based on past experience.

#### Accuracy

Accuracy of determination of thrust should be, of course, compatible with the accuracy of measurement of drag. Since the aircraft senses net thrust and the procedures yield gross thrust, it is necessary to have a more precise measurement of gross thrust. The ratio  $F_g/F_{net}$  is 2 to 3 for transonic flight. Assessment of accuracy is complicated by the many instruments employed in the measurement sequence, the many models used for obtaining drag increments and separate portions of overall drag, and the complex test apparatus. Desired accuracy in the transonic region is 0.5 per cent for  $F_g$ .

#### Isolated Nozzle Versus Complete Model Tests

Isolated nozzle tests are a very close approximation to a two-dimensional flow problem. The geometry is usually axisymmetric without fins, elevators, or other features. An afterbody or complete model test duplicates the geometry of the aircraft. This is a three-dimensional problem. Figure 11 illustrates the 3-D nature of the external flow by showing local Mach number and boundary layer thickness. The influence of wings, tails, and other upstream features is clearly evident.

Isolated nozzle tests, which are valuable for comparing different nozzle designs, are usually conducted early in the development phase. In later phases of the aircraft development, absolute values for nozzle performance parameters are needed. For these purposes complete model tests are usually conducted. Advantages and disadvantages for isolated and complete model tests are summarized in Tables II and III. Figure 12 illustrates two test arrangements for a wind tunnel. Figure 13 is a photograph showing an example where the feed pipe enters from the plenum.

TABLE II. ISOLATED NOZZLE TESTS

Advantages	Disadvantages
Larger Scale, Hence Larger Re	Flow is 2-D Instead of 3-D
Larger Scale, Easier to Instrument	Installation Effects May Require Nozzle Redesign
Larger Scale, Exact Detailing Possible	Do Not Form Basis for Predicting Interference in 3-D Models
Necessary for Checking New Nozzle Concepts and Basic Studies	Support Structure Eliminates Possibility for True Isolated Tests
Baseline for Uninstalled Performance	Not Adequate for Interference Between Multiple Nozzles
Substantiate Calculations; Easier Geometry for Which to Make Predictions	
Relatively Economical	

TABLE III. COMPLETE MODEL TESTS

Advantages	Disadvantages
Better External Flow Simulation	Small Size Nozzle or Else Very Large Tunnel Needed
Only Means Available to Predict Installed Nozzle Performance	Complex Shape Requires More Extensive Instrumentation
Verifies Aircraft Design	Simulation of Secondary or Tertiary Flow Difficult
Influence on Aircraft Aerodynamics Can Be Measured	Support System Interference Needs Careful Checking
Influence of Exhaust Plume on Control Surface Effectiveness Can Be Determined	Models Are Complex and Costly
Fylon Design Verified	Low Re for Nozzle Due to Size
Flow Visualization Possible	Changes in Geometry Are Difficult to Make
Multiple Nozzle Designs Verified	Hot Jets Difficult to Incorporate Profile into Nozzle May Be Poor
	Difficult to Measure Mass Flow Accurately

#### Jet Simulation

Jet simulation involves duplication in a model scale exhaust features from the full scale jet by using suitable scaling criteria. The relative importance of a particular jet flow property depends on the use of the test results. Extent of simulation depends on type of nozzle, installation of the propulsion system on the aircraft, and the required accuracy of the test data.

Actual installations are almost always three dimensional in character. Model size is limited by blockage restrictions in a transonic tunnel. Jet simulation must be incomplete. Laws of fluid mechanics quite precisely define the scaling rules and the necessary conditions for similitude. The problem is to determine the consequence when some of the conditions are violated.

Figure 14 illustrates different nozzle tests. Static tests are conducted without external flow and closely parallel engine tests in sea level static test stands or in altitude test facilities. When external flow is added, the tests can be separated into two categories: (1) nozzle flow immune to external flow and (2) nozzle flow sensitive to external flow.

In regard to thrust, the key question is whether or not the external flow can influence flow at the nozzle exit plane. To obtain drag, the pressure distribution on external surfaces is needed. The key feature is the location of these surfaces relative to the nozzle exit. Surfaces immediately upstream, e.g., a nozzle boattail, require less strenuous jet simulation. Adjacent surfaces located in the far field regions of the jet require more precise jet simulation in order to obtain suitable accuracy.

For thrust evaluation with the exit plane flow immune to external flow, duplication of nozzle pressure ratio,  $NPR$ , and jet heat capacity ratio,  $\gamma_j$ , is of primary importance. Distortion into the nozzle entrance and stagnation temperature are of secondary importance. For gross thrust determination when the exit plane flow is sensitive to the external flow, many more flow quantities must be duplicated. One obvious set of flow quantities is that defining the external flow. The primary flow quantities to be duplicated are  $NFR$ ,  $\gamma_j$ ,  $\gamma_\infty$ ,  $M_\infty$ ,  $\delta_j/D$ , and  $\delta_\infty/D$ . Lack of total temperature duplication can be accounted for although the ratio  $T_{Tj}/T_{T\infty}$  is significant.

Considering drag due to flow over surfaces in the near field of the jet, e.g., base flow, the plume shape at the nozzle exit must be duplicated. This requires a duplication of  $NFR$ ,  $\gamma_j$ ,  $\gamma_\infty$ ,  $M_\infty$ , and  $M_j$ . When mixing is important,  $(RT_{Tj})_j/(RT_{T\infty})_\infty$  should be duplicated.

For determining jet interference effects on adjacent surfaces in the far field, plume shape at the exit, reflection coefficients at the jet boundaries, and mixing both from momentum and heat transfer point of view are important. Jets are usually turbulent as in the external flow. Duplication of plume shape is probably the most severe case for jet simulation requiring duplication of  $NFR$ ,  $\gamma_j$ ,  $\gamma_\infty$ ,  $M_\infty$ ,  $M_j$ ,  $T_{Tj}$ , and  $T_{T\infty}$ . Turbulent and laminar Reynolds and Prandtl numbers are also important.

### Wind Tunnel Testing Schemes

There are numerous schemes for obtaining drag, thrust, and thrust minus drag. One such method will be discussed here to illustrate the scope of a complete test and to show how the afterbody tests fit into the procedures.

Aircraft performance is defined in part by thrust minus drag. The engine company sells thrust, and the airframe manufacturer minimizes drag. Since there are items in the force bookkeeping procedure which must be assigned to drag or to thrust, careful definitions are required.

Bookkeeping of forces usually involves increments to drag or thrust for operation at some point other than the reference condition. At a given  $M_\infty$ , three variables are usually specified as standard or reference values. These are NFR, nozzle area ratio, and angle of attack; subscript r denotes reference values. Deviation from these reference conditions gives rise to force increments. One philosophy for assignment of the force increments is to alter thrust if the increment results from a throttle change. If the increment is due to a change in angle of attack, it is assigned to drag.

The drag of inlets depends on mass flow ratio,  $m$ , into the air induction system. The drag of exhaust systems depends on nozzle pressure ratio,  $P$ , for a given flight condition. Variable geometry of inlets or nozzles adds complexity and alters drag. Changes in  $m$ ,  $P$ , and area ratios are mainly due to throttle changes and hence, assigned to thrust.

The aeroforce model is mounted on a sting and force  $F_1$  determined; see Figure 15. For this test there are reference values of  $m_r$  and  $P_r$  which may not be the same as, or even close to, the values chosen as the standard flight configuration and denoted by subscript r. At  $m_r$  and  $P_r$ , drag increments due to the inlet or nozzle flow are set equal to zero.

Figure 15 shows schematically how drag is obtained from the aeroforce model, the inlet model, and the exhaust model. Variation of force due to variation of  $m$  or  $P$  is readily obtained from the test data. The change in the force on the inlet represented by  $F_3 - F_4$  would be charged to thrust since it is a result of throttle (mass flow) changes. The change of force represented by  $F_7 - F_8$  would also be charged to thrust since nozzle pressure ratio is a function of throttle setting.

Propulsion system installed gross thrust is obtained from

$$\left\{ \begin{array}{c} \text{installed} \\ \text{gross} \\ \text{thrust} \end{array} \right\} = \left\{ \begin{array}{c} \text{test cell} \\ \text{gross} \\ \text{thrust} \end{array} \right\} + \left\{ \begin{array}{c} \text{increment} \\ \text{due to} \\ \text{inlet} \end{array} \right\} + \left\{ \begin{array}{c} \text{increment} \\ \text{due to} \\ \text{exhaust} \end{array} \right\} + \left\{ \begin{array}{c} \text{increment} \\ \text{due to} \\ \text{engine} \end{array} \right\} + \left\{ \begin{array}{c} \text{increment} \\ \text{due to} \\ \text{secondary} \\ \text{flow} \end{array} \right\} \quad (10)$$

The test cell  $F_g$  was discussed previously; Eq (6) is relevant. The increment terms need to be defined and discussed.

The increment due to the inlet includes the following: (1) spillage drag, (2) bleed drag, and (3) bypass drag. Spillage drag consists of additive drag and the change in force on the inlet cowl. Usually data are reported in terms of  $C_{D_{inlet}}$  or  $C_{D_{inlet}}^{\text{add}}$  plus  $C_{D_{inlet}}^{\text{cowl}}$ . To control shock-wave-boundary-layer interaction, it is necessary to partially remove the boundary layer at critical portions of the inlet. The bleed air is dumped overboard. For some flight conditions it is better to take excess air on board and then dump it overboard. Inlet stability or the trade off between spillage and bypass drag may make it desirable to swallow air in excess of engine needs.

Several factors determine the size of the drag increment due to the exhaust: (1) correction for external flow, (2) base drag, (3) boattail drag, and (4) exhaust interference. Installed gross thrust is at some flight Mach number. The test cell gross thrust is at static conditions. A correction must be made for the external flow influence on internal flow. For the CD nozzle illustrated in Figure 14, this correction may be very small. For the CONV, FLUG, or BIDE nozzles of Figure 14, this may be a relatively large correction. The correction is obtained from the subtraction of static nozzle thrust from the thrust of the same nozzle installed in an afterbody model. The nozzle is metric within the afterbody model. An example of the correction for external flow is shown in Figure 16 for a plug nozzle. Also the boattail and base drag corrections are shown.

Before proceeding with additional discussion of base drag, boattail drag, etc., it is worthwhile to examine Figure 17 which illustrates areas for drag definitions. Notice the split between the forebody and afterbody of the aircraft model; this implies the afterbody is metric as we shall see. Afterbody drag includes tail, fairings, and boattail. The boattail is the surface which reduces the area from the forebody-afterbody split to the area at the nozzle exit. For variable geometry nozzles, there are usually external nozzle surfaces exposed to the external flow giving rise to external nozzle drag,  $D_e$ . The drag,  $D_e$ , may be included with boattail drag. Base flow is a downstream flow region where the streamlines do not follow the body contour. Such an annular area is illustrated in Figure 17. The internal nozzle drag is not important for these discussions having been accounted for by  $C_{FG}$ .

When the base flow region is an annulus surrounding the nozzle exit, as shown in Figure 17, the correction for base drag can be lumped into boattail drag. When there are multiple exhaust nozzles, there may be base flow regions not at the nozzle exit plane. If this is the case, the base drag can be included with the exhaust interference term.

Changes in nozzle pressure ratio, use of afterburner for thrust augmentation, and other propulsion system operating points cause changes in the exhaust plume geometry. As a result, the external flow is modified. Changes in the external flow may alter the pressure distribution on the elevator, rudder, wing, or fuselage. The drag increment termed exhaust interference accounts for this aspect of the exhaust.

Continuing with the various terms on the right-hand side of Eq (10), consider now the increment due to the engine. As a result of  $m$  different from  $m_0$ , inlet pressure recovery and level of distortion at the compressor face may change. These changes can influence engine operation. Based on data obtained from test programs in sea level static test cells or altitude facilities, corrections can be made.

Power may be extracted from the engine either by bleeding air off the compressor or by driveshafts for alternators, pumps, etc. Bleed air from the compressor to provide boundary layer control on the wing, air conditioning for the crew, or to actuate pneumatic devices causes a loss of thrust. This thrust loss is accounted for in the term "increment due to engine."

The final term in Eq (10) is the increment due to secondary flow. (Secondary flow can be defined as air taken on board from freestream conditions and returned to the ambient atmosphere without forming part of the engine working fluid.) When the secondary flow, e.g., cooling air, forms part of the nozzle flow, there is a thrust increment which changes with the engine operating conditions. The secondary air may be dumped overboard through its own nozzle or exit door. Pressures on the aircraft may be changed. The ram drag associated with secondary air is the mass flow rate of secondary air times vehicle velocity.

Equation (10) indicates the corrections which must be made to convert test cell gross thrust to installed gross thrust. The number of corrections becomes quite large as the preceding discussion has indicated. Each correction or increment has its own accuracy and is a source of error. The bookkeeping schemes should strive for the minimum number of increments required to adequately describe forces on an aircraft. The increments may be based on a variety of model sizes. Typical model sizes providing data are indicated in Table IV.

TABLE IV. TRANSONIC TESTING MODEL SIZES* (TYPICAL FIGHTER AIRCRAFT)	
Model	Percentage of Full Scale
Aeroforce Model	5
Inlet Model	8-10
Isolated Nozzle Test	25
Afterbody Model	8-10
*Models less than 1/20 scale have so many compromises relative to geometric detail and Reynolds number that tests are not attempted.	

#### Afterbody Tests

The models illustrated in Figure 15 do not show the details of the output of powered afterbody tests. Additional discussion of the various approaches is worthwhile.

Figures 18 to 21 show four afterbody models. The arrangement of Figure 18 has only one balance which measures  $F_e - D_a - D_e$ . In Eq (10) these would be the terms installed gross thrust and the increment due to the exhaust. This scheme has the disadvantage that  $F_e$  is an order of magnitude larger than  $D_a$ . Results of modifications of the afterbody to improve  $D_a$  are not readily determined.

The arrangement shown in Figure 19 permits direct measurement of  $D_a + D_e$ . The balance size can be selected to fit the level of  $D_a + D_e$ . An arrangement such as that shown in Figure 20 decreases force on the balance compared to Figure 18. The balance reading can be interpreted differently using a momentum control volume. Seal problems are difficult with the system of Figure 20.

Tandem balances offer many advantages. Figure 20 shows one possible arrangement. Both balance (A) and (B) can be sized to match the force. The main disadvantage is the complexity of the model.

#### Simulation Techniques

There are general requirements for afterbody models, some of which are dictated by practical constraints. Here are some of these requirements:

- |  |   |
|--|---|
| (1) small diameter feed pipes for small struts or struts             | (5) no deformation of model due to thermal stresses   |
| (2) minimum interference of feed pipes with balance system           | (6) controllable and accurately repeatable jet simulator  |
| (3) momentum of flow in feed pipes normal to drag axis               | (7) low model costs   |
| (4) balances isolated from heat flux within model due to hot exhaust | (8) low operating costs   |
|  | (9) safe operation  |
|  | (10) compatible with wind tunnel; no contamination of air in closed circuit wind tunnel; no explosion hazard in wind tunnel |

There are several techniques for obtaining a jet; these are: cold gases, hot gases, and cold jet powered turbine engines.

When the jet is simulated using cold gases, air or  $N_2$  are most commonly used. As indicated in Figure 10,  $\gamma$  of exhaust gas is not 1.4 for a turbojet with afterburner. Table V gives flow data for different conditions. Rows 1 and 2 have the same NPR. The Mach number for  $\gamma = 1.3$  is higher, and the area ratio is also larger. Rows 1 and 3 have the same area ratio as would be the case for geometrically similar nozzles. A larger NPR is required for  $\gamma = 1.4$  to obtain ideal expansion; the exit Mach number is also larger. For a gas with large  $\gamma$ , the NPR is higher which means the density in the feed pipes should be larger. Since small struts are desired, this is an advantage. Cold gases do not provide simulation

of jet momentum. For underexpanded nozzles, the plume shape is not correctly simulated when NPR is duplicated; however, by adjusting NPR, the exhaust plume near the nozzle exit can be duplicated.

TABLE V. COMPARISON OF NOZZLE FLOWS FOR DIFFERENT RATIOS OF HEAT CAPACITIES

Row Number	Ratio of Heat Capacity, $\gamma$	Nozzle Pressure Ratio, NPR	Area Ratio, $A/A^*$	Mach Number
1	1.3	5.0	1.41	1.74
2	1.4	5.0	1.34	1.71
3	1.4	5.5	1.41	1.77

Gas mixtures have been suggested to tailor gas density and heat capacity ratio. Polyatomic gases decrease  $\gamma$ ; gases with small molecular weight adjust gas density and speed of sound. Many nozzle test rigs have flows of 2 to 8 lb<sub>m</sub>/sec. Gas mixtures are expensive. The wind tunnel becomes contaminated.

Use of hot gases is much more complicated requiring careful model design. Ignition sources, thermal shielding, safety precautions, fuel supply, and a control system increase complexity. Due to small geometric scale, combustion may be incomplete so that there can be burning in the exhaust plume. Incomplete combustion makes it difficult to determine the gas temperature.

Hot gas can be obtained using hydrogen peroxide decomposition or combustion of a fuel and oxidizer, usually air. The fuel may be propane, hydrogen, methane, ethylene, gasoline, or kerosene.

By using hot gas,  $\gamma$ , and  $T_{t1}$  can be simulated. Figure 22 shows  $\gamma$  as a function of  $(RT_{t1})_1 / (RT_{t1})_{\infty}$  for hydrogen peroxide decomposition. The values for a turbofan are also shown. A good match is obtained. Decomposition is initiated by a catalyst pack which fits within the volume constraint of a scale model.

A new technique being rapidly developed is the use of miniature turbine-powered compressors. Figure 23 shows a propulsion system simulator. The compressor air does not go through the turbine. The turbine is powered with an external supply of gas. To modify the mass flow in the nozzle, some of the supply gas can be mixed with the compressor flow. Both inlet and exhaust flows can be simultaneously simulated with this device. Since the turbine removes considerable energy from the supply gas, the exhaust gas will be extremely cold. Ice formation within the model can be a problem. Since powered simulators are important, a complete section, to follow, has been devoted to that topic.

Nozzle tests can be conducted in a wind tunnel with a repeatability of thrust minus drag of 0.2 per cent for supersonic tests and 1.0 per cent or less for transonic tests. Standard nozzles are available for verification of balances. A theoretical prediction of thrust of standard nozzles is possible. These predictions agree with measurements. For isolated nozzles, the accuracy of 0.5 per cent previously stated as being required seems to be possible.

Experimenters in this field are encouraged to report data as measured without scale corrections. Corrections, which are given in sufficient detail to be understandable, can then be applied. One such correction is for real gas effects. Variable  $\gamma$  can be handled readily by existing computer programs. Other corrections may involve viscous effects.

Reynolds number is rarely duplicated in model tests with the result that boundary layer thickness and boundary layer transition are not simulated. Flow separation on the boattail occurs more frequently on models due to low Reynolds number.

Variable geometry nozzles have leakage between leaves. This is not simulated in model tests. Correction of model data to account for leakage would be desirable if it could be done accurately; however, this is not the case. In addition, manufacturing tolerance will result in production nozzles with different leakage rates.

#### Exhaust-Airframe Interference Other Than Thrust Minus Drag

There are numerous interference effects other than thrust minus drag. These are listed in Table VI. Tests very similar to those described previously are conducted to determine increments in lift and moment coefficients. Partial models are used less frequently; the complete aircraft is tested to obtain the external flow. Semi-models or half-span models mounted on the tunnel wall may be used.

TABLE VI. INTERFERENCE OTHER THAN THRUST MINUS DRAG

Alter pressure distribution on surfaces changing $C_L$ , $C_M$ .	Alter unsteady flow effects.
Subject surfaces to heating.	Alter external nozzle pressure.
Distort boundary layer due to heating.	Alter thrust axis at low $p_j/p$ .
Reduce or augment control effectiveness.	Change shock wave locations.
	Stimulate panel flutter; acoustic fatigue.

Three different engine installations will be discussed from the point of view of exhaust and propulsion interference. These are wing mounted fan engine, fuselage mounted fan engine, and the engine buried in the airframe.

High bypass engines, pylon mounted on the wing, can have an influence on wing circulation and, at transonic speeds, on shock formation. Due to the large mass flow of air through the engine, a significant deviation of external streamtubes can be caused by changes in engine mass flow.

To duplicate the interference effects, the exhaust plume of the fan should be reproduced. The fan exhaust stream is transonic. An estimate of exhaust Mach number,  $M_e$ , is given by

$$\frac{M_e}{M_\infty} = \sqrt{\frac{\tau_r \tau_c - 1}{\tau_r - 1}} \quad (11)$$

where  $\tau_r$  is the ram temperature change given by  $1 + (\gamma - 1)M_\infty^2/2$ , and  $\tau_c$  is the stagnation temperature change due to fan work. Typical values are  $M_\infty = 0.84$  and  $\tau_c = 1.12$ . For these values,  $M_e = 1.2$ . Since the jet flow is high transonic or supersonic, the exhaust plume shape is determined by jet Mach number and  $\gamma$ . Wave reflections are duplicated leading to a similar jet structure. Jet Mach number is a strong function of NPR.

Viscous mixing occurs at the shear layer between the jet and the external stream. Growth of the mixing region, or shear layer, has a displacement thickness similar to a boundary layer. When the jet boundary increases in area, the jet acts as a source distribution. When the jet streamtube area decreases, the external flow moves toward the jet axis. Figure 24 shows the results of a calculation of jet area,  $A_x$ , compared to streamtube area,  $A_m$ , entering the inlet.

Case 1 in Figure 24 is for a turbojet with turbulent mixing. Case 1a is a slight modification with a laminar jet for  $0 < x/D < 2$  followed by turbulent mixing. Case 2 is a turbofan simulator with a bypass ratio of 2. The core and fan pressure and temperature ratios are shown. Case 3 is a turbofan simulator with cold gases. Mass flow has been increased so that  $A_x$  and  $M_e$  are equal to that of Case 2. Finally, Case 4 is for a flow-through nacelle with the correct  $A_x$ . The influence of laminar versus turbulent mixing, hot versus cold jets, and low stagnation pressure versus high stagnation pressure jets is shown by Figure 24.

A difficulty with simulation of high bypass engines is the duplication of both inlet and exhaust flows. One approach is to use a turbine driven fan. Another technique is to use ejectors within the fan cowl. Another method is to close a portion of the inlet with a bullet-shaped insert and to feed the nozzle with externally supplied air.

For a pylon mounted engine on a wing, there are three interactions: wing-inlet, wing-exhaust, and inlet-exhaust. An important question is whether or not the interference effects are additive. If the interference is additive, one can run a series of experiments varying only inlet flow and examine influence on the wing. A second set of experiments can be conducted varying only exhaust conditions and examining the influence on the wing. For a combined deviation of both inlet and exhaust flow, the influence on the wing would be obtained from addition of the two experimental results. Evidence indicates that the exhaust-wing interference is much greater than inlet-wing interference. Addition of effects may be valid.

A rear fuselage mounted engine can alter forces on the aircraft either by direct jet impingement, wave impingement, or constraints on the external flow. The rear mounted engine can influence effective angle of attack on tail surfaces, change aircraft drag, heat surfaces due to jet impingement, or stimulate vibration of panels leading to acoustic fatigue.

In contrast to pylon mounted engine simulators where thrust measurements are made, the rear mounted engine makes balance installation difficult. Semi-models are frequently used with wing mounted engines. With rear mounted engines, this is not feasible. Models with rear mounted engines may be supported in the wind tunnel by struts at the wing tips.

For buried engine installations, e.g., a fighter aircraft, the jet plume may cause separation with an oblique shock interacting with tail surfaces. Some installations have the nozzle planes at the rearmost station. Other installations have the exhaust exits upstream of the fuselage aftend. In this case, the exhaust plume can have a more pronounced influence on the aircraft drag, control effectiveness, surface heating, boundary layer characteristics controlling skin friction, etc.

Although this report focuses on thrust minus drag, it is apparent that a complete aircraft development program will examine the interference effects briefly introduced in the preceding paragraphs.

#### Comparison of Wind Tunnel and Flight Test Results

There are only limited data available in the transonic region comparing flight test results with wind tunnel results. One such paper is that by Samanich and Burley.<sup>(1)</sup> Figure 25 is reproduced from that paper. This figure compares flight test data for nozzle gross thrust coefficient with that obtained from isolated nozzle tests. In the Mach number range 0.8 to 1.2, installation effects cause considerable difference between the two measurements. Figure 26 gives the circumferential variation in pressure coefficient on the primary nozzle flap of the plug nozzle. Also shown are the data for the same nozzle tested isolated with cold flow in a wind tunnel. The flap location can be seen in the top graph of Figure 25. The data tend to emphasize the comments made previously concerning the three-dimensional character of flow in installed nozzles. In extreme cases it has been found experimentally with BIDE nozzles that flow may enter one door and leave through another.

As aircraft development programs proceed, the configuration evolves and changes. By the time the actual aircraft flies, there is little motivation to obtain wind tunnel data on an exact replica of the flight test aircraft. This fact hinders comparison of aircraft flight test results with wind tunnel data. Usefulness of future wind tunnel programs is degraded by lack of careful comparison of data.

Wind tunnel data should be digested, corrected, and otherwise modified before comparison with flight test data. There is a natural tendency to factor in that one last correction for boundary layer separation, or other good cause, so that the two test results agree.

#### Unsteady Aerodynamics of Exhausts

One aspect of aircraft exhausts which may be overlooked is unsteady flow. (Unsteady flow may be overlooked from the point of view of its influence on nozzle performance, e.g.,  $C_{FC}$ . Aeroelastic phenomena leading to destructive instabilities are certainly not overlooked.) There are several ways in which time dependent flow manifests itself: (1) shock wave oscillation in the external flow as the result of a large plume from an underexpanded nozzle, (2) unsteady separation zones in the external flow, (3) unsteady separation zones in the internal nozzle flow, (4) time varying flow from door to door into blow-in-door-ejector nozzles, (5) flutter of leaves in variable geometry nozzles, and (6) pulsations in secondary flows. The unsteadiness of the flow may be spatial and/or temporal.

There are experimental results which indicate the existence of large fluctuating pressure. See Figure 27. Base pressure coefficient is given for  $M_\infty = 0.9, 1.0, \text{ and } 1.2$ . For a stagnation pressure ratio of 2 at unity Mach number, the unsteady pressure fluctuation exceeds 20 per cent of the steady value.

Due to the compression of the external flow caused by the plume of an underexpanded nozzle, one might expect unsteady motion of the oblique shock wave. This is analogous to transonic buffet on airfoils.

#### Summary Remarks on Exhausts

In this part of the "Exhausts" section various items will be listed and briefly discussed.

- (1) Models tested in the wind tunnel do not represent accurate scaled models of the actual airplane. Development programs are paced by schedules and constrained by resources. In a development program wind tunnel data are of importance only to the extent that the data help to produce a good performing airplane. The wind tunnel data are relegated to the file cabinet as soon as the aircraft is certified. Most aircraft programs do not include resources to reexamine the quality of wind tunnel data in the light of flight test results. Since the model may not match the airplane, some key points may need checking in the wind tunnel with a new, accurate model.
- (2) Similarity rules of fluid mechanics are violated in nearly every wind tunnel test. Rarely is Reynolds number correctly duplicated. The problem with interpretation of wind tunnel exhaust data is to know the consequence of inexact similitude and scaling. With the advances in computational fluid mechanics coupled with analytical approaches, new insight may be gained.
- (3) Unsteady aerodynamics certainly occurs in the external flow field in the transonic regime. Time dependent exhaust flow may be an overlooked feature when evaluating exhaust system performance - or when evaluating the lack of performance.
- (4) Thrust coefficients are based on an ideal nozzle. Thrust coefficients are a one-dimensional concept trying to quantitatively define performance of a three-dimensional flow device. Thrust coefficients and ideal thrust neatly tie cycle analysis to exhaust system hardware and its performance. The tie becomes confusing and has sources of error in the number to assign to ideal thrust when there are profiles of  $p_T$  or  $T_T$ .
- (5) Bookkeeping procedures based on increments have several advantages such as conceptual simplicity; however, to fully exercise the complete bookkeeping procedure, numerous additions and subtractions of data obtained from many different models of widely varying scales must be accomplished. Bookkeeping procedures which do not clearly define the division of responsibility between the engine and airframe companies do not gain acceptance. Being practical and astute, this is a recognized requirement on bookkeeping procedure; however, the aircraft responds to thrust minus drag. Is the split of responsibility a factor which hinders optimization of thrust minus drag?
- (6) Present methods of defining thrust permit verification of full scale engine quality by testing outside the aircraft. This is certainly desirable.
- (7) Inlet spillage may have an influence on exhaust performance. Remember the accuracy goals are 0.5 per cent. Limited work has been done to define inlet interference on exhausts for engines buried in the fuselage. More extensive work has been done on pylon mounted turbofan engines. Fairled inlets may distort installed nozzle performance.
- (8) A Mach number of unity is difficult to achieve in a wind tunnel. Wind tunnel tests near  $M = 1$  are difficult to conduct without tunnel interference.
- (9) Pressure ratios are small in the streamtube passing through the fan. The potential for mutual interference between a wing and a turbofan is great.
- (10) Sources of error in exhaust testing include struts to hold model, roughness in the model flow channel, omission of small detail due to model scale, and incorrect profiles at nozzle entrance.

#### SIMULATORS

##### Introduction

As the preceding discussion has shown, separate forebody - inlet and afterbody - exhaust tests are conducted. These tests are in addition to the aeroforce model. Some exhaust systems and

bookkeeping procedures require a propulsion model also. One reason the numerous models and tests are necessary is that the aeroforce model cannot be designed to take on board the full inlet mass flow and eject the gas with a proper scale exhaust. Only by adding energy to increase  $p_m$  and  $T_m$  can both inlet and exhaust flows be simulated. The power requirements are large, and the space available in the model is small.

One approach would be to drive a suitable compressor with an electric motor. To obtain the correct pressure ratio having a reasonable number of stages, the compressor speed is high - 60,000 to 80,000 RPM. The electric motor with enough horsepower will not fit in the model. Electric motors driven by variable frequency generator sets were used in the old days of wind tunnel testing to power propellers on models.

Another approach would be to pipe the inlet air to a compressor and/or burner outside the wind tunnel. Of interest is transonic testing. At  $M = 1$ , the product,  $\rho u$ , which is mass flow rate per unit area, is a maximum. This means that the pipes leading from the inlet to a position outside the tunnel must be as large in cross section as the inlet capture area. This is a lower bound on pipe size assuming frictionless pipes. To power the nozzle, smaller feed pipes could be used at higher pressure. Semi-models or half-span models with engines in the fuselage can use this approach since there is room for the necessary plumbing.

#### Power Requirements

To indicate power requirements, consider the simulator shown in Figure 23. Designate the entrance to the compressor as station 2 and the exit as station 3. Denote freestream conditions by a subscript  $o$ . From Figure 10 pick a typical operating point, e.g.,  $MFR = 8$  and  $M_o = 1.4$ . The horsepower is given by

$$HP = \dot{m} C_p (T_{T3} - T_{T2}) \quad (12)$$

Assume an inlet capture area of 3 inch diameter. Smaller sizes would hardly be practical. Using values of  $a_o = 1100$  ft/sec,  $M_o = 1.4$ ,  $\rho_o = 1.4 \times 10^{-4}$  lb/ft<sup>3</sup> (equivalent to 45,000 ft altitude), and  $A_o = 0.08$  ft<sup>2</sup>, the mass flow is found to be  $1.7$  lb<sub>m</sub>/sec. Define the following symbol

$$\tau_o = T_{T3}/T_{T2}$$

The horsepower becomes

$$HP = \dot{m} C_p T_{T2} (\tau_o - 1) \quad (13)$$

Using a compressor ratio of 2.52 along with ram pressure recovery, the nozzle pressure ratio of 8 can be achieved. With an efficiency of 0.85 for the compressor, the stagnation temperature ratio,  $\tau$ , is 1.36. A value of  $\tau_o$  consistent with  $\tau$  is chosen; also  $T_{T3} = T_{T2}$ . The value of  $C_p$  is 0.24 BTU/lb<sub>m</sub>·sec. Finally, with these values inserted in Eq (13) and using the conversion factor  $HP = 1.415$  s<sup>2</sup>c/BTU, the horsepower is calculated to be 150 HP. This is like stuffing two VW engines in a three-inch pipe!

#### Simulators with Energy Addition in the Model

To begin, a few symbols will be defined:

$\dot{m}_f$	mass flow in the fan exhaust	$\dot{m}_t$	mass flow in the turbine (left-hand pipe in Figure 23)
$\dot{m}_c$	mass flow in the exhaust of the core of turbofan	$\dot{m}_e$	mass flow in the turbine-exhaust (right-hand pipe in Figure 23)
$\dot{m}_j$	mass flow in the exhaust of a turbojet	$\dot{m}_o$	inlet mass flow

There are several possible designs. For a turbojet simulator

$$\dot{m}_j = \dot{m}_o + \dot{m}_t \quad (14)$$

To conserve mass

$$\dot{m}_e = (1 - f)\dot{m}_t \quad (15)$$

The fraction of the turbine mass flow mixed with the compressor flow is  $f$ . This permits flexibility in controlling jet plume parameters. Figure 28 is an exploded view of a turbojet simulator for supersonic flight speeds. Figure 29 is a photograph of the same simulator on the test stand.

For turbofan simulators the inlet mass flow is used as the fan mass flow, i.e.,  $\dot{m}_f = \dot{m}_o$ . Such a turbofan is illustrated in Figure 30. The turbine drive gas forms the engine core exhaust, i.e.,  $\dot{m}_t = \dot{m}_c$ . An actual turbofan has  $\dot{m}_c = \dot{m}_t + \dot{m}_f$  if fuel addition is neglected. Bypass ratio,  $B$ , is defined as  $\dot{m}_f/\dot{m}_c$  which becomes in terms of  $\dot{m}_o$

$$B = \frac{\dot{m}_o - \dot{m}_c}{\dot{m}_c} = \frac{\dot{m}_o}{\dot{m}_c} - 1 \quad (16)$$

For the simulator, the effective bypass ratio is

$$B = \frac{\dot{m}_f}{\dot{m}_c} = \frac{\dot{m}_o}{\dot{m}_c} \quad (17)$$

Comparing Eqs (16) and (17), it is apparent there is an error. For high bypass engines, this is relatively insignificant. When the mass flow in the exhaust of both core and fan are properly simulated, there is a deficiency of mass flow into the simulator inlet compared to the actual engine. Spillage drag becomes a factor.

As discussed previously, when a nacelle is pylon mounted on a wing, it is possible to use semi-span models as shown in Figure 31. The wing is vertical, and the model is mounted on a turntable. The turntable is above the tunnel floor to divert the tunnel boundary layer. One difficulty with semi-span models is the tunnel wall boundary layer.

The exhaust temperature of the flow,  $\dot{m}_t$ , is very low. Consider the turbojet simulator previously discussed in connection with Eqs (12) and (13). The power to drive the compressor equals the turbine output power. Using this fact, the turbine exhaust temperature can be estimated. The equality of power is

$$\dot{m}_o c_p T_{T2} (\gamma_c - 1) = \dot{m}_t c_p T_{T4} (1 - \gamma_t) \quad (18)$$

Stations 4 and 5 are upstream and downstream of the turbine;  $\gamma_t$  is defined as  $T_{T5}/T_{T4}$ . Solving for  $\gamma_t$  yields

$$\gamma_t = 1 - \frac{\dot{m}_o}{\dot{m}_t} \frac{T_{T2}}{T_{T4}} (\gamma_c - 1) \quad (19)$$

It is apparent from Eq (19) that the smaller  $\dot{m}_t$ , the smaller  $T_{T5}$ . For  $T_{T5}$  equal to room temperature, the values of  $T_{T5}$  are  $-260^\circ\text{F}$  ( $-144^\circ\text{K}$ ) for equal mass flow through the compressor and turbine. If the mass flow through the compressor is roughly 1.4 times larger than that through the turbine, one begins to liquify oxygen in the air. To avoid this problem, dry  $N_2$  can be used to drive the turbine.

The technique of internally powered simulators is being developed. The most significant motivation for developing and using simulators is the high degree of simultaneous simulation of both inlet and exhaust flows. For turbofans, bypass ratio is not correct. For both turbofan and turbojet simulators, the exhaust temperatures are much too low. Burners are being developed to correct the exhaust temperature.

Similar procedures can be used for both the turbojet or turbofan simulator and the full scale engine. Static tests can be run. Figure 29 is a photograph of the supersonic turbojet simulator undergoing such a sea level static test. Tests in the wind tunnel with the simulator can duplicate aircraft mass flows.

Powered simulators offer high fidelity testing; however, there are disadvantages. Tests are expensive to operate. Simulators must be tailored to the particular engine being modeled. Extensive instrumentation is necessary to control and monitor simulator operation. Bearings are small and subjected to severe loads with the consequence that life is limited. Past experience has indicated that repeatability is limited. Two simulators manufactured under similar conditions may show different performance characteristics; variations of 5 per cent in net thrust have been observed. Separation of thrust and drag terms is difficult due mainly to inaccurate determination of nozzle coefficients. Further, development will undoubtedly improve many of the adverse features.

#### Ejectors

Ejectors have no moving parts. There are no rotating components. As a consequence, ejectors are easier to manufacture. Ejectors are relatively easy to scale, and the prediction of performance can be quite precise. The nozzle pressure ratio is limited. Mass flow into the inlet is also less than desired for turbojet or turbofan installations. There are large distortions in the  $p_p$  profile at the nozzle entrance. Characteristics of an ejector powered nacelle do not match that of an engine in the nacelle. Ejectors are not used for simulation of thrust but are useful for interference studies. Due to the low NFR, ejectors can be used for simulation of lift engines and V/STOL propulsion installations. Ejectors offer economy and simplicity; for these two reasons, ejectors deserve more attention for propulsion system simulation.

Figure 32 shows an ejector system developed for a V/STOL fighter or attack aircraft. In spite of the sizable plumbing, the system is used with a balance so that forces on the model aircraft can be measured. The usual ejector has the high-momentum stream interior to the low-momentum stream. The ejector shown in Figure 32 has different topology; the high velocity stream is external to the low-velocity flow. This arrangement is necessary to induce the flow into the inlet and provide for suitable seals. The combined flow from the inlet and high pressure air into the model supplies the nozzles.

#### Simulators with Energy Addition External to the Model

Using a semi-model for a buried engine installation, it is possible to route large pipes into and out of the model. By adding energy external to the model, the severe volume constraints are eliminated. Control of the inlet and exhaust mass flows is flexible. The main difficulty is the boundary layer on the reflection plane.

Effort should be directed to developing the semi-model technique for the case of engines within the fuselage. This technique is not being used currently.

#### ACKNOWLEDGEMENTS

Almost all of the material presented in this paper was obtained from the information supplied by various NATO countries participating in the ad hoc study on Transonic Testing and Engine Airframe Interference. Mr. Fygerk Jaarsma of National Aerospace Laboratories (NRL) of The Netherlands prepared the detailed report (2) on the ad hoc study. Many of the figures in this paper were reproduced from reference (2). Except for two figures, the specific source of each figure has not been identified. Reference (2) gives an extensive list of references and indicates sources for most of the information and figures.

Since the completion of the report on the ad hoc study, some new photographs of simulators were obtained by the author from Mr. Frank Montgomery of the Turbine Engine Division, AF Aero Propulsion Laboratory, WPAFB, Ohio, USA. Use of the photographs is appreciated.

#### REFERENCES

- (1) N. E. Samanich and R. R. Burley, "Flight Performance of Auxiliary Inlet Ejector and Plug Nozzle at Transonic Speeds," AIAA Paper No. 70-701.
- (2) F. Jaarsma, Editor, Engine-Airplane Interference in Transonic Tests, Report on the 1970 AGARD ad hoc Study (in-press).

#### ILLUSTRATIONS

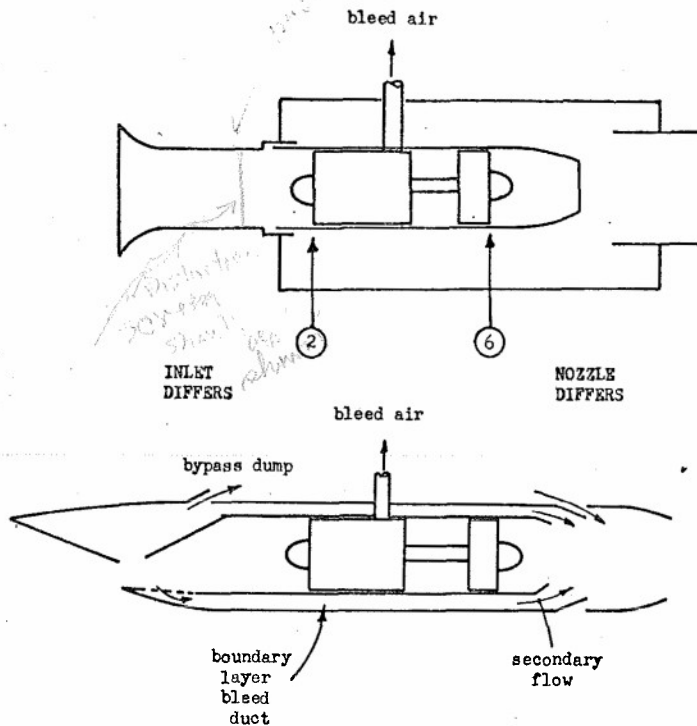


Figure 1. Jet Engine in Test Stand and Installed in Aircraft.

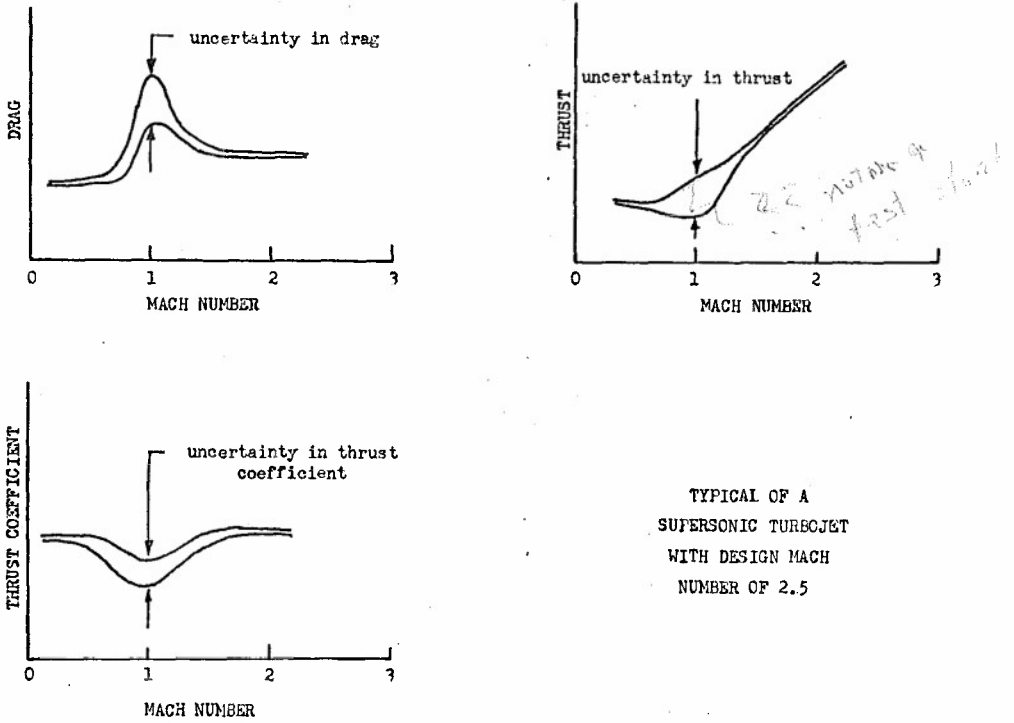


Figure 2. Thrust and Drag as a Function of Mach Number.

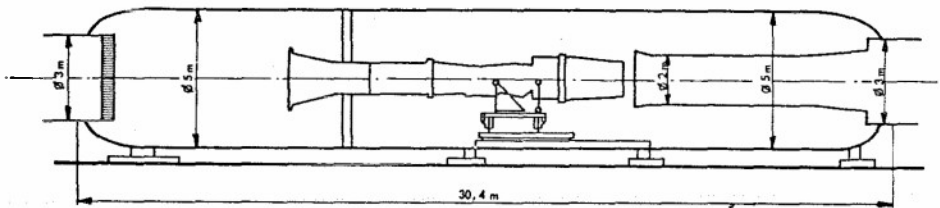


Figure 3. Altitude Static Test Facility.

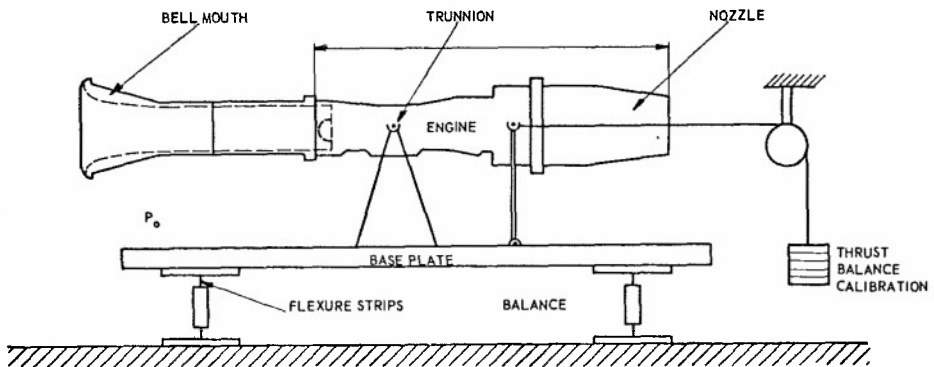
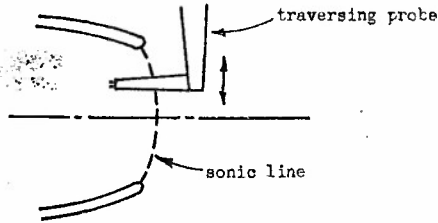


Figure 4. Engine Static Thrust Measurement at Sea Level Conditions.

CONVERGING NOZZLE



CONVERGING DIVERGING NOZZLE

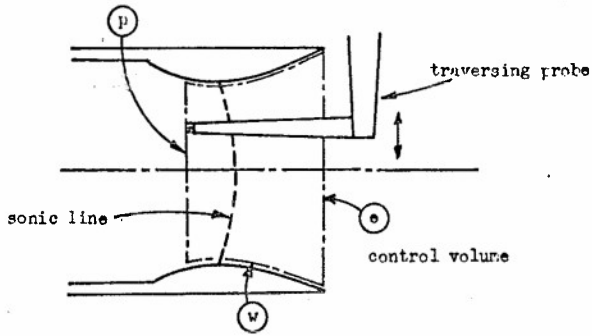


Figure 5. Exhaust Survey for Converging and Converging Diverging Nozzles.

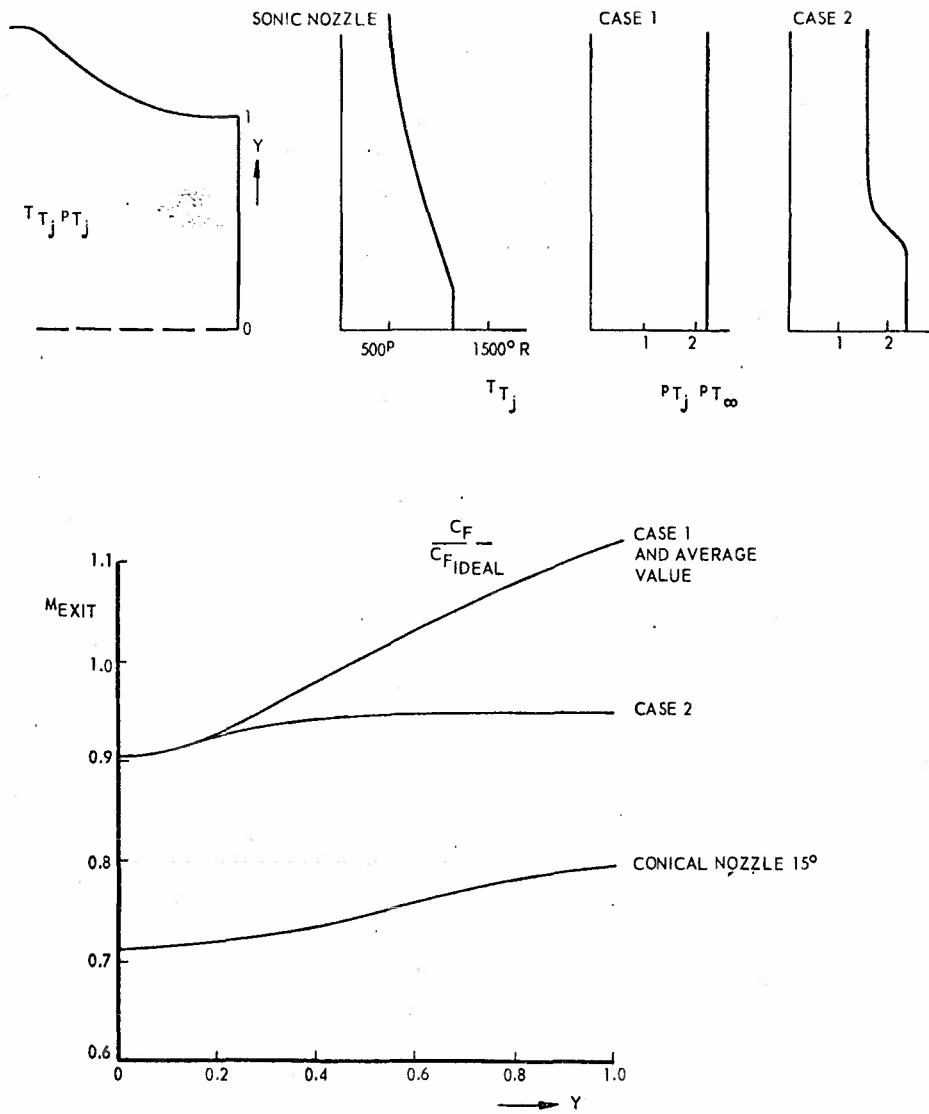


Figure 6. Mach Number Distribution at the Exit of a Nozzle for Nonuniform Stagnation Conditions.

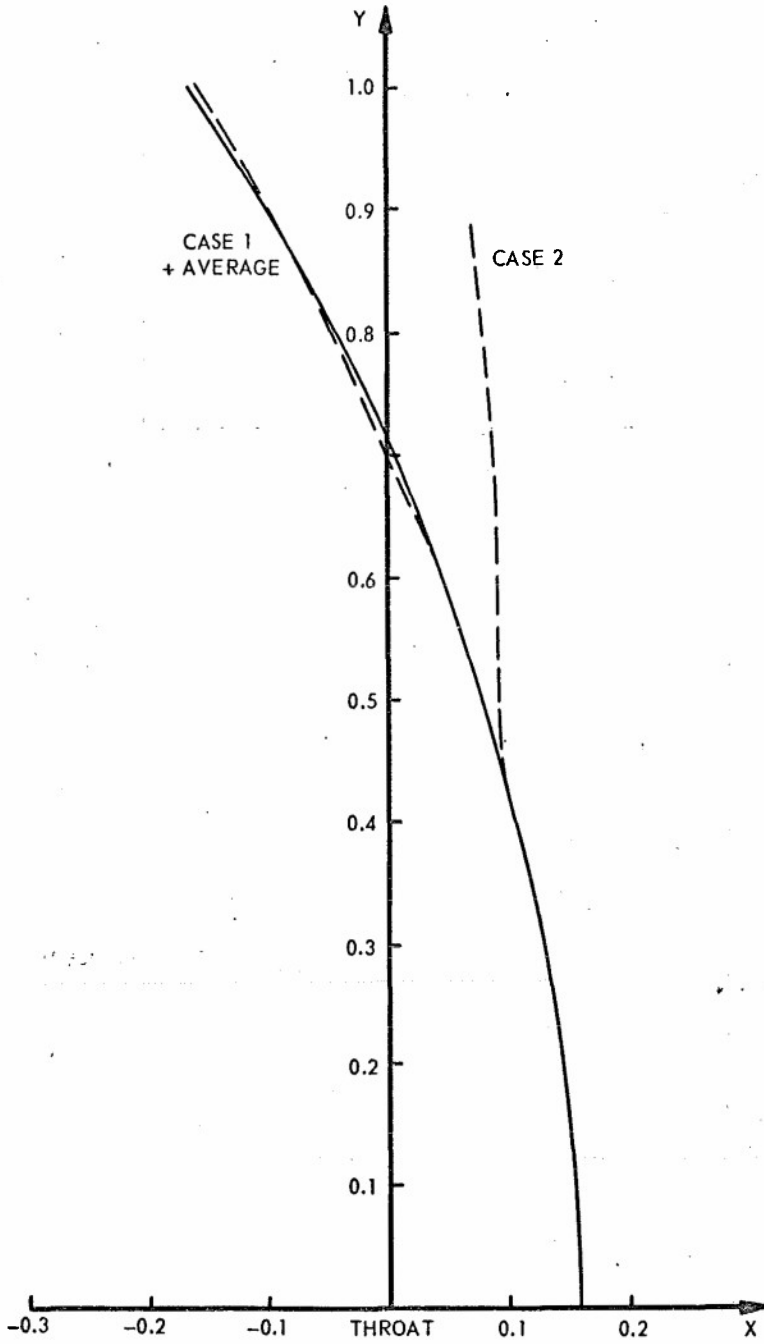


Figure 7. Shape of Sonic Line at Nozzle Geometric Throat.

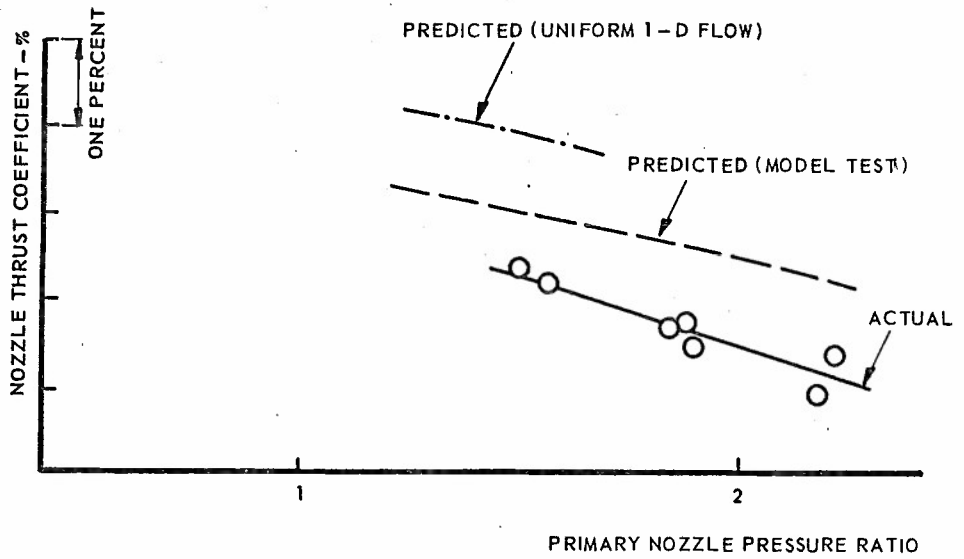


Figure 8. Comparison of Theoretical and Experimental Losses in a Nozzle.

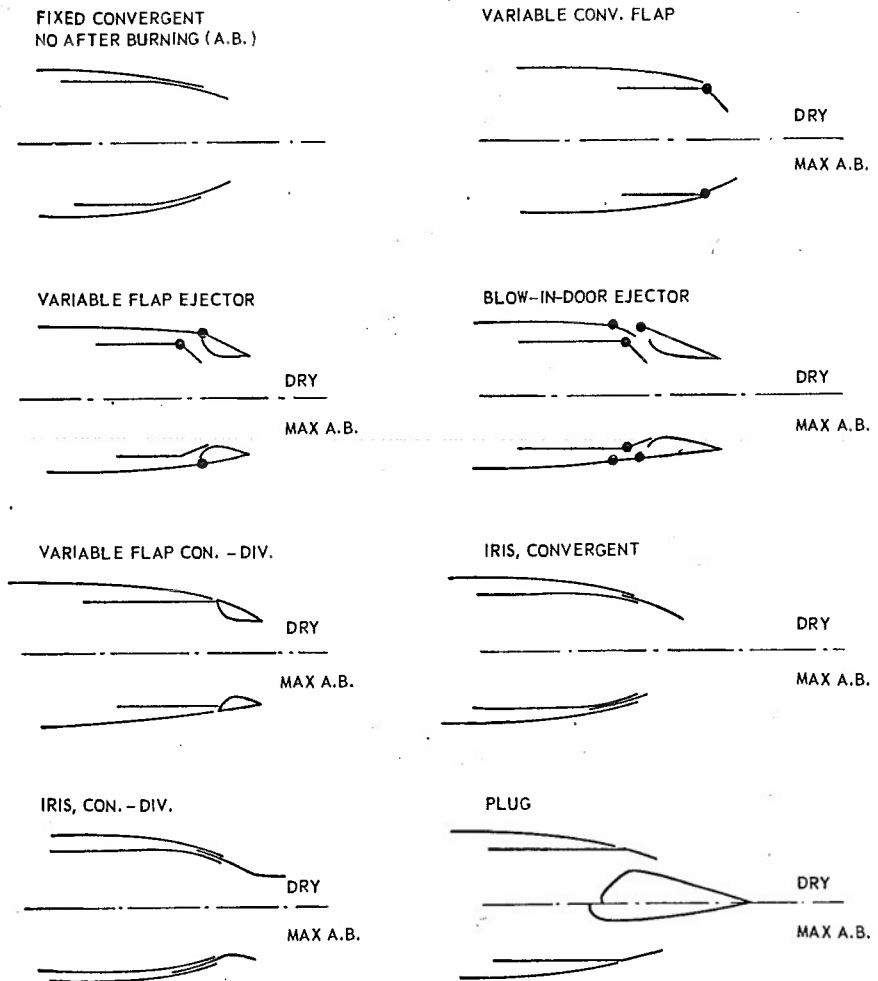


Figure 9. Schematic of Various Nozzle Designs.

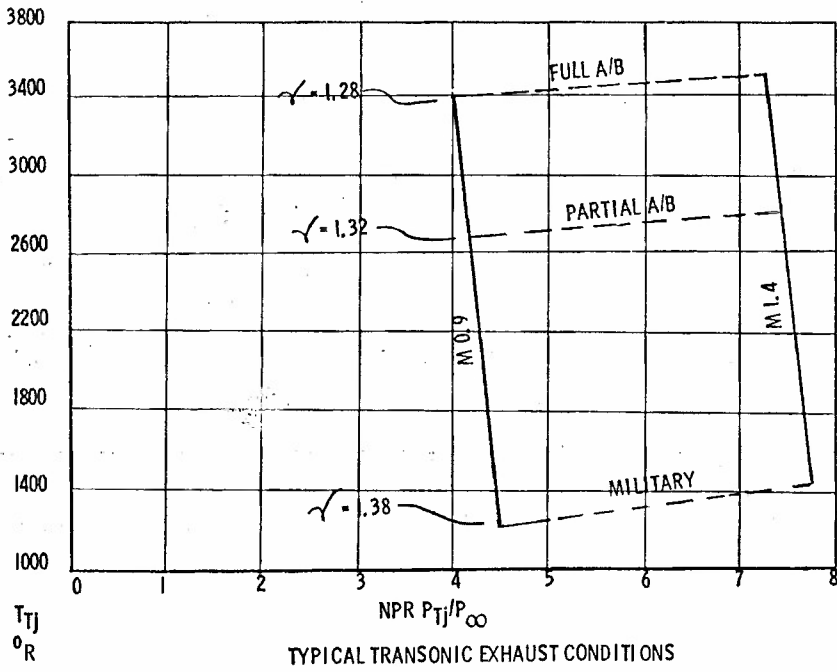


Figure 10. Map of Exhaust Variables for a Fighter Aircraft.

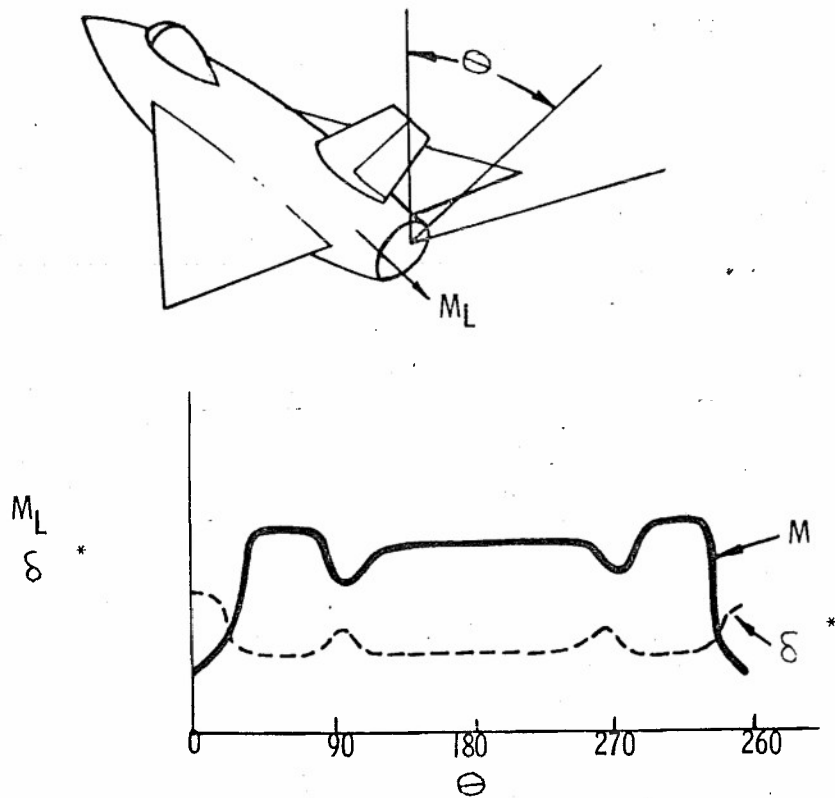


Figure 11. Three-Dimensional Flow Environment for Nozzle.  $M_L$  is local Mach number.

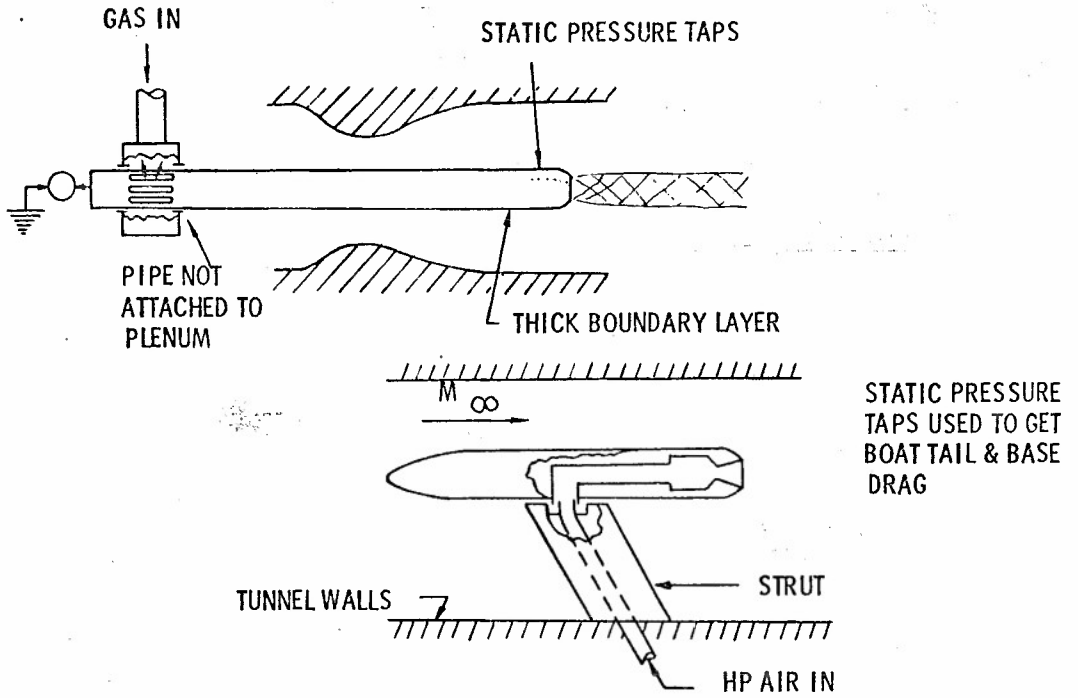


Figure 12. Isolated Tests in Wind Tunnel.

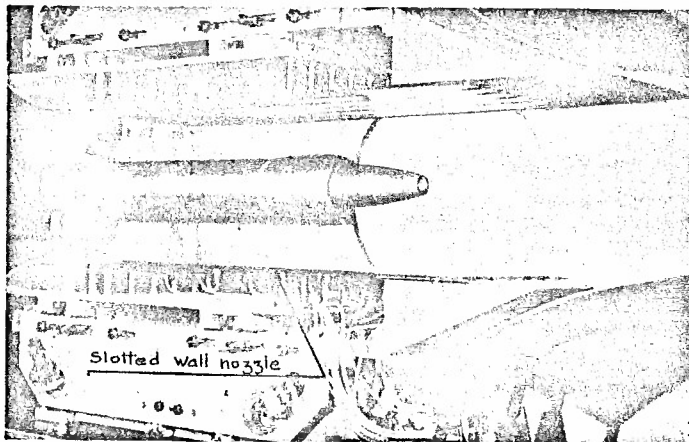
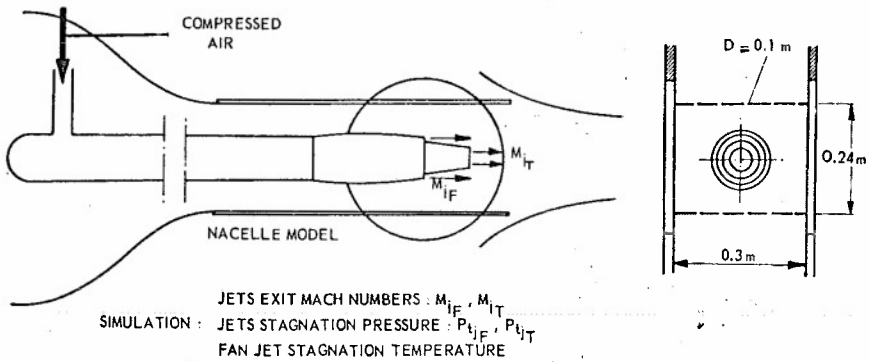
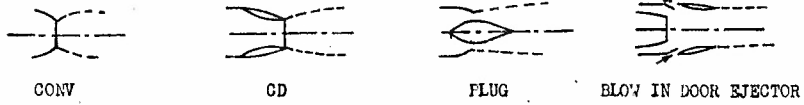
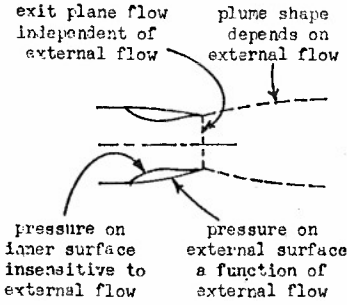


Figure 13. Fan Engine Afterbody Study.

STATIC



IMMUNE TO EXTERNAL FLOW



SENSITIVE TO EXTERNAL FLOW

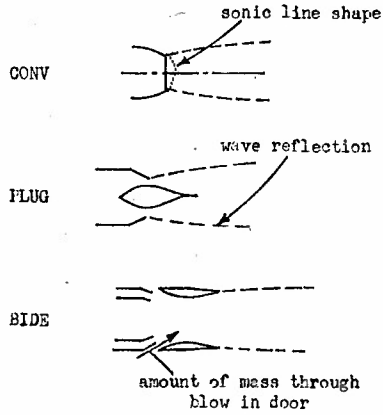
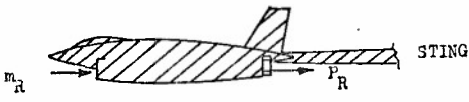


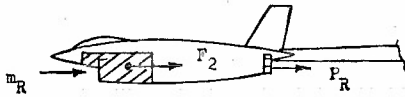
Figure 14. Static and Dynamic Nozzle Tests.

FIXED  $M_o$ ,  $\alpha$ , and NOZZLE AREA RATIO

CROSS HATCHED IS METRIC



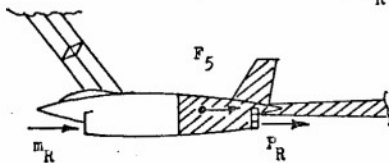
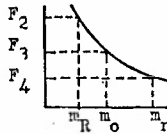
$$F_1 = D + D_I + \Delta D_I(m_R) + \Delta D_E(P_R) + D_{st}$$



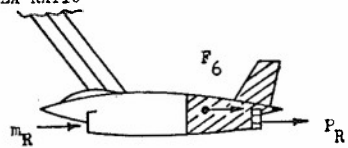
$$F_2 = D_I + \Delta D_I(m_R)$$

$$F_3 = D_I + \Delta D_I(m_o)$$

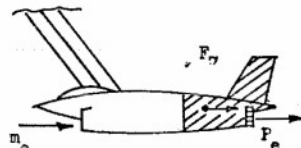
$$F_4 = D_I$$



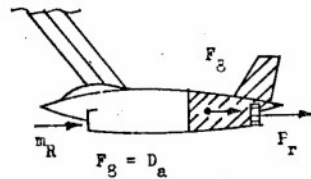
$$F_5 = D_a + \Delta D_E(P_R) + D_{st}$$



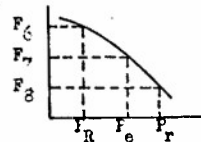
$$F_6 = D_a + \Delta D_E(P_R)$$



$$F_7 = D_a + \Delta D_E(P_e)$$



$$F_8 = D_a$$



$$D(m_R, P_R) = F_1 - \underbrace{[D_I + \Delta D_I(m_R)]}_{F_2} - \underbrace{[\Delta D_E(P_R)]}_{-(F_6 - F_8)} - \underbrace{D_{st}}_{-(F_5 - F_6)}$$

Figure 15. Bookkeeping for Drag.

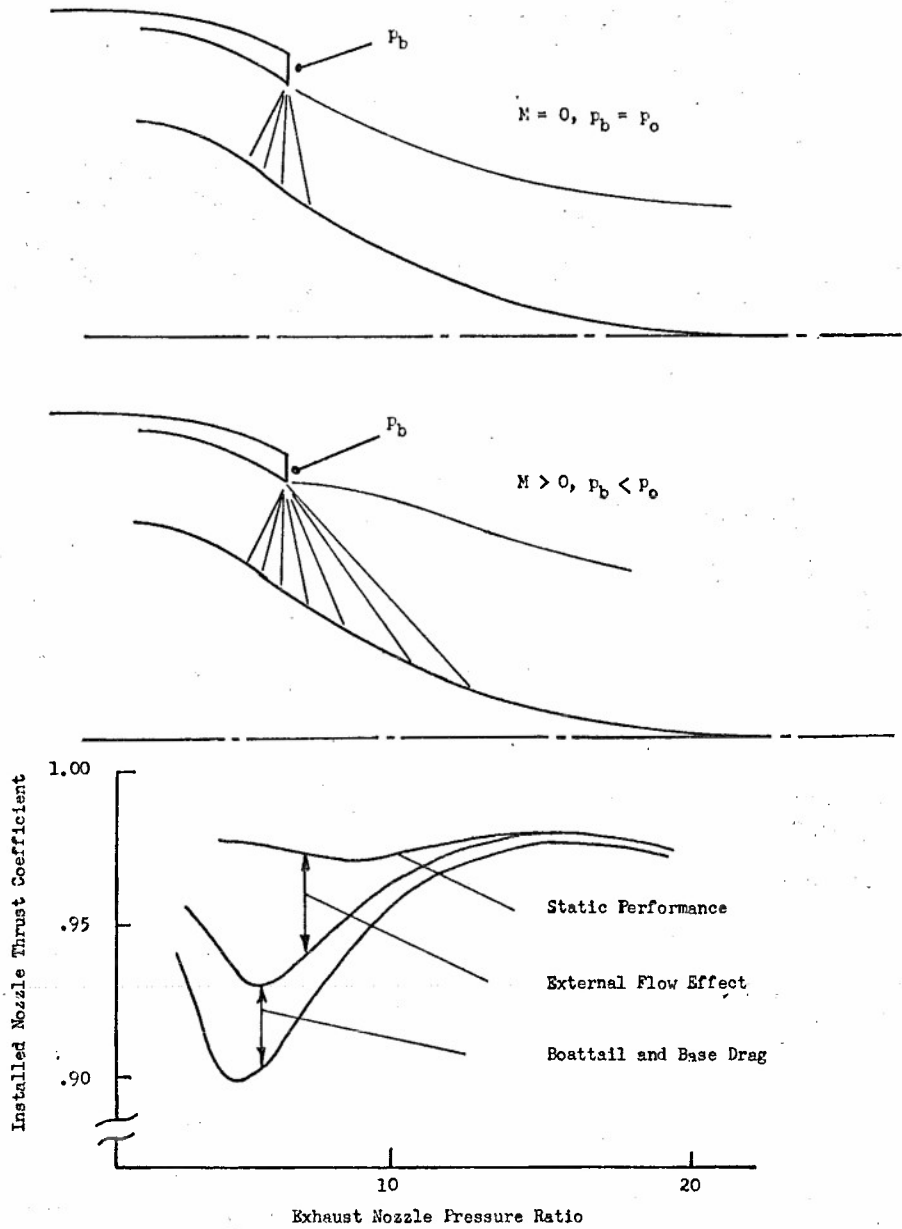


Figure 16. Static and Installed Thrust Coefficient for a Plug Nozzle.

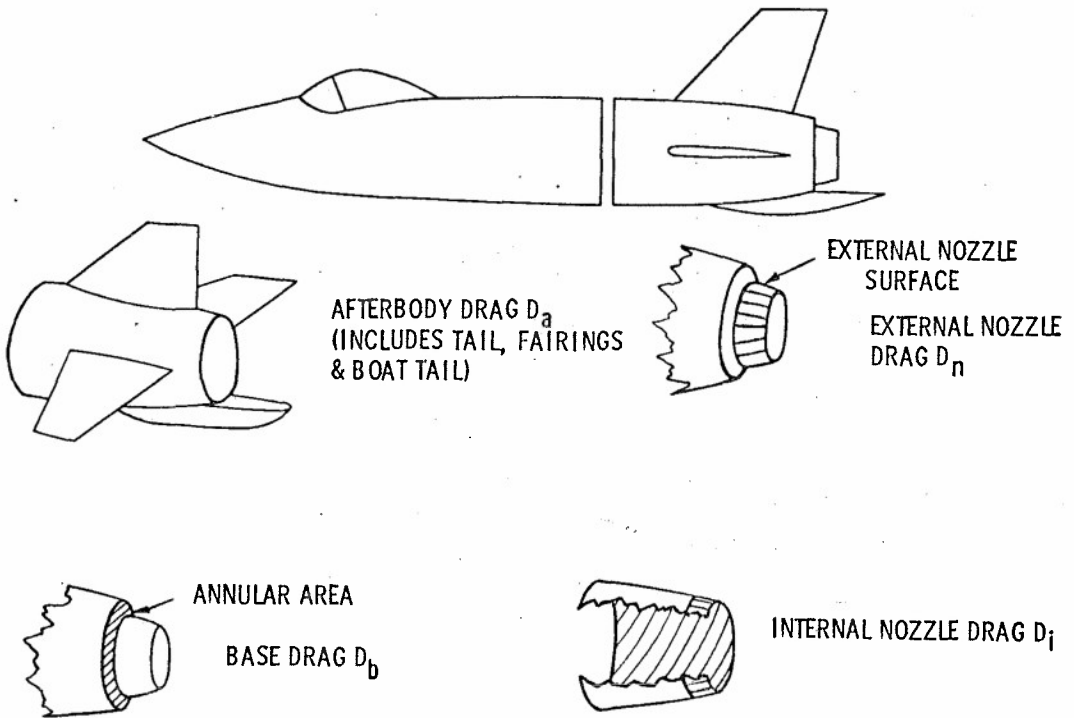


Figure 17. Areas for Drag Definitions.

CORRECTIONS REQUIRED FOR SPLIT PRESSURE,  
SEAL FORCES, AND ANY MOMENTUM OF AIR  
ENTERING NOZZLE

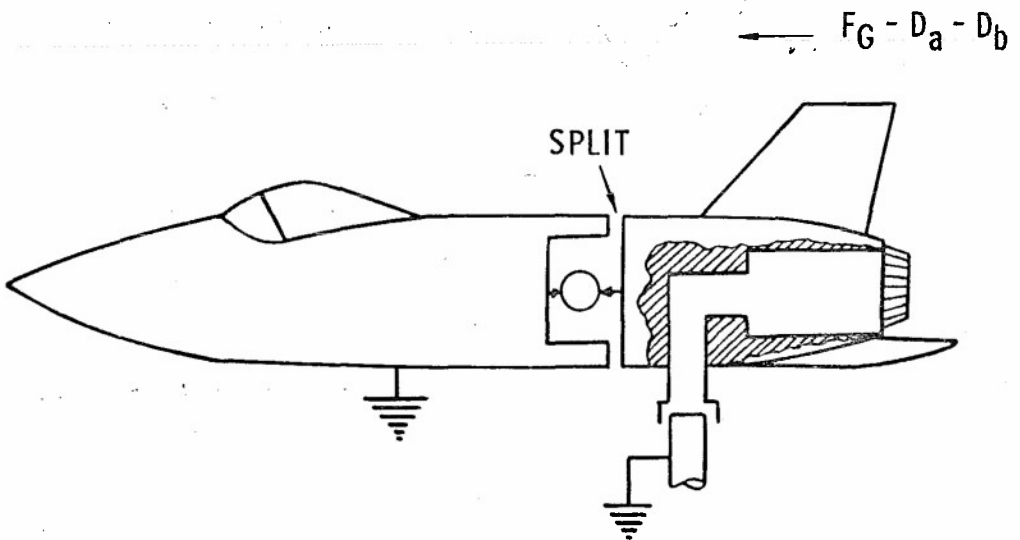


Figure 18. Gross Thrust Minus Drag.

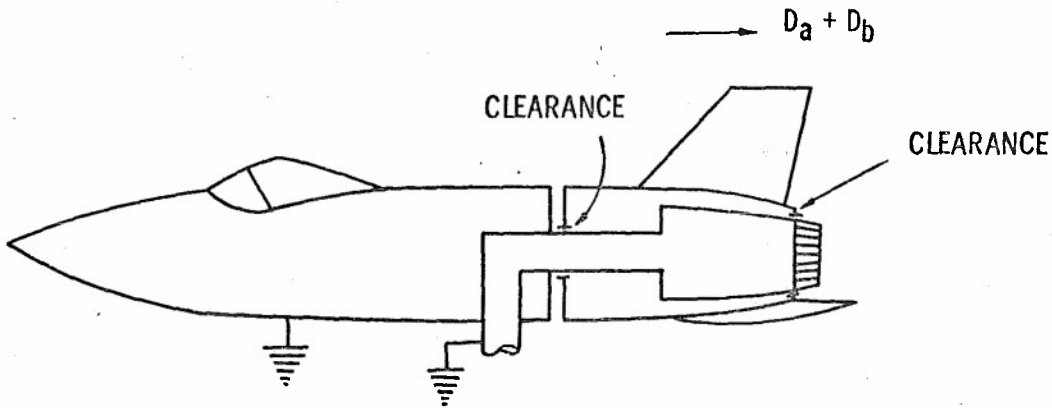


Figure 19. Metric Shell; Afterbody Plus Base Drag.

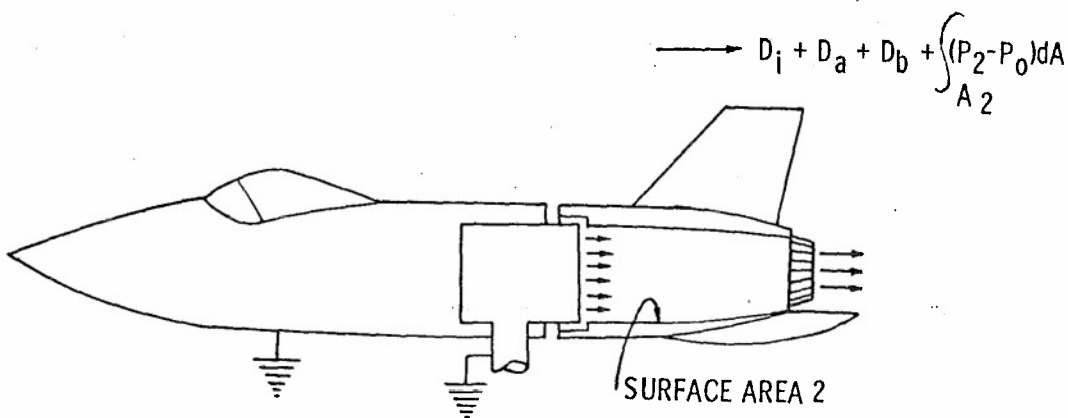


Figure 20. Afterbody, Base, External, and Internal Nozzle Drag.

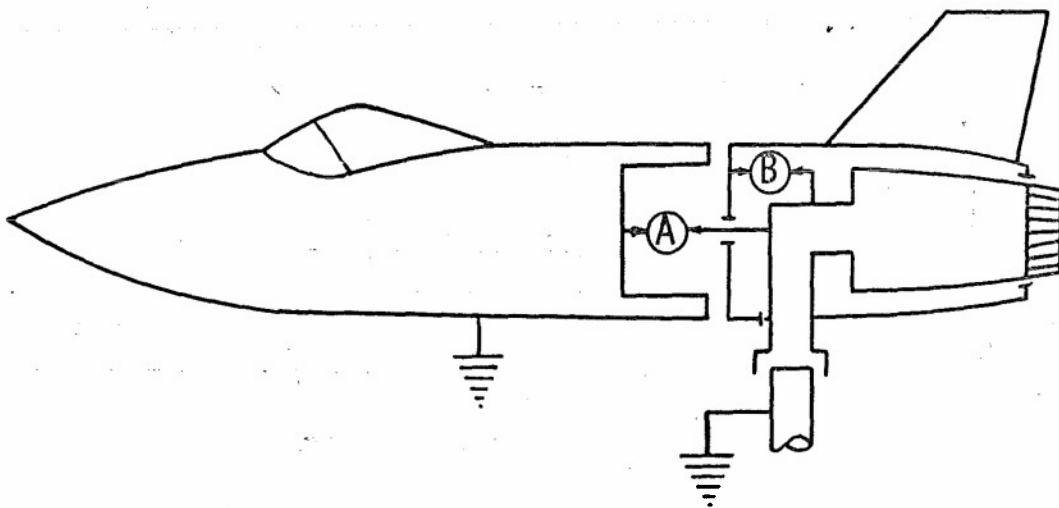


Figure 21. Tandem Balances. Balance (A) reads  $F_g - D_a - D_b$ . Balance (B) reads  $D_a + D_b$ .

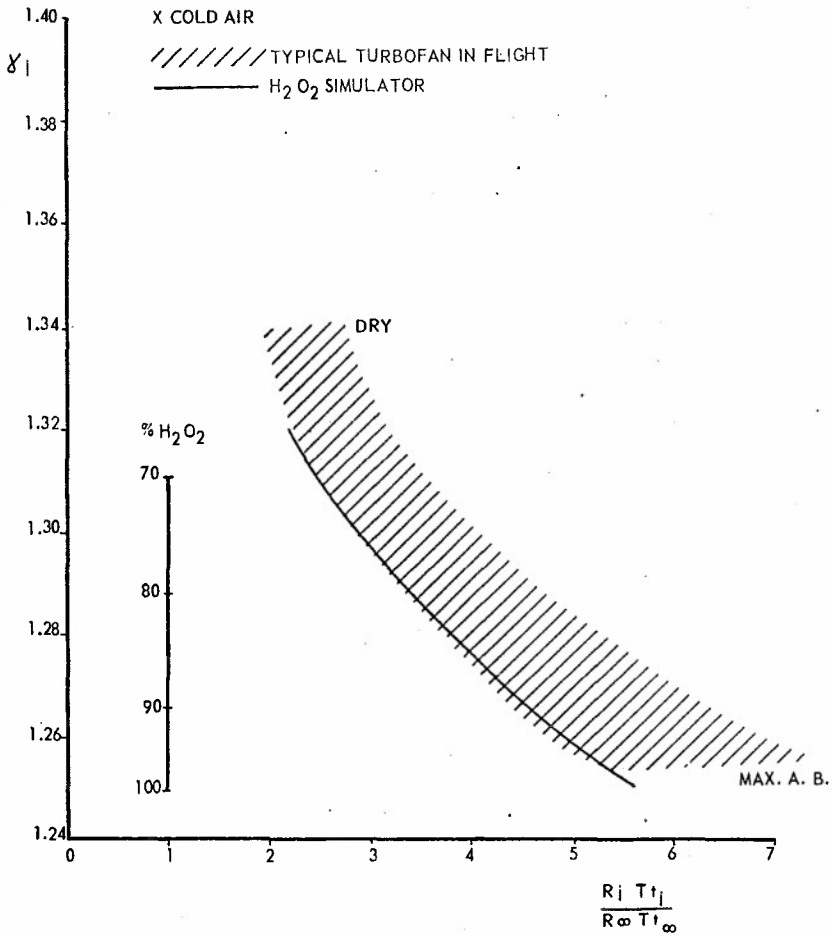


Figure 22. Ratio of Specific Heats Versus Ratio of  $(RT_T)_j / (RT_T)_\infty$  of Turbofans, Air, and Decomposed H<sub>2</sub>O<sub>2</sub> as Experienced in Flight and in Wind Tunnels.

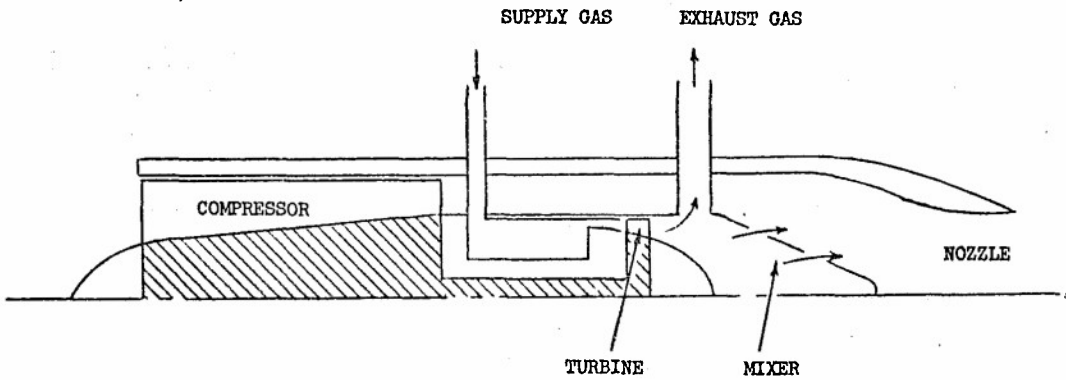


Figure 23. Propulsion System Simulator.

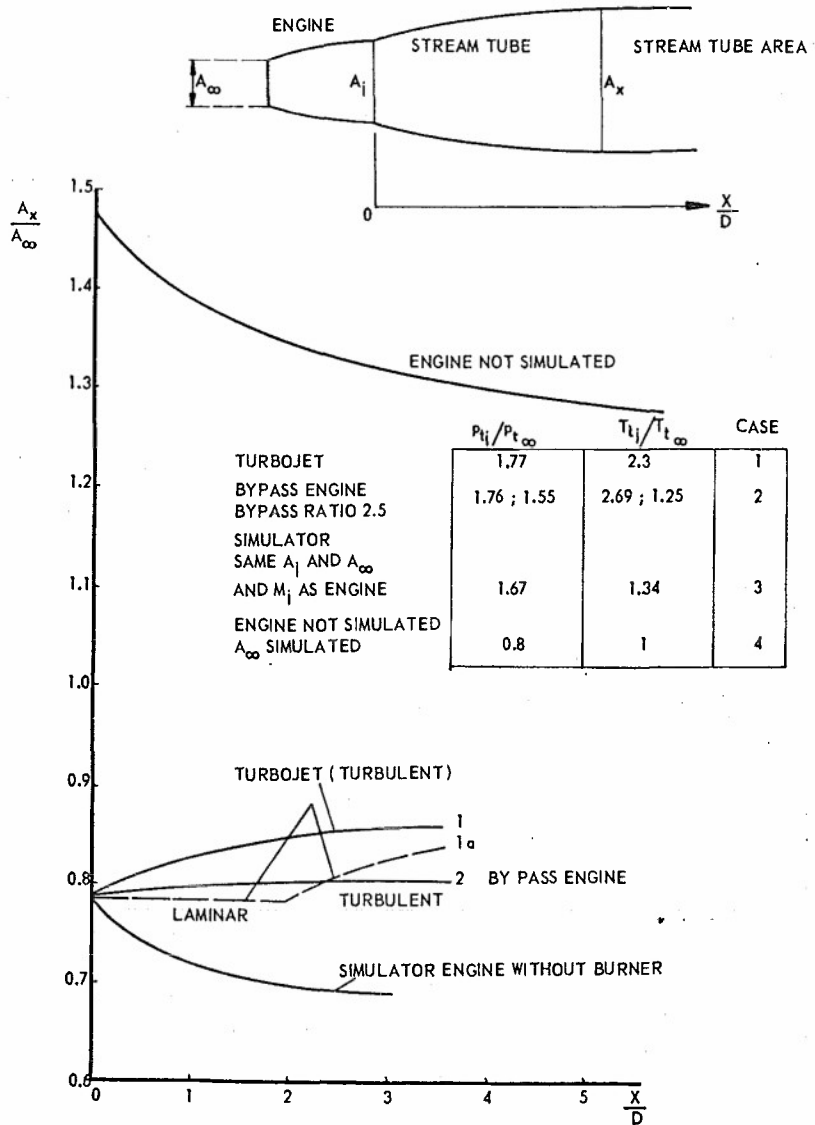


Figure 24. Variation of Jet Engine Stream Tube Due to Mixing.

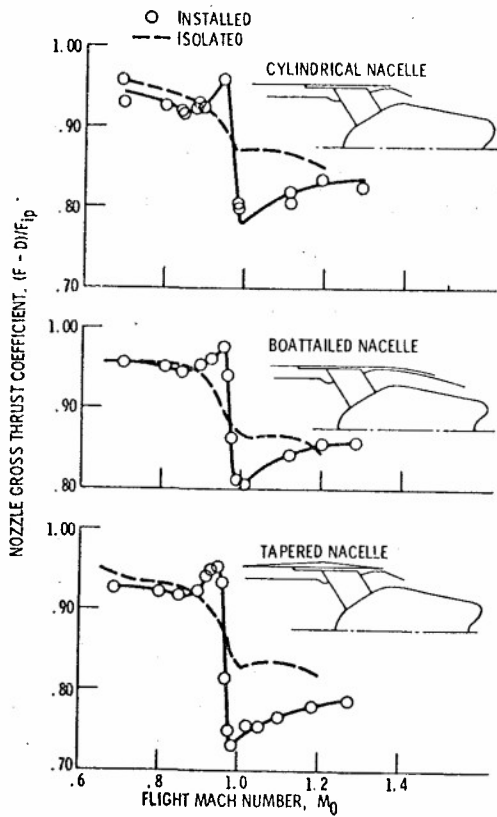


Figure 25. Installation Effect on Plug Nozzle Performance.

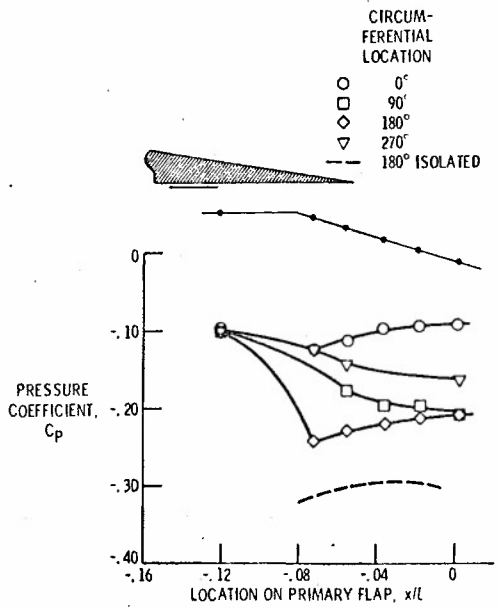


Figure 26. Circumferential Pressure Variation on Primary Flap of Cylindrical Nacelle Assembly.

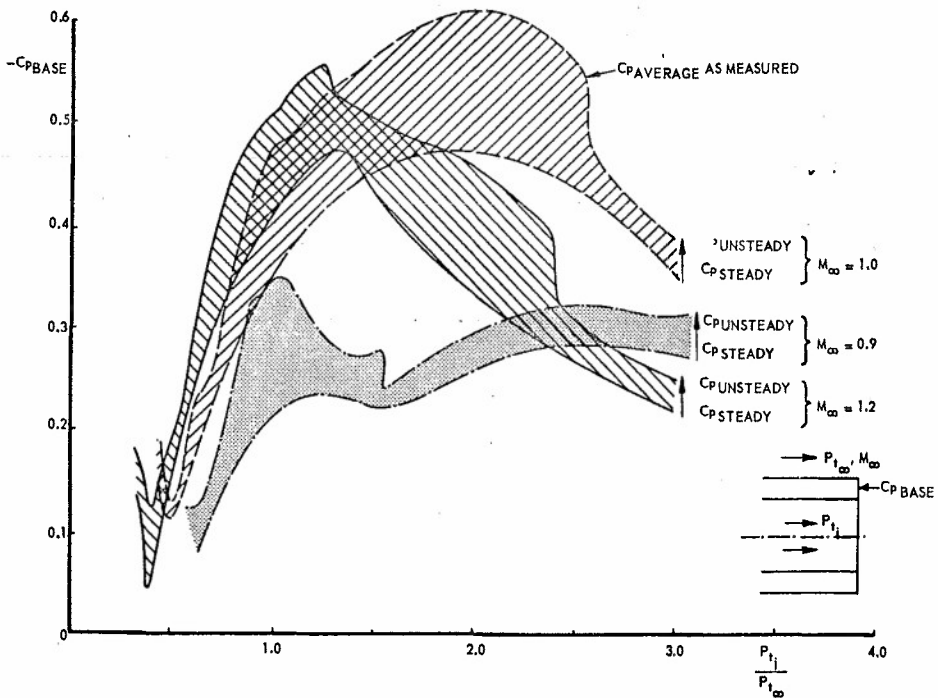
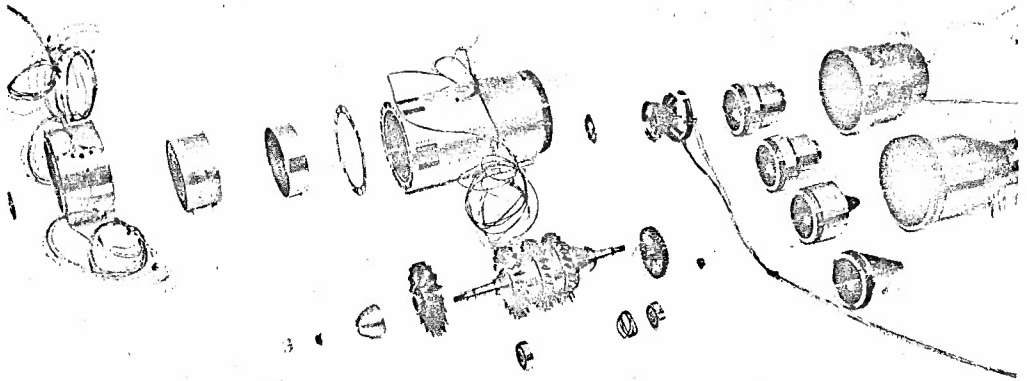


Figure 27. Time Average and Unsteady Pressures on the Base of a Bluff Afterbody.



**SUPERSONIC PROPULSION SIMULATOR**

CONTRACT NO. F33615-69-C-1909

TD 680

TECH DEVELOPMENT, INC.

DAYTON, OHIO

Figure 28. Exploded View of a Supersonic Propulsion Simulator.

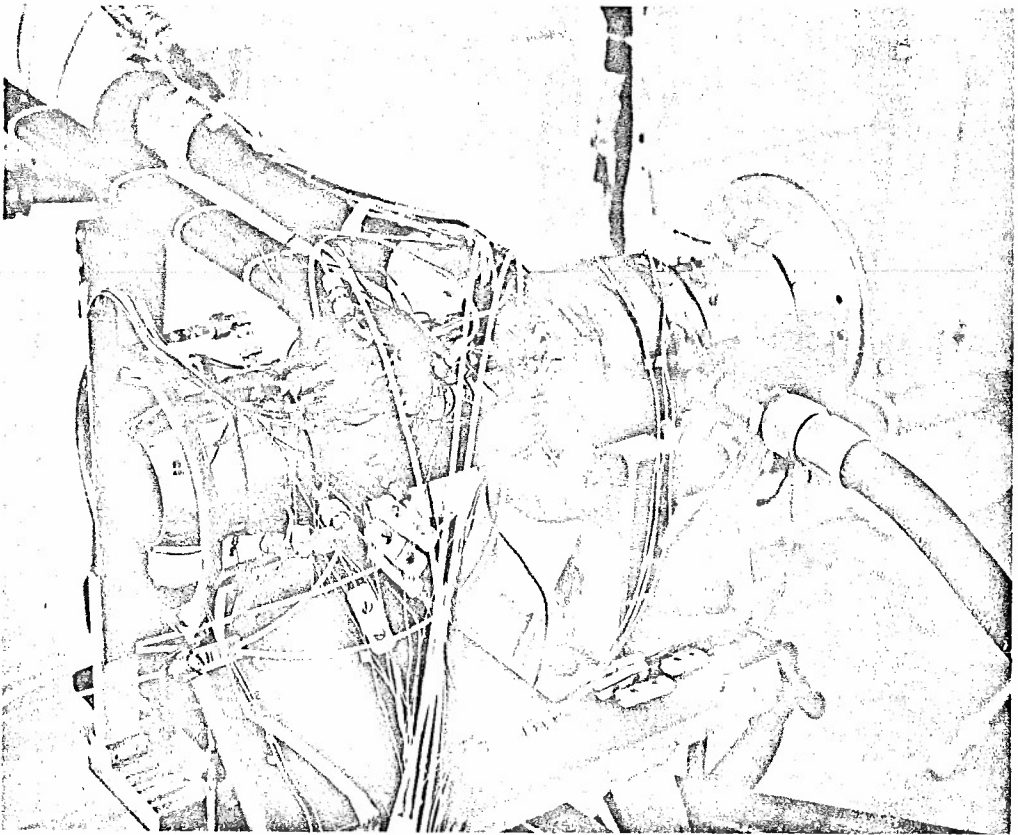


Figure 29. A Supersonic Propulsion Simulator on Test Stand.

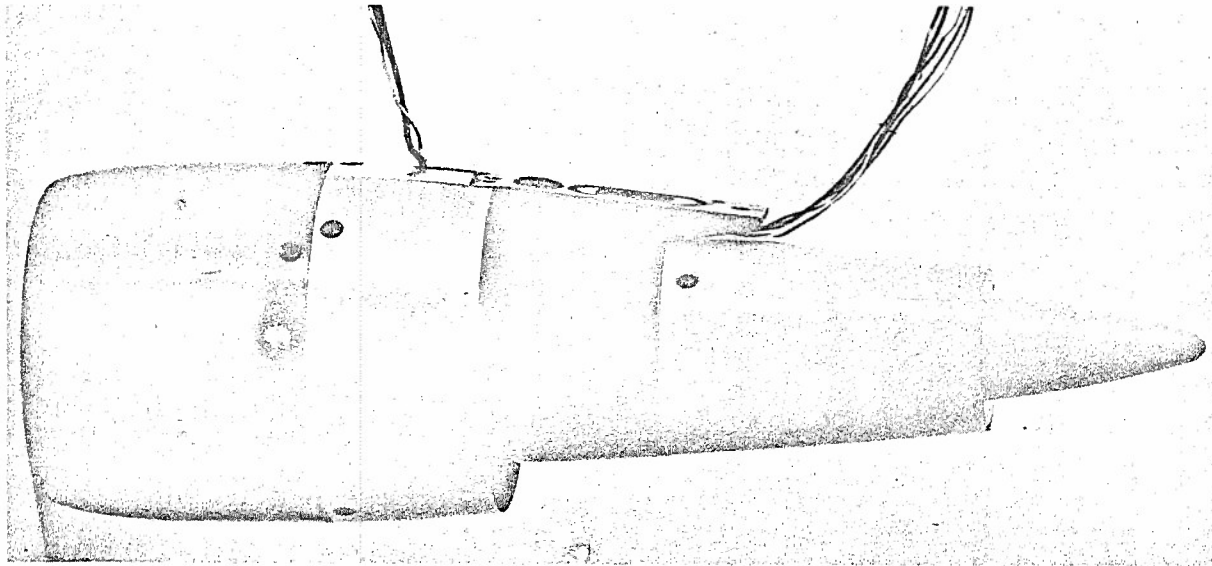
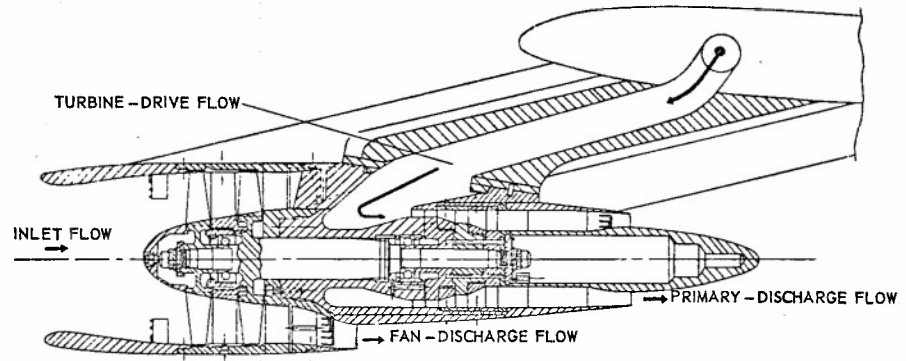


Figure 30. Cross-Sectional View of a Powered Model of a Turbofan.

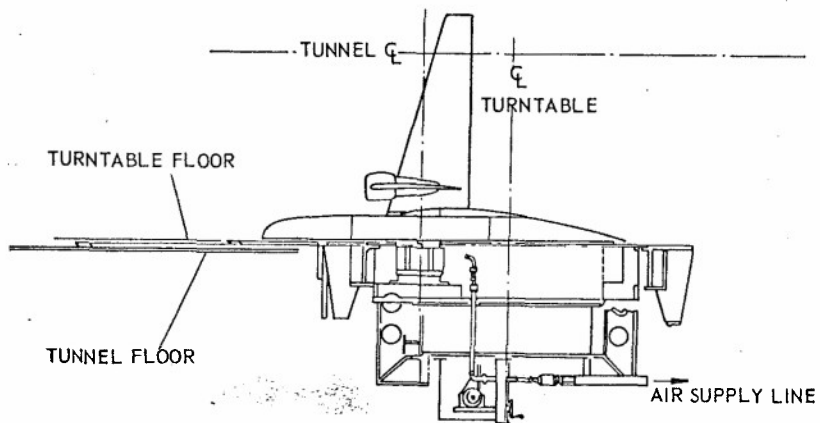


Figure 31. Semi-span Model Tunnel Installation.

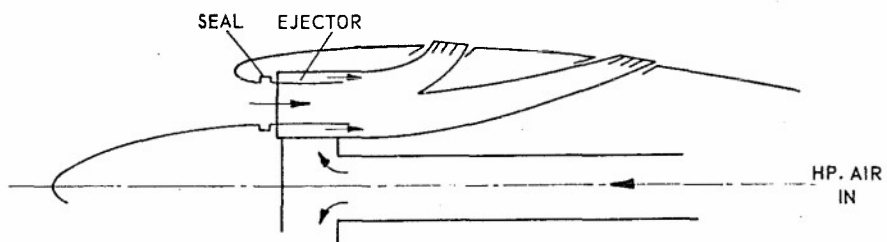
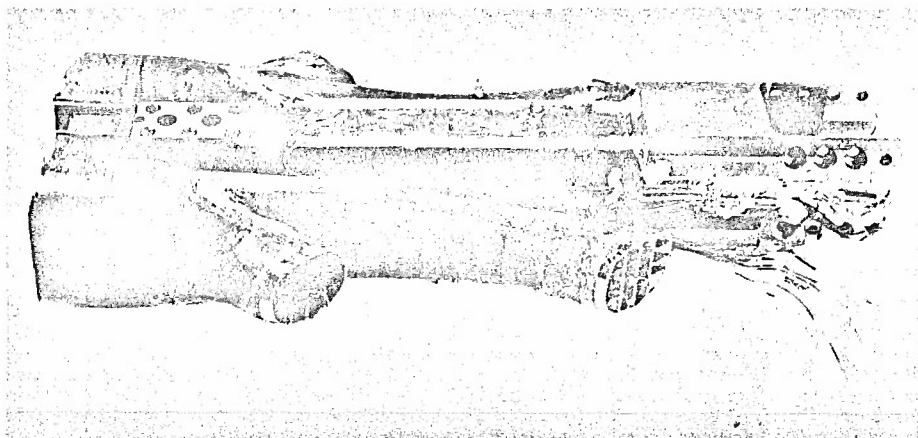


Figure 32. Ejector System for Inlet and Exhaust Flow.

## APPENDIX - SIGNIFICANCE OF TRANSONIC REGIME

It is worthwhile to state why transonic flow is particularly difficult and, being difficult, why it remains important and cannot be avoided.

First of all, look at the influence coefficient formulation for fractional velocity change in a one-dimensional flow

$$\frac{du}{u} = \frac{1}{M^2 - 1} \frac{dA}{A} \quad (A1)$$

In transonic flow, i.e.,  $M$  near unity, the factor multiplying  $dA/A$  is large. A very small change in  $dA/A$  causes a very large change in  $du/u$  and other flow properties. This sensitivity accounts for the extremely low blockage factors which can be tolerated.

Consider the linearized solution for wavy wall in both subsonic and supersonic flows. For a subsonic flow, the solution is

$$u = \frac{U \epsilon \alpha}{\sqrt{1 - M^2}} \left\{ \exp \left[ -\alpha y \sqrt{1 - M^2} \right] \right\} \sin \alpha x \quad (A2)$$

for a flow,  $U$ , over a wavy wall,  $y = \epsilon \sin \alpha x$ . Note that in subsonic flow the perturbation velocity,  $u$ , decays with  $y$ . As  $M$  approaches one, the decay becomes less and less. Of course, the solution is not valid for  $M$  near one, but the trend is clear. This trend indicates that perturbations are experienced at great distances laterally as one approaches Mach number unity.

For supersonic flow over the same wavy wall,

$$u = - \frac{U \epsilon \alpha}{\sqrt{M^2 - 1}} \cos \alpha (x - y \sqrt{M^2 - 1}) \quad (A3)$$

In supersonic flow there is no decay. A line given by  $x = y \sqrt{M^2 - 1}$  has constant amplitude of perturbation. As  $M$  approaches one, this approaches  $x = \text{constant}$ , which means perturbations occur laterally to the main stream. Three points have been illustrated: (1) extreme sensitivity of the flow to small changes in streamtube area, (2) little decay of perturbations laterally, and (3) perturbations perpendicular to the flow.

Difficulty of transonic flow analytically arises from the nonlinear nature of the equations of motion. Solutions depend either on rather specialized approximations which may not be valid everywhere in the flow or else on numerical calculations. In the case of transonic flow, the analytical companion to experimentation is very weak.

Examine the reasons transonic flow cannot be avoided. For the best range consistent with the desire for maximum speed, the flight Mach number usually is on the doorstep of the transonic drag rise. Ferry operations are transonic. Due to sonic boom restrictions, SST aircraft will fly transonically over populated land. Supersonic aircraft must accelerate through the transonic regime which is a region of increasing drag and decaying thrust. Supersonic fighter aircraft do not have sufficient thrust to pull high-g maneuvers and maintain supersonic flight. Aerial combat moves toward transonic speeds due to this limitation. Transonic flight is as important as it is difficult.

PROBLEMES DE MESURE SUR MAQUETTE DE LA POUSSEE D'UN ARRIERE-CORPS D'AVION SUPERSONIQUE  
TUYERES DE REFERENCE .

par Bernard MASURE (\*)

OFFICE NATIONAL D'ETUDES ET DE RECHERCHES AEROSPATIALES (ONERA)

92 - CHATILLON - FRANCE

RESUME -

La technique de mesure de la poussée d'un arrière-corps en soufflerie, couramment utilisée à l'O.N.E.R.A., à l'aide d'un support cylindrique amont est décrite. Cette mesure sert en particulier à corriger les mesures globales effectuées sur maquette complète avec fuseau creux simplifié. La précision est contrôlée par divers tarages comprenant en particulier l'essai d'une tuyère convergente-divergente de référence.

Le contrôle et l'analyse des résultats d'étude de configurations complexes comportant une tuyère primaire convergente s'appuient sur la connaissance des débits et poussées des tuyères soniques correspondantes. Les données concernant de telles tuyères pour une assez large variété de formes résultent d'essais précis effectués à l'atmosphère sans écoulement externe. Les résultats en sont présentés et sont comparés aux données théoriques actuellement disponibles.

SUMMARY -

PROBLEMS OF MEASUREMENT ON MODEL OF THE THRUST OF A SUPERSONIC AIRCRAFT AFTER-BODY .  
STANDARD NOZZLES .

The technique, currently used at ONERA, for measuring in wind tunnel, through an upstream cylindrical strut, the thrust of an after-body is described. With this measurement it is possible, in particular, to correct the global measurements made on complete models with simplified hollow nacelles. Precision is checked by various calibrations including, among others, tests on a standard convergent-divergent nozzle.

Checking and analysing the results on complex configurations including a primary convergent nozzle are based on the knowledge of mass flow rates and thrusts of corresponding sonic nozzles. Data concerning such nozzles for a rather broad variety of shapes result from precise tests performed within the atmosphere, without external flow. Their results are presented and compared with theoretical data currently available.

1 - INTRODUCTION -

La mise au point d'un avion de transport supersonique nécessite une optimisation poussée de ses divers constituants et une estimation aussi correcte que possible de ses futures performances. Il en est ainsi de l'avion "CONCORDE" dont le fuseau moteur et, plus particulièrement, l'arrière-corps sont l'objet d'une étude expérimentale minutieuse qui est poursuivie depuis plusieurs années dans les souffleries de l'O.N.E.R.A. et à l'étranger.

- La note présente se propose de rappeler les techniques mises en oeuvre à l'O.N.E.R.A. pour évaluer, en gaz froid et sur une maquette d'arrière-corps isolé, les performances de poussée du système d'éjection qui complètent les mesures effectuées dans d'autres laboratoires sur un modèle d'avion complet et à partir desquelles il est possible de classer les diverses évolutions d'arrière-corps envisagées.
- Les caractéristiques essentielles de la balance de poussée utilisée dans la soufflerie supersonique S5 Ch de l'O.N.E.R.A. seront donc rappelées et la voie suivie pour évaluer les débits, poussées et taux de détente sera décrite. La précision des mesures est contrôlée par divers tarages comprenant en particulier l'essai d'une tuyère convergente-divergente étalon dont le coefficient de poussée peut être évalué théoriquement. Le calcul de ce coefficient, qui met en jeu diverses corrections, est développé : l'occasion est ainsi donnée de mettre l'accent, en ce qui concerne la poussée, sur les distorsions des lois de détente de l'air par rapport à celles d'un gaz parfait de chaleurs spécifiques constantes à  $\gamma = 1,4$ .
- Les mesures effectuées en soufflerie sur arrière-corps isolé et avec écoulement externe sont complétées à l'O.N.E.R.A. par des mesures exécutées au point fixe permettant une optimisation séparée de la géométrie interne de l'arrière corps puisque, en configuration de croisière supersonique, les caractéristiques aérodynamiques des écoulements internes sont indépendantes de celles de l'écoulement externe. Le banc au point fixe qui permet ces mesures est brièvement décrit. Quelques résultats obtenus sur ce banc et concernant des tuyères convergentes coniques de formes variées sont d'abord donnés et comparés à quelques données théoriques actuellement disponibles. Ils peuvent servir de point de départ pour aborder, sous l'angle du calcul, l'étude de configurations plus complexes. Un exemple d'une recherche d'optimisation de la géométrie interne d'une tuyère biflux type "CONCORDE", mettant bien en lumière le degré de précision atteint dans les mesures effectuées sur le banc au point fixe, est enfin présenté.

2 - DETERMINATION DES PERFORMANCES D'UN ARRIERE-CORPS EN PRESENCE D'ECOULEMENT EXTERNE -

2.1. - Mesures sur maquette -

Les mesures sur arrière-corps isolé, avec simulation des jets internes à l'aide d'air comprimé froid, sont d'une exécution relativement simple. Elles complètent, comme nous l'avons dit dans l'introduction, les mesures réalisées sur une maquette d'avion complet où la simulation des écoulements internes du fuseau moteur n'est en général pas respectée. Pour préciser notre propos, considérons par exemple le cas des mesures exécutées à l'O.N.E.R.A., à la demande de la S.N.E.C.M.A., pour l'avion "CONCORDE".

(\*) Ingénieur Chef de Groupe de Recherches, Direction Aérodynamique.

Nous avons représenté sur la figure 1, d'une part, le schéma de l'avion CONCORDE complet muni de ses deux nacelles bi-moteurs et d'autre part, la partie de ces nacelles effectivement étudiée en soufflerie à l'O.N.E.R.A.

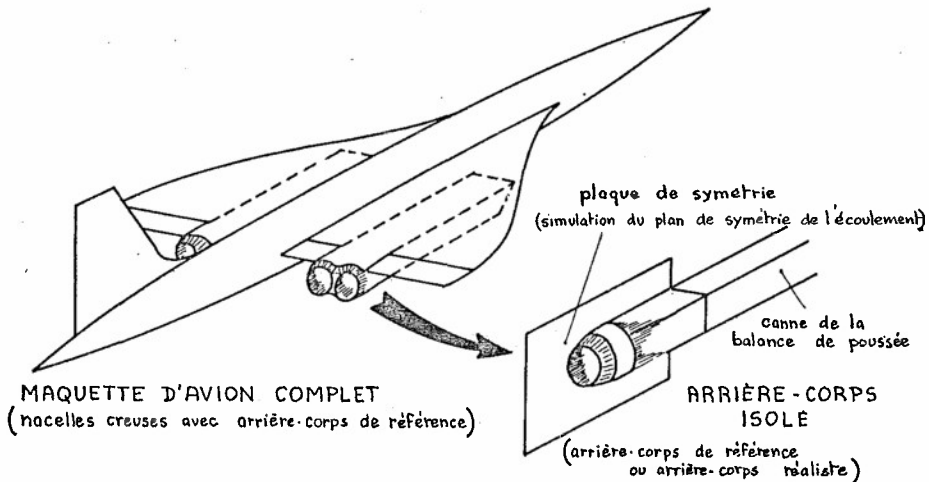


Fig. 1 - Mesure de poussée sur arrière-corps isolé.

En raison de la symétrie approchée que présentent les deux systèmes propulsifs d'une même nacelle, on se contente en soufflerie d'étudier la partie arrière d'une demi-nacelle en matérialisant, par une plaque, le plan de symétrie de la nacelle. Ce demi arrière-corps muni de sa plaque de symétrie est placé à l'extrémité de la canne pesée d'une balance de poussée que nous décrivons plus loin.

Les différentes étapes nécessaires pour évaluer les performances globales sont les suivantes :

#### 2.1.1. - Mesures sur maquette d'avion complet -

La maquette d'avion complet est équipée de deux nacelles creuses présentant dans leur partie aval des formes externes dites de "référence". Les conduits internes de ces nacelles, volontairement simplifiés par rapport au cas réel dans leur partie terminale, sont parcourus par un écoulement naturel qui, pénétrant dans les prises d'air à l'amont, est évacué en régime sonique ou légèrement supersonique à l'aval. La loi de section des conduits internes est telle que le débit qui y circule est égal au débit exact qui pénétrerait dans les prises d'air si la maquette était motorisée.

L'écoulement externe est, en conséquence, correctement simulé au voisinage de l'entrée des nacelles.

Dans le plan de sortie par contre, l'écoulement interne ne possède pas les caractéristiques aérodynamiques du cas réel : la simulation y est donc incorrecte.

Les mesures exécutées en soufflerie sur ce type de maquette permettent de soustraire de l'effort total mesuré la traînée due à l'écoulement interne et de déduire celle due à l'écoulement externe.

Imaginons maintenant le cas réel de l'avion motorisé et muni de nacelles, identiques dans leur partie amont à celles du cas précédent, mais possédant dans leur partie aval les caractéristiques géométriques d'un arrière-corps réaliste tant du point de vue externe que du point de vue interne. Si l'on veut alors déterminer les performances globales dans ce dernier cas, il faut compléter la mesure de la traînée externe précédemment évoquée de celles de la poussée interne du système propulsif et de l'écart des traînées externes existant entre l'arrière-corps "réaliste" et l'arrière-corps "de référence".

C'est la somme de ces deux derniers termes qui est estimée, en première approximation, en soufflerie à l'aide de notre balance de poussée en simulant la propulsion au moyen d'air comprimé froid.

#### 2.1.2. - Mesure en soufflerie de la traînée de l'arrière-corps de référence (O.N.E.R.A.)

On place à l'extrémité de la canne pesée de la balance de poussée un demi arrière-corps de référence muni de sa plaque de symétrie. La canalisation interne de cet arrière-corps, identique à celle de la maquette d'avion complet, est parcourue par un écoulement de mêmes caractéristiques que celles de l'écoulement naturel qui traversait les nacelles creuses de la maquette d'avion complet. L'écoulement externe a pour nombre de Mach  $M_0$ . On tire alors de la relation qui traduit l'équilibre de la partie pesée de la balance une grandeur  $X_A$  égale à la somme algébrique de la poussée de l'écoulement interne  $X_{i,REF}$ , d'un frottement parasite  $X_{f_A}$  le long de la partie cylindrique de la canne pesée et de la traînée externe  $D_{REF}$  de l'arrière-corps de référence :

$$(1) \quad X_A = X_{i,REF} + X_{f_A} - D_{REF}$$

La poussée interne  $X_{i,REF}$  est, par ailleurs, déduite de la connaissance du débit interne et de celle du coefficient de poussée de la tuyère sonique ou légèrement supersonique que constitue la canalisation interne. Ce coefficient de poussée interne est évalué sur le banc au point fixe que nous décrivons brièvement plus loin.

Connaissant par conséquent  $X_{L\text{REF}}$ , on déduit de (1) la grandeur  $X'_1 = X_1 - X_{L\text{REF}}$ , soit encore :

$$(2) \quad X'_1 = X_{f1} - D_{\text{REF}}$$

### 2.1.3. - Mesure en soufflerie sur l'arrière-corps réaliste (O.N.B.R.A.) -

On remplace le demi arrière-corps de référence par un demi arrière-corps réaliste muni, lui aussi, d'une plaque de symétrie. L'écoulement externe a le même nombre de Mach  $M_0$  que lors de la mesure précédente et l'on simule la motorisation (écoulement primaire et secondaire) au moyen d'air comprimé froid.

On tire de l'équation d'équilibre de la partie pesée une grandeur  $X_2$  égale, comme plus haut, à la somme algébrique de trois termes :

$$(3) \quad X_2 = X_{L\text{RÉALISTE}} + X_{f2} - D_{\text{RÉALISTE}}$$

### 2.1.4. - Synthèse -

Connaissant maintenant, grâce aux deux mesures précédentes, les valeurs des grandeurs  $X'_1$  et  $X_2$ , on déduit par différence :

$$X_2 - X'_1 = X_{L\text{RÉALISTE}} + \Delta X_f - \Delta D$$

$$\text{en posant} \quad \begin{cases} \Delta X_f = X_{f2} - X_{f1} \\ \Delta D = D_{\text{RÉALISTE}} - D_{\text{RÉFÉRENCE}} \end{cases}$$

Comme, de plus, le niveau de la pression génératrice de la soufflerie est le même pour les deux types de mesure :  $\Delta X_f = X_{f2} - X_{f1} = 0$

Les mesures réalisées à l'O.N.B.R.A. permettent donc d'évaluer, comme il le fallait, la somme :

$$X_{L\text{RÉALISTE}} - \Delta D$$

Décrivons donc maintenant les caractéristiques essentielles de l'installation expérimentale utilisée pour les mesures précédentes.

### 2.2. - Description succincte de la balance de poussée (Fig. 2) -

Le modèle étudié est placé à l'extrémité d'une conduite cylindrique qui traverse le col de la soufflerie et permet le passage des flux d'air comprimé froid simulant les jets primaire et secondaire.

Cette conduite, constituant la partie mobile de la balance de poussée, est suspendue par l'intermédiaire d'un parallélogramme déformable à l'intérieur d'un caisson placé dans le collecteur de la soufflerie. La poussée de l'arrière-corps est équilibrée par une contre pression réglable s'exerçant sur un piston lié à la conduite.

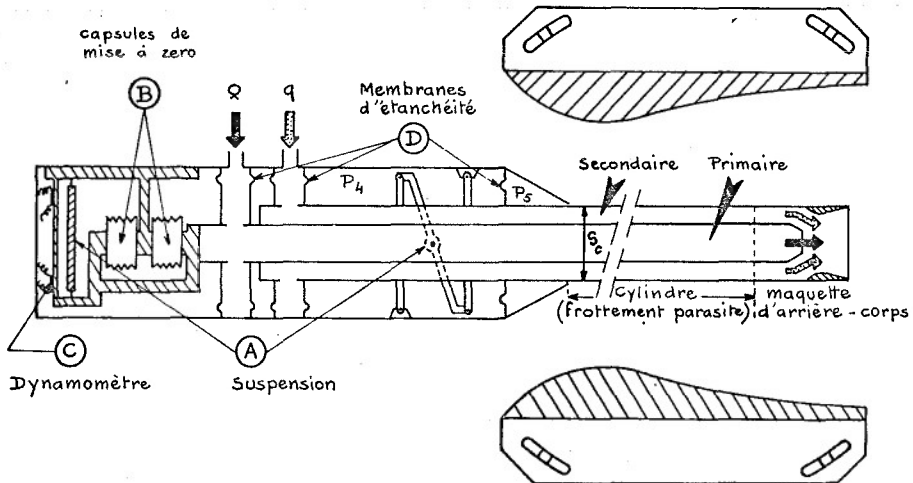


Fig. 2 - Balance de poussée (soufflerie supersonique S5 de CHALATS-MEUDON)

Afin d'éviter tout effort parasite à l'admission d'air comprimé, les alimentations se font perpendiculairement à l'axe de la poussée.

Nous remarquons en A les branches de la suspension dont l'une est composée d'un trois barres pour éviter les contraintes dues à des déformations provoquées par les dilatations ; en B les capsules servant à afficher la

pression nécessaire au retour à zéro de la partie suspendue ; en C le dynamomètre utilisé pour vérifier cette remise en équilibre. Enfin en D nous voyons les membranes de caoutchouc qui sont utilisées pour assurer l'étanchéité au niveau des alimentations en air comprimé. Ces membranes roulent très légèrement sur elles-mêmes lors du déplacement de la partie suspendue. Ce déplacement a été réduit au minimum ( $\pm 0,04$  mm) grâce à des butées, non représentées sur la figure. On pourra se reporter à [1] pour de plus amples détails relatifs à la balance de poussée.

La veine de la soufflerie, bidimensionnelle, est constituée de deux blocs tuyères identiques susceptibles de subir, indépendamment l'un de l'autre, une légère rotation par rapport à leurs positions nominales. Il est ainsi possible de corriger, partiellement, la perturbation provoquée par la canne de la balance et d'obtenir, au niveau du plan de raccordement avec la maquette, un nombre de Mach sensiblement constant et égal au nombre de Mach moyen qui existe, sur la maquette d'avion complet, dans le même plan.

Le montage décrit ici ne peut cependant pas représenter exactement les phénomènes réels et nous considérons que les résultats obtenus ont surtout une valeur relative et permettent de classer entre elles les diverses solutions car nous avons constaté que la similitude était assez correctement réalisée en ce qui concerne les épaisseurs de couche limite externe au niveau de l'arrière-corps.

Précisons maintenant quelques grandeurs :

- Dimensions de la veine de soufflerie :  $300 \times 300$  mm <sup>2 entrées et 2 sorties</sup>
- Dimensions de la canne de soufflerie :  $400 \times 70$  mm<sup>2</sup> (environ 6 % d'obstruction) <sup>~ module cross section</sup>
- Pression génératrice de la soufflerie :  $\sim 1/2$  bar
- Température génératrice de la soufflerie :  $\sim +40^\circ\text{C}$
- Effort moyen mesuré par la balance :  $\sim 15$  daN
- Débit d'air comprimé traversant la maquette :  $\sim 300$  g/s.

6% blockage

Posons :

X : résultante des actions mécaniques exercées sur la canne et la maquette par l'écoulement extérieur et les écoulements internes

$S_c$  : section de la canne

H : effort transmis par les capsules après remise à zéro

$P_4$  : pression régnant dans le carter

$P_5$  : pression régnant sous la coiffe de raccordement (voir fig. 2).

$\alpha_4$  : aire efficace d'action de la pression  $P_4$  (évaluée par un tarage préliminaire)

L'équation d'équilibre de la partie pesée s'écrit alors :

$$X + (\alpha_4 - S_c) P_5 = H + \alpha_4 P_4$$

ou

(4)

$$X = H + \alpha_4 P_4 - (\alpha_4 - S_c) P_5$$

Pour simplifier, nous avons omis dans la relation (4) les réactions parasites légères que les tarages mettent quelquefois en lumière au niveau des membranes d'alimentation.

C'est en utilisant la relation (4) et en procédant à deux mesures successives qu'il est possible, comme nous l'avons expliqué aux § 2.1.2. et 2.1.3., d'évaluer les performances d'un arrière-corps.

Analysons maintenant la voie suivie pour caractériser les propriétés des flux internes.

### 2.3. - Calcul des débits -

Les débits sont évalués par la méthode du col sonique, universellement reconnue comme la plus précise, et au sujet de laquelle divers travaux ont été entrepris à l'O.N.E.R.A. ces dernières années [2], [3], [4].

Rappelons la formule :

(5)

$$q = \bar{q} \times C_{D_v} = \left[ k \times \frac{p_1}{\sqrt{T_1}} \times A \times (C_{D_s} \times C_{D_k}) \right] \times C_{D_v}$$

dans laquelle :

$$- k = \text{constante} = \sqrt{\frac{\gamma}{\pi R}} \left( \frac{2}{\gamma + 1} \right)^{\frac{\gamma + 1}{2(\gamma - 1)}}$$

avec :  $\gamma = 1,4$

$\pi$  = nombre de molécules-gramme d'air par unité de masse

$R$  = constante universelle des gaz parfaits.

-  $p_1$  = pression d'arrêt isentropique de l'écoulement en dehors de la couche limite

-  $T_1$  = température d'arrêt isentropique (en degré absolu)

-  $A$  = aire géométrique du col

-  $A(C_{D_s} C_{D_k})$  = aire sonique aérodynamique

avec  $C_{D_s}$  = coefficient de réduction de débit due à l'effet de la viscosité

$C_{D_k}$  = coefficient de réduction de débit due à la courbure de la ligne sonique (écoulement non uniforme dans le plan du col)

-  $C_{D_V}$  = facteur multipliant le débit  $\bar{Q}$  calculé pour un gaz calorifiquement parfait à  $\gamma$  compte de l'effet de compressibilité (effet viriel). Ce dernier facteur est donné simple suivante [2] :

$$C_{D_V} = 1 + 0,035 \frac{p_i (atm)}{T_i - 210}$$

Le calcul d'un débit par (5) nécessite donc, outre la mesure de  $p_i$  et  $T_i$ , l'évaluation des coefficients  $C_{D_S}$  et  $C_{D_K}$ .

**Coefficient  $C_{D_S}$**  : Ce coefficient, égal, dans le cas d'un col débitmétrique à symétrie de révolution, à  $1 - 2 \delta_c^2/h$  ( $\delta_c$  : épaisseur de déplacement de la couche limite au col ;  $h$  : rayon du col) peut être relié [5] au nombre de Reynolds  $Re_{L,h} = \frac{\rho_i a_i R}{\mu}$  par une loi simple qui, dans le cas d'une couche limite turbulente, prend la forme :

$$(6) \quad (1 - C_{D_S}) Re_{L,h}^{-1/6} = C_{St}$$

Il suffit donc de calculer la couche limite, pour une géométrie donnée, dans un cas particulier (intégration approchée de l'équation intégrale de von Karman) pour connaître  $C_{D_S}$  dans tous les cas par application de (6).

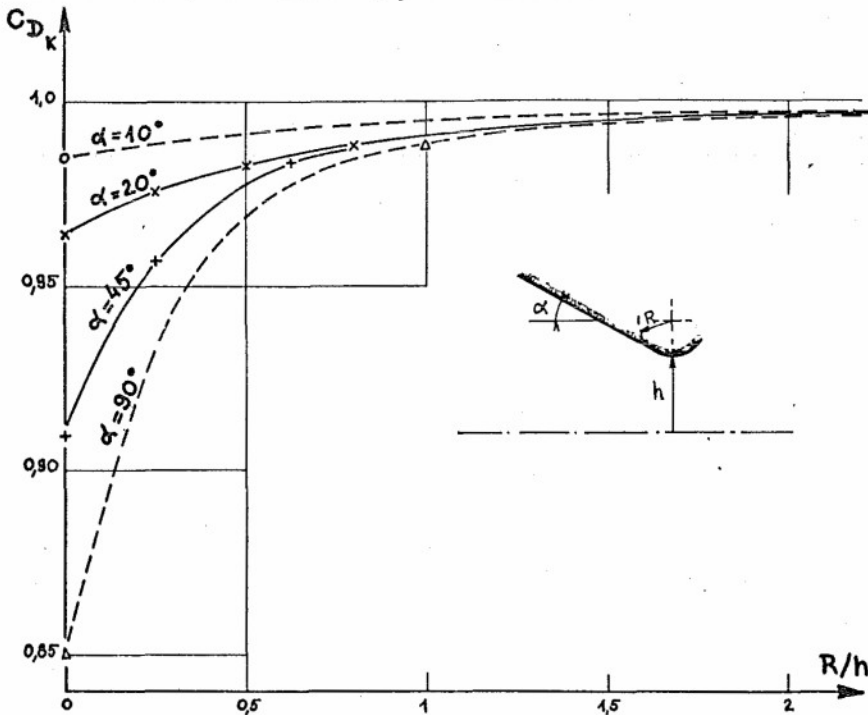
**Coefficient  $C_{D_K}$**  : Le calcul par développements limités de la fonction potentielle d'un écoulement irrotationnel à symétrie de révolution permet de définir complètement l'écoulement au voisinage du point sonique sur l'axe. Il est alors possible, par une simple intégration, de calculer le coefficient de débit  $C_{D_K}$  d'une tuyère dont le profil serait identique à une ligne de courant matérialisée de l'écoulement calculé.

Comme les développements mathématiques mis en oeuvre pour calculer la fonction potentielle ne sont valables qu'au voisinage immédiat du point sonique sur l'axe, on ne retient du champ d'écoulement calculé que la partie proche de ce point sonique et l'on se contente de caractériser les lignes de courant par leurs taux de courbure  $h/R$  en leurs sommets. On peut ainsi établir une correspondance entre ce taux de courbure local et le coefficient de débit  $C_{D_K}$ . Attribuant alors à cette correspondance un caractère d'universalité, on peut calculer le coefficient de débit  $C_{D_K}$  d'une tuyère quelconque pourvu que celle-ci présente au col une courbure modérée.

C'est ainsi que l'on procède à l'O.N.E.R.A. où les méridiennes des cols débitmétriques sont circulaires avec un taux de courbure égal à 0,25 ( $R/h = 4$ ). Le coefficient  $C_{D_K}$  vaut alors :  $1 - 1,4 \cdot 10^{-3}$ .

Si l'on voulait par contre utiliser un col débitmétrique à courbure prononcée, afin de réduire par exemple la correction due à la couche limite et limiter de cette façon la part d'incertitude que comporte toujours une telle correction, il y aurait lieu de tenir compte non seulement du taux de courbure de la paroi au col mais aussi de la nature exacte du profil de celle-ci à l'amont du col, pour calculer  $C_{D_K}$ .

La figure 3, tirée de [4] en apporte la preuve. Les résultats expérimentaux présentés sur cette figure montrent, en effet, que pour des taux de courbure élevés au col, le coefficient  $C_{D_K}$  est, comme il fallait l'attendre, très sensible à l'angle de la paroi à l'amont du col.



Donnons pour terminer et fixer les idées les valeurs que nous attribuons à  $C_{D_K}$ ,  $C_{D_S}$  et  $C_{D_V}$  pour évaluer, au moyen de la relation (5), le débit primaire pour les conditions d'essais habituelles rencontrées sur l'installation de poussée de la soufflerie S5 Ch :

$$C_{D_K} \approx 1 - 1,4 \cdot 10^{-3}$$

$$C_{D_S} \approx 1 - 5 \cdot 10^{-3}$$

$$C_{D_V} \approx 1 + 4 \cdot 10^{-3}$$

Fig. 3 - Coefficient de débit  $C_{D_K}$  d'une tuyère axisymétrique à courbure élevée

## 2.4. - Calcul du taux de détente -

Nous appelons taux de détente le rapport de la pression génératrice  $\varphi_{LJ}$  de l'écoulement principal (le jet primaire) à la pression statique  $p_0$  de l'écoulement externe :  $\varphi_{LJ}/p_0$

La pression statique  $p_0$  est calculée à partir du nombre de Mach moyen de l'écoulement externe au niveau du plan de raccordement du modèle avec la canne et de la pression génératrice de la soufflerie mesurée dans le collecteur.

La pression génératrice  $\varphi_{LJ}$  de l'écoulement primaire pourrait être évaluée tout simplement au moyen d'une ou plusieurs prises de pression d'arrêt (tube "pitot"), judicieusement réparties dans l'écoulement et dont les mesures permettraient, après pondération, de définir une pression génératrice moyenne.

Cette méthode n'a pas été retenue et on lui a préféré une méthode moins directe où la pression génératrice est déduite du débit réduit  $q\sqrt{T_{LJ}}$ , ce qui permet de s'affranchir des difficultés qui surgissent toujours quand il s'agit de définir une pression génératrice moyenne dans un écoulement qui présente, inévitablement, certaines distorsions de pression d'arrêt.

Cette méthode nécessite, comme nous allons le montrer, la mesure de la température génératrice  $T_{LJ}$  et la détermination au préalable de l'aire sonique aérodynamique de l'écoulement.

La loi de conservation de la masse en écoulement permanent conduit en effet à la relation suivante, avec les indices D et J respectivement pour le débitmètre et la tuyère en essais (fig. 4):

$$(7) \quad q = \left[ k \frac{\varphi_{LD}}{\sqrt{T_{LD}}} A_D (C_{D\delta} C_{D\kappa})_D \right] C_{DvD} = \left[ k \frac{\varphi_{LJ}}{\sqrt{T_{LJ}}} A_J (C_{D\delta} C_{D\kappa})_J \right] C_{DvJ}$$

Cette relation permet de calculer le groupement  $(\varphi_{LJ} A_J)^*$  auquel nous rapportons les efforts mesurés :

$$(8) \quad (\varphi_{LJ} A_J)^* = \left[ \varphi_{LJ} A_J (C_{D\delta} C_{D\kappa})_J \right] C_{DvJ} = q \sqrt{T_{LJ}} / k \quad \text{par}$$

$$(9) \quad (\varphi_{LJ} A_J)^* = \left[ \varphi_{LD} A_D (C_{D\delta} C_{D\kappa})_D \right] C_{DvD} \sqrt{\frac{T_{LJ}}{T_{LD}}}$$

La relation (9) montre que le groupement  $(\varphi_{LJ} A_J)^*$  est connu si l'on mesure, outre  $\varphi_{LD}$  et  $T_{LD}$ , la température  $T_{LJ}$ . Il est alors possible par (8) de calculer  $\varphi_{LJ}$  si l'on connaît, par ailleurs, le coefficient de débit  $(C_{D\delta} C_{D\kappa})_J$  de la tuyère (la présence du coefficient correctif  $C_{DvJ}$  ne fait que compliquer légèrement la situation en nécessitant un calcul itératif).

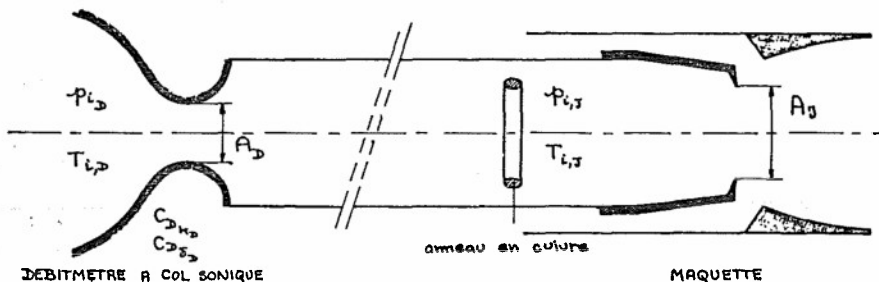


Fig. 4 - Débitmètre et tuyère d'éjection primaire.

- La température d'arrêt isentropique  $T_{LJ}$  est mesurée au moyen d'un anneau en cuivre qui relie entre eux trois thermocouples et qui est placé légèrement à l'amont du col de la tuyère primaire. Des mesures précises ont montré que le coefficient de récupération  $\lambda$  de cet anneau est égal au coefficient de récupération d'un thermocouple à fil tendu ( $\beta = 0,8$  mm). La valeur trouvée  $\lambda = 0,62$  est en bon accord avec [6]. La température  $T_{LJ}$  est ainsi donnée par :

$$T_{LJ} = T_{\text{anneau}} \frac{1 + 0,2 M_J^2}{1 + \lambda \times 0,2 M_J^2} \quad \text{où } M_J \text{ est le nombre de Mach moyen de l'écoulement au niveau de l'anneau.}$$

- Quant au coefficient de débit  $(C_{D\delta} C_{D\kappa})_J$  (appelé aussi coefficient de striction), il est déterminé hors soufflerie sur un banc, spécialement aménagé à cet effet et situé à CHALAIS-NEUDON, comportant un col sonique débitmétrique et une chambre de tranquillisation en amont de la tuyère étudiée. Les dimensions de cette chambre de tranquillisation sont telles que la pression génératrice de l'écoulement peut y être définie sans ambiguïté. Il suffit donc de compléter la mesure de la température génératrice dans cette chambre par celle de la pression génératrice pour calculer le coefficient de débit  $(C_{D\delta} C_{D\kappa})_J$  de la tuyère en utilisant encore la relation (8).

Nous présenterons plus loin quelques résultats de coefficient de débit obtenus récemment à l'O.N.E.R.A., non pas sur l'installation de CHALAIS mais sur le banc de mesure au point fixe de MODANE qui fait aussi office de banc de striction.

## 2.5. - Définition et calcul d'autres grandeurs -

En ce qui concerne l'écoulement secondaire (S) l'usage veut qu'on le caractérise par sa pression génératrice  $-p_{iS}$  et le paramètre sans dimension  $\mu$  défini par :

$$\mu = \frac{q_S}{q_J} \sqrt{\frac{T_{iS}}{T_{iJ}}}$$
 où  $q_S, q_J$  sont les débits et  $T_{iS}, T_{iJ}$  les températures génératrices des écoulements secondaire et primaire respectivement.

En soufflerie  $T_{iS} \sim T_{iJ}$ . On pose donc 
$$\mu = \frac{q_S}{q_J}$$

La pression génératrice de l'écoulement secondaire  $-p_{iS}$  est, soit mesurée directement avec un tube "pitot", soit calculée à partir de la mesure d'une pression statique et du débit secondaire  $q_S$ .

Quant aux poussées, elles sont rapportées systématiquement au groupement  $(p_{iJ} A_J)^* = q_J \sqrt{T_{iJ}} / k$  mais nous n'entrerons pas ici dans la définition des différents coefficients de poussée que l'on déduit des mesures faites en soufflerie.

## 3 - MESURE SUR UNE TUYÈRE ÉTALON -

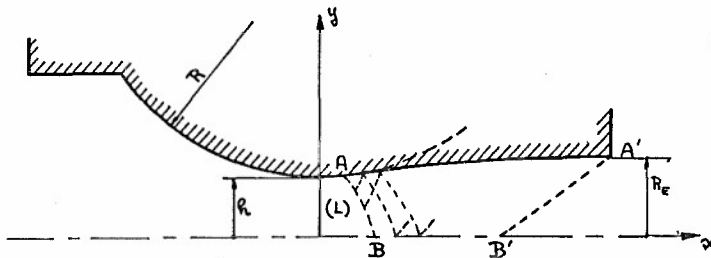
### 3.1. - Introduction -

Il est intéressant de pouvoir se prononcer sur la précision absolue des mesures réalisées en soufflerie. On utilise à cet effet une tuyère étalon de caractéristiques géométriques simples et dont le coefficient de poussée peut être calculé par voie théorique. En procédant alors à des mesures directes sur cette tuyère avec la balance de poussée, on peut effectuer un contrôle global de l'installation de mesure en comparant les valeurs expérimentales du coefficient de poussée aux valeurs calculées.

Nous allons présenter cette tuyère, rappeler les étapes nécessaires pour évaluer théoriquement le coefficient de poussée et présenter la technique expérimentale adoptée.

### 3.2. - Présentation de la tuyère étalon -

La tuyère étalon choisie est à symétrie de révolution. Son profil évolutif a été calculé par la méthode des caractéristiques, à partir d'une ligne de départ (L) de la région transsonique et appliquée à un gaz parfait non visqueux de chaleurs spécifiques constantes



[ $\gamma/C_v = \gamma = 1.4$ ] de façon telle que l'écoulement dans le plan de sortie soit uniforme et parallèle à l'axe de la tuyère, le nombre de Mach étant dans ce plan égal à 2. Dans la région du col, la méridienne est circulaire. Si  $R$  et  $h$  représentent respectivement le rayon de la méridienne et le rayon géométrique du col, on a  $R/h = 4$ .

Fig. 5 - Schéma de la tuyère étalon

### 3.3. - Calcul du coefficient de poussée -

Nous appellerons coefficient de poussée interne absolu le rapport de la poussée interne absolue (dans le vide)  $F_v$  au groupement  $(p_{iJ} A_J)^*$  égal, comme nous l'avons vu, à  $q \sqrt{T_{iJ}} / k$ . Nous poserons :

$$(10) \quad K_{TAI} = \frac{F_v}{(p_{iJ} A_J)^*} = \frac{F_v}{q \sqrt{T_{iJ}} / k}$$

Calculons ce coefficient.

#### 3.3.1. - Coefficient de poussée en gaz caloriquement parfait ( $\gamma = 1,4$ ) non visqueux -

$$\begin{cases} F_v = -p_E A_E + q V_E \\ (p_{iJ} A_J)^* = -p_{iJ} A_J \times C_{D_{HJ}} \end{cases}$$

$$\text{où } \begin{cases} -p_E & = \text{pression statique uniforme dans le plan de sortie} \\ A_E = \pi R_e^2 & = \text{aire de sortie ; } A_J = \pi h^2 & = \text{aire géométrique du col} \\ q & = \text{débit masse} \\ V_E & = \text{vitesse uniforme dans le plan de sortie} \end{cases}$$

En appelant  $M_E$  la solution de l'équation en  $M$  (détermination supersonique) :

$$\frac{A_E}{A_J C_{D_{KJ}}} = \Sigma(M) \quad \text{avec} \quad \Sigma(M) = \left(\frac{2}{\gamma+1}\right)^{\frac{\gamma+1}{2(\gamma-1)}} \frac{1}{M} \left(1 + \frac{\gamma-1}{2} M^2\right)^{\frac{\gamma+1}{2(\gamma-1)}}$$

et en posant  $\omega(M) = \left(1 + \frac{\gamma-1}{2} M^2\right)^{\frac{\gamma}{\gamma-1}}$ , un calcul simple montre que le coefficient  $K_{TAL}$  peut s'écrire :

$$K_{TAL} = \Phi(M_E) \quad \text{avec} \quad \Phi(M) = \omega(M) \Sigma(M) (1 + \gamma M^2)$$

Dans notre cas :  $\gamma = 1,4$  et  $M_E = 2$  et l'on trouve :

$$K_{TAL} = 1,42342$$

(gaz parfait à  $\gamma = 1,4$  sans viscosité)

### 3.3.2. - Coefficient de poussée en gaz calorifiquement parfait ( $\gamma = 1,4$ ) et visqueux -

Il se développe, à la paroi de la tuyère, une couche limite dont les effets essentiels sont de réduire le débit et d'altérer le nombre de Mach dans le plan de sortie.

Le coefficient de poussée  $K_{TAL}$  calculé plus haut doit subir, de ce fait, une correction que nous allons préciser.

Considérons donc la tuyère étalon que nous supposons alimentée en gaz parfait ( $p = \rho RT$  ;  $\gamma = 1,4$ ) mais maintenant visqueux et soient  $p_{iJ}$  et  $T_{iJ}$  la pression génératrice et la température génératrice de l'écoulement. La poussée dans le vide  $F'_V$  de la tuyère n'est autre que l'intégrale, dans le plan de sortie, de la grandeur  $-p + \rho V^2$ . (Nous supposons, malgré la présence de la couche limite, l'écoulement parallèle à l'axe dans le plan de sortie).

$$(11) \quad F'_V = \int_0^{R_E} (-p + \rho V^2) 2\pi y dy$$

En appelant maintenant  $M'_E$  la valeur du nombre de Mach vérifiant :

$\Sigma(M'_E) = \frac{A_E - 2\pi R_E \delta_E^{(0)}}{A_J C_{D_{KJ}} C_{D_{\delta J}}}$  où  $C_{D_{\delta J}}$  est le coefficient de réduction de débit dû à la viscosité et où  $\delta_E^{(0)}$  est l'épaisseur de déplacement de la couche limite dans le plan de sortie, la poussée  $F'_V$  s'écrit :

$F'_V = p'_E A_E + \int_0^{R_E} \rho V^2 2\pi y dy$ , la pression  $p'_E$ , uniforme dans le plan de sortie, étant reliée à la pression génératrice  $p_{iJ}$  par :

$$p'_E / p_{iJ} = \omega(M'_E) \quad (\text{ nous rappelons que } \omega(M) = \left[1 + \frac{\gamma-1}{2} M^2\right]^{\frac{\gamma}{\gamma-1}}).$$

Soient  $\rho'_E$  et  $V'_E$  les valeurs de la densité et de la vitesse de l'écoulement dans le plan de sortie de la tuyère, à l'extérieur de la couche limite : ces valeurs sont reliées à l'état générateur par l'intermédiaire du nombre de Mach  $M'_E$  introduit ci-dessus.

Le débit  $q$  de la tuyère, égal à  $K \frac{p_{iJ} A_J C_{D_{KJ}} C_{D_{\delta J}}}{\sqrt{T_{iJ}}}$  est aussi donné par :

$$(12) \quad q = \rho'_E V'_E (A_E - 2\pi R_E \delta_E^{(0)}) \sqrt{T_{iJ}}$$

Compte tenu de (12), l'expression (11) prend, après quelques développements simples, la forme :

$$(13) \quad F'_V = p'_E A_E + q V'_E - 2\pi R_E \delta_E^{(2)} \rho'_E V'^2_E$$

avec  $\delta_E^{(2)}$  : épaisseur de quantité de mouvement de la couche limite dans le plan de sortie.

Montrons maintenant, en reprenant le raisonnement proposé dans [7], que la relation ci-dessus peut prendre une forme simplifiée.

Considérons dans ce but une tuyère fictive, alimentée en gaz non visqueux, de même pression génératrice  $p_{iJ}$  et température génératrice  $T_{iJ}$  que la tuyère réelle, ayant la même aire de sortie  $A_E$  et traversée par le même débit  $q$  que la tuyère réelle.

Puisque, par hypothèse,  $p_{iJ}$ ,  $T_{iJ}$ ,  $q$  sont les mêmes dans les deux tuyères, l'aire aérodynamique critique de la tuyère fictive  $A_{J,f}^*$  est donnée par :

$$A_{J,f}^* = A_J C_{D_{KJ}} C_{D_{\delta J}}$$

Soit  $F''_V$  la poussée dans le vide de cette tuyère fictive alimentée en air non visqueux :

$$F''_V = p''_E A_E + q V''_E$$

avec  $p''_E / p_{iJ} = \omega(M''_E)$  et  $\Sigma(M''_E) = \frac{A_E}{A_J C_{D_{KJ}} C_{D_{\delta J}}}$

Formons la différence  $F_v' - F_v''$

$$F_v' - F_v'' = -p_E' A_E + q V_E' - 2\pi R_E \delta_E^{(2)} \zeta_E' V_E'^2 - (-p_E'' A_E + q V_E'')$$

Comme  $q = \zeta_E'' V_E'' A_E$

$$F_v' - F_v'' = A_E [(p_E' - p_E'') + \zeta_E'' V_E'' (V_E' - V_E'')] - 2\pi R_E \delta_E^{(2)} \zeta_E' V_E'^2$$

Or  $-p_E'$  et  $-p_E''$  peuvent être considérées comme les valeurs de la pression ds deux états voisins au cours d'une détente isentropique à partir ds la pression génératrice  $-p_{i,T}$ , états caractérisés par les nombres de Mach proches l'un ds l'autre  $M_E'$  et  $M_E''$

Ds même pour  $V_E'$  et  $V_E''$ .

On peut donc écrire

$$\begin{aligned} -p_E' - p_E'' &= \delta p_E \\ V_E' - V_E'' &= \delta V_E \end{aligned}$$

Or, les relations  $dH = T ds + \frac{dp}{\rho}$  (thermodynamique)

et  $H + \frac{V^2}{2} = \text{constante}$  (énergie)

donnent avec  $ds = 0$   $\rho V \delta V + \delta p = 0$

On a donc

$$(14) \quad F_v' - F_v'' = -2\pi R_E \delta_E^{(2)} \zeta_E' V_E'^2$$

Le coefficient ds poussée  $K_{TRAL}$  en air visqueux, égal par définition à  $\frac{F_v'}{q\sqrt{T_{i,T}}/k}$  ss calcule alors facilement en utilisant (14).

On trouve, après quelques calculs très simples :

$$(15) \quad \left( \begin{array}{l} K_{TRAL} \\ \text{(tuyère réelle)} \\ \text{air visqueux } \gamma = 1,4 \end{array} \right) = \phi(M_E'') - \gamma w(M_E'') \Sigma(M_E'') M_E''^2 2 \frac{\delta_E^{(2)}}{R_E}$$

Nous rappelons que  $\phi = w \Sigma (1 + \gamma M^2)$  et que le nombre de Mach  $M_E''$  est donné par

$$\Sigma(M_E'') = \frac{A_E}{A_c C_D K_T C_D \delta_E}$$

Ce nombre de Mach n'a donc aucune signification physique.

On voit ainsi qu'il est nécessaire, pour appliquer (15), de connaître l'épaisseur ds déplacement  $\delta_c^{(1)}$  au col ds la tuyère et l'épaisseur de quantité de mouvement  $\zeta_E^{(2)}$  dans le plan de sortie. Nous donnons une application numérique plus loin.

### 3.3.3. - Correction due à l'effet de compressibilité -

La loi  $-p = \zeta RT$  doit être remplacée par la relation exacte :  $-p = \Xi \zeta RT$  où  $\Xi$  est le facteur de compressibilité. Il en résulte en particulier, qu'au cours d'une détente isentropique par exemple, des écarts apparaissent à la fois sur les débits, les poussées et les modes de détente par rapport aux lois ds l'écoulement ds l'air supposé parfait et à  $\gamma = 1,4$ .

Ces écarts ont été calculés pour le cas simplifié ds détentes monodimensionnelles à partir ds tables thermodynamiques tenant compte de l'effet de compressibilité [8] pour des températures génératrices assez proches de l'ambiant ( $0^\circ \leq T_{i,T} \leq 75^\circ \text{C}$ ) et des pressions génératrices s'élevant jusqu'à 50 atm environ. Ces résultats ont été reportés en [2]. Rappelons-en l'essentiel :

Pour les débits mesurés par la méthode du col sonique, l'écart atteint presque 2% pour  $T_{i,T} = 288^\circ \text{K}$  et  $-p_{i,T} = 40$  atm par exemple, comme on peut le constater en appliquant la relation donnant  $C_{Dv}$  que nous avons rappelée au § 2.3.

Pour les poussées, le mode de comparaison est le suivant : nous considérons deux tuyères géométriquement identiques, d'aire sonique  $A_c$  et d'aire de sortie  $A$ .

- La première est alimentée par un gaz parfait et à  $\gamma = 1,4$ , de même masse moléculaire que l'air, de pression génératrice  $-p_{i,T}$  et température génératrice  $T_{i,T}$  et nous calculons la poussée  $F_v$  et le débit  $Q$  par les lois ds détente des écoulements monodimensionnels à  $\gamma = 1,4$ . D'où :

$$\left( \frac{F_v}{Q\sqrt{T_{i,T}}} \right)_{\text{parfait}}; \gamma = 1,4$$

- La seconde est alimentée en air réel, à la même pression génératrice  $-p_{i,T}$  et même température génératrice  $T_{i,T}$ . Les tables thermodynamiques [8] permettent alors de calculer de même la grandeur

$$\left( \frac{F_v}{Q\sqrt{T_{i,T}}} \right)_{\text{air réel}}$$

(Nous rappelons qu'il est fait abstraction des effets de la viscosité dans ce calcul).

On constate alors que le rapport  $\frac{\left( \frac{F_v}{Q\sqrt{T_{i,T}}} \right)_{\text{air réel}}}{\left( \frac{F_v}{Q\sqrt{T_{i,T}}} \right)_{\text{parfait}}; \gamma = 1,4}$  est, à température  $T_{i,T}$  invariable, une fonction pratiquement linéaire de  $-p_{i,T}$ . La figure 6 montre nos résultats dans le cas particulier  $T_{i,T} = 288^\circ \text{K}$  pour les trois types de tuyère  $A/A_c = 1; 1,7; 3$ .

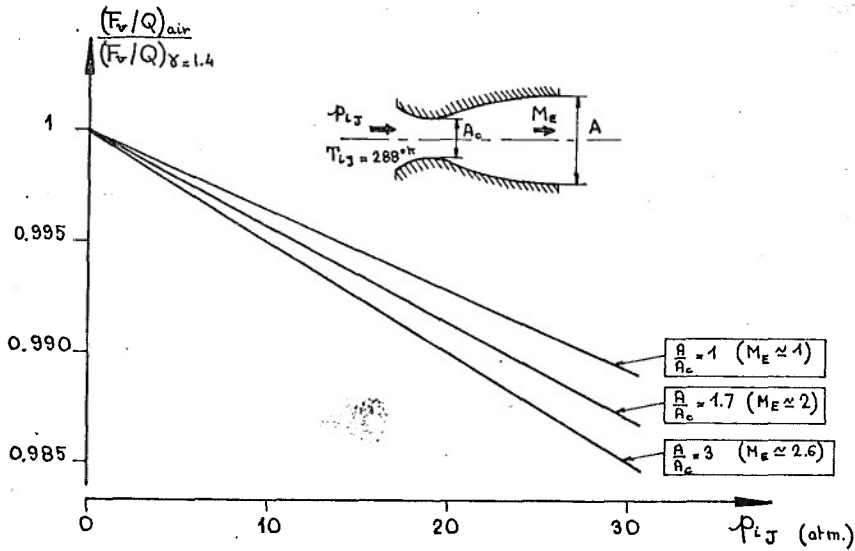


Fig. 6 - Effet viriel sur la poussée

Remarque :

On a supprimé, sur la figure 6, le radical  $\sqrt{T_{LJ}}$  qui figure au numérateur et au dénominateur du rapport précédent puisque la comparaison est faite pour la même valeur de  $T_{LJ}$ .

On voit ainsi sur la figure 6 que, pour une tuyère  $A/A_c = 3$ , il existe un écart d'environ 1 % entre les 2 coefficients de poussée pour  $-p_{LJ} = 20$  atm.

## 3.3.4. - Application numérique -

Les dimensions de la tuyère sont  $\left\{ \begin{array}{l} \text{diamètre du col} = 37,40 \text{ mm} \\ \text{diamètre de la sortie} = 48,54 \text{ mm} \end{array} \right.$

Pour ces dimensions et les conditions génératrices que nous adoptons pour les essais de cette tuyère ( $-p_{LJ} \approx 1$  atm,  $T_{LJ} \approx 320^\circ\text{K}$ ), les épaisseurs caractéristiques de la couche limite, supposée turbulente, sont :

$$\delta_c^{(0)} = 0,05 \text{ mm (épaisseur de déplacement au col)}$$

$$\delta_E^{(2)} = 0,13 \text{ mm (épaisseur de quantité de mouvement dans le plan de sortie).}$$

Ces épaisseurs sont obtenues par intégration de l'équation intégrale de von Karman en commençant l'intégration en un point situé à l'amont du col de la tuyère où le nombre de Mach est égal à 0,3 et en suivant la méthode proposée en [9].

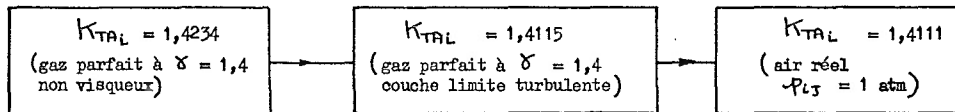
$$\text{d'où } \left. \begin{array}{l} C_{D\delta_J} = 1 - 5,5 \cdot 10^{-3} \\ C_{D\kappa_J} = 1 - 1,4 \cdot 10^{-3} \end{array} \right\} C_{D\delta_J} \cdot C_{D\kappa_J} = 0,9931$$

En appliquant la relation (15), on trouve alors :

$$\boxed{\begin{array}{l} K_{TAL} = 1,4115 \\ \gamma = 1,4 \\ \text{(couche limite turbulente)} \end{array}}$$

La correction d'effet viriel est insignifiante dans le cas considéré ici en raison du niveau très modéré de la pression : elle est en effet égale à  $-0,3\%$ .

En résumé :



## 3.4. - Mesures expérimentales sur la tuyère étalon -

La tuyère étalon est vissée à l'extrémité du canal primaire de la balance de poussée. Elle est entourée d'un carénage qui prolonge la canne de la balance, comme les arrière-corps présentés au § 2.1., mais qui est cylindrique. On procède, comme pour les mesures sur arrière-corps, en deux temps : on évalue tout d'abord, en l'absence de jet, la traînée externe qui est ici une traînée de frottement uniquement. Cette traînée est ensuite déduite de la mesure effectuée avec jet : la poussée interne et le coefficient  $K_{TAL}$  en résultent.

Pour ce type de mesure, le débit qui circule dans la tuyère est égal à celui qui traverse, lors d'une mesure courante, le modèle d'un arrière-corps. On se place ainsi délibérément, pour les mesures de contrôle, dans des conditions d'essais identiques à celles adoptées pour les mesures sur arrière-corps.

Afin de contrôler les calculs de la couche limite, un sondage expérimental de la couche limite a été effectué dans le plan de sortie de la tuyère. Les résultats sont :

$$\left\{ \begin{array}{l} \delta_E^{(1)} \text{ expérimental} = 0,37 \text{ mm} \\ \delta_E^{(2)} \text{ expérimental} = 0,12 \text{ mm} \\ H = \frac{\delta_E^{(1)}}{\delta_E^{(2)}} = 3,14 \end{array} \right.$$

Ces valeurs sont en excellent accord avec les valeurs calculées en couche limite turbulente et qui sont :

$$\left\{ \begin{array}{l} \delta_E^{(1)} = 0,41 \text{ mm} \\ \delta_E^{(2)} = 0,13 \text{ mm} \quad (\text{couche limite turbulente}) \\ H = 3 \end{array} \right. \left. \begin{array}{l} \text{alors que l'accord ne serait pas du tout satisfaisant avec} \\ \text{les valeurs calculées en couche limite laminaire :} \end{array} \right.$$

$$\left\{ \begin{array}{l} \delta_E^{(1)} = 0,23 \\ \delta_E^{(2)} = 0,04 \quad (\text{couche limite laminaire}) \\ H = 5,3 \end{array} \right.$$

Les hypothèses retenues pour le calcul de la couche limite sont ainsi justifiées.

Il serait fastidieux d'énumérer ici les diverses valeurs expérimentales du coefficient de poussée de la tuyère étalon que nous avons obtenues au cours des mesures répétées qui accompagnent toutes nos campagnes d'essai. Ces valeurs sont habituellement très proches de la valeur théorique, l'écart étant en général inférieur à 0,5%. Elles permettent d'affirmer qu'aucune erreur grave n'est commise dans nos mesures ; elles permettent aussi d'améliorer, par recalage, la cohérence entre les diverses campagnes d'essais.

#### 4 - MESURES EFFECTUEES SUR UN BANC AU POINT FIXE -

##### 4.1. - Introduction -

Le Centre d'essais de l'O.N.E.R.A. à MODANE-AVRILEUX possède, en service depuis 1967, un banc de poussée au point fixe destiné à chiffrer les performances internes de tuyères de réacteurs à échelle réduite et à un ou plusieurs flux. La simulation est obtenue, là encore, au moyen d'air comprimé froid. Les débits peuvent atteindre 20 kg/s et les taux de détente réalisables sont d'un niveau identique à ceux de l'avion de transport supersonique "CONCORDE". C'est à l'étude des performances de poussée de cet avion qu'a été consacrée jusqu'à maintenant cette installation expérimentale.

Après avoir présenté très brièvement l'installation, nous donnerons quelques résultats obtenus en monofluxeur des convergents de formes variées, résultats qui peuvent servir de point de départ à l'étude théorique ou expérimentale de configurations de tuyères plus complexes. Nous présenterons enfin un exemple d'une recherche d'optimisation interne d'une tuyère à deux flux.

##### 4.2. - Description de l'installation -

La figure 7, extraite de [10], montre l'installation. La balance de poussée comporte un équipage mobile suspendu élastiquement et bridé par un dynamomètre très rigide dont la capacité actuelle est de 1 000 daN.

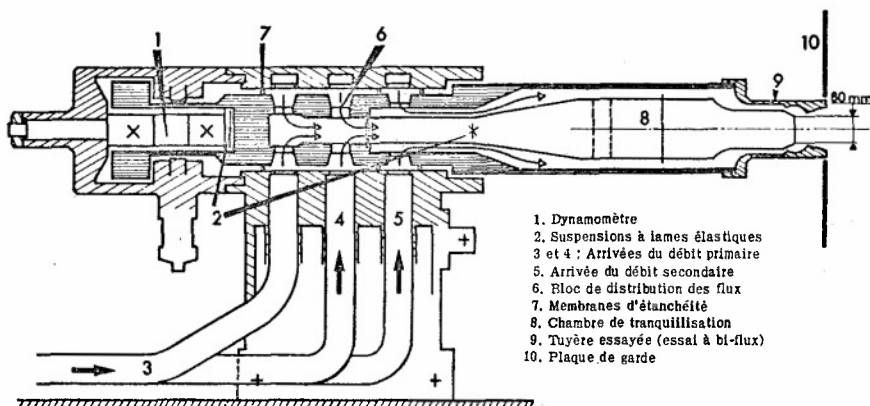


Fig. 7 - Banc de poussée au point fixe

Le système propulsif étudié, à un ou deux flux, est fixé à cet équipage mobile par l'intermédiaire d'une chambre de tranquillisation centrale pour l'écoulement principal et, éventuellement, d'une chambre périphérique pour l'écoulement auxiliaire.

La chambre centrale a été largement dimensionnée : les conditions génératrices d'éjection de l'écoulement primaire peuvent ainsi y être définies avec précision au moyen de thermocouples à fil tendu pour la température génératrice  $T_{L_j}$  et de prise de pression statique à la paroi pour la pression génératrice  $p_{L_j}$ . Cette installation de mesure de poussée est donc simultanément un banc de striction.

L'air comprimé, prélevé sur des bouteilles à haute pression, alimente, après conditionnement thermique, un réservoir tampon dans lequel pression et température sont maintenues constantes en cours d'essai. Après passage dans des débitmètres à col sonique, l'air pénètre dans la balance de poussée normalement à l'axe de mesure de l'effort.

4.3. - Coefficient de striction de convergents coniques axisymétriques -

En raison de l'intérêt pratique que présente l'étude des convergents coniques axisymétriques, puisque ce type de tuyère équipe habituellement les réacteurs d'avion, une série d'essais a été récemment effectuée à MODANE sur des convergents coniques (2 h, h) (voir figure 8) et dont le 1/2 angle  $\alpha$  a varié de 2° à 80°.

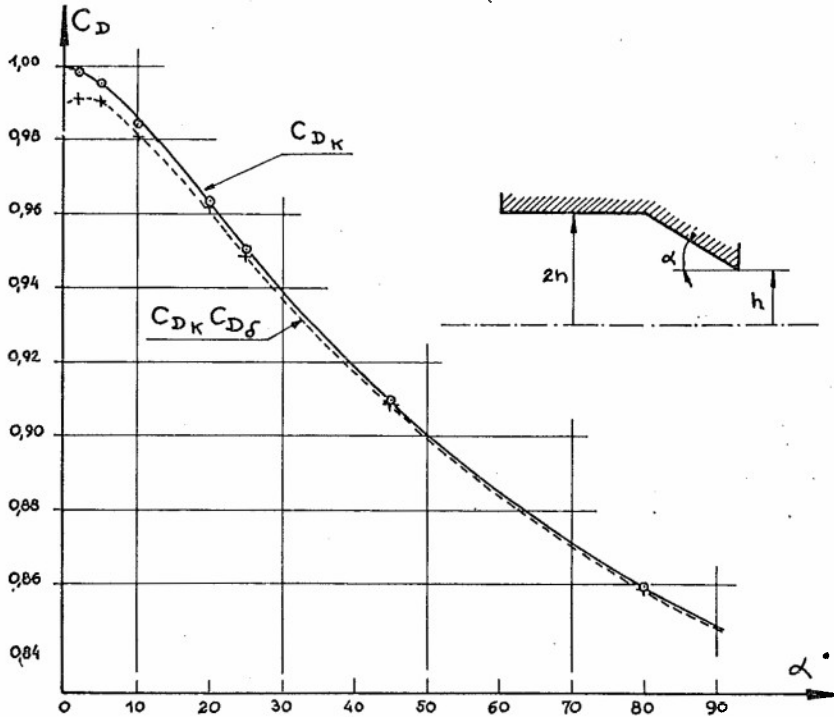


Fig. 8 - Coefficient de striction de convergents coniques

La figure 8, extraite de [4], donne les résultats de cette étude en ce qui concerne le coefficient de débit  $C_{D\delta}$ ,  $C_{D_K}$ . Les valeurs expérimentales sont représentées par des signes +. Toutes ces mesures ont été réalisées dans des conditions d'écoulement supercritique [par exemple, si  $\alpha = 80^\circ$ , le taux de détente critique ("choked pressure ratio"), est  $\geq 20$ ]

Pour donner plus de généralité à ces résultats, nous avons calculé approximativement la valeur de  $C_{D\delta}$  pour chaque tuyère, en intégrant, depuis un point situé bien à l'amont, l'équation intégrale de von Karman. Il en a résulté les valeurs de  $C_{D_K}$  représentées par les signes  $\odot$ . La courbe en trait continu qui joint ces points semble très cohérente : elle passe bien par le point [ $\alpha = 0^\circ$ ;  $C_{D_K} = 1$ ]

4.4. - Influence du taux de contraction sur le coefficient de débit d'un convergent conique -

Les résultats de la figure 8 concernent des tuyères convergentes coniques dont le taux de contraction est égal à 4. Qu'advient-il du coefficient de débit d'un convergent conique quand le taux de contraction varie ? C'est une question que peut se poser l'ingénieur qui doit calculer la tuyère d'un réacteur. Nous avons donné en [4] une première réponse pour un convergent conique de 1/2 angle  $\alpha = 20^\circ$ . Nous donnons sur la figure 9 une réponse beaucoup plus générale : les résultats présentés sur cette figure résultent de calculs en écoulement plan par la méthode de l'hodographe [11]. Il apparaît que le coefficient  $C_{D_K}$  est d'autant plus sensible au coefficient de contraction que l'angle  $\alpha$  est plus élevé. Ce résultat est logique. Dans le domaine d'utilité pratique pour un réacteur d'avion [ $0^\circ \leq \alpha \leq 25^\circ$ ;  $M_\infty \leq 0.6$ ] le taux de contraction, que nous caractérisons sur la figure 9 par le nombre de Mach  $M_\infty$ , ne joue pratiquement pas. Ces résultats mériteraient d'être généralisés au cas de l'écoulement de révolution.

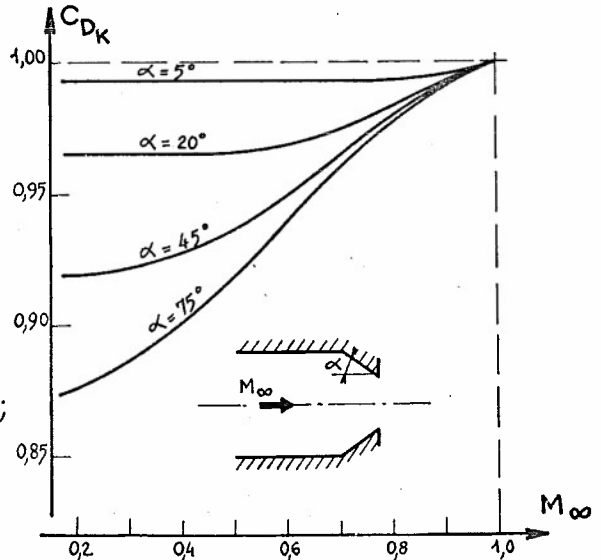


Fig. 9 - Coefficient de débit  $C_{D_K}$  en écoulement plan (méthode de l'hodographe)

## 4.5. - Coefficient de poussée de convergents coniques -

Avant de donner nos résultats expérimentaux, montrons que l'on peut prévoir de façon approchée, le coefficient de poussée  $K_{TA_L}$  d'un convergent.

Rappelons à cet effet la relation (15)

$$K_{TA_L} = \phi(M_E'') - \gamma \omega(M_E'') \sum(M_E'') M_E''^2 \cdot 2 \frac{\delta_E^{(2)}}{R_E}$$

air visqueux  
 $\gamma = cte$

Le nombre de Mach  $M_E''$  est donné par la solution (détermination supersonique) de l'équation :

$$\sum(M_E'') = \frac{A_E}{A_J C_{D_{\delta J}} C_{D_{KJ}}}$$

Admettons que la relation (15) puisse être appliquée au cas limite d'un convergent.

En ce cas  $A_E = A_J$

$$D'où \sum(M_E'') = \frac{1}{C_{D_{\delta J}} C_{D_{KJ}}}$$

Or

$$\frac{1}{C_{D_{\delta}} C_{D_K}} = \frac{1}{C_{D_{\delta}}} \times \frac{1}{C_{D_K}} = \left[ \frac{1}{1 - 2 \frac{\delta_c^{(0)}}{h}} \right] \frac{1}{C_{D_K}} \approx \left(1 + 2 \frac{\delta_c^{(0)}}{h}\right) \frac{1}{C_{D_K}} \approx \frac{1}{C_{D_K}} + 2 \frac{\delta_c^{(0)}}{h}$$

Remarquant que  $\phi$ , considérée comme une fonction de  $\sum$ , vérifie  $\frac{d\phi}{d\sum} = \omega$ ,

on a :

$$\phi(M_E'') \approx \phi\left(\sum = \frac{1}{C_{D_K}}\right) + 2 \frac{\delta_c^{(0)}}{h} \omega$$

Comme le nombre de Mach moyen de l'écoulement est proche de l'unité, on déduit pour  $K_{TA_L}$

$$K_{TA_L} = \phi\left(\sum = \frac{1}{C_{D_K}}\right) + 2 \frac{\delta_c^{(0)}}{h} \omega(1) - \gamma \omega(1) \times 2 \frac{\delta_c^{(2)}}{h}$$

air visqueux  
 $\gamma = cte$

ou, en posant  $H_c = \frac{\delta_c^{(0)}}{\delta_c^{(2)}}$

$$(16) \quad K_{TA_L} = \phi\left(\sum = 1/C_{D_K}\right) + \omega(1) \left[1 - C_{D_{\delta}}\right] \left[1 - \frac{\gamma}{H_c}\right]$$

air visqueux  
 $\gamma = cte$

Pour  $\gamma = 1,4$  et une couche limite turbulente au col ( $H_c = 1,8$ ), la relation (16) devient

$$(16') \quad K_{TA_L}^{\gamma=1,4} = \phi\left(\sum = 1/C_{D_K}\right) + 0,12 (1 - C_{D_{\delta}})$$

viscosité, turbulente

**REMARQUE** - Nous avons admis que la relation (15) est applicable au cas d'un convergent. Rien ne le justifie a priori puisque l'hypothèse qui a été retenue pour établir (15), à savoir que la pression statique est constante dans le plan de sortie de la tuyère, n'est manifestement pas respectée si  $C_{D_K} \neq 1$ . On peut montrer cependant, par un raisonnement tout à fait différent qui met en jeu le développement limité des fonctions  $\sum$  et  $\omega(1 + \gamma M^2)$  autour de  $M = 1$ , que la relation approchée (16) est bonne [12].

**Examinons maintenant nos résultats expérimentaux -**

Les valeurs expérimentales brutes du coefficient de poussée dans le vide  $K_{TA_L}$  ont tout d'abord été ramenées aux valeurs qu'aurait prises ce coefficient si l'air était un gaz parfait à  $\gamma = 1,4$ . Ces nouvelles valeurs sont appelées  $K_{TA_L}(\gamma=1,4)$ .

L'écart entre  $K_{TA_L}$  et  $K_{TA_L}(\gamma=1,4)$  est ici appréciable.

Par exemple, pour  $\alpha = 80^\circ$ , la pression nécessaire pour atteindre le régime supercritique a été de l'ordre de 20 atm et l'on a :

$$K_{TA_L}(\gamma=1,4) = K_{TA_L} (1 + 0,75\%)$$

pour  $T_{iJ} = 15^\circ C$

Les valeurs du coefficient  $K_{TA_L}$ , "ramenées à  $\gamma = 1,4$ ", ont été reportées sur la figure 10 de la page suivante, pour chaque convergent, en fonction du coefficient  $C_{D_K}$ .

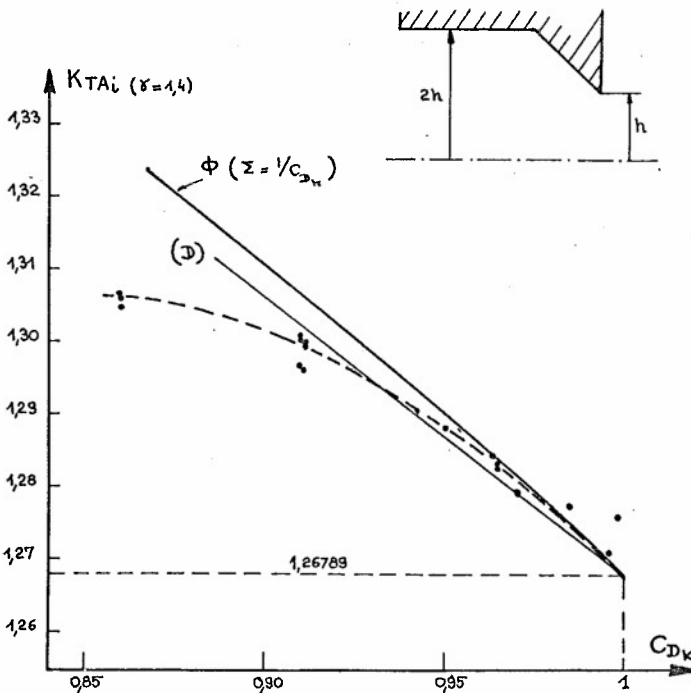


Fig. 10 - Coefficient de poussée de convergents coniques.

On a aussi tracé sur cette figure la courbe  $K_{TAL} = \phi(\zeta = \frac{1}{2} C_{DK})$  en trait continu épais. Si l'on remarque que le terme  $0,12(1 - C_{DK})$  est tout à fait négligeable puisque  $1 - C_{DK}$  est de l'ordre de quelques millièmes, on peut juger la valeur de la relation approchée (16') en comparant la courbe en trait continu épais et la courbe expérimentale en trait interrompu qui joint au mieux les points expérimentaux.

L'approximation est bonne pour  $0,95 \leq C_{DK} \leq 1$  ou encore:

$$0^\circ \leq \alpha \leq 25^\circ$$

On a aussi tracé sur la figure, en trait continu fin, la droite (D) qui traduit la relation

$$\frac{K_{TAL} / \phi(\zeta) - 1}{1 - C_{DK}} = 0,3$$

proposée dans [13].

Cette dernière relation, non justifiée dans [13], est une bonne approximation.

4.6. - Exemple d'une étude d'optimisation interne d'une tuyère biflux -

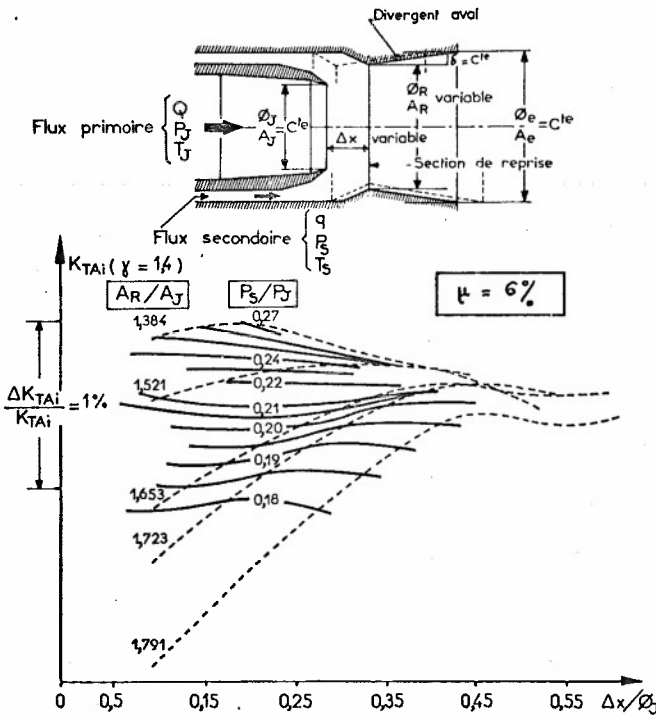


Fig. 11 - Performance interne d'une tuyère biflux type "CONCORDE" Influence du paramètre  $\Delta X$ .

Pour terminer cet exposé, nous présentons enfin les résultats d'une étude d'optimisation de la géométrie interne d'une tuyère biflux. Cette étude expérimentale a été effectuée, à la demande de la SNECIA, sur le banc au point fixe de MODANE. La tuyère biflux expérimentée, du type "CONCORDE", est présentée sur la figure 11. Elle comportait des éléments fixes : tuyère primaire, divergence ( $\delta$ ) et aire de sortie ( $A_E$ ) du divergent aval et des éléments variables : aire ( $A_R$ ) de la section de reprise, distance ( $\Delta X$ ) séparant celle-ci du plan de sortie de la tuyère primaire.

L'étude consistait à évaluer les variations du coefficient de poussée  $K_{TAL}$  en fonction de  $\Delta X$ , pour des valeurs données du coefficient  $\mu = \frac{q}{Q} \sqrt{\frac{P_s}{P_j}}$  ( $\mu = \frac{q}{Q}$  dans le cas des essais en gaz froids) et du rapport  $P_s/P_j$  ( $P_s, P_j$  pressions génératrices de l'écoulement secondaire et primaire respectivement). Les résultats présentés sur la figure 11 concernent le cas  $q/Q = 6\%$  et fournissent la synthèse finale de l'étude pour ce cas.

Les 5 courbes en trait interrompu correspondent à 5 valeurs différentes de la section de reprise  $A_R$  et, par conséquent, à 5 types de divergent.

Chacune de ces courbes a été obtenue en traduisant longitudinalement le divergent correspondant et en mesurant, pour différentes valeurs de  $\Delta X$ , le coefficient de poussée  $K_{TAL}$  (que l'on a ramené ensuite à  $\gamma = 1,4$ ).

On a ensuite superposé sur le réseau des courbes en trait interrompu, celui, en trait continu, des courbes iso.  $P_5/P_T$ . On peut alors tirer, de l'observation de ce dernier réseau, la conclusion suivante, valable pour  $\mu = 6\%$  :

La valeur optimale de  $\Delta X$  dépend du niveau de  $P_5/P_T$ . S'il y a intérêt, pour les faibles valeurs de  $P_5/P_T$ , à donner à  $\Delta X$  des valeurs importantes, il faut inversement réduire  $\Delta X$  pour les valeurs élevées de  $P_5/P_T$ .

**REMARQUE** - Si l'on tient compte de ce que représente, sur l'échelle des ordonnées, une variation relative du coefficient de poussée égale à 1 %, on voit qu'une grande précision des mesures était nécessaire pour pouvoir définir ce réseau de synthèse et donner les éléments d'appréciation suffisamment sûrs au constructeur.

#### 5 - CONCLUSION -

5.1. - Les méthodes de mesure utilisées à l'O.N.E.R.A. pour la détermination des performances d'un arrière-corps ont été présentées et les dispositifs expérimentaux utilisés dans les centres de l'O.N.E.R.A. à CHALAIS-MEUDON et à MODANE ont été décrits.

5.2. - Le contrôle de la validité des mesures est obtenu en comparant les performances calculées d'une tuyère étalon et les résultats obtenus expérimentalement. Pour ce faire, des coefficients correcteurs prenant en compte les effets de viscosité et de compressibilité de l'air utilisé dans les essais sont introduits. L'accord obtenu sur les coefficients de poussée est en général meilleur qu'à 0,3 % près.

5.3. - Des résultats de calcul ou de mesure de débits et de poussée de tuyères ont été présentés, ainsi qu'une synthèse partielle concernant les recherches d'optimisation au point fixe d'un arrière-corps de type "CONCORDE".

#### REFERENCES

- [1] ROLLIN G. Thrust balance for Turbo-jet exhaust studies in transonic and supersonic wind-tunnels. O.N.E.R.A. - T.P. n° 172 (1964) (non publié).
- [2] MASURE B. Virial and viscosity effects on the measurement of mass flow rates by means of a sonic throat. Virial effect on nozzle thrust. - Communication présentée à la 28ème réunion de la Supersonic Tunnel Association. DENVER 30-31 octobre 1967.
- [3] MASURE B. Etude de la précision des mesures de débits gazeux par la méthode du col sonique. A.T.M.A. 6-10 Mai 1968 -
- [4] MASURE B. SOLIGNAC J.L. LAVAL P. Mass flow rates measurement by means of a sonic throat. - Flow Symposium - PITTSBURGH (Pennsylvania) - 10-14 Mai 1971 -
- [5] CARRIERE P. Viscous effects on propulsion nozzles. - Short Course on Internal Aerodynamics of Rocket Engines - von KARMAN INSTITUTE FOR FLUID DYNAMICS - Rhode-Saint-Genève (Avril 1966).
- [6] McADAMS W.H. Heat Transmission, 3rd Edition - McGRAW-HILL (1954).
- [7] CARRIERE P. Tuyères propulsives - AGARD lectures series on supersonic turbomachinery - VARENNE (Italie) (15-20 Mai 1967).
- [8] MICHELS A. WASSENAAR T. WOLKERS G.J. Thermodynamical properties of air temperatures between +75°C and +170°C and pressures up to 1 200 atmospheres. - Appl. Sc. Res. Section A, vol. 5 (1955) pp. 121 à 136.
- [9] MICHEL R. Couches limites turbulentes et calcul pratique des couches limites en fluide compressible - Cours de l'Ecole Nationale Supérieure de l'Aéronautique - PARIS (1963).
- [10] FASSO G. PLETIN M. BROUSSAUD P. Installation pour l'étude de tuyères de réacteurs à plusieurs flux - Note Technique O.N.E.R.A. n° 160 (1970)
- [11] FENAIN M. Application des méthodes de résolution hodographique à l'étude de jets et de profils euphoristiques - Note Technique ONERA (Novembre 1970) - non publiée -.
- [12] MASURE B. Etalonnage d'un banc de dynalpie au point fixe à MODANE - S3 MA - Note Technique ONERA (Avril 1968) - non publiée -.
- [13] HERBERT M.V. MANTLEW D.L. The design-point performance of model internal-expansion propelling nozzles with area ratios up to 4. - National Gas Turbine Establishment - Rapport NGTE R 258 (1963).

## MOYENS ET EXEMPLES D'ESSAIS AU C. E. Pr.

par

Jean-Claude RIPOLL Ing. en Chef de l'Armement et Jean-Bernard COCHETEUX Ing. de l'Armement  
Centre d'Essais des Propulseurs - SACLAY 91-ORSAY - FRANCE

RESUME. - Le C. E. Pr. est un Etablissement d'Etat qui participe au développement des moteurs aéronautiques en mettant à la disposition des Industriels des moyens d'essais en vol simulé uniques en Europe Continentale.

L'installation comprend principalement des machines de traitement de l'air et des gaz d'échappement mues soit par l'électricité soit par la vapeur, un réseau complexe de conduites, 8 cellules d'essais de moteurs en vol simulé et 7 veines d'essais de sous ensembles. Les mesures sont principalement assurées par un ordinateur central.

Parmi les nombreux types d'essais relatifs aux entrées d'air et aux tuyères, on donne à titre d'exemples des indications sur deux essais pour Concorde et sur les études couplées de bruit et de poussée.

-----oo0oo-----

## Première partie : Moyens d'essais

1. - Introduction. - Le C. E. Pr. a été créé et développé par les autorités étatiques chargées de l'armement aéronautique. Il dépend actuellement de la D. M. A. au sein du Ministère d'Etat chargé de la Défense Nationale.

Sa mission comporte deux aspects essentiels :

- c'est le lieu des épreuves officielles d'homologation des moteurs aéronautiques fabriqués en France.
- Il met à la disposition des Industriels des moyens d'essais de recherches et de développement constituant des investissements lourds dont le regroupement est plus rentable.

Depuis plusieurs années des constructeurs étrangers y sont également venus réaliser des essais, dont certains pour la certification de leurs matériels.

Installé à l'origine dans l'enceinte d'un fort désaffecté qui contient toujours la plupart des bancs d'essais au sol, le C. E. Pr. a rapidement débordé sur le plateau de Saclay pour établir les installations d'essais en vol simulé, en profitant de la présence des étangs, créés par Louis XIV, qui constituent la " source froide " indispensable à l'ensemble des machines thermiques.

L'emplacement retenu apparaît aujourd'hui comme particulièrement favorable car il se situe sur l'axe intellectuel du sud ouest parisien avec la proximité de l'ONERA, du CEN, des Universités (Orsay) et grandes Ecoles (Polytechnique, Centrale) et une liaison facile avec les usines de la S. N. E. C. M. A. par les autoroutes en construction.

L'Etablissement compte aujourd'hui 1000 personnes dont :

350 pour les services administratifs et d'assistance technique

100 pour le Laboratoire d'essais sur les carburants et équipements

550 pour le service des essais de moteurs et les méthodes et mesures associées.

2. - Le vol simulé. - Le caractère spécifique du C. E. Pr. réside essentiellement dans ses installations de vol simulé qui sont uniques en Europe continentale. Ces moyens ont pu être heureusement adaptés jusqu'à ce jour aux orientations successives de l'effort aéronautique : avènement du réacteur, tendance vers le statoréacteur, développement des post-combustions, réacteurs évolués pour avions supersoniques ; les moteurs à grand rapport de dilution posent un nouveau problème d'investissements complémentaires.

Les essais en vol simulé sont surtout des essais de développement, qu'ils portent sur des sous-ensembles ou sur des moteurs complets ; cependant la certification de nacelles complètes en givrage et des épreuves d'endurance à grande vitesse sont la source d'une activité notable.

3. - Le Bâtiment B. - Le complexe principal, dit "Bâtiment B", s'étend actuellement sur 48 000 m<sup>2</sup>, une extension de 5 000 m<sup>2</sup> étant en cours de réalisation. Schématiquement il s'agit de 2 halls rassemblant les caissons et veines d'essais, séparés par le hall des machines dans le prolongement duquel se trouvent les chaufferies.

En effet la plupart des compresseurs et extracteurs sont mus par des turbines à vapeur qui autorisent plus de souplesse dans les régimes de fonctionnement. D'autre part l'électricité actionne quelques compresseurs et surtout les pompes qui puisent jusqu'à 50 000 m<sup>3</sup>/h dans les étangs pour alimenter les réfrigérants disposés sur les circuits. Le tableau I rassemble les caractéristiques générales des sources de puissance. Les graphiques du tableau II montrent l'évolution des consommations en électricité et en fuel lourd, carburant des chaufferies, correspondant à l'accroissement de la charge en essais.

Les machines de traitement de l'air et des gaz d'échappement sont connectées à un réseau de tuyauteries qui dessert les bancs d'essais. Ce réseau comprend trois circuits, l'un d'extraction, les 2 autres d'alimentation, l'un en air comprimé et chaud, l'autre en air déprimé et froid. De nombreuses liaisons entre ces circuits permettent toute sorte de combinaisons et de joindre pratiquement n'importe quel banc à n'importe quelle machine. Sur ces circuits se placent également les réchauffeurs d'air, les échangeurs et les sécheurs fournissant aux machines l'air conditionné nécessaire. (tableau III).

Mode	Installation	Fluide	Puissance	
Vapeur	Chaufferie I	24 bars 370 °C	360 t/h	Surchauffeur à 370°C ) en cours de réalisation ) mise en service 1973
	Chaufferie II	24 bars 300 °C	200 t/h	
	Chaufferie III	62 b 490 °C	140 t/h	
	Chaufferie IV	62 b 490 °C	140 t/h	
Electricité	Réseau H T	63 kV $\pm$ 8 % 50 Hz	26 MW	Limite à 3 MW aux H. P. Hiver Puissance installée $\approx$ 50 MVA
	Réseau MT	2 postes 63 15 kV	2 x 20 MVA	
Chaleur	Fours RC <sub>1</sub> RC <sub>2</sub> Fours RC <sub>3</sub> RC <sub>4</sub>	3 bars 675° C 3,5 et 25 b 250°C	2 x 28 MW 2 x 11 MW	Combustion de fuel lourd
Refroidissement	Château d'eau	Industriel 1,5 bar Incendie 4,5 bars	50 000 m <sup>3</sup> /h 2500 m <sup>3</sup> /h	Température variable 4° C en hiver 30°C en été

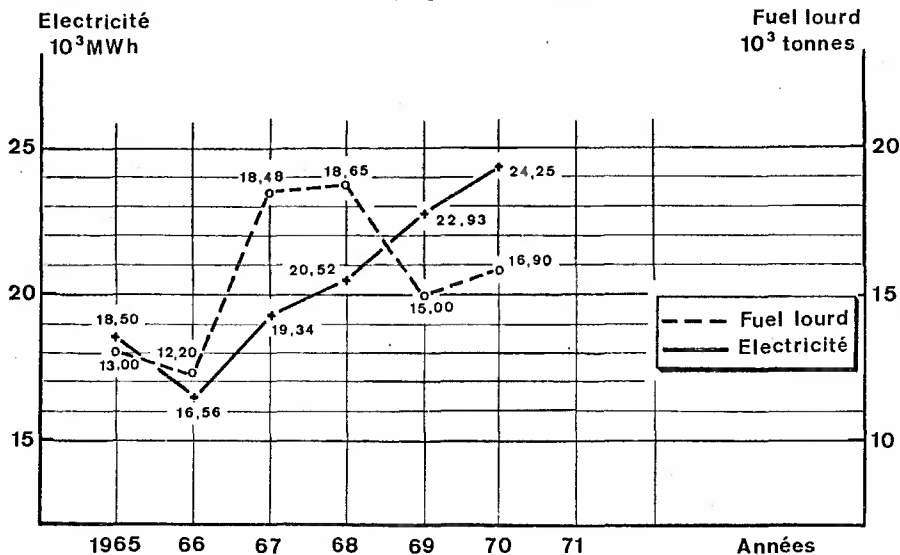


Tableau II Consommations d'énergie

TABLEAU III		DISPOSITIFS		STATIQUES	
<b>Sécheur</b>	Alumine activée 170 t	absorption 9 t d'eau			
S N	Air 100 kg/s	entrée 100 kPa	15°C	point de rosée 10°C	
		sortie 98	35	- 22	
<b>Réchauffeurs</b>	Pression maxi bars	Débit kg/s	Température °C		
RC 1	7	50	140 à 675		
RC 2	7	50	140 à 675		
RC 3	16	20	160 à 675		
RC 4	25	22	200 à 650		
<b>Réfrigérants</b>	Alimentation en froid		TS 8 tours à saumure 80 kg/s sous 90 kPa à - 10°C		
Sortie des Compresseurs	RCV 15	débit	1500 m <sup>3</sup> /h	tubes d'air	
	RCN 35	d'eau	2000 m <sup>3</sup> /h	-	
Circuits d'extraction	RS 1		5000 m <sup>3</sup> /h	tubes d'eau	
	RN 2		4250 m <sup>3</sup> /h	-	
	RN 6		4200 m <sup>3</sup> /h	-	
Entrées d'extracteurs	RV 8		2100 m <sup>3</sup> /h	tubes d'air	
	RV 15		800 m <sup>3</sup> /h	-	
	ER (6 appareils)		2400 m <sup>3</sup> /h	-	
	BBO (3 appareils)		2800 m <sup>3</sup> /h	tubes d'eau	
Sorties de Caissons	RP 5		2500 m <sup>3</sup> /h	tubes d'eau	
	RP 6		2500 m <sup>3</sup> /h	-	
	RLN 7		600 m <sup>3</sup> /h	-	

Le réseau de tuyauteries ne peut être représenté facilement sur une figure de petites dimensions ; il fait l'objet d'une planche en couleurs projetée qui est un diagramme fonctionnel, le plan géographique étant sensiblement plus compliqué. Ce réseau construit pas à pas est en permanente évolution et s'enrichit chaque année de branchements nouveaux qui en accroissent la souplesse ; cependant l'espace disponible se sature progressivement.

4. - Les machines. - Les machines de traitement des gaz et de l'air présentent également une grande diversité de missions qui contribue notablement à élargir le domaine d'emploi de l'installation. Ainsi :

- le groupe G. P. O. peut fournir de l'air comprimé à température réglable de + 30° à + 180° C mais également de l'air froid détendu grâce à une turbine placée sur le même arbre.
- les deux chaînes " Rateau " de trois extracteurs chacune peuvent être associées de différentes manières en parallèle.
- les groupes " Verdon " peuvent être utilisés soit en extracteurs soit en compresseurs et peuvent être connectés en série.
- il en est de même des 2 compresseurs T A et de 2 des 4 compresseurs T B
- les extracteurs T B peuvent être mis en série avec les " Verdon " ou avec les " Rateau ".
- le groupe B. B. O peut fournir de l'air haute pression (24 bars), de l'air froid, ou servir d'extracteur à basse pression.
- dans sa configuration finale le nouveau groupe C A C B offrira la mise en parallèle en compression, en parallèle ou série en extraction, de l'air haute pression (25 ou peut être 40 bars), de l'air froid à la pression ambiante.

Les performances obtenues de ces machines dont les caractéristiques sont rappelées dans le tableau IV dépendent donc des combinaisons adoptées ; seules les principales figurent sur les planches suivantes relatives aux valeurs " machines " proprement dites.

1 : Compression                      2 : Extraction                      3 : Production d'air froid

TABLEAU IV		CARACTERISTIQUES DES MACHINES		
<u>Electricité</u>	B B O	7 MW	B P Axial 16 étages MP Centrif. 5 étages  Turbine Axiale 2 étages Détente	- Haute Pression MP + HP Surchauffe par R C 4 - Extraction B P + MP
		7 MW	H P Centrif. 5 étages	- Air froid MD + HD + TD à pression atmosphérique
	G P O	4 MW	Compresseur Cent. 3 étages Turbine Détente Ax. 4 ét.	- Air comprimé à température régulée - Air froid détendu
<u>Vapeur</u>	T A	25 MW	2 compresseurs axiaux à 17 étages	- Compression 1 ou 2 T A - Extraction 1 ou 2 T A
	T B	25 MW	4 compresseurs axiaux à 17 étages	- Compression 1 ou 2 T B - Extraction 1-2-3-4 T B
	V 15	11 MW	3 compresseurs centrifuges 1 étage	- Compression <sub>1-2-3</sub> V 15 - Extraction
	V 8	6 MW	2 compresseurs centrifuges 1 étage	- Compression 1 ou 2 V 8 - Extraction
	E R Nord	3 MW	B P centrif. 2 étages M P centrif. 2 étages	- Extraction seulement - B P + M P - B P + M P + H P - M P seul - H P seul
		1,7 MW	H P centrif. 2 étages	- M P en parallèle avec H P
	E R Sud		Même définition et mêmes possibilités que ER Nord.	
Mises en série possibles		T B → V 15 ou V 8      T B → ER V 15 ← V 8              V 15 → ER		
En construction : C A		25 MW	2 compresseurs	Mêmes utilisations que T A et T B
(fin 1973) C B		25 MW	4 compresseurs	
Autre possibilité		: extraction 4 C B → 1 C A		
Ultérieurement		: haute pression, turbine de détente.		

Les pertes de charge dans les conduits, la recompression dans les éjecteurs et les limitations en vitesse dans les tuyauteries font que chaque cas particulier doit être examiné attentivement à partir de ces données de base. Nous avons également fait figurer sur ces diagrammes les possibilités supplémentaires qui seront offertes par le nouveau groupe CA-CB de 2 x 25 MW qui entrera en service à la fin de 1973.

5. - Les veines d'essais. - Ces installations ont pour mission les essais de sous-ensembles :
- compresseurs aux bancs C<sub>1</sub> et C<sub>2</sub> ; le montage en caisson et le raccordement au système d'air conditionné permet de faire varier largement le nombre de Reynolds et d'obtenir des vitesses équivalentes élevées,
  - chambres de combustion aux bancs K 3, K 6, K 7 et L 2
  - turbines aux bancs T U et K 5
  - canaux de post-combustion au banc R 4
  - tuyères de dimensions réduites au banc K 5

Les possibilités de ces veines sont résumées dans le tableau V.

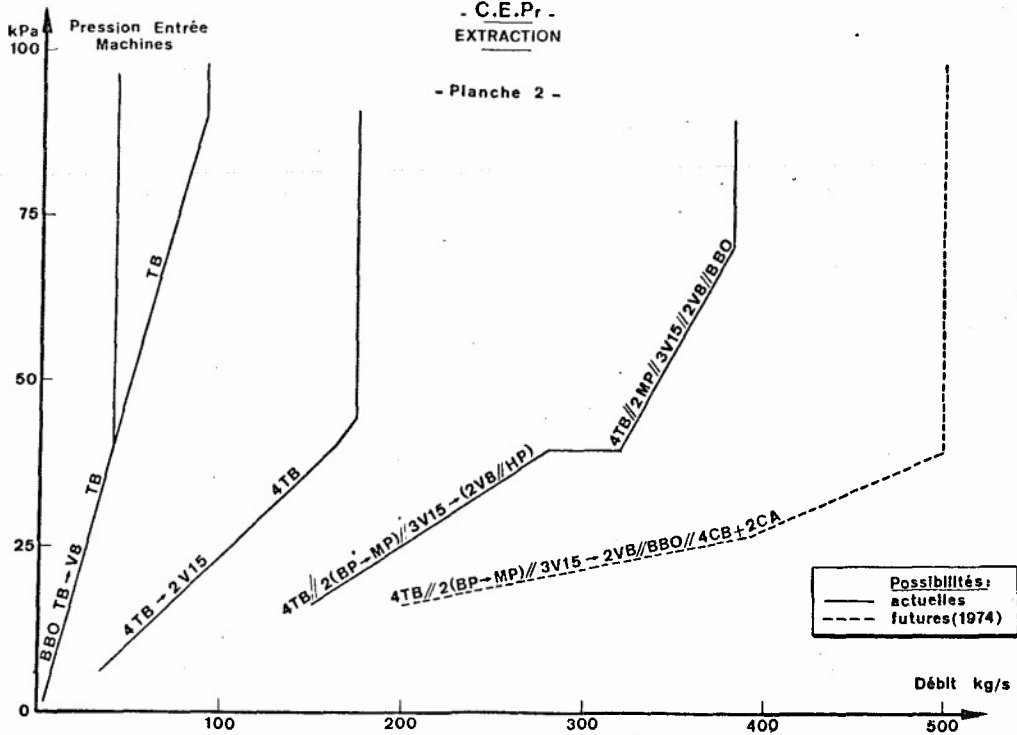
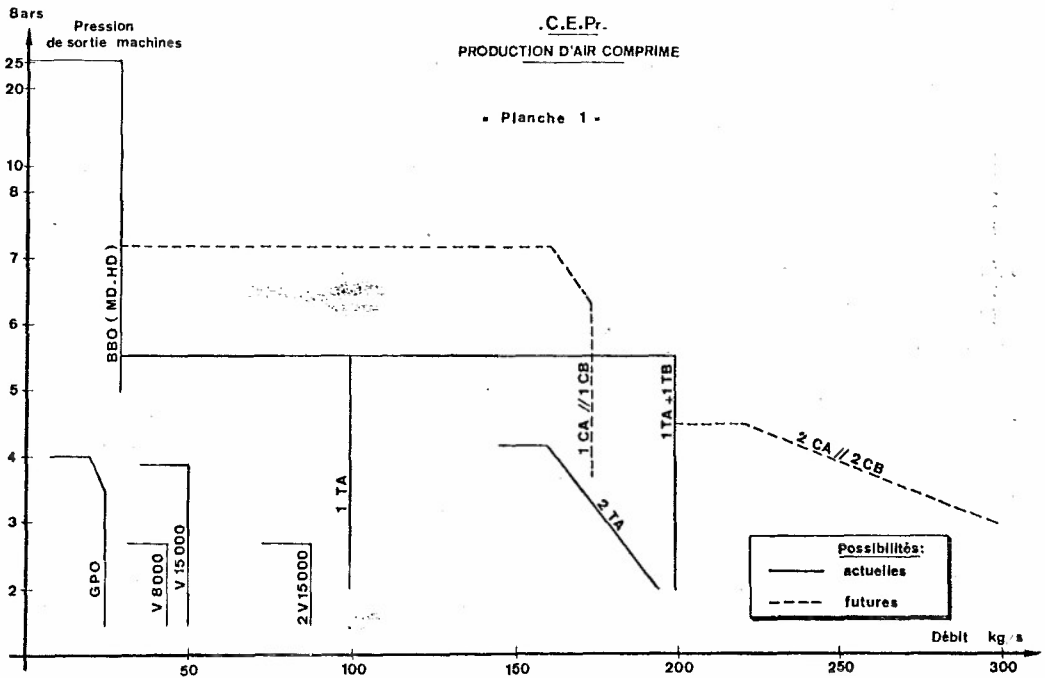
TABLEAU V		C. E. Pr.		Veines d'essais			
Compresseurs	Puissance	Vitesse de rotation	Limites				
C 2	11 MW Turbine à vapeur	600 à 18 000 un seul sens (horaire vu de l'amont)	Admission Pression 5 à 105 kPa Température -50° à +50°C Echappement Débits primaire 40 kg/s réduits secondaire 120 kg/s			Caisson Ø 3,2 m Echappement double flux	
C 1	1000 kW	11 000 tr/mn deux sens	Admission Pression 5 à 120 kPa Température -50° à +80°C Echappement Débit réduit 40 kg/s			Caisson Ø 3,2 m Motorisation en cours de réalisation	
Combustion	Débit normalisé maximal	Pression	Alimentation Température		Diamètre	Echappement Température Diamètre	
K 3	50 kg/s	7 b	- 50 à 570°C		900 mm	1,5 b	800° C 2000 mm.
K 6 K 7	25 kg/s	25 b	50 à 600° C		500 mm	25 b	650° C 1000 mm.
Turbines	Puissance	Vitesse de rotation	Limites				
T U	11 MW	1000 à 12 000 tr/mn	Alimentation Débit standard		4,5 bars 65 kg/s	350° C Echappement 800° C	
	5,5 MW	25 000 tr/mn	En cours de réalisation				
P. C.	Dimensions	Débit	Limites			Carburant	
R 4	Caisson Ø 3,7 m. Admission Ø 1,2m. Echappement Ø 1,5m.	normalisé maximal 90 kg/s	Pression kPa	Entrée 650	Sortie 150	Normal 27 m <sup>3</sup> /h 80 b Chaud 200° C 5 m <sup>3</sup> /h 80 b	
			Température	350°C	600°C		

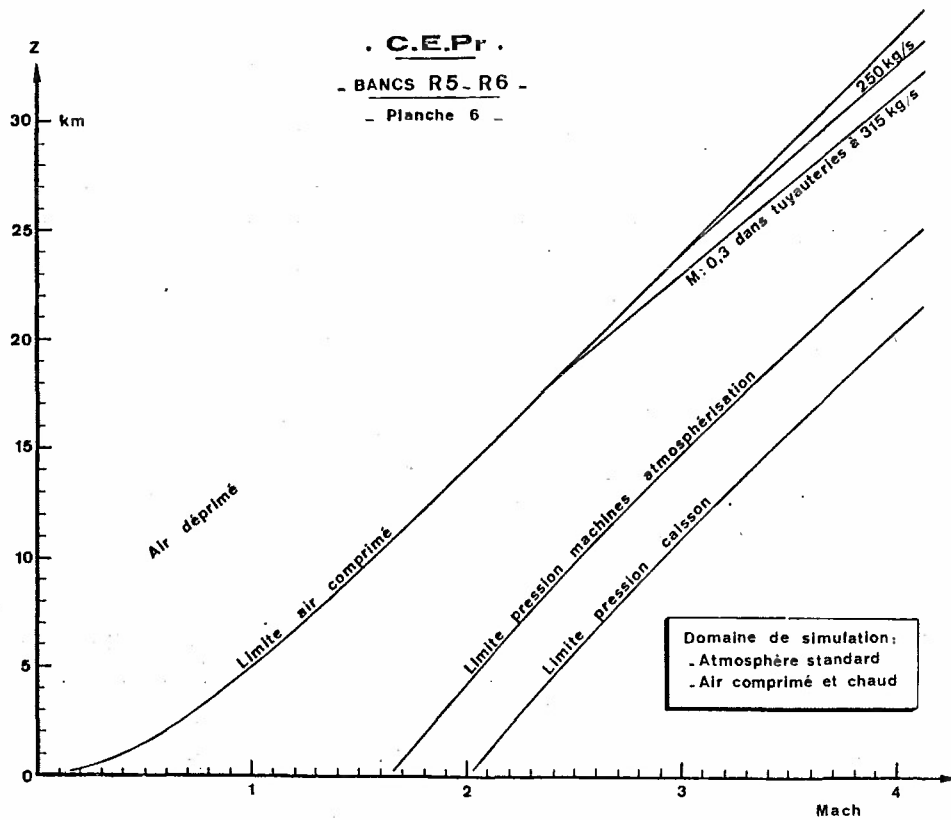
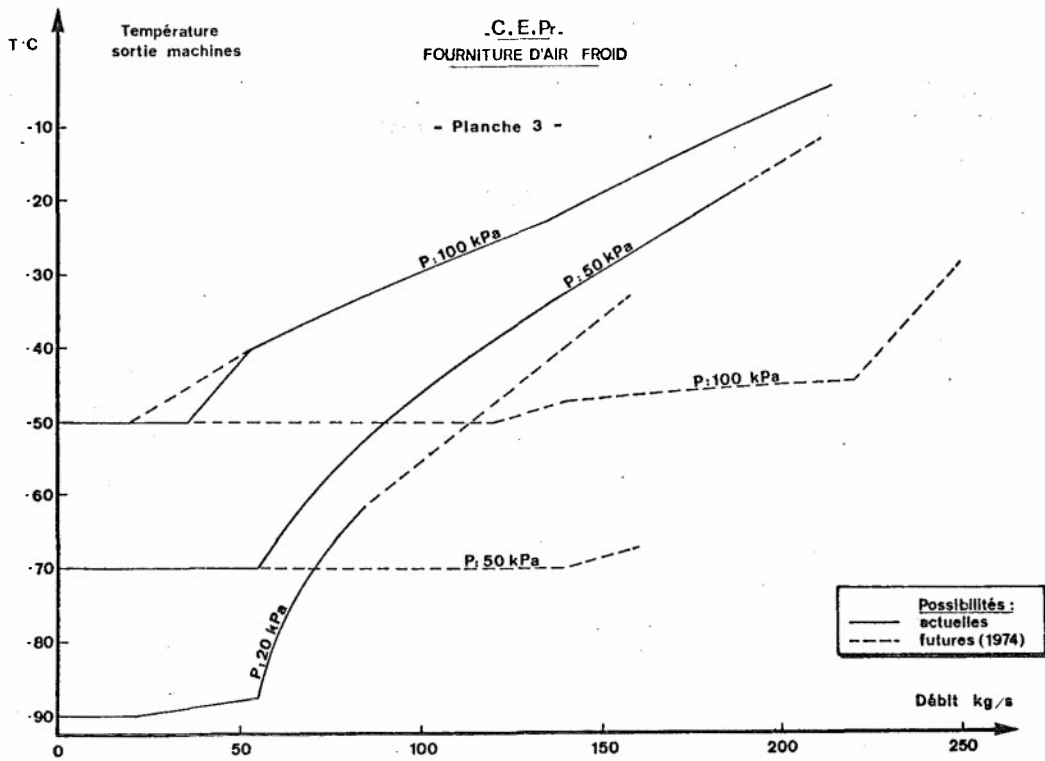
6. - Les caissons d'essais. - Ces caissons se prêtent à tous les essais aérodynamiques et aux essais de moteurs complets en veine forcée ou en jet libre. La planche 4 compare les caractéristiques générales des 7 caissons du C. E. Pr. Nous allons examiner plus particulièrement les caissons R 5 et R 6 qui ne diffèrent que par la température maximale d'entrée. On remarquera que la valeur de 675°C fournie par les fours permet de simuler exactement Mach = 4,1 à Z = 23 km ; en effet ces caissons ont d'abord été destinés à des essais de statoréacteurs.

Le domaine de simulation effectivement accessible dépend de nombreux facteurs attachés tant aux machines de traitement qu'aux tuyauteries et au caisson. Le point de vue industriel se traduit par un diagramme débit-pression (planche 5) et celui des essais par des diagrammes Nombre de Mach, Altitude (planches 6 et 7). Lorsque la pression génératrice est voisine de l'ambiante les configurations peuvent être très variables, c'est pourquoi les limitations représentées dans ces régions ne doivent pas être prises au sens strict.

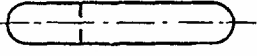
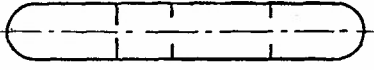
Le banc R 5 est équipé pour les essais "chauds". Le banc R 6 est équipé d'une installation de production de nuages givrants capable de traiter d'assez gros moteurs (planche 8).

7. - Mesures. - Il en sera plus amplement question dans la seconde partie. Le diagramme de la planche 9 montre l'organisation générale du central numérique dont les services ont considérablement modifié et amélioré les méthodes d'essais. Les programmes particuliers permettent outre le relevé des points stabilisés l'enregistrement des transitoires (essais de fusées) et l'analyse des vibrations acoustiques.





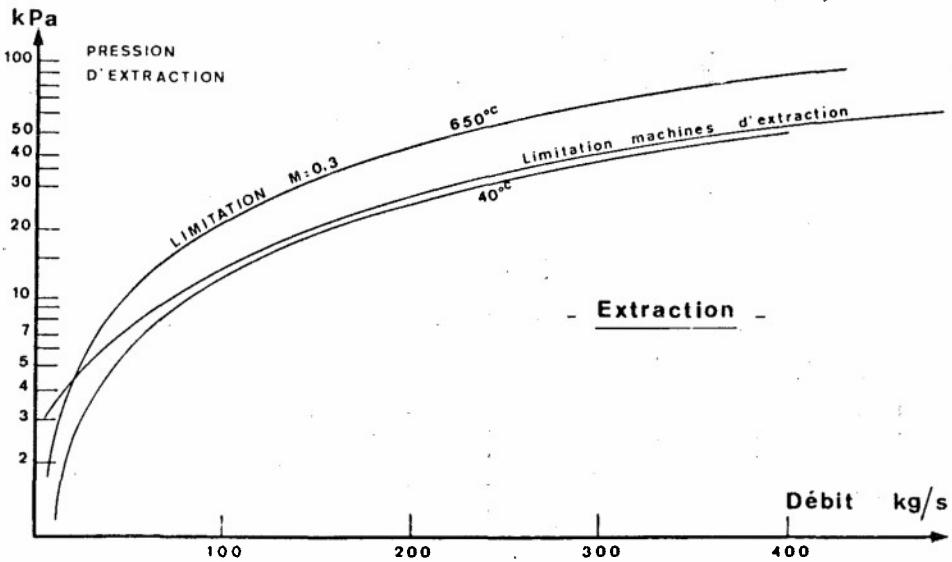
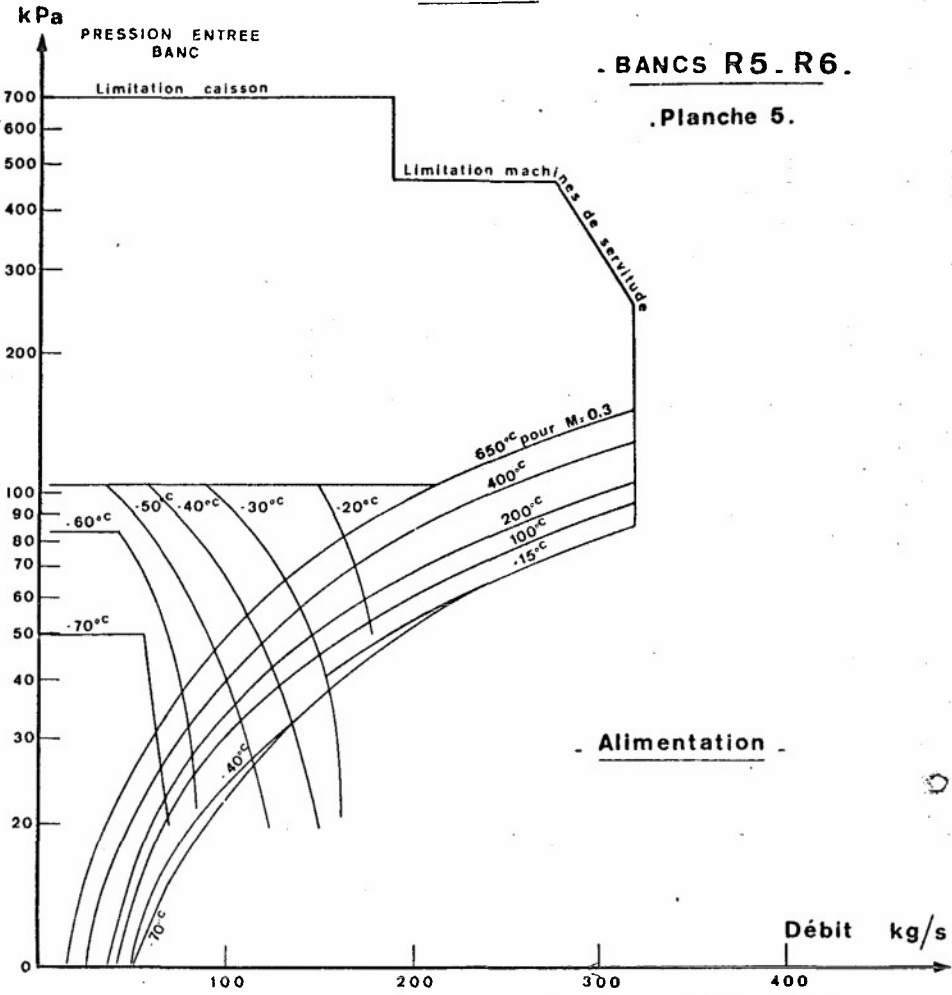
C.E.Pr

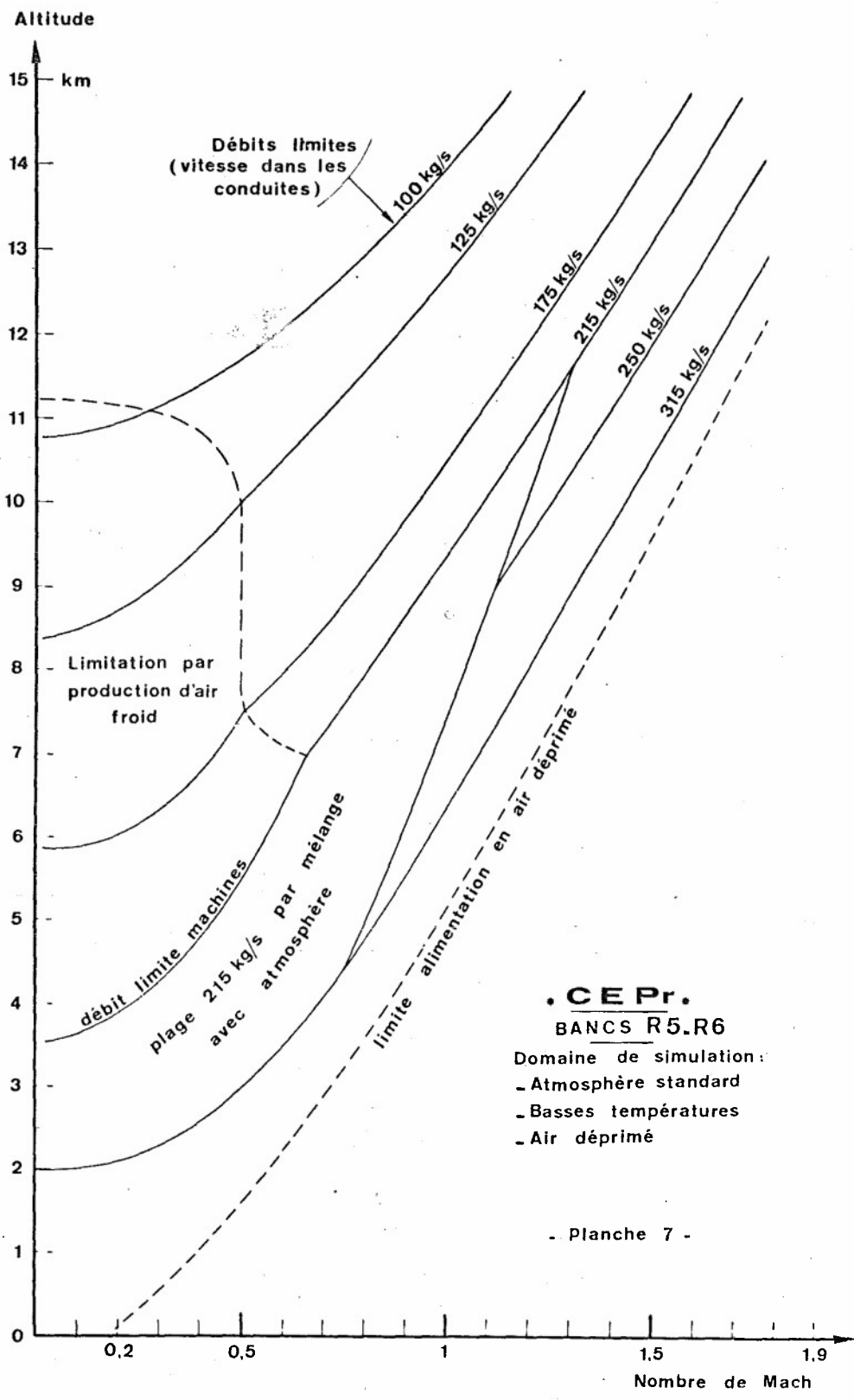
Planche 4	CAISSONS		Débit max. Standard	Dimensions Ø x long	Admission Pression Température		Echappement Température	Poussée ( 1971 )	Equipements spéciaux
	R 1	160	3,5 x 16	120 kPa	200° C	750° C 1200° intermittent	10 000 da N	Pluie artificielle veine 600 x 600 mm <sup>2</sup>	
	R 2	135	3,5 x 16	120 kPa	200° C	750° C 1200° intermittent	10 000 da N	Givrage ( grille Ø 1150 mm )	
	S 1	100	3,5 x 15,5	700 kPa	350° C	800° C 1200° C intermittent	5 000 da N	Tuyère supersonique Extraction latérale	
	R 3	135	3,7 x 18,4	200 kPa	200° C	800° C 1300° C intermittent	20 000 da N		
	R 4	135	3,7 x 18,4	200 kPa 650 kPa	350° C	900° C 1300° C intermittent	10 000 da N	Montage de post-combustion	
	R 5	375	5,0 x 30	650 kPa	700° C	1800° C pré-réfrigérant	30 000 da N	Admission haute température Extraction latérale	
	R 6	375	5,0 x 30	700 kPa	380° C	1800° C pré-réfrigérant	30 000 da N	Tuyère supersonique Extraction latérale Givrage ( grille Ø 2000 mm )	
	1975 ? R 7	Projet de caisson pour moteurs à grands rapports de dilution et turbopropulseurs avec hélices en vol simulé. Equipement de certification ( givrage, pluie ) Capable de la totalité des moyens d'extraction du C. E. Pr.							
Ech.	1/40		N. B. Balance latérale 3000 da N adaptable à tout banc.						

**. C.E.Pr. .**

**. BANCS R5 - R6 .**

**. Planche 5 .**





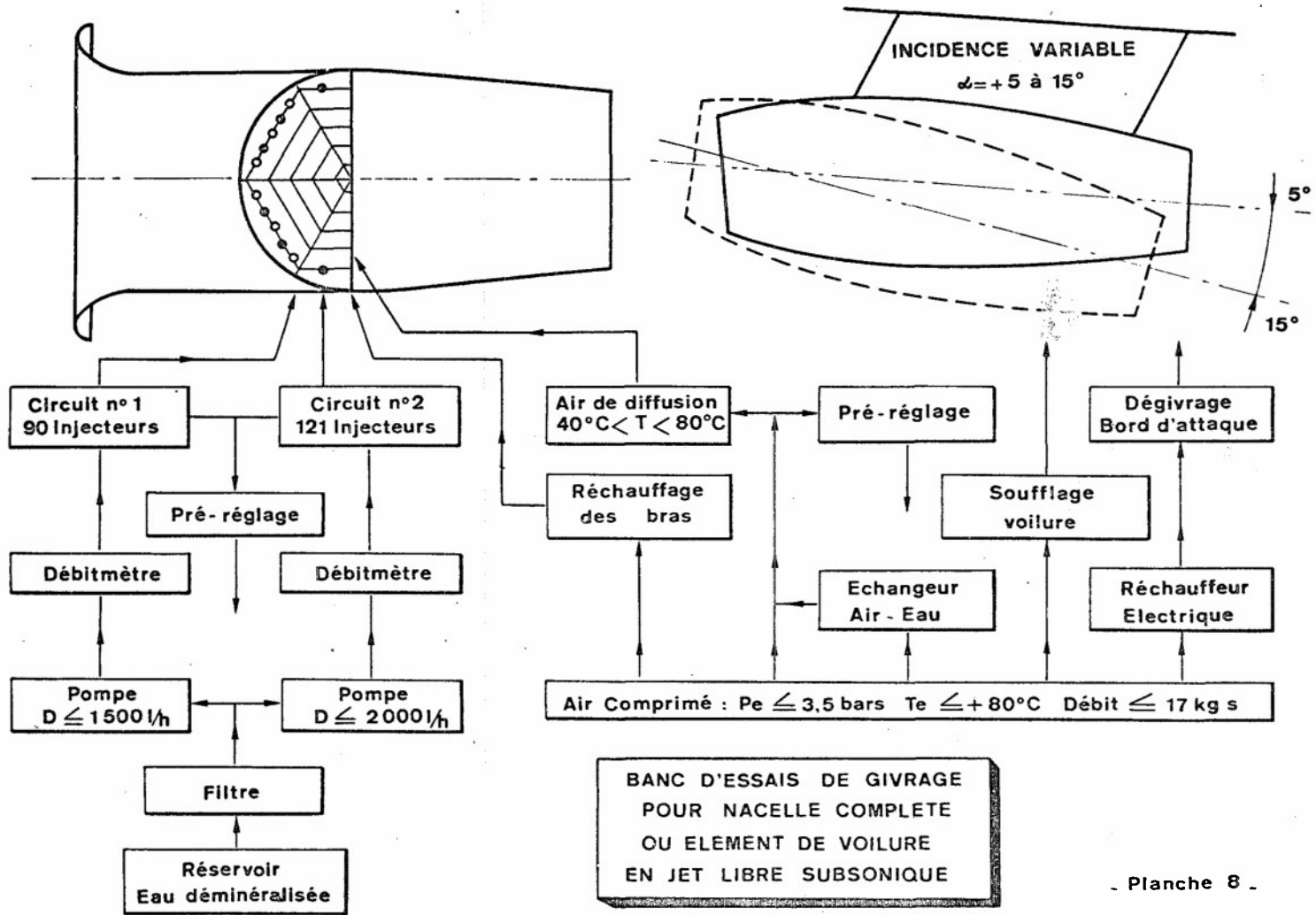
**. C E P r .**

**BANCS R5.R6**

Domaine de simulation :

- Atmosphère standard
- Basses températures
- Air déprimé

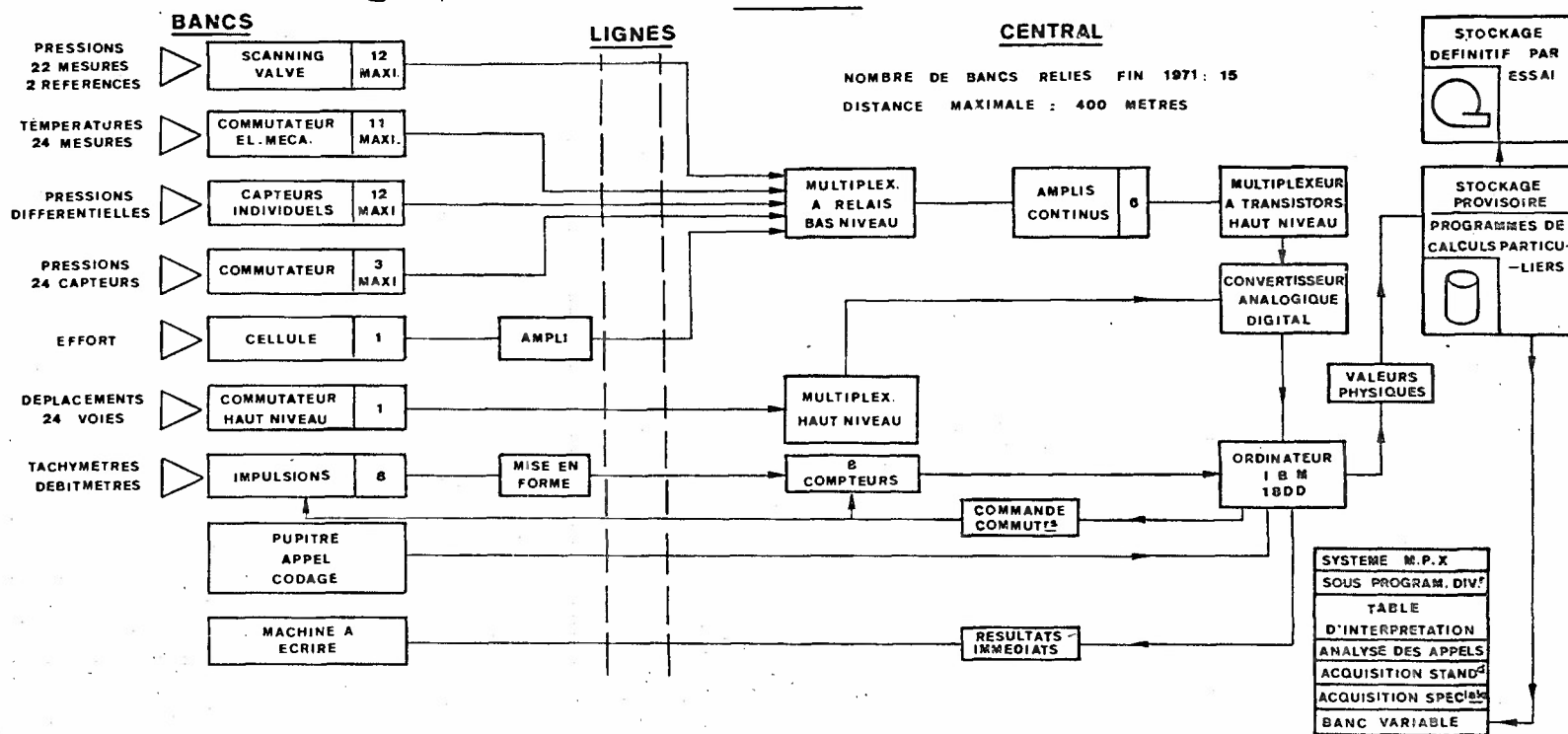
- Planche 7 -



# MOYENS ET EXEMPLES D'ESSAIS AU C.E.Pr.

## Planche 9

### Organisation des Mesures et de leur Traitement



## Deuxième partie : exemples d'essais

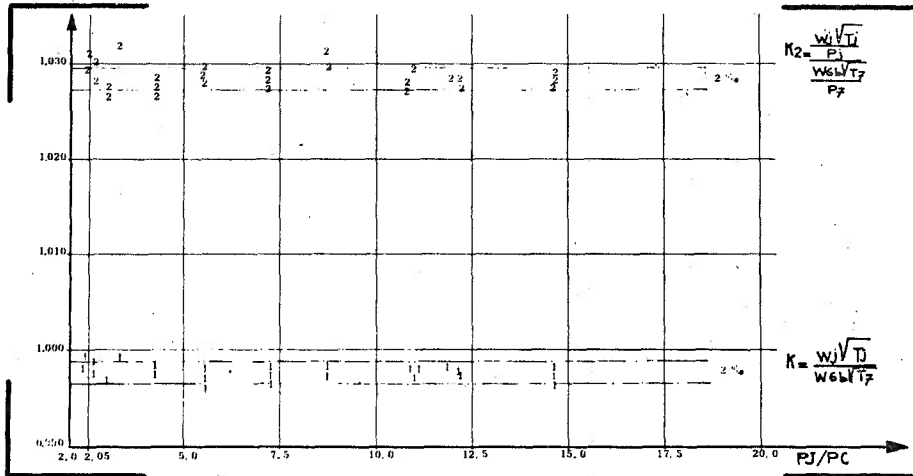
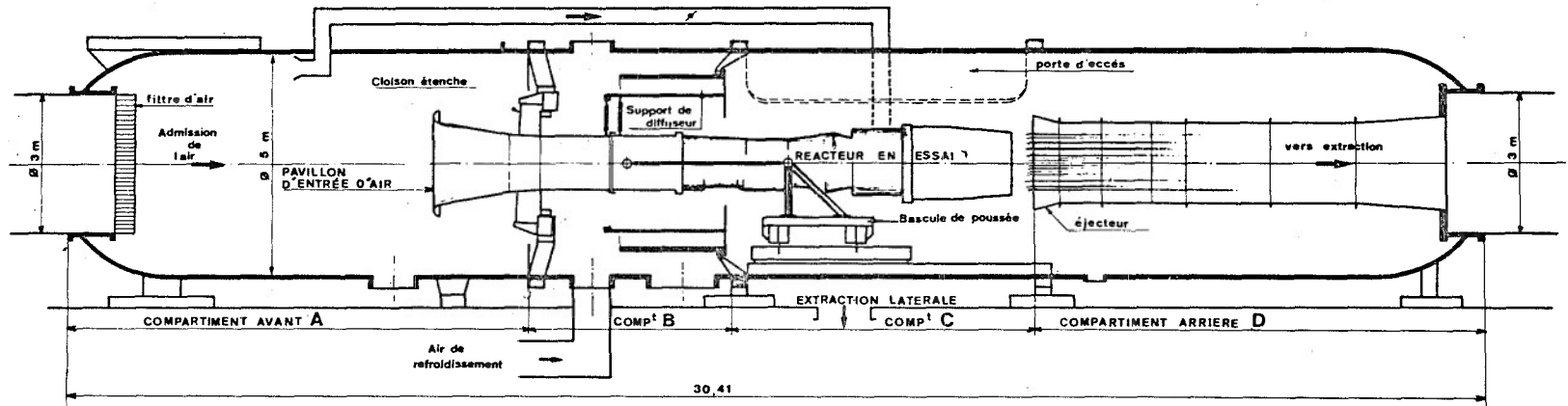
1. - Essai de turboréacteur en veine forcée Olympus 593 au banc R 5.

- 1.1. - Montage d'essai - Ce montage est orienté vers l'obtention d'une mesure précise des performances, la figure 1 en donne le principe.  
Les dimensions du compartiment de tranquillisation assurent une vitesse de l'ordre de 10 m/s favorable au fonctionnement du pavillon, à la mesure de la pression génératrice et à la protection du moteur en cas de rupture du filtre. Le débit d'air est calculable grâce à un étalonnage soigné du pavillon qui est identique à ceux des bancs de sol.  
La bascule de mesure d'effort d'un type habituel au C. E. Pr. , comporte un plateau reposant sur des lames élastiques. Le dynamomètre à jauges d'une grande raideur peut travailler en traction et en compression (suppression du système de précharge) : ceci garantit la fidélité de la mesure. La cellule, dont la gamme est adaptée à la poussée du réacteur, est placée dans un caisson isotherme non étanche ; la chaîne de mesure est réétalonnée régulièrement ; de plus un vérin et une cellule secondaire permettent de vérifier que la mise en place du moteur n'altère pas l'étalonnage et de contrôler la chaîne de mesure avant chaque séance d'essai. Au cours d'un point de mesures l'indication de la cellule est relevée 24 fois et moyennée ; grâce à ces précautions l'effort est mesuré avec une incertitude inférieure à 1 pour mille de la pleine gamme.  
Le pavillon d'aspiration n'est pas lié mécaniquement au moteur. Le dispositif d'étanchéité comporte un joint torique coulissant et gonflable et un labyrinthe pressurisé ; le joint, maintenu sous une différence de pressions très faible n'est gonflé qu'au moment du relevé de mesures ce qui lui évite toute déformation. Le montage permet également l'utilisation de grilles d'obstacles de distorsion.  
La tuyère divergente est alimentée en air secondaire à partir du compartiment amont ; le débit réglé est mesuré. Le montage, spécifique de l'Olympus, a été conçu pour ne pas perturber la mesure de poussée.

- 1.2. - Mesures - Le système d'acquisition automatique des données permet d'enregistrer plus de 300 paramètres en 6 secondes. Ceci améliore la précision grâce à la multiplication des mesures permettant de tenir compte d'effets secondaires, et au multiplexage des paramètres primordiaux. Un contrôle permanent et instantané de la chaîne de mesures est rendu possible par le calcul en temps réel. Enfin l'acquisition automatique réduit de 50 % la durée des essais par rapport au relevé manuel.  
1.3. - Essais effectués - La majeure partie des 300 heures d'essais effectuées sur Olympus au R 5 a porté sur l'étude des performances de la tuyère de propulsion. Cette étude pose un problème aigu de précision des mesures; elle ne peut se faire en effet que par comparaison de deux essais effectués, l'un avec une tuyère simplement convergente, l'autre avec la tuyère complète. La qualité des résultats peut se juger sur la figure 2 : la dispersion sur le coefficient de poussée d'une tuyère convergente de l'Olympus est de l'ordre de  $\pm 2\%$ . Ce résultat est d'autant plus remarquable que ce coefficient est fonction non seulement de la poussée mesurée, mais aussi des débits d'air et de carburant du moteur.

2. - Essai en jet libre : Maquette motorisée du fuseau moteur double du Concorde au R 6.

- 2.1. - But de l'essai - L'essai était destiné à l'étude des interactions entre les deux unités d'un même fuseau : Interactions liées au fonctionnement interne de chaque entrée d'air ou de chaque moteur ou résultant d'un phénomène externe (vol dérapé, rafale latérale etc. . . ). L'essai à échelle grandeur, souhaitable pour ce type d'essais, était incompatible avec les possibilités du C. E. Pr. L'échelle 1/3 rendait l'essai possible et avait le mérite de combler un vide entre les essais aérodynamiques au dixième et l'essai à échelle grandeur sur entrée d'air motorisée simple au N G T E.  
Pour confirmer les essais à petite échelle et apporter des enseignements à l'essai du N G T E, il était donc demandé au C. E. Pr. une caractérisation de la maquette de  $M = 1,6$  à  $M = 2,3$ . Le maître d'oeuvre de l'essai était Nord-Aviation constructeur de la maquette.  
2.2. - Description de la maquette (figure 3). - Le moteur de simulation devait avoir un débit surfacique aussi proche que possible de celui de l'Olympus et pouvoir fonctionner à 390°K, température génératrice minimale pour simuler  $M = 2,3$  sans choc de condensation avec les sécheurs du C.E.Pr. Seul le G. E. C J 610 remplit la deuxième condition dans la gamme des moteurs de 20 kg/s de débit d'air.  
Même en fonctionnant à une température inférieure de 50° à la température I S A, le C J 610 a un débit surfacique trop faible de 11 % d'où la nécessité de prolonger légèrement le divergent de la manche. Le C J 610 pouvait être équipé d'un obstruteur de tuyère destiné à le sensibiliser au pompage.  
L'échelle exacte de la maquette, fixée par le choix du moteur est de 1/3,06. Chaque entrée d'air peut être équipée soit du C J 610, soit d'un obstruteur variable (3 configurations d'essais possibles). Les prélèvements d'air inférieurs (Dunp door, échangeur) sont mesurés par des venturi. Le débit de prélèvement des rampes est réglé par deux vannes indépendantes simulant la tuyère moteur et le volet de décharge " Spill ". Les éléments mobiles de la maquette peuvent être réglés manuellement ou commandés par la régulation.  
2.3. - Montage d'essai (figure 4). - Le montage d'essai devait assurer un écoulement cylindrique et sain à l'entrée de la maquette ( $1,6 < M < 2,3$ ) et la simulation du dérapage (amplitude  $\pm 5^\circ$ , vitesse allant jusqu'à 5°/s), éviter toute interaction entre le système d'onde de chocs de la maquette et la tuyère, permettre une visualisation par ombroscopie, et alléger au maximum la charge des extracteurs.



## CAISSON R5

### ESSAIS D'UN REACTEUR

### EN VEINE FORCEE

Deux expérimentations furent réalisées pour définir le montage d'essai. L'une à l'ONERA pour étudier deux configurations d'essai (jet libre ou veine guidée) l'autre au banc A 10 du CE Pr. sur un ensemble à l'échelle 1/10 du montage du R 6.

La tuyère de Mach est bidimensionnelle ; ses parois latérales et supérieures sont fixes (cette dernière se continue par le plancher de la maquette simulant l'intrados) alors que le profil évolutif inférieur peut pivoter permettant une variation en essai du nombre de Mach de 0,2 par minute. Deux profils assurent la couverture de la gamme de nombre de Mach.

Le dérapage est obtenu par rotation de la tuyère autour d'un axe vertical ; l'amplitude est de  $\pm 5^\circ$  avec deux vitesses de variation ( $5^\circ/s$  et  $4^\circ/s$ ).

Le tableau ci-dessous donne le débit de la tuyère pour les conditions  $P_{10} = 100 \text{ kPa}$ ,  $T_{10} = 390^\circ\text{K}$

M	1,6	1,7	1,8	1,9	2	2,1	2,2	2,3
Débit tuyère kg/s	110,4	104,8	99,3	93,6	87,8	82,2	76,9	71,1
Débit maquette kg/s	40,7	38	35,3	32,7	30,1	27,6	25,4	23,2
Débit tuyère Débit maquette	2,72	2,76	2,81	2,87	2,92	2,97	3,02	3,06

La sortie de la tuyère est biseautée afin de permettre la visualisation par ombroscopie.

Le diffuseur destiné à augmenter la pression du compartiment C est réglable en position. Son efficacité est améliorée en extrayant dans le compartiment B une faible partie (1 %) du débit de la tuyère (extraction de couche limite). Ceci assure également un écoulement cylindrique.

Pour  $M = 2$  le rapport entre pression génératrice et pression d'extraction principale est de 3,8. L'extraction du débit de prélèvement des rampes (piège à couche limite) est assurée par une trompe à air fonctionnant entre les compartiments A et C. En effet, en régime fortement supercritique ; la pression du piège peut être inférieure à la pression du compartiment C.

- 2.4. - Mesures et dépouillements. - La maquette est équipée de très nombreuses prises de pression et en particulier d'un peigne tournant à quatre bras situé à l'entrée de chaque moteur et comportant une vingtaine de prises de pression totale et statique ainsi que 4 sondes directionnelles (clinomètre) permettant la mesure des vitesses radiale et circonférentielle en deux rayons.

Au total plus de 200 pressions étaient à mesurer.

En régime stabilisé deux types de manomètre ont été utilisés : appareil "Belin" (multimanomètre à liquide avec lecture par cellule photoélectrique et impression sur bande perforée) ; appareil "Scanivalve" avec impression sur bande perforée au début de l'essai, puis avec acquisition automatique.

En régime transitoire les indications des capteurs de pression C E C et O N E R A (fréquence de résonance respective 6 et 8 KHz) étaient enregistrées sur enregistreur photographique à grande bande passante et sur enregistreur magnétique fonctionnant en modulation de fréquence.

L'enregistreur magnétique s'est révélé très utile pour l'étude des fluctuations de pression à l'entrée d'un moteur en permettant les opérations suivantes :

- restitution graphique des signaux enregistrés avec utilisation de filtres passe-bas (50 Hz et 200 Hz) ou non.
- Analyse spectrale par tiers d'octave à l'aide d'analyseur Brüel et Kjoer de la chaîne d'analyse de bruit de la chambre anéchoïque du C. E. Pr. pour des fréquences de 5 Hz à 50 Hz, 20 Hz à 200 Hz, 50 Hz à 2000 Hz. Pour ces opérations la vitesse de lecture de la bande était quatre fois supérieure à la vitesse d'enregistrement (38 cm/s), (voir exemple figure 5).
- Analyse au pas de 1 Hz par densimètre spectral de Nord-Aviation.

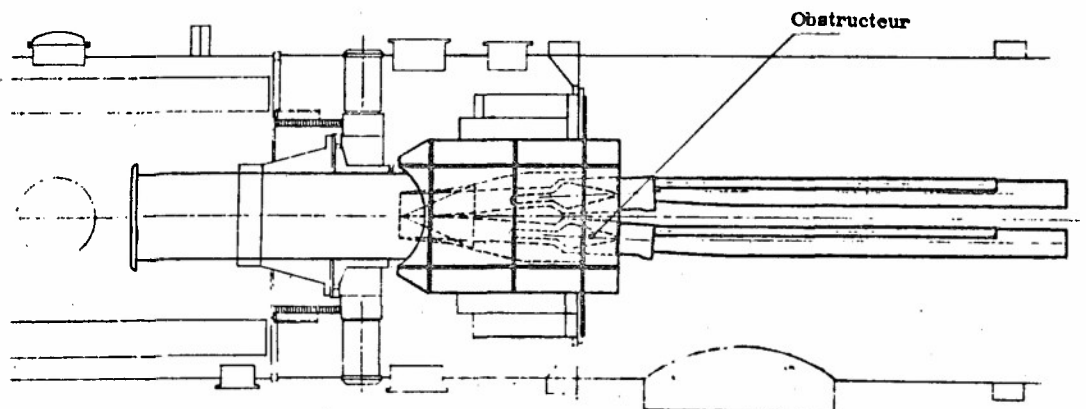
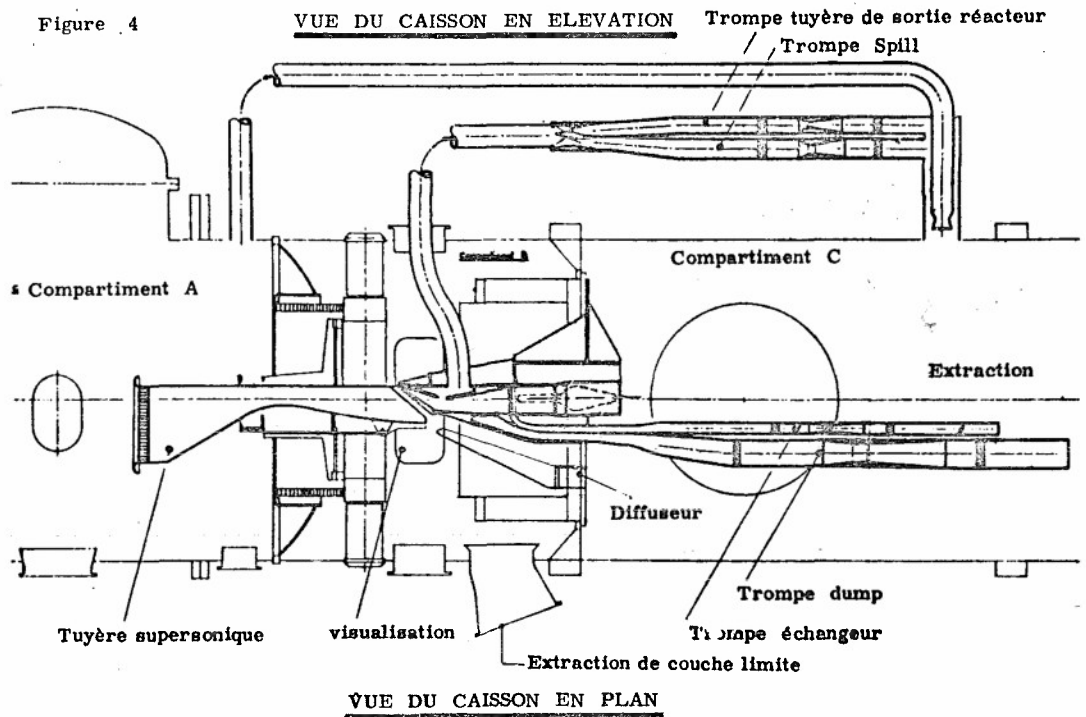
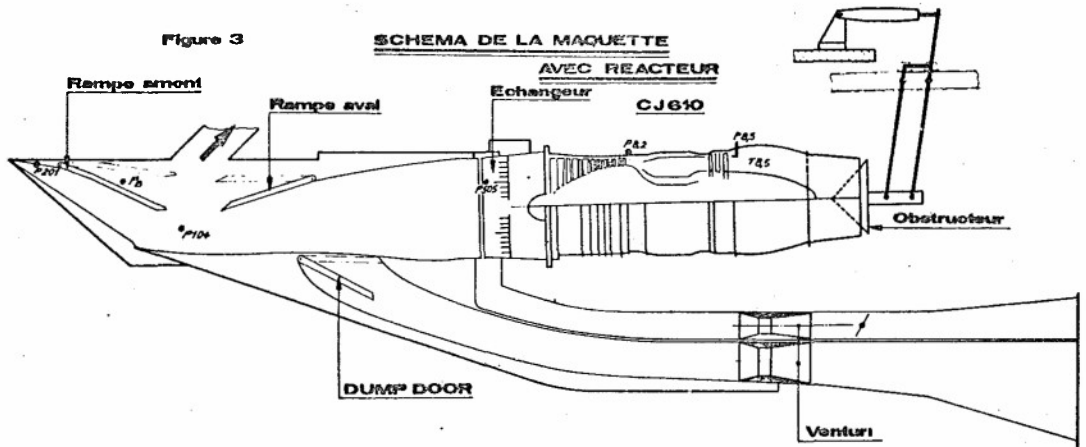
- 2.5. - Essais effectués. - Les essais se sont déroulés de juillet 65 à octobre 68 ; au total plus de 300 heures de fonctionnement ont été réalisées.

Les essais ont principalement porté sur les points suivants :

- caractérisation de l'entrée d'air
- Etude des paramètres de régulation
- Etude et optimisation de différents types de régulation
- Etude de l'influence du dérapage sur le pompage du moteur
- Etude de l'influence du pompage d'une entrée d'air sur l'autre
- Etude de l'influence du pompage d'un moteur sur l'autre entrée d'air
- Analyse des fluctuations de pression à l'entrée du moteur en fonction du dérapage.

3. - Essai de caractérisation d'un silencieux de tuyère. - La chambre anéchoïque A 17 et le banc de poussée A 04 du C. E. Pr. qui peuvent admettre des maquettes de tuyère de mêmes dimensions, permettent au constructeur de réaliser de meilleur compromis entre le gain acoustique et la perte d'un silencieux de tuyère.

- 3.1. - Le banc A 04 (figure 6) permet d'évaluer les performances de tuyères à simple ou double flux d'un débit maximal de 2,5 kg/s à des rapports de détente allant jusqu'à 16. La tuyère est fixée sur un canal cylindrique à deux parois supporté par des lames élastiques et limité en déplacement par une cellule à jauges.



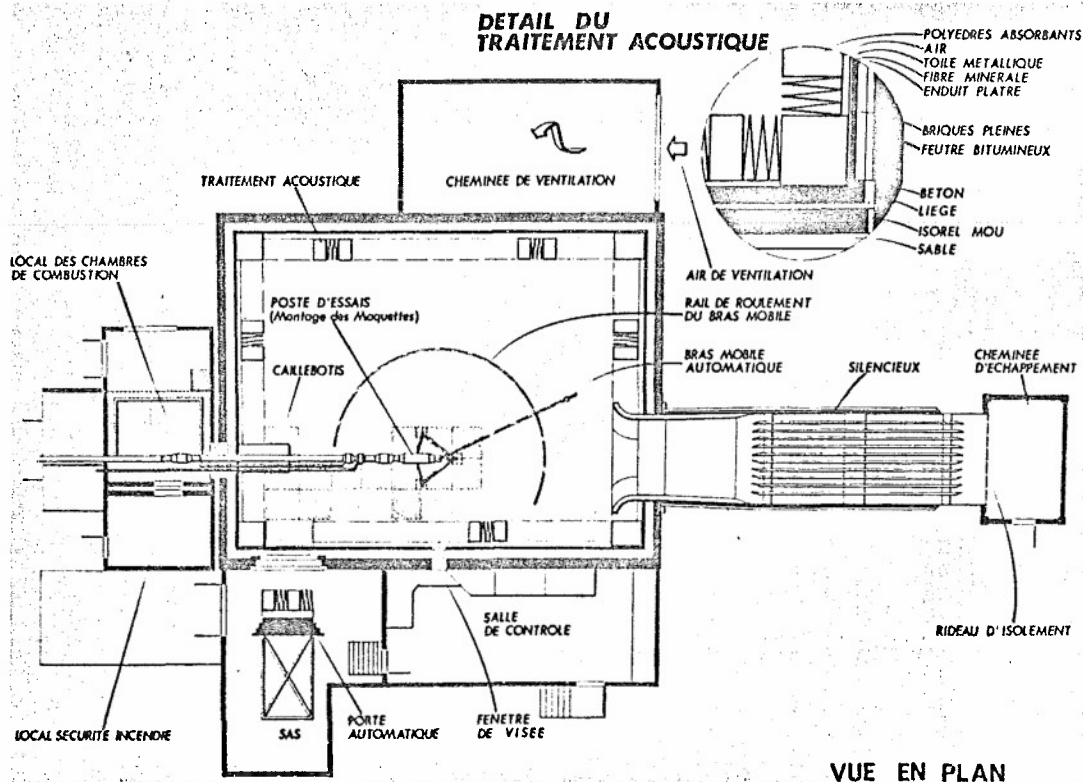


Les deux débits d'air sont mesurés par des cols soniques ; leur alimentation se fait radialement et sans aucun contact mécanique avec le canal : les fuites des labyrinthes de l'ordre de 5‰ du débit réel (jeu très faible 0,04 mm avec détection électrique de contact accidentel) sont périodiquement étalonnées. La bascule est étalonnée en statique avant chaque campagne par un système de pesons. L'ensemble de la chaîne de mesure est contrôlé avant chaque séance par une tuyère étalon. Une installation de stioscopie complète la connaissance aérodynamique du jet.

Pendant l'essai les conditions génératrices sont maintenues constantes, le taux de détente est réglé par la pression du compartiment d'essai. Les mesures et dépouillements entièrement automatiques permettent d'obtenir très rapidement les coefficients de poussée ( $\pm 2\%$ ) et de débit ( $\pm 1\%$ ) de la tuyère avec et sans silencieux.

- 3.2. - **Essai de performances acoustiques.** - La chambre anéchoïque A 17 a été spécialement conçue pour l'étude des bruits de jet. Il s'agit d'une chambre de 630 m<sup>3</sup> (figure 7) flottant à l'intérieur d'un premier local et reliée à un canal de dilution et à un conduit d'échappement des gaz. Elle peut recevoir des tuyères à simple ou double flux d'un débit maximal de 7,5 kg/s. La température génératrice maximale de 1350 °K est obtenue grâce à une chambre de combustion double au propane.
- Là encore le processus d'acquisition et de traitement des données est entièrement automatique : l'ordinateur suit le déplacement du microphone et commande l'acquisition. Une table traçante permet d'obtenir en temps réel le tracé correspondant au programme d'acquisition choisi au début du point. Un de ces programmes d'acquisition donne directement les niveaux de bruit moteur évalués en PNdB ou EPNdB et, grâce à un analyseur spectral au 1/3 d'octave (200 <math>f</math> <math>f</math> <math>100,000</math> Hz) les caractéristiques du spectre acoustique à l'angle d'émission sonore maximale.
- La chaîne de mesure est périodiquement réétalonnée à l'aide d'un générateur de bruit blanc parfaitement connu.

Figure 7



MEASUREMENT FULL-SCALE OF PROPELLING NOZZLE  
PERFORMANCE IN AN ALTITUDE TEST FACILITY

by

J C Ascough

National Gas Turbine Establishment, Pyestock  
Farnborough, Hampshire, England

SUMMARY

The Paper describes full-scale thrust-performance tests made in an altitude test cell at NCTE on a prototype two-stream propelling nozzle fitted to a turbojet engine installed within a simulated aircraft nacelle. The tests were made at conditions representing flight at Mach 2 at 20 km altitude.

Nozzle thrust efficiency obtained from these full scale tests is compared with that from a 1/10 scale model test rig. The preliminary analysis gave unexpectedly low full-scale efficiencies and, to investigate this, special tests were made with the secondary part of the nozzle removed. As a result of these primary nozzle tests, corrections were made to secondary nozzle test points giving satisfactory agreement between full-scale and model.

LIST OF SYMBOLS

(Note: strict S.I. units can be applied to every Eq. in this Paper)

A	area
$C_D$	discharge coefficient
[Inf.Coef]	influence coefficient
KCA	model test specific thrust
$K_J$	ratio of effective to observed flow in the jet pipe = $(W_J \sqrt{T_J})_{\text{effec}} / W_s \sqrt{T_s} \text{ calc}$
M	Mach number
P	total pressure
p	static pressure
T	total temperature
V	velocity
W	mass flow rate
x	distance between primary and secondary nozzle throats
$x_i$	a general measurement
$X_G$	gauge stream thrust (when this refers to a nozzle exit plane, it is usually called "the gross thrust")
$X_{GA}$	absolute stream thrust
$X_{PL}$	pre-load
$X_L$	load on the thrust meter
y	a performance result (= $\eta_{XG}$ )
$\Delta W$	leakage mass flow rate
$\eta_{XG}$	gauge thrust efficiency (sometimes called $\eta_F$ )
$\eta_{XGA}$	absolute thrust efficiency (sometimes called $\eta_s$ )
$\mu$	mass flow ratio = $W_s \sqrt{T_s} / W_J \sqrt{T_J}$
$\sigma$	standard deviation
	<u>Suffices which indicate location</u>
b	nozzle base
B	bleed flow exit
c	cell environment
E	exit plane of secondary nozzle
J	primary nozzle throat
S	secondary nozzle throat
SJ	slip joint
e	turbine exit
	<u>Other suffices</u>
calc	calculation, not direct measurement
con	convergent nozzle i.e. isentropic expansion limited to $M \leq 1$
cor	corrected for leakage
effec	effective, i.e. relating the observed full scale convergent nozzle thrust to model test performance
I	internal, i.e. does not include external effects
isen	isentropic value
J is $P_c$	isentropic expansion from $P_j$ to $P_c$
meas	measured by conventional test frame methods using readings external to the nozzle
model	model test value
M	measured flow, i.e. assuming no leaks
N	nozzle flow, after leaks have taken place
ref	reference instrumentation measurement
Sis $P_c$	isentropic expansion from $P_s$ to $P_c$

## 1. INTRODUCTION

In the interests of economy, most propelling nozzle research is carried out on scale models. But some questions can only be answered by tests on the full-scale engine and nozzle under flight conditions in an altitude test cell. One needs to know the effects of temperature and pressure profiles, of heat transfer, the effects of scale per se, and one must always expect the unexpected to turn up with the real hardware. Again in the interests of economy, it is the custom to fit full-scale performance tests into a programme of other features such as endurance tests, icing tests, re-lighting tests etc. And so it was that the opportunity arose to carry out some full-scale performance tests on a prototype two-stream nozzle with a turbojet engine installed within a simulated aircraft nacelle (SAN) in Cell 3 of the NGTE Engine Test Facility, for which the main test object was the investigation of heat transfer environment prior to aircraft flight tests.

In the present Paper, an account is given of these performance tests, with an analysis which concentrates on the efficiency of the nozzle, comparing the full-scale results with those obtained on a 1/10 scale model test rig.

## 2. COMPARISON BETWEEN FULL SCALE AND MODEL SCALE TEST ARRANGEMENTS

### 2.1 FULL SCALE TEST ARRANGEMENT

An impression of the arrangement is shown in Figure 1. The engine and primary nozzle are fitted inside the SAN which is mounted on the floating test frame. Dry air, at the correct conditions of simulated flight (in this case  $M = 2$  at 20 km altitude) is supplied to the engine through an inlet slip joint, having passed through the Cell 3 airflow meter. Secondary air is taken from the upstream plenum chamber and supplied to the SAN through four pipes with separate orifice plate air meters and separate slip joints. Unlike the model nozzle test rig, the inlet stream forces in Cell 3 are not zero, in fact they are of the same order of magnitude as that of powerplant gross thrust. The thrust equations are described in Section 3.

Details of the full scale prototype two-stream nozzle are shown in Figure 2. The jet pipe commences at the turbine exit annulus (engine station '6' where the instrumentation rakes are situated to measure  $P_6$ ;  $P_6$ ;  $T_6$ ). Within the jet pipe is the reheat flame holder. A variable primary nozzle of area  $A_J$  is fitted at the end of the jet pipe. For the first analysis of nozzle performance, it was assumed that the mass flow through the primary nozzle was equal to that at station '6' (i.e. no leaks). This primary flow is denoted  $W_6$  but it is based upon the cell air meter measurement. The primary nozzle temperature  $T_6(\text{calc})$  is based upon measured engine inlet temperature  $T_1$  together with temperature rise due to combustion of engine fuel flow, assuming manufacturer's data for combustion efficiency. Compressor work is balanced against turbine work (with small adjustments for air bleeds).

The secondary nozzle has a fixed throat of area  $A_S$  positioned an axial distance  $x$  away from the primary throat. Thrust-reverser buckets, positioned just ahead of the secondary nozzle throat, were locked open throughout the tests. Downstream of the secondary throat, the first part of the divergence is fixed but the second part consists of hinged flaps which are free to vary.

Extensive instrumentation was fitted at many stations within the secondary annulus and nozzle. Indeed, one object of the Cell 3 tests was to evaluate alternative sites for secondary pressure and temperature measurement. But for the present Report, the total pressure  $P_3$  and temperature  $T_3$  is taken to be that which was measured just ahead of the primary nozzle exit. The secondary mass flow  $W_3$  was given by the total flow measured at the four secondary inlet orifice plates.

### 2.2 MODEL SCALE TEST ARRANGEMENT

Model two-stream nozzles at 1/10 scale have been tested at NGTE on the rig depicted in Figure 3. A full discussion is given in Reference 1. Briefly, the model nozzle under test is mounted inside a depression box on the end of a pipe which is supported by air bearings. Dry air is supplied radially to the pipe inlet so that there is zero inlet stream force. Hence the measured gross gauge thrust of the test nozzle is simply:-

$$X_{\text{Gmodel}} = X_{\text{meter}} + A_{\text{piston}} (P_{\text{room}} - P_b) + X_{\text{inlet box leaks}} + X_{\text{depression box leaks}} \quad \dots(1)$$

Details of the model two-stream nozzle with its immediate upstream supply are shown in Figure 4. Different test arrangements could be built up of the secondary throat area  $A_S$  and for the axial distance  $x$  between primary and secondary throats. These geometric parameters are expressed non-dimensionally as  $A_S/A_J$  and  $x/D_J$ .

Variable fluid parameters are  $\mu = (W_S \sqrt{T_S}) / (W_J \sqrt{T_J})$ ;  $P_S/P_J$ ; and  $APR = P_J/P_b$ . In fact, the parameter  $\mu$  is equal to  $W_S/W_J$  because  $T_S = T_J (= 300K)$ . The primary flow ( $W_J \sqrt{T_J}$ ) is given by  $P_{\text{ref}}/P_{\text{ref}}$  making use of a previous calibration with a standard convergent nozzle. The secondary flow  $W_S$  is given by a British Standard orifice plate as shown in Figure 3.

For the model nozzle tests, the geometry was known very accurately while very uniform fluid conditions were measured as accurately as required.

## 3. THE SAN THRUST EQUATIONS IN CELL 3

The distribution of the various components in force is shown in Figure 5. The object of the Cell 3 tests is to evaluate the internal gross gauge thrust  $X_{GI}$  of the two-stream nozzle from readings of the thrust meters, after allowing for all the other forces at play.  $X_I$  is the load on the main thrust meter while  $X_{PI}$  is the pre-load which is sometimes applied to prevent  $X_I$  from becoming negative.

At the main engine inlet slip joint, and also at each of the four secondary slip joints, there is a Gauge Stream Force of the form:-

$$X_{GSJ(i)} = W(i) V(i) + A(i) (P(i) - P_0) \quad \dots(2)$$

and so, adding up the five elip joints we get:-

$$X_{GSJ} = \sum_{j=1}^5 X_{GSJ}(j) \quad \dots(3)$$

Again, there are three overboard bleeds from the engine which discharged rearwards to produce a little extra thrust of the form:-

$$X_{GB}(j) = W(j) V(j) + A(j) (P(j) - P_0) \quad \dots(4)$$

and so, adding up the three bleeds we get:-

$$X_{GB} = \sum_{j=1}^3 X_{GB} \quad \dots(5)$$

Finally, accounting for all the forces in Figure 5 we get:-

$$X_{GImeas} = (X_L - X_{PL}) + X_{GSJ} - X_{GB} \quad \dots(6)$$

Now, before we can evaluate the two-stream nozzle efficiency, we need to calculate the isentropic gauge thrust of the primary flow and secondary flow, with both flows completely expanded to cell pressure  $P_0$ . Thus, for the primary flow  $W_s$ , assuming no leaks, we have:-

$$X_{GJiePc} = W_s \sqrt{T_{scalc}} \left( \frac{V}{\sqrt{T}} \right)_{JisPo} = W_s V_{JiePo} \quad \dots(7)$$

and for the secondary flow, assuming no leaks, we have:-

$$X_{GSiePc} = W_s \sqrt{T_s} \left( \frac{V}{\sqrt{T}} \right)_{SisPo} = W_s V_{SisPo} \quad \dots(8)$$

Hence the gauge thrust efficiency is:-

$$\eta_{XG} = \frac{X_{GImeas}}{W_J V_{JisPc} + W_S V_{SisPc}} \quad \dots(9)$$

#### 4. COMPARISON BETWEEN FULL-SCALE AND MODEL SCALE NOZZLE EFFICIENCY

##### 4.1 PRELIMINARY ANALYSIS OF FULL-SCALE NOZZLE EFFICIENCY

Results from the preliminary analysis of the full-scale tests in Cell 3 are shown in Figure 6, together with the NGTE model test performance for the same range of flow ratio  $\mu$  as in the full-scale tests.

An immediate impression from the Figure is that the preliminary full-scale nozzle thrust efficiency is about 1.7 per cent low compared with model tests. One possible explanation is the presence of leaks from the jet pipe into the secondary annulus, and also from the nacelle into the cell environment. Alternative explanations include the possibility of errors of measurement. To examine these possibilities special tests were made on the primary nozzle alone with the secondary nozzle removed, as described in Section 4.2.

##### 4.2 TESTS ON PRIMARY NOZZLE ALONE

From tests on the model nozzle rig the absolute thrust efficiency of a convergent nozzle had previously been established, viz:-

$$\eta_{XGA,con,model} = \left[ \frac{\text{measured } X_G + A_J P_b}{W_J \sqrt{T_J} \left( \frac{X_{GA}}{W \sqrt{T}} \right)_{ieen,con}} \right]_{con,model} \quad \dots(10)$$

This efficiency can be carried across to the analysis of the full-scale tests (as Figure 1 but with primary nozzle only) to deduce the effective flow through the nozzle, from measurements of nozzle thrust, viz:-

$$(W_J \sqrt{T_J})_{effec} = \left[ \frac{\text{measured } X_G + A_J P_c}{\left( \frac{X_{GA}}{W \sqrt{T}} \right)_{ieen,con}} \right]_{con,Cell 3} \times \frac{1}{\eta_{XGA,con,model}} \quad \dots(11)$$

As a matter of convenience, the denominator of Eq.(11) was applied in the form of the parameter, KCA:-

$$KCA = \left( \frac{X_{GA}}{W \sqrt{T}} \right)_{ieen,con} \times \eta_{XGA,con,model} \quad \dots(12)$$

Results from the full-scale tests in Cell 3, expressed in the form:-

$$K_J = \frac{(W_J \sqrt{T_J})_{effec}}{W_s \sqrt{T_s oalc}} \quad \dots(13)$$

are shown in Figure 7.

A special difficulty with the full-scale tests is the measurement of variable nozzle area  $A_{J,meas}$  as used for the upper curves in Figures 7. The unexpected rapid rise of the  $K_J$  curve to values greater than 1.00 at low  $P_J/P_C$  is thought to be due to error in  $A_{J,meas}$ . An alternative analysis putting  $A_J = A_{J,isen}/C_{D,model}$  leads to the lower curve in Figure 7. Either way, for  $P_J/P_C$  greater than 4 the value of  $K_J$  (which is relatively insensitive to  $A_J$  at the higher values of  $P_J/P_C$ ) levelled out at about 0.984 whereas before these tests it would have been expected that  $K_J$  would be in the range 0.995 to 1.000 - here was a clue to the low performance of the complete two-stream nozzle (Figure 6).

#### 4.3 CORRECTION OF FULL-SCALE NOZZLE EFFICIENCY

##### 4.3.1 ALTERNATIVE HYPOTHESES

A more detailed expression for  $K_J$  can be assembled from Eqs. (13), (12), (11) and an equation similar to (6):-

$$K_J = \frac{(X_L - X_{PL}) + X_{GSJ} - X_{GB} + A_J P_o}{W_e \sqrt{T_e} \text{ calc} \left( \frac{X_{GA}}{W \sqrt{T}} \right)_{isen,con}} \times \frac{1}{\eta_{XGA,con,model}} \quad \dots(14)$$

con, Cell 3

and a correspondingly detailed expression for  $\eta_{XG}$  can be assembled from Eqs. (9), (8), (7), (6):-

$$\eta_{XG} = \frac{(X_L - X_{PL}) + X_{GSJ} - X_{GB}}{W_e \sqrt{T_e} \text{ calc} \left( \frac{V}{\sqrt{T}} \right)_{JisPo} + W_S \sqrt{T_S} \left( \frac{V}{\sqrt{T}} \right)_{SisPo}} \quad \dots(15)$$

con+esc, Cell 3

Both Eq.(14) and Eq.(15) show many explicit terms for which error of measurement could possibly cause the value of  $K_J$  and of  $\eta_{XG}$  to be low. Furthermore, it is conceivable that spurious effects upon the Cell 3 test system, such as test frame friction or stray pressure forces which are not explicitly measured at all in Eqs. (14) and (15), could also cause  $K_J$  and  $\eta_{XG}$  to be low. Then there is the possibility of leakage from the jet pipe such that  $W_J$  does not equal  $W_e$  and leakage from the secondary annulus such that  $W_S$  passing through the nozzle does not equal the measured value of  $W_S$ . All these possibilities can be classified into the following two extreme hypotheses:-

H(I): that the low value of  $K_J$  in the primary nozzle tests, and the low value of  $\eta_{XG}$  in the secondary nozzle tests is due to a combination of error in explicitly measured terms, together with the presence of spurious non-measured effects upon the Cell 3 test system. (This hypothesis assumes that there are no leaks.)

H(II): that leaks exist such that primary leakage is responsible for the low value of  $K_J$ , and such that both primary and secondary leakage is responsible for the low value of  $\eta_{XG}$  for the complete secondary nozzles.

The arguments and corrections developing from Hypotheses (I) and (II) are given in Sections 4.3.2 and 4.3.3.

##### 4.3.2 CORRECTION OF RESULTS UNDER HYPOTHESIS (I)

If we accept Hypothesis (I), this is to say that measurement error, or some other effect apart from leakage, causes full-scale performance to appear worse than model test performance as manifest by the departure of  $K_J$  from the value of 1.000. And so the 'effectiveness' properties of the gas entering the primary nozzles are given by:-

$$(W_J \sqrt{T_J})_{effeo} = K_J (W_e \sqrt{T_e} \text{ calc}) \quad \dots(16)$$

Returning now to the analysis of the full-scale secondary nozzle results, we can apply Eq.(16) to the calculation of isentropic thrust of the primary flow, as an alternative to Eq.(7):-

$$X_{GJisPo} = K_J (W_e \sqrt{T_e} \text{ calc}) \left( \frac{V}{\sqrt{T}} \right)_{JisPo} \quad \dots(17)$$

$$= K_J W_e V_{JisPo}$$

Thence the corrected full-scale nozzle thrust efficiency, under Hypothesis (I) is given by:-

$$\eta_{XG}^J = \frac{X_{GImeas}}{K_J W_e V_{JisPo} + W_S V_{SisPo}} \quad \dots(18)$$

The test points from the preliminary analysis in Figure 6, when re-evaluated by Eq.(18) with  $K_J$  from the upper curve in Figure 7, gives the corrected results shown in Figure 8.

Thus the full-scale nozzle efficiency when corrected under Hypothesis(I) becomes about 0.5 per cent less than that of NGTE model tests.

##### 4.3.3 CORRECTION OF RESULTS UNDER HYPOTHESIS (II)

Let us suppose that there are leaks  $\Delta W_J$  from jet pipe to secondary annulus and  $\Delta W_S$  from secondary annulus to cell environment, as shown in Figure 9. Then following Hypothesis (II), the proportional jet pipe leakage can be given by the  $K_J$  results, viz:-

$$W_{JN} = W_{JM} - \Delta W_J \quad \dots(19)$$

$$\frac{\Delta W_J}{W_{JN}} = 1 - \frac{W_{JM}}{W_{JN}} \quad \dots(20)$$

Referring back to Eq.(13) and putting

$$\frac{W_{JM}}{W_{JN}} = \frac{(W_J \sqrt{T_J})_{\text{effec}}}{W_g \sqrt{T_g \text{ calc}}} \quad \dots(21)$$

we obtain

$$\frac{\Delta W_J}{W_{JN}} = 1 - K_J \quad \dots(22)$$

The next problem is to find the secondary leakage  $\Delta W_g$ . This has been estimated by a treatment due to Lewis and Armstrong of NGTE using the secondary nozzle swallowing characteristics shown in Figure 10.

From Figure 10 we can find values of  $\Delta \mu$ , where:-

$$\Delta \mu = \mu_N - \mu_M = \frac{W_{SN} \sqrt{T_{SN}}}{W_{JN} \sqrt{T_{JN}}} - \frac{W_{SM} \sqrt{T_{SM}}}{W_{JM} \sqrt{T_{JM}}} \quad \dots(23)$$

Now, from Figure 9 we see that:-

$$\Delta W_S = W_{SM} - W_{SN} + \Delta W_J \quad \dots(24)$$

which can be combined with Eq.(23) to give:-

$$\frac{\Delta W_S}{W_S} = \frac{1}{\mu_M} \left\{ \mu_M + \frac{\Delta W_J}{W_{JM}} \sqrt{\frac{T_S}{T_J}} - (\Delta \mu + \mu_M) \left( 1 - \frac{\Delta W_J}{W_{JM}} \right) \sqrt{\frac{T_{SM}}{T_{SN}}} \right\} \quad \dots(25)$$

Eq.(25) has been evaluated for two specimen test points from Figure 6 to give the secondary leakage  $\Delta W_g/W_g$ , which was found to be of the order of 10 per cent.

Hence

$$W_{SN} = W_{SM} + \Delta W_J - \Delta W_S \quad \dots(26)$$

Then expanding the nozzle flows  $W_{JN}$  and  $W_{SN}$  isentropically to  $P_c$  we have for the nozzle gauge thrust efficiency, corrected for leakage:-

$$\eta_{XG}^n = \frac{X_{G \text{ meas}}}{W_{JN} V_{J \text{ is } P_c} + W_{SN} V_{S \text{ is } P_c}} \quad \dots(27)$$

Results of these corrections under Hypothesis (II) applied to the two specimen test points are shown in Figure 11. Thus the full-scale nozzle efficiency when corrected under Hypothesis (II) for both primary and secondary leakage becomes about 0.7 per cent less than the efficiency given by NGTE model tests.

## 5. PRECISION AND ACCURACY

Before discussing this topic, it is important to define the terminology. The word 'precision' refers to uncertainty of a value due to the presence of random error (i.e. noise). The word 'accuracy' refers to uncertainty of a value due to the presence of systematic error (i.e. bias).

An investigation by K F A Wallis of NGTE showed that the scatter of  $\eta_{XG}$  results in Figure 6 of the present Paper follows a Gaussian (i.e. Normal) distribution about the fitted line, with a standard deviation of  $\sigma = 0.0015$ . Thus the 95 per cent level of precision of  $\eta_{XG}$  is  $\pm 2\sigma = \pm 0.0030$  or  $\pm 0.3$  per cent for a single test point. The precision of the fitted line itself is improved by the factor  $1/\sqrt{n}$  approximately for  $n$  test points, and so the  $\eta_{XG}$  line in Figure 6 has a 95 per cent level of precision of  $\pm 0.0030/\sqrt{37} = \pm 0.0005 = \pm 0.05$  per cent, which is a negligible uncertainty.

Unfortunately, as a fundamental rule, one cannot be so definite about accuracy because systematic error is never obvious, although every precaution is taken to eliminate it by calibration of measuring instruments against other standards. To help identify the most important sources of such systematic error, Wallis made an analysis of the Influence Coefficients of the measurements which were made during the Cell 3 tests on the SAN. An Influence Coefficient is defined as:-

$$\left[ \text{Influence Coefficient of } x_1 \text{ relative to } y \right] = \left[ \frac{\partial y}{\partial x_1} \frac{x_1}{y} \right] \quad \dots(28)$$

where in this case

$$y = \eta_{XG}$$

and  $x_1$  = a general measurement (e.g. airmeter  $\Delta P$ ).

An alternative definition of Influence Coefficient would be the percentage change in  $\eta_{XG}$  resulting from a 1 per cent change in  $x_1$ . Hence each individual percentage measurement error ( $100 dx_1/x_1$ ) makes a corresponding percentage contribution ( $100 dy_1/y$ ) to error in  $y$  ( $y = \eta_{XG}$  here) thus:-

$$\left( 100 \frac{dy_1}{y} \right) = \left[ \text{Inf Coef} \right] \times \left( 100 \frac{dx_1}{x_1} \right) \quad \dots(29)$$

Then, assuming that these systematic error contributions follow a probability distribution, the total systematic error in  $y$  ( $= \eta_{XG}$ ) is calculated by root sum of squares:-

$$(\text{Total } \% \text{ systematic error in } y) = \left( \sum_1^a \left\{ [\text{Inf Coef}] \left( 100 \frac{dx_i}{x_i} \right) \right\}^2 \right)^{\frac{1}{2}} \quad \dots(30)$$

At the simulated flight condition of  $M = 2$  at 20 km altitude in Cell 3, the Influence Coefficients were as shown in Table I.

Now, a formal assessment of all the elements  $dx_i$  of systematic measurement error has not been made for these particular SAN tests in Cell 3 but, as an example, if we were to put  $(100 dx_i/x_i) = 1$  per cent for every element in Eq.(30) and taking values of Influence Coefficients from Table I we would have:-

$$(\text{Total } \% \text{ systematic error in } y(=\eta_{XG})) = \left( \sum_1^a \left\{ [\text{Inf Coef}] \right\}^2 \right)^{\frac{1}{2}} \quad \dots(31)$$

$$= 0.996 \text{ per cent}$$

This result is dominated by the greatest Influence Coefficient ( $= +0.81$ ) in Table I, which is that of the engine inlet slip joint total pressure  $P_{GJ1}$ . However, this particular pressure is measured very carefully by means of an array of 60 different pitot tubes, and so putting  $x_i =$  (mean of 60 measurements) we should have only a small error  $dx_i$  which will balance the large Influence Coefficient in Eq.(30) to produce an acceptable error contribution  $dy_i$ . And so, even though a complete formal systematic error analysis has not been made, one feels that the accuracy (due to systematic error or bias) of the  $\eta_{XG}$  results in Cell 3 should be better than Eq.(31) and is perhaps about 0.5 per cent.

## 6. DISCUSSION

Credibility of the full scale nozzle thrust efficiency is judged by comparison with model test results. The observed discrepancy of about 1.7 per cent in the preliminary analysis, after allowing for a full-scale 'technology loss' of about 0.5 per cent due to practical features not present in the model, is about 1.2 per cent. Now the accuracy, due to residual systematic measurement error, is thought to be within about 0.5 per cent (precision of the fitted  $\eta_{XG}$  line due to test measurement random error is practically perfect) and so there is a need to explain by other means a discrepancy of at least 0.7 per cent in  $\eta_{XG}$ .

The two extreme hypotheses, of H(I): explicit measurement errors plus spurious non-measured effects, and of H(II): leakage, are each separately able to explain the full-scale discrepancy but it is impossible to tell in retrospect which combination of H(I) and H(II) was actually responsible. It would be wise to guard against the future possibility of leakage - the full effects of which can only be detected by altitude cell tests such as described in the present Paper.

## 7. CONCLUSIONS

Performance tests were made on a prototype two-stream propelling nozzle fitted to a turbojet engine within a simulated aircraft nacelle. Conditions at engine inlet and at nozzle exit were selected to represent flight at Mach 2 at 20 km altitude.

Preliminary analysis of the two-stream nozzle thrust efficiency gave low performance compared with model tests. To throw light on this, the secondary part of the nozzle was removed and special performance tests were made with the primary nozzle alone - again low thrust performance was observed.

Two hypotheses are set up to explain the discrepancy between full-scale and model, representing either H(I): explicit measurement errors plus spurious non-measured effects, or H(II): leakage. Each hypothesis can by itself explain the shortfall in the full scale nozzle efficiency.

Only by making tests in an altitude cell under correctly represented flight conditions such as described in this Paper, including tests on the jet pipe and primary nozzle alone, is it possible to check the existence and magnitude of such full-scale performance problems.

Precision (due to random error, or noise) of the full-scale performance results is  $\pm 0.3$  per cent for a single test point, or  $\pm 0.05$  per cent for the fitted  $\eta_{XG}$  line. Accuracy (due to residual systematic measurement error or bias) is thought to be within  $\pm 0.5$  per cent.

## REFERENCE

1. W G E Lewis and F W Armstrong  
Some experiments on two-stream propelling nozzles for supersonic aircraft  
7th ICAS Congress, Rome, Italy, 1970 - September, Paper No. 70-48

The writer of this Paper wishes to acknowledge the contribution of Mr W G E Lewis and Mr F W Armstrong of NGTE to whom the concept of so much of the performance analysis is due. Credit is also due to Mr R G T Drage and Mr M R Nix who were responsible for controlling and analysing these very complex full-scale tests. Finally, a great deal of valuable help came from discussions with colleagues in engine firms outside of NGTE.

Thanks are also due to the MOD(AS) for permission to publish this Paper. The views expressed are entirely those of the writer.

Cell 3 measurements $x_i$	Influence Coefficient relative to $\eta_{XG}$
Primary air meter $\Delta P$	-0.23
Primary air meter $p$	-0.27
Primary air meter $T$	+0.27
Fuel mass flow	-0.03
Turbine exit pressures $P_e$	-0.14
Engins slip joint pressures $P_{SJ1}$	+0.81
Engine slip joint temperature $T_1$	-0.11
Thrustmeter load $X_L$	+0.25
Primary nozzle area $A_J$	0
Secondary nozzle exit area $A_E$	0
Secondary flow meters $\Delta P$	+0.03
Secondary flow meters $p$	+0.03
Secondary slip joint pressures $P_{SJ,S}$	+0.20

TABLE I - INFLUENCE COEFFICIENTS RELATIVE TO  $\eta_{XG}$  FOR  
SAN TESTS IN CELL 3

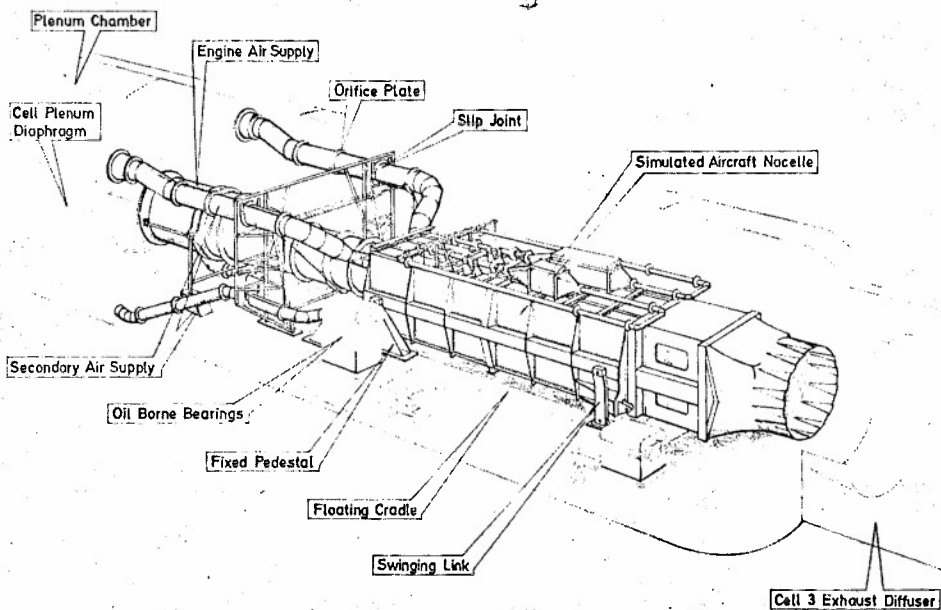


FIG.1 TURBOJET ENGINE WITH SIMULATED AIRCRAFT NACELLE AND PROTOTYPE NOZZLE IN NGTE ETF CELL 3

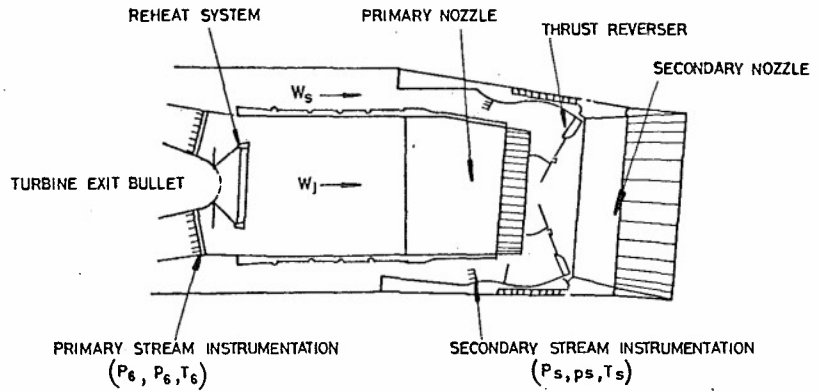


FIG.2 FULL SCALE JET PIPE AND PROTOTYPE SECONDARY NOZZLE

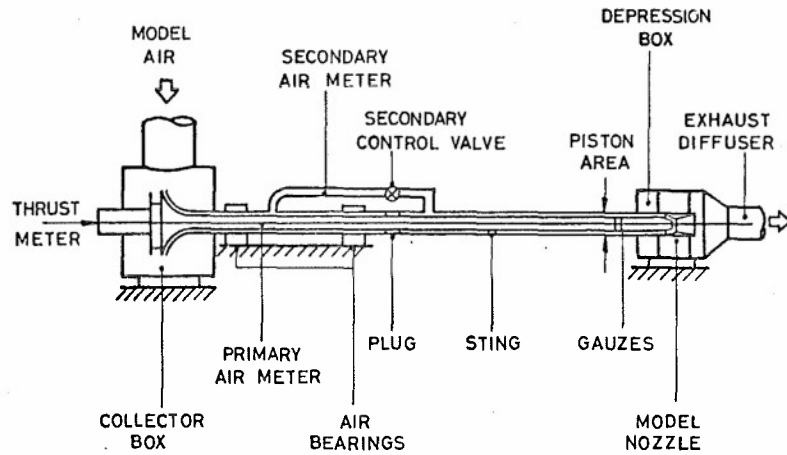


FIG.3 MODEL NOZZLE TEST RIG

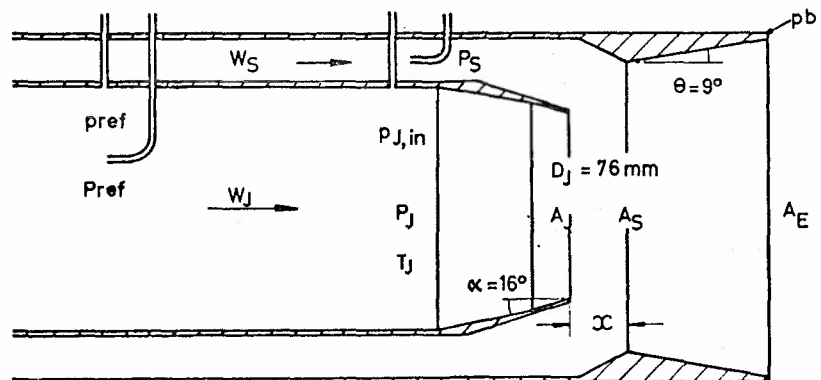


FIG.4 MODEL JET PIPE AND SECONDARY NOZZLE

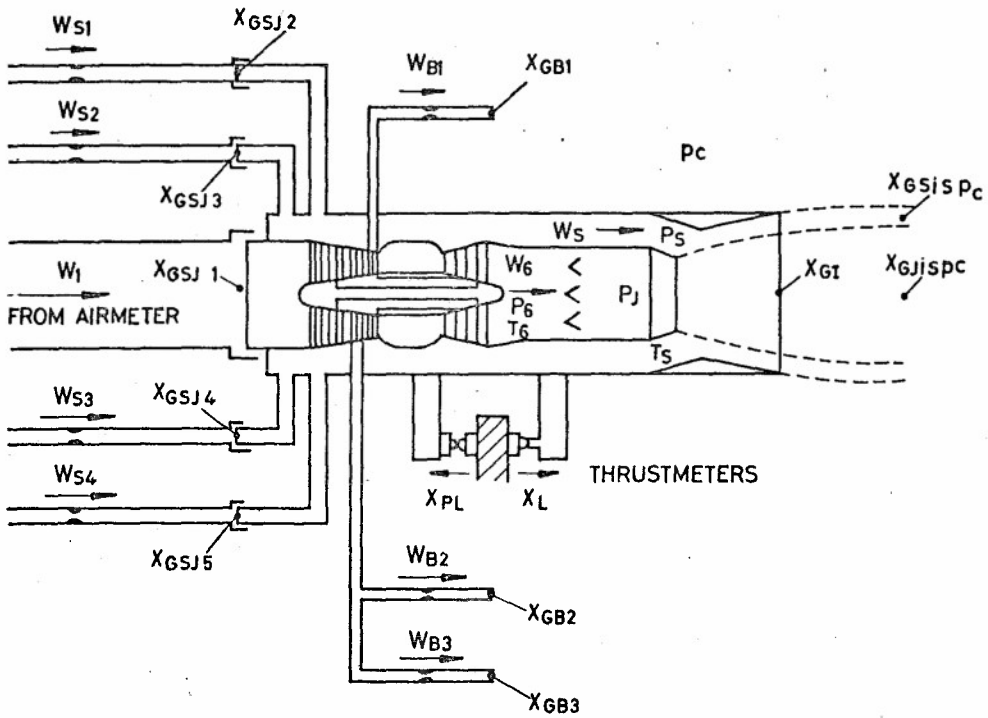


FIG.5 S.A.N. THRUST COMPONENTS IN CELL 3

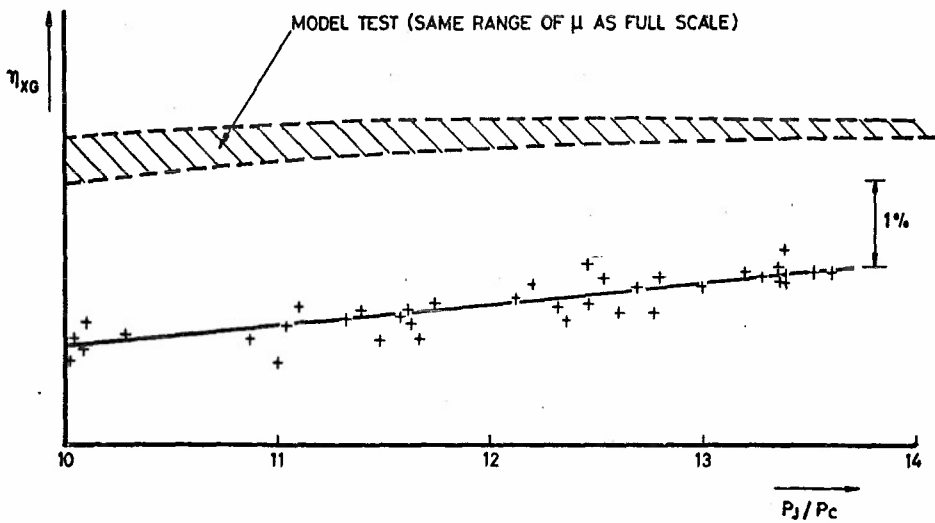
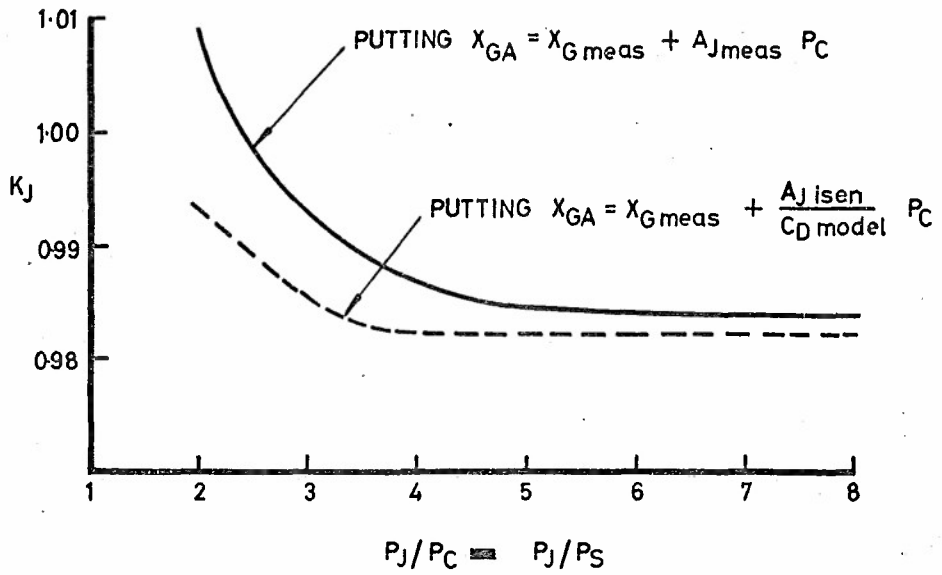
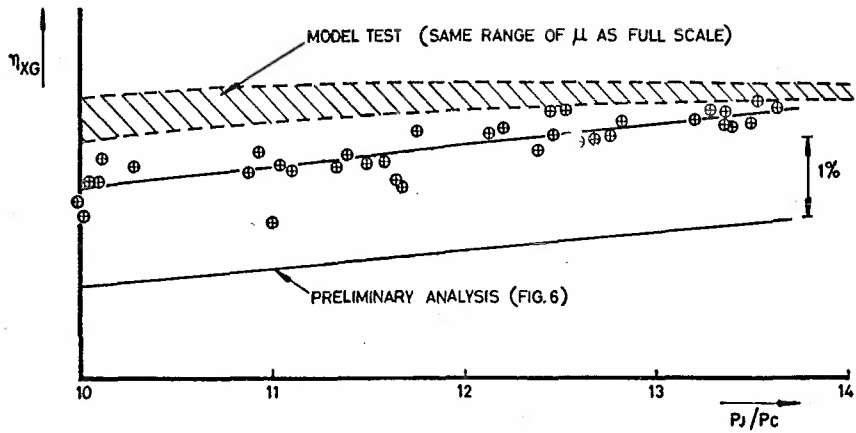


FIG. 6 PRELIMINARY ANALYSIS OF FULL SCALE NOZZLE EFFICIENCY



**FIG.7 EFFECTIVE FLOW PARAMETER OF ISOLATED PRIMARY NOZZLE**



**FIG.8 FULL SCALE NOZZLE THRUST EFFICIENCY - CORRECTED UNDER HYPOTHESIS (I)**

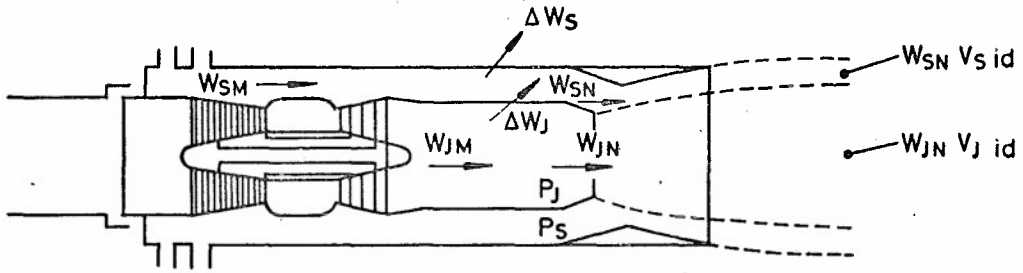


**FIG.9 LEAKAGE ASSUMPTIONS IN FULL SCALE TESTS**

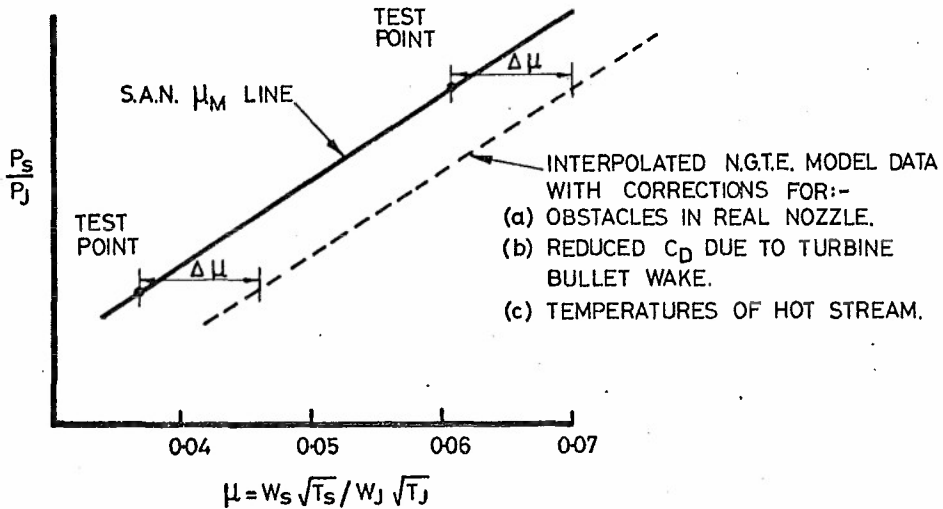


**FIG.10 SECONDARY NOZZLE SWALLOWING CHARACTERISTICS**

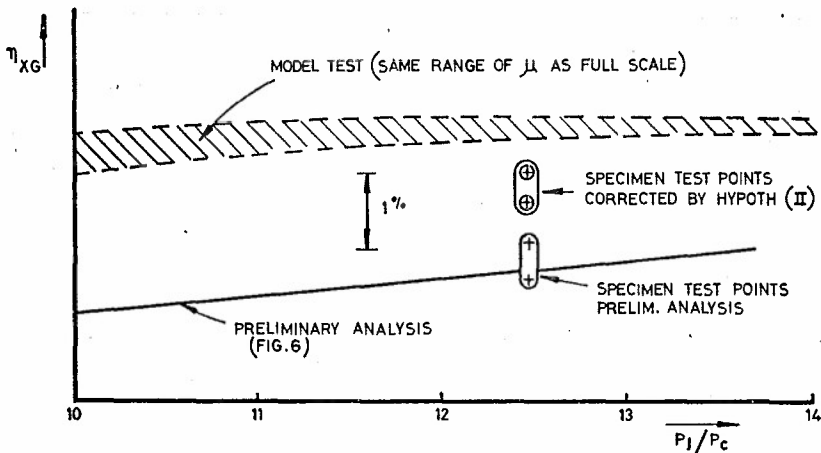


**FIG.11 FULL SCALE NOZZLE THRUST EFFICIENCY -CORRECTED UNDER HYPOTHESIS(II)**

## INLET-ENGINE-NOZZLE WIND TUNNEL TEST TECHNIQUES

by

D. N. Bowditch

Lewis Research Center

National Aeronautics and Space Administration

Cleveland, Ohio

## SUMMARY

Experimental investigations of the inlet, engine and exhaust nozzle of a supersonic propulsion system have been underway at the Lewis Research Center. Exhaust nozzle results are presented which compare wind tunnel and flight results and assess the accuracy of flight measurements. Comparisons are also presented for nozzle performance obtained with a cold jet, a powered turbojet simulator, and a solid jet boundary simulator. The effect of the local boundary layer on nozzle performance is also discussed. The need for good dynamic measurements during inlet-engine testing is illustrated for transients such as inlet unstart and engine stall. Also, the transient nature of inlet distortion and its effect on the engine is presented for two different operating conditions.

## SYMBOLS

$A_n$	nacelle cross sectional area
$C_g$	gross thrust coefficient, $T-D/T_{ip}$
$C_{D\beta}$	boattail drag coefficient, $D_\beta/qA_n$
$D$	drag
$D_\beta$	boattail drag
$d_n$	nacelle diameter
$d_c$	cowl lip diameter
$M_0$	free stream Mach number
$M_2$	compressor face Mach number
$N/N_D \sqrt{\theta}$	corrected portion of design engine speed
$P_0$	free stream total pressure
$P_2$	compressor face total pressure
$\bar{P}_2$	average compressor face total pressure
$P_3$	compressor exit total pressure
$\Delta P_{2rms}$	root mean square value of dynamic component of compressor face pressure
$\overline{\Delta P}_{2rms}$	average value of $\Delta P_{2rms}$
$P_2$	compressor face static pressure
$P_{2max}$	maximum compressor face static pressure during hammershock after surge
$q$	dynamic pressure
$r$	rounded boattail radius
$T$	thrust
$T_{ip}$	ideal primary thrust
$\alpha$	angle of attack
$\sigma$	standard deviation

## INTRODUCTION

Within existing ground test facilities experimental investigation of the aircraft propulsion system can rarely be done under the exact conditions that will exist in flight. Facilities are normally too small or models become too complex to simulate the actual flight conditions. Therefore, compromises are necessary and these must be made in such a way that their effect is negligible, or understood well enough so that the results can be corrected properly. Several experimental programs in this area of supersonic propulsion systems are currently underway at the Lewis Research Center, references 1-3.

Much testing of supersonic exhaust nozzles is required at off design speeds corresponding to high subsonic and transonic flight conditions. The geometry of a large area ratio nozzle that is efficient at supersonic pressure ratios of 20 and 30 must be changed at subsonic conditions in order to operate efficiently at much lower pressure ratios of 2 to 4. Collapsing the nozzle normally exposes a boattail or opens inlets on the nozzle which makes it a potential source of drag and the resulting performance is very sensitive to external flow conditions. These problems are investigated in the 8- by 6-foot wind tunnel using isolated nacelle models and subscale aircraft models. In addition, to overcome the size limitations of transonic wind tunnel testing, a flight test program utilizing underwing nacelles on an F-106 aircraft was initiated as illustrated in figure 1. This permits tests of a wide variety of complex nozzles on a complete aircraft configuration that is similar to that required for a supersonic cruise aircraft. The aircraft testing technique and its accuracy will be reviewed as well as several comparisons with wind tunnel data on similar configurations. Several other wind tunnel test techniques will also be described.

In the 10x10 supersonic propulsion wind tunnel, recent inlet-engine test programs have investigated the propulsion system stability and its integration with the airframe. Dynamic considerations are of primary importance in understanding the system operation under conditions such as inlet unstart, engine stall and high distortion. If the significance of the dynamic response of the propulsion system is not recognized, system instabilities may be encountered which could have been avoided by proper measurement and interpretation of dynamic conditions. To study the inlet-engine compatibility problem, several supersonic mixed-compression inlets have been tested with J-85 turbojet engines at Mach 2.5 cruise conditions. Highlights from these tests are used to demonstrate the test techniques used and the considerations necessary to properly evaluate the large-scale dynamic interactions of the propulsion system and airframe.

## EXHAUST NOZZLE TESTING

Typical models used for exhaust nozzle testing in the 8x6 foot wind tunnel are shown in figure 2. The isolated nacelle model is used to investigate external flow effects on nozzles. Separate primary and secondary flows are provided through the strut from an external source. The model is of sufficient length that the nozzle performance is not influenced by the disturbances caused by the closed nose of the nacelle and by the support strut at high subsonic speeds. Unfortunately it also provides an undesirably thick boundary layer. The two aircraft models are 5% and, 22% scale models of the F-106 aircraft. The smaller model has been used to investigate the effect of various nacelle shapes and results from those tests indicated the engine accessory bump had negligible effect on boattail drag. Because of transonic tunnel blockage limitations, the flow through nacelles were about 3 centimeters in diameter, and only capable of investigating simple boattails which simulated a variable flap ejector nozzle. The larger 22% scale model had a powered turbojet simulator in the underwing nacelle allowing both inlet and exhaust nozzle flows to be simulated. The model was also large enough to permit investigation of more complex exhaust nozzles. This model is large enough to cause concern about transonic wind tunnel wall interference, and comparison with F-106 flight data is being used to verify the interference-free speed range.

The smaller model utilized a cylindrical tube as a jet boundary simulator since a realistic jet was not practical for such small scale. This concept has been investigated on the isolated jet exit model where the boattail drag was measured with a fully expanded cold air jet and a cylindrical jet boundary simulator, reference 4. Results from that test are compared on figure 3. The drag coefficient of a sharp-edged  $15^\circ$  boattail is presented as a function of free-stream Mach number. The dashed and solid lines represent the drag for a fully expanded jet and jet-off respectively. The data symbols are

for the drag with a jet boundary simulator and it is obvious that the simulator is a good representation of a flowing jet for this case where the flow over the boattail was attached and well behaved.

Since model testing is obviously limited by transonic wind tunnel interference considerations, the F-106 flight test program was initiated at Lewis to permit investigation of propulsion systems at transonic speeds, references 5-8. The research nacelles are illustrated in figure 4. Two J85-13 afterburning turbojet engines are housed in nacelles under the aircraft wings. The nacelle location is typical of supersonic cruise aircraft, with the exhaust nozzle extended just beyond the trailing edge of the wing. The installation permits study of complex installed exhaust nozzles at relatively large size and at transonic speeds. The installation is also being used to make flyby noise measurements to determine flight velocity effects on the effectiveness of jet noise suppressors. This aircraft is particularly useful for this type of work because it is easy to make major changes in nozzle geometry and because a complete data system is available onboard the aircraft to monitor engine and aircraft operating conditions.

The method of nozzle evaluation is illustrated in figure 4. The nacelle is supported by a parallelogram linkage with a load cell restraining the nacelle along its axis to measure the net thrust minus drag. An accelerometer is used to determine any components of nacelle weight or inertia forces aligned with the thrust axis. The drag of the nacelle forward of the nozzle attachment station was evaluated throughout the aircraft operating envelope using a reference nozzle. The internal performance of this nozzle was calibrated and the drag of the well-defined base region was easily obtained with a few pressure measurements. The calibrated nacelle drag is added to the load cell reading of net thrust minus drag to determine research nozzle thrust minus drag. In order to evaluate nozzle performance, the primary conditions must be accurately determined. This was done by calibration of the J-85 engines in an altitude test facility prior to flight testing. Primary flow is obtained in flight testing by combining the airflow from the compressor calibration with the measured fuel flows. The nozzle total pressure and temperature were obtained from measurements at the turbine exit and an afterburner calibration of temperature rise and pressure drop. The ideal thrust of this primary flow is then compared with the measured thrust minus drag of the nozzle. Reference nozzle flights were performed at several times during the program to initially evaluate nacelle drag and later to evaluate system repeatability. The measurement accuracy of nozzle performance on the F-106 was determined from these flights, reference 9, and is presented in figure 5. The table contains the influence coefficient for each parameter on the nozzle gross thrust,  $C_g$ , the standard deviation for each parameter and the resulting standard deviation for the gross thrust coefficient. The standard deviation for each of the parameters was estimated by combining standard deviations of calibrations and required instrument accuracies. The resulting standard deviation of nozzle gross thrust coefficient of about one and one-half percent is consistent with observed data scatter.

In order to develop a testing technique that uses a model large enough to accommodate a powered turbojet simulator, the 22% scale F-106 model was tested. The model is shown installed in the 8x6 supersonic wind tunnel in figure 6. The total frontal area of the half-plane model was 1.8 percent of the wind tunnel cross sectional area and the splitter plate and supports added another percent blockage to that. The wing of the model is mounted on a multi-component balance and the nacelle is mounted to the wing on a thrust balance. A powered turbojet simulator is mounted in the nacelle where it provided simulation of both the J-85 inlet and exhaust nozzle flows.

A cutaway drawing of the turbojet simulator is shown in figure 7. It is designed to simulate a modern supersonic turbojet engine. The six-stage axial flow compressor provides a peak pressure ratio of 3.5. The compressor and turbine flows, which are matched in pressure and temperature, join just downstream of the turbine. Makeup air can be added to the resulting primary stream to provide the higher weight flows required to simulate afterburner operation. Secondary air is furnished by a third pipe for testing ejector nozzles. These pipes are mounted rigidly to the simulator, and are housed in the wing. They are connected to fixed mounts outside the wind tunnel by flexible connectors to permit thrust measurement.

A comparison of data from the three sources - flight, 5% scale, and 22% scale - is shown in figures 8 and 9. Sharp edged  $15^\circ$  boattail drag coefficients for the 5% scale model and flight data are compared with isolated values in figure 8. The installation effect of delaying the drag rise for the sharp edged boattail is obvious. Also the agreement of the model and flight data is very good except in the

region of Mach 1.0. The 5% scale data utilized cylindrical jet boundary simulators representing a fully expanded jet. The aircraft nozzle did not become fully expanded until slightly above Mach 1.0 which explains some of the difference between the two sets of data.

The nozzle gross thrust coefficient for a variable flap ejector nozzle is compared for the 22% scale model and flight, figure 9. This performance was derived from nacelle force measurements in both cases. Agreement is very good at subsonic Mach numbers less than 0.9. However, at higher speeds the flight thrust coefficient initially increases and then drops quickly at Mach 0.95 as the nacelle terminal shock passes over the nozzle. On the wind tunnel model, this shock movement was apparently delayed until a Mach number greater than 1.0. Above Mach 1.1 the agreement is only fair.

To illustrate the problems encountered in testing a complex nozzle, consider the auxiliary inlet ejector nozzle shown in figure 10. For this nozzle, part of the exit area variation required for efficient operation at all speeds is obtained by collapsing the trailing overlapping flaps and seals. The remaining area is too large for low pressure ratio operation, and doors are opened to provide air to fill the annulus between the primary jet and the leaves. To save actuator weight, these flaps and doors are positioned by the aerodynamic forces on the nozzle. Because the nozzle contains many complex moving parts, the tendency is to test with the boattail or doors fixed. This can lead to optimistic results as shown on figure 11, where the nozzle gross thrust coefficient is presented over a range of pressure ratios for several combinations of fixed and floating hardware. The best performance is obtained if the inlet doors and trailing flaps are fixed in the desired positions. If only the doors are allowed to float, they partially close, which reduces the thrust about 4 percent. Floating both the doors and flaps, reduces the performance an additional one to 3 percent depending on pressure ratio. Exact duplication of the floating linkage must be made to properly evaluate off-design performance. Another aspect of floating nozzles requiring similar investigation is the stability of the floating system. There are so many possible oscillation modes that testing the floating hardware is the only positive way to evaluate stability.

Another aspect of the nozzle flow field that is difficult to evaluate is the boundary layer. On many exit models used in tunnel testing the boundary layer is too thick due to excessive length or too low Reynolds number. In addition, the boundary layer is not uniformly thick at the nozzle when it is installed at the rear of an aircraft. It is nearly impossible to duplicate the actual installed condition. The effect of boundary layer thickness on boattail drag is presented in figure 12 and is discussed further in reference 10. In the case of both a sharp-edged boattail and a more rounded boattail, increasing boundary-layer thickness reduced drag. In this case, the thicker boundary layer appeared to effectively round the boattail corner thus reducing the drag.

A different problem is presented by the boattails in figure 13. These were designed with final angles of  $24^\circ$  and were to operate near to but without separation. They were investigated in flight on the F-106 aircraft at different altitudes to obtain Reynolds number effects. Case I and II were the same boattail with Case I extended farther beyond the wing trailing edge. Case III is a completely rounded boattail. Figure 14 shows that for all three boattails, the drag decreased as Reynolds number increased. Since boundary-layer thickness should be smaller relative to the body at higher Reynolds number, this is just the opposite of the previous case. By studying tuft pictures and boattail pressure distributions, it was possible to determine that separation regions on the boattails were decreasing with increasing Reynolds number. Therefore, the drag decrease was due to less separation in this case, causing drag to decrease with decreasing boundary-layer thickness. It is therefore necessary to determine the detailed flowfield causing drag before deciding how Reynolds number for boundary-layer thickness) will affect the drag.

#### DYNAMIC INLET-ENGINE TESTING

The Mach 2.5 mixed-compression inlet and J-85 engine installation used for propulsion system investigations is shown in figure 15. The inlet centerbody translates for inlet starting and for off-design Mach number operation. Bypass doors just ahead of the engine face provide control of the terminal shock position. Bleed is provided on the cowl and also on the centerbody where it is exhausted through support struts. Dynamic pressure measurements have been made at the compressor face with six 5-tube rakes, at the compressor exit, and throughout the inlet and compressor.

To investigate large transients for an axisymmetric nacelle located under a wing, the inlet-engine system was mounted just below a wing simulator (ref. 11) as shown in figure 16. Because of test section size limitations on the length of the simulator, it is difficult to obtain a thick enough boundary layer to simulate some engine installations, so the protuberances at the leading edge of the plate were used to artificially thicken the boundary layer. As described in more detail in reference 12, the desired momentum decrement was obtained with the leading-edge protuberances. The resulting boundary-layer profile near the leading edge was near separation, but was predicted to be well developed when it reached the area of interest ahead of the inlet. Separation tests with a forward-facing step showed it to be separated by a pressure rise almost exactly equal to that required for separation of a natural plate boundary layer. The location of the inlet relative to the plate is shown in more detail in figure 17. The cowl lip was tested at several heights equal to and larger than the boundary-layer height.

When the inlet unstarts, the shock system travels farthest forward during the initial transient. Several pictures from a movie of such a transient are presented in figure 18. These pictures show only the upper cowl lip and top half of the spike cone and the plate and boundary layer above the inlet. From these figures, it can be seen that the inlet shock system progresses clear to the spike tip during the transient, and also separates the plate boundary layer which transmits the disturbance even farther forward. The maximum extent of such a disturbance will determine how widely an adjacent nacelle must be separated in order to avoid one inlet unstart from disturbing an adjacent inlet. Either nacelle separation or some containment of the disturbance by fences must be used to prevent communication of disturbance between nacelles.

The extent of the unstart disturbance on the wing was measured by transient pressure instrumentation, and is presented in figure 19. Inlet unstart from different operating conditions cause variations in the extent of the disturbance. Without an engine installed, the inlet was unstarted by closing the bypass doors and forcing the terminal shock ahead of the inlet throat. The square and triangle represent data for a choke point at the engine face and for one about 2.5 meters downstream of the engine face, respectively. It is apparent that internal conditions affect the disturbance extent. For unstarts with an engine installed, the diamond represents the extent for an unstart initiated by bypass closure. However, by far the largest disturbance is caused by an unstart resulting from engine stall, which forces boundary-layer separation almost three diameters ahead of the inlet. Therefore, to avoid disturbing an adjacent inlet, its centerline would have to be about three and one-half diameters from the unstarted inlet centerline. It is worth noting again that this requirement is dictated by the extreme extent of the unstart transient and its amplification by the adjacent wing boundary layer. A criteria based on steady-state unstarted conditions without the wing would be totally inadequate.

The unstart not only could disturb adjacent inlets, but also presents a large transient to the engine operation (ref. 13). Unstart normally causes engine stall which can be easily understood by studying figure 20. The left transient is for a mild unstart at Mach 2 where the engine did not stall. The bottom curve of compressor face pressure shows that this pressure drops in about 8 milliseconds. From the center trace, it can be seen that the compressor exit pressure does not stop dropping until about 20 milliseconds after the transient is initiated due to the flow capacitance of the large combustor volume downstream of the compressor. As a result, the compressor pressure ratio increases momentarily to a value near stall but returns to the steady-state pressure ratio as shown in the top trace. Therefore, the transient pressure ratio did not exceed the stall value, and no stall occurred. The middle trace shows a similar case but this time the compressor pressure ratio starts from a higher value, reaches the steady-state stall line during the unstart transient and a stall occurs. The normal steady-state stall line therefore appears to be a valid criteria for engine stall during a transient such as unstart. This may not be surprising since the period for the compressor rotation is about 4 milliseconds. Since in distortion testing the critical distortion angle or rotation angle required for stalling a portion of a parallel compressor is considered to be less than half a compressor rotation, it is not surprising to see the compressor stall at its steady-state stall line during a transient requiring several compressor rotation periods. The traces at the far right are for an inlet unstart and engine stall at  $M = 2.5$ . While the compressor pressure ratio greatly exceeds the steady-state stall line before stall is reached, the compressor stalls in about 2.5 milliseconds or a little over one-half rotor revolution.

Another transient important to inlet design is the internal inlet overpressure caused by the hammer shock following compressor stall. Several values of this obtained during J-85 inlet tests are presented in figure 21. The figure presents the peak hammer shock static pressure ratioed to the compressor face total pressure  $\bar{P}_2$  just prior to stall. The most important points are the circles for which the compressor stalled at high pressure,  $\bar{P}_2$ , before inlet unstart, causing the highest internal overpressures. However, it is interesting to note the similarity of the pressure ratios obtained from stall after unstart when the compressor inlet pressure,  $\bar{P}_2$ , is about half the higher started value. The data shown correlate well with corrected weight flow per unit frontal area. However, it also correlates well with compressor exit pressure as proposed in reference 14. The overpressure has also been associated with the rate of flow stoppage within the duct during stall (ref. 15). However, this can be a function of duct geometry since compressor interstage and compressor face instrumentation show that compressor stall for the J-85 is not a uniform one-dimensional phenomenon, but a progressively growing rotating process. Therefore, in the test inlet which had the subsonic diffuser divided by three struts, the rotating stall process would stop the flow in one third of the duct in about one third of the time required to stop the full duct flow. Therefore, simple approximations to obtain hammer shock overpressure should be used with care.

Since most inlet testing is conducted without an engine present, it is important to determine the effect of the engine on inlet operation. A comparison of inlet distortion measured at similar inlet operating conditions is presented in figure 22. The dashed contours represent coldpipe data where the internal flow system was open from the compressor face station to a choke point about 2.5 meters downstream. The solid lines represent contours with the engine installed. Surprisingly little difference exist between the two total pressure distortions. However, a significant difference can be seen in the static pressures in the three portions of the subsonic diffuser between the centerbody support struts. With the coldpipe installed (dashed underlines) the static pressure in each of the ducts was about equal at the compressor face. With the engine installed, the static pressure in the bottom ducts were lower and the top duct static pressure increased. Therefore, the requirement for constant static pressure in cold pipe testing is changed by the pumping action of the compressor, giving more equal Mach numbers in each duct, reference 16.

Dynamic measurements have also contributed to understanding in the area of inlet distortion effects on compressor operation. In a recent inlet engine test in the 10x10 Foot Supersonic Wind Tunnel, the compressor face was instrumented with six 5-tube rakes which measured both the dynamic pressure variations and the steady-state or time-averaged pressures. During inlet operation at many different conditions, the J-85 engine was purposely stalled to determine the available stall margin. The steady-state and dynamic compressor face pressures were measured before and during stall so that comparisons could be made with steady-state stall parameters obtained from screen distortion testing references 17 and 18.

Distortion from a typical "drift" stall point is shown in figure 23 for a low recovery supercritical condition at zero angle-of-attack. Drift stalls occurred when the engine stalled during a period when no changes were made to any model or engine settings. They occurred most often at fairly high dynamic conditions. The distortion shown on the left is the normal steady-state radial distortion pattern, where the edges between constant density bands represents a line of constant total pressure recovery. Darker regions indicate lower recovery flow. It is a hub radial distortion. The distortion pattern on the right represents the amplitude of the dynamic component of total pressure at the compressor face. This amplitude is presented as the root mean square, rms, of the dynamic pressure component divided by the average compressor face pressure. The rms levels range from less than 0.04 to 0.08 of compressor face average pressure  $\bar{P}_2$ , with an average value of 0.066. Since these pressure fluctuations are random in nature, the peak-to-peak pressure fluctuations can reach four to six times the rms values. Here the darker bands represent higher dynamic pressure levels. It is interesting to note the location of the dynamics relative to the average total pressure bands. In the low total pressure region near the hub, the dynamic levels are lower. The high dynamic region, in this case, corresponds to the higher total pressure region, indicating that the major pressure fluctuations are occurring there.

A similar set of distortion profiles is shown in figure 24 for five degrees angle-of-attack with a total pressure recovery of 0.77. The steady-state circumferential distortion is typical for such an

operating condition with high recovery air at the top, leeward side of the inlet and low pressure air at the bottom. Now, however, the relationship between the high dynamic and high pressure regions is different in this case than for zero angle-of-attack. The dynamic level is again fairly low in the low total pressure region at the bottom of the inlet, but it is at an even lower dynamic level in the high total pressure region at the top of the inlet. In this case, the high dynamics occur between the high and low pressure regions. The different locations of the high dynamic regions in the zero and five degree angle-of-attack case will be discussed again when instantaneous distortions are presented.

In addition to the steady state and rms dynamic distortion plots, the pressure data were simultaneously digitized at a high rate for all thirty probes, and a steady-state distortion parameter and instantaneous distortion contour plots were made. The variation of the steady-state distortion parameter with time for the zero degree angle-of-attack case is presented in figure 25. The time of compressor stall was determined from compressor interstage dynamic pressure data. The parameter presented here is developed in reference 19 and is sensitive only to circumferential distortion, and would have a near zero value for the steady-state distortion pattern of figure 23. However, the instantaneous distortion pattern has an average value of about 0.04 and reaches the critical level required to cause stall once during the observed time span. Therefore, the instantaneous patterns must be considerably different for this case than the time-averaged pattern. A similar presentation of the distortion index variation with time is presented in figure 26 for the five degree angle-of-attack point. Here the average distortion level is higher, as would be expected from the steady-state distortion plot of figure 24. However, it can be seen that the average value is about 35 percent less than the value of 0.15 required for compressor stall. Transiently, however, the distortion does reach and exceed the critical level of distortion several times before compressor stall. A total of twelve stall points have been analyzed in a similar manner and in all but two cases, the time-varying distortion exceeded the critical level required to stall the engine.

To obtain a better understanding of the cause of the large transient distortion levels, an instantaneous contour plot of the peak transient distortion is compared with the steady-state contour in figures 27 and 28 for the zero and five degree angle-of-attack cases. At zero angle-of-attack, (fig. 27) the peak instantaneous distortion is primarily circumferential in nature. The pressures do not change drastically near the hub where the dynamics were low in the rms contour plot. Where the dynamics were high in the steady-state high pressure region, total pressure reaches as much as 20 percent less than the steady-state value in the lower left portion of the inlet. Since the rms contours were nearly symmetrical around the inlet at zero angle-of-attack, a similar pattern could probably occur in any orientation over a long period of time. The dynamics therefore indicated what appear to be large separate regions forming and disappearing which cause major circumferential distortions. A similar comparison of the instantaneous and steady-state distortion contours for five degrees angle-of-attack are presented in figure 28. Here the two contour plots are very similar, with the instantaneous plot having a broader high pressure region and lower pressure at the bottom of the inlet. Both effects tend to increase the circumferential distortion. The high dynamic regions were observed between the high and low pressure regions on the rms contour plots, and this can be correlated with the constant total pressure boundaries expanding and contracting across this region. Lower dynamics were observed at the top and bottom of the inlet where the high and low pressure region remain stably located, but vary somewhat in level.

Therefore inlet dynamics are apparently associated with unstable flow in the diffuser and not with turbulence in the classical sense. The dynamic level is not associated with any particular region of the steady-state distortion pattern. It is associated with the high pressure flow region passing back and forth over the measurement point as flow which is separating and attaching to a wall might do. This is a recognized operational regime for subsonic diffusers, reference 20. Therefore, the probable cause of most of the dynamic distortion measured in inlets, is transient flow separation in the subsonic diffuser combined with the terminal shock boundary layer interaction. Hence test techniques are required which determine if significant dynamic distortion is present, and if so, enough dynamic instrumentation is required to determine the instantaneous distortion pattern.

## CONCLUDING REMARKS

Most wind tunnel testing of supersonic exhaust nozzles is done to obtain off design performance in the speed range near Mach 1.0. Because of the complex internal and external flows, it is very difficult to duplicate all conditions simultaneously. It has been demonstrated that jet boundary simulators can provide good data if the flow is well behaved in the nozzle region. However, if separation is present, this method would probably become suspect. Then more complex models such as powered simulators should be used. Results from such a model were compared with flight data and were shown to agree up to high subsonic Mach numbers. However, viscous effects can still affect the nozzle drag and full Reynolds number testing is currently impossible in existing facilities. Two cases were presented where boundary-layer thickness affected the drag in opposite directions and demonstrated the need to fully understand the flow conditions. The viscous affects area is not completely understood yet and work in this area is continuing at Lewis.

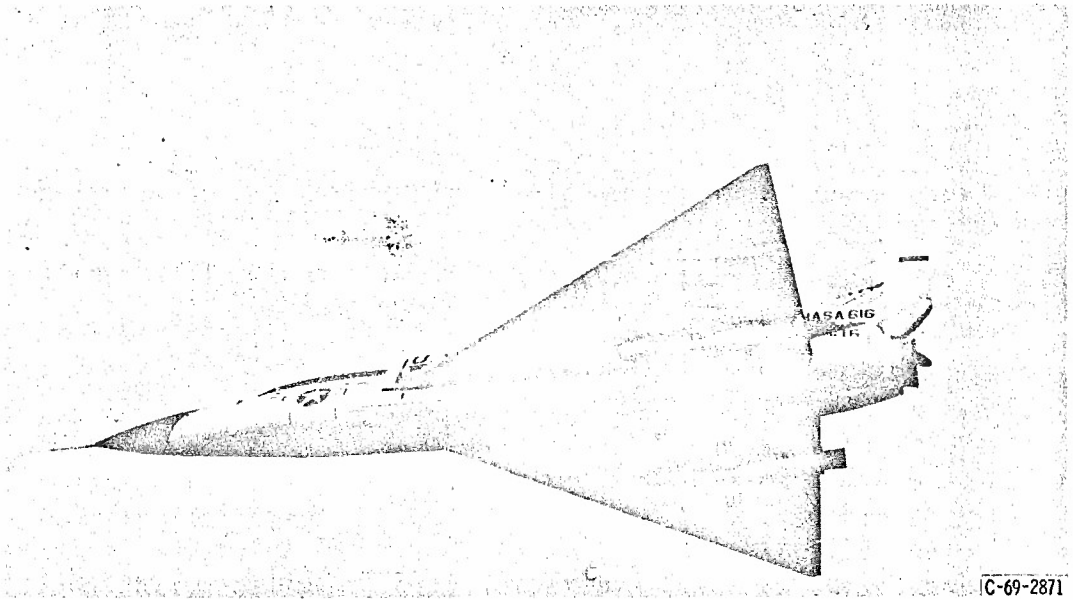
Dynamic measurements are absolutely necessary to understand the interactions of an inlet-engine combination. Nacelle spacing is determined by a maximum transient disturbance extent during unstart that is much larger than the steady-state disturbance. Engine stall during inlet unstart was easily explained by utilizing dynamic measurements of compressor pressure ratio. Nacelle strength is partially determined by the overpressures due to the hammer shock after compressor stall and it must be carefully measured with dynamic instrumentation. Probably the most complex flow phenomena revealed by dynamic measurements is dynamic distortion. Proper reduction of dynamic distortion data holds promise for explaining inlet-engine compatibility in terms of comparing the instantaneous distortion with the steady-state screen distortion required to stall the compressor. Several cases were presented demonstrating the nature of the flow fluctuations for different inlet operating conditions. The number of cases investigated so far has been limited due to the difficulty of data reduction but this is becoming easier with new methods. Work is continuing at Lewis on dynamic distortion, and should provide further understanding of the dynamic interaction of the inlet and engine.

## REFERENCES

1. Beheim, Milton A.; Anderson, Bernhard H.; Clark, John S.; Corson, Blake W., Jr.; Stitt, Leonard E.; and Wilcox, Fred A.: Supersonic Exhaust Nozzles. Aircraft Propulsion. NASA SP-259, 1971, pp. 233-282.
2. Bowditch, David N.; Coltrin, Robert E.; Sanders, Bobby W.; Sorensen, Norman E.; and Wasserbauer, Joseph F.: Supersonic Cruise Inlets. Aircraft Propulsion. NASA SP-259, 1971, pp. 283-312.
3. Povolny, John H.; Burcham, F. W., Jr.; Calogeras, James E.; Meyer, Carl L.; and Rudey, Richard A.: Effects of Engine Inlet Disturbances on Engine Stall Performance. Aircraft Propulsion. NASA SP-259, 1971, pp. 313-349.
4. Harrington, Douglas E.: Jet Effects on Boattail Pressure Drag of Isolated Ejector Nozzles at Mach Numbers From 0.60 to 1.47. NASA TM X-1785, 1969.
5. Wilcox, Fred A.; Samanich, Nick E.; and Blaha, Bernard J.: Flight and Wind Tunnel Investigation of Installation Effects on Supersonic Cruise Exhaust Nozzles at Transonic Speeds. 69-427, AIAA, June 1969.
6. Samanich, Nick E.; and Burley, Richard R.: Flight Performance of Auxiliary Inlet Ejector and Plug Nozzle at Transonic Speeds. Paper 70-701, AIAA, June 1970.
7. Mikkelsen, Daniel C.; and Head, Verlon L.: Flight Investigation of Airframe Installation Effects on a Variable Flap Ejector Nozzle of an Under wing Engine Nacelle at Mach Numbers From 0.5 to 1.3. NASA TM X-2010, 1970.
8. Mikkelsen, Daniel C.; and Blaha, Bernard J.: Flight and Wind Tunnel Investigation of Installation Effects on Underwing Supersonic Cruise Exhaust Nozzles at Transonic Speeds. Presented at the AGARD Aerodynamic Interference Specialists Meeting, Silver Spring, Md. Sept. 28-30, 1970.

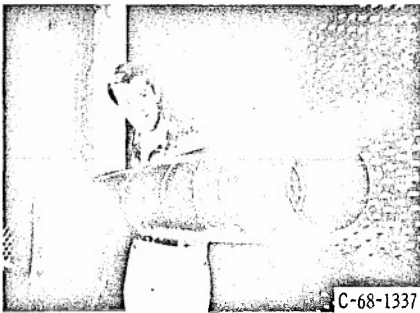
9. Groth, Harold W.: Nozzle Performance Measurements on Underwing Nacelles of an F-106 Utilizing Calibrated Engines and Load Cells. Paper 71-681, AIAA, June 1971.
10. Blaha, Bernard J.; and Bresnahan, Donald L.: Wind Tunnel Installation Effects on Isolated Afterbodies at Mach Numbers From 0.56 to 1.5. NASA TM X-52581, 1969.
11. Mitchell, Glenn A.; and Johnson, David F.: Experimental Investigation of the Interaction of a Nacelle-Mounted Supersonic Propulsion System with a Wing Boundary Layer. NASA TM X-2184, 1971.
12. Johnson, David F.; and Mitchell, Glenn A.: Experimental Investigation of Two Methods for Generating an Artificially Thickened Boundary Layer. NASA TM X-2238, 1971.
13. Choby, David A.; Burstadt, Paul L.; and Calogeras, James E.: Unstart and Stall Interactions Between a Turbojet Engine and an Axisymmetric Inlet With 60-Percent Internal-Area Contraction. NASA TM X-2192, 1971.
14. Bellman, Donald R.; and Hughes, Donald L.: The Flight Investigation of Pressure Phenomena in the Air Intake of an F-111 A Airplane. Paper 69-488, AIAA, June 1969.
15. Mays, Ronald A.: Inlet Dynamics and Compressor Surge. Paper 69-484, AIAA, June 1969.
16. Coltrin, Robert E.; and Choby, David A.: Steady-State Interactions From Mach 1.98 to 2.58 Between a Turbojet Engine and an Axisymmetric Inlet With 60 Percent Internal Area Contraction. NASA TM X-1780, 1969.
17. Calogeras, James E.; Mehalic, Charles M.; and Burstadt, Paul L.: Experimental Investigation of the Effect of Screen-Induced Total Pressure Distortion on Turbojet Stall Margin. NASA TM X-2239, 1971.
18. Calogeras, James E.; Burstadt, Paul L.; and Coltrin, Robert E.: Instantaneous and Dynamic Analysis of Supersonic Inlet-Engine Compatibility. Paper 71-667, AIAA, June 1971.
19. Calogeras, James E.; Mehalic, Charles M.; and Burstadt, Paul L.: Experimental Investigation of the Effect of Screen-Induced Total-Pressure Distortion on Turbojet Stall Margin. NASA TM X-2239, March 1971.
20. Sovran, Gino; and Klomp, Edward D.: Experimentally Determined Optimum Geometries for Rectilinear Diffusers with Rectangular, Conical or Annular Cross-Section. Fluid Mechanics of Internal Flow. Gino Sovran, ed., Elsevier Publ. Co., 1967, pp. 270-319.

NASA  
C-69-2871



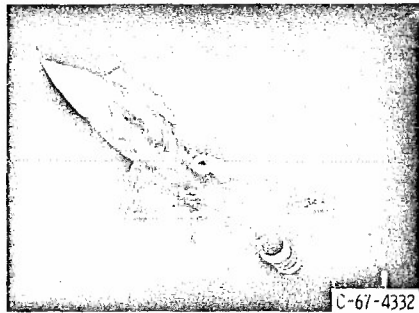
C-69-2871

Figure 1. - F-106 research flight with plug nozzle.



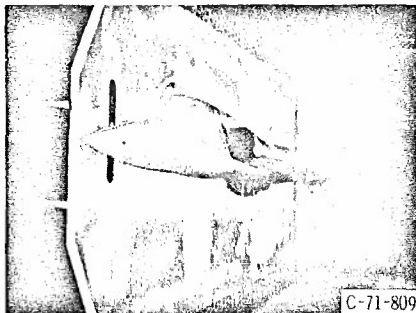
C-68-1337

ISOLATED NOZZLE



C-67-4332

5% SCALE F-106



C-71-809

22% SCALE F-106

Figure 2. - Exhaust nozzle test models.

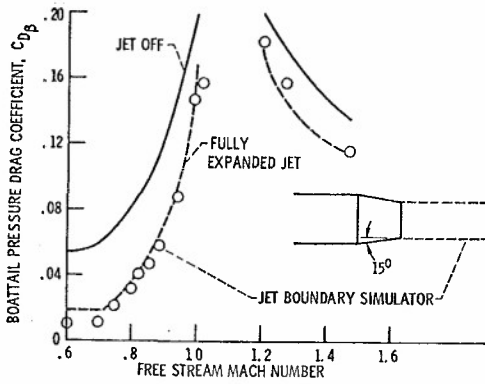


Figure 3. - Comparison of boattail drag for jet boundary simulator and jet on and off.

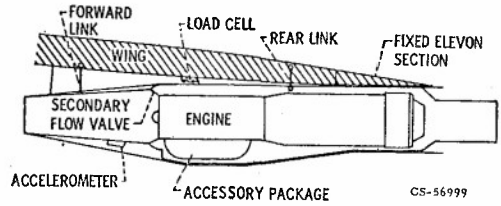


Figure 4. - Nacelle-engine installation.

PARAMETER	INFLUENCE COEFFICIENT FOR $C_g$	STANDARD DEVIATION $\sigma$
EXPERIMENTAL NACELLE TARE	0.598	1.50
IDEAL THRUST (GAS GENERATOR)	.994	1.11
LOAD CELL FORCE	.395	1.00
NOZZLE GROSS THRUST COEFFICIENT, $C_g$		1.47

Figure 5. - F106 Nozzle performance measurement accuracy.



Figure 6. - 22% F-106 model.

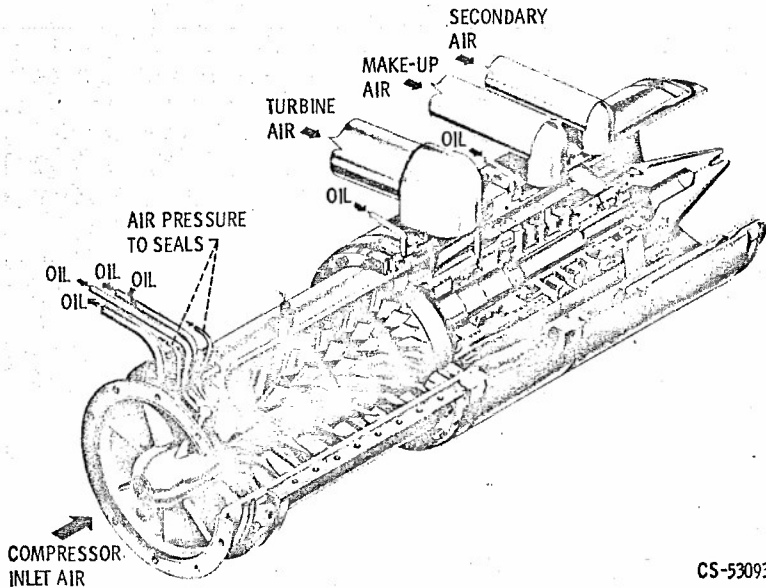


Figure 7. - Turbojet engine simulator.

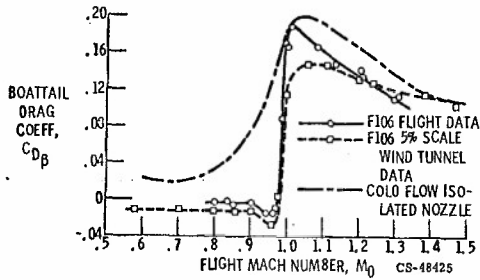


Figure 8. - Comparison of flight and wind tunnel data. Variable flap ejector nozzle  $r/d_n = 0$ .

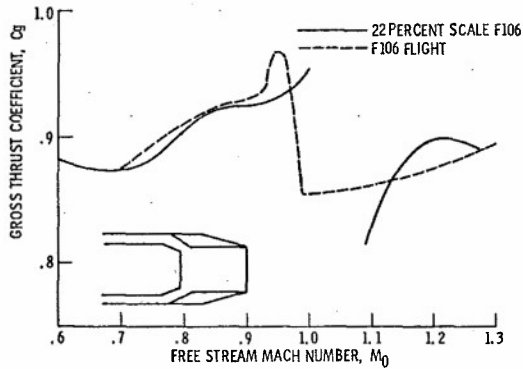


Figure 9. - Comparison of variable flap ejector performance from model and flight data.

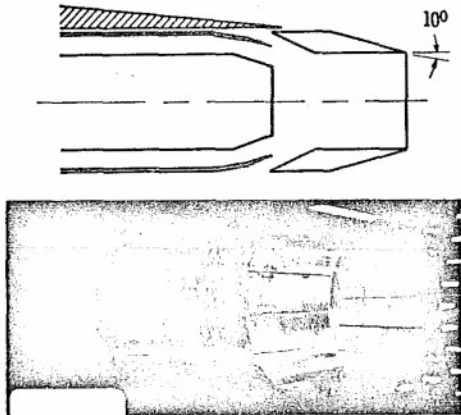


Figure 10. - Auxiliary inlet ejector.

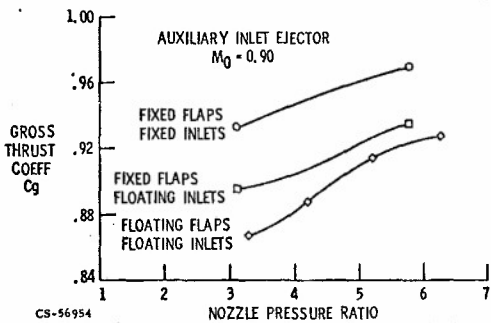


Figure 11. - Effect of floating components on performance.

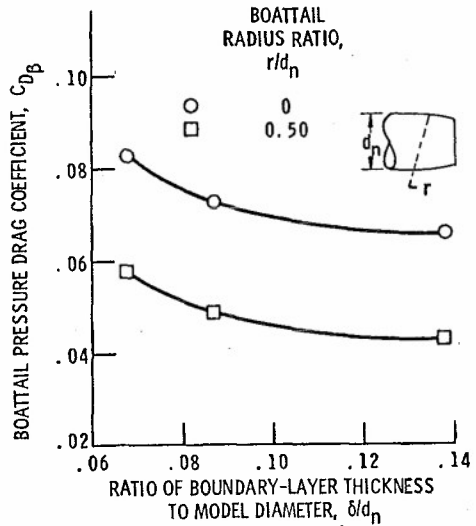


Figure 12. - Effect of boundary-layer thickness on boattail pressure drag;  $15^\circ$  - conical boattails at Mach 0.90.

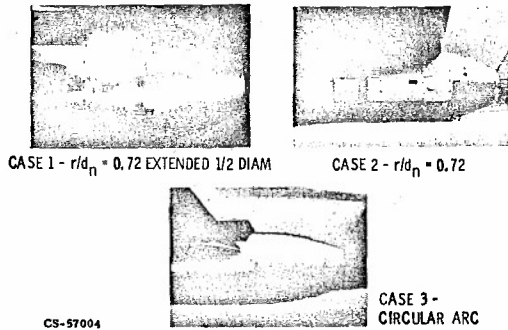


Figure 13. - Variable convergent-divergent nozzles.

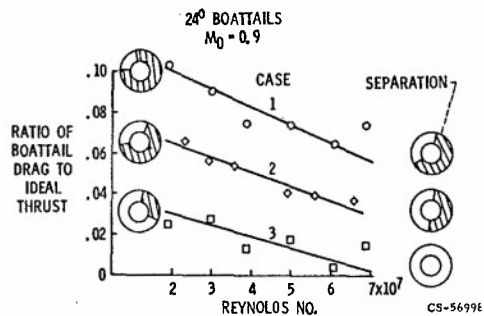


Figure 14. - Reynolds number effect on boattail drag.

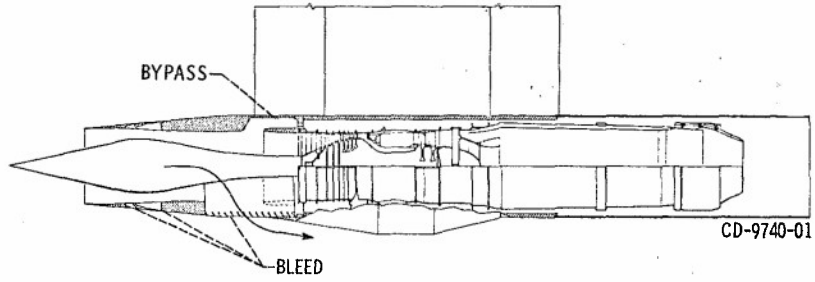


Figure 15. - Axisymmetric mixed compression and J85 turbojet installation.

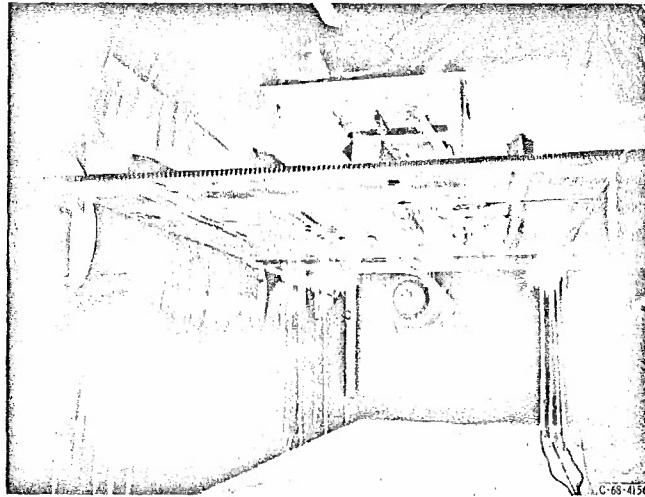


Figure 16. - Propulsion system and wing simulator installation in 10-by-10.

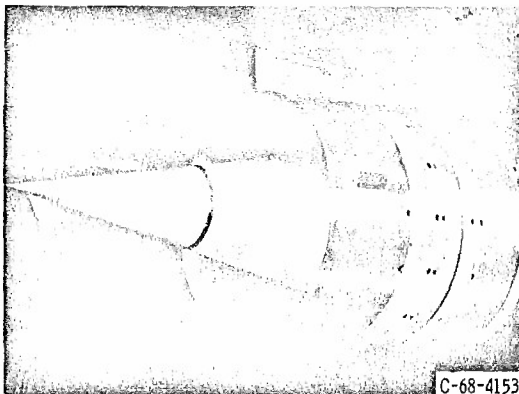


Figure 17. - Inlet location near wing simulator.

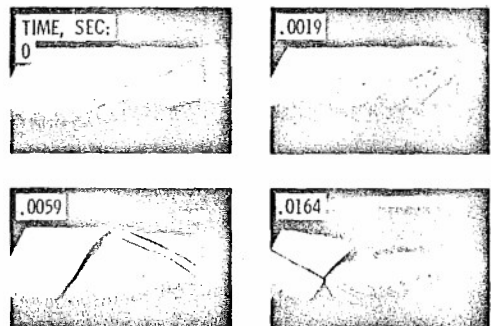


Figure 18. - Inlet unstart near a wing;  $Mo = 2.5$ .

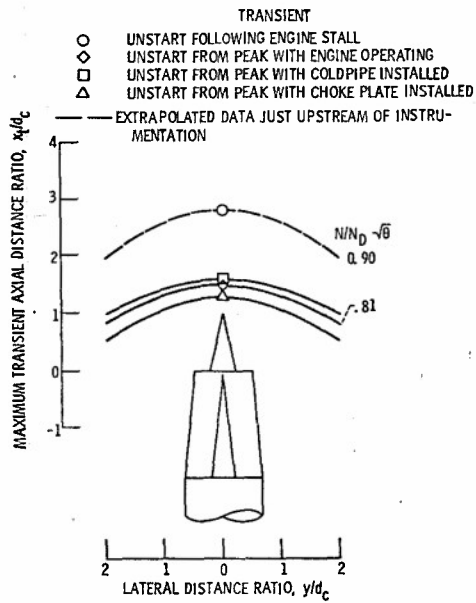


Figure 19. - Maximum wing surface disturbances during inlet unstart transients.  $M_0 = 2.5$ .

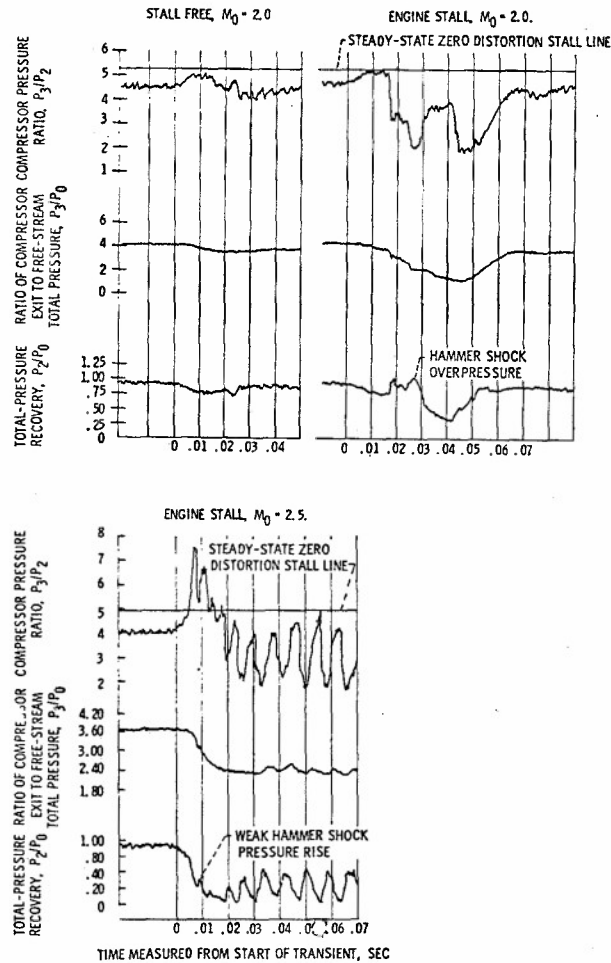


Figure 20. - Effect of inlet unstart on turbojet engine stability.

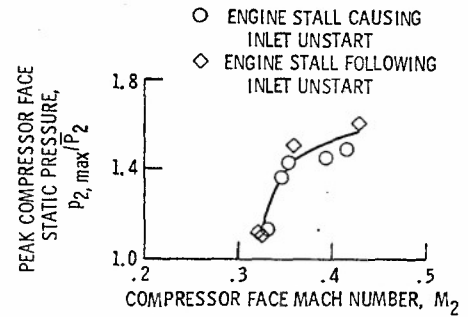


Figure 21. - Hammershock peak pressure following compressor stall.

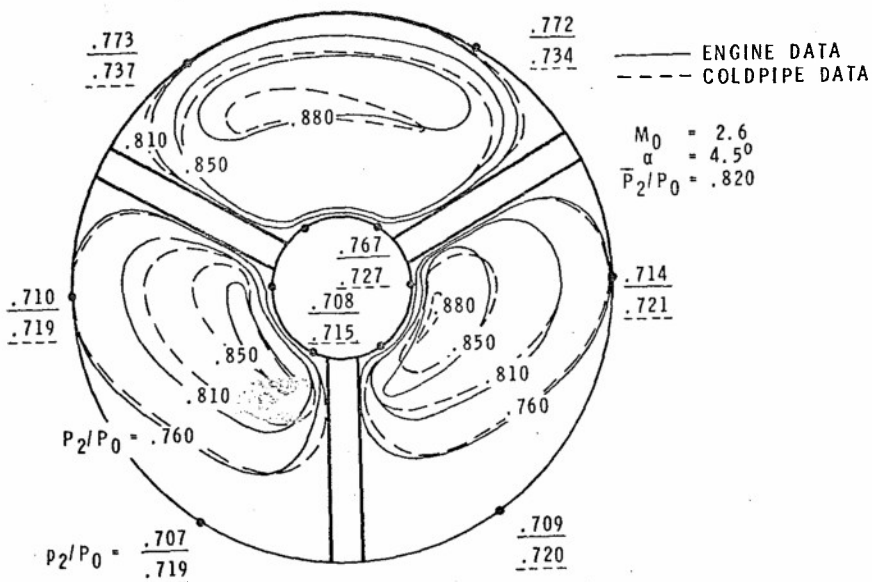


Figure 22. - Engine effect on distortion.

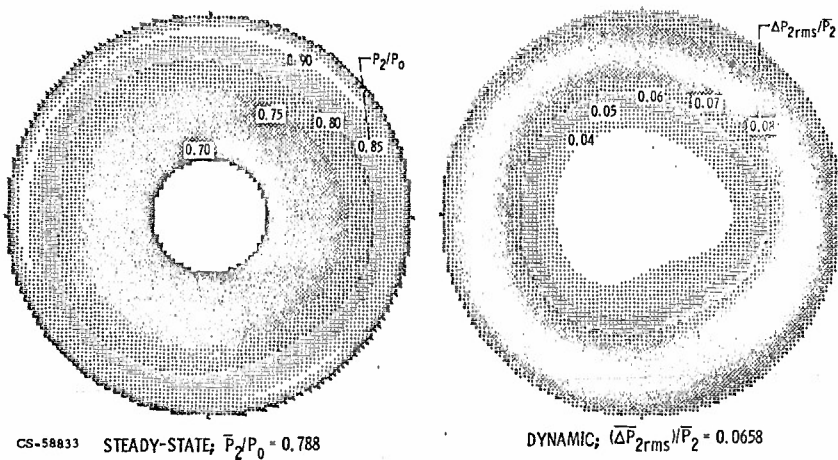


Figure 23. - Dynamic and steady state distortion.  $M_0 = 2.5$ ,  $0^\circ$  angle of attack.

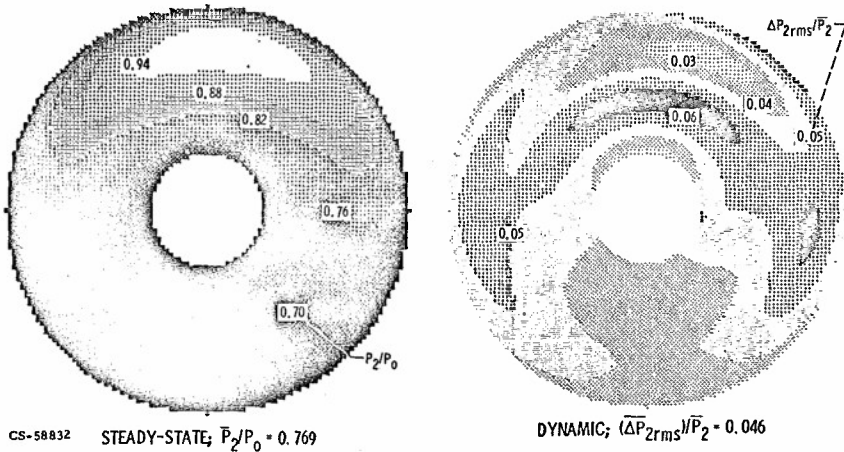


Figure 24. - Dynamic and steady state distortion.  $M_0 = 2.6$ ,  $5^\circ$  angle of attack.

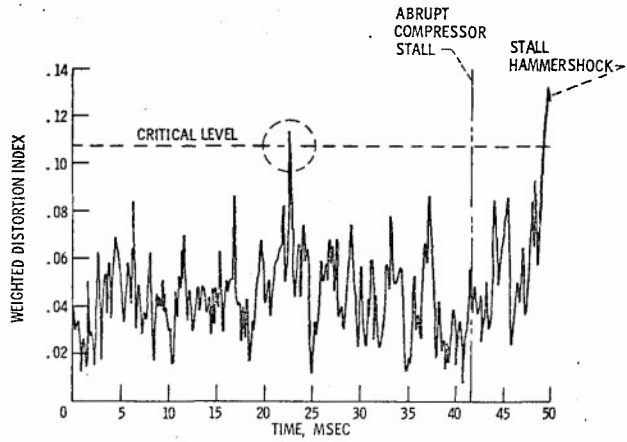


Figure 25. - Instantaneous distortion just prior to compressor stall.  $M_0 = 2.5$ ;  $0^\circ$  angle of attack.

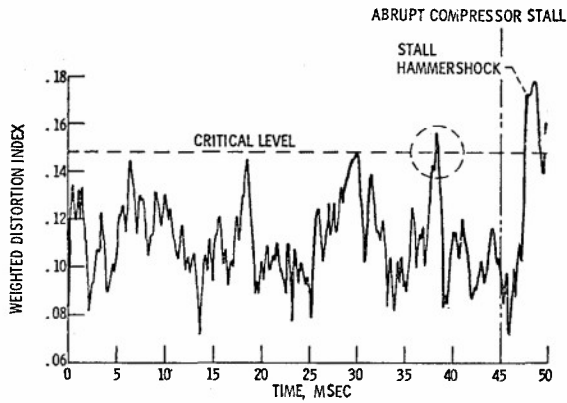
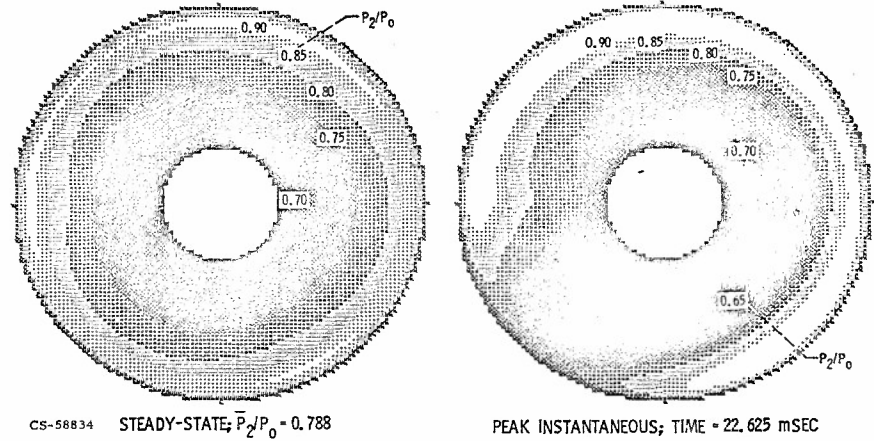


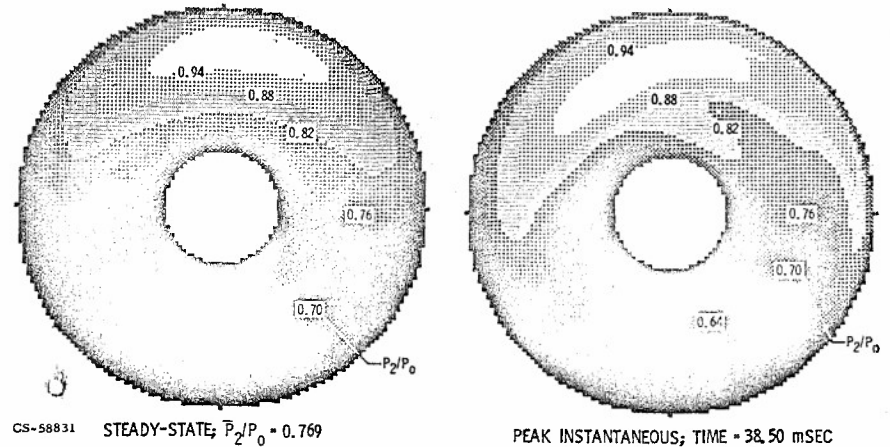
Figure 26. - Instantaneous distortion just prior to compressor stall.  $M_0 = 2.6$ ;  $5^\circ$  angle of attack.



CS-58834 STEADY-STATE;  $\bar{P}_2/P_0 = 0.788$

PEAK INSTANTANEOUS; TIME = 22.625 mSEC

Figure 27. - Comparison of steady state and peak instantaneous distortion.  $M_0 = 2.5$ ;  $0^\circ$  angle of attack.



CS-58831 STEADY-STATE;  $\bar{P}_2/P_0 = 0.769$

PEAK INSTANTANEOUS; TIME = 38.50 mSEC

Figure 28. - Comparison of steady state and peak instantaneous distortion.  $M_0 = 2.6$ ;  $5^\circ$  angle of attack.

WIND TUNNEL TESTING OF V/STOL ENGINE MODELS -  
SOME OBSERVED FLOW INTERACTION AND TUNNEL EFFECTS

R.A. Tyler and R.G. Williamson  
Gas Dynamics Laboratory  
Division of Mechanical Engineering  
National Research Council of Canada  
Ottawa K1A 0R6, Ontario, Canada

**SUMMARY**

The interpretation of force measurements on V/STOL-related models incorporating inflows and/or outflows is discussed in relation to continuing investigations concerned mainly with the transition performance of lift-fan configurations and utilising balance mounted powered models of about 1000 hp in the closed test section of the 10 ft x 20 ft N.R.C. V/STOL Propulsion Tunnel.

With models producing strong downwash an overriding testing limit arises in closed wind tunnels from the formation of a stable floor vortex system resulting from the interaction of stagnating model flow with the mainstream. An experimental study of this effect as it relates to downward directed jets is described. Vortex formation limits are correlated in terms of a jet force coefficient for a wide range of jet inclination to the vertical and for both single and paired jets. Interference velocity measurements, with limited data from the main programme and other sources, are used to deduce corresponding tunnel flow breakdown limits. These testing limits are indicated to be sensitive to model characteristics.

**SYMBOLS**

B	Test section width
$C_T$	$F/q_0 h^2$
$C_{TN}$	$C_T \cos \alpha$
d	Jet diameter at nozzle
$d_e$	Effective diameter based on total jet area at nozzles
D	Drag
F	$M_j V_j$
h	Nozzle distance from impingement wall
H	Test section height
M	Mass flow rate
q	$\rho V^2/2$
s	Nozzle spacing
V	Mean velocity
$V_R$	$\sqrt{q_0/q_j}$
x-axis	Axis through centre of nozzle exit parallel to mainstream (positive in mainstream direction)
$x_B$	x-coordinate of stagnation point, $X_B$ (Fig. 5)
$x_F$	x-coordinate of stagnation point, $X_F$ (Fig. 5)
$x_p$	x-coordinate of probe point
z-axis	Axis through centre of nozzle exit, perpendicular to impingement surface (positive towards surface)
$\alpha$	Inclination of nozzle axis (in xz-plane) to positive z-axis (positive in mainstream direction)
$\delta$	Boundary layer thickness
$\Delta$	Prefix denoting jet-induced increment
$\epsilon$	Flow pitch angle (positive upwards)
$\rho$	Mass density
$\psi$	Flow yaw angle (positive towards near sidewall)
<b>Suffix</b>	
o	Mainstream
j	Jet
*	Relative to datum value at incipient stagnation

## 1. INTRODUCTION

Prospective jet V/STOL developments in civil aviation have generated the need for the evaluation of reaction lift systems in transition flight by model tests. Since 1967 an experimental programme has been conducted in the NRC 10 ft x 20 ft V/STOL Propulsion Tunnel on balance-mounted V/STOL engine models predicated on the use of fan thrust. The tunnel is of the open circuit type with closed test section and is described in some detail in Reference 1. Unheated compressed air is available at the test section for driving fan equipped models absorbing up to several thousand horsepower. In the present context typical engine models incorporate turbine drives of about 1000 horsepower connected to thrusting fans of 12 to 15 in (0.30 to 0.38 m) tip diameter. Drive air is provided through the model mounting system. Typical studies have involved measurement of fan thrust in crossflow, i.e. in simulated transition. Tunnel speeds to about 200 ft/sec (60 m/sec) are available for this purpose. Models are characterized in general by inflow and efflux directions substantially at right angles to the mainstream.

To date, testing has been confined to relatively simple encased models involving single fans with minimal external structure. Interference forces arising from flow interactions are largely incidental to the model set-up, i.e. without full scale significance. Test conditions of main interest (distorted inflow) involve (high) ratios of tunnel/model flow rates at which tunnel effects are unlikely to be significant in relation to engine performance data. In line with existing proposals for civil V/STOL lift-fan aircraft, however, increasingly sophisticated models are anticipated. Current attention, for instance, is directed towards a model simulating sponson-housed multiple lift-fan systems. While interest remains centred on fan performance in transition, interactions among the freestream and individual fan flows (at intake and exit) in the presence of representative surfaces are of real concern. In addition, simulation of transition flight profiles calls in general for a significant range of fore-and-aft fan tilt and sponson incidence. Furthermore, increased lower limits on model size obtain - set basically by the lowest number of model fans needed for adequate representation of flow interaction effects and by the smallest fan diameter meeting blade Reynolds number requirements (3 fans of 12.0 in (0.30 m) tip diameter in current model).

The extent to which the wind tunnel remains a useful tool for the investigation of models of this kind is not clear at this time. Published experimental data and analytical treatments relevant to the tunnel testing of models incorporating inflows and issuing jets are few. The present paper outlines briefly some more or less relevant data arising from testing experience to date, together with the main results of an experimental investigation into a particular aspect of testing limits pertaining to jet models in closed test sections.

## 2. WIND TUNNEL LIMITATIONS

Various special problems attach to the wind tunnel testing of bodies incorporating inflows and jet effluxes. In general, the major sources of differences between test data obtained in wind tunnel testing and in free-flight are well known (scale effects, solid blockage, wall constraints, etc.). Corrections valid for lightly loaded models have been used with good results for many years. The advent of models generated by STOL and V/STOL research, involving large force coefficients and highly deflected wakes, has pointed up the inadequacies of the classical theory. Some progress has been made in establishing correction procedures for such cases, particularly with respect to wall constraints. Heyson has described the development of wall-induced interference calculation methods for arbitrary lifting systems based on increasingly sophisticated description of the deflected wake (Ref. 2). The methods proceed from the assumption of a straight wake passing downwards (with representation of the test section surfaces by an external image system) to vortex lattice methods capable of handling more realistic curved representations of the wake, including, through iteration, interference effects on wake position. In principle, at least, (and given adequate digital computer support) the latter method appears applicable to models incorporating discrete jets issuing at large angles to the mainstream. For models of this kind, wall-induced interference velocity will, in general, exhibit large spatial gradients, making valid correction procedures difficult to establish. In practice, the interference analysis might prove most useful in evaluating limits (on, for instance, the ratio of model/tunnel flow rates) within which wall-induced interference velocities are of a magnitude considered unimportant for a particular model type.

In free flight, bodies involving inflows and jet effluxes are subject, in general, to interference forces due to induced flows arising from body flow-freestream interaction. These interference forces are usually modified in proximity to the ground. Effects of this kind are encountered in jet-model tunnel testing, presumably modified by factors present in the wind tunnel but absent in free air. Little or no information appears to exist on this point.

Furthermore, the available wall constraint calculation methods are necessarily predicated on an ideal wind tunnel providing a uniform incoming flow. In real tunnels interaction between model flow and incoming tunnel flow can modify the latter to an extent rendering the measured data meaningless. Model flow impinging on a tunnel surface may penetrate forward in the boundary layer inducing separation of the tunnel flow upstream of the model (Ref. 3). Ground effect measurements on jet models, with and without moving ground plane (Ref. 4), indicated the data to be affected by floor boundary layer at model heights in the neighbourhood of one effective jet diameter ( $h = d_e \approx \delta$ ). Of more general significance in closed test sections is the flow

breakdown resulting from the stagnation of high energy downwash flow on the tunnel floor with the formation of a stable vortex system. This phenomenon was first reported, in connection with lifting rotor systems, in Reference 5. Tunnel flow breakdown limits for models with more or less uniform spanwise lift distribution (rotor, tilt wing, jet flap) have been presented in terms of a minimum wake impingement distance behind the model (Refs. 6, 7) or a maximum lift coefficient (Ref. 8). Little information appears to be available for models involving discrete jets. In view of the overriding limits imposed by this phenomenon some experiments were undertaken to investigate this effect in relation to jet-model testing in the NRC 10 ft x 20 ft tunnel.

### 3. OBSERVED INTERFERENCE EFFECTS

Various instances of jet, sink, and/or wall induced interference forces have been encountered in the experimental programme to date. These usually represent unwanted modification to indicated fan forces requiring direct assessment when relatively small and circumvention when large. A typical single-fan test model is shown installed vertically in the tunnel test section in Figure 1. The model proper is represented by the fan-intake configuration. The direction of fan gross thrust and model incidence are each independently variable through  $360^\circ$ . At  $90^\circ$  incidence, fan thrust was measured in essence as the increase in drag-balance reading on vectoring fan thrust through  $90^\circ$  downwards from a direction parallel to the tunnel axis (downstream). The second reading included intake momentum drag and interference force components induced by fan efflux and inflow. The interference forces were assessed directly by measurement in isolation on appropriate model mock-ups, as described in Reference 9. The results are shown plotted against non-dimensional fan flow rate in Figure 2. While the indicated inflow interference components are small (but not zero), the efflux effects are relatively strong and of similar magnitude to nominal momentum drag.

As indicated earlier, special difficulties arise at tunnel speeds sufficiently low relative to jet velocity to allow stagnation of downward directed jets on the tunnel floor. An extreme instance of this occurs at zero tunnel speed, for example in the attempted measurement of static thrust in a closed test section (Ref. 10). Figure 3 shows the effect of model-floor distance on lift-balance reading (ostensibly fan thrust) for the model of Figure 1 at zero incidence (fan axis horizontal) with fan efflux directed vertically downward. Constraint-enhanced ground effects are evident at all available model heights. In this particular case, satisfactory static thrust readings, at the required fan nozzle orientation, were obtained by simply rotating the model to  $90^\circ$  incidence or by completely inverting the model ( $180^\circ$  incidence) and removing the tunnel roof. A potentially more troublesome difficulty occurring at non-zero tunnel speeds is illustrated by the data of Figure 4. Drag-balance readings for the model at  $90^\circ$  incidence with fan efflux directed vertically downwards are shown plotted against fan rotational speed at constant nominal tunnel speed. A radical change in flow pattern at the higher fan speeds is indicated by a sharp break in the data trend. These data are representative of more than twenty sets of readings for the same model set-up equipped with different intake-fan configurations (Ref. 9). The effect is associated with the fan efflux, occurs at a critical low value of mainstream/fan efflux velocity ratio, and is evidently a manifestation of the stagnation phenomenon referred to earlier. In this instance the implied lower limit on useful tunnel speed was of no consequence. However, the implications for future models involving multiple and inclined jets are significant. As mentioned earlier, an experimental study was instituted to provide some background on tunnel flow breakdown limits with respect to jet-model testing in general.

### 4. TUNNEL FLOW BREAKDOWN

The development of tunnel flow breakdown in the presence of high-lift models has been described in Reference 11. The flow fields associated with several devices producing high energy downwash (jet flap, rotor and fan-in-wing models) were investigated visually at the floor, over a range of tunnel speed. The authors identify several stages in the development of unwanted tunnel secondary flows. For a given lift, tunnel flow is relatively undisturbed at high tunnel speeds. With reduction in tunnel speed model downwash becomes sufficiently deflected to interact with the tunnel boundary layer, causing agitation of tufts on the floor. With further decrease of tunnel speed a condition is reached in which the model wake penetrates the boundary layer to stagnate on the floor. This condition is unstable with intermittent periods of upstream surface flow forming small horseshoe vortices. The authors designate this condition as 'incipient stagnation'. With still further reduction in tunnel speed the flow becomes stable with well defined stagnation. A portion of the wake flows upstream to roll up into a stable vortex. The vortex size increases with decrease in tunnel speed. Finally the tunnel flow is rendered unrepresentative of free flow conditions to a degree beyond correction. This condition constitutes 'tunnel flow breakdown'.

Some simple experiments were set up in the NRC 10 ft x 20 ft tunnel to examine these phenomena as they arise from inclined circular jets originating in the tunnel test section. An initial objective was to relate quantitatively some observable elements of the breakdown process with jet conditions. These elements are illustrated schematically in Figure 5. Figure 5a indicates a typical flow breakdown situation at relatively low tunnel speed. In the plane through the nozzle axis parallel to the mainstream, the flow is characterized by two stable stagnation points on the tunnel floor,  $X_A$  and  $X_B$ . The positions of these stagnation points are easily determined in practice from wool tuft observations. A portion of the jet flows radially upstream from the vicinity of  $X_A$ , rolling up into a stable vortex to define  $X_B$ . The separation between  $X_B$  and  $X_A$  decreases with increasing tunnel speed (Figure 5b), tending to zero at the unstable condition of

incipient stagnation (Figure 5c). There is a corresponding reduction in vortex size. At higher tunnel speeds, any jet flow close to the floor is in the general downstream direction (Figure 5d).

The stable vortex formation implies lateral jet flow and can result in flow up the side walls at sufficiently low tunnel speed (Ref. 12). This is shown schematically in Figure 6. In the experiments to be described, this general picture was confirmed by flow visualization using smoke. The more forward origin, increasing size and steepening trailing arms of the floor vortex system were clearly indicated as tunnel speed was reduced.

From a practical standpoint it would be desirable to establish to what degree vortex formation could be allowed to proceed without significant effect on jet-model test results. This would determine the lowest useful tunnel speed. In detail however such a limit would depend not only on the specific jet arrangements but on other configurational aspects of the model and tunnel. Attention was directed first therefore towards the quantitative correlation of observed flow stagnation positions (corresponding to  $X_P$ ,  $X_B$ ) using selected basic jet arrangements encompassing parameter ranges relevant to foreseeable model testing. For the range of nozzle height/diameter ratio of interest such data should be broadly independent of tunnel characteristics (including floor boundary layer) and should provide a generally useful indication of the conditions pertaining to incipient stagnation. Such conditions define an operating limit for floor vortex formation, i.e. a conservative but safe minimum tunnel speed for meaningful model testing.

## 5. INCIPIENT STAGNATION LIMITS FOR SINGLE-JETS AND JET-PAIRS

Preliminary experiments employed plain cylindrical jet nozzles located at mid-width and directed vertically downward from various heights above the tunnel floor (Ref. 13). Three jet sizes ( $d = 6.63$  in (0.168 m), 8.19 in (0.208 m), 9.78 in (0.248 m)) at seven values of  $h/d$  (from 8.33 to 18.11) were operated at mean jet velocities up to 700 ft/sec (200 m/s). Observations, using wool tufts, were concerned mainly with the location of the stagnation point,  $X_B$ , relative to the nozzle. The correlation of approximately 250 data points indicated that, within the range of test variables, the non-dimensional distance  $x_B/h$  was a function of the parameter  $V_{RH}/d$ . A second experimental set-up utilized the fan efflux nozzle section of the lift-fan model of Figure 1. This arrangement allowed the observation of floor stagnation positions for a single-jet ( $d = 8.03$  in (0.204 m)) and a jet pair ( $s/d = 4.3$ ), operated at mean jet velocities up to 500 ft/sec (150 m/s) over a range of jet inclination to the vertical from  $-30^\circ$  to  $+30^\circ$  (Ref. 14). Two nozzle heights above the floor ( $h/d = 8.3$  and 12.4) were used with each jet arrangement. In conformity with the earlier results, both  $x_B/h$  and  $x_P/h$  were found to correlate reasonably well in terms of  $V_{RH}/d$ . The paired results for the single-jet case are shown in Figure 7. The curves illustrate the rearward migration and decreasing separation of the floor stagnation regions with increasing mainstream/mean jet velocity ratio. A minor extrapolation to intersection of the observation-based curves of  $x_B/h$  and  $x_P/h$  defines, at each  $\alpha$ , a critical  $V_{RH}/d$  corresponding to the state of incipient stagnation. (This condition is not amenable to direct observation by wool tufts owing to instability.) The curves of impingement stagnation position,  $x_P/h$ , of Figure 7, embody data observed at zero tunnel speed. Jet velocity was held constant (at about 200 ft/sec (60 m/s)) and inclination,  $\alpha$ , increased from zero in increments of  $5^\circ$ . Stagnation position was well defined (by wool tuft indications of strong radial flow) for values of  $\alpha$  up to  $50^\circ$ . At  $\alpha = 55^\circ$  a change in the character of the floor flow had become evident. The motion of the affected tufts nearest the nozzle had become highly irregular, indicating turbulence from the periphery of the jet. Apparently a state corresponding to incipient stagnation was achieved at a value of  $\alpha$  between  $50^\circ$  and  $55^\circ$ . The static data were used to extrapolate the incipient stagnation limits of Figure 7 to values of inclination beyond  $+30^\circ$ . Additional observations, using a third model set-up (described below), were made at negative values of inclination to  $-50^\circ$ . Figure 8 shows, in summary, an approximate representation of the conditions for incipient stagnation for a downward directed jet inclined to the vertical over a range of angle from  $-50^\circ$  to a limiting value of about  $+53^\circ$ . The curve indicates the single-jet operating limits for floor vortex formation in the NRC tunnel for values of  $h/d$  in the neighbourhood of 10. For this order of nozzle height and providing a solid floor is present, these limits should be broadly applicable to other tunnel configurations.

It is noted that the parameter  $V_{RH}/d$  can be expressed in terms of a force coefficient based on jet thrust,  $F (= M_j V_j)$ , dynamic pressure,  $q_0$ , and an appropriate area. Defining  $C_T = F/q_0 h^2$ , then  $V_{RH}/d = \sqrt{\pi/2C_T}$ . The results of Figures 7 and 8 can be recast in terms of  $C_T$  or, to facilitate comparison with other data, in terms of  $C_{TN} = C_T \cos \alpha$ , the coefficient based on jet force normal to the impingement surface. Figure 9 shows the single-jet incipient stagnation limits of Figure 8 replotted as limiting  $C_{TN}$  against  $\alpha$ . Over a range of jet inclination from about  $-5^\circ$  to  $+20^\circ$ , the conditions for incipient stagnation are represented by a constant value of  $C_{TN}$  ( $= 0.62$ ). Also shown on Figure 9 are the corresponding limits for a jet-pair ( $s/d = 4.3$ ) in both transverse and tandem alignment (i.e. with the line of nozzle centres perpendicular and parallel, respectively, to the tunnel axis). For these cases the force coefficient is based on total jet force (equivalent to the use of effective jet diameter based on total nozzle area in  $V_{RH}/d$ ). On this basis the incipient stagnation limits for the tandem jet-pair are quite similar to those for the single jet. A similar correspondence holds for observed stagnation positions. It is inferred that, from the standpoint of tunnel flow breakdown, a tandem jet-pair ( $s/d \leq 4.3$ ) may be regarded as a single jet of the same total nozzle area (centred at the mid-point of paired nozzle centres). It seems

probable, by extension, that a similar approach can be taken with respect to multiple in-line jets.

#### 6. INDICATED JET MODEL TESTING LIMITS ( $\alpha = 0$ )

The incipient stagnation limit defines the minimum tunnel speed for no vortex formation. In practice, tunnel flow breakdown will occur at a lower tunnel speed depending on the degree of vortex development that can take place without prejudice to measured data. This in turn depends, presumably, on the specific model and tunnel arrangements. The available experimental data on this point appear few, particularly for jet models. Vogler has reported force measurements on a jet equipped wing-fuselage model at various ground clearances in the 17-foot test section of the Langley 7 ft  $\times$  10 ft tunnel (Ref. 4). Owen has examined Vogler's lift data for evidence of tunnel flow breakdown (Ref. 15). The relevant lift data pertain to  $\alpha = 0$ ,  $h/d_e = 2$  to 10,  $d_e = 3.5$  in (0.089 m). In some cases a reversal in expected lift trend was noted (lift decreased as ground clearance was reduced). Owen's estimate of the implied testing limits for single-jet models is shown in terms of  $h/d$  and  $V_R$  in Figure 10. The incipient stagnation limit of Figure 8 is included for comparison. Apparently considerable floor vortex strength was developed before the lift data of Reference 4 reflected tunnel flow breakdown. Included in Figure 10 are the rectangular hyperbolas representing  $(V_{Rh}/d)^* = 0.45$ , 0.55, and 0.65. These curves straddle the Owen line and none is inconsistent with the (ill-defined) appearance of anomalies in the lift data of Reference 4. Very limited existing data suggest, therefore, that tunnel speed may be reduced to roughly 55% of the speed at which floor stagnation first appears before single-jet model data ( $\alpha = 0$ ) are invalidated by tunnel flow breakdown. The appearance of the anomalous drag-balance readings of Figure 4 (relating to the model type of Figure 1) corresponds to the operation of a transverse jet-pair at  $V_{Rh}/d_e = 0.86$  (the value of  $V_{Rh}/d$  associated with the turbine exhaust is well beyond that for stagnation). In this case the ratio of tunnel speed at breakdown to that at incipient stagnation is approximately 0.65 (Fig. 9). Considering the disparity in model-tunnel dimensions and configuration, this value is in reasonable conformity with the indications of the Langley data.

#### 7. LOCAL FLOW MEASUREMENTS AT NOZZLE HEIGHT (SINGLE JET)

To obtain more information on the allowable extent of vortex formation, additional measurements were made using the single-jet arrangement shown in Figure 11. The rotatable jet nozzle ( $d = 8.03$  in (0.204 m)) was centred between side-walls at a height 9.9  $d$  above the floor. Two five-hole probes were located at nozzle height, equidistant ( $4 d$ ) from the nozzle centre. Probe A was positioned directly ahead of the nozzle, probe B at  $45^\circ$  to the side and rear. The effect of jet operation on local flow conditions is illustrated, for  $\alpha = 0$ , in Figures 12 and 13. The data at both probe points show vortex-induced effects rapidly becoming dominant as mainstream/jet velocity ratio is reduced through the value for incipient stagnation. While the extreme values are beyond probe calibration and approximate, the trends are clear. At nozzle height, increasingly strong downwash and longitudinal interference effects reflect growing vortex size with reduction in  $V_R$ . Yaw readings at the off-centre position B demonstrate explicitly the corresponding steepening in the vortex trailing arms. Furthermore, while only two probes were used, it is evident from Figures 12 and 13 that considerable point-to-point differences exist in the response of local flow conditions to vortex development. This is illustrated in Figure 14 which shows the variation of  $(V_R)^*$  with longitudinal position at nozzle height (non-dimensionalized by  $h$ , as suggested by the observations of stagnation position) for various constant values of vortex-induced downwash angle. The data of Figure 12 are augmented here by measurements made with the jet nozzle (and attached probe) repositioned at 5.4  $d$  above the floor. Over the limited test range of  $x_p/h$ , vortex effects at nozzle height occur earlier (i.e. at higher  $V_R$ ) the farther downstream the point of measurement. Clearly the overall testing conditions representing tunnel flow breakdown will depend ultimately on the model arrangements associated with the jet. A general testing limit will provide at best a useful guide to minimum tunnel speed in a specific jet-model situation.

Figure 15 shows flow pitch angle, at positions A and B, plotted against  $(V_R)^*$  for a range of jet inclination from  $-30^\circ$  to  $+30^\circ$ . In the regime of vortex-induced downwash the data for all values of inclination are represented reasonably well by a single curve. The longitudinal interference data show similar trends. These results suggest that model testing limits and incipient stagnation limits vary similarly with jet inclination, tunnel flow breakdown occurring at an essentially constant value of  $(V_{Rh}/d)^*$  over the test range of  $\alpha$ . The single-jet testing limits for  $\alpha = 0$ , indicated by the lift data of Reference 4,  $(V_{Rh}/d)^* = 0.45$  to 0.65, are shown extended on this basis to other values of jet inclination in Figure 16. Included for reference in Figure 16 are curves of constant vortex-induced downwash angle,  $-\Delta\epsilon$ , measured at positions A and B for the specific single-jet arrangement of Figure 11.

While of limited coverage and tunnel-dependent, these data suggest that the indicated testing limits are unduly optimistic even for approximate purposes (at least in relation to the NRC tunnel). The indicated limits appear to be associated with significant vortex-induced downwash in the vicinity of the model. It is noted that, in the vortex-free regime, the probe measurements at nozzle height indicate appreciable induced upwash ahead of the jet. Figure 17 shows jet-induced flow pitch angle,  $\Delta\epsilon$ , at positions A and B for a range of jet inclination from  $-50^\circ$  to  $+50^\circ$ . The limited data show a marked dependence of vertical interference velocity on position and on jet inclination. In distinction to the vortex-induced interference, these effects, insofar as they arise from wall constraints, are in principle calculable (Ref. 2). The resulting

corrections to incidence are positive. The actual presence near the model of vortex-induced downwash indicates tunnel flow deterioration beyond the point where constraint corrections are useful, i.e. beyond the correctability limit properly defining tunnel flow breakdown. This limit is not necessarily the same as that indicated by manifest anomalies in observed data and is, in general, more restrictive. The limited single-jet data of Figure 15 indicate that little reduction in tunnel speed below the incipient stagnation level is necessary for flow conditions at nozzle height to be noticeably affected by the floor vortex system. From the correctability standpoint, it would seem advisable in practice to avoid vortex effects altogether by testing jet-models to the incipient stagnation limits only.

In the NRC tunnel it may be possible in some circumstances to circumvent the rather severe restriction on minimum tunnel speed implied by the incipient stagnation limits. The tunnel was designed ab initio, to meet what were envisaged (in 1960) as the requirements for the transition testing of V/STOL propulsion systems involving reaction jets. The general features of the installation reflect this approach, e.g. the high test section rectangularity ( $H/B = 2$ ). The entire test section (40 ft (12 m) long) is carried on a steel plenum chamber (vertical walls,  $4\frac{1}{2}$  ft (1.4 m) deep) supporting the adjustable floor. Some probe measurements were made with the test section floor plates removed, allowing jet penetration to the underlying chamber through an open aluminum grid. The results shown in Figure 18 are directly comparable with those obtained with the solid floor (Figure 15). While further assessment is required, the device appears to offer lower usable mainstream/jet velocity ratios and may prove useful in future testing.

## 8. CONCLUSION

Special problems attach to the transition testing of V/STOL propulsion system models involving inflow and efflux directions at large angles to the mainstream. Wall constraint, flow interference and real tunnel effects are discussed briefly in relation to data from a continuing experimental programme employing high-powered models in the closed test section of the NRC 10 ft x 20 ft wind tunnel.

Overriding limits to free-flight simulation arise from the stagnation of high energy downwash on a solid floor with the formation of a stable vortex system. An investigation of this real tunnel effect, as arising from circular jets, is described in some detail. Operating limits for floor vortex formation (incipient stagnation) are presented for single-jet and jet-pair arrangements encompassing typical parameter ranges and a wide range of fore-and-aft inclination to the vertical. The limits should be applicable, by extension, to models incorporating multiple in-line effluxes.

The initial appearance of anomalous trends in some existing jet-model force data is shown to correspond to tunnel speeds of from  $1/2$  to  $2/3$  the tunnel speed for incipient stagnation. Limited local flow measurements at nozzle height suggest that (a) such implied testing limits are associated with significant vortex interference in the vicinity of the model and (b) effective flow breakdown, defined by the limits of usefulness of data correction procedures, occurs at conditions close to those for incipient stagnation.

## 9. REFERENCES

1. Bachmeier, A.J. VTOL Propulsion Tunnel. Feature Article in Quarterly Bulletin No. DME/NAE 1968 (1), National Research Council of Canada, Ottawa, March 1968.
2. Heyson, H.H. Wind-Tunnel Wall Effects at Extreme Force Coefficients. N.Y. Acad. of Sci. Annals, Vol. 154, Art. 2, 1967.
3. Werlé, H. Simulation de l'Effet de Sol au Tunnel Hydrodynamique. La Recherche Aérospatiale, No. 95, July-August 1963.
4. Vogler, R.D. Ground Effects on Single- and Multiple-Jet VTOL Models at Transition Speeds over Stationary and Moving Ground Planes. NASA TN D-3213, January 1966.
5. Rae, W.H. Jr. An Experimental Investigation of the Effect of Test Section Geometry on the Maximum Size Rotor that can be Tested in a Closed Throat Wind Tunnel. AIAA Aerodynamic Testing Conference, AIAA Paper No. 66-736, September 1966.
6. Heyson, H.H. Grunwald, K.J. Wind-Tunnel Boundary Interference for V/STOL Aircraft and STOL Aircraft. NASA SP-116, April 1966.
7. Heyson, H.H. Theoretical Study of Conditions Limiting V/STOL Testing in Wind Tunnels with Solid Floor. NASA TN D-5819, June 1970.
8. South, P. Measurements of Flow Breakdown in Rectangular Wind Tunnel Working Sections. NRC NAE Aero Report LR-513, National Research Council of Canada, Ottawa, November 1968.
9. Tyler, R.A. Williamson, R.G. Balance Measured Thrust Performance of Various Cowl Axial Fan Configurations in a Mainstream at  $90^\circ$  Incidence. NRC DME Aero Report LR-543, National Research Council of Canada, Ottawa, October 1970.
10. Tyler, R.A. Williamson, R.G. System Considerations and Preliminary Model Tests on a Form of Vectored Thrust Power Plant for Commercial V/STOL Operations. C.A.S. Journal, Vol. 15, No. 5, May 1969.

11. Lazzeroni, F.A. Carr, L.W. Problems Associated with Tunnel Tests of High Disk Loading Systems at Low Forward Speeds. Proc. Third CAL/AVLABS Symposium, Aerodynamics of Rotary Wing and V/STOL Aircraft, Vol. II, June 1969.
12. Rae, W.H. Jr. Shindo, S. Comments on V/STOL Wind Tunnel Data at Low Forward Speeds. Proc. Third CAL/AVLABS Symposium, Aerodynamics of Rotary Wing and V/STOL Aircraft, Vol. II, June 1969.
13. Tyler, R.A. Williamson, R.G. Observations of Tunnel Flow Separation Induced by an Impinging Jet. NRC DME Aero Report LR-537, National Research Council of Canada, Ottawa, April 1970.
14. Tyler, R.A. Williamson, R.G. Tunnel Flow Breakdown from Inclined Jets. NRC DME Aero Report LR-545, National Research Council of Canada, Ottawa, March 1971.
15. Owen, T.B. Wind Tunnel and Other Facilities Required for V/STOL Model Testing. RAE Tech. Memo Aero 1198, February 1970.

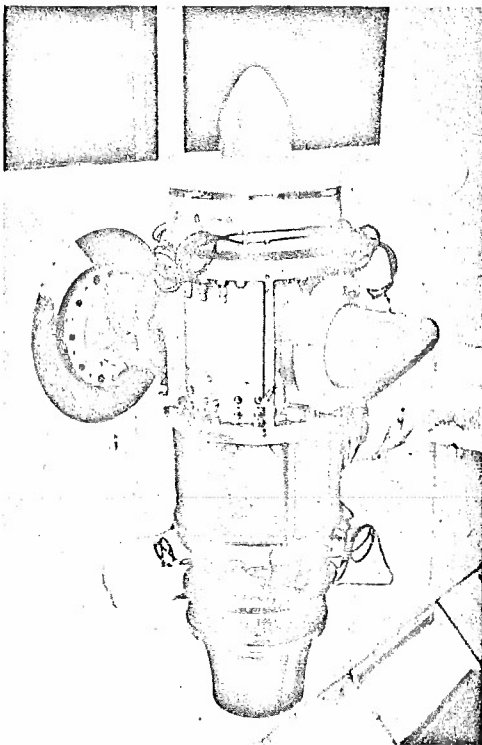


FIG. 1 TYPICAL SINGLE FAN TEST MODEL

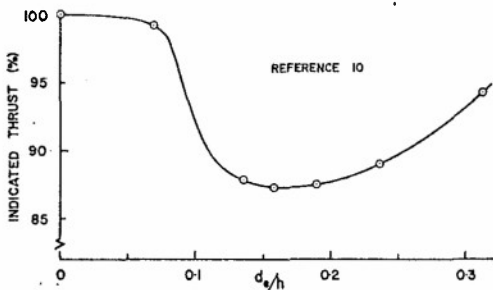


FIG. 3 TUNNEL EFFECTS ON STATIC THRUST MEASUREMENTS

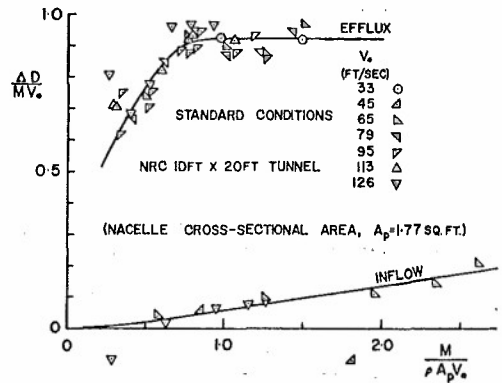


FIG. 2 INFLOW AND EFFLUX INTERFERENCE DRAG COMPONENTS

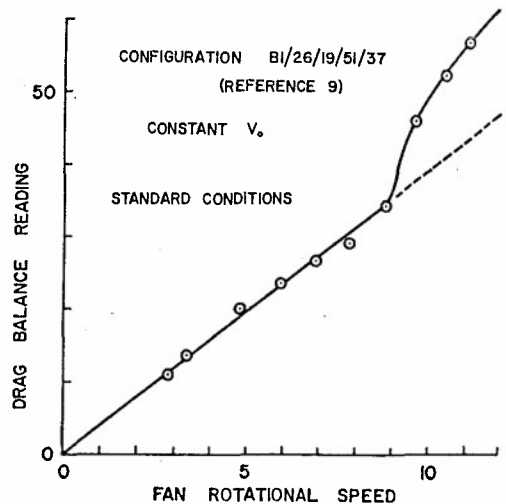


FIG. 4 EXAMPLE OF VORTEX-AFFECTED DATA

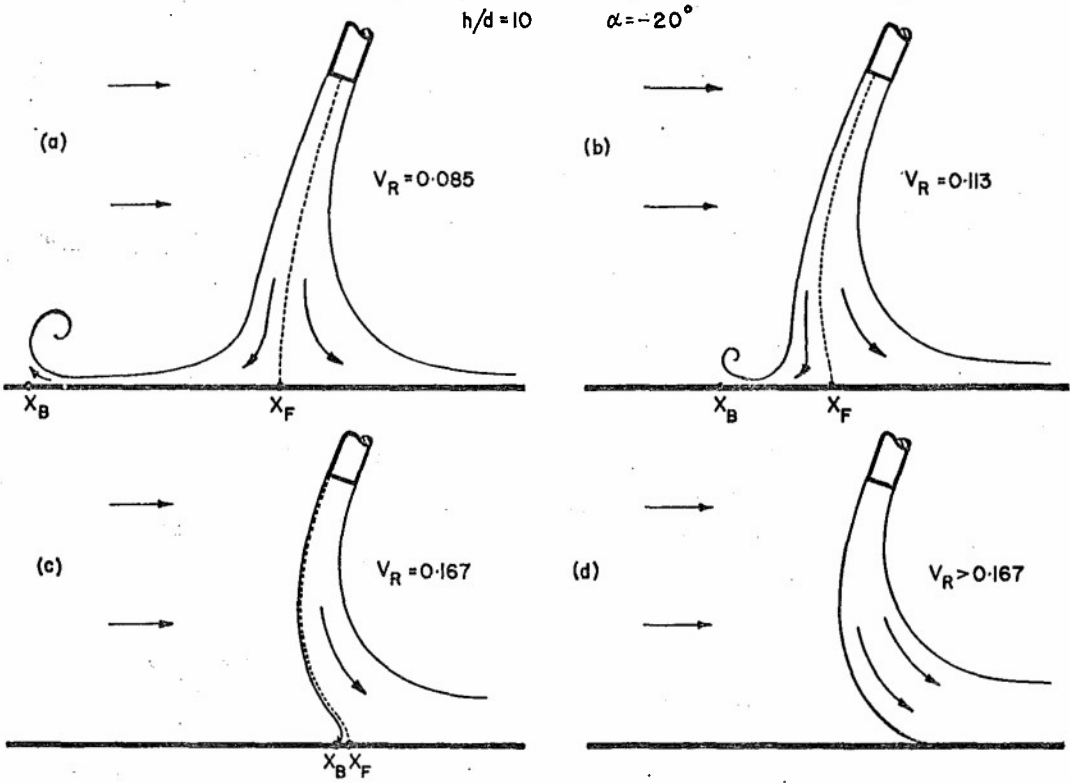


FIG. 5 SCHEMATIC JET FLOW PATTERNS

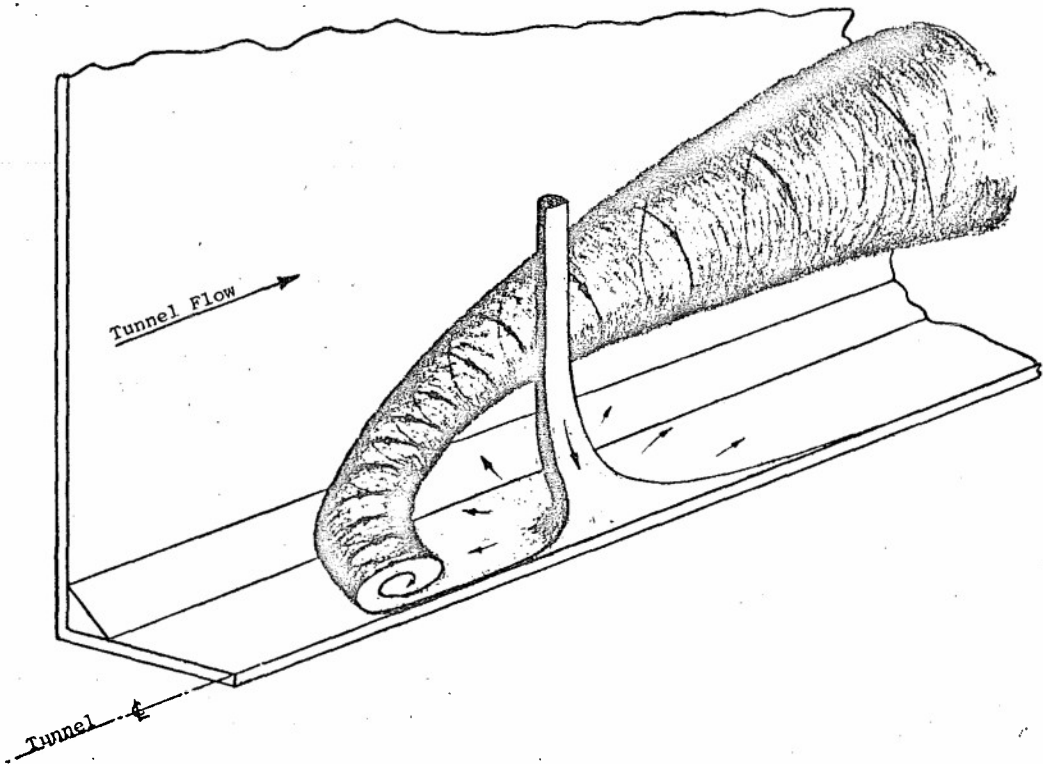


FIG. 6 IDEALISED REPRESENTATION OF VORTEX FORMATION BY IMPINGING JET

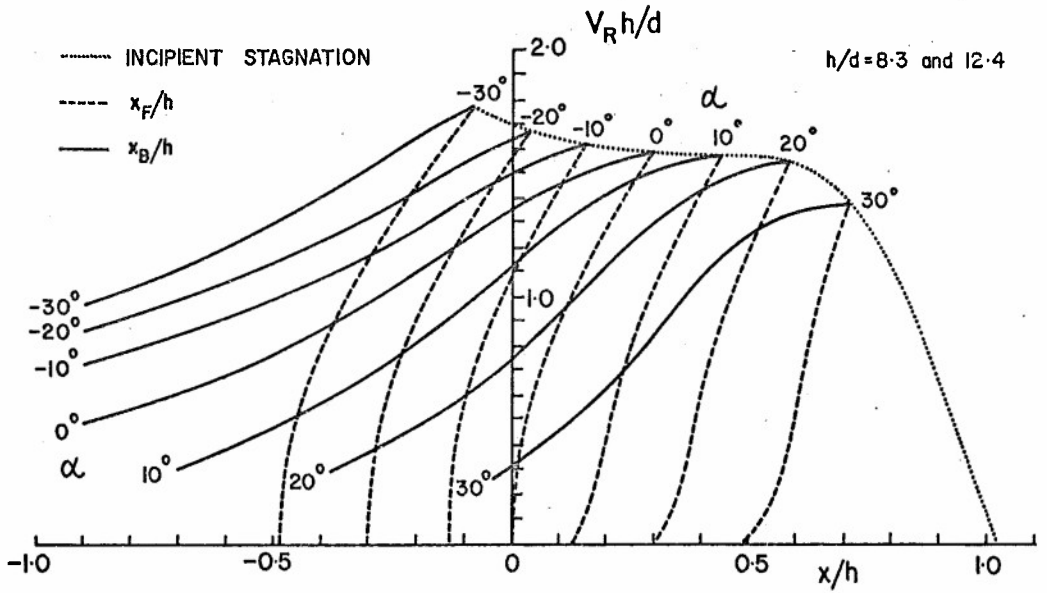


FIG. 7 FLOOR STAGNATION POSITIONS FOR INCLINED SINGLE JETS

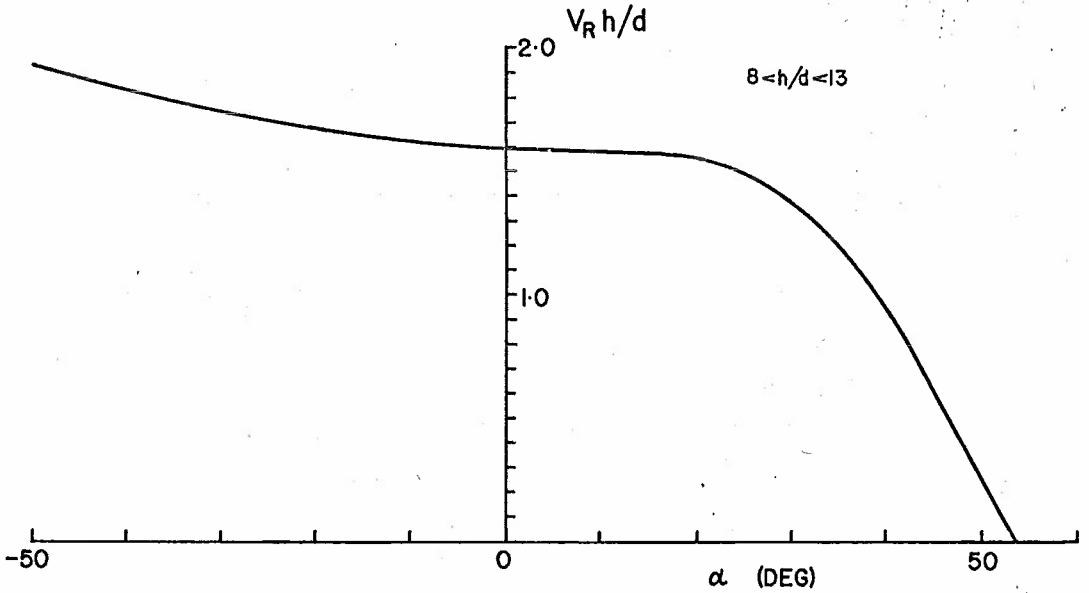


FIG. 8 INCIPIENT STAGNATION LIMIT (SINGLE JET)

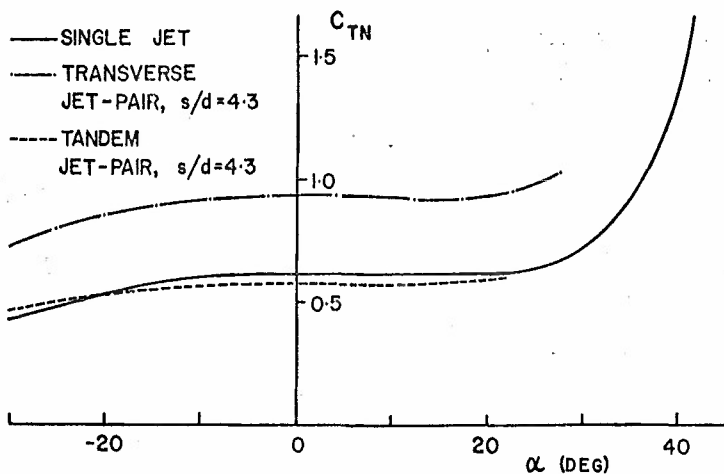


FIG. 9 FORCE COEFFICIENTS AT INCIPIENT STAGNATION

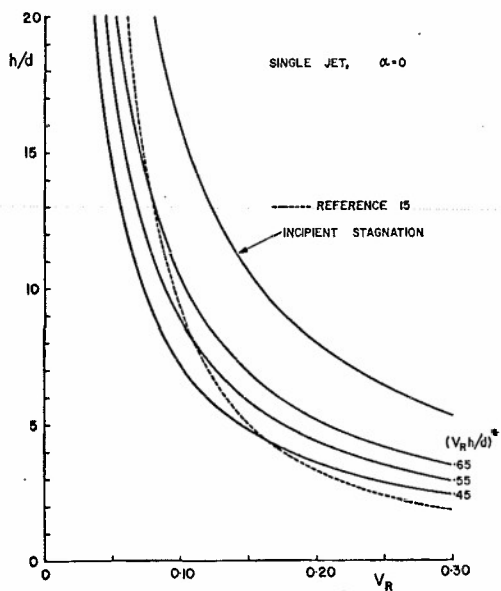


FIG. 10 TESTING LIMITS IMPLIED BY THE LIFT DATA OF REFERENCE 4

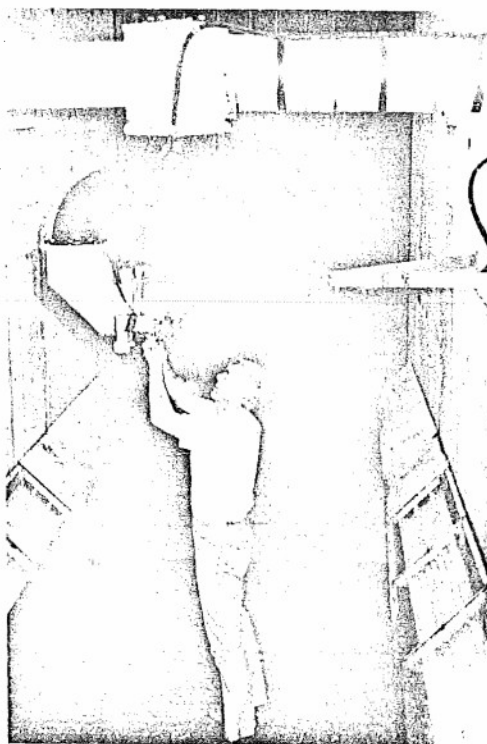


FIG. 11 TEST ARRANGEMENTS, SINGLE JET AND PROBES AT  $h/d = 9.9$

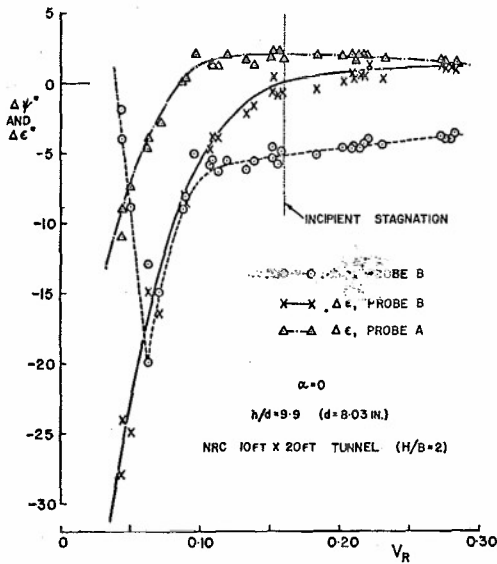


FIG. 12 JET-INDUCED INTERFERENCE AT NOZZLE HEIGHT; LOCAL FLOW ANGLES

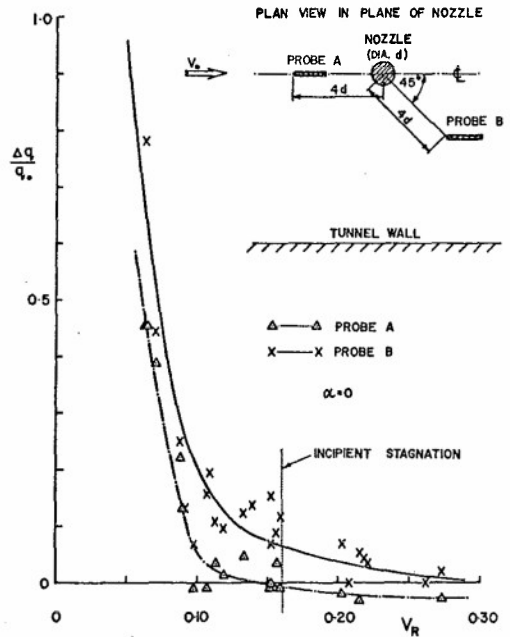


FIG. 13 JET-INDUCED INTERFERENCE AT NOZZLE HEIGHT; LOCAL DYNAMIC PRESSURES

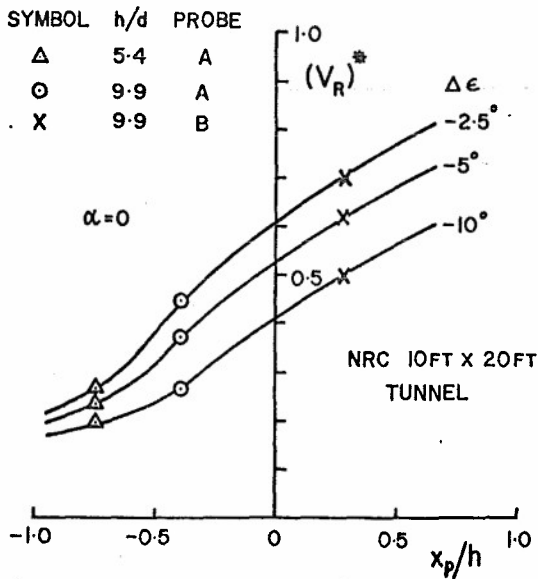


FIG. 14 LOCAL RESPONSE AT NOZZLE HEIGHT TO VORTEX DEVELOPMENT

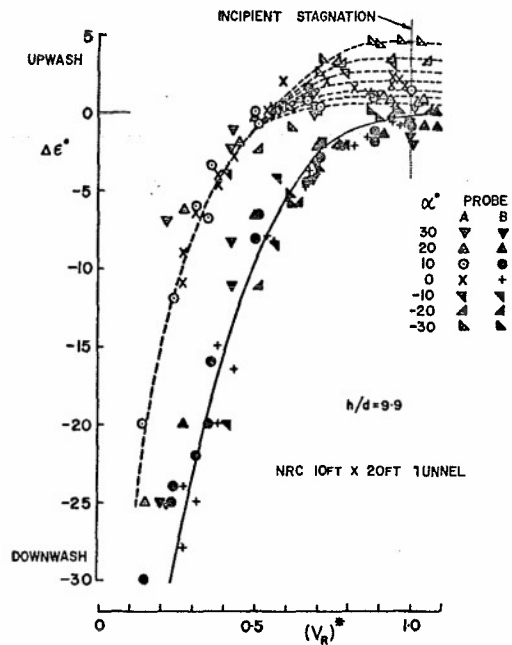


FIG. 15 CORRELATION OF  $\Delta\epsilon$  WITH JET INCLINATION ( $-30^\circ \leq \alpha \leq 30^\circ$ )

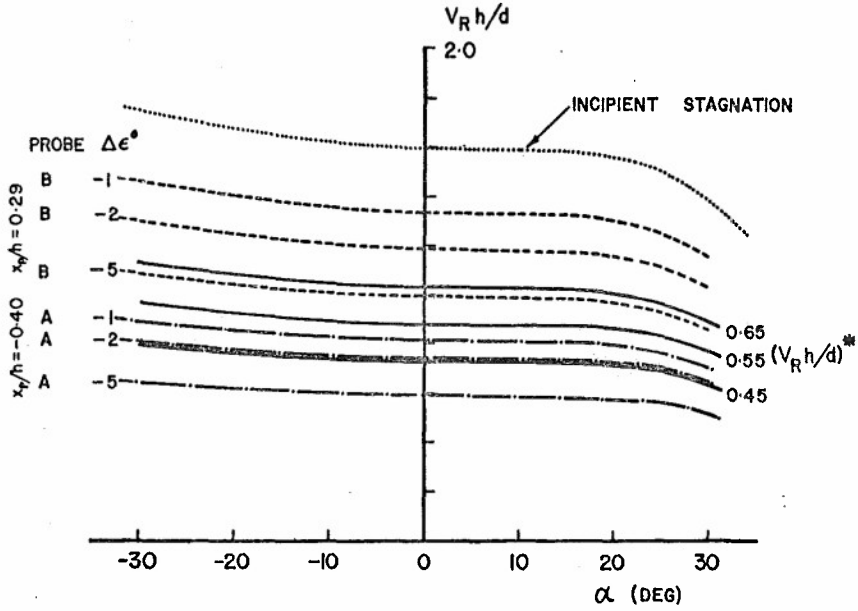


FIG. 16 VARIATION OF INDICATED TESTING LIMITS WITH JET INCLINATION

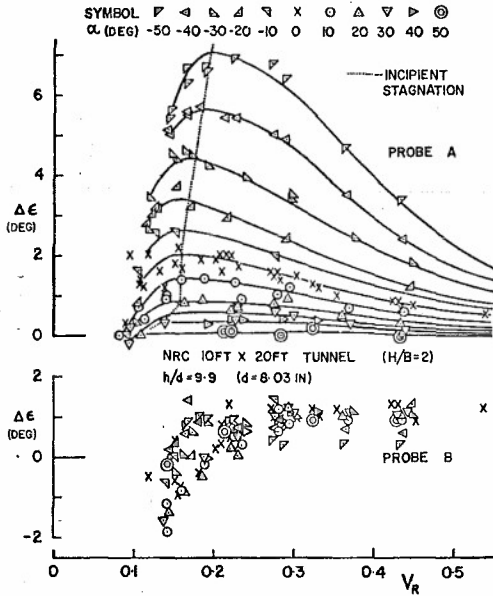


FIG. 17 LOCAL PITCH ANGLE AT NOZZLE HEIGHT IN VORTEX-FREE REGIME ( $-50^\circ \leq \alpha \leq 50^\circ$ )

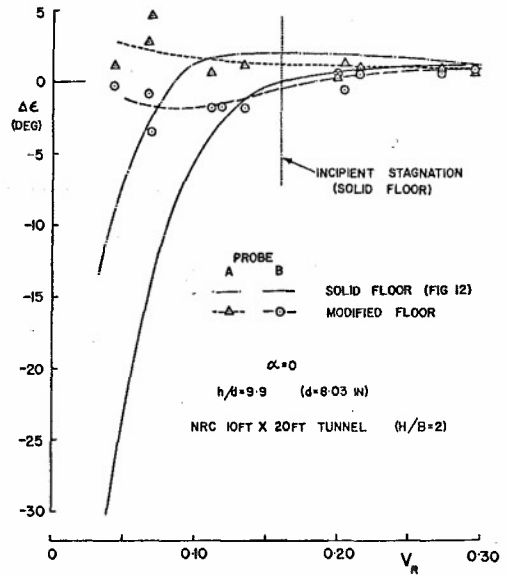


FIG. 18 EFFECT OF FLOOR MODIFICATION ON JET-INDUCED INTERFERENCE AT NOZZLE HEIGHT

## VECTORED THRUST IN AIR COMBAT

by

C. R. James, Jr.  
 Supervisor, Flight Performance  
 VOUCHT AERONAUTICS COMPANY  
 LTV Aerospace Corporation  
 P. O. Box 5907  
 Dallas, Texas 75222

## SUMMARY

Advantages of thrust vectoring in air combat are evaluated using the Vought Aeronautics manned air combat simulator. This simulator consists of two fighter cockpits linked by digital computer-driven visual displays which present each pilot with a properly oriented image of the opponent aircraft. Real time digital computation permits each pilot to "steer" his aircraft anywhere within the performance and strength limits of the airframe as he strives to maneuver into position to fire his weapons.

Engagements include three cases: (1) a baseline conventional fighter, (2) a vectored thrust version of the baseline and (3) the vectored thrust configuration with a 1500-pound weight penalty. The conventional fighter is the common opponent for all engagements. Engagements are scored by relative time in advantageous positions and by win-lose-draw results. Advantages of thrust vectoring are quantified and the sensitivity of advantages to weight penalty is determined. This paper describes the experiments, summarizes results, and presents analyses based on aircraft performance parameters. Results are also correlated with previous experiments.

## PREFACE

The close-in aerial combat or dogfighting mission presents the aircraft designer a demanding test. Maneuver requirements are severe and the proper tailoring of airframe-engine characteristics to assure a superior fighting machine is essential. From the early days of air combat in World War I, propulsion improvements have paced the development of fighter aircraft and the advent of lighter, more powerful engines has resulted in increasingly higher fighter performance levels. In addition, propulsion innovations such as the air cooled engine, supercharging, and turbojet propulsion have been widely exploited in fighter design. Recently a new innovation, the capability to alter thrust direction, has been incorporated in developmental and production aircraft. This capability, termed thrust vectoring, provides potentially a new dimension to air combat. Additional turning forces perpendicular to the flight path may be developed by properly directing thrust. These forces, however, are realized only at some loss in thrust component along the flight path.

In order to evaluate these trade-offs and to quantify the effects of thrust vectoring in air combat, a systematic experiment has been carried out using the Vought manned air combat simulator. A brief description of this simulator is presented in Appendix A.

## 1. DESCRIPTION OF EXPERIMENT

Three fighter configurations were evaluated: (1) a baseline conventional fighter, (2) a vectored thrust version of the baseline and (3) the vectored thrust configuration with a 1500-pound weight penalty. The conventional fighter was the common opponent for each engagement. Complete aerodynamic and propulsion data were programmed for each configuration as described in Appendix A. Since the primary objective of the experiment was to quantify gross effects, it was assumed that the gross thrust vector passed through the airplane center of gravity for all deflections; thus no trim changes were encountered as thrust was deflected. A maximum thrust deflection rate of 20 degrees per second was assumed and a control handle was located near the throttle quadrant to be used for thrust vector control. In the forward position the nozzle angle was -2 degrees (nozzle exit up); in the aft position, +100 degrees (down). The conventional fighter had a reference combat thrust-to-weight ratio of 0.91 and a combat wing loading of 70 pounds per square foot.

Engagements were initiated at a position of neutral advantage: Mach number 0.85 and 25,000 feet altitude with the aircraft on a collision course with a 90-degree track crossing angle. Initial separation distance was 24,000 feet. Each pilot was aware of the initial location of his opponent. The engagements each lasted five minutes and three pilots experienced in air combat participated. Thirty engagements were flown per configuration and the pilots were switched from cockpit to cockpit to provide a balanced matrix and thus minimize the effects of pilot skill on the outcome. A training and orientation period preceded the actual engagements. During this period, the pilots became familiar with the flight envelope and performance characteristics of each configuration. Tactics were also developed at this time.

Two types of scoring were used: time advantage ratio and win-lose-draw results. Time advantage ratio is defined as the ratio of the time the winning pilot maintains an advantageous position to the time the losing pilot maintains this advantageous position. Three types of time advantage criteria were applied: forward hemisphere, forward hemisphere within a range of 10,000 feet and forward hemisphere within a range of 3000 feet. Three different criteria were also applied to define win-lose-draw results: (1) bullet conversion, (2) pipper conversion, and (3) a missile launch zone conversion. The pilot first to satisfy the conversion criteria was scored the winner of that engagement. If neither satisfied the criteria within the five minute limit, the engagement was declared a draw. Scoring was by percent wins of A,  $P_{CA}$ ; percent wins of B,  $P_{CB}$ ; and percent draws,  $P_D$ . An additional parameter, Advantage Ratio, defined as wins plus draws divided by losses plus draws was also used to quantify results.

2. RESULTS

Figure 1 shows results in terms of time advantage ratio. The conventional baseline case advantage ratio is 1.0 for each criterion. With the forward hemisphere criterion the vectored thrust time advantage ratio is near 5.0. With the 1500-pound weight penalty, this ratio drops to about 3.4. Similar trends are noted for the 10,000-foot and 3000-foot range cases. With the 3000-foot range requirement, the effect of the weight penalty is more pronounced with a time advantage ratio of about 2.7.

Figure 2 summarizes win-lose-draw results based on bullet conversions. In order to score a bullet conversion, a pilot must be the first to satisfy three simultaneous constraints. He must be in the rear hemisphere of his opponent, within a range of 3000 feet and must fire a bullet within a distance of 100 feet of the center of gravity of the opposing aircraft.

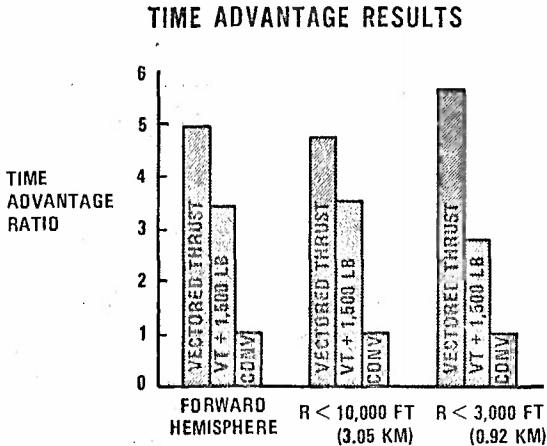


Figure 1.

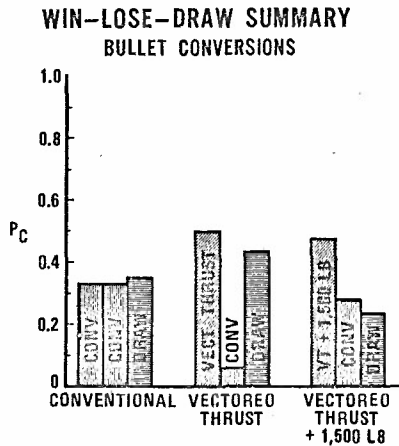


Figure 2.

The conventional baseline fighters each won about 32 percent of the engagements and 36 percent were draws. With vectored thrust, the wins increased to about 50 percent while the conventional fighter won only 7 percent. Between this pair of aircraft, 43 percent of the engagements were draws. With the 1500-pound weight penalty, the vectored thrust aircraft still won about 48 percent of the engagements. Now, however, the conventional aircraft was able to win about 27 percent of the engagements and about 25 percent were draws.

In terms of Advantage Ratio (wins plus draws divided by losses plus draws) Figure 3 compares results for bullet conversions. The advantage ratio for the vectored thrust aircraft was 1.86. Adding the 1500-pound weight penalty reduced this ratio to 1.40.

Similar trends are shown for the pipper conversion criteria. In order to score a pipper win the pilot must satisfy three simultaneous constraints: (1) place the pipper of the lead computing gun-sight on the target, (2) be within 3000 feet, and (3) have the trigger depressed. Figure 4 summarizes those results. Advantage ratio for the vectored thrust configuration is 1.88. The weight penalty reduces this ratio to 1.79. The degrading effect of weight penalty appears to be somewhat less with pipper conversion than with bullet conversions.

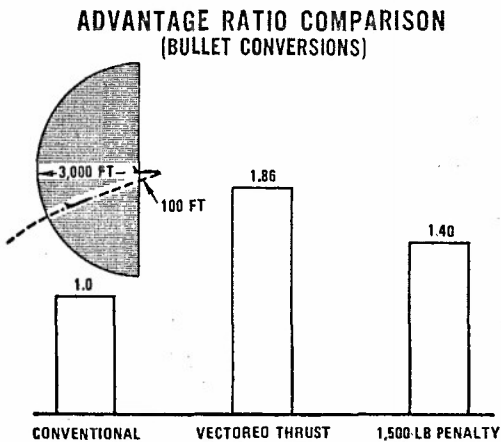


Figure 3.

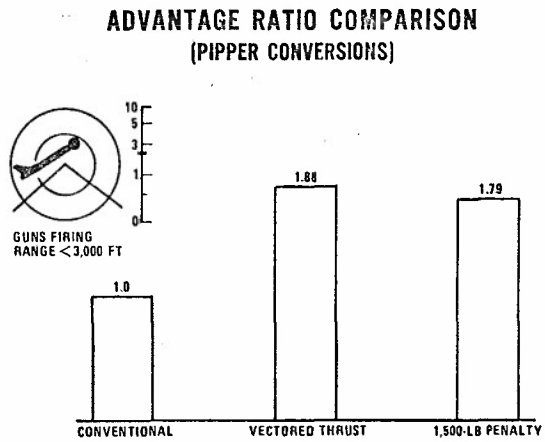


Figure 4.

The benefits of vectored thrust are even more pronounced in providing missile firing opportunities. Figure 5 summarizes advantage ratios for launch zone conversions. In order to score a missile conversion a pilot must be within the rear 40-degree cone of his opponent and have the opponent within his own forward 40-degree cone. He must be within a range of 6000 feet and hold these conditions for 3 seconds. The vectored thrust aircraft has a 2.42 advantage ratio in this situation. The 1500-pound weight penalty reduces this advantage ratio to 1.91.

For these experiments, the pilots were briefed on the performance characteristics of the aircraft and the calculated effects of vectoring thrust. Using this information, each pilot developed, during orientation and practice engagements, his own tactics and strategy for using the vectoring capability. With very little practice, the pilots discovered the tremendous built-in "speed brake effect" of high thrust deflection. These high deflections were used quite sparingly in the engagements. Figure 6 shows the frequency distribution of thrust deflection angle for the 30 engagements of the vectored thrust aircraft against the conventional aircraft. Note that 50 percent of the time the deflection was 13 degrees or below and that 85 percent of the time the deflection was 30 degrees or below. A "spike" of 4 percent is evident in the 90- to 100-degree deflection region.

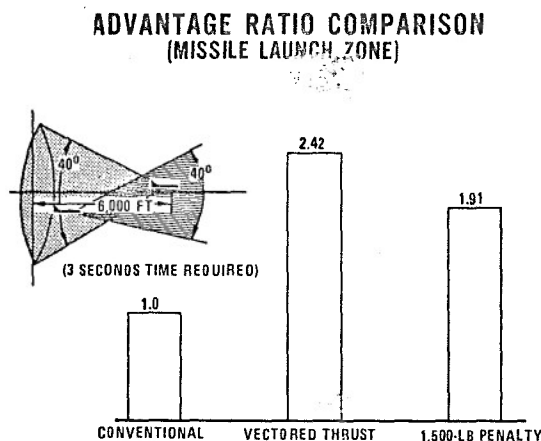


Figure 5.

**THRUST ANGLE FREQUENCY DISTRIBUTION**

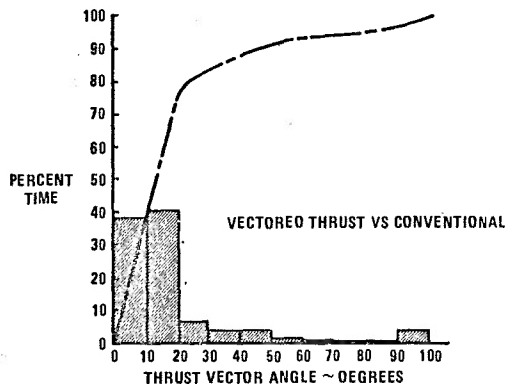


Figure 6.

### 3. CORRELATION WITH PREVIOUS EXPERIMENTS

Insight to the factors contributing to these results may be obtained by correlation with previous experiments. A dimensionless Measure of Performance (MOP) has been developed empirically to relate air combat effectiveness to aircraft performance, weight and geometry. The MOP combines three important elements of aircraft performance: (1) sustained (thrust limited) maneuvering, (2) longitudinal acceleration, and (3) maximum instantaneous (lift limited) maneuvering capability. This parameter is defined as follows:

$$MOP = n_s \sqrt{\frac{T/W}{M_B}}$$

where:

$$\left. \begin{aligned} n_s &= \text{maximum equilibrium "g"} \\ T &= \text{installed maximum thrust} \\ W &= \text{combat weight} \\ M_B &= \text{minimum Mach number for pulling 6.5 "g" at 10,000 feet} \end{aligned} \right\} \begin{aligned} M &= 0.8 \\ h &= 10,000 \text{ feet} \end{aligned}$$

The conditions for evaluating these parameters ( $M = 0.8$ ,  $h = 10,000$  feet) have been shown by simulation experience to be near the centroid of the combat arena. Analysis of Mach number and altitude frequency distributions show that aircraft typically spend as much time in combat below  $M = 0.8$  as above and as much time above 10,000 feet as below.

The effect of thrust vectoring on these parameters is shown in Figure 7. Maximum instantaneous (lift limited) and sustained or equilibrium "g's" are shown as functions of Mach number for both the conventional and thrust-vectored configurations. Maximum lift or instantaneous turning for the thrust-vectored aircraft is realized when the sum of the angle of attack and thrust vector angle equals 90 degrees. Approximately 1 "g" of additional load factor is obtained at a given Mach number with these large deflection angles. However, the resultant longitudinal decelerations are quite large. At any given speed and altitude a unique thrust deflection angle maximizes sustained turn performance. This angle balances the trade-off between longitudinal thrust loss and reduced drag due to lift to increase sustained turn rate above that attainable without vectored thrust. This optimum angle is shown in the insert of Figure 7.

Pertinent performance parameters used in MOP determination are tabulated below:

ITEM/CONFIGURATION	CONVENTIONAL	VECTORED THRUST	VECTORED THRUST + 1500 POUNDS
T/W	0.91	0.91	0.86
W/S	70	70	73.9
$n_g$	7.14	7.29	6.95
$M_B$	0.703	0.635	0.654
MOP	8.11	8.73	7.98

Note the improvement in sustained "g" and instantaneous maneuvering (lower  $M_B$ ) afforded by thrust vectoring. Note also that the degrading effect of weight penalty more than offsets the advantages of thrust vectoring so that the MOP of this configuration is lower than that of the conventional fighter.

The comparison of thrust-vectoring effects is based on a large data base of simulator and flight test results of air combat engagements. Figure 8 shows the matrix of configurations tested. Wing loadings vary from 55 pounds per square foot to 95 pounds per square foot and reference thrust-to-weight ratios from 0.4 to almost 1.0. Note that the vectored-thrust configurations are near the upper limit of thrust-to-weight ratios tested and on the lower side of wing loadings.

**MANEUVERING PERFORMANCE COMPARISON  
(10,000 FT ALTITUDE)**

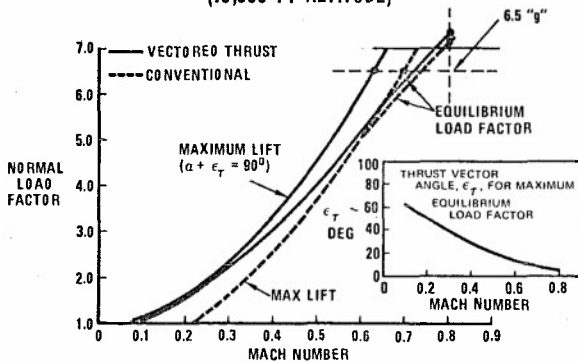


Figure 7.

**CONFIGURATION MATRIX FOR CORRELATION**

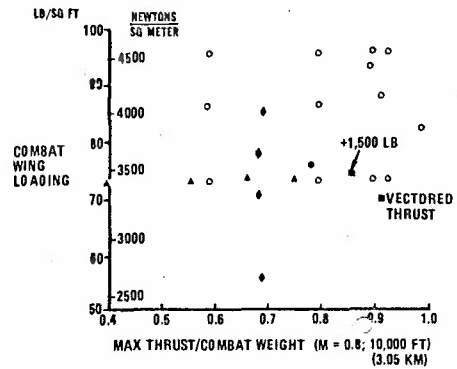


Figure 8.

Results of the vectored-thrust experiments are shown on Figure 9 and compared with a correlation of results from previous experiments. (A complete discussion of the development of this correlation is presented in Reference (1)). Advantage ratio is shown as a function of MOP. The solid trend line is that established from previous simulator and flight tests. The dashed line is drawn through the two points from the vectored-thrust experiments. Note that the trend due to weight penalty is consistent with previous studies but that the thrust-vectored points are displaced from the non-vectored trend line to the extent that a thrust-vectored aircraft with an MOP equal to that of a non-vectored aircraft would be expected to have an Advantage Ratio of about 1.45. Results from previous studies indicate that it would take a wing loading differential of 12 to 16 pounds per square foot or a thrust-to-weight advantage of 0.08 to 0.16 to achieve this level of combat advantage without thrust vectoring.

**COMPARISON OF VECTORED THRUST RESULTS WITH PREVIOUS CORRELATION**

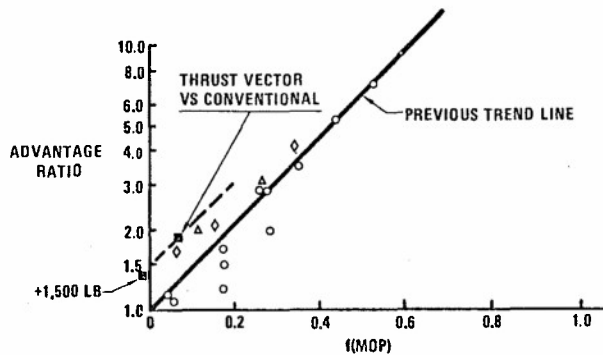


Figure 9.

#### 4. CONCLUSIONS AND RECOMMENDATIONS

Results of limited manned air combat simulator experiments indicate that significant benefits to air combat capability may be realized through thrust vectoring. Large increments in positional time advantage ratios and improvements in wins, losses and draws are realized when thrust vectoring is applied to a high performance fighter. Particular benefits were derived for air combat with missiles. Inspection of frequency distributions of thrust-vector angles show most usage in the low deflection range where loss in longitudinal thrust component is small. A spike exists near 90 degrees, however, where thrust vectoring functions quite well as a speed brake due to the ram drag momentum of the incoming air. The effects of weight penalties are pronounced, particularly in gun engagements.

Comparison of results with previous experiments indicates that thrust-vectoring advantages beyond those accounted for in the correlation parameter MOP may exist. These advantages may accrue from the shortened response time to pull "g" with thrust vectoring at the low end of the speed regime. At 0.4 Mach number, for example, it takes over twice as long to develop 0.25 "g" using elevator control as it does using thrust vectoring (1.2 seconds compared to 0.5 seconds). Another factor not reflected in MOP is the tactical advantage of using high deflection angles as a speed brake to avoid overshoot. This feature was rated quite useful by the pilots.

Two recommendations are identified from this study:

- (1) These limited ~~simulator~~ engagements should be expanded to better identify the benefits of thrust vectoring. In particular, the tactical limitations of restricting maximum angles to the order of 20 degrees to 30 degrees should be explored.
- (2) Configuration development for thrust-vector aircraft should be directed toward minimizing trim changes and unfavorable induced effects with thrust deflection. These effects were neglected in this study but could negate much of the potential benefits of thrust vectoring unless careful attention is given to configuration arrangement.

#### 5. REFERENCES

- (1) "Aerial Gun Duels: A comparison of Flight Tests and Simulator Results," by C. R. James, Jr., a paper delivered at the AIAA Fighter Conference, March 1970.

## APPENDIX A

## SIMULATOR DESCRIPTION

The Vought Aeronautics manned air combat simulator consists of two single seat fighter airplane cockpits equipped with individual flight controls, instruments, and interconnected visual display systems. The simulator is operated in real time through associated digital and analog computer equipment. During test runs, many output parameters are generated and recorded on magnetic disc tape and strip chart recorders for subsequent analysis. This system engages two pilots in a realistic air-to-air dogfight with each pilot constrained only by his capabilities and those of his simulated aircraft.

## 1. CONTROLS AND INSTRUMENTS

Cockpit controls include a two-axis control stick incorporating a longitudinal beep trim switch and gun trigger, a throttle with afterburner controls and a speed brake control. An auxiliary control lever can be used for control of variable wing sweep, maneuvering flaps or vectored thrust, depending on the configuration being simulated.

Flight instruments include a three-axis attitude director indicator, altimeter, airspeed/Mach indicator, vertical velocity indicator, angle-of-attack indicator, normal accelerometer, fuel gauge and speed brake extended warning light. Also, a missile launch light is pulsed in the attacking aircraft when certain missile launch criteria are satisfied.

## 2. AIRFRAME CHARACTERISTICS REPRESENTATION

A six-degree-of-freedom dynamic representation of the aircraft is provided. Appropriate aerodynamic, thrust, and fuel flow characteristics are programmed in table look-up form.

Longitudinal and lateral stick forces are simulated through a mechanical spring system. Static, dynamic and maneuvering longitudinal control characteristics are mechanized by programming the ratio of longitudinal control stick displacement to simulated elevator movement.

Additional simulated flight characteristics are provided by "stick shaker" and "wing rock" systems. The "stick shaker" system commences at computed buffet onset and increases in amplitude with increased angle of attack. The "wing rock" system simulates lateral instability of maximum attainable lift coefficient by introducing 1 cps oscillation in roll. Further increase in angle of attack results in a simulated departure from controlled flight by hard over roll input.

## 3. VISUAL DISPLAY

The visual display provides the pilots with near full peripheral field of view. Each cockpit is enclosed in a 16-foot diameter sphere, as illustrated in Figure A-1. These spheres serve as spherical projection screens. The projected visual scene consists of the opponent aircraft image in proper orientation and size, a representation of the earth horizon, and gunsight imagery with lead compensation pipper and range marker.

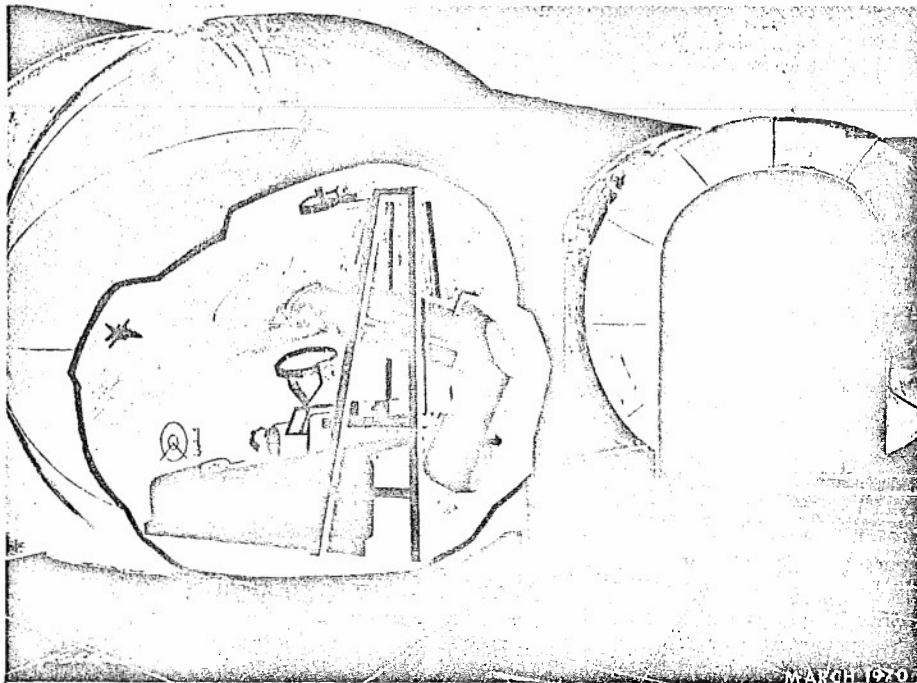


Figure A-1. Artist's Concept of Vought Air Combat Simulator

As shown in Figure A-2, the visual system is mounted on a derrick-shaped frame directly behind the pilot. The opposing aircraft image is computer generated onto a fixed high brightness cathode ray tube and is projected onto the spherical screen through a refractive optics system and center-mounted gimbal mirror assembly.

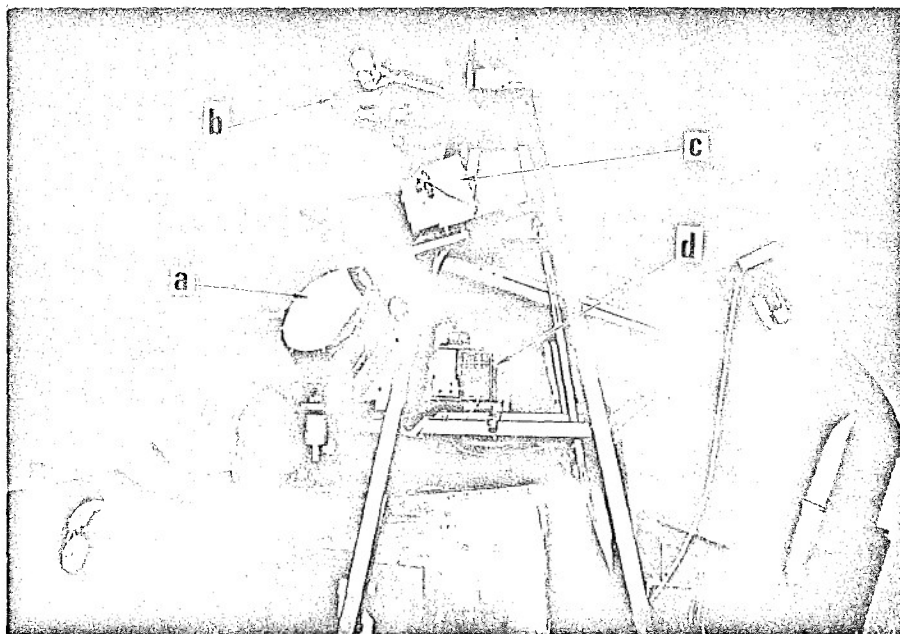


Figure A-2. Simulator Visual Display System

The gimbal mirror (Item a of Figure A-2) is a servo-driven two-axis system which can be rotated 360 degrees in both pitch and yaw to position dynamically the target image at the proper azimuth and elevation on the projection sphere.

The earth horizon projector (Item b of Figure A-2) consists of a high intensity light source mounted in a tube. The tube is mounted on a two-axis, servo-driven gimbal system which allows it to rotate 360 degrees in both pitch and roll. The light source is driven axially in the tube to keep the horizon line in the proper location with respect to the pilot's eye.

The gunsight system is displayed on the projection sphere in front of the pilot by two slide projectors. The gunsight consists of fixed 50- and 100-mil radius rings, 45-degree bank reference, a gunsight pipper, a logarithmic 10,000-foot range scale, a variable range marker, and an in-range reference bracket. The gunsight is automatically "uncaged" within a 10,000-foot range, with the pipper displaying a computed lead pursuit tracking solution. See Figure A-3. One slide projector (Item c of Figure A-2) projects the gunsight reticle and range scale and contains a slide gate that produces a black line which moves vertically along the gunsight range scale to provide target range information. The second slide projector (Item d of Figure A-2) projects the lead compensating pipper onto the screen through two mirrors rotating about orthogonal axes. The position of the rotating mirrors provides X-Z motion of the pipper image on the spherical screen.

### GUNSIGHT IMAGERY

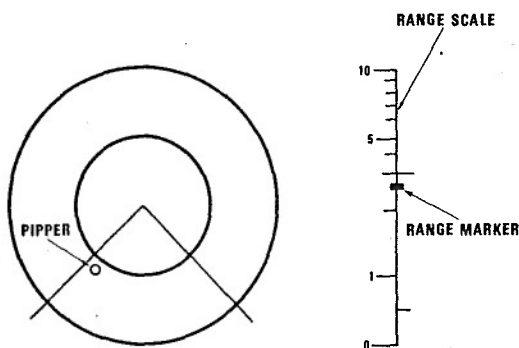


Figure A-3.

4. FLIGHT OPERATING CUES

Several synthetic operating cues are incorporated in each cockpit to enhance the pilot's ability to extract maximum performance from his aircraft. The cues include "g" suits, a grayout/blackout load factor warning light system, low altitude warning lights, and maximum dynamic pressure panel warning lights.

The "g" suit system consists of a standard inflatable "g" suit that is connected to an air supply system and inflates at a linear rate with aircraft load factor. This system provides the pilot with load factor cues that he is naturally accustomed to in actual flight.

The grayout/blackout load factor warning light is a white floodlight of two intensities located forward of the instrument panel and directed toward the pilot. The light comes on at low intensity to represent grayout when a certain load factor dosage is exceeded and then switches to high intensity if the dosage is further increased to an unacceptable limit. When load factor is reduced, the light is turned off by a reverse load factor dosage integration process. This light illuminates at high intensity immediately upon exceeding the structural limit load factor.

Three red floodlights of low intensity provide the pilot with a low altitude warning cue. They are located in front and on either side of the cockpit. These lights are pulsed at a prescribed altitude level and then become steady at a lower prescribed altitude. For the vectored thrust experiment the lights were pulsed between an 8000-foot and 10000-foot altitude and were steady below a 1000-foot altitude.

AERODYNAMICS OF THRUST REVERSER DESIGN.

by

W.J. Lewia

Rolla-Royce (1971) Limited,  
Bristol Engine Division,  
P.O. Box 3,  
Filton,  
Bristol BS 12 7QE

and

H. Prechter

Motoren- und Turbinen-Union,  
München GMBH  
8000 München 50  
Postfach 500640

SUMMARY

For a number of applications the clamshell target-type thrust reverser is an attractive solution to produce a braking force from a jet engine. This type of reverser consists of a pair of buckets which, in the stowed position, form part of the aircraft fuselage or engine nacelle and are moved into the jet efflux downstream of the final nozzle to provide thrust reversal.

The important geometric design parameters can be determined from consideration of the flow in the thrust reverser system. Their effect on the aerodynamic performance is established from model tests and will be discussed in detail. For the optimization of the operating mechanism in connection with fail-safe requirements, the load on the bucket and its point of application is important and is related to the reverser geometry. The problem of hot gas and debris ingestion into the engine intake is pointed out. Several solutions to overcome this problem are investigated together with the implications they have on performance and design.

1.0. NOTATION.

- $d_j$  - Nozzle diameter.  
 $h$  - End plate depth.  
 $l$  - Reverser bucket height.  
 $l_F$  - Height of point of application of bucket load.  
 $s$  - Reverser bucket spacing.  
 $w$  - Reverser bucket width on the nozzle axis.  
 $\beta$  - Bucket wrap angle.  
 $\theta$  - Bucket sweep angle.  
 $\phi$  - Direction in which bucket load acts.  
 $A_j$  - Nozzle area.  
 $C_D$  - Nozzle discharge coefficient.  
 $M$  - Mass flow.  
 $P_j$  - Jet total pressure.  
 $P_\infty$  - Ambient pressure.  
 $v$  - Velocity.  
 $X_Q$  - Nozzle gross thrust.  
 $\alpha$  - Jet inclination angle viewed from the side.  
 $\gamma$  - Jet inclination angle viewed from the rear.  
 $\delta$  - Bucket rotation angle viewed from above.  
 $\epsilon$  - Bucket rotation angle viewed from the side.  
 $\zeta_R$  - Reverser thrust efficiency -  $\frac{\text{Reverse Thrust}}{\text{Nozzle Thrust}}$

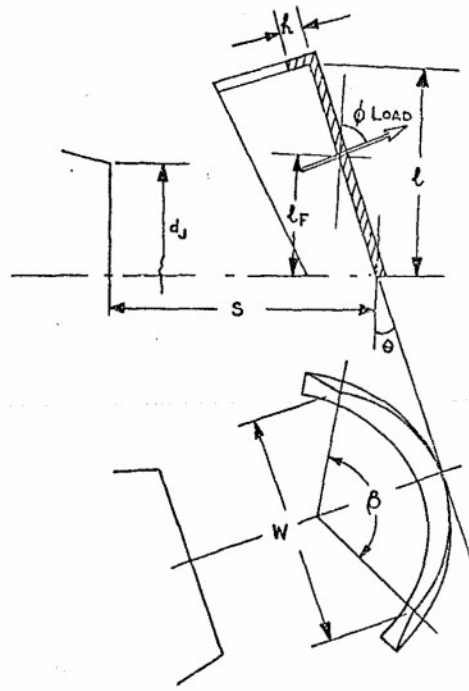


Fig. 1. Diagram of Target-Type Thrust Reverser.

## 2.0. INTRODUCTION.

The majority of civil transport aircraft and the latest military aircraft require thrust reversal to supplement the conventional wheel braking system in order to reduce landing distances. It is also useful to assist stopping during a rejected take-off or for in-flight operation. The landing distance of a reverser equipped aircraft is typically about 70% of that without a reverser. On wet and icy runways, where the wheel brakes are less effective, thrust reversers can stop an aircraft in about the same distance as on a dry runway with brakes alone.

From the various reverser designs currently in use on aircraft the target type will be dealt with in detail. With this type of reverser the clamshells (or buckets) are placed directly behind the exhaust nozzle when deployed, thus turning the exhaust gases into the required forward direction to produce a braking force on the aircraft. In the retracted position the reverser buckets blend in with the rear part of the engine nacelle, having small incremental drag. The installation is completely external to the engine exhaust system and does not compromise the exhaust system design. When stowed, it is not exposed to the adverse conditions (high temperature and vibration) of the exhaust, and causes no engine performance penalty in the forward thrust condition.

## 3.0. DESIGN FEATURES.

There are a number of parameters which have a significant effect on the aerodynamics and performance of the thrust reverser system. These are as follows :-

- (a) the reverser bucket width in the plane of the nozzle axis.
- (b) the reverser bucket height measured from the nozzle axis.
- (c) the reverser spacing (i.e. the distance of the bucket from the nozzle exit plane measured along the nozzle axis).
- (d) the bucket end plate depth and angle.
- (e) the bucket sweep angle and wrap angle.
- (f) special means to reduce the reingestion problem.

In this paper all of the above dimensions have been non-dimensionalised by dividing by the nozzle diameter. Obviously it is not practical to test all the various combinations of the above parameters and some form of selection is desirable. This has been done by analysis of the flow processes in the reverser system.

## 4.0. REVERSER AERODYNAMICS.

The aim of any thrust reverser design must be to catch as much of the nozzle flow as possible and eject it efficiently in the required direction. These two aims conflict to a certain extent insofar as the entire jet can be collected if the reverser buckets are made efficiently wide, but control of the efflux direction then becomes virtually impossible because large amounts of flow spill from the sides of the bucket. A diagrammatic representation of the flow for a target-type thrust reverser is shown on Fig.2. This flow pattern is common to nearly all reverser geometries and only the magnitude and strengths of the various flows are changed with change in the geometry.

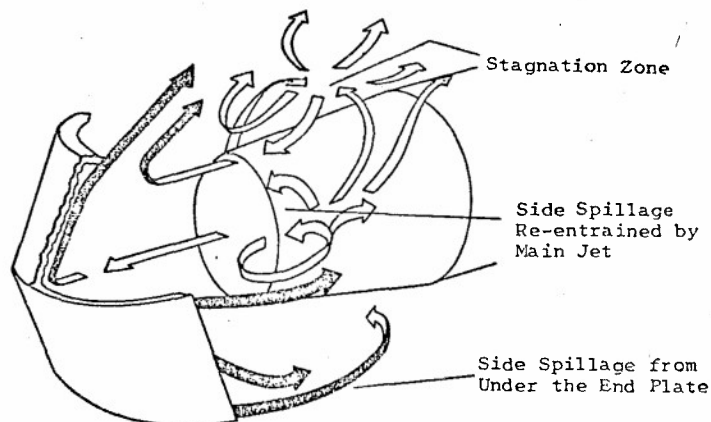


Fig.2. Diagrammatic Representation of Thrust Reverser Flows.

## 4.0. (continued)

In order to see how this flow occurs consider the plane of the nozzle axis and the bucket mating line. There are two aerodynamic effects, the upstream pressure effect due to the stagnation region in the reverser and the flow turning between the jet boundary and the reverser bucket surface. If the reverser bucket has a width similar to but not less than the nozzle diameter, i.e. is narrow, then the former of the two above aerodynamic effects is the more significant. The side spillage is low but the magnitude and direction varies with jet pressure ratio and bucket wrap and sweep angles. Fig.3(a) shows the observed flow pattern in this plane. Decreasing the bucket wrap angle but maintaining a constant width reduces the local turning angle at the edge of the jet and also reduces the axial distance between the edges of the bucket and the stagnation zone. Because of the higher pressure in the jet at the edge of the bucket the flow shown in Fig.3(b) is produced. A reduction in jet pressure or an increase in the bucket sweep angle will produce the same effect - in the former case because the upstream pressure rise increases in extent, and in the latter case because the effective axial distance between the bucket edge and the stagnation zone is reduced.

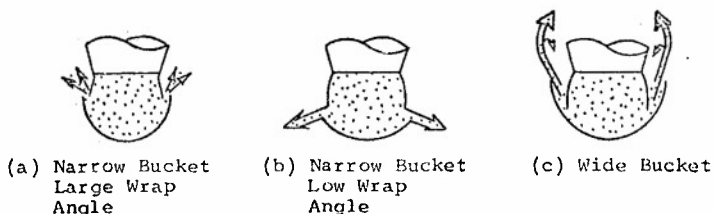


Fig.3. Effect of Reverser Bucket Wrap Angle and Width on the Flow in the Bucket Mating Plane.

In the case of the wide bucket, although the entire jet is caught in the bucket the turning angle at the jet edge is low. Consequently, as width is increased, more and more of the flow is able to spill sideways and then forwards off the edge of the bucket (Fig.3(c)). In the limit the reverser is a flat plate with the jet spreading uniformly over it. Not only does the large side spill cause the entire rear end of the engine nacelle to be enveloped in exhaust gas - which may cause local structural overheating, engine bay pressurisation and sooting and possibly hot gas reingestion - but the ability to change reverser performance significantly, by changing the sweep angle and the end plate depth, is lost since only a small proportion of the total exhaust gas flows along the bucket over the end plate.

Qualitative experiments have indicated that the minimum side spillage occurs for reverser width ratios of the order of 1.1:1, and is acceptable for width ratios between 1.0:1 and 1.25:1, and for sweep angles up to  $15^\circ$ . In this range of geometries, however, the magnitude and the direction of the side spillage is very sensitive to the geometry and to jet pressure ratio. On some installations it is impossible to design a reverser bucket with sufficient wrap in the above width range; for example, on an engine fitted with a reheat system, very much wider buckets are necessary to allow stowage over the reheat barrel. In this case, means of reducing the effective width of the bucket are necessary. One method of doing this is by using fixed or retractable fences inside the bucket.

4.1. Reverser Performance.

Having caught as much of the exhaust flow as possible in the reverser buckets, the next problem is to eject it in the required direction to achieve the necessary reverse thrust. Considering a section through the reverser system in the plane of symmetry, Fig.4 indicates the flow pattern for a bucket with no end plate. As the bucket height is reduced, the flow is turned less and less and leaves the end of the bucket at a large angle to the direction of it. A bucket height of about one nozzle diameter is necessary for the directional change between the flow and the bucket to be negligible. (Figs.4(a) & 4(b)).

The same reasoning can be used to explain the effect of the end plate (Fig.4(c)). The major difference is the separation of the flow over the bucket surface caused by the adverse pressure gradient. In certain cases, particularly with wide reverser buckets where flow is diverging over the bucket surface, a deep end plate will cause a circumferential flow in this separation zone and there will be spillage from the bucket edges in the corner formed by the end plate and the bucket. In any case, the separation and mixing on the separation boundary will cause a loss of reverse thrust. Since complete turning of the exhaust flow is not usually required, both end plate depth and bucket height may be less than the respective critical values. In practice, it is usual for the end plate to be relatively short in order that the bucket can be stowed without the need for very high boat-tail angles. The bucket height then must be near to the critical value to achieve worthwhile reverse thrust levels.

4.1. (continued)

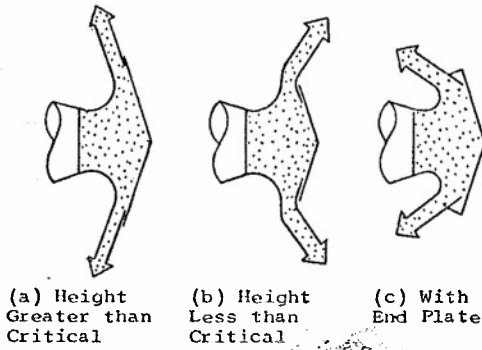


Fig. 4. Flow Patterns to demonstrate the effect of Bucket Height and End Plates.

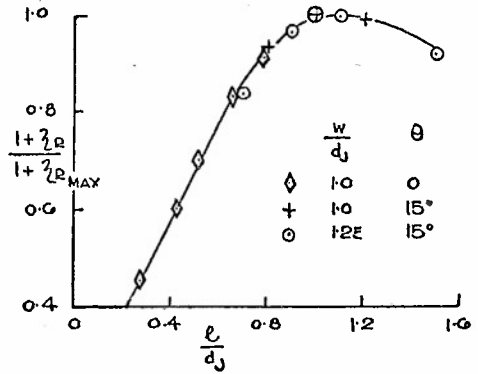


Fig. 5. Variation of Reverse Thrust Efficiency with Bucket Height. (no end plates).

The effect of bucket height is shown quantitatively on Fig. 5. With no end plate the maximum reverse thrust occurs with a bucket height of the order of 1.0 to 1.1 nozzle diameters. Any reduction below this height leads to a large loss in reverse thrust. The addition of an end plate does not significantly change the critical bucket height but may have a large effect on the slope of the line for heights less than critical. The value of the maximum reverse thrust efficiency used in Fig. 5 is a function of sweep angle and bucket width. This variation is shown on Fig. 6, and a number of results are included for wide buckets in which some methods of reducing the effective width were applied. On the assumption of no total pressure losses in the main flow, Fig. 6 also indicates the variation of the side spillage with sweep angle and width. For a width ratio of unity the side spillage has a small forward thrust component which increases slightly up to a sweep angle of 15°. Above this sweep angle the forward thrust component is more significant. For width ratios above a value of about 1.1 : 1 the side spillage has a small net rearward component leading to reverse thrusts slightly higher than the theoretical value.

It is obvious from Fig. 6 that only small amounts of reverse thrust are obtained without the use of an end plate. Fig. 7 shows the increment in reverse thrust with end plate depth, and it will be noted that increments of 30% and more are easily obtainable with relatively small end plates. There is a limiting value of end plate depth beyond which no further increase of reverse thrust is achieved. This limiting depth appears to be a function of the reverser bucket length and sweep angle. However, it will be seen from Figs. 6 & 7 that by careful selection a reverser can be obtained which has a reverse thrust efficiency greater than 60%.

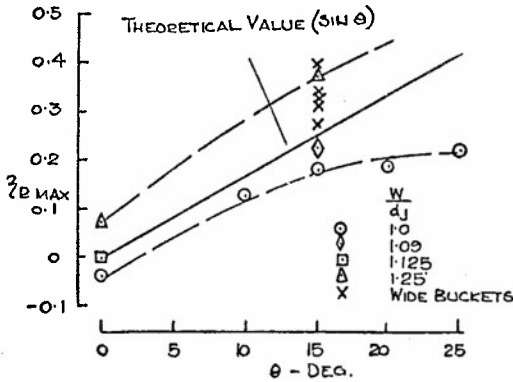


Fig. 6. Variation of Maximum Reverse Thrust with Bucket Width and sweep (no end plates).

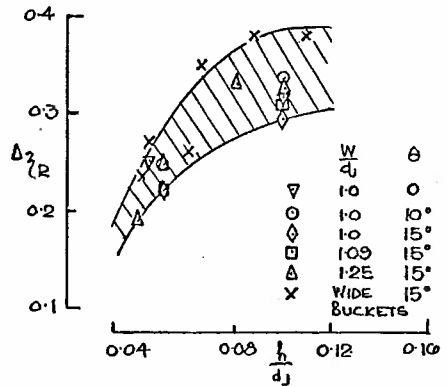


Fig. 7. Increment in Reverse Thrust Efficiency due to end plate depth.

4.2. Spacing Ratio.

Although the distance of the reverser buckets downstream of the nozzle has a small effect upon the reverser thrust efficiency, the main interest in the spacing ratio occurs because of possible effects on the nozzle discharge coefficient - and consequently on the engine internal operating conditions. From the point of view of weight - and, in some cases, ground clearance - it is desirable to position the reverser buckets as close to the nozzle as possible. However, at too small spacing ratios the upstream pressure field of the stagnation region in the reverser will lead to a local pressure around the nozzle which is higher than the ambient pressure, with a consequent possible reduction in nozzle discharge coefficient (particularly at low jet pressure ratios). Whether or not a reduction in the nozzle discharge coefficient is permissible depends upon the type of engine, the likely throttle movements in reverse thrust and, in the case of an engine with a variable nozzle, the control system.

A critical spacing ratio has been defined as that position of the reverser buckets which gives a reduction of 1% in the nozzle discharge coefficient. Fig. 8 & 9 show typical effects of width and sweep angle on the critical spacing ratio for different jet pressure ratios.

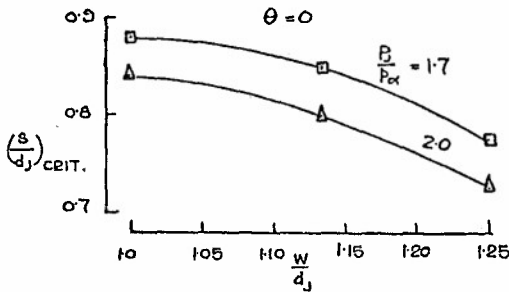


Fig. 8. Effect of Bucket Width on Critical Spacing Ratio.

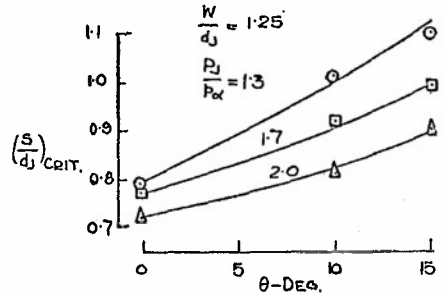


Fig. 9. Variation of Critical Spacing Ratio with Bucket Sweep Angle.

Since the reductions in nozzle discharge coefficient are due to the upstream effect of the stagnation zone in the reverser it is clear that bucket sweep angle should have a significant effect as is shown on Fig. 9. However, there is a further consideration: the upstream effect cannot be uniform across the jet and can be expected to be a maximum on the centre line. Fig. 10 shows the critical spacing ratio for a system representative of an unmixed long duct bypass engine (two coaxial nozzles). This shows that considering the inner (hot) nozzle alone leads to a larger critical spacing ratio than for the combined system. At the critical spacing ratio for the combined system the reduction in hot nozzle discharge coefficient has been determined and is shown on Fig. 11.

Co-axial, Coplanar Nozzles  $\frac{A_{J \text{ cold}}}{A_{J \text{ hot}}} = 1.12$   
 Equal Hot & Cold Total Pressures.

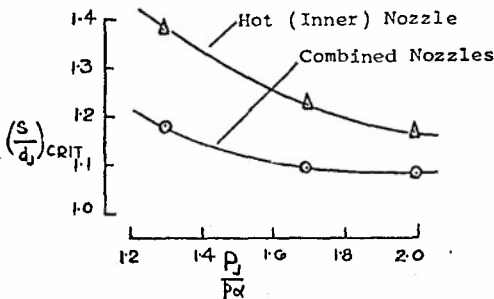


Fig. 10. Critical Spacing Ratio.

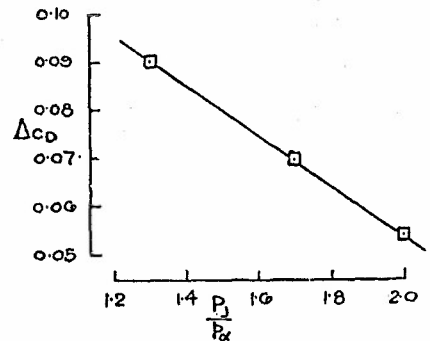


Fig. 11. Reduction of Hot Nozzle Discharge Coefficient at the critical spacing for the combined nozzle.

## 4.2. (continued)

The end plate depth will also affect the critical spacing ratio; very large end plates would tend to reduce the area around the exhaust system through which the reversed jet is able to pass. However, in the range of interest, end plate depth effects on the critical spacing can be ignored.

5.0. REVERSER BUCKET LOADS.

Knowledge of the loads on the thrust reverser buckets, both during deployment and in full reverse thrust is essential when designing the system in order to meet any fail-safe requirements and to minimize the actuator sizes. So many factors affect the loads, for instance the choice of linkage system, that only the full reverse thrust case at zero forward speed conditions will be considered. For a typical case with a simple double linkage with each link pivoted at both ends - one end on the fixed structure and the other on the reverser bucket - the instantaneous centre in full reverse is approximately 1.5 nozzle diameters from the reverser surface. If a moment arm of 0.05 nozzle diameters is assumed, this implies a moment of about 4200 Nm (39,000 lb.in.) on a 90 kN (20,000 lb.) thrust engine, then a shift in the point of application of the load of 0.025 nozzle diameters, or in the direction by  $1^\circ$ , is sufficient to change the moment by 50%. It is therefore essential that the direction and point of application of the load be known to a high accuracy. As a result, data based upon previous experience must be used with great caution.

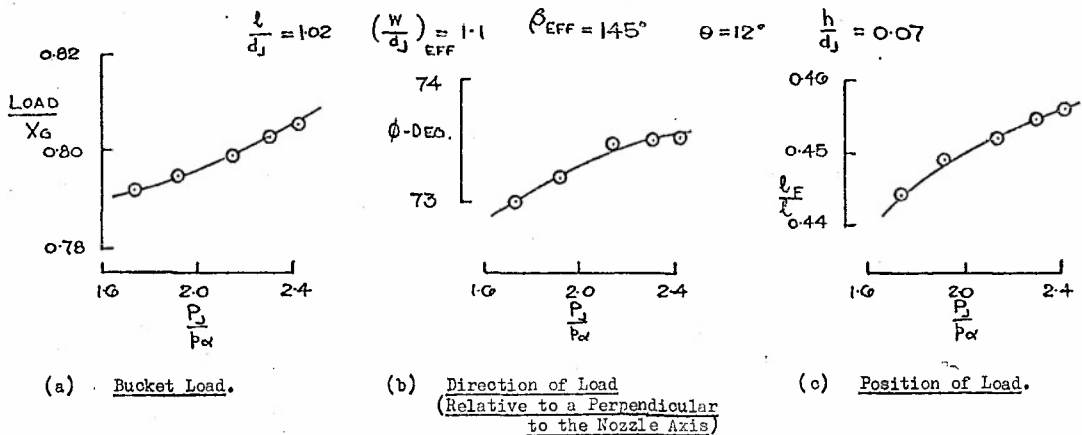


Fig. 12. Typical Thrust Reverser Loading Data.

Fig. 12 shows the measured magnitude, direction and position of the bucket load for a typical reverser system. In this case the component of the magnitude of the load in the axial direction is approximately equal to half the sum of the nozzle thrust and reverser thrust, although forces induced on the boat-tail which, in turn, react on the bucket, can change this magnitude by up to one-tenth of the nozzle gross thrust. The direction of the load is not perpendicular to the bucket surface due to the effect of the end plate. The difference from the perpendicular increases with the amount of flow turning done by the end plate. For the maximum practical end plate the direction of the force may be as much as  $5^\circ$  from the perpendicular to the bucket surface. If the mean direction of the reversed flow can be determined, then a crude approximation of the direction of the load (within about  $\frac{1}{2}^\circ$ ) can be made if the axial component of the load is assumed to be half the sum of the nozzle thrust and the reverse thrust. No successful method for predicting the point of application of the load has yet been discovered.

6.0. INSTALLATION FEATURES.

For a given aircraft/engine configuration, there are three major problem areas arising from the installation of a thrust reverser :-

- i) Aircraft stability.
- ii) Overheating of the adjacent structure.
- (iii) Ingestion of exhaust gases into an engine inlet.

The latter problem will be dealt with in more detail.

## 7.0. HOT GAS REINGESTION AND METHODS OF REDUCTION.

Reingested gases cause pressure and temperature distortions at the compressor face of the engine. Besides the thrust loss associated with an increase in average inlet temperature, the variation of pressure and temperature across the engine inlet may in general be above the tolerance limit. As a result, compressor surge is encountered with violent effects on the engine.

Due to the jet spread characteristics in a cross-flow with varying velocity, the amount of usable reverse thrust will be a function of the aircraft speed at which the reverser efflux may be reingested into the engine inlet. At this condition it becomes necessary either to cut off the reverser or throttle back the engine gradually with reduction in aircraft velocity. It is therefore essential for effective thrust reverser operation to design for a low reingestion speed.

The problem of hot gas reingestion discussed is associated with that part of the thrust reverser efflux which impinges on the ground, spreads along the ground, curls upward due to buoyancy and forward speed effects, and is eventually drawn into the engine air intakes.

Abbott and Cox, Ref.1, have carried out a systematic investigation into the effect of the important parameters on the flow characteristics of round jets impinging on the ground. Although these results are not strictly applicable to the efflux from a target-type thrust reverser, where the jets are no longer round, useful conclusions can be drawn. It is possible to estimate the variation in aircraft forward speed at which reingestion occurs. The governing flow parameters are found to be :-

Jet dynamic head or nozzle pressure ratio.

Jet inclination relative to the ground.

Mass flow or equivalent jet diameter.

The effect of these parameters on the aircraft speed at which reingestion occurs is shown in Fig.13.

For the influence of nozzle pressure ratio,  $P_J/P_{\infty}$ , the following relation holds :-

$$V \propto \sqrt{P_J/P_{\infty} - 1}$$

Starting from a reference nozzle pressure ratio  $(P_J/P_{\infty})_{REF}$  of 2.0, which is typical for a jet engine at take-off conditions, an aircraft speed - or otherwise reverser cut-off speed - of 30% less than at the reference pressure ratio is possible with the engine throttled back to 75% of the reference nozzle pressure ratio.

The influence of jet inclination relative to the ground is given by :

$$V \propto \frac{1}{\sqrt{\cos \alpha}} + 2 \sin \alpha$$

where the angle  $\alpha$  is measured from the vertical to the ground. This relation plots as a straight line in the diagram. Reducing the inclination from about  $\alpha = 50^\circ$  to  $\alpha = 35^\circ$  results in a 20% reduction in cut-off speed. From the point of view of reingestion it is therefore of advantage to direct the jet as vertically as possible to the ground.

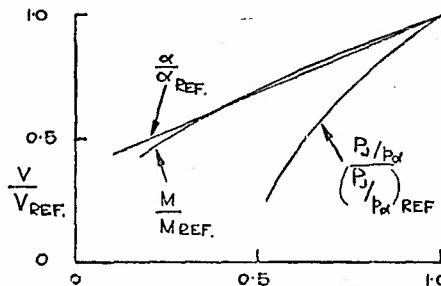


Fig.13. Variation of Speed at which Reingestion is predicted to occur.

## 7.0. (continued)

The mass flow,  $M$ , of the ground jet enters into the problem by a characteristic geometric dimension which, in this case, is the equivalent nozzle diameter  $d_j$  :-

$$V \propto d_j \propto \sqrt{M}$$

If it is possible with a given engine mass flow to reduce the mass flow from the lower reverser bucket by 30%, a gain of about 10% in cut-off speed is envisaged. In this case the ratio of mass flows from the upper and lower bucket is about 2:1 against the usual 1:1 split.

To reduce the speed at which reingestion occurs it is then demonstrated that the most important parameter is jet pressure ratio, whereas mass flow gives the smallest reduction.

Another parameter (not shown in Fig.13) is the sideways deflection of the lower jet out of the vertical plane. Tests indicate a considerable reduction in the reingestion speed if side deflections of the order of 30° to 40° can be achieved.

7.1. Nozzle Pressure Ratio.

The speed at which reingestion occurs, on a given installation, is shown in Fig.13, to be very sensitive to nozzle pressure ratio. As a reduction in pressure ratio will lead to a loss of thrust, the normal procedure on current aircraft is to reduce nozzle pressure ratio progressively as the speed falls during the ground roll. Two methods of reducing pressure ratio are (i) to reduce engine r.p.m. or (ii) in those cases where there is the facility and the engine can withstand the changed internal conditions, to open the final nozzle. The latter method gives a higher thrust at a given pressure ratio.

Because of the thrust loss associated with reducing jet pressure, it is usual for other methods of lowering the reingestion speed to be applied - particularly for STOL aircraft when the maximum retardation is required. On this type of aircraft, having made use of other methods, progressive throttling of the engine may not be possible since the engine run-down time may be such that the change in reingestion speed is similar to the change in aircraft speed.

7.2. Jet Inclination relative to the Ground.

It has already been demonstrated that the final direction of the flow leaving the bucket is determined by the end plate height. Reducing the end plate height on the lower bucket only in order to have a more vertical jet would exert a pitching movement on the aircraft because the vertical thrust component of the lower jet increases with the cosine of the inclination angle. To balance the vertical thrust components the deflection of the upper jet must be reduced by the same amount. This, however, will result in a considerable loss in reverse thrust - which amounts to about 25% if the jet efflux angle is decreased from 50° to 35°.

7.3. Mass Flow Split.

A very simple method to achieve unequal mass flows from the upper & lower bucket is shown in Fig.14. The mass flows from a jet impinging normal to a plane wall will split in the ratio 1:1. Rotating the wall by an angle  $\epsilon$  from the jet axis requires for the upper flow to turn through an angle  $(90 - \epsilon)$  and for the lower flow through the larger angle  $(90 + \epsilon)$ . Ideally, this would result in a mass flow split between the upper and lower part of :

$$\frac{M_U}{M_L} = \frac{1 + \sin \epsilon}{1 - \sin \epsilon}$$

Taking into account turning losses, this ratio would increase further.

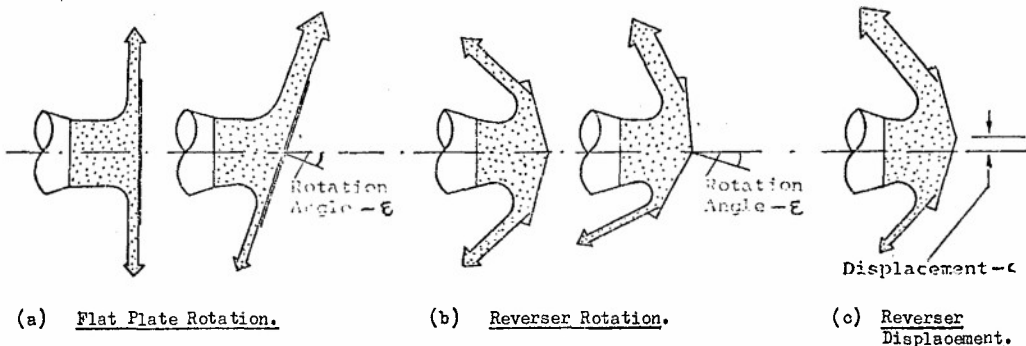


Fig.14. Diagrammatic Representation of the Effects of Reverser Bucket Rotation & Displacement.

## 7.3. (continued)

Using this principle on a thrust reverser to obtain unequal mass flows, it can be realised by the methods shown in Fig.14. Assuming that the apex angle ( $180 - 2\theta$ ) remains unchanged, the whole thrust reverser has either to be rotated by an angle  $\epsilon$  in the vertical plane, or must be offset from the nozzle axis upward by an amount  $c$ . Both methods of course imply a change in the actuating mechanism, leading to a complicated mechanical design - but this can be solved. It is obvious that with unequal mass flows from the upper & lower buckets the vertical loads are no longer balanced. The resulting pitching moment on the system, however, is of opposite direction to the one obtained from reducing the jet efflux angle from the lower bucket. To balance the vertical loads associated with a smaller mass flow from the lower bucket, this flow should have, in addition, a more vertical direction to the ground. It has been shown before that both measures tend to reduce the reingestion problem. Another important point is that the loss in reverse thrust can be kept small because of the increasing amount of thrust being produced by the upper jet with the higher mass flow.

Fig.15 shows test results from a model thrust reverser with rotation in the vertical plane. The apex angle was  $150^\circ$  and the ratio of upper to lower end plate height was 7:1. This ratio was chosen to deflect the upper jet well forward and to have only a small deflection for the lower jet. The test results show that, in fact, high mass flow ratios may be obtained with moderate rotation but coupled with unacceptable vertical loads. For the investigated configuration a rotation of  $3^\circ$  yields a mass flow ratio of 1.5:1 with the vertical loads balanced. The mean efflux angles from vertical are about  $50^\circ$  for the upper and  $30^\circ$  for the lower jet. Reverse thrust drops to 90% relative to the fully symmetric configuration with  $50^\circ$  flow angles for both the upper and lower stream. To achieve a similar improvement in reingestion by changing flow angles only, i.e.  $30^\circ$  for upper and lower jet, reverse thrust would be only 70% relative to the symmetric configuration, thus demonstrating the advantage of changing the mass flow split.

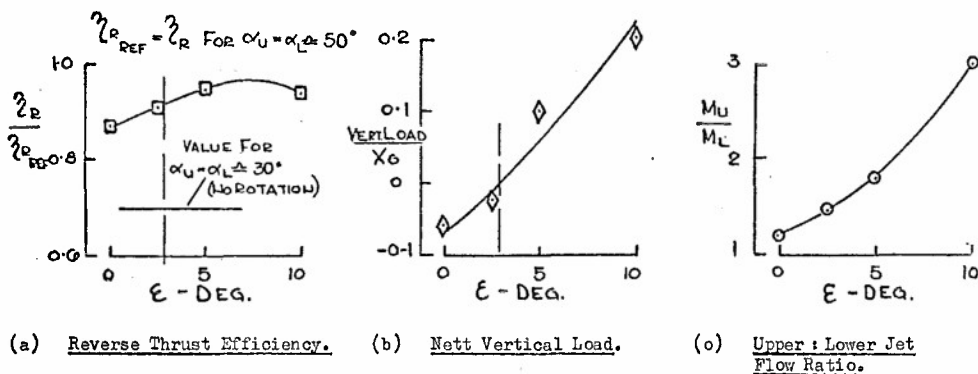


Fig.15. Reverser Performance with Bucket Rotation.

Corresponding tests with buckets offset from the nozzle centre-line have also been carried out. It was found that the same results as with a  $3^\circ$  rotation can be obtained by offsetting the buckets about 10% of nozzle diameter above the centre-line.

From Fig.13 it is estimated that with the combined mass flow and inclination effect, the reverser cut-off speed should reduce by about 25%. This order of gain was, in fact, substantiated by reingestion tests.

## 7.4. Side Deflection.

Improving reingestion by deflecting the lower jet sideways out of the vertical plane, requires considerable turning angles because the jet, in impinging on the ground, spreads to all sides.

A very simple and effective method for side deflection is to rotate the reverser around the nozzle axis, Fig.16. If there is insufficient clearance to rotate the entire reverser system on a given installation, an angled configuration may be possible with the upper bucket position unchanged. This, however, raises considerable actuation and stowage problems.

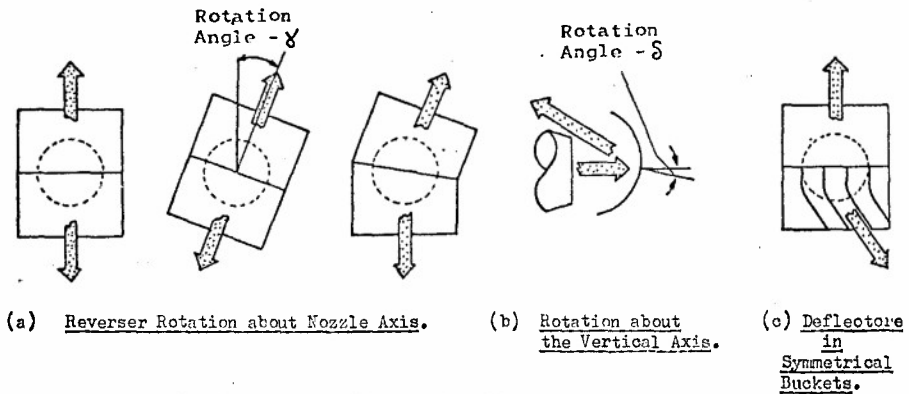


Fig.16. Methods of Jet Deflection.

7.4. (continued)

A rotation around the vertical axis of the reverser also causes side deflection. In model tests a side deflection of  $12^\circ$  was obtained with a  $7^\circ$  rotation. Although this method seems to be very effective, it will be generally limited to small angles of rotation from design considerations.

If none of the above-mentioned methods for side deflection is feasible with a given installation, the only way seems to lie in fitting suitable deflecting features in an otherwise symmetrically-operated reverser bucket. Either profiled or simple sheet metal turning vanes may be used and they must be of sufficient depth to avoid part of the flow spilling over the vanes.

Fig 17 is a flow visualisation picture of a model thrust reverser with flow deflectors incorporated in symmetrical buckets. A mean side deflection, viewed from the rear, of about  $35^\circ$  is achieved.



Fig.17. Flow Visualisation of Reverser with side deflection.

There is, of course, a penalty in reverse thrust associated with the side component of the thrust vector and the flow turning losses. A reverse thrust of the order of 45% of the bare nozzle thrust can be obtained.

## 7.4. (continued)

In combination with a derived mass flow split between the upper & lower bucket flow, the rotation  $\epsilon$  of  $3^\circ$ , which gave a balance of the vertical loads, must be reduced with increasing side deflection in order to maintain the load balance. However, even with no rotation ( $\epsilon = 0$ ), there still exists an unequal mass flow split because of the increased losses which the flow from the lower bucket has to overcome. With this principle of side deflection of the lower efflux only, the problem lies with the considerable side forces acting upon the system. This brings about design complexity to the operating mechanism, and adds weight. The application may be restricted to a multi-engined aircraft configuration where the side forces can be compensated by corresponding engines.

8.0. REFERENCE.

- (1) M. Cox & W.A. Abbott J. Sound Vib.  
Vol.3. Part 3. 1966. pp.393 - 406

INFLUENCE DE QUELQUES PARAMETRES CARACTERISTIQUES SUR

LES PERFORMANCES DES EJECTEURS

Jean Marie HARDY  
S.N.E.C.M.A.  
Centre de VILLAROCHE  
77 - MOISSY-CRAMAYEL

RESUME

Ayant posé le problème de l'adaptation d'un arrière-corps nous dénombrons les paramètres permettant son optimisation.

Après avoir rappelé le principe de la méthode de calcul théorique des performances de l'éjecteur, nous présenterons une étude de la répercussion des paramètres géométriques sur les performances interne et externe de la tuyère, basée sur un ensemble de résultats de calculs théoriques et expérimentaux.

Nous étudierons en particulier l'adaptation interne de l'éjecteur et nous discuterons du choix de la position de la ventilation secondaire compte-tenu de l'effet de gaz chaud. Des idées sur l'optimisation des performances globales par choix de la valeur et de la forme de la section d'éjection seront également présentées. Nous profiterons de ce qui est proposé pour donner plusieurs confrontations théorie-expérience.

LISTE DES NOTATIONS

Écoulement primaire : indice j

- $P_j$  Pression génératrice
- $T_j$  Température génératrice
- $W_j$  Débit de gaz
- $A_j^*$  Section critique isentropique de l'écoulement primaire

Écoulement secondaire : indice s

- $P_s$  Pression génératrice
- $T_s$  Température génératrice
- $W_s$  Débit d'air
- $A_s^*$  Section critique isentropique de l'écoulement secondaire
- $\mu_s = \frac{W_s \sqrt{T_s}}{W_j \sqrt{T_j}}$

Écoulement externe :

- $M_o$  Nombre de Mach
- $P_{io}$  Pression génératrice
- $P_a$  Pression statique

Effort de poussée ou traînée :

- L'indice i caractérise les valeurs internes
- L'indice \* caractérise les valeurs isentropiques
- $R_X$  Traînée externe du carénage

- $X_G$  Poussée brute
- $X_{GA}$  Poussée brute absolue

$$K_T = \frac{X_G}{P_j A_j^*} \quad \text{Coefficient de poussée brute}$$

$$K_T^* = \frac{X_G^*}{P_j A_j^*} \quad \text{Coefficient de poussée brute isentropique mono-dimensionnel, détente à } P_a$$

$$K_{TA}^* = \frac{X_{GA}^*}{P_j A_j^*} \quad \text{Coefficient de poussée brute absolue isentropique mono-dimensionnel}$$

$$K_{TA} = \frac{X_{GA}}{P_j A_j^*} \quad \text{Coefficient de poussée brute absolue}$$

$$C_T = \frac{K_T}{K_T^*}$$

$$\eta_F = \frac{X_G/P_j A_j^*}{\frac{X_G^*}{P_j A_j^*} + \frac{X_{Gs}^*}{P_s A_s^*} \mu_s} = \frac{K_T}{K_{Tj}^* + \mu_s K_{Ts}^*}$$

Pour  $T_s = T_j$  en air pur

$\eta_F$  Coefficient d'efficacité de l'éjecteur

## 1. INTRODUCTION

Le développement des avions de transport supersoniques à long rayon d'action est largement conditionné par leur rentabilité. Le faible rapport de la charge marchande au poids de l'appareil, la masse de carburant nécessaire au vol et aux réserves, l'augmentation du taux de motorisation (20 à 25 % pour les avions actuels, 35 à 40 % pour les avions de transport supersoniques) conduisent en particulier à une recherche exceptionnelle de qualité des éléments du groupe propulsif et à une étude de l'organisation optimale du fuseau moteur. La réalisation d'une entrée d'air d'efficacité élevée nécessite des prélèvements importants de débit qu'il convient de détendre au mieux. De ces conditions d'installation et d'optimisation du fuseau moteur est née la tuyère bi-flux où l'adaptation aux différents régimes de fonctionnement est obtenue par des moyens aérodynamiques. Cette solution offre deux avantages : la simplicité technologique et la possibilité d'évacuer dans de bonnes conditions le débit d'air provenant des pièges à couche limite de la prise d'air.

On se convaincra aisément de la nécessité d'une étude soignée de l'arrière-corps en sachant que 1 % de rendement tuyère, sur l'ensemble de la mission, correspond sensiblement à 10 % de la charge marchande. C'est pourquoi le choix d'une organisation de nacelle étant fait, il y a lieu de faire une étude paramétrique permettant de définir la géométrie de l'ensemble d'éjection afin d'obtenir la performance maximale.

## 2. DEFINITION DU PROBLEME

### 2.1. Cadre de l'étude

Le problème à résoudre consiste à réaliser la confluence de trois écoulements avec un minimum de pertes, compte tenu d'un certain nombre de contraintes géométriques (pl.1). Les caractéristiques des écoulements externes et du flux primaire sont imposées par le choix des conditions de vol, du point de fonctionnement du moteur et des caractéristiques de la manche. Les caractéristiques du flux secondaire sont également imposées par les conditions de fonctionnement de la prise d'air, les pertes de charge dans la nacelle et les échanges thermiques au contact du moteur. Les contraintes géométriques sont liées au maître couple Am de la nacelle et à la longueur de l'arrière-corps qui est imposée par ailleurs. Le choix d'une solution à double flux étant fait, il subsiste un certain nombre de paramètres sur lesquels on peut agir en vue d'obtenir la performance maximale.

Dans le cas qui nous préoccupe, ces paramètres sont :

- Distance  $\Delta X$  entre la section de reprise et la section d'éjection primaire
- La section de reprise  $A_R$
- La section de sortie  $A_R$
- L'angle de la génératrice du divergent
- La forme de la génératrice externe de l'arrière-corps
- La forme de la section d'éjection
- Le taux interne de détente du jet primaire (forme de la tuyère primaire).

Rappelons que le point de fonctionnement d'un éjecteur résulte de l'équilibre des pressions secondaires au plan de raccordement nacelle-tuyère. En effet, il existe deux relations : une dite courbe d'alimentation qui relie le niveau de pression secondaire au débit secondaire, compte tenu du rendement des pièges à couche limite de la manche, des pertes de charge dans la nacelle et des échanges de chaleur, l'autre dite caractéristique tuyère qui lie la pression secondaire au débit secondaire éjecté, compte tenu de la géométrie de l'éjecteur et des conditions d'éjection du flux primaire. C'est la satisfaction de ces deux relations pour une même valeur du débit secondaire qui détermine le point de fonctionnement de l'éjecteur.

Dans la suite de l'exposé, nous allons analyser l'influence de chacun des paramètres dénombrés ci-dessus sur les performances de l'arrière-corps. Ensuite, nous étudierons spécialement l'influence du taux de détente interne du jet primaire, c'est-à-dire l'introduction d'une tuyère primaire convergente-divergente à la place d'une tuyère primaire simplement convergente.

### 2.2. Base de l'étude

#### 2.2.1. Base expérimentale

Les essais sur les diverses configurations ont été effectués dans les installations de l'O.N.E.R.A. :

- à MODANE : en ce qui concerne les essais sans écoulement externe visant à déterminer les performances internes
- à la Soufflerie S5 à CHALAIS MEUDON : en ce qui concerne les essais avec écoulement externe visant à déterminer soit les performances externes, soit les performances globales.

#### 2.2.2. Bases théoriques

- Calcul des traînées externes :  
Méthode des caractéristiques pour l'écoulement non visqueux, puis calcul de couche limite intervenant sous forme de correction.
- Calcul des performances internes :  
Méthode de calcul présentée Réf. 1 - 2 - 3 - 4, basée sur les hypothèses suivantes :
  - . l'écoulement primaire est calculable par la méthode des caractéristiques correctement formulée pour tenir compte des variations des chaleurs spécifiques au cours de la détente
  - . l'écoulement secondaire est isentropique et mono-dimensionnel
  - . la compatibilité des écoulements est imposée par l'égalité des pressions statiques de part et d'autre de la surface de glissement.
  - . l'unicité de la solution est assurée par la condition critique de l'écoulement secondaire.

Au calcul en fluide parfait est associée une correction pour tenir compte des phénomènes visqueux à l'interface des jets et sur la paroi du divergent ainsi que des transferts de chaleur.

## 3. RESULTATS DE L'ETUDE

### 3.1. Performances externes

#### 3.1.1. Etude de la forme de la méridienne du rétreint

Nous avons étudié l'influence de la génération externe sur la traînée d'un arrière-corps défini par sa section au maître couple, sa section de sortie et sa longueur.

Nous avons constaté que dans le cas de vol considéré, croisière supersonique, les arrières-corps à méridienne rectiligne présentaient le minimum de traînée. Ces résultats sont illustrés planche 2.

- La figure 1 reproduit les répartitions de pression le long de l'arrière-corps associées à la forme de la méridienne
- La figure 2 montre l'évolution de la traînée en fonction de la courbure de l'arrière-corps à méridienne parabolique. Sur cette même figure sont portés les points correspondant à un arrière-corps conique et à un arrière-corps dont la génératrice présente un point d'inflexion.

Notons que ces résultats sont en plein accord avec ceux publiés dans la référence n° 9.

### 3.2. Performances internes

#### 3.2.1. Ejecteur à détente libre du jet primaire (tuyère ventilée au col)

##### 3.2.1.1. Etude de l'adaptation interne

Les deux variables géométriques apparemment indépendantes  $\Delta X$  et  $A_R$  sont en réalité liées par la nécessité d'évacuer un certain débit secondaire caractérisé par une température  $T_s$  et une pression génératrice  $P_s$ . Pour un angle de divergent fixé, il existe une série de couples de valeurs ( $A_R$ ,  $\Delta X$ ) répondant à la condition ( $P_s/P_j$ ;  $\mu_s$ ).

Sur la planche 3 nous avons représenté l'évolution des pressions pariétales dans le divergent secondaire pour 3 couples de valeurs ( $A_R$ ,  $\Delta X$ ) assurant l'évacuation d'un  $\mu_s = 6\%$  à  $P_s/P_j = 0,20$ .

On remarque en particulier que l'accroissement de  $\Delta X$  semble régulariser la détente et laisse inchangée la pression dans le plan d'éjection du divergent. Cette dernière constatation montre que l'organisation de la confluence des écoulements internes peut être étudiée indépendamment de la section d'éjection  $A_e$ .

La planche 4 présente une confrontation théorie-expérience relative à l'influence de  $\Delta X$ . La courbe du haut illustre une loi  $A_R = f(\Delta X)$  à  $\mu_s$  et  $P_s/P_j$  donnés. La figure n° 2 montre que, si les niveaux de pressions théorique et expérimentale diffèrent légèrement, leur accord en détente est parfait. La figure 3 met en évidence que, dans les conditions considérées, les valeurs de  $P/P_j$  et  $\mu$  fixent la valeur de  $\eta_F$  quels que soient  $A_R$  et  $\Delta X$ , cette démonstration étant faite aussi bien expérimentalement que théoriquement. Toutefois, on pourrait déceler au vu de l'étude théorique une légère tendance à la croissance de  $\eta_F$  avec  $\Delta X$ , ce qui pourrait être associé à la régularisation de la détente observée sur la planche précédente.

La planche 5 présente une généralisation de la planche précédente; elle donne l'influence de  $\Delta X$  pour différentes valeurs de  $A_R$ . On remarquera que :

- jusqu'à une certaine valeur maximale de  $P_s/P_j$  voisine de 0,215, les performances sont indépendantes du choix du couple ( $A_R$ ,  $\Delta X$ )
- le lieu des optima de performances pour chaque  $A_R$  correspond à un  $\Delta X$  décroissant quand  $P/P_j$  décroît. Toutefois, pour les  $A_R$  importants ( $P_s/P_j \approx 0,215$ ), la valeur de l'optimum est indépendante de  $\Delta X$  dans le domaine exploré.
- pour toutes les pressions secondaires inférieures à la pression secondaire optimale, on retrouve le résultat de la planche précédente, à savoir que les couples de valeurs ( $A_R$ ,  $\Delta X$ ) assurant un même  $P_s/P_j$  à  $\mu_s$  donné conduisent à des performances constantes de l'éjecteur.

Sur la planche 6 nous avons présenté l'évolution de  $\eta_F$  en fonction de  $P_s/P_j$  pour une valeur donnée de  $\mu_s$  ( $\mu_s = 5,75\%$ ); on remarque :

- pour des  $P_s/P_j$  inférieurs à 0,215 la courbe "a", lieu des optima, les courbes  $\eta_F = f(P/P_j)$  à  $A_R$  donné et  $\Delta X$  variable, ainsi que la courbe  $\eta_F = f(P_s/P_j)$  à  $\Delta X$  donné et  $A_R$  variable, sont sensiblement confondues.
- pour des  $P/P_j$  supérieurs à 0,215, ces mêmes courbes sont nettement différenciées, mettant en évidence l'existence d'un couple de valeurs ( $A_R$  et  $\Delta X$ ) assurant la performance maximale.

Cette planche précise les constatations faites sur la planche précédente.

##### 3.2.1.2. Influence de l'angle de la génératrice du divergent

Pour des sections  $A_R$  et  $A_e$  données, l'angle d'un divergent conique a une répercussion sur les performances et sur le diagramme de trompe d'un éjecteur. Nous avons cherché à exprimer les résultats sous forme de  $\eta_F$ , efficacité du divergent, à  $P/P_j$  donné, étant donné que cette efficacité reste pratiquement inchangée par de petites variations de  $\mu_s$  autour de la valeur optimale.

Sur la planche 7 nous avons illustré, pour une géométrie donnée de la zone de confluence et une section d'éjection fixée, l'influence de l'angle de la génératrice. On remarque, figure de gauche, l'existence d'un angle optimum. D'autre part, la figure de droite met en évidence l'influence de l'angle du divergent sur le diagramme de trompe. Ceci s'explique facilement par le fait que, le débit secondaire étant déterminé par l'existence d'un col sonique dans le divergent, un changement de l'évolution de la section en fonction de la longueur du divergent entraîne une modification en position et en valeur du col secondaire. Des essais effectués dans la zone de l'angle optimum ont confirmé les résultats théoriques.

Sur la planche 8 nous avons fait figurer l'évolution des pressions pariétales en fonction de leurs abscisses pour plusieurs valeurs de la génératrice.

On peut remarquer que :

- l'augmentation de l'angle entraîne une variation de plus en plus irrégulière de la détente à l'entrée du divergent secondaire et peut même conduire à des recompressions
- à  $P_s/P_j$  donné et  $A_e$  donné, la pression d'éjection diminue légèrement avec l'angle du divergent
- compte tenu de la variation de  $\mu_s$  associée à la variation d'angle, on peut admettre qu'à  $\mu_s$  donné, la pression d'éjection varie peu.

De ceci on peut conclure que l'influence de l'angle sur  $\eta_F$  est principalement due, à  $A_e$ ,  $P_s/P_j$ ,  $\mu_s$  donnés, à sa répercussion sur la régularité de la détente dans le divergent et sur le frottement pariétal.

### 3.2.1.3. Influence de forme de la génératrice du divergent

Nous avons entrepris une série d'études expérimentales et théoriques en vue d'optimiser la forme de la méridienne du divergent. Ces études ont principalement porté sur la forme de la génératrice en aval de la section de reprise (conique ou parabolique) et sur la zone de raccordement du divergent à la partie amont.

La planche 9 illustre quelques résultats obtenus au cours de cette étude. Sur la figure de droite, nous avons étudié l'influence de la longueur de la partie aval du divergent pour une partie amont fixée, le divergent étant alors formé de deux troncs de cône. Nous avons également fait figurer les performances de divergent à génératrice parabolique de même  $A_p$ ,  $A_e$  et longueur. On peut alors remarquer que l'écart entre un divergent bi-conique et parabolique est faible et que, compte tenu des frottements interne et externe, il apparaît dans les deux cas un optimum de longueur à  $A_e$  donné. Sur la figure de gauche, nous avons étudié l'effet de l'adjonction d'un arrondi au col de reprise du divergent, cela aussi bien pour des divergents coniques que paraboliques.

De ces résultats, on peut retenir que l'introduction d'un arrondi au col de reprise serait plutôt néfaste alors que l'introduction d'une forme parabolique ne serait que légèrement favorable, les faits théoriques et expérimentaux le confirmant. Mais il est vraisemblable que cette conclusion, en particulier en ce qui concerne le divergent à méridienne parabolique, serait remise en cause pour d'autres valeurs de  $P_s/P_j$  et  $\mu_s$ .

L'organisation de cette zone est un cas d'espèce. En effet, la forme de la méridienne en aval de la section de reprise est largement conditionnée par la pression et la direction des écoulements dans cette région qui sont tributaires des formes amont. En tout état de cause, on doit veiller à obtenir une détente aussi régulière que possible.

### 3.2.1.4. Remarque sur l'effet de l'excentration du convergent par rapport au divergent

Au cours de nos études, nous avons été amenés à étudier la répercussion du centrage du canal primaire par rapport au divergent secondaire. La planche 10 présente une série de résultats.

Figure 1 : Influence sur les pressions pariétales à  $\mu_s$  donné

Figure 2 : Influence sur les poussées internes

Figure 3 : Influence sur les pressions secondaires

On peut remarquer que, du point de vue performances globales et dans la gamme des  $\mu_s$  usuels, des excentrations raisonnables sont tolérables. Par contre, pour des éjecteurs adaptés à de faibles valeurs de  $\mu_s$ , le centrage de la tuyère primaire par rapport à la tuyère secondaire doit être assuré avec une bonne précision. On voit donc que, de ce point de vue, le choix d'une solution à débit secondaire élevé est bénéfique. On peut encore remarquer que la distorsion importante des pressions pariétales associée à l'excentration subsiste jusque dans le plan d'éjection.

### 3.2.2. Ejecteur à détente du jet primaire contrôlé Introduction d'une tuyère primaire convergente-divergente

Dans les cas précédemment étudiés, les pressions statiques des écoulements dans le plan de leur confluence étaient très différentes. On peut se proposer de détendre l'écoulement primaire jusqu'à une pression statique voisine de celle de l'écoulement secondaire afin d'améliorer les conditions de confluence. Ceci entraîne l'utilisation d'une tuyère primaire convergente-divergente. Le schéma d'une telle solution est présenté planche 11. L'introduction d'un divergent primaire qui peut être mobile permet, à  $\mu_s$  donné, de régler la détente de l'écoulement primaire en fonction de la pression secondaire. Nous verrons par la suite que cette solution apparemment séduisante entraîne des pertes de performances.

Pour l'optimisation du divergent interne et son adaptation, nous disposons de trois paramètres indépendants :

- $\Delta X$  : distance entre le plan d'éjection du divergent primaire et la section de reprise
- $\theta_p$  : angle des volets du divergent primaire
- $L_p$  : longueur des volets du divergent primaire

#### 3.2.2.1. Influence de $\Delta X$

Dans ce qui suit, nous nous intéresserons uniquement au cas où la section d'éjection du divergent primaire est placée dans le même plan que la section de reprise du divergent, soit  $\Delta X = 0$ . En effet, cette solution semble donner les meilleures performances et en plus, elle correspond au souci d'éviter toute détente non contrôlée des écoulements internes.

#### 3.2.2.2. Influence de la longueur des volets du divergent primaire

Sur la planche 12 figure, pour une géométrie figée de l'ensemble secondaire, la répercussion, à  $\theta_p$  constant, de la longueur des volets primaires sur les performances internes de l'éjecteur.

Figure supérieure : influence sur le diagramme de trompe

Figure inférieure : influence sur la poussée

Sur cette planche, on note que :

- à chaque valeur  $\theta_p$ , angle du divergent, correspond une longueur optimale  $L_p$  des volets
- pour un rapport de pression donné  $P_s/P_j$ , il existe un couple de valeurs  $\theta_p$  et  $L_p$  donnant la performance maximale (courbe a)
- à longueur donnée, toute variation d'angle, en vue de régler la pression secondaire, entraîne une variation de performance de même sens.

#### 3.2.2.3. Etude de l'adaptation interne

La longueur des volets du divergent primaire étant fixée, ainsi que la longueur et la section de sortie du divergent secondaire, on peut se proposer de déterminer le couple de valeurs  $A_p$  et  $\theta_p$  qui assurera, à  $P_s/P_j$  donné, la performance maximale. La planche 13 illustre une telle recherche d'optimisation. Sur

cette planche figure également une confrontation théorie-expérience qui, une fois de plus, montre le bon accord des deux méthodes d'analyse.

- La figure supérieure est relative au diagramme de trompe
- La figure inférieure présente les performances internes.

Sur cette planche on peut faire les mêmes remarques que sur la planche précédente, en ce qui concerne l'effet du contrôle de  $P_s/P_j$  par l'angle du divergent primaire, sur les performances.

D'autre part, à  $P_s/P_j$  donné et  $\mu_s$  donné, il existe un couple de valeurs  $A_R$  et  $\Theta_p$  assurant la performance maximale.

#### 3.2.2.4. Discussion du choix de cette solution

On voit donc que l'introduction d'un divergent primaire permet d'adapter la pression d'éjection de l'écoulement primaire à la pression de l'écoulement secondaire dans le même plan, ce qui implique que le choix de cette solution sera conditionné par le niveau de la pression secondaire. Sur la planche 14, nous avons tracé l'évolution de  $\eta_F$  en fonction de  $P/P_j$  pour diverses valeurs de l'angle  $\Theta_p$  des volets du divergent primaire et trois valeurs de la section de reprise.

On remarque que :

- à chaque valeur de la section  $A_R$  correspond un  $\Theta_p$  donnant la valeur maximale de  $\eta_F$
- à la géométrie définie ci-dessus correspond une certaine valeur de la pression secondaire
- la courbe "a" définissant le lieu des maxima correspond, pour un  $\mu_s$  donné, à l'efficacité maximale du dispositif
- si l'on veut rester sur la courbe d'efficacité maximale, à toute réduction de la pression secondaire correspond un changement de géométrie, soit un accroissement de  $A_R$  et  $\Theta_p$

Sur cette même planche, nous avons fait figurer la courbe  $\eta_F = f(P_s/P_j)$  obtenue pour une tuyère primaire simplement convergente (courbe b).

La comparaison des courbes "a" et "b" met en évidence l'intérêt de la solution tuyère primaire convergente-divergente au lieu de celle à tuyère simplement convergente. On peut remarquer, en particulier, que le gain de  $\eta_F$  obtenu pour les pressions secondaires supérieures à 0,20 est illusoire, compte tenu du poids et de la complexité du dispositif. Par contre, pour les pressions secondaires faibles, cette solution peut présenter un intérêt. Le niveau de pression secondaire conditionne le choix du dispositif dans la mesure où le bilan aérodynamique-technologie est positif.

#### 3.2.3. Remarque sur l'effet de gaz chaud

Les résultats des essais comme ceux des calculs théoriques que nous venons d'analyser ont été obtenus en gaz froid. A ces résultats, il y a lieu d'appliquer une correction de gaz chauds "effet de  $\chi$ ". En effet, quand le  $\chi$  du jet primaire décroît, le volume de celui-ci croît, entraînant une réduction du débit secondaire ou une augmentation de la pression secondaire si l'on désire maintenir le  $\mu_s$ . Cette correction s'applique donc à la fois sur les pressions secondaires et sur les poussées à  $\mu_s$  donné. Sa valeur dépend de l'organisation de l'éjecteur. Actuellement la correction de " $\chi$ " est déterminée par le calcul théorique à l'aide de la méthode de calcul utilisée en gaz froids, mais cette fois, en effectuant le calcul pour les valeurs de la température primaire et de la richesse correspondant au vol. Nous pensons développer prochainement une installation d'essais permettant de vérifier le calcul théorique. Notons que ces installations nécessitent des précisions très élevées et qu'elles se heurtent à de grosses difficultés de réalisation.

Sur la planche 15, nous avons présenté l'effet de gaz chauds pour trois valeurs de la détente du flux primaire avant confluence.

- a) Dans le cas d'une tuyère primaire convergente
- b) Dans le cas d'une tuyère primaire convergente-divergente d'angle  $\Theta_p = 9^\circ$  (pression d'éjection supérieure à la pression statique secondaire)
- c) Dans le cas d'une tuyère primaire convergente-divergente d'angle  $\Theta_p = 11^\circ$ , c'est-à-dire où la pression dans le plan d'éjection est plus faible que pour "b" et adaptée à la pression secondaire.

On remarque que :

- les corrections de pression secondaire et de poussée sont de même signe
- la correction est d'autant plus faible que la détente primaire est plus poussée
- à  $P/P_j$  donné, l'effet de  $\chi$  réduit le débit secondaire pour une tuyère primaire convergente alors qu'il laisse inchangé celui de la tuyère primaire convergente-divergente  $11^\circ$ .

De ces remarques, il résulte que la comparaison des solutions tuyère primaire convergente et tuyère primaire convergente-divergente doit s'effectuer après correction des essais soufflerie au même  $\mu_s$  et à même  $P_s/P_j$ . Si cette opération réduit effectivement les gains apportés par une tuyère primaire convergente-divergente, il n'en reste pas moins, qu'à faible pression secondaire, cette solution garde son intérêt.

### 3.3. Performances globales

#### 3.3.1. Détermination de la section $A_e$ optimale

L'optimisation de la section  $A_e$  résulte d'un compromis entre les performances interne et externe. Nous nous intéresserons ici aux arrière-corps de révolution sans culot. La traînée externe croît lorsque l'angle de rétreint croît. La performance interne passe par un maximum pour une certaine valeur de la section  $A_e$  voisine de celle assurant la détente complète des deux flux jusqu'à la pression ambiante. Dans le cas de vol que nous considérons, cette section est inférieure à la section maximale de l'arrière-corps. De ce fait, l'optimum est trouvé pour une section  $A_e$  supérieure à celle assurant le maximum de performance interne. Ce résultat est en accord avec ceux publiés dans la référence n° 9.

Sur la planche 16, nous avons tracé en fonction de  $A_e$  la contribution à la performance globale de la traînée externe de la poussée interne pour un arrière-corps de révolution de  $A_m$  et de longueur donnée.

Sur cette planche, la courbe "a" donne l'évolution de la traînée externe liée à l'angle du rétreint en fonction de  $A_e/A_m$ . La courbe "b" donne l'évolution de la performance interne calculée, compte tenu de la variation de l'angle du divergent. La courbe "c" correspond à la performance globale. On note que, si la

section  $A_e$  optimale est inférieure à la section  $A_m$ , elle est nettement supérieure à la section assurant le maximum de performance interne.

Remarque : Ce qui précède serait remis en cause pour l'optimisation d'arrière-corps destinés à des avions volant à des Mach supérieurs où la section  $A_e$  de détente complète serait supérieure à  $A_m$ .

### 3.3.2. Influence de la forme de la section d'éjection

Dans tout ce qui précède, nous nous sommes intéressés au divergent de révolution. Pour des fuseaux moteur non de révolution, ou pour un avionnage en bi-moteur, on peut être conduit à rechercher une forme de la section d'éjection non circulaire pour améliorer les performances globales. Dans le cas où la section optimale en divergent de révolution conduit, du fait des contraintes amont, à un arrière-corps présentant à la fois des rétreints et des anti-rétreints, on peut déformer la section de sortie afin de minimiser les rétreints et de supprimer les anti-rétreints. Cette opération améliore bien sûr les performances externes, mais entraîne une perte de performance interne due aux distorsions imposées à l'écoulement. La figure 17 illustre une telle recherche d'optimisation. Les valeurs portées au bas de la planche mettent en évidence, là encore, le bon recouplement théorie-expérience et montrent que, dans le cas considéré, un gain non négligeable de performances a été obtenu.

## 4. CONCLUSION

De tout ce qui précède, il résulte que le nombre de paramètres permettant l'optimisation d'un arrière-corps est important, que la recherche de la valeur optimale de chacun peut quelquefois conduire à des contradictions géométriques. L'étude paramétrique peut montrer que la répercussion sur les performances de petites variations de chacun des paramètres est faible, mais il ne faut pas pour autant la négliger, car c'est par la somme de ces améliorations que l'on aboutira à la définition d'un arrière-corps de qualité.

D'autre part, il faut remarquer que ces améliorations étant dans la limite de la précision des souffleries, l'étude expérimentale doit être menée sur une base statistique et appuyée sur une méthode de calcul théorique appropriée, afin de contrôler, d'analyser les essais, et de les transposer un cas de vol.

Les confrontations théorie-expérience données ici, ainsi que celles que nous avons présentées réf. 1 - 2 - 3 - 4, montrent que maintenant il est possible de définir complètement l'avant-projet d'un arrière-corps par calcul théorique.

Si l'optimisation d'un arrière-corps n'est pas une chose aisée pour le cas de vol de croisière supersonique, cette difficulté est encore accrue quand on doit tenir compte dans sa conception de suggestion destinée à permettre son bon fonctionnement dans les autres cas de vol.

## LISTE DES REFERENCES

- 1 - Possibilités actuelles d'étude théorique d'une tuyère supersonique à double flux  
Réunion AGARD sur l'aérodynamique des groupes propulseurs AEDC - Tullahoma 25-28 octobre 1965  
par J.M.HARDY et J.DELERY
- 2 - Les tuyères supersoniques à double flux - méthode de calcul  
Conférence SFIM-6-12-1967 publiée dans la revue française de Mécanique n° 24 (1967)  
par J.M.HARDY et H.LACOMBE
- 3 - Problèmes d'adaptation de tuyère - 32<sup>e</sup> réunion AGARD du Groupe Propulsion et Energie -  
Toulouse - 9-13 septembre 1968  
par P.CARRIERE - M.SIRIEIX et J.M.HARDY
- 4 - Etude théorique d'une tuyère convergente-divergente bi-flux - 3<sup>e</sup> symposium franco-soviétique -  
novembre 1969 - Paris - par J.M.HARDY
- 5 - Calcul du mélange turbulent de deux écoulements hétérogènes dans un éjecteur - N.T. ONERA avril 1962  
par P.CARRIERE
- 6 - Contribution à l'étude des éjecteurs supersoniques - Association Technique Maritime et Aéronautique 1963  
par M.SIRIEIX
- 7 - Interaction between primary and secondary streams of supersonic ejector systems and their performance characteristics - A.I.A.A. Journal Vol. 2 - avril 1964  
par W.L.CHOW - A.ADDY
- 8 - A theory for base pressure in transonic and supersonic flow - University of Illinois MG TN 3922 - 1955  
par H.H.KORST
- 9 - Contours extérieurs et intérieurs d'une tuyère assurant la poussée efficace maximale d'un propulseur  
3<sup>e</sup> Symposium franco-soviétique - Paris - novembre 1969  
par LI.SORKINE et IA.IVANOV
- 10 - Same experiments on two - stream propelling nozzles for supersonic aircraft - The seventh congress  
for the International Council of the Aeronautical Sciences - Rome - sept. 14-18/1970  
par W.G.E.LEWIS - F.W.ARMSTRONG
- 11 - Adaptation de l'arrière-corps des réacteurs d'un avion supersonique  
O.N.E.R.A. Colloque Aérodynamique appliquée AFITAE - 12-13 novembre 1964  
par J.M.BRASSEUR

SCHÉMATISATION DU PROBLÈME POSÉ PI. 1

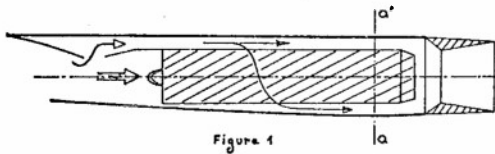


Figure 1

INFLUENCE DE ΔX SUR LES PRESSIONS PI. 3  
À LA PAROI DU DIVERGENT

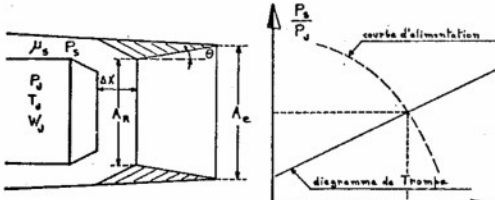
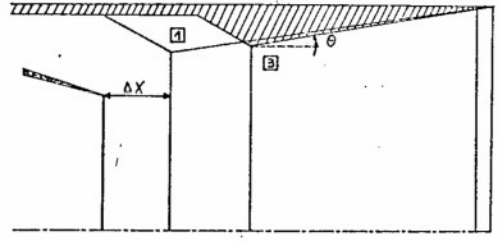


Figure 2

Figure 3

Paramètres imposés

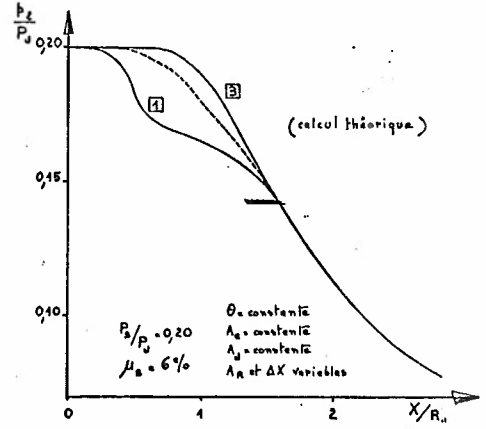
Section aa' =  $A_m$   
 $\left. \begin{matrix} W_0 \\ T_0 \\ P_0 \end{matrix} \right\} A_0 \text{ et } P_0/p_a$

Paramètres d'adaptation

$P_2/P_1$  et  $\mu_s$

Paramètres libres

$\Delta X$  : distance entre le col de reprise et le col principal.  
 $A_R$  : section de reprise.  
 $A_0$  : section d'éjection.  
 $\theta$  : angle du divergent.  
 géométrie externe  
 géométrie interne.



ETUDE DE LA FORME DE LA GÉNÉRATRICE D'UN RETREINT PI. 2

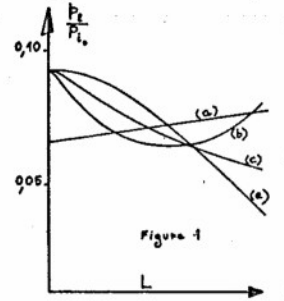
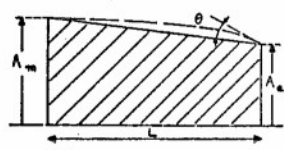


Figure 1

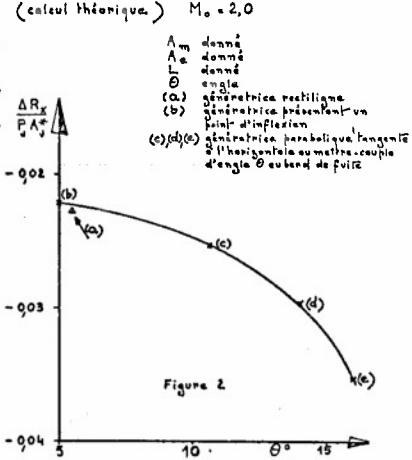
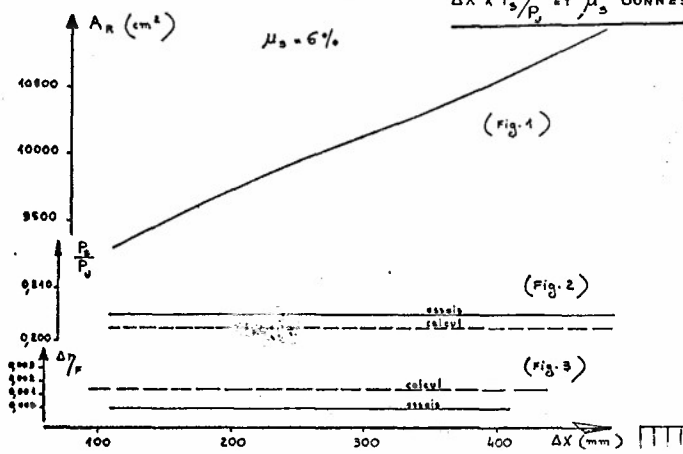


Figure 2

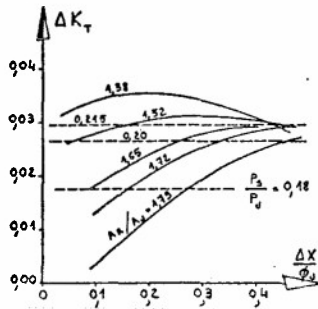
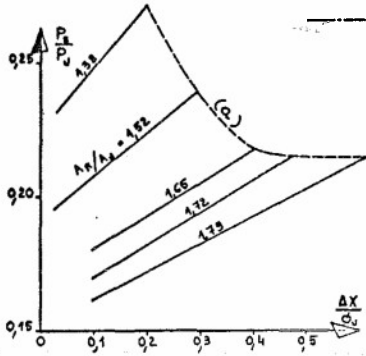
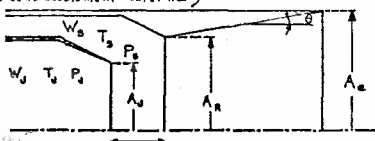
COMPARAISON THÉORIE - EXPÉRIENCE SUR L'INFLUENCE DE  $\Delta X$  A  $P_3/P_0$  ET  $\mu_3$  DONNÉS



ETUDE DE L'ADAPTATION INTERNE

PI-5

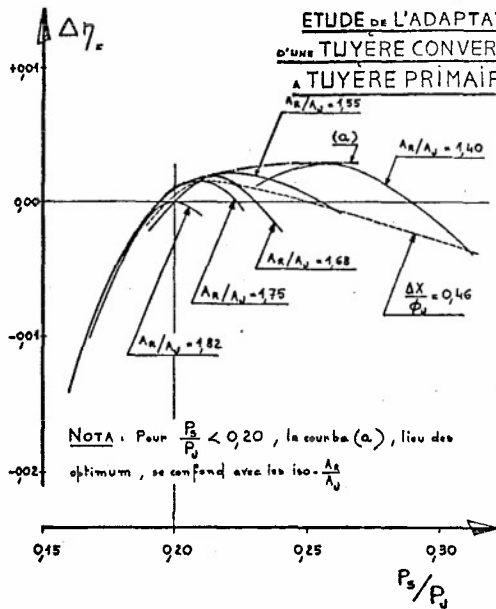
$\mu_3 = \frac{W_3 \sqrt{T_3}}{W_0 \sqrt{T_0}} = 6\%$   
 $K_T = \frac{X}{P_0 A_0^2}$   
 $A_0$  et  $\theta$  donnés



ETUDE DE L'ADAPTATION INTERNE D'UNE TUYÈRE CONVERGENTE-DIVERGENTE

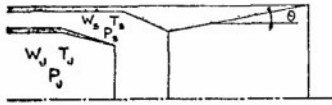
PI-6

À TUYÈRE PRIMAIRE CONVERGENTE



**INFLUENCE DE L'ANGLE DU DIVERGENT SUR LES PERFORMANCES INTERNES** <sup>Pl. 7</sup>

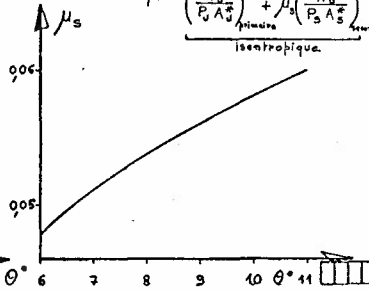
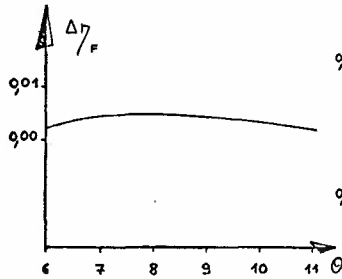
(calcul théorique.)



$P_2/P_0 = 0,21$   
 $A_2, A_0, \Delta X$  donnés

$\mu_s = \frac{W_2 \sqrt{T_2}}{W_0 \sqrt{T_0}}$

$\eta_F = \frac{\left(\frac{X_{gr}}{P_0 A_0^*}\right)_{\text{réel}}}{\left(\frac{X_{gr}}{P_0 A_0^*}\right)_{\text{idéale}} + \mu_s \left(\frac{X_{gr}}{P_2 A_2^*}\right)_{\text{idéale}}}$   
 isentropique.



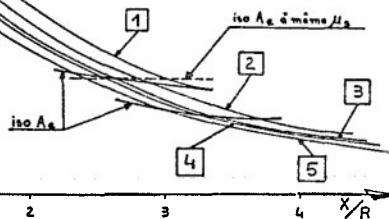
**INFLUENCE DE L'ANGLE DE DIVERGENT SUR LES PRESSIONS A LA PAROI**

(calcul théorique.)

Pl. 8



Divergent conique			
	$P_2/P_0$	$\theta$ divergent	$\mu_s$ %
1	0,22	6°	5,8
2	0,22	7° 50'	6,3
3	0,22	8° 50'	6,6
4	0,22	9°	6,7
5	0,22	10° 26'	7

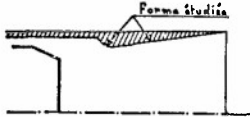


**INFLUENCE DE LA FORME DE LA GÉNÉRATRICE DU DIVERGENT**

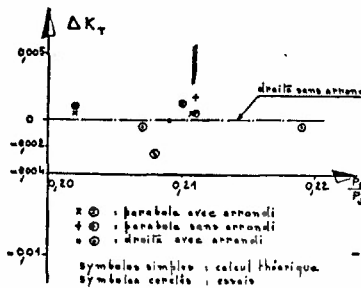
$M_0 = 2,00$

$A_0, A_2, \Delta X = \text{constantes}$

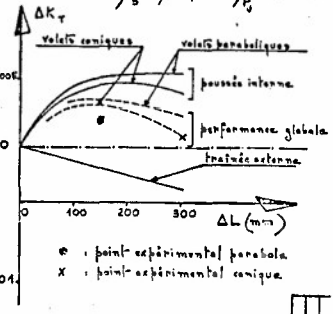
Pl. 9



$\mu_s = 6,25\%$   $P_2/P_0 = \text{constante}$



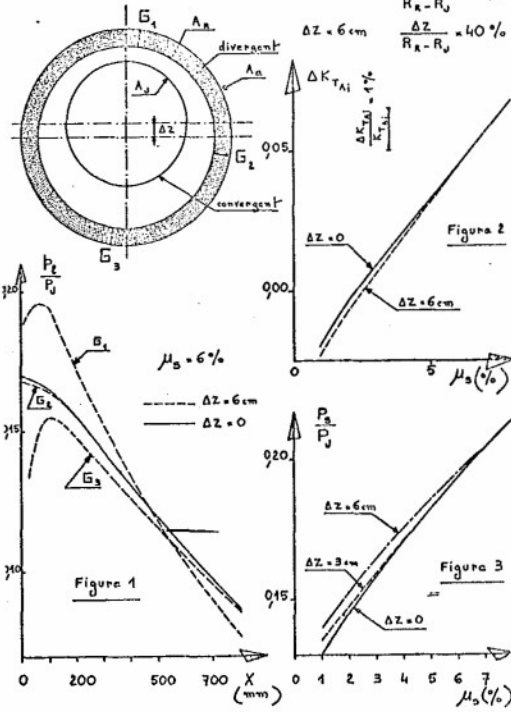
x ⊗ : parabola avec arrondi  
 + ⊗ : parabola sans arrondi  
 ⊙ : droit avec arrondi  
 Symboles simples : calcul théorique.  
 Symboles cercles : essais



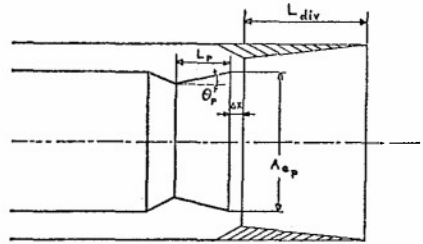
⊙ : point expérimental parabola  
 x : point expérimental conique

**INFLUENCE DE L'EXCENTRATION**

(Essais dans écoulement externe)



**TUYÈRE A VENTILATION EN COURS DE DÉTENTE**



**Paramètres libres de la tuyère à ventilation au col**

- $\Delta X$  : distance plan d'injection primaire - col de reprise
- $A_R$  : section de reprise
- $A_p$  : section d'injection
- $\theta$  : divergent secondaire, génératrice divergent, génératrice externe

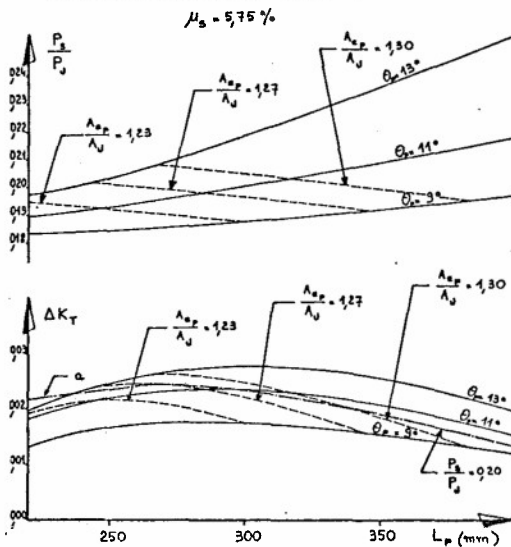
**Paramètres supplémentaires**

- $\theta_p$  : divergent primaire
- $A_{ep}$  : section d'injection primaire
- $L_p$  : longueur des volets primaires

**Avantage**

Possibilité d'une pré-détente du jet primaire pour adapter la confluence des deux jets

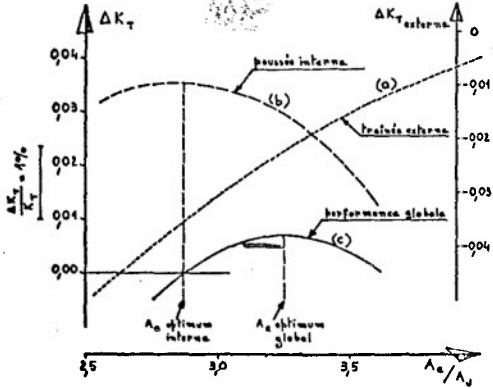
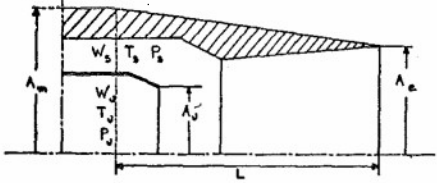
**INFLUENCE DE LA LONGUEUR DES VOILETS OU DIVERGENT PRIMAIRE**





LPI-16

**DÉTERMINATION DE LA SECTION  $A_e$**   
(calcul théorique)



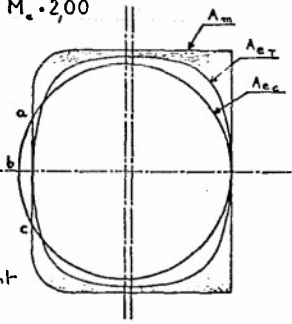
$\frac{A_m}{A_t} = 4,65$        $P_s/P_e = 0,21$        $L$  : donné  
 $\frac{W_s \sqrt{T_s}}{W_e \sqrt{T_e}} = 8\%$        $M_e = 2,00$

LPI-17

**OPTIMISATION DE LA FORME DE LA SECTION D'ÉJECTION**

$\mu_s = 6\%$   
 $P_s/P_e = 13,5$   
 $P_s/P_e = 0,20$

$A_m = \text{constante}$   
 $A_{e_c} = A_{e_T}$   
 $A_R$  circulaire  
 $a, b, c$  entré-entré



Gain de traînée externe sur la forme  $A_m - A_e$  entraîné par la modification de  $A_{e_c}$  en  $A_{e_T}$   
Théorique  $\Delta K_T = +0,006$

Perte de performance interne entraînée par la modification de  $A_{e_c}$  en  $A_{e_T}$   
Théorique  $\Delta K_T = -0,0015$

Bilan global  
Théorique  $\Delta K_T = 0,0045$   
Essais avec écoulement interne et externe  $\Delta K_T = 0,0045$

## SOME APPLICATIONS OF BOUNDARY-LAYER CONTROL BY BLOWING TO AIR INLETS FOR VSTOL AIRCRAFT

by

I. McGregor

Aerodynamics Department, Royal Aircraft Establishment, Bedford, England.

## SUMMARY

The use of jet blowing as a means of BLC in intakes has not received much attention, but it appears to have several advantages for VSTOL aircraft.

This paper first reviews the principles involved and then discusses briefly two examples - a two-dimensional inlet under static conditions, and a ducted lifting-fan at low forward speed - where the method was used to improve performance.

Some results of the effects of slot blowing on the behaviour of the intakes of a model of a VSTOL strike aircraft at subsonic speeds are presented, and compared with those obtained using a naturally-aspirated suction bleed. It is concluded that BLC by blowing could lead to a small improvement in nett thrust and a significant reduction in flow distortion at entry to the compressor: sensitivity of intake performance to incidence is also much reduced.

## PRINCIPAL NOTATION

A	area of entering streamtube	X	engine thrust
DC <sub>60</sub>	} flow distortion parameters defined in section 4.3	$\alpha$	incidence
DV <sub>max</sub>		<u>Suffices</u>	
m	rate of mass flow	B	suction bleed
M	Mach number	e	at edge of boundary layer
p	static pressure	f	mean value at compressor face
P	total pressure	G	gross
q	dynamic pressure	J	jet blowing
R	rate of increase of pressure recovery for zero change in nett thrust	N	nett
T	total temperature	t	at intake throat
u, v	velocity	$\infty$	freestream
W $\sqrt{T/P}$	engine airflow parameter	*	choking conditions
		O	without BLC

## 1 INTRODUCTION

The primary task of the intake in any gas-turbine powered aircraft is to deliver an adequate supply of air to the engine with the minimum loss of total pressure and distortion of the flow, with the minimum external drag. At subsonic speeds, these undesirable effects mostly arise from the viscosity of the air: boundary layers grow in the duct between inlet and engine, flow separation can occur in the duct and around the lips of the intake, secondary flows can develop if the duct is excessively curved, boundary layers can be ingested from parts of the aircraft adjacent to the intake, and flow separation can be induced on these parts by the adverse pressure field ahead of the inlet when it is not running full. The adverse effects of viscosity can be reduced by good aerodynamic design, but trouble is still likely to occur under certain conditions, such as at take-off and low-speed, and at high angles of incidence. This is true of any aircraft, but the problem can be particularly severe in VSTOL machines. It may, therefore, be necessary to improve the state of the airflow arriving at the fan or compressor face of the engine. There are several possible methods: auxiliary inlets can be used to mitigate the effects of flow separation from the lip of a conventional type of inlet at zero or low forward speed, and control of the boundary layer may be possible by suction, by vortex generators, or by the injection of high-pressure air. It is with the latter technique that this paper is concerned.

The principle of re-energising a turbulent boundary layer by means of a thin jet of air discharged tangentially to the wall through a slot has been known for many years, and numerous experiments have been made, both in windtunnels and on full-scale aeroplanes<sup>1</sup>. This work has been mainly directed at improving the maximum lift coefficient of wings by delaying boundary-layer separation on trailing-edge flaps at high deflection angles. In spite of achieving a considerable measure of success, the method has rarely been adopted on production aircraft. This is probably because of the weight and complication involved but, in the much more restricted environment of an intake, and with a supply of high-pressure air available nearby, these objections would seem to be far less serious.

This paper first reviews the principles involved in controlling boundary layers by blowing, and then discusses briefly two examples - a twodimensional inlet under static conditions and a ducted lifting-fan

at low forward speed - where the method was used to improve performance. Some results obtained at RAE Bedford on the effects of slot blowing on the behaviour of the intakes of a model of a VSTOL strike aircraft at subsonic speeds are then presented, and compared with those obtained using a naturally-aspirated suction bleed.

## 2 PRINCIPLES OF BLC BY BLOWING

Consider the situation shown in Fig.1, where a thin jet of air is injected tangentially beneath a turbulent boundary layer. The excess momentum of the jet relative to the freestream is  $m_j(u_j - u_e)$ , where  $m_j$  is the rate of air injection per unit width,  $u_j$  the injection velocity and  $u_e$  the velocity at the edge of the boundary layer. The corresponding momentum defect in the boundary layer is  $\theta \rho_e u_e^2$  where  $\theta$  is the momentum thickness and  $\rho_e$  the stream density. If we make the simplest possible assumption, that mixing takes place instantaneously and without loss, then the momentum of the boundary layer will be fully restored when these two quantities are equal. In fact, of course, mixing occurs gradually downstream of the blowing slot - the maximum velocity of the jet decreases, and a new boundary layer forms underneath the jet. Thus a greater jet excess momentum than that just sufficient to counteract the deficit in the boundary layer will be required to re-energise the flow (ratios of the order 2 to 5 have been suggested<sup>2,3</sup>), but lower values have been found adequate to delay or suppress separation in an adverse pressure gradient<sup>4</sup>.

That jet momentum is the most significant parameter is supported by its successful use in correlating the results of blowing over trailing-edge flaps. However, this does not mean that any combination of jet mass flow and velocity giving the same excess momentum will produce the same velocity profile at the same distance downstream of the blowing slot (Fig.2). This can be important if the blowing slot is a relatively short distance from the engine face, as the peak velocity produced by a narrow, high-pressure jet may still be greater than that at the edge of duct-wall boundary layer at engine entry, causing an increase in flow distortion there.

Although a reduction in the extent of the separated region has been reported when air is injected downstream of separation<sup>5</sup>, best results are normally obtained when the blowing slot is located upstream of this point. Peake<sup>4</sup> suggests a distance of six boundary-layer thicknesses ahead of a rapid rise in pressure sufficient to cause separation. If the blowing slot is located too far forwards, the energy of the jet is dissipated by friction with the wall, and a higher jet total pressure will be needed to produce the same effect. On the other hand, if the slot is placed in a region of rapidly rising pressure, flow reversal can occur in the wake region between the jet and boundary layer (Fig.3).

Theoretical work on the interaction of a wall jet with a turbulent boundary layer in an adverse pressure gradient is not very advanced, and the restrictions that have to be imposed in the analysis make the results difficult to apply in practice. Hubbard and Bangert<sup>6</sup> have recently reviewed the position, but the method of calculation they present is only applied to two limiting cases - a simple wall jet (i.e. one without an initial boundary layer) and a flow in which the initial boundary layer is just separated and a zero minimum velocity persists in the wake downstream.

Even without air injection, the calculation of the boundary layer on the walls of a curved duct, of varying and perhaps non-circular cross-section, is a quite formidable problem. Consequently, the development of an efficient BLC system must rely largely on experiment. Indeed, as applied to an intake, it would seem inadvisable to define the objectives of BLC in purely boundary-layer terms: what matters is the overall behaviour of the intake-engine system. Thus eliminating flow separation may not be the best criterion, and the optimum compromise (taking into account such factors as flow distortion and the loss of thrust due to bleeding air from the compressor) may be obtained at a different rate of blowing. Ideally, therefore, data on pressure recovery and flow distribution at the compressor face is required for a range of slot heights, positions and blowing pressure ratios, over a range of intake operating conditions, before the usefulness of this form of BLC can be properly assessed in a particular installation.

## 3 TWO EXAMPLES OF INTAKES WITH BLC BY BLOWING

3.1 Gregory<sup>7</sup> has considered the design of a family of twodimensional intakes for static conditions, which have a uniform suction over the lip, followed by a fairly rapid rise in pressure in a parallel section downstream. To avoid the possibility of separation in this region, boundary-layer control by blowing was proposed. Three models with varying contraction ratios were tested, and the one that appears most promising is shown in Fig.4. This has a highlight-to-throat area ratio of 1.17, and strikes a reasonable compromise between the need for a thin lip for efficient operation at high speeds, whilst providing sufficient lip area for a reasonably high flow rate to be reached before limiting suction on the lip occurs and the flow breaks away due to inability to satisfy the momentum equation. In the latter event, boundary-layer control is of no avail and other means, such as doors that permit air to be drawn directly into the diffuser, would be necessary to increase pressure recovery and mass flow.

Fig.5 demonstrates that, for a given intake flow, the blowing flow necessary to just prevent separation depends on slot height, and that with narrow slots the blowing pressure ratio required is greater. However, as might be expected, the influence of slot size is almost eliminated when the correlation is made in terms of blowing momentum ratio.

The variation of pressure recovery with intake mass flow ratio,  $m_e/m^*$ , is shown in Fig.6a. The results with blowing are maximum values, normalised with respect to the theoretical total pressure that would prevail in the absence of any viscous or mixing losses between the two streams. The increase in recovery (defined in this way) due to blowing is about 2%. With the largest slot height tested, the blowing pressure ratio at which maximum efficiency of pressure recovery occurred coincided with that at which

separation was just completely suppressed, but with smaller slot sizes the corresponding blowing pressure ratio tended to be lower, higher mixing losses outweighing the improvement possible by further reduction in the extent of the separated flow region.

To assess the effect on performance, it is convenient to consider the actual pressure recovery  $P_f/P_\infty$  as a function of  $m_f P_\infty / m P_f$ , which is directly related to the 'reduced' airflow  $W \sqrt{T/P}$  normally used to specify engine demand. Fig. 6b shows the actual recovery without blowing, and that obtained with the largest size slot at a blowing pressure ratio of 2.0. This is about the maximum value that may be obtained from the LP stage of a typical compressor, and is similar to that required to just suppress separation with this particular slot. For a given engine operating condition, the pressure recovery would be increased by about 3% for a blowing quantity equal to 2.2-2.4% of engine airflow. The analysis made in section 5 suggests that this would result in an increase in static thrust of about 2.5%.

3.2 The second example concerns a project study of a lifting pod<sup>8</sup> containing five lightweight, high-bypass-ratio engines, vertically mounted and arranged in line astern (Fig. 7). The pod was intended for mounting on or beneath a wing, and the design was based on criteria of minimum frontal area and minimum spacing between the engines. This required that the engines should be as close to the top of the pod as possible, with a small intake-lip radius (6.25% of the duct diameter, highlight-to-throat area ratio = 1.267).

Preliminary windtunnel tests on a small model showed that separation occurred at the front part of the lip of the first intake at all velocity ratios except zero, causing poor flow distribution and a significant loss in pressure recovery. Further work was therefore concentrated on improving the performance of this intake. Various fixed mechanical devices that were tried were only effective over parts of the range of velocity ratio, and it was decided to attempt control of the flow around the lip by air injection, using a considerably larger model of the front intake only.

The blowing slot was located on the intake highlight, as oil-flow tests had shown that separation occurred downstream of this under all conditions, and it discharged a jet in a direction initially perpendicular to the axis of the intake. Both the height and angular extent of the slot could be varied, best results being obtained when the slot extended completely around the front half of the intake. Comparative results without blowing and with just sufficient blowing to eliminate separation are shown in Fig. 8 for a velocity ratio of approximately unity. The blowing flow was about 2.2% of the duct flow, and the reduction in flow distortion is quite spectacular. It was found that for each slot tested the blowing flow required was directly proportional to freestream velocity. Denning and Gardiner concluded that, for a typical installation with a maximum transition speed of  $M = 0.2$ , the blowing flow requirement would amount to about 0.7% of the maximum engine airflow, with a blowing pressure ratio of around 1.85.

A similar, and equally successful, application of BLC by slot blowing to the intake of a lifting fan mounted in a thin delta wing has recently been reported in Ref. 9.

#### 4 TESTS ON A MODEL OF A VSTOL STRIKE-FIGHTER WITH FUSELAGE-SIDE INTAKES

4.1 The model which formed the subject of this investigation is shown in Fig. 9. The semicircular intakes on each side of the fuselage are connected by short, highly curved ducts to a single, centrally mounted engine, the area ratio between the intake throat and compressor face being approximately 0.9. The intakes ingest the boundary layer from the fore part of the fuselage, and the combination of curvature and rising pressure produces on the inner walls of the duct a thick boundary layer that is prone to separation and to complex interactions with the boundary layers on the top and bottom of the duct. Consequently, in the absence of any form of BLC, intake losses tend to be high and flow distribution at the compressor face poor.

Considerable work has been done at RAE Bedford on the development of a bleed system for this intake<sup>10</sup>. At conditions corresponding to cruising flight, a considerable improvement in pressure recovery and flow distribution was obtained. However, at conditions of high Mach number, high mass flow and high incidence, the bleed (which was vented to the top of the fuselage behind the canopy, and relied on the difference in static pressure between this point and the bleed slot in the duct wall for its operation) was not very effective. Slot blowing was proposed as an alternative.

4.2 Four slot configurations were tested. The slots were designed to produce an approximately tangential jet of high-pressure air on the curved inner wall of the diffuser. Two longitudinal positions for the slots were used, called for simplicity the 'rear' and 'forward' positions. The 'rear' position corresponded to that of the suction bleed slot. Three slot arrangements were tried in this position - slots the full height of the diffuser, with nominal throat sizes of 0.5 mm and 1.0 mm, and shorter slots extending over the top and bottom quarter of the diffuser height, with a nominal throat size of 1 mm. The 'forward' position was 2.5 mm behind the intake entry plane. Here, slots with a nominal throat size of 0.5 mm and extending virtually the full height of the intake were used, the slots being curved in front view to conform with the cross-sectional shape of the fuselage.

High-pressure air was supplied by a pipe which entered the top of the model just ahead of the intakes. Oil-flow tests showed that disturbances in the fuselage boundary layer due to the presence of the pipe did not enter the intakes under any conditions.

A bleed was provided on the forward part of the fuselage so that the thickness of the boundary layer on the fuselage side at the intake entry was roughly the same, relative to the height of the intake, as full-scale.

4.3 The blowing pressure  $P_j$  was measured with a total pressure tube in the supply pipe just upstream of the model: the blowing mass flow  $m_j$  was determined using a British Standard orifice plate. The temperature of the blowing air was always within 2 to 3°C of tunnel total temperature.

The pressure distribution at the compressor-face station was measured with a cruciform pitot rake, the six tubes in each arm being so disposed that they governed annuli of equal area. The rake was rotatable and was used in six angular positions, giving 144-point coverage of the compressor face: the area-mean total pressure  $P_f$  is defined as the average of these 144 pressures. Static pressures were measured at eight points around the periphery of the compressor face, and the mean static pressure  $p_f$  has been taken as the average of these.

Flow through the intakes was controlled by a movable exit plug, some distance downstream of the measuring station. The total mass flow  $m_f$  at the compressor face was computed from

$$m_f = \sqrt{\frac{\gamma}{RT}} \frac{A_f}{144} \sum_{i=1}^{144} P_i \frac{M_i}{(1 + 0.2M_i^2)^{3/2}}$$

where  $R$  = gas constant

$P_i$  = pitot pressure at  $i$ th tube

$\gamma$  = ratio of specific heats

$M_i$  = local Mach number calculated from  $P_i$  and  $p_f$

$T$  = tunnel total temperature

$A_f$  = area of compressor face

The mass flow of air entering the intake is  $m_f - m_j$ , and the intake mass flow ratio is defined as

$$\frac{A_\infty}{A_t} = (m_f - m_j) \left\{ \sqrt{\frac{\gamma}{RT}} \frac{P_\infty A_t M_\infty}{(1 + 0.2M_\infty^2)^{3/2}} \right\}$$

where  $A_t$  is the intake throat area.

Two measures have been used to describe flow distortion. The first is the parameter  $DC_{60}$ , originated by Rolls-Royce, which is defined as

$$DC_{60} = (\bar{P}_{60} - P_f) / q_f$$

where  $\bar{P}_{60}$  is the mean total pressure in the worst  $60^\circ$  sector and  $q_f$  the mean dynamic pressure at the compressor face (calculated, here, from  $P_f$  and  $p_f$ ). Quantitatively, this is mainly of value in predicting the likelihood of engine surge at high mass flows, but it is also useful for comparing distributions at lower flow rates. However, it is insensitive to even quite large distortions if they are very localised in extent, and an alternative parameter is needed to detect these. There are effectively six rings of pitot tubes at the compressor face, and the pressure is measured at 24-points around each ring. The quantity  $(V_{\max} - V_{\min})/V_f$  is evaluated for each ring:  $DV_{\max}$  is the greatest of these. Physically,  $DV_{\max}$  may be interpreted as the greatest variation in inflow velocity experienced at any point along a compressor blade during one revolution.

4.4 The model was sting-mounted in the transonic working section of the 3ft x 3ft tunnel at RAE Bedford. The majority of the tests were made at a single Mach number of 0.85, as earlier work had shown that the general character of the intake flow did not vary greatly over the speed range, but some tests were also made with the 0.5 mm blowing slots at  $M_\infty = 0.5, 0.7$  and  $0.95$ . The Reynolds number, based on entry height, was  $1.5 \times 10^6$ .

During a test, the blowing pressure was held constant and the intake mass flow varied. Fig.10 is typical of the results obtained at  $M_\infty = 0.85$ . The shape of the pressure recovery - mass flow curve is characteristic of an intake ingesting the boundary layer from a surface ahead of it, and is determined by two distinct factors<sup>11</sup>. At high mass flows, the pressure recovery falls due to increasing viscous losses in the duct, but with reducing mass flow the adverse pressure field that develops ahead of the intake first thickens and, finally, the external boundary layer separates, causing a rapid drop in recovery and increase in flow distortion. At this Mach number, pre-entry separation occurs at a mass flow ratio of about 0.65. Slot blowing inside the intake cannot be expected to have any effect on pre-entry separation, and the general variation of pressure recovery with mass flow is similar with and without blowing. For a given blowing pressure, the increase in pressure recovery is almost constant between mass flow ratios of about 0.7 to 0.9, falling slightly at higher or lower flow rates. The increase in pressure recovery with blowing is due partly to improving the flow in the duct and partly to the excess pressure of the blowing air, but it is a rather difficult problem to apportion the increases between these two causes. From a practical point of view it is the actual pressure recovery that matters, as this determines engine thrust.

Slot blowing also produces a considerable reduction in flow distortion, as exemplified by the  $DC_{60}$  parameter. As with pressure recovery, the greatest improvement occurs between mass flow ratios of roughly 0.7 to 0.9.

Further discussion of the results is simplified by considering intake performance under two conditions of operation. The first approximates to 'cruise' conditions, and is  $(A_\infty/A_t) = 0.80$ ,  $\alpha = 4.5^\circ$ . At this incidence the intake is most nearly aligned with the local flow direction and pressure recovery is at a maximum. The second condition approximates to maximum engine demand, and is  $(A_\infty/A_t) = 0.90$ ,  $M_\infty = 0.85$ .

4.5 Fig.11 summarises the results at 'cruise' conditions at  $M_\infty = 0.85$ . The differences in blowing mass flow ratio for the three slot configurations tested in the rear position are greater than would be expected from the nominal differences in dimensions, but manufacturing tolerances are likely to be responsible - it is extremely difficult to make a slot of this length with a variation in throat height of less than 0.05 mm, or 10% of the nominal height of the narrowest slot.

The pressure recovery grows steadily with increasing values of  $P_J/P_\infty$ , the 1 mm slot naturally showing the most rapid rise. Judged in terms of increase in recovery for mass injected, the 0.5 mm slot in the rear position appears to be the most effective arrangement. However, the most interesting feature of the results concerns flow distortion. Whereas  $DC_{60}$  decreases continuously with  $P_J/P_\infty$ , the value of  $DV_{max}$  for the three full-height slots has a minimum at a blowing pressure ratio of about 1.5 (slots in the rear position) or 1.6 (forward position). For values of  $P_J/P_\infty$  greater than this optimum, the peak total pressure in the jet layer at the compressor face is higher than freestream, resulting in a localised increase in distortion.

Similar behaviour was found at other Mach numbers, and Fig.12 shows this optimum blowing pressure ratio for the 0.5 mm slots in the rear and forward positions, together with the intake performances under these conditions. The optimum value of  $P_J/P_\infty$  increases with  $M_\infty$ , and is 0.1 to 0.2 higher for the forward slot - due mainly to the greater distance and consequently greater frictional losses between the slot and measuring station - but differences in the other quantities are, in general, little greater than the experimental error. It is interesting that the blowing flow required, about 2.5%, is constant over the Mach number range. Compared with the suction bleed (with  $m_B/m_f = 0.05$ ), blowing at the optimum pressure ratio with the 0.5 mm slots gives an almost identical pressure recovery between  $M_\infty = 0.65$  and 0.90, but a significantly lower value of  $DC_{60}$ .

Pressure recovery and flow distortion with the 0.5 and 1.0 mm slots in the rear position are shown in Fig.13 as functions of the excess momentum ratio of the jet,  $m_J(u_J - u_e)/(m_f - m_J)V_\infty$ . The velocity  $u_e$  was calculated from  $P_\infty$  and the static pressure  $p_e$  on the duct wall immediately upstream of the blowing slot, and the jet velocity  $u_J$  was calculated from  $P_J$  and  $p_e$ : both streams were assumed to be at the same total temperature. Use of this parameter correlates the  $DC_{60}$  values very well and also (reasonably successfully) the values of  $DV_{max}$  for blowing pressure ratios below the optimum, where  $DV_{max}$  is decreasing with increasing  $P_J/P_\infty$ . However, the pressure recovery does not appear to be a function solely of the excess momentum, but depends on slot size as well.

4.6 Considering now the performance at a mass flow ratio of 0.90, Fig.14 shows the variation of the distortion parameters with  $P_J/P_\infty$  for the 0.5 mm blowing slot in the rear position. The distortions at incidences of  $-2.5^\circ$  and  $10.5^\circ$  are greater than at  $4.5^\circ$ , but it is noteworthy that the much higher value of  $-DC_{60}$  at  $-2.5^\circ$  is not reflected in a correspondingly higher value of  $DV_{max}$ : this emphasises the desirability of using more than one parameter to describe flow distortion. At all incidences,  $DV_{max}$  has a minimum value at a blowing pressure ratio of 1.5 to 1.6, although the minimum is not so well-defined as at the lower mass flow ratio.

The variation of pressure recovery and  $DC_{60}$  with incidence at a blowing pressure ratio of 1.5 is shown in Fig.15 for the various slot arrangements. The increment in pressure recovery and decrement in  $DC_{60}$  with slot blowing are nearly constant over the incidence range, whereas the effectiveness of the suction bleed declines rapidly at incidences away from  $4.5^\circ$ . The improvement in flow distribution at the compressor face at  $\alpha = 10.5^\circ$  is clearly demonstrated in Fig.16.

## 5 EFFECT ON PERFORMANCE

5.1 A detailed analysis of the effects on engine performance of applying ELC to the intake is outside the scope of this paper, and would have to take account of the changes in flow distribution as well as in the mean values of the parameters. However, an indication of the improvement possible may be obtained quite simply, and in such a way that the relative merits of ELC by blowing into, or bleeding from, the intake duct can be compared. It will be assumed that the engine is operating at constant speed, so that the reduced airflow  $W\sqrt{T}/P$  is constant. With a blowing system taking air directly from the compressor, the injected air will be at a slightly higher total temperature than freestream, but if this is ignored it follows that  $m_f/(P_f/P_\infty)$  is constant. Therefore any change  $\Delta(P_f/P_\infty)$  in recovery must be accompanied by a corresponding change  $\Delta m_f$  in the mass flow entering the engine, such that

$$\frac{\Delta m_f}{m_{f0}} = \frac{\Delta(P_f/P_\infty)}{(P_f/P_\infty)_0},$$

suffix 0 referring to conditions without ELC.

If a mass flow  $m_j$  is bled from the compressor and injected back into the intake, the gross thrust is given by

$$X_G = X_{G_0} - \frac{\partial X_G}{\partial m_J} m_J + \frac{\partial X_G}{\partial (P_f/P_\infty)} \Delta(P_f/P_\infty) ,$$

and if engine speed is constant, the mass flow of air entering the intake from upstream is

$$m_{f_0} \left[ 1 + \frac{\Delta(P_f/P_\infty)}{(P_f/P_\infty)_0} \right] - m_J .$$

Thus the nett thrust will be

$$X_N = X_{G_0} - \frac{\partial X_G}{\partial m_J} m_J + \frac{\partial X_G}{\partial (P_f/P_\infty)} \Delta(P_f/P_\infty) - \left\{ m_{f_0} \left[ 1 + \frac{\Delta(P_f/P_\infty)}{(P_f/P_\infty)_0} \right] - m_J \right\} V_\infty$$

compared with the value  $X_{G_0} - m_{f_0} V_\infty$  without blowing. Therefore the change in nett thrust is

$$\Delta X_N = \frac{\partial X_G}{\partial (P_f/P_\infty)} \Delta(P_f/P_\infty) - \frac{\partial X_G}{\partial m_J} m_J - \left\{ m_{f_0} \frac{\Delta(P_f/P_\infty)}{(P_f/P_\infty)_0} - m_J \right\} V_\infty .$$

The rate of increase of pressure recovery with rate of blowing to just make good the loss of thrust due to bleeding air from the compressor is therefore

$$R_J = \frac{\Delta(P_f/P_\infty)}{(m_J/m_{f_0})} = \left( \frac{\partial X_G}{\partial (m_J/m_{f_0})} - m_{f_0} V_\infty \right) / \left( \frac{\partial X_G}{\partial (P_f/P_\infty)} - \frac{m_{f_0} V_\infty}{(P_f/P_\infty)_0} \right)$$

If a mass flow  $m_B$  is bled from the duct walls and discharged with negligible momentum in the streamwise direction, a similar argument shows that the rate of increase in recovery with bleed flow for the increase in thrust to just balance the drag of the bleed is

$$R_B = \frac{\Delta(P_f/P_\infty)}{(m_B/m_{f_0})} = m_{f_0} V_\infty / \left( \frac{\partial X_G}{\partial (P_f/P_\infty)} - \frac{m_{f_0} V_\infty}{(P_f/P_\infty)_0} \right) .$$

The variation of  $R_J$  and  $R_B$  with Mach number for a typical engine under maximum continuous rating conditions at sea level is shown in Fig.17. The curve for  $R_B$  is extended down to  $M_\infty = 0$ , but in practice there would be insufficient pressure difference for a naturally-aspirated bleed system to work below a Mach number of about 0.6, and it would probably be necessary to incorporate some form of control to prevent air being inadvertently drawn into the intake from the bleed under these conditions. The factor  $R_J$  has a nearly constant value between 0.5 and 0.6, and is less than  $R_B$  for  $M_\infty > 0.9$ . For each per cent change in pressure recovery from the 'break-even' value  $R_J(m_J/m_{f_0})$  or  $R_B(m_B/m_{f_0})$  there will be a change in nett thrust of, typically, 1.5 to 1.7% at subsonic speeds.

5.2 Fig.18 shows, for the model described in the previous section, the increment in pressure recovery at  $M_\infty = 0.85$ ,  $\alpha = 4.5^\circ$ , as a function of blowing mass flow ratio. To accord with the assumption of constant engine speed, the increments were evaluated at a constant value of  $m_f/P_f$ , equal to that at  $A_\infty/A_t = 0.90$  without blowing. Of the various arrangements tested, the 0.1 mm slot in the rear position gives the greatest nett thrust, but in view of the quite large difference between the 0.5 and 1.0 mm slots, this is not necessarily the best possible configuration. A slot somewhat smaller than 0.5 mm may perhaps give a superior thrust, but this must be balanced against the greater reduction in flow distortion possible with a larger slot. Due, presumably, to the complicated nature of the flow in the duct, there does not appear to be a unique slot size and location that will give both maximum thrust and minimum distortion: this might have been expected if the function of the blowing jet was just to eliminate flow separation.

Compared with slot blowing, the performance of the intake with a suction bleed appears distinctly inferior. Since a constant value of  $m_f/P_f$  is assumed, this is due, in small part, to the intake operating at about a 7% higher mass flow ratio. This could, however, be off-set to some extent by a reduction in spillage drag. At a blowing pressure ratio of 1.5, the 0.5 mm blowing slot would give an increase in thrust of just over 2% and some improvement in flow distortion compared with the suction bleed: the 1 mm slot would give an increase in thrust approaching 1% and a large decrease in distortion. These benefits would be even more pronounced at higher incidences.

## 6 CONCLUSIONS

Three examples of the application of BLC by blowing are discussed in this paper - an intake under static conditions, a lifting fan at low forward speed, and a fuselage-side intake at high-subsonic speed. They clearly demonstrate its versatility and effectiveness in improving intake performance, and, in the two latter examples, its superiority over other forms of BLC.

The blowing mass flow required is quite modest and the blowing pressure is well within the capacity of the LP stage of the average compressor. A simple method for estimating the overall change in nett thrust is described.

In particular, adoption of a slot blowing system in place of the suction bleed in the intakes of the VSTOL strike aircraft could lead to an increase in maximum thrust of 1 to 2% and a considerably lower level of flow distortion at entry to the compressor: the variation of intake performance with incidence would also be much reduced.

REFERENCES

<u>No.</u>	<u>Author(s)</u>	<u>Title, etc.</u>
1	G.V. Lachmann (Editor)	Boundary layer and flow control. Vol.1 - Its principles and application. Pergamon Press (1961)
2	B.S. Stratford	Boundary layer control by injection from aircraft gas turbine engines. ARC 16137, FM 1949 (1953)
3	P. Bradshaw M.T. Gee	Turbulent wall jets with and without an external stream. ARC R&M 3252 (1962)
4	D.J. Peake	The use of air injection to prevent separation of the turbulent boundary layer in supersonic flow. ARC CP 890 (1966)
5	A. Chinneck Miss G.C.A. Jones Miss C.M. Tracy	Interim report on the use of blowing to reduce the fall in control effectiveness associated with shock induced separation at transonic speeds. ARC 17564, FM 2231 (1955)
6	J.E. Hubbart L.H. Bangert	Turbulent boundary layer control by a wall jet. AIAA Paper 70-107 (1970)
7	N. Gregory	On the static performance of two-dimensional intakes with momentum injection in the form of boundary layer control by blowing. ARC R&M 3656 (1971)
8	R.M. Denning R.G. Gardiner	An experimental investigation of boundary layer control on intakes for vertically mounted lift engines. Bristol Siddeley Engines Ltd., Unpublished Report (1965)
9	B.K. Hodder J.V. Kirk L.P. Hall	Aerodynamic characteristics of a large-scale model with a lift fan mounted in a 5 per cent thick triangular wing, including the effects of BLC on the lift-fan inlet. NASA TN D-7031 (1970)
10	M.M. Shaw Mrs. D. Musselle	Wind tunnel measurements of intake performance on a model of a subsonic strike aircraft with VSTOL capability. Unpublished RAE Report (1970)
11	J. Seddon	Air intakes for aircraft gas turbines. Journal R.Ae.Soc., pp.747-781, October 1952

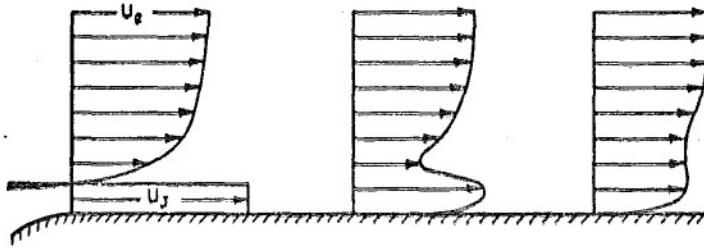
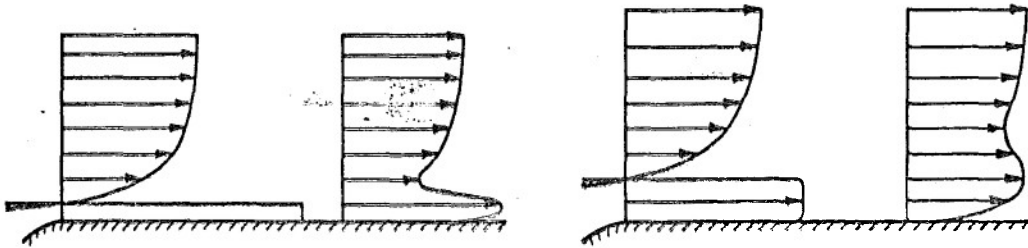


Fig. 1 Principle of re-energising a boundary layer by means of a wall jet



a Narrow, high velocity jet

b Wide, low velocity jet

Fig. 2 Two jets with the same excess momentum,  $m_j(u_j - u_e)$

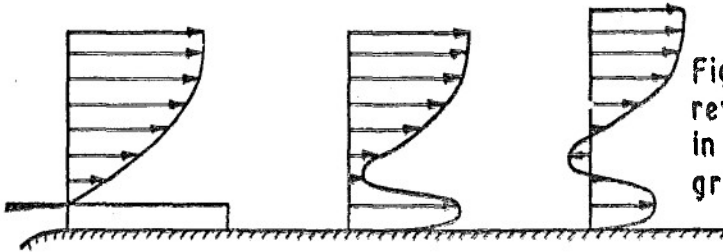


Fig. 3 Possible flow reversal in wake region in strong adverse pressure gradient

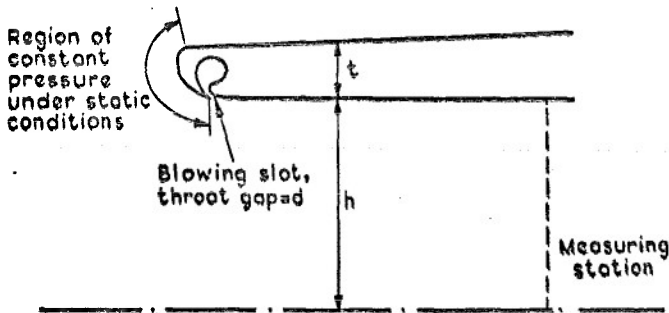


Fig. 4 Two-dimensional intake with blowing BLC (Ref. 7)

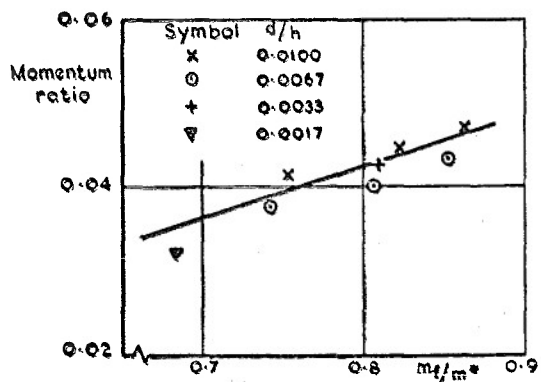
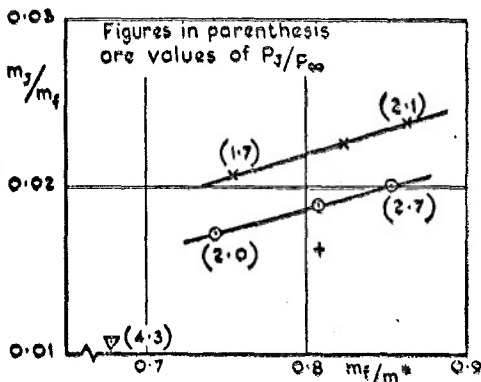


Fig. 5 Jet blowing required to suppress separation under static conditions ( $t/h = 0.25$ )

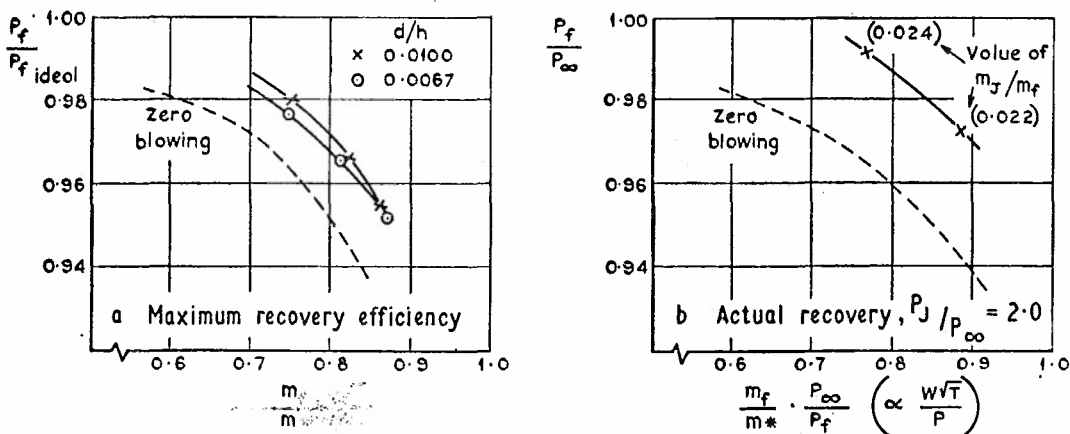


Fig. 6 Effect of jet blowing on pressure recovery under static conditions

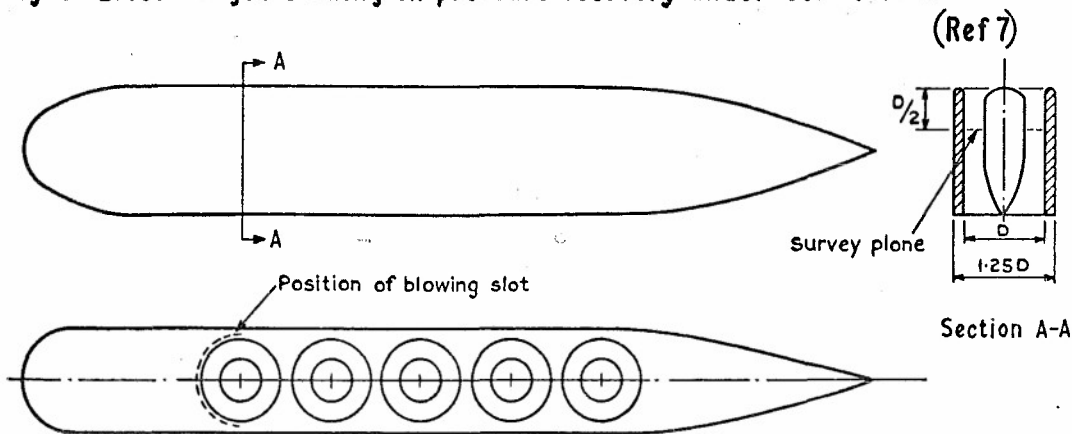


Fig. 7 Design of a pod with 5 lifting engines (Ref 8)

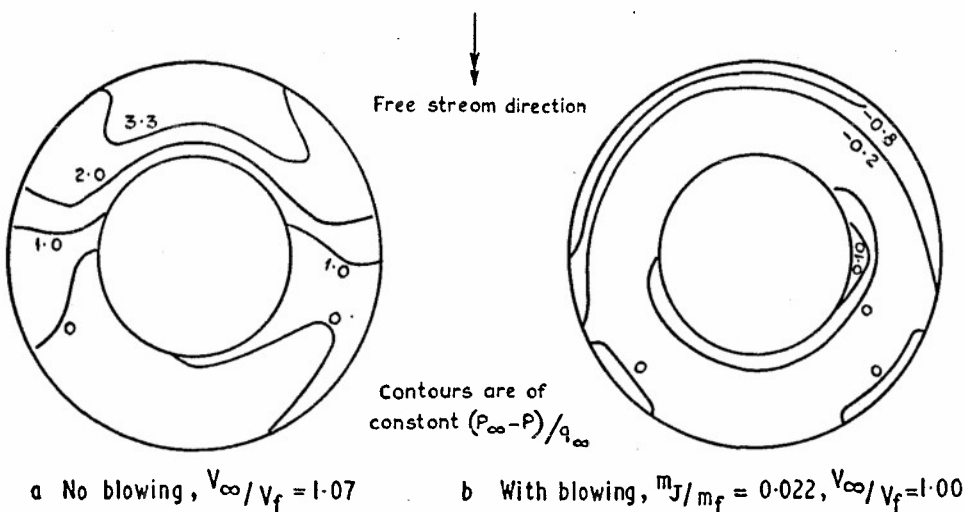


Fig. 8 Effect of jet blowing on flow distribution in leading intake (Ref 8)

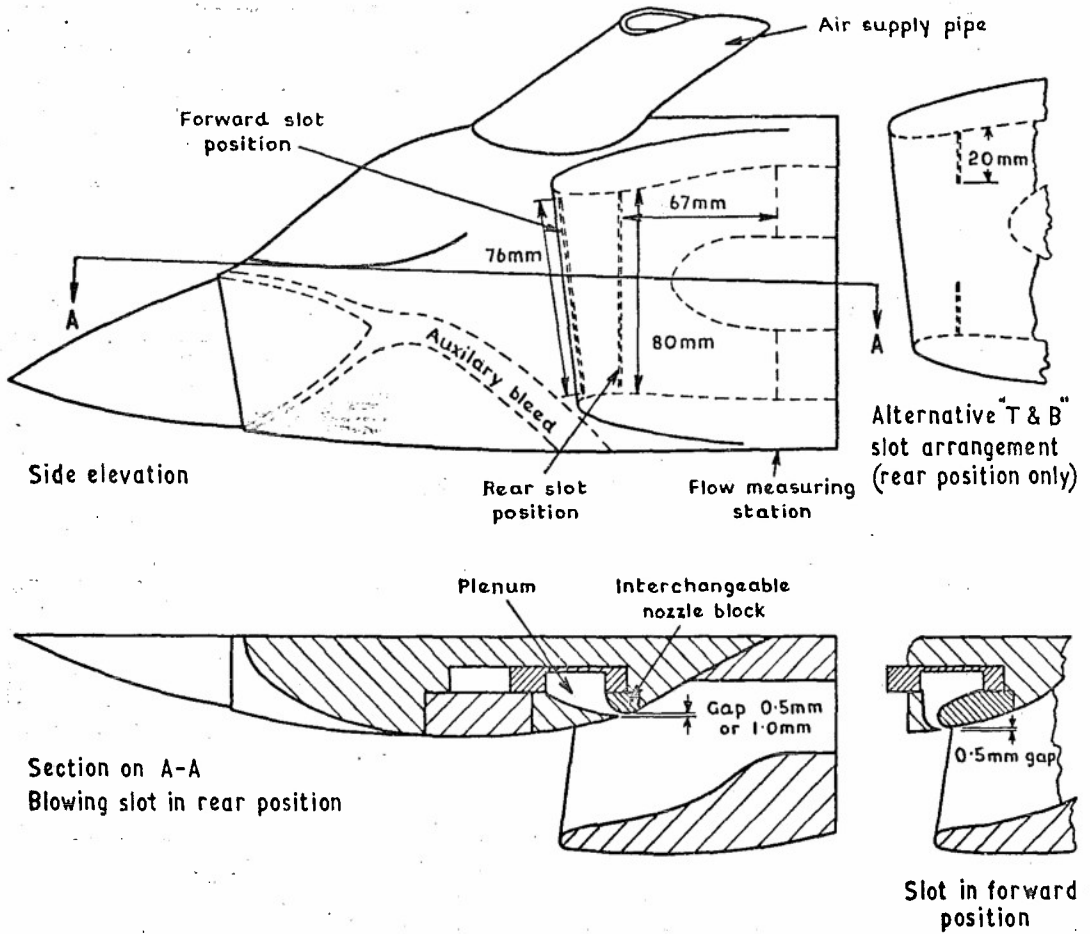


Fig. 9 Details of fore part of model with slot blowing in the intakes

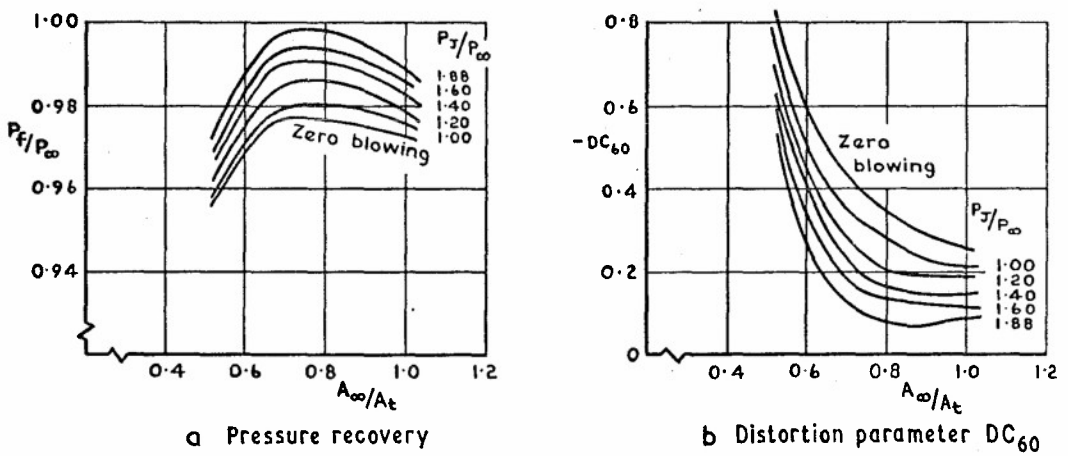


Fig. 10 Intake performance with 0.5mm blowing slot, rear position.  $M_\infty = 0.85$   $\alpha = 4.5^\circ$

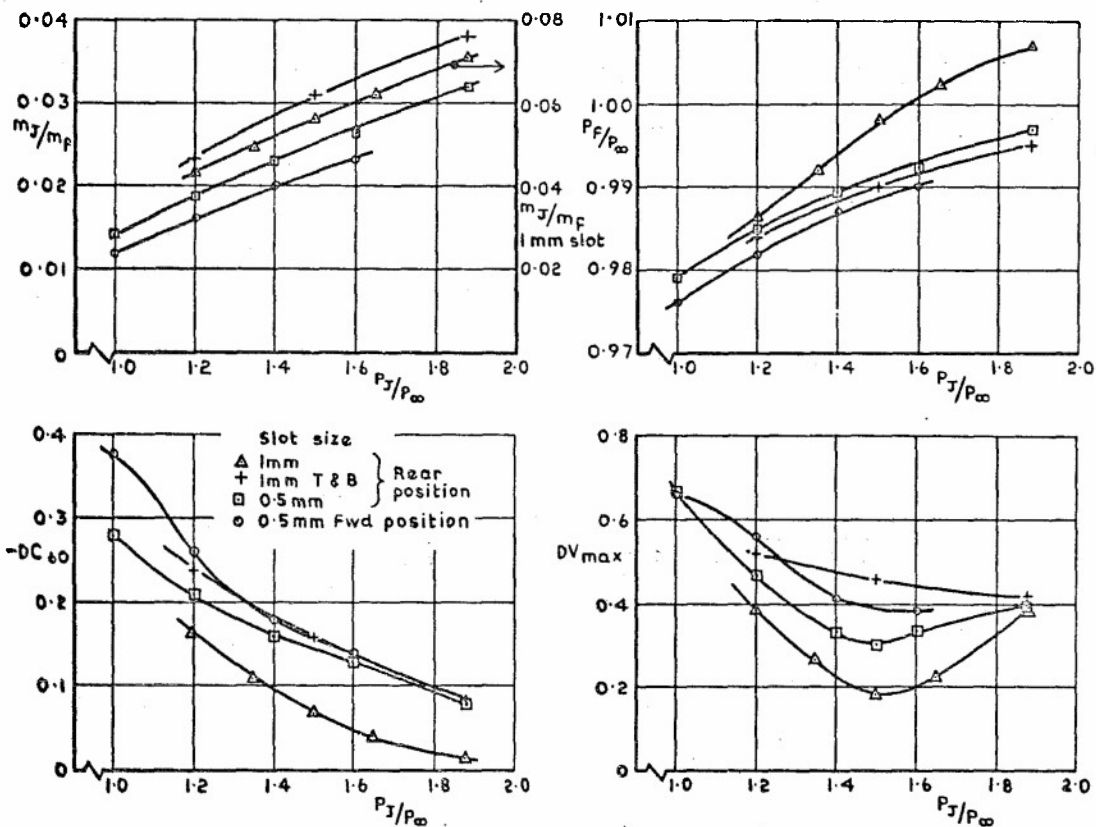


Fig.11 Effect of slot size, position and blowing pressure ratio on intake performance.  $M_\infty = 0.85$ ,  $\alpha = 4.5^\circ$ ,  $A_\infty/A_t = 0.80$

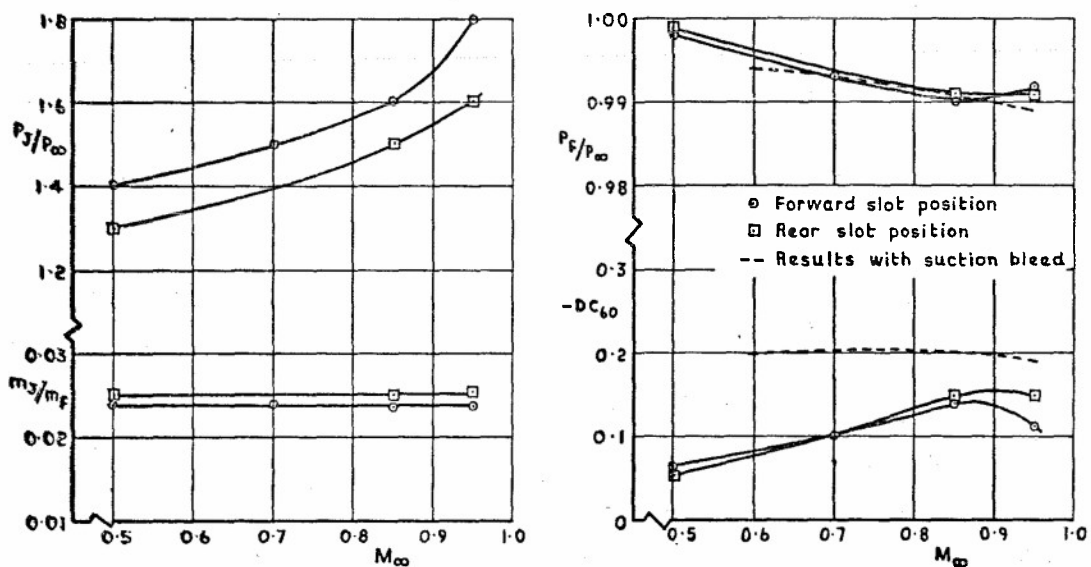


Fig.12 Blowing condition to produce lowest velocity distortion and corresponding intake performance. 0.5mm slot,  $A_\infty/A_t = 0.80$ ,  $\alpha = 4.5^\circ$

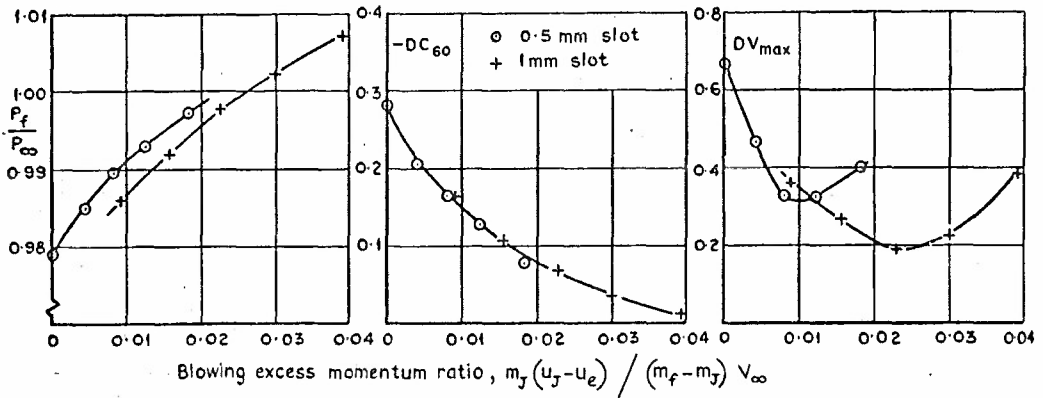


Fig.13 Performance of 0.5 and 1.0 mm blowing slots in rear position  
 $M_\infty = 0.85$ ,  $\alpha = 4.5^\circ$ ,  $A_\infty/A_t = 0.80$

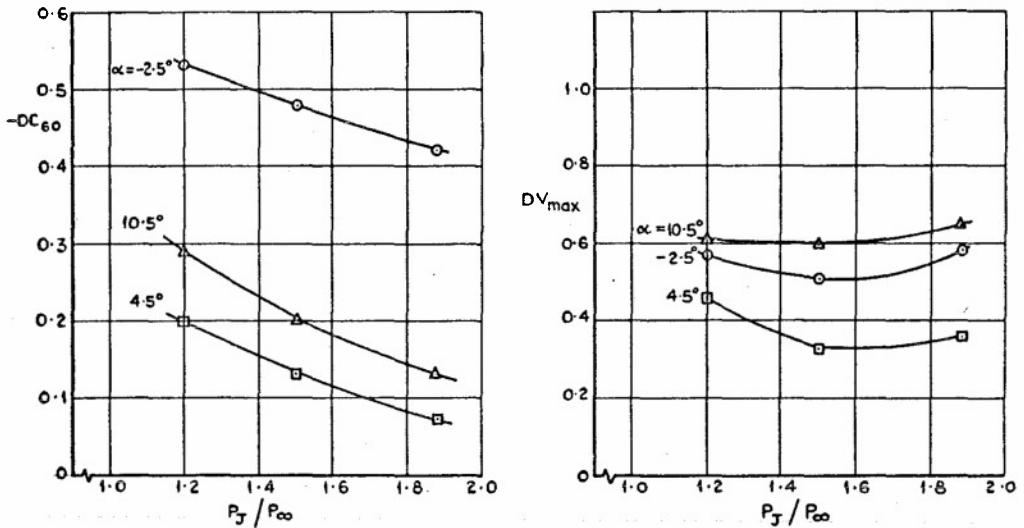


Fig.14 Effect of blowing on flow distortion at incidence. 0.5mm slot, rear position  
 $M_\infty = 0.85$ ,  $A_\infty/A_t = 0.90$

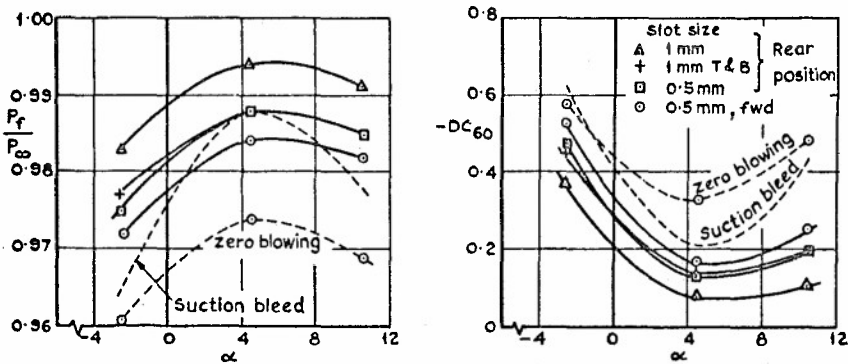


Fig.15 Effect of incidence on intake performance,  
 $P_j/P_\infty = 1.5$ ,  $M_\infty = 0.85$ ,  $A_\infty/A_t = 0.90$



a Without BLC

b With suction bleed,  $m_B/m_f = 0.045$

c With 0.5 mm blowing slot,  $P_J/P_\infty = 1.50, m_J/m_f = 0.023$

Fig.16 Contours of constant  $V/V_f$  at compressor face,  $A_\infty/A_t \approx 0.92, M_\infty = 0.85, \alpha = +10.5^\circ$

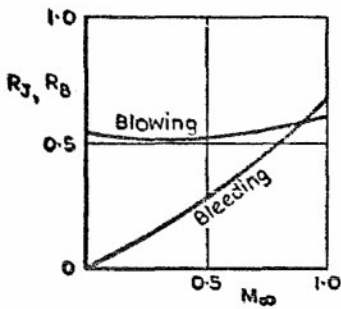


Fig.17 Rate of increase of pressure recovery with blowing or bleed flow for zero change in nett thrust. Max continuous rating conditions, sea level

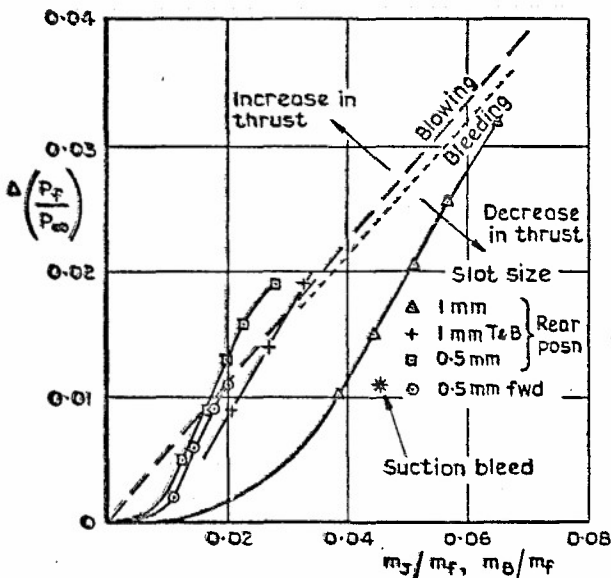


Fig.18 Increase in pressure recovery with blowing or bleed flow at approx maximum continuous rating conditions.

$W\sqrt{T}/P$  const  
 $M_\infty = 0.85, \alpha = 4.5^\circ$   
 $\frac{A_\infty}{A_t} = 0.90$  without BLC

SOME ASPECTS OF PROPULSION FOR THE  
AUGMENTOR-WING CONCEPT

by

D. C. Whittley  
Deputy Director - Research  
The De Havilland Aircraft of Canada, Limited  
Downsview, Ontario, Canada

SUMMARY

Many modern concepts for STOL and V/STOL aircraft rely on integration of the propulsion system with the wing to create favourable lift interactions and therefore they have become known as "powered-lift" concepts. A study of powered-lift concerns the management and control of the various propulsive streams or jets, with each concept having its own particular objectives and requirements. This paper describes some specific objectives of this kind which relate to the Augmentor-Wing.

Consideration is given to three aspects of the subject, namely: the augmentor flap itself, the wing ducting and augmentor primary nozzle and the choice of powerplant or engine cycle. More generally, comments are made regarding noise attenuation and the prospect for achieving a low overall noise level for jet-STOL aircraft of the future.

INTRODUCTION

Previous papers (references 1 and 2) have described how small scale tests of the augmentor flap led to the design and construction of a large 42 foot span straight wing model for tests in the NASA Ames 40' x 80' wind tunnel. (Figure 1.) These early tests placed emphasis on performance and longitudinal stability and control. Subsequently, tests have been directed toward investigation of lateral stability and control and toward aerodynamic interference due to vectored propulsive thrust and to the addition of pylon and nacelles to the model. (Figure 2.) A parallel program on one of the large moving base flight simulators at the Ames Research Center was carried out to study stability and control and handling qualities of a projected flight research aircraft. (Figure 3.) These extensions to the original program provided the technical foundation for flight research experiments and have resulted in a joint USA/Canada program to incorporate the Augmentor-Wing concept in a de Havilland Buffalo airframe using two Rolls-Royce Spey turbo-fan engines. (Figure 4.) The Boeing Company is the airframe contractor for NASA in this flight program with de Havilland under contract to the Canadian Department of Industry for provision of the powerplant and nacelle assembly. Thus, following a period of nearly five years' research on the large straight wing model, sufficient confidence has been gained to justify flight experiments with a straight wing. The need to extend research to swept wings was realized early in 1966 and long term plans were made in Canada to build a swept wing to fit on the same fuselage and use the same compressed air unit as for the large straight wing model. (Figure 5.) Agreement was eventually reached and the swept wing has now been built and has undergone one test series early this year in the Ames 40' x 80' wind tunnel. The straight wing has a thickness/chord ratio of .16 whereas the new swept wing has a thickness/chord ratio which varies from 0.125 at the root to 0.105 at the tip, and therefore is more representative of a modern high speed subsonic transport aircraft. Both wings have an aspect ratio of eight approximately.

This paper describes some of the small scale tests and background work which has been undertaken in Canada to ensure success of the large scale model tests in the NASA Ames 40' x 80' wind tunnel. This work dealt mostly with internal aerodynamics and development of the augmentor flap. Also some comments are made regarding the special requirements and constraints which an internal blowing concept, such as the Augmentor-Wing, places on the choice of powerplant.

THE AUGMENTOR FLAP

In Canada, the first suggestion for a powered spanwise slot in the wing was made by T. Higgins in 1960. The concept had three or four spanwise slots located in a multi-spar wing and was powered by the primary exhaust gas of a turbo-jet engine. (Reference 1.) This idea was modified and much simplified by the author to just a single slot located behind a conventional wing box and powered by the relatively cold by-pass air from a turbo-fan engine and this, together with the engine off-take and ducting arrangement, has become the Augmentor-Wing concept as we know it today. Optimization of the ejector has been carried out by D. B. Garland and the idea for a slot in the upper flap element to provide boundary layer control by suction is due to J. E. Farbridge.

In the following, consideration is given to the reasons for choice of an augmentor flap, the objectives from a design point of view and the performance of the flap as a propulsion device.

Many of the reasons for choice of the augmentor flap relate to its aerodynamic characteristics. These have been described in some detail in a recent paper (reference 3). In particular, it has been shown that the suction pressure set up by induction of secondary air into the flap provides a powerful mid-chord control and that this leads to satisfactory stalling characteristics of the wing, whether straight or

swept, at quite high values of lift coefficient. However, not all of the advantages relate to the aerodynamics of the wing, some, in fact, relate to the augmentor flap as a device for propulsion.

One of the earliest ideas for powered lift relates to blowing over a plain flap and using the minimum of air so that the flow just remains attached. Air for blowing the flap is obtained by bleeding the compressor of a turbo-jet or turbo-fan engine. It now appears that the level of lift which can be obtained in this way is not very much greater than available from a highly developed mechanical flap and that thrust for take-off is degraded by bleeding the compressor. The Augmentor-Wing concept represents an attempt to overcome these two objections: firstly, sufficient air is ducted to the flap so that it operates in the region of supercirculation and therefore generates substantially more lift than that available from a mechanical or "BLC" flap and also,  $CL_{max}$  now becomes speed dependent, and therefore, a wider stall margin can be achieved. Secondly, by-pass air is used to power the flap so that thrust degradation due to compressor bleed is avoided, also the degree of thrust augmentation achieved is sufficient to more than offset the duct loss and therefore, the previous trend toward degradation of thrust is reversed.

For take-off, at moderate flap angles (say, less than  $50^\circ$ ), the principle of thrust recovery holds true for a deflected jet sheet so that the propulsive thrust advantage is maintained even though the jet is deflected. For landing, the augmentor flap provides a very positive means of thrust deflection through the large angles which are required to achieve a steep descent gradient.

**Design and Optimization of Augmentor Flap Geometry.** Design of the flap takes place within fairly well defined limits. To retain a reasonable wing box for torsional stiffness, the rear spar is located at about mid-chord therefore the ducting and flap (when stowed) must be housed within the remaining wing contour. The thickness of wing nozzle "t" is established by the desired thrust in the wing (about 35% of total) and by the corresponding pressure ratio (between 2 and 3). In order to achieve a reasonable augmentation of thrust the throat width of the ejector should be at least twelve "t" and, to establish good mixing, the length to width of the ejector should be at least five. The radius of the Coanda surface should be as large as possible (consonant with other geometric requirements) so as to give a wide operating range of flap angle.

These constraints largely define the augmentor flap geometry and the chosen design is obtained by iteration using a drafting layout. There remains one important factor, namely, the choice of location of the Coanda surface relative to the nozzle.

By experience it has been found desirable to direct the jet downward fifteen degrees relative to the chord line. In earlier designs the Coanda surface was isolated from the main lower flap element (Figure 6) and, by a small rotation of the Coanda surface relative to the flap, a position could be found which was optimum for augmentation of thrust - the objective being to adjust the geometry so as to arrange for the velocity profile at exit to have a peak close to the centre of the passage. Subsequently it was determined that this secondary slot in the lower surface could be eliminated and a new position found for the flap (relative to the nozzle) which gave comparable results.

The optimum position for the flap is found experimentally for a range of flap angles (typically  $30^\circ$  to  $80^\circ$ ) by systematic testing within a geometric grid. It has been found by experience that performance of the flap depends upon the magnitude of the "jump" which the jet takes as it turns and attaches itself to the Coanda surface. This jump distance is defined by the parameters "z" and " $l_z$ " where the distance "z" is a measure of the gap and " $l_z$ " is a measure of the horizontal displacement of the Coanda surface relative to the nozzle.

Contour plots are made of constant augmentation on graphs of z vs  $l_z$  showing departure from optimum for each flap angle, an example of which is shown in Figure 7. Finally, a single pivot point is chosen which locates the flap close to its optimum position over the range of flap angles chosen.

Performance of the augmentor is defined in terms of net augmentation ratio  $\phi_s$ , where

$$\phi_s = \frac{\text{Measured thrust}}{\text{Isentropic thrust supplied to the pipe}}$$

Within the geometric confines and requirements for an augmentor flap, the value of  $\phi_s$  appear to lie in the range 1.3 to 1.6.

#### Effects of Forward Speed.

- **Optimization.** The procedures for optimization outlined in the previous section relate to static tests. Clearly it is considerably more difficult to carry out such an optimization in the wind tunnel because for one reason, the detailed performance of the ejector tends to become masked by the aerodynamic loads generated by the wing. In general, it has been found that a deflected flap, chosen on the basis of static tests, also gives best performance in the wind tunnel at values of blowing coefficient appropriate to take-off and landing.

- **Experimental Performance.** At first sight it would seem that the effect of speed on performance of the augmentor flap could be deduced from pressure surveys at the exit plane. Whereas this is possible, in practice it becomes very tedious and time consuming because of the variation in exit distribution from point to point along the span. However, by careful analysis of force data, some understanding of

performance has been obtained from various wind tunnel model tests.

There are two questions of fundamental interest. How does the augmentation ratio of the ejector vary with forward speed? and, to what extent does the thrust recovery hypothesis apply to the rather thick deflected jet sheet which issues from the augmentor flap?

Consider a wing blown with a jet strength defined by the coefficient  $C_{J1}$  which is based on the isentropic thrust supplied to the wing nozzle. Statically the flap generates a thrust corresponding to  $\phi_s C_{J1}$  where  $\phi_s$  is the net static augmentation ratio which takes into account both nozzle loss and ejector gain. Two multiplying factors are introduced, one which is a measure of the loss in thrust with forward velocity due to the fundamental characteristic of the ejector ( $K_V$ ) and one which is a measure of the departure from a performance corresponding to full thrust recovery ( $K_R$ ). Normally  $K_R$  would not be less than  $\cos \delta_f$ , where  $\delta_f$  is the angle of flap deflection.

Thus the thrust experienced in the wind tunnel would correspond to  $C_T = K_V K_R \phi_s C_{J1}$  when expressed in coefficient form. The highest value of  $C_T$  would result with full thrust recovery ( $K_R = 1$ ) and no loss of ejector performance with velocity ( $K_V = 1$ ) giving  $C_T = \phi_s C_{J1}$ . The lowest expectation might correspond to complete loss of augmentation ( $K_V = 1/\phi_s$ ) and a recovery factor  $K_R = \cos \delta_f$  giving  $C_T = C_{J1} \cos \delta_f$ . Assuming  $\phi_s = 1.3$  and  $\delta_f = 50^\circ$ , then the ratio of the maximum to minimum values of  $C_T$  would be  $\phi_s : \cos \delta_f = 1.3 : 0.64$ . It is quite possible to detect differences of this order of magnitude by analysis of wind tunnel test data especially since experimental values of  $C_{J1}$  of interest may reach as high as 2:5. However, the accuracy of the method may be open to some criticism.

An expression for thrust and drag is written as follows:

$$C_D - T = C_D - C_T = C_{D0} + \frac{C_L^2}{\pi A + r C_J} - K_V K_R \phi_s C_{J1}$$

The wind tunnel data is plotted in the form  $C_D$  vs  $C_L^2$  and the intercepts at  $C_L^2 = 0$  are plotted versus  $C_{J1}$ . The slope of this curve gives an experimental value of  $K_V K_R \phi_s$ . This process requires extrapolation of the  $C_D$  vs  $C_L^2$  to zero  $C_L$  which introduces some loss in accuracy. Alternatively, cross plots can be made at fairly high  $C_L$  (say 3 or 4) and thereby avoid the extrapolation. This latter process is justified in the belief that the value of "r" in the expression for induced drag is small (as suggested in reference 4), and much less than the value of two given by Spence.

A typical plot using the intercepts at  $C_L^2 = 0$  is shown in Figure 8 and is taken from tests of a quasi-2D model in the 6' x 9' tunnel at the National Aeronautical Establishment, Ottawa. The particular configuration shown has a value of  $\phi_s = 1.30$  whereas the factor  $K_V K_R \phi_s$  is shown to be 1.21. Thus  $K_V K_R = 0.93$  but it is not possible to determine whether the departure from ideal performance ( $K_V = K_R = 1$ ) is due to a reduction in  $K_V$  or  $K_R$  or a combination of both.

Results from the same model show that lift and drag data collapse using  $C_{J1}$  as parameter over the likely range of speed and blowing coefficients appropriate to operation in the STOL mode. (Figure 9.) A possible reason for the invariance of drag coefficient with speed (at constant  $C_{J1}$ ) is given in the following section.

- Theory. Much work has been carried out on ejector theory but it would appear to be of limited value to the designer (see conclusion one of reference 5). A theory has been developed by the author for use at de Havilland based on the original work of Von Kármán published in the Reissner Anniversary Volume. Space allocation does not permit this work to be presented here, nevertheless one comment is appropriate. The theory of Von Kármán accounts for a non-uniform inlet velocity distribution but assumes a uniform exit profile. His theory has been extended to account for a non-uniform exit profile (which is very much to the point from a practical point of view) and for the effect of forward speed. Theory then shows that the effect of forward speed is to reduce thrust to some new level in an asymptotic fashion. However, experiments indicate that the exit profile becomes more uniform as speed increases which, as is known, gives rise to an increase in augmentor efficiency. Thus these two effects are offset, one against the other, so that augmentor thrust seems to remain substantially constant over the speed range of interest for STOL operation. This result can only hold true if the exit distribution is non-uniform in the first place (that is, at zero forward speed), which tends to be the case for an augmentor flap because of geometric limitations which allow only a moderate mixing length between the two flap elements.

#### WING DUCTING AND AUGMENTOR PRIMARY NOZZLE

Ducting and Pressure Loss. The primary design objective of the ducting arrangement which supplies air to the augmentor flap is to avoid roll asymmetry in the event of engine failure. In the case of a twin-engined aircraft this can be achieved using a twin-slot nozzle arrangement with independent ducting from each engine. (See Figure 10.) Two possible arrangements for duct routing are shown in Figure 11. In the case of a four-engined aircraft, a similar duct/nozzle assembly may be used with each engine being independent; alternatively the by-pass flow may be fed to a common duct with a single slot nozzle (see Figure 12). In this latter case, since the engines feed a common duct, various two-way valves are required and the design scheme must account for starting engines individually, for engine failure and for the appropriate matching of nozzle area. One such scheme has been proposed by G. Wright of Rolls-Royce.

Experience has shown that, for an internal blowing system of the kind being considered, the pressure ratio lies somewhere between two and three depending upon choice of aspect ratio, thrust to weight ratio etc. At a pressure ratio of 2.5, the complete loss of one dynamic head represents a pressure loss of about 5% whereas a carefully designed right angle bend need only account for a loss given by  $\Delta P/q = 0.25$ . Calculations suggest that, for a typical duct installation, the overall pressure loss need not exceed 8 to 10% of total pressure which would correspond to a thrust loss of 4 to 5%. The large swept wing tunnel model provides one example of a ducting system for which pressure loss measurements are available (Figure 13). The flow experiences a sudden expansion and high loss where the compressor feeds into the plenum chamber but in this respect, it is not considered to be representative of a full scale aircraft.

**Nozzle Design.** Experience at de Havilland relates largely to a long thin type of nozzle which is "closely coupled" to the supply pipe and which is fed from one end. If the pipe is short (as in the case of the segment used for component test in the de Havilland research laboratory), then the inlet Mach number is quite low (say 0.05), conditions in the pipe are substantially plenum and guide vanes in the nozzle are straight and set normal to the pipe. In the large model which has been tested in the NASA 40' x 80' wind tunnel (Figure 1), the pipe inlet Mach number is approximately 0.3 falling to zero at the end so that curved guide vanes must be ~~designed accordingly~~. In the case of the swept wing for the large model, the complete semi-span is fed by a single pipe from root to tip and is tapered so as to maintain a constant pipe Mach number of approximately 0.29. Thus the jet issues from the swept nozzle at a constant angle to form a jet sheet which is in line with the free stream. Under these circumstances the guide vanes are curved and geometrically similar but do not act as turning vanes; they merely form a fairing to hold the duct/nozzle assembly together.

The efficiency of the nozzle has been shown to depend upon its perimeter/area ratio which, for long thin nozzles is inversely proportional to nozzle thickness 't' and independent of length. For a nozzle of thickness  $t = 0.25$  in., efficiency is typically about 0.95.

If the guide vanes are spaced reasonably for structural purposes they do not affect the nozzle efficiency to any appreciable extent. However, the disturbance or wake created by the vanes has been shown to increase the augmented thrust when operating as part of a complete ejector. Presumably these disturbances promote better mixing and can lead to improvement up to 10% in augmentation ratio as compared to a "clean" nozzle without guide vanes. This rather surprising result has led to an increase of interest in segmented or piccolo type nozzles.

Simple piccolo type nozzles have been constructed by squeezing a tube (Figure 14). This results in a slight fish-tail shape so that, at the edges, jets from adjacent nozzles tend to impinge on each other and create "humps" in the flow. Again, this promotes greater mixing and leads to an improvement in augmentation as compared to a "clean" slot nozzle. End fed pipes fitted with piccolo type nozzles have been designed without undue loss as compared to the vane type duct/nozzle assembly.

**Noise.** It has long been maintained that the ejector flap provides a means for noise attenuation for the following reasons:

- a) The long thin nozzle changes the characteristic dimension of the jet thus shifting the noise generated to higher frequencies when it is then more easily attenuated by the surroundings.
- b) The entrainment action of the ejector reduces the relative shearing velocity between the jet and surrounding air thus greatly reducing the fundamental jet noise which is dependent on the jet shearing velocity to the eighth power.
- c) The inner surfaces of the flap elements can be lined to absorb sound energy before it emanates from the exit of the ejector.

It is only fairly recently that some specific tests have been carried out to demonstrate this; for example see reference 6.

Further to this, research work is in progress at de Havilland to attenuate noise at the source by changes to design of the nozzle itself. Figure 15 shows an augmentor model mounted on an outside stand for purposes of noise measurements. Microphones are located at a radius of 25 feet at a height which corresponds to the centre line of the jet. Reductions in noise of up to 5 dB have been achieved by appropriate modifications to the nozzle as compared to a plain slot nozzle. This result helps to reinforce the view that noise generated by the augmentor flap can be attenuated so that it need not predominate relative to other noise from the propulsion system.

#### CHOICE OF POWERPLANT

The previous sections of the paper have described directly or indirectly some of the constraints placed upon the designer of the airframe on account of integration of the powerplant and wing. This section deals with some of the constraints on the powerplant itself.

The Requirement. Firstly, a reminder that the following comments apply to a transport type aircraft designed to operate in and out of a field length of about 2000 ft or less, having a wing loading about 75 lb/sq ft, an aspect ratio of 8 to 10 and requiring an installed thrust to weight ratio in the order of 0.4 to 0.5

Calculations have been shown that the percentage of blowing thrust to total thrust is about 35 to balance take-off and landing distances. The take-off distance considers failure of one engine at rotation speed and the landing field length is derived from the landing distance using the conventional factor of 1.67. Project design studies have shown that the ideal pressure ratio for blowing is approximately 2.5.

Three possible powerplant arrangements have been considered to suit this requirement.

- (1) Separate engines for propulsion and blowing.
- (2) A two stream twin spool engine with relatively high by-pass pressure ratio (to satisfy the requirement of duct sizing).

If low noise is a requirement, then cold to hot stream thrust is in the ratio of 80 : 20 approximately and all the cold flow is ducted to the wing where the noise generated by the fairly high pressure stream is attenuated by the augmentor flap. If low noise is not a primary requirement (say, for military application), then, in the case of the 80 : 20 engine only, about half of the by-pass flow need be ducted to the wing. Alternatively the engine may be like the Rolls-Royce Spey with a low by-pass ratio (i. e., less than one), but with a substantial hot thrust - by percentage about 70.

- (3) A three stream engine with fairly high by-pass ratio (about 5) which generates two by-pass streams, one at a low pressure ratio (say 1.2) and a second stream at about 2.5 for blowing.

Such an engine having either two or three spools would provide low noise levels and be suited to civil STOL application.

The preferred powerplant arrangement has not been clearly identified and might vary depending on the particular aircraft requirement.

Solution one tends to be favoured by the engine manufacturer but meets some resistance from potential operators because they prefer a single type of engine for ease of maintenance. Also, use of separate engines results in a high installed thrust to weight ratio and therefore in higher operating and powerplant first costs.

Solution number two requires a fairly simple two-spool engine but, if low noise is prescribed with this class of engine, then it presents the designer with the difficult task of accommodating a high proportion of the thrust in the wing. Nevertheless this solution seems to be preferred by Boeing and NASA (see references 6 and 7). If low noise is not specified, then the Spey type of engine seems reasonably well suited to the requirement.

On the basis of present knowledge, de Havilland considers the three-stream engine as the best solution for a quiet civil STOL airliner of the future. A comprehensive review of the various options is beyond the scope of the present paper and therefore the remainder of the section will be devoted to a discussion of the three stream engine.

For take-off there is a need to generate both blowing thrust and propulsive thrust whereas for descent there remains a need for blowing thrust only - in fact, propulsive thrust becomes an embarrassment and, if present, it must be "spoiled" either by vectoring ( $90^\circ$  deflection) or by partial reverse. However, for the baulked landing case, it is necessary to quickly regain the propulsive thrust to minimize loss of height and complete the "go-around". It is quite obvious that separate powerplants for propulsion and for blowing will provide the necessary flexibility, but if this solution is rejected, then it is desirable that the single type of powerplant remaining should have the capability of operating in different modes so as to generate thrust from the various streams in suitable proportion for take-off, for cruise and for landing. This implies an engine with variable geometry, that is, a variation in such parameters as fan blade pitch, guide vane setting or nozzle area.

For landing, the engine is required to operate as a turbo-compressor with a minimum of propulsive thrust. For take-off there is a requirement for both blowing air and propulsive thrust whereas for cruise, the primary requirement is for propulsive thrust and the blowing air should be zero or small. Furthermore, the propulsive thrust should be derived from a fairly low pressure stream (high by-pass ratio) in order to reduce noise for take-off and to achieve low sfc for cruise. This represents a demanding specification for the engine designer, because, in addition to meeting the requirement, every attempt should be made to achieve a substantial degree of commonality between the STOL blowing engine and other variants of the same engine for CTOL operation.

It is for the powerplant fraternity to consider this specification and to make a judgement as to practical feasibility. As far as the author is concerned, it is appropriate only to hint of some of the possible solutions which have arisen in the past few years as a result of collaboration between de Havilland Canada and Rolls-Royce.

**The Rolls-Royce Split-Flow Spey.** Before introducing some examples of a three stream engine it will be helpful to consider briefly the engine presently under development for the Buffalo/Spey research aircraft. (Figure 16.) Designated the Spey 801 SF, it is a version of the engine in which the by-pass flow has been ducted away separately and not allowed to mix with hot stream as in the case of the standard Spey. A Pegasus type nozzle has been fitted to vector the hot propulsive thrust. Figure 17 shows the level of thrust for the hot and cold streams for an engine of this general type and what would be the effect of introducing variable geometry, which in this case is a variation in primary or hot nozzle area. It can be seen that an increase in nozzle area greatly reduces the hot propulsive thrust while increasing the cold blowing thrust. Thus, by a relatively simple change, the engine behaves more like a compressor unit and therefore becomes more suited to the power demands for approach and landing.

Figure 18 shows a proposed pylon type installation for the Spey 801 SF with separate off-takes from the engine by-pass duct for blowing the wing and for cruise. Also shown is a variable primary nozzle with target type reverser.

**The Two-Spool Engine with Aft Fan.** Consideration has been given to an aft-fan version of the split-flow Spey. (Figure 19.) It could be argued that this is, in fact, a three-spool engine and thereby provides the required flexibility of operation. One option is to locate a thrust reverser/spoiler ahead of the fan with an effective nozzle area much greater than the standard value. Thus, in this mode of operation on approach, not only could the unwanted thrust of the fan be eliminated, but cold blowing thrust could be increased.

**The Three-Spool Engine with Front Fan.** It would seem that the Rolls-Royce three-spool engine (such as the Trent or the RB-211) lends itself naturally to the requirement for three streams and for variable geometry of a simple nature which could vary the relative strength of these streams to suit the three modes of operation described previously. Changes to nozzle area and guide vane angle would be appropriate in this case. (Figure 20.) Figure 21 shows an artist's impression of a proposed DHC 150-passenger Augmentor-Wing airliner based on the front fan engine. The design was prepared in response to the specification established by Eastern Airlines.

**The Two-Spool Engine with Variable-Pitch Fan.** The Rolls-Royce RB 419 engine represents a third proposal for a three stream engine. This engine is a derivative of the RB 410, which is a two-spool, high by-pass ratio design with geared front fan (for low noise). The 419 derivative takes air from the intermediate or I. P. compressor for flap blowing. During approach the variable pitch control is used to unload the front fan and transfer power to the I. P. compressor thus destroying propulsive thrust in exchange for blowing thrust. (Figure 22.) The engine provides the necessary flexibility to meet the requirements for cruise since it is possible to reduce or eliminate blowing thrust. Nevertheless there remain some penalties in terms of sfc and engine weight as compared to the simple high by-pass ratio engine such as RB 410.

## CONCLUSIONS

The paper has described some areas of interface between engine and airframe for an augmentor-wing jet STOL transport aircraft. Project studies based on large scale wind tunnel tests have shown that there are considerable benefits to be obtained in terms of performance from the concept of powered-lift. The practical realization of these gains depends upon the development of simple and reliable design schemes for integration of powerplant and wing. It would appear that, with the Augmentor-Wing concept, it is possible to combine safety and low noise with short field performance and thereby in these respects meet the requirements for civil STOL operation.

## ACKNOWLEDGEMENTS

The research programs described in this paper have been funded in part by The Defence Research Board of Canada, The Canadian Department of Industry, N. A. S. A., and de Havilland (Canada). The opinions expressed are those of the author.

## REFERENCES

- D. C. Whittley "The Augmentor-Wing: A New Means of Engine Airframe Integration for STOL Aircraft"  
Fourth ICAS Conference, Paris 1964  
AIAA Paper 64-574
- D. C. Whittley "The Augmentor-Wing Research Program: Past, Present and Future"  
Tenth Anglo-American Aeronautical Conference, Los Angeles, California 1967  
AIAA Paper 67-741
- D. C. Whittley "The Aerodynamics of High Lift Illustrated by Augmentor-Wing Research"  
Twelfth Anglo-American Aeronautical Conference, Calgary, Alberta 1971

- D. C. Whittley "Maximum Lift Coefficient for STOL Aircraft: A Critical Review"  
 CAL/USAAVLABS Symposium, Buffalo, New York 1966
- K. P. Huang "An Investigation of the Thrust Augmentation Characteristics of Jet Ejectors"  
 E. Kisielowski USAAVLABS Technical Report 67-8, April 1967
- J. E. Middlebrooks "The Evolutionary Development and Current Status of the Augmentor-Wing Concept"  
 H. C. Tinney S. A. E. Meeting, Los Angeles, California, October 1970  
 D. C. Whittley S. A. E. Paper No. 700812
- B. H. Wick "Turbofan STOL Research at NASA"  
 R. E. Kuhn Astronautics and Aeronautics, May 1971

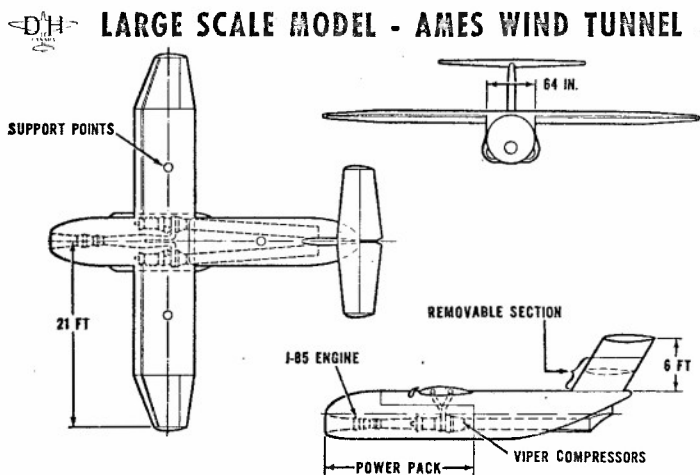


Figure 1

**AUGMENTOR-WING**  
**STRAIGHT WING MODEL IN THE AMES 40' X 80' TUNNEL**

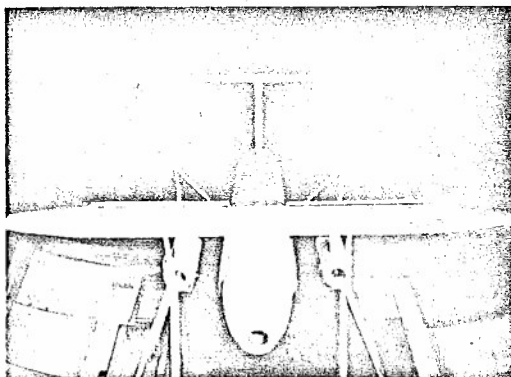


Figure 2

# AUGMENTOR-WING SIMULATION STUDIES

NASA-AMES VISUAL DISPLAY

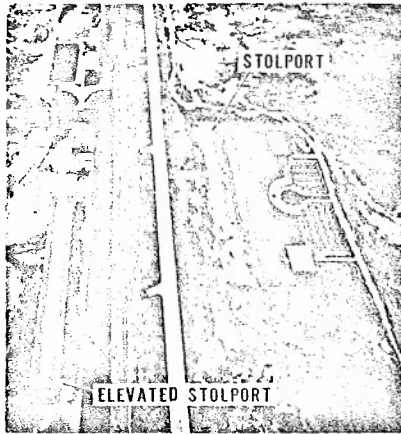


Figure 3



## AUGMENTOR-WING RESEARCH AIRCRAFT

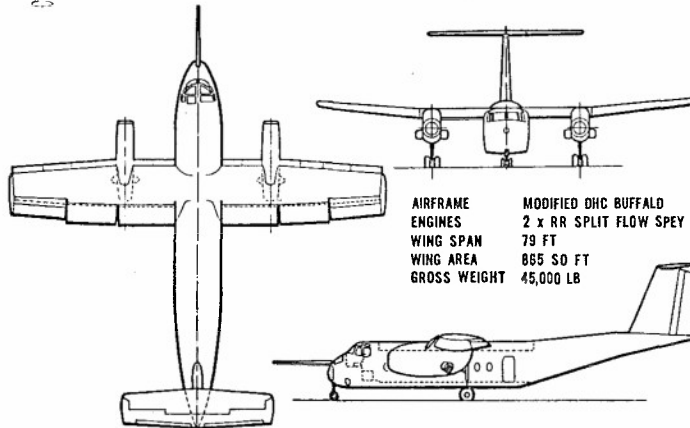


Figure 4



## AUGMENTOR-WING SWEEP WING MODEL IN THE AMES 40' X 80' TUNNEL

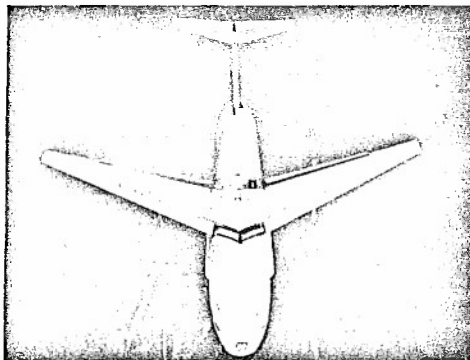


Figure 5

**AUGMENTOR-WING SECTION**

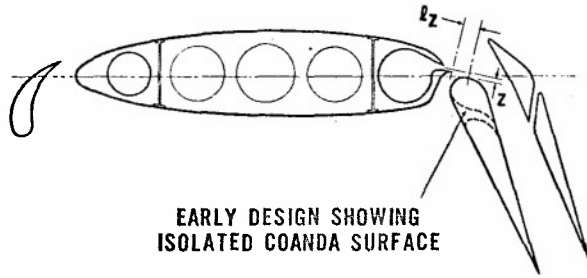


Figure 6

**GEOMETRIC OPTIMIZATION  
CONTOUR LINES OF  
AUGMENTATION LOSS**

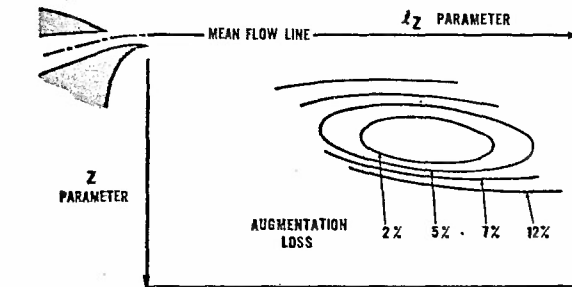


Figure 7

**AUGMENTOR PERFORMANCE  
AT FORWARD SPEED**

QUASI 2-D MODEL, FLAP ANGLE 40°

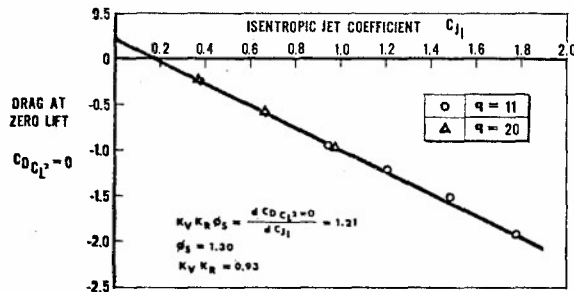


Figure 8

### COLLAPSE OF LIFT AND DRAG DATA

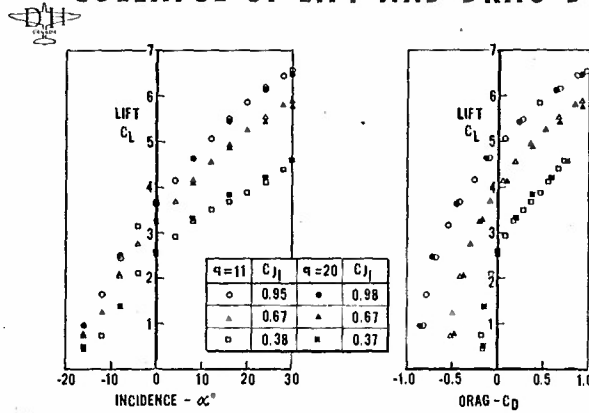


Figure 9

### SCHEMATIC SHOWING DUCT AND TWIN NOZZLE FOR AUGMENTOR FLAP

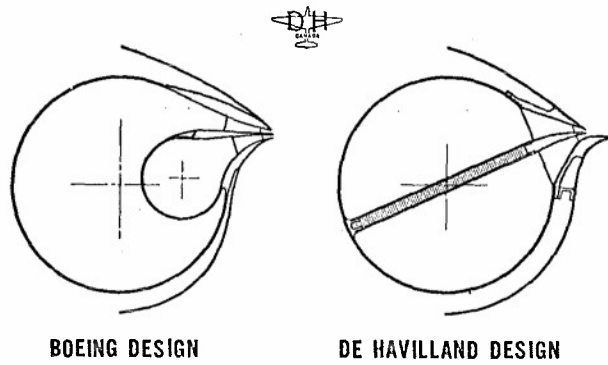


Figure 10

### DUCTING ARRANGEMENTS FOR TWIN ENGINE AIRCRAFT

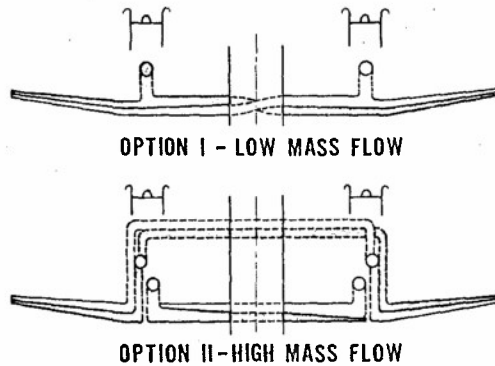
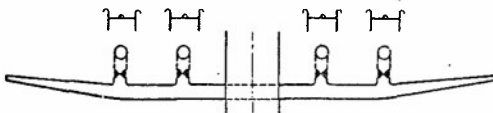
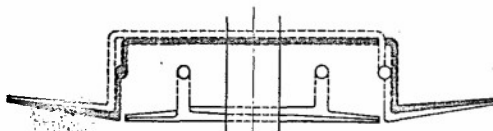


Figure 11

**DUCTING ARRANGEMENTS FOR FOUR ENGINE AIRCRAFT**



PLENUM DUCT SHOWING DIVERTER VALVE FOR EACH ENGINE



INDEPENDENT DUCTING WITH CROSS-OVER

Figure 12

**DUCT SYSTEM PRESSURE LOSS**

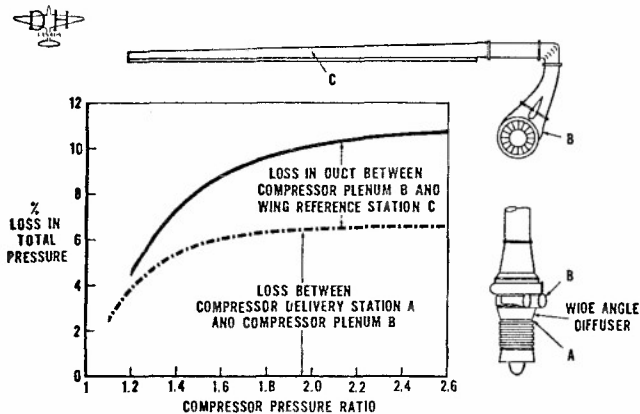


Figure 13

**SEGMENTED NOZZLE**

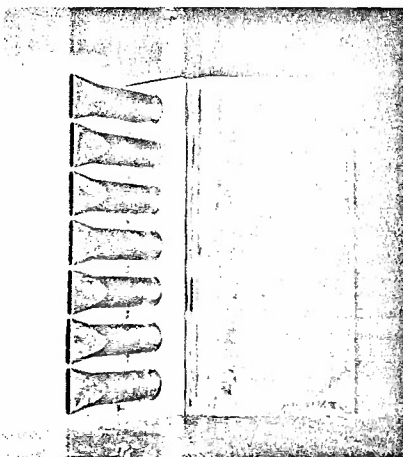


Figure 14

  
**TEST RIG  
FOR  
NOISE  
MEASUREMENT**

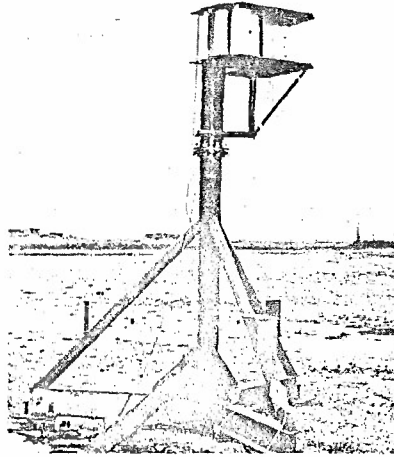


Figure 15



**ROLLS-ROYCE  
SPEY MK 801-SF**

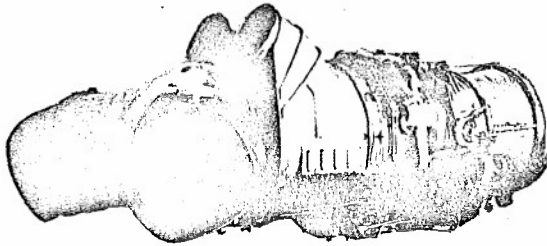


Figure 16

**TYPICAL THRUST OF SPLIT-FLOW ENGINE**

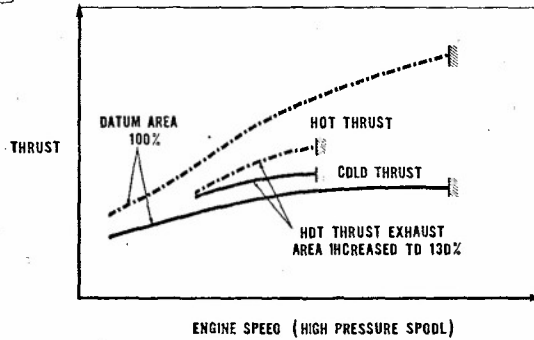


Figure 17

### PYLON MOUNTED SPLIT-FLOW ENGINE

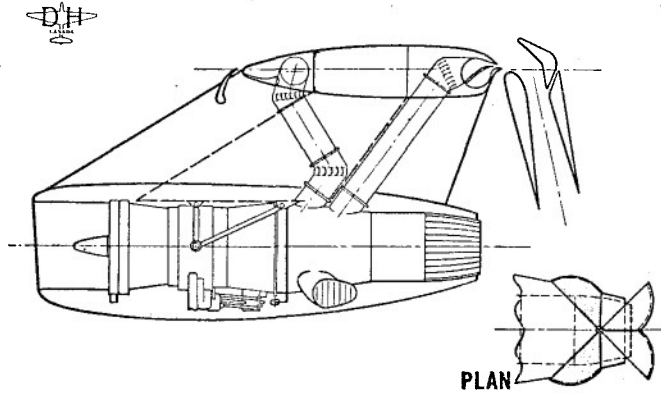


Figure 18

### PYLON AND NACELLE-AFT FAN ENGINE

CRUISE CONFIGURATION

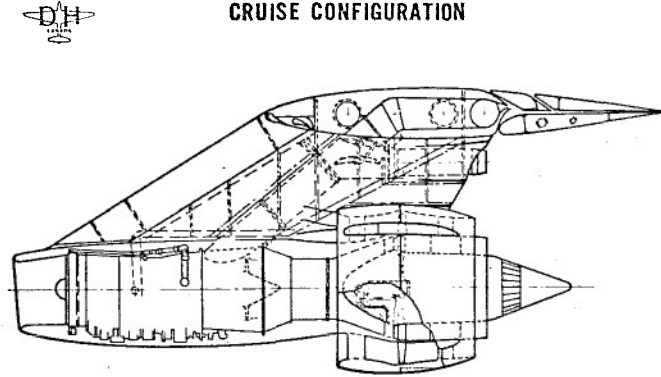


Figure 19

### FRONT FAN ENGINE TECHNOLOGY

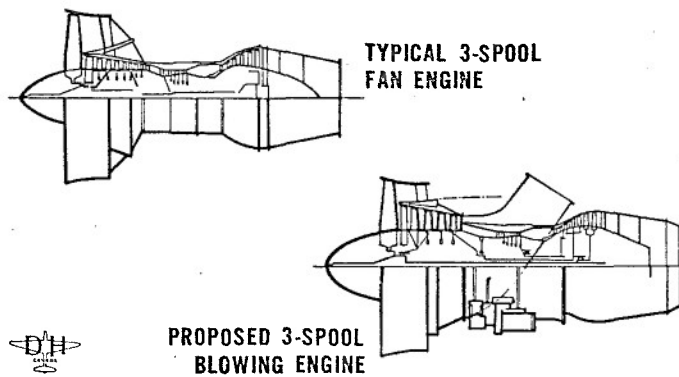


Figure 20

# AUGMENTOR-WING JET-STOL AIRLINER

150 PASSENGERS, FRONT FAN CONFIGURATION

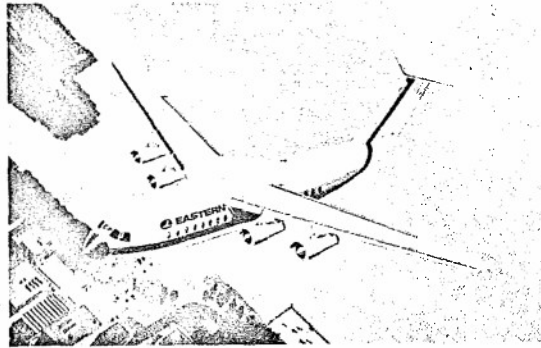


Figure 21



# ROLLS-ROYCE RB 419 TYPE PROPULSION/BLOWING ENGINE

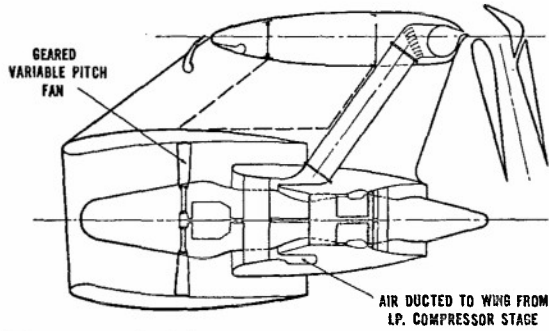


Figure 22

## RAPID MIXING NOZZLES FOR V/STOL APPLICATIONS

by

C.M. Chesters,  
 Installation Aerodynamics Research Engineer,  
 Rolls-Royce (1971) Limited,  
 Derby Engine Division,  
 Derby,  
 England.

## SUMMARY

If the maximum potential of a V/STOL aircraft is to be achieved it must be capable of operating from a variety of both prepared and unprepared sites. The use of high thrust to weight ratio jet lift engines with convergent or annular nozzles restricts this capability due to: ground erosion; debris and hot gas recirculation; and noise. Model and full scale tests have demonstrated the benefits to be obtained from the use of rapid mixing nozzles with acceptable thrust loss and engine length penalties. The scope of the investigation extended to an examination of the possibilities of thrust vectoring and of the performance of thrust augmentors using rapid mixing nozzles.

## SYMBOLS

See Figure 1

$P_L$  total pressure measured by a pitot tube mounted close to the ground surface

$P_L$  static pressure measured by a surface static pressure tapping

$P_J$  nozzle total pressure

$P_0$  ambient static pressure

$P_L - P_L$  ground dynamic pressure ratio

$P_J - P_0$

R radius from nozzle centre line

D diameter of circle with total nozzle area

$P_J/P_0$  nozzle expansion ratio

H nozzle exit to ground height

H/D non dimensional nozzle height

W maximum width of inter outlet fairing at outlet mid radius

L length from turbine exit plane to inter outlet maximum width

$L_J$  length from turbine exit plane to nozzle exit plane

$D_T$  Turbine exit diameter

$L_J/D_T$  non dimensional nozzle length

$\theta_{eq}$  Semi angle of circular section convergent nozzle equivalent in inlet area, exit area and length to one outlet.

$r_0$  radius of circle with outlet exit area

$r_c$  radius of circle circumscribing outlets

$r_c/r_0$  outlet spacing parameter

$\theta_C$  mean wall convergence angle for one outlet measured at outlet mid radius

$\theta_D$  mean wall divergence angle for one outlet measured on outlet major axis

$\theta_C + D$  Wall angle fishtailing parameter

Thrust efficiencies are expressed relative to an ideal one dimensional convergent thrust.

## 1. INTRODUCTION

The turbojet engine can be made to offer a high thrust to weight ratio within a small installed volume. Vertically or near vertically mounted jet engines have been used and are projected to provide direct lift. This lift can be used on its own to provide V.T.O.L. capability or it can be used to augment a lift vector from a propulsion engine or the wings to provide V/S.T.O.L. capability. In addition to high noise level the high temperature and velocity of the jet efflux pose installational and operational problems through:

- a) jet impingement onto the ground causing erosion with a subsequent risk of foreign object damage to the engine compressor and airframe
- b) thermal damage to the airframe and undercarriage
- c) ingestion of hot gas by the engine causing loss of thrust, reduction in handling margins and in the limit engine surge.

The erosion and some allied problems can be alleviated if the jet mixing process is accelerated. The rapid mixing nozzle achieves this by replacing the conical convergent engine nozzle with a number of smaller outlets having the same total area. In the absence of interference between the outlets and if the outlets are of circular section the rate of mixing is increased in proportion to the square root of the number of outlets (reference 1). A further increase in the rate of mixing can be achieved if the outlet periphery is increased through the use of non circular sections (reference 2).

The acceleration of the mixing process will tend to reduce the temperature of gas impingement onto the airframe. The effect of rapid mixing will reduce the velocity at a given streamwise distance from the nozzle more rapidly than the temperature. Thus encouraging the dominance of convective forces over the inertial forces. The effect of both of these factors on airframe and undercarriage thermal damage and on hot gas recirculation will be strongly dependent on the installation configuration.

In practice nozzle length is at a premium. Thus the outlets are placed around the turbine exit annulus. Interference, which increases with the number of outlets, then occurs between the outlets. It reduces the rate of mixing on boundaries between and within the outlets. In addition the pressure acting on the base area contained within and between the outlets is depressed causing a base thrust loss.

The overall nozzle diameter must also be consistent with the dressed engine diameter to ensure that engine spacing can be minimized for multi engine layouts. A further loss of axial thrust is caused by the increased internal surface area and asymmetry in the individual outlets.

Successful nozzle aerodynamic design lies in optimization between reduction in ground erosion through increased mixing and the thrust efficiency within the limitations imposed by nozzle length and diameter. The following detailed design trends have been established from a large number of both full and model scale tests carried out on a wide variety of rapid mixing nozzle types.

## 2. GROUND EROSION

The ground surface structure (including both the material and the condition), and the jet temperature and velocity close to the ground are the factors likely to affect ground erosion. Dent in reference 3 describes the test technique used to measure erosion. The main parameter used is the time between jet impingement onto the surface and the onset of erosion, or limiting residence time.

The results of tests carried out on a wide variety of ground surfaces show this to be a critical factor. Water cured concrete and linked aluminium track way were undamaged by multiple take off cycles. Air cured concrete suffered surface flaking. With asphalt the tar bonding melted allowing rapid erosion of the aggregate. However for versatile military operation deployment to unprepared grass land is desirable. Thus the majority of testing was carried out using consolidated grass typified by the grass land at Hucknall airfield.

Consistency of a series of full scale tests carried out under summer (1962 and 1965) and winter (1965) conditions, and using the exhaust from an RB.108, unheated Avon (740°C) and reheated Avon (1000°C), indicate that for this consolidated grass neither the annual variation in surface condition and surface moisture content, nor the jet temperature are critical parameters. A possible explanation of this is that the surface is reduced to a friable state in an immeasurably short time. The onset of erosion being determined by the jet velocity adjacent to the surface.

Comparison between the ground dynamic pressure ratio for a full scale conical convergent nozzle and a 9 outlet rapid mixing nozzle is shown on Figure 2. A substantial reduction in the ratio can be noted for the rapid mixing nozzle. This gave a marked increase in limiting residence time (from less than 1 sec for the convergent nozzle to 100 secs for the rapid mixing nozzle at an expansion ratio of 2.0). The agreement between full and a  $\frac{1}{4}$  linear scale model test is also illustrated.

The ground dynamic pressure measurement was derived from surface static pressure tappings and pitot tubes mounted at a fixed distance from the ground. The instruments were located on a radial line beneath the major axis of one of the outlets. Use of this technique provides a reduction of dynamic pressure close to the nozzle axis. This is attributed to a cumulation of angular effects on the instruments, the curvature in the flow, and a somewhat arbitrary total pressure measurement. This measurement may lie in the ground boundary layer, the turned under mixing layer from the inner boundaries of the jets, the core region or the ambient mixing region. Figure 3 diagrammatically illustrates the flow processes involved.

The measurement does not take account of the circumferential variation in dynamic pressure away from the outlet major axis. Model testing showed that this simple technique provides a parameter which is a maximum at a non dimensional radius of 1.5. This corresponds to the region at which erosion is first observed and is most rapid.

Figure 4 illustrates the relationship between the ground dynamic pressure ratio at non dimensional radius of 1.5 and limiting residence time. The large scatter in the results is attributed to the simplified description of the ground dynamic pressure ratio and the difficulty in assessing the exact point of the onset of erosion particularly at the higher nozzle dynamic pressures. The lack of a consistent trend with jet temperature supports the hypothesis that this is not a dominant parameter.

Assuming there to be a causal relationship between the ground dynamic pressure ratio and ground erosion then the effect of rapid mixing nozzle geometry on the ground dynamic pressure ratio has to be established. Cox and Abbot in reference 4 show that for a convergent nozzle the maximum dynamic pressure at a radial position away from the nozzle axis in the jet spreading over the ground, is a fixed proportion of jet exit dynamic pressure irrespective of the nozzle non dimensional height. They also show that close to the nozzle axis the velocity is in agreement with the velocity decay rate at the non dimensional height reported by Squire (reference 1) and others. Even allowing for the limitations in the measuring technique the rapid mixing nozzles do not exhibit this behaviour, Figure 5. The decay rate is more rapid than would be expected from a convergent nozzle of the same total area. At lower values of non dimensional height it is less rapid than would be expected from a convergent nozzle equivalent to one outlet yet more rapid at higher values of non dimensional height. The decay rate is strongly non dimensional height dependent.

This behaviour can be ascribed to the number of outlets (affecting the core length), the radius of the circumscribing circle (affecting the amount of jet boundary free to mix with ambient air), the gully geometry between the outlets (affecting the extent of mixing on the jet boundaries between and within the outlets) and the radial corrugations produced by the outlets in the flow over the ground. It has not yet been found possible to provide an exact description of the complex situation in terms of geometric parameters. However the use of the simple parameter, inflow area ratio, gives the correlation on Figure 6. Although the curve will vary with non dimensional nozzle height, the trend is valid for all heights. The low number of outlets and the large ventilation inflow area occurring at high values of airflow ratio give the highest attenuation of ground surface dynamic pressure. Less attenuation occurs as the inflow area ratio is decreased but at a value of .2 about 75% of the possible attenuation is achieved.

### 3. ISOLATED NOZZLE DESIGN AND PERFORMANCE

The three factors affecting nozzle performance are:-

- a) Pressure perturbation at turbine exit plane
- b) Discharge coefficient
- c) Thrust efficiency. This can in turn be divided into base thrust loss and residual or internal thrust loss.

These factors are affected by nozzle expansion ratio and the swirl in the flow at nozzle inlet (or turbine exit). The effect of inlet swirl is to decrease the discharge coefficient and thrust efficiency. The effect on the rapid mixing nozzles is less marked than for a convergent nozzle due to the straightening effect of the inter outlet fairings and the discrete nature of the outlets. Comparisons and correlations of nozzle performance are presented at a nozzle expansion ratio of 2.0 and at an inlet swirl of  $10^\circ$  relative to the performance of a convergent nozzle at the same expansion ratio but with  $0^\circ$  swirl. If this convergent nozzle were subject to  $10^\circ$  swirl at this condition it would suffer a thrust decrement of 1.6%. Use of straightening vanes within the nozzle of course reduces this decrement.

The order of the pressure perturbation at the turbine exit plane is equal to the number of outlets. The amplitude is largely independent of nozzle expansion ratio and mainly depends on the inter outlet fairing width and the separation between this fairing and the turbine outlet plane, as shown on Figure 7. This factor has an effect on the fatigue life of the turbine. It is necessary to ensure that the back pressure perturbation does not excite any natural frequency in the turbine.

The effect of swirl is to produce a phase change between the pressure perturbation at the turbine outlet plane and the inter outlet fairings. This feature is also important in the alignment of the rapid mixing nozzle outlets so that any hot streaks generated by the combustor are directed through the outlets rather than onto the inter outlet fairings.

The variation of nozzle discharge coefficient with expansion ratio affects the starting and acceleration performance of an engine. The absolute level of discharge coefficient at operating expansion ratio affects engine matching. With the rapid mixing nozzles the variation with expansion ratio is less marked than for a convergent nozzle. Thus an engine that will start and accelerate with a convergent nozzle will not be adversely affected by fitment of a rapid mixing nozzle. If the expansion ratio is defined as the ratio of nozzle total pressure to outlet exit pressure, taking account of the variation of static pressure around the outlet periphery caused by the base depression, the absolute level of discharge coefficient is comparable to that of an equivalent circular section convergent nozzle defined by the inlet area, exit area and length of the outlet.

The base depression is another way of expressing the efficacy of ventilation to the mixing region within and between the outlets. However in addition to the factors already discussed with respect to ground dynamic pressure attenuation the distribution and amount of base area within and between the outlets contributes to the base thrust loss. Again it has not yet been possible to determine an exact relationship between the numerous factors affecting this complex situation. Correlation has been achieved by the use of a simple radius ratio parameter Figure 8. High values of this parameter give low base thrust loss, ultimately at unity the value is zero equivalent to a single convergent nozzle. Low values give increasing thrust loss as the ventilation of the base is reduced by closer spacing of smaller outlets around the nozzle periphery. A reasonable compromise appears at a radius ratio of around .2 with a base thrust loss of about 1%. The residual axial thrust loss, or internal thrust loss, is dependent on the individual outlet design. It is inherent in the rapid mixing nozzles due to the outlet asymmetry. It is increased as the outlet shaping is made more asymmetric to increase the outlet periphery and to increase the ventilation air inflow between the outlets. A simple description of the outlet asymmetry is provided by the wall angle fishtail parameter, Figure 9.

The scatter of the results indicates that this parameter requires supplementing to provide an adequate description of the wall shaping for the complex outlet shapes tested. High values of the wall angle parameter in general occur with a small number of outlets, low values with a large number of outlets. Thus it should be noted that the trend for the internal loss is in direct opposition to the trend for the base thrust loss and the ground erosion behaviour.

At this point it is worth examining the performance of a near optimum 9 outlet rapid mixing nozzle, with attention paid to the detailed design of the outlets.

	Rapid Mixing	Convergent nozzle, with no internal straightening vanes.	
Expansion Ratio	2.0	2.0	2.0
Inlet Swirl	10°	0°	10°
Limiting residence time	20 msec	< 1 sec	< 1 sec
Ground dynamic pressure ratio	.28	1.0	1.0
H/D = 3.0 R/D = 1.5			
Thrust loss	1.5% base 3.0% internal 4.5% total	0% base 1.5% internal Datum total	1.5% total

Although at first sight the thrust losses appear to give a large penalty it should be noted that in practice the alternative is unlikely to be a convergent nozzle but an annular nozzle of the same length as the rapid mixing nozzle. In the latter case the thrust loss penalty is marginal.

This however only relates to an isolated installation. This is typified by a stowable lift engine swung out from a fuselage for use, when sufficiently remote from the fuselage to be out of interference effects. The rapid jet decay induced by mixing can become an embarrassment if the inflow is impeded by either surrounding aircraft structure or adjacent jets. Figure 10 illustrates this. The total thrust loss of an isolated nozzle is increased by a staggering 33% when it is surrounded on all sides. This would be the condition if it were mounted in an unventilated multiple engine lift bay, or aircraft fuselage, with side doors opening only sufficiently to allow ingress of the jet and with adjacent end walls or jets.

Reduction of this installation loss to 4.5% can be achieved by allowing ventilation air to pass through the bay and around the nozzle, around the top of the doors and by opening the doors as far as possible. The need for this, increases the number of factors to be considered in the engine - nozzle - installation design compromise to include the additional weight and mechanical complexity required for bay installations.

#### 5. THRUST AUGMENTATION POSSIBILITIES

The rapidity of achieving mixing with ambient air may however be used to provide thrust augmentation by surrounding the nozzle with an augmentation tube. If the inlet to the tube is well designed and the inflow to it unrestricted considerable augmentation of the bare nozzle thrust can be achieved at the expense of weight and installed volume (or mechanical complexity if the tube is made telescopic).

Figure 11 summarises the results of a series of tests in which the tube length, diameter and inlet dimensions were systematically varied. A volumetric increase of 2.5 gives a thrust gain of 5% over the basic nozzle thus bettering the reference convergent nozzle with no inlet swirl and no augmentor tube by 2%.

The use of an augmentor tube also provides a surface for acoustic lining. This would enhance the marginal noise attenuation observed during the full scale tests (a reduction of 5dB for a 9 outlet nozzle from 154.5dB for a single convergent nozzle measured at a height from the ground of 7 ft, 3 ft 6 inches below the nozzle and 9 ft radial distance from nozzle).

As thrust augmentation relies on efficient mixing of the jet to induce secondary flow, achievement of a high thrust augmentation should not greatly detract from the ground erosion performance.

## 6. VECTORING POSSIBILITIES

An alternative to the obvious approach of rotating the engine-nozzle assembly to give thrust vectoring and hence accelerative or decelerative vectors in addition to lift, is to mount the engine at a compound angle relative to the aircraft.

If the nozzle is mounted to the engine via a wedge type elbow a wide degree of thrust vectoring can be achieved simply by rotating the elbow. (Figure 12) at the expense of a high single order turbine back-pressure and side loads. Model tests (Figure 13) illustrate that the increased thrust loss for the addition of the elbow is of the order to 1.5%.

## LIST OF REFERENCES

- 1) H.B. Squire - Jet flow and its effects on aircraft, Aircraft Engineering Vol. 22, No. 253 March 1950.
- 2) N. Rajaratnan - Three - dimensional free jets, and K. Subramanga Journal of the Royal Aeronautical Society, Vol. 71 December 1967 pages 858, 859.
- 3) J. Dent - Paper read at the 27th meeting of the AGARD Flight Mechanics panel in Rome 11 - 12th October 1965.
- 4) M. Cox and W.A. Abbott - Studies of the flow fields created by single vertical jets directed downwards N.G.T.E. Memorandum M390.

## ACKNOWLEDGEMENT

I would like to acknowledge the debt owed to all my colleagues who have taken part in the execution of the tests described in this paper.

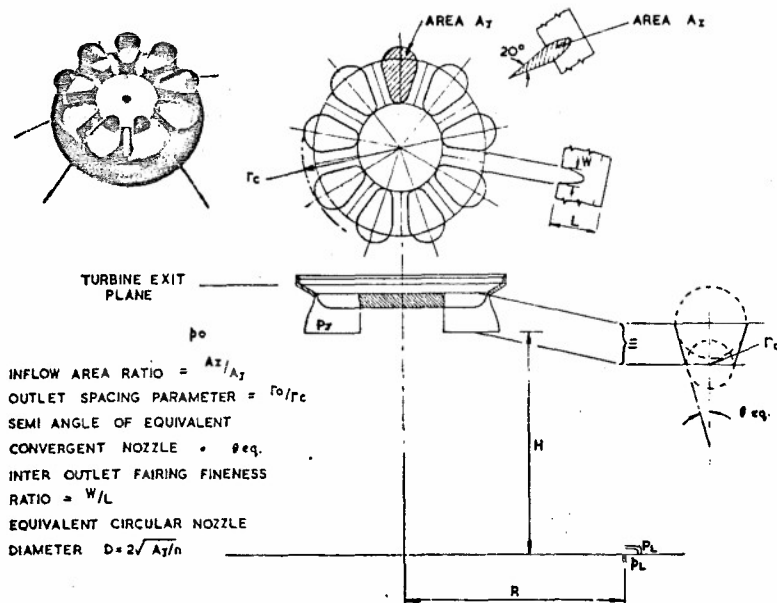


FIG. 1. DEFINITION OF SYMBOLS

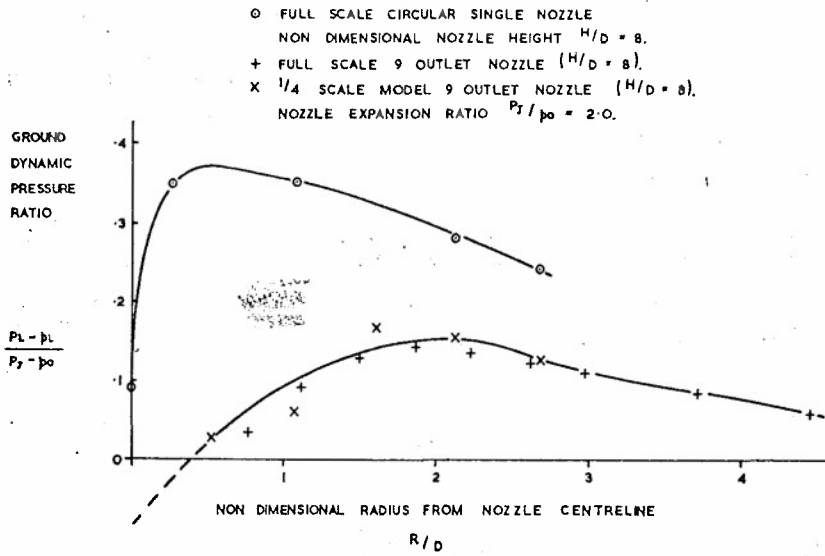


FIG. 2. GROUND DYNAMIC PRESSURE RATIO.

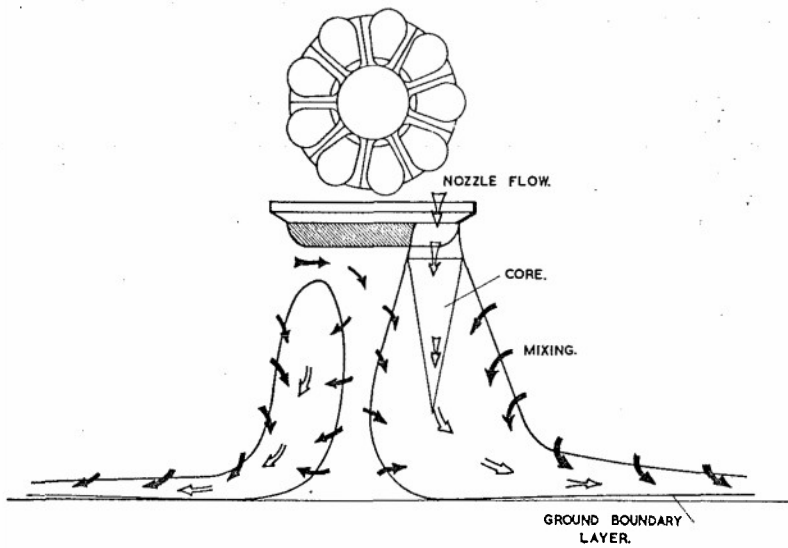


FIG. 3. RAPID MIXING NOZZLE FLOW PROCESSES.

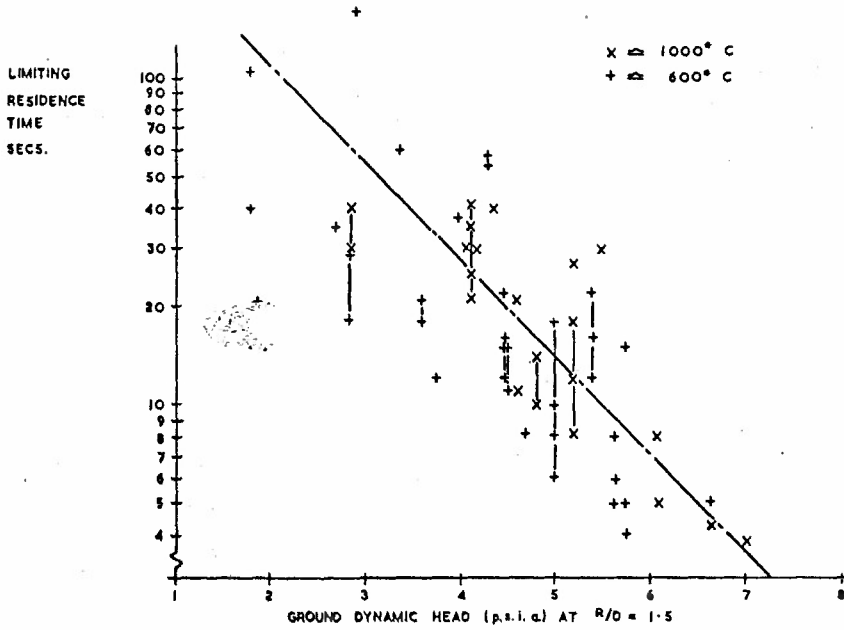


FIG. 4. LIMITING RESIDENCE TIME.

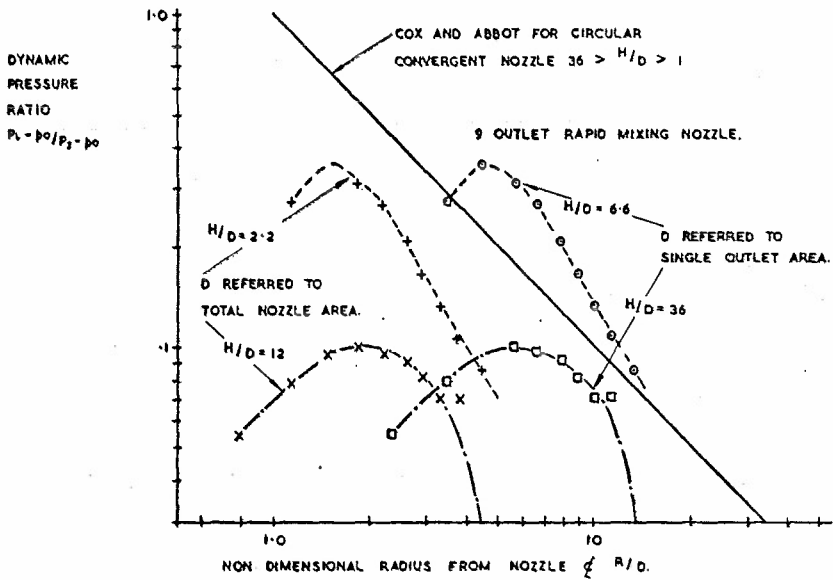


FIG. 5. GROUND DYNAMIC PRESSURE RATIO COMPARISON WITH CONVERGENT NOZZLE.

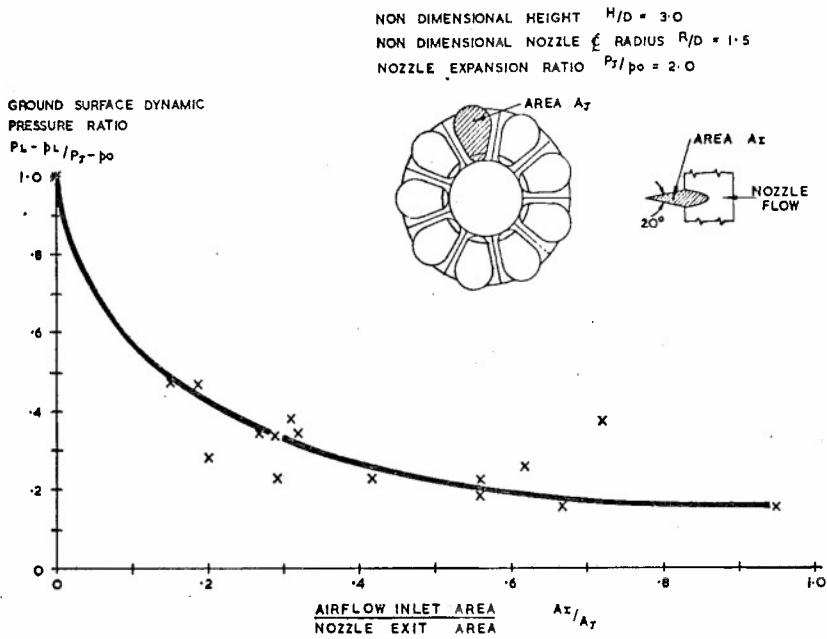


FIG. 6. EFFECT OF INFLOW AREA RATIO ON GROUND DYNAMIC PRESSURE

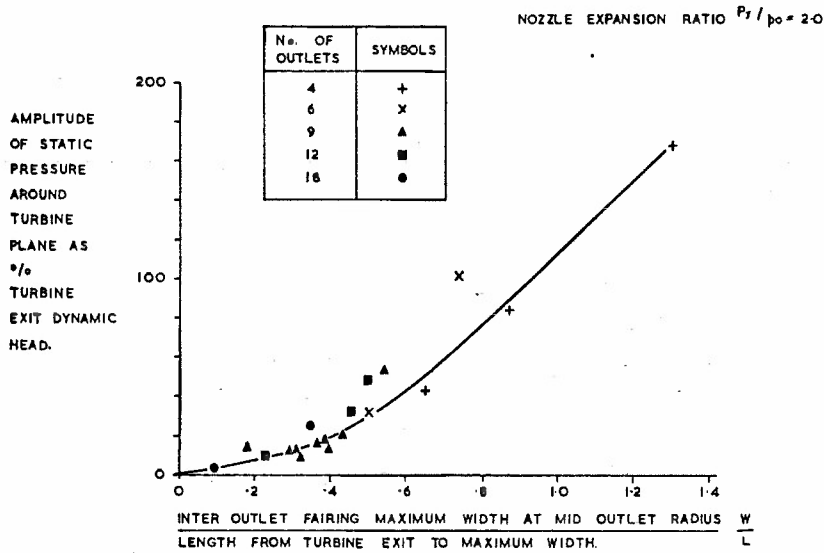


FIG. 7. PRESSURE INFLUENCE ON TO TURBINE.

NOZZLE EXPANSION RATIO  $P_T/p_o = 2.0$   
 10° INLET SWIRL.

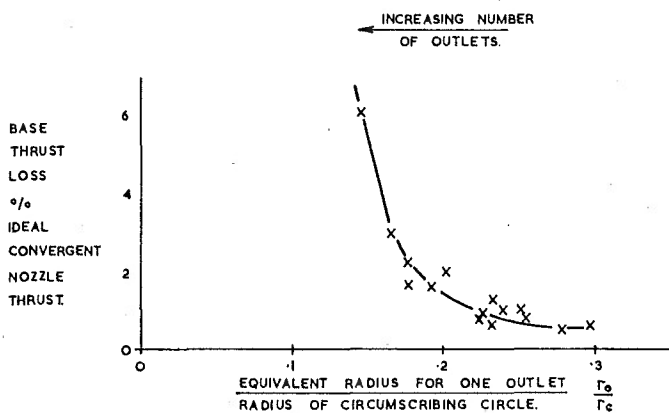


FIG. 8. BASE THRUST LOSS.

$\theta_c$  MEAN WALL CONVERGENCE ANGLE MEASURED AT OUTLET MID RATIO.  
 $\theta_o$  MEAN WALL DIVERGENCE ANGLE MEASURED ON OUTLET MAJOR AXIS.

NOZZLE EXPANSION RATIO  $P_T/p_o = 2.0$   
 10° INLET SWIRL.

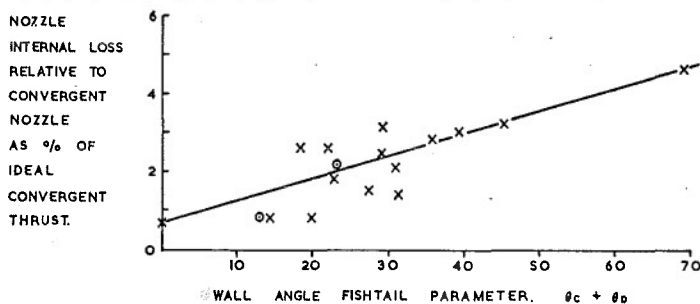


FIG. 9. INTERNAL AXIAL THRUST LOSS.

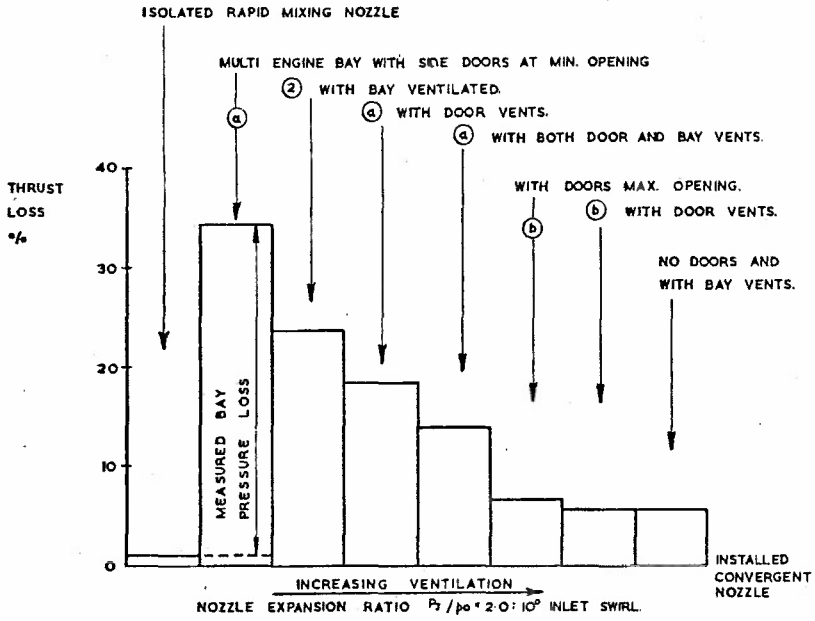


FIG. 10. MULTI ENGINE BAY INSTALLATION PENALTIES.

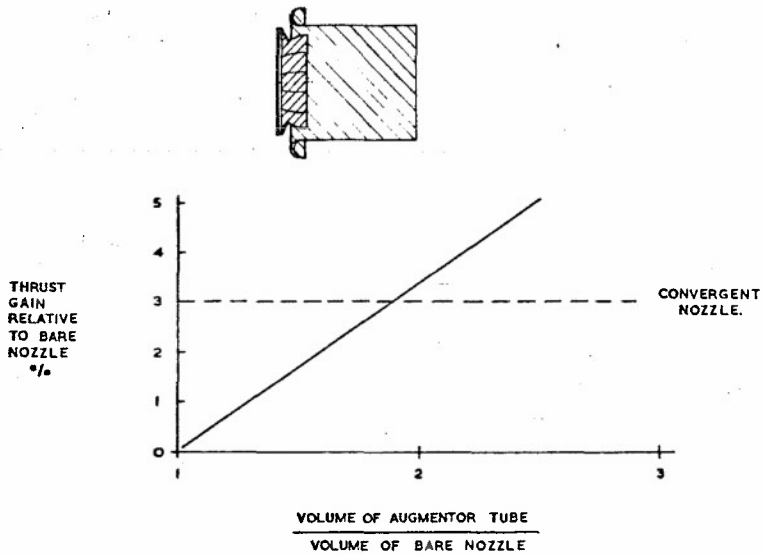


FIG. 11. THRUST AUGMENTATION POSSIBILITIES.

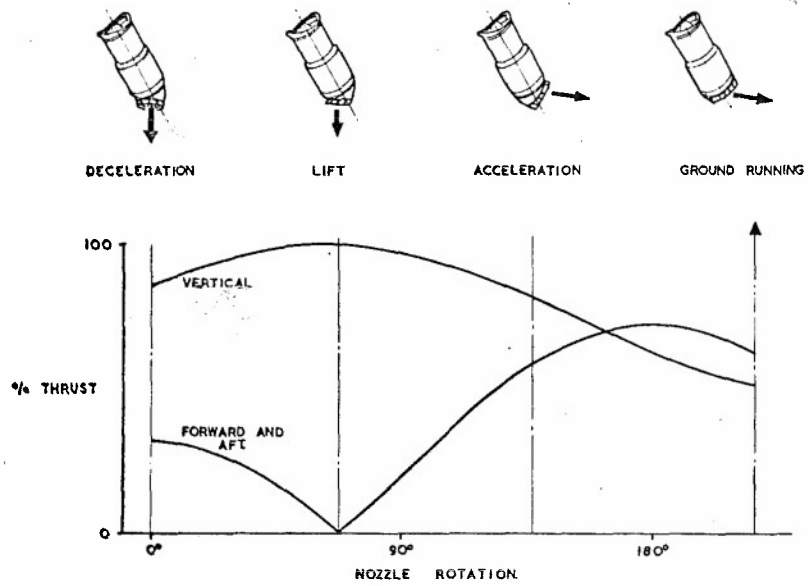


FIG. 12. THRUST VECTORING.

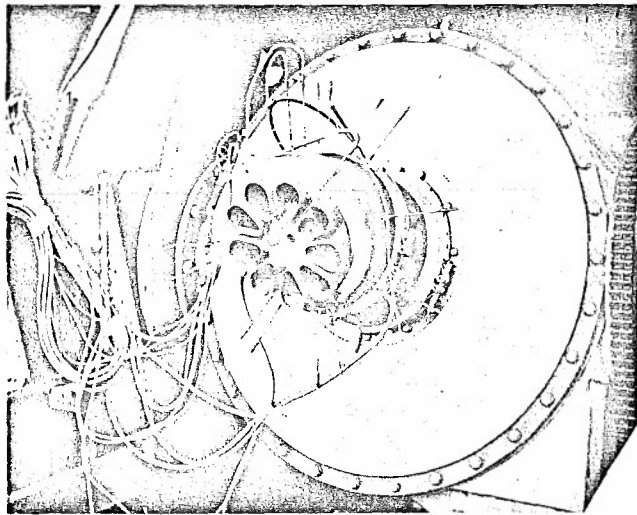


FIG. 13. MODEL TEST ON RAPID MIXING NOZZLE TO DEMONSTRATE VECTORING CAPABILITY.

## THE PROPULSION JET OF A VTOL AIRCRAFT

Dipl.-Ing. E. Schwantes

DEUTSCHE FORSCHUNGS- UND VERSUCHSANSTALT

FÜR LUFT- UND RAUMFAHRT E.V.

Institut für Luftsaugende Antriebe

Braunschweig, Germany

## SUMMARY

The three regions of a VTOL propulsion jet, the free jet, the wall jet and the zone of separation of the wall jet from the ground, due to wind-effects and buoyancy forces are investigated with a three dimensional model-jet with critical nozzle pressure ratio and temperatures up to 1000°C above ambient at the DFVLR Braunschweig. Behind the convergent nozzle the jet accelerates up to supersonic velocity maintaining in the core nearly 5 nozzle diameters. Because of the lower turbulence of the jet with high speed the decay of the jet and the three dimensional spread are lower than those of the jet with small nozzle velocity. At the hot wall jet there is a strong influence of the nozzle distances from the ground on the velocity profiles. The decisive parameter to characterize the recirculation flow is the radius of separation of the wall jet from the ground. The behaviour of the radius of separation for different jet parameters and several wind velocities is represented.

SYMBOLS

D	nozzle diameter
H	distance of the nozzle exit from the ground
h	distance from the ground
M	mach number
$\dot{m}$	mass flow
R	radius of the wall jet, beginning at the stagnation point
r	radius of the free jet, beginning at the centre of the jet
$R_{0,5u_{\max}}$	radius on which half the value of the axial velocity appears
T	absolute temperature
U,u	component of velocity in x-direction
V	wind velocity
$V_1$	wind velocity at 1 m above the ground
$V_z$	wind velocity at the distance z from the ground
x	coordinate in jet direction
z	vertical coordinate
$\theta$	temperature minus ambient temperature
$\rho$	density
$\varphi$	angle

INDICES

O	condition in the nozzle exit
u, <sup>*</sup>	ambient conditions
Stau	condition at the stagnation point
max	maximum value or value at axis
ges	total value

## 1. INTRODUCTION

The propulsion jet of a VTOL-lift-engine spreads behind the engine nozzle as a hot jet. With critical nozzle pressure ratio the core flow accelerates up to supersonic velocity and keeps it for about 5 nozzle diameters (fig.3). Reactions of the ground on the development of the free jet exist only up to 2 nozzle diameters above ground referring to Gauntner-Livingood-Hrycak [11] and Tani-Komatsu [26]. Impinging on the ground the free jet is deflected to the wall jet and spreads radially to all directions. By mixing with the surrounding air the wall jet increases its mass and reduces its velocity. The static underpressure which exists just as in the total free jet, makes the wall jet adhere to the ground against the thermic buoyancy (Coanda effect). Only when the static underpressure becomes weaker than the buoyancy, the wall jet separates from the ground. If there is a wind flow against the wall jet the point of separating will be reached earlier. The separated wall jet is taken back to the engine inlet by the wind flow and the sinking effect of the wall jet. This back flow of hot air is a dangerous recirculation flow, as it causes operating-troubles at the engine and propulsion losses. For calculating the recirculation flow the mechanism of wall jet spreading must be known. According to [22] there have been published only a few investigations about hot wall jets up to now, e.g. Cox-Abbot [7], Hall-Rogers [13], Higdon-Kelly-Wainwright [15]. But they give no data about the growth of mass flow of the wall jet which is very important for calculating the recirculation. Nearly all the fundamental investigations deal with undercritical jets. But at the lift-engine the jet leaves the nozzle with supersonic velocity and has a jet spreading very different from that of the jet of low velocity.

That is why there have been made extensive investigations on a single VTOL propulsion jet with a nozzle temperature up to 1000°C and a critical nozzle pressure ratio at the DFVLR. We started with free jet measurements without ground influence. Then we investigated the wall jet and its separation from the ground due to wind and the secondary flow field.

## 2. TEST SETUP

The investigations of VTOL-propulsion jets have been taken place on the Bodeneffekt-Versuchsanlage of the DFVLR Institut für Luftschiff-Antriebe in Braunschweig, which is described in [8]. A rotary compressor served as an air generator delivering 1 kg/s at a maximum pressure of 3 atmospheres absolute. Through a pipe system of 10 m length (113 mm internal diameter) the air was delivered to a combustion chamber and there heated by combustion of JP 1. The pipe for the hot gas behind the combustion chamber consisted of a cylindrical pipe of 2 m length (80 mm internal diameter), made of stainless steel with an extremely smooth surface and interchangeable test-nozzles at the exit so that the free jet exhausted horizontally. The passage from the hot-air-pipe to the nozzle was so smooth that the internal flow was not disturbed in any way.

For the free jet investigations five convergent nozzles have been used, each of them with a different shape. Three of them had a bell-shaped contraction area followed by a cylindrical exit with a length of 2,1 or 0 diameter. Then there was used a cone-shaped nozzle corresponding to the engine nozzles of present usage if not considering the hub core. Further there was an orifice with a very short cylindrical exit under the investigated nozzles. The exit diameter was 50 mm  $\pm$  0,05 mm at each nozzle. The internal outlines ended sharp edged at the nozzle exit. The measurements of the free jet have been made with a probe rake which could be moved by a remote-controlled movable support along the jet axis. On the probe rake 31 pitot tubes and 20 NiCr-Ni thermocouples were distributed over a width of 200 mm.

For the wall jet investigations the hot-air-pipe behind the combustion chamber consisted of a steel pipe of 1 m length and an internal diameter of 113 mm, on the end of which there was fastened a test nozzle with the opening facing to the ground (fig.2). The nozzle diameter converged from 80 mm to 50 mm at the exit. The nozzle had a cylindrical exit of 50 mm. A measurement of the total head in the nozzle exit area delivered a satisfactory rectangular profile and made expect an axially symmetrical wall jet. The wall jet has been investigated on a platform of 12 m<sup>2</sup>, the distance of which was hydraulically variable to the nozzle. There was a great problem in choosing a proper material for the platform surface. On the one hand it had to be like the concrete ground as the natural starting-place of VTOL-aircrafts and on the other hand the material had for a longer time to bear the enormous erosion effect due to the hot jet with a temperature of up to 1000°C and its supersonic velocity. After many experiments we thought Eternit-plates most appropriate, 25 mm thick with a heat-shield of Promabest (silicon-asbestos) 200 mm thick. We used them for all our tests. After 30 minutes blowing-time the Promabest-plates have always been changed. The roughness of the platform surface was below 0,3 mm.

The wall jet measurements have been carried out with a remote-controlled movable support, which could be moved on rails beside the platform. After an examination of the axial symmetry of the wall jet we have taken measurements with the probe rake only in one plane at right angle to the pipe axis. On the probe rake of 268 mm length there were distributed 20 pitot tubes made of V2A-steel and 20 thermocouples.

The wind influence for the investigations of the separation of the wall jet has been provided by a blower producing a large volume of a spinless wind flow by means of straighteners, the exit of the blower having a rectangular cross section with a width of 2 m.

The visualization of the VTOL-propulsion jet was obtained by means of a light-intersection-method (fig.8). For this purpose an incombustible contrast powder was blown in by compressed air and gave white colour to the propulsion jet. In the dark a light-plane-projector with a power of 6000 W lit an arbitrary plane of only a few millimeters thickness of the whole flow field, so that the flow in this plane was visible to an observer looking rectangular to it. The flow was photographed by a camera of high intensity and an aperture of diaphragm of 1:0,95. The exposure time amounted to 1/15s.

The record of the measured data was made by means of a digital data logger asking the test results with a speed of 5 measuring points per second and registering them by means of a punch. The pneumatic scanner for the probe rake worked only with 3 Hz because of the longer transient time.

### 3. THE FREE JET

If today you are looking for facts about the spread of the engine jet you often must refer to 20 or 40 years old investigations of free jets. These older fundamental reports about the spread of free jets deal nearly almost with those of low temperature and low nozzle exit velocity. But the jet of a turbo engine leaves the nozzle with supersonic velocity and high overtemperature and makes expect a jet spread which is different from that of the incompressible cold jet. Recent American reports (Laurence [18], Higgins-Wainwright [14]) confirm, that the nozzle mach number and the nozzle temperature are important parameters for jet spread.

At the DFVLR we have made extensive fundamental investigations with circular hot free jets. Annular shaped nozzles with a hub core - corresponding to the realistic engine nozzles - have not been investigated, the same applies to nozzle flow with spin. Yet Higgins-Wainwright [14] give some facts that the spin has very little influence on the decay of the free jet on the jet axis. All our investigations have been made with the same nozzle pressure ratio  $p_{ges}/p_{\infty}=1.95$ , the total temperature in the nozzle exit being 40°C and 550°C resp. above ambient temperature. The measurements were taken just behind the nozzle exit up to a distance of 30 nozzle diameters, a range which is especially interesting for VTOL techniques. In the following the free jet results refer to the bell-shaped nozzle with a cylindric exit of one diameter length.

The velocity in the jet core with critical nozzle pressure ratio is higher than sonic velocity. Fluctuations of the static pressure in the range of the first five diameters behind the nozzle have been identified as compression-shocks of a supersonic flow by means of a Schlierenphotograph (fig.3). All the investigated nozzles had a supersonic flow of mach 1.02 to 1.04 in the core. Even with exactly critical pressure ratio there was an over-expansion to supersonic flow behind the nozzle, which can be explained by the sinking-effect of the jet: Just near the nozzle exit the static pressure of the surrounding is decreased for the amount of the total head of the external flow. That is why the existing nozzle pressure ratio increases to an overcritical value and the over-expansion behind the nozzle accelerates the flow to supersonic velocity. In figure 4 and 5 the velocities on the axis of the free jet are shown. They have been calculated from the values which are corrected by the error of measurement of the pitot tubes due to turbulence. The influence of the mach number is described in figure 4. The smaller turbulence of the mach-1-jet causes the smaller decay of the jet with high speed in contrary to the subsonic free jets. Figure 5 shows the influence of temperature on the axial velocity. Higher nozzle temperatures cause a quicker decay of jets.

For the jet extension the value  $R_{0,5u_{max}}$  is a proper dimension, that is the distance from the jet centre to that point where you will find half the axial value of the velocity. Figure 6 shows that the spread depends very much on the nozzle mach number as you can take from the results of Laurence [18]. The nozzle temperatures have no more influence on the development of the mach-1-free-jet. For this reason we must not assume a greater spread angle for all of the hot jets than for cold jets as e.g. Abramowitch [2]. The only responsible parameter for spread is turbulence. But as there have not been any investigations of turbulence on hot jets with high nozzle exit velocity up to now, it is impossible to determine the error of measurement for pitot tubes caused by turbulence, to give exact total head profiles and to deduct laws for spread of hot jets.

For calculating the mass flow

$$\dot{m} = \rho \int_0^R \int_0^{2\pi} u(r) dr d\varphi \quad (1)$$

in a certain cross section of free jets the density and velocity and from these a partial mass flow are determined for each measurement of the probe rake. The sum of these partial mass flows gives the total mass flow of a cross section. Figure 7 shows that in the region behind the nozzle the growth of mass flow of the hot jet is very different from that of the cold jet. While the cold jet hardly grows in the region of 3 to 6 nozzle diameters, the hot jet absorbs most of the secondary air just here. For  $x/D = 6$  the mass flow of the cold jet is only 1.3 times the mass flow at the nozzle while the hot jet already has come up to 1.8. In this initial region the hot jet absorbs nearly three times the mass of the cold jet. Up to  $x/D = 25$  the hot jet has the greater volume, but from this point the nozzle temperature seems not to have influence on the growth of mass of the free jet any longer, the curves of mass flow of the cold and hot jet meet on the straight line

$$\frac{\dot{m}}{\dot{m}_0} = 0.412 + 0.144 \frac{x}{D} \quad (2)$$

For the area beyond  $x/D = 30$ , mass determinations have not yet been made.

#### 4. THE WALL JET

Corresponding to [22] only a few results about hot wall jets have been published up to now, e.g. Cox-Abbott [7], Hall-Rogers [13], Higgins-Kelly-Wainwright [15], which give no data about growth of mass of the wall jet which is important for calculating the recirculation-flow. Nearly all of the fundamental investigations of wall jets deal with undercritical jets. But the jet of the lift-engine leaves the nozzle with supersonic velocity and produces a spread very different from the jet of lower velocity.

The investigations of the hot wall jet were made with the jet impinging on the ground in right angle. In all our tests we had a nozzle pressure ratio  $p_{ges}/p_{\infty}$  of 1.95 which is nearly the same as of lift-engines and corresponds to a nozzle mach number of one. In the nozzle exit the total temperature amounted either to 60°C, 550°C or 1000°C over the ambient temperature. The distance between the nozzle and the ground varied from 2 to 10 nozzle diameters. The measurements in the wall jet were made on radii of 3 to 20 nozzle diameters from the jet stagnation point.

If you compare total heads for different nozzle distances  $H/D$  at a certain radius in the wall jet you will find out that the maximum total heads grow with increasing distance from the ground up to  $H/D = 8$ . Although at 3D nozzle clearance from the ground, the distance covered by the jet up to the measuring point at  $R/D = 5$  is nearly half the way of that at 10D nozzle clearance from the ground, the maximum total head of the greater nozzle clearance is for 24% higher than that of the smaller clearance. This "reversal effect" cannot be stated for the temperature profiles. At the same point of measuring narrow nozzle distances cause higher temperatures.

If you plot the maximum flow velocity against the radius, the maximum velocities in the wall jet increase when the nozzle distance grows up to 8D (fig.9). If the distance of the nozzle from the ground comes up to 10D the velocity keeps constant as Cox-Abbott [7] and Hölscher-Jünke [16] remarked. The growth of the wall jet velocity with decreasing nozzle distance from the ground may be explained by the free jet spreading: An engine jet accelerates its core flow up to supersonic velocity at critical pressure ratio (fig.3). When the supersonic jet impinges on the ground, the deflection to the wall jet is combined with higher loss of momentum than we can find with the subsonic jet.

Figure 10 shows that similar to the free jet the wall jet decays faster with high nozzle temperature. So the maximum velocity in the wall jet amounts to 24% of the nozzle velocity for a distance of 5 nozzle diameters from the stagnation point at an overtemperature of 60°C; if the nozzle temperature is increased to 550°C the velocity decreases to 18%, up to 1000°C it falls to 15% of the original value.

For calculating the mass flow

$$\dot{m} = \rho \cdot 2\pi \cdot R \cdot h \cdot u \quad (3)$$

of the wall jet at a certain radius from the stagnation point, density and velocity and from these a partial mass flow are determined for each measuring point of the probe rake. The sum of these partial mass flows gives the local total mass flow of the wall jet. In figure 11 the mass flow for different values of  $H/D$  and nozzle temperatures are plotted against the radius, it grows linear and depends very much on the nozzle temperature and nozzle distance.

The nozzle temperature and the distance of the nozzle from the ground have very strong influence on the increase of the mass flow of the wall jet. If normalizing the mass flow of the wall jet, not with the mass flow  $\dot{m}_0$  in the nozzle exit but with the free jet mass flow at the stagnation point  $\dot{m}_{stau}$  on the ground, which can be taken from fig.7, this mass flow ratio for different temperatures and values of  $H/D$

may be described by the linear equation

$$\frac{\dot{m}}{\dot{m}_{\text{stau}}} = 0.4 \cdot \frac{R}{D} \quad (4)$$

for ground clearances  $H/D \geq 5$  (fig.11).

##### 5. SEPARATION OF THE WALL JET DUE TO WIND INFLUENCE

The lengths covered by the wall jets against wind flow have been investigated by the light-intersection-method with constant nozzle diameters of 50 mm for different nozzle mach numbers, nozzle temperatures and ground clearances of the nozzle (fig.12). A wind flow with a realistic velocity profile has been blown against the wall jet. The velocity profile of the wind near the ground may be expressed by an exponential law

$$V_z = V_1 \cdot z^{\left( \frac{\lg V_z - \lg V_1}{\lg z} \right)} \quad (5)$$

In figure 13 measured velocity profiles of wind flows near the ground are opposed to the profile used in the test. Figure 14 shows the radii of separation as a function of wind velocity for  $H/D = 8$  and critical nozzle velocity for different nozzle temperatures. The plotted wind velocities in the diagram are maximum velocities of the velocity profile investigated. The radius of separation decreases with increasing wind velocity. An influence of the nozzle temperature on the point of separation cannot be found for wind velocities of more than 7 m/s. But the nozzle mach number is very important for the radius of separation. With decreasing nozzle pressure ratio the jet momentum also decreases and therefore the way covered by the wall jet against the wind becomes shorter (fig.15).

The strong dependence of the nozzle distance from the ground on the length of separation of the wall jet is striking very much. The reduced wall jet momentum at small  $H/D$  values (fig.9) causes shorter lengths of separation. In figure 16 the radius of separation of  $H/D = 3$  is opposed to that of  $H/D = 8$ .

Separations of the heated wall jet, caused only by thermic effects, as they are discussed by Cox-Abbott [7], have not been investigated because of technical difficulties of measuring greater separation lengths and their little practical importance for the recirculation flow.

##### 6. THE SECONDARY FLOW FIELD

The whole secondary flow field around the VTOL primary jet, which consists of free jet, wall jet, and area of separation, may be seen as a potential flow field, as there is no friction on solid walls and as the difference between the jet temperature and the ambient temperature may be neglected in a certain distance from the stagnation point. If covering the engine inlet, the free jet and the wall jet borders and the point of separation with a proper source-sink-distribution, which is determined by the measured mass flow distribution, the induced secondary flow field can be calculated according to a method described in [24]. The wind influence may be represented by simple superposition of velocities. Figure 17 shows the computed secondary flow field around a single lift engine, once without wind influence and once with a wind blowing with a velocity of 10 m/s. The pictures illustrate distinctly that the recirculation flow of a single jet can appear only with wind influence. Then indeed the warm wall jet enters the engine inlet in a very short time. Light intersection photographs of the secondary flow field on the Bodeneffekt-Versuchsanlage confirm the calculated flow fields.

##### 7. RESULTS

The behaviour of the wall jet of high velocity is different from the behaviour of the wall jet of low velocity. If you intend to produce a realistic propulsion jet of a lift-engine only the geometrical proportions may be varied, nozzle mach number and temperature must be kept. The results of the investigations of axially symmetrical jets blown downwards with critical jet pressure ratios are:

###### Free Jet

1. The core flow of the free jet is a supersonic flow if using convergent nozzles with a critical nozzle pressure ratio  $p_{ges}/p_{\infty}$ .
2. The jet turbulence decreases with increasing nozzle mach number, and the decay of the jet will be reduced.

3. The jet spread angle for velocity, total head, and temperature decreases with increasing nozzle mach number. In contrary to the free jet with lower nozzle velocity the jet spread angle of the mach-1-jet is nearly independent of the jet temperature.
4. The hot jet enlarges its mass far more than the cold jet along the distance of about 5 nozzle diameters.

#### Wall Jet

1. With decreasing distance of the nozzle from the ground the maximum total heads and the velocities in the wall jet are reduced.
2. The mass flow of the wall jet grows little with increasing nozzle distance from the ground, it grows very much with the increase of the nozzle temperature. Normalizing it with the free jet mass flow at the stagnation point, the increase of mass flow may be described by a single straight line.

#### Separation

1. The length of separation of the wall jet grows linear with decreasing wind velocity.
2. The separation of the wall jet due to wind blowing is not dependent on the nozzle temperature, however the nozzle mach number has a great influence on the point of separation.

#### Secondary Flow Field

1. The single VTOL propulsion jet has no recirculation without wind-blowing.

### 8. REFERENCES

- [1] Abbott, W. Studies of Flow Fields Created by Vertical and Inclined Jets when Stationary or Moving over a Horizontal Surface, National Gas Turbine Establishment, England NGTE Memorandum No. 391
- [2] Abramowitch, G. The Theory of Turbulent Jets, M.I.T. Press, Cambridge Massachusetts, 1963
- [3] Bakke, P. An Experimental Investigation of a Wall Jet, J. Fluid. Mech. 2, 1957, S. 467-472
- [4] Bradshaw, P. Ferries, D. Turbulence in the Noise-Producing Region of a Circular Jet, AGARD-Report 450, April 1963
- [5] Bradshaw, P. Love, E. The Normal Impingement of a Circular Air Jet of a Flat Surface, British Aeronautical Research Council, Reports and Memoranda R.+M. No. 3205, Sept. 1959
- [6] Corrsin, S. Uberoi, M. Further Experiments on the Flow and Heat Transfer in a Heated Turbulent Jet, NACA Report 998, 1950
- [7] Cox, M. Abbott, W. Studies of the Flow Fields Created by Single Vertical Jets Directed Downwards upon a Horizontal Surface, National Gas Turbine Establishment, Pyestock, England, NGTE M 390, Okt.64
- [8] Dissen, H. Schwantes, E. Versuchsanlage für Bodeneffektuntersuchungen bei Kurz- und Senkrechtstartern, DLR-Mitteilung 68-29, Oktober 1968
- [9] Ebrahimi, I. Turbulenz in isothermen Freistrahlen und Freistrahlfammen, Diss. TU Karlsruhe, Dez.1967
- [10] Eickhoff, H. Statischer Druck und Turbulenz in drehsymmetrischen Freistrahlen und Freistrahlfammen, Diss. TU Karlsruhe, Juli 68
- [11] Gauntner, J. Livingood, J. Hrycak, P. Survey of Literature on Flow Characteristics of a Single Turbulent Jet Impinging on a Flat Plate, NASA TN D - 5652 Feb. 1970
- [12] Glauert, M. The Wall Jet, J. Fluid. 1, 1956, pp. 625-643
- [13] Hall, G. Rogers, K. Recirculation Effects Produced by a Pair of Heated Jets Impinging on a Ground Plane, NASA CR - 1307, May 1969
- [14] Higgins, C. Wainwright, T. Dynamic Pressure and Thrust Characteristics of Cold Jets Discharging from Several Exhaust Nozzles Designed for VTOL Downwash Suppression, NASA TN D-2263, 1964
- [15] Higgins, C. Kelly, D. Wainwright, T. Exhaust Jet Wake and Thrust Characteristics of Several Nozzles Designed for VTOL Downwash Suppression, NASA CR-373, 1966
- [16] Höltscher, F. Jünke, E. Systematische Untersuchungen von Freistrahlen, Bodenstrahlen und Heißgas-Fontänen bei VTOL Konfigurationen mit Strahltriebwerken, Lift-Fans und Luftschrauben, Dornier ZTL Endbericht 4, Dezember 1969, VT 483 B5

- [17] Hrycak, P.  
Lee, D.  
Gauntner, J.  
Livingood, N. Experimental Flow Characteristics of a Single Turbulent Jet Impinging on a Flat Plate, NASA TN-D 5690, March 1970
- [18] Laurence, J. Intensity, Scale and Spectra of Turbulence in Mixing Region of Free Subsonic Jet, NACA Report 1292, 1956
- [19] Liem, K. Strömungsvorgänge beim freien Hubstrahler, Luftfahrttechnik 8, 1962, S. 198-207
- [20] Shapiro, A. The Dynamics and Thermodynamics of Compressible Fluid Flow, The Ronald Press Company, New York Vol. I 1953
- [21] Schrader, H. Trocknung feuchter Oberflächen mittels Warmluftstrahlen, VDI Forschungsheft 484, 1961
- [22] Schwantes, E. Übersicht über den Bodeneffekt bei strahlgestützten V/STOL-Flugzeugen - Literaturbericht - DLR-Mitteilung 68-28, Dezember 1968
- [23] Schwantes, E. Untersuchungen an Abgasstrahlen von TL-Triebwerksmodellen, Vortrag Nr.70-055 auf der 3. Jahrestagung der DGLR am 3.12.70 in Düsseldorf, DLR-Mitteilung 70-28
- [24] Schwantes, E. Theoretische Untersuchung des Betriebsverhaltens eines Hubtriebwerks unter Berücksichtigung der Rezirkulation, Diplomarbeit im Institut für Strahltriebwerke der TU Braunschweig, November 1966
- [25] Skifstad, J. Aerodynamics of Jets Pertinent to VTOL Aircraft, Journal of Aircraft, Vol.7, No.3, May-June 1970
- [26] Tani, I.  
Komatsu, Y. Impingement of a Round Jet on a Flat Surface, Appl.Mech.Proc.of the 11. International Congress of Appl. Mech. München 1964, Springer-Verlag 1966

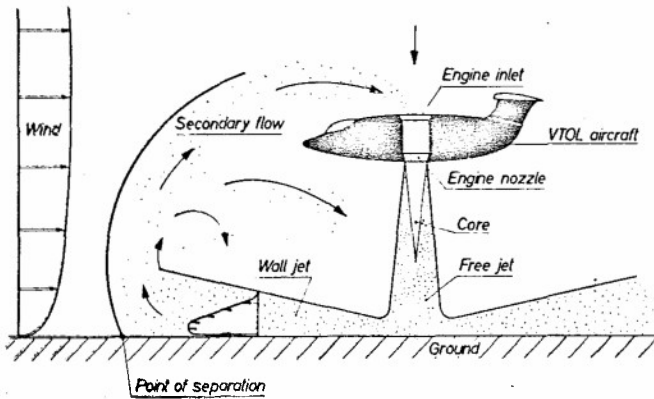


Fig.1 VTOL propulsion jet

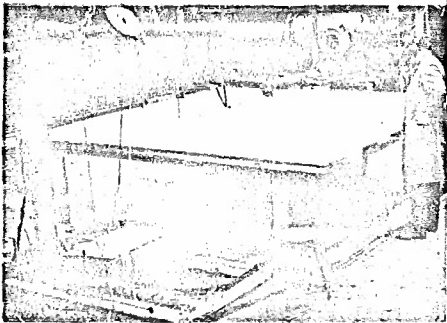


Fig.2 Test setup

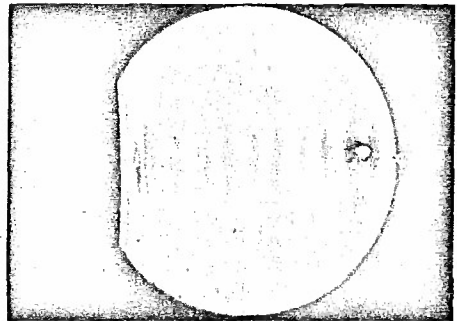


Fig.3 Schlierenphotograph of the free jet, just behind the nozzle exit, nozzle pressure ratio  $p_{ges}/p_m=1.9$

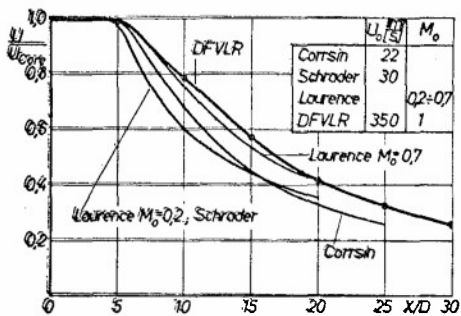


Fig.4 Axial velocity distribution at different nozzle mach numbers

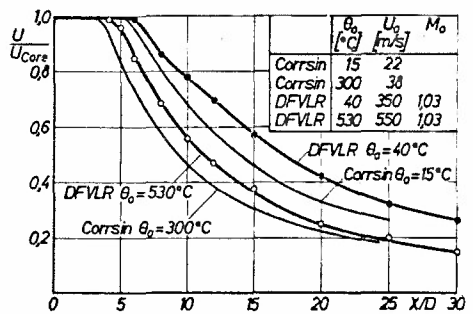


Fig.5 Axial velocity distribution at different nozzle temperatures

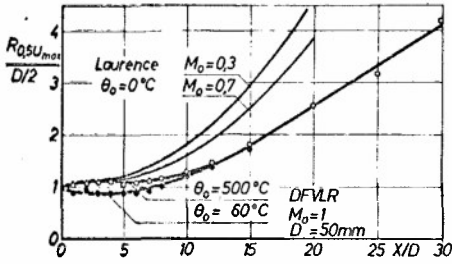


Fig.6 Spread of the velocity, influence of the nozzle mach number and temperature

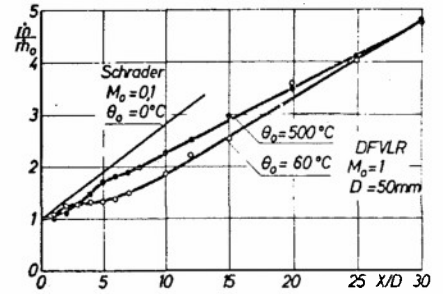


Fig.7 Entrainment of mass in the free jet, influence of the nozzle temperatures

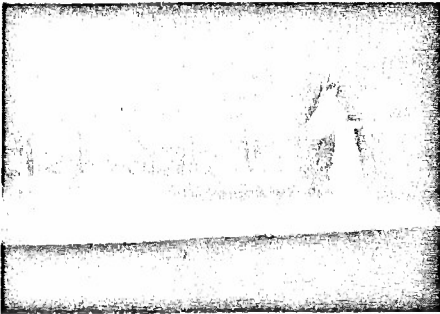


Fig.8 Light-intersection photograph of the wall jet

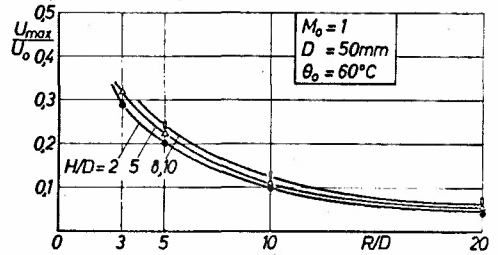


Fig.9 Decay of the maximum velocity of the wall jet, influence of H/D

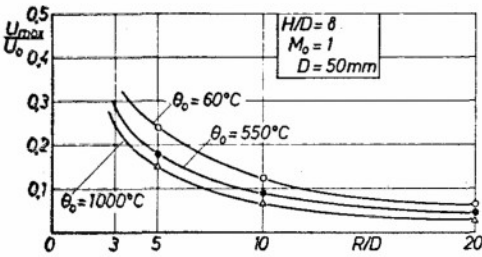


Fig.10 Decay of the maximum velocity of the wall jet, influence of nozzle temperature

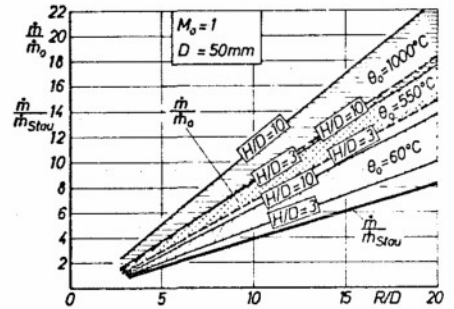


Fig.11 Entrainment of mass in the wall jet, influence of nozzle temperature and H/D

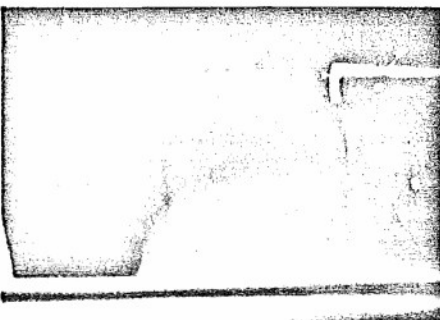


Fig.12 Light intersection photograph of the wall jet with separation due to wind-effects

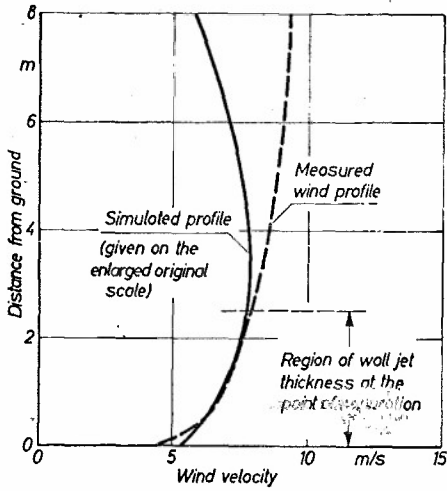


Fig. 13 Wind profile

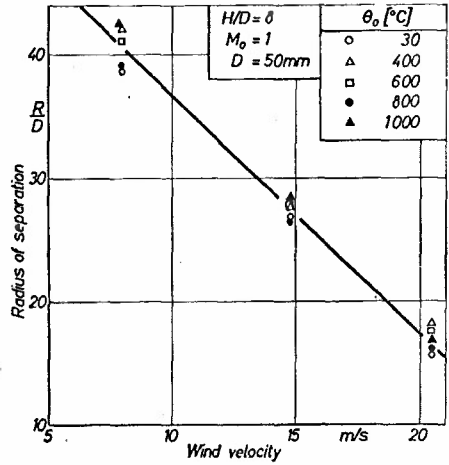


Fig. 14 Radius of separation of the wall jet, influence of nozzle temperature

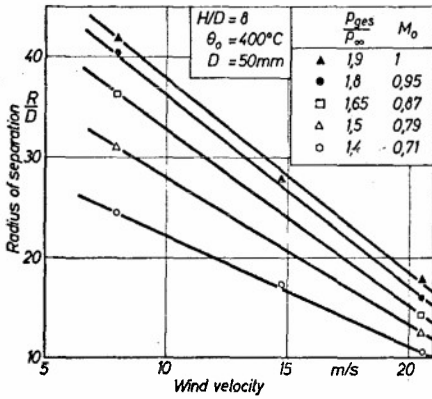


Fig. 15 Radius of separation of the wall jet, influence of nozzle mach number

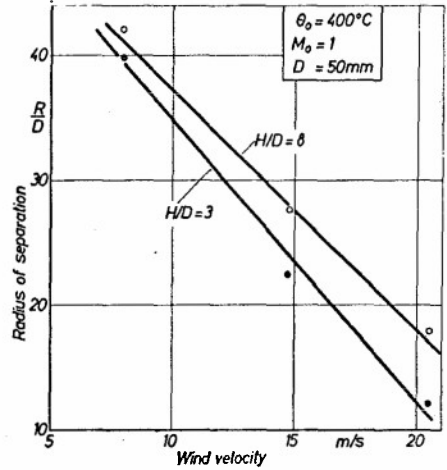


Fig. 16 Radius of separation of the wall jet, influence of H/D

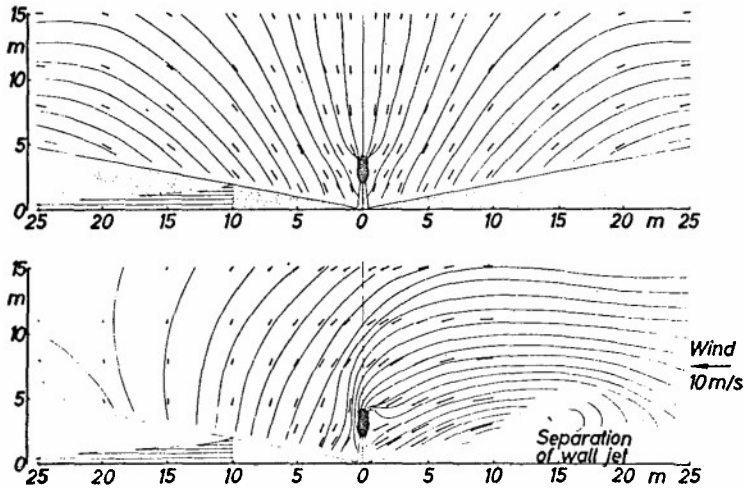


Fig. 17 Computed secondary flow field of a VTOL propulsion jet

FLOW ANALYSIS IN AXISYMMETRIC SUBSONIC INLETS  
OF SMALL GAS TURBINES.

by

P.N. GALLET

von Karman Institute, Rhods-St-Genèse  
and  
Royal Military School, Brussels  
Belgium.

SUMMARY.

Complicated axisymmetric air inlets are used in small gas turbines. The flow at the compressor entrance is therefore disturbed. A streamline curvature method to calculate the flow in the passage and at the compressor eye is presented. A new universal theory of the discontinuities of curvature is applied. Additional annulus boundary layer calculations can help in the analysis of a channel. Some experimental and theoretical results are shown, which tend to confirm the validity of the theory.

RESUME.

Les petites turbines à gaz utilisent des entrées d'air assez compliquées. L'écoulement à l'entrée du compresseur est de ce fait perturbé. Nous présentons une méthode basée sur la courbure des lignes de courant qui permet de calculer les caractéristiques de l'écoulement dans le passage et à l'entrée du compresseur. Une nouvelle théorie, assez universelle, basée sur les discontinuités de courbure est appliquée. Le calcul complémentaire de la couche limite annulaire parfait l'analyse du canal. Nous présentons également quelques résultats théoriques et expérimentaux qui confirment la validité de la méthode.

+ + + + +

## NOTATIONS

am <sub>0</sub>	velocity of sound at stagnation conditions.
A	coefficient of the velocity equation.
$b_1$	curvature application length for simulating a corner.
B	coefficient of the velocity equation.
of	friction coefficient.
CRV	curvature..
d	distance.
D	mass flow.
Dc	influence of curvature.
es	auxiliary length.
F	entrainment function of Head.
G	auxiliary function of Head.
H	enthalpy.
H <sup>12</sup>	momentum form factor.
H( $\delta$ - $\delta$ )	Head's form factor.
L( $\delta$ - $\delta$ )	Truckenbrodt's form factor.
m	meridional line.
n	normal line.
R	radius.
Rc	radius of curvature.
Re	Reynolds number based on reference length and velocity.
Re $\theta$	Reynolds number based on momentum thickness.
Rex	local Reynolds number.
R <sub>G</sub>	gas constant.
s	trajectory length.
T	total temperature.
V <sup>0</sup>	velocity.
x	axial coordinate.
$\alpha$	angle of the m-line with the axis.
$\beta$	flow angle.
$\gamma$	specific heats ratio.
$\delta^*$	displacement thickness.
$\varphi$	angle of a corner.
$\theta$	angular coordinate.
$\theta^*$	momentum thickness.
$\nu_s$	camber correction.
$\nu_q$	blockage correction.
$\rho$	density.

## SUBSCRIPTS.

A	corrected.
i	inner.
m	meridional.
n	normal.
r	radial.
u	tangential.
x	axial.

+ + + + + + + + +

## 1. INTRODUCTION.

In the last few years, small gas turbines have been improved considerably. In these machines, the role of the centrifugal compressors is increasingly important. Its compactness, reliability and ease of manufacturing are some factors for its success.

In many applications, the small gas turbines are associated with a big reduction gearbox (fig.1). This leads to the use of air inlets which are generally radial and their shape can become rather complicated.

Flow analysis of these inlets is necessary to avoid a flow separation due to an inadequate deceleration and to calculate correctly the inlet angles for the blades of the inducer. It can, for example, be demonstrated, that the inlet absolute velocity can never be uniform for a radial compressor preceded by a radial inlet.

For high performances compressors, where the tip relative velocities are almost sonic or even slightly supersonic, it is absolutely necessary to calculate with very much accuracy the shock free flow angle.

In this paper, we will first present the basic flow equations leading to our method of analysis. The most important factor in this method is the curvature of the walls. We will also present a new method for computing the curvatures of the meridional streamlines at any point of the channel.

Boundary layer calculations are introduced. We will, then, discuss the effects of the inlet flow on the design of the impeller and present some experimental and theoretical results.

## 2. BASIC EQUATIONS FOR AXISYMMETRIC FLOW.

We consider the motion of the point M in an  $(x, R, \theta)$  coordinate system represented in fig.2. The motion of M can also be described in an axisymmetric orthogonal system  $(m; n)$  where the m lines are streamlines projected on a meridional plane and the n lines, normal lines.

If we assume that the flow is permanent, isentropic and non viscous, the general equation of the flow is :

$$\nabla H = \vec{V} \times (\nabla \times \vec{V})$$

where  $\nabla H$  denotes eventually enthalpy gradients.

Considering the equilibrium of the forces in the  $(m; n)$  system, the equations of the flow can be written :

$$V_m \frac{\delta V_m}{\delta n} + \frac{V_m^2}{Rc} + \frac{V_u}{R} \cdot \frac{\delta(R \cdot V_u)}{\delta n} - \frac{\delta H}{\delta n} = 0, \quad (1)$$

$$\frac{V_u}{R} \cdot \frac{\delta(R \cdot V_u)}{\delta m} = 0$$

and  $\frac{\delta H}{\delta m} = 0$ .

Rc is the radius of curvature of the m curve at the considered point.  $V_m$  is the meridional component of the velocity V, and  $V_u$  the tangential component.

If the initial values of  $\frac{\delta H}{\delta n}$  and  $R \cdot V_u$  are known along a special normal line  $n_0$ , we have :

$$\frac{\delta H}{\delta n} = \frac{\delta H_0}{\delta n_0} \cdot \frac{\delta n_0}{\delta n},$$

$$V_u = V_{u_0} \cdot \frac{R_0}{R},$$

and 
$$\frac{V_u}{R} \cdot \frac{\delta(R \cdot V_u)}{\delta n} = V_{u_0} \cdot \frac{R_0}{R^2} \cdot \left( \frac{\delta(R \cdot V_u)}{\delta n} \right)_0 \cdot \frac{\delta n_0}{\delta n}.$$

Equation (1) can finally be written :

$$\frac{\delta V_m^2}{\delta n} + 2 \cdot \frac{V_m^2}{Rc} + 2 \cdot (V_{u_0} \cdot \frac{R_0}{R^2}) \cdot \frac{\delta(R_0 \cdot V_{u_0})}{\delta n_0} - \frac{\delta H_0}{\delta n_0} \cdot \frac{\delta n_0}{\delta n} = 0. \quad (2)$$

Equation (2) is a linear differential equation with  $V_m^2$  as variable. All the coefficients are functions of n. The solution of that equation is :

$$V_m^2 = e^{-\int_0^n \frac{2}{Rc} \cdot dn} \cdot \left( C - \int_0^n 2 \cdot (V_{u_0} \cdot \frac{R_0}{R^2}) \cdot \frac{\delta(R_0 \cdot V_{u_0})}{\delta n_0} - \frac{\delta H_0}{\delta n_0} \right) \cdot e^{\int_0^n \frac{2}{Rc} \cdot dn} \cdot dn_0 \quad (3)$$

The integrations are performed from the inner contour to the outer one, i.e. from  $n = n_1 = 0$  to n.

If n is equal to zero, we are along the inner wall and we have :

$$V_m^2 = C.$$

Equation (3) can therefore be written :

$$V_m^2 = A^2 \cdot (V_{m_1}^2 - B^2) \quad (4)$$

where  $A^2 = e^{-2 \int_{n_1=0}^n \frac{dn}{Rc}}$

and  $B^2 = 2 \int_{n_0=0}^{n_0} (V_{u_0} \cdot \frac{R_0}{R^2} \cdot \frac{\delta(R_0 \cdot V_{u_0})}{\delta n_0} - \frac{\delta H_0}{\delta n_0}) \cdot e^{\int_{n=0}^n \frac{2}{Rc} \cdot dn} \cdot dn_0$

If there is no swirl, or a free vortex swirl, and no enthalpy gradients, the term  $B^2$  is equal to zero; equation (3) is simpler and becomes :

$$\frac{V_m}{V_{m_1}} = e^{\int_0^n \frac{dn}{Rc}}$$

### 3. METHOD OF SOLUTION.

#### 3-1. DETERMINATION OF $V_{m_1}$

$V_{m_1}$  is calculated by means of the continuity equation. The mass flow passing through the channel is imposed. The mass flow passing through a passage section defined by a normal line  $n$  is equal to

$$D = \int_0^n \rho \cdot R \cdot V_m \cdot dn. \quad (5)$$

The local static density  $\rho$  is calculated from the known total conditions of the gas.

$$\rho = \rho_0 \cdot \left( 1 - \frac{\gamma-1}{2} \cdot \frac{V_m^2 + V_u^2}{a_{m0}^2} \right)^{\frac{1}{\gamma-1}}$$

$a_{m0}$  is the velocity of sound at stagnation conditions :

$$a_{m0} = \sqrt{\gamma \cdot R_G \cdot T_0}$$

The correct value of  $V_{m_1}$  is determined by an iterative trial and error method.

A first value of  $V_{m_1}$  is assumed. The ratio of the local meridional velocity to  $V_{m_1}$  is known by equation (4), and so a first value of the meridional velocities is calculated along the normal line. Integrated in equation (5), the velocities give a mass flow which is compared to the actual one.  $V_{m_1}$  is corrected until the computed and actual mass flows correspond.

Special case has to be taken when the iterations are handling velocities close to the sound velocity. There, a large increase in velocity give only a small increase in mass flow and the iterations could put some local velocity higher than sound speed. In this case, the method is no longer valid, in its present form.

#### 3-2. ITERATIVE PROCEDURE.

The calculations are performed from a first net of meridional and normal lines (fig.3). The meridional lines are defined as equal mass flow lines. The first net can be obtained by a rheoelectrical analogy or by calculations assuming that the velocities are uniform in a section.

The velocities are computed for the first net and their integration show that the first net was not an equal mass flow net. It is thus necessary to change the position of the points because the calculations are only valid if the points of the net are located at the intersection of true meridional streamlines and normal lines.

The correction  $\Delta n$  along the normal line is computed by interpolation on the velocity profile. The new coordinates are then given by :

$$X_A = x - \Delta n \cdot \sin \alpha$$

$$R_A = R + \Delta n \cdot \cos \alpha$$

where  $\alpha$  is the local angle of the meridional line with the axis of symmetry. The points along the inner wall are initial points and do never change of position. But, the points along the upper wall are changing and they must always stay on the upper wall. The new intersection of the corrected normal line with the outer wall is given by the intersection of a straight line perpendicular to the last meridional line and a line tangent to the wall through the point of the previous iteration.

A new net of meridional and normal lines is so defined. In fact, the corrections must be small enough to allow the application of the theory. A relaxation factor multiply therefore the computed correction  $\Delta n$  before defining the new net.

The calculations are performed again, until the corrections are small enough, i.e. smaller than 0,001 mm. Convergence of the procedure is more or less rapid depending on the value of the relaxation factor (0,1 to 0,4).

## 4. LIMITING SWIRLING FLOW.

It can be seen from equation (4) that if the term  $B^2$  becomes greater than  $V_m^2$  there is no more a real solution for  $V_m$ . It means that the energy of the flow is not large enough to assure the equilibrium of the forces. Therefore, any mass flow cannot be combined with any swirling property of the flow.

This phenomenon cannot occur if the flow is without rotation, or of the free vortex type. But, in a actual flow, there is always a boundary layer where the flow does not follow the same rules as in the main flow. In fact, purely free vortex flows do not exist. Therefore, there is also in the free vortex flows a minimum mass flow under which unstability occurs.

In the design of an inlet for swirling flow, it is very important to know the unstability mass flow. Unstability is the cause of theoretically unexpected separations of the boundary layer and of important back flows.

## 5. MERIDIONAL STREAMLINES CURVATURE.

The most important parameter coming into the equation is the curvature of the meridional lines. In ref. (2), Vavra uses a linear interpolation between the boundary values of the curvature (curvature of the walls). He demonstrates that the error introduced is not important.

However, this procedure becomes unsuitable when the curvatures of the walls are discontinuous, especially when the contours are made from straight lines and circular arc as encountered many times in practice. Other methods must be used to determine the curvatures in the channel. The most widely used methods are best fit or spline fit methods associated with smoothing. But, these calculations are long and generally unsuitable for automatized procedure.

We have developed a new method, more in relation with the physic meaning of the problem which is that the curvatures inside of the channel are generated by the curvatures of the walls. The method is called "method of the discontinuities" because we consider first the effect of one discontinuity and then the effect of a contour having more than one discontinuity. If the curvature of the wall is continuous it can easily be approximated by a large number of small discontinuities.

## 5-1. EFFECT OF ONE DISCONTINUITY.

In ref.(1), we demonstrate that the curvature induced by a discontinuity ( $R_{c1}; R_{c2}$ ) at a point P (fig. 4) with coordinates ( $d; \xi$ ) is equal to :

$$\frac{1}{R_c} = \frac{1}{R_{c2}} + \left( \frac{1}{R_{c1}} - \frac{1}{R_{c2}} \right) \frac{1}{\pi} \tan^{-1} \frac{d}{\xi} \quad (6)$$

Equation (6) is extended in a more general case, where the abscissa of a discontinuity is  $m_i$  and a point when the curvature has to be calculated is given by the abscissa  $m$  and the distance  $n$  along a normal line. So, the influence of a discontinuity of curvature ( $CRV_i; CRV_{i-1}$ ) can be written :

$$\begin{aligned} D_c &= CRV_i - (CRV_{i-1} - CRV_i) \frac{1}{\pi} \tan^{-1} \left( \frac{n}{m-m_i} \right) - CRV_{i-1} & \text{for } m < m_i \\ D_c &= CRV_i - (CRV_{i-1} - CRV_i) \frac{1}{\pi} \tan^{-1} \left( \frac{n}{m-m_i} \right) - CRV_i & \text{for } m > m_i \\ D_c &= \frac{1}{2} (CRV_i - CRV_{i-1}) & \text{for } m = m_i \end{aligned}$$

## 5-2. EFFECT OF SEVERAL DISCONTINUITIES ; EFFECT OF THE OTHER WALL.

We will made the assumption of the additivity of the influences of curvature. Thus, a wall having  $j$  discontinuities will give at a point which coordinates are ( $m; n$ ) a curvature equal to :

$$CRV_{m,n} = CRV_{m,o} + \sum_{i=1,j} D_c(j)$$

where  $CRV_{m,o}$  is the curvature along the wall at the root of the considered normal line.

Now, it is obvious that the other wall has also an influence on the curvature at a point. Since along a wall the curvature can only have its geometrical value, it has to be assumed that there exists a "conter-curvature" generated by a wall on the other. Fig. 6 presents the distribution of curvature along a normal line of a channel. The two main influences can be seen and the conter-curvatures too. The resulting curvature along the line is also shown.

Actually, the linear subtraction (with the length of the normal) of the overlaying curvature on the other wall give the same results.

## 5-3. EFFECT OF A CORNER.

In many applications, not only the curvatures of the walls are discontinuous but also the wall itself. It was therefore interesting to include this case in the general theory. An approximate method has been developed leading to the following theory.

A corner represents two infinitely large discontinuities of curvature, infinitely close one to the other. If we assume that the distance between the two discontinuities is equal to  $b_1$ , small but finite, the presence of a corner can be demonstrated to be equivalent to two discontinuities whose value is equal to:

$$CRV = \frac{-2\pi \sin\varphi}{b_1}$$

where  $\varphi$  is the angle of the corner (fig. 7).

With our method, the curvature can be calculated at any point of the channel, knowing only the curvature distribution along the walls. However, this procedure is complicated and the automatic calculations can only be performed with a very large computer. Therefore a graphic method has also been established to determine an equivalent wall curvature. The complete calculation is performed separately along each normal line. The composition of the influences is made graphically and a linear interpolation is defined giving the same integral as the actual "curvature profile" along the normal line. In this way, an automatic program working with the interpolation of the equivalent wall curvature can be used on a small computer.

## 6. THREE DIMENSIONAL FLOW PICTURE.

If there is no rotation the flow is completely described in a meridional plane. But, if the flow is rotational, it is important to know the effective length of the trajectory of a fluid particle. And therefore we must know the complete coordinates of a point  $x, R$  and  $\theta$ .

Since  $V = \sqrt{V_m^2 + V_u^2}$ ,

$$V_u = R \cdot \frac{d\theta}{dt},$$

$$\tan \alpha = \frac{dR}{dx}, \quad \tan \beta = \frac{V_u}{V_m},$$

$$V_x = V_m \cdot \cos \alpha = \frac{dx}{dt},$$

and  $V_r = V_m \cdot \sin \alpha = \frac{dR}{dt},$

we find  $d\theta = \frac{\tan \beta}{\cos \alpha} \cdot \frac{dx}{dR} = \frac{\tan \beta}{\sin \alpha} \cdot \frac{dR}{R}$

and so  $\theta = \int_0^x \frac{\tan \beta}{R \cdot \cos \alpha} dx = \int_0^R \frac{\tan \beta}{R \cdot \sin \alpha} dR.$

Knowing  $x, R$  and  $\theta$ , the actual length of the trajectory is calculated:

$$ds = \sqrt{dx^2 + R^2 \cdot d\theta^2 + dR^2} \quad \text{so that}$$

$$s = \int_0^x \sqrt{1 + \left(\frac{\tan \beta}{\cos \alpha}\right)^2 + \tan^2 \alpha} dx = \int_0^R \sqrt{1 + \frac{(\tan \beta)^2}{\sin^2 \alpha} + \frac{1}{\tan^2 \alpha}} dR$$

It is also interesting to define the auxiliary variable  $es$  so that:

$$des = \sqrt{dx^2 + R^2 \cdot d\theta^2}$$

and  $es = \int_0^x \sqrt{1 + \left(\frac{\tan \beta}{\cos \alpha}\right)^2} dx = \int_0^R \sqrt{1 + \left(\frac{\tan \beta}{\sin \alpha}\right)^2} dR$

The trajectory of a particle along the walls can now be represented in a plane ( $es; R$ ). The advantage of this representation is that the curvature of the curve ( $es; R$ ) is the curvature that feels the boundary layer along the walls. The trajectory is longer than in a meridional plane but the curvature is less strong.

## 7. BOUNDARY LAYER CALCULATIONS.

In the inlet channels the flow is generally accelerating. But, in complicated cases, large decelerations can occur locally. Boundary layer calculations are therefore very useful.

Using the assumption of an axisymmetric flow we will calculate a two dimensional axisymmetric boundary layer. The length of the trajectory is known, as well as the local radius, and by means of the curve ( $es; R$ ) the curvature that the boundary layer feels.

It is well known that in the axisymmetric case the momentum equation combined with the continuity equation gives the general boundary layer equation:

$$\frac{1}{V^2 \cdot R} \cdot \frac{d}{de} (V^2 \cdot Re\theta) + \frac{\delta^*}{V} \cdot \frac{dV}{ds} = \frac{cf}{2}, \quad (7)$$

where  $Re\theta$  is the Reynolds number related to the momentum thickness  $\theta^*$ ,  $\delta^*$  is the displacement thickness

and of a skin friction coefficient.

We will also make use of the momentum form factor  $H_{12} = \frac{\delta^*}{\theta^*}$ .

In most of the cases, the boundary layer is very quickly turbulent. But it is necessary to calculate the laminar part to locate the transition point and to have the initial values for a turbulent boundary layer calculation.

The calculations are performed for an incompressible case.

### 7-1. LAMINAR BOUNDARY LAYER.

The development of the laminar boundary layer is easily computed by the method of Truckenbrodt (ref.3)

The momentum thickness is calculated from the following equations.

We have

$$C_f^* = \frac{cf1}{2} \left( \int_0^{\xi} V^5 \cdot R^2 \cdot d\xi \right)^{1/2}$$

where  $cf1$  is a laminar skin friction coefficient equal to

$$cf1 = \frac{1,328}{\sqrt{Re_x}}$$

$Re_x$  is the local Reynolds number defined as  $Re_x = \frac{V \cdot x}{\nu}$ . We obtain, by Truckenbrodt's theory, the local value of

$$\theta^* = \frac{C_f^{*5/4}}{R \cdot V^3}$$

With the local value of the auxiliary variable  $\xi$  defined as  $\xi = (C_f^*)^k$ , where  $k$  is equal to 6,5 for an accelerating flow and 8 for a decelerating flow, we find the local value of Truckenbrodt's form factor  $L$

$$L = \ln V - \frac{1}{\xi} \int_0^{\xi} \ln V \cdot d\xi$$

Truckenbrodt says that there is a unique relation between  $L$  and  $H_{12}$  (Fig.8) and so for a given value of  $L$ , we find  $H_{12}$  and thus  $\delta^*$ .

In our cases, the boundary layer is mostly turbulent. It is thus necessary to determine the zone of transition.

We will, therefore, assume that the transition occurs when the local Reynolds number  $Re_x$  becomes higher than  $5 \cdot 10^5$ .

### 7-2. TURBULENT BOUNDARY LAYER.

The calculation of the turbulent boundary layer is performed by the entrainment method of Head (ref.4).

Equation (7) is combined with the entrainment equation

$$\frac{1}{V} \frac{d}{dx} (R \cdot V \cdot (\delta - \delta^*)) = R \cdot F(H_{\delta - \delta^*}) \quad (8)$$

The main assumption of Head is to say that the quantity of fluid entrained in the boundary layer is a function  $F$  of the form factor  $H_{\delta - \delta^*}$  defined as  $\frac{\delta - \delta^*}{\theta^*}$ .

He assumes too that the form factor is a unique function  $G$  of  $H_{12}$ .

In an analytical form we have :

$$F = 0,0306 \cdot (H_{\delta - \delta^*} - 3)^{-0,653} \quad (9)$$

$$\text{and } H_{\delta - \delta^*} = 1,535 \cdot (H_{12} - 0,7)^{-2,715} + 3,3 \quad (10)$$

If ' denotes that the variables are non-dimensionalized, and with  $Re = \frac{V_{ref} \cdot C_{ref}}{\nu}$ , the boundary layer equation can be written

$$\frac{d}{dx'} \left( \frac{Re \theta}{Re} \right) + \left( \frac{Re \theta}{Re} \right) \cdot \left( H_{12} + \frac{1}{V'} \right) \cdot \frac{dV'}{dx'} = \frac{1}{2} cf \cdot V' - \left( \frac{Re \theta}{Re} \right) \cdot \frac{dR'}{dx'} \cdot \frac{1}{R'}$$

and the auxiliary entrainment equation becomes :

$$H_{\delta - \delta^*} \cdot \frac{d}{dx'} \left( \frac{Re \theta}{Re} \right) + \left( \frac{Re \theta}{Re} \right) \cdot \frac{d}{dx'} \cdot (H_{\delta - \delta^*}) = V' \cdot F(H_{\delta - \delta^*}) - \frac{H_{\delta - \delta^*}}{R'} \cdot \left( \frac{Re \theta}{Re} \right) \cdot \frac{dR'}{dx'}$$

These two differential equations with  $H_{\delta - \delta^*}$  and  $Re \theta / Re$  as unknowns can be solved on a computer. Equations (9) and (10) are used as auxiliary equations.

The turbulent friction coefficient  $cf$  is estimated by the formula of Ludwig and Tillman

$$cf = 0,246 \cdot 10^{-0,678 \cdot H_{12}} \cdot Re^{-0,268}$$

The effect of the curvature of the wall is given by the radius of curvature  $R_c$  of the curve ( $es;R$ ). That effect is found principally in the function  $F$ , by mean of the formula suggested by Horton (ref.5).

$$F_{\text{curv}} = F_{\text{(without curv.)}} \cdot \left[ 1 + kb \cdot \frac{\delta}{R_c} (H_{\delta-s} - 2,3) \right]^{-1,38}$$

$kb$  is a content equal to 7 for a convex contour and to -4,5 for a concave one.

Classical separation criterias can be used to determine an eventual separation of the boundary layer. For example, we may consider that separation occurs when  $H_{12}$  becomes higher than 2,6 or when the friction coefficient  $cf$  becomes equal to zero.

If the boundary layer is thick enough it can be useful to calculate again the complete flow in a new channel defined by the displacement thickness added to the original contours. It is so possible to take into account of the annulus boundary layer blockage at the compressor eye.

### 8. CORRECTION OF THE INLET FLOW ANGLES.

It is well known that, especially for high speed compressors, the best efficiency is obtained for a "shock free" (in the sens of hydraulic shock) inlet flow. This condition is also called "zero work" condition at the leading edge.

If the blade angles are made without incidence regarding the relative flow in front of the wheel, some work at the leading edge appears due to the blockage effect of the blades that changes the meridional velocity. A large curvature of the blading introduces also a work near the leading edge. However, important turnings near the leading edge are usually not used in high speed compressor. This is to avoid or limit the appearance of shock waves (in the fluid mechanic sense).

The "hydraulic shock free" blade angle  $\beta_{1c}$  is defined as

$$\beta_{1c} = \beta_1 - (v_s + v_q).$$

$\beta_1$  is the relative flow angle in front of the wheel,  $v_s$  is the correction due to camber effects and  $v_q$  the correction due to the blockage. Fig. 9 shows a typical velocity triangle at leading edge.

According to Schnell (ref.6) the influence of the camber is

$$v_s = \frac{-t_1}{\pi \cdot \rho_N} \cdot (\cos \beta_{1c} \cdot \ln(2 \cdot \cos \beta_{1c}) + \beta_{1c} \cdot \sin \beta_{1c}) ;$$

$t_1$  is the pitch of the blading at the leading edge and  $\rho_N$  the radius of curvature of the camber line.

The influence of the blockage is calculated from the following formulas. With the "blockage factor"  $q$  defined as

$$\frac{th}{\cos \beta_{1c}} = \frac{2\pi}{N} \cdot R (1 - q)$$

where  $th$  is the thickness of the blading, and  $N$  the number of blades, we find that

$$\tan v_q = \frac{(1 - q) \cdot \tan \beta_{1c}}{1 + q \cdot \tan^2 \beta_{1c}}.$$

In modern designs the correction  $v_s$  is generally neglected because the curvature of the blading is inexistant near the leading edge.

The final value of  $\beta_{1c}$  is obtained by a check and trial procedure from the initial value  $\beta_1$ .

Many improvements of the compressors efficiencies can be obtained by the application of this theory, when the local calculated value of the inlet velocity is considered.

### 9. PRESENTATION OF SOME EXPERIMENTAL RESULTS.

The method has been checked in a classical inlet similar to the one presented in Fig.1. The non-dimensionalized velocity distribution along the shroud is shown in Fig.10 and compared with the tests. We can see that the design of the inlet was not too good because there is a large deceleration occurring in front of the inducer. A modified shape gave the velocity distribution represented in dotted line.

Fig. 11 shows the computed and measured velocity distributions in a traverse along the radius made some millimeters in front of the inducer. We remark that, here too, we have a good agreement between the tests and the calculations.

Fig. 12 presents a typical cross-over duct for a radial compressor. The computed and measured velocities distributions are shown and compared in Fig.13. They also agree quite well with each other.

## 10. EXAMPLE OF INLETS CALCULATIONS.

In Fig.14 we have presented a meridional view of a typical inlet channel and radial compressor. The meridional lines are given in the inlet.

Fig. 15-a presents the velocity distribution calculated along the shroud. We see also the local curvature and the displacement thickness of the boundary layer. Fig. 15-b makes the same thing for the hub. In Fig.16, we can see the velocity distribution at the impeller eye. The velocities are very much different from the velocity computed for an uniform flow. The blade angles are also calculated for an impeller running at 35000 RPM. We see that there is a significant difference in blade angle when our calculations are used. An undesired incidence of  $\pm 5^\circ$  can result from a one-dimensional design leading to a smaller range in mass flow for the compressor. In a other way, the inlet blading varies less in our case and the compressor is then easier to manufacture.

Fig.17-a, -b, -c, and -d present a different (bad) inlet, the velocity distribution along the contours and the velocity distribution at impeller eye.

## 11. CONCLUSIONS.

The method presented here is not a design method but can help very much to avoid errors. It is also of great help in the design of a radial compressor while our theory of curvatures show that the impeller has also an influence on the velocity distribution at the eye.

The method, combined with a classical method of analysis of a blading, can be easily used to study what happens in an inlet with prewhirl.

The boundary layer calculations are not very important for most of the inlet designs, when the flow is continuously accelerating. But, if the method is applied to the analysis of axisymmetric diffusers they become very usefull.

The new method giving the curvatures in the channel by the knowledge of the curvature of the contour has more physical meaning than a spline or best fit method, and is of general use. For example, this method is now used in three-dimensional analysis of rotating machines (through-flow theories).

As conclusion, we may say that the correct design of a good inlet, checked by a good analysis, can greatly improve the range and the efficiencies of the compressors and so of the complete gas turbine.

+ + + + +

## REFERENCES.

1. P.M. GALLET      Ecoulement dans les canaux axisymétriques de géométrie méridienne quelconque.  
Ph.D.Thesis. Univ. of Louvain. Sept. 1970.
2. M.H. VAVRA      Aero-Thermodynamics and flow in Turbomachines.  
John Wiley & Sons. Inc. N.Y. 1960.
3. E. TRUCKENBRODT      A method of quadrature for calculation of the laminar and turbulent boundary layer  
in case of a rotationnally symmetric flow.  
NACA TM 1379. May 1955.
4. M.R. HEAD      Original entrainment method for the calculation of form parameter development.  
VKI LS P-3      March 1968.
5. H.P. HORTON      The calculation of compressible turbulent boundary layer by the entrainment history.  
H.S.A.Ltd. R.1048. Aug. 1969.
6. E. SCHNELL      L'écoulement au travers de roues radiales à charge limite.  
V.K.I. CN 53      1965.

+ + + + +

## ACKNOWLEDGEMENT.

The author would like to thank the von Karman Institute where he has done the most part of this work, and the Chair of Applied Mechanics of the Belgium Royal Military School which allowed him to prepare and present this paper.

+ + + + +

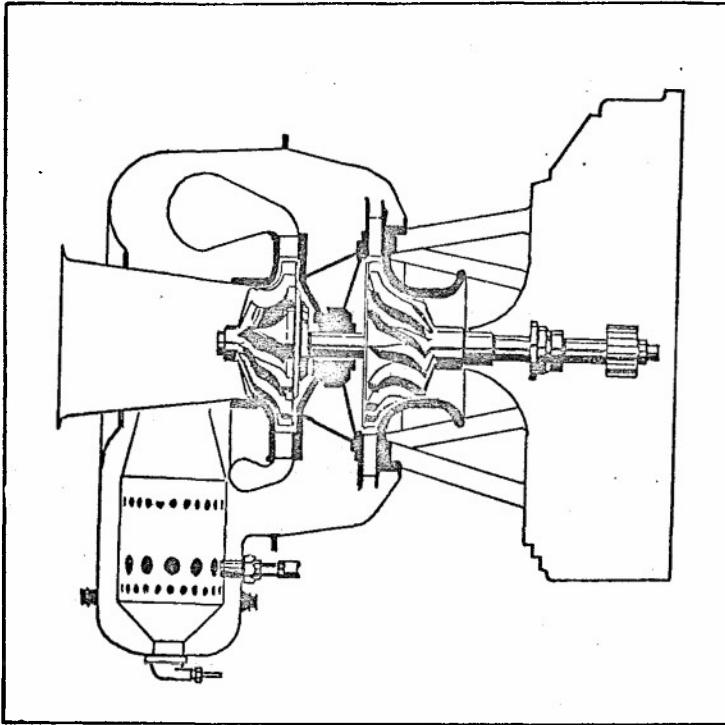


Fig. 1. Typical small gas turbine inlet.

Fig. 2. Nomenclature.

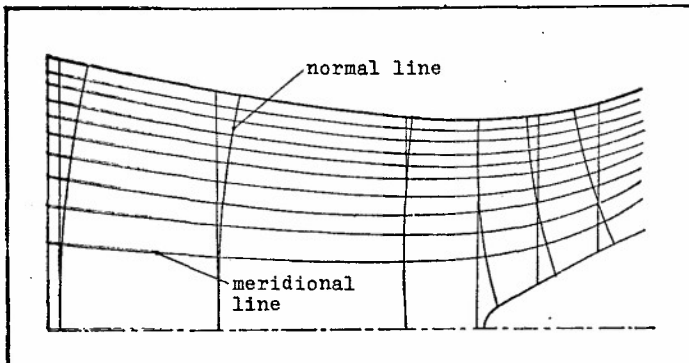
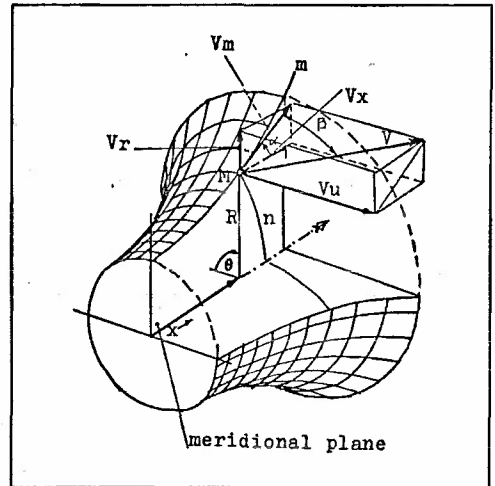


Fig. 3. First net of meridional and normal lines.

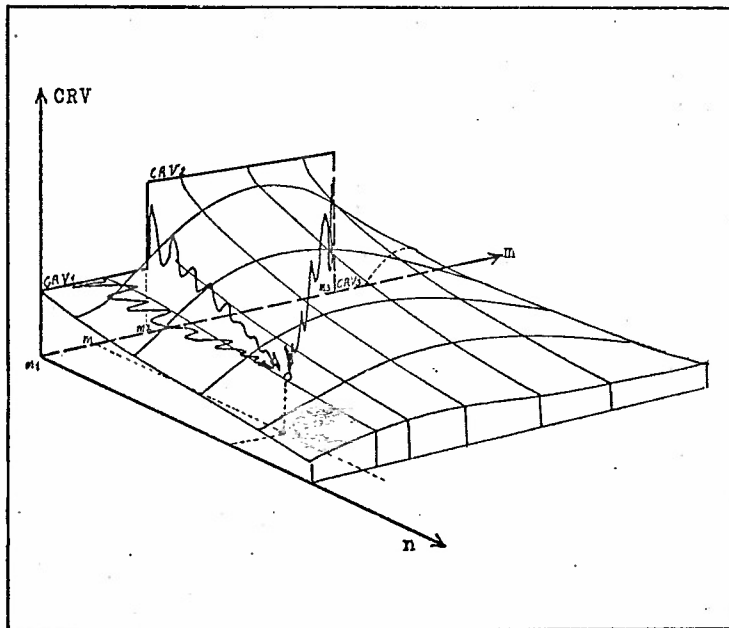


Fig. 5. Effect of the discontinuities on a point P.

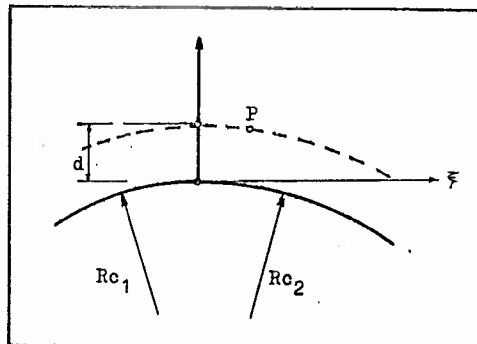


Fig. 4. Discontinuity of curvature.

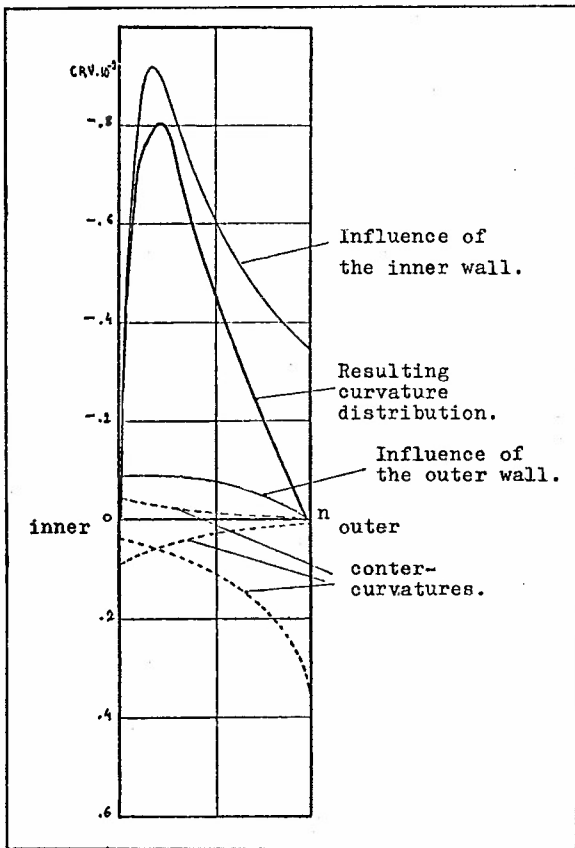


Fig. 6. Distribution of the curvature effects along a normal line.

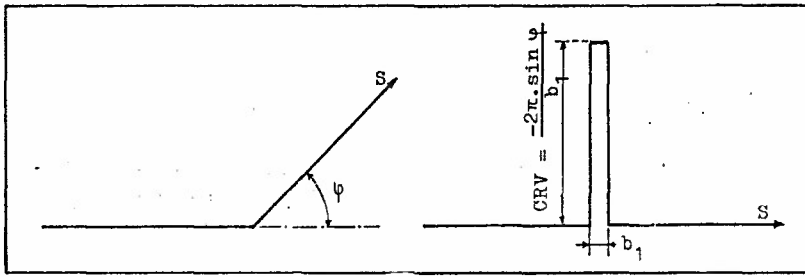


Fig. 7. Curvature generated by a corner.

Fig. 8. Relation between  $L$  and  $H_{12}$

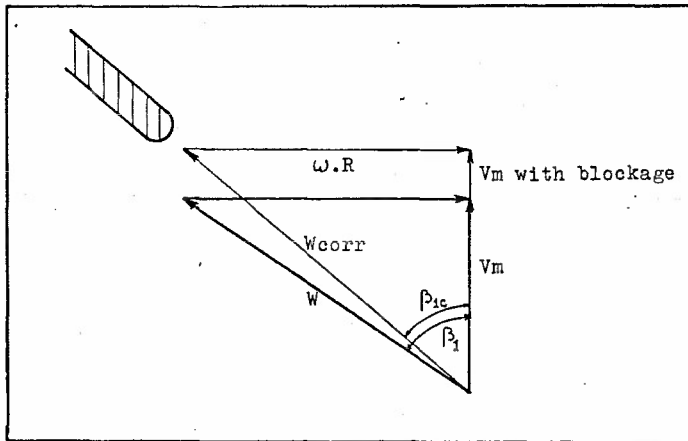
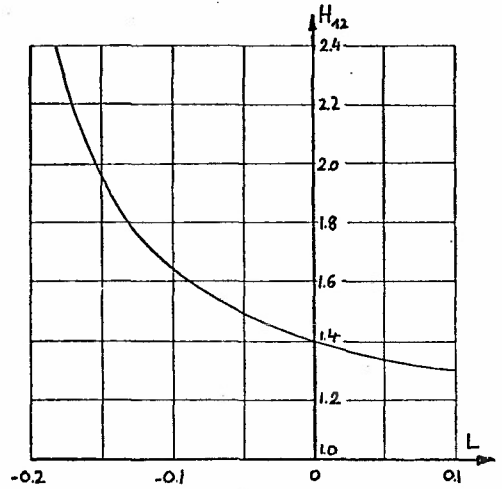
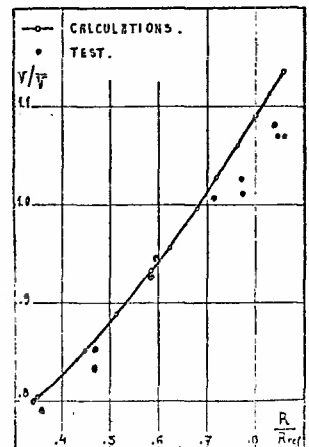


Fig. 9. Inlet velocity triangle.

Fig. 11. Non dimensional traverse.



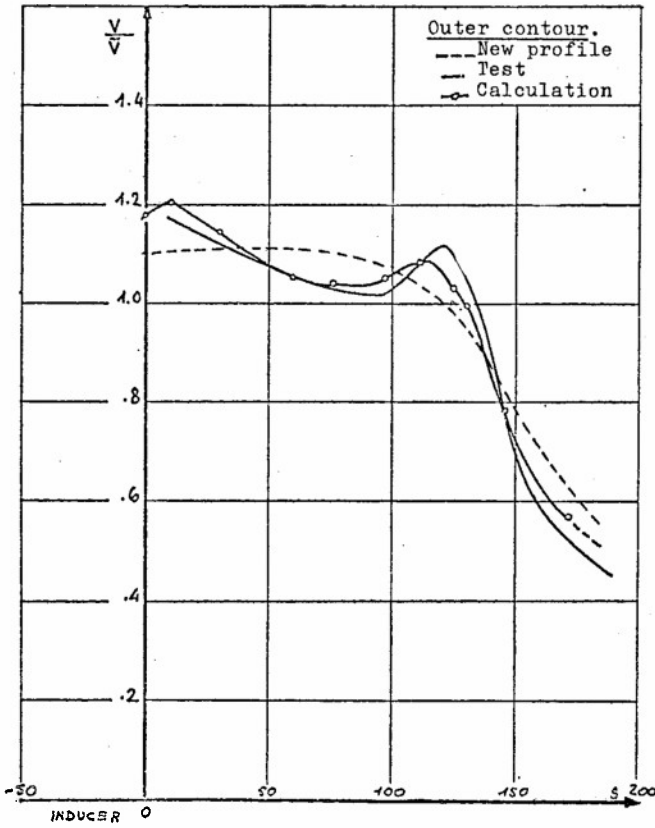


Fig. 10. Velocity distribution along the shroud of a typical inlet.

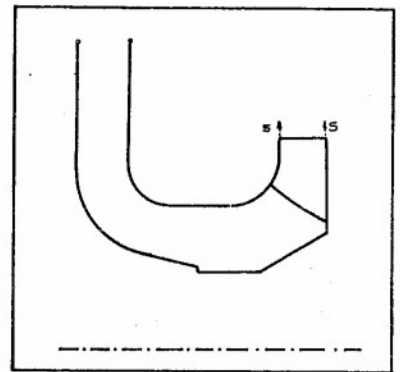


Fig. 12. Typical cross-over duct.

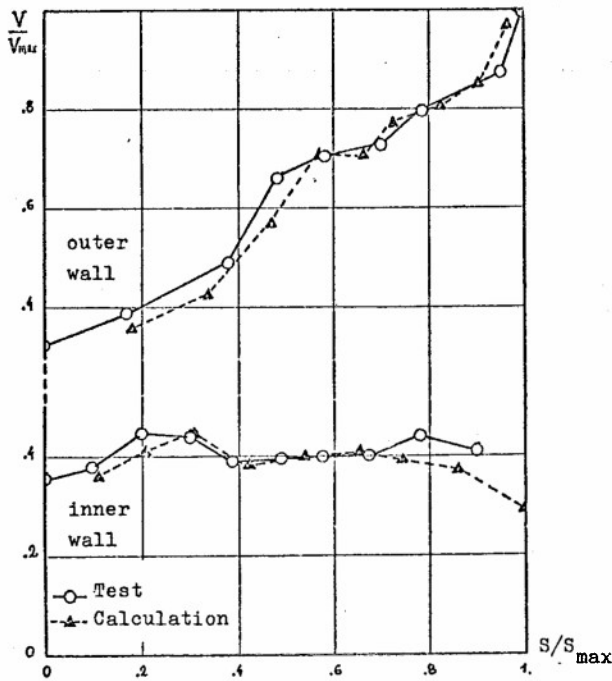


Fig. 13. Velocity distribution along the walls of the cross-over duct.

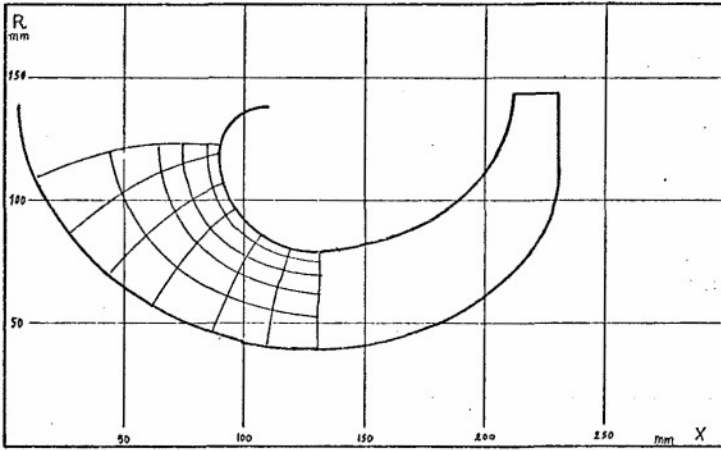


Fig. 14. Typical inlet channel and compressor.

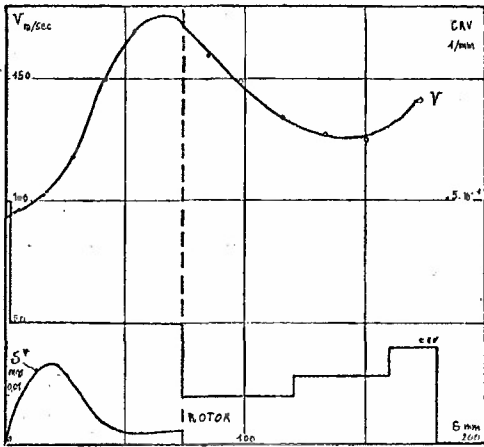


Fig. 15-a. Velocity and curvature distribution along the shroud.

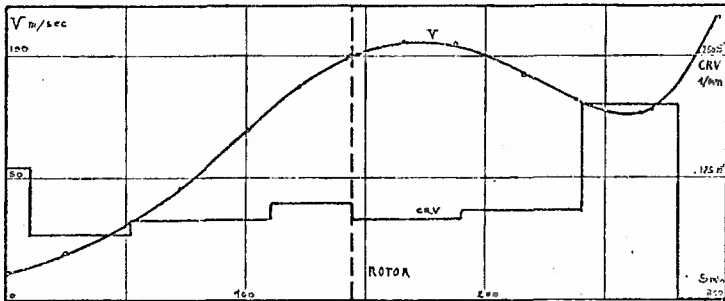
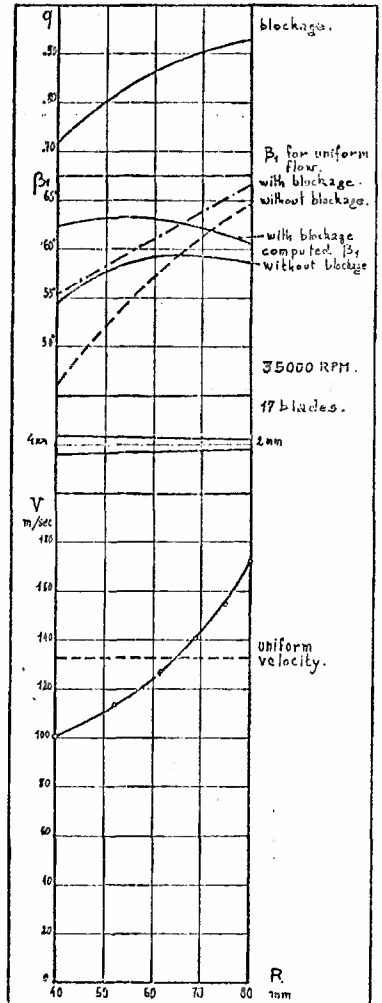


Fig. 15-b. Velocity and curvature distribution along the hub.

Fig. 16. Inlet velocities and angles.



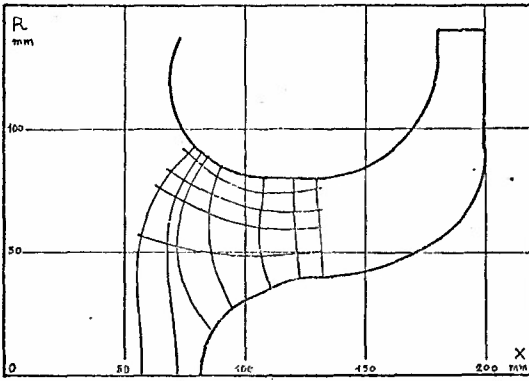


Fig. 17-a. Example of short inlet and compressor.

Fig. 17-b. Velocity distribution along the hub

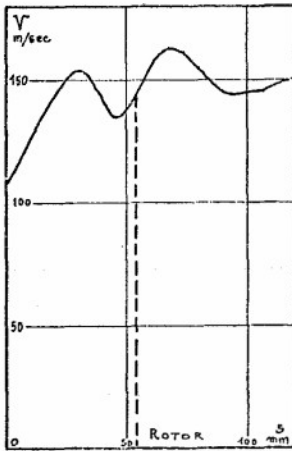
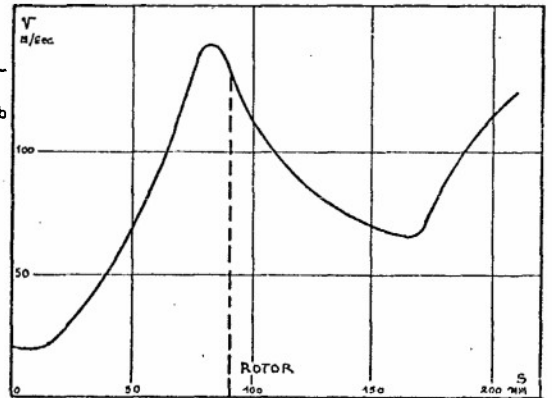
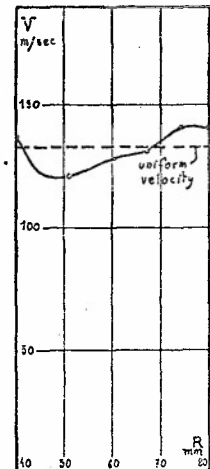


Fig. 17-c. Velocity distribution along the shroud.

Fig. 17-d. Velocity distribution at inducer eye.



FLOW DISTORTION AND PERFORMANCE MEASUREMENTS ON A 12" FAN-IN-WING  
MODEL FOR A RANGE OF FORWARD SPEEDS AND ANGLE OF ATTACK SETTINGS

Uwe W. Schaub, Associate Research Officer  
Robert W. Bassett, Technical Officer  
Division of Mechanical Engineering  
National Research Council of Canada  
Montreal Road, Ottawa, Canada, K1A 0R6

SUMMARY

The performance of a typical fan-in-wing model was examined under representative transition conditions. The model, comprising a 12-in. (30,5 cm) diameter fan buried in a N.A.C.A. 0015 section wing with a constant chord of 40-in. (1,02 m), was tested at various angles of attack and air speeds in the 10x20-ft (3x6 m) closed working section of the Propulsion Wind Tunnel at the National Research Council of Canada.

Tunnel interference corrections were estimated by a novel method. Typical corrections were indicated for the whole testing range which became limited at very low crossflow ratios as a result of uncertainty in the correction in angle of attack.

Flow distortion due to crossflow occurred in both the inlet and exit planes. In the crossflow ratio range zero to 0.27, inflow distortion was observed to be velocity distortion at essentially constant total pressure, whereas outflow distortion appeared to be a distortion of the exit plane static pressure field.

The fan thrust was seen to fall off with crossflow ratios greater than 0.2 and appeared to be a direct result of increasing distortion. However, it seemed to be insensitive to relatively large changes in angle of attack. Input power measurements indicated little dependence on approach air speed or angle of attack.

Despite high levels of distortion in the inlet at large crossflow ratios, the fan demonstrated considerable tolerance in operating under these conditions. This was evidenced by the very large flow redistributions that took place within the fan stage which almost completely attenuated the inlet distortion at the exit plane.

LIST OF SYMBOLS

$C_{\theta}$	local swirl velocity, component of V
$C_z$	local axial velocity, component of V
D	fan diameter
H	blade height
$P_t$	total pressure
$P_{t\infty}$	total pressure of the crossflow
$q_a$	fan axial dynamic pressure based on inlet mass averaging
$q_n$	crossflow dynamic pressure, free air equivalent
$q_{\infty}$	tunnel dynamic pressure far upstream of the model
$T_t$	total temperature
U	blade velocity
V	local velocity in the inlet and outlet planes
$V_a$	fan axial velocity based on inlet mass averaging
$V_n$	crossflow velocity, free air equivalent
$V_{\infty}$	tunnel velocity, far upstream of the model
$\dot{w}$	fan mass flow, summed in the inlet plane
$\alpha$	wing pitch or setting angle
$\alpha_n$	angle of attack
$\Delta$	denotes change in a quantity
$\theta$	circumferential angle
$C_p$	static pressure coefficient: local static pressure referenced to crossflow static pressure divided by crossflow dynamic pressure
$\frac{\Delta P_t}{q_a}$	loss coefficient
$\frac{V_n}{V_a}$	crossflow ratio

## INTRODUCTION

The general attractiveness of lifting fans to serve as thrusters for V.T.O.L. aircraft has been amply demonstrated (1). For safety reasons alone, it is essential that such fans are capable of stable operation under all powered forward flight conditions.

Although a great deal of experience exists with both fan and compressor inlet flow distortions, it is usually associated with total pressure losses (2). In very shallow installations where the total axial length may be only half the fan diameter or less, there is insufficient surface ahead of the fan for such distortions to develop, and consequently such installations are less apt to suffer from large amounts of total pressure distortion (3). The relatively short inlet region cannot, however, provide adequate guidance for the entering flow (4) and hence the dominant inflow problem is a velocity distortion, both magnitude and direction being involved.

This distortion is likely to occur in V.T.O.L. lifting fans during transition manoeuvres from vertical to horizontal flight, and vice versa, because the flow entering the inlet plane is still in the process of turning as it reaches the fan.

The efflux jet, emerging in a direction essentially normal to the external crossflow, experiences a distortion in the static pressure field in and around the jet.

The combined effect of these two distortions imposes a fluctuating load on the rotor blading and causes the fan performance to vary noticeably from the axisymmetric case.

The experimental work reported herein represents part of a study at the National Research Council of Canada on V.T.O.L. lifting fans. The data presented show in detail the inlet and outlet distortions that are associated with representative transition conditions. An attempt is made to correlate these distortions with the appropriate performance parameters and measurements under similar crossflow conditions.

## EXPERIMENTAL METHOD

Test Model

The model, shown in Figures 1 and 2, comprised a constant 40-in. (1,02 m) chord wing of 15% section thickness (N.R.C.A. 0015) completely spanning the 10x20-ft. (3x6 m) N.R.C. Propulsion Tunnel working section at the 10-ft. (3 m) elevation, and a 12-in. (30,5 cm) diameter fan mounted in the wing plane at mid-span and 35% of the chord. Six inch (15,2 cm) high fences were fitted to the wing ends 10 in. (25,4 cm) away from the tunnel walls.

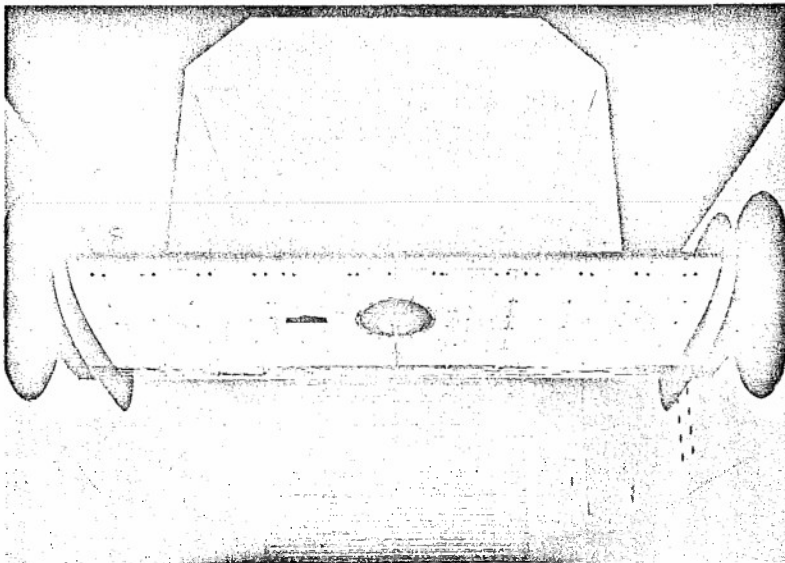


Fig. 1. Powered fan-in-wing model in the NRC propulsion wind tunnel.

The main aerodynamic specifications of the fan are described in Reference 5; it was a single stage fan designed for operation up to 18,000 r.p.m. The rotor and stator had 18 and 11 blades, respectively, and the fan's axial length to diameter ratio was nominally 1/4. The rotor was driven by an air turbine powered shaft which passed through a thick stator blade at the starboard side of the model and a bevel gear set inside the hub. The fan inlet plane was 0.50 in. (1,27 cm) above the wing symmetry plane, and coincided

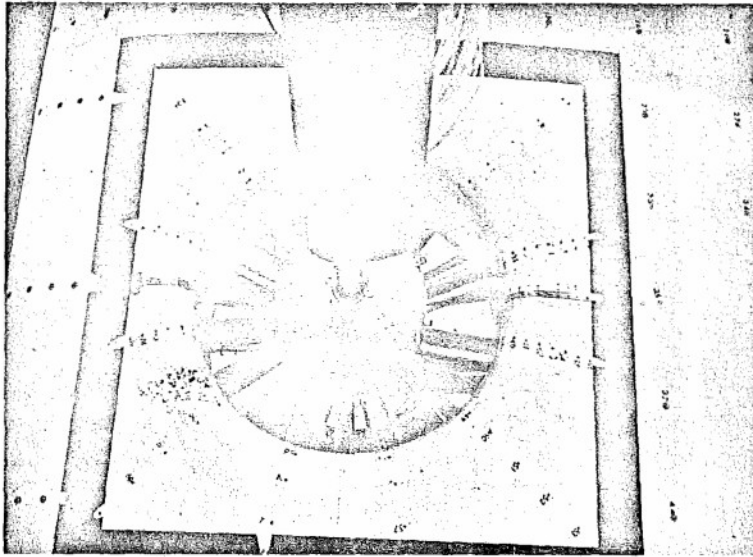


Fig. 2. View of inlet side of fan-in-wing model.

with the beginning of the cylindrical portion of the outer shroud. The inlet and centre-body walls had elliptic profiles (2:1 ellipse, with major axis parallel to fan axis). The fan is illustrated schematically in Figure 3.

#### Measurements

Measurements reported herein were made at test conditions of fan speeds from 6,000 to 13,500 r.p.m., crossflow speeds from zero to 130 ft/sec (39,6 m/s), and wing pitch angles from  $-12.5^\circ$  to  $+12.5^\circ$ .

Overall performance measurements comprised drive shaft torque and speed, total lift, and some wing surface pressures. Fan thrust was derived from total lift and wing surface pressure measurements.

Detailed aerodynamic measurements were made in an inlet plane, 0.75 in.

(1.90 cm) forward of the rotor's leading edge, and in an exit plane, 0.375 in. (9.50 mm) downstream of the stator's trailing edge by means of traversing pressure probe rakes.

Measurements in the inlet were made at five radial stations; the equally spaced probes extending to within 0.25 in. (6.35 mm) of the annulus walls. Traversing was done circumferentially at  $18^\circ$  increments.

Radial spacing of the exit plane probes was identical to that of the inlet, but a circumferential positioning of  $16.36^\circ$  was selected for traverses. Outlet measurements could not be made far enough downstream of the stator for adequate wake profile smoothing to take place, lest the whole efflux stream become greatly changed by the crossflow. It was therefore necessary to measure in a plane of near proximity to the stator exit; but in order to maintain some reasonable balance between the number of sampling points required and the prime information sought, wake detail was omitted. The sampling stations were carefully placed between the stator wakes so that an indication of the "healthy" flow - and thereby rotor performance - could be obtained. Consequently, efflux measurements were made at every  $16.36^\circ$  of circumference. These measurements were estimated to yield prime information on distortion and overall trends; but it is known that appreciably large errors were introduced into the efflux parameter averaging.

Boundary layer measurements were not made and so the value of stream variables in the near-wall region are uncertain. The mass flow was based on inlet measurements.

#### Tunnel Interference Corrections

Established conventional wind tunnel correction methods are known to be unreliable

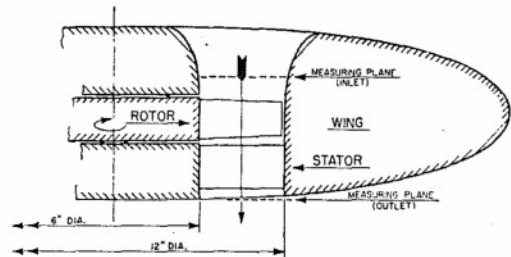


Fig. 3. Diagrammatic cross section of fan-in-wing model.

for many high-lift configurations, and in spite of more recent correction procedures fan-in-wing data remain difficult to handle. The difficulty arises because in addition to being a high-lift device a large surface area is offered on which the interference can act. The lift data and tunnel test conditions presented here have been corrected to an equivalent free air state by means of a simple correction method devised at the National Research Council for this type of model (7). This method makes use of measured control pressures on the surface of the wing away from the source-sink field of the fan and a prior calibration of the same pressure orifices on the two-dimensional wing (fan openings faired-in) at known tunnel conditions. A more detailed account of the application of the method and the nature of corrections involved is given in the Appendix.

The indicated corrections, particularly to angle of attack, become uncertain however at tunnel speeds of less than 40 ft/sec (12.2 m/s) and crossflow ratios less than 0.1, and so a different technique was devised to obtain the overall performance data at zero forward speed. The efflux was ducted away from the model across an air gap, carefully optimized to avoid interference.

#### FLOW DISTORTIONS

The particular type of distortion associated with shallow-mounted lifting fans can be studied by comparing inlet and outlet flow fields. The examples offered are: two crossflow ratios, a nominal one of 0.03 and another at 0.26, at zero pitch angle; and two additional pitch angles of  $-12.5^\circ$  and  $+12.5^\circ$  for nearly the same large crossflow ratio. The 0.03 crossflow ratio data, representing an unavoidable tunnel draft condition, was chosen as the only available datum case since zero crossflow ratio data were not available directly. Both inlet and efflux distributions are presented as viewed from above.

#### Inlet Plane

The distribution of inlet total pressure in the form of loss coefficients at the above conditions are given in Figure 4. These distributions show that, except for unmeasured boundary layer losses, the inflow field is essentially loss-free. The only observed losses were those associated with a well-defined but small region on the leeward side of the centrebody. Independent experiments involving an airflow suction intake with boundary layer control on the outer wall demonstrated the possibility of separated flow in this region (4,8). The observed loss was a result of a natural tendency of the boundary layer to thicken rapidly in a rising pressure field coupled with the de-stabilizing effect of the upstream obstruction offered by a porous cluster of inlet instrumentation tubes shown in Figure 2. It was the only evidence of the more usual total pressure distortion associated with long inlets and multi-stage compressors.

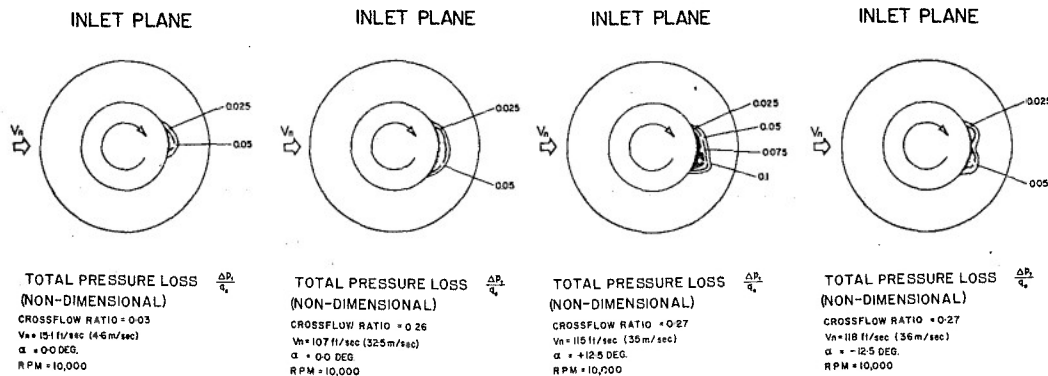


Fig. 4. Inlet total pressure loss distributions.

The fan's proximity to the upper surface of the wing evidently inhibited the formation of large regions of flow separation that are likely with long intake duct installations exposed to the same crossflow. The fan achieved this condition presumably because the rotor blading near the tips provided a diffusion rate more conducive for attached flow than would otherwise have been the case. Pressure loss therefore did not appear as a prime distortion problem in the shallow lifting fan installation.

Velocity distributions are presented in separate forms of magnitude and direction. The direction of inlet velocity was resolved into swirl and meridional plane angle components so that the distortion could be viewed in a co-ordinate system natural to the fan rotor. Of these, swirl angle is of prime importance because it modifies the inlet air angle of the rotor blades thereby shifting the fan blade passage operating point. This is discussed later. The meridional plane angle is of less significance, it is only a measure of spanwise flow on the rotor blades.

Figure 5 illustrates the associated contours of inlet velocity magnitude. The 0.03 crossflow ratio case has the characteristic features of zero crossflow, that is ambient

still air, with highest velocities near the outer wall and velocities near the hub wall generally larger than in the mid-annulus region. Such a profile is typical of entrance flows, including long intake ducts using airflow suction. Generally, it is found that the velocity increases with decreasing radius of curvature, as required by free vortex flow. With increasing crossflow a second curvature effect became progressively more significant giving rise to a higher velocity at the front of the annulus than at the rear. This variation is associated with the approach flow bending into the inlet. It is

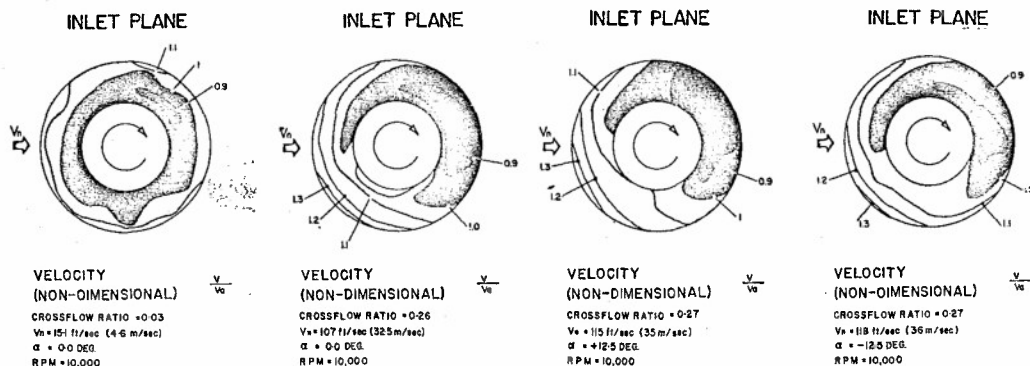


Fig. 5. Inlet velocity distributions.

a characteristic feature of the crossflow-inlet flow velocity field which was also observed earlier during intake airflow tests on a suction model (8). A comparison of the suction model and powered fan results (1) demonstrated the similarity between these experiments as a function of crossflow ratio. The noted velocity distortion was, in fact, quite unlike that normally identified with compressor flows at the inlet face, which is purported to be a flow field of constant velocity, but non-uniform total pressure (2). The general skewness of the velocity contours in a counter-rotational sense is direct evidence of a feedback from the fan as will be explained later. A comparison of velocities at the larger crossflow ratios shows that the indicated changes in pitch angle influenced neither velocity magnitude nor distribution.

Figure 6 shows the measured swirl angle distribution. As expected, there was little evidence of crossflow distortion when the crossflow ratio was 0.03. The average swirl

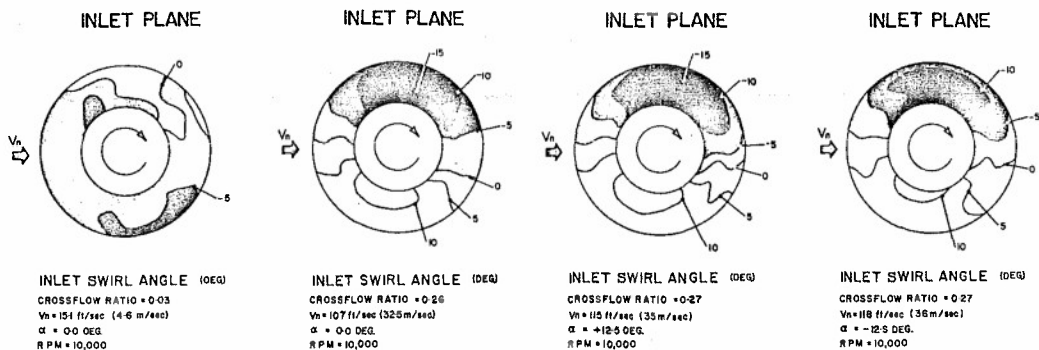


Fig. 6. Inlet swirl angle distributions.

angle, in the direction of fan rotation, of two or three degrees seems representative of rotor-induced effects. The swirl distribution attained a distinctive appearance with increasing crossflow, with counter-clockwise swirl on the advancing blade side and clockwise on the retreating blade side. Swirl was largest - swirl velocity tending toward the crossflow velocity value - at the sides of the centrebody where a minimum of flow guidance was available from the walls. In fact, the radial variation of swirl, particularly noticeable on the port and starboard sides of the annulus, is consistent with a combination of residual velocity and secondary flow effects associated with flow in a bend. The feedback effect of the fan on the inlet flow, which under still air conditions appeared solely as the fairly uniform swirl mentioned, now also manifested itself as a skewness in the distribution in the sense of fan rotation. Port to starboard symmetry can be approximately restored by removing the 3° datum effect.

The effect of wing pitch angle on swirl distribution is also illustrated in Figure 6. Here again it was at the sides of the centrebody, where least guidance was provided by the inlet walls, that the swirl angle changed most. The swirl angle became less as the fan was inclined toward the crossflow. It should be noted though that the change in swirl

angle was negligible in the region of the inlet annulus forward and in the lee of the centrebody.

Certain features of the distortion are better illustrated by circumferential plots of non-dimensional axial ( $C_z/V_a$ ) and swirl ( $C_\theta/V_a$ ) velocities. Figure 7 depicts the 0.26 crossflow ratio, zero pitch angle condition. Three radial stations are represented: near tip (83% of blade height, H), mid (50% of H), and near hub (17% of H). These profiles exhibited a definite wave form with a fundamental wavelength equal to the circumference; but the waves were not centred on  $\theta=0^\circ$ , a feature referred to above as skewness. The swirl velocity profiles were in phase with one another; indicating thereby that this component of distortion was much more a result of crossflow than of feedback from the fan. The axial velocity profiles, however, were noticeably out of phase with each other, which demonstrated a strong mutual interaction between the crossflow and the fan flow. It is seen from Figure 8 that crossflow and pitch angle distorted the meridional plane angle by only a token amount. The dominant variation was in a radial sense and appeared to be solely determined by sink-flow effects (static operation) and perhaps the fan design.

Since none of the inflow variables demonstrated very strong dependence on pitch angle and hence wing angle of attack, within the specified test range, it is deduced that the wing performs a powerful flow alignment function and thereby shields the inlet almost completely from angle of attack changes of the approaching stream. This quality is viewed as an important advantage of the fan-in-wing configuration relative to other V.T.O.L. lift schemes. It is the magnitude

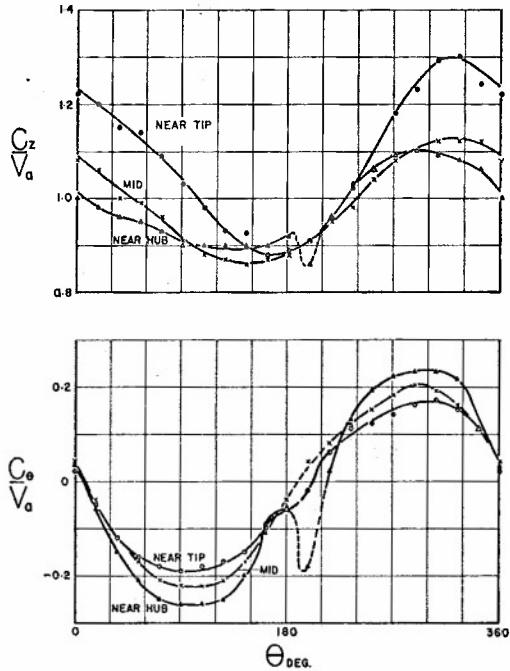


Fig. 7. Circumferential inlet velocity profiles.

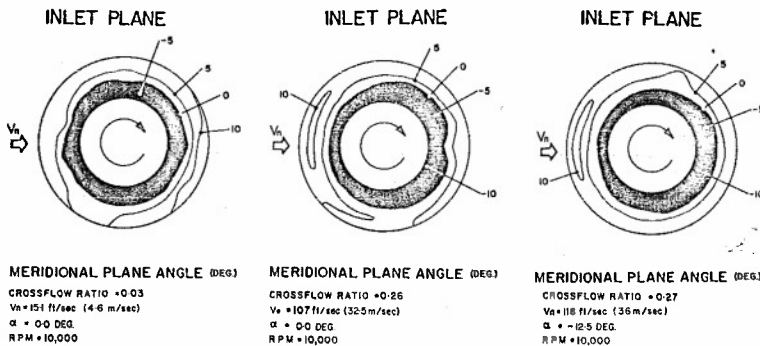


Fig. 8. Inlet meridional plane angle distributions.

of crossflow, rather than the direction, that emerges as the prime cause of inflow distortion. As crossflow increases, progressively more flow comes directly from the front of the wing and there results a distortion in both magnitude and direction of the inlet velocity that is consistent with stream curvature causing agents: entering flow bending from the original direction towards the axial direction and local contraction effects. The latter agent is,

associated with the shape of the inlet surfaces and inlet depth. of course, present even under static inflow conditions.

Outlet Plane

Inlet distributions alone are not sufficient to describe the total distortion effect for, as will be shown, the fan also suffers an exit plane distortion which appears to be largely independent of the inflow.

Figure 9 illustrates how velocity changed across the fan at a crossflow ratio of 0.03. The dominant variation (radial) persisted through the fan. At the larger crossflow ratio case, in Figure 10, almost complete attenuation of the inlet distortion took place and only remnants of the more prominent distortion features remained: higher velocity in the front annulus sector than in the rear, distortion skewness, and the low energy region at the rear of the centrebody. A complete transition had taken place, and the dominant variation appearing in the efflux was a radial one, quite similar in fact,

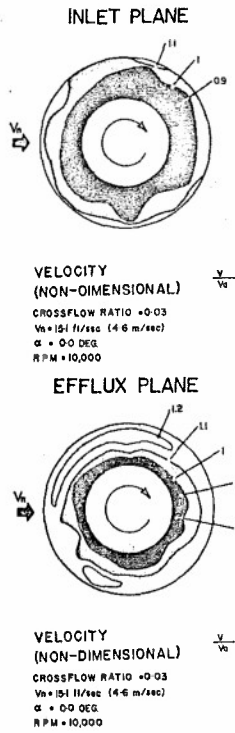


Fig. 9. Inlet-efflux comparison: velocity distributions at 0.03 crossflow.

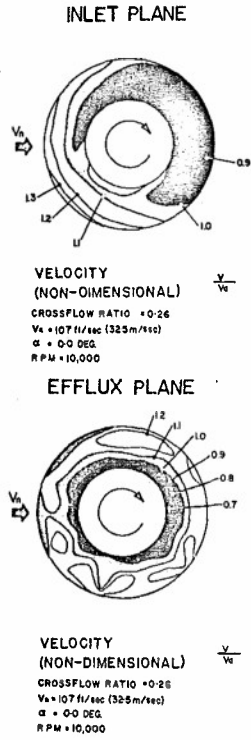


Fig. 10. Inlet-efflux comparison: velocity distributions at 0.26 crossflow.

to the low crossflow ratio case. The fan evidently operated powerfully on the major distortion problem, and so it was not surprising to find that the efflux velocity distribution was not altered significantly by changes in the wing pitch angle setting, as Figure 11 shows.

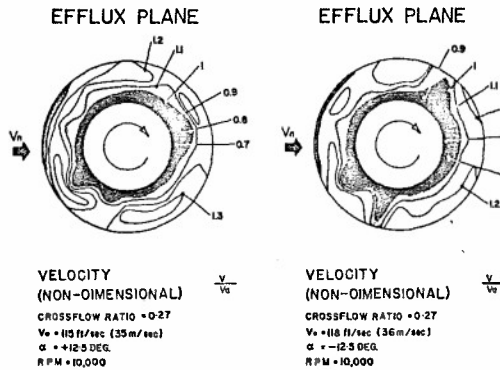


Fig. 11. Efflux velocity comparison: distributions at 0.27 crossflow and pitch angles of  $+12.5^\circ$  and  $-12.5^\circ$ .

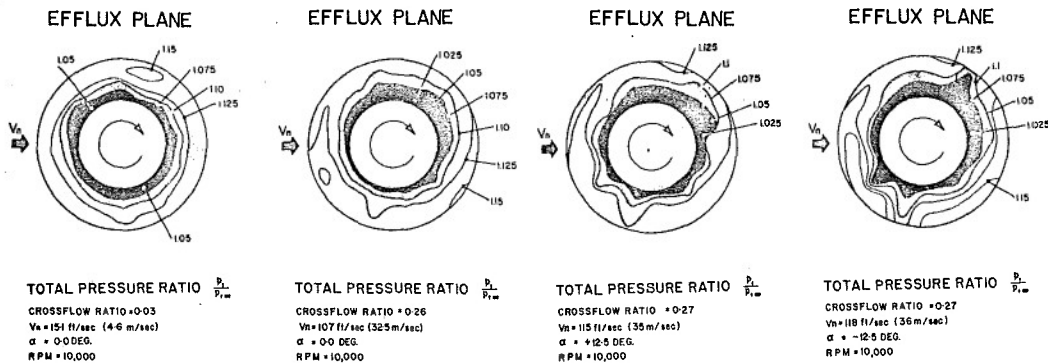


Fig. 12. Efflux total pressure ratio distributions.

The fan's capability in dealing with the inlet distortion was also indicated by the general invariance with crossflow and pitch change of the total pressure distribution (since inlet total pressure distribution was reasonably constant hence also pressure ratio distribution), see Figure 12. The advancing rotor blades, subjected to more positive incidence, appeared to work a little harder - as shown by somewhat larger pressure ratios on the port side of the efflux plane. The observed radial variation of total pressure ratio is considered to be a function of fan design and is not attributed to crossflow in any way.

As might be expected, the efflux swirl bears no relationship to the inlet swirl distribution. In fact, as Figure 13 shows, the distributions are quite similar at both crossflow ratios and remarkably uniform circumferentially. Angles of 15° to 20° are indicated except near the centrebody and below

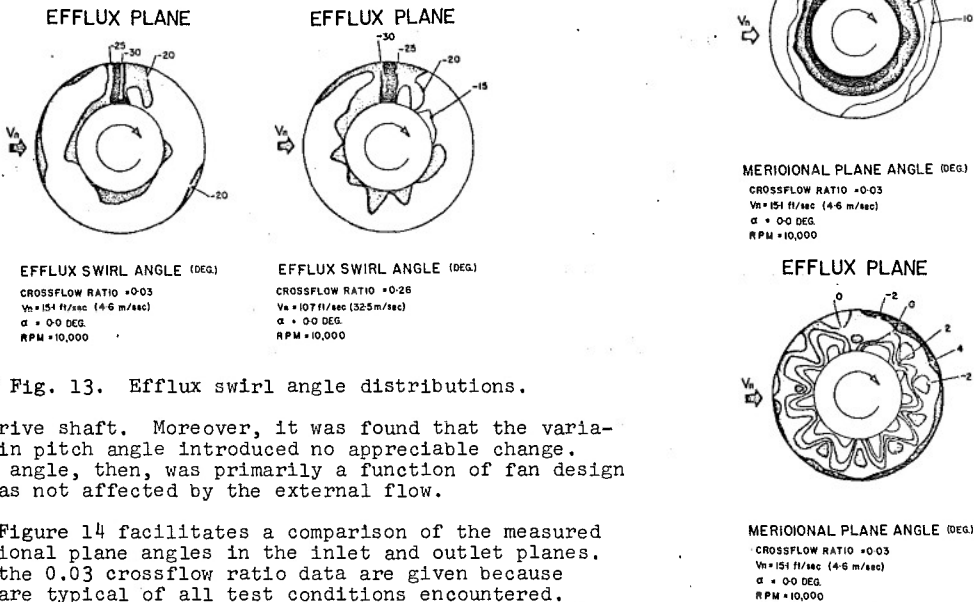


Fig. 13. Efflux swirl angle distributions.

the drive shaft. Moreover, it was found that the variation in pitch angle introduced no appreciable change. Swirl angle, then, was primarily a function of fan design and was not affected by the external flow.

Figure 14 facilitates a comparison of the measured meridional plane angles in the inlet and outlet planes. Only the 0.03 crossflow ratio data are given because they are typical of all test conditions encountered. The most important feature here was the degree of radial flow redistribution across the fan: the inflow converged and the efflux diverged. The general lobular appearance of the outlet distribution is associated with blade-to-blade flow variations and is therefore not of prime relevance to the distortion issue.

Fig. 14. Inlet-efflux comparison: meridional plane angle at 0.03 crossflow and zero pitch angle.

By far the most interesting and crossflow-sensitive variable in the efflux plane was the static pressure; distributions in coefficient form (referenced to free stream static pressure and normalized by average inlet dynamic pressure) are depicted in Figure 15. Generally, in the presence of crossflow, the distributions exhibited negative pressures on the starboard side (retreating blades) and positive pressures in the outer annulus on the port side (advancing blades). Pressures in the front of the annulus were positive and those in the lee of the efflux jet, relative to the crossflow direction, exhibited

considerable recovery - unlike that expected had crossflow separated fully at the sides of the efflux jet. The lack of side-to-side symmetry was presumed to be associated with efflux swirl. This circumferential pressure distribution suggests a fundamental similarity between the observed interaction of the crossflow with the swirling jet and

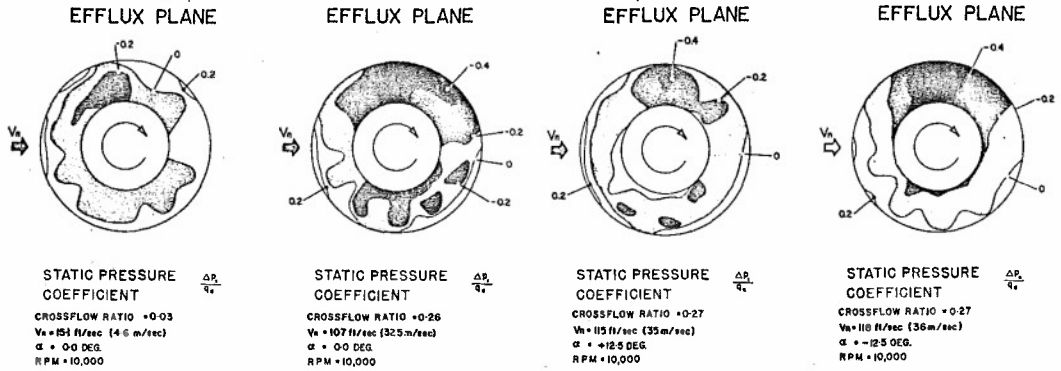


Fig. 15. Efflux static pressure distributions.

potential streaming flow around a rotating cylinder. The recovery in the lee of the jet is reasoned to be the result of a substantially reduced wake and is probably assisted by the boundary layer control capabilities of the efflux jet. A short film showing a flow visualization of these crossflow effects (9) illustrates this region of interaction.

The overall level of static pressure seemed somewhat dependent on wing pitch angle; the +12.5° distribution being generally more positive as might be expected.

It is demonstrated, therefore, that the static pressure field at the exit of a shallow lifting fan configuration during crossflow is far from being uniform and that it represents a well defined crossflow distortion in its own right, i.e. it is independent of the inlet distortion but dependent on the presence of crossflow.

POWER REQUIREMENTS

Input power (including transmission losses) computed from measured torque and speed is shown in Figure 16. Although the data shown pertain to zero pitch, the lines drawn are typical for the +12.5° and -5° pitch conditions as well. Power, as is readily seen, was independent of crossflow velocity and dependent only on fan speed. The implication appears to be therefore that thrust losses associated with high crossflow speeds must have resulted from a falling efficiency.

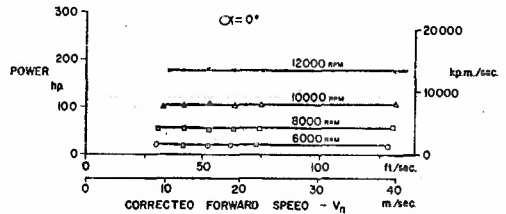


Fig. 16. Input power v. corrected forward speed ( $\alpha = 0^\circ$ ).

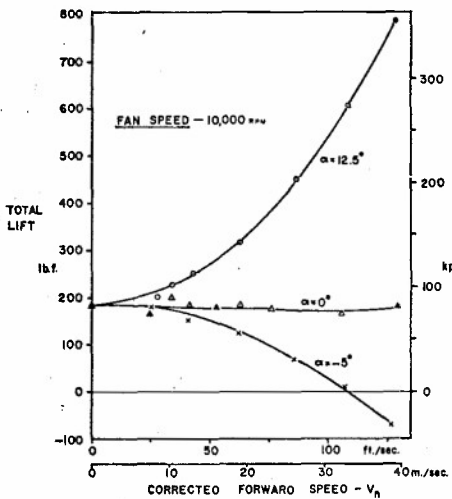


Fig. 17. Total lift v. corrected forward speed at 10,000 r.p.m.

FAN THRUST

Total lift measurements for a fan speed of 10,000 r.p.m. and three pitch angles (-5°, 0°, +12.5°) are shown in Figure 17. The existence of two individual contributions are demonstrated here: fan thrust and a two-dimensional wing contribution. The latter tends to be relatively large at high forward speed and angle of attack. The wing, however, is viewed without special interest; in fact, it can be thought of as providing merely a support role: it holds the fan and ensures smooth inlet flow typical of a fan-in-wing environment. The wing contribution, based on a span of 100 in. (2.54 m), was therefore subtracted from the total measurement to yield fan thrust (a force normal to the wing plane). No attempt was made to divide fan thrust into efflux thrust and induced lift

contributions. It is hoped, though by no means proven, that fan thrust can be treated simply as an increment for combined system lift involving wings other than tested here.

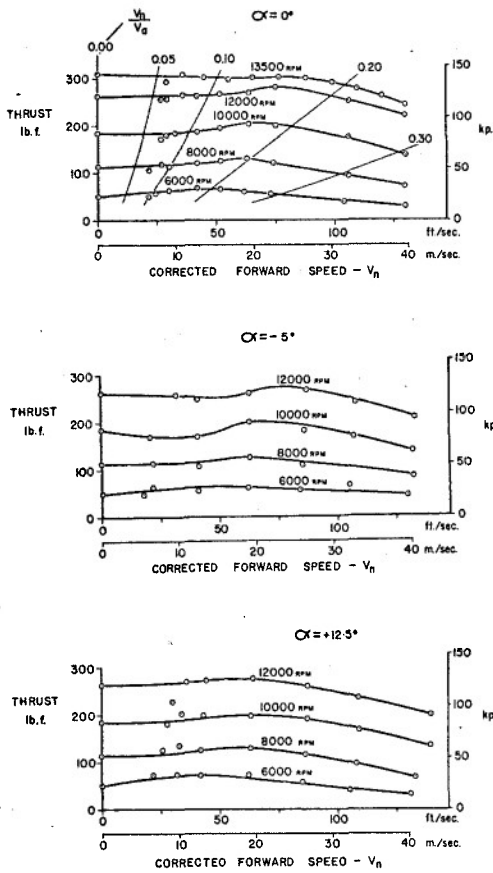


Fig. 18. Fan thrust v. corrected forward speed.

faced with a circumferential total pressure distortion. The shallow lifting fan however does not appear to behave this way. When exposed to crossflow, it tends to induce a more uniform total pressure in the inlet, and while accepting and supporting a non-uniform inlet velocity field, it experiences an increased mass flow.

It is obviously inadequate to explain this unusual performance in terms of the characteristic of the complete fan unit. Since the crossflow caused a circumferential distortion around the fan, it may be helpful to view the fan as comprising a large number

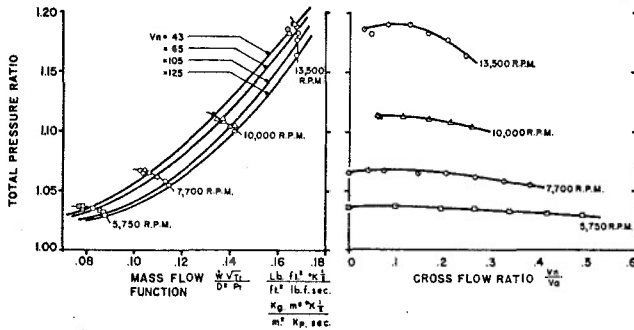


Fig. 19. Fan characteristics.

Figures 18a, b, and c illustrate the so-calculated fan thrust as a function of crossflow velocity. Initially at a low forward speed thrust was augmented, subsequently at higher speed after reaching a maximum, it diminished. The initial improvement over datum thrust was accompanied by a markedly noticeable reduction in fan speed fluctuation. Thrust appeared to be independent of angle of attack within the given range of pitch angle, thereby substantiating in a qualitative way a similar tendency observed from the independently measured flow distribution. Hence an important simplification to performance testing may be justifiably introduced, that is to say, the number of test variables can be reduced by one, provided that the two-dimensional wing contribution is first removed from the total measurement. As far as overall fan performance is concerned, prime information can be obtained at only one pitch setting.

FAN CHARACTERISTICS

The total pressure ratio of the fan, subject to the previously mentioned sources of error, is given as a function of corrected mass flow and crossflow ratio in Figure 19. The influence of crossflow is clearly indicated. The crossflow effect on the constant speed performance of the fan was somewhat similar to, but not as simple as, varying the back pressure, i.e. increasing crossflow generally induced greater mass flow through the fan, as Figure 20 shows. The effect of crossflow on total pressure ratio was novel: at low crossflows there appeared to be a small enhancement while at large crossflows the total pressure ratio fell off noticeably. A similar variation was indicated for fan thrust.

This manifestation of distortion was unexpected in view of the acquired experience on the effects of total pressure distortion on compressors and fans. In this connection it is held that a reduction of flow is the result of an observed tendency of compressors to operate with uniform inlet velocity when faced with a circumferential total pressure distortion. The shallow lifting fan however does not appear to behave this way. When exposed to crossflow, it tends to induce a more uniform total pressure in the inlet, and while accepting and supporting a non-uniform inlet velocity field, it experiences an increased mass flow.

It is obviously inadequate to explain this unusual performance in terms of the characteristic of the complete fan unit. Since the crossflow caused a circumferential distortion around the fan, it may be helpful to view the fan as comprising a large number of small compressors working in parallel. This concept is already a well-established aid in understanding the response of compressor performance under conditions of total pressure distortion. It has, for example, led to the theory that spoiled and unspoiled compressor sectors are like separate compressors operating on a unique characteristic, at least away from stall at maximum flow (2). The shallow lifting fan problem may be resolved similarly by examining the individual rotor blade passages in the light of deviations from a standard characteristic, as indicated by periodic and interactive effects.

The prime crossflow distortion in a shallow intake was seen to be a velocity maldistribution which, as was suggested, could be characterized by a mostly circumferential variation of swirl and axial velocity components. The swirl caused a swing in rotor blade incidence which resulted in higher axial velocities and pressure rise on the advancing blades, and lower axial velocities and pressure rise on the retreating blades. In addition, there was the basic fore-to-aft variation in axial velocity associated with flow bending which, when combined with the swirl-induced axial velocity variation gave an anti-rotational skewed velocity distortion. In fact, the fan operated with the inflow distortion as if there existed a set of loss-free inlet guide vanes providing different degrees of pre-swirl. The fan blade passages therefore functioned with differing characteristic lines depending on the blades' instantaneous circumferential position, as indicated schematically in Figure 21. This inlet guide vane analogy, proposed in Reference 10, together with the parallel compressor concept admits the observed trend of increasing total pressure ratio with mass flow at low crossflow ratios, depending upon the chosen aerodynamic design of the fan. Acceptance of this theory is however not necessary for appreciating that it is mandatory to look 'inside' the fan in order to ascertain if the crosswind has a stabilizing influence on the fan.

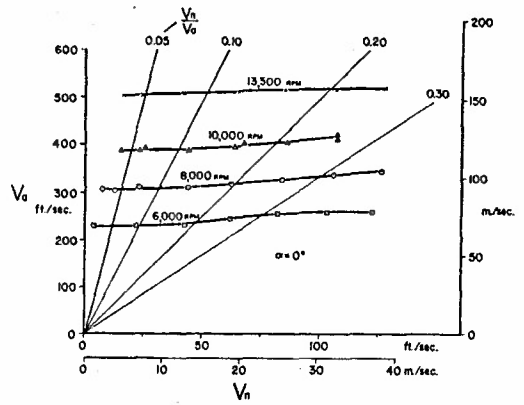


Fig. 20. Fan axial velocity  $v_a$  corrected forward speed ( $\alpha = 0^\circ$ ).

Detailed consideration is a prerequisite to the design of a high-performance shallow lifting fan tolerant of crossflow distortion with adequate surge margin.

CONCLUSIONS

1. The crossflow-induced distortions in a fan-in-wing flow field comprises two parts. First, there is a basic interaction between the flow fields which would be present even without the fan. Second, there is a feedback effect of the fan on this flow field, due to the fan's proximity to the external flow.
2. Both inlet and outlet planes experienced flow distortion. In the crossflow ratio range zero to 0.27 inflow distortion was observed to be a non-uniformity of velocity magnitude and direction. The flow field appeared to be consistent with one effected by stream curvature-producing agents, viz. crossflow bending and contracting, and secondary flow effects, and was one of essentially constant total pressure. Outflow distortion was observed to involve primarily static pressure. The distribution of static pressure around the jet can be related to that around a rotating cylinder in streaming potential flow.
3. The fan's feedback on the inlet flow was to introduce considerable skewness to the velocity distribution. Axial velocities were increased from their basic distortion magnitudes on the advancing blade side of the fan. The fan also induced a pre-swirl that caused side-to-side differences in flow angle.
4. Despite severe velocity maldistribution in the inlet of the fan, substantial flow redistribution took place within the fan stage and almost completely attenuated the inlet distortion. The fan imparted an almost uniform swirl to the efflux.
5. Over the crossflow ratio range tested there was no first order variation of fan performance with angle of attack - hence the wing may be regarded as an effective flow alignment device. Second order effects included a small reduction of inlet swirl at negative angle of attack and a small increase in the level of outlet static pressure at positive angles of attack.
6. The changes in fan thrust and total pressure ratio with increasing crossflow ratio were gradual, initially an enhancement and finally a falling-off.
7. Fan input power was found to be invariant with crossflow velocity and to vary only with fan speed.

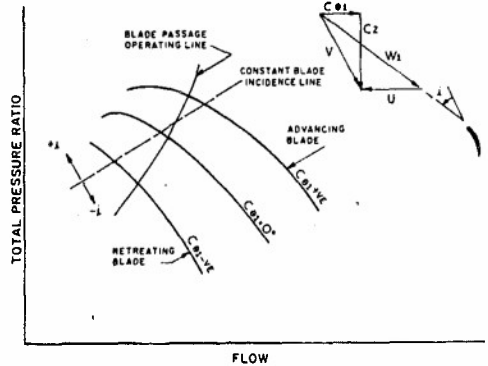


Fig. 21. Diagrammatic representation of variation in rotor blade passage characteristic with inlet swirl at crossflow,  $U = \text{constant}$ .

## REFERENCES

1. Cockshutt, E.P., "VTOL Propulsion - 1970 Perspective", Canadian Aeronautics and Space Journal, Vol. 17, No. 4, April 1971, pp 117-130.
2. Reid, C., "The Response of Axial Flow Compressors to Intake Flow Distortion", A.S.M.E. Paper No. 69-GT-29, Gas Turbine Conference & Products Show, Cleveland, Ohio, March 9-13, 1969.
3. Lieblein, S., Yuska, J.A., Diedrich, J.H., "Wind-Tunnel Tests of a Wing-Installed Model VTOL Lift Fan with Coaxial Drive Turbine", NASA TMX-67854, 1971.
4. Schaub, U.W., Cockshutt, E.P., "Analytic and Experimental Studies of Normal Inlets, with Special Reference to Fan-in-Wing VTOL Powerplants", Proceedings of the International Council of the Aeronautical Sciences, Spartan, 1965, pp 519-553.
5. Schaub, U.W., Bassett, R.W., "Analysis of the Performance of a Highly Loaded 12-inch VTOL Z-Axis; Fan-in-Wing Model at Zero Forward Speed", DME Aero Rept. LR-439, National Research Council, Ottawa, Canada, September 1965.
6. Schaub, U.W., Sharp, C.R., Bassett, R.W., "An Investigation of the Three-Dimensional Flow Characteristics of a Non-Nulling Five-Tube Probe", DME Aero Rept. LR-393, National Research Council, Ottawa, Canada, February 1964.
7. Schaub, U.W., Bassett, R.W., "Low-Speed Aerodynamic Testing of VTOL Models: A Method for the Compensation of Wind-Tunnel Interference Effects", Canadian Aeronautics and Space Journal, Vol. 17, No. 6, June 1971, pp 245-249.
8. Schaub, U.W., "Experimental Studies of VTOL Fan-in-Wing Inlets", Aerodynamics of Powerplant Installation, AGARDograph 103, Pt. 2, AGARD, October 1965, pp 715-747.
9. Bassett, R.W., (Directed by), "Fan-in-Wing Crossflow Studies", Film Serial 22, Division of Mechanical Engineering, National Research Council, Ottawa, Canada, 1970.
10. Beeler, E.F., Przedpelski, Z.J., "Lift Fan Design Considerations", Annals New York Academy of Sciences, Vol. 154, Art. 2, November 22, 1968, pp 619-640.

## APPENDIX

## TUNNEL INTERFERENCE CORRECTIONS

It is well known that high-lift models tend to produce considerable tunnel interference, particularly at low tunnel speeds. The classical tunnel interference correction methods are invalid because no account is made for the efflux jet. More recently developed interference rules are more useful as guidelines for maximum model size and test range, and tend to relate to pure high-lift configurations such as isolated rotors, ducted fans, etc., which feature no or very small external lifting surfaces in the vicinity of the high-lift element. Yet to neglect interference effects and to revert to

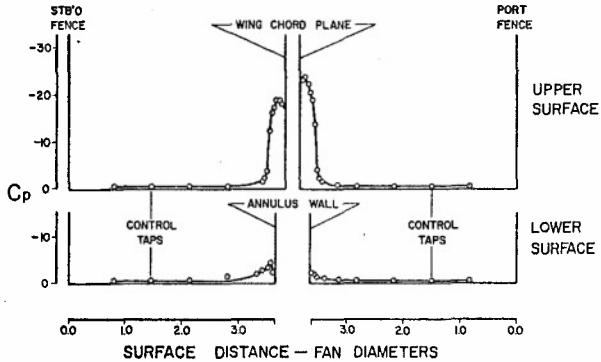


Fig. 22. Spanwise surface pressure distributions at 35% of chord.

dimensional wing (fan openings faired-in) at known tunnel conditions. To demonstrate that the control pressures were free of fan induced effects, upper and lower surface spanwise pressure distributions at the 35% chord station for a crossflow ratio of 0.26 and a fan speed of 10,000 r.p.m. are shown in Figure 22.

the use of uncorrected data leads to errors that are unacceptably large in instances where the model size is not negligibly small relative to the test section dimensions. Such was deemed to be the case for the N.R.C. fan-in-wing model. Consequently, a simple correction method was devised at N.R.C. to give equivalent free air conditions (7), and it appears to give reasonable corrections for tunnel speeds larger than 40 ft/sec (12.2 m/s) or crossflow ratios (simulated forward speed divided by average fan axial velocity) greater than 0.1, whichever is the larger constraint.

This method makes use of measured control pressures on the surface of the wing away from the source-sink field of the fan and a prior calibration of the same pressure orifices on the two-

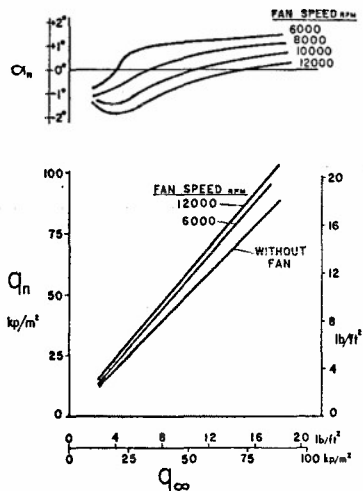


Fig. 23. Tunnel corrections for zero wing pitch angle.

The magnitude of the corrections for the zero pitch angle case are shown in Figure 23. It can be seen that without the fan the ratio of dynamic pressures was unity because datum corrections, in accord with classical theory, were negligible for this particular installation. Appreciable corrections were indicated however for the powered fan-in-wing model, viz.  $q_n/q_\infty = 1.12$  for 6000 r.p.m. and 1.18 for 12,000 r.p.m. and higher. This result seems reasonable since the efflux jet may be regarded as a swept-back cylinder which offers solid blockage. The lower the crossflow ratio, the less sweep-back there is, and hence the greater the approach air overspeed at the model. The indicated angle of attack corrections are more complex to understand. They are believed to be controlled by two opposing effects. At low fan speeds or high tunnel speeds, i.e. large crossflow ratios, at which the free air state is approached, the fan-in-wing causes a high-lift condition that results in an effective positive angle of attack. As fan speed is increased or tunnel speed is decreased, i.e. low crossflow ratios, progressively more tunnel constraint is felt and a reduction of angle of attack is effected, which in sense is also indicated by classical correction theory.

## THE DESIGN, DEVELOPMENT, AND TESTING OF A SUPERSONIC TRANSPORT INTAKE SYSTEM

by E. Tjonneland  
The Boeing Company  
Seattle, Washington, USA

## SUMMARY

The performance criteria, including engine airflow matching requirements, of an axisymmetric mixed-compression intake for a supersonic transport application are described and related to the selection of the design features of the intake variable-geometry components. Viscous technology is applied to the design and development of the boundary layer control system to account for intake viscous interactions and to scale model results to full-scale designs. Small, low-angle bleed holes  $20^\circ$  to the surface yield high flow coefficients. Hole diameters of approximately half the height of the boundary layer displacement thickness are used to improve the cleanliness of the supersonic diffuser flow and to maximize pressure recovery of the bleed air. Vortex valves are incorporated in a fluidic normal shock stability system to allow operation at peak intake recovery and remain started during atmospheric or engine transients.

## INTRODUCTION

A supersonic transport air intake system for future commercial operations should be designed to achieve a level of performance in excess of that achieved in supersonic aircraft currently in service. A wide range of operating conditions, engine and airplane interactions, and operating reliability require a careful balance of the design. Various advanced design features were incorporated in an SST air intake system suitable for commercial application in a Mach 2.7 cruise speed vehicle. Improvements in the state of the art of intake design, especially in the areas of viscous technology, intake stability, and intake/engine airflow matching, were required to determine the various features of the intake. They also greatly reduced efforts during development by providing better predictions and correlation with experimental data. The major design criteria imposed on the system are shown as related to the overall design, realizing that many iterations are carried out before the final set of design features and criteria mutually agree.

## PERFORMANCE CONSIDERATIONS

The intakes on a supersonic long-range transport aircraft receive early attention in configuration and performance studies. The expected configuration problems for best pod shape, interference effects, inflow conditions, exhaust effects, engine-out conditions, etc., are quickly recognized. The performance studies soon show that the intake is also responsible for a significant cruise range penalty. In contrast to the intakes used on long-range subsonic aircraft, the intakes of a supersonic aircraft have total pressure losses and viscous effects (resulting in bleed air drag) which are very significant. Even with optimistic recovery and bleed estimates, an SST with a range of 3500 miles has an airplane cruise range loss, resulting from intake total pressure losses and bleed drags, which is in excess of 12%. There are also numerous other performance loss items during airplane off-design operation. The net effect is to set very high performance objectives in supersonic intake designs. These must be based on firm experimental or analytic design data to prevent goals being set too high. Influence factors for key intake performance items are shown in Figure 1. The considerable effect on aircraft range of bleed drag (both the amount of bleed and bleed air recovery), cruise bypass drag, and intake recovery clearly show the incentive to set high performance goals. While weight trades are important, Figure 1 shows that weight savings can rarely be justified if they compromise performance.

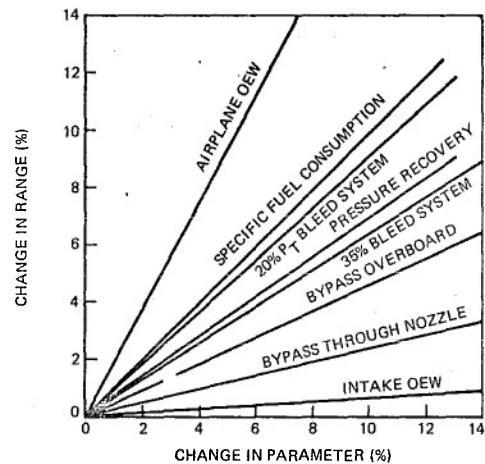


FIG. 1 INTAKE PERFORMANCE TRADE FACTORS FOR CRUISE

## PERFORMANCE CRITERIA

Specific performance objectives of the SST intake described in this paper are shown in Figures 2 and 3. The steady-state performance levels of Figure 2 were to be met simultaneously, with the intake providing inherent stability margins and tolerances to disturbances. For example, with the intake started at Mach 2.65 and operating at a recovery of 91%, the intake was designed to tolerate a step reduction of 5% in engine corrected airflow, without controller action, and remain started. Similarly, with the intake operating on-design at Mach 2.65, a step reduction of Mach 0.05 was not to cause an intake unstart. These criteria were established from considerations of the intake control system performance as well as the steady-state operating characteristics of the intake. The first criterion was met by incorporating vortex valves in the intake throat section as an auxiliary normal shock stability system. The second criterion specifies the minimum allowable throat Mach number during on-design, started intake operation. With the incorporation of vortex valves in the intake throat section, another design criterion is immediately established: the intake throat station should be fixed relative to the intake cowl throughout the started Mach number range. This will allow

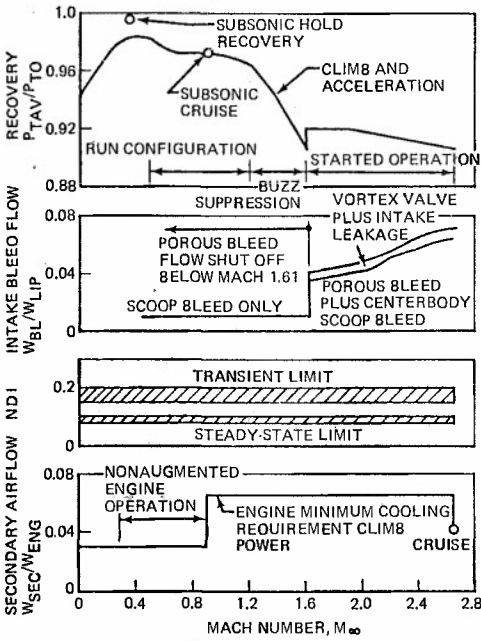


FIG. 2 INTAKE PRIMARY PERFORMANCE OBJECTIVES

maximum intake performance to be maintained while using the vortex valves when dynamically needed to guard against intake unstarts.

Another important performance parameter is that of cowl thickness. To obtain a favorable interference between the pod and the wing, the intake cowl lip thickness had to be minimized. Structural requirements dictated a cowl lip thickness angle of 2.5°. An increase of 1° would have resulted in a range loss in excess of 1%. The inside cowl and the centerbody cone angles determine the strength and pattern of the internal shock waves. For a 2.5° cowl thickness angle, an inside cowl angle of 0° and a centerbody half-cone angle of 11° resulted in the desired internal shock strength.

In determining intake sizing, it was essential to avoid overboard bypass airflows during cruise. The intake size (i.e., lip radius) was chosen to match a standard-day engine cruise power demand. For maximum power demand on a standard or cold day, engine rpm is trimmed back to avoid excessive supersonic intake operation. On a hot day with the engine operating at design rpm, the excess intake airflow supply is discharged through the secondary nozzle via the secondary air system. The overall system was matched such that essentially no overboard bypass airflow was needed for intake/engine airflow matching during normal climb and cruise intake operation.

INTAKE DESIGN AND OPERATION

The following sections describe in detail the variable-geometry components of the intake, their use in the operation of the intake, and the intake performance for the various flight regimes. Reference is made to the design objectives stated earlier, including the major analytical tools used in determining the intake design. Ten major areas are emphasized: intake variable geometry, intake takeoff/landing configurations, noise abate operation, intake run and bypass configurations, buzz suppression operation (including subsonic cruise), supersonic diffuser/bleed system design, intake bleed drag, auxiliary normal shock stability system, and supersonic, started mode performance.

Intake Variable Geometry

A schematic view of the intake lines is shown in Figure 4. The intake is axisymmetric, with mixed external-internal compression. Two major geometry components are incorporated to obtain the necessary geometry variations needed for engine airflow matching at transonic speeds and for proper flow area contraction at supersonic speeds.

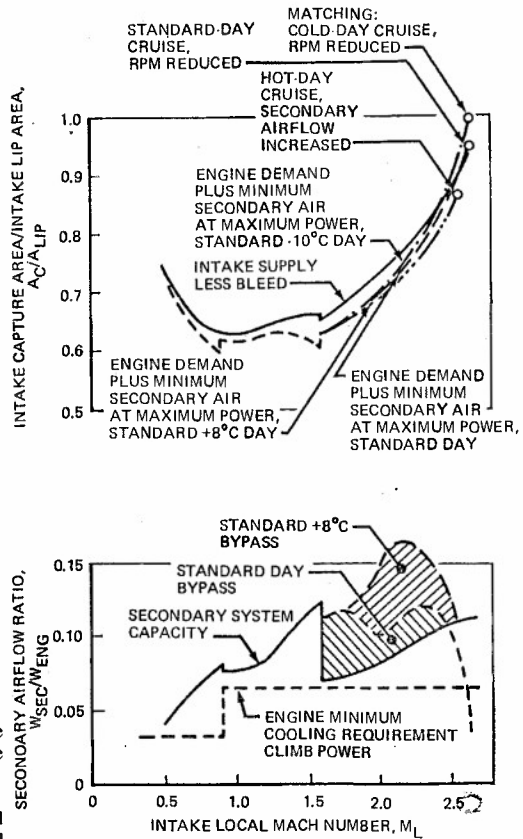


FIG. 3 INTAKE SUPPLY/ENGINE DEMAND AIRFLOW MATCHING

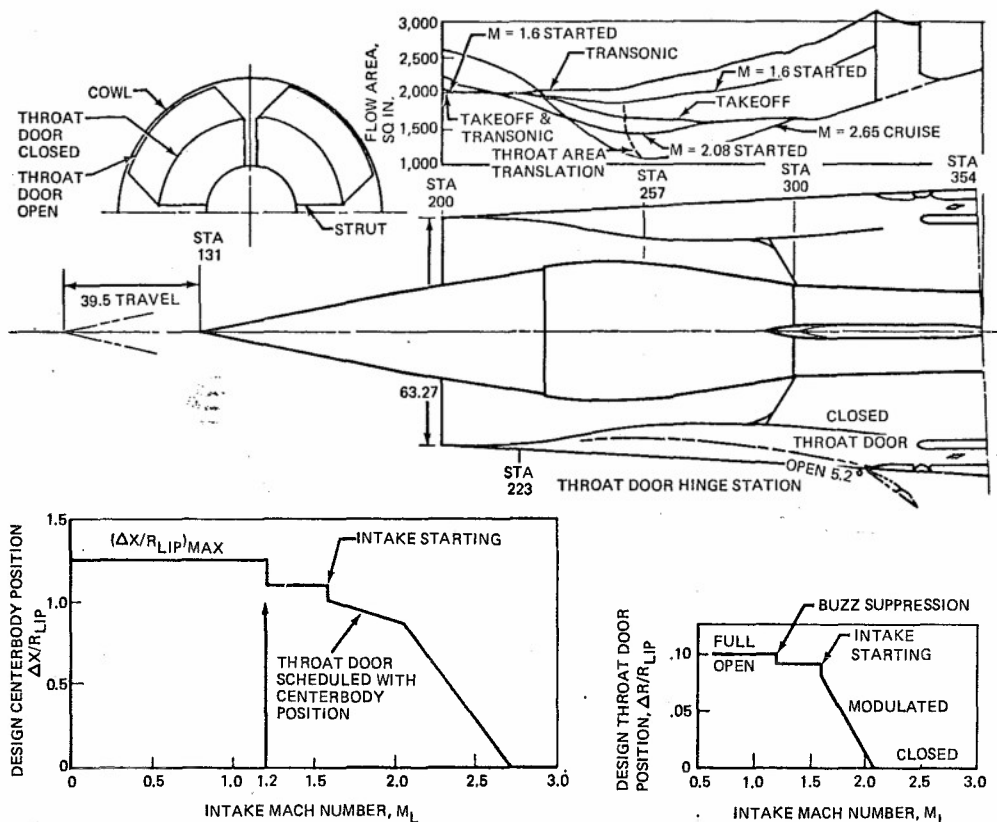


FIG. 4 INTAKE GEOMETRY

**Throat Doors/Centerbody**—The flow area required for transonic engine airflow matching is shown in Figure 4 as the minimum flow area just aft of the intake cowl lip station. This area allows a flow Mach number of 0.85 at full engine power and includes allowance for the engine secondary air cooling flows as shown earlier in Figure 3. To obtain the flow area variation required between the curves labeled "takeoff" and "transonic", a set of four cowl throat doors is used. These are 90° segments of the inner cowl, hinged at the forward end and rotated outward between parallel-sided (90°) structural beams in the intake. For supersonic airflow matching the centerbody retracts from its fully extended position a distance of 1.25  $R_{LIP}$ . The intake internal flow-area variation provided by this translation is shown in the area progression curves of Figure 4 as the area decrease between the curves labeled "takeoff" and "cruise."

The design translation schedules for these two components are also shown in Figure 4. It should be noted that during started intake operation, the centerbody is modulated via a closed-loop control to maintain a throat Mach number of 1.25, and the throat doors are scheduled as a function of centerbody position<sup>(1)</sup>.

**Secondary Air Valves/Bypass and Takeoff Doors**—A schematic of the secondary air valves and overboard bypass and takeoff doors is shown in Figure 5. There are eight butterfly-type secondary air valves, two per 90° segment in the intake secondary flow channel. They are used to regulate cooling air to the engine secondary nozzle, to serve as a fine control for positioning the normal shock during started intake operation, and to provide a means of intake/engine airflow matching during normal and hot-day cruise without having to open the overboard bypass doors.

There are four overboard bypass doors, one per 90° segment. These doors perform the well known function of spilling the large amounts of intake excess airflow that occur during airplane descent and inoperative engine conditions.

The bypass doors contain the secondary or bellmouth-contoured takeoff doors (see Figure 5), as a door within a door. The primary takeoff doors are separately hinged, free-floating inward to open the auxiliary flow passage to the engine. These primary doors are mechanically linked to the throat doors. Ten percent throat door travel outward from the cruise position forces the primary takeoff doors closed. During takeoff, when both primary and secondary takeoff doors suck in, the bypass door frames remain closed. At higher speeds, when intake internal pressures exceed external pressures, the secondary takeoff doors follow the bypass door frames to form the bypass doors, and the primary takeoff doors remain closed.

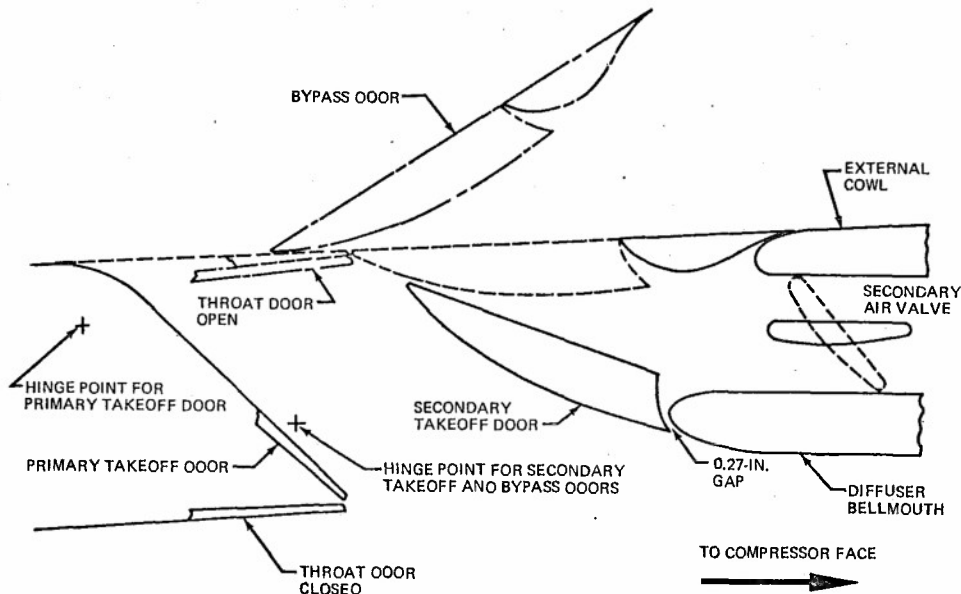


FIG. 6 SCHEMATIC OF SECONDARY AIR VALVES/BYPASS AND TAKEOFF DOORS

#### Intake Takeoff/Landing Configuration

The intake is shown in the takeoff/landing configuration in Figure 6. In this configuration the centerbody is extended, the throat and overboard bypass doors are closed, and the secondary air valves are open. The minimum duct flow area now occurs well aft in the intake as shown in Figure 4. This reduces the intake lip flow velocities and the resulting sharp-lip losses associated with low-speed intake operation. With the throat doors in the closed position, the auxiliary takeoff doors are allowed to float free of the overboard bypass door frames. The takeoff doors suck in as necessary to satisfy engine airflow demands. Details of intake low-speed performance are shown in Figure 7, where model and full-scale test data are compared. To achieve the low-speed recovery goals shown in this figure, a takeoff door size of  $29\% A_{LIP}$  is required. This was determined by model tests and analysis using Reference 2, and is based on main intake duct and takeoff door passage Mach numbers of 0.5 and 0.7, respectively. Detail design restraints later compromised the full-scale design such that a takeoff door area of only  $23\% A_{LIP}$  was available. The full-scale recovery and distortion data shown in Figure 7 were obtained from tests of the intake/engine combination shown in Figure 8. Smooth operation of the free-floating takeoff doors during unrestricted engine throttle operation was observed. Crosswind operation up to 35 knots at  $90^\circ$  showed no significant increase in distortion values. Takeoff performance was primarily a function of the bellmouth contours of the aft wall of the passage. A lemniscate-shaped bellmouth gave best results. The maximum primary takeoff door angle is  $35^\circ$ .

As the takeoff doors suck open to form a bellmouth contour, they also open a passage to the engine secondary air system (see Figure 6). This allows an opening through which the engine primary nozzle can pump the required nozzle-cooling air.

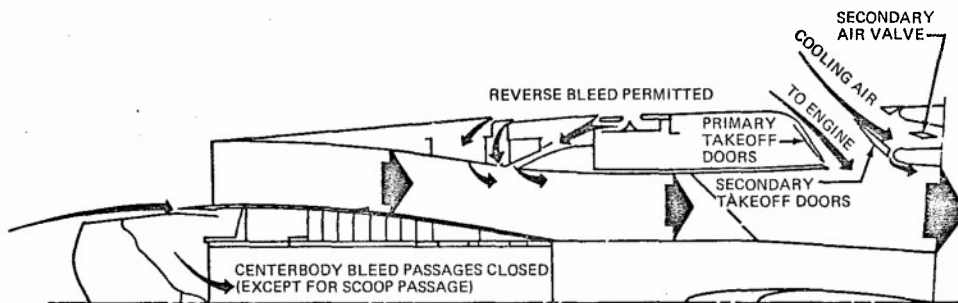


FIG. 6 TAKEOFF/LANDING CONFIGURATION,  $0 \leq M_L \leq 0.5$

SYM	A <sub>TO</sub> A <sub>LIP</sub>	MODEL SCALE	TAKEOFF DOORS
○	0.29	1/10	AXISYMMETRIC
□	0.29	1/10	DEVELOPED
△	0.23	1/1	AXISYMMETRIC
△	0	1/1	AXISYMMETRIC

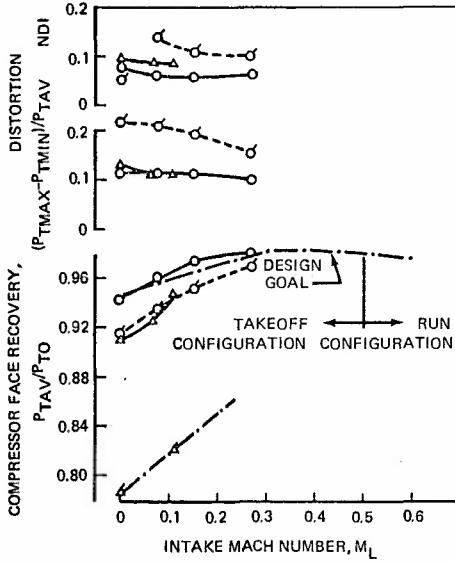


FIG. 7 INTAKE LOW-SPEED PERFORMANCE

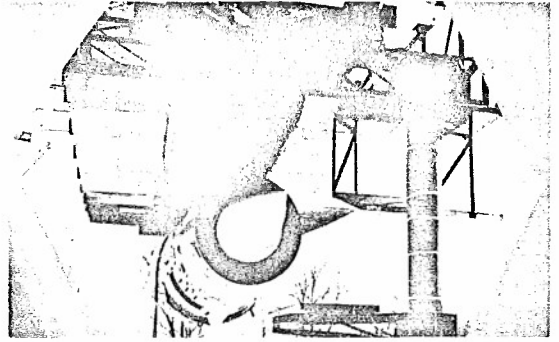


FIG. 8 FULL-SCALE INTAKE, ENGINE LOW-SPEED TEST CONFIGURATION

The intake takeoff configuration is automatically obtained when the engine mode selector is placed in the takeoff/landing position. This, of course, occurs during airplane taxi and takeoff and during descent when the airplane slows to a Mach number of approximately 0.5.

**Noise Abate Mode**

The noise abate mode is an optional intake control mode which may be manually initiated by the flight crew during intake operation in the 0.0 to 0.5 Mach range. In this mode the primary takeoff doors are held closed by positioning the intake throat doors at an intermediate opening. The secondary takeoff doors remain free-floating, and due to aerodynamic loading, they assume a full-open position. The overboard bypass door frames are held closed, while the secondary air valves remain

full open. A schematic of the noise abate mode showing the throat and bypass door configurations is shown in Figure 9. Holding the primary takeoff doors closed prevents compressor noise from radiating out these openings. Forward compressor noise radiation is significantly reduced by modulating the centerbody to maintain an intake throat Mach number of 0.85. The noise abate mode is automatically disengaged and the takeoff configuration engaged should high engine thrust operation (e.g., during airplane go-around) be required.

**Intake Run Configuration**

The intake run configuration is used between Mach 0.5 and 1.2. This configuration is automatically obtained during climb when the pilot places the engine mode selector in the run position at approximately Mach 0.5. In this configuration the centerbody is fully extended, the throat doors and secondary air valves are fully opened, and the overboard bypass doors are held closed. A schematic of the run configuration is shown in Figure 10. No controller action is used in the run configuration, and the bypass doors remain closed even when the engine airflow is decreased as in airplane descent. Thus, for low engine airflows, intake/engine airflow matching is obtained via intake foreshallage. An exception to this is the Mach 0.85 subsonic cruise condition. To reduce intake drags during subsonic cruise, the buzz suppression mode, which is described in a following section, is used.

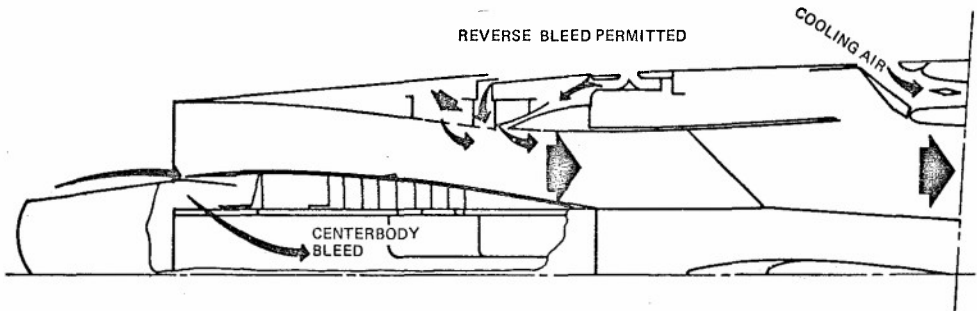


FIG. 9 NOISE ABATE MODE,  $M \leq 0.5$

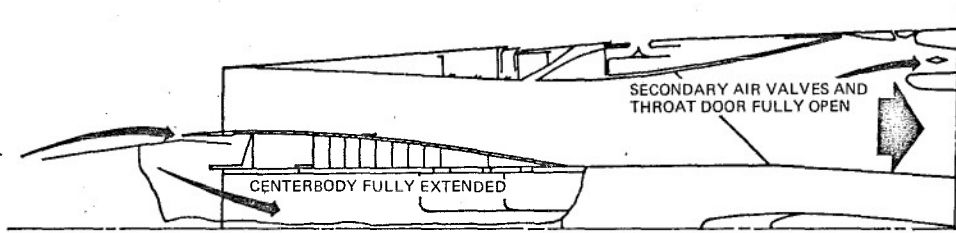


FIG. 10 RUN CONFIGURATION,  $0.5 \leq M \leq 1.2$

Figure 3 shows that throat doors were used to obtain adequate transonic flow area. Other ways were explored to solve this flow matching problem. For design comparisons, fixed-cowl intakes (no throat doors) with translating centerbodies only, were used. The flow capacities of two such intakes are shown in Figure 11 together with the variable-throat-door, translating-centerbody intake supply. A Boeing solid-cowl intake with essentially equal centerbody translation and cone angle, equal external cowl lip angle, and constant throat area station for started operation provided 12% less transonic flow than the throat door intake. A later design by NASA improved this to 8% less transonic flow than a throat door intake, but at a cost of 24% more centerbody translation,  $1.5^\circ$  higher external cowl angle, and a nonstationary throat station with centerbody translation. All three intakes were designed to provide acceptable recovery and low distortion characteristics, with a minimum duct area Mach number of 0.85. Earlier testing had shown that this was permissible to obtain maximum lip area flow coefficients, as long as a reasonable diffusion process was provided.

Because the throat station is constant with centerbody translation, which facilitates the incorporation of vortex valves, the Boeing solid-cowl design was further analyzed via intake/engine and performance/airplane integration studies. For these studies the available engine rpm trim control loop was studied for use during transonic operation to reduce engine rpm and obtain intake/engine airflow matching. It should be noted here that during climb at Mach numbers between 0.33 and 0.90, the engine operates without augmentation. At Mach 0.9, full engine augmentation is applied as the airplane approaches the transonic drag rise condition. On the maximum altitude placard on a cold day, the engine rpm is reduced by the normal engine control, holding constant corrected engine speeds, to an rpm close to the lowest engine operating rpm at which afterburner operation can be sustained. This left insufficient rpm trim capability to use for intake/engine airflow matching on cold-day flights. It would have resulted in flight restrictions on cold days if rpm trim had been chosen as a means to achieve transonic flow matching. On a standard-day flight, engine rpm trimming could have been used to reduce engine airflow 12% to match the Boeing solid-cowl intake supply shown in Figure 11, but would have reduced the normal rpm margin from augmentor blowout by 80%. Also, severe reduction in the standard-day transonic thrust margins associated with the engine rpm reduction would occur. Thus, the Boeing solid-cowl intake sized for cruise (see Figure 11) was deemed unfeasible for the engine being considered. Oversizing the solid-cowl intake for cruise was considered, but drag penalties for cruise bypass as shown in Figure 1 ruled this out, especially since the outboard intake was already oversized by 4% due to a lower outboard local Mach number 2.61 versus 2.65 for the inboard intake on the airplane being considered. The intake was designed for the higher local inboard Mach number of 2.65 (for Mach 2.7 cruise). All curves and design data are shown for this intake; the outboard intake was identical and simply operated at a 0.04 lower local Mach number.

Data obtained from scale-model tests of the variable-cowl intake operating in the run configuration are shown in Figure 12. Design recovery at low engine face distortion levels was obtained for the full range of operation in this "uncontrolled" run configuration. Data shown in Figure 12, from Mach 1.2 to 1.6, are for the intake operating in the suppression mode as explained in a following section. Figure 13 shows secondary air duct pressure recovery for Mach numbers to 1.2. The solid curve with data points shows that at flight speeds up to Mach 0.5, in takeoff configuration, the secondary air supply is greater than required (even for maximum augmentation). From Mach 0.5 to 0.8 the secondary air supply is shown to be adequate for engine operation at continuous maximum dry power. Maximum augmentation operation is allowed above Mach 0.8 or well below the speeds where augmentation is applied for transonic and supersonic acceleration.

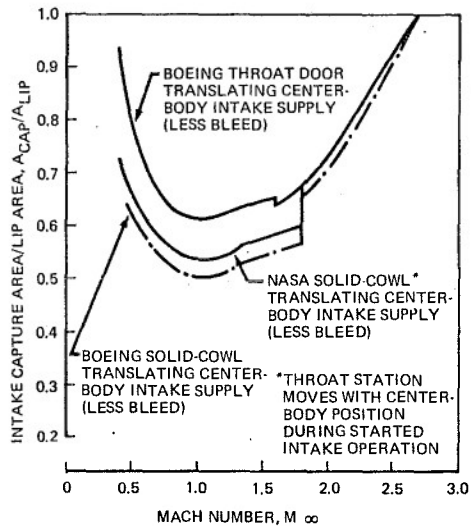


FIG. 11 AIRFLOW SUPPLY OF FIXED AND VARIABLE COWL INTAKES

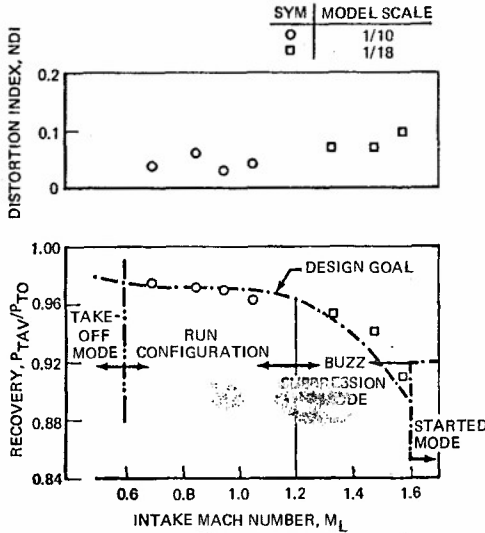


FIG. 12 EXPERIMENTAL TRANSONIC INTAKE PERFORMANCE

Intake Bypass Configuration

The maximum overboard bypass door opening of 45%  $A_{LIP}$  at an angle of  $33^\circ$  was chosen to provide buzz-free intake operation (above Mach 1.3) with all intake hydraulic power shut off and the engine rotor essentially stopped (aerodynamic engine windmill brake applied). During this failure condition, aerodynamic forces cause the centerbody to extend fully and the throat doors, secondary air valves, and overboard bypass doors to open fully. The full-open throat doors provide a smooth airflow passage to the overboard bypass doors as shown in Figure 5. Figure 14 shows the buzz margins and bypass corrected airflows for the intake bypass configuration. For local Mach numbers greater than 2.4, the maximum bypass door area of 45%  $A_{LIP}$  is sufficient to maintain a started intake. For Mach numbers less than 2.4, the combined corrected airflows of the windmill braked engine and the secondary and overboard bypass doors are not sufficient to start the intake, and the unstarted normal shock spills excess airflow externally. The full centerbody extension of the intake bypass configuration locates the centerbody bleed scoop (as discussed later) just forward of the intake cowl lip. By removing approximately half the centerbody boundary layer at this point, considerable normal shock spillage could be obtained before the onset of buzz. This reduces the maximum bypass door opening design requirement which, as noted from Figure 14, occurs at a local Mach of 1.3 with an intake angle of slideslip of  $3^\circ$ . An angle of slideslip of  $5^\circ$  at Mach 1.3 is not used as the maximum bypass door opening requirement because of the low probability of its occurrence.

Buzz Suppression Operation

The buzz suppression control mode is manually initiated during climb at approximately Mach 1.2. A generalized schematic view of the buzz suppression mode is shown in Figure 15. In this mode the centerbody is fixed at an extended position of 90% of full travel and the throat doors are placed at 90% of the full-open position. The slightly retracted centerbody position locates the centerbody bleed scoop in the best position relative to the cowl lip for buzz suppression. Boundary layer bleed at this point allows stable operation with large amounts of normal shock spillage. The slightly closed throat door position unports

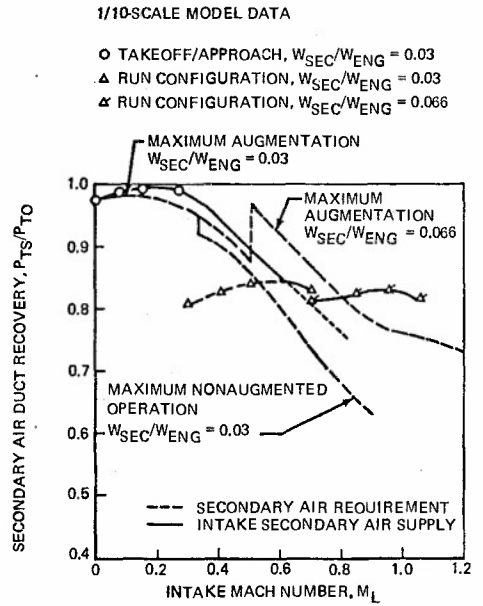


FIG. 13 SECONDARY AIR RECOVERY REQUIREMENTS

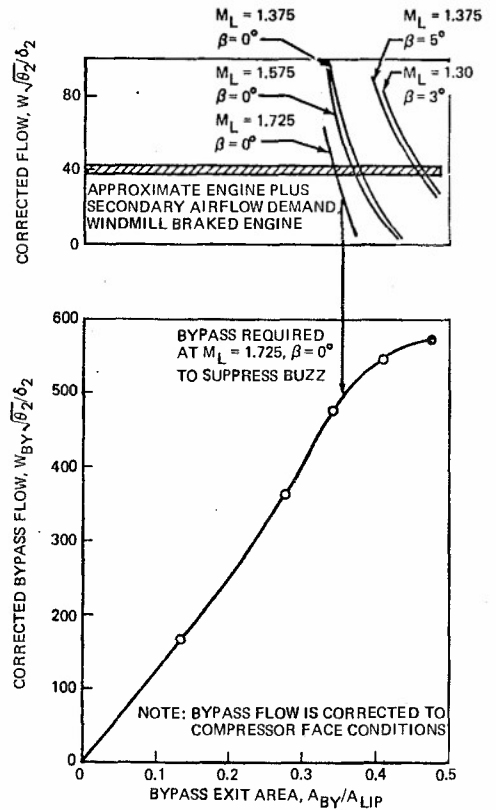


FIG. 14 BYPASS DOOR SIZING REQUIREMENTS

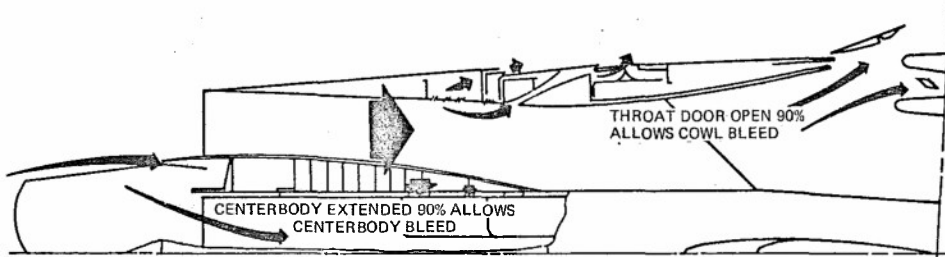


FIG. 15 SCHEMATIC OF BUZZ SUPPRESSION MODE INTAKE OPERATION,  $1.2 \leq M \leq 2.9$

the bleed exits in the outer cowl and allows the cowl boundary layer bleed system to function. When the throat doors are fully open, all cowl bleed exits are closed by mechanical valving action of the doors to prevent loss of unnecessary bleed below Mach 1.2 when intake air supply is critical. This also prevents negative bleed (recirculation) at low Mach numbers around 0.5 when duct Mach number is higher than external Mach number.

In this mode the secondary air valves and overboard bypass doors are modulated to maintain a duct Mach number of approximately 0.7 as determined by a static-to-total-pressure ratio located at the intake throat station<sup>(1)</sup>. For any given local Mach number, controlling the intake throat Mach number is essentially the same as specifying the desired amount of external normal shock spillage. It is interesting to note that the intake throat Mach number is far from being choked during buzz suppression control. This is often considered a requirement for buzz-free operation of an unstarted internal compression intake.

The key performance parameters for the intake in buzz suppression operation are shown in Figure 16. The data show that during standard-day climbout approximately 1.5% engine airflow trim is needed for matching at Mach 1.2. This reduces to zero at Mach 1.35. During cold-day operation continuous engine trim is used between Mach 1.2 and 1.6. Figure 17 shows a comparison of intake supply in the run configuration with the supply available in the buzz suppression mode for the Mach 1.2 to 1.6 range. It is noted that if the run configuration is used in this Mach range, the standard-day engine plus minimum secondary airflow needed for nozzle cooling may be supplied without engine rpm trimming. However, the run configuration does not contain control loops, and hence does not contain the capability for trimming engine rpm. If the run configuration were used between Mach 1.2 and 1.6, cold-day engine plus minimum secondary airflow demands would cause an inadvertent intake start (swallowing the normal shock) above Mach 1.2. Since the bleed system is designed to allow controlled, started operation only above Mach 1.6, premature starts produce large increases in distortion as the normal shock goes more and more supercritical. Furthermore, with descent engine-power settings, intake buzz would occur between Mach 1.2 and 1.6 if bypass doors remained closed as in the run configuration. For these reasons, the buzz suppression control mode is used between Mach 1.2 and 1.6.

The throat Mach/secondary air valve/bypass door control loop of the buzz suppression mode operates in the same manner as the normal shock/secondary air valve/bypass door control loop of the started mode. When engine airflow is increased as occurs during cold-day operation, the overboard bypass doors would be closed and the secondary air valves would close down to the minimum area needed to maintain secondary nozzle cooling. If engine airflow demand is sufficiently high, the throat Mach number of the buzz suppression mode would increase above its design value, and similarly the normal shock of the started intake would move downstream (i.e., higher supercritical) from its design position to achieve an airflow balance. This increase above the design values for these variables would activate the engine rpm trim control loop, and engine rpm is reduced until the control loop design values are again satisfied. The opposite occurs during hot-day conditions when the intake airflow supply exceeds the engine plus minimum secondary airflow demand. During this condition the engine rpm remains at its operating point and the secondary air valves open as necessary to achieve matching. Figure 18 shows the corrected airflow of the secondary air valves with valve displacement. During

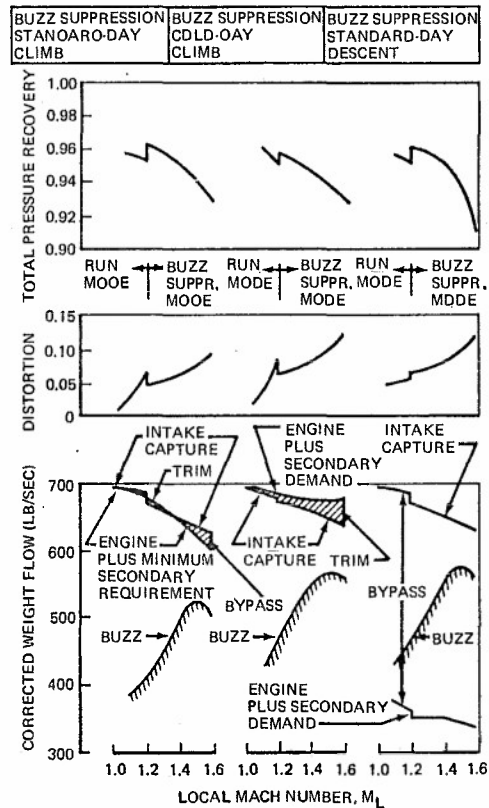


FIG. 16 INTAKE PERFORMANCE IN BUZZ SUPPRESSION MODE

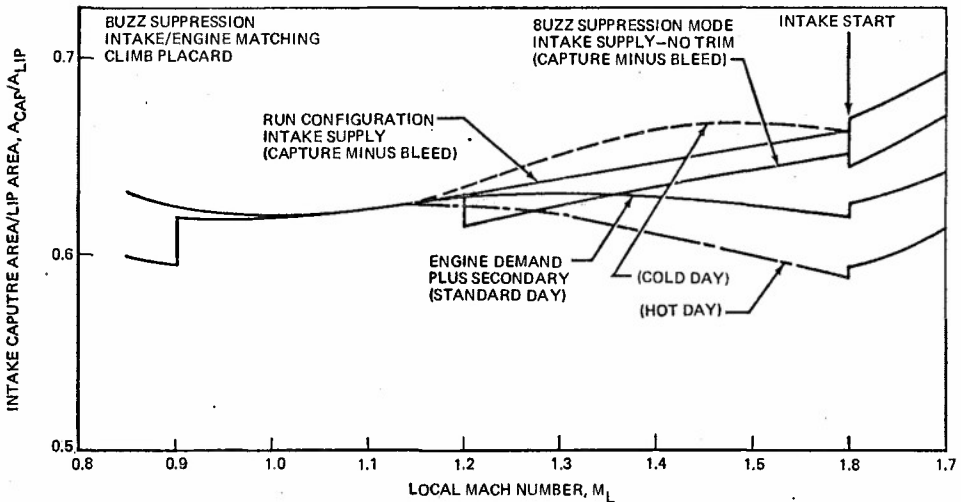


FIG. 17 COMPARISON OF RUN CONFIGURATION AND BUZZ SUPPRESSION MODE INTAKE SUPPLY

controller action the maximum allowable steady-state secondary air valve opening is  $0.07 A_{LIP}$ . This position, shown as the upper break point in Figure 18, is specified from stability analyses of both of the above control loops. For extremely hot day matching, the secondary air valves remain at  $0.07 A_{LIP}$  and the overboard bypass doors open to spill excess air.

The buzz suppression control mode is also used for two other purposes: (1) as a mode which provides stable airflow with low distortion level following an inadvertent unstart at Mach numbers greater than 1.6, and (2) for subsonic cruise.

Following inadvertent intake unstarts, a buzz-free mode was required that would allow continued engine operation until the pilot elected to initiate the restart sequence. The buzz suppression mode described provided the lowest engine face distortion levels during the unstarted operation. At Mach 2.65 the distortion was only around 2%. The restart could also be accomplished with the lowest distortion transients<sup>(1)</sup> when restarts were initiated with the intake in the buzz suppression configuration.

During subsonic cruise the pilot would select the buzz suppression mode to minimize long-range subsonic cruise drags by trading the forespillage drag of the run configuration for the lower overboard bypass door drag of the buzz suppression mode.

Supersonic Diffuser/Bleed System Design

The supersonic mode of operation, between Mach 1.6 and 2.7, called the "started mode," occurs when the normal shock moves to a position downstream of the intake throat at Mach 1.6. The intake configuration for this mode is shown in Figure 19. The throat Mach number is maintained constant at 1.25 by translation of the centerbody and the throat doors as the airplane Mach number changes. Between Mach 1.6 and 2.1 both the centerbody and the throat doors translate to maintain a constant throat Mach number and to minimize movement of the geometric throat station. Above Mach 2.1, the throat doors remain closed and the throat Mach number is controlled to 1.25 by translation of the centerbody only. The normal shock is maintained in a less than 1% supercritical position through the use of the secondary air valves, bypass doors, vortex valves, and rpm trim.

The design of the supersonic diffuser contours for the translating-centerbody axisymmetric intake was a complex procedure involving numerous iterations. Key features that influenced the contour selection were the selection of a throat Mach number of 1.25, the fixed positioning of the throat with respect to the cowl with centerbody translation, and the requirement that there be no spillage or bypass from the intake at cruise.

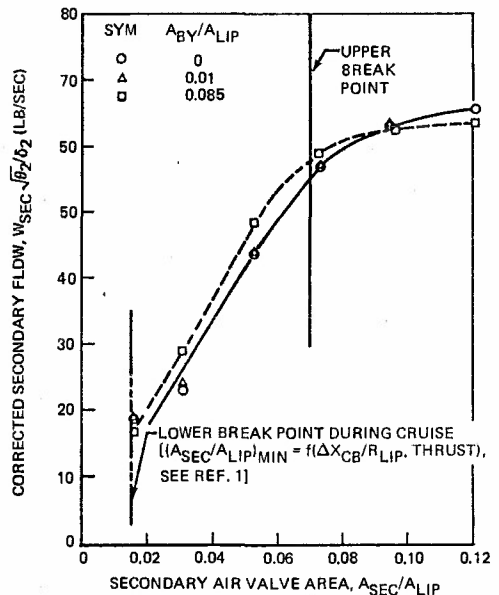
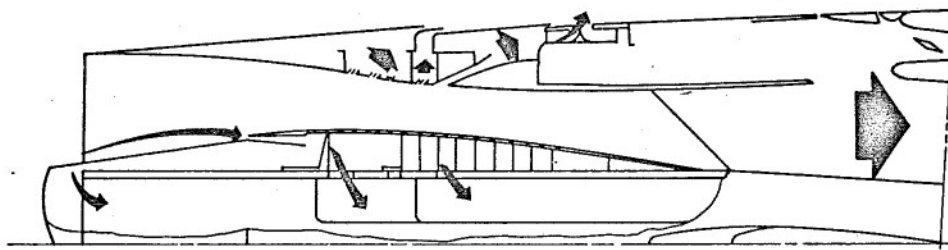


FIG. 18 SECONDARY AIR VALVE FLOW CHARACTERISTICS

FIG. 19 STARTED MODE,  $1.60 \leq M_{\infty} \leq 2.90$ 

The lip area of the intake was determined by the cruise standard-day engine demand with allowances for bleed, leakage, and minimum secondary airflow for nozzle cooling. Experimental data had shown that the throat blockage or boundary layer displacement effects could be allowed to occupy between 4% and 5% of the throat area, if this boundary layer was controlled to "arrive" at the throat with full velocity profile, equivalent to a power law exponent of 6 to 7. The subsonic diffuser including the normal shock effects would then be nonseparating or not pose undue restraints on the overall design. Since a 4% to 5% boundary layer bleed was also being predicted upstream of the throat, the throat area at cruise was simply defined by the requirement of a 1.25 throat Mach number. The maximum centerbody diameter was defined by requirements at transonic Mach numbers, when the maximum diameter of the centerbody is at the cowl lip station. The transonic engine airflow demand then defines the area to pass the required flow, at a chosen lip Mach number of 0.85. The additional requirement was that there be a continuous diffusion of the minimum flow area at the cowl lip, as shown in Figure 4.

Within the above constraints, the design of the diffuser contours involved an iteration to achieve an intake with acceptable recovery, distortion, weight, and drag. Additional considerations include achieving a uniform throat flow and avoiding strong adverse pressure gradients or shocks which would require excessive boundary layer control, cause restart problems, or give poor tolerance to angle-of-attack operation.

Uncontrolled viscous effects related to boundary layer growth and interactions can cause performance degradations that may seriously limit the effectiveness of the intake. Intake performance is directly related to the way in which the boundary layer develops through an intake. A boundary layer developing through a strong, adverse pressure gradient tends to thicken rapidly and has a velocity profile "less full" than a boundary layer developing through a zero pressure gradient. Interactions between the boundary layer and shocks also cause the boundary layer thickness to change and the velocity profile to become distorted. These changes affect the inviscid flow field, increase the likelihood of separation, and reduce intake recovery. The adverse effects associated with the boundary layer can be partially eliminated by using a "bleed" system to control boundary layer development through the intake.

General features of the boundary layer bleed system are shown in Figure 20. Cowl bleed is removed through three separate bleed plenums. Boundary layer bleed from these plenums is discharged overboard through exit nozzles located along the outer cowl

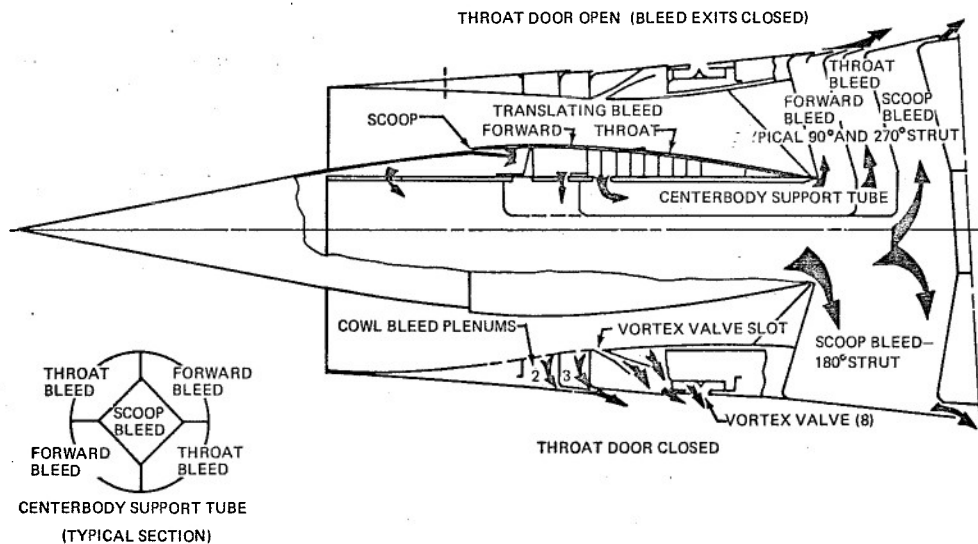


FIG. 20 BOUNDARY LAYER BLEED SYSTEM

surface. The centerbody bleed system consists of a boundary layer bleed scoop, a translating forward bleed region, and a translating throat bleed region. Centerbody bleed is removed through the centerbody support tube, ducted to the cowl through the centerbody support struts, and discharged overboard through nozzles located in the cowl. Bleed from the three centerbody bleed regions is ducted separately to the exit to prevent recirculation of high-pressure bleed from one region into a bleed plenum at a lower pressure. Separate ducting also reduces bleed drag by allowing each bleed plenum to operate at a maximum total pressure corresponding to the local surface pressure for each region.

A unique feature of the design is the traveling centerbody bleed system, illustrated in Figure 20. It is used to optimize the location of the bleed regions over the range of flight conditions encountered. As the centerbody translates forward, ports in the centerbody support tube slide across the bases of the vertical dividers which separate the various centerbody bleed plenums. Bleed is removed from a given bleed region if a support tube port is located beneath a bleed plenum. The locations on the centerbody where bleed is being removed can thus be scheduled as a function of centerbody translation through locating the support tube ports and the dividers between the bleed plenums.

The bleed system was designed through application of an analytic procedure for the rapid and inexpensive development of a system with high performance within certain external constraints. The procedure is based on years of SST intake test experience, analyses that accurately predict the flow through the supersonic portion of the diffuser, empirical information on the subsonic diffuser performance, and empirical information on the flow through and the boundary layer development across a given bleed region.

The bleed system design procedure is briefly as follows. The intake inviscid flow is computed over the started Mach range of the intake with a method of characteristics program<sup>(3)</sup>. Plots of the static pressure distributions along intake surfaces as a function of freestream Mach number are prepared, as shown in Figure 21 for the centerbody. Using the inviscid static pressure distributions, the boundary layer development along intake surfaces is computed<sup>(4)</sup> over the started Mach range of the intake. A boundary layer velocity profile parameter, usually the incompressible power law exponent,  $N_i$ , which represents the velocity profile distortion, is plotted along intake surfaces as a function of freestream Mach number over the started Mach range of the intake, as shown in Figure 22, again for the centerbody.

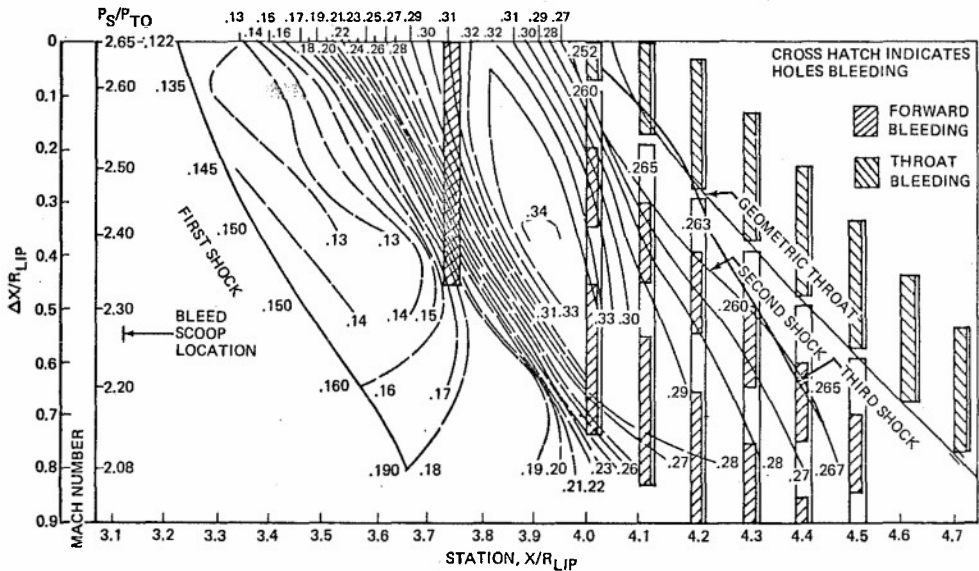


FIG. 21 CENTERBODY SURFACE PRESSURES

The vertical cross-hatched bands in Figures 21 and 22 depict regions of bleed holes on the centerbody. At cruise Mach number (zero  $\Delta X/R_{LIP}$ ) two bleed bands are shown as throat bleed and one bleed band as forward bleed, plus the bleed scoop which is allowed to bleed at all times. To exemplify the use of these design curves and to see which bleed holes are flowing, follow a horizontal line across the figure, say for Mach 2.3 ( $\Delta X/R_{LIP} = 0.5$ ). The forward bleed band is indicated as not bleeding below about Mach 2.35, i.e., the holes are still there but there is no port in the center tube under these holes when the centerbody is in this position, and hence bleed flow from these holes is shut off. Following the horizontal line further a bleed band is shown cross hatched as forward bleed region, which at Mach 2.65 was a throat bleed region. The next band is closed off, followed by two more forward bleed bands, and one closed band, followed by three throat bleed bands. At Mach 2.3 there are thus three open forward bleed bands, three closed (nonbleeding) bands, and three throat bleed regions being used for centerbody boundary layer control in addition to the bleed scoop.

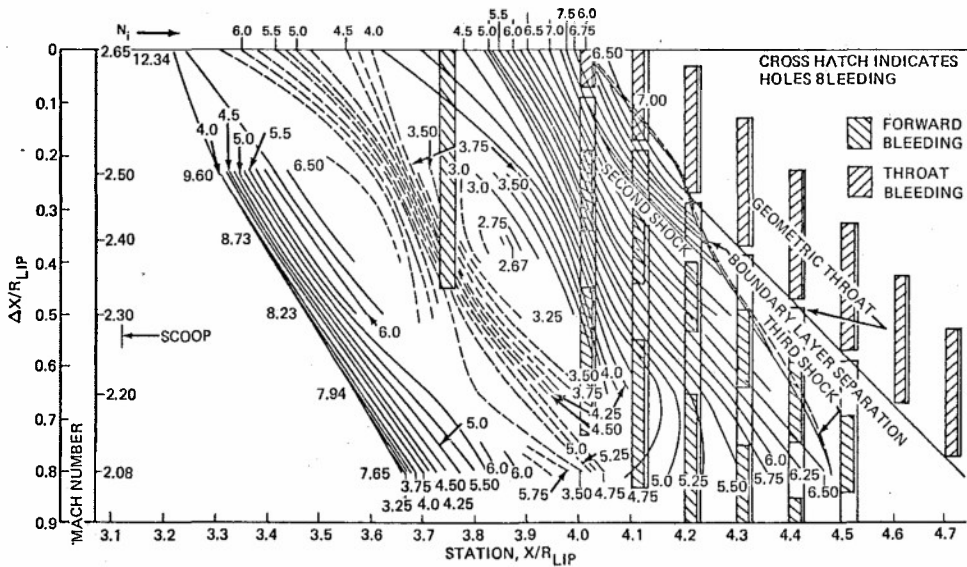


FIG. 22 CENTERBODY BOUNDARY LAYER POWER LAW EXPONENTS

The plots of  $N_1$  as a function of Mach number for a given intake surface are used to define regions where bleed is required over the started Mach range. A fully developed boundary layer (a boundary layer developing through zero pressure gradient) has a power law exponent of seven or larger. A boundary layer that has been distorted by an adverse pressure gradient or a shock will have an  $N_1$  less than seven.  $N_1$  decreases to about one as the boundary layer approaches separation. Normally, boundary layer control is used to prevent  $N_1$  from going below four. Experience has shown that if the profile exponent is allowed to deteriorate much below four, the boundary layer entrains mass rapidly, throat blockage (the displacement thickness in the intake throat) is high, and intake recovery and angle-of-attack tolerance are generally poor.

The plots of surface static pressures as a function of Mach number are also used to define the possible bleed regions and the maximum bleed plenum pressure obtainable without recirculation from other forward bleed holes. A number of possible bleed configurations are examined with the boundary layer programs. Bleed configurations (type, location, and amount) that appear promising (low throat displacement thickness and high bleed plenum pressures for a given bleed rate) and satisfy all intake external constraints are selected for further study.

Bleed flow rates, plenum pressures, and changes in the boundary layer properties across a given bleed region are computed for the various bleed plenums over the started Mach range for the systems selected for further study, using bleed system performance<sup>(5,6,7)</sup> data. The boundary layer program is rerun over the started Mach range using the predicted bleed flow rates. Improvements suggested by the initial runs are made and the boundary layer and bleed plenum pressures recomputed until an acceptable system is defined.

Cowl bluntness, boundary layer displacement, bleed, and shock/boundary layer interactions can significantly modify the locations and strengths of shocks and pressure gradients predicted from an inviscid analysis. An analysis procedure<sup>(8)</sup> that accounts for the above effects is used to compute the inlet flow at cruise and at selected off-design Mach numbers. The bleed system is then modified, if necessary, to correct for predicted changes in the location and strength of shock interactions and/or pressure gradients.

Application of the bleed system design procedure results in specification of the location and amount of bleed, bleed plenum pressure, bleed hole size, inclination, compartmentation, and pattern, as well as a prediction for the recovery that can be achieved with the system specified. Application of this procedure to a given intake usually results in an intake with good performance for the predicted type, location, and amount of bleed. The precise location and amount of bleed for optimum intake performance is then relatively easy to determine by experiment. Adjustments in intake model scale bleed geometry are made using the same tools to account for different test model Reynolds numbers and construction (larger wall thickness, etc.).

The bleed system design procedure removes much of the "black magic" from intake design and can be used to eliminate many of the costly development tests which have been necessary in the past. It also provides a basis for scaling small-scale bleed test results to larger model scales. Typically, the bleed required to achieve a given level of intake performance decreases as intake size increases. Data indicate that the boundary layer growth rate across a bleed region increases as the ratio of the diameter to boundary layer displacement thickness increases, an effect which has been attributed to vortex shedding from the bleed holes. As illustrated in Figure 23, this effect is usually a problem for small models and becomes less of a problem as the size of the model increases. The bleed system design procedure accounts for this effect and allows small-scale intake bleed and recovery results to be scaled.

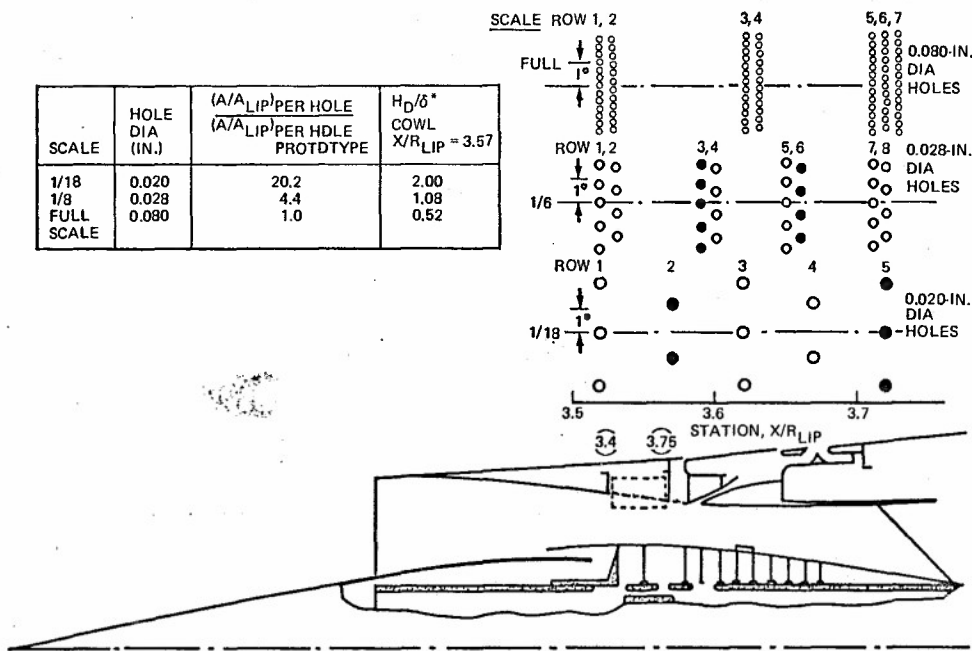


FIG. 23 BLEED HOLE SIZE COMPARISON—COWL PLENUM NUMBER 2

In Figure 23 a bleed hole pattern is shown as it would appear in a typical bleed region (as indicated on the cowl), when each model provided essentially the same flow area through the bleed holes. Note that with 1/6-scale (or larger) models, bleed patterns and hole size relative to the boundary layer displacement thickness compare reasonably well, as did the test results. Comparisons for 1/18-scale models are poor, and significant higher bleed rates were required on this model to obtain equal intake recovery levels.

The bleed hole diameter for the full-scale intake was selected as 0.080 inches. This resulted in a ratio of hole diameter to displacement thickness of 0.5 in the forward cowl bleed region to around 1.0 in the throat region, both on the cowl and centerbody. In the forward bleed region on the centerbody, as shown in Figure 22, the ratio is also in this range, about 0.7, due to the effect of the bleed scoop in reducing the displacement thickness, even with the much longer distance over which boundary layer bleed is generated on the centerbody.

The bleed hole inclination to the surface determines the maximum allowable plenum pressure for choked flow through the bleed holes. In general, the maximum plenum pressure increases with decreasing hole angle. An angle of 20° was selected for the SST intake to minimize bleed drag. A 1/6-scale model, which provided final design information for the full-scale bleed system, used bleed holes located at 40° to the surface. Figure 24 illustrates how bleed hole mass flow coefficient curves for 40° and 20° holes were used to transform the 1/6-scale model data to full-scale application. The curves show clearly the large improvement in flow coefficient for the 20° holes, requiring less bleed hole area. The 20° holes also operate at higher plenum pressures and in all cases operate closer to the choked flow limit for the holes with more tolerance to plenum pressure changes before the bleed rates are significantly affected.

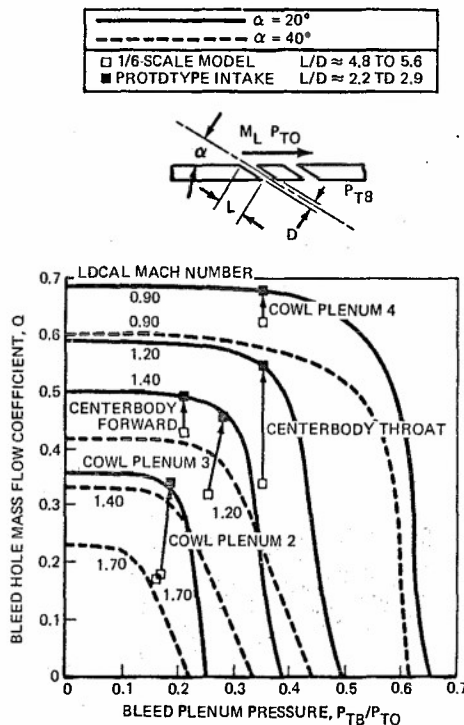


FIG. 24 BOUNDARY LAYER BLEED HOLE PERFORMANCE—MODEL SCALE VS FULL SCALE



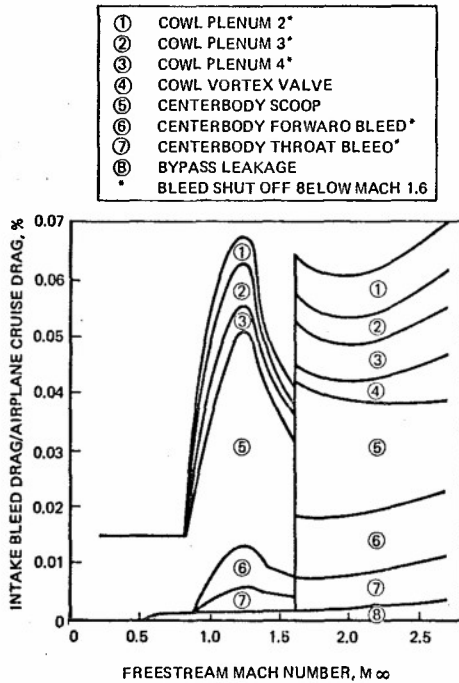


FIG. 26 INTAKE BLEED DRAG

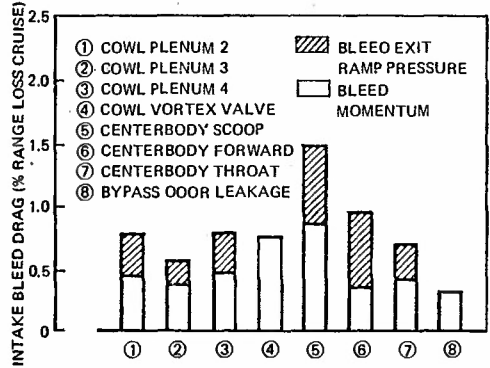


FIG. 27 AIRPLANE RANGE LOSS DUE TO INTAKE DRAG

normal shock movement toward the intake throat, thus increasing the total pressure recovery across the normal shock, and reduces the corrected weight flow supply to the engine. The limit to this, of course, would be an intake unstart.

Vortex valves installed within the intake cowl alleviate intake unstarts and increase the normal shock stability by bleeding excess air. The vortex valves operate when the throat doors are closed (intake in started mode) and are shut off when the throat doors are open. When the throat doors are closed a small amount of high-pressure airflow from the compressor face (0.4% of intake captured flow at supersonic cruise) is received from the outer cowl ducts and is directed tangentially through two converging nozzles (spaced 120° apart) into the vortex chamber from the chamber's outer periphery (Figure 28). With the intake normal shock near critical, these nozzles are choked, and the swirl established in the vortex chamber provides a back pressure at the valve's throat bleed entrance equal to the throat duct pressure, preventing intake air from escaping through the throat slot.

When a disturbance occurs that forces the normal shock to move toward critical, the shock travels across the throat bleed slot raising the pressure in the throat duct above the initial back pressure of the vortex valve and reducing the swirl intensity in the vortex chamber. The rise in throat duct pressure and the corresponding reduction in swirl strength permits a large increase in throat bleed flow (over 5% of lip flow) as the normal shock moves to critical. The throat duct plenum pressure can also be increased by a decrease in throat Mach number, which increases the internal cowl pressures. By locating the vortex valve bleed slot in the intake's throat region, as shown in Figure 28, the intake will be able to operate normally at a total pressure recovery level just below the maximum recovery obtained in an intake with no throat slot (less than 1% supercritical). At the same time, the throat slot/valve combination also helps to maintain an upstream Mach number tolerance of 0.05 and a subsequent increase in intake angle-of-attack tolerance.

Supersonic, Started Mode Performance

Cruise intake performance versus corrected engine airflow obtained on a 1/6-scale model of the intake is shown in Figure 29. A rise in the throat slot plenum pressure occurs at a full-scale engine airflow of 333 lb/sec. This pressure rise activates the vortex valves, and the vortex valve flow increases continuously as the engine airflow is decreased. As shown, the vortex valves provide a stability margin of 6.3% from an operating point recovery of 92.4%. Cowl static pressure profiles for the operating and the critical points are shown in Figure 30. The normal shock is located just downstream of the throat slot at the operating point. At critical the normal shock has moved in front of the throat slot, i.e., in front of the geometric throat due to the removal of mass flow through the slot.

Supersonic, Started Mode Performance

Figure 31 shows the intake performance in the Mach number range from 2.1 to 2.65. Both critical and operating point (5% stability margin) performance levels are shown. The slightly degraded performance below Mach 2.4 is partly caused by the centerbody vortex generators, which are located in front of the intake throat in this Mach number range due to the translation of the centerbody.

CONCLUSIONS

The intake system described was designed to meet high overall performance levels with enhanced controllability. Extensive use was made of analytical tools which would minimize the risk and effort involved in the test verification and development of the intake. Key elements in the design that allowed these basic objectives to be met were the use of:

- Engine rpm trim and nozzle secondary cooling flow systems to eliminate cruise bypass drag or intake oversize for engine airflow matching.

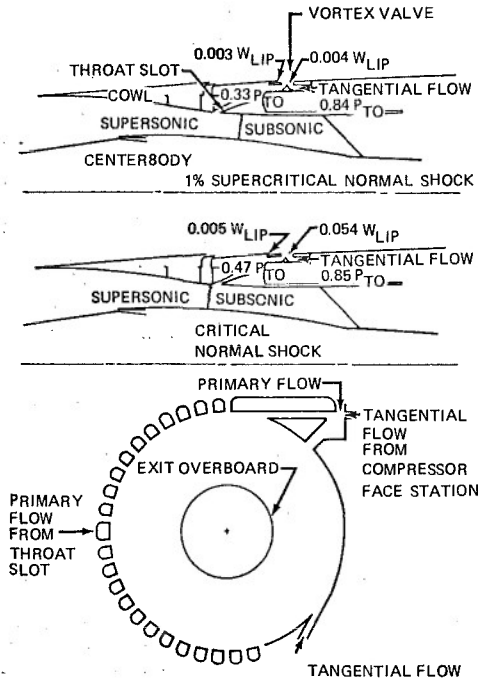


FIG. 28 VORTEX VALVE SCHEMATIC

SYM	$\Delta$	$\circ$	$\square$
MACH	2.65	2.65	2.65
$\Delta X/R_{LIP}$	0.013	0.013	0.013
$P_{TAV}/P_{TO}$	0.802	0.924	0.927
DISTORTION	0.153	0.076	0.080
$W_{ENG}/W_{LIP}$	0.886	0.864	0.814

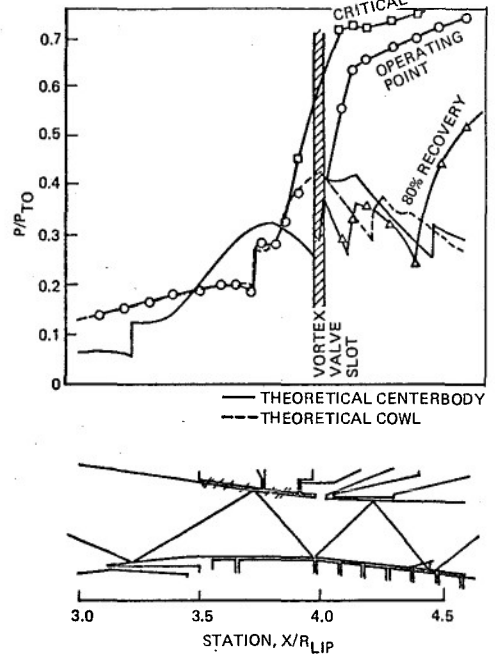


FIG. 30 COWL STATIC PRESSURE PROFILES, MACH 2.65,  $\Delta M = 0.05$

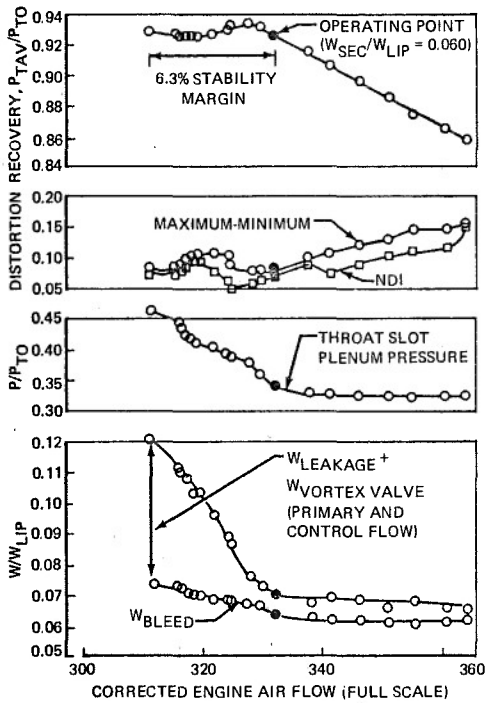


FIG. 29 INTAKE PERFORMANCE, MACH 2.65, 1/6 SCALE MODEL

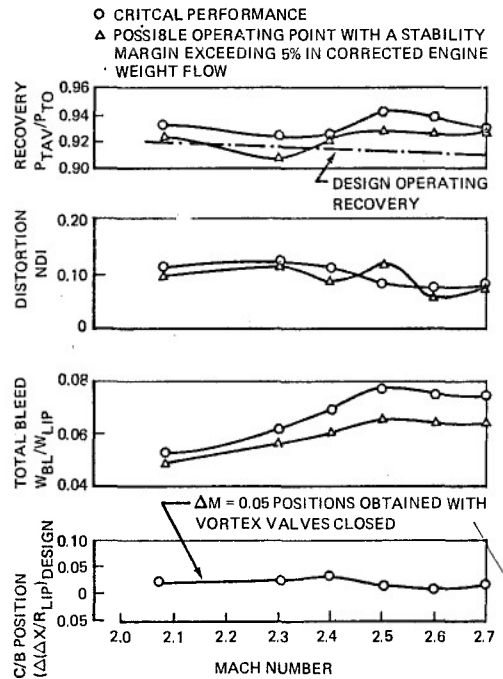


FIG. 31 INTAKE PERFORMANCE

- o A fluidic normal shock stability system (vortex valves) and good control of supersonic diffusion/boundary layer development for clean throat flow to give high steady-state stability margins. A -5% corrected flow,  $\pm 2.5^\circ$  angle of attack, and -0.05 Mach number change could be tolerated without controller action.
- o Slanted boundary layer bleed holes,  $20^\circ$  to the surface, to give maximum bleed pressure recovery. Small hole dimensions scaled from half to full height of the boundary layer displacement thickness gave minimum disturbance effects from the bleed holes (or maximum bleed removal effectiveness).
- o A boundary layer bleed scoop on the centerbody (located at the cowl lip station with centerbody extended) to provide good supersonic buzz margins and high transonic flow capacity. Cruise distortion of only 2% allowed stable operation with an unstarted intake. A transonic lip Mach number of 0.85 or higher was permitted, with the minimum flow area located just inside the cowl lip.
- o Cowl throat doors to provide geometric flow area variations (in addition to centerbody translation) to give unrestricted flow matching to an engine with high transonic flow demand, optimum flow area control for intake restarts, throat area location for transonic and supersonic conditions, and bleed exit control (shutting off unnecessary bleed).

#### REFERENCES

1. H. Larsen and G. Schweikhardt, *Control Concept and Wind Tunnel Testing of a Supersonic Intake Control System*, AGARD Propulsion and Energetics Panel 38th Meeting, September 1971
2. E. A. Fradenburgh and D. D. Wyatt *Theoretical Performance Characteristics of Sharp Lip Inlets at Subsonic Speeds*, NASA Report 1193
3. *MOCHA—The Generalized Method of Characteristics Program*, Boeing document D6-29625, to be published.
4. T. A. Reyhner, *A Computer Program for Finite-Difference Calculations of Compressible Turbulent Boundary Layers*, Boeing document D6-23236, June 17, 1970
5. G. McLafferty and E. Ranard, *Pressure Losses and Flow Coefficients of Slanted Perforations Discharging from Within a Simulated Supersonic Inlet*, VAC R-0920-1
6. A. L. Schuehle and C. W. Landgraf, *Boundary Layer Bleed System Development and Performance Test*, Boeing coordination sheet SST-PROP-3364, June 17, 1970
7. A. L. Schuehle, *Boundary Layer Bleed System Development and Performance Test—Boundary Layer Development Results*, Boeing coordination sheet SST-PROP-3720R, July 22, 1970
8. T. A. Reyhner and T. A. Hickcox, *A Procedure for Coupling Viscous and Inviscid Analyses for Supersonic Inlet Flow Field Determination*, Boeing METM-69-49, December 8, 1969

FREE-JET TESTS OF A FULL-SCALE SUPERSONIC  
INTAKE/ENGINE COMBINATION

by

P. F. Ashwood

Head, Engine Test Department, National Gas Turbines  
Establishment, Pyestock, Farnborough, Hampshire,  
United Kingdom

SUMMARY

Results are presented from an experimental investigation on a full-scale Concorde powerplant in the NQTE 5 ft x 5 ft free-jet test facility (Cell 4) to investigate intake/engine compatibility at supersonic speeds under both steady-state and transient conditions.

The main aim of the test programme was to study the behaviour of the powerplant when running under the control of its flight systems, in particular during the transients that result from the sudden application of sideslip or from rapid engine power changes.

Initial tests with the intake alone enabled detailed surveys to be made of the engine face pressure distribution and fluctuation over a wide range of test conditions. The major part of the programme was undertaken with an Olympus 593 two-spool turbojet engine coupled to the intakes in a test configuration which reproduced the precise geometry of the port outer powerplant of the prototype Concorde aircraft.

Results of typical tests made during the programme are presented including: steady-state surge margin determinations at supersonic flight speed; response to rapid engine throttle movements; effects of sideslip; operation at Mach numbers in excess of the cruise value, and the influence of atmospheric temperature changes.

NOTATION

$A_j$	jet pipe nozzle area
$DC_{e0}$	pressure distortion parameter = $(P_1 - P_{1min0})/\bar{q}$
$HP/4$	HP compressor fourth stage static pressure
$LP/5$	LP compressor fifth stage static pressure
$LP/6$	LP compressor sixth stage static pressure
$M_0$	intake Mach number
$N_1$	engine LP rotor speed
$N_2$	engine HP rotor speed
$P_1$	mean total pressure at LP compressor entry
$P_{1min0}$	minimum mean total pressure over a 60 degree sector surrounding the region of lowest total pressure at the engine face
$P_{2e}$	LP compressor outlet static pressure
$P_{3e}$	HP compressor outlet static pressure
$\bar{q}$	mean dynamic head at LP compressor entry
$T_1$	total temperature at LP compressor entry
$\beta$	sideslip angle
$\delta_2$	intake ramp angle
$\eta_1$	intake pressure recovery
$\eta_B$	throat bleed pressure recovery
$\theta_{DD}$	dump door angle
$\theta_{PL}$	pilot's throttle lever angle
$\theta_t$	engine throttle angle

## 1.0 INTRODUCTION

The development of a supersonic transport aircraft for use in commercial airline service requires wide ranging and extensive ground test facilities to ensure that the necessary high standards of performance, reliability and safety can be met and fully guaranteed. In no area is this more important than in the field of powerplant performance where a high efficiency at cruise conditions is essential to enable an economic payload to be achieved. In the case of the Anglo-French Concorde project the National Gas Turbine Establishment has contributed to every aspect of propulsion development, and especially through its programmes of work on intakes and propelling nozzles at model scale and by the use of its extensive altitude test facilities for tests involving full-scale engines and complete propulsion systems. The work described in this Paper formed part of this general programme.

## 2.0 THE AIRCRAFT POWERPLANT

The Concorde is powered by four Rolls-Royce/SNECMA Olympus 593 two-spool turbojet engines mounted in pairs in underwing nacelles. Each of the four powerplants operates as an independent unit in all important respects and each has its own intake, propelling nozzle and associated control gear. The intakes are inclined inwards towards the aircraft centreline to match the wing flow field and the wing boundary layer is diverted around the nacelles by a double wedge located above each pair of intakes. Due to the influence of the wing the Mach number of the air entering the intake is slightly lower than that at which the aircraft is flying; the difference amounts to slightly under 0.1 Mach for the outboard intakes and it is this value which is appropriate to the test installation considered in this Paper. To avoid aerodynamic interference between neighbouring intakes the wall separating each pair is extended a short distance forward of the outer side walls of the nacelle. This extension is termed the "splitter plate".

The intake is a multi-shock external compression design with a fixed geometry front wedge, variable second ramp and with a variable aft spill ("dump door") located in the subsonic diffuser. The boundary layer which accumulates on the supersonic compression surface is removed through a bleed slot at the throat and passes around the engine to provide the secondary flow to a dual-stream propelling nozzle. Comprehensive reviews of the aerodynamic factors governing the intake design and the considerations influencing intake/engine matching are given in Reference 1.

## 3.0 THE TEST INSTALLATION

The test installation in the NGTE supersonic free-jet facility (Cell 4) simulates as closely as possible the port outer powerplant in the aircraft, except that special arrangements are made to deal with the intake bleed and dump door flows. A full account of the development and capability of this test facility is given in Reference 2 from which Figure 1 is taken.

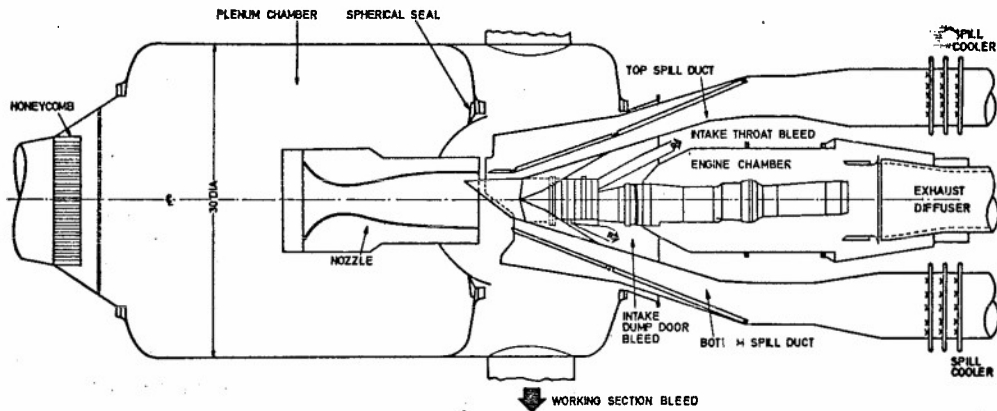


Figure 1 NGTE free-jet test facility (Cell 4)

Air is supplied to the cell plenum chamber at the total pressure and temperature corresponding to the flight condition being simulated whilst the working section is maintained at the required altitude pressure by the exhaustor plant. Air passing through the supersonic nozzle is thus accelerated to the required flight Mach number and forms the free-jet stream. The test intake is mounted in the central part of the nozzle efflux and is subjected to the same conditions as those experienced in free flight. The air which does not enter the intake is captured by a variable geometry supersonic diffuser within which it undergoes an increase of pressure, thereby minimizing the total power required for exhaust extraction. The Mach number of the jet can be varied while the cell is in operation over the range 1.8 to 2.3 at rates of change representative of aircraft accelerations, and the entire nozzle can be yawed to  $\pm 4$  degrees to simulate operation in sideslip conditions.

Setting up the required test conditions has proved to be relatively simple, the procedure being to move the blowing nozzle walls to the position for minimum Mach number, adjust the intake ramp to the corresponding angle and partly open the dump door. The engine is then lit and run up to a throttle setting intermediate between idle and cruise whilst the flow from the blowing nozzle is kept subsonic by bleeding atmospheric air into the working section. The inbleed is then closed and the flow from the blowing nozzle caused to become supersonic by the consequent reduction of the working section pressure. Final adjustments are then made to the engine throttle, intake ramp and dump door settings and the spill diffuser adjusted to equalize the nozzle outlet and working section pressures to ensure parallel shock-free jet flow.

4.0 TEST RESULTS

4.1 INTAKE TESTS

The first phase of the programme was aimed at investigating the aerodynamic performance of the intake on its own and at determining suitable control laws for managing the intake during engine and aircraft transients. The arrangement for these tests is shown in Figure 2.

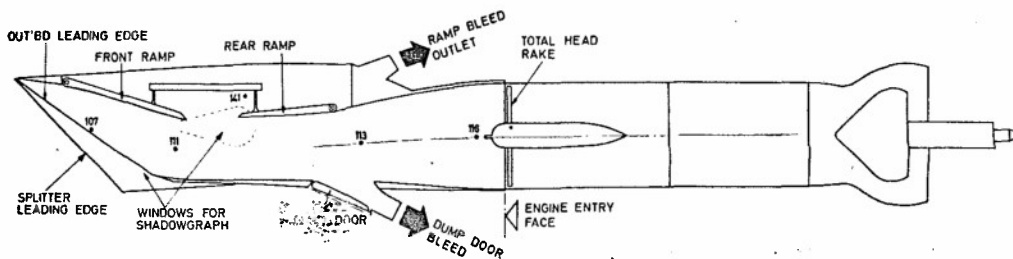


Figure 2 Concord intake test installation  
(Numbers identify locations of transient pressure transducers - see Figure 4)

A "dummy" engine, consisting of a parallel duct and variable plug nozzle, was coupled to the intake and this allowed the flow rate to be changed. A 72-point total pressure rake enabled the flow uniformity in the plane of the engine inlet to be determined. The internal surfaces of the intake were provided with numerous pressure taps, most being grouped in regions of specific interest such as the edges of the throat bleed slot, inside the cowl lip and over the supersonic compression surfaces. Each of the pressure taps was connected to the Facility steady-state data acquisition system, and about one-third were also coupled to transient recording equipment.

A large amount of testing was done to evaluate the performance of the intake control system in terms of response and stability. Transient conditions were induced by making either step or ramp changes in the position of the dummy engine plug, and some tests were made with the plug translating in simple harmonic motion. Some results from these tests are given in References 3 and 4.

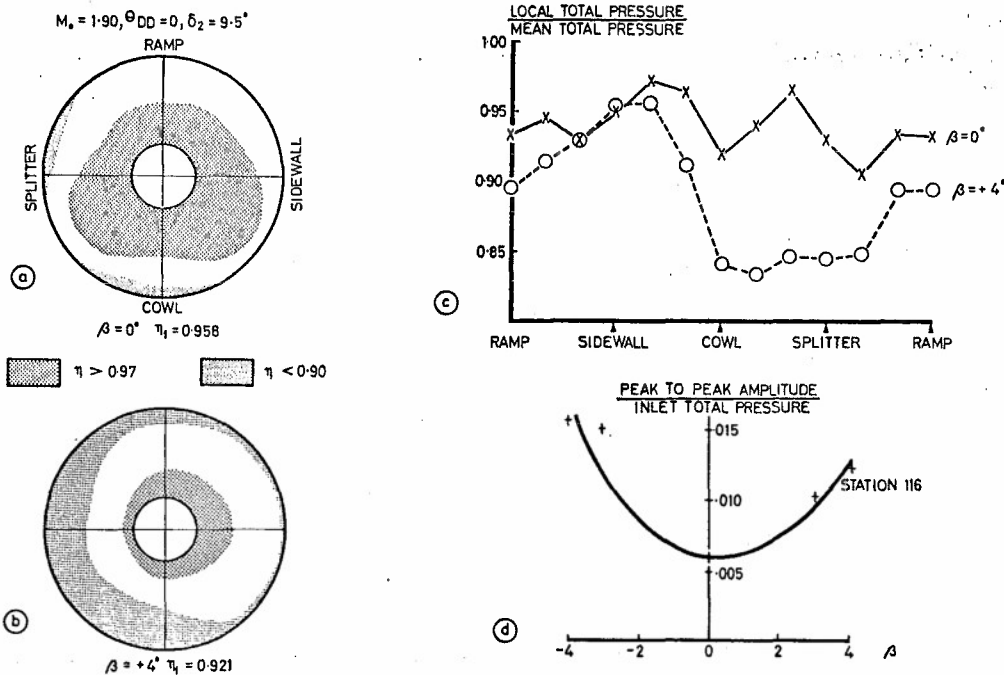


Figure 3 Effects of sideslip on engine face pressure distortion

Figures 3a and 3b show the effect of positive sideslip (i.e. the airstream coming from the splitter plate side) on the steady-state total pressure distribution measured at the engine face plane. In the no sideslip case, Figure 3a, the distribution is symmetrical and except for small areas close to the wall in line with the splitter plate and cowl lip, the total pressure is everywhere greater than 90 per cent of the free-stream value. With +4 degrees of sideslip, Figure 3b, the flow is distorted laterally with a

low pressure region close to the duct wall, centered on the splitter plate side and extending circumferentially to affect areas in line with the cowl and ramp. The distortion is reflected in a deterioration in the steady-state distribution factor,  $DC_{80}$ , from -0.079 to -0.263.

The effect is shown in another way in Figure 3c which plots the time-averaged total pressures measured by the individual pitots of each rake in the outermost position but one, that is at a radius 0.874 that of the duct. At this radius the peak to peak "steady-state" variation with zero sideslip is 6.6 per cent of the mean total pressure, whilst with +4 degrees of sideslip it becomes 12.2 per cent.

Figure 3d shows the effect on the amplitude of the fluctuations in wall static pressure measured at Station 116, a point a short distance ahead of the engine face plane. The influence of sideslip is again marked, with little difference discernible between positive and negative sideslip angles.

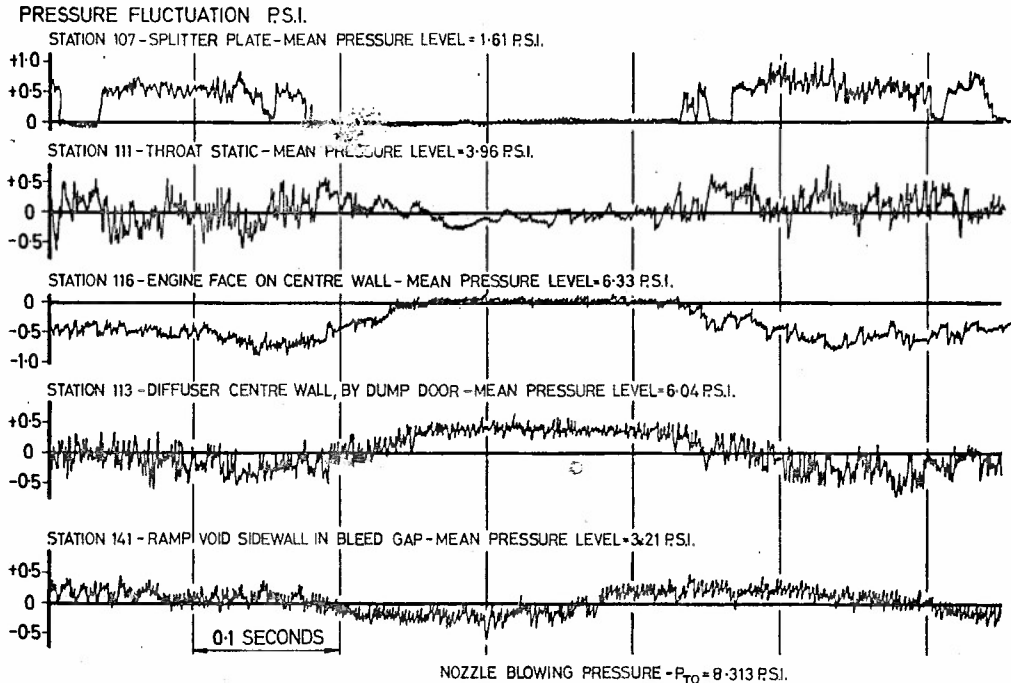


Figure 4 Intake pressure fluctuations

Figure 4 shows some typical records of wall static pressure fluctuations taken at conditions generally similar to those of Figure 3b (i.e. +4 degrees of sideslip) but with the throat bleed pressure recovery increased above the level specified by the flight standard control system, thus moving the operating point into the sub-critical regime. Under these conditions non-periodic fluctuations occur, a feature which is particularly marked at Station 107 on the splitter plate surface. Detailed investigation on model scale, coupled with visualisation tests on the full-scale intake using a mixture of white pigment and oil painted on the internal surfaces, revealed that the instability was due to separation of the boundary layer from the splitter wall. Observations of the surface pattern while the test was in progress showed that the region of separated flow continually changed as the fluctuating shock system passed back and forth over it. From a practical point of view this regime is unimportant as the powerplant is controlled in such a way that operation within it is impossible, but it is of considerable fundamental interest in that it has been shown that similar pressure fluctuations can be the direct cause of engine surge.

#### 4.2 INTAKE/ENGINE TESTS

Since all the tests described in this Paper were undertaken as part of the Concorde powerplant development programme, much of the work was of a semi-empirical nature. The main emphasis was placed on establishing the optimum control laws for both the engine and the intake and on proving their effectiveness over as wide a test envelope as the Facility could achieve.

The test arrangement was similar to that shown in Figure 2, with an Olympus 593 engine replacing the dummy engine used for the intake tests. The engine was equipped with its standard reheat system and variable area primary nozzle, but the secondary nozzle was not fitted as it was not necessary for this programme. Conventional instrumentation was used to measure the normal engine parameters: pressures, temperatures, rotor speeds, fuel flows, etc. Variations in "steady-state" total pressure at the engine face were measured by 35 pitot tubes mounted in the inlet guide vanes of the LP compressor.

Although the test programmes undertaken on individual engines were in the main arranged to provide answers to specific development problems, it is possible to identify six main types of test. In the following Sections each of these will be considered in turn and typical results quoted by way of illustration.

## (A) MATCHED INTAKE TESTS

The purpose of this type of test is to establish the engine running point with the powerplant operating at supersonic cruise conditions, one objective being to compare the measured performance with that predicted from a ground level test bed calibration.

From an experimental viewpoint determination of the engine airflow to the required degree of precision presents a difficulty since in a free-jet test it cannot be measured directly with an air-meter as in a connected test and the flow measuring instrumentation that can be accommodated within the engine itself is normally inadequate. A simple and convenient solution is to use the test intake as an air-metering device and this has been done throughout the Concorde programme with excellent results.

The matched intake point was achieved by setting the appropriate intake ramp angle and dump door opening and adjusting the engine speeds by altering the jet pipe nozzle area until the required intake bleed pressure recovery and turbine inlet temperature were obtained. Since engine speed can be determined very accurately, it has proved possible to distinguish the effects on the intake/engine matching point of quite minor changes to the compressor blading. It has also enabled similar comparisons to be made between engines built to the same nominal standard.

## (B) ENGINE THROTTLING TESTS

At supersonic flight speeds the Olympus 593 engine is controlled so that a linear relationship is maintained between the non-dimensional speeds of the LP and HP rotors thus:

$$N_1 / \sqrt{T_1} = a N_2 / \sqrt{T_1} + b \quad \dots(1)$$

where a and b are constants.

Some of the engines tested at NGTE were fitted with a control system in which b varied automatically as a function of  $T_1$ . This had the effect of moving the running line away from the surge line as  $T_1$  was reduced and vice versa. The effect of this on the performance of the powerplant is described in Section 4.2 F. The control system incorporates all the normal safeguards to prevent mechanical overspeeding or excessive turbine inlet temperature and provision is also made to avoid engine surge during aircraft sideslip by reducing the LP compressor speed, a process known as "N<sub>1</sub> dip".

If the engine is throttled from cruise power when flying supersonically the nozzle area reaches its minimum value before the flight idle throttle setting is reached and when this occurs the control schedule is changed to allow a different rotor speed relationship to be established. This is done by reducing the value of the constant 'a' in Eq (1).

Tests were made to examine the behaviour of the powerplant when throttled from the matched intake point to flight idle at conditions corresponding to flight at various Mach numbers and altitudes. Data scans were taken at a number of steady-state running points on the normal engine control line between the matched intake point and flight idle and these were followed by acceleration and deceleration at various rates up to "slam" movement of the throttle lever with the intake and engine operating on automatic control. Typical variations of LP and HP compressor speeds, nozzle area and engine throttle angle occurring during a slam acceleration are shown in Figure 5.

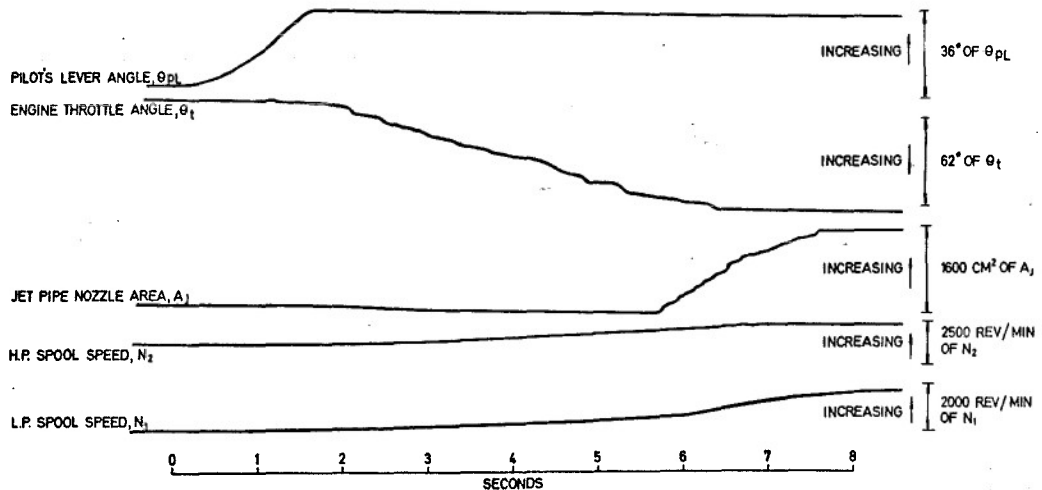


Figure 5 Slam acceleration test

## (C) SURGE MARGIN TESTS

A valuable feature of the NGTE free-jet test facility is that it enables deliberately provoked engine surges to be studied in a controlled manner, and monitored using extensive instrumentation, without incurring any of the hazards that would attend such an investigation in flight. Moreover, distortions of

the intake flow to the engine, both steady-state and time variant, are automatically provided by the intake so that exact representation of flight conditions is achieved.

All the Olympus 593 engines so far run in Cell 4 have been subjected to surge margin investigations and in most cases the tests have also included an examination of the effects of aircraft sideslip. Results from some early tests at zero sideslip have already been published (see for example Figure 5 of Reference 3), but Figure 6 presents a more comprehensive set of data with a greater number of results at the lower end of the engine speed range.

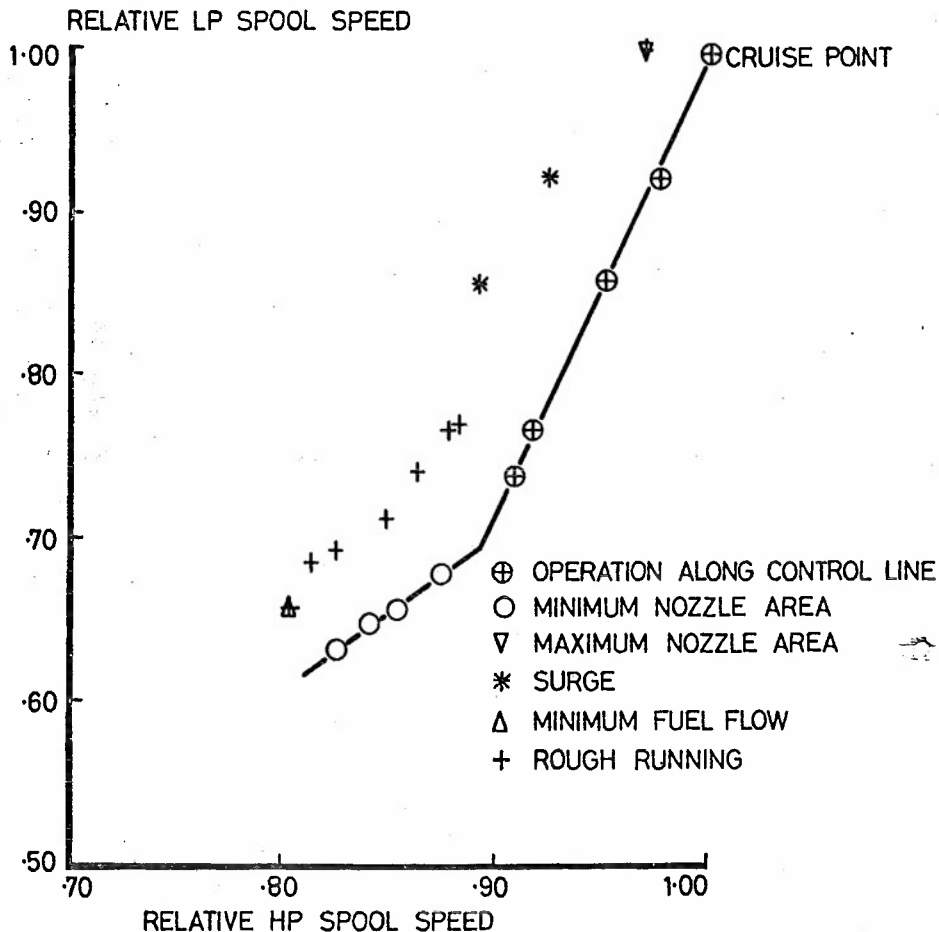


Figure 6 Surge and rough running points

In this low speed region the engine could not be surged, even with  $N_2$  reduced to the lowest achievable value (determined by the minimum fuel flow permitted by the control system), but occasional flashes of flame from the jet pipe were observed and these indicated a condition of "rough running" symptomatic of partial compressor stall followed by recovery. Figure 7 shows the "steady-state" surge points for three different engines two of which were tested in different build configurations. The surge points for all five tests group closely around a mean line.

It should be noted that due to a temporary shortage of plant exhaust capacity at the time the tests illustrated in Figure 7 were made it was not possible to manage the intake in accordance with the flight system control laws over the entire test range. In particular the amount of forespill had to be limited and the excess intake capture flow removed via the dump door. The net effect was that at the lower engine speeds the flow distortion at the engine face was worse than would occur in flight. The interaction of the relevant parameters is shown in Figure 4 of Reference 3 from which it can be seen that if  $\delta_2$  has to be limited to 13.5 degrees (the value appropriate to the tests of Figure 7)  $DC_{e0}$  exceeds -0.6 compared with -0.28 achieved when the intake is managed to its normal schedule.

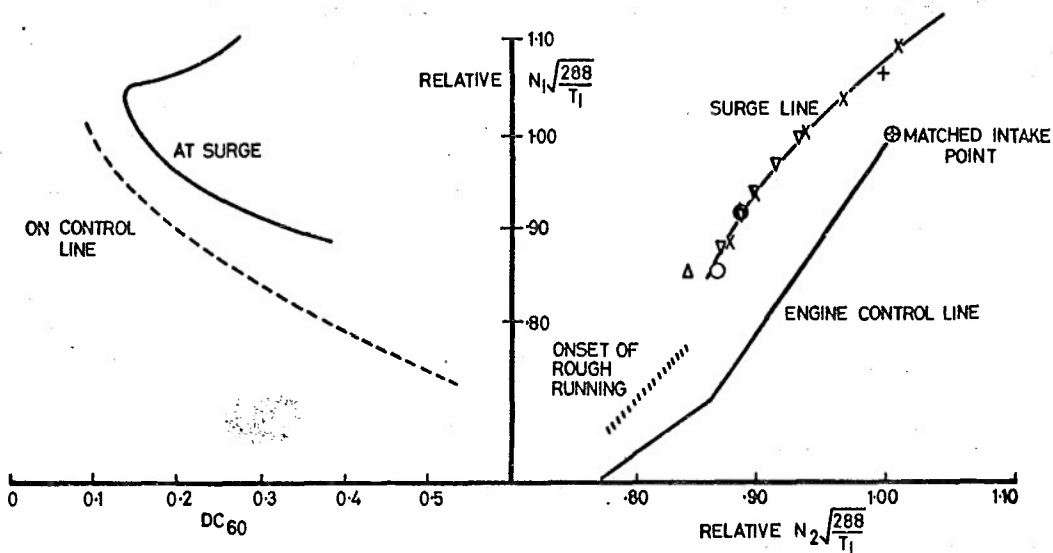


Figure 7 Surge line determination

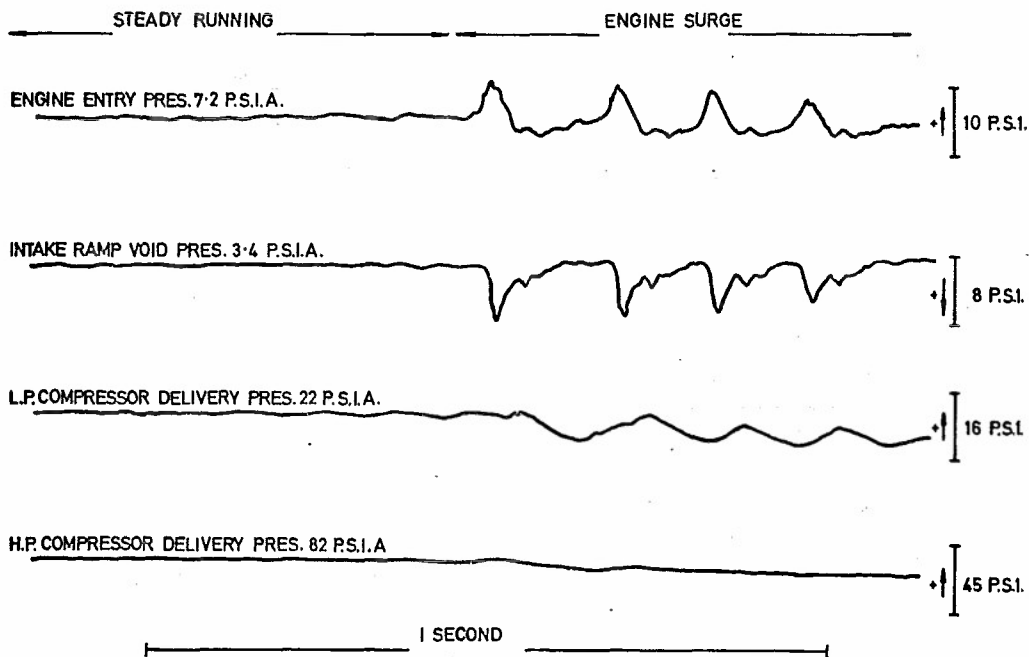
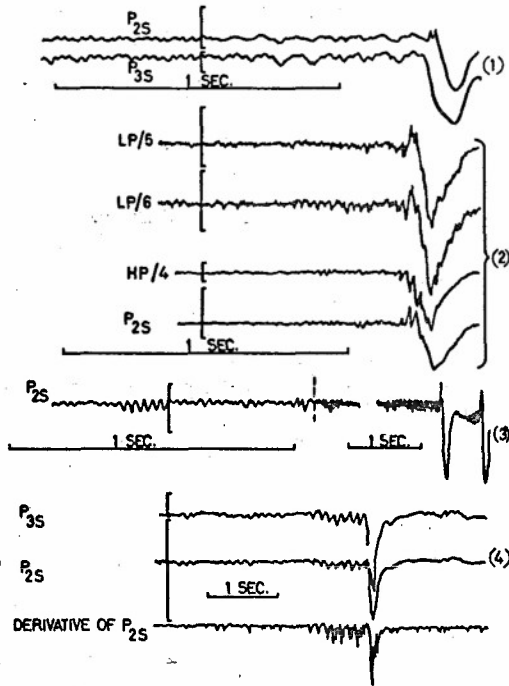


Figure 8 Engine and intake pressures during an engine surge

Figure 8 illustrates the transient variations of pressure experienced during a deliberately induced surge at Mach 2 cruise conditions initiated by progressively restricting the intake bleed flow. The first indication of the onset of surge can be seen as a sharp rise on the trace of engine entry pressure, with a similar rise of intake ramp void pressure evident some 15 milliseconds later. A study of transient pressure signals at various stations within the LP and HP compressors at conditions immediately preceding surge has revealed a wide diversity of amplitudes and frequencies and it is evident that several varieties of stall or surge phenomena can exist either separately or in combination. Furthermore, different builds of engine, or even the same engine running at different conditions, can generate quite dissimilar traces. Some typical examples, obtained at various times from several engines, are shown in Figure 9. The traces have been classified into four groups; those in each group were recorded simultaneously, but the different groups were obtained during four separate tests. Traces 1 and 2 were recorded during surges initiated by increasing the nozzle area, whilst traces 3 and 4 were obtained

with surge induced by applying sideslip without using  $\eta_B$  suppression. Since the Figure is intended to illustrate comparative waveforms only, it was not thought necessary to identify the sense of the pressure changes.



Basic frequency of about 8 Hz with a higher frequency (30 Hz) evident in certain areas

Rather irregular but with much of the oscillation in the 30-40 Hz frequency band

35 Hz oscillation shown at two recording speeds

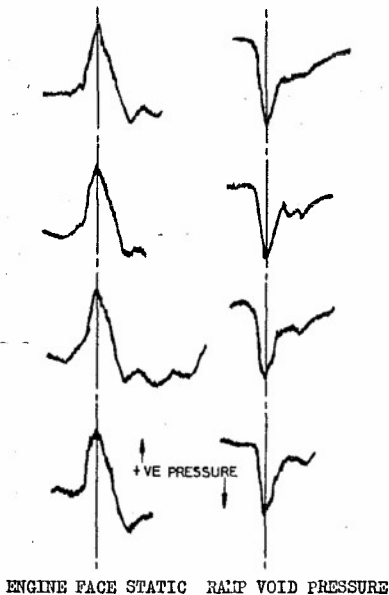
Basic frequency of 8 Hz but sub-divided. Each of the main oscillations has three minor peaks most clearly seen on the time derivative of  $P_{2S}$

Amplitude markers indicate 5 psi except for  $P_{2S}$  in Group (1) which indicates 2 psi

Figure 9 Pressure traces preceding surge

In contrast to the situation immediately preceding surge, the gross pressure changes occurring in the intake during the surge cycle follow a very consistent pattern which does not depend on the method by which surge is induced.

Method of inducing surge



Increasing ramp angle

Reducing throat bleed flow

Driving engine to maximum nozzle area at low throat bleed flow

Applying sideslip at high throat bleed flow without  $N_1$  dip or  $\eta_B$  suppression

ENGINE FACE STATIC RAMP VOID PRESSURE

Figure 10 Surge pulse repeatability

Figure 10 shows four engine face static pressure traces obtained at Mach 2.0 flight conditions with the engine caused to surge in different ways: by increasing the ramp angle at a fixed engine speed until surge occurred due to supercritical operation; by progressive reduction of the throat bleed flow; by increasing the nozzle area at low throat bleed flow and by the application of sideslip without using either  $N_1$  dip or  $\eta_B$  suppression. No significant differences in the surge pulse waveforms can be detected.

#### (D) OPERATION IN SIDESLIP

Tests with the dummy engine confirmed that the engine face distortion in sideslip conditions could be improved by reducing the intake bleed pressure recovery and allowing the intake to operate supercritically ( $\eta_B$  suppression). The intake control system incorporates means for doing this if the aircraft sideslip angle exceeds  $1\frac{1}{4}$  degrees.

Tests were made to investigate the adequacy of the system, first in steady-state conditions at sideslip angles up to the maximum achievable in the Cell ( $\pm 4$  degrees) and subsequently with sideslip applied at various rates up to 2 degrees per second. Figure 11 shows the results of a typical transient sideslip test to  $-4$  degrees at Mach 2.0 cruise conditions with  $\eta_B$  suppression and  $N_1$  dip control features operative. Satisfactory surge-free operation was achieved.

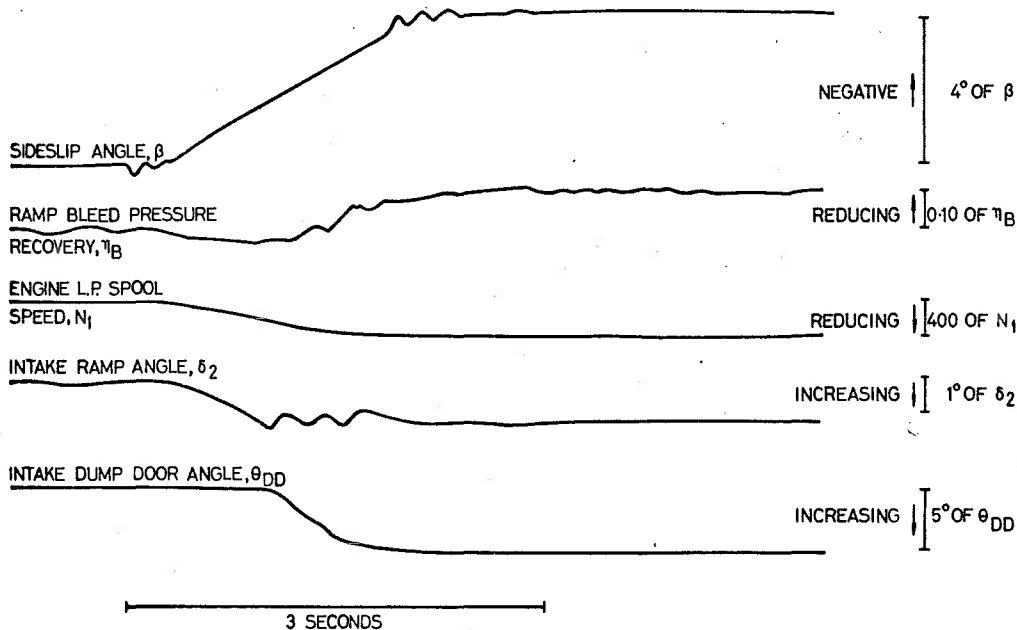


Figure 11 Transient yaw test

#### (E) AIRCRAFT OVERSPEED EVALUATION

Tests were made to assess the ability of the powerplant to function satisfactorily at intake Mach numbers higher than the normal cruise value, representing a transient aircraft overspeed. In these tests, which were made with zero sideslip, the intake Mach number was increased in small increments until surge occurred, the engine conditions being held constant. Before each increment the appropriate intake control parameters ( $\delta_2$  and  $\eta_B$ ) were set up, and the Mach number then slowly increased to the new value. The results are shown in Figure 12 in terms of the engine face distortion parameter,  $DC_{60}$ .

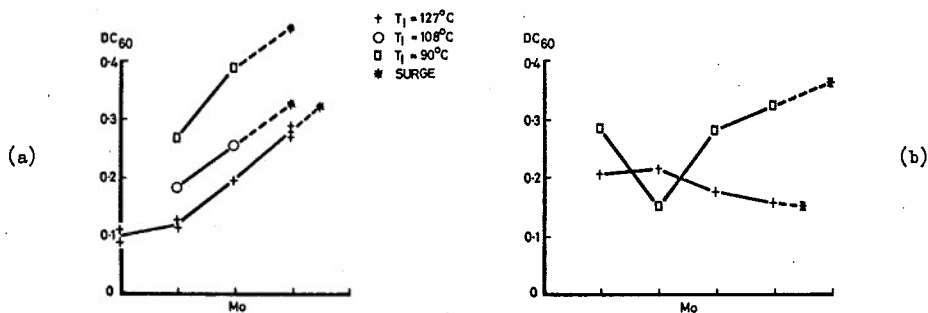


Figure 12 Effects of aircraft overspeed

Figure 12a shows the results of three tests made with the engine running at its cruise throttle setting with inlet air temperatures of 90°C, 108°C and 127°C respectively. The HP rotor speed was the same for each test but the LP speed increased with inlet temperature in accordance with the engine control schedule described in Section 4.2 B. At each temperature level there was a consistent trend for  $DC_{50}$  to increase with Mach number, a result in line with intake test data, with the highest values reached under the coldest day conditions when the intake was running most supercritical. Even though  $DC_{50}$  varied appreciably over the test range all the surges occurred at approximately the same intake Mach number.

Figure 12b shows the results of similar tests with the engine running at a partly throttled condition. Except for one point, which is clearly a rogue, the highest values of  $DC_{50}$  were again recorded at the lower temperature, but in contrast to the other tests in this series the one made at an inlet temperature of 127°C showed an improvement in engine face distortion with increase of intake Mach number. The explanation is that for this test in addition to the intake being scheduled to operate critically there was a small amount of aft spill through the dump door, and this latter feature is known to contribute significantly to the achievement of a good flow distribution at the engine face.

#### (F) "COLD DAY" TESTS

Some tests were undertaken to examine the effects of non-standard atmospheric temperature (i.e. "cold day" conditions) on the operation of the powerplant. The standard cruise condition (aircraft Mach No. 2.0; air inlet temperature 127°C = ISA + 5°C) was set up as datum and the inlet air temperature progressively lowered in steps of approximately 10°C. Performance parameters were obtained at each condition.

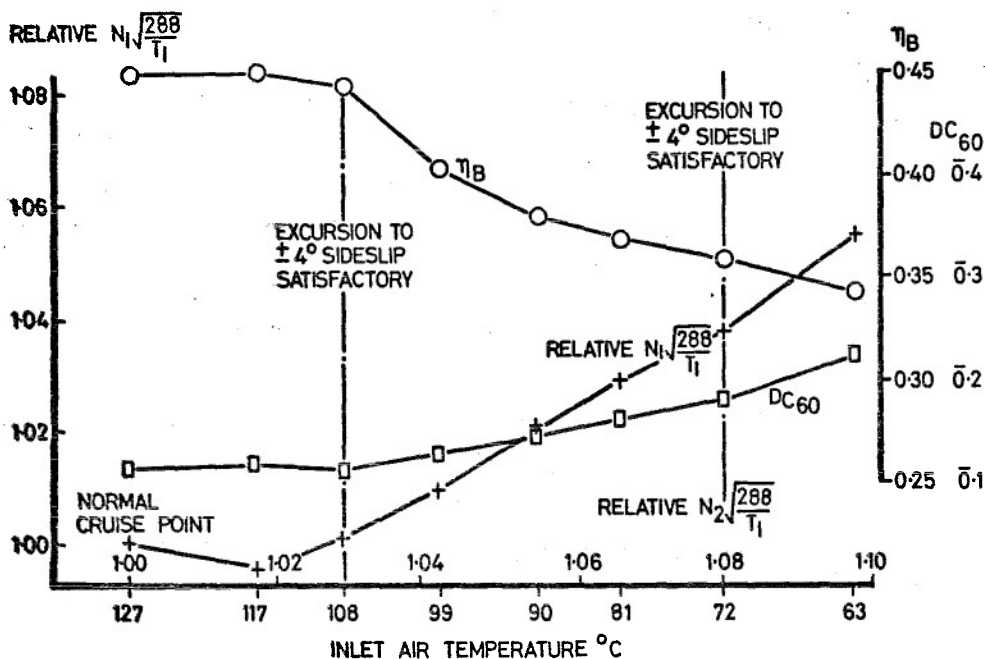


Figure 13 Influence of inlet air temperature at Mach 2 cruise

Figure 13 shows how the intake bleed pressure recovery, engine face distortion parameter and LP rotor speed varied with inlet temperature. In the particular test illustrated the engine was controlled to a schedule which required the LP rotor speed to fall as the air temperature was lowered whilst the HP rotor speed remained constant. It will be seen that as a consequence of the intake operating point moving into the supercritical regime as the air temperature was reduced, the bleed pressure recovery decreased and the engine face flow uniformity deteriorated.

Finally it is worth recording that successful surge-free excursions to  $\pm 4$  degrees of sideslip were made at temperatures of 108°C and 72°C using  $\eta_B$  suppression but without  $N_1$  dip.

#### 5.0 CONCLUDING REMARKS

This Paper has attempted to summarise the highlights of an extensive test programme extending over several years and carried out as a joint undertaking by teams from several organisations.

The NGTE Test Facility has enabled powerplant performance to be explored in advance of the flight test programme over a wide range of conditions, including some well outside the normal limits of operation in flight. The ability to determine surge margin by direct experiment has been particularly useful and the extensive test programme undertaken with the intake and engine running under automatic control has provided a valuable background of experience and has established a high degree of confidence in the performance of these systems.

An indication of the magnitude of the test and data analysis effort involved can be gained from the fact that more than 600 hours of testing at supersonic flight conditions has now been accumulated during which over two million items of information have been recorded from some 500 data channels.

My thanks are due to my colleagues at NGTE, Rolls-Royce, and BAC on whose work this Paper has been based. It is impossible to mention every individual by name, but I am particularly indebted to Mr. P. Philpot of NGTE who has been personally in charge of virtually every test in Cell 4 and whose efforts have contributed so much to the success of the programme.

Thanks are also due to the Ministry of Defence (Aviation Supply) for permission to publish the Paper. The views expressed are entirely my own.

#### REFERENCES

- 1 Rettie I. H. and Lewis W. G. E. The design and development of an air intake for a supersonic transport aircraft. Journal of Aircraft Vol.5 No. 6, November-December 1968
- 2 Ashwood P. F. The design and development of a large supersonic free-jet test cell J.R. aero. Soc. Vol.74 pp.205-212, 1970
- 3 Morriss D. P. and Williams D. D. Free-jet testing of a supersonic engine/intake combination. J.R. aero Soc. Vol.74 pp.212-218, 1970
- 4 Ashwood P. F. Intake/engine compatibility at supersonic speeds - A resume of tests made in the NGTE Engine Test Facility on the Concorde powerplant. Proc. ninth conference on environmental effects on aircraft and propulsion systems. NAPTC Trenton N.J. USA, October 1969

CONCORDE POWERPLANT DEVELOPMENT

by

C.S. Leyman, Chief Aerodynamicist (Concorde)  
D.P. Morriss, Assistant Chief Powerplant Development Engineer

British Aircraft Corporation Limited  
Commercial Aircraft Division  
Filton House  
Filton, Bristol, U.K.

SUMMARY

The paper describes the development of the Concorde power unit, with particular reference to the problems encountered during flight testing. The extent to which these problems were predicted by altitude test cell experience and the use of such facilities in the development of the design is also discussed.

1. INTRODUCTION

The design of high efficiency supersonic propulsion systems represents an exacting task. Particularly in the case of the supersonic transport aeroplane, in which the balance is finely drawn between often conflicting requirements, the challenge is stimulating, and has occupied the attention of many people on both sides of the Channel for several years.

Much has already been published concerning the fundamental design philosophy and pre-flight development aspects of the Concorde powerplant e.g. Refs. 1 and 2. The primary objectives of the present paper are to present some of the more interesting aspects of the flight test experience so far. The impact of this experience on the development of Prototype aircraft powerplant and management techniques, and also on the definition of the Production aircraft powerplant, is discussed in some detail.

For convenience, flight experience is presented under appropriate topics. Where considered necessary to ease understanding, brief recapitulation of design aspects are included in the interests of self containment, although free reference is made to previously published documentation.

2. OVERALL POWERPLANT DESCRIPTION

Although the main design features of the Concorde powerplant have already been presented many times e.g. Ref. 1 it would be useful to recapitulate the major features. (Fig. 1).

Starting from the front, the intake is mounted off the wing with a vertical separation calculated to eliminate wing boundary layer ingestion at 1g conditions at 2.0M. The space between intake proper and wing is filled by a diverter of the original prototype triangular planform on 002 and of the compound sweep production design on 001. (see Fig. 6).

The intake compression geometry is predominantly external compression, designed for first shock on lip at a local Mach number of 2.1M.

Intake geometry is varied by means of the moveable front compression surface (front ramp) and a spill door mounted in the floor of the main diffuser (dump door).

One dominant feature of the intake design is the full width, large chord bleed slot immediately behind the moveable front ramp.

The bleed air is used to ventilate the engine bay before being exhausted via the dual stream secondary nozzle.

On the Prototype, there is additional circumferential bleed from the main diffuser just ahead of the engine face. This bleed feeds the cabin air heat exchangers and is then mixed and exhausted with the throat bleed air. On the Production aircraft this air is taken from a localised bleed on the upper surface of the diffuser.

The Olympus 593 engine is a twin spool design of 14:1 pressure ratio. The engine mass flow is controlled by adjustment of the primary nozzle area which controls the LP RPM ( $N_1$ ) by varying the pressure drop across the LP turbine. The HP spool speed ( $N_2$ ) is effectively a function of fuel flow only. The exact relationship between the two spool speeds and hence the proximity of the engine operating point to the surge line is defined by a law known as the 'E' Schedule. This 'E' Schedule on the prototype engine is a variable function of total temperature. The schedule can also be altered by injecting appropriate signals into the control amplifier. This has an important bearing on the M2.0 operation of the propulsion system as will be described later.

The prototype dual stream secondary nozzle features blow-in 'tertiary doors' for nozzle ventilation at low Mach number and high power, and free floating secondary petals which reduce the exit area in like conditions. At cruise Mach numbers, the tertiary doors are shut and the petals fully open.

### 3. PRE-FLIGHT INTAKE CONTROL SYSTEM DEVELOPMENT

#### 3.1 General

Over a wide range of intake geometry, the flow conditions on the Concorde intake design which give low compressor face distortion and good pressure recovery are characterised by a particular range of pressure recovery in the throat bleed passage.

In addition, for a given Mach number, altitude and intake geometry, the throat bleed pressure rises and falls monotonically as the engine mass flow is varied, and is directly affected by ramp and dump movement at constant engine demand.

It is therefore a natural choice for use in the intake control system. Conveniently non-dimensionalised by free stream total pressure, the parameter

$$\eta_B = \frac{P_{TB}}{\text{Free stream total pressure}} \quad (\text{see Fig. 2 for } P_{TB})$$

becomes a very useful yardstick to define intake operating conditions.

The original Prototype intake control system (I.C.S.) described in Ref. 1 was based on defined limits of this parameter  $\eta_{BMAX}$ ,  $\eta_{BMIN}$  which were scheduled as a function of Mach number. The necessary total pressure and Mach number information was supplied by the aircraft Air Data Computers (A.D.C.).

The function of the I.C.S. was simply to position the ramp and dump surfaces so as to prevent operation above  $\eta_{BMAX}$ , and to signal the presence of  $\eta_B < \eta_{BMIN}$  by means of a warning light. On the Prototype aircraft a manual facility to reduce the engine mass flow by LP RPM adjustment was (and is) provided to eliminate this condition.

The primary spill surface is the ramp, which is allowed to operate between limits  $\delta_{2MIN}$  and  $\delta_{2MAX}$  which at any given Mach number are fixed by second shock on lip and flow distortion limits respectively. These limits are also scheduled functions of Mach number.

In the initial definition described in Ref. 1, on attainment of maximum ramp angle, control was switched to the dump door, with ramp overtravel available to cater for engine shut down cases.

Several changes were made to the system described in Ref. 1 before flight testing with I.C.S. operative began. These are described below.

When the full scale tests began at Cell 4 N.G.T.E. Fyestock, it was evident that the throat bleed flow entered the secondary system as a discrete jet, and that the flow at the proposed  $P_{TB}$  measurement station was not fully mixed.

This was judged to be unacceptable from the point of view of intake control, and another suitable parameter was sought. Investigations revealed that the static pressure in the space above the front ramp bore an acceptable relationship to  $P_{TB}$ , and it was decided to use this pressure (PRVS in Fig. 2) as the intake control pressure using the ratio PRVS/ $P_{\infty}$ .

### 3.2 I.C.S. Response

In parallel with the Cell 4 development work, the theoretical I.C.S. response characteristics were studied on an analogue simulation of the complete system.

This work revealed that the proposed system had an undesirably sluggish response to atmospheric disturbances. This was primarily due to the response of the A.D.C. mechanical output which furnished Mach number information to the I.C.S.

In certain extreme cases, the phase lags introduced from this source caused amplification of the disturbance. Since this amplification occurred at frequencies where sympathetic engine response could not be ruled out, it was decided to find a reference pressure source which instantaneously reflected changes in local Mach number at the intake entry.

### 3.3 I.C.S. Reference Pressure

Several schemes for reference pressure sensing were examined, and finally it was decided to use the static pressure given by a  $15^\circ$  cone mounted on the first (fixed) intake compression surface. This source had the added attraction that when used in association with P<sub>RVS</sub> as defined above, it was predicted to give a good simulation of the desired  $\eta_{BMAX}$  - Mach number relationship without needing an external source of Mach number information.

The cone installation initially devised for the Prototype aircraft featured twin cones located just forward of the front ramp hinge (aft cones) (Position 'A' Fig. 2). Two cones per intake were required for systems monitoring purposes.

With this arrangement, the original relationship between control and reference pressure was reversed because whereas  $P_{TP}/P_\infty$  is less than unity,  $P_{RVS}/P_0$  is greater than unity. To enable the original pressure ratio sensors to be retained, the connections to the sensor casing and bellows were reversed and the control parameter  $\eta_B$  replaced by a new parameter  $r_B = P_0/P_{RVS}$ .

It was expected that the value of  $r_B$  corresponding to the original  $\eta_{BMAX}$  law would be independent of Mach number. However further testing showed that it was necessary to retain some form of Mach scheduling to avoid intake buzz at low supersonic Mach Numbers. This Mach scheduling is only required for fine trim, and the rapid response to Mach changes which caused rejection of the earlier system is not required.

### 3.4 Intake/Engine Compatibility

It would be difficult to over emphasise the role played by the tests on the complete intake/engine/I.C.S. system at Cell 4 in the successful development of the Prototype system.

Apart from the developments in  $P_0$  and P<sub>RVS</sub> mentioned in the previous sections, the facility has had considerable impact on the development of additions to the basic control laws necessary to give trouble free operation in all cases.

One of the first discoveries was that the concept of using ramp and dump surfaces individually to give increasing spill was not viable. It was found that above  $\delta_2_{MAX}$ , use of the dump door alone to provide the extra spillage caused unacceptable flow separations on the upper surface of the diffuser.

The system was altered to provide a unique relationship between ramp angle ( $\delta_2$ ) and dump door ( $\theta_{DD}$ ) deflections above  $\delta_2_{MAX}$ . This was so arranged that dump door opening commenced at  $\delta_2_{MAX}$  and the maximum physical travel of ramp coincided with two thirds travel of the dump. This has been shown (Ref. 2) to provide an optimum arrangement giving minimum DCGO for all throttle settings.

The most important development from Cell 4 testing was that of the I.C.S. sideslip protection systems.

### 3.4 Intake/Engine Compatibility (Cont'd)

It was found that the compressor flow quality deteriorated significantly in sideslip at high Mach number. A full discussion of the problem can be found in Ref. 2. For the purposes of the present paper, it may be noted that additional I.C.S. laws were developed with the following functions

- a) Reduced  $\eta_{BMAX}$  with increased aircraft sideslip angle ( $\beta$ )
- b) Reduced permissible maximum ramp angle ( $\delta_{2MAX}$ ) with increased  $\beta$ .

Fig. 3 shows how the addition of  $\eta_{BMAX}$  reduction keeps the intake flow quality (Distortion and flow unsteadiness) inside acceptable limits.

A further development was the use of reduced engine LP spool RPM ( $N_1$ ) to increase the surge margin in cases of excessive sideslip. Fig. 4 shows the principle of this device (termed  $N_1$  dip) which significantly increases the basic engine surge margin.

$N_1$  dip is triggered by two signals :

- a) Sideslip angles greater than  $1.25^\circ$
- b) Asymmetric rate of change of HP compressor delivery pressure between corresponding engines, port and starboard.

This second feature provides  $N_1$  dip on the live engines in the case of engine failure.

On the basis of the results obtained at Cell 4, 500 RPM dip was selected for the Prototype engine.

It should be noted that an important factor in the intake sideslip protection philosophy is the auto rudder function of the aircraft flight control system. Peak sideslip angles in response to engine failure are significantly reduced by rudder application automatically introduced by the same signal as triggers  $N_1$  dip in this case.

## 4. FLIGHT TEST EXPERIENCE

### 4.1 Intake Control System

#### 4.1.1 Reference Pressure Sensing

Fig. 5 presents the variation of  $P/P_\infty$  (The ratio cone static/stagnation pressure) with ramp angle and  $P_{RYS}/P_\infty$ , for the aft cones.

The deficiencies of the aft cones design were found to be :-

- a) The cone reference signal proved extremely sensitive to variation of ramp angle due to ramp shock interference
- b) In the illustrated rapid throttling case, at  $M = 1.67$ , beyond a ramp angle of  $13.5^\circ$  potential control reversal occurs, supercritical intake operating conditions being signalled to the I.C.S., commanding reduced ramp angle, when in fact the intake operation is subcritical. This is indicated by the fact that the  $P_c/P_{RYS}$  ratio is above the control value of  $r_b$  (0.844 in this case) although the actual  $P_{RYS}$  is significantly subcritical. The ramp angle command was not immediately reversed in this case, however, because the system response was dominated by the engine  $N_1$  inputs. However this excursion into buzz during a rapid throttling transient emphasises the unacceptable nature of this signal source.

#### 4.1.1 Reference Pressure Sensing (Cont'd)

Following this disappointing experience, the cones were relocated at more forward positions on the front wedge, as shown in Fig. 2 Position 'B'. Lateral cone separation in the revised system was only approximately 3", but in spite of this, the cones exhibited significantly different adverse effects of incidence and sideslip in flight. The consequent continual spurious warnings of system failure forced abandonment of the twin cone arrangement in favour of a single cone installation. The chosen cone provided the more acceptable signal characteristics. Cross comparison of signals between paired intakes was used as the basis of a revised monitoring system.

Fig. 6 presents flight measurements from the revised Prototype installation (single, forward mounted cones). The data are shown relative to the predicted  $3^{\circ}$  incidence value.

Marked behaviour differences in incidence variations are shown between inboard and outboard intake cones and this presented problems in choice of I.C.S. monitoring threshold.

Modification of the wing boundary layer diverter planform to that appropriate to the Production aircraft (Aircraft 001 only) effects considerable improvement of the inboard intake in terms of incidence sensitivity and agreement with prediction. However, no significant improvement can be identified in relation to the outboard intake cone signal. This reflects the dominating influence of local flow conditions at the intake wedge leading edge. The major factors may be presumed as follows :-

- a) Wing boundary layer diverter flow conditions. It is known from model data that the Prototype diverter system remains unstarted up to Mach 2.0 hence thickening and causing partial ingestion of the wing boundary layer.
- b) Wing undersurface boundary layer/shear layer thickening as aircraft incidence is reduced (see later section). This thickening is known to have a more pronounced effect on the outboard intake. The cone pressure could clearly be affected by immersion into this thicker boundary layer.
- c) Incidence variation of cross flow components relative to the cones.

The inference from this experience is that tests to determine local reference sensing points must be made on the full scale aircraft, and this is programmed for future development aircraft, which have slightly different geometries.

Fig. 7 shows typical flight measured intake operating  $\eta_B$  values on 001 compared with the predicted  $\eta_{BMAX}$ . Inevitably, the cone reference pressure problems are reflected in these data and incidence/sideslip sensitivity contributes to the scatter. Nevertheless, inboard intake operation closely approaches the target condition. The outboard intake is shown to operate supercritically relative to the target datum.

#### 4.1.2 I.C.S. Response

The external compression, large throat bleed intake design selected for Concorde is characterised by a very wide operating range with smooth transition from supercritical to subcritical operation.

These characteristics have a significant effect on the intake control system response requirements.

## 4.1.2 I.C.S. Response (Cont'd)

Rapid response is not required, neither is there a need for special devices to improve stable subcritical margins etc. On top of this, the system lacks the complexities associated with automatic restart - there is no unstart in the classical sense.

Hence the required intake control system response characteristics are quite modest. For example, the Prototype system is only required to reduce the effects of transients up to frequencies of  $1\frac{1}{2}$  Hz. The Production system cross-over frequency is boosted to approximately 4 Hz but even so this eliminates the closed loop stability problems associated with more ambitious designs.

The highest rate response requirements are set by the engine failure case, in which the normal closed loop system is dominated by the phase advance signal  $N_1$ .

Typical flight measured characteristics of the system are illustrated in Figs. 8, 9, 10.

Fig. 8 illustrates system response in a pull up and pushover manoeuvre at  $M = 2.0$ . Both intake cones on No. 1 engine show broadly similar effects of varying incidence. The variation of ramp angle ( $\delta_2$ ) and  $PRVS$  indicates the system response to cone pressure disturbances,  $PRVS$  following the outer (driving) cone signal very well.

The inboard (No. 2) intake cones exhibit differing forms of signal variation with incidence, more particularly in the reduced incidence case (pushover) in which opposite signs of incremental cone pressure are shown. This example is typical of the phenomenon which dictated revision of the sensing system to a single cone per intake installation. Once again system response reflects the signal distortion of the 'driving' (outer) cone.

Fig. 9 illustrates the functioning of the sideslip protection devices during sideslip investigation at  $M = 2.0$ . Both outboard and inboard intake/engine combinations exhibit similar correct responses.

$N_{1DIP}$  and  $\eta_{BDIP}$  (indicated by the reduction of  $PRVS$  and an incidence in  $r_B$ ) are shown to be triggered as sideslip angle is increased. The apparent 'delay' in the achievement of the maximum  $r_B$  change ( $\eta_{BDIP}$ ) is due to the hesitation in the application of sideslip, bearing in mind the 'ramped' function of sideslip angle (Fig. 3). The maximum ramp angle ( $\delta_{2MAX}$ ) reduction is masked in this particular example, but the final supercritical operating state of the intakes is achieved by dump door deflection (not shown).

Fig. 10 presents data from a simulated engine failure at  $M = 2.0$ . Response of the intake in the case of the 'failed' No. 1 engine indicates the dominant influence of the anticipation signal  $N_1$ , the ramp ( $\delta_2$ ) and the dump door ( $\theta_{DD}$ ) angles following the decay of engine LP RPM independently of  $PRVS$  in the initial phase. Following the achievement of windmilling RPM, variation of  $PRVS$  and sympathetic dump door response is associated with cone signal distortion due to incidence and sideslip variation.

The major point illustrated by the inboard intake is the functioning of the  $N_{1DIP}$  system in response to asymmetry of engine thrust signalled from differential HP spool delivery pressure.  $N_{1DIP}$  is established rapidly following the simulated failure of the outboard engine. The intake response parameters indicate the consequent subcritical excursion.

Fig. 11 compares a typical flight measured response with prediction. The source of the prediction in this case is a sophisticated analogue simulation of the complete powerplant developed at B.A.C. Filton. The contributions made by this simulation to the design and development of the intake control system have proved invaluable. Prior to aircraft flight with an operational intake control system, the simulation was set up permanently to support flight investigations in the event of running into unexpected problems associated with powerplant

#### 4.1.2 I.C.S. Response (Cont'd)

dynamics. The gratifying agreement between predicted and measured response characteristics illustrated by this particular example adequately explains why the simulation has not been needed in support of flight investigations.

### 4.2 Intake/Engine Compatibility

#### 4.2.1 General

The importance of intake/engine compatibility in the design of supersonic aircraft and the somewhat unpredictable nature of the problem leads to a degree of preoccupation on the part of the design teams, so that the search for potential problem areas becomes almost a way of life.

In parallel with flight exploration, model investigations continued with the primary objective of extending the assessment of intake behaviour to operating regimes appropriate to Production aircraft. Notably, this included systematic investigation of an increased aircraft incidence range compared with previous investigations, which were limited to the range typifying planned initial Prototype flight investigations with somewhat limited freedom of manoeuvre.

Before proceeding to discussion of flight test data, it is interesting to briefly summarise this model experience which had considerable impact both on the course of Prototype flight investigation and subsequent aircraft development.

Low speed wind tunnel investigations including incidences compatible with zero 'g' flight conditions exposed potential problems of outboard engine malfunction. Flow visualisation investigations at low speed revealed an underwing flow separation vortex partly ingested by the outboard intakes. Fig. 12 presents the pattern typifying these flow conditions.

Fundamental aerodynamic reasoning suggested aggravation of the problem at supersonic speeds, and led to a systematic investigation at high Mach No. based on a 1/15th scale twin intake model with fully representative wing. Various modified wing leading edge section profiles were assessed, leading to the current Production aircraft definition (BA10). The modified standard features reduced forward camber and increased leading edge radius compared with the Prototype (BA1).

Fig. 13 illustrates the impressive beneficial effects of the revised wing leading edge. The influence of wing incidence and  $\gamma_B$  on compressor face distortion level (DC60) are shown for the outboard intake under Mach 2.0 operating conditions for both standards of leading edge. Incidence for the possible onset of surge (DC60 > 0.3) is shown to be reduced by approximately  $1\frac{1}{2}^\circ$  and little problem is indicated in preserving surge free engine operation down to less than zero 'g' flight condition consistent with Airworthiness Requirements.

#### 4.2.2 Early Flight Operation with Fixed Geometry

Although inevitably the problems of high Mach number operation have more glamour, the problems of obtaining optimum performance at low speed are technically quite interesting.

With the sharp lipped intake design, it is to be expected that at low speed flow separations at the intake leading edge will cause substantial deteriorations in flow uniformity and pressure recovery at the engine face.

The classic solution to this problem is to provide some form of auxiliary intake. On Concorde prototypes, this now takes the form of a dual hinged door in the intake floor which doubles as an auxiliary intake at low speed and a spill door at high speed. For the first 30 or so flights 001 was equipped with a simple auxiliary intake consisting of a hole with fixed guide vanes in place of the dump door. This was installed because of early fears concerning the flow distortion measured on small scale models and apparently

#### 4.2.2 Early Flight Operation with Fixed Geometry (Cont'd)

associated with the door design at low forward speed. This excessive distortion was eventually traced to model deterioration which was accepted as indicative of the need at full scale for a high standard of surface finish and sealing at the door hinge. The doors were consequently installed and have functioned excellently as shown by Fig. 14.

It is worth noting how quickly the DC60 level subsides to a low value and also the slight but noticeable change in recovery during rotation.

#### 4.2.3 Subsonic/Transonic Flight Regime

High subsonic exploration confirmed light airframe buffet due to an intake oscillation at windmilling mass flow which was first noticed on the Vulcan Flying Test Bed. The consequences of this oscillation were magnified by the particular Vulcan installation, but nevertheless, the presence of this oscillation on Concorde has dictated a need for provision of an open loop subsonic spill door function in the Production aircraft standard intake control system. Deflection of the spill door has been demonstrated to eliminate the buffet which is believed to be due to flow separation on the intake cowl.

Initial investigation of less than 1.0 'g' flight conditions at low supersonic speeds exposed a further intake instability. During pushover manoeuvres at  $M = 1.45$  repeatable intake oscillation/engine rough running conditions were established at approximately 0.75 'g'. The initial judgement that this confirmed the potential low incidence intake/engine compatibility problem predicted by model tests (described above) proved to be incorrect. Model tests (Fig. 15) showed discontinuous variations of intake pressure recovery ( $\eta_1$ ), main duct flow ratio ( $\epsilon_1$ ) and DC60 with ramp angle. These effects are indicative of flow separation at the ramp hinge. This is shown to occur under these particular simulated flight conditions at  $4^\circ$  ramp angles which in fact is consistent with a flow expansion around the ramp hinge.

Clearly, the adverse effects of incidence reduction, possibly aggravated by unstated wing boundary layer diverter flow conditions, are factors which are peculiar to the Prototype aircraft and which could dominate the origin of this flow separation. However, to completely eliminate any residual problem in the case of service aircraft (which has improved wing/diverter geometry), the Production intake control system provides for increased minimum ramp angle to  $7^\circ$  minimum (hence eliminating the expansion at the ramp hinge) below a selected value of aircraft incidence. This over-rides the normal  $\delta_{MIN}$  - Mach number relationship.

#### 4.2.4 Supersonic Flight Regime

Supersonic investigations under nominally level flight and near Maximum Continuous Power engine operating conditions showed no intake/engine compatibility problem with the intakes under automatic control. Transient changes of intake geometry associated with the establishment of intake control at the switching Mach number (1.3M) also introduced no problems.

Fig. 16 indicates levels of flow distortion measured in specific flights in nominally level flight conditions up to Mach 2.0. These may be taken as typical and are illustrative of the excellent flow quality capabilities of the intake. The associated oscillatory pressure component at the engine face is less than 2% of stagnation pressure.

#### 4.2.4 Supersonic Flight Regime (Cont'd)

The model prediction of low incidence problems demanded the addition of systematic pushover manoeuvres to the scheduled powerplant handling assessment programme. At Mach Numbers in excess of  $M = 1.70$  the problem became evident and was demonstrated to be considerably aggravated under engine throttled conditions. Fig. 17 presents the variation of outboard intake flow distortion with aircraft incidence for full and partially throttled engine operating conditions. Oscillatory flow component levels in  $P_1/P_{\infty}$  terms ( $P_1 = P_{PF}$  on Fig.2) and typical surge points are also indicated. The data clearly exposes deteriorating compressor face flow quality with reduction of incidence and the significant adverse impact of engine throttling. A by-product is the inferred quite remarkable tolerance of the Olympus 593 engine to flow distortion.

The adoption of quite restrictive engine throttling limits, based on the results of these investigations enabled completion of an impressive volume of flight testing without the occurrence of inadvertent surging.

The Production aircraft leading edge, shortly to be tested on OO1, is expected to eliminate the need for these throttling restrictions.

#### 4.3 Intake Interaction and Engine Surge

The twin intake arrangement of the Concorde entrains problems of intake interaction by virtue of the mutual interference associated with subcritical intake operation. Clearly, subcritical excursions, involving significant shock expulsion, distort the external shock system of the neighbouring intake.

The centre wall leading edge extension or 'splitter' between paired intakes is designed to limit these adverse effects to major disturbances, for example, those associated with high intensity engine surge (i.e. near Max. RPM engine operation). The splitter design was selected on the basis of systematic model tests to provide freedom from significant interaction to just beyond the buzz threshold in either intake. Protection from interaction in the surge case was not a design objective, the probability of success in such an endeavour without impairing intake performance to an unacceptable degree being problematical. The design philosophy is that the complete system shall be so designed as to make the probability of engine surge extremely remote, and that the aircraft characteristics shall be such that no hazard results from such surges, even if two engines should be affected.

Attempts to express engine tolerance of interaction effects in tangible terms, failed because of the lack of a definitive criterion. The results of such analysis provoked the simple conclusion that the confidence level attached to the prediction of interaction malfunctioning thresholds was extremely low, and that there was no substitute for flight investigation in this context.

The systematic flight investigation of low incidence and throttling surge thresholds consequently furnished vital information on surge interaction.

Another aspect of surges which gave cause for some anxiety was the associated intake loading. In the initial design and development stages the problems could be sub-divided into three categories :-

- 1) Data relevant to the 'overpressure' (sometimes termed 'hammer shock') loading imposed on the ducting ahead of a surging turbojet engine was hard to come by.
- 2) The predicted pressure propagation within the intake under surge conditions, i.e. relationship between peak pressure levels and phasing in various zones of the intake, was by no means straightforward.
- 3) The possibility of interaction induced surge in the adjacent engines introduced the problem of phasing and hence differential pressure variation across the centre wall between intakes in the case of double surges.

#### 4.3 Intake Interaction and Engine Surge (Cont'd)

Systematic programmes of testing were set up including using a small scale model equipped with a surge simulation valve, engine surge investigations using the Vulcan aircraft in subsonic conditions and the full scale intake/engine installation in Cell 4. These investigations were supported by theoretical studies of pressure propagation undertaken by Aerospatiale (then Sud Aviation).

These endeavours led to the formulation of aerodynamic loading information to assess structural integrity in surge. Rolls Royce, for example, exposed the dependence of duct peak surge pressure on the initial overall compression ratio. American work in this field confirms this type of correlation. Surge induced transient pressures measured on the full scale Cell 4 intake installation confirmed the small scale model results, both showing measurements compatible with the results of the theoretical approaches.

The doubts associated with interaction surge loads remained, however, and structural integrity was assessed on the basis of unique application of assumptions of worst phasing appropriate to each component.

The initial surge programme associated with the low incidence investigations confirmed the assumed transient pressure levels in intake subjected to 'primary' surges. Initial belief that loadings in the interaction case were in fact less rigorous than those in the primary surge case was based on the reduced duct peak pressure levels which were measured in the former. This, in association with the evidence of completion of the surge programme with no apparent structural effect, was interpreted as indicative of a successful outcome in this potential problem area. Then came flight 122 of aircraft 001.

#### 4.4 Intake Structural Failure in Surge

During Flight 122 with the aircraft under Mach 2.0 conditions at an altitude of 49,000 ft. No. 3 engine surged following cancellation of reheat. No. 4 engine surged due to interaction, operating at Maximum Continuous Power at this time. Following 7 secs. of double surging, during which continuous bewildering warnings of intake control system failure defied interpretation on the part of the crew, engine No. 4 flamed out. The aircraft was decelerated to subsonic speeds. No. 3 engine was relit at 1.2M, and No. 4 relit but failed to accelerate. Visual inspection of the intakes (using the aircraft hyperscope) revealed the loss of No. 4 intake forward ramp and heavy damage to the lower intake cowl lip.

The sequence of events surrounding the failure as indicated by interpretation of the data given by the airborne recording system and by inspection of the damaged intake by accident investigations experts from RAE Farnborough, agreed in all major respects.

The cause of surge of engine No. 3 results from an error of technique in the cancellation of reheat with the obsolescent standard of reheat control amplifier fitted to that particular engine. Engine overspeed into a transient surge condition could happen, unless reheat cancellation was undertaken with care. The modified amplifiers now fitted do not suffer this disadvantage.

The interaction surge of No. 4 engine was to be expected but in this instance one of the two rear attachments of the forward ramp failed, freeing the ramp to oscillate about the front hinge and remaining rear attachment. Coupled surge/ramp response maintained a cyclic surge condition which resulted in progressive failure of the front hinge. The final surge pulse (in a train of approx. 35 pulses) caused failure of the sole remaining ramp attachment at the rear as the ramp rotated rapidly hinge edge downwards striking the lip. The ramp left the intake moving forward and downwards rotating around the lip (hence severe lip damage), finally leaving the aircraft passing rearwards beneath the nacelle.

The damage evidence emphasised that the failure was due to exceedance of the design strength of a component in the ramp drive mechanism and there was no question of fatigue or faulty materials being involved. The source of the phenomenal load causing the failure then became the subject of much debate.

#### 4.4 Intake Structural Failure in Surge (Cont'd)

Further systematic surge investigations were immediately planned using aircraft 002, the British Prototype. For these investigations, the ramp and drive mechanism were suitably strengthened and stiffened and the test engines were equipped with special amplifiers allowing surge to be induced at will. Based on destructive strength tests the modified design possesses some 2.25 times the strength of the original design. Instrumentation systems were augmented to more precisely define pressure propagation over the forward and rear ramps and the transient loading in various components.

Model scale twin intake tests scheduled in support of the full scale exploration included investigation of flexible ramp behaviour under simulated interaction surge.

Fig. 18 shows examples from flight records made during the systematic interaction surge investigation. These data are appropriate to  $M = 2.0$  flight conditions and show for both intakes the time variation of pressure on the underside of the forward ramp trailing edge, the throat bleed sensor pressure  $P_{RVS}$  and the wall static pressure in the intake lower diffuser floor just forward of the compressor face ( $P_{EF}$ ).

Considering firstly the mechanism of interaction surge, the first surge of the inboard engine (No. 2) occurs following a significant pressure reduction forward of the engine face, which is believed to be the primary cause of interaction surge. The reduced pressure arises from the rapidly reducing intake pressure recovery due to distortion of the external shock system by shock expulsion of the neighbouring intake (primary surge). A possible contributory factor to the reduced pressure is choking of the intake throat due to flow separation along the splitter leading edge. The flow separation could arise from cross flow at the splitter leading edge associated with the pressure gradient generated by shock expulsion in the primary surging intake. It is interesting to speculate on the transient compressor face flow quality in this event.

The first interaction surge (No. 2 engine) is notable for its low intensity at the engine face, the peak pressure merely achieving the steady state initial level. However, a noticeable peak occurs in the intake ramp void (space above the ramps). Careful inspection of the toothed pressure variations reveals a local trough in the underside ramp trailing edge pressure coincident with this peak. However, although the peak pressure levels achieved in this case are lower than those appropriate to the primary surge (first surge in intake 1) the downward load on the front ramp is at least as large. In numerous cases the differential ramp loading has been found to be greater in the interaction than the primary case and furthermore, the largest ramp differential loadings so far measured are associated with interaction surge cases.

Two types of interaction surge signature (form of compressor face pressure variation) are identifiable in investigations so far. The one is typified by the first interaction surge of No. 2 engine with low absolute peak level and low initial starting pressure and the other has a form more closely approaching a primary surge, with small reduction of initial pressure and high achieved peak level. An example of this second type is the second surge shown in the case of No. 2 engine.

This second type of interaction surge signature has associated large peak pressures above and below the ramp. Inspection of the traces indicates only moderate differential ramp loading as assessed from peak differences. However, a large trough in the under ramp pressure almost coincident with the peak ramp void pressure gives large differential ramp loading. Attention is drawn to the unusual second primary surge of No. 1 engine. This effect is more typical of interaction surge, although by no means fully understood. Exact phasing of such peaks and trough, which in the example shown re-establishes normal undisturbed external ramp pressure, would in fact result in the initial design load being approached.

The investigation so far has not succeeded in achieving more than 75% of the load which must have been experienced in Flight 122. However, although the latter has not been re-produced, the contributory elements have been exposed. We could by no means claim an understanding of the phenomena. Investigations continue.

#### 4.4 Intake Structural Failure in Surge (Cont'd)

Despite all these worries about the structural integrity, the aircraft's handling behaviour has been impeccable. A considerable amount of pre-flight effort was devoted to consideration of simultaneous double engine failure, and from this an auto rudder system was adopted which was triggered by asymmetric rapid variations of HP compressor delivery pressure.

The result of this effort can be seen in Fig. 19 which shows the actual aircraft response to the double engine surge on Flight 122. A bank angle change of only  $2^\circ$  coupled with  $1^\circ$  sideslip in this severe case at 2.0M is proof enough of the efficiency of the protective systems.

Installation of similar systems on the production aircraft will ensure that even if such a severe case should occur in service there will be no hazard to aircraft or occupants.

#### 4.5 Performance

Although the technical problems associated with intake/engine compatibility are fascinating they must eventually be solved, and the viability of a commercial supersonic transport then rests on the achievement of performance claims.

It is therefore interesting to examine how the powerplant behaviour compares with predictions in this respect.

Unfortunately direct measurement of intake recovery cannot be shown because of instrumentation problems which are not yet resolved. However it can be said that by using indirect measurements it becomes obvious that the recovery is not significantly different from that measured on small scale models at full scale in N.G.T.E.

The analysis of engine and nozzle behaviour is of course in the hands of Rolls Royce (1971) Ltd. and SNECMA. They have kindly consented to allow us to use some of their material so that a reasonably complete performance picture can be presented.

One of the major concerns of the performance testing to date has been to develop an acceptable means of 'reed across' from Prototype to Production aircraft. It was decided that in view of the detailed differences between the two aircraft it would not be sufficient to apply overall percentages derived from prototype experience to the Production estimates. In fact, it is necessary to subject each component of the performance to detailed scrutiny so that appropriate adjustments can be made to the Production aircraft component characteristics.

For example Fig. 20 shows a comparison of flight and brochure engine s.f.c. (flange to flange). It is evident that the agreement is excellent. However this overall result conceals some interesting side effects.

It is found that the engine measured mass flow and fuel flow at a particular  $N_1$ ,  $N_2$  combination differ from the values given by the engine brochure. The in-flight mass flow is higher than predicted at all speeds, but the measured fuel flow is higher than predicted at subsonic Mach numbers but lower than predicted at 2.0M.

When all these factors are combined, it is found that the thermodynamic cycle of the engine is unchanged, but that the 'effective' spool speeds differ from the measured speed. The explanation is believed to lie in the effect of intake radial flow distortion on the compressor characteristics.

In practice, it means that to get the true performance, one must work with a modified  $N_1$  and measured fuel flow in order to correctly estimate thrust and spill drag.

The measured internal pressure distribution of the secondary nozzle is compared with wind tunnel results in Fig. 21. One minor difference arises from the fact that the aircraft free floating secondary petals are a shade over-expanded in cruise, as shown by the difference between full and dotted lines on the figure. As a result of this, the static pressure over the after part of the nozzle shroud diverges slightly from the tunnel model result.

#### 4.5 Performance (Cont'd)

Despite this minor discrepancy, the overall nozzle gross thrust (calculated from measured pressures on the nozzle) is in excellent agreement with predictions as shown by Fig. 22. From this it is concluded that there is no reason to modify the predicted cruise performance of the production nozzles.

On the debit side, it was found that the nacelle as a whole was leaking badly, and it was necessary to take steps to establish how much performance was being lost from this source.

By sealing as much of the Prototype nacelle as is physically possible, and ground measurements of leakage rate before and after sealing, the assumptions on the exchange rate between leakage and thrust loss are being verified.

When this is done, the Production aircraft performance will be modified if necessary, but it is not expected that significant changes will arise from this cause since most of these leak sources do not exist on the Production aircraft. For example the Gas Turbine Starter exhaust, tertiary doors and reverser grilles have all been eliminated.

#### 5. CONCLUSION

This presentation has attempted to show some of the problems met and overcome. Much work remains to be done of course, but the Concorde designers are enormously encouraged by their experience so far.

It is now known that a supersonic transport can be built which is technically sound and which will meet the performance claims advanced many years ago.

The judgements as to whether this aircraft is economically viable is outside the scope of this paper. BAC/Aerospatiale believes emphatically that it is viable, and look forward to the day when the world's airlines confirm this judgement.

#### REFERENCES

1. The design and development of an Air Intake for a Supersonic Transport Aircraft  
I.H. Rettie and W.G.E. Lewis  
Journal of Aircraft, Volume 5, Number 6, November-December 1968.
2. Free Jet Testing of a Supersonic Engine/Intake Combination  
D.P. Morris and D.D. Williams  
Journal of the Royal Aeronautical Society, Vol. 74 pp. 213-218  
March 1970.

#### ACKNOWLEDGEMENTS

The Authors wish to thank the British Aircraft Corporation Limited for permission to publish this paper, also Rolle Royce (1971) Limited and SNECMA for permission to publish data as described in the text.

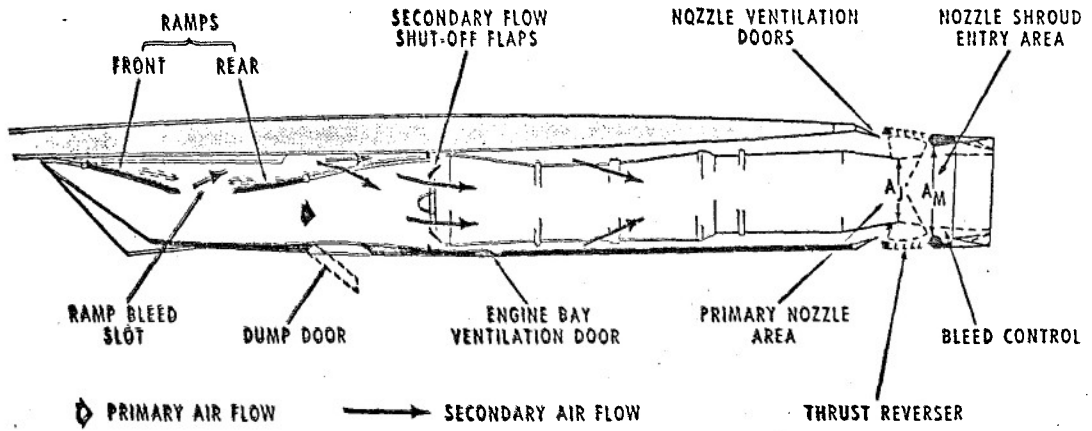


Fig. 1. Powerplant layout

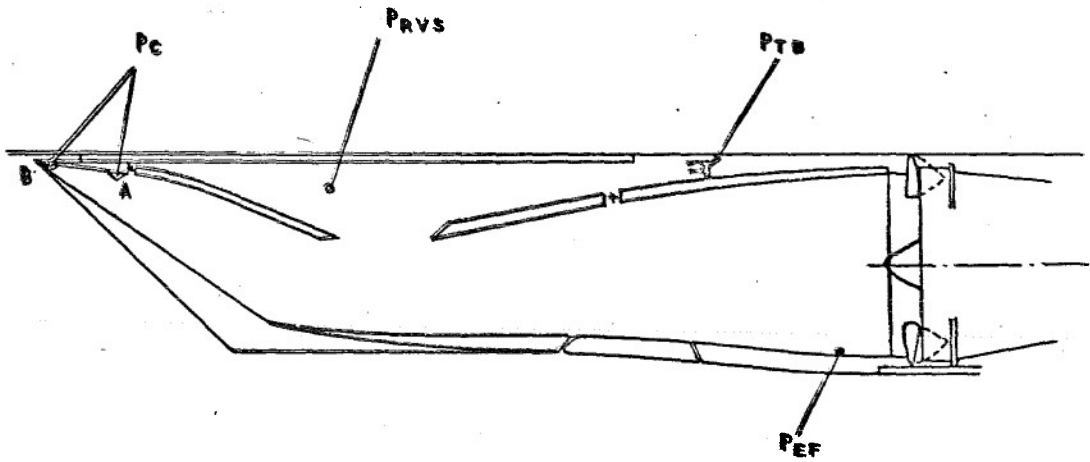
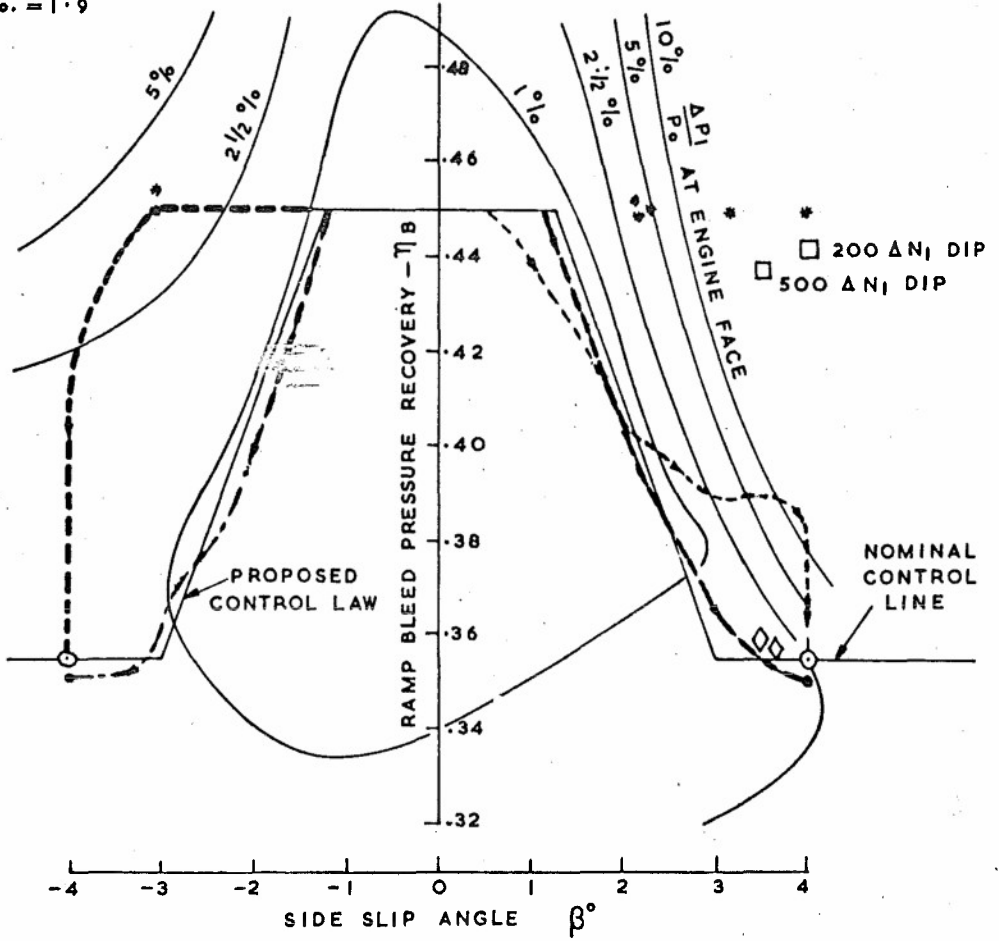


Fig. 2. Intake control aerodynamic instrumentation

CELL MACH  
No. = 1.9

MAXIMUM CONTINUOUS POWER

$A_B^* = 110$  FIXED



SURGES

- \* - NO  $\eta_B$  OR  $\eta_i$  DIP
- -  $N_1$  DIP ALONE
- ◇ -  $\eta_B$  DIP ALONE
- - SMOOTH RUNNING  $N_1$  DIP AND  $\eta_B$  DIP

--- TRANSIENT EXCURSIONS

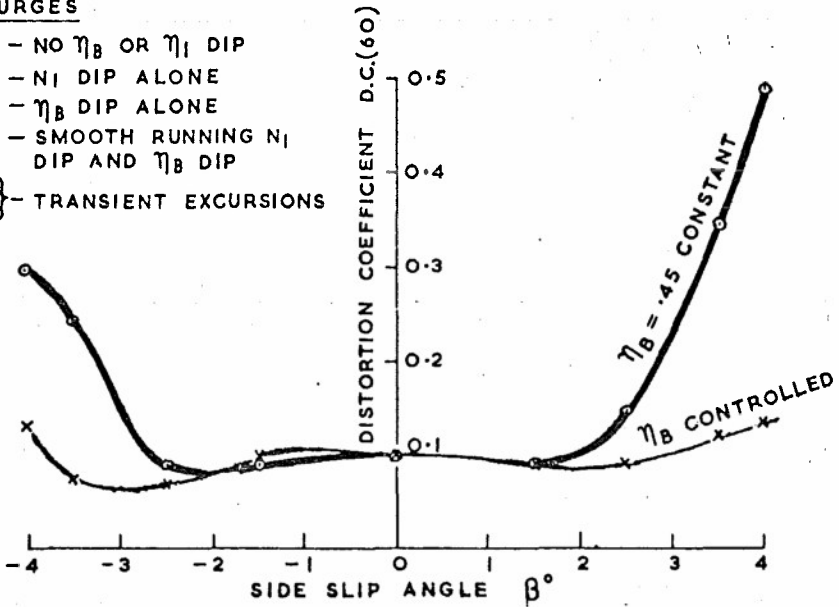


Fig. 3. Engine face flow distortion levels during sideslip

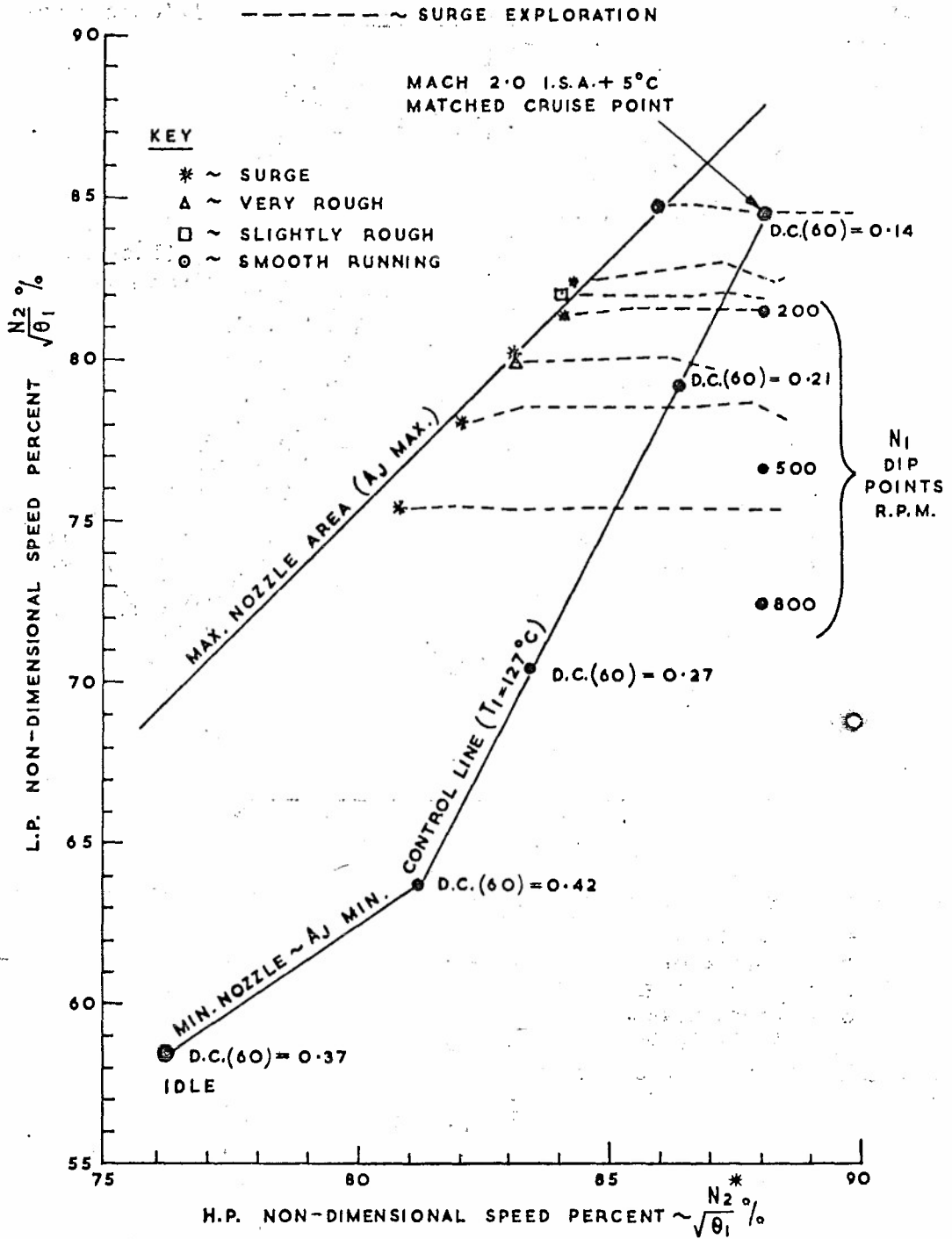


Fig. 4. Typical engine operating characteristics N.G.T.E. cell 4 ~ cell mach number = 1.9

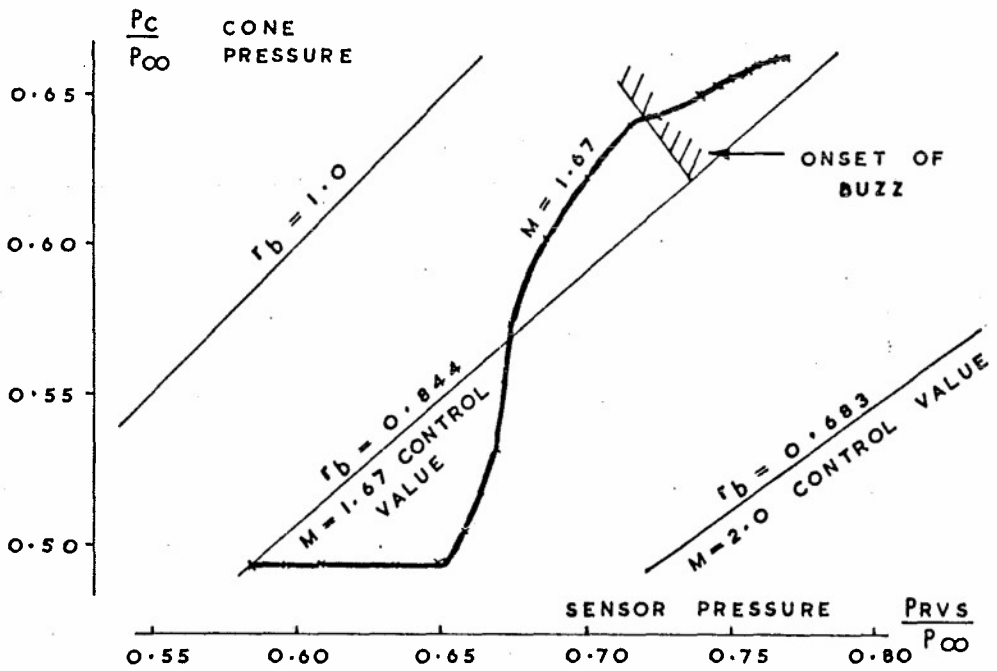
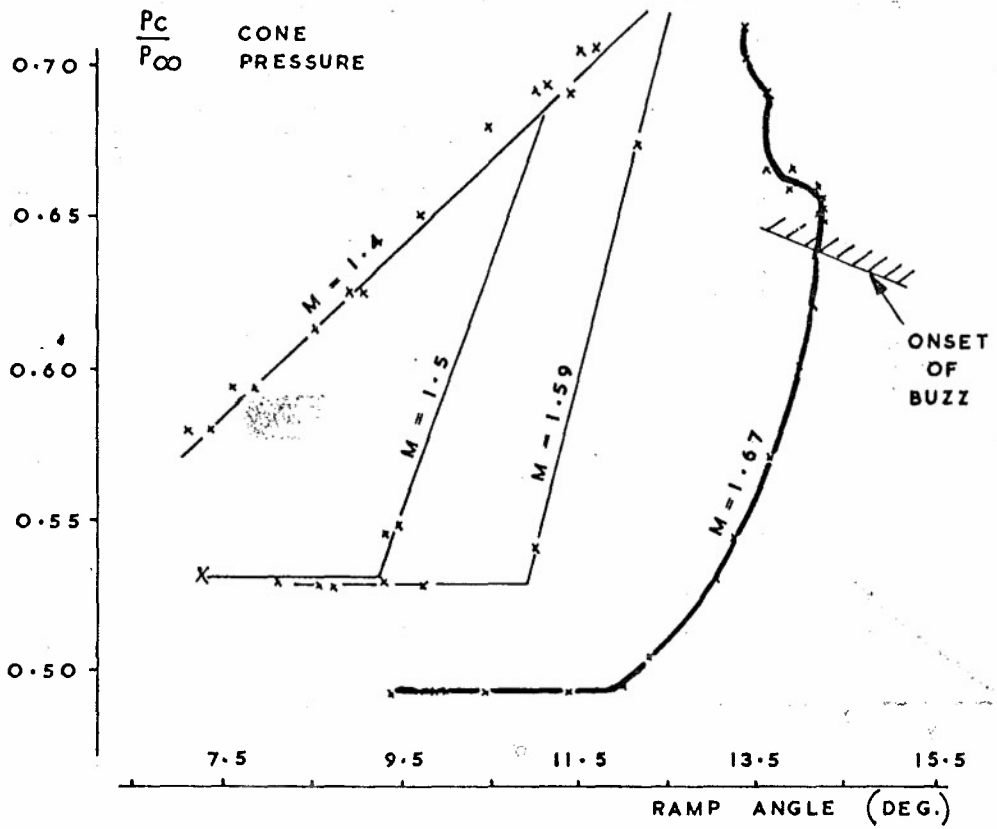


Fig. 5. Cone reference pressure interference during throttling at low mach number

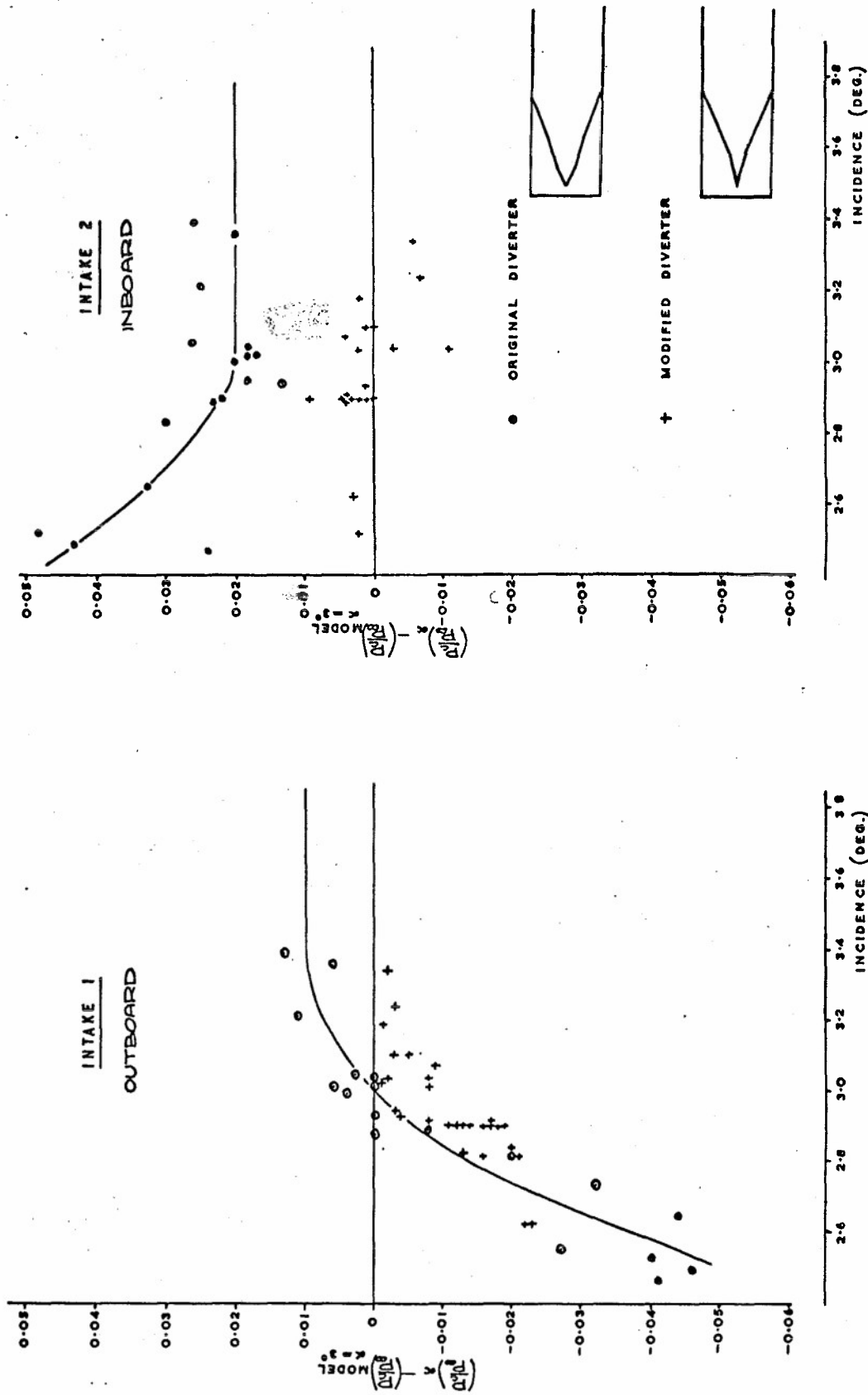


Fig. 6. Effect of incidence on forward cone pressure at M = 2.0



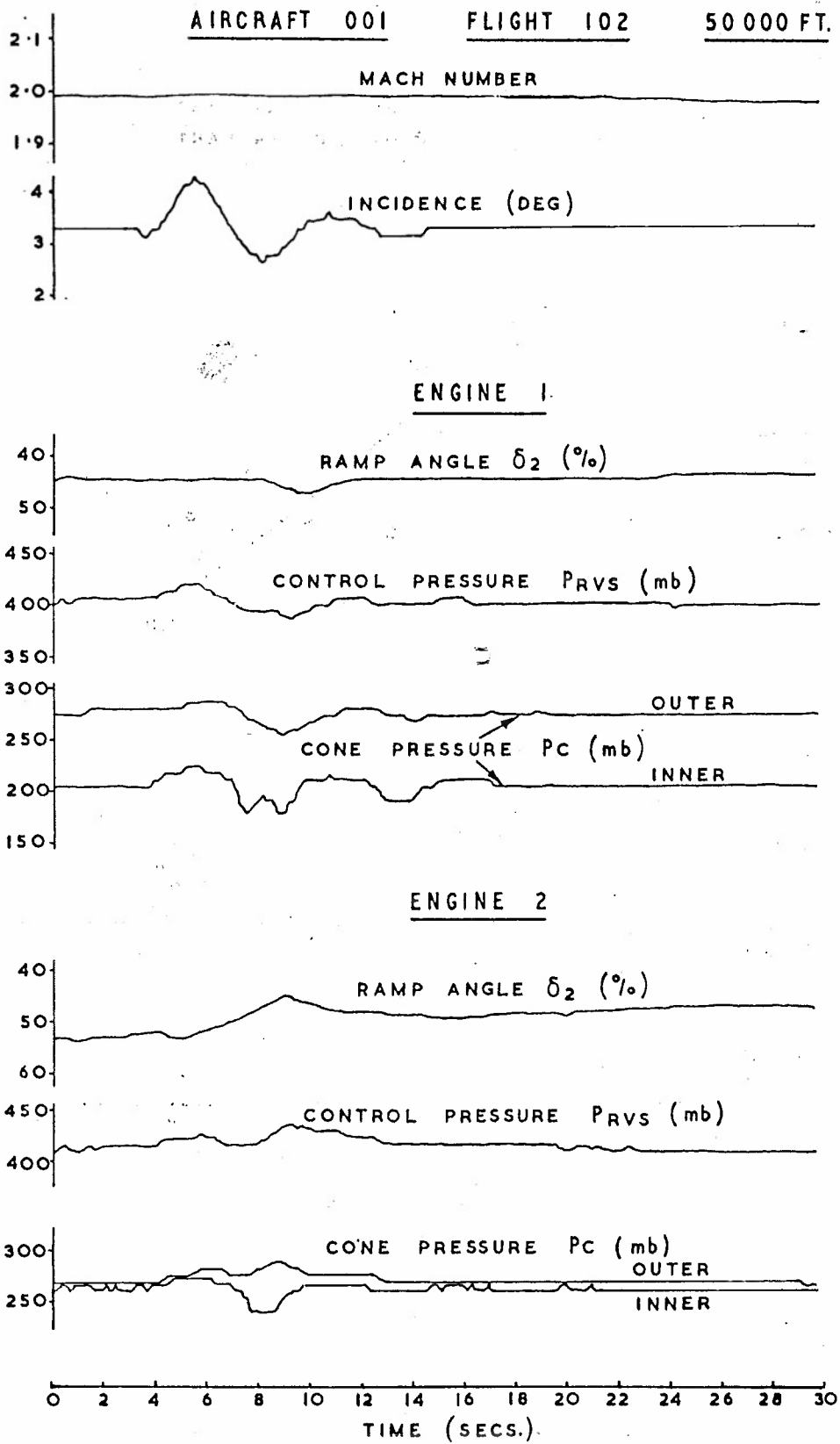


Fig. 8. Pitch manoeuvre

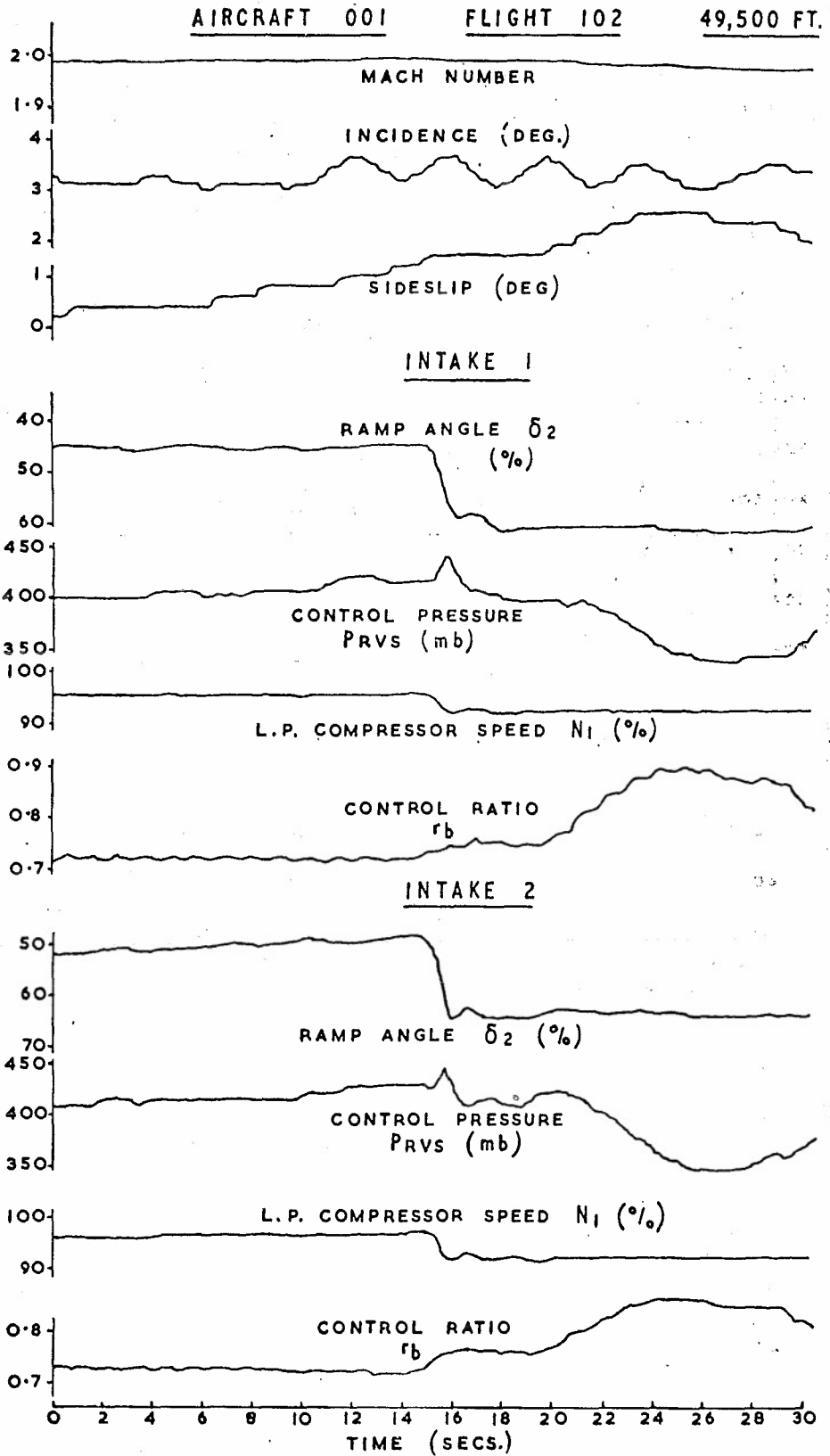


Fig. 9. Sideslip manoeuvre

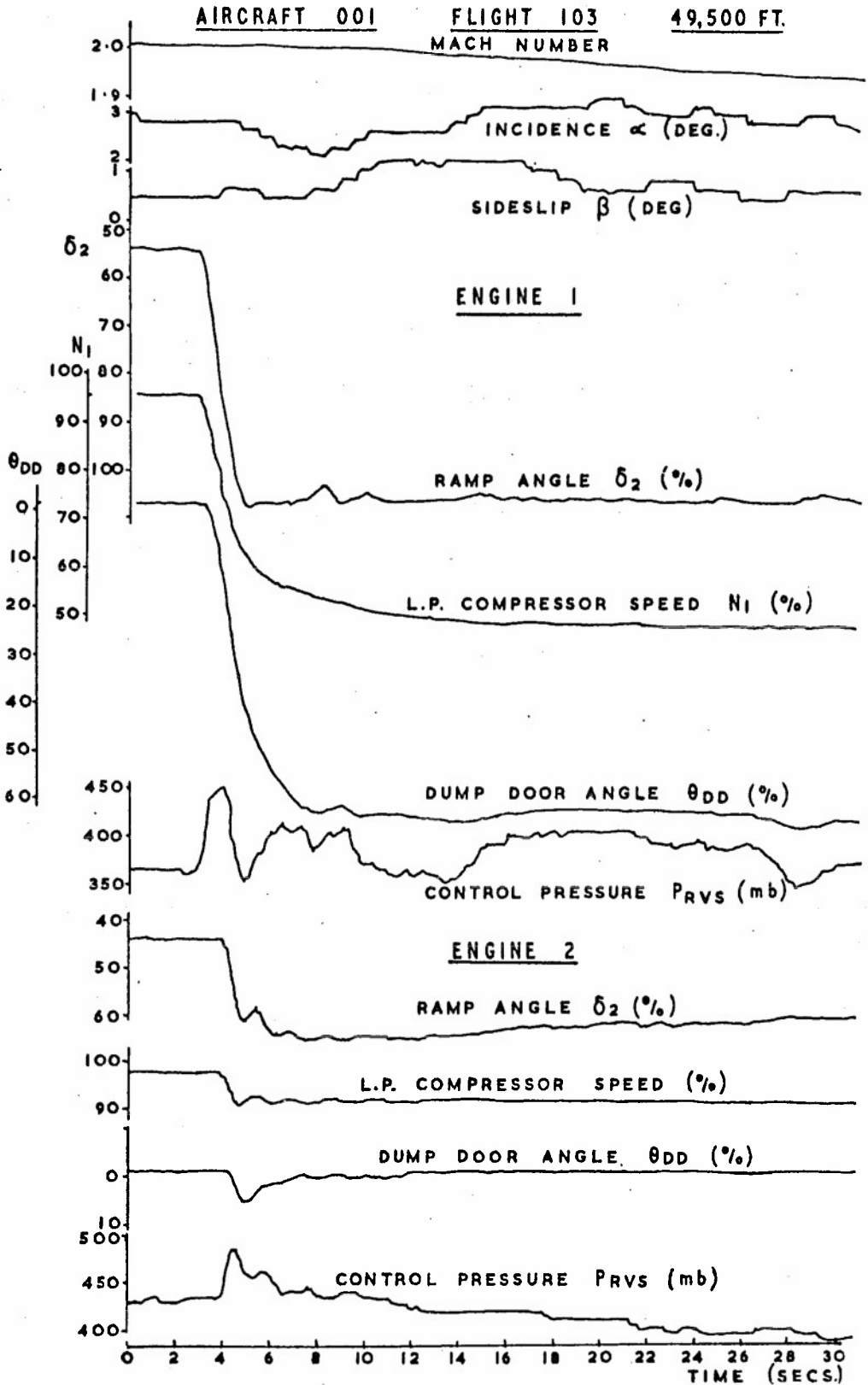
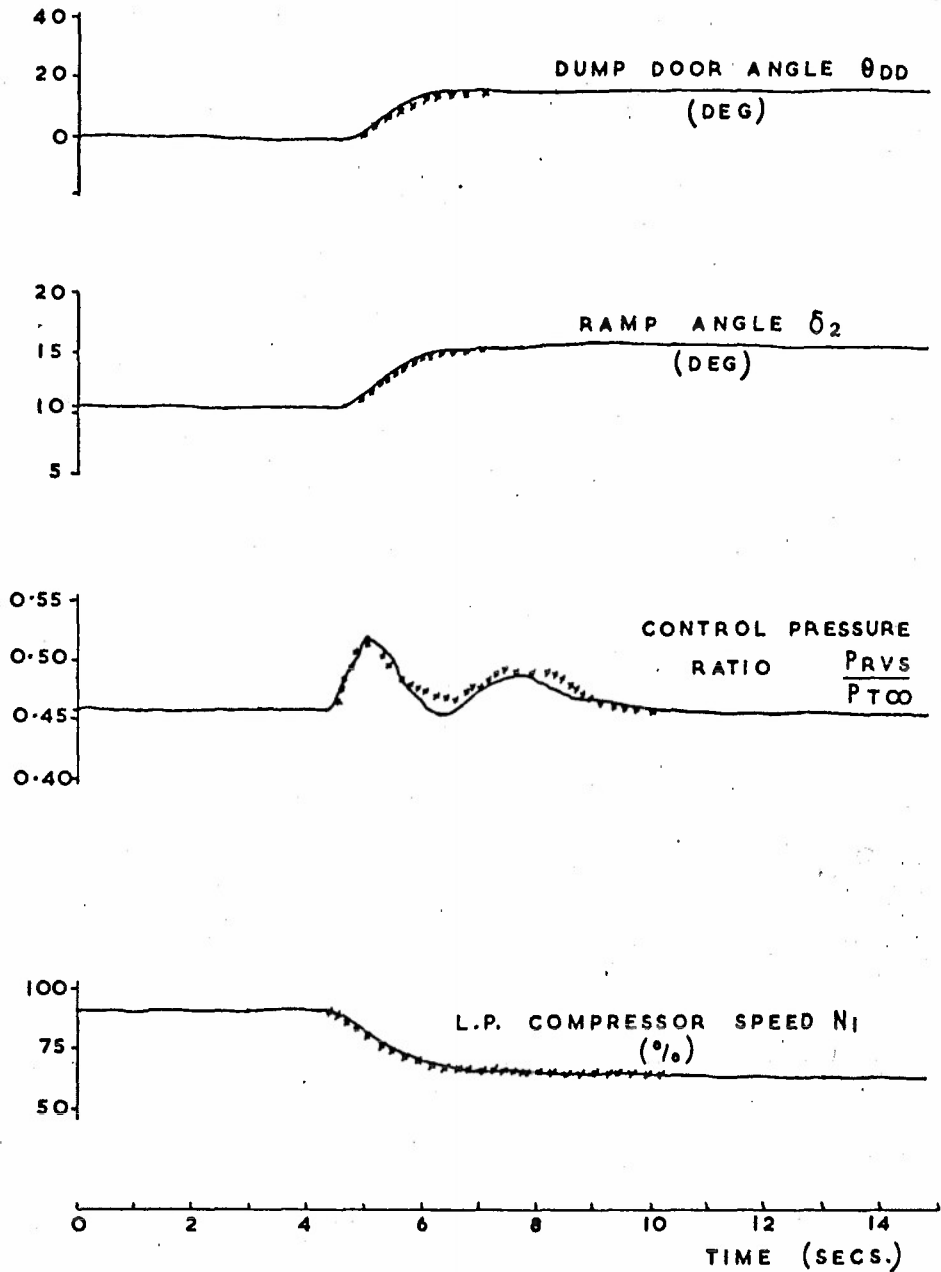


Fig. 10. Shut down of no. 1 engine



——— SIMULATION  
 xxxxxxxx MEASURED  
 ( AIRCRAFT 002 FLIGHT 58  
 M = 1.833  $Z_p = 45\ 000$  FT.)

Fig. 11. Engine slam deceleration comparison between prediction and measurement

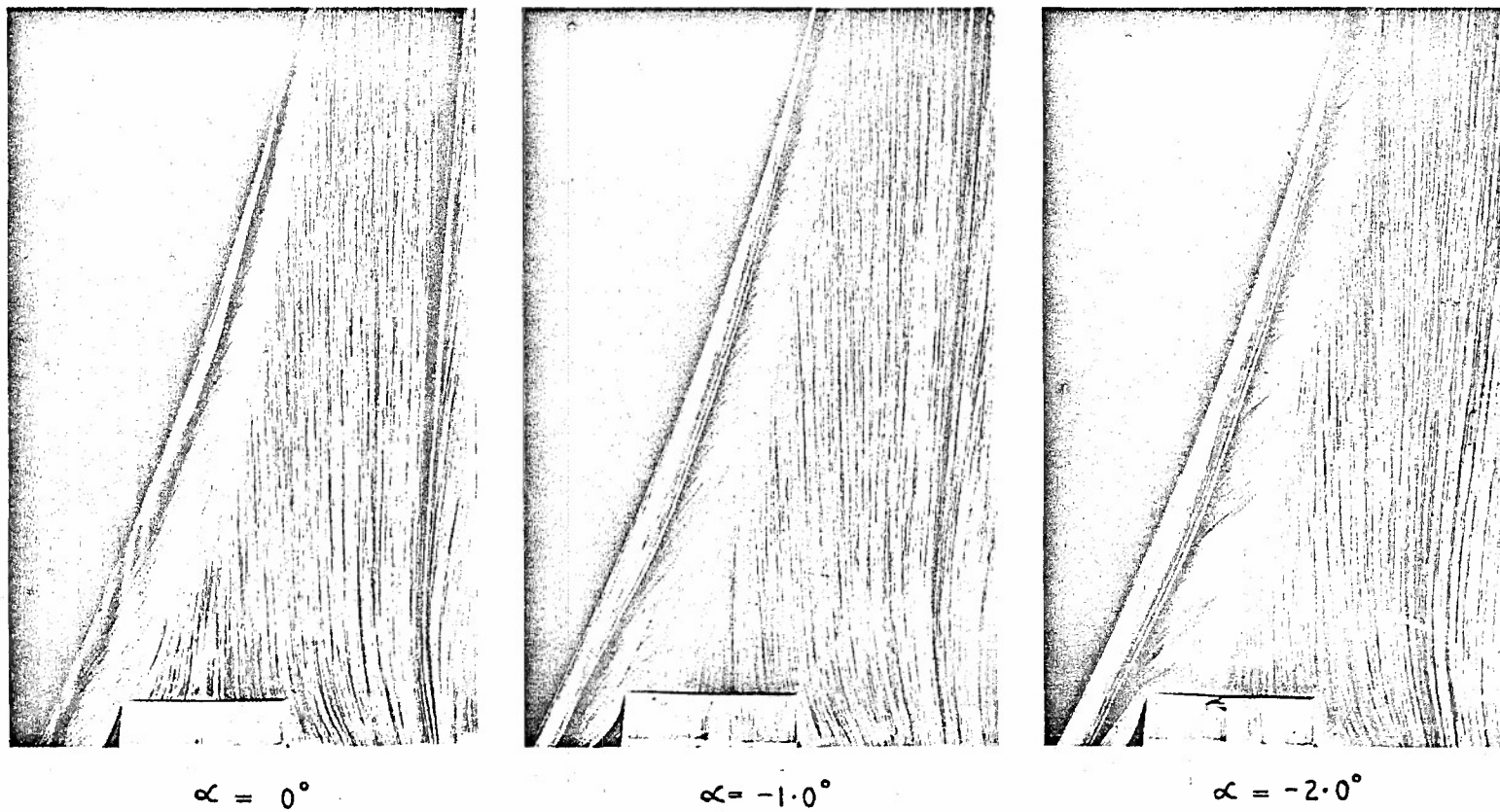


Fig. 12. Underwing flow at low incidence (subsonic) prototype wing leading edge (BAI) zero sideslip

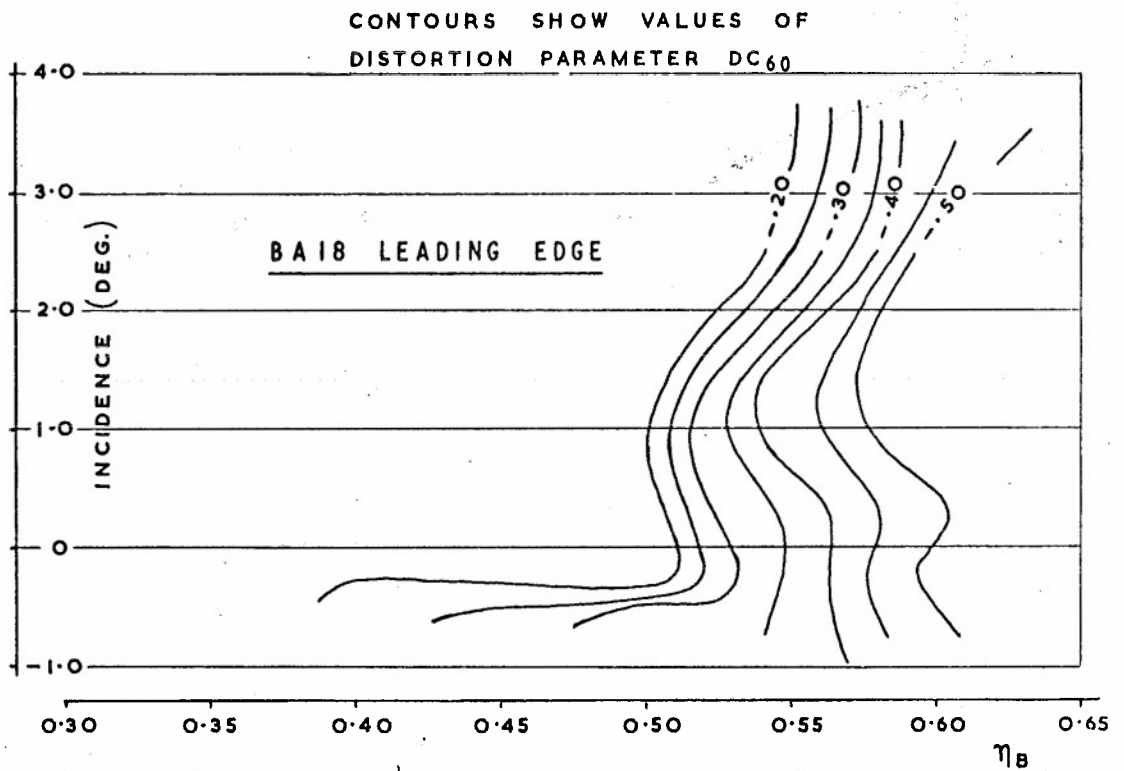
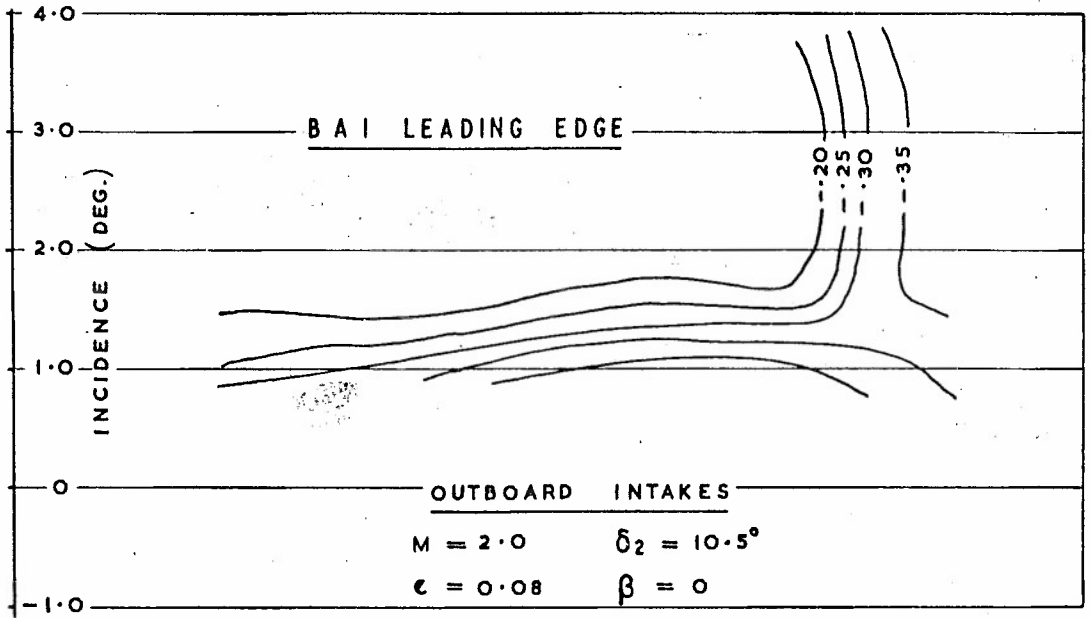


Fig. 13. Effect of wing leading edge design on intake flow distortions

AIRCRAFT 001 FLIGHT 40

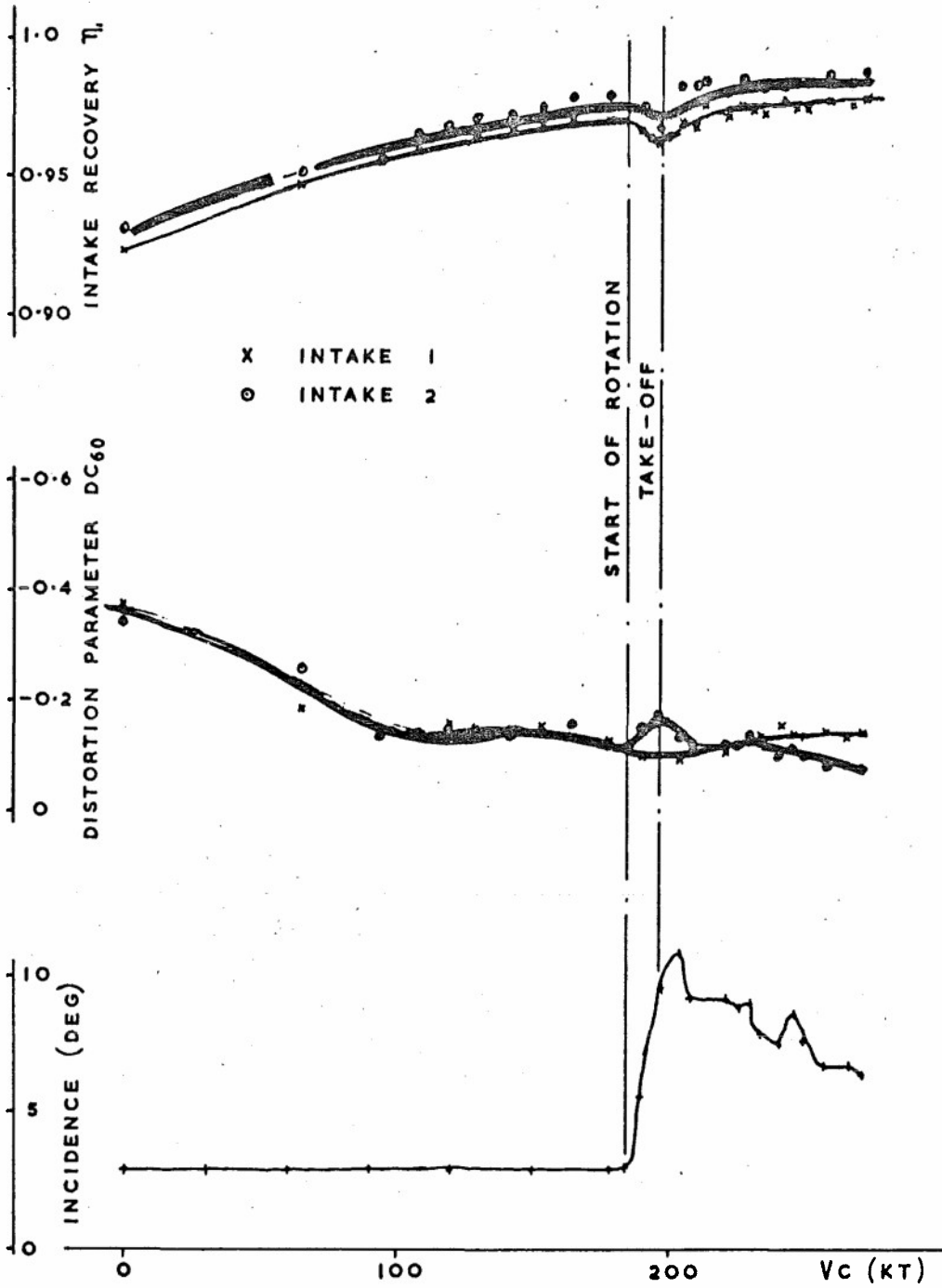


Fig. 14. Intake measurements during take-off

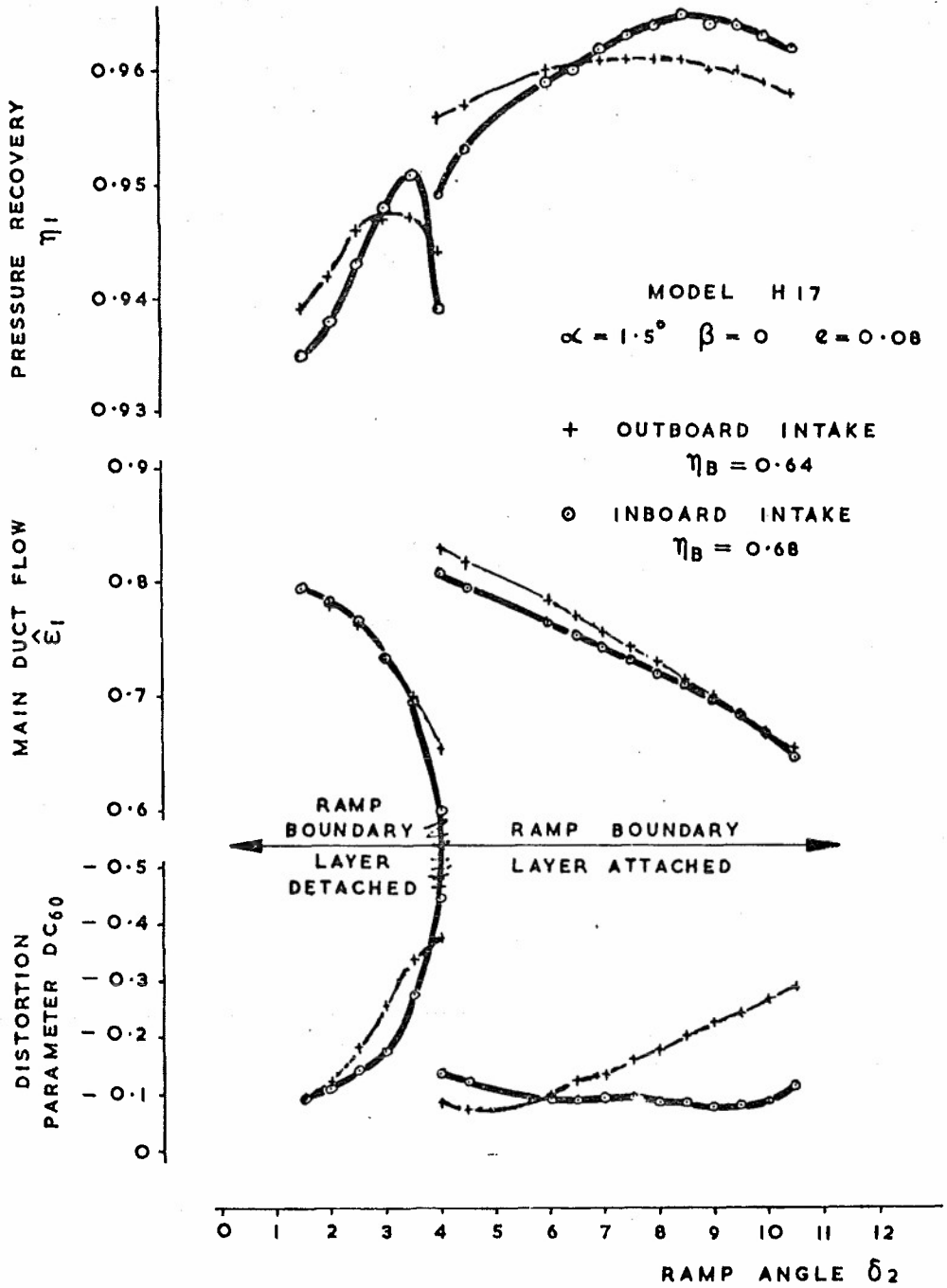


Fig. 15. Intake boundary layer separation at  $M = 1.6$

+ PHASE 1, FIXED INTAKE GEOMETRY      ⊙ PHASE 2, VARIABLE INTAKE GEOMETRY

1g FLIGHT AT MAX. RECOMMENDED POWER

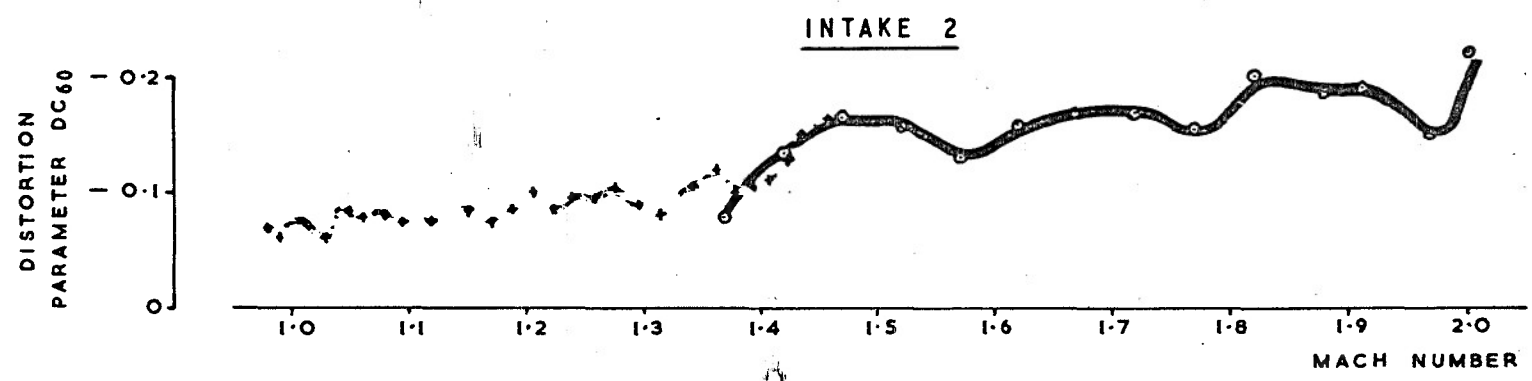
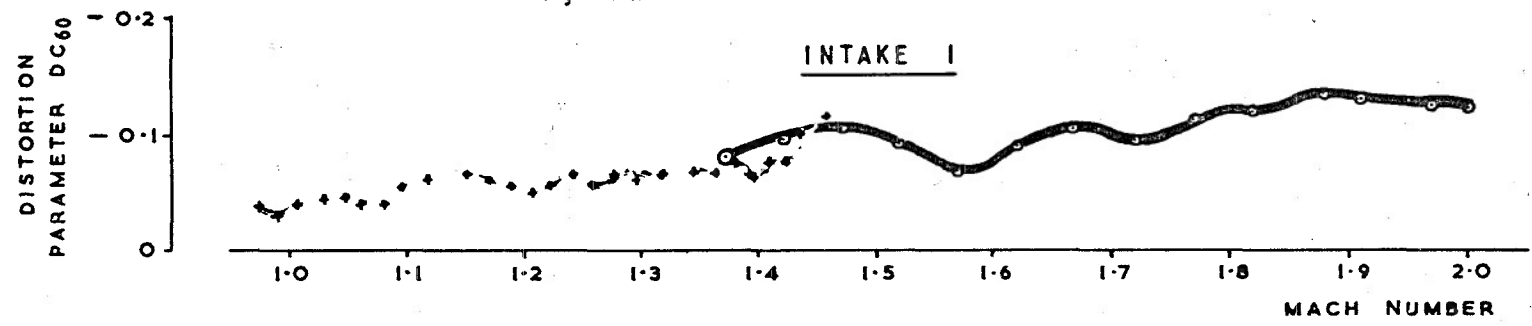


Fig. 16. Intake flow distortion at supersonic speeds

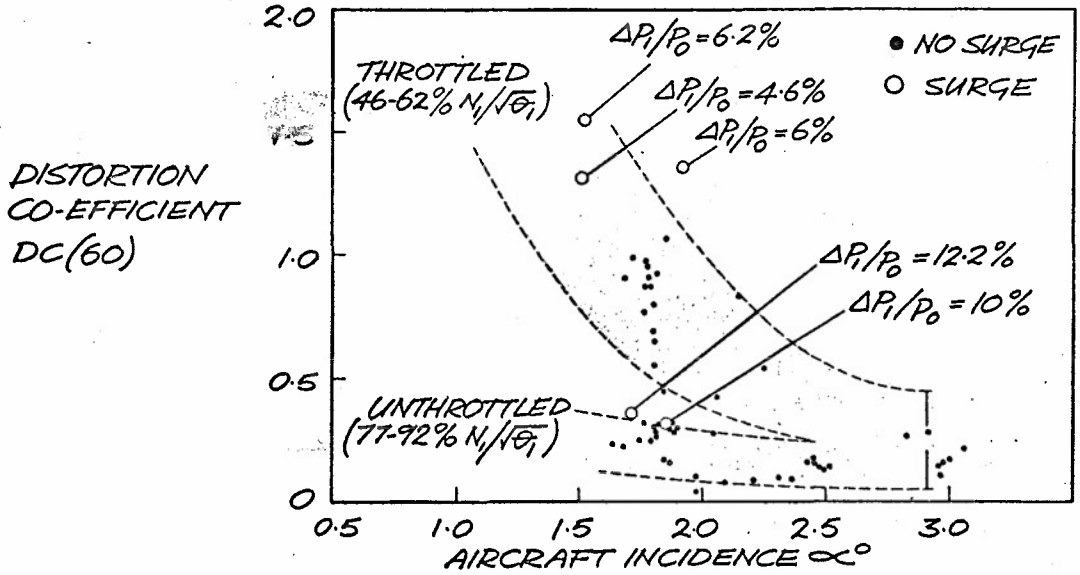


Fig. 17. Typical surge events supersonic flights  $M > 1.7$  no. 1 (outboard) intake

AIRCRAFT 002 FLIGHT 82 M=2.01

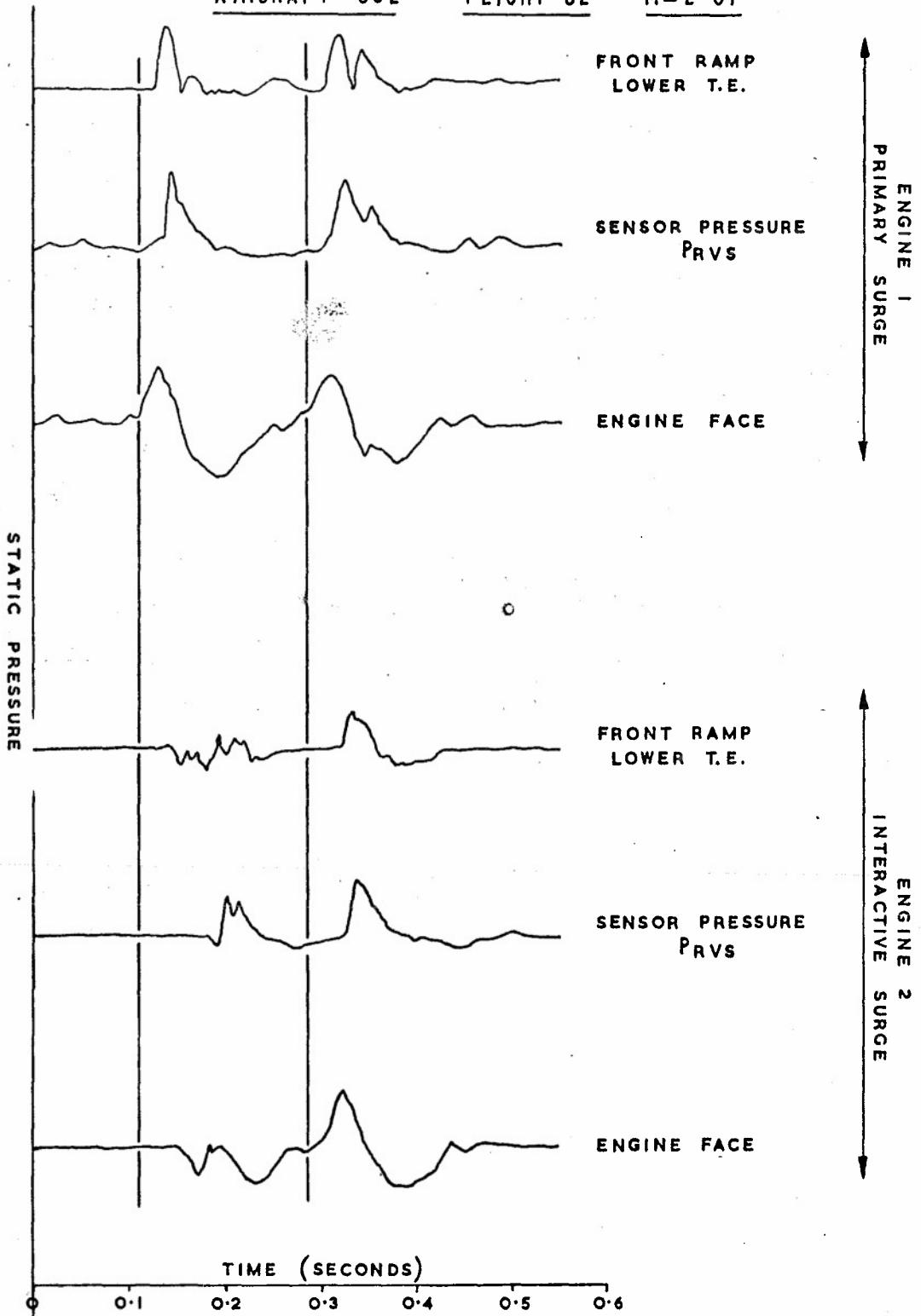


Fig. 18. Intake pressures in surge

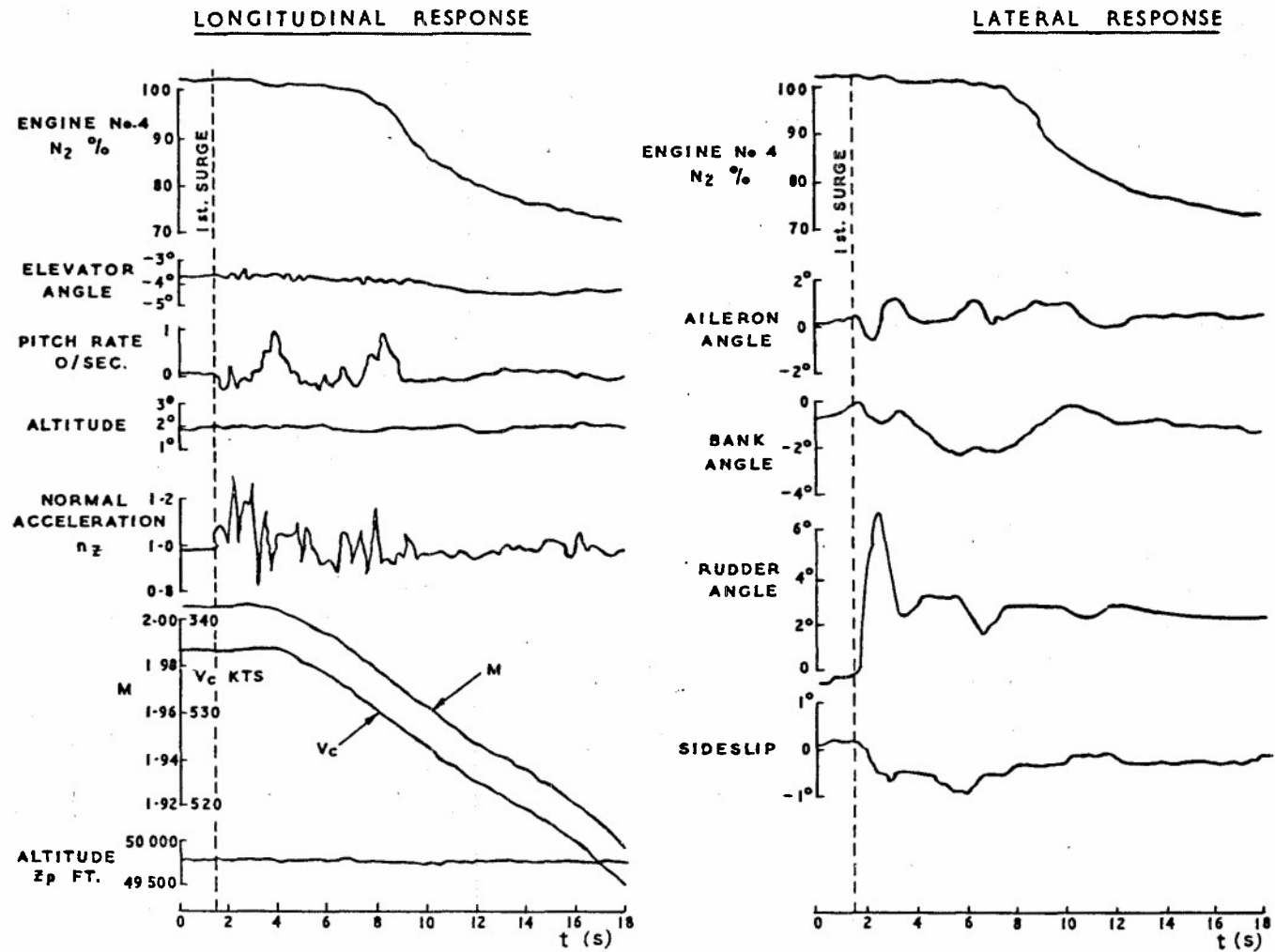


Fig. 19. Aircraft response to double engine surge

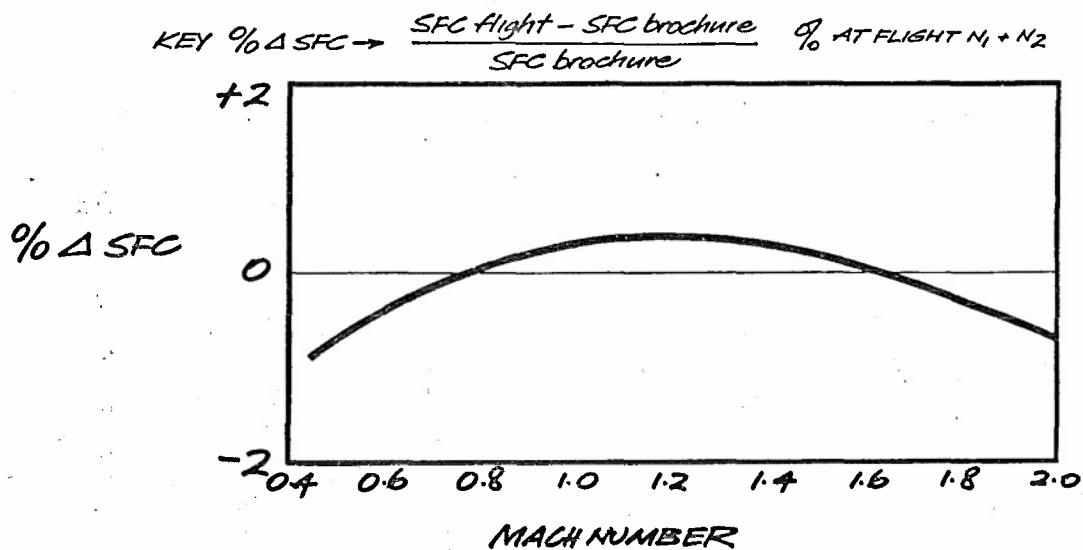


Fig. 20. Comparison between flight and brochure SFC (flange to flange) olympus 593-3B flight analysis

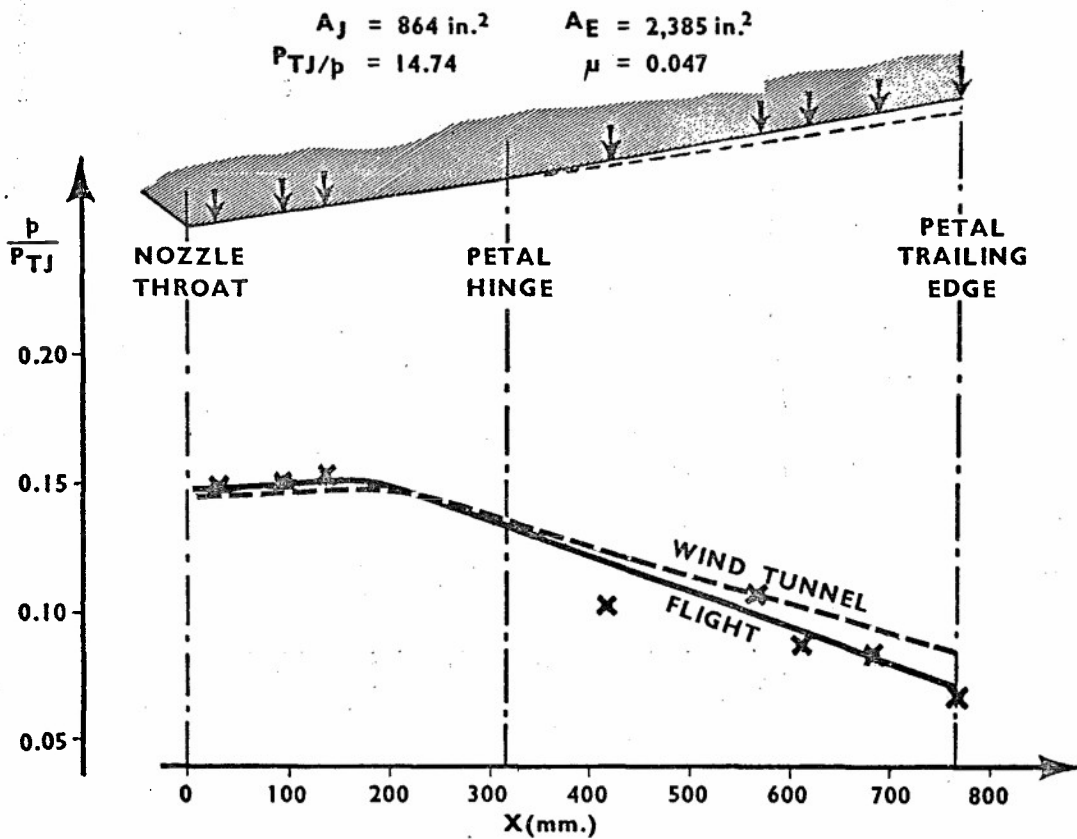


Fig. 21. Nozzle internal pressure

Concorde 001 - flight 117 - mach 2

## CONTROL CONCEPT AND WIND TUNNEL TESTING OF A SUPERSONIC INTAKE CONTROL SYSTEM

by H. N. Larsen and R. G. Schweikhardt  
The Boeing Company  
Seattle, Washington, USA

## SUMMARY

The design, development, and performance criteria of a control system for an axisymmetric mixed compression intake are described. The controller is independent of other intake controllers and of airplane data systems. During started intake operation, throat Mach number is controlled with a translating centerbody and variable position cowl throat doors; normal shock position is controlled with secondary air valves and overboard bypass doors. These two control loops use intake duct pressure ratio signals for feedback. The desired pressure ratio reference value is scheduled with centerbody position and biased with intake controller error signals to provide for varying intake Mach number and angle of sideslip. Using vortex valves as an auxiliary normal shock stability system, model tests showed that the controller can maintain peak intake recovery while accommodating the required disturbances. Hot- and cold-day engine/intake airflow matching is automatically controlled with increased secondary valve airflow or an intake-activated engine rpm trim control. An external compression mode which maintains stable intake airflow with low compressor face distortion provides for unstarted supersonic intake operation.

## NOMENCLATURE

ABY	overboard bypass door area	t	time
ALIP	intake lip area	$\frac{W\sqrt{\theta_2/\delta_2}}$	corrected airflow rate
ASA	secondary air valve area	X <sub>BY</sub>	overboard bypass door actuator displacement
DIST	$P_{T2 \text{ avg}} - P_{T2 \text{ min}}/P_{T2 \text{ avg}}$	X <sub>SA</sub>	secondary air valve actuator displacement
K	controller gains	X <sub>TRIM</sub>	trim motor position
M <sub>L</sub>	local Mach number	$\Delta_{CC}$	cross coupling bias (PRU)
M <sub>TH</sub>	throat Mach number	$\Delta_{PC}$	half position coordination deadzone
N	mechanical engine speed	$\Delta_{PP}$	half parallel path deadzone
P <sub>TO</sub>	local total pressure	$\Delta_{PCB}$	$(P_{CB \text{ max}} - P_{CB \text{ min}})/P_{TNS}$
P <sub>C</sub>	cowl static pressure	$\Delta_{RTD}$	throat door displacement
P <sub>CB</sub>	intake throat static pressure	$\Delta_{XCB}$	centerbody displacement
P <sub>NS</sub>	static pressure aft of normal shock	$\Delta_{\alpha}$	angle-of-sideslip bias (PRU)
P <sub>TNS</sub>	intake throat total pressure	$\epsilon$	error signal
P <sub>T2</sub>	compressor face total pressure	$\zeta$	damping ratio
P <sub>VV</sub>	vortex valve exit total pressure		
PRU	pressure ratio units	Subscripts	
R <sub>LIP</sub>	intake lip radius	c	actuator command position
rpm	revolutions per minute		
S	La Place operature		

## INTRODUCTION

A control system for an axisymmetric intake suitable for supersonic transport application has been developed. The design combines simplicity and relative self containment with the unique capability to maintain the high intake performance necessary for efficient commercial supersonic flight. The airplane which utilizes four intakes has a design cruise Mach number of 2.7, the local intake Mach numbers being 2.65 and 2.60 for the inboard and outboard intakes, respectively. Each intake is provided with two identical automatic control systems, each controller having its own set of sensors, feedbacks, and outputs. Dual redundant two-stage servovalves and actuators are also provided for each control surface. One intake control system is used for normal control, and the second is used as a standby. Either system may be manually selected for control by the flight crew and, in addition, automatic transfer of control occurs between systems following the detection of a failure condition, such as failure to maintain the correct intake takeoff geometry, failures of either hydraulic or electric power for the control system in operation, inadvertent intake unstart, or detection of intake buzz.

Within each control system are control loops which use intake pressure ratios for feedback. These pressure ratios (control signals) are used by the control system to position the intake variable geometry components, which consist of a translating centerbody, variable position cowl throat doors, and a bypass system comprising secondary air valves and overboard bypass doors. The control laws governing the control system actions are divided into several modes, sequences, and configurations. Switching between these various sets of control laws is generally automatic; however, in some instances flight crew action is utilized to reduce system hardware. In addition to the control surfaces, the intake incorporates vortex valves at the throat section. During mixed compression operation, these valves are aerodynamically triggered to bleed airflow just aft of the normal shock should the shock traverse forward into the throat section. Maximum vortex valve bleed capacity<sup>(1)</sup> is 5% of the cruise engine airflow demand. This capability provides 5% additional stability margin against unstarts due to downstream transient disturbances. Figure 1 shows a schematic of the intake with the locations of the control surfaces and vortex valves.

This paper describes the intake control system with emphasis on operation between Mach 1.6 and 2.9. To maintain high started intake performance across this Mach range, it is generally necessary to vary control signal references with intake operating conditions: intake Mach number, angle of attack, and intake throat Mach number. To keep all intakes from being dependent on an airplane-generated air data Mach signal without the addition of intake Mach sensors, each intake control system schedules its pressure ratio

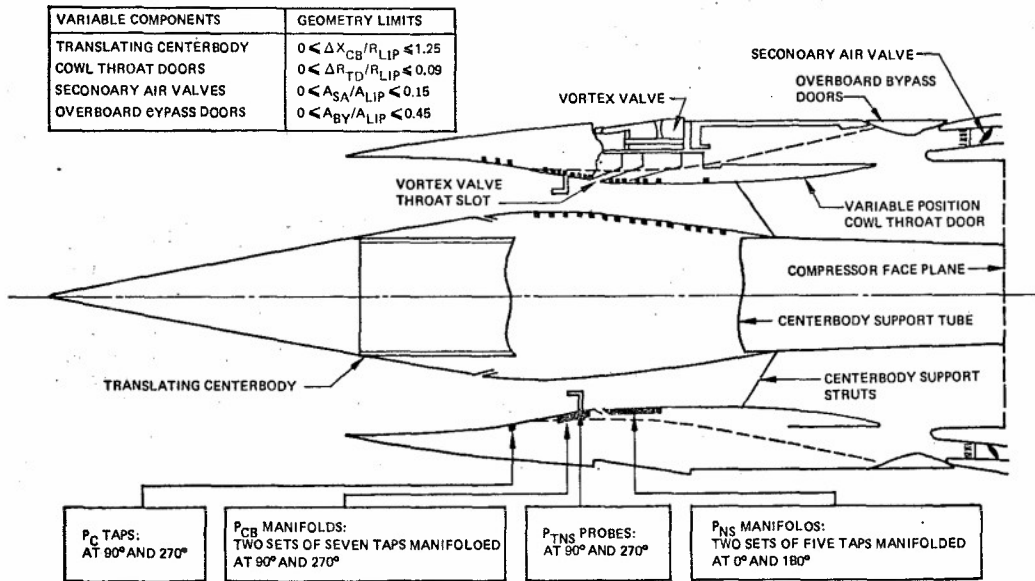


Figure 1. Intake Variable Geometry, Vortex Valves, and Control Signal Locations

references with centerbody position. Thus, during started operation each intake control system uses centerbody position as a Mach meter. Angle of attack and intake throat Mach number information is inherent in error signals within the intake control system. These error signals are used to bias the pressure ratio references and maintain started intake operation during off-design conditions. Internal aerodynamic analyses, control system performance and stability analyses, and steady-state wind tunnel test results were used in the synthesis of the intake control system.

Dynamic testing of the control system was performed using a 1/6-scale model (5.28-in. lip radius). The intake was fully instrumented with pressure taps and probes along the cowl, centerbody, and at the compressor face. Dynamic instrumentation in two distinct response ranges was provided. Relatively slow response (30 Hz) pneumatic lines and transducers were used for control signal sensing. Flush-mounted transducers at the compressor face provided dynamic measurements (2000 Hz) of intake recovery and distortion. These transducers were located on a compressor face rake which consisted of eight equally spaced arms with five probes per arm. Compressor face rake data from these 40 transducers were tape recorded, whereas data of control system variables were saved using three strip chart recorders of eight channels each. A cold pipe, terminated with a variable-area plug valve, was fitted to the rear of the intake to simulate engine weight flow changes.

## CONTROL MODES

The positioning of the variable-geometry components for the intake control modes, sequences, and configurations is shown in Table 1. Airplane takeoff and the large engine airflow requirements below Mach 0.5 are accommodated by the takeoff configuration. This configuration is automatically obtained when the engine mode selector is placed in the takeoff/landing position. Below Mach 0.5, "noise abate" is an optional mode which may be manually selected during low engine thrust operation such as descent airport approach. The mode modulates the centerbody to maintain a near-sonic throat to prevent the forward propagation of compressor noise. The noise abate mode is automatically disengaged and the takeoff configuration engaged should high engine thrust be demanded. This occurs during airplane go-around and engine thrust reverser operation. The run configuration is a simple and reliable method of supplying engine air demands during subsonic and low supersonic climb. This mode is automatically obtained when the engine mode selector is placed in the run position at approximately Mach 0.5. Control is manually switched from the run configuration to the buzz suppression mode at approximately Mach 1.2. Buzz suppression mode control is maintained until the flight crew starts the intake by activation of the restart sequence.

Between Mach 1.6 and 2.9, the intake control system consists of two modes and two sequences: a started mode, a buzz suppression mode, a restart sequence, and a sympathetic unstart sequence. The started mode maintains mixed compression operation for efficient supersonic climb and cruise. The buzz suppression mode maintains satisfactory external compression operation in the event of an inadvertent intake unstart or a sympathetic unstart. The restart sequence transfers intake operation from the buzz suppression mode to the started mode. The sympathetic unstart sequence unstarts an outboard intake following an inadvertent unstart of the other outboard intake combined with a sensed high airplane lateral acceleration. Thus, sympathetic unstart is used to reduce airplane yaw excursions.

Table 1. Intake Control System Summary

Control Mode Configuration or Sequence	Mach Number Range	Intake Components					
		Centerbody	Cowl Throat Doors	Primary Bypass Doors	Secondary Air Valves	Takeoff Doors	RPM Trim
Takeoff configuration	0 to 0.5	Fully extended	Closed	Closed	Fully open	Unrestricted	Inactive
Noise abate mode	0 to 0.5	Modulated for $M_{TH} = 0.85$	19% open	Closed	Open	Closed	Inactive
Run configuration	0.5 to 1.2	Fully extended	Open	Closed	Open	Closed	Inactive
Buzz suppression mode	1.2 to 2.9	Fixed at $\Delta X_{CB}/P_{TR} = 1.15$	Fixed at $\Delta R_{TD}/R_{LIP} = 0.09$	Modulated to position normal shock in front of cowl lip		Closed	Active
Started mode high performance	1.6 to 2.9	Modulated for $M_{TH} = 1.25$	Scheduled function of centerbody position	Modulated to position normal shock downstream of intake throat (i.e., just aft of vortex valves)		Closed	Active
Started mode high stability	1.6 to 2.9	Modulated for $M_{TH} = 1.30$	Scheduled function of centerbody position	Modulated to position normal shock downstream of intake throat		Closed	Active
Restart sequence	1.6 to 2.9	Retracted at maximum rate	Fixed at $\Delta R_{TD}/R_{LIP} = 0.09$	Modulated to position normal shock downstream of translating throat		Closed	Active
Sympathetic unstart sequence	1.6 to 2.9	Commanded to $\Delta X_{CB}/R_{LIP} = 1.15$	Commanded to $\Delta R_{TD}/R_{LIP} = 0.09$	Commanded closed		Closed	Active

The started mode uses two feedback control loops: one to control intake throat Mach number utilizing the translating centerbody and variable-position cowl throat doors. The second loop controls normal shock position by modulating secondary air valves and overboard bypass doors. For transient off-design throat Mach numbers a signal path (cross-coupling function) is provided between the two loops to maintain started intake operation. Either a high-stability or a high-performance option can be selected during started mode control. These options offer a choice between a higher intake pressure recovery or a larger stability margin from unstarts caused by upstream or downstream disturbances.

In the buzz suppression mode the centerbody and cowl throat doors are commanded to fixed positions and a duct pressure ratio signal is used to modulate the secondary air valves and primary bypass doors to maintain stable intake airflow. The resulting normal shock position is just forward of the cowl lip and the entire intake airflow is subsonic. A pressure ratio near the cowl lip is used as a start/unstart detector. This pressure ratio is compared to a reference to determine whether the intake controller should be in the started or buzz suppression mode. Sensing an unstart, this detector will cause the intake controller to automatically engage the buzz suppression mode. Sensing an intake start after initiation of a restart sequence will activate the started mode.

The intake is restarted at the most opportune time following an unstart and the establishment of buzz suppression control. Flight crew action initiates the restart sequence, which consists of the following control system actions:

- 1) The centerbody is retracted at maximum rate from the fixed buzz suppression position while the cowl throat doors remain open. The intake throat position moves downstream from the cowl lip as the centerbody is retracted.
- 2) Simultaneous with the centerbody retraction, the buzz suppression control signal reference is decreased causing the primary and secondary bypass doors to open and ingest the normal shock just downstream of the intake throat.
- 3) When the moving normal shock crosses the start/unstart detector, the control system automatically switches to the started mode control logic.
- 4) Using the cross-coupling function, the intake geometry moves to the high-stability condition of the started mode.

Activation of the sympathetic unstart sequence immediately commands the centerbody and throat doors to their buzz suppression positions and causes the primary and secondary bypass doors to close and unstart the intake.

#### STEADY-STATE CONTROL SIGNALS

The intake control system design uses a system of pneumatic pressure taps and probes located within the intake. Signals from these sources are used as the feedback parameters for control loop operation. To obtain the control signal characteristics, steady-state wind tunnel measurements were made with intake models operating over a wide range of conditions. The results of these tests were

used to select the control signal tap configurations and locations, to determine the control signal references, and to define the control signal gain variation for closed-loop stability analyses. Control signals were sought which could utilize constant reference values, or references which could be scheduled as functions of parameters available within an intake control system. This was desired in order to keep all four intakes from being dependent upon an airplane-generated signal. Reference schedules use piecewise linear functions to reduce system complexity and increase system reliability. In addition, it was desired to have the signal slope be uniform over a wide range of operating conditions in order to maintain the desired closed-loop response and to minimize problems of closed-loop stability. Figure 1 shows the final tap configurations and locations selected for closed-loop testing.

The intake throat Mach number control signal pressure source,  $P_{CB}$ , is obtained from a manifold of several static pressures just upstream of the intake throat. Manifolding in this manner minimizes the adverse effects on the  $P_{CB}$  signal from intake oblique shocks which cross the pressure taps as the centerbody translates. The location upstream of the throat helps to reduce the effects of the normal shock boundary layer on the  $P_{CB}$  signal. The total pressure source,  $P_{TNS}$ , is derived from a conventional total pressure probe located at the throat. The variation of the intake throat Mach control signal,  $P_{CB}/P_{TNS}$ , with centerbody position is shown in Figure 2 for several intake Mach numbers. The signals in the mid Mach number range are relatively uniform in level and slope, whereas variations are evident at the higher and lower Mach numbers. The decreased signal level at the higher Mach numbers is associated with a compression wave crossing the  $P_{TNS}$  probe, and the increased level at the lower Mach numbers is caused by the movement of the cowl throat doors. A three-segment reference schedule, as a function of centerbody position, is readily adapted to these characteristics to obtain a constant throat Mach number for the entire operating Mach range. Shown in the plot are two such schedules, one for high performance and one for high stability. Tests show that these schedules correspond to throat Mach numbers of approximately 1.25 and 1.30, respectively. The signal gain variation across the Mach range is ten to one.

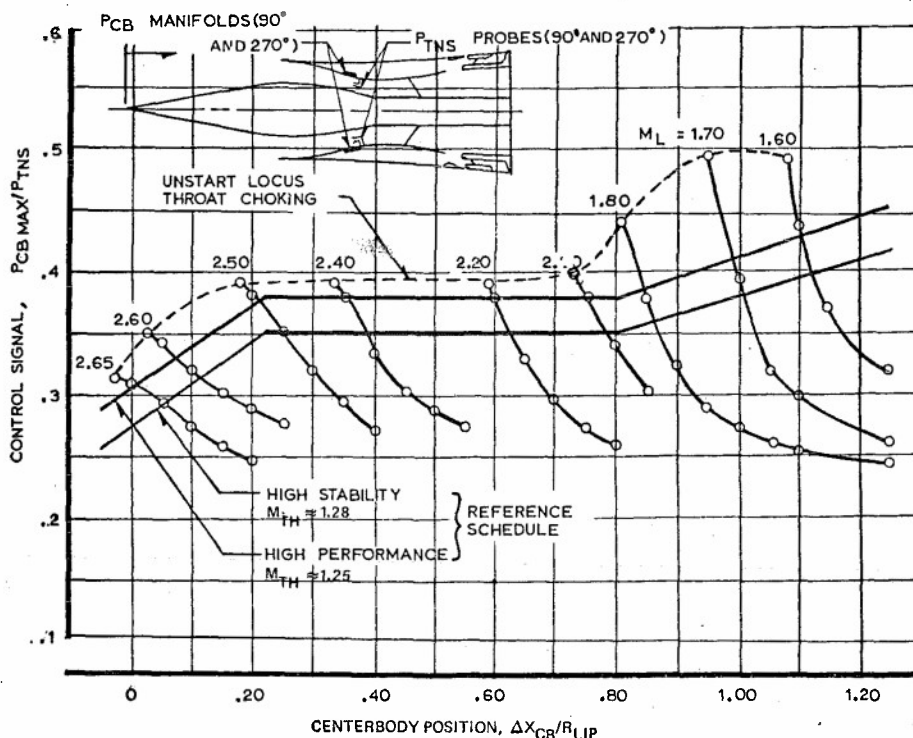


Figure 2. Started Mode—Intake Throat Mach Control Signals and Reference Schedules

Intake angle-of-sideslip operation results in a nonuniform throat Mach number distribution, and for sufficiently high angles of sideslip, one segment of the annular throat would eventually choke and unstart the intake if the centerbody position is not changed. To induce compensating centerbody movement, the control system selects the maximum reading from either of two  $P_{CB}$  manifolds as the control signal. Because the airplane wing shields the intake from flow angles normal to the wing surface, the manifolds are located in the intake sideslip plane at  $90^\circ$  and  $270^\circ$ . Thus, the minimum throat Mach number during intake angle of sideslip is held approximately constant.

A manifolded series of static pressure taps located downstream of the intake throat is used for normal shock control. The average signal from two manifolds at circumferential positions of  $0^\circ$  and  $180^\circ$  is ratioed to the throat total pressure to provide a  $P_{NS}/P_{TNS}$  signal which is relatively uniform in magnitude and slope for the started mode Mach number range. The resulting signals, which are used to modulate the primary and secondary bypass doors, are shown as a function of full-scale intake corrected airflow for several Mach numbers in Figure 3. These control signals were obtained with the centerbody at the on-design high-performance operating position as given by Figure 2. A  $P_{NS}/P_{TNS}$  reference schedule was sought which would control the normal shock just on the verge of vortex valve bleed activation during high-performance started mode operation. Such a schedule would maintain near-peak pres-

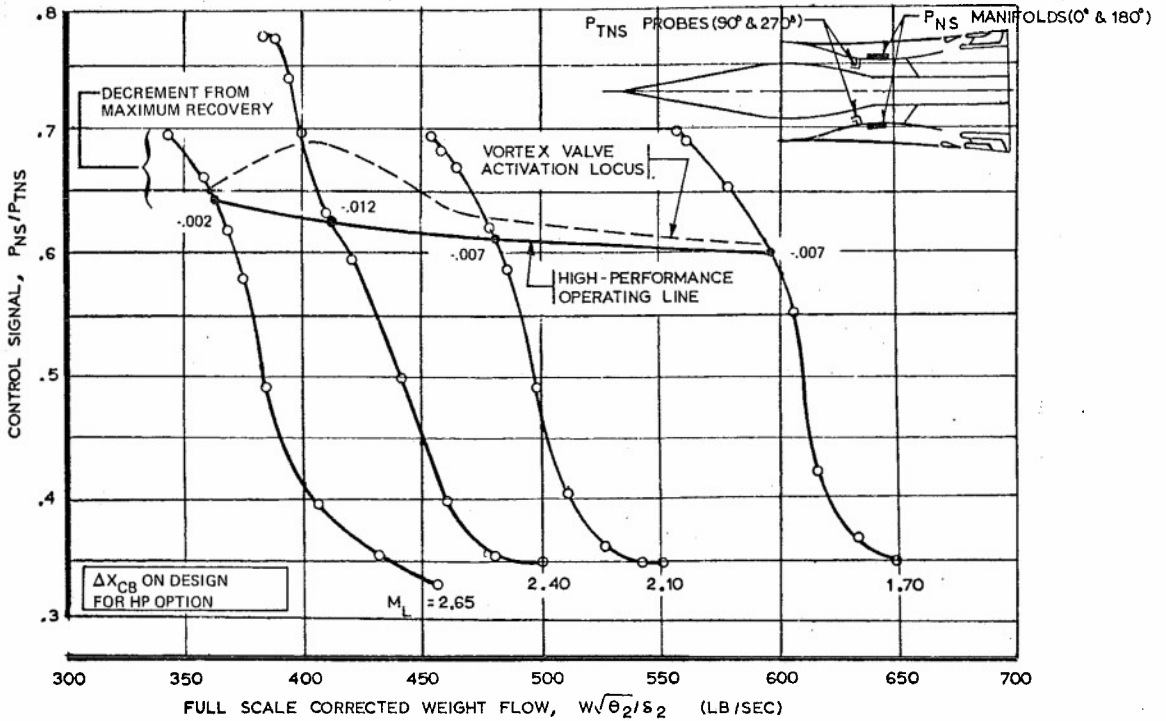


Figure 3. Started Mode-Normal Shock Control Signals and Reference Schedule for H.P. Option

sure recovery and approximately 5% unstart stability margin due to the potential vortex valve bleed. The high-performance  $P_{NS}/P_{TNS}$  operating line and the associated intake recovery along this operating line are also shown in Figure 3. The operating line is determined by scheduling the  $P_{NS}/P_{TNS}$  reference with centerbody position as shown in Figure 4.

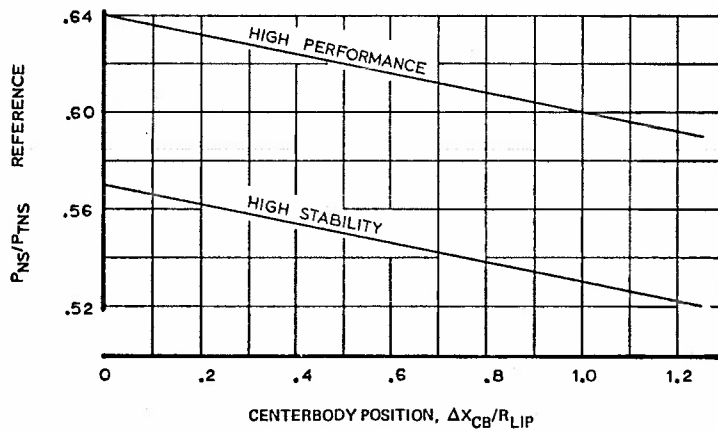


Figure 4. Started Mode-Normal Shock Reference Schedules

Off-design centerbody and cowl throat door positions, which occur transiently during restart and upstream disturbances, cause the throat Mach number to change from its design condition. The sensitivity of the normal shock control signal to off-design throat Mach number operation is shown in Figure 5 for two intake local Mach numbers. During high throat Mach number operation, the value of the  $P_{NS}/P_{TNS}$  signal at intake unstart is below the reference level established by centerbody position (Figure 4). To avoid intake upstart the centerbody control loop error signal which exists during this condition is utilized in a cross-coupling function to bias the normal shock reference schedule down to a level which would maintain a started intake with acceptable performance. Figure 6 shows this function as it was implemented for closed-loop testing.

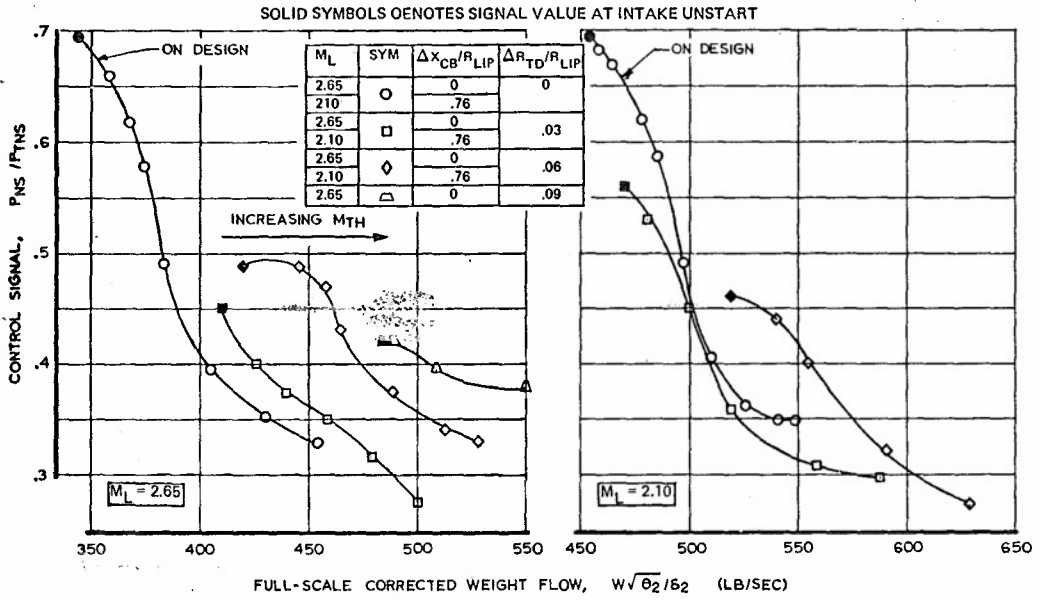


Figure 5. Effect of "Off-Design" Throat Mach Number on Normal Shock Control Signals

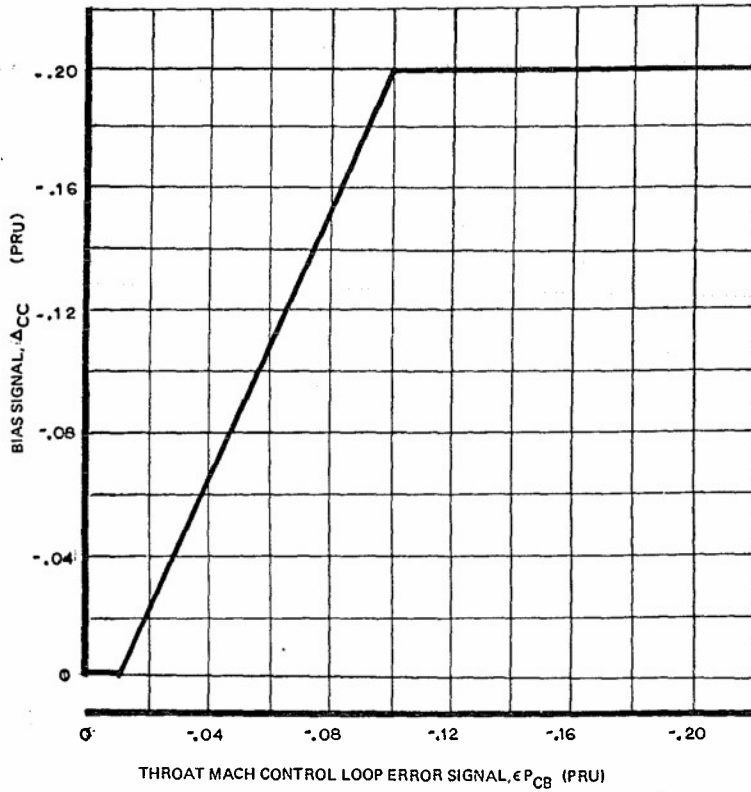


Figure 6. Normal Shock Reference Schedule Bias

The control signals of Figure 7 indicate the need for an additional bias when the intake is operating at angle of sideslip. Again, the control signal level at unstart is below the scheduled reference, and this would cause the overboard and secondary doors to induce an unstart. The angle-of-sideslip signal required as an input to this bias is provided by the difference of the two intake throat Mach control signals,  $P_{CB}/P_{TNS}$ . Figure 8 shows the sensitivity of this parameter to angle of sideslip. Using this input parameter, the function of Figure 9 provides the necessary bias. The observed data spread of Figure 8 requires a compromise selection for the function. This schedule will maintain a started intake up to 5° intake angle of sideslip. Intake sideslip is expected to remain within 2° during 90% of all flight above Mach 1.6.

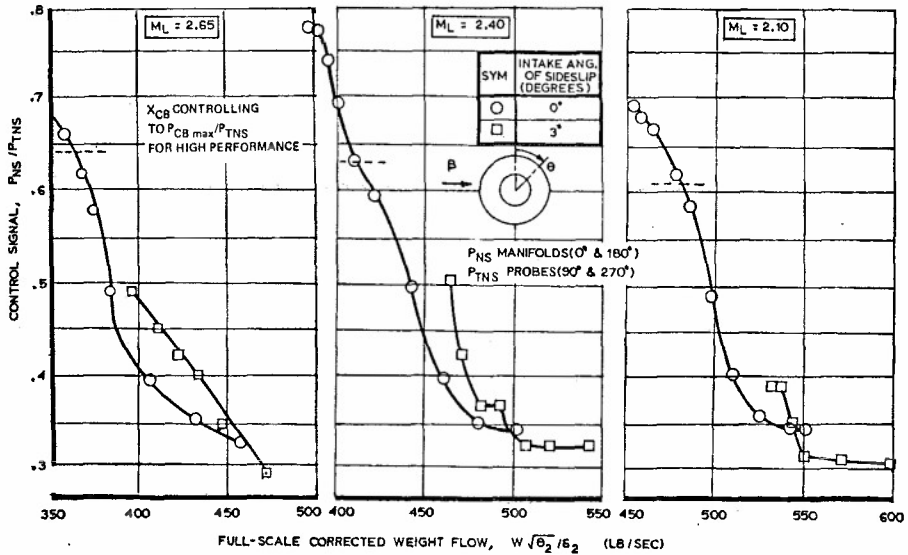


Figure 7. Effect of Intake Angle of Sideslip on Normal Shock Control Signals

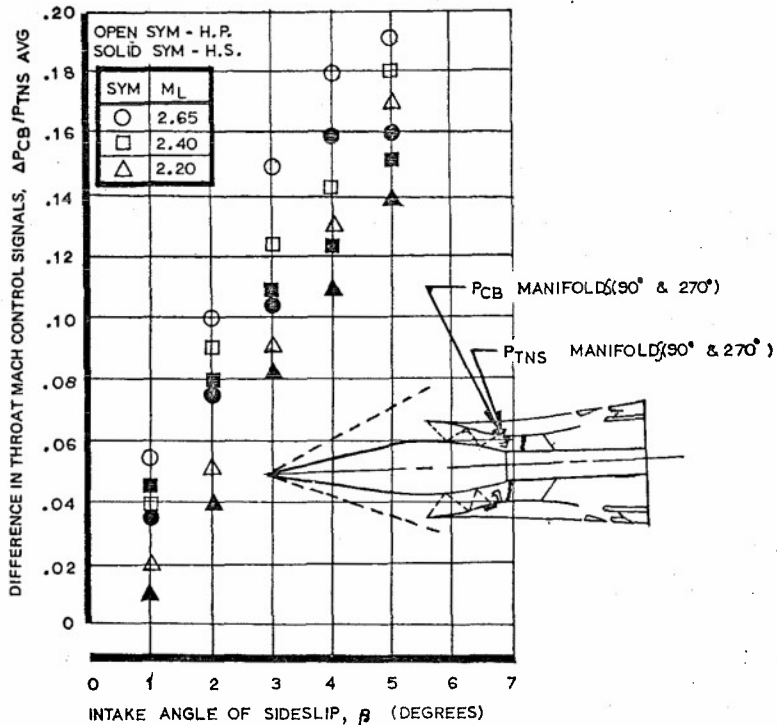


Figure 8. Intake Angle of Sideslip Indicator

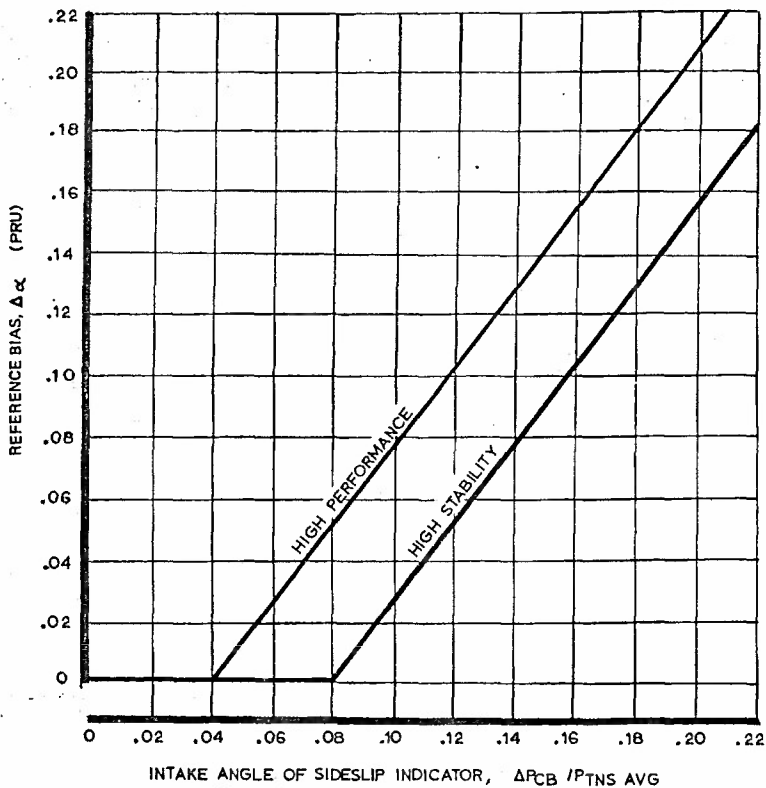


Figure 9. Normal Shock Reference Bias  $\Delta \alpha$ , for Intake Angle of Sideslip Operation

The start/unstart signal is the ratio of a static pressure,  $P_C$ , located between the throat and the cowl lip and the throat total pressure,  $P_{TNS}$ . The static pressure used is the maximum of two static taps located at circumferential positions of  $90^\circ$  and  $270^\circ$  (Figure 2). The value of this pressure ratio is shown for many started and unstarted intake operating conditions in Figure 10. Also shown in Figure 10 are the start/unstart reference schedules. If the intake controller is in the started mode and an unstart signal is received, the buzz suppression mode is activated and the start/unstart reference schedule is decreased to a very low value (see the dashed line in Figure 10). This is done by the system logic to "lock in" the buzz suppression mode. Thus, intake buzz or rapid engine airflow fluctuations which yield lower  $P_C \text{ max} / P_{TNS}$  signals than the solid line reference shown in Figure 10 cannot cause the intake controller to switch to the started mode. The start/unstart reference schedule is reset to the solid line shown in Figure 10 upon activation of the restart sequence.

Stable unstarted intake operation and low compressor face distortion are provided with the buzz suppression mode. Using the existing  $P_{NS}$  and  $P_{TNS}$  tap locations, the  $P_{NS} / P_{TNS}$  buzz suppression control signals for Mach 2.65 and 2.10 are shown in Figure 11. These data indicate that intake airflow may be stabilized at several centerbody and throat door positions. The centerbody and throat door positions of the buzz suppression mode (see Table 1) were chosen because of the low compressor face distortion associated with unstarted, unchoked throat intake operation. For the fixed centerbody and throat door positions of the buzz suppression mode, the compressor face distortion and corrected airflow supply of the intake are shown for several values of the  $P_{NS} / P_{TNS}$  control signal in Figure 12. The chosen reference value of 0.75 provides low distortion with airflow sufficient to meet engine demands. The  $P_{NS} / P_{TNS}$  reference for the buzz suppression mode is shown as a function of centerbody position in Figure 13. A constant reference value may be used, but a sloped reference will help suppress buzz following an intake unstart. Also shown in Figure 13 is the  $P_{NS} / P_{TNS}$  reference used during the restart sequence. The level of this reference should be low enough to start the intake before the centerbody retracts beyond the starting area ratio of the intake. The centerbody is retracted during the restart sequence to obtain a lower throat Mach number immediately following an intake start. This decreases the normal shock Mach number and the associated compressor face distortion.

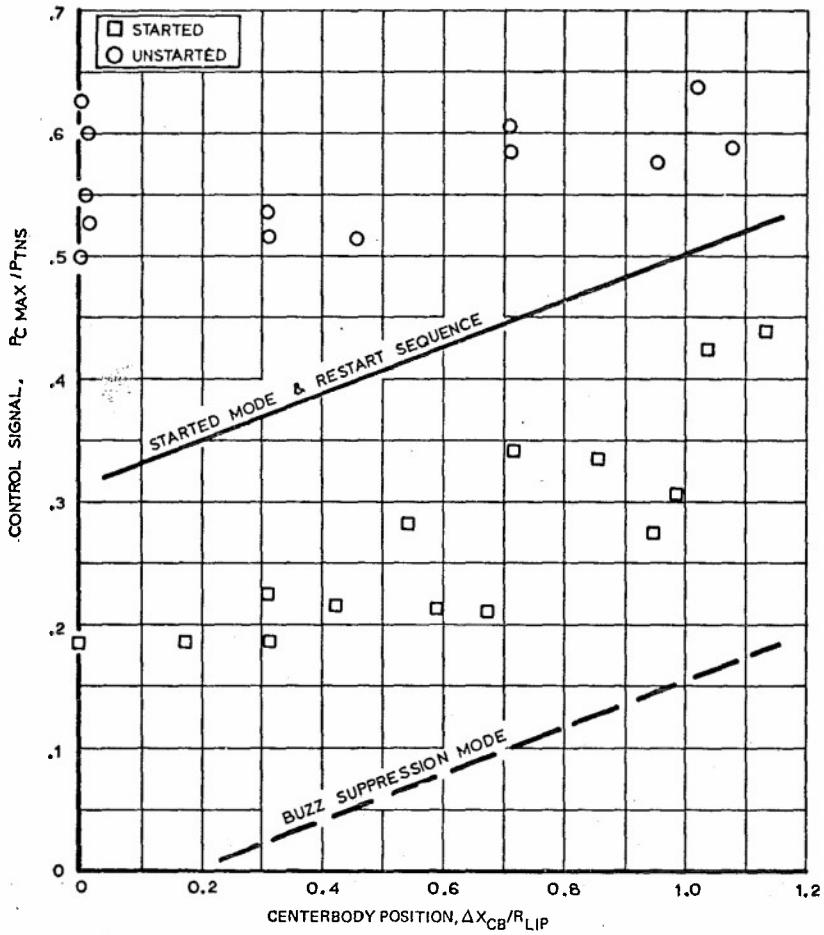


Figure 10. Start/Unstart Control Signal and Reference Schedules

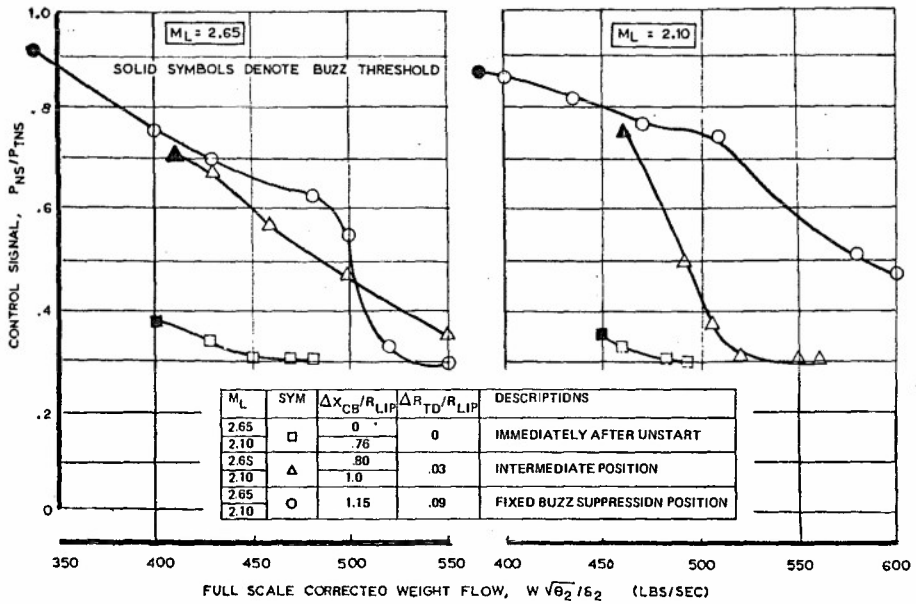


Figure 11. Buzz Suppression Mode Control Signals

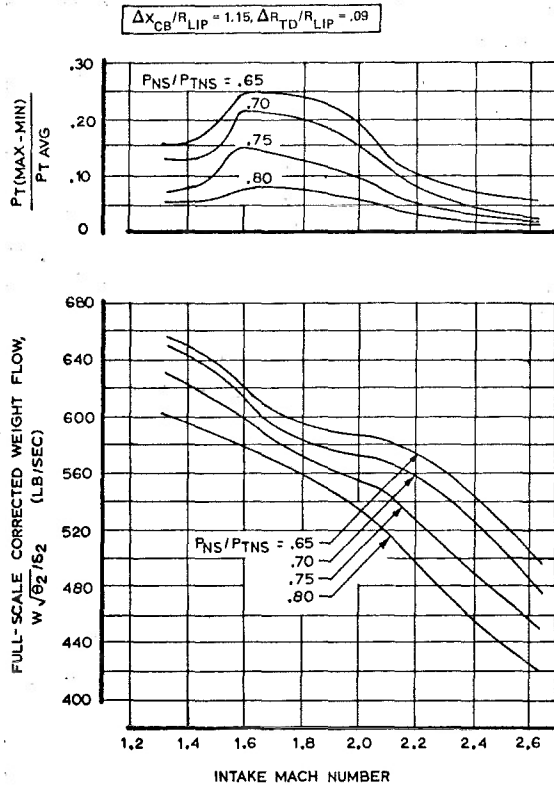


Figure 12. Intake Operation—Buzz Suppression Mode

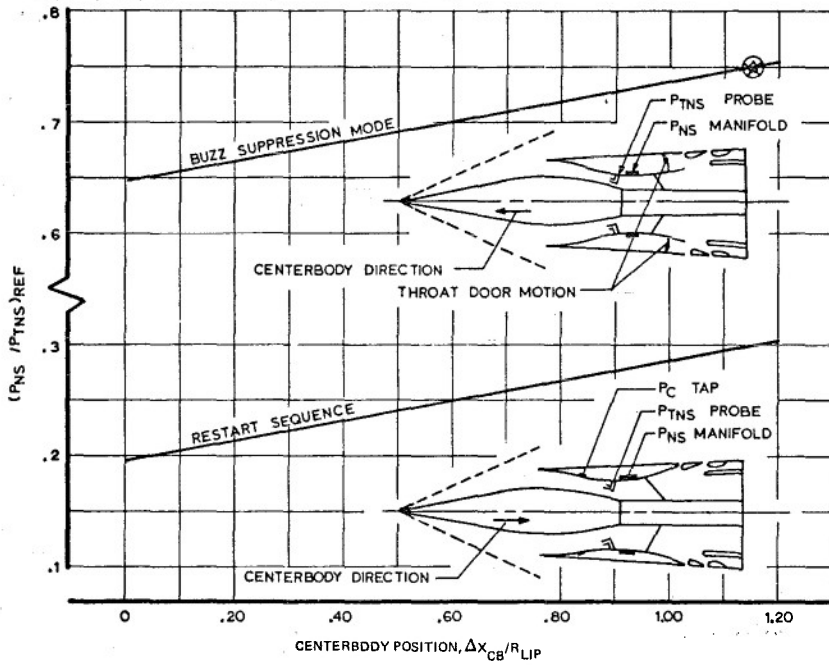


Figure 13. Unstarted Intake Reference Schedules

CONTROL SYSTEM DESCRIPTION

The function block diagram of the control system used during intake operation at Mach numbers greater than 1.2 is shown in Figure 14. This consists of the started and buzz suppression modes and the restart and sympathetic unstart sequences. Started mode operation, the normal control mode above Mach 1.6, modulates the centerbody to control the throat Mach number as measured by  $P_{CB\ max}/P_{TNS}$ . The difference between the control signal and the reference schedule is amplified by a nonlinear gain,  $K_{CB}$  and a proportional plus integral operator is used to obtain an actuator position command,  $(X_{CB})_C$ . A hydraulic servocontrol loop is used to position the centerbody. The gains and time constants used in the centerbody controller are shown in Table 2. The variable position cowl throat doors are scheduled with centerbody position as shown in Figure 15a. The nonlinear gain,  $K_{CB}$ , shown

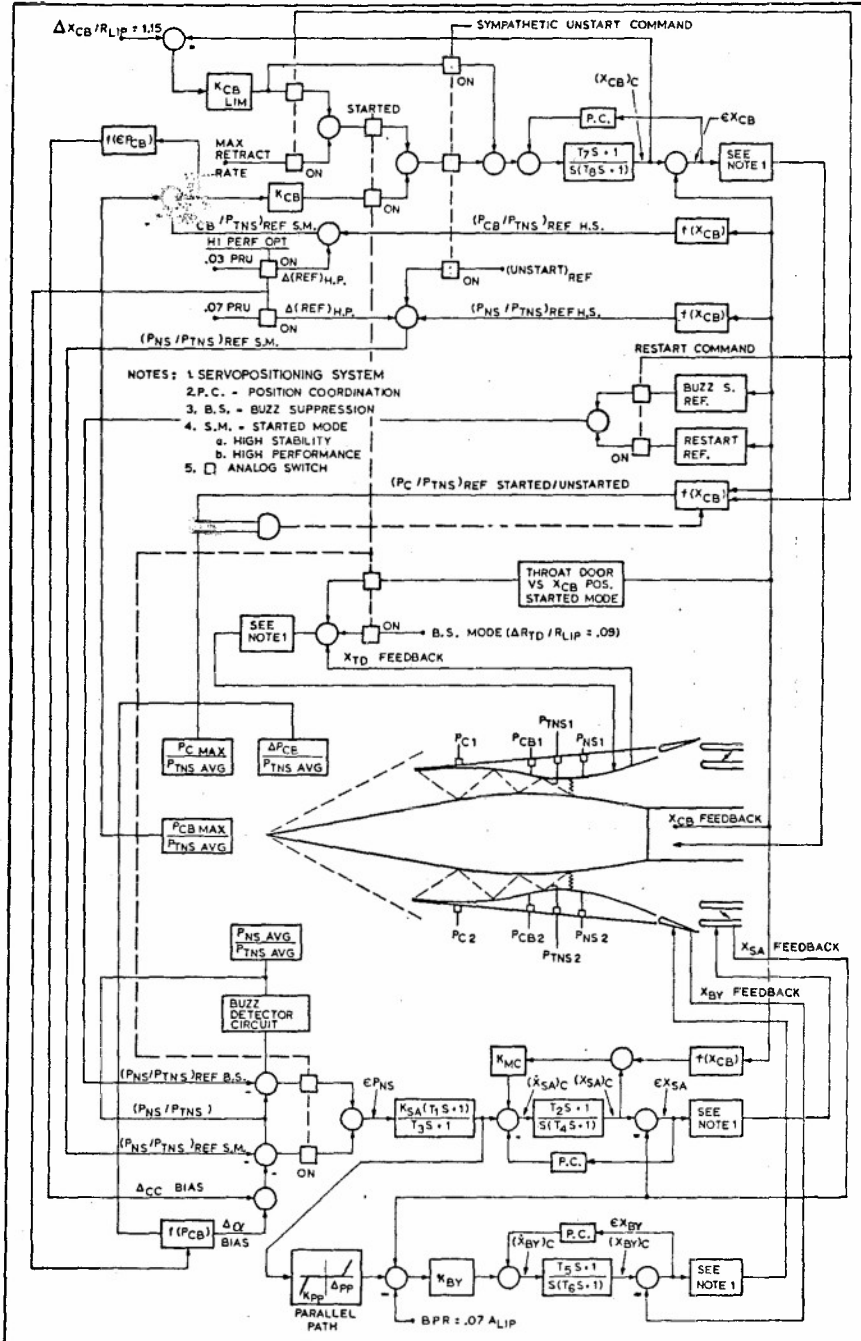


Figure 14. Intake Control System

in Figure 15b, was developed by analysis using the results of an analog simulation of the throat Mach control loop to random gust inputs. For error signals,  $\epsilon P_{CB}$ , greater than  $\Delta_{CB}$  pressure ratio units (PRU), the overall centerbody loop gain is very high, and a linear analysis would show the loop to be unstable at this gain. However, using the describing function for the gain,  $K_{CB}$ , a non-linear analysis of the throat Mach control loop indicates no instabilities, and for the expected random gust input disturbance, simulated control loop time histories show the loop to have high performance and good stability. Fast Mach ramp wind tunnel time histories have verified these nonlinear analyses.

Table 2. Centerbody Controller

Parameter	Symbol	Engineering Units
Overall loop gain	$K_V$	$\text{sec}^{-1}$
Started mode controller gain	$K_{CB}$	$(X_{CB}/R_{LIP})/\text{sec}/\text{PRU}$
Controller compensation time constants	$T_7$	sec
	$T_8$	sec
Buzz suppression controller gain	$K_{CB LIM}$	$\text{sec}^{-1}$

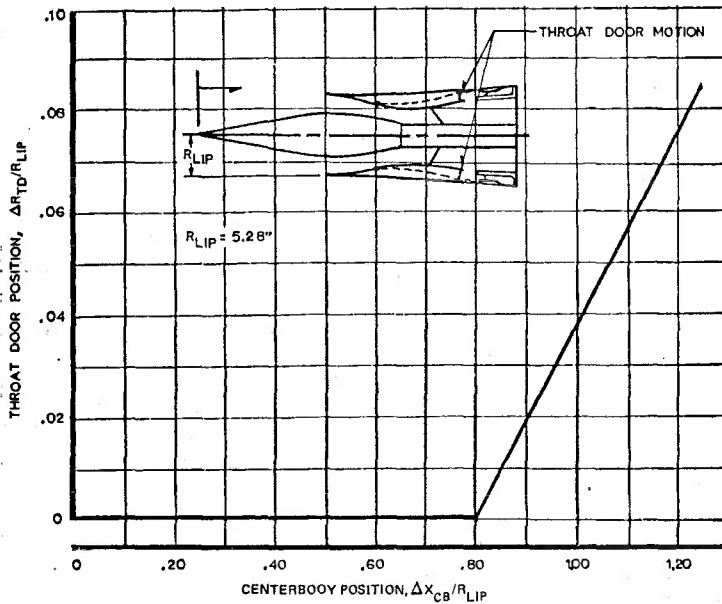


Figure 15a. Started Mode-Throat Door Schedule

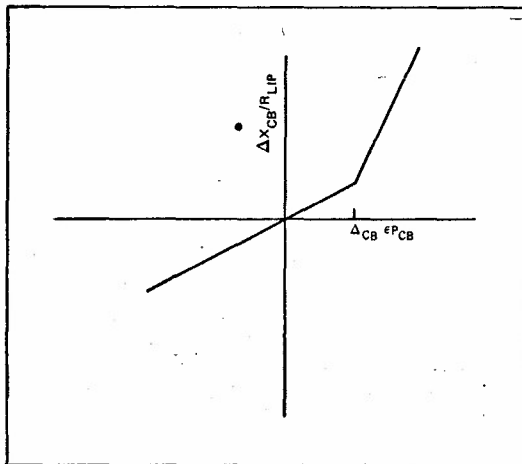


Figure 15b. Centerbody Controller Gain,  $K_{CB}$

The feedback gain during centerbody controller operation is the composite of the aerodynamic signal gain minus the reference schedule gain. The nonzero slopes of the  $P_{CB}/P_{TNS}$  reference schedule as a function of centerbody position provide additional negative feedback for the control loop. The variation of the composite feedback gain is expected to be approximately 5:1. A position loop for centerbody actuation is used primarily to obtain overall control-loop accuracy (i.e., the servovalve null shift is eliminated in the error analysis). A theoretical autonomous limit cycle analysis of this control loop yielded negligible throat Mach number variations.

The secondary air valves and overboard bypass doors control the normal shock position as measured by the  $P_{NS}/P_{TNS}$  control signal in the started mode. The forward loop gain,  $K_{SA}$ , is linear, and a lead-lag compensation filter in addition to a proportional plus integral operator is used to obtain the secondary air valve actuator position command,  $(X_{SA})_C$ . The overboard bypass door actuator position command  $(X_{BY})_C$  also uses a proportional plus integral operator, with the input signal being  $X_{SA}$  minus a constant (BPR) plus the parallel path output,  $f(K_{PP})$ . For small error signals,  $\epsilon P_{NS}$ , the normal shock control is of the follow-up type.

That is, overboard bypass door rate is dependent on secondary air valve position. For large error signals, the control used is of the follow-up plus parallel type where both surfaces respond directly to the error signal. The gains and time constants used in this loop are given in Table 3. The normal shock control loop was designed from a theoretical performance and stability analysis which included several items: (1) an autonomous limit cycle analysis yielded results indicating the need for a trimmer door (secondary air valve) to reduce normal shock and pressure recovery oscillations, (2) stability analyses indicated the need to keep the overboard bypass door gain  $K_{BY}$  low, (3) performance studies showed the need for an overboard bypass door kicker (or parallel path) circuit to maintain a started intake during normal engine decelerations, (4) control signal data for normal operation, angle of attack, and restart indicated the loop would have to be stable for control signal gain variations of approximately 10:1, and (5) aerodynamic nacelle drag studies showed the obvious need to keep the overboard bypass doors closed during normal and hot-day cruise.

The values for the parallel path circuit deadzone,  $\Delta_{PP}$ , and gain,  $K_{PP}$ , were chosen to maintain a started intake when the disturbance is an engine airflow deceleration from maximum augmented operation to idle. The control concept for the parallel path circuit was determined using a discrete disturbance (i.e., an engine deceleration) which can be approximated by a ramp function. If  $K_{PP}$  is too large, the bypass doors will oscillate during this transient and the intake can unstart.

Table 3. Bypass System Control-Loop Design

Parameter	Symbol	Engineering Units
Overall loop gain for $A_{SA}$	$K_V$	$\text{sec}^{-1}$
Secondary valve gain	$K_{SA}$	$[(A_{SA}/A_{LIP})/\text{sec}]/\text{PRU}$
Compensation time constants	$T_1$	sec
	$T_3$	sec
Secondary valve controller time constants	$T_2$	sec
	$T_4$	sec
Break point reference	BPR	$0.070 A_{SA}/A_{LIP}$
Overall loop gain for $A_{BY}$	$K_A$	$\text{sec}^{-2}$
Overboard bypass door controller gain	$K_{BY}$	$[A_{BY}/A_{LIP})/\text{sec}]/(A_{SA}/A_{LIP})$
Overboard bypass door controller time constants	$T_5$	sec
	$T_6$	sec
Parallel path gain	$K_{PP}$	sec
Parallel path deadzone	$\Delta_{PP}$	$(A_{SA}/A_{LIP})/\text{sec}$

The variable-geometry components of the intake are positioned with hydraulic actuators controlled with closed-loop servo systems. The position coordination (PC) circuits (Figure 14) used as feedback on the centerbody, secondary air valve, and bypass door position command integrators prevent the integrators from demanding rates in excess of actuator capability. A general PC circuit is shown in Figure 16, where  $\Delta_{PC}$  is set to a voltage 20% greater than the error voltage associated with maximum actuator rate. The gain,  $K_{PC}$ , is high. Thus, if the actuator is traveling at maximum rate, the electronic integrator is prevented from "over-integrating" the command position.

The engine RPM trim loop, shown in Figure 17, is used for cold-day engine/intake airflow matching; this loop was not simulated for the 1/6-scale test. During cold-day operation, when engine weight flow increases, the overboard bypass doors will be fully closed and the secondary air valves will close to the minimum cooling schedule (see Figure 18). If the day is sufficiently cold, the engine will pull the normal shock downstream, lowering the intake recovery to achieve a corrected airflow match. When the resulting normal shock error signal,  $\epsilon P_{NS}$ , becomes greater than  $-0.04$  PRU, the RPM trim motor will integrate down to lower the engine airflow demand and decrease the magnitude of the error signal. The  $-0.04$  level of error signal was chosen to keep the normal shock from moving far downstream and causing high distortion. The minimum cooling schedule provides the minimum airflow level needed to cool the secondary nozzle. The secondary air valves are prevented from closing below this schedule by using a high-gain feedback,  $K_{MC}$ , around the secondary air valve position command integrator (Figure 14).

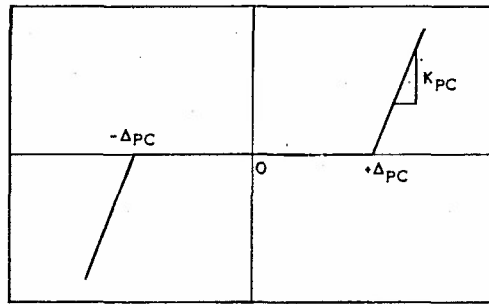


Figure 16. Generalized PC Circuit

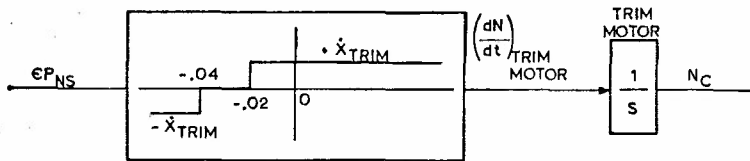


Figure 17. Engine Trim Control

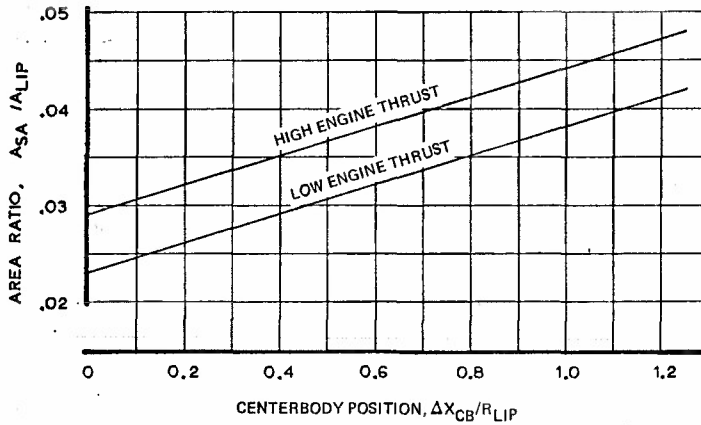


Figure 18. Secondary Air Valve Minimum Cooling Schedule

The secondary air valves and overboard bypass doors are controlled during the buzz suppression mode with the same loop as the started mode. A control loop gain change was not necessary because the buzz suppression control signal gains were compatible with the started mode gains. The buzz suppression control signal gains were relatively invariant with intake freestream conditions.

**Time Scaling the Test Controller**

A comparison of the relative sizes of the full-scale intake and the 1/6-scale intake model and flow sting is shown in Figure 19. The long flow sting used to obtain an accurate calibration of airflow on the 1/6-scale intake significantly affects the duct dynamics (i.e., transfer function) between the secondary air valves (and bypass doors) and the normal shock position. Using a small-perturbation mathematical model,<sup>(2)</sup> a comparison of the theoretical duct dynamics during started intake operation is given in Figure 20. These characteristics are similar for unstarted intake operation. The comparison shows that for frequencies less than 40 rad/sec the 1/6-scale intake as installed is slower than the full-scale intake. The pneumatic lines and sensors used on the 1/6-scale model were faster than those expected to be used with the full-scale model; therefore, the combined theoretical frequency response of duct, line, and sensor was found to be approximately the same for both models in this frequency range. Since the full-scale bypass door (normal shock) control loop was designed to have a maximum closed-loop frequency response of approximately 30 rad/sec for the highest expected control signal gain, the 1/6-scale bypass door controller was tested in real time relative to the full-scale bypass door controller. The aerodynamic response of throat Mach number to centerbody movement during started intake operation is essentially negligible for both models. Thus, the centerbody control loop was also tested in real time.

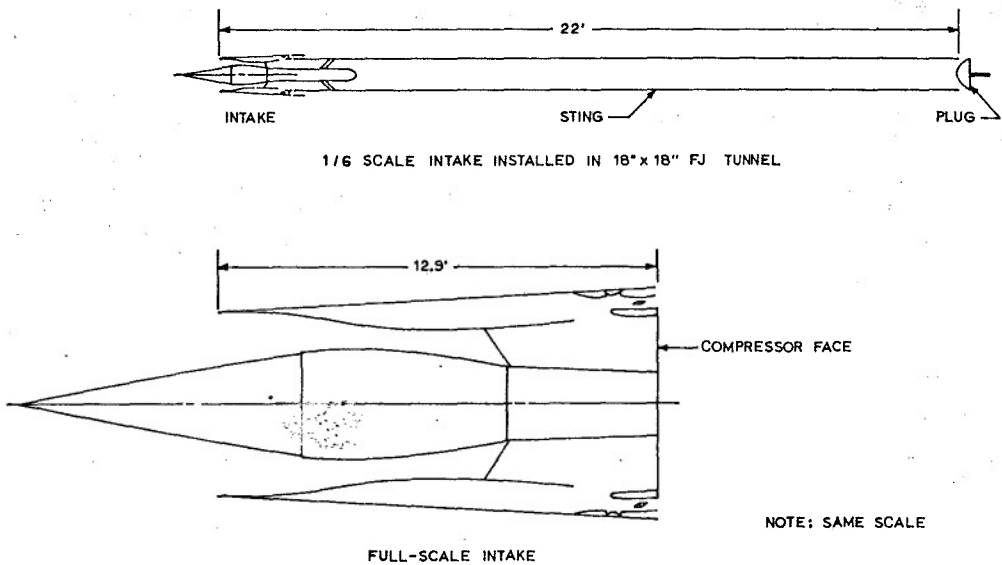


Figure 19. Comparison of 1/6 and Full Scale Intakes

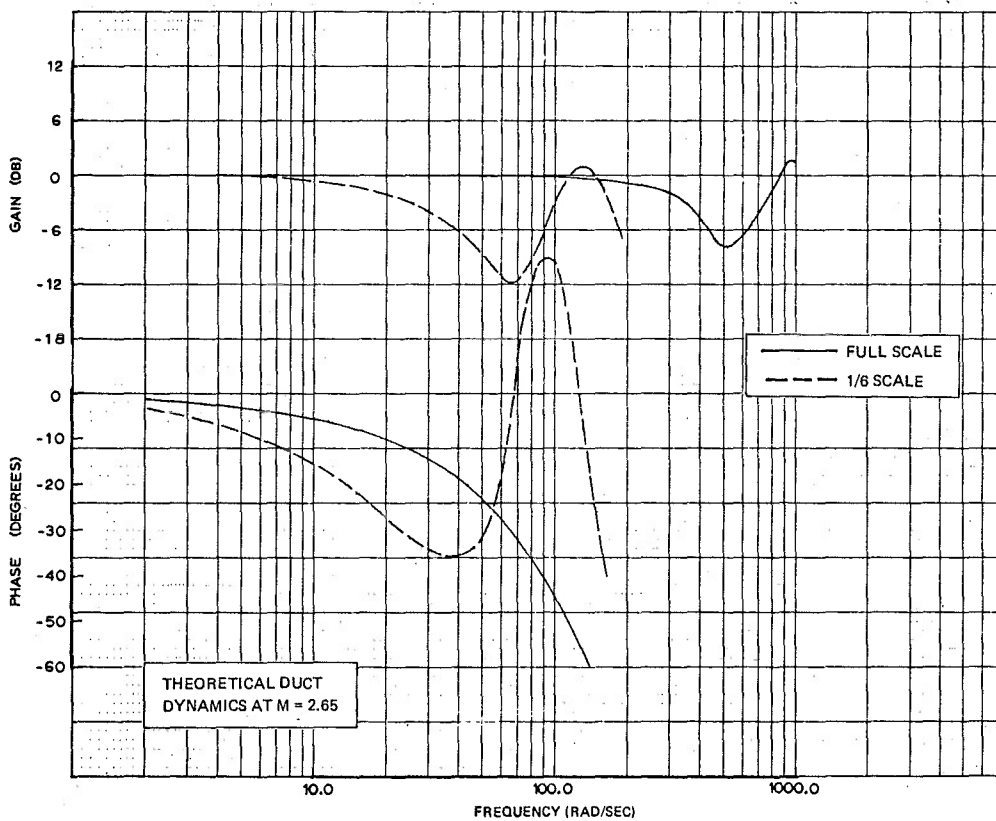


Figure 20. Comparison of Theoretical Duct Responses

## Test Model Geometry

Simulating the dynamics of the full-scale intake and controller with the test model is accomplished using the full-scale normalized gains and maximum rates. This is easily done for centerbody control since both full- and 1/6-scale intakes have centerbody translations that are integral with actuator strokes. The maximum centerbody extension is  $1.25 R_{LIP}$  in. Similarly, the openings versus actuator strokes of the throat doors and secondary air valves of the 1/6-scale model closely approximate those of the full-scale intake. The throat door opening versus actuator stroke of the model is essentially linear with actuator stroke and has a maximum displacement,  $(\Delta R/R_{LIP})_{max}$ , of 0.09 units as measured at an axial location of  $1.83 R_{LIP}$  in. (i.e., the throat station) aft of the intake cowl lip. The normalized displacement of the secondary air valves for the model is shown in Figure 21. Also shown in Figure 20 is the normalized bypass door opening with actuator stroke for the model. Since the full-scale design incorporates a non-linear bypass door opening with actuator stroke that can be closely approximated with a logarithmic function, the bypass door controller gain,  $K_{BY}$ , for the 1/6-scale model is scheduled with actuator position as shown in Figure 22. Thus, this function is used on the 1/6-scale controller to simulate full-scale bypass door dynamics.

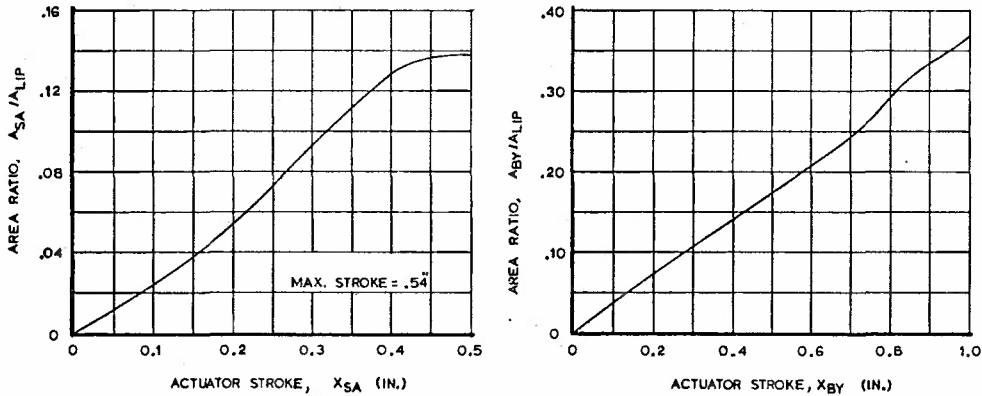


Figure 21. 1/6-Scale Bypass System

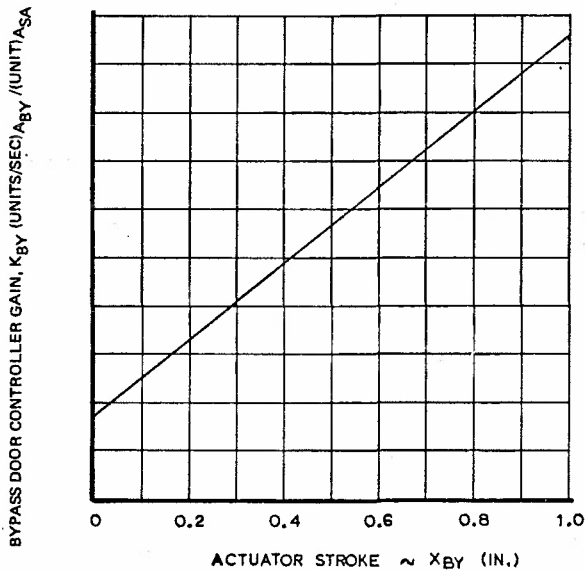


Figure 22. 1/6-Scale Bypass Door Controller Gain

## CONTROLLED INTAKE TIME HISTORIES

The 1/6-scale intake including controller was wind tunnel tested between Mach 1.6 and 2.9. Analog computers simulated the controller. The responses of the controlled intake were measured during simulated airplane, engine, and environmental transient disturbances.

### Plug Transients (Engine Airflow Disturbances)

The intake throat Mach number is not affected by engine airflow disturbances in the started mode; hence, plug transients provide a means of assessing secondary air valve/bypass door control loop stability and performance. Maintaining a started intake during a 2-sec engine throttle chop from maximum augmentation to idle is the minimum performance requirement of this loop. The engine corrected airflow deceleration rate and magnitude of change at Mach 2.65 for this disturbance are  $70 \text{ lb}_m/\text{sec}^2$  for a change of  $20 \text{ lb}_m/\text{sec}$ . At Mach 2.1 these values are  $105 \text{ lb}_m/\text{sec}^2$  for a change of  $50 \text{ lb}_m/\text{sec}$ .

Time histories in Figure 23a at Mach 2.65 in the high-performance option of the started mode show ramp plug transients with a fixed magnitude of change of  $37 \text{ lb}_m/\text{sec}$  and increasing deceleration rates. The intake remained started for a deceleration rate of  $60 \text{ lb}_m/\text{sec}^2$  but unstarted for a deceleration rate of  $80 \text{ lb}_m/\text{sec}^2$ . The controller gains for this run were the design values listed in Table 3. Since this run was approximately 38% more severe in magnitude of change than the requirement, the control loop should meet the above performance requirements at Mach 2.65 without difficulty. Ramp plug transients with a magnitude of change of  $55 \text{ lb}_m/\text{sec}$  and increasing deceleration rates were input at Mach 2.1. With the design control loop gains in effect, the intake remained started for deceleration rates up to  $210 \text{ lb}_m/\text{sec}^2$ . The improved performance at this lower Mach number is due to higher control signal gain,  $\partial(P_{NS}/P_{TNS})/\partial(A/A_{LIP})$ . The time history for this run is shown in Figure 23b. The above plug transients that did not unstart the intake were generally accompanied by negligible changes in engine face distortion and pressure recovery.

### Mach Transients

Two types of Mach transients were simulated to determine the feasibility of using the centerbody position to schedule control signal reference values and to evaluate the response of the centerbody to upstream disturbances during the started mode. A relatively slow Mach number variation from 2.65 to 1.9 with the plug concurrently opened to simulate increasing engine airflow was used to demonstrate the validity of scheduling the reference values with centerbody position. The centerbody extended with decreasing Mach number in response to varying  $P_{CB}/P_{TNS}$  signal and reference schedule changes. The scheduled references,  $P_{CB}/P_{TNS}$  and  $P_{NS}/P_{TNS}$ , maintained the pressure recovery greater than 90% during the entire transient.

Mach ramps with faster rates but small magnitudes of change were used to evaluate dynamic centerbody response and stability characteristics. A series of such ramps with changes between Mach 2.60 and 2.50 and rates up to 0.8 Mach/sec are shown in Figure 24. The control system kept the intake started for transients up to 0.8 Mach/sec; design requirements specify 0.6 Mach/sec for a Mach change of 0.1. The nonlinear gain,  $K_{CB}$ , utilized in the loop gave quite rapid centerbody response in the extend direction as compared to the retract direction, but the overshoot is small. The test thus confirmed the dynamic advantages of the nonlinear gain, as well as the stability of the centerbody control loop. During these transients the secondary air valves and bypass doors responded to the  $P_{NS}/P_{TNS}$  signal and reference changes, and these responses also indicate excellent stability.

It should be noted that when the Mach number increases, the secondary air valves and overboard bypass doors start in what appears to be the wrong direction by opening, and then as the centerbody retracts, they close. There are two reasons for this initial response: (1) the ramp local Mach number increase causes the intake throat Mach number to increase transiently, and this activates the cross-coupling,  $\Delta_{CC}$ , circuit to drive the bypass system open, and (2) the transient increase in throat Mach results in an increased shock Mach with an associated lower recovery, which drives the normal shock into the vortex valves, and the vortex valve bleed increases the  $P_{NS}/P_{TNS}$  control signal, which also helps drive the bypass system open. The combination of these two events prevents an intake unstart. Vortex valve bleed is also used during decreasing Mach ramps. When local Mach is decreased the intake throat Mach number is decreased but the corrected airflow supply of the intake is increased. Since the engine corrected airflow demand is constant (i.e., plug position is fixed), the normal shock moves forward into the vortex valve to establish an intake diffuser airflow balance. The vortex valve bleed again causes the bypass system to open and the normal shock just aft of the valve is quickly stabilized.

### Angle-of-Sideslip Transients

The intake was subjected to both slow and fast angle-of-sideslip changes while operating in the high-performance option of the started mode. Figure 25 shows the intake operation at Mach 2.6 as the intake angle of sideslip was varied slowly from  $+5^\circ$  to  $-5^\circ$ . The centerbody extended as a result of controlling the  $P_{CB \text{ max}}/P_{TNS}$  signal, and the intake remained started over the test range; however, at a  $5^\circ$  angle of sideslip the pressure recovery dropped to 57% and the distortion level was 23%. Since probability estimates indicate that the intake is not expected to see local angles of incidence greater than  $2^\circ$  at high Mach numbers, the performance during the brief stop at  $-3^\circ$  is more significant. Here the recovery was 75% and the distortion only 10%.

The intake was subjected to fast  $3^\circ$  angle-of-sideslip ramps at increasing rates to demonstrate dynamic angle-of-sideslip capability. The time histories of Figure 26 show no unstarts at the maximum rate of 3 deg/sec. The recovery varied between 69% and 87% and the distortion between 6% and 12%. Notice that as the angle of sideslip is approaching zero from either minus or plus  $3^\circ$ , the cross-coupling function,  $\Delta_{CC}$ , provides a bias to lower the  $P_{NS}/P_{TNS}$  reference as the magnitude of the  $\Delta_{\infty}$  bias is decreasing to zero. This is because the slower retract capability of the centerbody allows the throat Mach number to become greater than 1.25 and the cross-coupling bias is activated. This bias is necessary to prevent the secondary air valves and bypass doors from closing and unstarting the intake.

### Restart, System Unstart, and Buzz Suppression

The time histories of a restart sequence followed by the activation of the high-stability started mode, and a sympathetic unstart sequence followed by activation of the buzz suppression mode at Mach 2.65 are shown in Figure 27. The  $(P_{NS}/P_{TNS})_{REF}$  strip chart recording shown in this figure indicates the mode of controller operation. The time history begins with the control system in the buzz suppression mode. Initiation of the restart sequence causes the centerbody to retract and the bypass system to open. When the  $P_C/P_{TNS}$  control signal indicates that the intake has started, the controller automatically switches to the high-stability option of the started mode. The throat doors are commanded to close via the schedule of throat door position with centerbody position (see Figure 15). The controller moves the intake to the high-stability operating point using the cross-coupling function,  $\Delta_{CC}$ . The distortion during the shock swallowing transient is quite high, with a peak at about 30% following initiation of the started mode.

The intake was then unstarted by selecting the sympathetic unstart sequence. The sequence, which sets the  $P_{NS}/P_{TNS}$  reference to 1.0 PRU, unstarted the intake within 0.4 sec and caused a buzz condition. To suppress this condition, a buzz detector circuit was implemented in addition to the scheduled  $P_{NS}/P_{TNS}$  reference for the buzz suppressor mode. The buzz detector circuit is a dynamic device that detects an oscillation in the  $P_{NS}/P_{TNS}$  signal between frequencies of 7 and 14 Hz (the expected intake buzz frequency range) and has an output proportional to the magnitude of the input oscillation. Moreover, the output increases quite rapidly with the onset of buzz, but decays to zero more slowly with the suppressing of buzz. The output of this device is shown in Figure 27.

Figure 28 shows a restart sequence at Mach 2.1. After starting, the centerbody overshoots the design position because the throat doors are open. As the throat doors close, centerbody motion reverses, and the centerbody extends to the design position as determined by the high-stability  $P_{CB}/P_{TNS}$  reference and control signal. In this restart case, the high-performance option was selected about 5 sec after the start, and the recovery increased from approximately 88% to 90.5%. Figure 29 shows a restart sequence at Mach 2.65 with the intake at a  $-2^\circ$  angle of sideslip. The restart sequence is successful despite considerably turbulent control signals.

### CONCLUSIONS

The control system described is designed to meet the following basic objectives:

- 1) be accurate to maintain peak intake performance
- 2) be relatively self-contained for reliability
- 3) contain self-generated information of intake local sideslip and Mach gradients to maintain a started intake during these localized disturbances
- 4) contain sufficient transient performance to meet expected atmospheric and engine disturbances

The accuracy and self-containment of the control system are maintained by scheduling the intake pressure ratio references with centerbody position and biasing these references with controller error signals for intake sideslip and off-design throat Mach number conditions. Controlling to near-peak intake recovery while maintaining a started intake during atmospheric and engine disturbances is obtained using vortex valves as an auxiliary normal shock stability system.

The intake control system design requires a minimum of flight crew action and monitoring. This is provided by using dual redundant automatic control systems on each intake. A manual backup control system was deemed unfeasible because of the difficulty and complexity of displaying information with sufficient accuracy to allow for manual operation even close to peak recovery. Thus a second automatic control channel, with only minor mode selection required of the pilot, was deemed necessary to ensure continued high intake performance following an in-flight malfunction.

### ACKNOWLEDGEMENT

The authors wish to acknowledge the work of the many members of the engineering staff of The Boeing Company whose very detailed work has formed the basis of the design and development of the intake control system. In particular, we wish to thank R. H. Burr for his many contributions in the preparation of this paper.

### REFERENCES

1. E. Tjonneland, *The Design, Development, and Testing of a Supersonic Transport Inlet System*, AGARD Propulsion and Energetics 38th Meeting, 1971
2. Ross G. Willok, *A Mathematical Analysis of Supersonic Inlet Dynamics*, NASA TN D-4969, December 1968

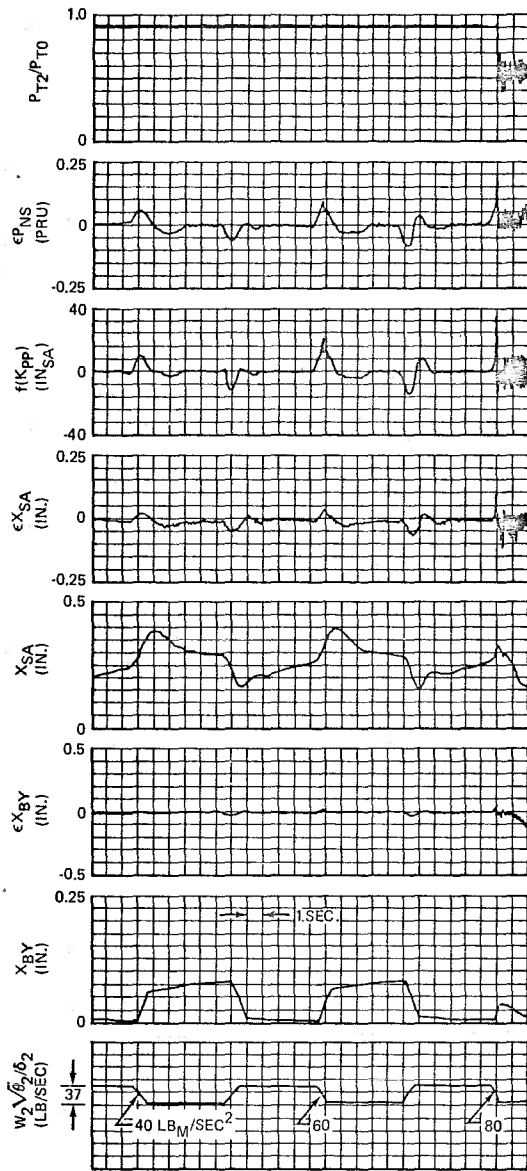


Figure 23a. Plug Ramps at Mach 2.65

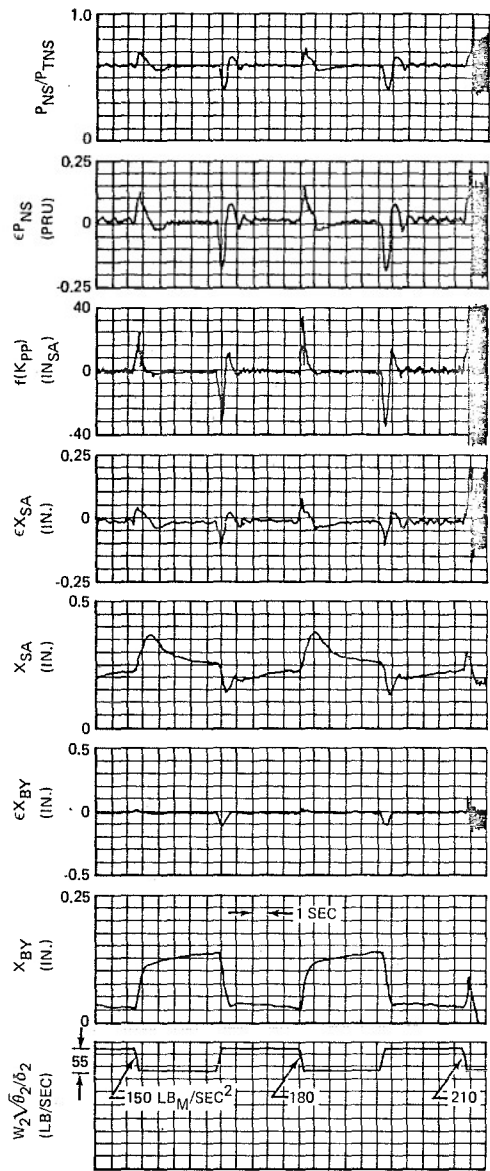


Figure 23b. Plug Ramps at Mach 2.10

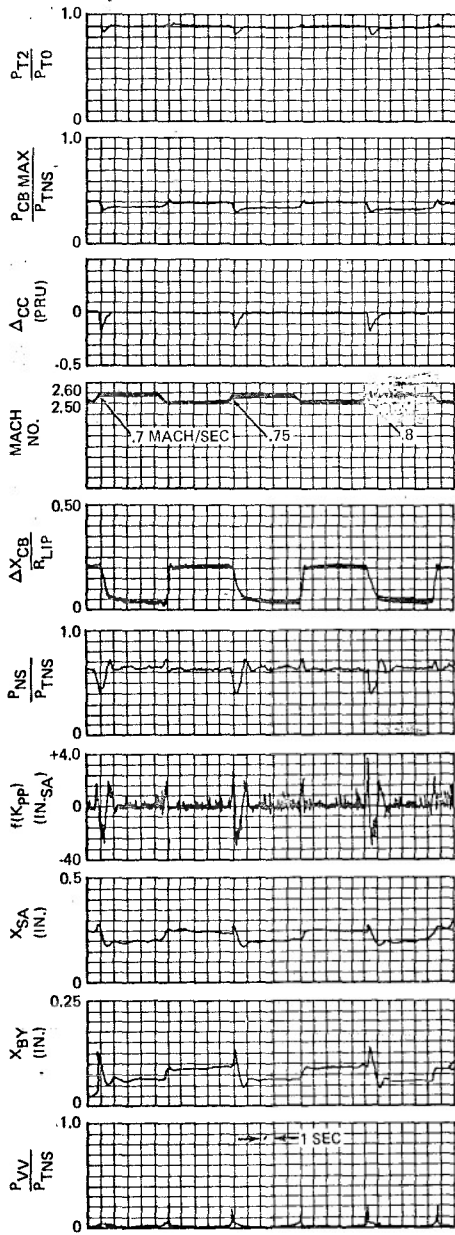


Figure 24. Mach Ramp Transients at Mach  $2.55 \pm 0.05$

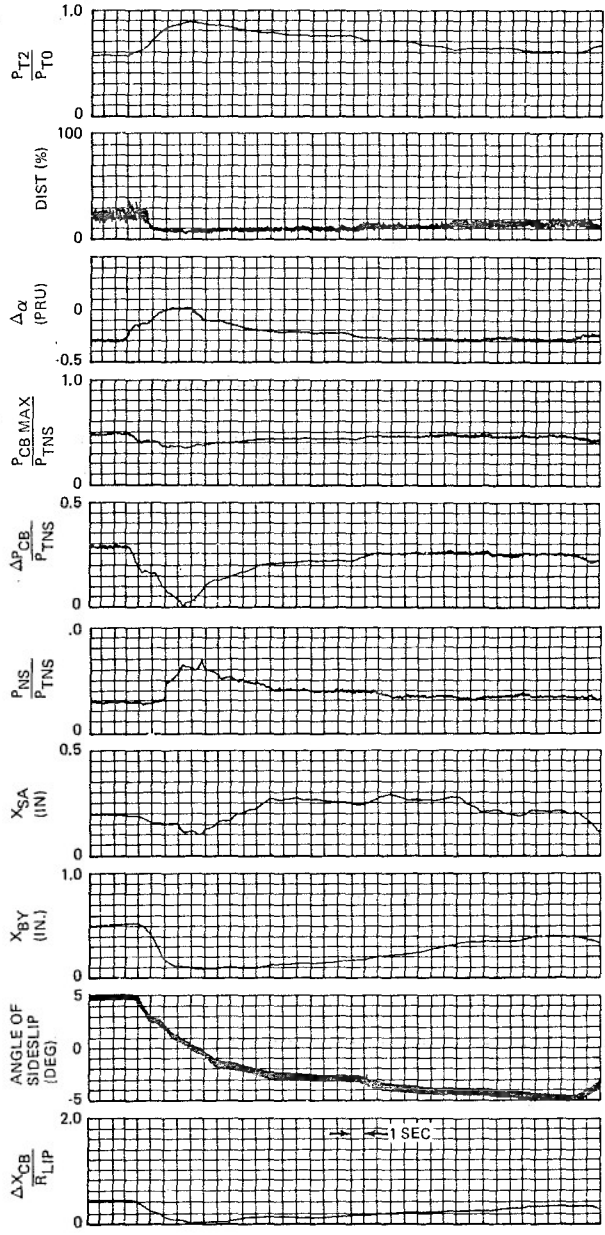


Figure 25. Slow Sideslip Transient at Mach 2.60

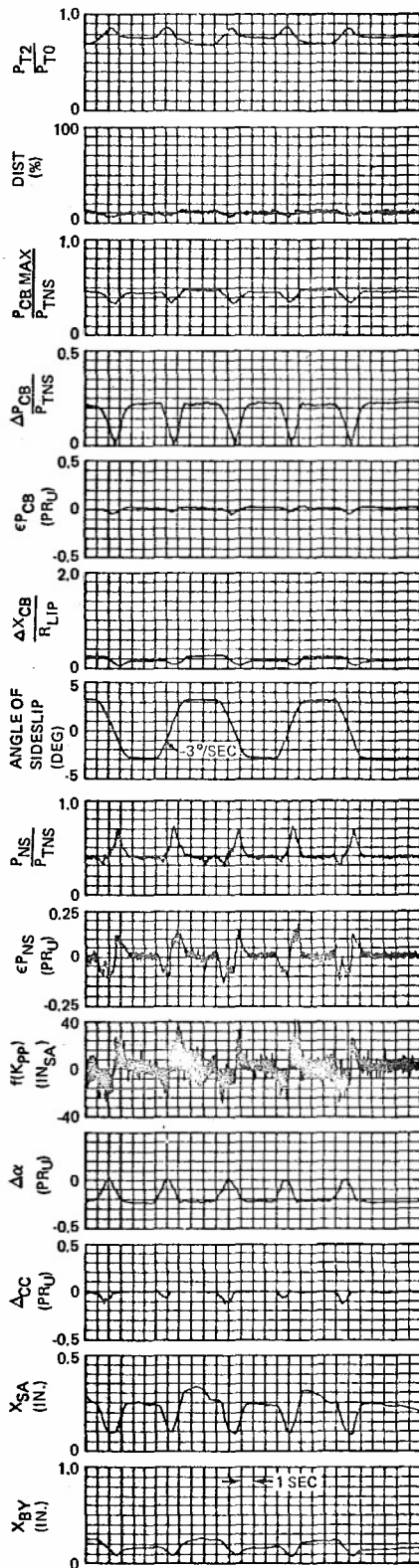


Figure 26. Fast Sideslip Transients at Mach 2.60

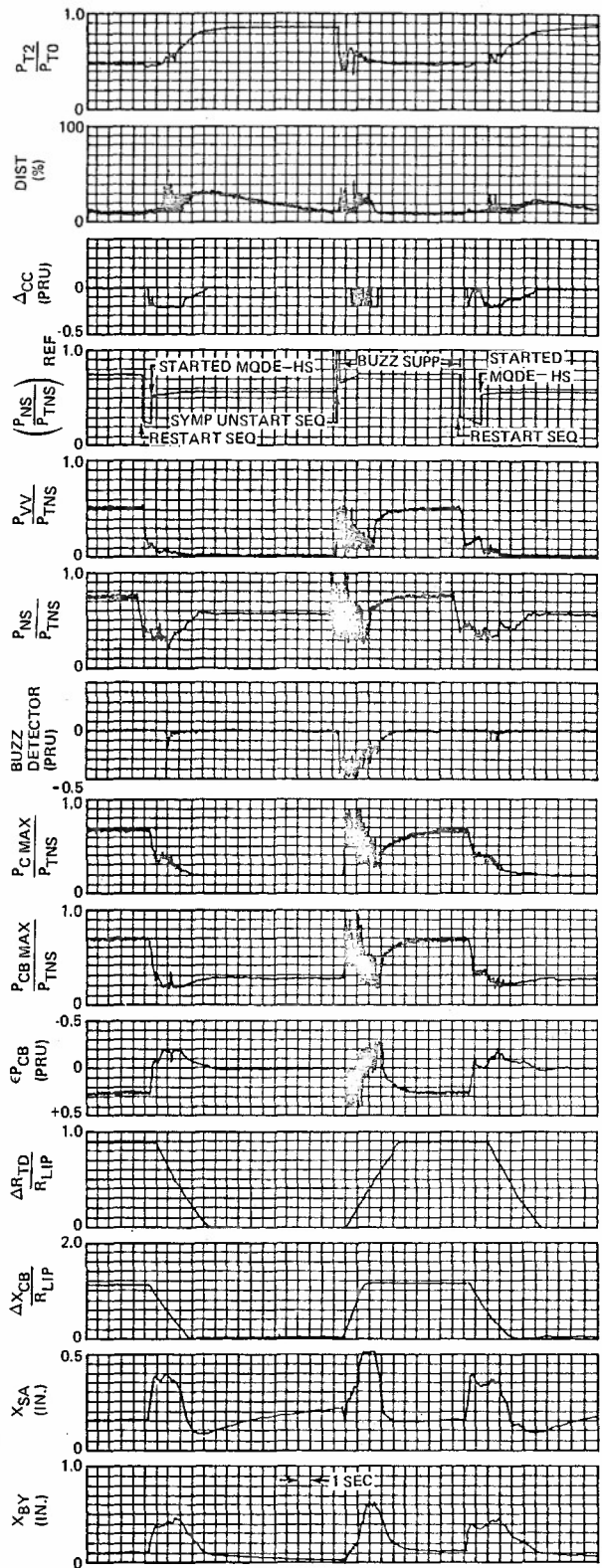


Figure 27. Restart, Sympathetic Unstart, and Buzz Suppression at Mach 2.65

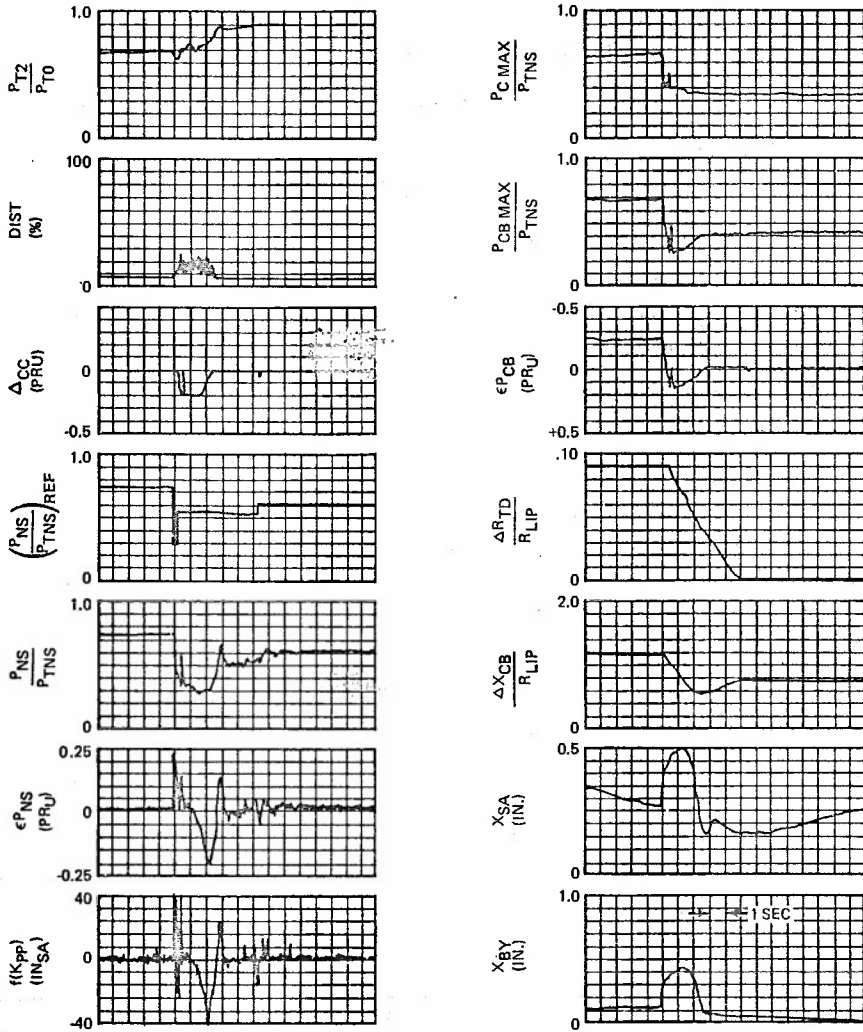


Figure 28. Restart Sequence at Mach 2.10

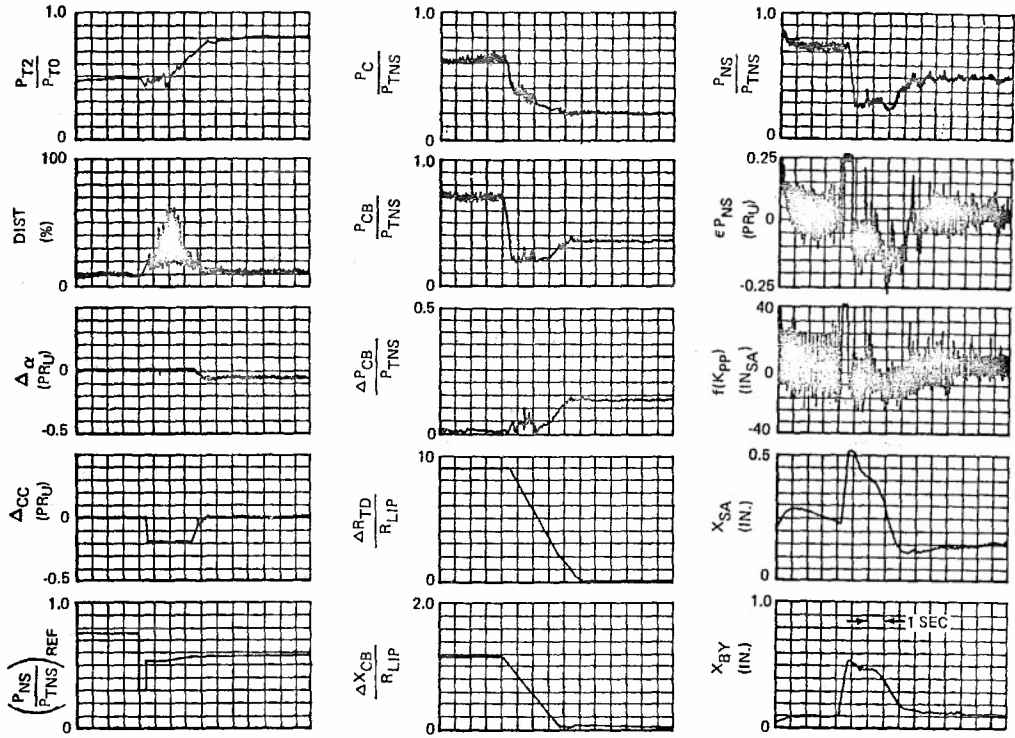


Figure 29. Restart Sequence at Mach 2.65, Intake Angle of -2 degrees

AN AERODYNAMIC DRAG STUDY OF  
JET ENGINE NOZZLES

by

Dave Bergman  
Convair Aerospace Division of General Dynamics Corp.  
P. O. Box 748  
Fort Worth, Texas 76101

SUMMARY

Exhaust nozzle drag is often a significant part of total airplane drag but, unfortunately, accurate techniques for predicting nozzle internal/external flow interactions are not yet known. For example, the viscous mixing, or entrainment, of surrounding flow created by high velocity exhaust jets has a definite effect on external drag; however, at the present, this phenomenon cannot be calculated. The same holds true for other effects, such as jet plume shape, nozzle contour, free-stream Mach number, etc. To aid nozzle analysis in areas where analytical methods are lacking, the Convair Aerospace Division of General Dynamics recently conducted a wind-tunnel program to investigate and measure the external drag characteristics of several nozzles at both on- and off-design exhaust conditions. This study involves nozzles of the centerbody plug, the convergent, and the convergent-divergent types. In addition, flow-through-nacelle nozzles and solid-wall jet plume simulators, each used frequently in airplane model tests, were included in the program. The data from these subsonic tests were substantiated by comparison with National Aeronautics and Space Administration data in the cases where model configurations were similar. Results of the General Dynamics tests show large changes in external drag with variations in exhaust flow, and describe the behavior of jet plume shape and entrainment effects. The results also provide insight into methods for simulating exhaust flow effects on airplane models which do not incorporate high-pressure exhaust flow.

SYMBOLS

- A = cross-sectional area
- $A_e/A_0$  = nozzle expansion ratio
- $C_D$  = boattail drag coefficient,  $\left(\frac{\text{Drag}}{qA_m}\right)$
- $C_{Dp}$  = boattail pressure drag coefficient,  $\left(\frac{\text{Pressure Drag}}{qA_m}\right), \left(\frac{1}{A_m}\right) \int_{A_m}^{A_b} C_p dA$
- $C_p$  = pressure coefficient,  $\left(\frac{p-p_0}{q_0}\right)$
- d = diameter
- L = length
- $L/d_m$  = boattail fineness ratio
- $M_0$  = freestream Mach number
- NPR = nozzle pressure ratio,  $P_{T0}/P_0$
- $P_T$  = total pressure
- p = static pressure
- q = dynamic pressure,  $\frac{1}{2} \rho V^2$
- X = distance

SYMBOLS (Cont'd)

$V$	= velocity
$\alpha$	= solid-wall extension angle, angle between solid-extension exterior and axial direction
$\beta$	= boattail chordal angle, angle between axial direction and line connecting the boattail tangency point at $d_m$ with the boattail trailing edge
$\theta_c$	= nozzle internal convergence angle
$\theta_d$	= nozzle internal divergence angle
$\rho$	= gas density

SUBSCRIPTS

$b$	= boattail base
$\odot$	= nozzle exhaust station
$m$	= maximum
$o$	= free-stream
$T$	= total
$\ominus$	= nozzle internal throat station

INTRODUCTION

In less than 70 years, aviation has progressed from aircraft with maximum speeds comparable to that of an automobile to present-day aircraft capable of flight measured in multiples of the speed of sound. Along with growth in airplane size and speed, advances in technology have also made it possible to attain more aircraft performance for the same amount of expended fuel. Part of the efforts to continue this trend is the work being done to extend knowledge concerning airframe/propulsion system integration (Reference 1). A considerable portion of this effort is aimed at examining in detail the manner in which jet engine inlets and nozzles interact with external flow fields and the resulting effects on system performance.

In this paper, the effects that nozzle exhaust flows have on surrounding flow fields are examined. Specifically, emphasis is placed on the flow fields enveloping the exhaust-nozzle exterior, which, in terms of performance, creates "boattail drag" forces.

PROBLEM STATEMENT

Sketches of various types of nozzles with the nomenclature to be used are presented in Figure 1. The nozzles shown are representative of non-afterburning engine operation during subsonic flight. This condition corresponds to a maximum amount of boattail aft-facing projected area as compared to afterburning, in which the nozzle exhaust opens and the exterior approaches a cylindrical shape.

Because of geometrical differences, each nozzle type produces its own characteristic plume shape. And, of course, jet plumes change during flight as changes occur in nozzle pressure ratio (exhaust jet total pressure divided by free-stream static pressure).

Related to these circumstances is the situation that results during scale model testing when, for one reason or another, the model is not provided with engine pressure-ratio exhaust jets. In such instances, a hollow "flow-through" nacelle, such as shown in Figure 2, often takes the place of the propulsion system and, sometimes, a tubular sleeve is attached to the nozzle in an effort to simulate a plume (Reference 2). A plug-type engine nozzle and its corresponding airplane force-model nozzle are shown. Both have identical external boattails, but there are two important differences

between these nozzles. First, the force-model nozzle centerbody plug is smaller than that of the engine plug in order to allow enough flow to pass through the nacelle for proper inlet mass-flow setting. The force-model plug is usually truncated at the exit to ease measurement of its drag force, which is subsequently subtracted from the overall airplane force data. Second, because the nozzle pressure ratio of force-model nozzles is determined by free-stream Mach number and flow-through-nacelle duct losses, force-model nozzles always "operate" at much lower pressure ratios than engine nozzles. Similarly, the force-model counterpart of a non-plug engine nozzle has a larger throat area and lower pressure ratios; hence, the boattail shape for these two nozzles becomes different. In any case, applying jet-plume simulation to scale models presents a formidable problem, one that requires detailed attention.

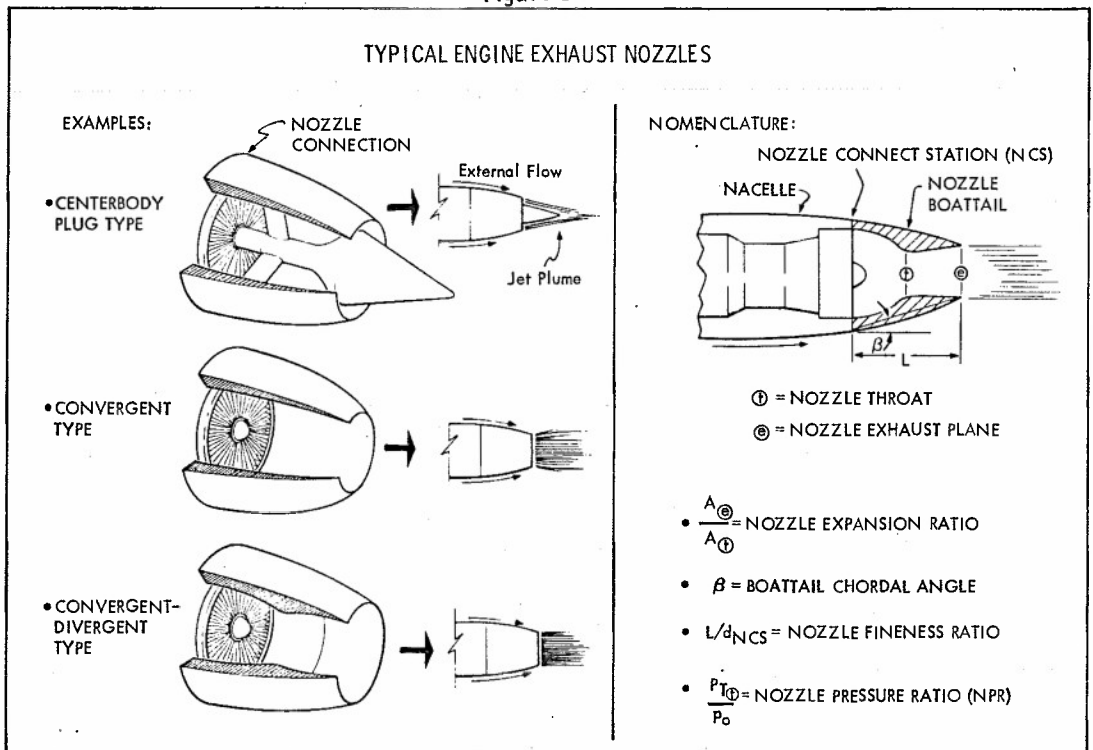
The above situations lead to the following questions:

1. With the realization that during subsonic flight an engine exhaust plume has the potential of propagating flow-field disturbances both upstream and downstream of the nozzle exit, how strong is this effect on, for example, nozzle boattail drag, and, if these effects are significant, what factors cause them to occur?
2. How can knowledge concerning jet-interference effects be applied to airplane scale models that do not incorporate engine-pressure-ratio exhaust flow?

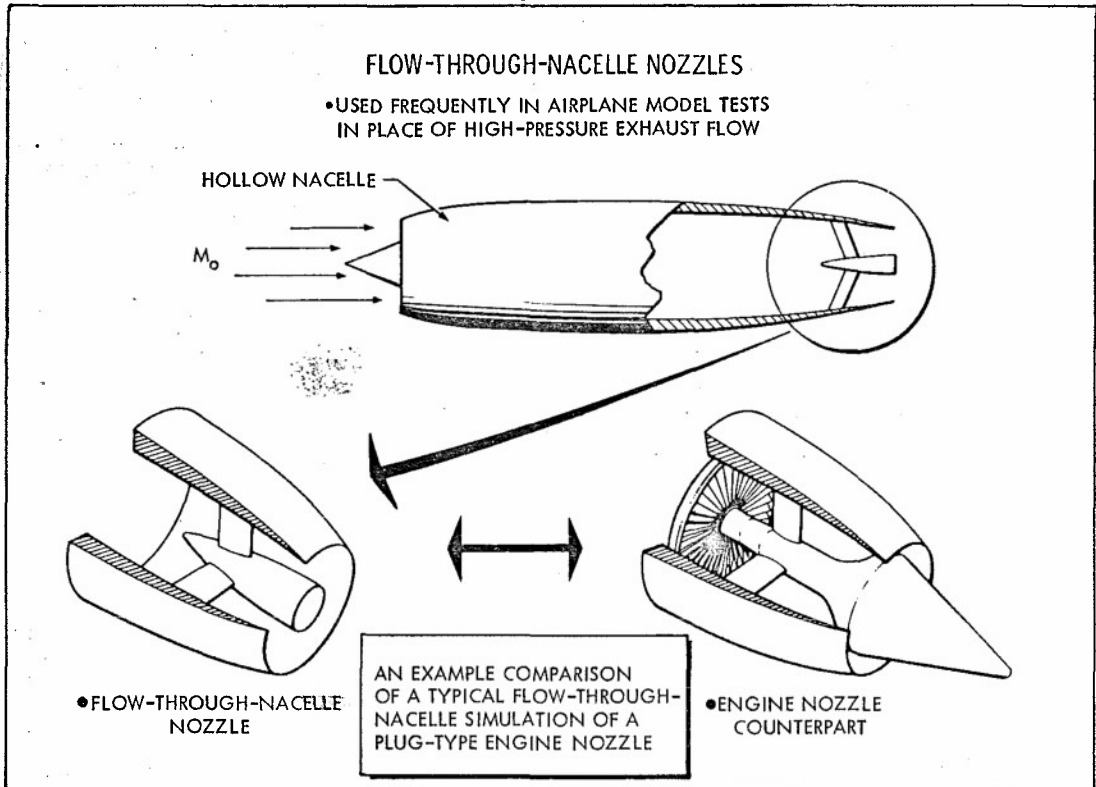
#### METHOD OF APPROACH

Fully answering the above questions is difficult since there obviously are an infinite number of possible airplane/engine-nozzle combinations, each with its own characteristic performance. Nevertheless, worthwhile descriptions of jet interference effects and trends can be derived to some extent by examining specific cases. With this in mind, a series of isolated nozzles were wind-tunnel-tested to examine jet effects on boattail drag. Note that, in this instance, attention is focused primarily on the jet effects rather than on the resulting absolute drag levels. This distinction is important because the drag levels of nozzles installed in an aircraft, as opposed to the same nozzles isolated, will depend on, in addition to jet effects, the flow-field interference produced by surrounding structure.

- Figure 1 -



- Figure 2 -



Nozzle testing was performed in a continuous-flow wind tunnel having a subsonic free-jet test section. A schematic of the tunnel is presented in Figure 3. A steam-ejector system pulls outside air into a 12-foot-wide bellmouth inlet from which the air then flows through a 9-1/4-inch-wide square channel. This channel terminates inside a large plenum chamber, and it is here that a subsonic free-jet test section is formed. At a Mach number of .85, the Reynolds number per foot in this section is  $4 \times 10^6$ . A nozzle forebody support pipe extends through the center of the test section and serves to deliver pressurized exhaust flow. The nozzle flow is not heated, thus its total temperature is ambient. Measurements show that the external flow on the pipe at the nozzle connect station has a turbulent boundary layer with a thickness approximately 17 percent that of the pipe diameter. An aft-fuselage nozzle installation would involve boundary-layer heights near this value, whereas a podded-nacelle nozzle installation would normally involve less boundary-layer growth. All the configurations have circular-arc boattails tangent at the nozzle-connect station (maximum diameter). The forebody support pipe is cylindrical and attaches at this station. All the nozzles are axisymmetric and have identical maximum diameters.

A problem that frequently arises in nozzle analysis involves the generalized use of published subsonic boattail drag data, the majority of which concerns purely convergent nozzles (minimum internal flow area located at the nozzle exit plane). With the advent of higher-pressure-ratio engines, published data may not be directly applicable to nozzle concepts that incorporate slight amounts of internal flow expansion during subsonic flight. If the nozzle expansion ratio is greater than unity, then changes in internal flow conditions occurring downstream of the nozzle throat create external exhaust plumes unlike those of convergent nozzles. In turn, boattail flow can possibly be altered by such changes in exhaust jet conditions. The issue is then whether, for a given boattail shape, changes in internal expansion ratio significantly affect external drag. To help resolve this question, the convergent and convergent-divergent nozzles shown in Figure 4 were tested.

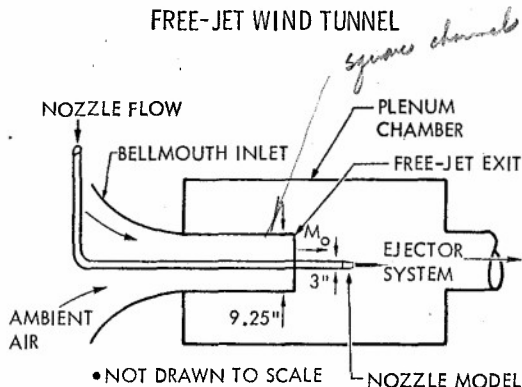
As stated earlier, emphasis is placed on examining jet exhaust effects on boattail drag. Therefore, comparisons of the nozzles in Figure 4 are made on the basis of varying the exhaust flow conditions while retaining the identical nozzle exterior. This approach is different from the methods used to choose the optimum nozzle for a given thrust-class engine (particular throat area), wherein boattail shapes change when comparing one nozzle type with another.

It is important to note that although the important criterion for rating nozzle performance is thrust-minus-drag level, thrust levels were not measured in these tests -- in fact, they are not needed to accomplish the objectives of this study. Therefore, these results are intended as an aid in understanding jet exhaust/external-flow interference rather than as a rating of the performance of one nozzle type versus another.

Boattail drag in these tests was determined by integrating pressure/projected-area distributions along the boattail surface. The pressure data come from several rows of static pressure orifices located along the length of the nozzle exterior. These drag values are thereby termed boattail "pressure" drag. Predictions of the boattail friction drag are subsequently presented.

Model internal instrumentation were total-pressure tubes for determining nozzle pressure ratio. Diagrams showing the location of the various instrumentation are presented in Figure 5.

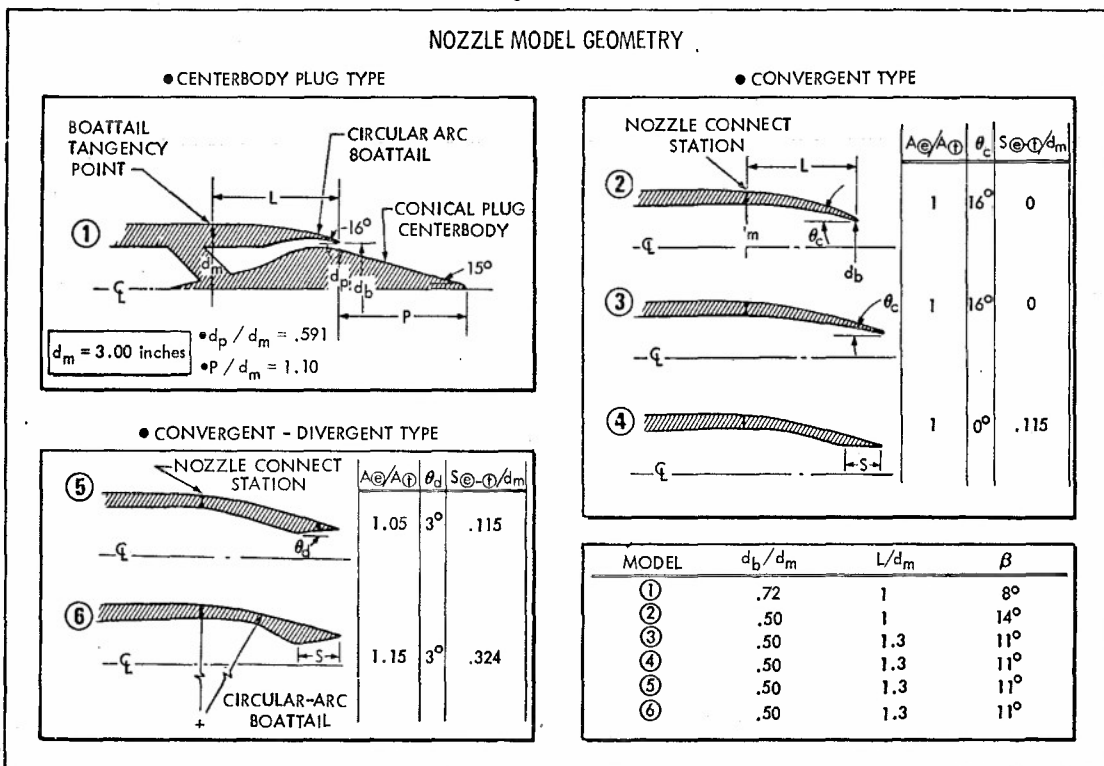
- Figure 3 -  
FREE-JET WIND TUNNEL



RESULTS AND ANALYSIS

Some of the boattail pressure distributions measured during the tests are shown in Figure 6. Note the flow expansion around the nozzle/forebody juncture and then the rapid flow recompression near the nozzle trailing edge. This speed-up/slow-down flow pattern is characteristic of boattails and can be attributed to the positive and negative centrifugal forces imposed upon the flow as it envelopes the nozzle. It is evident from these pressure measurements that exhaust jets can cause significant flow-field disturbances upstream of the nozzle exit. In fact, the measurements show that these disturbances can be felt over the entire nozzle exterior.

- Figure 4 -



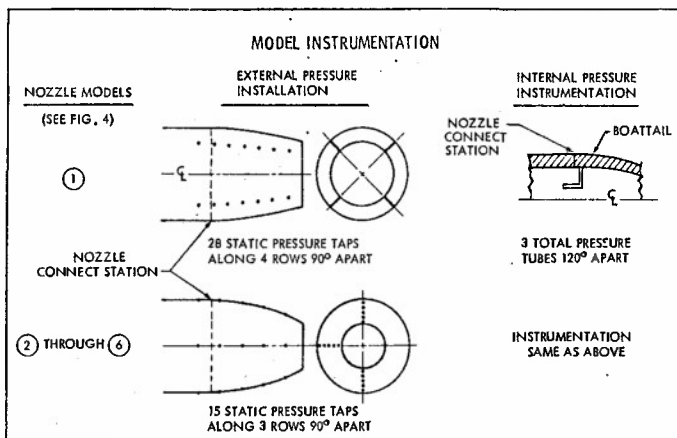
Summing, or integrating, the boattail pressure-area distribution provides the nozzle pressure drags presented in Figure 7. Nozzle pressure ratio and exhaust flow direction (flow along tapered centerbody plug as opposed to axial exhaust flow) are each seen as important elements affecting nozzle drag levels. The drag coefficients shown are referenced to nozzle maximum cross-sectional area.

To get a better understanding of the factors which create jet interference effects, a

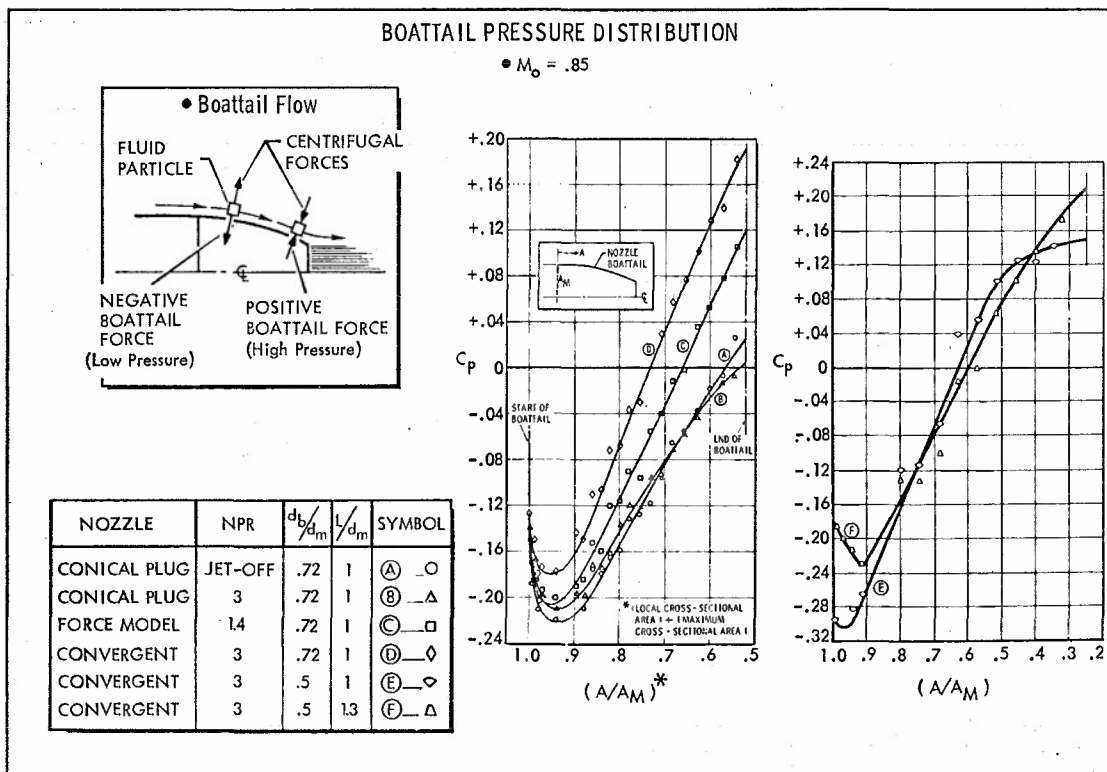
rough attempt was made to separate the jet plume shape effects from the jet plume entrainment effects. The shape of the jet plume can be thought to produce flow blockage about which the external flow must "navigate". A further complication is that jet engine exhaust velocity is greater than that of the surrounding flow. This velocity differential results in flow entrainment, or "pulling", of the external flow. This effect is brought about by the mixing along the jet-plume/external-flow interface. As a result, external flow is speeded up adjacent to the jet, and this disturbance can alter boattail flow fields.

The approach for simulating plume shape effects was that of using isentropic flow relationships at specific nozzle pressure ratios to describe an approximate (inviscid) plume shape. As shown in Figure 8, a nozzle was tested three ways: (1) with the jet off, (2) with a solid body simulating a plume shape, and (3) with the true exhaust flow. The difference in boattail drag between the jet-off situation and the situation with the solid-body plume simulator is denoted as the jet-plume shape effect, whereas the difference in drag between jet-on and the solid-body plume is denoted as the

- Figure 5 -

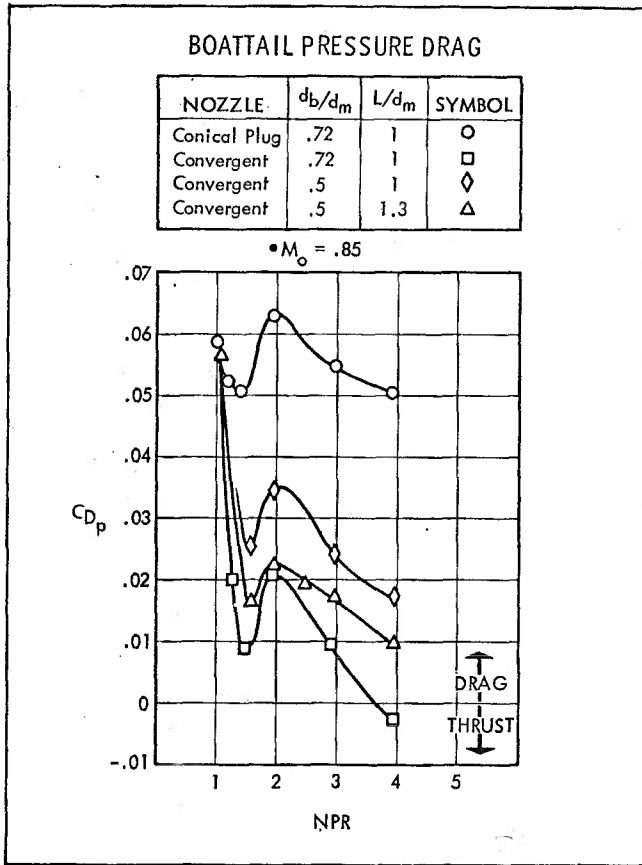


- Figure 6 -

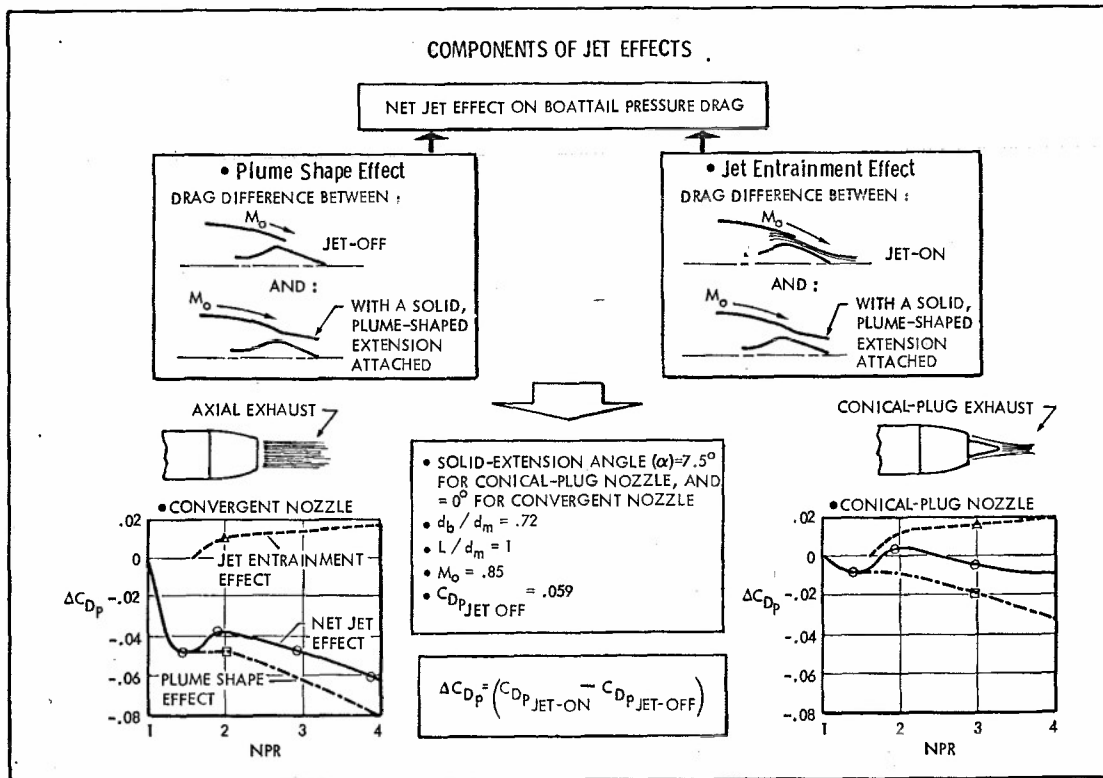


- Figure 7 -

jet entrainment effect. Because of the extrapolation involved, the curves in Figure 8 are meant to depict a qualitative rather than a precise quantitative description. Jet entrainment is shown to begin its effect on boattail drag at a jet velocity approximating free-stream velocity and then to gain in strength with increasing pressure ratio. As suggested earlier, this effect is detrimental since jet entrainment creates an induced speed-up of boattail flow, which lowers boattail pressures. In contrast, the jet plume-shape effect is shown as beneficial since it acts to move boattail flow streamlines away from the centerline, thereby causing stronger flow re-compression on the boattail surface as compared to jet-off conditions. The jet plume is unable to "billow out" beyond the exit area until a sonic exhaust is established; thus, the plume-shape effect is assumed to be virtually constant from a jet velocity equal to free-stream to a just-choked exit (NPR≈2). As nozzle pressure ratio is increased past the just-choked condition, the plume expands and its effect on drag becomes more pronounced by causing further displacement of boattail flow streamlines. The



- Figure 8 -



net, combined effect of jet entrainment and plume shape shown in Figure 8 results in the same general trends for both the plug and convergent nozzles.

The larger levels of drag with the conical plug nozzle compared to the convergent nozzle seen in Figure 7 can then be explained by differences in plume shape. The plug-nozzle plume causes boattail flow to be turned axially downstream of the boattail surface, whereas the convergent-nozzle plume forces an earlier re-compression at the boattail end. As a result, boattail pressures with the conical plug remain relatively low while further external flow re-compression occurs downstream, adjacent to the plug flow. For this reason, plug nozzles are often said to have "aerodynamic boattails".

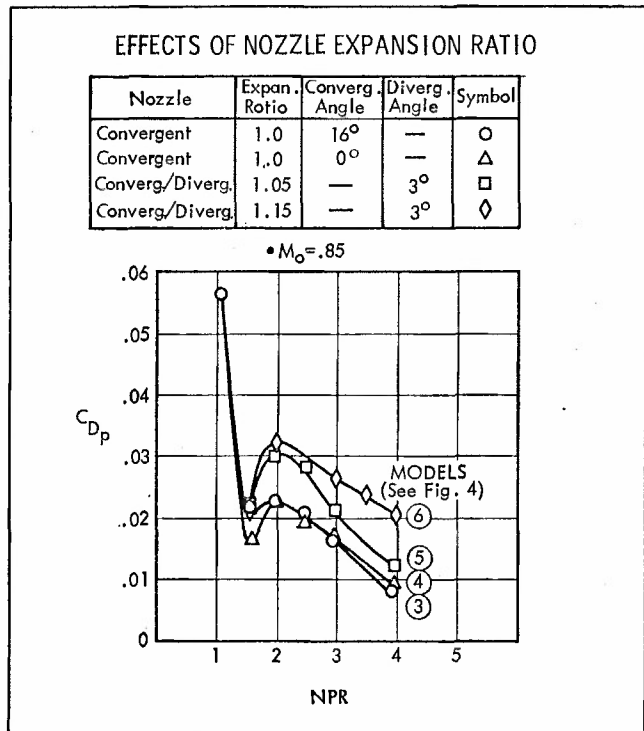
The effects of nozzle expansion ratio on the drag of a particular boattail shape are shown in Figure 9. Also included in the tests was a configuration in which the half-angle approach to the throat of a convergent nozzle (unity expansion ratio) was changed from 0 to 16 degrees. The results show that this change has a noticeable effect on drag at unchoked, subsonic, exhaust flow (nozzle pressure ratios less than approximately 2), but this change has only a very slight effect during choked-flow operation. Evidently the sonic throat tends to hamper these internal upstream geometry changes from propagating a strong effect into the external plume. However, this result probably does not adequately describe nozzles with quite large convergence half-angles in which vena contracta effects become more prominent. Adding internal expansion downstream of the throat to form a convergent-divergent passage results in more boattail drag, at the identical nozzle pressure ratios, as compared to the same boattail with purely convergent flow. This trend is not unexpected, since the boattail effectively "sees" a narrower exhaust plume, compared to a convergent nozzle, if a portion of the plume expansion is internal. These results suggest that drag data pertaining to a desired boattail shape but obtained with unity expansion ratio should be corrected for application to convergent-divergent nozzles by (1) correlating data on the basis of exhaust-static-to-freestream-static pressure ratios in order to account for plume shape, and (2) adding an additional entrainment increment to the data to account for differences in plume velocity.

It can be gathered from remarks up to now that force-model, flow-through-nacelle nozzles probably affect boattail flow fields quite differently than do their engine-nozzle counterparts. Indeed, the drag data shown in Figure 10 illustrate this fact. Also shown in Figure 10 are means whereby jet effects can be simulated to an extent on a force-model nozzle by adding hollow-sleeve extensions. Notice that a conical rather than a cylindrical tube shape more closely simulates the effects of fully-expanded convergent nozzle flow. This result can be attributed to the flow-entrainment properties of the jet. In other words, because of mixing, the effective shape of the jet plume is narrower than that which would be predicted on an inviscid basis.

However, in practical terms, solid-body jet simulators have rather limited applications since angle of attack effects, installation effects, and forces incurred on the simulator itself can inhibit or restrict their actual use. In any event, the basic point remains that airplane force data obtained with flow-through-nacelle nozzles can require significant corrections to account for true jet effects.

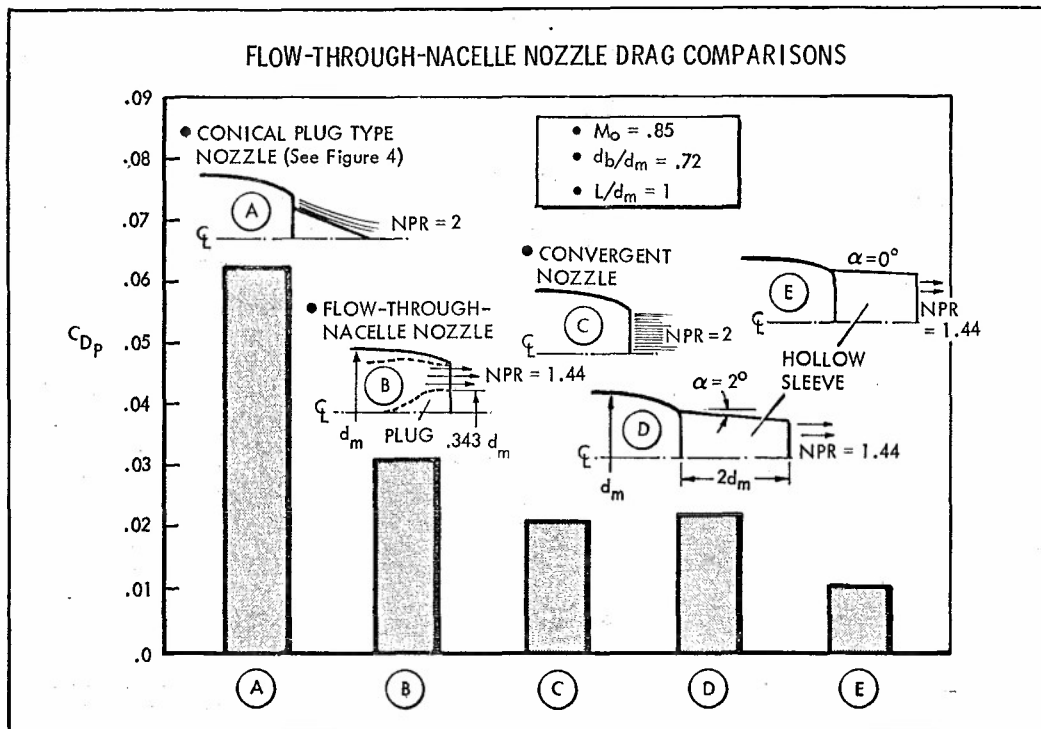
One of the convergent nozzle configurations is similar to a nozzle tested at the National Aeronautics and Space Administration's Langley Research Center in their 16-foot transonic wind tunnel. Therefore, a comparison of the General Dynamics data with the NASA data (Reference 3) was made. The results, shown in Figure 11, are in good agreement both in level and trend. Although the General Dynamics' free-jet tunnel

- Figure 9 -

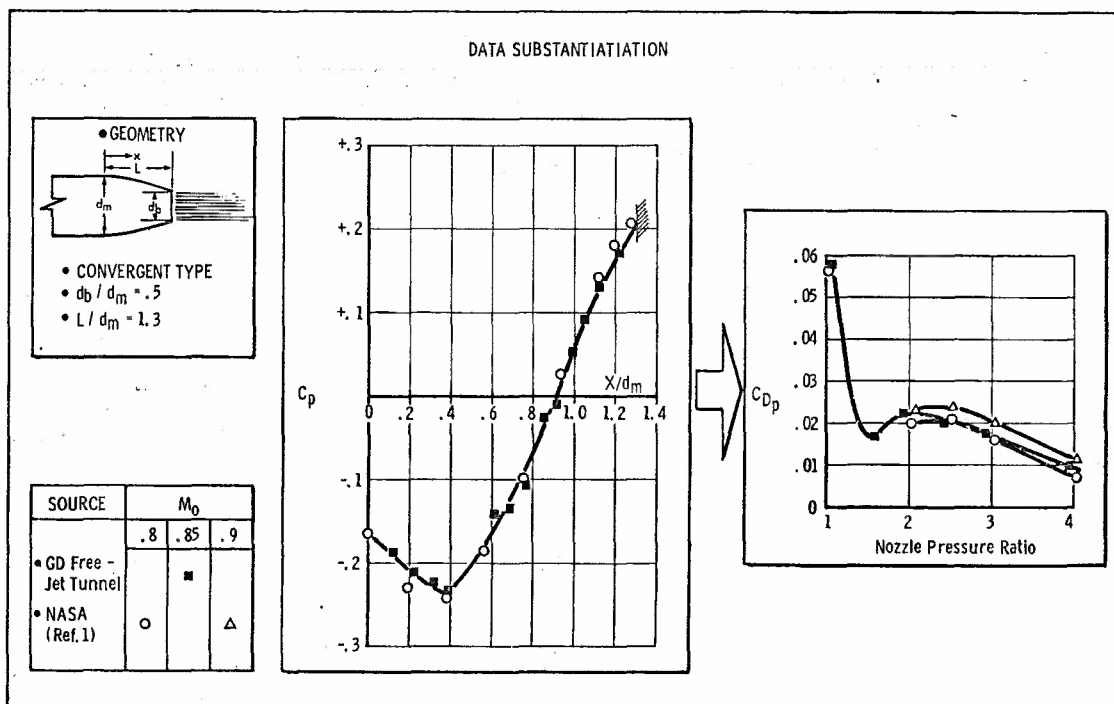


is rather small, the data from these boattail drag tests appear to be valid. A comparison of NASA data with other drag data obtained in this free-jet tunnel is found in References 4 and 5.

- Figure 10 -



- Figure 11 -



### EXTENDING THE RESULTS

At this point it is worthwhile to theorize or postulate somewhat beyond the specific conclusions resulting from the preceding test data. For example, there is a question in airplane model testing concerning the consequent effects on drag brought about by the simulation of exhaust jets with cold rather than hot flow. Cold-flow (ambient temperature) jets are often used in tests since they lend considerably less complication and expense to model construction and operation. By adjustment of nozzle pressure ratio, the portion of the plume near the boattail can be kept a particular shape for either hot or cold flow; however, once this matching of shape has been accomplished with cold flow, there still remains a mis-match in jet entrainment, since the momentum differential between the jet flow and the free-stream is unlike that which occurs with hot flow. In other words, adjustments in nozzle pressure ratio can force cold flow to simulate either the plume shape or the entrainment of a hot jet, but not both simultaneously. Plume shape is usually the predominant of the two; therefore, the normal test procedure involving cold jets is to concentrate on simulating as closely as possible the shape of the true jet exhaust. One must then judge or predict the significance of the resulting entrainment mis-match on airplane forces.

Past tests (Reference 4) indicate that, for isolated nozzles operating at or near design conditions, the part of the jet plume from the nozzle exhaust plane to no more than one to two nozzle diameters downstream is the portion of the plume that primarily affects boattail flow. Thus, it is within this initial region where jet entrainment differences must occur if boattail drag is to be noticeably altered. On the other hand, any airplane structure near downstream portions of the jet will be subjected to much larger effects due to jet entrainment since, by then, more mixing of the jet flow has had a chance to occur. Data and Schlieren photographs in Reference 6 show very slight changes for hot versus cold jet flow within this initial length of the plume (one to two nozzle diameters), but do show large changes in the flow field farther downstream because of the different mixing (momentum) characteristics of cold as opposed to hot flow.

Therefore, it would seem that whether hot exhaust flow is actually needed in airplane model testing really depends upon the particular nozzle location on the airplane. For example, the least consequences of using cold-jet flow probably occur if the nozzle plume does not flow adjacent to any airplane structure such as in an aft-fuselage engine location; the opposite would be the case in an underwing or side-fuselage installation. An exception might be an aft-fuselage nozzle located in a highly separated flow region such as aft of a blunt base. The entrainment effects for this situation are radically multiplied because of the larger momentum differential between the low-velocity separated flow and the jet. As a result, proper jet temperature simulation can gain importance for this case.

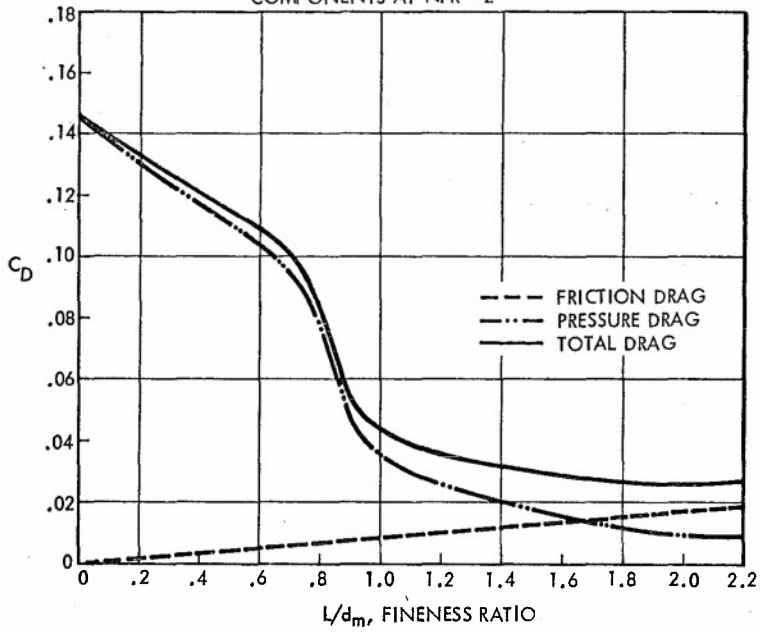
Variations in boattail fineness ratio (length divided by diameter) have strong effects on external drag. Rapid changes in pressure drag and friction drag occur if the boattail surface is made either shorter or longer. Of course, the total of the two drags, pressure plus friction, is the important drag level to consider. The curves in Figure 12, constructed by correlating data from several sources, show changes in drag with fineness ratio. Since many extrapolations and simplifying assumptions were used in developing these curves, they are intended as rough predictions, or indications, of fineness-ratio effects. Friction drag was calculated by use of wall-friction formulas and, as would be expected, continually increases in magnitude with increases in boattail length. In proceeding from a fineness ratio of 0 (blunt base) to larger fineness ratios, pressure drag decreases continuously as a result of increased boattail flow attachment. The major attachment phase occurs at a fineness ratio of approximately 1. The total drag (pressure plus friction) appears to minimize near a fineness ratio of 2, whereas further increases in boattail length produce an increase in drag due to friction. These drag curves pertain to isolated nozzles attached to cylindrical forebodies; however, airplane nacelles having larger cross-sections upstream of the nozzle ("upstream boattailing"), as well as the presence of the fuselage, wings, etc., can significantly change these drag levels.

As was stated earlier, thrust-minus-drag is the important nozzle performance criterion; therefore, fineness ratio must also involve tradeoffs in weight and in nozzle internal performance. It is also important to note in Figure 12 that increases in nozzle pressure ratio appear to cause an increase in external drag at low fineness ratios (separated boattail flow), but that the opposite is true at high fineness ratios (attached boattail flow). Apparently jet entrainment effects are considerably amplified near separated-flow regions, whereas plume shape is a more important factor for afterbodies with generally attached flow.

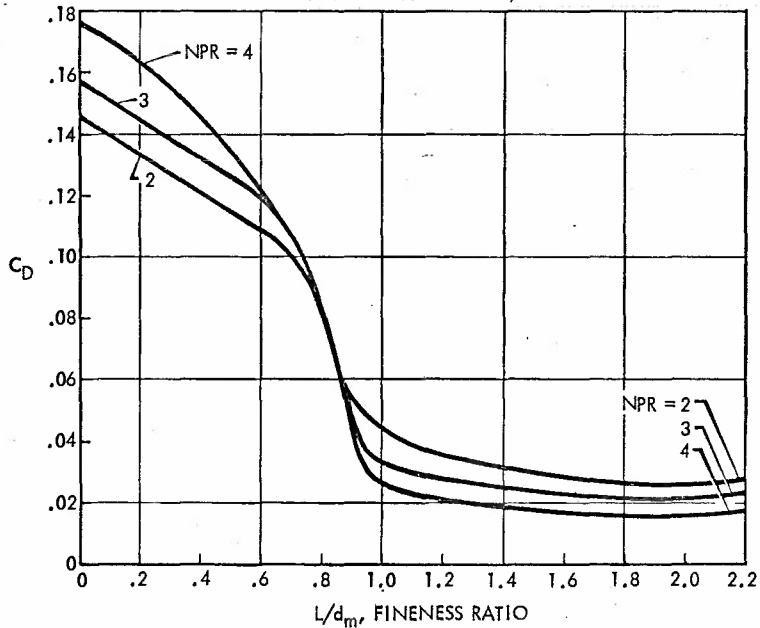
### ESTIMATED EFFECTS OF BOATTAIL FINENESS RATIO (CORRELATION INCLUDING DATA FROM REFERENCES 4, 5, 7, 8, 9, 10)

- $d_b / d_m = .5$
- SUBSONIC EXTERNAL FLOW
- CONVERGENT NOZZLE ( $A_0 / A_1 = 1$ )
- SMOOTHLY CONTOURED BOATTAIL (E.G., CIRCULAR ARC)
- ISOLATED NOZZLES WITH CYLINDRICAL FOREBODIES

● PRESSURE AND FRICTION DRAG COMPONENTS AT NPR = 2



● BOATTAIL TOTAL DRAG (PRESSURE DRAG PLUS FRICTION DRAG)



### CONCLUSIONS

For the configurations tested, it is found that:

1. Nozzle external drag is a strong function of exhaust jet conditions. The flow field disturbances created by the presence of exhaust jets can be described as being due to a combination of plume shape and plume mixing, or entrainment. These properties affect boattail flow fields differently at each nozzle pressure ratio and for each nozzle type.
2. Because of their exceedingly low pressure ratios, airplane model flow-through-nacelle nozzles have external drag levels unlike those of their engine nozzle counterparts. This simulation error can be lessened to a limited extent by adding hollow-sleeve extensions to the nozzles. These extensions, or plume simulators, should have contours with an "effective" plume shape in which jet entrainment has also been accounted for.
3. External drag, for a given boattail shape, is measurably affected by changes in internal expansion ratio. This effect occurs at low expansion ratios common to many convergent-divergent nozzles during subsonic flight. At a constant nozzle pressure ratio and boattail shape, the trend is that of increases in external drag with increases in internal expansion ratio. Therefore, drag data for purely convergent nozzles are not directly applicable, at identical nozzle pressure ratios, to the same boattails having internal plume expansion.

### REFERENCES

1. Proceedings of the Air Force Airframe-Propulsion Compatibility Symposium, Air Force Aero Propulsion Laboratory AFAPL-TR-69-103, June 1970.
2. Blaha, B. J., "Effect of Underwing Engine Nacelle Shape and Location on Boattail Drag and Wing Pressures at Mach Numbers From 0.56 to 1.46", NASA TM X-1979, March 1970.
3. Compton III, W. B. and Runckel, J. F., "Jet Effects on the Boattail Axial Force of Conical Afterbodies at Subsonic and Transonic Speeds", NASA TM X-1960, February 1970.
4. Bergman, D., "Effects of Engine Exhaust Flow on Boattail Drag" AIAA Paper No. 70-132, January 1970.
5. Bergman, D., "Exhaust Nozzle Drag: Engine vs. Airplane Force Model", AIAA Paper No. 70-668, June 1970.
6. Lee, G., "An Investigation of Transonic Flow Fields Surrounding Hot and Cold Sonic Jets", NASA TN D-853, April 1961.
7. Harrington, D. E., "Performance of Convergent and Plug Nozzles at Mach Numbers From 0 to 1.97", NASA TM X-2112, October 1970.
8. Henry, Jr., B. Z. and Cahn, M. S., "Additional Results of an Investigation at Transonic Speeds to Determine the Effects of a Heated Propulsion Jet on the Drag Characteristics of a Series of Related Afterbodies", NACA RM L56G12, September 1956.
9. Cabbage, Jr., J. M., "Jet Effects on the Drag of Conical Afterbodies for Mach Numbers of 0.6 to 1.28", NACA RM L57B21, April 1957.
10. Rustemeyer, A. H., and Twomey, E. J., "Thrust and Drag Characteristics of Several Turbojet Exhaust Models at Supersonic and High-Subsonic Mach Numbers", United Aircraft Corporation R-0922-16, June 1957.

Jet Effects on Boattail Pressure Drag at  
Supersonic Speeds

J.A.P. Stoddart  
British Aircraft Corp., Preston Division, Warton Aerodrome,  
Nr. Preston, Lancs. U.K. PR4 1 AX.

SUMMARY

An analysis is presented of supersonic boattail pressure drag measurements in the presence of single or twin propulsive jets. Using theoretical inviscid pressure distributions as a datum, the decrease in boattail pressure drag coefficient with increasing nozzle pressure ratio is shown to be a function of the difference between the measured base pressure coefficient and a reference base pressure coefficient which is theoretically just high enough to cause separation of the boattail terminal shock wave. The boattail shapes considered are shown to fall into two groups one of which experiences a much stronger influence of the propulsive jet than does the other. Correlations of measured base pressure coefficient in the presence of a propulsive jet are also presented for convergent and con-di nozzles.

An example of the use of the analysis is given in which the installed performance of a convergent nozzle is compared with that of a con-di nozzle.

1. INTRODUCTION

It has long been recognised that the presence of propulsive jets issuing from the base of a body can have a considerable effect on the external flow over the boattail and in the base region. These interferences can give rise to large changes in external drag which, at sufficiently high values of jet total pressure ratio, can be favourable relative to jet-off or inviscid conditions.

Over the years, a vast amount of experimental data on the effects of a propulsive jet on boattail drag has been accumulated and the high subsonic aspects of these phenomena have received some attention, e.g. Reference 1. From the performance engineer's viewpoint no similar analysis seems to be available for supersonic speeds.

In this note, simple correlations are made of the effects of single and twin propulsive jets on the boattail pressure drag and base pressure of afterbodies of mainly parabolic or conical shape. A range of Mach numbers from 1.4 to 2.4 is covered together with various types of propelling nozzle.

2. LIST OF SYMBOLS

M	Mach Number
H	total pressure
p	static pressure
$C_{D\beta}$	boattail pressure drag coefficient based on maximum cross sectional area
$C_p$	pressure coefficient
d	diameter
x	axial distance from start of boattail
A	cross sectional area
$\beta$	maximum boattail angle
$\epsilon$	nozzle exhaust angle (+ v.s. diverging)
D	drag force on boattail and base annulus
$X_G$	nozzle exit gross thrust force
$\infty$	free stream
m	position of maximum afterbody diameter
b	base
CON	convergent nozzles
J	jet exit
T	jet throat
at	theoretical inviscid conditions at end of boattail
bc	theoretical critical base value for onset of separation of terminal shock wave
t	theoretical inviscid value
AS	asymptotic drag value

3. DESCRIPTION OF THE PHENOMENA AND PRELIMINARY ANALYSIS

Some typical jet effects on boattail and base flow are taken from Reference 2 and are shown in Figure 1. The model afterbody has a parabolic form with a final boattail angle of approximately 12 degrees. A single variable plug nozzle was fitted which gave either a convergent nozzle or a con-di nozzle of area ratio 1.45. A sketch of the model is shown in Figure 1(a).

Figure 1(b) shows the measured effects of jet total pressure ratio on the boattail pressure drag coefficient at  $M_\infty = 2.0$ . The convergent nozzle exhibits a rapid decrease in boattail pressure drag beyond a total pressure ratio of about 5 whereas the con-di nozzle shows no such effect up to pressure ratios of 15.

Figure 1(c) shows the corresponding effects on base pressure coefficient. Both nozzles show a minimum base pressure which corresponds to the choking pressure ratio for the convergent nozzle and to the design

pressure ratio ( $H_j/p_b = 5.9$ ) for the con-di nozzle. At pressure ratios above these minima the convergent nozzle shows a more rapid pressurisation of the base region and the base pressure coefficient is typically 0.10 to 0.15 higher than the con-di nozzle values at the same engine operating condition. At pressure ratios greater than 5 the convergent nozzle installation has a thrust force on the base annulus which, when taken in conjunction with the reduced boattail wave drag, will offset some of the gross thrust augmentation due to the con-di nozzle. This point will be discussed in Section 6. The measured change in boattail pressure drag coefficient is about 0.035 over the range of pressure ratios investigated. This drag change corresponds to about 7 percent of the total zero lift drag coefficient based on fuselage maximum cross sectional area for typical supersonic military aircraft.

The aerodynamic effects of jet induced interference on boattail flow can be illustrated by static pressure distributions measured along the boattail as shown in Figure 1(d) for the convergent nozzle model of Reference 2. In this Figure, the static pressure coefficient is plotted against boattail cross sectional area for different values of jet total pressure ratio so that pressure drag changes can be easily seen.

An inviscid theoretical calculation of the boattail pressure distribution for this model by the method of Reference 3 is also shown in Figure 1(d) and this highlights the changes in pressure drag due both to the jet and to viscous effects.

For low jet total pressure ratios, the measured boattail pressure level is higher than the inviscid estimate by an amount which can only be a function of boundary layer displacement effects and interference from the model forebody or support system. At minimum base pressure (nozzle choking pressure ratio) the base pressure is lower than the boattail pressure measured at the static hole closest to the base. Thus the boattail flow is 'insulated' from the base flow by a weak expansion centred at the base lip. As the nozzle pressure ratio rises, the base region is pressurised by the expanding jet boundary and a condition is reached when the base expansion fan changes into a weak compression fan. When this obtains the relatively high base pressure can feed forward on to the boattail through the inner subsonic regions of the boattail boundary layer and thus the boattail pressure level close to the base is increased. ( $H_j/P_{0j} = 4.0$  and  $5.3$  on figure 1(d)). However, referring to Figure 1(b), no appreciable reduction in boattail pressure drag has accrued thus far.

As the nozzle pressure ratio is further increased, the base pressure continues to rise until the weak compression fan has strengthened to include one or more shock waves of finite strength. In this condition quite substantial over-pressures can feed forward on to the boattail via the boundary layer and the boattail pressure drag reduces dramatically ( $H_j/P_{0j} > 8$  on Figure 1(d)). At successively higher nozzle pressure ratios the boattail terminal shock wave begins to move forward along the boattail leaving a separated region behind it and the rate of change of base pressure with nozzle pressure ratio begins to decrease (Figure 1(c)) on account of the increased region of separated flow but the boattail pressure drag continues to reduce steadily (Figure 1(b)).

Figure 1(e) shows the method of analysis which forms the basis of the present correlation of jet induced boattail pressure drag changes. The data of Figures 1(b) and 1(c) is replotted in the form of boattail pressure drag coefficient  $C_{D\beta}$  versus base pressure coefficient  $C_{pb}$ . In this form the results from both nozzles become coincident (including the jet off value) as far as the data goes. A complete correlation between the two nozzles cannot be claimed because of the restricted range of the con-di nozzle measurements in these variables.

However, because of the partial data collapse a hypothesis is advanced which is tested by further analysis in Section 4. That is, for a given afterbody at a given Mach Number, the boattail pressure drag is determined only by the base pressure as a first approximation. Hence such variables as nozzle geometry, pressure ratio and secondary flow ratio which strongly influence base pressure, may be expected to have only second order effects on the  $C_{D\beta} \sim C_{pb}$  relationship. This form of analysis if valid, should expedite the correlation of jet induced boattail pressure drag changes because the independent variables are reduced to base pressure, Mach Number and boattail geometry. The question of base pressure determination is left open for the present and will be discussed in Section 5.

At low values of base pressure, the data of Figure 1(e) tend towards an asymptotic value of boattail pressure drag denoted by  $C_{D\beta AS}$  and which lies below the inviscid boattail drag coefficient  $C_{D\beta t}$  calculated by the method of Reference 3. The departure of the convergent nozzle drag data from the asymptotic value as base pressure increases must in some way be related to the rise in static pressure in the base region which is required to separate the terminal shock wave. From theoretical calculations, the inviscid pressure coefficient at the end of the boattail,  $C_{p at}$ , and the inviscid terminal Mach Number can be found. Assuming that the terminal shock wave occurs at this Mach number, the static pressure rise required to separate this shock wave can be computed from Mager's correlation of shock induced separation data given in Figure 3 of Reference 4. Thus a critical base pressure,  $C_{pb c}$ , can be found which is calculable for all configurations. Figure 1(e) indicates that the value of  $C_{pb c}$  thus calculated for the afterbody of Reference 2 corresponds quite well with the departure of the convergent nozzle drag data from the asymptotic level. It is likely that in actuality the terminal shock wave does not begin to separate the boattail boundary layer until  $C_{pb c}$  has been exceeded by some margin but this does not prevent this parameter from being used as a correlation variable.

The analysis of this typical data suggests that the effects of jet induced boattail pressure drag changes might be correlated approximately for other test data by shifting the origin of Figure 1(e) to the point ( $C_{pb c}$ ,  $C_{D\beta AS}$ ).

In passing, it may be noted that Figure 1(e) suggests that the con-di nozzle drag measurements shown in Figure 1(b) did not show any significant change with nozzle pressure ratio simply because the critical base pressure  $C_{pb c}$  was not reached in the tests.

#### 4. CORRELATION OF FURTHER BOATTAIL DRAG DATA

To substantiate the hypothesis of the previous section, test data from References 5 to 15 was examined. Details of the model geometries and flow conditions are shown in Table 1. It can be seen that a wide variety of afterbody shapes and nozzle types were included as were the effects of secondary flow in References 6, 10, 11 and 15. Most of the data is from NACA sources of about 15 to 20 years ago but recent B.A.C. (References 13 and 15) and R.A.E. (Reference 14) results are included. With the exception of Reference 15 which had a twin jet afterbody, the data refers to single jet models.

The reference inviscid calculations for each afterbody were obtained either by the method of characteristics or by Van Dyke's second order method (Reference 3) where presented in the original data sources.

The results of the analysis are shown in Figures 2(a) and 2(b). In each figure it appears that, to a reasonable degree of approximation, the departure of the measured boattail pressure drag  $C_{Dp}$  from the asymptotic value  $C_{DAS}$  is a function of  $C_{pb} - C_{pbc}$  only, thus confirming the hypothesis of Section 3. The effects of variations of free stream Mach number, nozzle and afterbody geometry, nozzle pressure ratio and secondary flow ratio are included. In the interests of legibility only about half of the points analysed are shown in Figure 2(a) but it can be seen in both Figures that the data points are within  $\Delta C_D = \pm 0.01$  of the mean lines. This scatter corresponds to about  $\pm 2$  percent of typical military aircraft supersonic lift drag.

The data of Figure 2(a) (References 2, 5 to 9, 11 to 14) shows a much more powerful effect of a propulsive jet on boattail pressure drag than does the data of Figure 2(b) (References 10 and 15) and the difference in behaviour can be related qualitatively to the corresponding inviscid flow fields. The afterbody shapes included in Figure 2(a) are mainly parabolic or conical and thus exhibit monotonic inviscid pressure distributions of which that shown in Figure 1(d) is typical. In these cases the terminal shock is able to move freely forward along the boattail as the base pressure increases and the increasing boattail pressure level acts over an increasing projected area. Thus the parabolic nature of Figure 2(a) can be anticipated for this type of shape.

The radius distribution of the single jet model of Reference 10 and the equivalent radius distribution of the twin jet model of Reference 15 are similar to each other and have different characteristics to the other boattail shapes. The first 85% to 90% by length of these two radius distributions is almost linear with a slope of about 5 degrees. The remaining 10 to 15 percent consists of a rapid near-parabolic contraction to a final boattail angle of about 25 degrees. Figure 2(c) shows a sketch of the boattail shape for the model of Reference 10. The corresponding inviscid calculations show that a considerable flow expansion exists over the rear parts of these shapes (see Figure 2(d)). Examination of measured boattail pressure distributions in Reference 10 indicated that the rapid flow expansion was limiting the forward movement of the terminal shock wave at increasing nozzle pressure ratios. Thus, although successively higher pressures were acting on the rear portion of the model the projected area over which they were acting was increasing at a relatively low rate. A similar phenomenon probably existed on the twin jet model of Reference 15 since the character of the overall pressure distribution is largely determined by the equivalent volume distribution.

The data of Figure 2(a) is therefore characteristic of 'smooth' idealised boattails, the term smooth being used in the sense of smooth continuous slopes and curvatures and the data of Figure 2(b) is probably more characteristic of 'non smooth' or more practical afterbody shapes.

Clearly, these 'non smooth' boattails exhibit comparatively high values of pressure drag in the presence of a propulsive jet at supersonic speeds since the basic inviscid pressure drag is likely to be relatively high, on account of the high degree of final boattailing and the jet induced drag alleviation is comparatively small. Severe final boattailing can arise from the realities of aircraft layout where it is often necessary to fit a very large, strong frame around the engine or jet pipe to carry the tailplane and its actuating mechanism. The problem is more acute on twin jet installations in which the fuselage volume between the engines is being faired out at the same time.

Figures 2(a) and 2(b) suggest that for the class of 'smooth' boattails the jet induced boattail drag reduction begins when

$$C_{pb} - C_{pbc} = 0.06$$

and rather later for 'non smooth' boattails at

$$C_{pb} - C_{pbc} = 0.01$$

Finally, comparison of theoretical boattail pressure drag coefficients with the asymptotic measured values indicated that

$$C_{DAS} - C_{Dpt} = 0.0075 (1 - \beta/6) (D/E)$$

with most of the data lying about the mean line within a tolerance band of  $\Delta C_D = \pm 0.0050$ . These drag differences are partly due to boundary layer effects and partly due to the influence of the model forebodies and support hardware, none of which was accounted for in the theoretical calculations.

#### 5. CORRELATION OF BASE PRESSURE COEFFICIENT

In order to utilize the data of Figures 2(a) and 2(b), an estimate of the jet-on base pressure coefficient is required. Analytic estimation of this quantity is usually rather tedious and a simple correlation of experimental data is generally preferable from the performance analyst's viewpoint.

By a trial and error inspection of the measured data of the various references, Figures 3(a) and 3(b) have been prepared. Figure 3(a) is a correlation of the difference between the measured jet-on base pressure coefficient,  $C_{pb}$ , and the inviscid theoretical pressure coefficient at the end of the boattail,  $C_{pb}^{pat}$  for choked,  $C_{pb}^{con}$  coplanar convergent nozzles. The ordinate is, in fact, proportional to  $(C_{pb} - C_{pb}^{pat})/C_{pb}^{con}$  and the abscissa can be regarded as a reduced nozzle total pressure ratio which depends upon nozzle and boattail geometry. Figure 3(b) shows the corresponding analysis for underexpanded con-di nozzles, i.e. running at above the design expansion pressure ratio. The effects of secondary flow ratio are not included in Figure 3 but nozzle pressure ratios of up to about 20 have been correlated for each type of nozzle.

Figure 3 shows that for low values of the reduced nozzle total pressure ratio, convergent nozzles produce a greater degree of base pressurisation than do con-di nozzles and at higher reduced pressure ratios the two mean curves appear to become coincident.

Clearly, these base pressure correlations are not universal since meaningful predictions are not obtained from the Figures for an axial exit nozzle in a cylindrical boattail ( $\epsilon = 0, \beta = 0$ ). The Figure should not be used outside the geometry ranges of Table 1.

The range of jet to free stream total temperature ratio for the data considered was from 1.0 to 2.6 and within this relatively small range no significant effects on base pressure were observed.

#### 6. EXAMPLE CALCULATION

The preceding correlations of jet induced boattail drag changes and base pressures have been used to compare the installed performances of a convergent and a con-di nozzle in related parabolic boattails. Sketches of the installations and relevant geometrical details are shown in Figure 4(a). The con-di nozzle installation is formed by extending the convergent nozzle boattail downstream by one throat diameter and then shifting the parabolic contour to pass through the resulting base area. The con-di nozzle has a design pressure ratio of 8 which corresponds to an area ratio of 1.7 and a fully expanded jet Mach number of 2.0. The throat and maximum areas of the two installations are identical and are supposed to be matched to a typical modern reheated turbofan which has operating pressure ratios of approximately 8 and 10 at Mach numbers of 1.6 and 2.0 respectively. The con-di nozzle is therefore operating at its design pressure ratio at  $M_{\infty} = 1.6$  and at  $M_{\infty} = 2$ , the nozzle is underexpanded so that the jet Mach number and the free stream Mach numbers are equal.

The nozzles are compared in terms of a gross thrust efficiency defined by

$$\frac{X_G - D}{X_G \text{ CON}}$$

where  $X_G$  is nozzle exit gross thrust and  $D$  includes both the boattail and base annulus pressure drags.

Figure 4(b) shows that  $M_{\infty} = 1.6$ , the 6 percent uninstalled gross thrust advantage possessed by the con-di nozzle relative to the convergent nozzle on the operating line is reduced to less than 2 percent when the different levels of jet on afterbody drag are accounted for. If the con-di nozzle was replaced by an ejector nozzle of the same design pressure ratio, the comparative performance of the sophisticated nozzle would be worse on account of the momentum drag of the secondary flow. The net force on the boattail plus base annulus changes from a drag to a thrust at jet pressure ratios of approximately 9.5 and 22.5 for the convergent and con-di nozzles respectively. However at  $M_{\infty} = 2.0$  where the con-di nozzle is appreciably underexpanded, the installed efficiency of the con-di nozzle is some 7 percent better than that of the convergent nozzle. This difference is only slightly less than the uninstalled gross thrust advantage. The efficiency of the con-di nozzle installation on the engine operating line is increased by about 2.5 percent between Mach numbers of 1.6 and 2.0 whereas the efficiency of the convergent nozzle installation is reduced by almost the same amount. This is mainly due to the different effects of Mach number and jet pressure ratio on the drags of the two boattails on the operating line as shown in Figure 4(c). The dotted lines in Figure 4(c) indicate extrapolation to the asymptotic drag value  $C_{DAS}$  and the calculation suggests that the effects of jet flow on boattail pressure drag are likely to be more significant at say  $M_{\infty} = 1.6$  than at  $M_{\infty} = 2.0$  especially for convergent nozzles.

The results of the example calculation raise two important points. Firstly, are sophisticated nozzles, which rely mainly on thrust augmentation either by geometric or aerodynamic means, a better overall proposition than the simple convergent nozzle, which can experience a large amount of favourable jet interference? Secondly, experimental comparisons between simple and sophisticated nozzles could be misleading if the nozzles are mounted in afterbodies which are not comparable from an aircraft layout viewpoint. For example, if various nozzles are being matched to a given engine in a given aircraft, the ratio  $d_n/d_m$  should be the same for each of the nozzle installations being compared, but the ratio  $d_n/d_m$  and the boattail angle  $\beta$  should be matched to each nozzle. Such a test technique would be more costly but more representative than fitting a number of different nozzles into a common afterbody.

#### 7. CONCLUDING REMARKS

It has been shown that jet induced boattail pressure drag alleviation at supersonic speeds can be related to the difference between the measured base pressure coefficient  $C_{pb}$  and a critical base pressure coefficient  $C_{pb}^{crit}$ . This critical value is theoretically just high enough to separate the boattail terminal shock wave which is assumed to occur at the inviscid Mach number at the end of the boattail. The use of base pressure as a correlation variable eliminates to first order the independent effects of nozzle geometry, nozzle pressure ratio and secondary flow ratio.

Idealised conical or parabolic boattails exhibit much larger jet induced pressure drag reductions than do more practical shapes which may involve a high degree of boattailing in the region close to the base.

Convergent nozzles in general experience larger jet induced effects than con-di nozzles which in some flight conditions can offset a large proportion of the thrust gain of the con-di nozzle.

#### 8. REFERENCES

1. H. McDonald  
P.F. Hughes      A Correlation of High Subsonic Afterbody Drag in the Presence of a Propulsive Jet or Support Sting.  
J. Aircr. Vol.2 No.3 May-June 1965, pp. 202-207.
2. D.P. Hearsh  
G.C. Gorton      Investigation of Thrust and Drag Characteristics of a Plug-Type Exhaust Nozzle.  
NACA RM E53L16 December, 1953.
3. M.D. Van Dyke      First and Second Order Theory of Supersonic Flow past Bodies of Revolution.  
J. Aeronaut. Sci. Vol 18 No.3 March 1951 pp 161-178.
4. A. Mager      Transformation of the Compressible Turbulent Boundary Layer.  
J. Aeronaut. Sci. Vol.25 No.5 May 1958, pp 305-311.
5. G.W. Englert  
D.J. Vargo  
R.W. Cubbison      Effect of Jet Nozzle Expansion Ratio on Drag of Parabolic Afterbodies.  
NACA RM E54 B12 February, 1954.
6. G.C. Gorton      Pumping and Drag Characteristics of an Aircraft Ejector at Subsonic and Supersonic Speeds.  
NACA RM E54D06 March 1954.
7. D.J. Vargo  
G.W. Englert      Effect of Nozzle Contour on Drag of Parabolic Afterbodies.  
NACA RM E54D02 March 1954.
8. L.E. Baughman  
F.D. Kochendorfer      Jet Effects on Base Pressures of Conical Afterbodies at Mach 1.91 and 3.12.  
NACA RM E57E06 May 1957.
9. R.M. O'Donnell  
R. W. McDearman      Experimental Investigation of Effects of Primary Jet Flow and Secondary Flow through a Zero-length Ejector on Base and Boattail Pressures of a Body of Revolution at Free Stream Mach Numbers of 1.62, 1.93, 2.41.  
NACA RM L54I22 September 1954.
10. A.S. Valerino  
R.A. Yeager      External Stream Effects on Gross Thrust and Pumping Characteristics of Ejectors Operating at Off Design Mach Numbers.  
NACA RM E56C14 March 1956.
11. J.L. Klann  
R.G. Huff      Characteristics of Five Ejector Configurations at Free Stream Mach Numbers from 0 to 2.0.  
NASA TM X-23 August 1959.
12. C. Pel  
A. Rustmeyer      Investigation of Turbojet Exhaust - Interference Drag.  
U.A.C. Research Report R-0801-12 November 1955.
13. C. Davenport  
A. Watson      Axisymmetric Afterbody Tests.  
B.A.C. Warton Report AX/VG/5 February 1966
14. J. Reid      R.A.E. Farnborough Wind Tunnel Results.  
Private Communication April 1971.
15. Unpublished      B.A.C. Warton Wind Tunnel Results.

REFERENCE NUMBER	BOATTAIL TYPE	$\beta$ (DEG)	$d_b/a_m$	NOZZLE TYPE	$d_j/d_b$	NOZZLE AREA RATIO	$\epsilon$ (DEG)	$M_\infty$	SYMBOL
2	PARABOLIC	11.9	0.79	CON PLUG	0.94	1.00	-5.0	1.6,2.0	$\Delta$
				CON-DI PLUG	0.94	1.45	-5.0	1.6,2.0	$\nabla$
5	PARABOLIC	17.1	0.55	CON	0.90	1.00	0	1.6,2.0	$\circ$
		15.3	0.64	CON-DI	0.92	1.44	18.8		$\square$
		13.7	0.72	CON-DI	0.93	1.83	26.4		$\diamond$
6	PARABOLIC	15.7	0.62	EJECTOR	0.79	1.44	-12.0	1.6,2.0	$\beta$
7	PARABOLIC	17.1	0.55	CON	0.90	1.00	-12.0	1.6,2.0	$\Delta$
		17.1	0.55	CON	0.90	1.00	0		$\Delta$
		15.3	0.64	CON-DI	0.92	1.44	18.4		$\Delta$
		15.3	0.64	CON-DI	0.90	1.39	3.6		$\Delta$
		15.3	0.64	CON-DI	0.92	1.44	0		$\Delta$
8	CONICAL	5.6	0.53	CON	0.90	1.00	0	1.91	$\gamma$
9	CIRC. ARC	21.2	0.55	CON	0.64	1.00	0	1.62,1.93,2.41	Y
		21.2	0.55	CON-DI	0.55	5.25	12.0		$\lambda$
10	PARABOLIC- CONICAL- PARABOLIC	24.5	0.56	EJECTOR	0.81	1.35	-2.9	1.5,1.8,2.0	X
					0.55	2.90	-4.0		
					0.65	2.09	-8.8		
11	CONICAL- CONICAL	12.5	0.61	EJECTOR	0.52 TO	1.69 TO	- VE	1.5,1.8,2.0	N
					0.73	3.24			
12	CONICAL	15.0	0.75	CON	0.56	1.00	-15.0	1.50	+
13	PARABOLIC	16.0	0.58	CON	0.59	1.00	0	1.42	$\gamma$
14	PARABOLIC	16.0	0.63	CON	0.80	1.00	0	2.00	$\gamma$
		16.0	0.71	CON	0.70	1.00	0		$\gamma$
		16.0	0.83	CON	0.60	1.00	0		$\gamma$
		12.0	0.71	CON	0.70	1.00	0		$\gamma$
		20.0	0.71	CON	0.70	1.00	0		X
15	TWIN JET AFTERBODY MODEL			CON				1.80	*

TABLE 1.

SUMMARY OF EXPERIMENTAL DATA USED

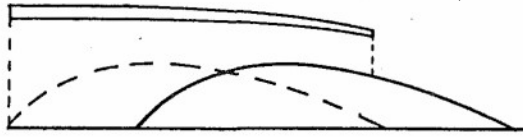


Figure 1(a) Sketch of Afterbody Model of Reference 2.  
 — Plug in Convergent Position.  
 --- Plug in Con-Di Position.

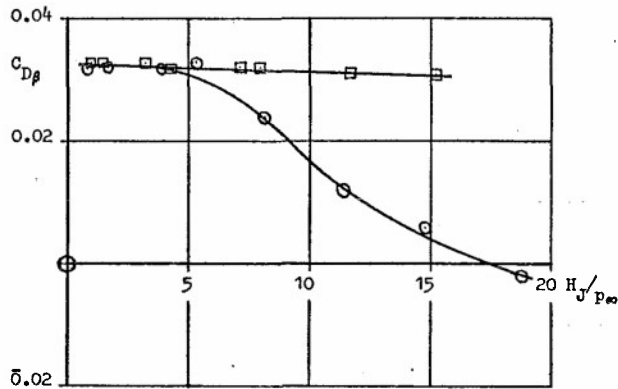


Figure 1(b) Typical Effects of Nozzle Pressure Ratio on Boattail Pressure Drag Coefficient.  
 $M_\infty = 2.0$  Data from Reference 2.  
 ○ Convergent Nozzle. □ Con-Di Nozzle.

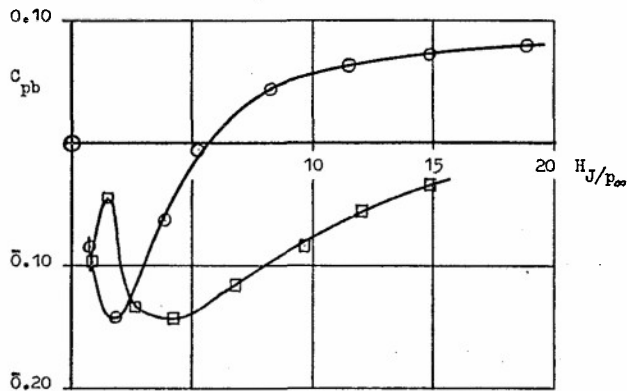


Figure 1(c) Typical Effects of Nozzle Pressure Ratio on Base Pressure Coefficient.  
 $M_\infty = 2.0$  Data from Reference 2.  
 ○ Convergent Nozzle. □ Con-Di Nozzle.

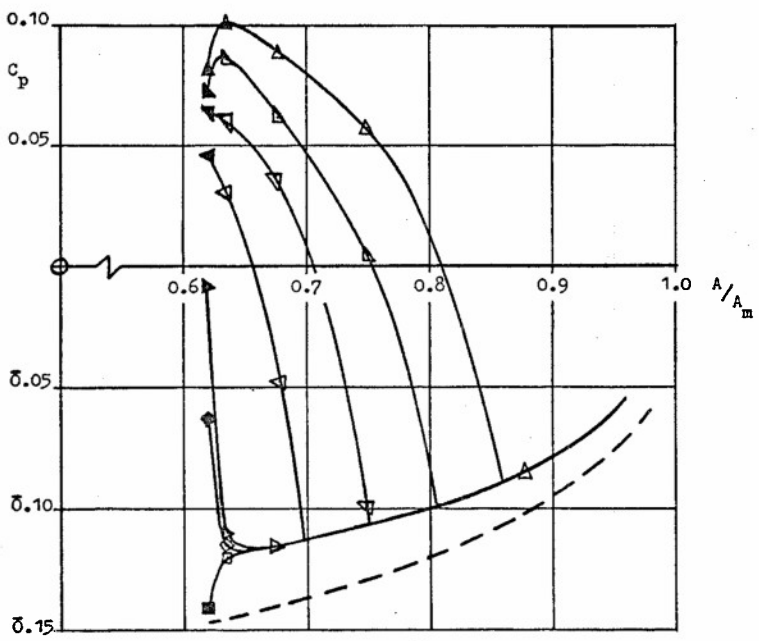


Figure 1(d) Typical Effects of Nozzle Pressure Ratio on Boattail Static Pressure Distribution.  
 $M_{\infty} = 2.0$ . Data from Reference 2. Convergent Nozzle.  
 $\square H_j/p_{\infty} = 1.8$   $\triangleleft H_j/p_{\infty} = 8.1$   $\triangle H_j/p_{\infty} = 18.8$   
 $\diamond 4.0$   $\nabla 11.3$   
 $\triangleright 5.3$   $\blacktriangle 14.8$   
 --- Inviscid Theory from Reference 3. *Van Dyke 1951*  
 Solid Symbols indicate Base Pressure Measurements.

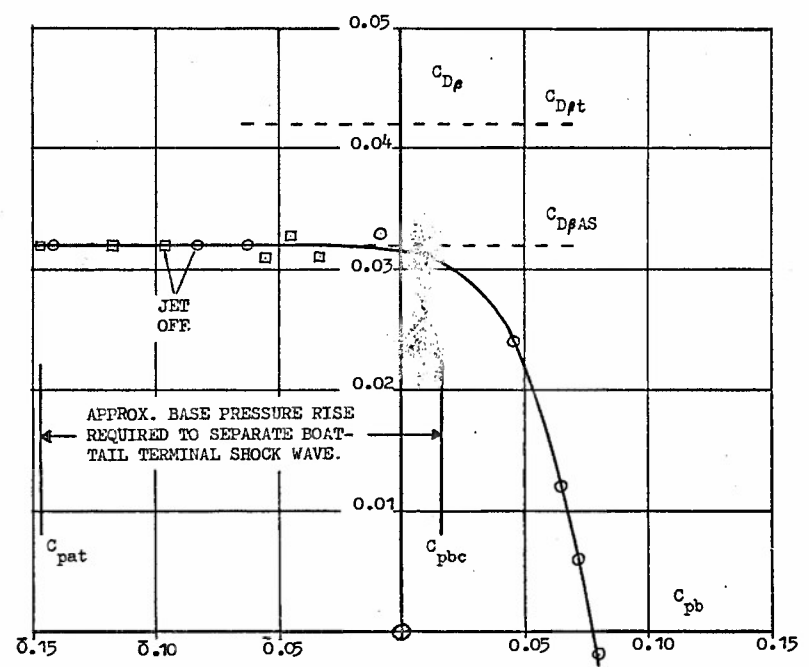


Figure 1(e) Analysis of Typical Propulsive Jet Effects on Afterbody Drag.  
 $M_{\infty} = 2.0$ . Data from Reference 2.  
 O Convergent Nozzle. E Con-Di Nozzle.

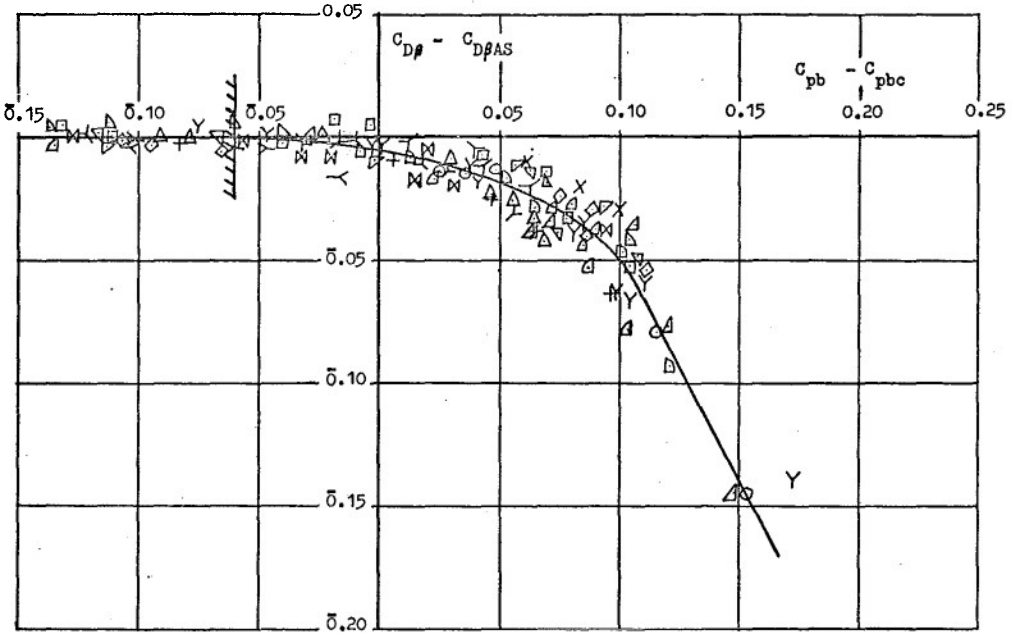


Figure 2(a) Jet Induced Boattail Pressure Drag Reduction at Supersonic Speeds for 'Smooth' Shapes.  $M_\infty = 1.4$  to  $2.4$ . For Symbols, see Table 1.

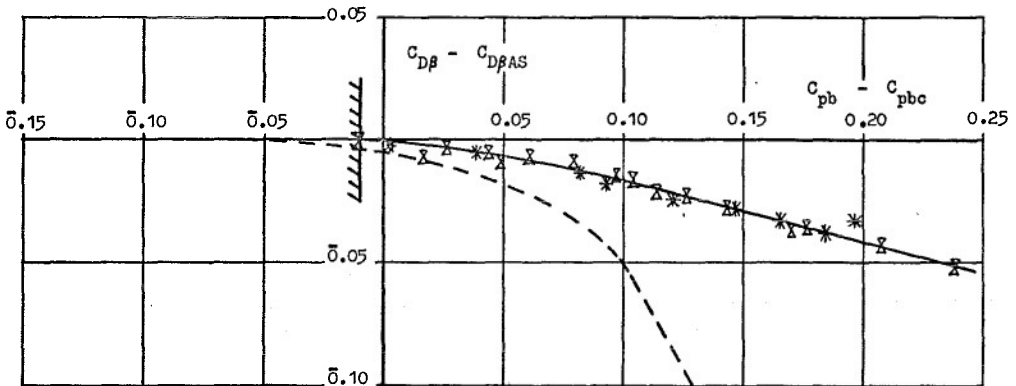


Figure 2(b) Jet Induced Boattail Pressure Drag Reduction at Supersonic Speeds for 'Non-Smooth' Shapes.  $M_\infty = 1.5$  to  $2.0$ . For Symbols, see Table 1. ----- Mean line from Figure 2(a).

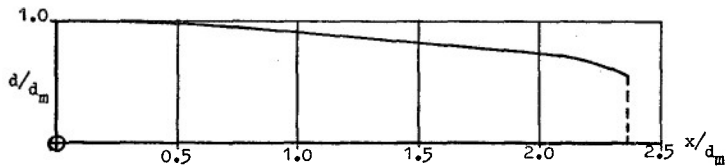


Figure 2(c) Boattail Shape of Reference 10.

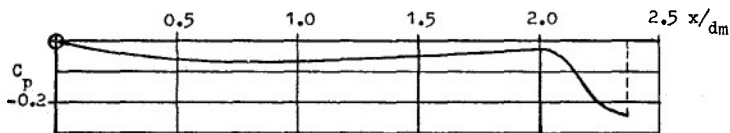


Figure 2(d) Inviscid Pressure Distribution for Boattail of Reference 10.  $M_\infty = 2.0$ . Method of Characteristics.

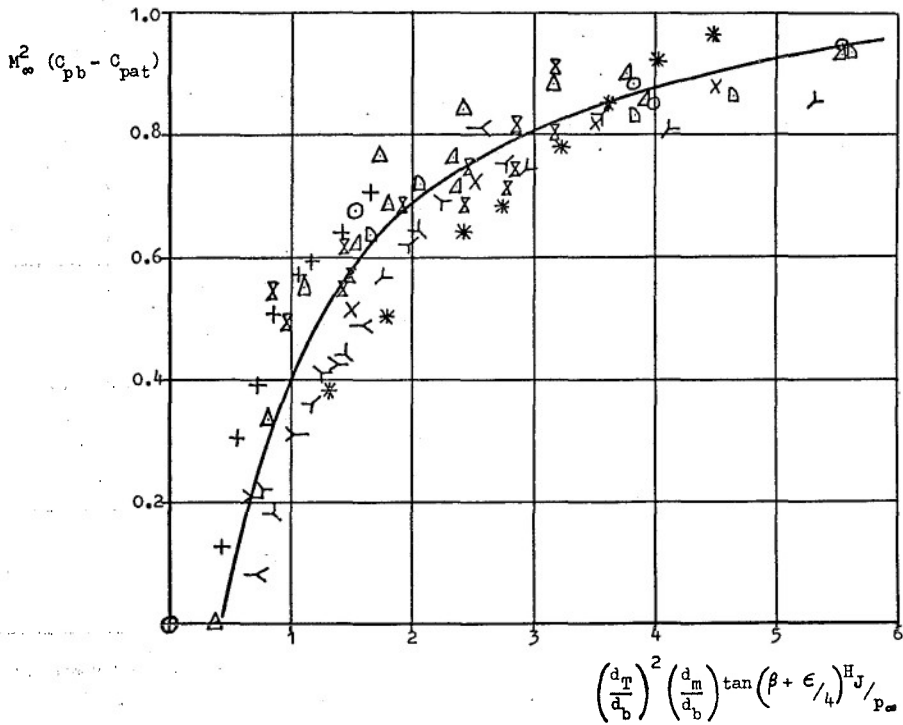


Figure 3(a) Base Pressure Coefficient at Supersonic Speeds for Choked Convergent Nozzles.  $M_\infty = 1.4$  to  $2.0$ . For Symbols, see Table 1. Coplanar Nozzles, No Secondary Flow.  $H_J/P_\infty > 2.5$ .

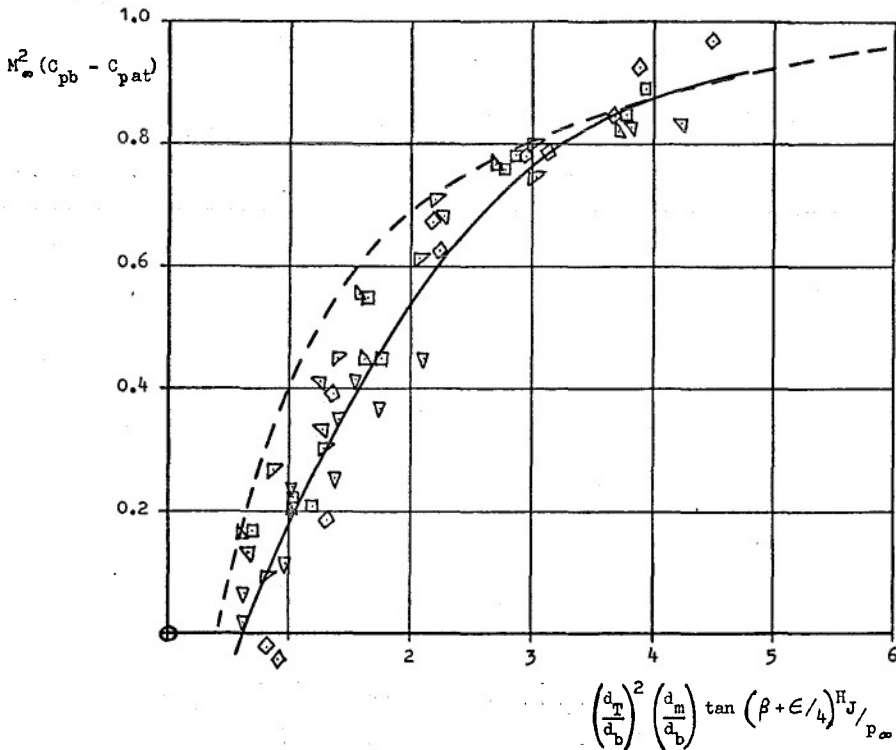
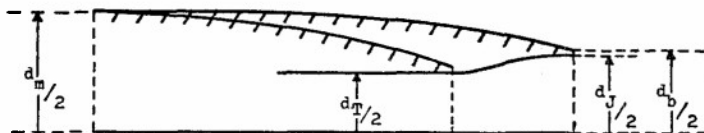


Figure 3(b) Base Pressure Coefficient at Supersonic Speeds for Under-expanded Con-Di Nozzles.  $M_\infty = 1.6$  to  $2.0$ . For Symbols, see Table 1. Coplanar Nozzles, No Secondary Flow.  $H_J/P_\infty$  Design Pressure Ratio. --- Mean Line from Figure 3(a).



	$d_b/d_m$	$\beta$	$d_J/d_b$	$\epsilon$	$d_T/d_m$	$(d_J/d_T)^2$	$M_J$
Con Nozzle	0.55	17.1	0.91	0	0.50	1.0	1.0
Con-Di Nozzle	0.70	13.7	0.93	0	0.50	1.7	2.0

Figure 4(a) Installation of Convergent and Con-Di Nozzles.

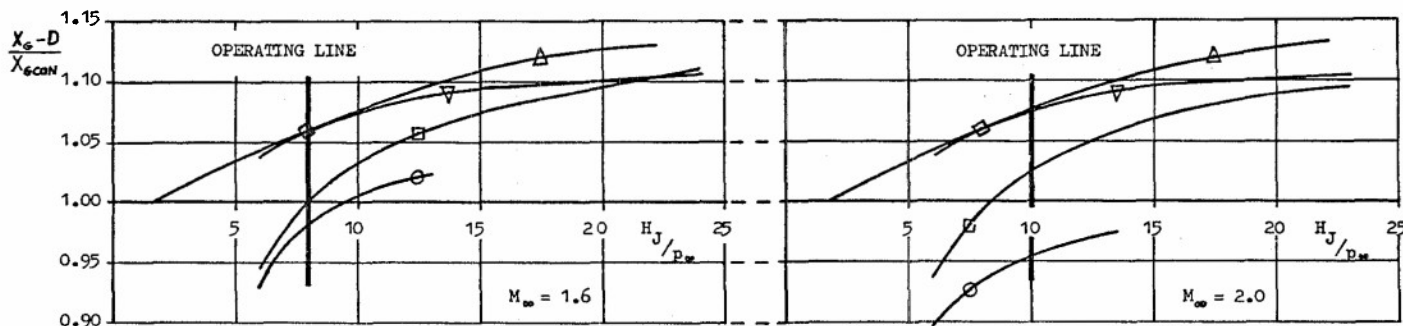


Figure 4(b) Gross Thrust Efficiency

$\Delta$  Uninstalled Envelope of Possible Con-Di Nozzles.  $\nabla$  Uninstalled Example Con-Di Nozzle.  
 $\diamond$  Example Con-Di Nozzle Design Point.  $\square$  Installed Example Con-Di Nozzle.  
 $\circ$  Installed Example Convergent Nozzle

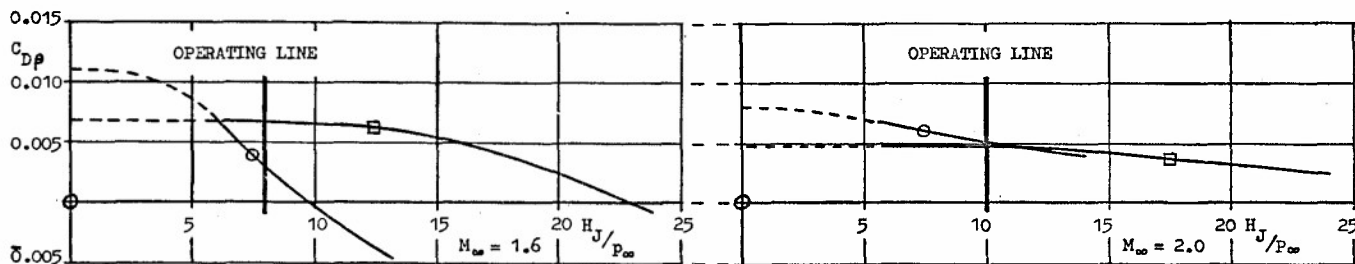


Figure 4(c) Boattail Pressure Drag

$\circ$  Installed Convergent Nozzle.  $\square$  Installed Con-Di Nozzle





Figure 1. Photograph of the two F-111A test airplanes.

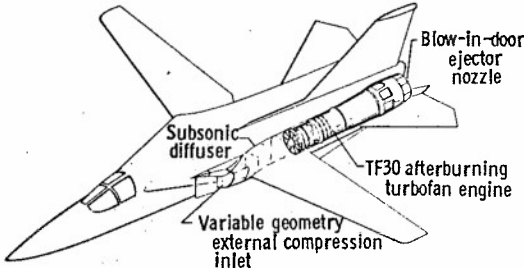


Figure 2. F-111A left propulsion system.

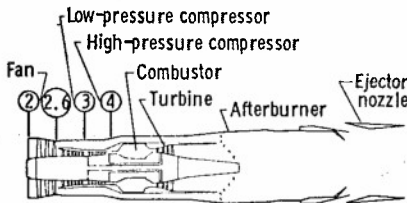


Figure 3. TF30 afterburning turbofan engine and appropriate station designations.

varied by translating the compression spike fore and aft and by varying the second conical ramp (cone) angle from  $10.5^\circ$  to  $24^\circ$ . The first conical ramp is fixed at  $12.5^\circ$ .

At low speeds the spike is forward and the cone is collapsed, as shown in figure 4. At high supersonic speeds, the spike is aft and the cone is fully expanded. This configuration is shown in figure 5. Positions of the spike and cone are normally controlled by an automatic inlet control system, described in reference 6. The left inlet geometry could be manually positioned by the pilot to any desired position on both test airplanes.

Two different cowl lip configurations were tested. A sharp lip cowl (fig. 4) was tested on both airplanes. A cowl with a blunted lip (fig. 5) was flown on airplane number 6 for several flights. This cowl, in addition to the more rounded lip, was drooped and cut back 5 centimeters over the inboard part and had a slightly larger capture area.

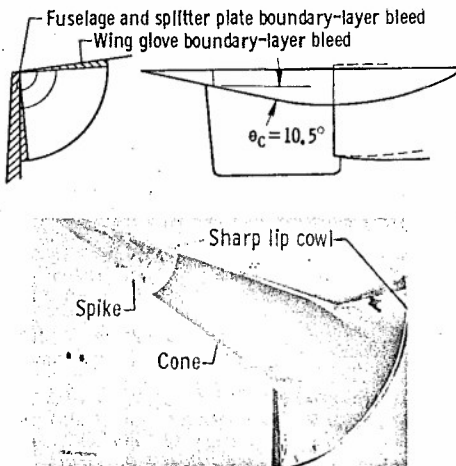


Figure 4. Photograph and two-view drawing of the F-111A inlet with sharp lip cowl installed, spike full forward, and cone fully collapsed.

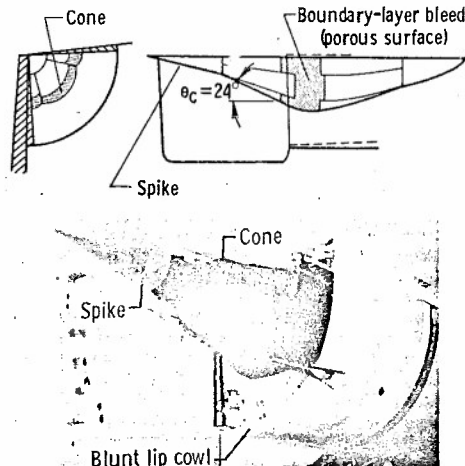


Figure 5. Photograph and two-view drawing of the F-111A inlet with blunt lip cowl installed, spike full aft, and cone fully expanded.

**Subsonic diffuser.**— The inlet subsonic diffuser (fig. 2) turns inboard and changes in shape from a one-quarter circle near the inlet to a circular shape at the compressor face in a relatively short length. The cross-sectional area

swept, the airplane is designed for supersonic dash capability at sea level and Mach 2.5 at altitude.

The two F-111A airplanes used in the NASA tests were both early models, numbers 6 and 12 (fig. 1). The only significant differences between the airplanes for these tests were in the inlet, as discussed later.

**Propulsion System**

The left propulsion system of the F-111A airplane is shown in figure 2. Thrust is provided by two TF30 afterburning turbofan engines mounted in the aft fuselage. The engines are equipped with blow-in-door ejector nozzles that admit external air at low speeds to control nozzle expansion. Air is supplied to the engine by an inlet mounted under the wing glove followed by a short subsonic diffuser.

**Engine.**— The TF30-P-1 engine has approximately 80,000 newtons of thrust and a nominal bypass ratio of 1.0. Figure 3 is a schematic view of the engine. A three-stage fan and a six-stage low pressure compressor is driven by a three-stage turbine at  $N_1$  speed. A seven-stage high pressure compressor is driven by a separate turbine. Rated airflow is 110 kilograms per second and overall compression ratio is 17 to 1. A five-zone afterburner is located in the combined fan and core streams. The engines tested were equipped with sixth-stage bleeds to increase the distortion tolerance of the compressor. These bleeds were usually opened for Mach numbers above 1.8. The engines tested in the two airplanes were essentially identical. More information on the engine is included in references 4 and 5.

**Inlet.**— The air inlet shown in figures 4 and 5 is a variable-geometry external-compression type and is approximately a  $90^\circ$  segment of a double cone axisymmetric inlet. Inlet geometry can be

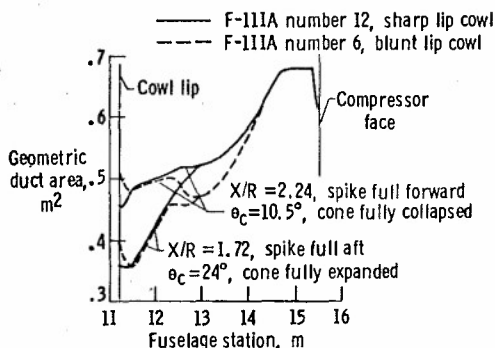


Figure 6. Inlet duct area distribution for F-111A number 6 and number 12.

distributions for both airplanes are shown in figure 6. It can be seen that the latter configuration (airplane number 12) diffuses the air more gradually in the middle part of the duct. Vortex generators (fig. 7) are installed to minimize separation in the duct and to improve the pressure distribution at the compressor face.

**Boundary-layer removal system.**—The F-111A inlet incorporates several regions of boundary-layer removal to prevent low energy air from entering the inlet. Fuselage, splitter plate, and wing glove bleed scoops are shown in figure 4 and porous bleed on the second cone surface in figure 5.

#### INSTRUMENTATION

Figure 7 shows the location of pressure measurements in the left inlet of the F-111A airplane. Table 1 describes the number of measurements, their sampling rates, and their frequency responses for the airplanes. Miniature

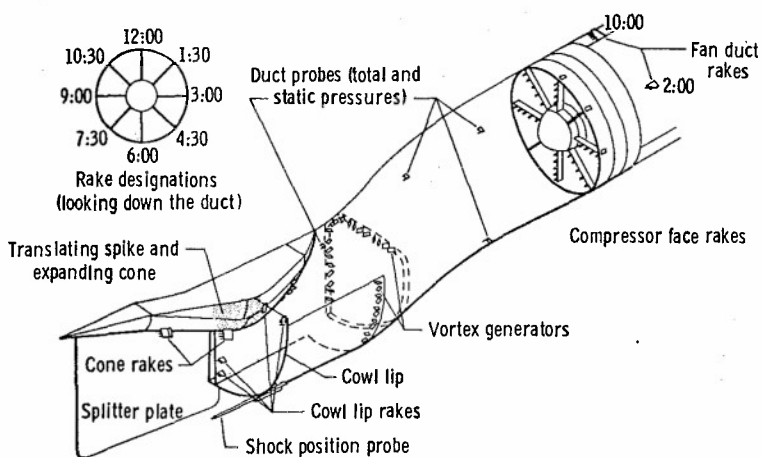


Figure 7. Inlet and compressor face pressure instrumentation.

TABLE 1. — NUMBER OF MEASUREMENTS, SAMPLING RATE, AND FREQUENCY RESPONSE OF PRESSURES IN THE F-111A INLET

Location of pressures	Number of measurements		Samples per second	Frequency response, Hz
	F-111A no. 6	F-111A no. 12		
Cone rake:				
Total pressure	8	--	400	200
Static pressure	2	--	400	200
Cowl lip:				
Total pressure	12	--	200	100*
Static pressure	4	--	200	100*
Shock position probe	6	--	200	100*
Inlet duct:				
Total pressure	4	--	200	100
Static pressure	4	--	200	100
Compressor face:				
Total pressure, low response	20	--	50	10
Total pressure, high response	20	40	400	200
Compressor face:				
Total pressure	2	2	Analog	1000
Static pressure	16	4	200	100*
Fan duct total pressure	8	--	200	100*
Low compressor discharge static pressure	1	1	200	100*
High compressor discharge static pressure	1	1	200	100*

\*Parameter filtered at 40 hertz prior to digitizing; amplitude uncertain above 40 hertz.

subject to large zero shifts due to temperature changes, and their steady-state values were not reliable. Eight high response compressor face rakes were flown in airplane number 12. These were a special type with in-flight nulling capability to determine the transducer zero, as often as desired, so that steady-state as well as dynamic values could be obtained. Details of the rake design are presented in reference 7. Figure 8 is a photograph showing the rake installation at the engine compressor face. A schematic view of this rake is shown in figure 9. Figure 10 shows an example of the rake zero checks made on two compressor face total pressures before and after a compressor stall.

transducers were located in the two cone rakes, the shock position probe, the duct rakes, and the diagonally oriented compressor face rakes to provide high frequency response. Conventional probes connected by tubes to remotely located transducers were used for the cowl lip rakes, the horizontal and vertically oriented compressor face rakes, and internal engine instrumentation. The tube lengths limited flat frequency response to about 50 hertz. Details of the instrumentation on airplane number 6 are included in references 1 and 3 through 6. Differential pressure transducers were used for all measurements except the internal engine measurements. Some of the techniques used to obtain the dynamic pressure measurements are described in reference 7.

The miniature transducers gave good values for dynamic pressure but were

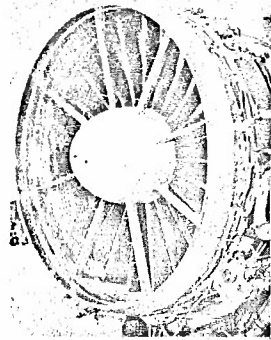


Figure 8. Photograph of the TF30 engine showing the compressor face rakes with in-flight nulling capability.

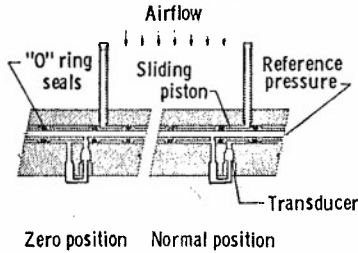


Figure 9. High response compressor face rake with in-flight nulling capability.

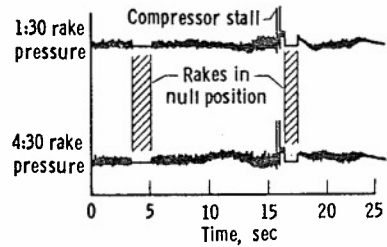


Figure 10. Compressor face rake pressure zeros before and after a stall.

The need for the zero checks can be seen in figure 11, which shows the traces of 2 compressor face rake pressures over a 3-minute period of flight.

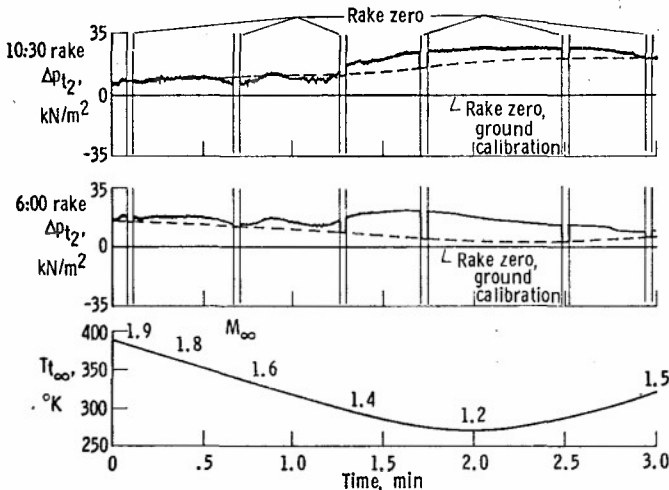


Figure 11. Time history of F-111A compressor face rake pressures showing zero shifts with temperature during supersonic flight.

number, altitude, angle of attack, inlet spike and cone position, and the value of the reference pressure supplied to the differential transducers.

#### DATA RECORDING

Output signals from the transducers were digitized by pulse code modulation (PCM) systems and recorded on magnetic tape. Two PCM systems were used, each with 77 channels sampled 200 times per second. The compressor face pressures were sampled 400 times per second by using two channels for each pressure, thus allowing frequency analysis to be extended from 100 hertz to 200 hertz. All compressor face pressure signals were filtered electrically prior to digitizing, to remove high frequencies, with cutoff starting at 200 hertz. Two of the compressor face pressures were also recorded on a wide-band frequency modulation (FM) system to permit analog analysis to much higher frequencies. These two channels were filtered, with cutoff starting at 1000 hertz, prior to recording.

Outputs of the PCM and FM systems were recorded on an onboard tape recorder. Part of the data was also telemetered to the ground to permit real time data monitoring and analysis.

#### DATA REDUCTION

Flight tapes containing the digital data were processed using a digital computer. Voltage monitor corrections and zero corrections were incorporated, and calibrations were applied. Output data were available in the form of parameter listings, calculated performance time histories, time history plots, and cross plots. The digital data were statistically analyzed by a digital computer program.

Analog pressure data and digital pressure data converted to analog data were processed by using a hybrid spectrum analyzer. In some instances, this system was used for real time analysis of pressures during flights.

#### DATA ANALYSIS

Several parameters are used in this paper to describe and analyze the pressure fluctuations observed in the inlets.

##### Instantaneous Parameters

A parameter which can be calculated with one sample of data from each pressure may be said to be "instantaneous,"

within the limitation of the sampling rate of 400 per second.

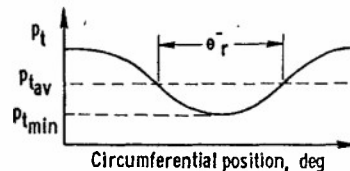
**Pressure recovery.**— The compressor face average total pressure recovery is calculated by averaging the probe values and dividing by the free-stream total pressure.

**Distortion factor,  $K_D$ .**— A distortion parameter derived by Pratt & Whitney for the TF30 engine is the  $K_D$  parameter. It considers the circumferential extent of distortion and weighs distortion near the engine hub more heavily than at the tip. The  $K_D$  parameter is defined as follows:

$$K_D = \frac{\sum_{r=1}^n \left[ \left( \frac{\Delta p}{p} \right)_r \left( \frac{d_o}{d_r} \right)^2 \theta_r \right]}{\sum_{r=1}^n \left( \frac{d_o}{d_r} \right)^2}$$

where

- $r$  a particular ring of total pressure probes
- $\left( \frac{\Delta p}{p} \right)_r = \frac{p_{t_{av}} - p_{t_{min}}}{p_{t_{av}}} \times 100$ , in percent, for a particular ring
- $p_{t_{av}}$  average pressure per ring
- $p_{t_{min}}$  minimum pressure per ring
- $d_o$  outer diameter of duct
- $d_r$  diameter of a particular ring
- $\theta_r$  circumferential extent of largest single pressure depression below  $p_{t_{av}}$ , in degrees, for a particular ring (see adjacent sketch)
- $n$  number of measurement rings



#### Statistical Parameters

Computation of statistical parameters such as those discussed below requires a considerable amount of data. These parameters are described briefly here; more rigorous definitions are presented in reference 8.

**Turbulence factor,  $T_u$ .**— The dynamic activity of a fluctuating pressure is indicated by the turbulence parameter,  $T_u$ , defined as the root mean square total pressure level divided by the average total pressure.

$$T_u = \frac{p_{t_{rms}}}{p_{t_{av}}}$$

**Power spectral density, PSD.**— A useful parameter for detecting predominant frequencies in a fluctuating pressure is the power spectral density parameter, PSD. It is also useful in comparing data from separate sources, such as flight data to wind-tunnel data or ground facility data. The square root of the area under the PSD curve is equal to the turbulence factor.

**Coherence.**— The coherence function provides a measure of the extent to which the pressure fluctuations at two probes arise in common sources, that is, the linear interdependence of the two pressures, at a specific frequency. Coherence ranges from 0 (no interdependence) to 1.0 (perfect interdependence). Coherence values less than 0.2 generally indicate no significant interdependence.

**Phase angle.**— The phase angle function provides an indication of the time delay between the two pressures as a function of frequency. For example, two pressures with a common frequency are  $180^\circ$  out of phase if at an instant of time one pressure is at a maximum while another pressure is at a minimum.

**Calculation of statistical parameters.**— The statistical parameters were calculated from the digital data by using a fast Fourier transform digital program. Input data were detrended prior to analysis to remove any very low frequencies. A total of 2048 data points (5.12 seconds) was used for the 400 samples per second compressor face pressure data, with an equivalent filter bandwidth of 2 cycles. A total of 1024 data points (5.12 seconds) was used for the cowl lip rake, shock position probe, duct total and static pressures, and engine pressures, all of which were sampled 200 times per second. The statistical parameters were valid for frequencies up to one-half of the sampling rate (ref. 8); however, some of the pressures were filtered to less than one-half of the sampling rate because of the probe resonant frequencies.

Power spectral densities calculated from the analog recording system were extended to 1000 hertz, even though the probe response was not flat beyond about 400 hertz. Eight seconds of data were used with an equivalent two-cycle bandwidth filter.

#### Duct Resonance Analysis

The formula for the resonant frequency of a pipe open at one end is given in reference 9 by

$$f_1 = \frac{c}{2(l + 0.82a)}$$

where

- $f_1$  first fundamental frequency of the pipe
- $c$  speed of sound, m/sec
- $l$  pipe length, m
- $a$  average pipe radius, m

If the flow velocity in the pipe is not small, the following correction can be made:

$$f_1' = f_1 (1 - M_{d_{av}}^2)$$

where

- $f_1'$  first fundamental frequency corrected for flow
- $M_{d_{av}}$  average Mach number of the flow

The quantity  $M_{d_{av}}$  was determined by calculating the Mach number at several duct stations using the known engine air-flow and the duct area distribution, and averaging the results. Substituting for the speed of sound, this becomes

$$f_1' = 20.4 \frac{\sqrt{T_t}}{2(l + 0.82a)} \sqrt{1 + 0.2M_{d_{av}}^2} (1 - M_{d_{av}}^2)$$

For the F-111A inlet duct

$$l = 4\text{m}, a = 0.4\text{m}$$

so

$$f_1' = 2.38 \sqrt{T_t} \frac{(1 - M_{d_{av}}^2)}{\sqrt{1 + 0.2M_{d_{av}}^2}}$$

For the engine fan duct resonance

$$l = 2.74\text{m}, a = 0.3\text{m}$$

$$f_1' = 3.4 \sqrt{T_t} \frac{(1 - M_{d_{av}}^2)}{\sqrt{1 + 0.2M_{d_{av}}^2}}$$

RESULTS AND DISCUSSION

Steady-State Performance

The steady-state performance of the inlet is shown in terms of the inlet total pressure recovery and distortion factor, as a function of mass-flow ratio and angle of attack, for a Mach number of about 2.15. Wind-tunnel data from a 1/6-scale model (ref. 10) are also shown for comparison. As shown in figure 12, the flight recovery data are relatively insensitive in the sub-critical region to mass flow ratio and are slightly lower than the wind-tunnel results. The inlet becomes unstable at a mass flow ratio of about 0.80, as predicted by the wind-tunnel results. An inlet duct resonance discussed in a later section occurs between  $m/m_0 = 0.89$  and  $0.94$ .

The operating point,  $m/m_0$  of 0.97, is above the resonance mass flow and appears to represent slightly supercritical operation. The lower mass flow and recovery are probably due to fuselage boundary-layer ingestion which did not occur in the wind-tunnel tests. The  $K_D$  distortion factor increases rapidly with increasing mass flow ratio except for mass flow ratios near the stability limit. Values of  $K_D$  at the operating point are near the stall value, as will be discussed in the compressor stall section. Data obtained at a slightly lower Mach number are shown in figure 13 as a function of angle of attack. Both recovery and distortion increase as angle of attack increases from  $2^\circ$  to  $6^\circ$ . Further increases in angle of attack have only a small effect on recovery and distortion. A single wind-tunnel data point at  $\alpha = 5.5^\circ$  agrees well with the flight data.

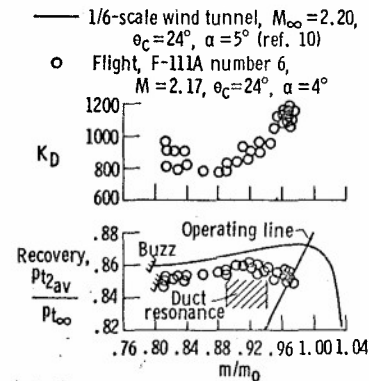


Figure 12. Effect of mass flow ratio on inlet recovery and distortion.

cone position are reported in reference 6 for F-111A number 6. A typical example is shown in figure 14 at a Mach number of 1.60. Recovery, distortion factor, and turbulence factor are plotted as functions of spike position with the cone fixed and as functions of the cone angle with the spike fixed. The automatically scheduled positions are nearly optimum at this flight condition. Moving the spike aft has only a small effect, but moving the spike forward increases the turbulence factor and  $K_D$  and results in compressor stall. The cone can be fully retracted, but  $K_D$  and turbulence

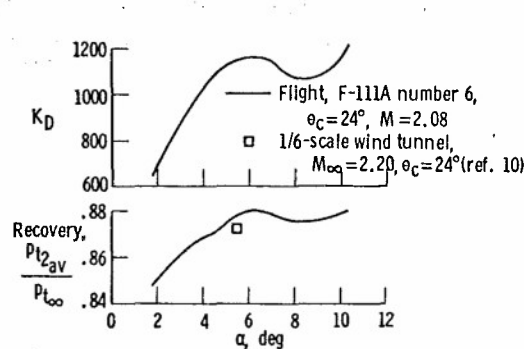


Figure 13. Effect of angle of attack on inlet recovery and distortion.

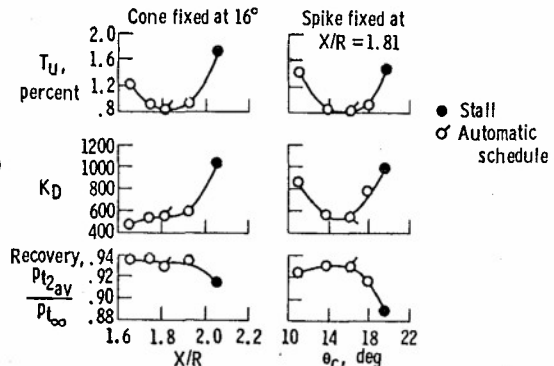


Figure 14. Effect of spike and cone position on inlet performance at Mach 1.60.

rise to near the stall level. Expanding the cone decreases recovery and increases turbulence and distortion and causes a compressor stall.

### Dynamic Analysis

**Compressor stall analysis.**— The occurrence of TF30 engine compressor stalls in the F-111A airplanes could not be satisfactorily correlated with inlet conditions until dynamic pressure measurements were made at the engine compressor face (ref. 4). Four of the eight compressor face rakes tested in F-111A number 6 were low response types and were used to obtain low response inlet recovery and distortion. A typical time history of the inlet distortion leading to compressor stall is shown in figure 15. At the time the stall was initiated, the low response distortion calculated at 50 samples per second was slowly decreasing with no indication of the approaching stall. The other four compressor

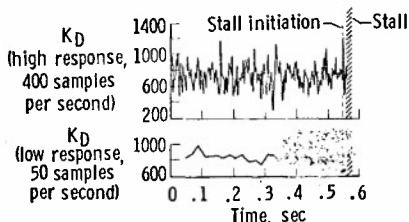


Figure 15. High and low response distortion factor for a compressor stall at Mach 1.60.

This peak in distortion factor 15 milliseconds prior to a compressor stall occurred in each of the 25 stalls analyzed from F-111A number 6. However, in some instances, this peak was not as high as other peaks during a previous data run. This was attributed mainly to the use of only four high response rakes. Reference 12 shows that five or more rakes are desirable. F-111A number 12 tests with eight high response rakes yielded more consistent distortion peaks prior to stall. Because of their in-flight nulling capability, the absolute level of each pressure, and, hence, the overall distortion factor levels were more accurate. Figure 16 compares the distortion factors for a stall using all eight rakes, only the diagonal rakes, and only the vertical and horizontal rake for the same set of data. The eight rake  $K_D$  value at the time of stall initiation is higher than any previous peaks, but the  $K_D$  value calculated from the horizontal and vertical rakes is lower than many previous peaks and is therefore not a good indication of the stall. The diagonal rakes give almost as good an indication as all eight rakes because, in this instance, the lowest total pressure and the highest turbulence is in the region surveyed by the 7:30 rake.

Instantaneous total pressure maps were made from the F-111A number 12 40-probe data. A series of six maps taken in 23 milliseconds is shown in figure 17 for the compressor stall data of figure 16. The first two maps were taken prior to the stall initiation. Map 3 shows the high distortion that caused the stall with the  $K_D$  value of 1367. Maps 4 and 5 were taken while the stall was developing in the compressor, and in map 6 the high pressure hammer shock wave appeared in the middle of the compressor face.

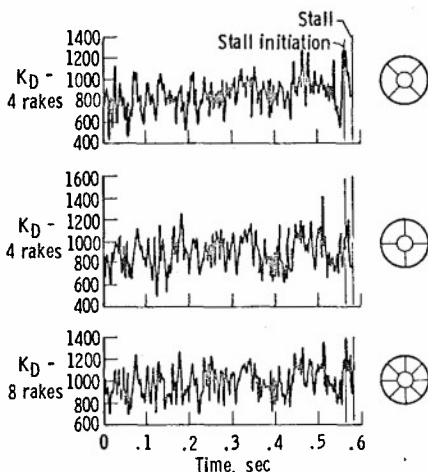


Figure 16. Effect of the number of rakes on the distortion factor,  $K_D$ , for a stall at  $M_\infty = 2.0$ .

A buildup in the distortion is evident in maps 1, 2, and 3 as the low pressure (dark) area moved toward the hub and enlarged and the high pressure area increased in size. The high distortion lasted only 3 milliseconds (about 1/2 rotor revolution) and in the next sample, map 4, the distortion was considerably lower. The appearance of the hammer shock near the hub is consistent with the occurrence of the stall in the compressor stages and not in the fan.

Studies of the pressure fluctuations that occur in the inlet flow just prior to stall often reveal an out-of-phase relationship. This is shown in a "drift" type of stall (fig. 18), with the 1:30 rake pressures all rising and the 7:30 rake pressures all dropping at the same time. Although no particularly high or low pressure peaks occurred, the out-of-phase effect raised the distortion factor to a predominant peak and caused a compressor stall.

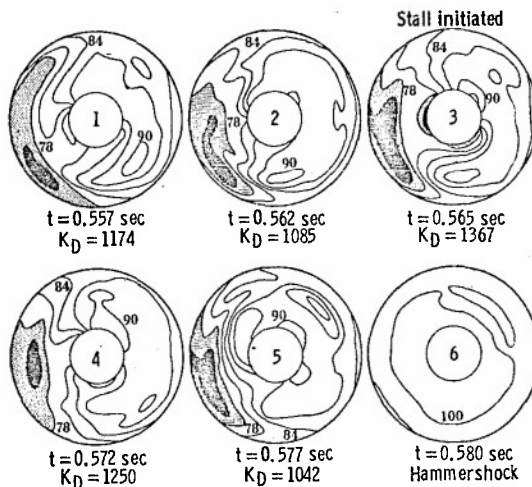


Figure 17. Instantaneous compressor face maps for a stall at Mach 2.0. Numbers indicate total pressure recovery, percent.

The  $K_D$  values at stall are summarized in figure 19 as a function of corrected engine airflow. Most of the data points are from F-111A number 6, but a few points from F-111A number 12 are shown and agree well with the F-111A number 6 data. Values of  $K_D$  at stall increase with corrected engine airflow. The sixth stage bleeds increase the  $K_D$  values at stall about 200. Stalls encountered without afterburning showed an additional  $K_D$  margin of about 150.

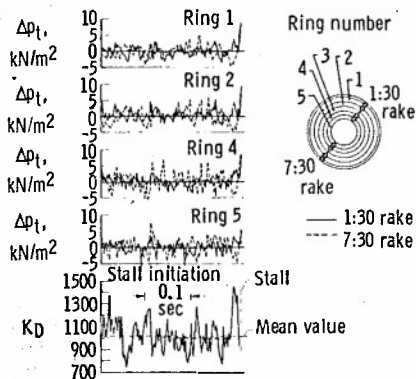


Figure 18. Pressure traces on opposite sides of the compressor face and distortion factor,  $K_D$ , for a stall at  $M_\infty = 2.17$ .

In the previous discussion, only the distortion parameter,  $K_D$ , was presented; however, several other distortion parameters were also used. Some of these were discussed in reference 4. The Pratt & Whitney  $K_\theta$  parameter and the Rolls Royce DC ( $\theta$ ) parameter have also been used for the F-111A number 12 data. Evaluation of these parameters is continuing.

The "instantaneous" distortion type of analysis is ideally suited to flight-test analysis of stalls, because only a few seconds of data leading up to the stall must be analyzed. In ground facility tests, many hours of test time are accumulated and it becomes prohibitively expensive to calculate instantaneous distortion factors for all the data. Reference 13 discusses statistical techniques for predicting the maximum distortion and relates it to the measured instantaneous distortion. Data from ground facility tests using actual engines may be analyzed by using the instantaneous distortion technique. Reference 14 presents results of wind-tunnel and altitude facility tests of a variety of engines, in addition to the flight data shown here.

**Inlet duct resonance.**—A resonant mode of the inlet duct has been observed in the inlet pressure data at certain flight conditions. The resonance was first detected in PSD plots of compressor face total pressures, for example, figure 20, which shows a PSD of four compressor face pressures from F-111A number 6 at  $M = 2.0$ . The resonant frequency of 27 hertz is evident on these probes, and a harmonic at 54 hertz can also be seen. Pressure traces for these same four probes are presented in figure 21. The 10:30 and 1:30 rakes have an obvious 27 hertz fluctuation. The 4:30 and 7:30 rake pressures show very little evidence of the resonance, and the power spectral densities of figure 20

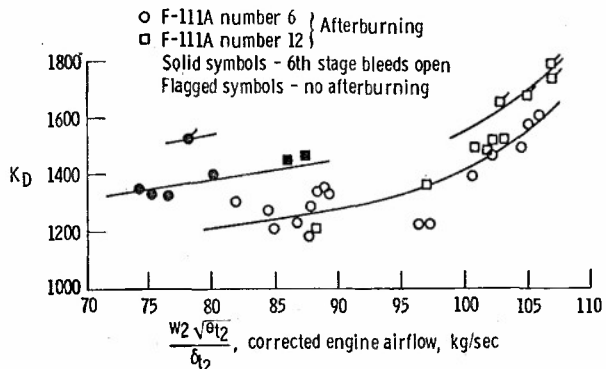


Figure 19. Summary of instantaneous distortion factor,  $K_D$ , values causing stall for F-111A number 6 and number 12. All data adjusted to Reynolds number index of 1.0.

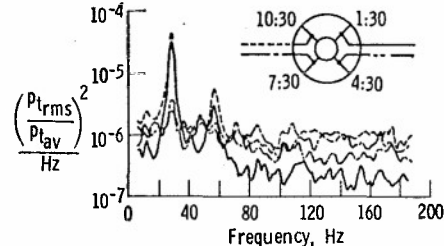


Figure 20. PSD's of four compressor face total pressures during duct resonance at  $M_\infty = 2.0$ .

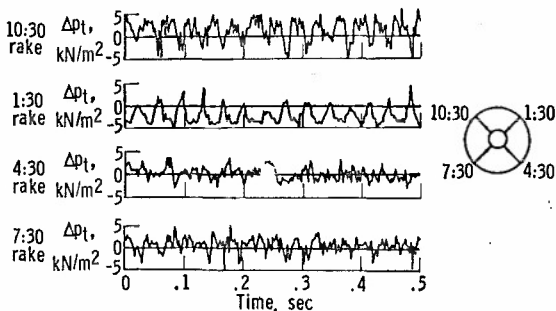


Figure 21. Time history of compressor face total pressures during duct resonance at  $M_\infty = 2.0$ .

are required to detect its presence. Coherence plots showing the degree of interdependence between two pressures are presented in figure 22. The 10:30 rake pressure is compared to the 4:30, 7:30, and 1:30 rake pressures, and the coherence is highest for the 1:30 pressure. Phase angle plots between five pressures on the 1:30 and 10:30 rakes are shown in figure 23. At the 27 hertz resonance, phase angles of about  $180^\circ$  are seen, whereas at other frequencies, phase angles are random. This  $180^\circ$  phase angle can also be seen in figure 21 between the 1:30 and 10:30 rake pressure traces.

The magnitude of these fluctuations and the out-of-phase condition suggested that the compressor face distortion might be strongly affected by the resonance. The distortion factor was calculated for the data shown in the previous figures, and the 27 hertz fluctuation is obvious in figure 24. The peak  $K_D$  values are almost high enough to cause a compressor stall. An instantaneous map taken at the high  $K_D$  value shows a very high recovery region at the 1:30 rake and a very low recovery region at the 10:30 rake. This contrasts with the normal map at the lower  $K_D$ .

This duct resonance was usually observed at Mach numbers between 1.8 and 2.1. Its occurrence, strength, and frequency were found to be functions of the inlet geometry position, engine airflow, and free-stream Mach number. Intensity of the resonance was plotted qualitatively on a plot of spike position versus cone angle (fig. 25). A region of

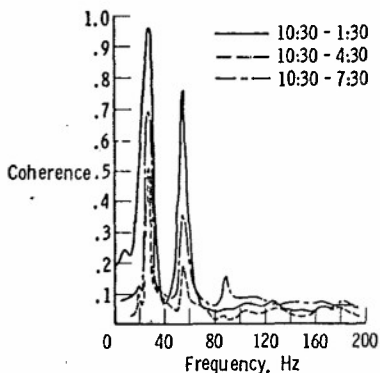


Figure 22. Coherence between 10:30 rake pressure and three other pressures during duct resonance at  $M_\infty = 2.0$ .

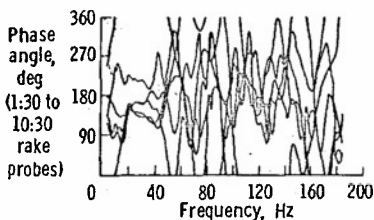


Figure 23. Phase angle between 1:30 rake and 10:30 rake pressures during duct resonance,  $M_\infty = 2.0$ .

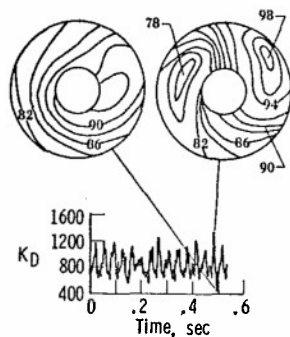


Figure 24. Distortion factor,  $K_D$ , and instantaneous compressor face maps during duct resonance at  $M_\infty = 2.0$ .

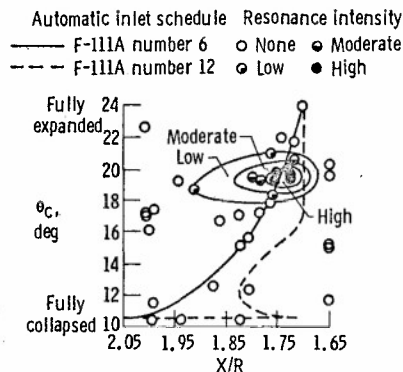
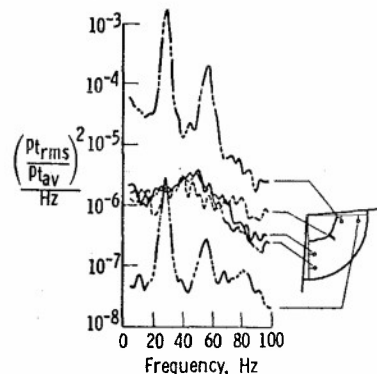


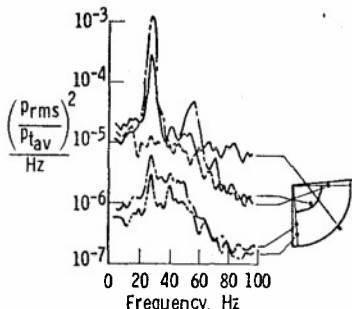
Figure 25. Effect of spike and cone position on the intensity of resonance.

the strongest resonance existed at a particular combination of spike and cone settings. The inlet control system automatically set the spike and cone in this region between Mach 1.9 and 2.05 on F-111A number 6 as indicated; however, with the manual inlet control system, the pilot could set the inlet geometry to off-schedule positions. The F-111A number 12 automatic schedule positioned the spike farther aft, and only weak resonance was encountered in the automatic mode. The spike position for strongest resonance places the inlet minimum area slightly inside the cowl lip (figs. 5 and 6) particularly with the blunt lip cowl, whereas the cone position results in an inlet throat Mach number of about 1.0. This situation might permit the inlet terminal shock wave to oscillate between the normal external position and an abnormal internal position.

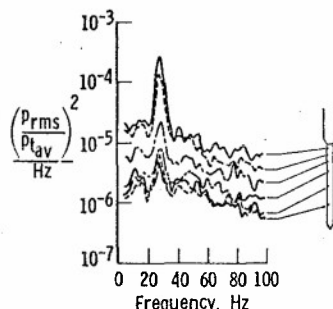
Power spectral density plots for the cowl lip rake total pressures, cowl lip rake static pressures, inlet duct total and static pressures, and shock position probe static pressures are presented in figures 26(a) to (d), respectively. These plots show evidence of the resonant frequency everywhere except on the cowl lip total pressures on the inboard side of the inlet. The resonance is extremely strong at the upper part of the inlet near the cone surface. A rake located in this area shows a



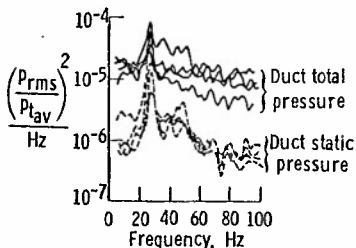
(a) Cowl lip total pressures.



(b) Cowl lip static pressures.



(c) Shock position probe static pressures.



(d) Inlet duct total and static pressures.

Figure 26. Power spectral density plots of inlet pressures during duct resonance at  $M_\infty = 2.0$ .

low and high recovery areas seen at the compressor face in figure 24. As this is happening, the shock wave returns to the internal position. Numerous phase angle and coherence plots and studies of time histories that are not shown substantiate this explanation.

predominant separation and reattachment cycle, as seen in figure 27, which shows the rake total pressure and the static pressure at the rake base. The distortion factor from figure 24 is repeated, and the direct effect can be easily seen at the compressor face with the slight delay due to the duct transport time. The highest  $K_D$  peaks follow the lowest inlet rake pressure levels.

These results suggest that the normal shock wave oscillation occurs as shown in figure 28. The shock wave is inside and nearly stable at the lower part of the inlet and jumps from the internal to the external position at the top. The shock wave moving forward separates the boundary layer on the cone, causing the extreme fluctuations seen in figure 27 near the cone surface. This separation generates additional oblique shock waves upstream of the normal shock, which momentarily result in high pressure recovery near the upper cowl lip. This combination of low energy separated flow inboard and high energy air outboard then flows down the duct and causes the

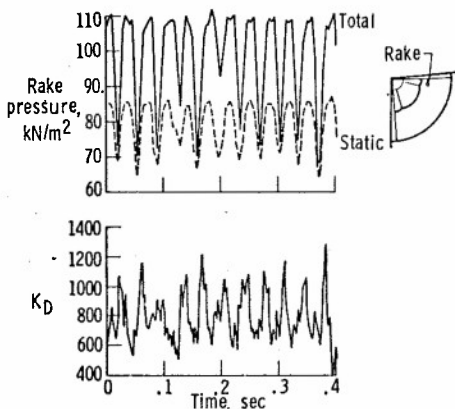


Figure 27. Comparison of inlet cowl lip rake total and static pressures with compressor face distortion factor,  $K_D$ , during duct resonance at  $M_\infty = 2.0$ .

The precise frequency of this cycle is governed by the static pressure pulse generated by the movement of the normal shock wave. The duct acts as an open pipe and, at or slightly inside the compressor face, the wave is reflected back to initiate another shock movement. A simple formula for a pipe open at one end corrected for flow effects was described earlier and approximately predicts the observed resonance frequencies and their variation with engine airflow (duct Mach number) and free-stream Mach number (total temperature).

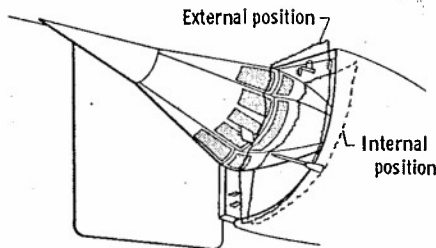


Figure 28. Sketch of the inlet showing the normal shock wave in the external and internal position.

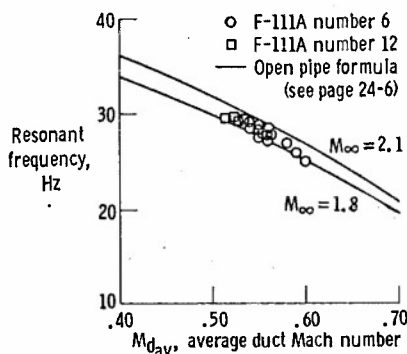


Figure 29. Comparison of measured resonant frequency to theoretical open pipe frequency. F-111A inlet duct;  $M_\infty = 1.8$  to 2.1.

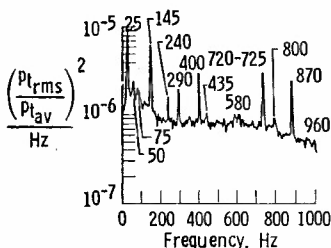
At Mach numbers between 2.1 and 2.3, the resonance is not seen except at reduced mass flow ratio (fig. 12). At the higher mass flow operating point, the normal shock appears to be inside the inlet (supercritical); and at lower mass flows (below  $0.89 \text{ m/m}_0$ ), the shock is stable outside the inlet (subcritical operation). Only in the  $0.89$  to  $0.94 \text{ m/m}_0$  range is the shock wave sufficiently unstable to sustain the resonance.

Figure 29 shows the frequency predicted by this formula as a function of the average duct Mach number for a total temperature representative of Mach numbers of about 1.8 to 2.1. Data points shown are the measured frequencies from F-111A number 6 and agree well with the calculated frequencies. Data from F-111A number 12 are also shown and are consistently higher in frequency and lower in average duct Mach number than those for the number 6 airplane because of the different duct area distribution (fig. 6).

The resonance disappears from digital power spectral densities at airplane Mach numbers below about 1.8, probably because the normal shock wave is stably positioned outside the duct. However, very weak resonant fluctuations can be seen in the analog power spectral densities in certain regions of the compressor face where random fluctuations are very small, at lower supersonic and even subsonic Mach numbers.

Rotor Speed Harmonics

Other discrete frequencies detected in the compressor face total pressures are the rotor speed frequencies and their harmonics. These frequencies are generated by shock waves from the blade tips operating at supersonic speeds and result in the multiple pure tone noise discussed in reference 15. The low pressure compressor frequency is typically 150 hertz and was detected in digital power spectral densities. Analog power spectral densities of pressures filtered above 1000 hertz showed the 150 hertz peak and many more peaks due to the high pressure compressor rotor speed and harmonics of both rotor speeds. An example is shown in figure 30. The most predominant peaks in these data and in most other data are the fundamental and the fourth and fifth harmonics of the  $N_1$  speed. Peaks at 400 and 800 hertz are due to the 400 hertz power supply frequency in the airplane. When the fan tip speed was subsonic, these frequencies were not evident.



Source	Fundamental, Hz	Harmonics, Hz				
		1	2	3	4	5
Duct resonance	25	50	75	---	---	---
Low rotor speed	145	290	435	580	725	870
High rotor speed	240	480	720	960	---	---
Electrical power	400	800	---	---	---	---

Figure 30. Analog PSD of a compressor face total pressure showing various peaks due to duct resonance, rotor speeds, and power supply.

The instrumentation in the engine was not designed for high response; however, the sampling rate is sufficient for valid power spectral densities to 100 hertz. Probe resonance and data filtering make amplitude response uncertain above 40 hertz, but the predominant 50 hertz resonance is believed to be valid. Power spectral densities showing the eight fan duct total pressures and the low and high pressure compressor discharge static pressures are shown in figure 31. Figure 31(a) shows data for a Mach number of 2.04 with partial afterburning of the left engine. The spike at 50 hertz is evident in all the pressures. Figure 31(b) shows power spectral densities for the

Fan Duct Resonance

A resonance detected in the fan duct and engine is believed to be due to a fan duct oscillation at a frequency of about 50 hertz.

same pressures at  $M_\infty = 2.08$  with the afterburner not lit, and there is a complete absence of any predominant frequencies up to the maximum value of 100 hertz. A third PSD is shown in figure 31(c) at  $M_\infty = 2.15$  with maximum afterburning. It shows a definite resonance at 50 hertz, but the resonance is not on all probes and is of much less magnitude than that for the partial afterburning condition in figure 31(a).

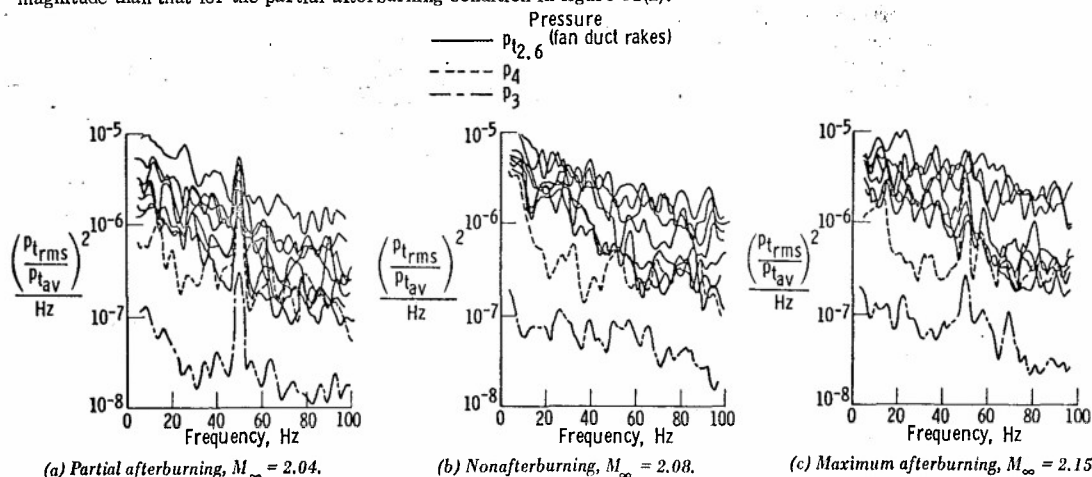


Figure 31. PSD of fan duct and engine pressures.

The fact that the resonance appears in the low and high pressure compressor as well as in the fan duct indicates that the pressure fluctuation is propagating through the fan stages into the compressor. This may explain the observed decrease in engine compressor stall margin with the afterburner lit, shown in figure 19. The relationship between the fan duct resonance and the afterburner operation suggests that a combustion instability is involved. The afterburning flame front may oscillate and generate pressure pulses which propagate back up the fan duct and reflect off the fan stages.

Although there are many modes of combustion instability, the most common is probably the longitudinal mode. Using the distance from the fan discharge to the afterburner flameholder, and a fan duct Mach number of 0.4, the same organ pipe equation used in the inlet duct estimates a fan duct frequency of 53 hertz, which is sufficiently close to the observed frequency of 50 to suggest that it may be the mode causing the fluctuation. Phase angles between the 10:00 and 2:00 fan duct pressures at 50 hertz are near  $0^\circ$  which also suggests a longitudinal mode. Reference 16 discusses afterburner instabilities and analytical techniques for predicting the frequencies and amplitudes.

#### FUTURE PROGRAMS

To acquire the depth of understanding necessary to apply generally the information obtained on the nature of inlet dynamics to future aircraft, several different types of inlets need to be studied. The F-111A tests are now complete, and preparations are being made to conduct a comparable program on a YF-12 airplane. This airplane (fig. 32) will permit the study of an axisymmetric, mixed compression type of inlet. Such an inlet presents new problem areas not encountered with the external compression F-111A inlets. Included are inlet unstarts and the effect of bypass flows on airplane aerodynamics. The large unsymmetrical drag resulting from one inlet unstarting while at cruise speeds near Mach 3 can cause severe handling problems and possibly complete loss of control.



Figure 32. Photograph of the YF-12 airplane.

Like most mixed or internal compression inlets the YF-12 inlet requires air to be bypassed ahead of the compressor at some speed and power conditions in order to maintain the terminal shock at the proper position. Preliminary flight studies in which tufts were photographed with a motion picture camera mounted in the fuselage showed that the bleed and bypass flows from the nacelle caused a large separated area in the wing-nacelle juncture region and pulsating flow along the surface of the nacelle. These flow effects are illustrated in figure 33, which was taken from reference 7. One-twelfth-scale model tests in a wind tunnel at the Ames Research Center showed that bypassing 37 percent of the intake air, a realistic value for some flight conditions, causes an increase in the overall airplane drag by an amount nearly equal to the zero-lift drag.

A schematic view of the inlet showing the location of the various sensors is shown in figure 34. Measurements at the tip of the centerbody will indicate the total pressure and direction of the airstream reaching the inlet. Static pressure orifices will show the location of the terminal shock, even when the inlet is unstarted, and enough of these sensors will be of the high response type that shock oscillations can be measured. There will be three internal boundary-layer rakes, one close to the throat and two farther downstream. These boundary-layer probes will be connected to dynamic pressure transducers so that rapid variation and oscillations of the boundary-layer pressures can be measured. Altogether, 50 to 70 dynamic pressure measurements will be made in the inlet.

Bleed and bypass flows will also be measured in flight. To make such measurements without an excessive amount of instrumentation, tests will be run on a full-scale inlet in the 10-by-10-foot wind tunnel at the NASA Lewis Research Center to define and calibrate the duct flow probes. The wind-tunnel tests will also give an indication of leakage flow through various joints and cracks. Sealing small cracks is extremely difficult because of the temperatures encountered by the inlet, and the leakage flow is believed to be significant.

The flight-measured performance of the YF-12 inlet will be correlated with data from the full-scale inlet in the Lewis 10-by-10-foot wind tunnel and with data on 1/3-scale and 1/12-scale models tested at the NASA Ames Research Center. Thus it should be possible to get an indication whether differences are due to scale effects or to basic

differences between wind-tunnel and flight testing.

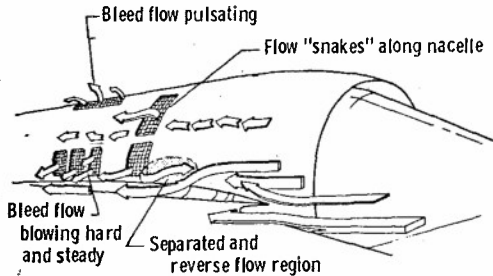


Figure 33. Flow patterns on nacelle of YF-12 airplane as determined from tuft studies. Mach 1.5, forward bypass open.

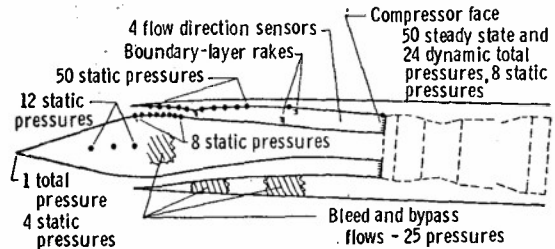


Figure 34. Instrumentation for YF-12 tests.

#### CONCLUDING REMARKS

The steady-state and dynamic pressure phenomena in the inlets of two F-111A airplanes were investigated. A new pressure survey rake incorporating miniature transducers and a slide valve to permit in-flight zero checks was used at the compressor face and was found to yield excellent steady-state and dynamic pressure data. Analysis of the high response pressure data showed the cause of compressor stalls to be high levels of instantaneous distortion lasting for times as short as 3 milliseconds. In many instances, the distortion causing the stall was due to an out-of-phase situation in total pressures on opposite sides of the compressor face. An inlet duct resonance at Mach numbers above 1.8 was analyzed by using time history and statistical parameters and was found to result from a normal shock oscillation at the duct fundamental frequency. Another resonance in the fan duct of the engine during afterburning operation may have affected the compressor stall margin. Plans for studies of the inlets of the YF-12 interceptor include flight tests and comparison with full-scale, 1/3-scale and 1/12-scale wind-tunnel tests.

#### REFERENCES

- Smith, Ronald H.; Bellman, Donald R.; and Hughes, Donald L.: Preliminary Flight Investigation of Dynamic Phenomena Within Air Breathing Propulsion Systems of Supersonic Aircraft. AIAA Paper No. 68-593, 1968.
- Martin, Richard A.: Dynamic Analysis of XB-70-1 Inlet Pressure Fluctuations During Takeoff and Prior to a Compressor Stall at Mach 2.5. NASA TN D-5826, 1970.
- Bellman, Donald R.; and Hughes, Donald L.: The Flight Investigation of Pressure Phenomena in the Air Intake of an F-111A Airplane. AIAA Paper No. 69-488, 1969.
- Burcham, Frank W., Jr.; and Hughes, Donald L.: Analysis of In-Flight Pressure Fluctuations Leading to Engine Compressor Surge in an F-111A Airplane for Mach Numbers to 2.17. AIAA Paper No. 70-624, 1970.
- Burcham, Frank W., Jr.: An Investigation of Two Variations of the Gas Generator Method to Calculate the Thrust of the Afterburning Turbofan Engine Installed in an F-111A Airplane. NASA TN D-6297, 1971.
- Martin, Richard A.; and Hughes, Donald L.: Comparisons of In-Flight F-111A Inlet Performance for On- and Off-Scheduled Geometry at Mach Numbers of 0.68 to 2.18. NASA TN D-6490, 1971.
- Bellman, Donald R.; Burcham, Frank W., Jr.; and Taillon, Norman V.: Techniques for the Evaluation of Air-Breathing Propulsion Systems in Full-Scale Flight. NASA paper presented at AGARD 38th Flight Mechanics Panel Meeting, Toulouse, France, May 10-13, 1971.
- Bendat, Julius S.; and Piersol, Allan G.: Measurement and Analysis of Random Data. John Wiley & Sons, Inc., c. 1966.
- Kinsler, Lawrence E.; and Frey, Austin R.: Fundamentals of Acoustics. Second ed., John Wiley & Sons, Inc., 1962, p. 201.
- Hartin, J. P.: Wind Tunnel Investigation at Transonic and Supersonic Mach Numbers of Duct Modifications to the F-111A Inlet. AEDC-TR-66-19, Arnold Eng. Dev. Center, Feb. 1966.
- Braithwaite, Willis M.; and Vollmar, William R.: Performance and Stall Limits of a YTF30-P-1 Turbofan Engine With Uniform Inlet Flow. NASA TM X-1803, 1969.
- Oates, Gordon C.; Sherman, Dale A.; and Motycka, David L.: Experimental Study of Inlet-Generated Pressure Fluctuations. Tech. Rep. AFAPL-TR-69-103, Air Force Aero Propulsion Lab., Wright-Patterson Air Force Base, June 1970, pp. 427-457.
- Kimzey, William F.; and McIlveen, Milton W.: Analysis and Synthesis of Distorted and Unsteady Turbo Engine Inlet Flowfields. AIAA Paper No. 71-668, June 1971.
- Anon.: Aircraft Propulsion. NASA SP-259, 1971, pp. 283-349.
- Pickett, Gordon F.: The Prediction of the Spectral Content of Combination Tone Noise. AIAA Paper No. 71-730, June 1971.
- Dix, Donald M.; and Smith, George E.: Analysis of Combustion Instability in Aircraft Engine Augmenters. AIAA Paper No. 71-700, 1971.
- Johnson, Clarence L.: Some Development Aspects of the YF-12A Interceptor Aircraft. AIAA Paper No. 69-757, 1969.

SUPERSONIC INLET PERFORMANCE AND DISTORTION  
DURING MANEUVERING FLIGHT

by

L. E. SUREER and D. J. STAVA  
Air Force Flight Dynamics Laboratory  
Wright-Patterson AFB  
Ohio, USA

SUMMARY

This paper reports selected results from several investigations of engine air inlet design and performance. Several possible vehicle configurations are presented and discussed to point out inherent advantages and disadvantages in terms of airframe-inlet integration and mission accomplishment. Important features of the forebody and forebody/wing configurations are presented together with wind tunnel test data comparing the inlet flow fields of these models. The paper describes techniques used to design air inlets for the airframe flow fields. It also describes the instrumentation employed to document inlet performance. Air inlet performance and duct flow distortion from wind tunnel tests of different model designs are compared to show the effects of aircraft geometry, air inlet design, and maneuver condition over the 0.6 to 2.5 Mach Number range. The paper also summarizes basic conclusions reached during these research efforts concerning the effects of model scale on air inlet flow.

ACKNOWLEDGEMENT

This paper has made use of source material from several USAF contracts which have not, as yet, resulted in final documents suitable for referencing. Consequently, the authors gratefully acknowledge the work of engineering personnel from the General Dynamics, North American Rockwell, Fairchild Hiller, and Northrop Corporations whose efforts have made this paper possible.

## INTRODUCTION

The performance and stability of aircraft turbine engine propulsion systems is, in part, dependent upon the design of the engine air inlet and the manner in which it is integrated with the aircraft. In the case of a highly maneuverable supersonic fighter or interceptor aircraft, this dependency becomes critical. Operation of these types of aircraft over a broad matrix of Mach Number, altitude, engine power setting, and aircraft maneuver condition demands that the inlet efficiently diffuse a great variety of distorted airflows. If missiles, gun ports, or other protuberances are located ahead of the inlet, the degree of flow distortion at the face of the inlet can be substantially increased.

A concerted effort has been made over the past several years to investigate these problems and establish a better understanding of the factors which influence supersonic air inlet performance. This paper draws information from several investigations in order to suggest a supplement to existing design philosophy as applied to supersonic external compression inlets and their integration with flight vehicles. Separate investigations involving airframe-inlet integration, inlet development, and subsonic diffuser development, have generated a wealth of theoretical and empirical information which has shed light on various aspects of the inlet design problem. The investigations considered here have concentrated on the problem of inlet total pressure recovery performance and inlet-engine compatibility. Design practices employed have attempted to avoid high drag configurations, but no measurement has been made of inlet drag increments.

One investigation in particular, Project Tailor-Mate, has embraced nearly the entire spectrum of inlet development problems in a rather comprehensive investigation; consequently, the results of that work will form the primary thesis of this paper with the results of other programs being brought in to emphasize or expand particular points of interest. Inlet flow fields and subsequent inlet performance of side-mounted and wing-shielded configurations will be compared primarily at Mach 2.2.

## FOREBODY FLOW FIELDS: BASIC DESIGN CONSIDERATIONS

The first point of interest in the development of air inlets for highly maneuverable supersonic aircraft is the flow field in which the inlet is to be immersed. Extreme flight maneuver conditions create a wide variety of flow conditions around an aircraft in terms of local flow angularity, total pressure, and Mach Number. Since inlets must operate efficiently in these environments, the fuselage flow fields must be sufficiently well defined at all aircraft operating conditions to enable realistic inlet design requirements and test conditions to be established. In preliminary aircraft design, inlet placement and basic airframe configuration must be determined simultaneously. If the inlet is to be shielded by the wing or fuselage, it is normally possible to employ an inlet which performs well only at relatively low incident flow angles. Conversely, inlets placed in the free stream or other regions of high flow angularity, Mach Number gradient, and/or pressure distortion must be designed to operate satisfactorily throughout at least the same envelope which the aircraft can experience.

The Project Tailor-Mate investigation was initiated with a mission analysis for supersonic tactical fighter aircraft to determine basic mission Mach Number and maneuver requirements. A matrix of designs was reduced to eight candidate designs for which actual mission performance was determined. Finally, four aircraft configurations (Figure 1) including examples of side-mounted inlets (A-1, A-2), fuselage-shielded inlets (A-3), and wing-shielded inlets (B-3/B-4) were selected for 1/4-scale forebody model fabrication and wind tunnel testing. The test program defined fuselage static pressure distributions, boundary layer development, and inviscid flow fields at proposed inlet stations.

## FOREBODY FLOW FIELDS: SIDE-MOUNTED INLETS

Local angle-of-attack ( $\alpha_L$ ) and sideslip ( $\beta_L$ ) mappings of side-mounted inlet flow fields (Figure 2) at aircraft angles-of-attack equal to  $0^\circ$  and  $15^\circ$  reveal rather large local  $\alpha_L$  gradients with the average value of  $\alpha_L$  near the aircraft angle-of-attack,  $\alpha_0$ . The  $\alpha_L$  gradient noted at  $\alpha_0 = 0^\circ$  on the A-1 and A-2 models is primarily due to the presence of a rather prominent aircraft canopy. Negative values of  $\alpha_L$  in the lower outboard corner of the flow field apparently originated far upstream by the canopy windshield, and the positive  $\alpha_L$  in the upper inboard portion of the field is the result of local flow expansion over the aft end of the canopy. At  $\alpha_0 = 15^\circ$  this canopy effect is overshadowed, for the most part, by a fuselage effect in which flow in the lower portion of the field is expanding inboard and upward over the aft part of the fuselage. It is further noted that the lower inboard corner of the inlet flow field exhibits rather large values of  $\beta_L$  due to the outwash of flow from the bottom of the fuselage.

In comparing the two side-mounted inlet fuselage shapes from the Tailor-Mate program, it is seen that the forebody flow fields are quite similar, but that the more rounded underbody (A-2) produces somewhat lower sideslip angularity in the flow field adjacent to the fuselage.

Large differences in fuselage cross-section shape produce more substantial variations in the forebody flow fields ahead of side-mounted inlets. Examples of these variations can be illustrated by results from an Airframe-Inlet Interaction Investigation (Figure 3). In this program, many different aircraft configurations were represented by a series of 1/12-scale aircraft forebody models with provisions for variations in nose droop, fuselage cross-section, canopy shape, and wing geometry. Measurements obtained during transonic and supersonic wind tunnel testing were similar to those outlined in the Tailor-Mate test description.

The large difference between flow fields measured in the Tailor-Mate program and flow fields measured in the Airframe-Inlet Interaction Investigation are due to a combination of major geometric differences including forebody camber, fuselage cross-section, aspect ratio, and canopy design. Additional comparative analysis will be required to completely understand the differences between the two sets of experimental flow fields, but in both cases the more gently rounded fuselage underbody produces more uniform flow fields at high aircraft angles-of-attack.

#### FOREBODY FLOW FIELDS: SHIELDED INLETS

In the Airframe-Inlet Interaction Investigation, flow surveys were also taken further aft under a top-mounted wing. Although this type of wing offers inlet shielding at high  $\alpha_0$ , flow field interaction problems arise when flow washes from under the fuselage upward toward the inlet region (Figure 4). It has been concluded for this type of wing-shielded inlet configuration that it is preferable to design an approximately rectangular shaped fuselage with rounded corners in order to provide the least distorted inlet flow field during flight maneuvers. Rounded fuselages appear to give rise to heavy vortex action at the wing-fuselage junction at high angle-of-attack. On the other hand, the rectangular body tends to channel the flow somewhat, resulting in more uniform flow adjacent to the fuselage.

The integration problem associated with shielded inlets is simplified considerably in the Tailor-Mate low wing configurations. In this case the wing-shielded and forebody-shielded inlet flow fields experience little change in local angle-of-attack up to  $\alpha_0 = 15^\circ$ , but increasingly larger values of sideslip are generated at the higher  $\alpha_0$  (Figure 5a). Comparing the average flow field properties of the wing-shielded and side-mounted inlet configurations from Project Tailor-Mate (Figure 5b) indicates the considerable degree of protection offered by wing shielding.

#### INLET PERFORMANCE: BASIC DESIGN CONSIDERATIONS

The next important design consideration is that of the supersonic inlet itself. Taking an example from the 1/12-scale Airframe-Inlet Interaction Investigation, it is seen that a very simple side-mounted two-dimensional inlet operating somewhat off design at  $Mo = 2.2$  responded quite differently to flow fields generated by four different fuselage shapes (Figure 6). In this case the average flow field angle-of-attack was slightly negative, resulting in significantly lower inlet performance than in the isolated inlet test case.

Much more detailed inlet performance tests were conducted in the larger scale Project Tailor-Mate program. Two side-mounted and two shielded external compression inlets (Figure 7) were "tailored" for the flow fields defined by the forebody test program. Wind tunnel models of these inlets had provisions for variation in inlet compression surface arrangement, cowl shape, sideplate shape, boundary layer bleed, and subsonic diffuser length. Instrumentation used to document inlet performance (Figure 8) included static pressure measurements throughout the inlet and diffuser and total pressure rakes near the cowl lip, in the diffuser, and at the simulated compressor face. All of the compressor face instrumentation and some of the inlet static pressures incorporated high response transducers.

It is beyond the scope of this paper to cover all of the inlet design information generated in this effort. There are, however, a few basic points which have emerged from the Tailor-Mate program - supplemented by information from other investigations - which are worthy of note for future design practices.

#### INLET PERFORMANCE: EFFECT OF WING-SHIELDING

First it is useful to compare the general reaction of the different inlet systems to the simulated flight environment (Figure 9). The effect of inlet shielding is readily seen in this comparison, the more severe problems being encountered with the side-mounted axisymmetric inlet. Judging from the angle-of-attack data alone, the wing-shielded two-dimensional (2-D) inlet appears the best choice for Mach 2.2 airframe propulsion compatibility. However, a more accurate compatibility assessment can be made by making use of a screening process developed during analysis of the Tailor-Mate data. This method of screening makes use of a plot of time-averaged inlet flow distortion (a typical engine manufacturer's parameter) versus compressor face flow turbulence for all inlet test points. Definition of the region of distortion and turbulence levels for which stable engine operation can be assured has been the result of this effort. Some of the  $\alpha_0, \beta_0$  "compatibility envelopes", for the individual inlet installations (Figure 10) indicate that adverse sideslip generally has a much more unfavorable effect on the shielded 2-D inlet. The shielded axisymmetric inlet, therefore, is found to offer the best performance potential due to its relatively high pressure recovery and low flow distortion throughout the entire flight maneuver envelope. Shielding by the wing produces high pressure recovery at high angles-of-attack for both inlets, but the axisymmetric cowls are much less sensitive to the resulting sideslip flow than the 2-D inlet sideplates.

#### INLET PERFORMANCE: EFFECT OF FOREBODY SHAPE

The importance of careful integration of the inlet and fuselage can be illustrated by a test from the Tailor-Mate program, in which the 2-D side-mounted inlet, A-1, was tested on both the A-1 and A-2 forebodies. Making use of the screening process mentioned earlier, the envelope of distortion index versus turbulence has been plotted for each of these installations and compared with the region of assured compatibility (Figure 11). In terms of propulsion system compatibility, flow fields generated by the more rounded fuselage underbody (A-2) were found to be substantially better than the other (A-1). It is difficult to identify the exact reason for this difference, but the A-2 fuselage with the more rounded contour exhibited lower values of local flow outwash (see again Figure 2) at high  $\alpha_0$ , reducing the tendency toward flow separation on the inboard inlet sideplate during maneuvering flight. At the

very least, this comparison of inlet compatibility for two slightly different flow fields illustrates the potential sensitivity of integration problems and one possible avenue for improving inlet flow distortion characteristics in supersonic maneuvering flight.

#### INLET PERFORMANCE: EFFECT OF FOREBODY FLOW FIELD DISTORTION

A recent supersonic inlet investigation can also be used to improve understanding of the effect of fuselage or wing flow field distortion on inlet performance. In this program - Supersonic Inlet Development - a 2-D external compression inlet and a half-axisymmetric external compression inlet were designed and wind tunnel tested in approximately 1/8-scale (Figure 12). Instrumentation in the inlets included static pressure distributions through the inlet and duct, a movable total pressure throat rake to assess flow entering the subsonic diffuser, and total pressure rakes at the simulated compressor face.

This program was split into two phases with the first phase devoted to isolated inlet performance/compatibility wind tunnel tests and the second phase exploring the sensitivity of the inlets to artificially generated flow field distortion. The flow field distortion was created in the wind tunnel by means of a large variable angle-of-attack wedge incorporating an expansion corner on its lower surface (Figure 13). This wedge spanned the wind tunnel ahead of the inlet and its variable angle-of-attack feature was used to generate a well defined gradient of Mach Number and flow angularity at the face of the inlet.

Both inlets were tested in this environment, but the 2-D inlet was also tested in the inverted position (Figure 14). In the case of the upright 2-D inlet, very little effect of the distorted flow field was observed because the inlet shock system had been oriented in such a way that there was very little Mach Number or flow angularity gradient across the initial oblique shock wave. This had the effect of placing the inlet in a flow field which it "saw" as nearly uniform. On the other hand the flow field intercepted by the half axisymmetric inlet initial shock wave varied from nearly uniform at the lower part of the inlet to highly distorted along the upper surface of the shock sheet. By testing the 2-D inlet in the inverted position, a large gradient in Mach Number, flow angularity, and pressure was imposed on the initial inlet shock sheet. As expected, increased flow distortion across the initial shock resulted in decreased pressure recovery performance and increased compressor face flow distortion.

These tests have pointed out the importance of definition of flow distortion actually reaching the inlet face in supersonic flow. In the case of the Project Tailor-Mate flow field definition program, the distortion of fuselage flow fields does not vary significantly with axial distance; therefore, it has been concluded that the measured invicid flow fields give an accurate description of the flow distortion in which the inlets have been tested.

#### INLET PERFORMANCE: EFFECT OF SUBSONIC DIFFUSER DESIGN

Under the project Tailor-Mate investigation, very little work has actually been done on the development of subsonic diffusers. Part of the reason for this lack of emphasis is the existence of a wide variety of subsonic diffuser information from a Subsonic Diffuser Development investigation which has explored pertinent diffuser problems. In this particular diffuser investigation, great care has been taken to establish realistic duct entrance flow profiles. This has been accomplished by providing a flow generating device ahead of the diffuser (Figure 15) which by means of trips, bleed flow variations and throat inserts provides realistic subsonic and supersonic flight inlet throat flow conditions including shock wave-boundary layer interaction effects. The flow profiles are defined by steady state and dynamic total pressure rake instrumentation at both the diffuser entrance and the simulated compressor face. A wide variety of diffuser shapes with static pressure distribution instrumentation has been tested with several different entrance flow conditions. As with the other programs mentioned, a great deal of useful information has been gathered, but a few results of the test are particularly applicable to the problems of supersonic maneuvering flight (Figure 16).

Analysis of the subsonic diffuser data shows clearly that the large levels of flow distortion and turbulence normally associated with the interaction of throat boundary layer and terminal shock wave at high  $Co$  can be reduced significantly by means of throat bleed flow. In one case in particular (Figure 16a) the levels of distortion and turbulence associated with a uniformly thick throat boundary layer profile were several times higher than the levels obtained with a profile which has been thinned by considerable throat bleed.

Long diffusers provide good inlet performance conditions over a wide range of inlet throat conditions whereas the equivalent performance in a short diffuser is contingent upon uniform flow and a thin boundary layer at the inlet throat (Figure 16b). The effect of duct length has also been shown in Project Tailor-Mate by testing the A-1 inlet/A-1 forebody combination with a simple extension to the subsonic diffuser (increasing duct length by approximately 40%). This duct extension results in an even more remarkable improvement in inlet/engine compatibility (Figure 17) than the adjustment of fuselage contour.

The use of vortex generators, in cases where flow would otherwise separate, can improve performance when located upstream of the separation point (Figure 16c).

These results illustrate the fact that carefully designed diffusers result in lower levels of flow turbulence, pressure loss, and flow distortion. The Subsonic Diffuser Development work, coupled with the Tailor-Mate program results, indicates that the more exposed inlets such as the side-mounted configurations would normally be longer and require low diffusion rates in order to achieve acceptable performance in maneuvering flight. Conversely, shielded inlets can produce more uniform diffuser entrance conditions

which, in turn, allow the effective use of much shorter ducts, perhaps making use of vortex generators in regions of high turning.

#### INLET PERFORMANCE: EFFECT OF MODEL SCALE

The Project Tailor-Mate program has explored only wind tunnel test models in 1/4-scale, but another investigation conducted during the same time period (Wind Tunnel/Flight Test Correlation) compares results of inlet wind tunnel test models in approximately 1/8 and 1/4-scale with flight test results of the RA-5C aircraft inlet (Figure 18). The RA-5C incorporates two-dimensional, horizontal ramp, external compression inlets. The objective of this investigation has been to determine the relationship of model scale to the measured performance of supersonic inlets for typical fighter aircraft. Complete and exhaustive analysis results are not yet available, but some interesting comparisons of inlet performance can be made and are well worth a brief examination.

The comparison of total pressure recovery at  $Mo = 1.8$  (Figure 19a) indicates very little difference between the three sets of test results from  $\alpha_o = 2^\circ$  to  $\alpha_o = 11^\circ$ , but the pressure recovery results of the two scaled models begin to diverge above  $\alpha_o = 14^\circ$ . This difference is thought to be due to the failure to duplicate an external underbody fairing on the 1/4-scale model. Comparison of the circumferential inlet flow distortion values of the three scale models again shows minor differences among the model sizes (Figure 19b). In terms of average RMS levels of turbulence, (Figure 19c), the similarity of scaled inlet performance is also seen.

On the other hand, when maps of compressor face total pressure are examined at  $Mo = 1.8$  - even for very small  $\alpha_o$  - it can be seen that there are some significant differences in the characteristics of the inlet flow between the various scales. One representative example at  $Mo = 1.8$  (Figure 20) shows that the zone of maximum total pressure is not at the same position in the .125 scale as in the .228 scale and flight test. This difference is not sufficient to become obvious in the average total pressure recovery or average turbulence levels. Repetition of this circumstance at other flight conditions has led to the conclusion that very close approximation of full scale compressor face flow distortion should not be relied upon in inlet model sizes much below 1/4-scale when testing supersonically with unit Reynold's Numbers in the range of one to two million per foot.

The differences observed between 1/8 and 1/4-scale test results are felt to be a combination of Reynold's Number and scale effects. In order to allow for increased boundary layer thickness on the scaled model fuselages, the inlet diverter height has been increased accordingly. This alteration coupled with other Reynold's Number effects has placed the inlet in a slightly different flow field which (as is seen from the project Tailor-Mate data) can easily result in inlet flow variations. Also, thicker boundary layers on the inlet side walls, coupled with the small scale inlet size, results in an altered throat shock wave-boundary layer interaction and subsequent altered responses of the viscous layer to adverse pressure gradients in the subsonic diffuser.

#### INLET PERFORMANCE: EFFECT OF REYNOLD'S NUMBER

From the foregoing considerations, it is reasonable to expect some change in inlet performance and flow distortion with changes in test Reynold's Number. It has been anticipated in the past that the higher Reynold's Numbers associated with full scale flight operation tend to result in thinner fuselage and inlet boundary layers, reduced viscous interaction problems, and, consequently, lower inlet flow distortion. This hypothesis has been verified in part by the results of both Project Tailor-Mate and RA-5C Wind Tunnel/Flight Test Correlation programs which indicate that (at engine match points) total pressure recovery tends to increase slightly with Reynold's Number while flow distortion and RMS levels of duct turbulence tend to decrease.

A brief exploration of Reynold's Number variations in the Tailor-Mate program and comparison with other work suggests that inlet flow conditions generally improve with increasing Reynold's Number when inlet and engine are well matched, but there is a tendency toward higher inlet turbulence with increased inlet mass flow (Figure 21). It is considered encouraging that the most recent data trends are consistently continuous over the range of Reynold's Numbers and scale sizes tested. Judging from work done under Project Tailor-Mate, it must be considered advisable to carry out supersonic inlet development tests at unit Reynold's Numbers greater than two million per foot.

#### CONCLUSIONS:

Several conclusions have been drawn from recent investigations of inlet designs for high maneuverable supersonic fighter aircraft.

1. There is no "best" engine air inlet design for this class of aircraft. However, a great deal of care must be taken to determine aircraft maneuver requirements from mission analysis. The subsequent airframe/inlet design development must be accomplished with sufficient care to assure that the supersonic inlet can efficiently diffuse captured mass flow, and that the subsonic diffuser design is compatible with inlet throat flow profiles at all Mach Number and maneuver conditions.
2. Fuselage forebody design can have a significant effect on side-mounted inlet performance. Its shape should be considered one of the variables during inlet development.

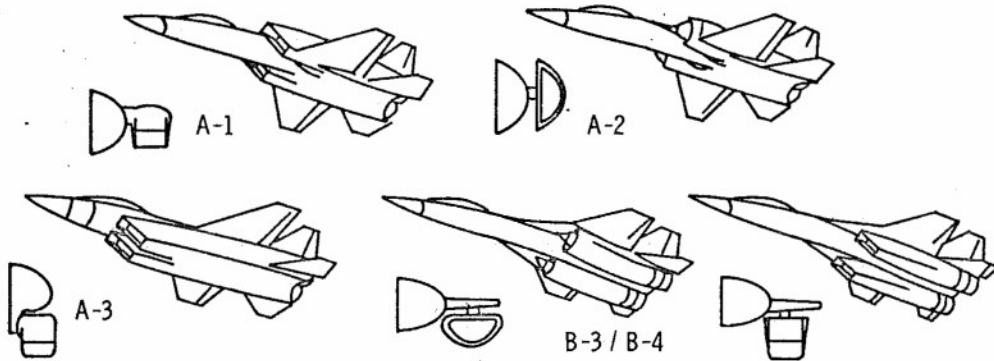
3. Wing-shielding can provide inlets with significant protection from local angle-of-attack, but greater sideslip flow angularity is associated with low wing installations and viscous interaction problems must be solved in high wing installations.

4. Artificial techniques of simulating distorted aircraft forbody flow fields can be used in inlet tests to derive, in a qualitative sense, the response of inlet designs to installed maneuvering flight.

5. Increased subsonic diffuser length may be employed effectively to achieve substantial reductions in compressor face levels of flow distortion and turbulence.

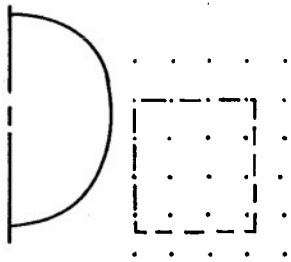
6. Relatively small scale tests ( $1/8$  to  $1/10$ ) may be used to determine inlet average pressure recovery and compressor face turbulence in supersonic flight; but in order to be reasonably certain of duplicating basic compressor face flow patterns, larger scale models (possibly  $1/3$  to  $1/6$ ) are recommended along with minimum unit Reynold's Numbers of approximately two million per foot.

7. Inlet flow distortion and turbulence are somewhat sensitive to Reynold's Number, but recent studies show no indication of sharp changes in sensitivity from model to full scale.

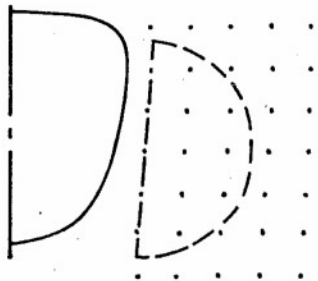
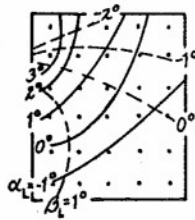


PROJECT TAILOR-MATE: CONFIGURATIONS CHOSEN FOR FOREBODY TESTS

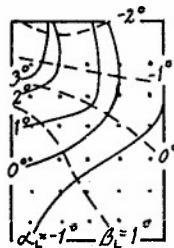
FIG. 1.



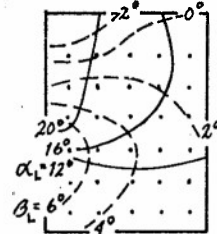
CONFIGURATION A-1



CONFIGURATION A-2



$M_0 = 2.2, \alpha_0 = 0^\circ, \beta_0 = 0^\circ$



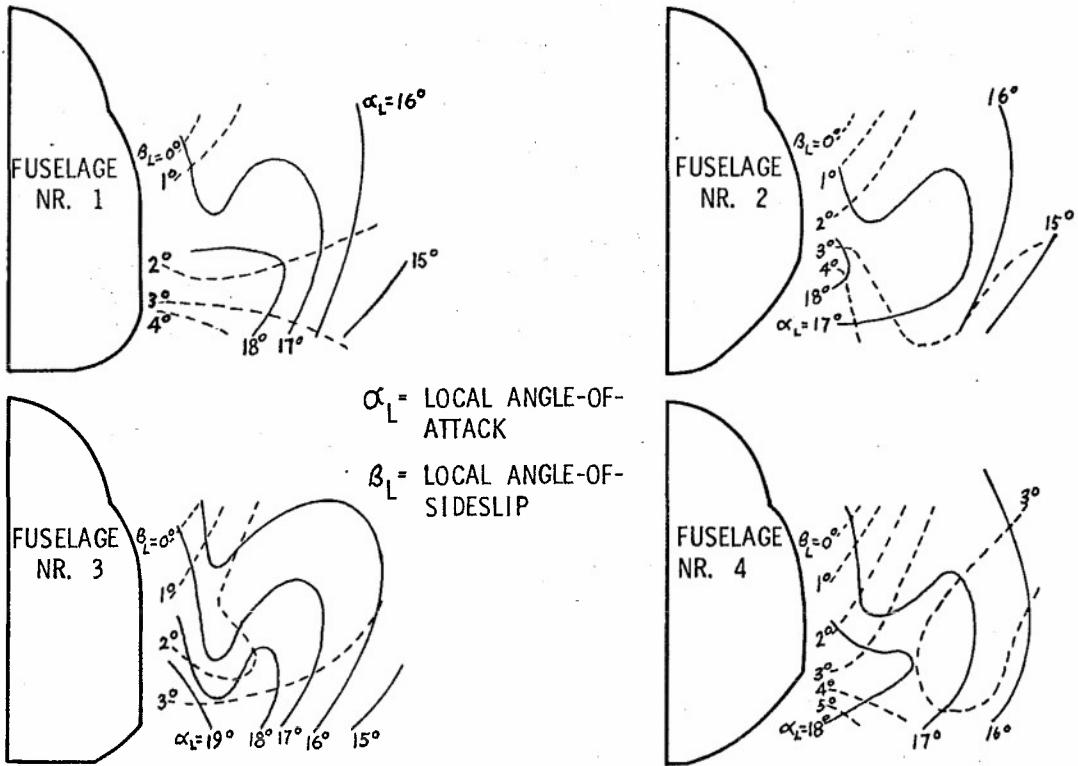
$M_0 = 2.2, \alpha_0 = 15^\circ, \beta_0 = 0^\circ$

• DENOTES POINT IN CONE-PROBE SURVEY MATRIX

$\alpha_L$  = LOCAL ANGLE-OF-ATTACK  
 $\beta_L$  = LOCAL ANGLE-OF-SIDESLIP

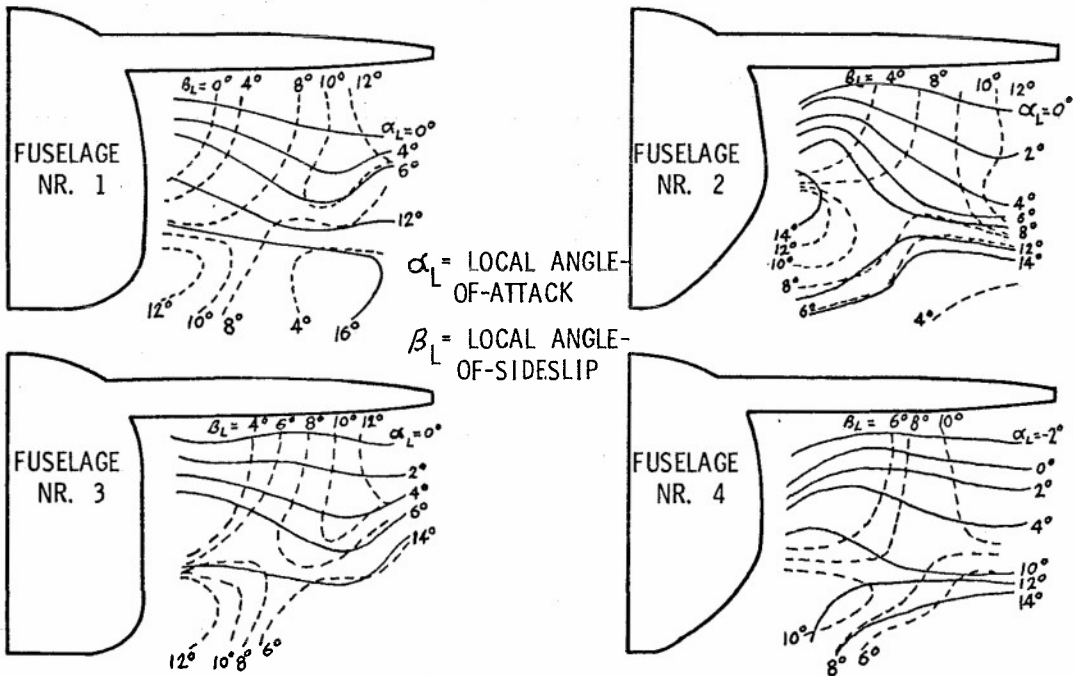
PROJECT TAILOR-MATE: FOREBODY FLOW FIELD ANGULARITY AT  $M_0 = 2.2$  FOR SIDE-MOUNTED INLETS,  $\alpha_0 = 0^\circ, 15^\circ$

FIG. 2



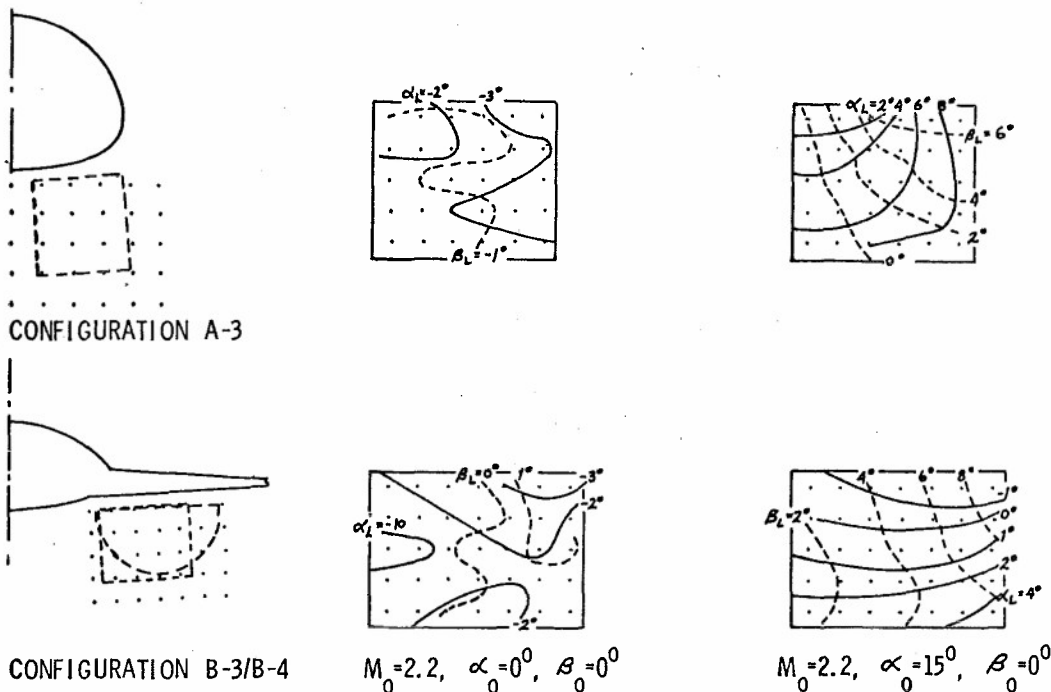
AIRFRAME-INLET INTERACTION: EFFECT OF FUSELAGE SHAPE ON FLOW FIELD ANGULARITY AT  $M_0=2.2$ ,  $\alpha_0=15^\circ$  FOR UNSHIELDED SIDE-MOUNTED INLETS

FIG. 3



AIRFRAME-INLET INTERACTION: EFFECT OF FUSELAGE SHAPE ON FLOW FIELD ANGULARITY AT  $M_0=2.2$ ,  $\alpha_0=15^\circ$  FOR WING-SHIELDED SIDE-MOUNTED INLETS

FIG. 4

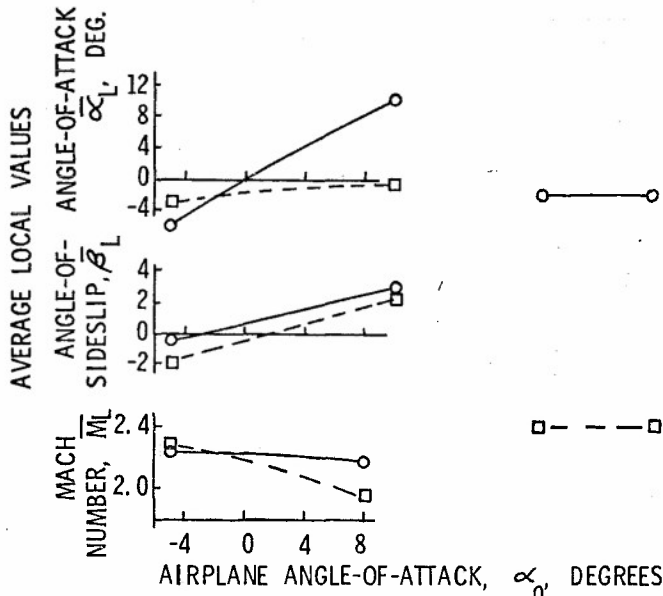


• DENOTES POINT IN CONE-  
PROBE SURVEY MATRIX

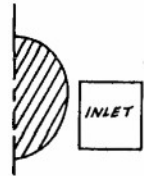
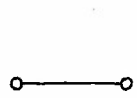
$\alpha_L$  = LOCAL ANGLE-OF-ATTACK  
 $\beta_L$  = LOCAL ANGLE-OF-SIDESLIP

PROJECT TAILOR-MATE: FOREBODY FLOWFIELD ANGULARITY AT  $M_0=2.2$  FOR FOREBODY-AND WING - SHIELDED INLETS,  $\alpha_0=0^\circ, 15^\circ$

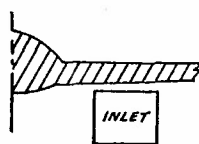
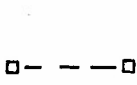
FIG. 5a



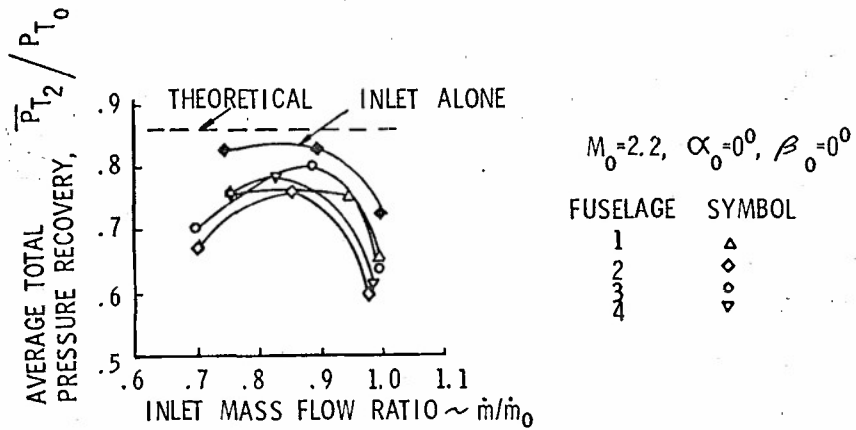
CONFIGURATION A-1



CONFIGURATION B-4

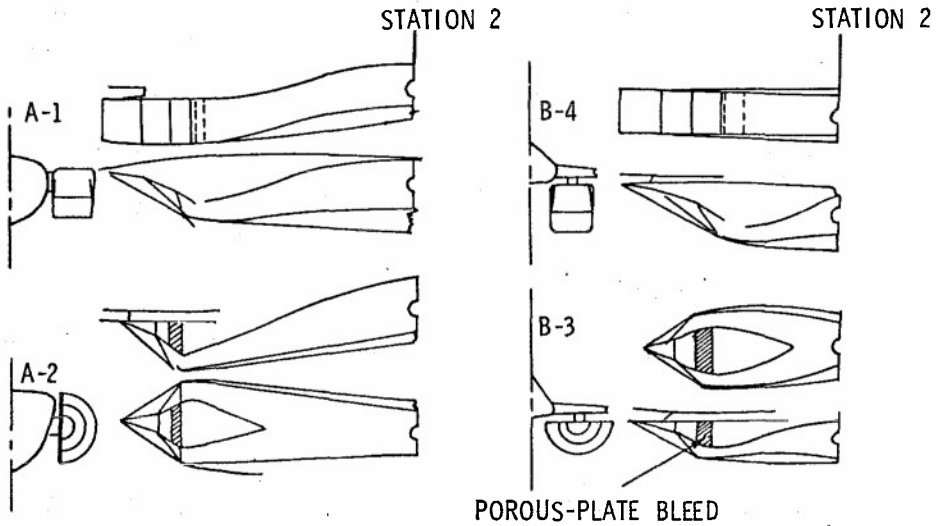


PROJECT TAILOR-MATE: COMPARISON OF AVERAGE FLOW FIELD PROPERTIES FIG. 5b



AIRFRAME-INLET INTERACTION: COMPARISON OF INLET PERFORMANCE

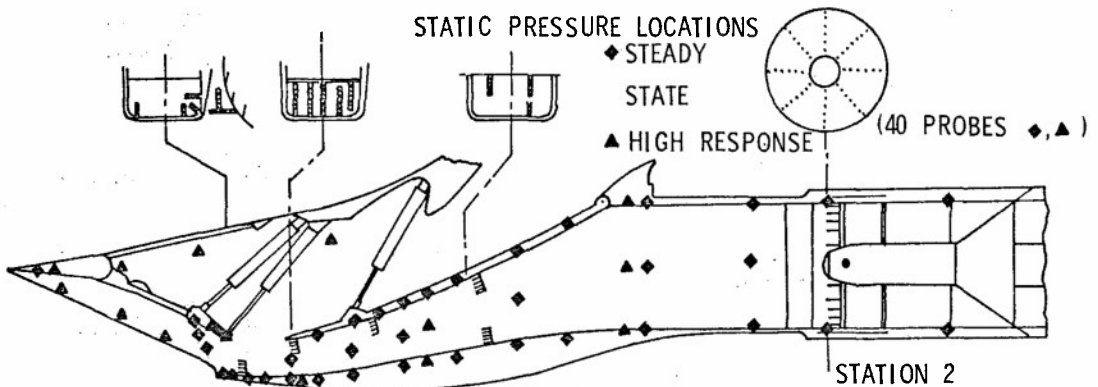
FIG. 6



STATION 0 IS FREE STREAM

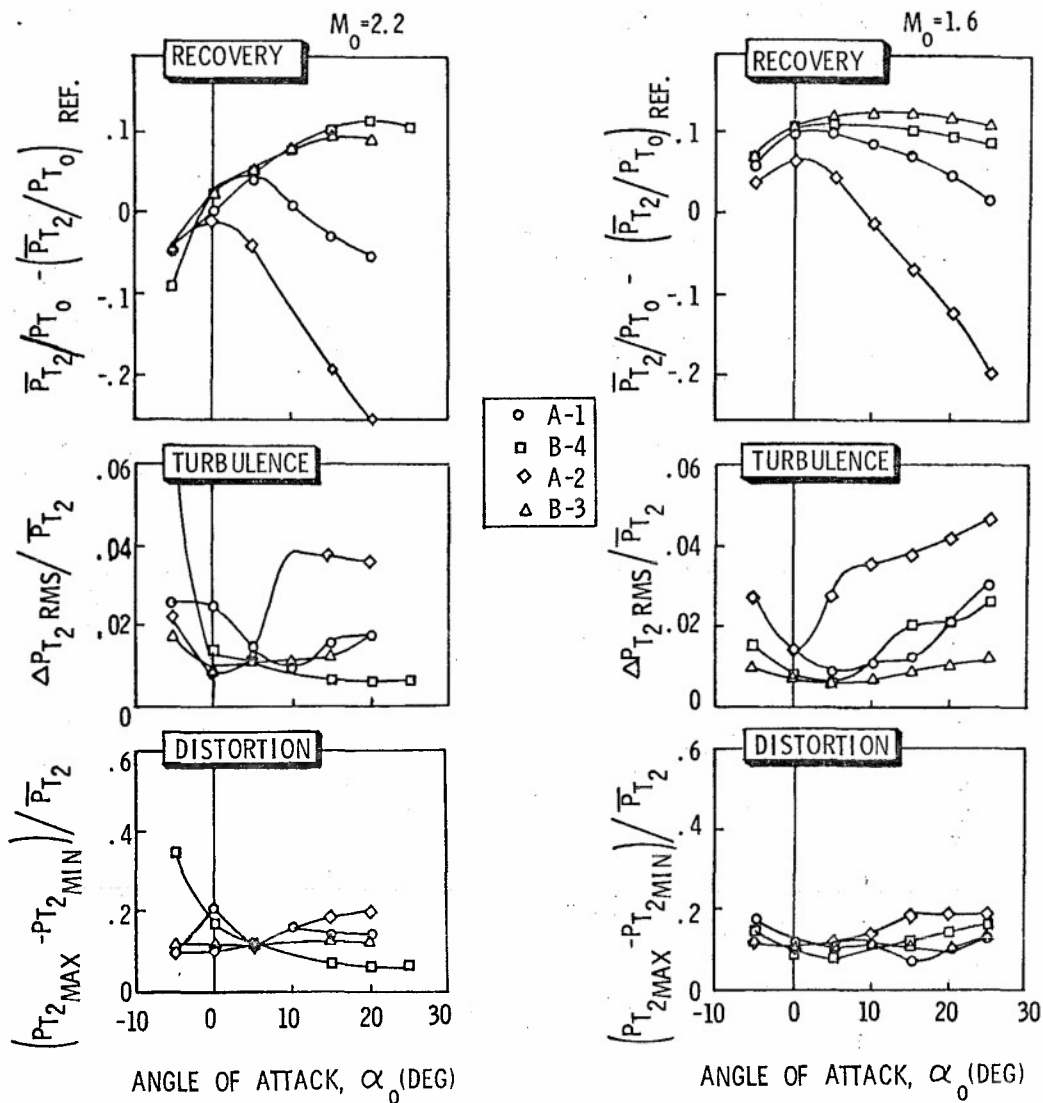
PROJECT TAILOR-MATE: COMPARISON OF INLET DESIGNS

FIG. 7



PROJECT TAILOR-MATE: TYPICAL INLET INSTRUMENTATION

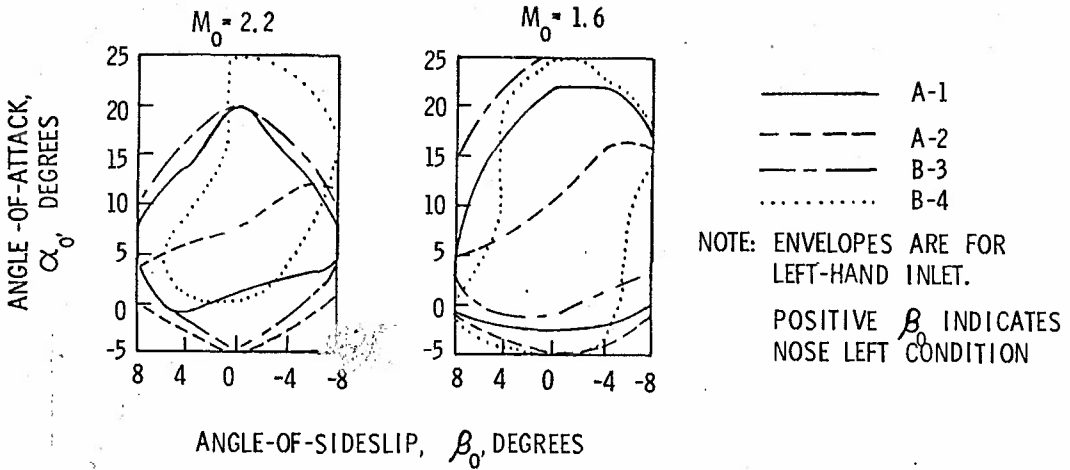
FIG. 8



NOTE: REF. CONDITION IS  $M_0=2.2, \alpha_0=0^\circ$  FOR A-1 INLET

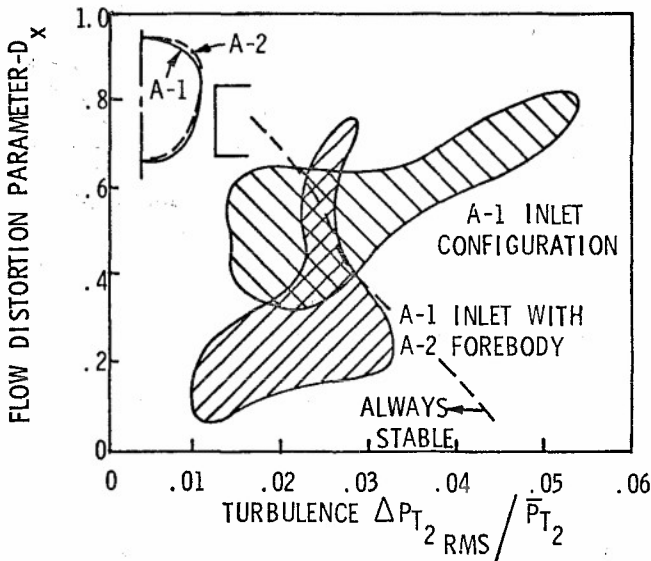
PROJECT TAILOR-MATE: COMPARISON OF INLET PERFORMANCE VARIATIONS IN MANEUVERING FLIGHT

FIG. 9



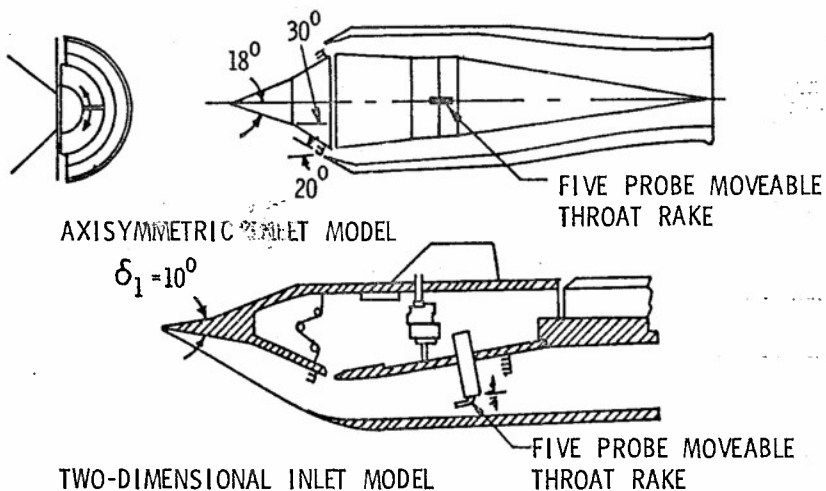
PROJECT TAILOR-MATE: FLIGHT MANEUVER COMPATIBILITY ENVELOPES

FIG. 10

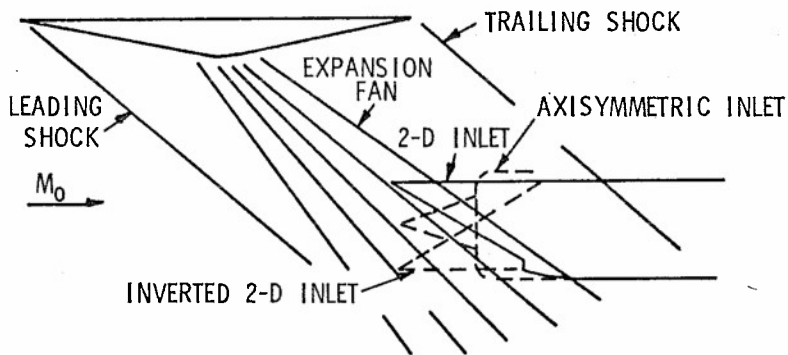


PROJECT TAILOR-MATE: EFFECT OF FOREBODY CONTOUR ON INLET / ENGINE COMPATIBILITY,  $M_0 = 2.2$

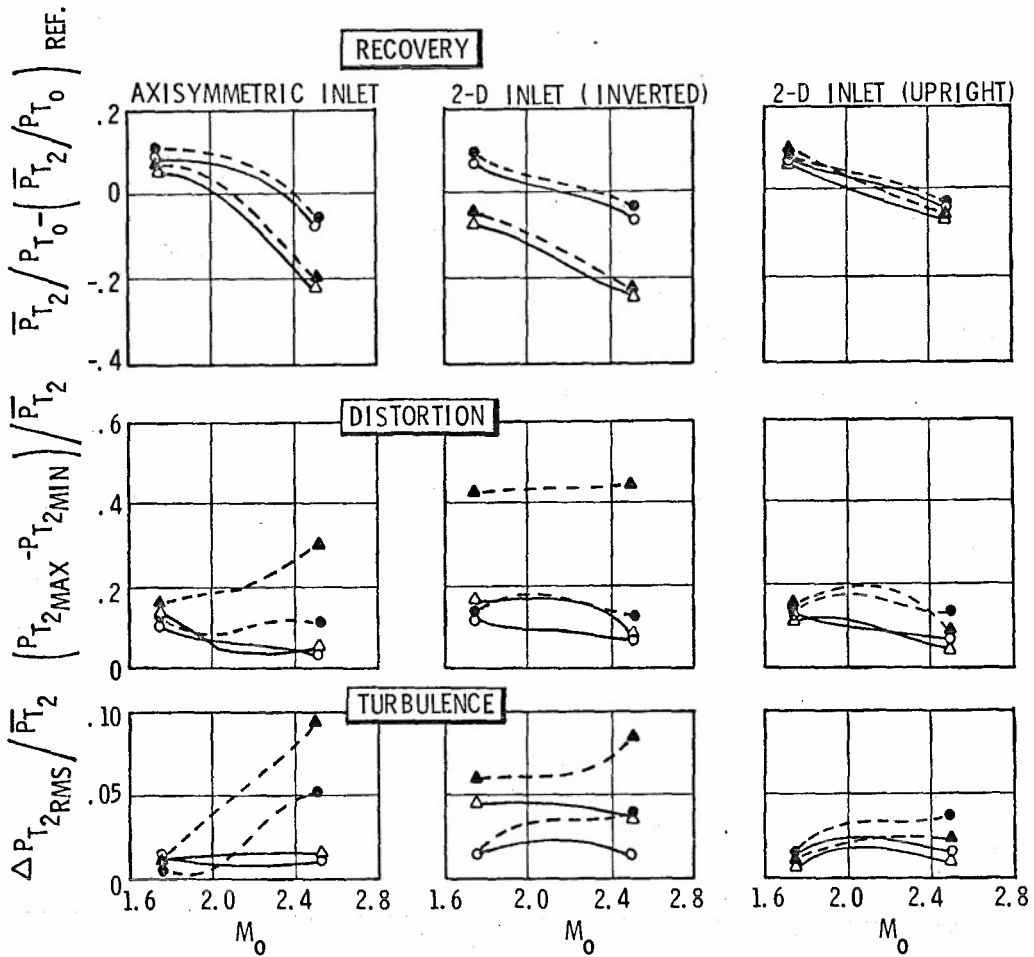
FIG. 11



SUPERSONIC INLET DEVELOPMENT: EXTERNAL COMPRESSION INLET MODELS FIG. 12



SUPERSONIC INLET DEVELOPMENT: INLET FLOW FIELD GENERATOR CONCEPT FIG. 13

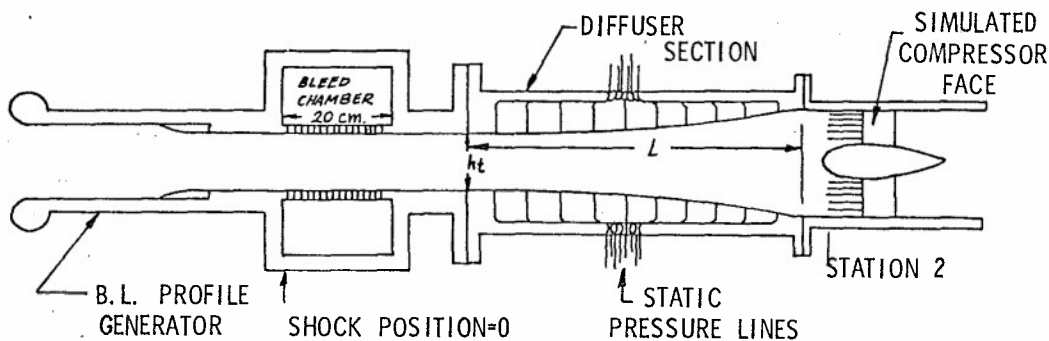


$\frac{\Delta M}{M_0}$	DISTORTION	—	COMPRESSOR FACE
o	0 (UNIFORM)	- - -	MOVEABLE RAKE
Δ	.20	· · ·	(FILLED SYMBOLS)

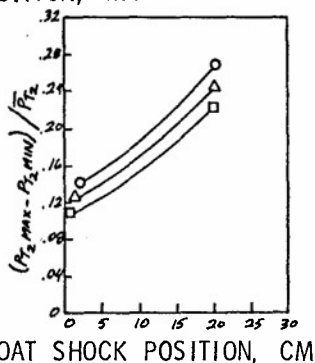
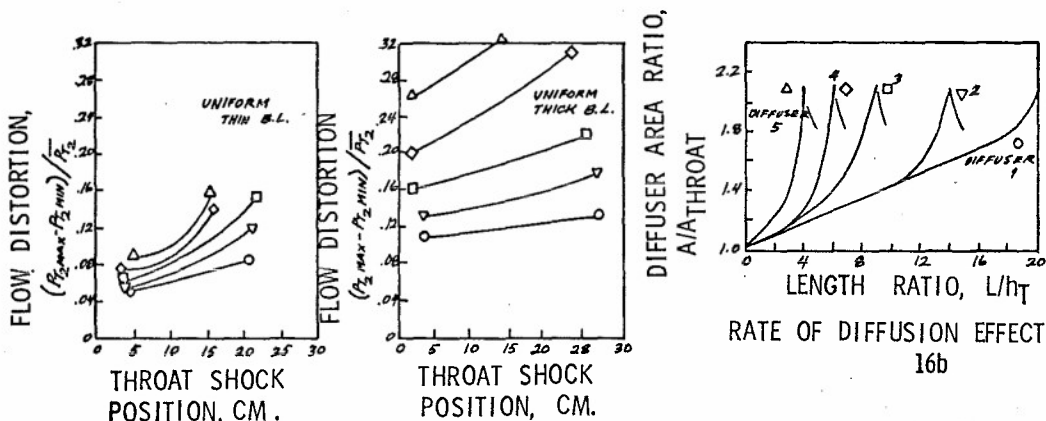
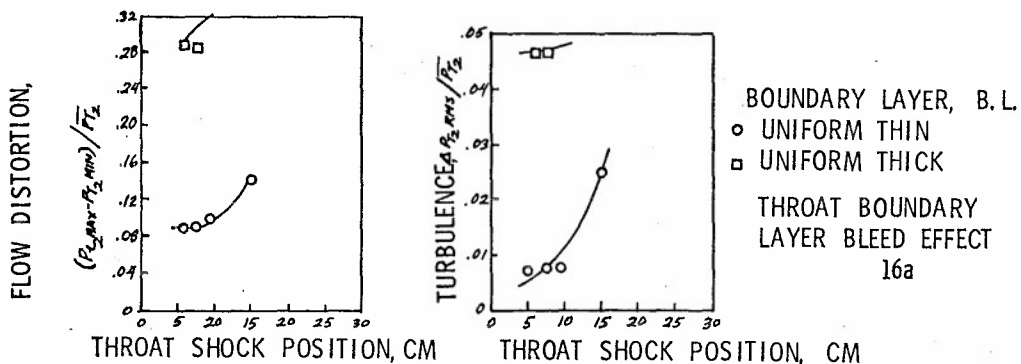
$$\frac{\Delta M}{M_0} = \frac{M_{LMAX} - M_{LMIN}}{M_0}$$

NOTE: REF. CONDITION IS  $M_0=2.2, \alpha_0=0$  FOR THE 2-D INLET (UPRIGHT)

SUPERSONIC INLET DEVELOPMENT: EFFECT OF FLOW DISTORTION UPSTREAM OF INLET,  $\alpha_0 = 0$  FIG. 14



SUBSONIC DIFFUSER DEVELOPMENT FLOW GENERATING DEVICE AND DIFFUSER TEST INSTALLATION CONCEPT FIG. 15



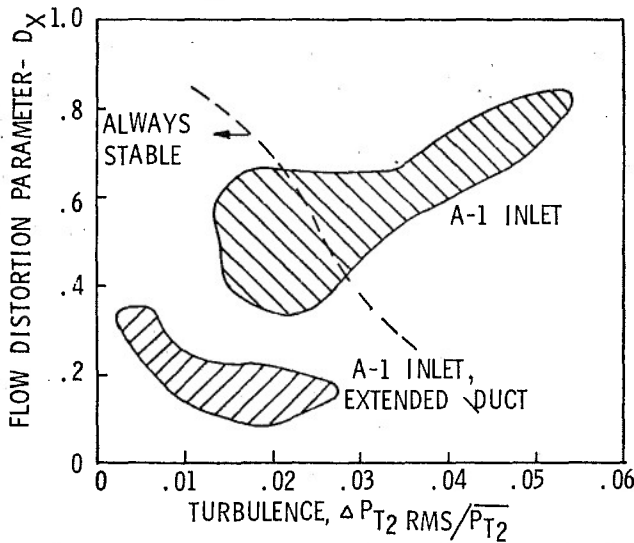
SYMBOL	VORTEX GEN. CONFIG.
○	BASIC DIFFUSER 4
△	X/L = 10%, RAMP ONLY
□	X/L = 10%, RAMP AND SIDES

WHERE X/L DENOTES DIFFUSER POSITION  
 VORTEX GENERATOR EFFECT  
 16c

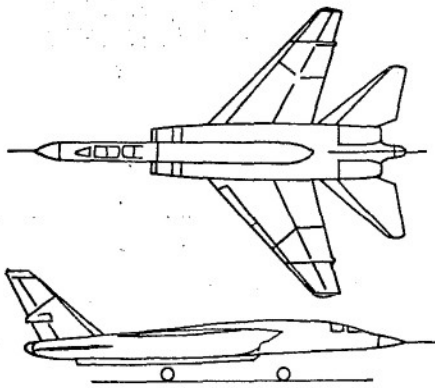
THROAT SHOCK POSITION, CM

SUBSONIC DIFFUSER DEVELOPMENT: EFFECTS ON PERFORMANCE

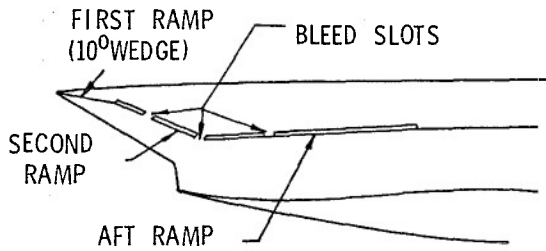
FIG. 16



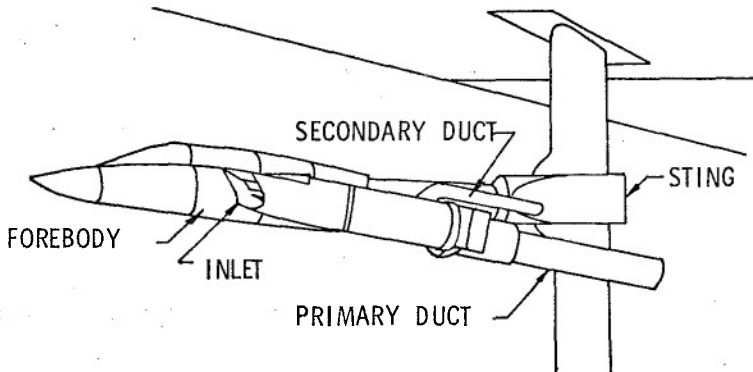
PROJECT TAILOR-MATE: EFFECT OF DUCT LENGTH ON INLET / ENGINE CAPABILITY,  $M=2.2$   
 FIG. 17



RA-5C AIRCRAFT - 18a



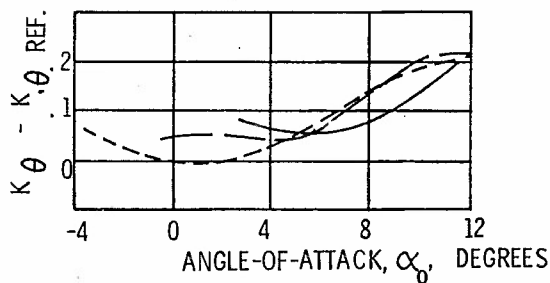
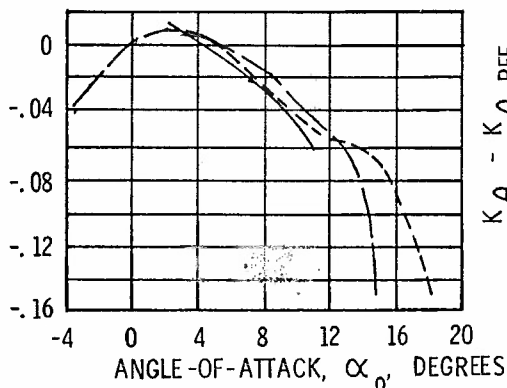
RA-5C INLET SCHEMATIC-18b



RA-5C 1/4 SCALE INLET TEST ARRANGEMENT - 18c

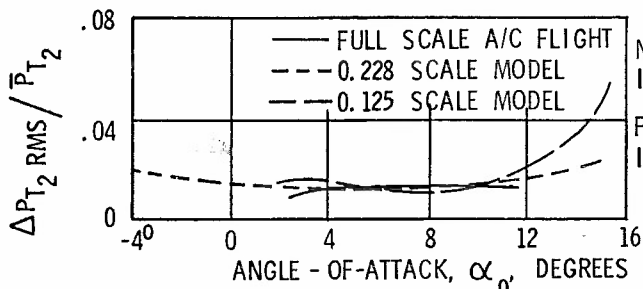
WIND TUNNEL / FLIGHT TEST CORRELATION: RA-5C AIRCRAFT AND INLET TEST MODEL  
 FIG. 18

$$\bar{P}_{T_2} / P_{T_0} - \left( \bar{P}_{T_2} / P_{T_0} \right)_{REF.}$$



CIRCUMFERENTIAL DISTORTION  
PARAMETER COMPARISON - 19b

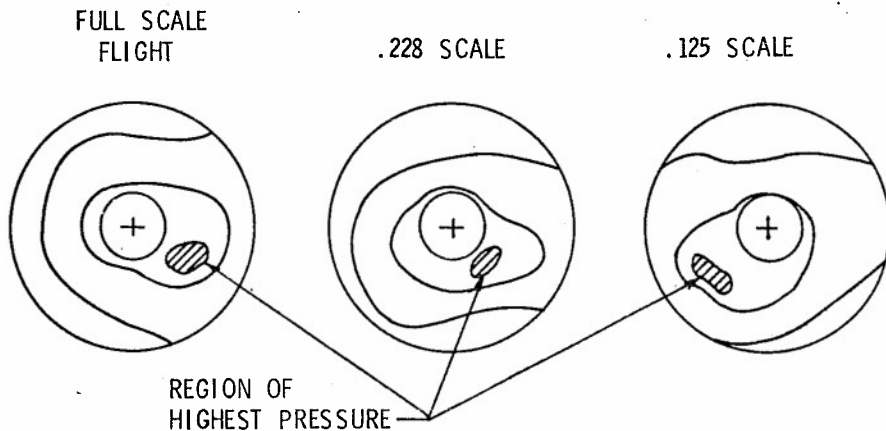
PRESSURE RECOVERY COMPARISON - 19a



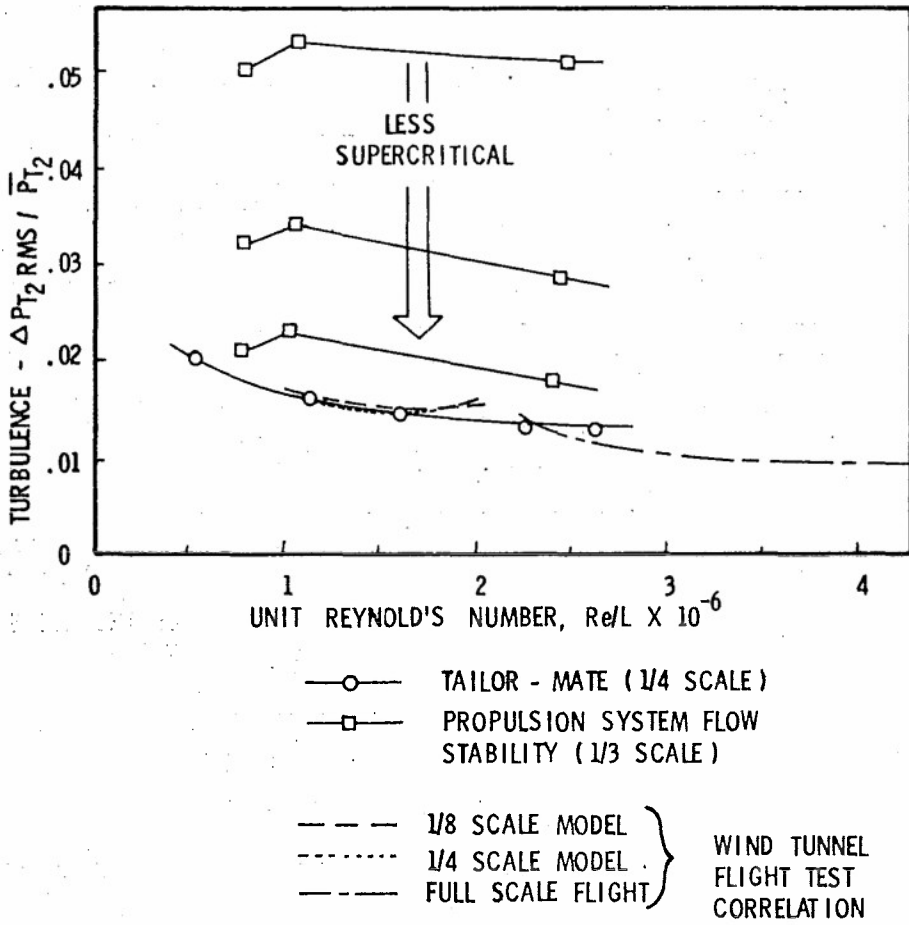
NOTE: REF. CONDITION  
IS  $M_0 = 1.8, \alpha_0 = 0$   
FOR THE .228 SCALE  
INLET

TURBULENCE COMPARISON - 19c

WIND TUNNEL/FLIGHT TEST CORRELATION: INLET PERFORMANCE COMPARISON  
FIG. 19



WIND TUNNEL/FLIGHT TEST CORRELATION: COMPARISON OF COMPRESSOR  
FACE TOTAL PRESSURE MAPS  
FIG. 20



REYNOLD'S NR. EFFECT ON TURBULENCE

FIG. 21

## INLET-ENGINE COMPATIBILITY ANALYSIS

by

S. H. Ellis  
 Senior Project Engineer  
 Pratt & Whitney Aircraft  
 P. O. Box 2691  
 West Palm Beach, Florida 33402

### SUMMARY

The destabilizing factors considered in compatibility analysis are reviewed, instrumentation and test techniques are discussed, and examples of compatibility data are given for a propulsion system consisting of a supersonic inlet and a turbofan engine. The primary destabilizing factor, inlet distortion, is measured with high response instrumentation capable of describing complex time-variant distortion patterns. The maximum-time variant distortions, determined from model inlet tests, are simulated during component and engine testing to define both loss in stall margin with distortion and the attenuation of distortion as it passes through the engine. The losses in stall margin due to engine causes, such as throttle transients, control tolerances and component interactions, are analyzed by dynamic simulations to identify potential system problems prior to system testing. Attention is focused on potential problems by compatibility audits that show the allocation of stall margin between destabilizing influences and identify areas where component improvement is needed.

### INTRODUCTION

Improvements in propulsion system performance have been achieved by extending operating limits, such as turbine temperature and compressor pressure ratio, and by keeping component efficiencies close to peak levels with more use of variable geometry. Use of variable geometry results in components that are held close to limits over the entire operating range, whereas they used to have a single critical design point and wide margin for most operating conditions. At the same time, aircraft altitudes and speeds have been increasing, and military aircraft are required to operate over an expanded range of angles of attack and sideslip. All these factors increase the difficulty of successful propulsion system integration to achieve inlet-engine compatibility.

Inlet-engine compatibility is the required propulsion system operation when the pilot moves the controls. Any combination of power lever transients and aircraft maneuvers must result in all components remaining within operating limits. In particular, flow breakdown in the compression system (surge) must be avoided by maintaining stability margin at all times.

Solving inlet-engine compatibility problems during flight testing is both expensive and time consuming. A propulsion system designer's objective is, therefore, to identify and fix potential problems before flight. This objective places increased emphasis on compatibility analysis, modeling, and testing, with a resultant analytical integration of propulsion system components before they are assembled for flight test.

Compatibility analysis starts during preliminary design with trade studies between compatibility, performance and weight. These studies result in features, such as those shown on figure 1, specifically included in the engine to improve compatibility.

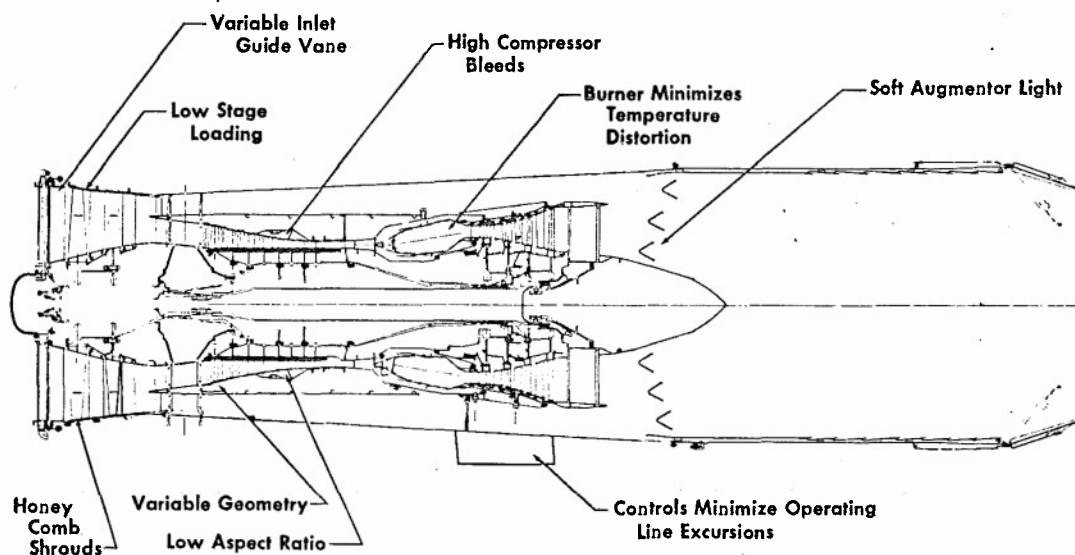


Figure 1. Design For Stability

A key decision during these trade studies is the stall margin allocated to destabilizing influences. The engine stability margin, which must be maintained at all times, can be conveniently represented on a compressor map by the residual stall margin after all influences that lower the surge line and raise the operating line have been accounted for (figure 2). Stall margin is defined as the difference between the undistorted surge line and the steady-state operating line at constant flow, expressed as a percentage of the undistorted surge line.

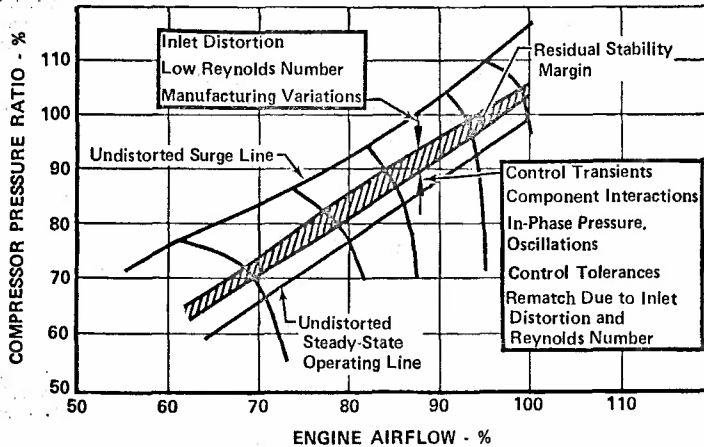


Figure 2. Many Factors Influence Stability Margin

The purpose of this paper is to review the principal factors affecting inlet-engine compatibility and the latest analysis and test techniques used during the time interval between engine cycle selection and first flight.

#### DISCUSSION

Airflow matching between the engine's flow requirements and the inlet supply changes the pressure field at the inlet-engine interface, which in turn, affects inlet compression system stability. Airflow matching is relatively easy for subsonic aircraft, because rounded inlet lips provide a large, stable flow range, and because engine corrected airflow varies little between takeoff, climb, and cruise. Flow matching is complex for supersonic aircraft, because both the engine and the inlet must operate over a larger flow range. Also, the flow characteristics are functions of different variables that do not have the same trends; the inlet airflow is a function of Mach number, angle of attack, angle of sideslip, and the bleed flow required to stabilize the shock system, while engine airflow demand is a function of engine inlet temperature, power lever position and, to a minor extent, inlet distortion level. Low airflow demand by the engine can force an external compression inlet into buzz and an internal compression inlet to unstall; both of these undesirable operating modes can cause surge. High airflow demand causes high distortion, which can again cause surge. The inlet and engine control systems must, therefore, maintain the airflow match in an acceptable corridor. Control schedules are selected to provide margin between the low-flow side of this corridor and inlet instability. The airflow used for stability analysis is at the high-flow side of this matching corridor, because the high inlet distortion associated with high flow gives the worst conditions for flow stability.

Inlet pressure distortion has a marked effect on the compression system surge boundary. In addition to inlet-airflow matching, distortion at the inlet-engine interface is a function of the shape of the aircraft forward of the inlet, angles of attack and sideslip, and aircraft speed. It is also a strong function of time because of turbulence produced by interactions between the aircraft flow field, the boundary layer, and the inlet compression system. The time-variant nature of typical supersonic inlet distortion is illustrated in figure 3, which shows a 25% change in distortion level over a period of 4 milliseconds. The maximum time-variant distortion is used in stability analysis (e.g., 25.4%  $\Delta P/P_0$  would be the level used from the data shown in figure 3).

High response instrumentation is required at the engine-inlet interface to measure distortion. This requirement is illustrated by figure 4, which shows inlet pressure contours measured by both low and high response instrumentation during a test where distortion was simulated by a turbulence generator. The high response probes measured more than five times the distortion of the low response probes. This testing established that a minimum of 40 total pressure probes with a frequency response of 1000 Hz are required for full-scale distortion testing. Reference 1 describes scale effects on model inlet data that require a frequency response inversely proportional to the model scale (e.g., 6000 Hz response required for a 1/6 scale model).

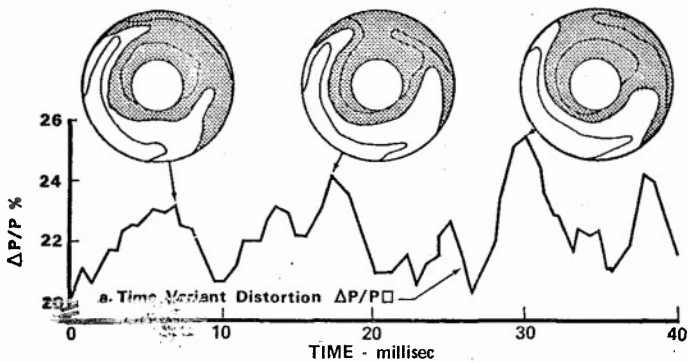


Figure 3. Time-Variant Distortion From A Supersonic Inlet Model

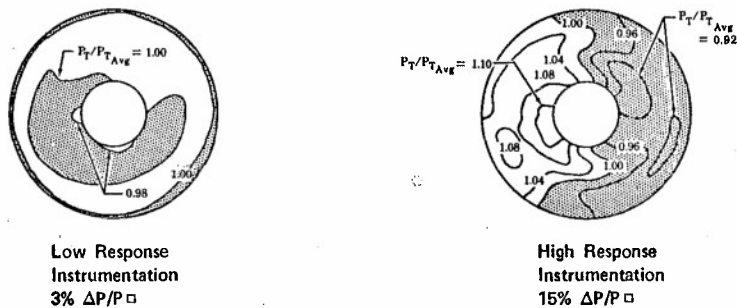


Figure 4. High Response Instrumentation Is Required To Measure Time-Variant Distortion

Maximum time-variant distortion was shown to be the surge-inducing event during research reported in Reference 2. Furthermore, simulation of maximum time-variant distortion by inlet screens will also cause surge (figure 5). The testing of reference 2 showed that pressure data should be filtered to match the compressor stability response. Digital data can be filtered by averaging pressures over a time period corresponding to 1/3 of a revolution. Equivalent analog filtering uses a third-order, linear-phase, low-pass filter that has 3 db attenuation at a frequency corresponding to rotor speed. When scale model inlet data are being processed, the filter cut-off frequency is increased inversely proportional to the model scale.

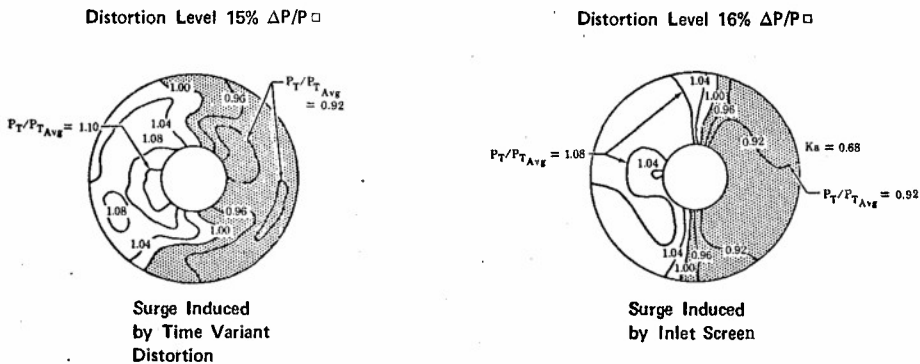


Figure 5. Simulation Of Maximum Time-Variant Distortion By Inlet Screens Reproduces A Surge

Inlet distortion data are generated during 1/6 scale model inlet testing at the rate of 20,000,000 patterns per hour for a test period which may be several weeks long; however, the data points of interest are included in the relatively brief periods of maximum time-variant distortion. This cost of analyzing all these data by normal digital techniques is prohibitive. Consequently, McDonnell Aircraft Company has designed an analog computer (Reference 3) to identify the points of peak distortion during model inlet testing. This computer records the maximum time-variant distortion for each run and the point in time at which it occurs. Digital data reduction is used in the neighborhood of points of peak distortion to provide a more accurate answer. Figure 6 shows that this analog computer correctly identifies the point of maximum distortion and gives peak values within 10% of the digital data.

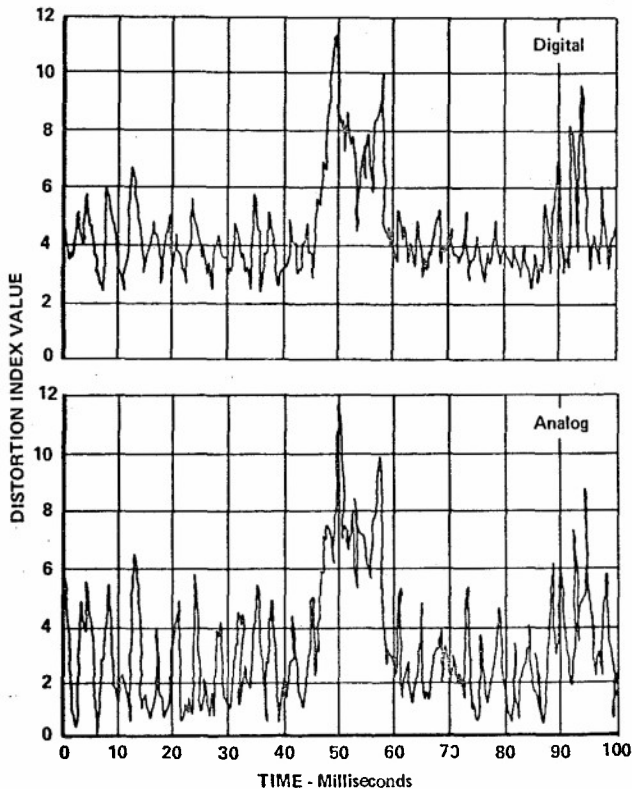


Figure 6. An Analog Computer Is Used To Identify Points Of Peak Distortion During Inlet Testing

Inlet temperature distortion can occur from ingestion of hot gas from armament firing or re-ingestion of exhaust gas. While pressure distortion is always present to some degree, temperature distortion at the engine inlet is infrequent and can usually be anticipated; consequently, special control action can be taken to minimize this effect. Downstream compressors are subjected to temperature distortion created by upstream compressors. Fortunately this effect is small compared to other destabilizing influences. Data showing the effects of temperature distortion on compressor stability are given in Reference 4.

Distortion factors describe an inlet distortion pattern by a number proportional to stall margin loss. They must account for pattern intensity, shape, and extent for all patterns which can be produced by the inlet. A distortion factor system with these elements has been used to translate complex and radial patterns into equivalent circumferential patterns, so that pattern severity can be compared. The unit of distortion used in this paper ( $\Delta P/P_0$ ) is the intensity of a 180 degree square wave pattern that will produce the same loss in stall margin as the pattern under consideration.

Loss in stall margin with distortion. Analytical tools for predicting the loss in stall margin with inlet distortion are in the early stages of development and have limited success. Consequently, component surge tests with and without distortion are required to define the effect of distortion on compressor stability (figure 7). The data for one value of corrected airflow and several inlet patterns are correlated by the distortion factor  $\Delta P/P_0$  in figure 8. The slope of the correlation in figure 8 is called the sensitivity to distortion. Both the sensitivity of the compressor and its undistorted stall margin are necessary to define stability.

Distortion attenuation by upstream components improves the operating environment and stability of downstream components. Maldistributed flow causes a performance loss in each compression stage that is exposed to distortion. It is important, therefore, to attenuate distortion early in the compression system, so that later stages may be designed for high performance. Figure 9 shows attenuation of a 180 degree circumferential square wave inlet pattern as it passes through a low hub-tip ratio fan. Almost all of the inlet distortion is removed by the fan tip, whereas substantial distortion still persists at the root discharge. Changing the square wave inlet distortion to the sine wave exit distortion at the root results in a pattern which causes lower stall margin loss, even though the intensity is only slightly reduced. The root therefore shows distortion attenuation that is higher than would be inferred from a comparison which only considered the change in intensity.

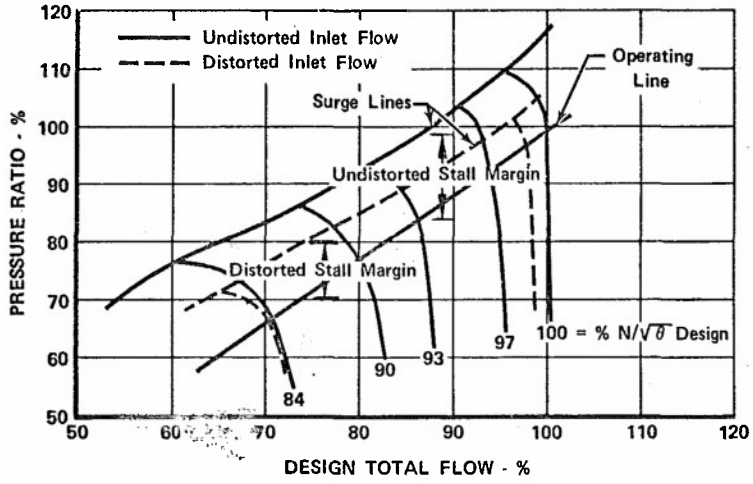


Figure 7. Component Testing With And Without Distortion Is Required To Define The Effect Of Distortion On Stability

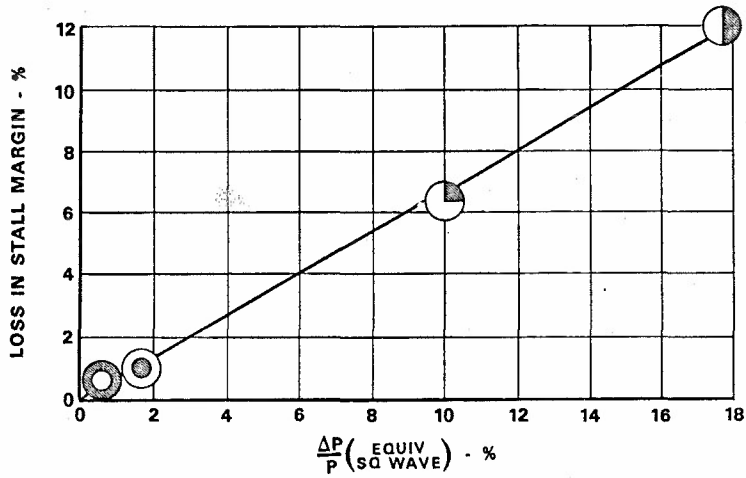


Figure 8. Sensitivity To Distortion - Loss In Stall Margin Due To Distortion Is Correlated By The Distortion Factor

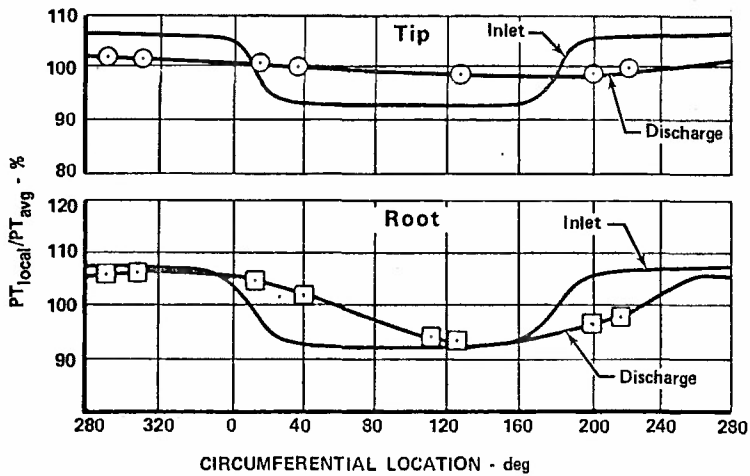


Figure 9. Attenuation Of Circumferential Distortion By A Fan

Figure 10 shows that data points taken with tip radial distortion are scattered evenly about the discharge profile without distortion. This complete attenuation of radial distortion is typical of most fans. Figure 11 shows the complete attenuation of hub-radial distortion. Here again the data points at the discharge with distortion are scattered evenly about the discharge profile determined without distortion. A compressor downstream of this fan must be designed to accept the radial flow pattern generated by the fan in addition to the residual component of the inlet circumferential pattern. Consequently, "undistorted" compressor testing is carried out with this radial pattern. Distorted testing has the circumferential distortion screen being tested superimposed on the normal radial pattern produced by the fan.

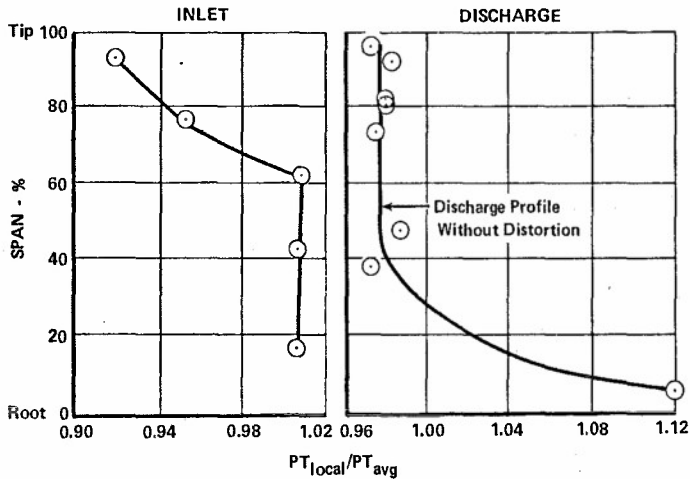


Figure 10. Complete Attenuation Of Tip Radial Distortion

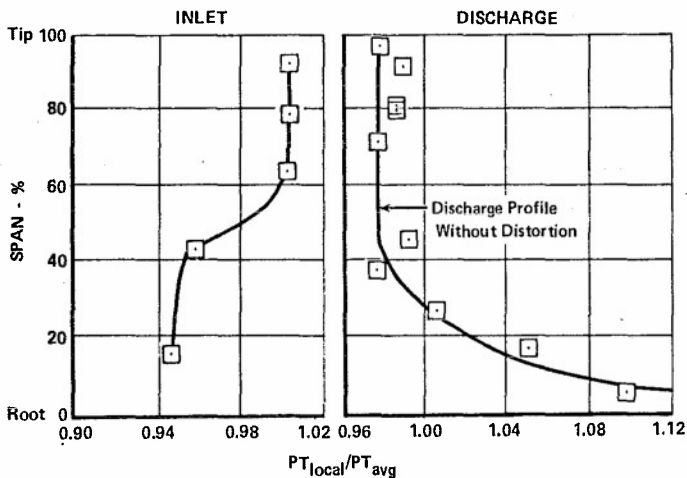


Figure 11. Complete Attenuation Of Hub Radial Distortion

Distortion simulation during early component and engine testing is accomplished by simple square wave circumferential and radial screens. Testing with simple patterns is relatively inexpensive and enables distortion to be tracked through the component to identify problem areas in stage matching and distortion attenuation. An important measurement is the temperature distortion produced at the discharge of a fan as a by-product of inlet pressure distortion attenuation. This temperature distortion causes loss in stall margin on the compressor following the fan.

Testing with simple distortion patterns defines the distortion factor that is used to sift inlet data and define a set of the worst time-variant patterns. These patterns are then simulated by complex inlet screens to check the superposition of radial and circumferential distortion. Changes in the formulation of the distortion factor may be required to correlate this new test data.

After components have been developed by screen testing to approach compatibility goals, testing is carried out with a turbulence generator or preferably an inlet simulator to check the correspondence between time-variant distortion and simulation of maximum time-variant distortion by inlet screens. Both a turbulence generator and an inlet simulator produce time-variant distortion by setting up a shock system. The difference is that the turbulence generator is designed to produce a given range of turbulence levels, while an inlet simulator is designed to set up the same type of shock system, flow passages, and bleeds as a specific inlet and thereby reproduce the flow field at the entrance to the engine in as realistic a manner as possible.

Reynolds number effects can cause a loss in stall margin as large as the loss due to inlet distortion for aircraft which operate over a wide Reynolds number range. Testing to define the effect of Reynolds number on stability should be accomplished in the early stages of an engine development program, because the results can have a significant effect on the stall margin required to meet compatibility goals. Reynolds number effects may also require control system revision to obtain the best compromise between performance and compatibility over the flight envelope.

The loss of stall margin due to time-variant distortion, temperature distortion, and Reynolds number has been discussed. The primary effect of these destabilizing factors is to lower the surge line. Loss of stall margin is also caused by steady-state and transient effects which raise the operating line. The transient operating line depends on the interaction of components in the propulsion system that are not operated together until late in the development program. Consequently, several levels of dynamic simulation are used to predict system operation and thereby obtain early knowledge of potential problems. These simulations are discussed below in conjunction with destabilizing phenomena which raise the operating line.

Power lever transients are analyzed by an engine and control digital dynamic simulation (Reference 5) to give a transient compressor operating line such as that shown in figure 12. The increase in fuel flow required to accelerate from idle raises the operating line toward the surge line, the maximum loss in stall margin being set by acceleration requirements. Conversely, a deceleration causes a drop in operating line with consequent increased stability margin.

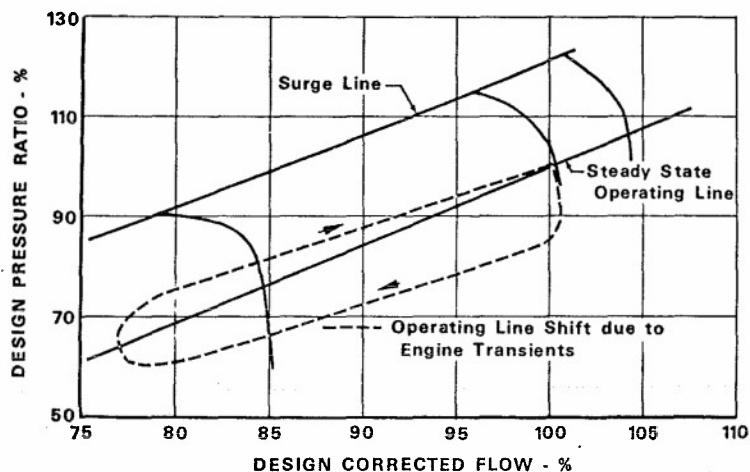


Figure 12. Power Lever Transients Analyzed By Engine And Control Dynamic Simulation

This engine and control simulation represents the entire engine from the fan through the nozzle with the interaction of all engine control systems. It is used for generating control schedules, studying engine transients, and evaluating methods of controlling around stability problems (e.g., control reset to accommodate gas ingestion disturbances caused by armament firing).

Component interactions are analyzed by a dynamic simulation which is correlated with the latest component and engine test data. In the majority of cases, interaction effects are predicted, and corrective action is taken before testing. Occasionally dynamic simulations do not contain sufficiently detailed knowledge to predict a problem. An example of a recent instance where dynamic simulation was used for diagnosis rather than prediction occurred during testing of a mixed-flow turbofan engine when interaction occurred between the augmentor control system, augmentor, and compression system. Pressure perturbations that destabilized both the fan and compressor were observed during sequential ignition of portions of an augmentor burner system. Additional instrumentation clearly showed a problem area. A more detailed dynamic simulation of the fuel system and augmentor was then used to isolate the cause of the problem in the augmentor fuel system and to define both an interim solution to complete the planned test program and a long-range solution for the production component.

**In-phase pressure oscillations.** If the pressures measured at the engine-inlet interface are uniform in space (no distortion) but variable with time, there will be a loss in stability that is not accounted for by the distortion factor. This type of time-variant inlet data is called "in-phase oscillation." The typical in-phase oscillations shown in figure 13 are small and do not have much effect on engine stability. A control system failure in the engine or the inlet, however, may create an airflow mismatch that forces the inlet into a buzz region. In this event pressure oscillations on the order of 30% can occur.

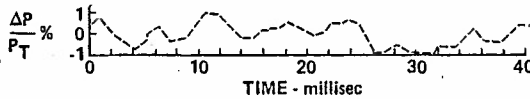


Figure 13. Typical In-Phase Oscillations From Supersonic Inlet Data

The large loss in stall margin caused by inlet buzz has been estimated from an engine and control simulation and is shown by the solid line in figure 14. This simulation had a frequency response limited to 10 Hz, because the volumes represented in the simulation had been lumped together to reduce operating cost. The conditions determined from the engine and control simulation at the inlet of the fan, the fan discharge, and the compressor discharge were input as boundary conditions to a fan and compressor stage-by-stage simulation (Reference 6) which has an order of magnitude better frequency response than the engine and control simulation. The fan and compressor simulation showed a greater loss in surge margin as shown by the dashed line in figure 14. This difference between the results of two simulations illustrates the need for several levels of dynamic simulation to analyze the propulsion system fully.

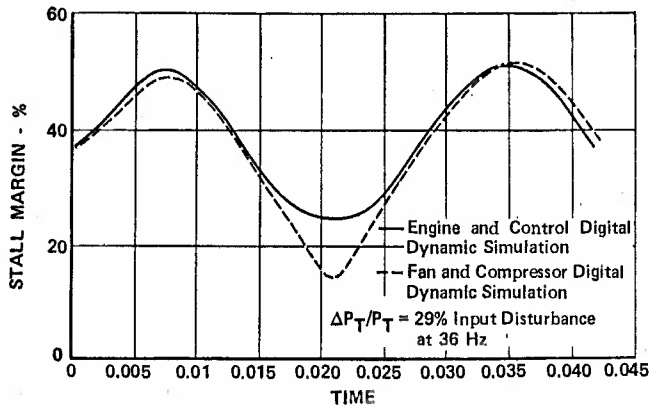


Figure 14. Fan Response To High Amplitude In-Phase Oscillations

Fan and compressor simulations are also used to evaluate component interactions by varying the amplitude of in-phase oscillations at a given frequency until instability occurs. In the example shown in figure 15, the compressor generates system instability at low disturbance frequencies and stabilizes the fan at high frequencies.

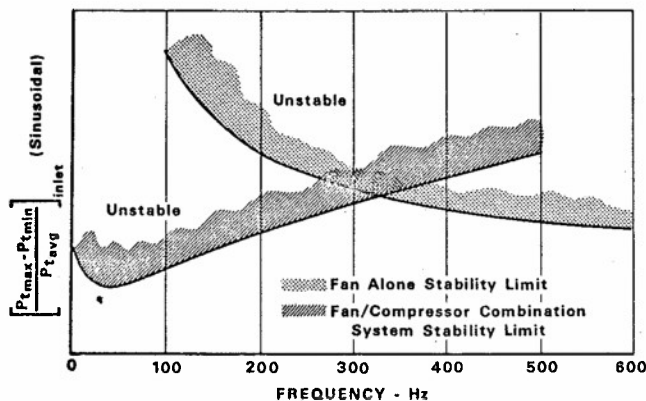


Figure 15. Amplitude-Frequency Stability Plot - Interactions Modify Stability Limits

Control tolerance and sensor errors cause movement of the operating line and can also change the surge line, if they cause variable geometry to deviate from the scheduled setting. The effect of tolerances and sensor errors on stability is normally studied using the steady-state mode of the engine and control dynamic simulation, because this simulation is required to have a complete description of both the control and the engine components. The most adverse movement of the operating point for stability is caused by control tolerances and sensor errors that result in a combination of reduced airflow and increased pressure ratio.

A study of control sensor errors is particularly important during the control definition phase of engine design. A control cannot distinguish between true and false signals; consequently, if the study shows large sensitivity to a particular control tolerance, or if the control uses a sensor with an inherently large error band, then the control mode should be changed before hardware is committed.

Rematch due to inlet distortion and Reynolds number. Both inlet distortion and low Reynolds number can cause losses in flow and efficiency. These losses can rematch the operating line in either a stabilizing or a destabilizing direction depending on the engine control mode, the type of inlet pattern, and the relative effect on the fan and compressor of both inlet distortion and Reynolds number. Component data from simple inlet screens is used to measure the loss in flow and efficiency with distortion. These effects are included in the engine and control simulation that is operated at steady-state conditions to determine the rematch. The average time-variant distortion is used to determine rematch in contrast to the maximum time-variant distortion that is used to determine the loss in surge line.

So far, the major factors causing loss in stability have been individually reviewed. These factors are combined into a "compatibility audit" to focus management attention on components needing improvement. In the example of a compatibility audit shown in figure 16, the fan has a small but adequate stability margin. This fan would require more development, if this level of inlet distortion persists in regions of the flight envelope where Reynolds number effects are significant. If the large compressor stability margin shown in figure 16 is also obtained at other flight conditions, then engine rematch to obtain more performance should be studied.

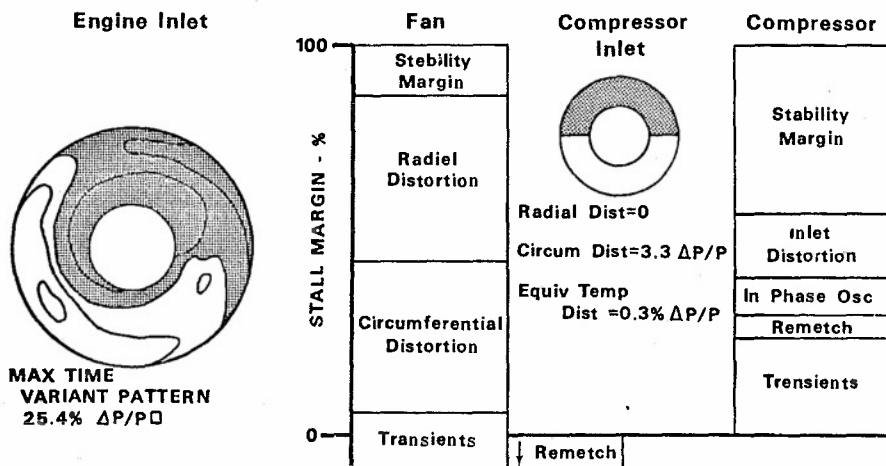


Figure 16. Compatibility Audits Identify Components Needing Improvement

As the development program proceeds, compatibility status is determined using better information. Testing with simple inlet screens is replaced by more realistic testing with an inlet simulator. Individual component test data are replaced by dual-spool test data. Dynamic simulation is replaced by engine transient testing. This procedure of analysis and testing should result in the first combined engine-inlet test in an altitude facility being a verification test rather than one in which new problems are discovered. If problems do develop, however, the information obtained during component testing and the subsequent updated dynamic simulations are available to identify early solutions.

#### CONCLUDING REMARKS

Compatibility analysis starts by allocating sufficient stall margin in a preliminary engine design to accommodate all destabilizing influences. Since high stall margin results in weight and performance penalties, this stall margin allocation focuses attention on components needing improvement. These may be an inlet which generates high distortion, a fan with low distortion attenuation, a compressor with high sensitivity to distortion, or a control system which has large transient excursions or high sensor errors.

Testing to develop compatibility requires specialized equipment to simulate distortion, high response instrumentation, and the resulting analysis and digestion of extremely large quantities of data. High response instrumentation is particularly needed at the engine-inlet interface during model inlet testing and during engine tests with an inlet or an inlet simulator, since low response instrumentation will only identify a fraction of the inlet distortion.

Component integration for compatibility relies heavily on dynamic simulations that are used to define design criteria, to obtain early knowledge of potential integration problems, and to identify solutions to problems. While dynamic simulations are key engineering tools, compatibility audits are the management tools used to focus attention on problem areas. The key to successful system integration lies in the use of these tools to recognize and solve potential problems early enough to avoid flow instability in flight.

## REFERENCES

- <sup>1</sup>Tjonneland, E. and O'Neill, E. B., "Total Pressure Turbulence in a Sharp Lip Axisymmetric Supersonic Intake Operating in the Flow Field of an Airplane Wing and Flap System in Takeoff Configurations," AIAA Paper No. 68-50, June 1968.
- <sup>2</sup>Plourde, G. A., and Brimelow, B., "Pressure Fluctuations Cause Compressor Instability," Airframe/Propulsion Compatibility Symposium, June 1969, Sponsored by Air Force Aero Propulsion Laboratory, Air Force Flight Dynamics Laboratory, Wright-Patterson Air Force Base, Ohio.
- <sup>3</sup>Lynch, F. R., and Slade, C. J., "Data Acquisition and Automated Editing Techniques for Engine-Inlet Tests," AIAA Paper No. 70-596, May 1970.
- <sup>4</sup>Rudey, Richard A. and Antl, Robert J., "The Effect of Inlet Temperature Distortion on the Performance of a Turbo-Fan Engine Compressor System," NASA TMX-52788, June 1970.
- <sup>5</sup>Przybylko, S. J., Hutcheson, L., Suder, B., and Warwick, T. R., "Advanced Integrated Digital Engine Simulation," AIAA Paper No. 70-633, June 1970.
- <sup>6</sup>Kulberg, J. F., Shepard, D. E., King, E. O., and Baker, J. R., "Dynamic Simulation of Turbine Engine Compressor," AIAA Paper No. 69-486, June 1970.
- <sup>7</sup>Cotter, H. N., "Integration of Inlet and Engine - An Engine Man's Point of View," SAE Paper No. 680286, April 1968.
- <sup>8</sup>Langston, C. E., "Distortion Tolerance - By Design Instead of By Accident," ASME Paper No. 69-GT-115, March 1969.
- <sup>9</sup>Campbell, J. L., and Ellis, S. H., "Engine/Inlet Compatibility Analysis Procedure," AIAA Paper No. 70-941, June 1970.

ON THE APPLICATION OF A TIME DEPENDENT TECHNIQUE  
IN TRANSONIC DOUBLE FLOW NOZZLE SOLUTIONS

by

CARLO OSNAGHI  
Lecturer of Turbomachinery - Politecnico of Milan

ENNIO MACCHI  
Assistant Professor - Politecnico of Milan

ISTITUTO DI MACCHINE - POLITECNICO DI MILANO  
Piazza Leonardo da Vinci, 32 - 20133 Milano-Italy

SUMMARY

The modern aeronautical industry calls for accurate methods of prediction of exhaust system performance. The interactions among the various streams of double flow nozzles make a rigorous fluid dynamic treatment difficult, particularly for subsonic and transonic flows.

In order to overcome these difficulties, the possibility of applying a time dependent technique using the method of characteristics was considered. A computer program was written, which proved to be able to solve axisymmetric, inviscid flows contemporarily, irrespective of their subsonic, transonic or supersonic nature.

In the present paper some results relating to a transonic nozzle and a subsonic double flow nozzle are presented and compared with experimental data.

LIST OF SYMBOLS

A	flow area	$\alpha, \beta$	functions defined by Eq(A1-2)
a	speed of sound	$\alpha_0, \beta_0$	arbitrary functions defined by Eq(A1-4). respectively for $Y=Y_0$ and $X=X_0$
$a_0$	speed of sound at total temperature $T_0$ .	$\gamma$	ratio of specific heats
$D_5, D_6, D_8$	quantities defined respectively by Eq(A2-13), Eq(15), and Eq(A2-14)	$\delta$	quantity defined by Eq(A2-17)
H	total enthalpy	$\xi$	quantity in compatibility equations, respectively equal to zero (plane flows) or to one (axisymmetric flows)
h	static enthalpy	$\theta$	angle between the axes x and $x_1$
M	Mach number	$\rho$	density
$\dot{m}$	mass flow rate		
P	total pressure		
p	static pressure		
S	entropy		
T	static temperature		
$T_0$	total temperature		
t	time		
$t_x$	time, at which perturbations on boundary geometry are stopped		
V	flow velocity		
X, Y	stretched coordinates, respectively in direction parallel and perpendicular to the flow, defined in Appendix 1.		
$X_0, Y_0$	coordinates, along which the function $\beta_0$ and $\alpha_0$ are defined		
x, y	coordinates in the physical plane		
$x_1, y_1$	coordinates respectively in direction parallel and perpendicular to the flow, in the natural coordinate system.		
XX	quantity defined by Eq (13)		
YY	quantity defined by Eq (14)		
Z	variable for isentropic flow of perfect gas with constant $\gamma$ , defined by Eq. (20)		

Subscripts :

A, B, C,	at base points of bicharacteristics
D, E, F	(see the figures in Appendix 2)
M, N	at points to be computed
0	at center of the ellipse, along which the characteristic surface cuts the plane $t=t_0$
P	at projection of M on plane $t=t_0$
$\infty, e, j, t$	at stations $x_\infty, x_e, x_j, x_t$ (see Fig.5 and 8)
1	for the internal stream
2	for the external stream
i	at initial time

## INTRODUCTION

The modern aeronautical industry calls for precise methods of prediction of all propulsion components. A variety of exhaust system configurations has been proposed for different flight situations (see Fig.1). In all the cases represented in Fig.1, the interactions among the various streams make a rigorous treatment of the fluid-dynamic problem difficult. In fact, the correct description of flow phenomena requires the contemporary solution of continuity, energy, and momentum equations for all considered streams. The numerical solution of the resulting system of differential equations is in general difficult, even under simplifying hypotheses, namely inviscid fluid and axisymmetric flow. While for supersonic flow the hyperbolic equations of motion can be fairly easily solved by the method of characteristics, the presence of subsonic flow regions requires the solution of an elliptic equation, with the well-known convergence-problems.

It is well-known (see for example (1) and (2)) that the introduction of the time variable leads to a hyperbolic equation. Hence, it is possible to solve unsteady flows with the method of characteristics, irrespective of their subsonic, transonic, or supersonic nature. Since steady flows can always be considered asymptotic limits of unsteady flow situations, the same method can also be applied for steady problems. The purpose of the present paper is to discuss the possibility of applying this time dependent technique using the method of characteristics to some unsolved double-flow nozzle problems. The above technique is suitable for general use, since it can be applied to any inviscid plane or axisymmetrical flow. To show the wide variety of possible applications of the method, some of the cases which have been successfully solved during the computer program set up are exhibited in Fig. 2.

The general proceeding carried on by the computer program is shown in Fig.3 for the simple case of an axisymmetric nozzle discharging into an infinite capacity reservoir. The mass flow variation (Fig.3a-b) and the flow area ratio  $A/A^*$  (Fig.3c) are represented along the axis at various phases of solution:

1. An initial steady flow condition (uniform flow in a constant area channel) is given at  $t=0$ .
2. Perturbations on the boundary are imposed during the interval of time  $0 < t < t_x$ ; they produce the unsteady flow situation represented in Fig. 3a.
3. When the desired final geometry is reached ( $t=t_x$ ), no more perturbations are given, and the flow evolves into a steady solution as shown in Fig.3b.
4. When a steady situation is reached in the region of interest (for  $x_\infty < x < x_1$  in Fig.3c), the calculations are stopped. An exactly similar proceeding can be followed when more than one stream is considered and/or more than one boundary is changed.

Besides all steady flows applications, it is obvious that this method allows one to investigate those situations in which unsteady states are of interest per se, as for instance the flow phenomena occurring during the opening and closing of an adjustable nozzle. The main obstacle to a wider engineering application of the above method is brought about by the large amount of computer time which is necessary to reach steady situations. Nevertheless, even if no cheap computer time is available, the adoption of this method will be any way useful for the control of simplified treatments of easier design use, such as linearized solutions (3) or one-dimensional approaches (4,5).

## METHOD OF ANALYSIS

The governing laws for an inviscid, adiabatic and unsteady flow are given by Eqs (1-3):

- continuity equation:

$$\frac{\partial \rho}{\partial t} + \nabla \cdot (\rho \vec{V}) = 0 \quad (1)$$

- energy equation along the flow path of a particle:

$$d'(H) = - \frac{\partial}{\partial t} \left( \frac{V^2}{2} \right) dt \quad (2)$$

where the operator  $d' ( )$  is defined by  $d' ( ) = \vec{V} dt \cdot \nabla ( )$

- equation of motion:

$$\frac{\partial \vec{V}}{\partial t} + \nabla H = \vec{\nabla} x (\nabla x \vec{V}) + T \nabla S \quad (3)$$

**COORDINATE SYSTEM.** The coordinate system given in Appendix 1 was introduced by Carriere and Capellier (2), and proved to be very useful for these applications. Besides all the peculiar advantages of a natural coordinate systems, it allows one to stretch the computational meshes by a proper choice of the function  $\alpha$  and  $\beta$  of Eq. (A1-4). The advantages related to this degree of freedom will be discussed later.

**COMPATIBILITY EQUATIONS.** Let us assume that flow conditions are known in the whole region of interest in the plane  $t=t_0$  (see Fig.4). The particle in the point  $O(X_0, Y_0, t_0)$  will be at point  $M(X_0 + dX, Y_0 + dY, t_0 + dt)$  after the increment of time  $dt$ . In order to identify the particle completely, the following four variables are required: the module of velocity  $V$ ; the

angle  $\theta$ ; and two parameters of state, for example pressure and density. In fact, any other function of state  $f$  can be derived by the equation of state of the fluid:

$$f = F(p, \rho) \quad (4)$$

From the theory of characteristics it is known that the characteristic surface passing through  $M$  is a conoid, which cuts the plane  $t=t_0$  along an ellipse, having center in  $O$  and axes  $AB$  and  $CD$  parallel to  $X$  and  $Y$ . Although the compatibility relations can be derived for any generatrix, they assume a very simple form along the four particular lines  $AM$ ,  $BM$ ,  $CM$ , and  $DM$ , which are called bicharacteristics. Total derivatives with respect to time and compatibility equations along the bicharacteristics and the trajectory  $OM$  are given in Table 1. They hold for plane ( $\xi=0$ ) and axisymmetric ( $\xi=1$ ) flows.

LINE	$\frac{d}{dt}$		COMPATIBILITY EQUATIONS
A-M	$\left(\frac{d}{dt}\right)_{AM}$	$= \frac{\partial}{\partial t} + \frac{V+a}{\alpha} \frac{\partial}{\partial X}$ (5a)	$\frac{1}{\rho a^2} \left(\frac{dp}{dt}\right)_{AM} + \frac{1}{a} \left(\frac{dV}{dt}\right)_{AM} = -\frac{V}{\beta} \frac{\partial \theta}{\partial Y} - \xi \frac{V \sin \theta}{y}$ (5b)
B-M	$\left(\frac{d}{dt}\right)_{BM}$	$= \frac{\partial}{\partial t} + \frac{V-a}{\alpha} \frac{\partial}{\partial X}$ (6a)	$\frac{1}{\rho a^2} \left(\frac{dp}{dt}\right)_{BM} - \frac{1}{a} \left(\frac{dV}{dt}\right)_{BM} = -\frac{V}{\beta} \frac{\partial \theta}{\partial Y} - \xi \frac{V \sin \theta}{y}$ (6b)
C-M	$\left(\frac{d}{dt}\right)_{CM}$	$= \frac{\partial}{\partial t} + \frac{V}{\alpha} \frac{\partial}{\partial X} - \frac{a}{\beta} \frac{\partial}{\partial Y}$ (7a)	$\frac{1}{\rho a^2} \left(\frac{dp}{dt}\right)_{CM} - \frac{V}{a} \left(\frac{d\theta}{dt}\right)_{CM} = -\frac{1}{\alpha} \frac{\partial V}{\partial X} - \xi \frac{V \sin \theta}{y}$ (7b)
D-M	$\left(\frac{d}{dt}\right)_{DM}$	$= \frac{\partial}{\partial t} + \frac{V}{\alpha} \frac{\partial}{\partial X} + \frac{a}{\beta} \frac{\partial}{\partial Y}$ (8a)	$\frac{1}{\rho a^2} \left(\frac{dp}{dt}\right)_{DM} + \frac{V}{a} \left(\frac{d\theta}{dt}\right)_{DM} = -\frac{1}{\alpha} \frac{\partial V}{\partial X} - \xi \frac{V \sin \theta}{y}$ (8b)
O-M	$\left(\frac{d}{dt}\right)_{OM}$	$= \frac{\partial}{\partial t} + \frac{V}{\alpha} \frac{\partial}{\partial X}$ (9a)	$\rho V \left(\frac{d\theta}{dt}\right)_{OM} = -\frac{1}{\beta} \frac{\partial p}{\partial Y}$ (9b)

Table 1 Total derivatives with respect to time and compatibility equations along the bicharacteristics and the particle path (for symbols see Fig. 4)

It is easy to show that the five equations (5-6-7-8-9) can be reduced to the three following independent equations, which are given already in a finite difference form:

$$V_M = \frac{1}{2} \left\{ V_A + V_B + \left[ \left(\frac{1}{\rho a}\right)_{BM} - \left(\frac{1}{\rho a}\right)_{AM} \right] P_M + \left(\frac{1}{\rho a}\right)_{AM} P_A - \left(\frac{1}{\rho a}\right)_{BM} P_B + \frac{1}{2} (YY_A - YY_B) \Delta t \right\} \quad (10)$$

$$\theta_M = \frac{1}{V_{CM} + V_{DM}} \left\{ V_{CM} \theta_C + V_{DM} \theta_D + \left[ \left(\frac{1}{\rho a}\right)_{DM} - \left(\frac{1}{\rho a}\right)_{CM} \right] P_M + \left(\frac{1}{\rho a}\right)_{CM} P_C - \left(\frac{1}{\rho a}\right)_{DM} P_D + \frac{1}{2} (XX_D - XX_C) \Delta t \right\} \quad (11)$$

$$P_M = \frac{1}{\Sigma \frac{1}{\rho a}} \left\{ \Sigma \frac{1}{\rho a} (p/\rho a) + V_A - V_B + V_{CM} \theta_C - V_{DM} \theta_D + \frac{\theta_M}{2} (V_D - V_C) - \frac{D_6}{2} \Delta t \right\} \quad (12)$$

where:

$$XX = \frac{a}{\alpha} \frac{\partial V}{\partial X} + \xi a V \frac{\sin \theta}{y} \quad (13)$$

$$YY = \frac{aV}{\beta} \frac{\partial \theta}{\partial Y} + \xi a V \frac{\sin \theta}{y} \quad (14)$$

$$D_6 = 2 YY_M + 2 XX_M + YY_A + YY_B + XX_C + XX_D \quad (15)$$

$$\Sigma \frac{1}{\rho a} (f) = f_A + f_B + f_C + f_D \quad (16)$$

$$(f)_{XY} = \frac{1}{2} (f_X + f_Y) \quad (17)$$

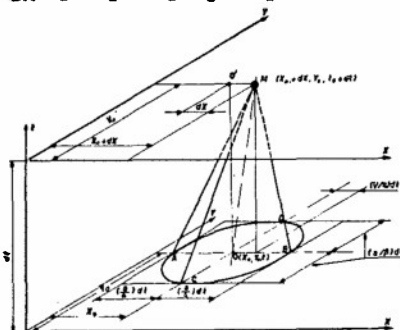


Fig. 4

To solve the problem, another relation is necessary, namely the energy equation along the path  $O-M$  of the particle. This equation is given, in a finite difference form, by:

$$h_M = h_O + V_O^2 - V_M^2 + \frac{V^2}{\alpha} \frac{\partial V}{\partial X} \Delta t \quad (18)$$

The density  $\rho$ , which is present in Eqs. (10-11), can be computed from known

values of pressure and enthalpy. For the simple case of a reversible and adiabatic flow, the energy equation becomes:

$$S_0 = S_M \quad (19)$$

If a perfect gas with constant  $\gamma$  is considered, the system of equations (10-11-12-19) can be simplified by the introduction of the variable  $Z$ :

$$Z = \frac{2}{\gamma-1} a \quad (20)$$

In fact,  $dp/\rho a = d(2a/(\gamma-1))/dZ$ . The resulting system of three equations is given below:

$$V_M = \frac{1}{2} \{V_A + V_B + (YY_{BM} - YY_{AM}) \Delta t + Z_A - Z_B\} \quad (21)$$

$$\theta_M = \frac{1}{V_{CM} + V_{DM}} \{V_{CM} \theta_C + V_{DM} \theta_D + (XX_{DM} - XX_{CM}) \Delta t + Z_C - Z_D\} \quad (22)$$

$$Z_M = \frac{1}{4} \left\{ \frac{2}{1} (z) + (V_A - V_B) + \theta_C V_{CM} - \theta_D V_{DM} + \frac{1}{2} \theta_M (V_D - V_C) - \frac{1}{2} D_0 \Delta t \right\} \quad (23)$$

METHOD OF SOLUTION FOR DIFFERENT POINTS. A variety of points, which must be solved in different ways, can be met during the calculation. A simple form of equations to be used is provided for all considered points in Appendix 2: on the left of the page the adiabatic flow of an inviscid fluid with the equation of state (A2-1) is treated, while on the right the isentropic flow of a perfect gas is considered. In the first case, pressure and enthalpy are computed, and density is derived by Eq (A2-1), while in the second case the variable  $Z$  is sufficient to identify the thermodynamic state.

It can be seen that both problems imply the solution of non linear systems of equations, which can be performed by an iterative method. However, a very rapid convergence is in general achieved, since all terms on the right side of the equations containing the unknowns are small enough.

BOUNDARY CONDITIONS. While interior, rigid wall, and slip-line points can be solved fairly easily, both indicated methods concerning inlet or outlet non-rigid boundaries in subsonic flow are often sources of trouble. In fact, the first one (extrapolation) can produce the well-known form of instability which is described for example by Collatz (6). As far as the second method is concerned (arbitrary conditions at boundaries), let us quote McKenzie and Moretti (7). "It is physically impossible to prescribe proper conditions on subsonic non rigid boundaries, since all signals from the interior region (computed) affect the exterior region (not computed) and viceversa", and again Moretti (8): "No arbitrary assumptions should be used during the time evolution, even if they are valid in a steady state and a steady state is to be reached eventually". Actually, while assignable boundary conditions are well known for steady flow problems (see for example (9)), they are not so well established for unsteady flows.

In order to circumvent the above quoted difficulties, the following method was worked out by the authors. Initial known conditions are given in an infinite (I.E. very large, since the method is numerical) region. The desired signals are induced, and calculations are performed in the perturbed regions, while the other regions of the field are unaltered. Obviously, the perturbed (calculated) region will spread with time in all directions. The problem is to reach a steady state solution in the region of interest, before some signal reaches the boundaries. The necessity follows of adopting wide regions of computation in the physical plane. On the other hand, a rather restricted number of meshes is required by computing time limitations. These opposite requirements can be matched by the adoption of the above defined coordinate system  $X, Y$ . In fact, the physical coordinates  $x, y$  can be stretched by a proper choice of functions  $\alpha_0$  and  $\beta_0$  of Eq. (A1-3).

Although in this way a steady solution can always be reached, another question arises: is the calculated solution the one of interest? For simplicity, let us consider the case represented in Fig. 3. We started with a given Mach number of 0.50 constant everywhere. A steady solution was reached, with the required geometry, corresponding to an upstream Mach number of 0.465. No easy relation between these two values can be established. On the other hand, one is in general interested in a particular solution, but cannot set a priori the right initial Mach number. However, the possibility exists of reaching every solution of interest, by gradually changing the discharge pressure. This proceeding was applied to the nozzle of Fig. 3, and the results are given in Fig. 5, where the various phases from the steady subsonic flow represented in Fig. 5a up to the steady supersonic flow represented in Fig. 5d are represented.

Unfortunately, a similar action cannot be applied when more than one subsonic stream is to be considered. Let us, for instance, look into the case represented in Fig. 8. First, the initial total pressure ratio  $P_1/P_2$  between the two streams 1 and 2 is fixed arbitrarily, then the boundary geometry is gradually changed. The induced perturbations change upstream conditions in both streams, so that the total pressure ratio  $P_1/P_2$  which is found for the steady situation corresponding to the final geometry, is in general different from the primary one. No possibility seems to exist of predicting these changes exactly.

NUMERICAL INTERPOLATIONS. There are obvious limitations to the number of meshes which can be used in the computations. They are due to both computer core capacity restrictions and

computational time requirements. The two problems are somewhat interrelated, since a larger computer capacity can allow one to decrease computational time by recording a greater number of intermediate results, which can be used in subsequent calculations. A node number around 3000 is allowed by the UNIVAC 1108 available at the Politecnico of Milan.

The adoption of rather coarse meshes requires therefore an accurate interpolation method. In (2) an example is reported, where linear interpolations proved to be inadequate. Since the nature of perturbations is undulatory, it would seem appropriate to describe flow phenomena with functions which can have flexes. The simplest function with flexes, a polynomial of third degree, was therefore adopted. No attempts were made to fit the whole calculated plane by means of polynomials of high degree, since in the authors' experience (10), these methods are often unsafe. The excellent precision of results, which was achieved even after a very large number of iterations, brings into evidence the potential of the adopted method.

**STEADINESS OF SOLUTION.** By definition, all variables do not change with time when a solution is fully steady. Nevertheless, small changes are always present in a numerical solution. The problem arises of understanding whether these changes are due to numerical inaccuracies, or reflect a still unsteady situation. A very intuitive way of checking steadiness consists in looking into the mass flow diagram (see for example Fig. 5.3 and 5), which must be flat in all the region of interest. A more precise method can be adopted for isentropic, irrotational flows. In this case, the term on the right side of Eq (3) is equal to zero, since entropy is constant ( $\nabla S=0$ ) and flow irrotational ( $\nabla \times \mathbf{V}=0$ ). Steady solutions require therefore total enthalpy, and consequently total pressure to be constant everywhere. In all cases treated in this paper, solutions were considered to be steady for total pressure fluctuations well below one thousandth of the absolute value.

#### DISCUSSION OF RESULTS

Specific calculations about transonic double flow nozzles could not be brought to an end, because of the unexpected unavailability, during the last two months, of the high speed computer which had been used for the research until then. However, the results presented in this chapter, concerning respectively a transonic nozzle discharging into an infinite capacity reservoir and a subsonic double flow nozzle, leave no doubt about the possibility of solving transonic double flow nozzles by the proposed method.

**TRANSONIC NOZZLE.** In Fig. 5a, the steady subsonic solution is represented, which was achieved at time  $t=2.1t_x$  after the unsteady phase described in Fig. 3. On the upper part of the figure, lines at constant Mach number are shown in a section along the axis, while the percentage mass flow rate variations at various stations with respect to the throat one are represented in the lower part of the figure. Besides results shown in Fig. 5a, steadiness in the region of interest can be noticed from Fig. 6. In fact, mass flow rates through the three stations  $x_0$ ,  $x_t$ , and  $x_s$  coincide (Fig. 6a) and Mach numbers are steady (Fig. 6b).

In order to establish a transonic flow through the nozzle, the reservoir pressure is gradually decreased up to the time  $t=4.3t_x$ , as shown in Fig. 6c. Results obtained during the transient phase ( $t=3.5t_x$ ) are represented in Fig. 5b, where the occurrence of a supersonic region is shown. Unsteady peculiarities of flow can be seen both in the lower part of Fig. 5b and Fig. 6. On the contrary, a nearly steady situation is found at  $t=5t_x$ , as indicated by small (0.7%) mass flow variations represented in Fig. 5c. However, the Mach number behavior at station  $x_j$ , represented in Fig. 6b, indicates an unsteady situation.

This fact can be explained by the appearance of shock waves, due to the overexpansion of the nozzle. No steady solution could be found, since calculations were carried out with the equations of isentropic flow, which cannot account for irreversible phenomena. However, results of Fig. 5c show the adaptability of the method, since shock waves are outlined with excellent precision. It can be of interest to notice that the sharp variations in static pressure density, and flow velocity across the shock waves, which are shown in the figure, are not due to an entropy increase, as in Hugoniot relations, but to a total pressure drop due to unsteady phenomena.

In order to investigate whether the occurrence of shock waves during the transient phase influences the final steady solution, the discharge pressure was decreased up to a value close to the pressure at station  $x_0$ , as shown in Fig. 6c. Results represented in Fig. 5d show that the correct steady solution could be achieved (mass flow variations below 0.3% can be considered very satisfactory, by accounting for a rather coarse computational mesh).

**SUBSONIC DOUBLE FLOW NOZZLE.** In the following a comparison between experimental tests, made at ONERA (11) and calculated results concerning a subsonic double flow nozzle is made. Sections of the experimental assembly and the model used during the calculations are shown respectively in the lower and upper part of Fig. 8c. During the transient phase, the internal nozzle turns from a cylindrical channel with infinitely thin walls into a converging nozzle with 5 mm. thick walls. Contemporarily the external cylindrical channel increases its diameter. Flow area variations versus time at station  $x_0$  for the external stream and at station  $x_t$  for both streams are shown in Fig. 7a.

Total pressure and Mach number variations along the center line and the middle streamline of the second stream (streamline No. 15) at stations  $x_0$ ,  $x_t$ , and  $x_c$  versus time are represented in Fig. 7b and c. Since, as discussed in previous chapter, total pressure variation is a good indication of steadiness, the almost perfect matching of total pressure curves represented in Fig. 7b indicates that flow is very close to a steady situation at  $t=3.6 t_x$ . The same information is given by constancy of Mach numbers with time (Fig. 7c).

However, results shown in Fig. 8a and b, where respectively total pressures and Mach numbers at streamlines 1, 11, 12, and 17 versus the axis are represented, indicate that total

pressure variations of 1.2% are still present. This can be easily explained by the presence of sharp corners, which cannot be interpolated correctly, and by the coarse meshes which were adopted in the computation (only 22x17 nodes in the region at finite).

In spite of these inaccuracies, the comparison with test results of static pressure, represented in Fig. 8a, is favorable. In fact, the difference between experimental and calculated values of static pressure can be ascribed to the fact that during the calculation, the coincidence of static pressure of the two separate streams (Kutta-Jukowski condition) was imposed in the first node after the real trailing edge. If the right condition would have been assumed, all results would be translated of one mesh in direction of the axis, and a fair agreement with experimental data achieved.

#### REFERENCES

- (1) Moretti, G., and Abbett, G. "A Time Dependent Computational Method for Blunt Body Flows", AIAA J, Vol. 4, No. 12, December 1966, pp. 2136-2141
- (2) Carriere, P., and Capelier, C. "Application de la methode des caracteristiques instationnaires au calcul numerique d'un ecoulement permanent compressible", AGARD Conference Proceedings No 35, 1968.
- (3) Labrujere, Th. E., Loeve, W., and Slooff, J. W. "An Approximate Method for the Determination of the Pressure Distribution on Wings in the Lower Critical Speed Range", AGARD Conference Proceedings No 35, 1968.
- (4) Chow, W. L., and Addy, A. L. "Interaction between primary and secondary streams of supersonic ejector systems and their performance characteristics", AIAA J, vol. 2, No. 4, April 1964, pp. 686-695.
- (5) Hardy, J. M., and Delery, J. "Possibilités actuelles d'etude theorique d'une tuyère supersonique à double flux", AGARDograph 103, part. 2, pp. 445-473
- (6) Collatz, L. "The Numerical Treatment of Differential Equations", 3rd ed., Springer, Berlin, 1960.
- (7) Mac Kenzie D., and Moretti G. "Time Dependent Calculation of the Compressible Flow about Airfoils" AGARD Conference Proceedings No 35, 1968
- (8) Moretti, G. "The Choice of a Time-Dependent Technique in Gas Dynamics", von Karman Institute for Fluid Dynamics, Lecture Series 26, May 1970.
- (9) Smolderen, J. J. "Transonic Flow Theory Applied to Turbine Cascades", von Karman Institute for Fluid Dynamics, Lecture Series 30, January 1971.
- (10) Angelino, G., and Macchi E. "Computation of Thermodynamic Properties of Carbon Dioxide in the Range 0-750 Deg. C.", Journal of Engineering for Power, 92/A, July 1970 pp. 301-309
- (11) Osnaghi, C., Unpublished Data, ONERA, Chalais-Meudon, France, February 69.

#### ACKNOWLEDGEMENTS

The authors wish to express their appreciation to the Director of Institute of Machines of Politecnico of Milan, Prof. Corrado Casci, for providing guidance and counsel during the investigation.

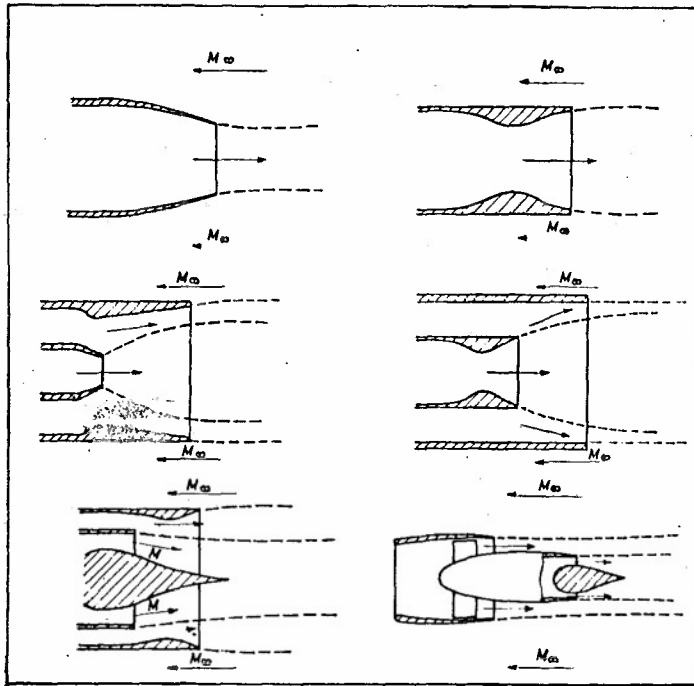


Fig. 1 Typical exhaust system configurations

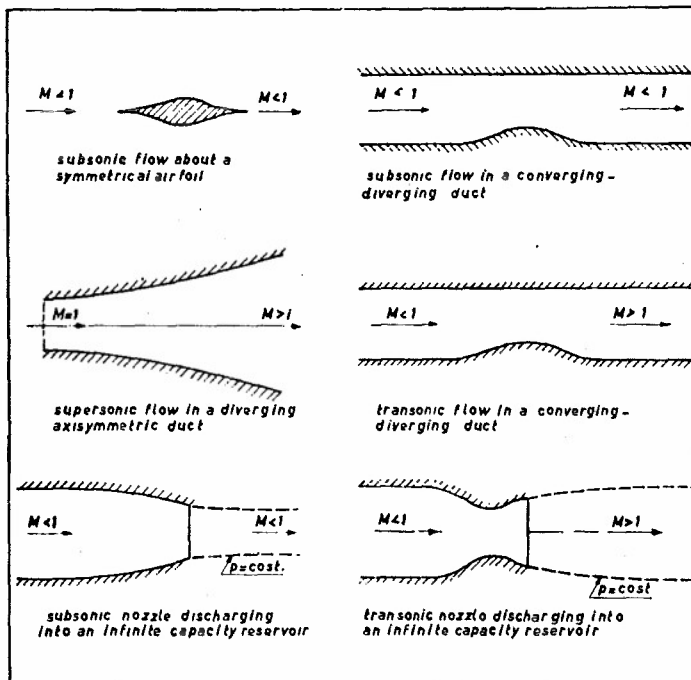


Fig. 2 Examples solved during the program set up

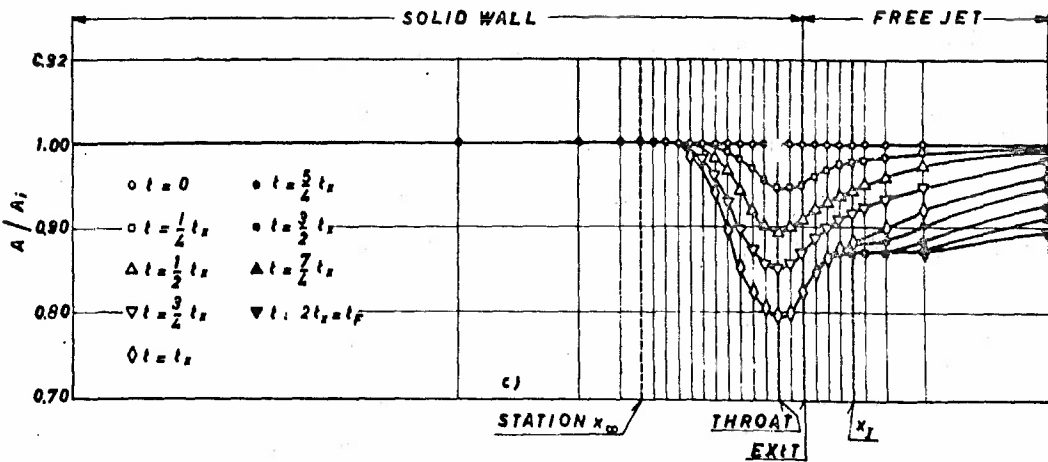
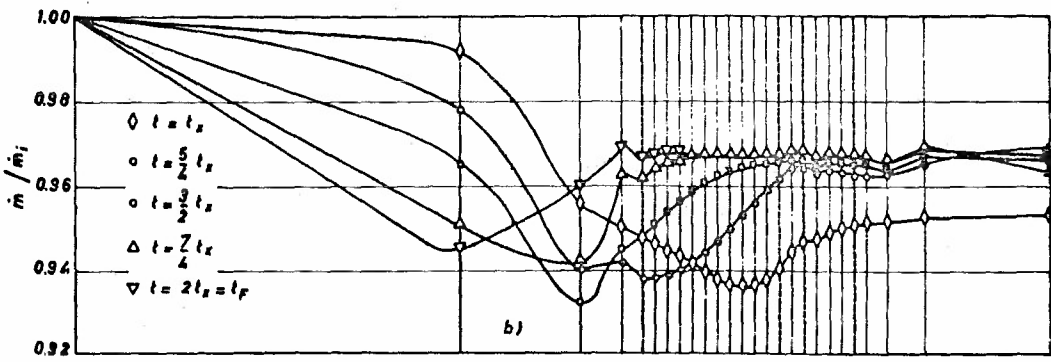
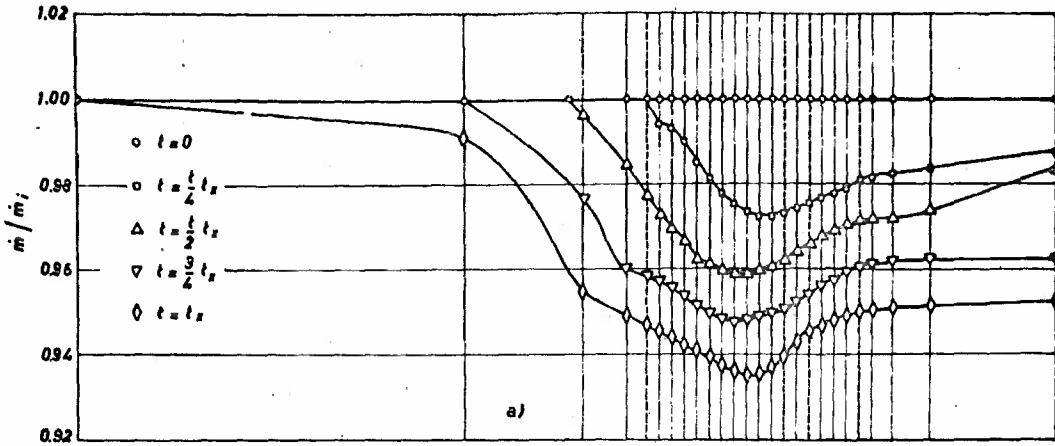
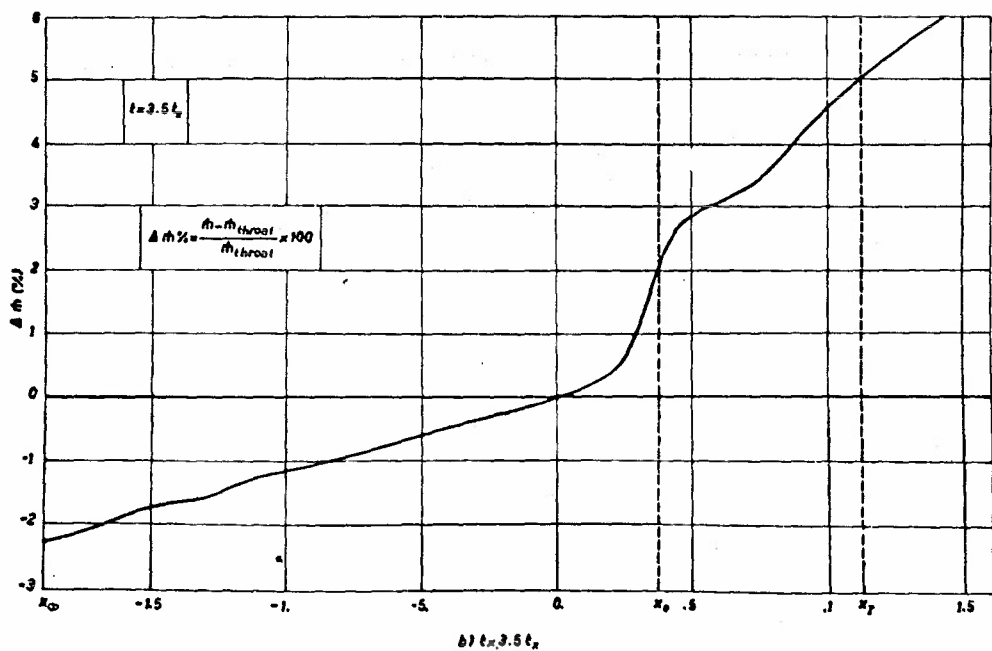
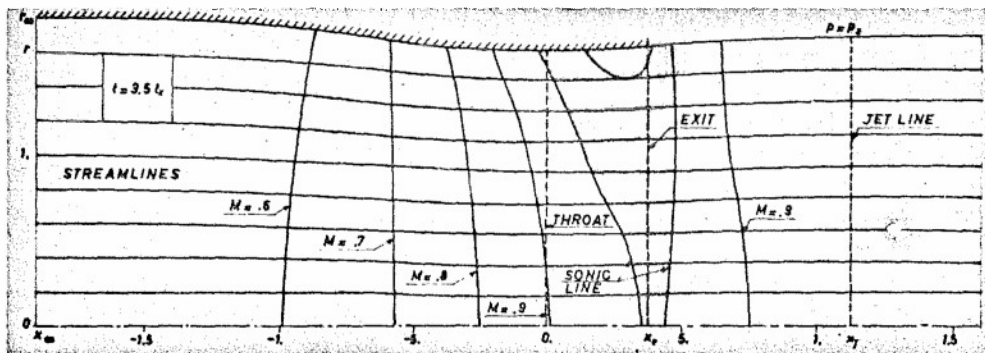
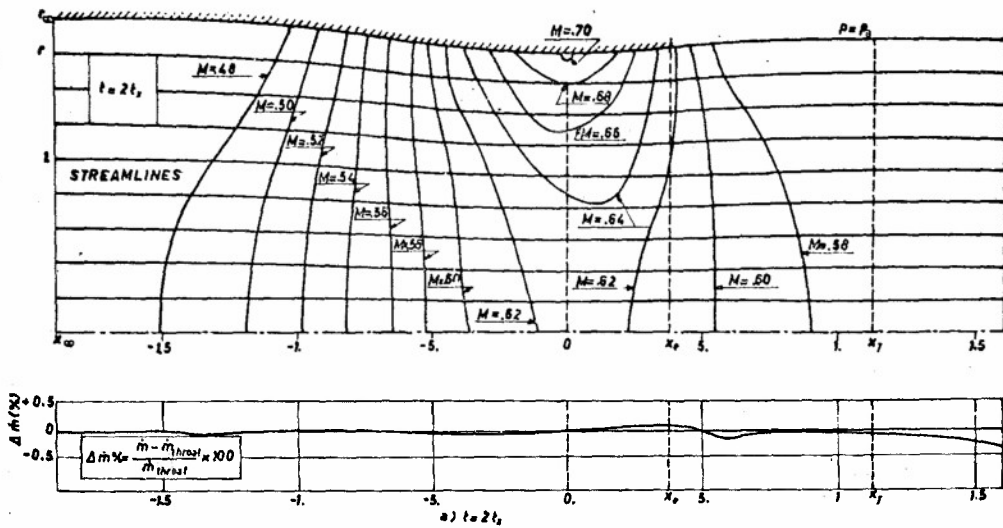


Fig. 3 Stages of the solution of a subsonic nozzle at different times.



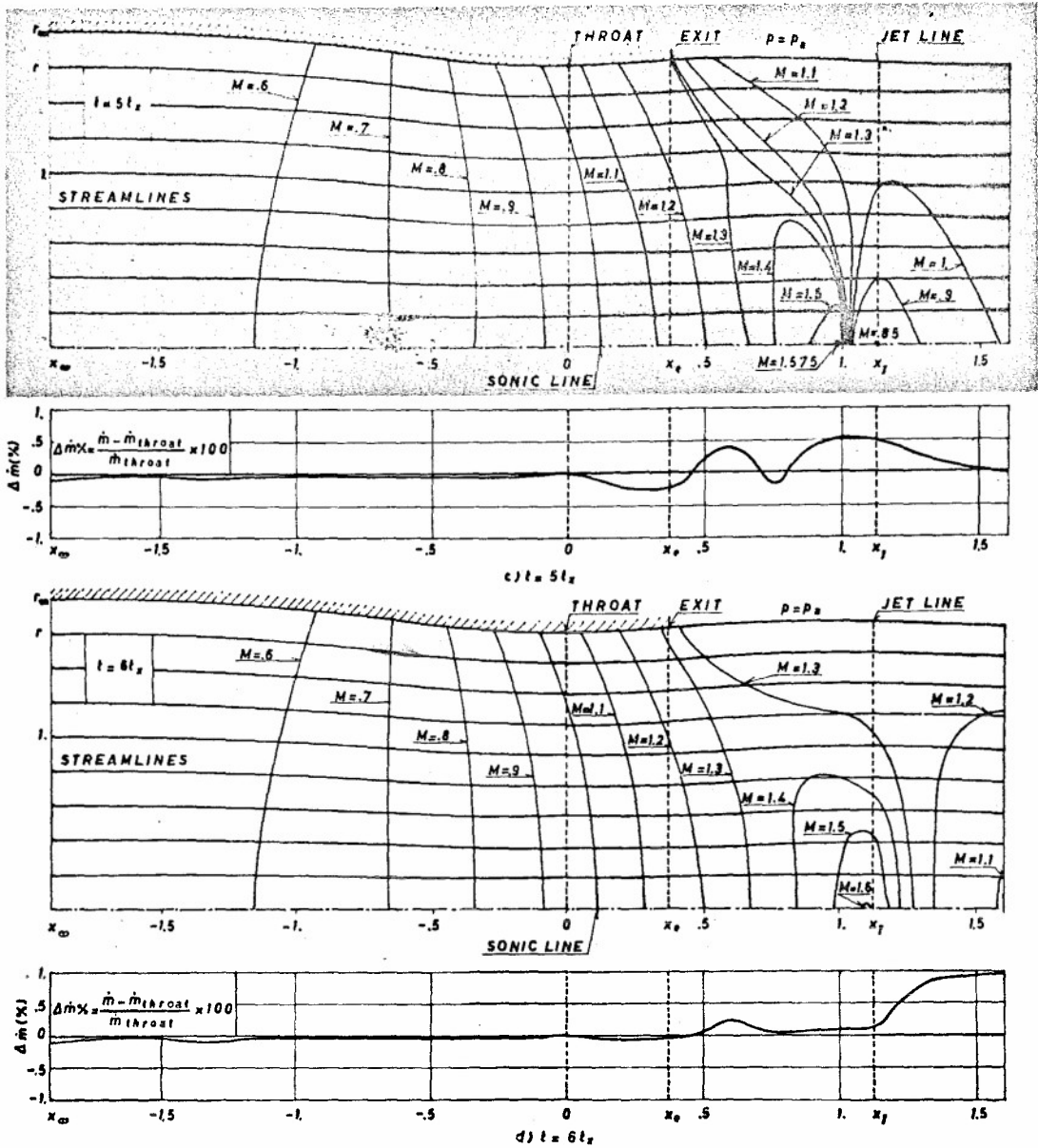


Fig. 5 Stages of the solution of a transonic nozzle at different times: streamlines and lines at constant Mach number.

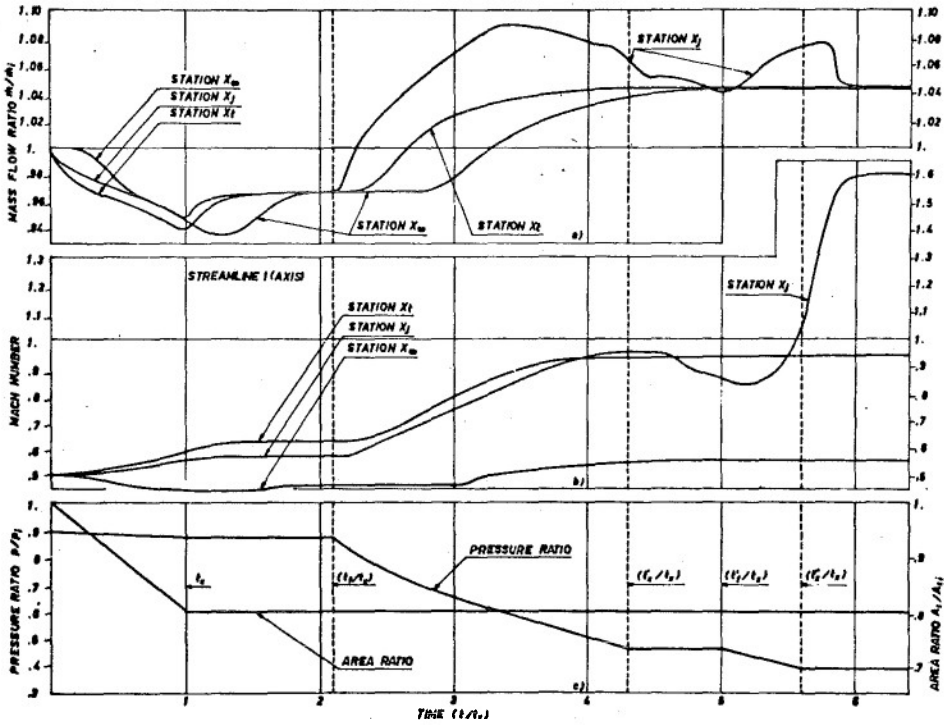


Fig. 6 Transonic nozzle solution: a-b) Flow rates (a) and Mach numbers (b) at stations  $x_0, x_t, x_j$  versus time. c) Throat area and jet pressure versus time.

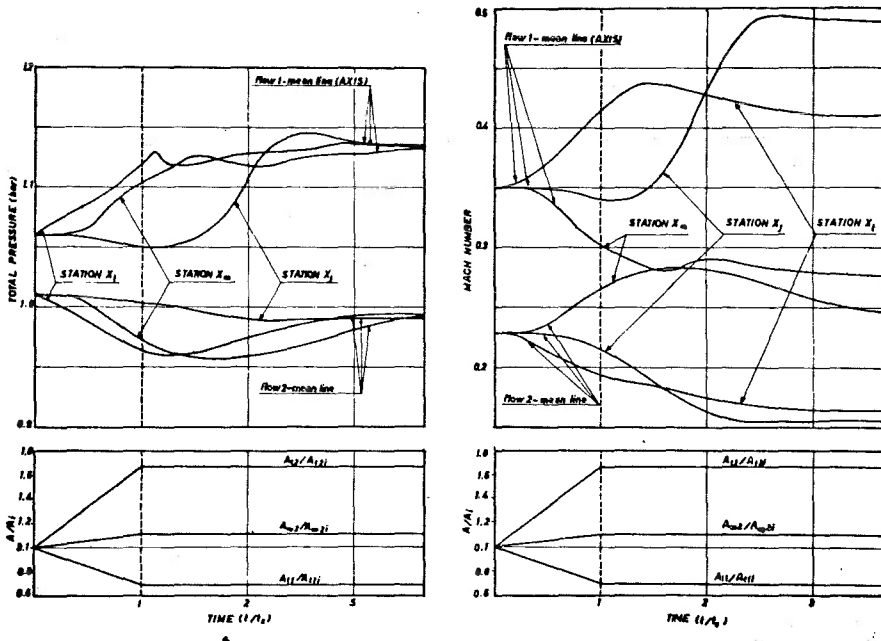


Fig. 7 Double flow nozzle solution: a) Areas of flows 1 and 2 versus time. b-c) Total pressures (b) and Mach numbers (c) at stations  $x_0, x_t, x_j$  versus time.

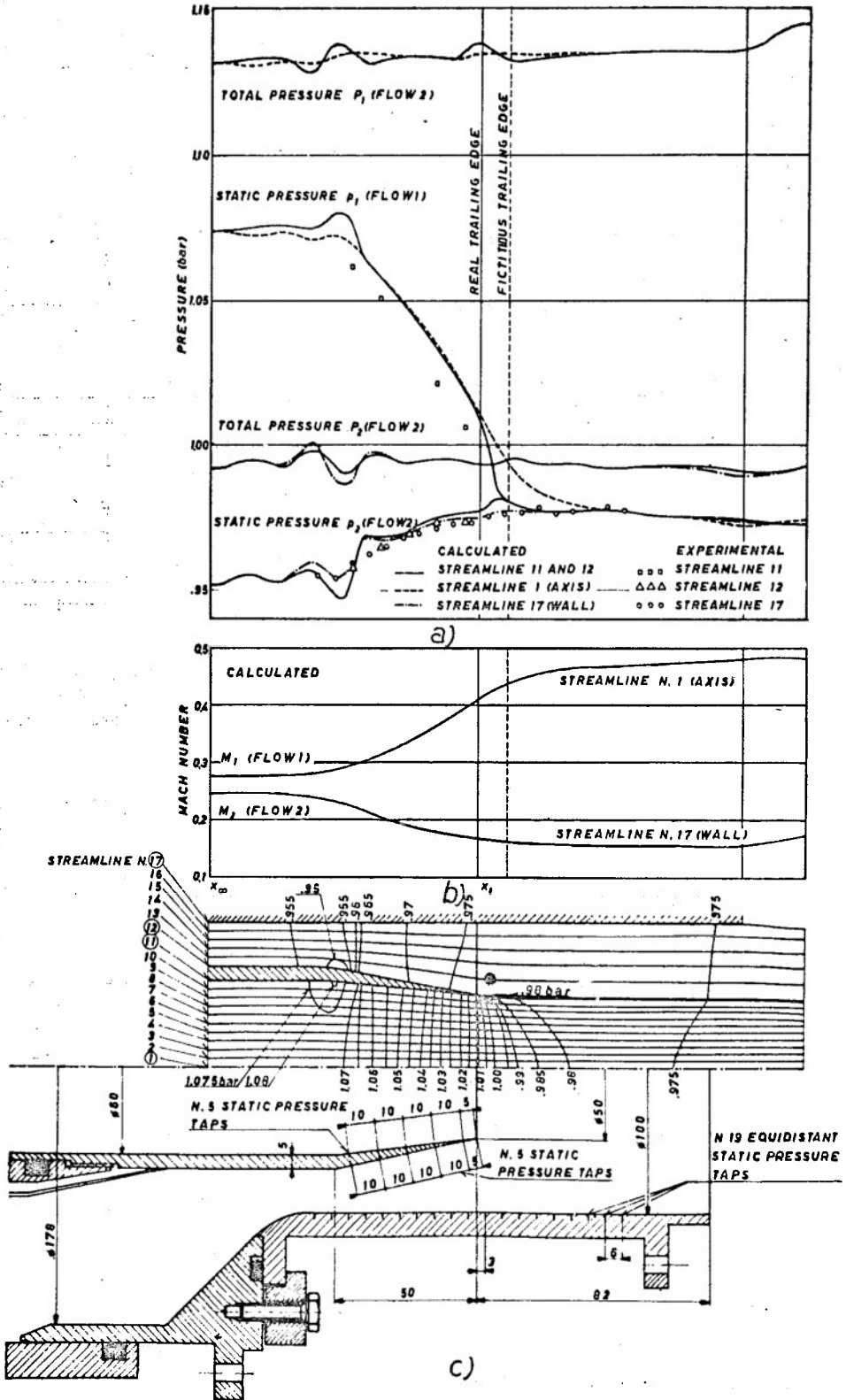


Fig. 8 Experimental assembly and calculated solution of a double flow subsonic nozzle.

APPENDIX 1

**COORDINATE SYSTEM.** Let us call  $x$  and  $y$  the coordinates in the physical plane;  $x_1$  and  $y_1$ , the curvilinear coordinates, respectively parallel and perpendicular to the streamlines; and  $\theta$  the angle between the axes  $x_1$  and  $y_1$ . From Fig. A1-1, the geometric relation between  $x$ ,  $y$  and  $x_1$ ,  $y_1$  is given by:

$$\begin{cases} dx = \cos\theta dx_1 - \sin\theta dy_1 \\ dy = \sin\theta dx_1 + \cos\theta dy_1 \end{cases} \quad (A1-1)$$

The new coordinate system is defined by the following relationships:

$$\begin{cases} dX = (1/\alpha) dx_1 \\ dY = (1/\beta) dy_1 \end{cases} \quad (A1-2)$$

where  $\alpha$  and  $\beta$  are functions of  $X$ ,  $Y$ , and  $t$ . The transformation  $x, y \rightarrow X, Y$  will be uniquely defined, only if the following conditions are satisfied:

$$\begin{cases} \frac{\partial \alpha}{\partial Y} = -\beta \frac{\partial \theta}{\partial X} \\ \frac{\partial \beta}{\partial X} = \alpha \frac{\partial \theta}{\partial Y} \end{cases} \quad (A1-3)$$

or, by integrating Eq(A1-3):

$$\begin{cases} \alpha(X, Y, t) = \alpha_0(X, Y_0, t) - \int_{Y_0}^Y \frac{\partial \theta}{\partial X} \beta dY \\ \beta(X, Y, t) = \beta_0(X_0, Y, t) + \int_{X_0}^X \frac{\partial \theta}{\partial Y} \alpha dX \end{cases} \quad (A1-4)$$

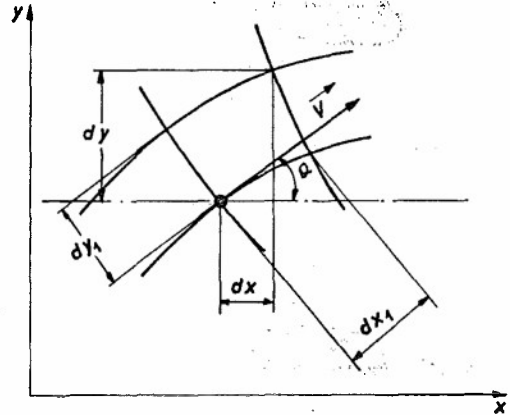


Fig. A1-1

where the functions  $\alpha$  and  $\beta$  can be fixed arbitrarily, respectively at  $Y=Y_0$  and  $X=X_0$

APPENDIX 2

List of equations used in the appendix:

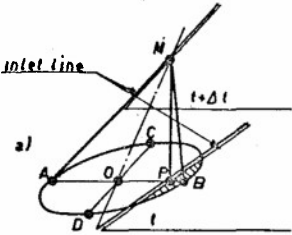
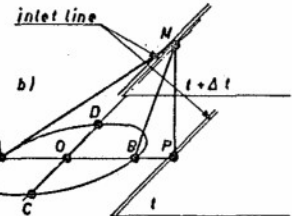
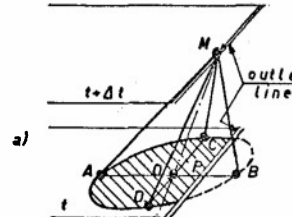
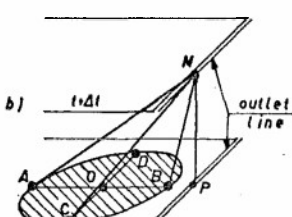
- $\rho = \rho(p, h)$  and  $a = a(p, h)$  (A2-1)
- $P_M = 1/(\Sigma_1^3(1/\rho a))(\Sigma_1^3(p/a) + V_A - V_B + V_{CM}(\theta_M - \theta_C) - \frac{1}{2} D_5 \Delta t)$  (A2-2a)
- $Z_M = 1/3 \Sigma_1^3(Z) + V_A - V_B + V_{CM}(\theta_M - \theta_C) - \frac{1}{2} D_5 \Delta t$  (A2-2b)
- $P_M = 1/(\Sigma_1^3(1/\rho a))(\Sigma_1^3(p/\rho a) + V_A - V_B - V_{CM}(\theta_M - \theta_C) - \frac{1}{2} D_5 \Delta t)$  (A2-3a)
- $Z_M = 1/3 \Sigma_1^3(Z) + V_A - V_B - V_{CM}(\theta_M - \theta_C) - \frac{1}{2} D_5 \Delta t$  (A2-3b)
- $\theta_M = \theta_C - 1/V_{MC} \{ (1/\rho a)_{MC} (P_M - P_C) + \frac{1}{2} (XX_C + XX_M) \Delta t \}$  (A2-4a)
- $\theta_M = \theta_C - 1/V_{MC} \{ 2_M - 2_C + \frac{1}{2} (XX_C + XX_M) \Delta t \}$  (A2-4b)
- $\theta_M = \theta_C + 1/V_{MC} \{ (1/\rho a)_{MC} (P_M - P_C) + \frac{1}{2} (XX_C + XX_M) \Delta t \}$  (A2-5a)
- $\theta_M = \theta_C + 1/V_{MC} \{ 2_M - 2_C + \frac{1}{2} (XX_C + XX_M) \Delta t \}$  (A2-5b)
- $P_M = P_N = 1/(\Sigma_1^6(1/\rho a))(\Sigma_1^6(p/\rho a) + V_A + V_E - V_B - V_F + V_{DM}(\theta_M - \theta_D) - V_{CN}(\theta_M - \theta_C) - \frac{1}{2} D_8 \Delta t)$  (A2-6a)
- $Z_M = 2_N/\delta = 1/(3+3\delta) \{ 2_A + 2_B + 2_D + \delta(2_E + 2_F + 2_C) + V_A - V_B + V_E - V_F + V_{DM}(\theta_M - \theta_D) - V_{CN}(\theta_M - \theta_C) - \frac{1}{2} D_8 \Delta t \}$  (A2-6b)
- $V_N = \frac{1}{2} (V_E + V_F + ((1/\rho a)_{FN} - (1/\rho a)_{EN}) P_M - (1/\rho a)_F P_F + \frac{1}{2} (YY_{FN} - YY_{EN}) \Delta t)$  (A2-7a)
- $V_N = \frac{1}{2} (V_E + V_F + 2_E - 2_F + (YY_{FN} - YY_{EN}) \Delta t)$  (A2-7b)
- $\theta_M = \theta_N = 1/(V_{CN} + V_{DM}) \{ V_{CN} \theta_C + V_{DM} \theta_D + ((1/\rho a)_{DM} - (1/\rho a)_{CN}) P_M + (1/\rho a)_{CN} P_C - (1/\rho a)_{DM} P_D + \frac{1}{2} (XX_{DM} - XX_{CN}) \Delta t \}$  (A2-8a)
- $\theta_M = \theta_N = 1/(V_{CN} + V_{DM}) \{ V_{CN} \theta_C + V_{DM} \theta_D + 2_M(1-\delta) + 2_C - 2_D + \frac{1}{2} (XX_{DM} - XX_{CN}) \Delta t \}$  (A2-8b)
- $V_M = V_B + (1/\rho a)_{BM} (P_M - P_B) + YY_{BM} \Delta t$  (A2-9a)
- $V_M = V_B + 2_M - 2_B + YY_{BM} \Delta t$  (A2-9b)
- $P_M = (\rho a)_{BM} (V_M - V_B) - YY_{BM} \Delta t + P_B$  (A2-10a)

(continue on page A2-3)

ADIABATIC FLOW  
OF AN INVISCID FLUID

ISENTROPIC FLOW OF A PERFECT  
GAS WITH CONSTANT  $\gamma$

<p><b>INTERNAL POINT</b></p>	<table style="width: 100%; border: none;"> <tr> <td style="width: 50%; vertical-align: top;">                     Eq (10) Eq (11) {Eq (12) Eq (18) Eq (A2-1)                 </td> <td style="width: 50%; vertical-align: top;">                     Eq (21) {Eq (22) Eq (23)                 </td> </tr> </table> <p>Since all base points of bicharacteristics are in the calculated region, the equations derived for the general case are used.</p>	Eq (10) Eq (11) {Eq (12) Eq (18) Eq (A2-1)	Eq (21) {Eq (22) Eq (23)		
Eq (10) Eq (11) {Eq (12) Eq (18) Eq (A2-1)	Eq (21) {Eq (22) Eq (23)				
<p><b>SIDE BOUNDARY POINT WITH SPECIFIED FLOW DIRECTION</b></p> <p>a)</p> <p>b)</p>	<table style="width: 100%; border: none;"> <tr> <td style="width: 50%; vertical-align: top;">                     Eq (10) {Eq (A2-2a) Eq (18) Eq (A2-1)                 </td> <td style="width: 50%; vertical-align: top;">                     Eq (21) {Eq (A2-2b)                 </td> </tr> </table> <p style="text-align: center;">a) right wall</p> <table style="width: 100%; border: none;"> <tr> <td style="width: 50%; vertical-align: top;">                     Eq (10) {Eq (A2-3a) Eq (18) Eq (A2-1)                 </td> <td style="width: 50%; vertical-align: top;">                     Eq (21) Eq (A2-3b)                 </td> </tr> </table> <p style="text-align: center;">b) left wall</p> <p>One base point of bicharacteristics, D, is out of the calculated region. Since the variable angle <math>\theta</math> is given, Eq (11) and Eq (22) are replaced by <math>\theta_M = \theta_{wall}</math></p>	Eq (10) {Eq (A2-2a) Eq (18) Eq (A2-1)	Eq (21) {Eq (A2-2b)	Eq (10) {Eq (A2-3a) Eq (18) Eq (A2-1)	Eq (21) Eq (A2-3b)
Eq (10) {Eq (A2-2a) Eq (18) Eq (A2-1)	Eq (21) {Eq (A2-2b)				
Eq (10) {Eq (A2-3a) Eq (18) Eq (A2-1)	Eq (21) Eq (A2-3b)				
<p><b>SIDE BOUNDARY POINT WITH SPECIFIED PRESSURE</b></p> <p>a)</p> <p>b)</p>	<table style="width: 100%; border: none;"> <tr> <td style="width: 50%; vertical-align: top;">                     Eq (10) {Eq (A2-4a) Eq (18) Eq (A2-1)                 </td> <td style="width: 50%; vertical-align: top;">                     Eq (21) Eq (A2-4b)                 </td> </tr> </table> <p style="text-align: center;">a) right wall</p> <table style="width: 100%; border: none;"> <tr> <td style="width: 50%; vertical-align: top;">                     Eq (10) {Eq (A2-5a) Eq (18) Eq (A2-1)                 </td> <td style="width: 50%; vertical-align: top;">                     Eq (21) Eq (A2-5b)                 </td> </tr> </table> <p style="text-align: center;">b) left wall</p> <p>One base point of bicharacteristics, D, is out of the calculated region. Since the variable pressure is given, Eq (12) and Eq (23) are replaced by <math>P_M = P_{jet}</math></p>	Eq (10) {Eq (A2-4a) Eq (18) Eq (A2-1)	Eq (21) Eq (A2-4b)	Eq (10) {Eq (A2-5a) Eq (18) Eq (A2-1)	Eq (21) Eq (A2-5b)
Eq (10) {Eq (A2-4a) Eq (18) Eq (A2-1)	Eq (21) Eq (A2-4b)				
Eq (10) {Eq (A2-5a) Eq (18) Eq (A2-1)	Eq (21) Eq (A2-5b)				
<p><b>SLIP LINE POINT</b></p>	<table style="width: 100%; border: none;"> <tr> <td style="width: 50%; vertical-align: top;">                     Eq (10) Eq (A2-6a) {Eq (A2-7a) Eq (A2-8a) Eq (18) Eq (A2-1)                 </td> <td style="width: 50%; vertical-align: top;">                     Eq (21) Eq (A2-6b) {Eq (A2-7b) Eq (A2-8b)                 </td> </tr> </table> <p>The equations of the two separate streams must be solved contemporarily at the geometrically coincident points M and N, since the conditions <math>p_M = p_N</math> and <math>\theta_M = \theta_N</math> must be satisfied. The other unknowns come out from the above equations, obtained from the six points indicated in the side figure.</p>	Eq (10) Eq (A2-6a) {Eq (A2-7a) Eq (A2-8a) Eq (18) Eq (A2-1)	Eq (21) Eq (A2-6b) {Eq (A2-7b) Eq (A2-8b)		
Eq (10) Eq (A2-6a) {Eq (A2-7a) Eq (A2-8a) Eq (18) Eq (A2-1)	Eq (21) Eq (A2-6b) {Eq (A2-7b) Eq (A2-8b)				

<p><b>INLET BOUNDARY POINT</b></p>  	<p>Eq (A2-9a) or Eq (A2-10a) Eq (A2-9b) or Eq (A2-10b)          Eq (18)          Eq (A2-1)</p> <p>a) <u>inlet Mach number less than unity</u>: the motion in M is influenced by both internal and external regions of preceding plane, since point A is internal, while points B,C, and D are external. Two ways of solution are possible:          - points B,C, and D are calculated by extrapolation in the plane <math>t=t_0</math>, so that M can be treated as an internal point.          - the angle <math>\theta_M</math> and one of the two unknowns <math>p_M</math> and <math>V_M</math> are fixed arbitrarily, while the other one is calculated by the above equations.</p> <p>b) <u>inlet Mach number equal or larger than unity</u>: no signal coming from the calculated region can reach the point M, since base points A,B,C and D are out of the calculated region. Hence, arbitrary values of <math>V_M</math>, <math>p_M</math>, and <math>\theta_M</math> can be assigned.</p>
<p><b>OUTLET BOUNDARY POINT</b></p>  	<p>{Eq(A2-11a) or Eq(A2-12a) Eq(A2-11b) or Eq(A2-12b)          Eq(11) Eq(22)          Eq(18)          Eq(A2-1)</p> <p>a) <u>outlet Mach number less than unity</u>: the motion in M is influenced by both internal and external regions of preceding plane, since points A,C, and D are internal, while point B is external. Two ways of solution are possible:          - point B is computed by extrapolation in the plane <math>t=t_0</math>, so that M can be treated as an internal point.          - one unknown, either pressure or velocity, is fixed arbitrarily, while the other ones are computed by the above equations.</p> <p>b) <u>outlet Mach number larger than unity</u>: the motion in M is entirely determined by the calculated conditions in the previous plane, since all base points of bicharacteristics are internal. Hence, the calculation is carried out with the same technique used for the interior points.</p>

$$Z_M = V_M - V_B + Z_B - YY_{BM} \Delta t \tag{A2-10b}$$

$$V_M = V_A - (1/\rho a)_{AM} (V_A - V_M) - YY_{AM} \Delta t \tag{A2-11a}$$

$$V_M = V_A - (Z_M - Z_A) - YY_{AM} \Delta t \tag{A2-11b}$$

$$P_M = P_A + (\rho a)_{AM} (V_A - V_M) - YY_{AM} \Delta t \tag{A2-12a}$$

$$Z_M = V_A - V_M + Z_A - YY_{AM} \Delta t \tag{A2-12b}$$

with:

$$D_5 = 2 YY_M + XX_M + YY_A + YY_B + XX_C \tag{A2-13}$$

$$D_8 = 2 YY_M + 2 YY_N + XX_M + XX_N + YY_A + YY_B + YY_E + YY_F + XX_C + XX_D \tag{A2-14}$$

$$\Sigma_1^3 (f) = f_A + f_B + f_D \tag{A2-15}$$

$$\Sigma_1^6 (f) = f_A + f_B + f_D + f_E + ff_F \tag{A2-16}$$

$$\delta = Z_N/Z_M = a_{oN}/a_{oM} (P_M / P_N)^{(\gamma-1)/2\gamma} \tag{A2-17}$$

## RÉPARTITION DES VITESSES A L'ENTRÉE D'UN COMPRESSEUR SUPERSONIQUE \*

par Bernard LEDOUX & Roger BAGOT

OFFICE NATIONAL D'ÉTUDES ET DE RECHERCHES AÉROSPATIALES (O.N.E.R.A.)

92 - CHATILLON - France

Les forts rapports de compression des compresseurs supersoniques nécessitent des sections de passage fortement évolutives, ce qui conduit à placer en amont du rotor un capotage qui induit des vitesses radiales importantes. La connaissance de ces vitesses et de l'influence qu'elles ont sur le profil des vitesses axiales est indispensable pour l'établissement d'un projet correct de compresseur.

Deux méthodes ont été élaborées à cet effet :

- une méthode directe consistant à déterminer, à partir de la forme du canal et de celle du capotage, l'écoulement en fluide parfait compressible qui s'établit dans le canal ; les répartitions de pression obtenues par le calcul sont comparées à celles relevées sur le carter externe et sur le capotage au cours d'essais effectués en soufflerie ; on en déduit la répartition des vitesses dans la veine ;
- une méthode indirecte partant des répartitions de pressions à la paroi externe et en déduisant le champ d'écoulement ; la vérification du calcul s'obtient par comparaison de la ligne de courant correspondant au débit à l'entrée du montage à la forme de la méridienne du capotage avant.

Les deux méthodes donnent des résultats cohérents.

### VELOCITY DISTRIBUTION AT a SUPERSONIC COMPRESSOR INLET

The high compression ratios of supersonic compressors entail widely varying duct sections, which leads to placing upstream of the rotor a cowl inducing important radial velocities. It is mandatory, to design correctly the compressor, to know these velocities and their influence on the axial velocity profile.

To this end, two methods were devised :

- a direct method in which the ideal, compressible flow in the duct is established from the duct and the cowl shapes ; the computed pressure distributions are compared with those read on the external shroud and on the cowl during wind tunnel tests ; from these, the velocity distribution in the duct is deduced ;
- an indirect method starting from the pressure distribution on the external wall and leading to the flow field ; the calculation is checked by comparing the streamline corresponding to the set-up inlet with the shape of the front cowl meridian.

The two methods give coherent results.

### NOTATIONS

$r, z$	coordonnées cylindriques ou planes
$\psi, x$	coordonnées du plan de calcul pour la méthode inverse
$f(r, z)$	fonction de compressibilité
$F$	fonction
$\psi(r, z)$	fonction de courant pour la méthode directe
$a^*$	vitesse critique du son
$M$	nombre de Mach
$M^*$	nombre de Mach critique
$p$	pression statique
$p$	pression génératrice de l'écoulement
$Q$	Constante
$R_1$	Rayon externe de la veine
$R_0$	Rayon interne de la veine
$T$	Température d'arrêt
$u$	composante de la vitesse normale à l'axe
$w$	composante axiale de la vitesse
$\alpha$	exposant ( $\alpha = 0$ écoulement plan, $\alpha = 1$ écoulement de révolution)
$\Delta r, \Delta z$	pas de calcul pour la méthode directe
$\Delta \psi, \Delta x$	pas de calcul pour la méthode inverse
$\rho$	masse volumique

### Indices

$i, j$	indices d'un noeud du réseau de calcul
$-\infty$	indice relatif au plan infini amont
$+\infty$	indice relatif au plan infini aval

\* Étude effectuée sous contrat de la Direction des Recherches et Moyens d'Essais

## 1. INTRODUCTION

Le calcul correct d'une roue de compresseur exige préalablement la connaissance de l'état de l'écoulement à l'entrée de cette même roue.

Dans le cas de compresseurs conventionnels (ni transsoniques, ni supersoniques), les veines sont en général peu convergentes et les vitesses radiales à l'entrée des roues sont pratiquement négligeables. Il est alors relativement aisé de connaître l'état de l'écoulement à l'entrée de ces roues soit par le calcul, soit par des méthodes expérimentales.

Dans le cas des compresseurs transsoniques ou supersoniques, les rapports de compression élevés nécessitent des sections de passage fortement évolutives, en particulier pour la roue de tête. Il existe par suite, à l'entrée de ces compresseurs, des vitesses radiales non négligeables qui compliquent beaucoup l'étude expérimentale. Celle-ci est également rendue difficile par le caractère hautement subsonique et même parfois transsonique de l'écoulement.

Les seuls résultats expérimentaux faciles à obtenir sont, dans le cas d'une entrée d'air de compresseur supersonique, les conditions génératrices de l'écoulement et les pressions statiques aux parois. La connaissance complète de l'écoulement ne peut donc être réalisée que par le calcul. La validité de la méthode de calcul choisie sera établie par la comparaison des résultats expérimentaux partiels obtenus avec les résultats correspondants du calcul. Ces considérations ont amené à envisager deux méthodes de calcul :

a) une méthode de calcul, dite directe, qui consiste à calculer l'écoulement à partir des données géométriques et des conditions génératrices de ce même écoulement. La comparaison des pressions statiques mesurées et calculées sur les parois permet de vérifier la validité des résultats obtenus.

b) une méthode de calcul, dite inverse, qui consiste, à partir des mesures expérimentales de pressions statiques sur une paroi, à calculer l'écoulement compte tenu des conditions génératrices. Dans ce cas, l'autre paroi est obtenue comme ligne de courant particulière. Deux comparaisons sont alors possibles, d'une part entre la paroi calculée et la paroi réelle, d'autre part entre les pressions statiques mesurées et calculées sur cette même paroi.

## 2. DEFINITION DU SCHEMA UTILISE

Qu'il s'agisse de la méthode directe ou inverse, le problème revient toujours à déterminer l'écoulement dans un canal, dans lequel est placée une roue de compresseur précédée par un capotage amont, ou bien simplement dans un canal qui constitue l'entrée d'air d'un moteur.

L'hypothèse fondamentale du calcul est de supposer que l'écoulement dans le canal, en amont de la roue, n'est pas modifié par l'absence de cette même roue. On est ramené ainsi à calculer l'écoulement dans un simple canal.

Dans tous les cas, la forme du canal n'est définie que dans une portion limitée de l'espace et, pour le calcul direct, il est indispensable de prolonger de façon fictive les contours internes et externes jusqu'aux infinis amont et aval où ils doivent être parallèles à l'axe. Dans le cas d'un capotage, c'est l'axe qui assure le prolongement du contour du moyeu vers l'infini amont (fig. 1). Il peut en être également ainsi vers l'infini aval. Les résultats trouvés dépendent plus ou moins du choix de ces contours, il y a là une difficulté que l'on retrouve dans l'expérimentation en soufflerie de ces mêmes entrées d'air. Les précautions élémentaires à prendre consistent à assurer la continuité de la tangente et de la courbure entre la paroi réelle et la paroi fictive et à éviter que par diminution excessive de la veine un blocage sonique n'apparaisse.

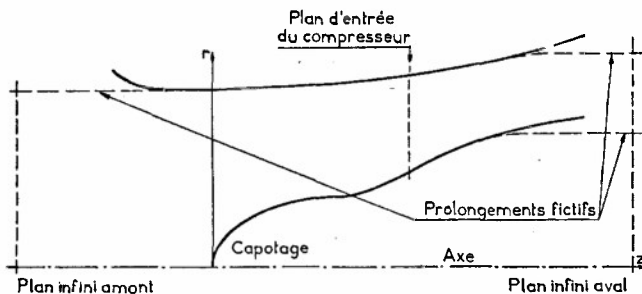


Fig. 1 - Domaine de calcul

## 3. EQUATIONS DE BASE

L'écoulement est supposé irrotationnel et fonction de deux variables seulement, l'abscisse  $z$  et l'ordonnée  $r$ , qui, dans le cas d'un capotage de révolution, représente la distance du point considéré à l'axe.

Les composantes ( $\mu$ ,  $w$ ) de la vitesse suivant les axes  $O_r$  et  $O_z$  sont liées par la condition d'irrotationnalité

$$\frac{\partial w}{\partial r} - \frac{\partial \mu}{\partial z} = 0 \quad (1)$$

valable de façon précise dans un écoulement accéléré du type de ceux étudiés ci-dessous et par la condition de conservation du débit

$$\frac{\partial(r^\alpha \rho \mu)}{\partial r} + \frac{\partial(r^\alpha \rho w)}{\partial z} = 0 \quad (2)$$

avec  $\left\{ \begin{array}{l} \alpha = 0 \text{ pour un écoulement plan} \\ \alpha = 1 \text{ pour un écoulement de révolution} \end{array} \right.$

$\rho$  représentant la masse volumique

Pour donner plus de généralité aux méthodes étudiées ici, le cas de l'écoulement plan est envisagé, bien qu'il n'intervienne pas dans les entrées d'air de compresseurs

Les équations (1) et (2) forment un système différentiel de deux équations à deux inconnues  $\mu$  et  $w$ . La relation (2) permet de définir une fonction de courant  $\psi$  par

$$\left\{ \begin{array}{l} \mu = \frac{Q}{\rho r^\alpha} \frac{\partial \psi}{\partial z} \end{array} \right. \quad (3)$$

$$\left\{ \begin{array}{l} w = \frac{Q}{\rho r^\alpha} \frac{\partial \psi}{\partial r} \end{array} \right. \quad (4)$$

où  $Q$  est une constante. A l'infini amont, l'écoulement est uniforme et axial. Il est caractérisé par une vitesse  $w_{-\infty}$  et une masse volumique  $\rho_{-\infty}$ .

La fonction de courant  $\psi$  est définie de telle sorte que pour  $r = R_0$ ,  $\psi = 0$  et  $r = R_1$ ,  $\psi = 1$ .

Les courbes  $r = R_0(z)$  et  $r = R_1(z)$  représentent respectivement les parois du moyeu et du carter.

Dans le cas d'un capotage, et en amont du nez  $R_0(z) = 0$ , la constante  $Q$  se calcule alors aisément à l'infini amont

$$Q = \rho_{-\infty} w_{-\infty} \frac{R_{1-\infty}^{\alpha+1} - R_{0-\infty}^{\alpha+1}}{\alpha+1} \quad (4)$$

#### 4. METHODE DE CALCUL DIRECT

##### 4.1 - Equations du calcul direct

En introduisant la fonction de courant  $\psi$ , l'équation (1) devient

$$\frac{\partial}{\partial r} \left( \frac{1}{\rho r^\alpha} \frac{\partial \psi}{\partial r} \right) + \frac{\partial}{\partial z} \left( \frac{1}{\rho r^\alpha} \frac{\partial \psi}{\partial z} \right) = 0$$

ou après transformations

$$\frac{\partial^2 \psi}{\partial r^2} + \frac{\partial^2 \psi}{\partial z^2} - \frac{\alpha}{r} \frac{\partial \psi}{\partial r} - \frac{\partial f}{\partial r} \frac{\partial \psi}{\partial r} - \frac{\partial f}{\partial z} \frac{\partial \psi}{\partial z} = 0 \quad (5)$$

où  $f = \text{Log}(\rho/\rho_{-\infty})$  représente la fonction de compressibilité.

En fluide incompressible l'équation (5) se réduit à la forme classique

$$\frac{\partial^2 \psi}{\partial r^2} + \frac{\partial^2 \psi}{\partial z^2} - \frac{\alpha}{r} \frac{\partial \psi}{\partial r} = 0 \quad (6)$$

##### 4.2 - Fonction de Compressibilité

La fonction de compressibilité  $f$  qui intervient dans l'équation (5) est liée de façon implicite à la fonction de courant  $\psi$ . L'écoulement étant supposé isenthalpique et isentropique (homotropique)

$$\frac{\rho}{\rho_{-\infty}} = \left( \frac{m^2 - M_*^2}{m - M_{*-\infty}^2} \right)^{\frac{m^2 - 1}{2}} \quad (7)$$

où  $m^2 = (\gamma + 1) / (\gamma - 1)$ ,  $M_*$  est le nombre de Mach critique local et  $M_{*-\infty}$  est le nombre de Mach critique amont.

Le nombre de Mach critique est lié à la vitesse

$$M_*^2 = \frac{\mu^2 + w^2}{a_*^2}$$

où  $a_* = \sqrt{2C_p T / m^2}$  représente la célérité critique du son, soit, compte tenu des relations (3) et (4)

$$M_* = M_{*-\infty} \frac{\rho_{-\infty}}{\rho} \frac{R_{1-\infty}^{\alpha+1} - R_{0-\infty}^{\alpha+1}}{(\alpha+1) r^\alpha} \sqrt{\left( \frac{\partial \psi}{\partial z} \right)^2 + \left( \frac{\partial \psi}{\partial r} \right)^2} \quad (8)$$

Les équations (7) et (8) forment un système de deux équations à deux inconnues  $M_*$  et  $\frac{\rho}{\rho_{-\infty}}$ . Ce système peut avoir deux solutions (une solution subsonique et une solution supersonique), une seule solution (qui correspond à  $M_* = 1$ ), ou pas de solution du tout.

Pour un écoulement entièrement subsonique, il y a toujours des solutions dont il ne faut retenir que la solution subsonique. La recherche systématique de cette solution subsonique permet donc de définir, connaissant la fonction de courant  $\psi$ , la fonction de compressibilité  $f$  sans ambiguïté.

Dans le cas de l'écoulement de révolution ( $\alpha = 1$ ), l'équation (8) est indéterminée pour  $r = 0$  (sur l'axe). Cette indétermination peut être levée au moyen de la règle de l'Hopital.

$$\lim_{r \rightarrow 0} M_* \frac{\rho}{\rho_{-\infty}} = M_{*-\infty} \frac{R_{1-\infty}^2 - R_{0-\infty}^2}{2} \lim_{r \rightarrow 0} \frac{\partial^2 \psi}{\partial r^2}$$

soit

$$\left( \frac{\rho}{\rho_{-\infty}} M_* \right)_{r=0} = M_{*-\infty} \frac{R_{1-\infty}^2 - R_{0-\infty}^2}{2} \left( \frac{\partial^2 \psi}{\partial r^2} \right)_{r=0}$$

#### 4.3 - Résolution numérique

La détermination de la valeur de la fonction de courant  $\psi$  dans le domaine de calcul se fait par une méthode de différences finies en utilisant l'équation (5). Le domaine de calcul est quadrillé par des droites  $r = \text{constante}$  (lignes) distantes de  $\Delta r$ , la première ligne étant nécessairement l'axe, et par des droites  $z = \text{constante}$  (colonnes) distantes de  $\Delta z$ , les droites  $z = z_{-\infty}$  et  $z = z_{+\infty}$  étant les colonnes extrêmes.

Le calcul des dérivées premières et secondes en un noeud du réseau se fait dans le cadre de l'approximation parabolique.

La résolution numérique se fait par des itérations en deux temps.

1) La fonction de compressibilité  $f_1$  étant donnée, calcul de la fonction de courant  $\psi$  par surrelaxation grâce à l'équation (5).

2) Au moyen de la nouvelle fonction de courant  $\psi$ , ainsi trouvée, calcul d'une fonction de compressibilité corrigée  $f_2$  grâce aux équations (7) et (8).

Un test de convergence sur la fonction de compressibilité  $f$  permet alors soit de recommencer le calcul de la fonction de courant  $\psi$  en 1) avec la nouvelle valeur  $f_2$  de la fonction de compressibilité  $f$  soit de procéder à l'impression des résultats.

#### 4.4 - Conditions aux limites

Sur l'axe et sur la paroi du moyeu qui constitue une ligne de courant particulière, on a  $\psi = 0$  et sur la paroi du carter  $\psi = 1$ .

Dans les plans infinis aval et amont, l'écoulement est uniforme. Grâce à l'équation (4) il est aisé de calculer la fonction de courant  $\psi$  dans ces plans

pour  $z = z_{-\infty}$  
$$\psi = \frac{r^{\alpha+1} - R_{0-\infty}^{\alpha+1}}{R_{1-\infty}^{\alpha+1} - R_{0-\infty}^{\alpha+1}}$$

$z = z_{+\infty}$  
$$\psi = \frac{r^{\alpha+1} - R_{0+\infty}^{\alpha+1}}{R_{1+\infty}^{\alpha+1} - R_{0+\infty}^{\alpha+1}}$$

(Dans le cas d'un capotage  $R_{0-\infty} = 0$ )

La résolution numérique de l'équation (5) exige la connaissance de la fonction  $f$  sur les frontières, c'est-à-dire des dérivées  $\frac{\partial \psi}{\partial r}$  et  $\frac{\partial \psi}{\partial z}$  sur ces mêmes frontières. Dans le cadre de l'approximation parabolique utilisée, on suppose près des parois que

$$\psi = ar^2 + br + cz^2 + dz + e$$

ce qui permet de calculer aisément les dérivées  $\frac{\partial \psi}{\partial r}$  et  $\frac{\partial \psi}{\partial z}$  sur les frontières. Dans les plans infinis amont et aval, il n'y a pas de problème puisque  $\frac{\partial \psi}{\partial z} = 0$ .

#### 5. METHODE DE CALCUL INVERSE

##### 5.1 - Equations du calcul inverse

Dans la méthode du calcul inverse, on suppose connue la répartition des vitesses sur une paroi. Les équations (3) et (4) permettent de définir un changement de variables et d'effectuer les calculs dans le plan  $(\psi, x)$  plus commode que le plan physique  $(r, z)$ . Ce changement de variables s'écrit

$$\begin{cases} \psi = \psi(r, z) \\ x = z \end{cases} \quad (9)$$

Les différenciations s'effectuent au moyen des opérateurs

$$\frac{\partial}{\partial z} ( ) = \frac{\partial \psi}{\partial z} \frac{\partial}{\partial \psi} ( ) + \frac{\partial}{\partial x} ( ) \quad (10)$$

$$\frac{\partial}{\partial r} ( ) = \frac{\partial \psi}{\partial r} \frac{\partial}{\partial \psi} ( )$$

et l'équation d'irrotationnalité devient

$$\frac{\partial u}{\partial \psi} \frac{\partial \psi}{\partial z} - \frac{\partial w}{\partial \psi} \frac{\partial \psi}{\partial r} + \frac{\partial u}{\partial x} = 0 \quad (11)$$

soit

$$\rho r^\alpha \left( u \frac{\partial u}{\partial \psi} + w \frac{\partial w}{\partial \psi} \right) - Q \frac{\partial u}{\partial x} = 0 \quad (12)$$

De même l'équation de conservation du débit s'écrit

$$\rho r^\alpha \left( w \frac{\partial u}{\partial \psi} - u \frac{\partial w}{\partial \psi} \right) + Q \left( \alpha \frac{u}{r} + \frac{\partial w}{\partial x} - \frac{(m^2-1)w \left( u \frac{\partial u}{\partial x} + w \frac{\partial w}{\partial x} \right)}{m^2 a_x^2 - u^2 - w^2} \right) = 0 \quad (13)$$

Quant au rayon  $r$ , il est lié aux variables utilisées par

$$\frac{\partial r}{\partial \psi} = \frac{Q}{\rho r^\alpha w} \quad (14)$$

## 5.2 - Résolution numérique

Le calcul de l'écoulement se fait par une méthode de différences finies. Le plan de calcul  $(\psi, x)$  est décrit au moyen d'un maillage de  $m$  lignes  $\psi = \text{cte}$  distantes de  $\Delta\psi$ , les lignes extrêmes étant  $\psi = 1$  pour le carter et  $\psi = 0$  pour le moyeu, et de  $n$  colonnes  $x = \text{cte}$  distantes de  $\Delta x$ .

En appelant  $F_{ij}$  la valeur prise par une fonction  $F$  au point du maillage situé sur la  $i^{\text{ème}}$  ligne et sur la  $j^{\text{ème}}$  colonne, on peut exprimer les équations (12), (13) et (14) sous forme de différences finies

$$\left\{ \begin{aligned} & \rho_{ij} r_{ij}^\alpha \left( u_{ij} \frac{u_{i+1j} - u_{i-1j}}{2\Delta\psi} + w_{ij} \frac{w_{i+1j} - w_{i-1j}}{2\Delta\psi} \right) - Q \frac{u_{ij+1} - u_{ij-1}}{2\Delta x} = 0 \\ & \rho_{ij} r_{ij}^\alpha \left( w_{ij} \frac{u_{i+1j} - u_{i-1j}}{2\Delta\psi} - u_{ij} \frac{w_{i+1j} - w_{i-1j}}{2\Delta\psi} \right) + \alpha Q \frac{u_{ij}}{r_{ij}} + Q \frac{w_{ij+1} - w_{ij-1}}{2\Delta x} \\ & - Q (m^2 - 1) \frac{w_{ij} \left( u_{ij} \frac{u_{ij+1} - u_{ij-1}}{2\Delta x} + w_{ij} \frac{w_{ij+1} - w_{ij-1}}{2\Delta x} \right)}{m^2 \Delta x^2 - u_{ij}^2 - w_{ij}^2} = 0 \quad (15) \\ & \frac{r_{i+1j} - r_{i-1j}}{2\Delta\psi} = \frac{Q}{\rho_{ij} r_{ij}^\alpha w_{ij}} \end{aligned} \right.$$

Ce système d'équations est linéaire en  $r_{i+1j}$ ,  $u_{i+1j}$  et  $w_{i+1j}$ . Il est donc possible en connaissant les valeurs des différentes fonctions sur la  $i-1^{\text{ème}}$  ligne et sur la  $i^{\text{ème}}$  ligne de déterminer les valeurs des mêmes fonctions sur la  $i+1^{\text{ème}}$  ligne et par suite de connaître tout le champ de l'écoulement. Comme critère de validité du calcul, la valeur de  $r$  déterminée sur la ligne  $\psi = 0$  donne la forme du moyeu.

## 5.3 - Conditions de départ

Pour débiter les calculs, il est nécessaire de connaître les différentes fonctions sur deux lignes consécutives or celles-ci ne sont connues que sur une seule ligne (la ligne  $\psi = 1$  ou  $i = 1$ ), celle qui représente la paroi où est donnée la répartition de vitesses (la paroi externe dans le cas considéré). Pour démarrer les calculs, il est nécessaire de faire une approximation supplémentaire. On a supposé que

$$\left( \frac{\partial F}{\partial \psi} \right)_{1,j} = \frac{F_{2,j} - F_{1,j}}{\Delta\psi}$$

Cette hypothèse n'est rigoureuse, dans le cas de la méthode de différences finies utilisée que si

$$\left( \frac{\partial^2 F}{\partial \psi^2} \right)_{1,j} = 0$$

## 6. MONTAGE EXPERIMENTAL

Le capot de moyeu (fig. 2 et 3), caractéristique de l'entrée d'air étudiée pour une veine cylindrique de diamètre intérieur 200 mm, est placé dans celle-ci (fig. 4).

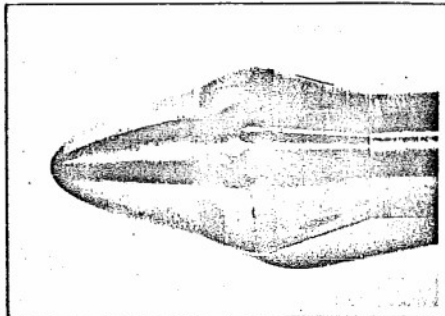


Fig. 2 - Photo du capotage

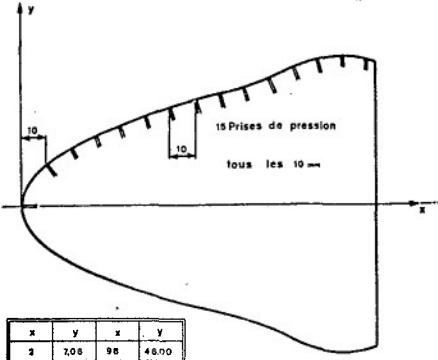


Fig. 3 - Plan du capotage

x	y	x	y
2	7,08	98	48,00
4	10,00	100	49,50
8	14,20	104	51,60
16	20,40	108	53,60
24	24,60	112	55,60
32	28,80	116	56,40
40	31,80	120	57,60
48	34,60	124	58,80
56	37,52	130	60,00
64	39,68	134	59,60
72	41,78	138	58,48
80	43,84	142	57,28
88	45,98	144	57,08

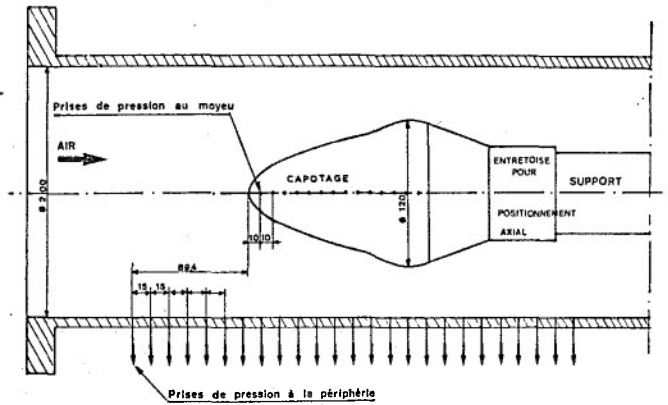


Fig. 4 - Schéma du montage expérimental

Le capot est tenu dans la veine par un dard cylindrique de diamètre 97 mm. Le calage du dard au centre de la veine se fait à l'aide de deux séries de trois bras-supports à 120°. Derrière le capot, se trouve un corps conique de raccordement et une entretoise cylindrique d'épaisseur variable dont le rôle est de modifier à l'occasion la position axiale de l'avant-roue. Sur le compresseur, seule la fraction du capot comprise entre l'axe et le parallèle de rayon 100 mm peut être utilement comparée aux essais en soufflerie, le reste étant masqué par les aubes.

Sur le montage, une prise de pression d'arrêt amont indique la pression génératrice de l'écoulement. Sur la périphérie et sur le corps central se trouvent un certain nombre de prises de pression statique (fig. 3 et 4). Les prises de la périphérie sont situées sur une méridienne ; les prises montées sur le capot sont placées sur une hélice dont le pas est de 40 mm (fig. 3).

7. COMPARAISON CALCULS-EXPERIENCES

Sur la figure 5, ont été tracées les courbes expérimentales donnant la répartition des nombres de Mach sur les parois pour deux pressions génératrices différentes. L'une de ces pressions génératrices (P = 1385 mmHg) donne un écoulement transsonique. La répartition expérimentale du nombre de Mach sur le carter externe a servi à calculer l'écoulement par la méthode inverse. L'autre pression génératrice (P = 885 mmHg) donne un écoulement entièrement subsonique. La méthode directe a été utilisée pour ce deuxième cas.

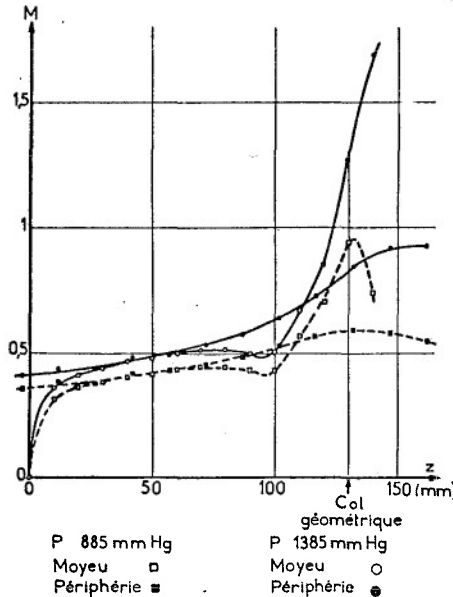


Fig. 5 - Evolution du nombre de Mach aux parois

## 7.1 - Méthode directe

La comparaison des résultats théoriques et expérimentaux a été réalisée sur les figures 6a et 6b. Les écarts entre calculs et expériences apparaissent assez faibles (de l'ordre de 1 à 2 %) mais systématiquement dans le même sens.

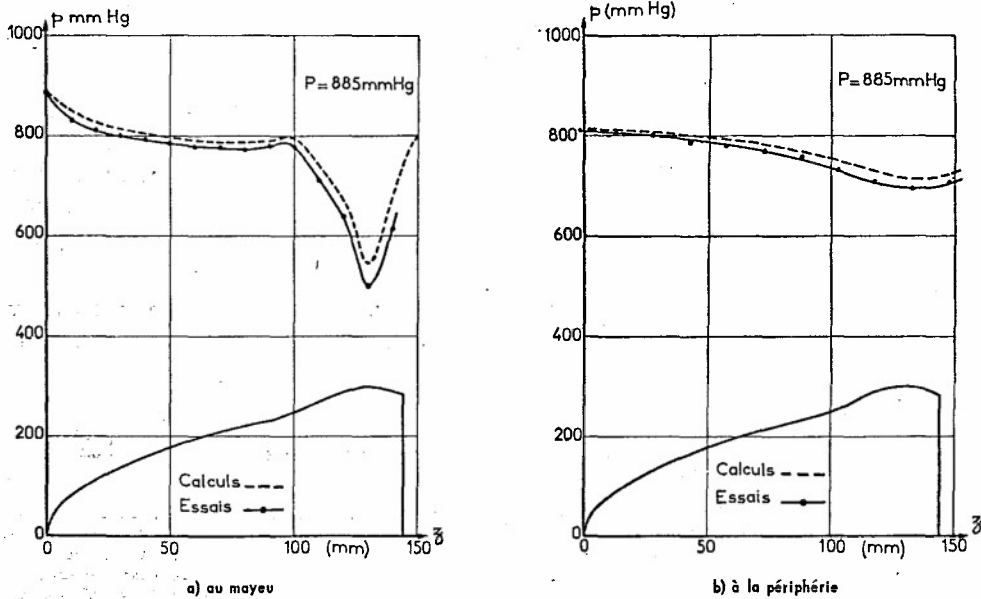


Fig. 6 - Méthode directe.  
Comparaison des pressions statiques calculées et mesurées

La figure 7 représente le tracé des isobares, qui sont graduées en nombres de Mach. Ce tracé montre de façon très précise les fluctuations de vitesses dans la veine.

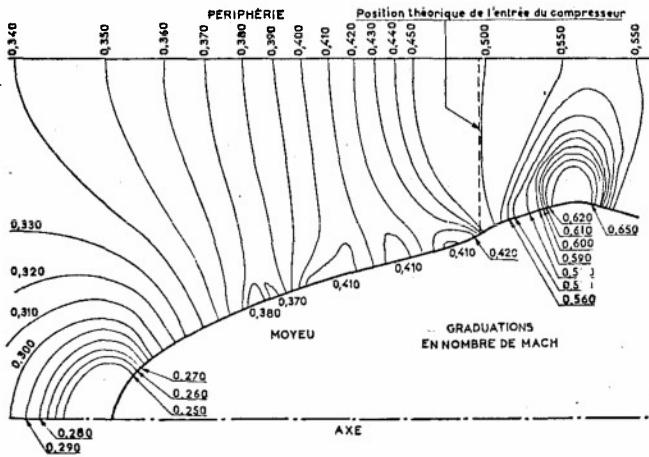


Fig. 7 - Tracé des courbes isobares

## 7.2 - Méthode inverse

Sur la figure 8 est tracée la répartition des pressions statiques à la paroi du carter, mesurées expérimentalement, pour la pression génératrice de l'écoulement  $P = 1385$  mm Hg. A partir de cette répartition longitudinale de pressions, préalablement lissée, a été effectué le calcul de l'écoulement.

La comparaison de la forme du moyeu trouvée par le calcul avec la forme du moyeu réelle est présentée sur la figure 9. La concordance est assez bonne. Il faut cependant noter que les résultats près du nez sont mauvais.

Le calcul donne même juste en avant du capot des rayons négatifs. Ceci n'est guère étonnant car une méthode de différences finies suppose la continuité des différentes fonctions et de leurs dérivées ce qui n'est pas le cas pour la fonction  $r$  près du nez.

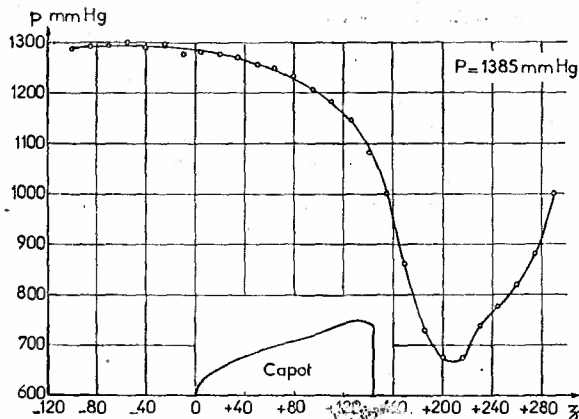


Fig. 8 - Méthode inverse.  
Répartition expérimentale des pressions à la périphérie

La figure 10 montre une comparaison entre le relevé expérimental des pressions statiques sur le capot et les valeurs déduites par le calcul. L'erreur est relativement faible.

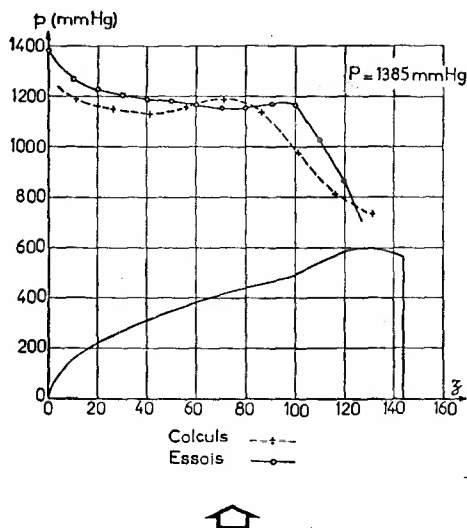


Fig. 10 - Méthode inverse.  
Comparaison des pressions statiques calculées et mesurées au moyeu

Fig. 9 - Méthode inverse.  
Comparaison de la forme calculée et de la forme réelle

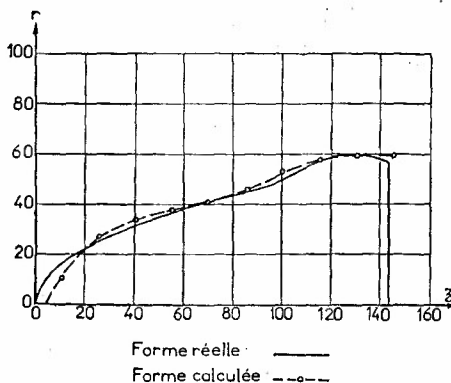
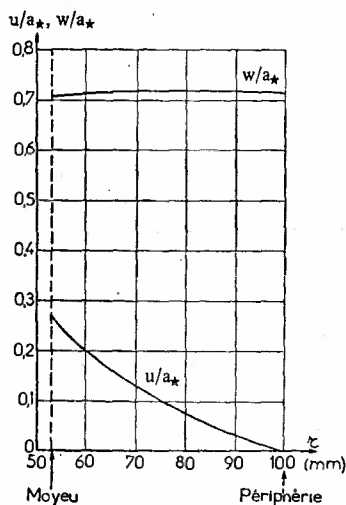


Fig. 11 - Méthode inverse.  
Répartition radiale des vitesses axiales et radiales à l'entrée d'un compresseur



Enfin, sur la figure 11, ont été tracées les répartitions radiales des vitesses axiales et radiales, calculées par la méthode inverse, dans le plan d'entrée de compresseur. On note la répartition très uniforme de la vitesse débitante.

## 8. CONCLUSION

Le calcul direct et indirect de l'écoulement autour d'un capotage de compresseur placé dans un canal cylindrique constitue un ensemble de méthodes permettant de connaître à partir de la forme du capot et de la veine d'une part, de la répartition de pression sur la paroi externe d'autre part, le champ de l'écoulement à l'entrée du compresseur.

L'intérêt de la méthode réside dans le fait que la détermination expérimentale de la répartition radiale de la vitesse est rendue difficile par la pente importante des lignes de courant ainsi que par les phénomènes de compressibilité non négligeables à l'entrée d'un compresseur axial moderne.

Chacune des deux méthodes proposées a des avantages et des inconvénients. La méthode directe ne nécessite de vérification expérimentale que lorsque la forme de capot choisie donne déjà satisfaction tant par l'uniformité de la vitesse obtenue à l'entrée du compresseur qu'à la répartition de pression sur le moyeu ; en revanche par les itérations qu'elle exige son temps de calcul peut être long et de toutes façons, elle ne s'applique pas aux écoulements transsoniques. La méthode inverse repose sur des résultats expérimentaux préalablement acquis. Ceux-ci doivent être précis et nécessitent donc une réalisation très soignée de montage : toute erreur dans la continuité correcte des valeurs de la pression introduites dans le calcul conduit inéluctablement à un blocage de celui-ci. Un lissage des valeurs expérimentales est donc nécessaire et ce n'est que lorsque le calcul a redonné de façon correcte le moyeu comme ligne de courant particulière de l'écoulement que l'on est assuré de l'exactitude des répartitions de vitesse déterminée par cette méthode. En revanche, le calcul inverse s'applique aussi aux écoulements légèrement transsoniques, ce qui en augmente le domaine d'application.

\*

THE ANALYSIS OF A SUBSONIC AXISYMMETRIC  
INLET FOR COMPRESSOR MATCHING

by

R. E. Stanley Senior Aerodynamicist  
Gas Turbine Division  
A/S Kongsberg Våpenfabrikk  
Postbox 25  
3601 Kongsberg, Norway

SUMMARY

The experimental analysis of the flow within an axisymmetric inlet will be presented. The purpose of this analysis will be set out, that is, the need to match the blade inlet angles of a centrifugal compressor to the inlet radial flow distribution.

The measured velocity distribution for the original inlet will be compared to the distribution obtained by a method of numerical analysis. It will be shown that the favourable results of this comparison led to the development of this inlet by a method of numerical analysis in preference to a model testing technique; the analytical work being contracted out to a consultant within a NATO country. The recommendations of the consultant will be presented, together with the results of an experimental analysis of the redesigned inlet configuration. The method of compressor matching will be touched upon, and finally conclusions will be drawn about the success of this development method.

LIST OF SYMBOLS

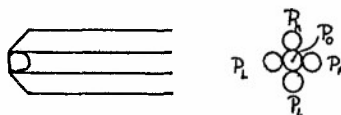
CRV	curvature, mm <sup>-1</sup>
R	radius from axis of inlet, mm
V	local velocity
$\bar{V}$	reference mean velocity
X	axial distance from inducer leading edge, mm
Z	contour path length, mm

Symbols for probe B figure 2:-

Probe Head

Side

Front



Symbols for figure 3:-

P	reference total pressure	} from windtunnel calibration for probe B
P <sub>s</sub>	reference static pressure	
$\Delta P_o$	P - P <sub>o</sub>	
Q	reference dynamic head P - P <sub>s</sub>	
Q <sub>p</sub>	probe dynamic head P <sub>o</sub> - P <sub>h</sub>	
$\beta^\circ$	flow yaw angle relative to probe B	
$\theta^\circ$	flow pitch angle relative to probe B	

INTRODUCTION

The inlet to be described is that from an all radial industrial gas turbine, the Kongsberg Viking. This engine is in the 1200 to 1600 kW power class and is developed and manufactured at Kongsberg in Norway. This paper describes part of the centrifugal compressor development programme, in which the flow characteristics of the original inlet were investigated by using pressure sensing instrumentation within the inlet of a development gas turbine. The same inlet was analysed by the streamline curvature technique described in reference 1. The analysis was contracted out to the von Karman Institute For Fluid Dynamics, who recommended an inlet redesigned by using the same technique. These recommendations were effected by installing a redesigned inlet into the development engine and repeating the experimental flow investigation. The experimental results were then compared to the predicted characteristics and subsequently used to rematch the blade angle distribution of the compressor inducer to the measured inlet flow distribution.

Figure 1 shows the engine inlet arrangement. This inlet, which is a radial inflow axial exit type, is manufactured to the redesigned standard and is now fitted to all production engines. Figure 4 shows the original inlet profile. The rectilinear channel, downstream of the inducer leading edge, was used in the numerical analysis to allow the calculation to proceed to the set boundary conditions. These boundary conditions are described later. In reality there exists the characteristic meridional channel shape of a radial compressor, downstream of the inducer leading edge. The shroud and hub curvatures are given in figures 5 and 6 as curves I. These two figures show that the inlet profile is solely constructed of circular arcs and straight lines, which give the step function plot as shown. The original inlet was designed on the basis of a smooth area distribution through the inlet, the shroud and hub profiles being constructed of circular arcs and straight lines in order to simplify component manufacture. However with the increasing use of numerically controlled machining processes, the restriction of a simple profile geometry is no longer warranted.

#### EXPERIMENTAL INVESTIGATION OF THE ORIGINAL INLET

The instrumentation associated with the experimental investigation of the original inlet is shown in figures 2 and 4. Total pressure at the entrance to the inlet was measured by using four kiel probes of the sharp-edged venturi type, which have a yaw and pitch angle range of  $\pm 45^\circ$ . An example of this type of probe is shown in figure 2 as probe A. Probe B, in figure 2, is a three dimensional pressure probe which was manufactured and calibrated by the von Karman Institute. Figure 3 shows a set of typical calibration curves which were supplied with the probe and used to reduce the test data. The probe was calibrated at a mach number of 0.4. The location of the pressure probes and static pressure taps is shown in figure 4. Also shown in the same figure are details of a static pressure tap which consists of a brass insert made flush with the inlet shroud profile and having a 1 mm diameter sensing hole. Only one set of static pressure taps could be installed into the hub surface because of the bearing and shaft arrangement located within the confines of the hub profile. Additional instrumentation, which was standard to the development engine test rig, consisted of an air mass flow measuring-venturi to DIN 1952 standard. The throat pressure drop was measured with a Betz micromanometer and the air total temperature was measured by two thermocouples which were external to the test rig.

The test procedure consisted of running the development engine at the design air mass flow rate of  $12.3 \text{ Kg sec}^{-1}$ , defined on a normalized basis, and also at 50% of design mass flow rate. Inlet preswirl vanes were not installed during these series of tests. Consequently the three dimensional probe was locked in a zero yaw—zero pitch position and traversed radially. It was assumed that the actual flow yaw and pitch angles at the radial traverse station would be within the calibration range of the probe,  $\beta = \pm 20^\circ$ ,  $\theta = \pm 10^\circ$ . This assumption proved to be correct. Consequently the testing time was reduced as the probe pressures were not balanced. The probe calibration curves were used to determine true values for  $\beta$  and  $\theta$ .

The results from this test series are presented in figures 7, 8 and 9 I, II. The shroud and hub velocity distribution, as measured by the individual static pressure taps, is presented in figures 7 and 8, and the probe traverse data, which have been transformed to the inducer leading edge station, are presented in figure 9.

The conclusions drawn from the results of this test were as follows.

- a) The shroud velocity distribution should be improved. The test data indicate an area of diffusion and hence possible flow separation in the region of  $Z = 140 \text{ mm}$ , see figure 7.
- b) No conclusion could be drawn concerning the hub velocity distribution. However this was of little consequence since no changes could be made to this surface due to the mechanical arrangement within the hub, and since there was no danger of separation of the flow.
- c) The radial velocity distribution at the inducer leading edge should be improved before attempting to rematch the inducer blade angle distribution. Figure 9, II indicates a non-uniformity in  $V/\bar{V}$  of  $+17.5\% - 11\%$ .

It should be mentioned at this point that the inducer blade angle distribution was originally matched for a completely uniform inlet velocity profile, i.e.  $V/\bar{V} = 1.0$ . Hence the actual inlet velocity profile results in an incorrect incidence distribution at the design operating point. Since the inducer tip relative mach number is high, this state of affairs is a cause for some concern.

A development programme for the inlet was set out as follows.

- i) An attempt should be made to analyse the flow within the original inlet by a method of numerical analysis, and then compare the theoretical and experimental results.
- ii) If good agreement between the two methods was obtained, a redesign of the inlet should be attempted, using the same method. It was hoped to obtain a monotonic pressure distribution in the inlet and an approximately constant axial velocity distribution at the inducer leading edge.
- iii) A redesigned inlet should be manufactured and tested. If the test results prove to be satisfactory, the existing inducer blade angle distribution should be modified to match the measured flow distribution.

A model test programme was not ventured upon owing to the length of time required for the manufacture of rig components and for the completion of the development testing, which could only be based on a process of trial and error.

#### NUMERICAL ANALYSIS

The aforementioned development requirements were presented to the von Karman Institute, who then accepted a contract for the analysis of the original intake. If the analysis proved encouraging, they agreed to redesign the shroud profile.

This numerical analysis required that the streamline curvature, which was infinitely close to the shroud and hub contours, should have a smooth variation with distance along the contour. This smoothing of the step function curvature for the shroud and hub profiles is shown in figures 5 and 6 as curves II. A rectilinear channel was assumed downstream of the inducer leading edge in order to allow the numerical analysis to proceed to the set boundary conditions of zero profile curvature and uniform flow velocity distribution 60 mm downstream of the inducer leading edge. In order to obtain sensible results from the analysis a great deal of thought was given to the setting up of these boundary conditions. The effect of revising these boundary conditions by replacing the rectilinear channel with the compressor meridional channel will be presented later.

The results of the analysis for the original inlet are presented as continuous curves in figures 7, 8 and 9 III. The measured shroud velocity distribution occurred in the results of the numerical analysis, and thus the area of diffusion for  $Z = 140$  mm was confirmed. The calculated radial velocity distribution at the inducer leading edge, was felt to be close enough to the measured distribution to assume that any  $\Delta V/V$  improvement achieved by future predictions would be realized in practice.

A redesign of the shroud profile was effected but four contours were examined before the peaked and continuously increasing shroud velocity distribution was eventually smoothed. This redesign shroud profile is shown in figure 10 where it is compared to the original shroud profile. The geometric curvature for this shroud is shown in figure 11 I along with the curvature used in the numerical analysis represented by II. Figures 12, 13 and 14 II give the velocity distribution for the shroud and hub profiles and the radial velocity distribution at the inducer leading edge. The extent of the improvement in calculated radial velocity distribution was restricted because of the impossibility of revising the hub profile. The calculated range of velocity distribution for the original inlet was + 18.5% - 14.5%, and for the redesigned inlet + 10% - 12.2%.

We accepted their redesign on the basis of the improvement in shroud velocity distribution along with the likelihood of marginal improvements in the radial velocity distribution at the inducer inlet.

#### EXPERIMENTAL INVESTIGATION OF THE REDESIGNED INLET

The development gas turbine engine was modified by fitting the redesigned inlet with instrumentation as shown in figure 10, and the test procedure was repeated as for the original inlet. Unfortunately the hub static pressure taps failed at the beginning of the test series owing to an oil leak on the development engine. Consequently no readings were available for this test series. The results for this investigation are presented in figures 12 and 14 I. The measured inlet radial velocity distribution had a measured variation of + 15.8% - 15.5% at the inducer leading edge, remaining substantially the same as for the original inlet. However it was encouraging to find that the measured shroud velocity distribution eliminated the possibility of separation.

#### COMPRESSOR MATCHING

The required inducer blade angle distribution was calculated using the measured inlet radial velocity distribution and blade blockage. The latter was based on the existing inducer blade thickness distribution. Zero incidence was regarded as the optimum for the inducer tip, and a radial blade angle distribution was used to give a radially stacked inducer blade. A radially stacked inducer blade is defined here as one in which the blade camber plane is generated by a radial line passing through the axis of rotation of the blade. Mathematically it is defined as  $\tan \alpha / R = \text{constant}$  where  $\alpha$  is the camber angle relative to the axial direction for a given radial generator line station. The blade inlet distribution derived from the above criterion gave increasing positive incidence of flow from the inducer tip section to the blade root. Complete zero radial incidence could have been achieved by keeping a radially stacked inducer blade with a swept back leading edge. However a reduced tip section chord, which would produce this swept back, could not be accepted because of inducer aerodynamic loading. Increasing the hub section chord was contemplated but finally rejected in preference to keeping a vertical inducer leading edge and obtaining the desired rematch by modifying an existing inducer wheel. This method reduced substantially the manufacturing time which was required to produce a rematched development inducer wheel.

## CONCLUDING REMARKS

A development philosophy has been described concerning the improvement of the flow within a subsonic axisymmetric inlet, and for the subsequent matching of the inducer of a centrifugal compressor to the measured inlet flow distribution. The problem of predicting the flow distribution within an accelerating channel, with low losses, is a relatively simple task for numerical flow analysis using modern computer facilities, but the upstream effects of the compressor inducer on the flow within the inlet is not fully understood. Finite inducer blade thickness, viscous effects and blade angle mismatch could cause some redistribution of the flow upstream of the inducer, but none of these effects could be taken into account in the numerical analysis.

The validity of the predicted velocity distribution is dependent upon the chosen streamline curvature distribution along the shroud and hub contours, and upon the downstream boundary conditions. The effect of changing these boundary conditions was investigated by replacing the downstream rectilinear channel of the redesigned inlet by the compressor meridional channel. The change to the radial velocity distribution is shown in figure 14 III, where the gradient of the predicted velocity distribution III is closer to the measured distribution I than the initial prediction II was.

The programme described in this paper has given us sufficient confidence in the method of numerical analysis for it to be used in the design phase of an inlet for the next generation of engine now being prepared at Kongsberg. This new inlet is another radial inflow axial exit type, and this time complete freedom was given to contouring the hub profile before the shaft and bearing designs were frozen. The downstream boundary conditions were set assuming that the compressor meridional shape was downstream of the inducer leading edge. The velocity distributions within this inlet will be measured and it is hoped that very little development will be required before the compressor inducer is matched to the measured flow velocity distribution.

## REFERENCE

1. GALLET, P.: Axisymmetric Subsonic Inlets - Small Gas Turbines.  
AGARD CP 38, 1971.

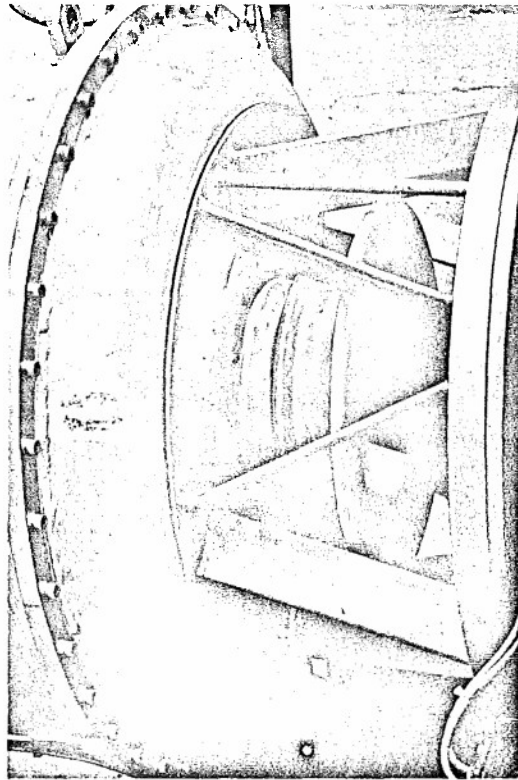


FIG. 1 ENGINE INLET

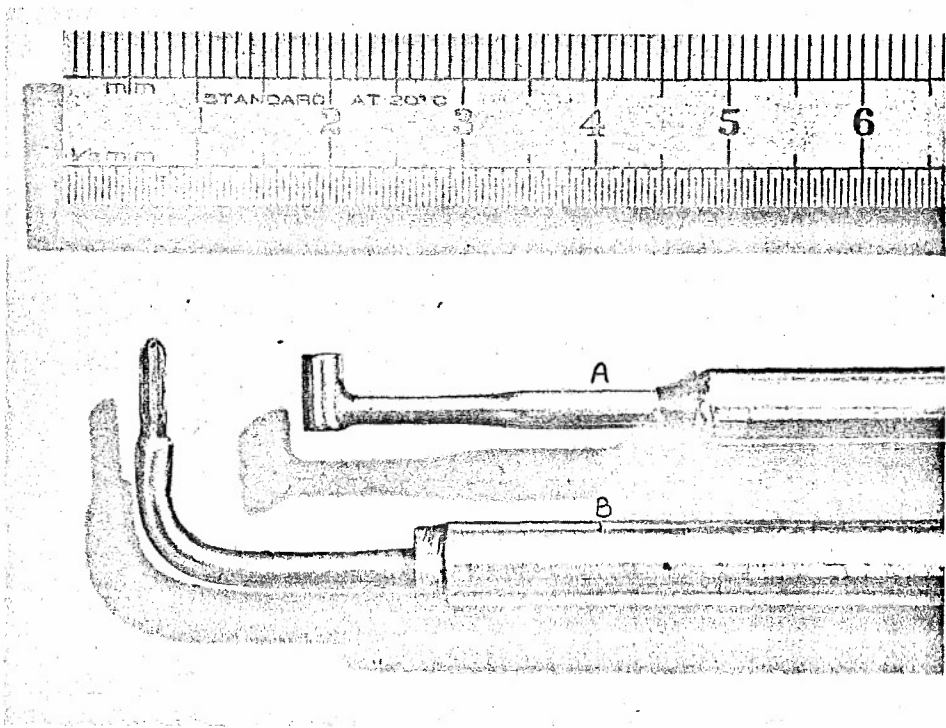


FIG. 2 PRESSURE PROBES

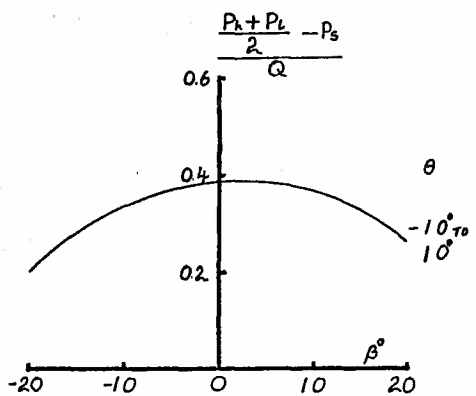
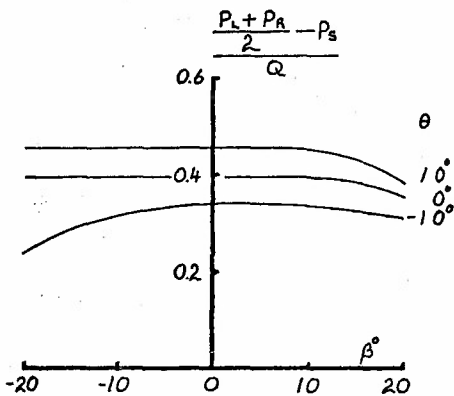
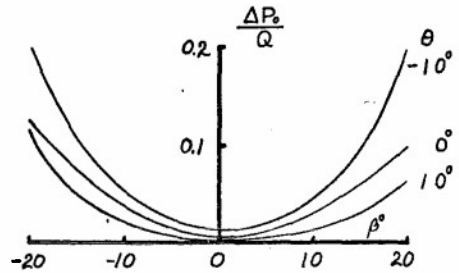
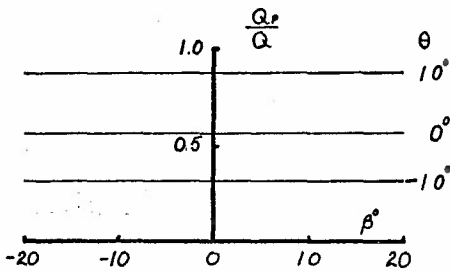
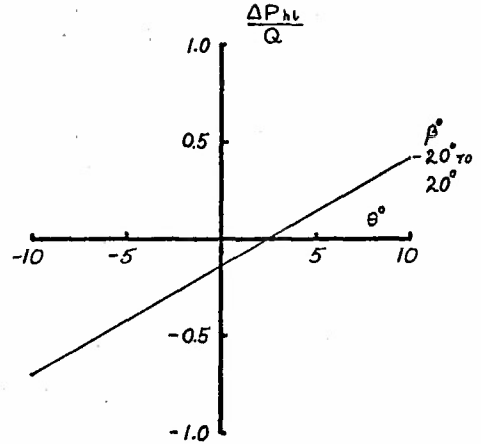
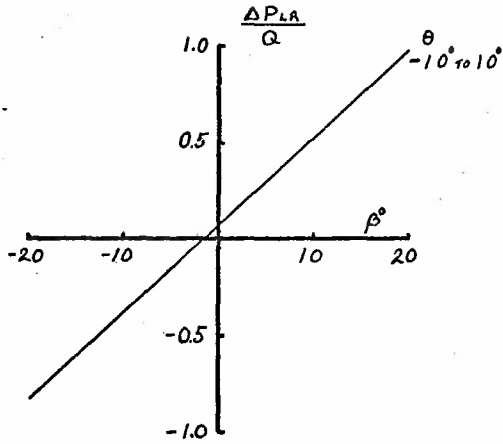


FIG.3 TYPICAL CALIBRATION CURVES FOR A 3-DIMENSIONAL PROBE

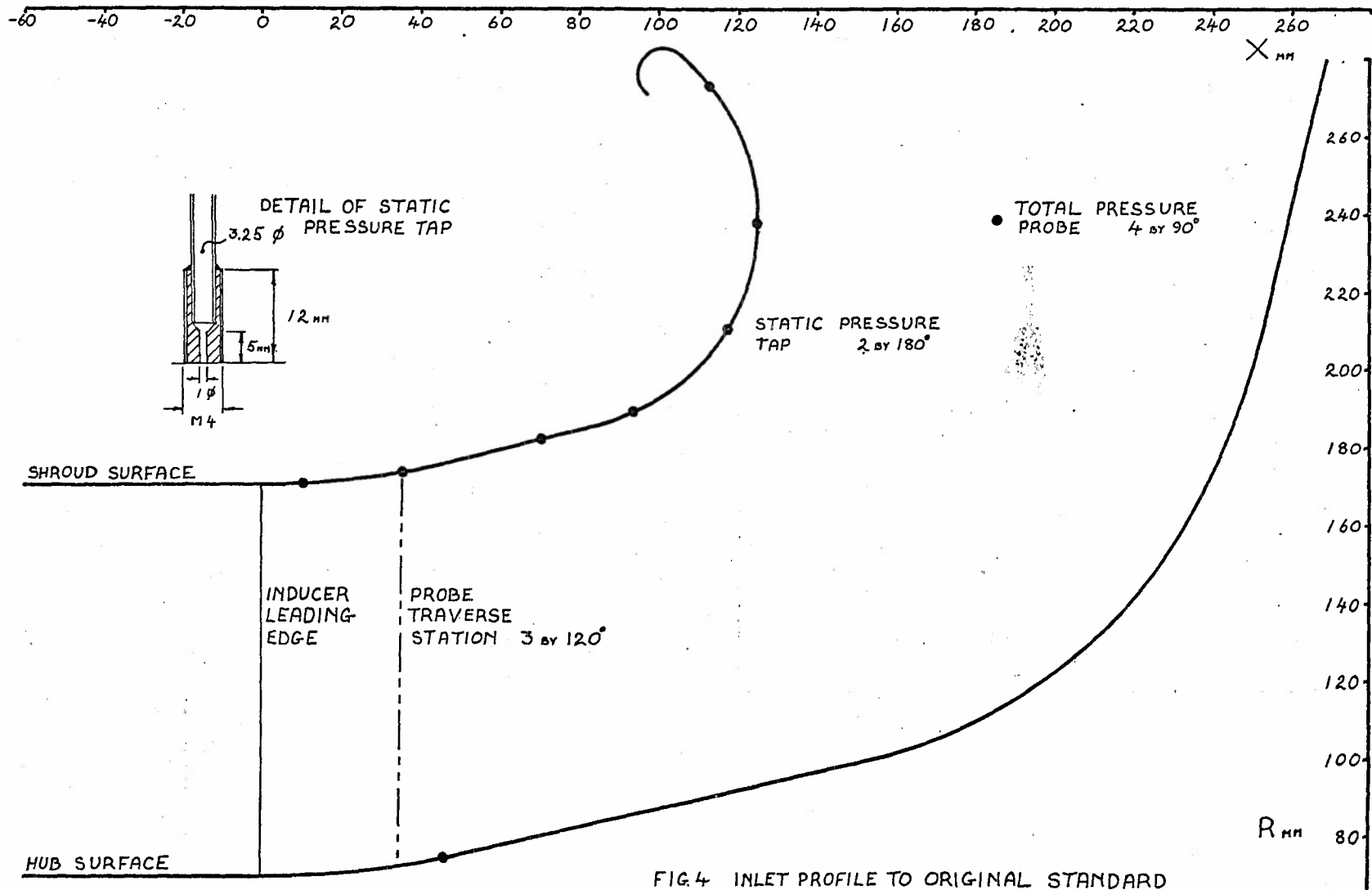


FIG. 4 INLET PROFILE TO ORIGINAL STANDARD

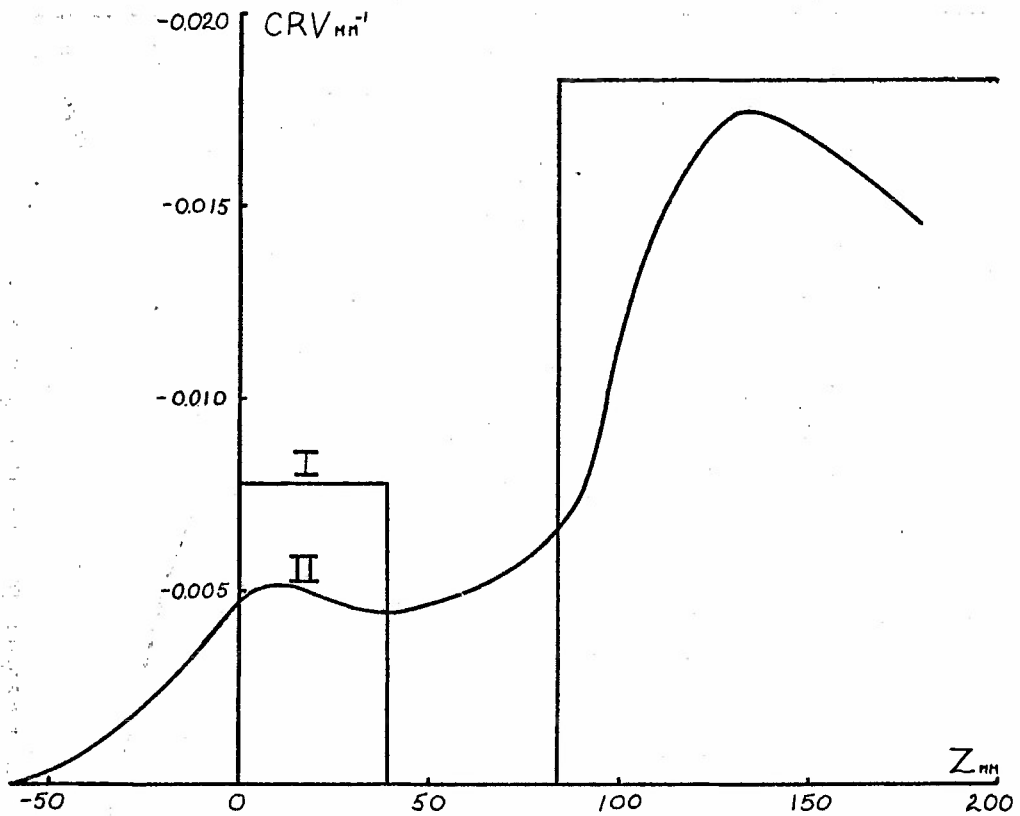


FIG. 5

INLET CURVATURE — SHROUD

- I INLET GEOMETRIC CURVATURE  
 II CURVATURE USED FOR NUMERICAL ANALYSIS

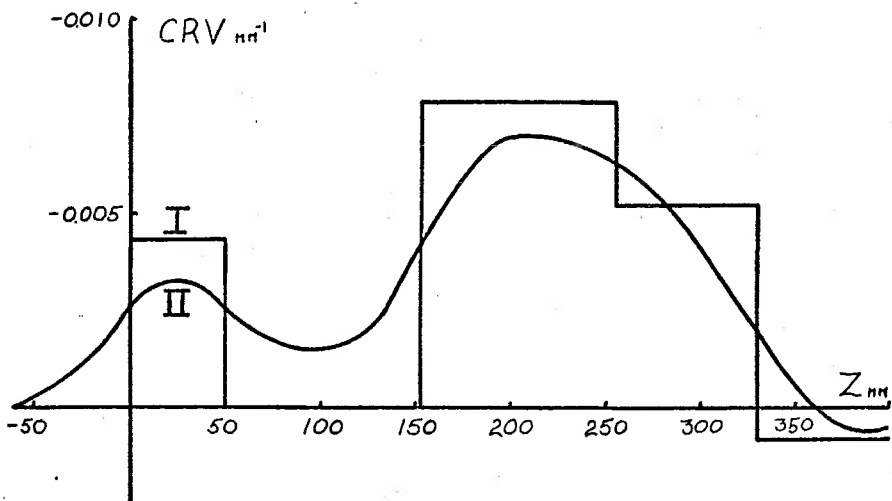


FIG. 6

INLET CURVATURE — HUB

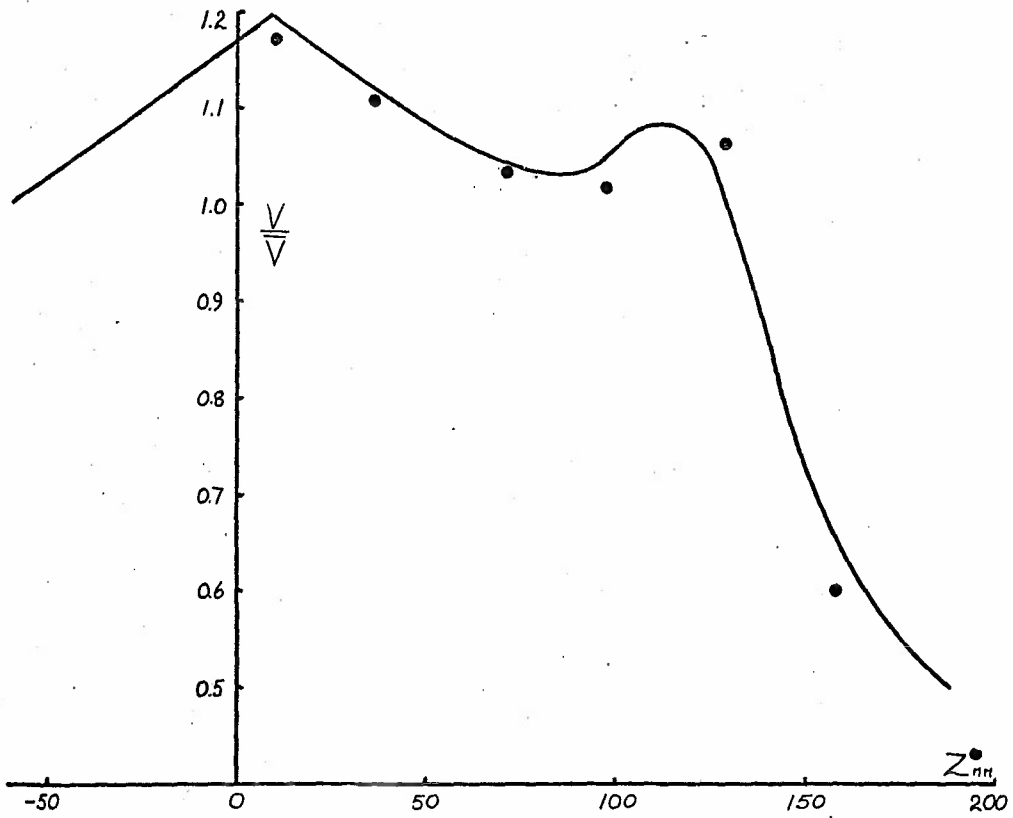


FIG. 7 INLET VELOCITY DISTRIBUTION - SHROUD

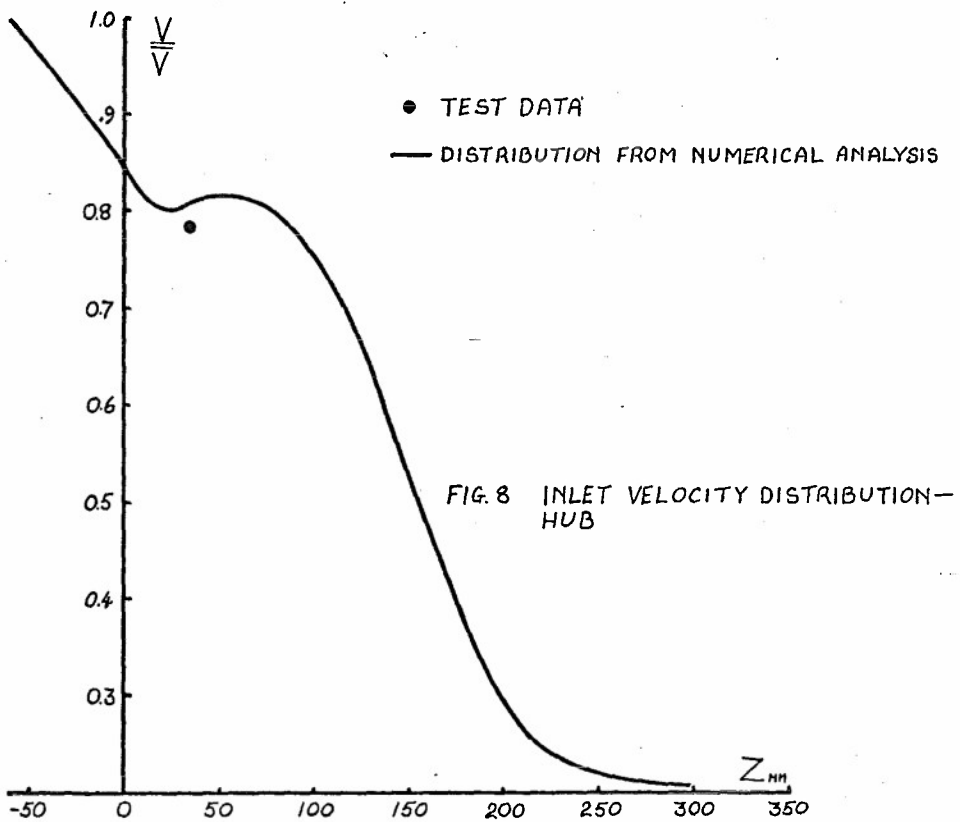


FIG. 8 INLET VELOCITY DISTRIBUTION - HUB

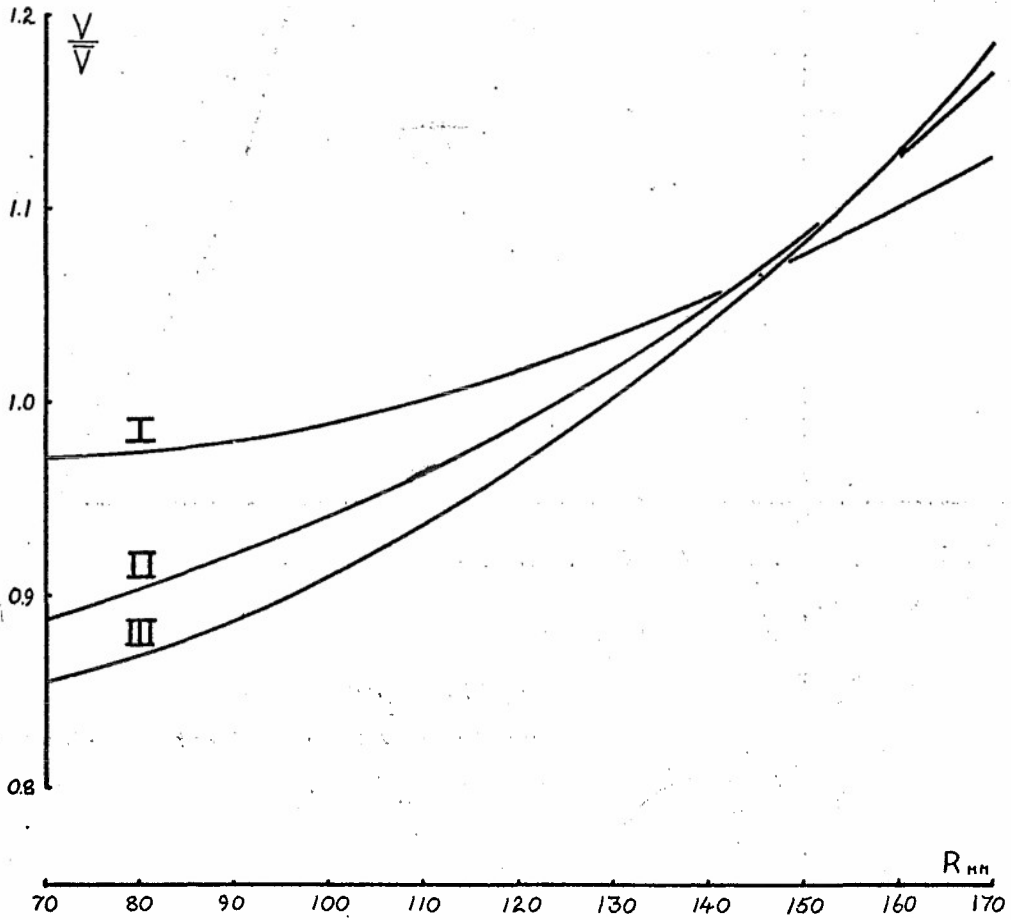


FIG.9 INLET RADIAL VELOCITY DISTRIBUTION AT INDUCER LEADING EDGE

- I DISTRIBUTION FROM TEST DATA FOR 50% DESIGN MASS FLOW
- II DISTRIBUTION FROM TEST DATA FOR DESIGN MASS FLOW
- III DISTRIBUTION FROM NUMERICAL ANALYSIS FOR DESIGN MASS FLOW

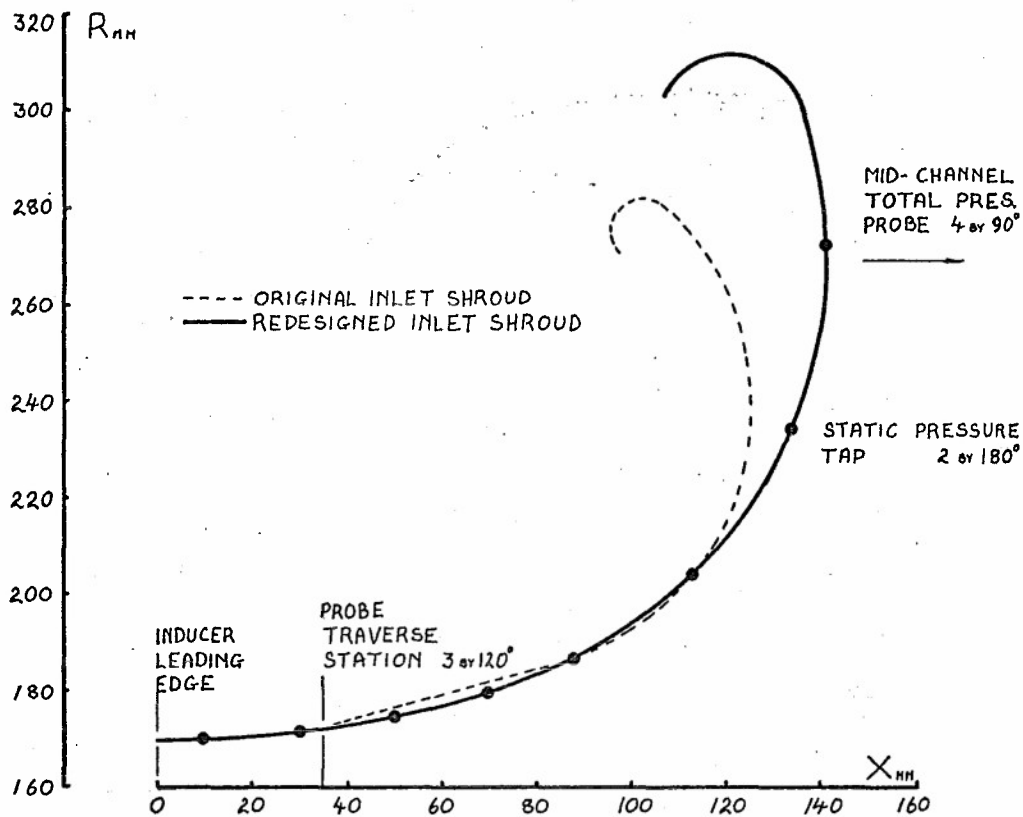


FIG. 10 INLET SHROUD PROFILE COMPARISON

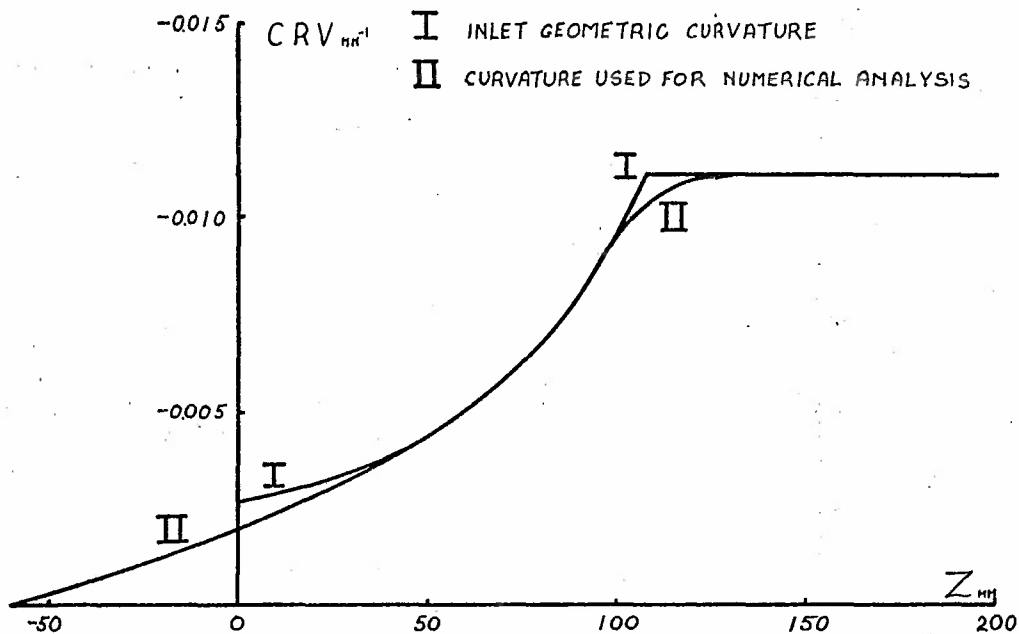


FIG. 11 INLET CURVATURE - SHROUD FOR REDESIGNED INLET

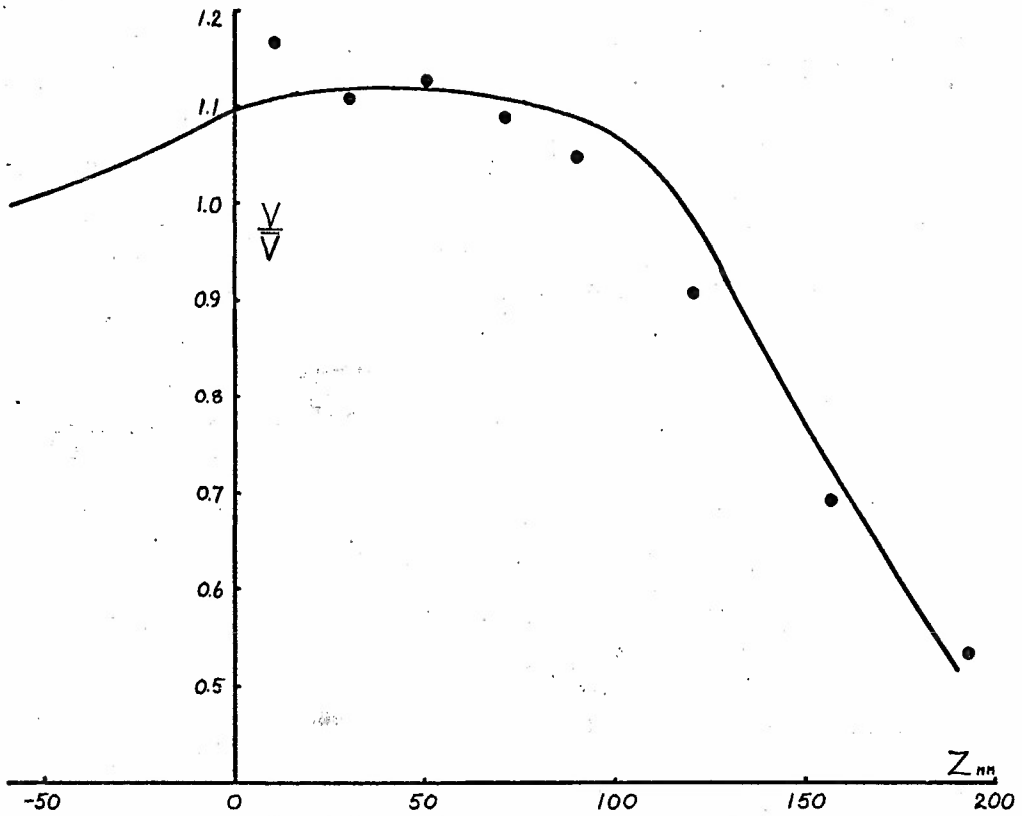


FIG. 12

INLET VELOCITY DISTRIBUTION - SHROUD FOR REDESIGNED INLET

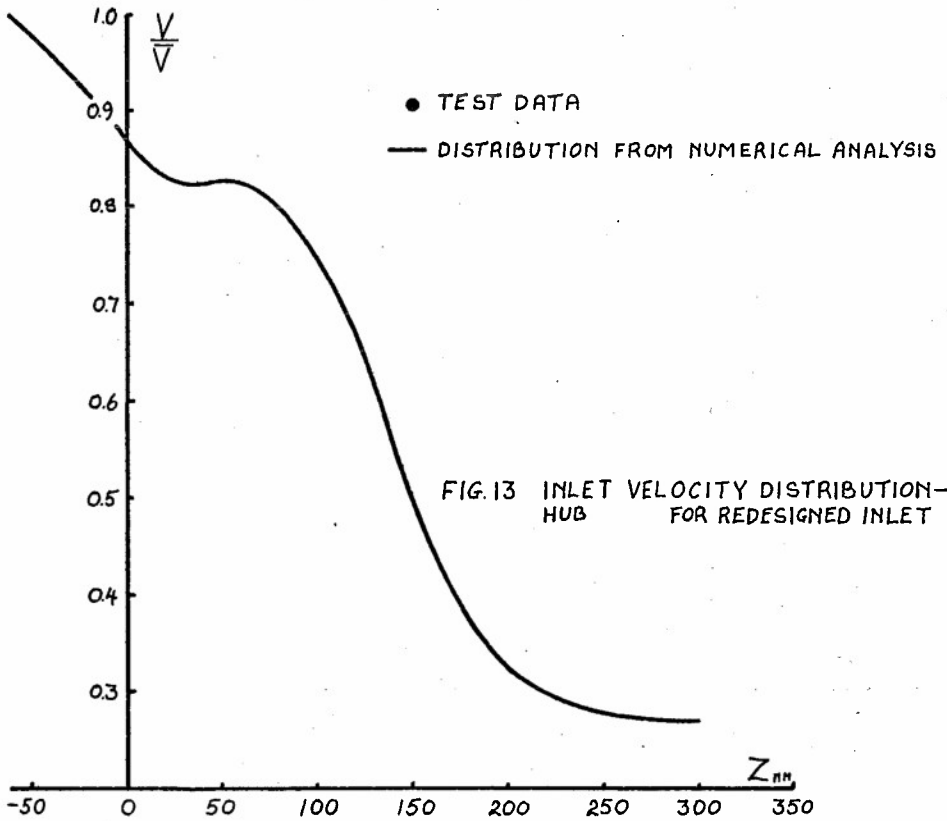


FIG. 13 INLET VELOCITY DISTRIBUTION - HUB FOR REDESIGNED INLET

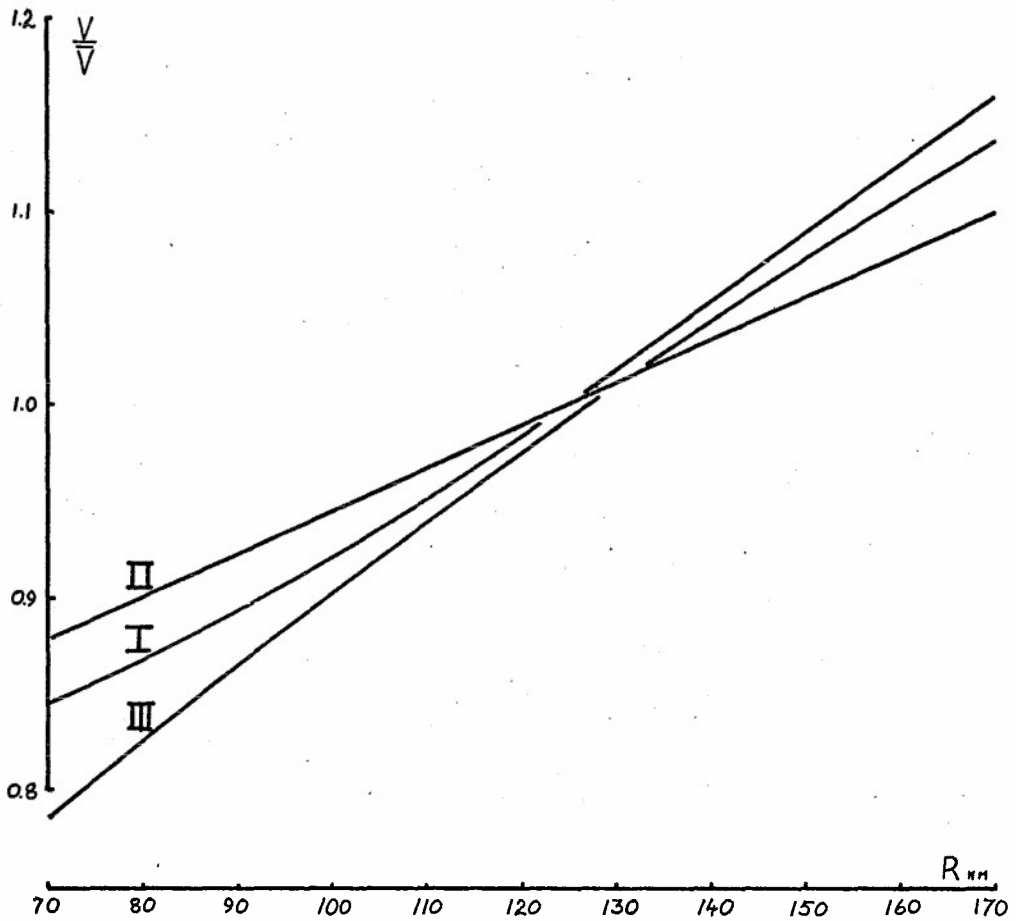


FIG. 14 INLET RADIAL VELOCITY DISTRIBUTION AT INDUCER LEADING EDGE FOR REDESIGNED INLET

- I DISTRIBUTION FROM TEST DATA FOR DESIGN MASS FLOW.
- II DISTRIBUTION FROM NUMERICAL ANALYSIS FOR DESIGN MASS FLOW.
- III DISTRIBUTION FROM NUMERICAL ANALYSIS WITH REVISED BOUNDARY CONDITIONS.

## AMORÇAGE D'UNE PRISE D'AIR HYPERSONIQUE DE REVOLUTION A COMPRESSION SUPERSONIQUE MIXTE

par G. LARUELLE (\*) et J. LEYNAERT (\*\*)  
OFFICE NATIONAL D'ETUDES ET DE RECHERCHES AEROSPATIALES (ONERA)  
92 - CHATILLON - FRANCE

## RESUME -

La définition théorique en fluide parfait des conditions d'amorçage d'une prise d'air à compression supersonique mixte correspond à une configuration telle qu'un choc droit vienne se situer juste à l'entrée du convergent interne.

Les essais montrent toutefois que cette représentation est mise en défaut par un processus d'interaction choc-couche limite, et que les conditions réelles d'amorçage sont moins sévères que celles ainsi calculées.

Un schéma amélioré a donc été utilisé, dans lequel le phénomène d'interaction est représenté de façon très élémentaire.

Son application permet de critiquer les résultats d'essais et de préciser l'influence de certains paramètres sur les conditions d'amorçage.

## SUMMARY -

## STARTING CONDITIONS OF A MIXED COMPRESSION AXISYMMETRIC HYPERSONIC INLET

In a perfect fluid, the starting conditions of a mixed supersonic compression inlet are theoretically to be found in a configuration such that a normal shock occurs right at the entrance of the internal convergent section.

However, tests indicate that this definition is not correct, due to a shock-boundary layer interaction process, and that the actual starting conditions are less strict than the computed ones.

Therefore, an improved diagram including an elementary representation of the interaction phenomenon is used.

By means of this diagram, test data on axisymmetrical inlets at high supersonic speeds can be discussed, and the influences of some parameters can be precised.

## 1 - INTRODUCTION -

Les études d'avant-projet des moteurs d'avions hypersoniques mettent en évidence l'intérêt de fuseaux très courts comportant une chambre de combustion de géométrie fixe et une prise d'air munie d'un dispositif de déformation limité au strict minimum.

Un schéma d'un tel ensemble propulsif est représenté figure 1, à titre d'illustration [1]. La prise d'air, destinée à alimenter une chambre de combustion fonctionnant en supersonique aux nombres de Mach maximaux du vol, comporte une pointe conique et un convergent supersonique interne annulaire (figure 2 a). Le seul mode d'ajustement de cette prise d'air est une translation du corps central qui permet à la fois d'ajuster la géométrie en fonction du nombre de Mach, et d'assurer le réamorçage de l'écoulement supersonique interne en cas de désamorçage accidentel du convergent.

Les limites de déplacement nécessaires du corps central sont par conséquent tributaires des conditions d'amorçage.

Le schéma de principe, en fluide non visqueux, de l'écoulement "désamorcé" est celui d'un choc droit émergeant de la section annulaire d'entrée (aire  $A_0$ ), suivi d'un écoulement subsonique, dont une partie est déviée à l'extérieur de la prise d'air de telle sorte que la section critique du débit capté soit égale à la section géométrique du col du convergent,  $A_c$  (figure 2 b).

Le déplacement du corps central vers l'amont permet de dévier un certain débit autour de la carène grâce au champ de l'écoulement conique : l'écoulement dévié en subsonique entre le choc et le carène est réduit d'autant, et ceci jusqu'à ce que le choc "droit" vienne se situer juste à l'entrée du convergent (figure 2 c). Cette configuration est instable et le choc franchit le convergent vers l'aval en même temps que se rétablit un écoulement supersonique interne, c'est-à-dire que l'amorçage est obtenu.

Les phénomènes d'interaction chocs-couches limites faussent toutefois notablement ce schéma et facilitent l'amorçage en le provoquant à des émergences de corps central nettement plus réduites que celles prévisibles par la représentation précédente.

Il est donc important de préciser si possible le processus réel de l'amorçage. Des schémas d'interaction chocs couches limites en écoulement stationnaire ont déjà été proposés à cet effet par divers auteurs [2], [3].

Dans les essais présents, l'amorçage se produit en écoulement instationnaire (pompage de la prise d'air) et met en jeu des configurations d'écoulement très complexes. Néanmoins, un même schéma stationnaire a été utilisé pour analyser les résultats et critiquer l'influence de certains paramètres. Cette schématisation fait l'objet de l'étude et des remarques qui suivent.

(\*) Ingénieur de recherches, Direction de l'Aérodynamique.

(\*\*) Ingénieur Chef de Subdivision, Direction de l'Aérodynamique.

## 2 - SCHEMATISATION DE L'ÉCOULEMENT -

L'effet prépondérant de la couche limite sur le phénomène d'amorçage résulte d'un décollement qui se forme au pied du choc droit supposé situé juste à l'entrée du convergent, dans la configuration limite d'amorçage (figure 3). Dans cette configuration, l'augmentation d'entropie de la zone non visqueuse est plus faible que s'il y avait un choc droit unique au nombre de Mach local amont  $M_0$ , puisque ce choc est remplacé par un choc oblique suivi d'un choc droit à un nombre de Mach  $M_1$  réduit par la déviation due au décollement.

Cette schématisation peut toutefois paraître illusoire lorsqu'on se réfère à l'écoulement dans un conduit de section constante (figure 4). Dans ce cas, en effet, le passage du supersonique au subsonique s'effectue par un "train de chocs" dont l'élément initial correspond aussi au cas du choc oblique suivi d'un choc droit moins intense qu'un choc unique. Toutefois, ce choc est alors suivi d'une détente supersonique et d'une succession de chocs-détentes de même nature que le premier, de sorte que, finalement, l'écoulement supposé redevient subsonique uniforme plus en aval est identique à celui qu'aurait donné un choc droit unique au nombre de Mach amont. Le calcul de cet écoulement à section constante s'effectue en effet par les mêmes relations de conservation que pour un choc droit, dans l'hypothèse acceptable en première approximation que le frottement aux parois du tube est négligeable, ce qui est d'autant mieux justifié que des décollements s'exercent sur la plus grande partie du conduit.

Cette remarque permet par conséquent de mettre en évidence que, dans le cas de la prise d'air, c'est la convergence du conduit qui permet à l'interaction choc-couche limite d'avoir un effet favorable, en limitant la détente supersonique qui se produit en aval du premier choc droit dans le cas du conduit cylindrique.

Un calcul des conditions d'amorçage sur un schéma simplifié qui négligerait la détente supersonique en aval du choc droit ne peut donc prétendre qu'à servir de référence pour des configurations ayant par ailleurs des taux de convergence comparables.

## 3 - MODE DE CALCUL -

La configuration du décollement (pente et longueur en amont du choc droit) étant supposée connue, l'écoulement amont jusqu'au choc d'entrée est déterminé en utilisant les méthodes de calcul de la couche limite [4] et la méthode des caractéristiques. Cet écoulement étant hétérogène (régions séparées par le choc de déviation, éventuellement par le choc conique amont, et zone de couche limite), le calcul se poursuit par assimilation à un écoulement moyen par tranches en aval du choc, dont l'état uniforme initial est déterminé par l'hypothèse d'un mélange à section constante sans frottement. La section critique de cet écoulement est enfin comparée à la section géométrique du col.

L'angle de décollement est donné par un critère usuel, à savoir que le rapport du nombre de Mach  $M_1$  de l'écoulement dévié au nombre de Mach amont  $M_0$  est égal à 0,78 [5]. Ce critère correspond à une couche limite initiale turbulente. Les calculs de couche limite indiquant que la transition se situe à peu près au niveau du décollement. Bien entendu, on pourrait aussi utiliser des critères plus raffinés prenant en compte l'état effectif de cette couche limite.

La longueur  $L$  de décollement est fonction des différents paramètres qui définissent la configuration et qui conditionnent notamment le recollement plus en aval. Elle n'est pas actuellement calculable. Le but des essais est précisément de donner une loi expérimentale d'évolution de  $L$  en fonction de ces paramètres, afin de permettre une prévision des limites d'amorçage.

D'une façon pratique, la valeur de  $L$  est déduite d'un essai en effectuant, pour la position du corps central qui permet l'amorçage, un calcul des sections critiques de l'écoulement aval pour plusieurs valeurs de  $L$  choisies a priori : la valeur de  $L$  retenue est celle pour laquelle la section critique est égale à la section du col, comme indiqué plus haut.

Il est bon de rappeler que cette longueur de décollement n'est qu'une longueur fictive, caractéristique du phénomène schématisé, et qu'elle ne se prête pas à une observation directe, l'écoulement réel étant plus complexe, et instationnaire, comme il sera précisé plus loin.

## 4 - CONFIGURATIONS ÉTUDIÉES ET RÉSULTATS D'ESSAIS -

Les essais ont porté sur l'étude, à plusieurs nombres de Mach compris entre 4 et 7, de prises d'air de révolution comportant des pointes coniques de  $10^\circ$  et  $15^\circ$  associées soit à une carène profilée de  $5,7^\circ$  de pente interne initiale, soit à une carène cylindrique.

Les formes des prises d'air et les schémas calculés d'écoulement à l'amorçage sont indiqués figures 5 à 8.

Les nombres de Reynolds des essais, rapportés au diamètre de la carène, sont de  $3 \cdot 10^6$ .

On remarquera sur ces figures l'extension du décollement en fonction du nombre de Mach, et aussi les effets minimes d'interaction calculés dans le cas particulier du cône de  $15^\circ$  associé à la carène cylindrique.

Les résultats bruts des essais, exprimés en rapport de contraction à l'amorçage ( $A_C/A_0$ ) en fonction du nombre de Mach à la surface du cône  $M_0$ , sont représentés figure 9.

L'importance de l'effet favorable de l'interaction choc couche limite ressort de l'écart des points expérimentaux à la courbe théorique d'un choc droit en fluide parfait.

Les résultats des calculs des longueurs de décollement sont reportés figure 10 où le rapport  $\frac{L}{h_e}$  est donné en fonction du nombre de Mach  $M_0$ . La valeur de  $\delta_1$  qui caractérise l'importance relative de la couche limite

( $\delta$  est l'épaisseur de déplacement en  $A_e$ , calculée en supposant la couche limite entièrement laminaire) et la valeur du paramètre de convergence initiale du conduit annulaire,  $K = \frac{dA/dx}{A_e}$ , sont indiquées en chaque point.

La comparaison des points relatifs au cône de  $10^\circ$  et au cône de  $15^\circ$ , respectivement associés à la même carène profilée, semble indiquer que l'effet favorable d'une convergence plus accentuée; pour le cône de  $15^\circ$ , est compensé par l'effet défavorable d'une couche limite relativement plus petite.

Toutefois, l'essai du cône de  $15^\circ$  associé à la carène cylindrique met en évidence qu'une convergence initiale trop élevée est défavorable à l'amorçage. L'essai du cône de  $10^\circ$  muni de la carène cylindrique indique également une limitation en ce sens, la valeur élevée du coefficient  $K$  ne permettant pas d'améliorer la limite d'amorçage. Par ailleurs, l'effet favorable de la couche limite doit également être marqué par un maximum.

Ces indications sont évidemment très sommaires, le nombre d'essais étant insuffisant pour isoler l'influence des paramètres désignés, et d'autres facteurs pouvant intervenir, tels que la courbure du profil du corps central (très marquée en position d'amorçage pour la configuration cône  $15^\circ$  + carène cylindrique) ou la forme précise de l'écoulement amont, qui est particulièrement hétérogène dans les cas étudiés.

Les quelques points reportés figure 10 ne peuvent donc servir que de repères pour des essais de configurations voisines de celles étudiées.

## 5 - NATURE INSTATIONNAIRE DE L'ÉCOULEMENT À L'AMORÇAGE -

Si l'on se réfère à une hypothèse d'écoulement quasi-stationnaire en pompage [6], on peut décrire qualitativement les phénomènes observés de la façon suivante :

- supposons (figure 11 a) qu'à un instant donné le choc "droit" se situe à l'entrée du convergent, avec une pression moyenne de l'écoulement subsonique interne comparable à celle que l'on aurait pour cette même configuration en écoulement stationnaire, mais que la section  $A_c$  du col soit inférieure à la section critique de cet écoulement : le blocage à la sortie se traduit par des ondes de compression qui remontent le convergent vers le choc. Selon la loi d'accroissement de l'efficacité du choc en fonction de sa pénétration dans le convergent, ces ondes peuvent soit être absorbées par le choc qui progresse vers l'aval, auquel cas l'amorçage se produit, soit refouler le choc en amont de la prise d'air, interdisant l'amorçage.

Dans ce dernier cas, l'accroissement de pression interne accentue le décollement, le débit interne alimentant la zone décollée qui peut, surtout en régime laminaire remonter jusqu'à la pointe du cône (figure 11 b).

Le débit d'entrée dans le convergent est alors diminué (si non négatif) et se retrouve inférieur au débit de sortie : la pression interne diminue et devient suffisamment basse pour que le décollement se résorbe progressivement. Mais, de ce fait, l'écoulement repasse par une phase de débit d'entrée supérieur au débit de sortie, d'où un nouvel accroissement de pression qui limite la résorption du décollement et, finalement, une situation identique à celle de départ, pour un nouveau cycle de pompage.

L'amorçage s'effectuant en phase de pompage se produit pour une section critique "stationnaire" de l'écoulement subsonique aval (c'est-à-dire calculée comme aux paragraphes précédents) supérieure à  $A_c$ , et, en ce sens, l'écoulement instationnaire est favorable à l'amorçage, mais l'importance de cet effet est difficile à apprécier.

Un film de visualisation stroboscopique [7] montre que le choc pénètre nettement dans le convergent en écoulement instationnaire avant que l'amorçage ne s'effectue, ce qui indique que l'effet de surdébit atténue largement l'effet favorable de progression temporaire du choc dans le convergent et, par conséquent, que le gain sur la limite d'amorçage par le processus instationnaire est sans doute assez limité ; cette remarque tend à justifier l'hypothèse admise pour rechercher une corrélation des résultats selon un schéma stationnaire.

## 6 - CONCLUSION -

L'amorçage d'une prise d'air à compression supersonique mixte est un phénomène complexe, et le nombre de paramètres en jeu ne permet pas de dégager des lois générales à partir d'essais en nombre très limités.

Néanmoins, on a tenté d'apporter quelques éléments à une discussion plus approfondie du problème ; les résultats rassemblés peuvent contribuer à une première estimation des limites d'amorçage en hypersonique de prises d'air d'un type voisin de celles étudiées.

## REFERENCES

- [1] LEYNAERT J. Prises d'air pour le vol à Mach 7  
O.N.E.R.A. - T.P. n° 658 (1968)  
L'Aéronautique et l'Astronautique n° 16
- [2] MITCHELL G.A. An experimental investigation of the restart area ratio of a Mach 3 axisymmetric mixed compression inlet.  
CUBBLISON R.W. N.A.S.A. TM X 1547 (1968).
- [3] HENRY J.R. Boundary layer and starting problems on a short axisymmetric scramjet inlet.  
ANDREWS E.H. Jr. N.A.S.A. SF 216 - Compressible boundary layer (1968).  
PINCKNEY S.Z.  
McCLINTON C.R.
- [4] MICHEL R. Couches-limites, frottement et transfert de chaleur.  
Cours de l'E.N.S.A.E. Toulouse-Lespinet - 31 - France.
- [5] CARRIERE P. Aérodynamique interne des réacteurs - Deuxième partie - Tuyères et jets.  
Cours de l'E.N.S.A.E. - Toulouse-Lespinet - 31 - France.
- [6] LEYNAERT J. Pompage dans les entrées d'air supersoniques.  
L'Aéronautique et l'Astronautique n° 22 (1970)
- [7] Film ONERA 696 Amorçage d'une prise d'air hypersonique par translation du corps central, à Mach 6.

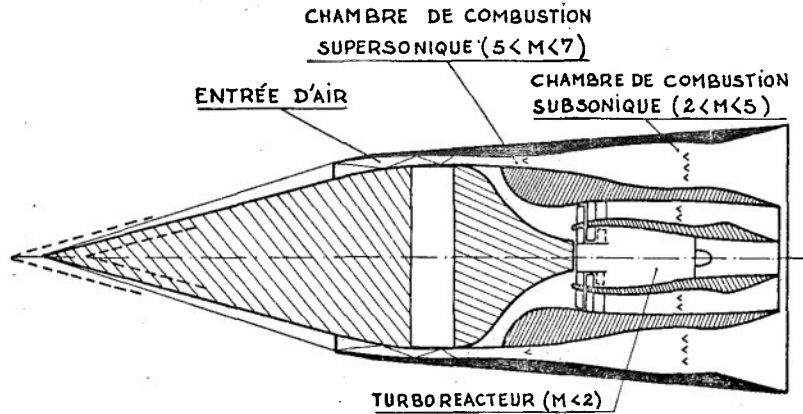


FIG.1 ENTRÉE D'AIR HYPERSONIQUE  
AIR-INTAKE FOR SCRAMJET OR TURBO-SCRAMJET

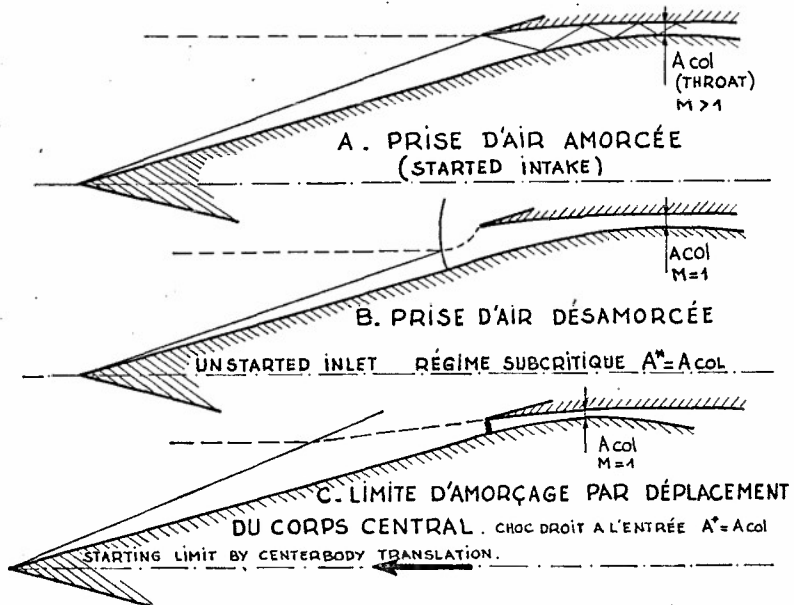


FIG.2 PROCESSUS THÉORIQUE D'AMORÇAGE (NON VISQUEUX)

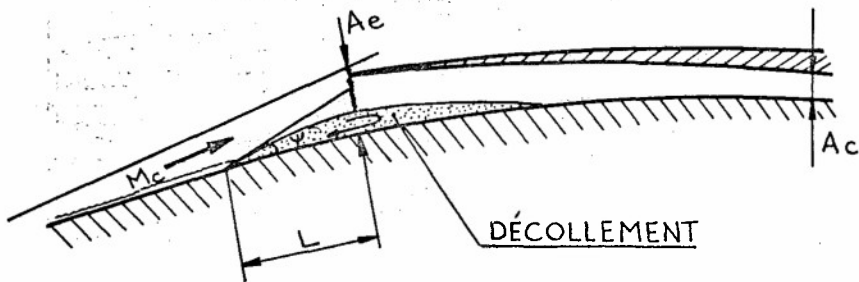


FIG.3 SCHÉMA THÉORIQUE D'AMORÇAGE STATIONNAIRE  
THEORETICAL VISCOUS STARTING SCHEME

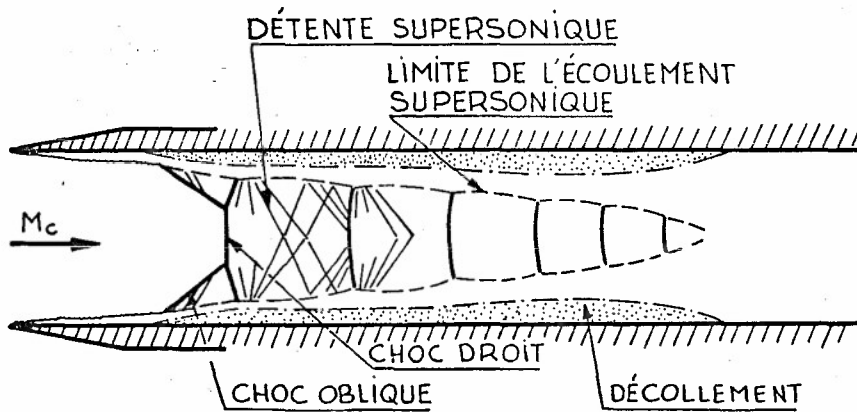


FIG.4 . INTERACTION CHOC- COUCHE LIMITE  
DANS UN CONDUIT  
SHOCK-BOUNDARY LAYER INTERACTION IN A CYLINDRICAL DUCT

LIMITES D'AMORÇAGE  
STARTING LIMITS

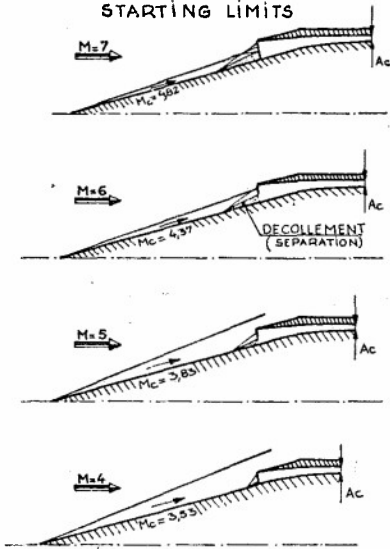


FIG. 5 CÔNE DE 15° - CARÈNE INCURVÉE

LIMITES D'AMORÇAGE  
STARTING LIMITS

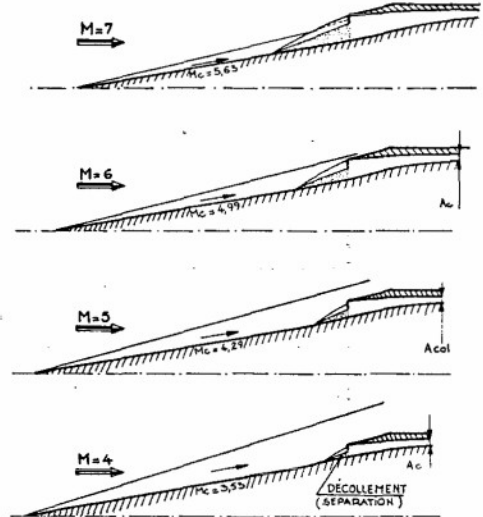


FIG. 6 - CÔNE DE 10° - CARÈNE INCURVÉE

LIMITES D'AMORÇAGE  
STARTING LIMITS

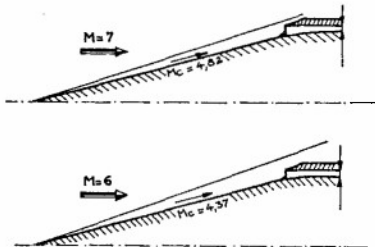


FIG. 7 - CÔNE DE 15° - CARÈNE CYLINDRIQUE



FIG. 8 - CÔNE DE 10° - CARÈNE CYLINDRIQUE

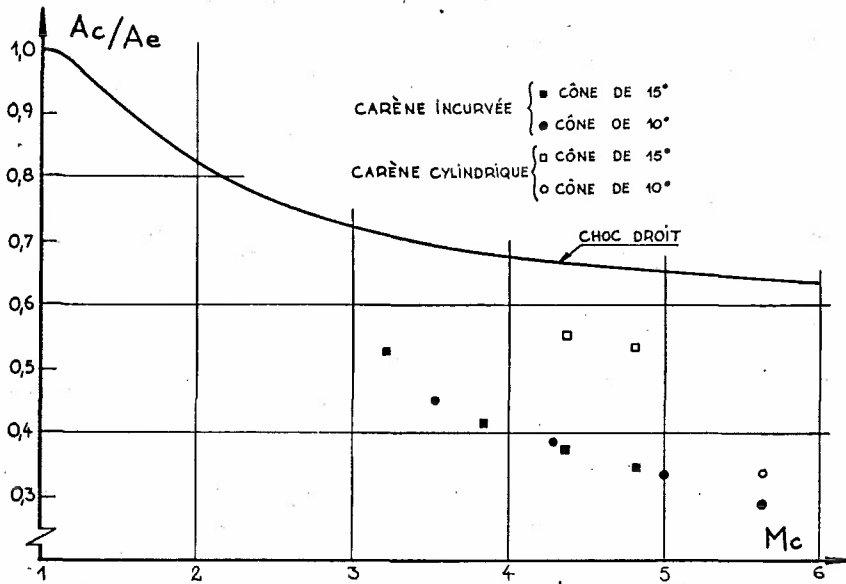


FIG. 9- RAPPORT DE CONTRACTION D'AMORÇAGE  
STARTING CONTRACTION RATIO

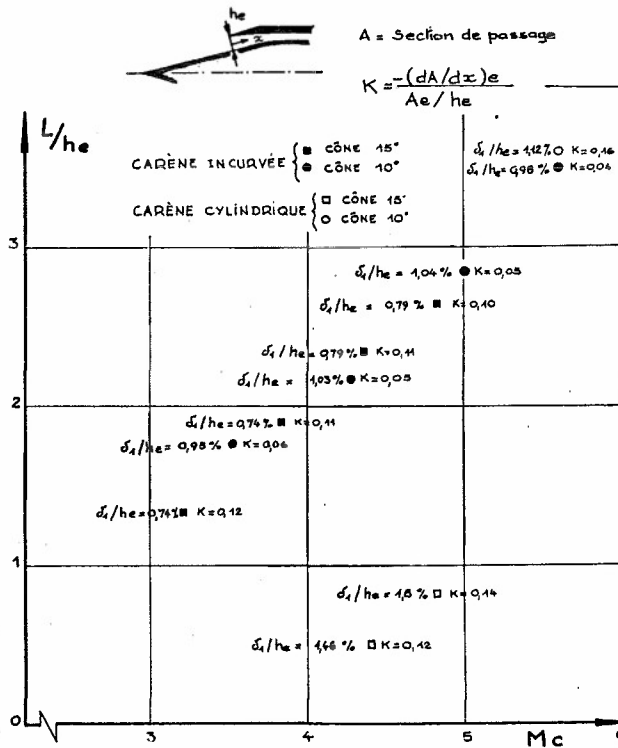


FIG. 10- LONGUEUR DE DÉCOLLEMENT A L'AMORÇAGE  
SEPARATION LENGTH AT STARTING

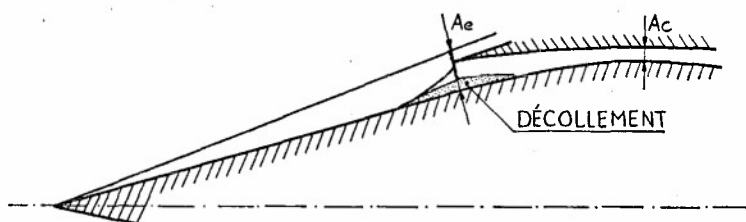


FIG. 11a. PASSAGE AU RÉGIME CRITIQUE  $Q_e > Q_c$

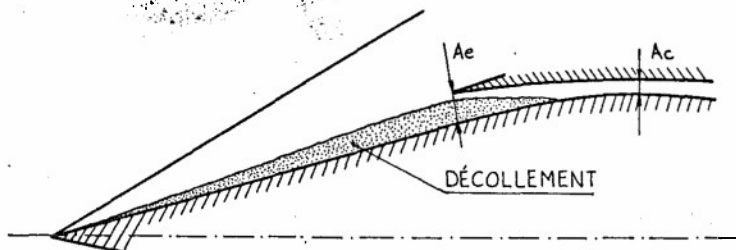


FIG. 11b. PHASE DE DÉCOLLEMENT MAXIMAL  $Q_e < Q_c$

FIG. 11. PHASES DE POMPAGE  
BUZZ FLOW PICTURES

ÉTUDE THÉORIQUE ET EXPÉRIMENTALE DE LA CO-EXISTENCE DE DEUX FLUX  
DANS UN CANAL DE SECTION CONSTANTE

par Jacques PAULON

OFFICE NATIONAL D'ÉTUDES ET DE RECHERCHES AÉROSPATIALES (O.N.E.R.A.)  
92 - CHATILLON - France

R É S U M É

Un montage plan et un montage de révolution de caractéristiques très voisines ont été réalisés pour étudier la coexistence dans un canal de section constante d'un jet supersonique à l'intérieur d'un jet subsonique.

L'analyse expérimentale de l'écoulement effectuée à partir de relevés de pression sur les parois et au sein du fluide a permis de caractériser les limites réelles de deux flux ainsi que le domaine de transition les séparant. Dans le cas du montage plan, la visualisation stroboscopique de l'écoulement confirme les mesures.

L'analyse théorique basée sur l'application de la méthode des caractéristiques confirme les mesures pariétales. Toutefois, la section d'épanouissement maximal du flux interne, indiquée par cette méthode, diffère de la section sonique de l'écoulement externe, ce qui peut conduire à des prévisions erronées dans le cas d'un éjecteur à contour évolutif.

S U M M A R Y

A two-dimensional, and an asymmetrical set-up of very similar characteristics, were built in order to study the coexistence, in a constant section duct, of a supersonic jet inside a subsonic jet.

The experimental analysis of the flow, made from pressure readings on the walls and inside the fluid, led to characterizing the actual limits of the two flows, and also the transition domain between them. In the two-dimensional case, the schlieren visualization of the flow confirms the measurements.

The theoretical analysis, based on the method of characteristics, confirms the parietal readings. However the maximum flaring section, given by this method, differs from the sonic section of the external flow, which may lead to faulty predictions in the case of a contoured ejector.

1. INTRODUCTION.

Peu sensibles à l'hétérogénéité des écoulements primaire et secondaire, les théories unidimensionnelles des mélangeurs à section constante où coexistent un flux primaire supersonique et un flux secondaire subsonique dans la section de confluence, fournissent avec grande précision les performances globales de ces montages. C'est ce qui explique le succès des théories par quasi-tranches planes des éjecteurs supersoniques [1] [2] qui, soumises au critère de l'expérience depuis bientôt 20 ans se sont avérées utiles et précises pour des montages de faibles dimensions utilisés dans les laboratoires aussi bien que pour les grands éjecteurs industriels.

Ces théories ne permettent cependant pas de prévoir le développement axial de l'écoulement et de situer avec précision la position de la section d'épanouissement maximal du flux primaire, condition nécessaire pour réaliser une optimisation en poids de ces installations. C'est pourquoi diverses études ont été entreprises en France [3] [4] et à l'étranger [5] pour parfaire le schéma unidimensionnel simplifié, de façon à y inclure une évolution longitudinale correcte des deux flux.

L'hypothèse essentielle retenue dans ces calculs dont l'importance est spécialement marquée pour les éjecteurs de turboréacteurs où le coefficient d'entraînement est faible (débit secondaire de l'ordre de 5 % au plus du débit primaire) est qu'il y a coexistence dans le canal d'un flux primaire supersonique se développant suivant la théorie des caractéristiques et d'un flux secondaire subsonique s'écoulant par quasi-tranches planes.

Ce schéma, s'il est accessible au calcul numérique et permet de prendre en compte lorsque le débit secondaire se réduit à une couche limite épaisse les interactions des ondes de choc avec cet écoulement pariétal, devient peu réaliste aux débits secondaires plus élevés par suite du développement notable de la zone de mélange entre les deux flux et de l'importance que prennent alors les forces de viscosité dans le domaine de transition correspondant.

Afin de mieux comprendre la structure fine d'un tel écoulement essentiellement hétérogène car comportant trois domaines de flux sensiblement parallèles, une étude expérimentale a été entreprise à une échelle suffisamment grande pour permettre une exploration détaillée du flux secondaire dans sa totalité. Seule une fraction du flux primaire est accessible aux sondages, compte tenu de la fragilité des sondes utilisées, profondément engagées dans le montage et soumises à des efforts aérodynamiques qui deviennent dangereux pour leur tenue, dès lors que la nécessité de ne pas perturber les écoulements primaire et secondaire conduit à limiter considérablement leur dimension.

## 2. MONTAGES EXPERIMENTAUX.

La source d'air comprimé disponible à l'Établissement O.N.E.R.A. de PALAISEAU a les caractéristiques suivantes :

- pression génératrice  $P_i$  : 14,5 bars
- température génératrice :  $370^\circ\text{K} < T_i < 390^\circ\text{K}$
- débit masse  $Q$  : 10 kg/sec.

Les montages expérimentaux ont été réalisés de façon à restituer sensiblement les mêmes conditions expérimentales. Les grandeurs caractéristiques de ces deux installations sont portées sur le Tableau I.

Le montage (A) est bidimensionnel et permet de ce fait une exploration systématique du champ des pressions statiques qui sont d'autre part mesurées par sondages au sein de l'écoulement, ainsi d'ailleurs que les pressions d'arrêt des deux flux.

### - TABLEAU I -

#### CHARACTERISTIQUES DES DEUX MONTAGES EXPERIMENTAUX

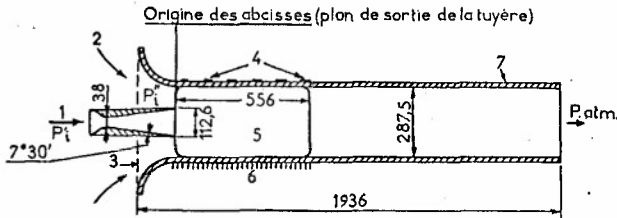
A - MONTAGE BIDIMENSIONNEL :	B - MONTAGE DE REVOLUTION :
<u>Mélangeur :</u>	<u>Mélangeur :</u>
Hauteur : 287,5 mm	Diamètre : 171 mm
Largeur : 80 mm	Longueur : 1490 mm
Longueur : 1560 mm	Section constante : 23.000 mm <sup>2</sup>
Section constante : 23.000 mm <sup>2</sup>	
<u>Tuyère primaire :</u>	<u>Tuyère primaire :</u>
Hauteur du col : 38 mm	Diamètre du col : 67 mm
Section du col : 3040 mm <sup>2</sup>	Section du col : 3530 mm <sup>2</sup>
Hauteur dans le plan de sortie : 112,6 mm	Diamètre dans le plan de sortie : 107 mm
Section de sortie : 8900 mm <sup>2</sup>	Section de sortie : 9000 mm <sup>2</sup>
Largeur : 80 mm	Angle d'ouverture du divergent : $12^\circ 70'$
Angle d'ouverture du divergent : $15^\circ$	Nombre de Mach théorique : $M'_{th} = 2,464$
Nombre de Mach théorique : $M'_{th} = 2,624$	
<u>Instrumentation de mesure :</u>	<u>Instrumentation de mesure :</u>
- 11 rangées de 23 prises de pression sur paroi latérale,	- 19 prises de pression statique sur une génératrice,
- 28 prises de pression sur paroi inférieure,	- 11 prises de pression statique réparties à $90^\circ$ dans 4 plans de mesure,
- 6 bossages pour introduction de sondes	- 7 bossages pour introduction de sondes sur une génératrice voisine de celle où se trouvent les 19 statiques,
- 2 hublots de visualisation.	- 11 bossages réparties à $90^\circ$ dans 4 plans de mesure.

Le montage (B) de révolution ne permet pas une étude aussi fine de la répartition des pressions par suite de l'hétérogénéité azimutale, difficile à éviter, et sur laquelle nous reviendrons plus loin. L'intérêt de l'expérimentation décrite ci-dessous tient à la possibilité d'évaluation des avantages et inconvénients de chacun de ces dispositifs fonctionnant tous deux en régime permanent.

### 2.1. Montage bidimensionnel (A).

La Figure 1 montre le schéma de principe de cette installation, tandis que la Figure 2 en montre une vue photographique qui permet de se rendre compte des dimensions et des principes constructifs.

Les buts recherchés étant l'analyse fine de l'écoulement et la visualisation de celui-ci, les parois latérales sont interchangeables.



- |                                    |              |                                 |
|------------------------------------|--------------|---------------------------------|
| 1 - Arrivée d'air primaire         | 4 - Bossages | 6 - Prises de pression de paroi |
| 2 - Arrivée d'air secondaire, patm | 5 - Hublot   | 7 - Mélangeur                   |
| 3 - Vannage                        |              |                                 |

Fig. 1 - Schéma de l'installation A (cotes en mm)

- |   |   |
|---|---|
| 1 - Plaque perforée créant une perte de charge pour l'écoulement secondaire | 4 - Injection du flux primaire                    |
| 2 - Porte sonde télécommandé  | 5 - Evacuation à l'air ambiant                    |
| 3 - Hublot de visualisation   | 6 - Plaque inférieure munie de prises de pression |
|   | 7 - Plaque latérale munie de prises de pression   |

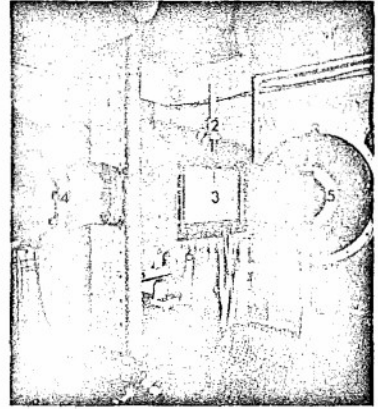


Fig. 2 - Vue de l'installation d'essais A

Une paroi équipée de 253 prises de pression est destinée à fournir le champ de pression statique, champ complété par le relevé des pressions mesurées sur la paroi inférieure dans son plan de symétrie.

Un porte-sonde télécommandé qui peut être installé sur 6 bossages régulièrement répartis sur la paroi supérieure a permis de relever les pressions d'arrêt et statique locales sur une grande partie de la hauteur de la veine. Une connaissance plus complète de l'écoulement jusqu'à l'axe de la veine n'a pu être effectuée par suite des difficultés de tenue mécanique des sondes, suffisamment petites pour ne pas perturber l'écoulement.

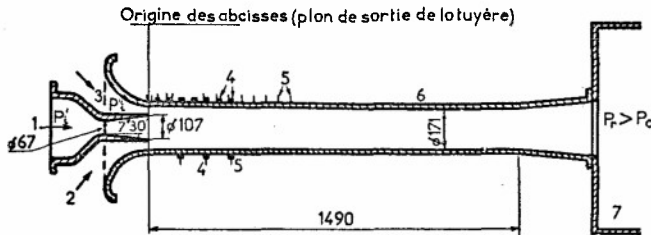
Comme on le verra sur les diagrammes présentant les résultats expérimentaux, la mesure de la pression statique n'a pu être effectuée que sur une fraction de la demi-hauteur de la veine. D'autre part, la répartition pariétale de pression a mis en évidence une très légère dissymétrie de l'écoulement due à une petite imperfection du montage. Les relevés ont systématiquement porté sur l'analyse d'une moitié du montage expérimental.

Dans une seconde phase, les parois latérales de cette installation ont été remplacées par deux panneaux comportant des hublots de visualisation de grandes dimensions. Néanmoins le montage stroboscopique utilisé a nécessité d'effectuer en deux fois la prise de vue de l'écoulement. La répétabilité et la bonne stabilité de l'écoulement ont permis une superposition correcte des vues stroboscopiques obtenues, dont l'analyse sera présentée ci-après.

## 2.2. Montage de révolution (B).

Le second montage expérimental décrit ici comporte une tuyère primaire et un mélangeur à symétrie de révolution ainsi que le montrent les Figures 3 et 4. Il présente l'avantage indiscutable d'être plus voisin des installations industrielles usuelles, bien que dans certaines applications comme les jets plate, on soit amené à rechercher un montage bidimensionnel.

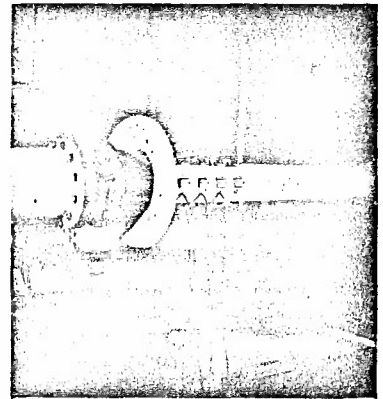
Le mélangeur utilisé a été réalisé en tôle roulée et soudée et ne présente donc pas la perfection de fabrication qui aurait été souhaitable pour l'analyse fine de l'écoulement telle qu'elle avait été envisagée au début des essais (\*).



- |                              |  |
|------------------------------|--|
| 1 - Arrivée d'air primaire   | 5 - Prises de pression de paroi                                    |
| 2 - Arrivée d'air secondaire | 6 - Mélangeur  |
| 3 - Vannage                  | 7 - Chambre de tranquillisation de la soufflerie de grille d'aubes |
| 4 - Bossages                 |  |

Fig. 3 - Schéma de l'installation B (cotes en mm)

Fig. 4 - Vue de l'installation d'essais B



(\*) Le montage expérimental est en réalité un augmentateur de débit réalisé pour une soufflerie de grille d'aubes supersonique [6] [7] et utilisé en second lieu pour les essais décrits ici.

La procédure expérimentale est donc plus simple sur ce montage et se limite à l'exploration azimutale de l'écoulement grâce à des prises de pression pariétales réparties dans quatre plans de mesures, à un relevé longitudinal de la pression sur une génératrice du montage et à l'étude de la répartition radiale des pressions totale et statique dans sept plans.

### 3. PERFORMANCES DU MONTAGE BIDIMENSIONNEL (A).

#### 3.1. Choix du point de fonctionnement.

Une vérification préalable a été effectuée afin de comparer aux prévisions théoriques les performances globales de l'éjecteur qui refoule à la pression atmosphérique  $P_a$ . Le régime supersonique s'établit pour une pression primaire  $P'_i/P_a = 10$  bars; aussi pour les essais ci-dessous, le point de fonctionnement retenu correspond aux conditions :

$$\frac{P'_i}{P_a} = 14,5 \text{ bars} \quad \frac{P''_i}{P_a} = 0,75 \text{ bar} \quad \mu = 0,20$$

$P''_i$  étant la pression génératrice secondaire et  $\mu$  le rapport du débit masse secondaire au débit masse primaire. (La valeur de  $P'_i/P_a$  de transition entre le régime supersonique et le régime mixte fournie par le calcul [2] est de 5,5. La différence importante provient de ce que nous sommes en montage plan où les pertes sont plus importantes qu'en montage de révolution).

Le coefficient de débit est suffisamment élevé pour que le flux secondaire ne se comporte pas comme une épaisse couche limite pariétale et il se trouve à des conditions expérimentales suffisamment distantes du fonctionnement en régime mixte pour échapper aux instabilités. Ce point se trouve effectivement sur la caractéristique théorique débit-pression du mélangeur [2].

#### 3.2. Relevés de pression sur la paroi inférieure.

L'analyse de la répartition de la pression  $P''$  mesurée sur la paroi inférieure, rapportée à la pression génératrice  $P''_i$  du flux secondaire, donne une idée exacte de l'évolution de ce dernier (Figure 5).

Entrant dans le mélangeur à un nombre de Mach modéré ( $M'' = 0,54$  dans la section de confluence des deux jets prise comme origine des abscisses), le flux secondaire se détend de façon continue jusqu'à atteindre les conditions critiques à une distance sensiblement égale à  $X_* = 450$  mm.

On remarquera (Figure 6) que cette distance critique est sensiblement celle qui correspond au point de rencontre d'une onde de Mach issue d'une lèvre de la tuyère primaire et de l'ordonnée de la section unidimensionnelle sonique de l'écoulement secondaire.

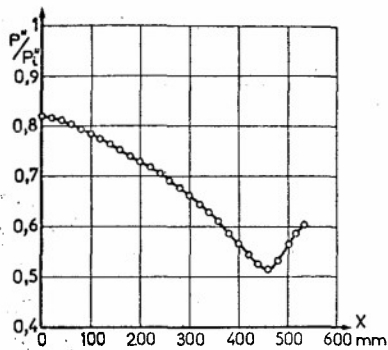


Fig. 5 - Evolution longitudinale de la pression statique à la paroi inférieure

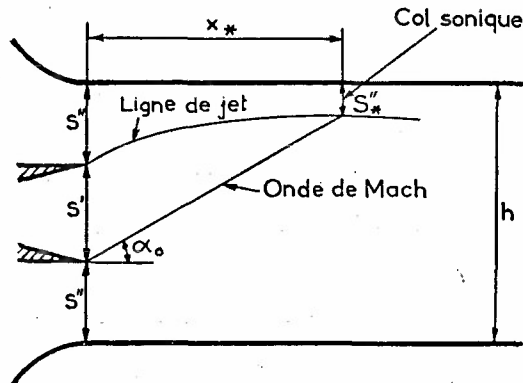


Fig. 6 - Schémo de colcul de la distance critique

En effet, la tuyère primaire ayant un nombre de Mach réel  $M' = 2,566$ , cette distance s'écrit avec les grandeurs portées sur la figure :

$$X_* = \frac{h - S'' \left[ 1 + 1,73 M'' \left( \frac{S}{S + M''^2} \right)^3 \right]}{\operatorname{tg} \alpha_0}$$

avec :  $\alpha_0 = \arcsin 1/M' = 7,50$

D'où  $X_* = 470$  mm.

Cette propriété s'est trouvée vérifiée sur un certain nombre de montages expérimentés par ailleurs au Laboratoire.

En aval de cette section critique, la pression pariétale croît, ce qui indique un désamorçage progressif de l'écoulement qui finit par atteindre la pression ambiante.

3.3. Relevée de pression sur la paroi latérale.

Une analyse plus fine du champ de l'écoulement s'obtient par l'étude des relevés de pression  $P$  sur la paroi latérale munie de 11 rangées de 23 prises. La répartition complexe des valeurs de la pression mesurée sur cette paroi (Figure 7b) s'explique aisément suivant le schéma porté en haut de la Figure 7a.

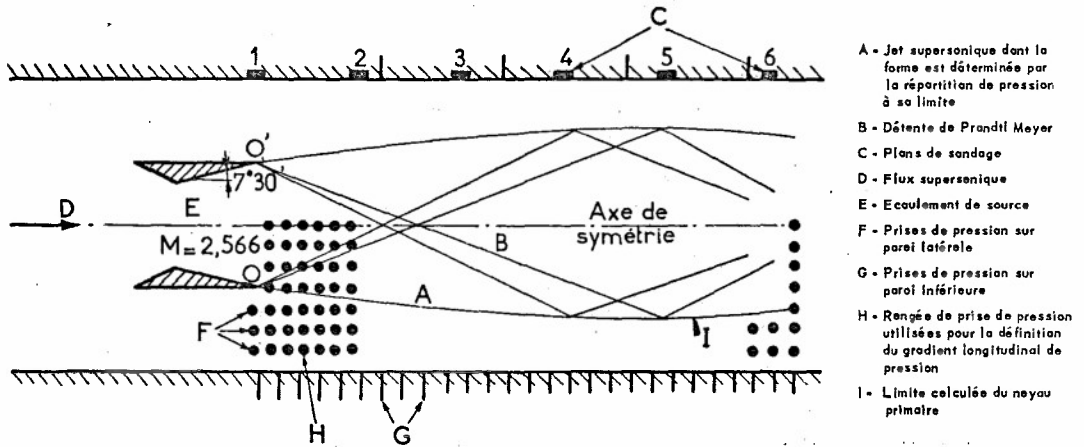


Fig. 7a - Schéma aérodynamique explicatif des hypothèses de calcul

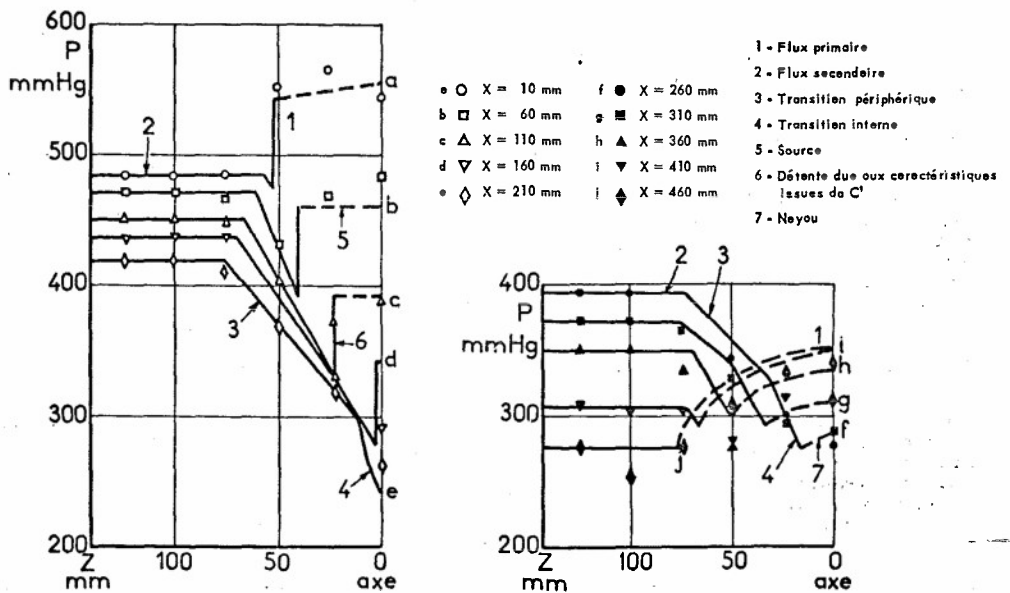


Fig. 7b - Répartitions de pression mesurées sur une paroi latérale - Comparaison avec les valeurs calculées

- le fluide primaire, supposé parfait, est assimilé à un écoulement de source plane, d'angle d'ouverture  $15^\circ$  et de nombre de Mach  $M' = 2,566$  au point de confluence des deux flux (valeur déduite des relevés de pression);
- ce fluide débouche dans un milieu où règne un gradient longitudinal de pression défini par les relevés pariétaux, mais en fait ce sont les indications de la première rangée de prises latérales qui ont été utilisées. Elles ne diffèrent guère des relevés sur la paroi inférieure du montage. La complexité des répartitions de pression relevées à la paroi du montage est due à l'existence simultanée de plusieurs gradients de pression;
- sur l'axe du montage l'écoulement de source issu de la tuyère primaire s'accélère fortement mais le profil des vitesses dans des plans normaux à l'axe est quasi-constant (coupe (a) à (d));
- à la périphérie du noyau central, l'accélération du flux externe induit un gradient longitudinal négatif de la pression, plus faible que celui correspondant à la source;
- la transition au point de confluence  $O$  des deux écoulements se fait par une détente de Prandtl-Meyer, puisqu'initialement la pression dans le noyau est supérieure à celle du flux externe (coupe (a)), et les caractéristiques correspondantes transportent une détente, de moins en moins accentuée (coupes (a) à (d));
- ces caractéristiques atteignant l'axe du montage au voisinage de la coupe (e) à laquelle correspond la pression minimale dans le noyau central;
- dans les coupes suivantes (f) à (i) le rôle des caractéristiques issues du point de confluence  $O$  des deux flux symétriques de  $O$  par rapport à l'axe du montage devient prépondérant et si, à la périphérie du jet primaire, la pression continue à diminuer, au centre elle augmente progressivement;

La confrontation calcul-expérience est très satisfaisante dans tout le domaine proche du plan d'injection du flux primaire. Elle devient plus imprécise près de la section d'épanouissement maximal du noyau supersonique, où la transition visqueuse entre les deux flux devient importante.

#### 3.4. Mesures au sein du fluide : exploration d'un plan normal à l'axe du montage.

Le domaine de transition séparant les flux primaire et secondaire ne peut être caractérisé par les relevés pariétaux de pression, dont le nombre est insuffisant pour une analyse détaillée du phénomène. L'exploration des deux veines au moyen d'une sonde traversant le montage dans son plan de symétrie suivant une normale à l'axe permet la description fine du passage du flux primaire au flux secondaire. Comme nous l'avons signalé plus haut cette exploration n'a pu être effectuée que sur une fraction de la hauteur de la veine.

La Figure 8 représente les relevés de pression statique  $P$  et de pression totale  $P_t$  dans les six plans de mesure équipés à cet effet. Pour obtenir la pression totale dans la partie supersonique de la veine (domaine interne de la zone de transition et portion du flux primaire où l'exploration de la veine a pu être effectuée) la pression d'arrêt ( $P_t$ ) choc mesurée par la sonde a été corrigée pour tenir compte du nombre de Mach local en amont de l'onde de choc droite qui s'établit devant la sonde. On remarquera essentiellement que la pression statique est sensiblement constante dans le flux secondaire aussi bien que dans la zone de transition, dont les limites externe et interne sont définies respectivement comme point où la pression d'arrêt  $P_t$  commence à croître et point où elle atteint sa valeur maximale. En revanche la pression statique varie rapidement dans tout le domaine du flux primaire non perturbé par la transition (Figure 7). Nous avons comparé sur la Figure 8 les pressions statiques mesurées à la paroi et celles données par la sonde d'exploration transversale. La concordance des deux mesures est correcte dans le flux secondaire non perturbé, elle l'est moins dans la zone de transition où il existe un fort gradient de pression d'arrêt risquant de fausser les mesures de pression statique fournies par la sonde.

#### 3.5. Mesures au sein du fluide : exploration transversale de la veine.

Comme dans tout montage plan, le mélangeur étudié présente l'inconvénient d'être tributaire du développement des couches limites sur les parois latérales du montage. Afin de mieux connaître l'importance des perturbations correspondantes une exploration transversale en pression totale a été effectuée à une distance  $X = 460$  mm du plan de confluence des deux jets, c'est-à-dire sensiblement au niveau de la section sonique du flux secondaire. La Figure 9 présente les résultats correspondants : dans le flux secondaire (Figure 9a) l'épaisseur de la couche limite est de l'ordre de 4 mm, ce qui correspond bien aux prévisions de calcul [8]; la surpression que l'on observe au voisinage de la paroi est vraisemblablement due à des échanges énergétiques entre les deux flux, échanges qui seraient favorisés par la couche limite; la valeur sensiblement constante mesurée dans le noyau sain du flux secondaire recoupe correctement les valeurs obtenues dans l'exploration de ce dernier (Figure 8).

Dans le flux primaire (Figure 9b) seule la pression pitot, directement donnée par la sonde, est présentée. La couche limite pariétale semble plus importante (de l'ordre de 9 mm), mais il faudrait pouvoir tenir compte ici des déperditions d'énergie qui ont conduit au maximum de pression mesuré dans le flux secondaire, et qui ont pour effet dans le flux primaire d'élargir le domaine voisin de la paroi, où l'écoulement n'est pas uniforme.

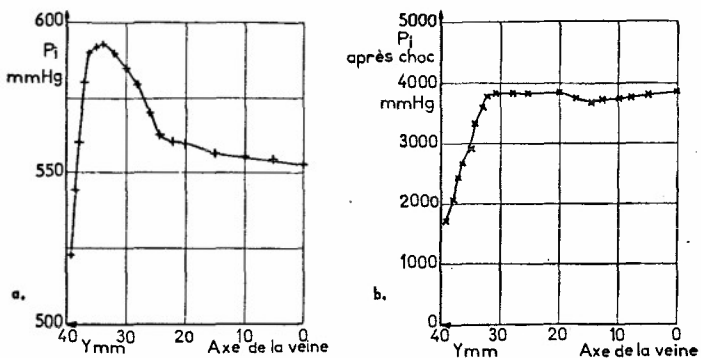
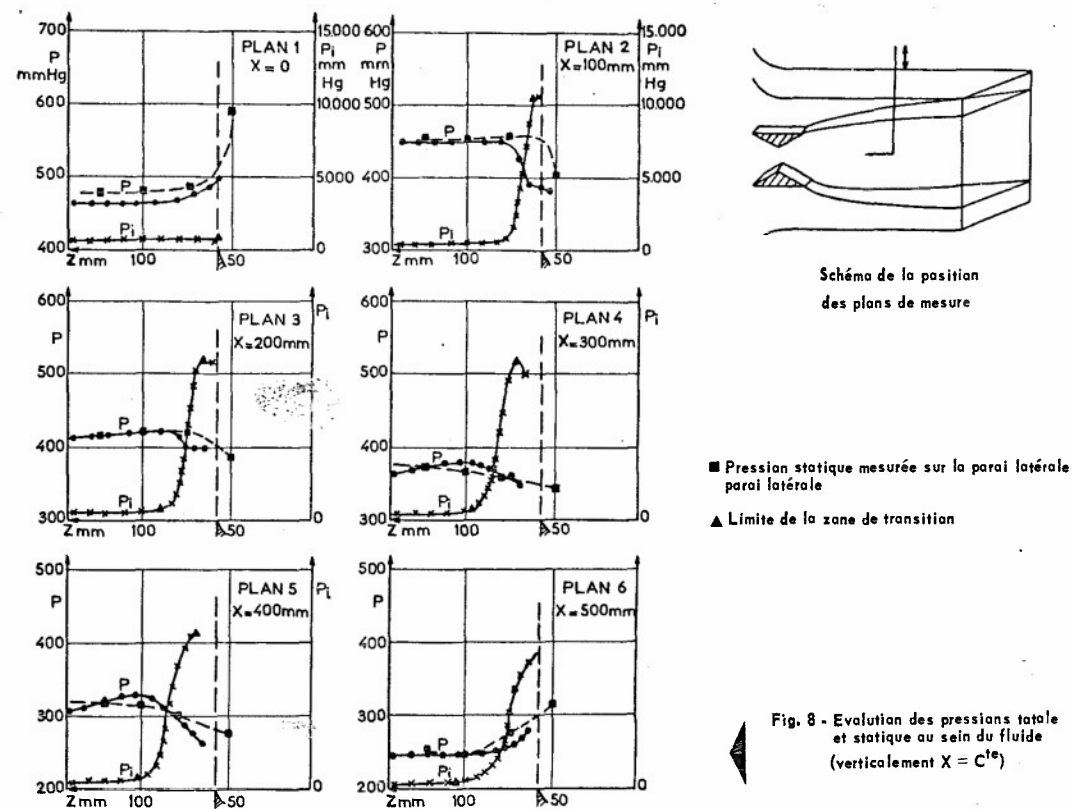


Fig. 9 - Evolution de la pression totale au sein du fluide

a. - Flux secondaire, X = 460 mm    b. - Flux primaire, X = 460 mm

### 3.6. Visualisation de la ligne de jet et de la zone de mélange.

Le jet supersonique primaire et la zone de transition à densité fortement variable peuvent être mis en évidence par striescopic de l'écoulement. Des hublots (en pyrex pour résister à la température de 390°K du flux primaire) ont été utilisés, mais deux clichés successifs correspondant à deux positions différentes du banc de striescopic ont été nécessaires pour permettre de voir tout le domaine intéressant. La légère déformation des bords de l'image due à la nécessité de travailler en lumière divergente dans le grand champ visualisé ne permet pas une superposition correcte des deux clichés.

On notera tout d'abord sur la Figure 10 qu'au point de fonctionnement étudié le jet primaire reste amorcé bien au delà du domaine exploré dans cette étude, c'est-à-dire au delà de la section sonique du flux secondaire. Sur cette figure ont été également portées les limites de la zone de transition déterminées au moyen des relevés de pression (Figure 8), ainsi que les caractéristiques limites ayant servi au calcul de l'écoulement dans le flux primaire.

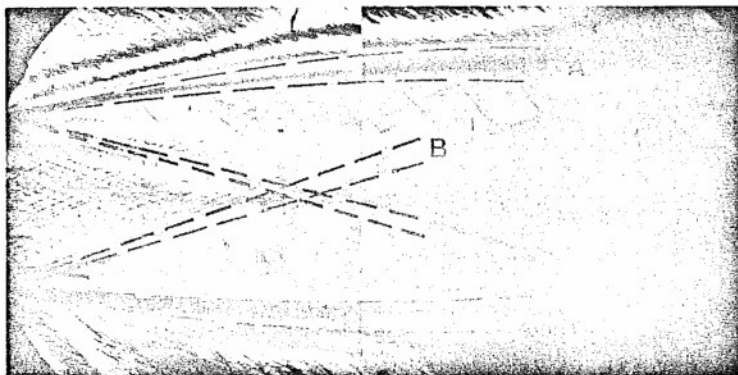


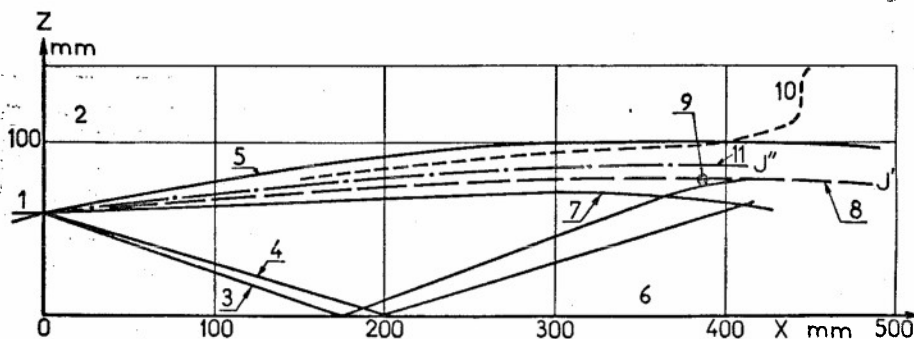
Fig. 10 - Visualisation de l'écoulement

A - Limites zones de mélange B - Faisceau de détente

La Figure 11 résume les résultats acquis et compare sur le même diagramme les limites de la zone de transition visqueuse entre les deux jets et la ligne de jet primaire  $J'$  calculée dans l'hypothèse d'un fluide parfait. Cette dernière se trouve bien au milieu des deux premières.

Sur la même figure a été portée la ligne sonique de l'écoulement déduite des relevés de pression (Figure 1). On remarquera cette fois que le schéma unidimensionnel ne semble plus valable : la ligne sonique, pratiquement confondue avec la ligne externe de la zone de transition visqueuse, n'est normale à l'écoulement qu'au voisinage de la section d'épanouissement maximal du flux primaire.

Supposant alors que la vitesse est peu inclinée sur l'axe du montage, on en déduit aisément l'ordonnée de la limite  $J''$  du flux secondaire, définie comme ligne de courant d'un écoulement ayant le même débit que l'écoulement secondaire entrant dans le mélangeur. On remarquera sur la Figure 8, où cette ligne limite  $J''$  a été portée, qu'elle diffère peu de la limite théorique du jet primaire.



- |                              |   |   |
|------------------------------|---|---|
| 1 - Tuyère                   | 5 - Limite externe de la zone de transition | 9 - Epanouissement maximal du flux primaire |
| 2 - Flux secondaire          | 6 - Flux primaire                           | 10 - Ligne sonique                          |
| 3 - Première caractéristique | 7 - Limite interne de la zone de transition | 11 - Limite du flux secondaire              |
| 4 - Dernière caractéristique | 8 - Limite théorique du jet primaire        |   |

Fig. 11 - Ligne de jet et zone de transition

#### 4. ANALYSE DES PERFORMANCES DU MONTAGE DE REVOLUTION (B).

##### 4.1. Choix du point de fonctionnement.

Géométriquement très voisin du montage plan par ses lois de section, le montage (B) a d'abord été testé globalement pour comparer ses performances aux prévisions théoriques. Cet éjecteur servant à augmenter le débit d'une soufflerie de grille d'aubes, la pression de refoulement n'est plus l'atmosphère mais une pression  $P_r$  de l'ordre de 2,45 bars.

De ce fait, le rapport  $P_c/P_r$  n'est guère supérieur à la valeur de transition théorique entre les régimes supersonique et mixte, d'où certaines fluctuations et instabilité.

Pour les essais décrits ci-dessous, le point de fonctionnement imposé correspond à :

$$\frac{P'_c}{P_r} = 5,5$$

$$\frac{P'_c}{P_r} = 0,37$$

$$\mu = 0,24$$

#### 4.2. Etude de l'homogénéité azimutale du flux secondaire.

Dans le montage bidimensionnel analysé au n° 3, le flux secondaire se compose de deux petits jets quasi-indépendants dont la seule condition de compatibilité tient à la même valeur de la pression génératrice. Grâce à une réalisation symétrique du montage, aux imperfections mécaniques près, les deux flux secondaires présentaient des configurations d'écoulement très voisines.

Le problème se pose tout différemment dans le cas du montage de révolution où il n'existe qu'un flux secondaire unique, injecté par un orifice annulaire et entourant le jet primaire. Une difficulté provient alors de ce que pour éviter toute interaction parasite entre les éléments du montage et les flux étudiés, il n'a pas été mis de bras supports à l'intérieur de la veine, ce qui rend délicat le centrage du jet primaire par rapport au jet secondaire. Il s'agit d'un centrage tridimensionnel, car il faut s'assurer que la tuyère primaire et le mélangeur cylindrique sont concentriques et que leurs axes sont confondus. Si cette difficulté peut être à peu près surmontée, il en existe une autre, très importante et incontrôlable. Le mélangeur, à sa sortie, est solidaire du caisson de tranquillisation de la soufflerie de grille dont l'éjecteur fait partie. Les températures génératrice primaire et secondaire sont respectivement de 390°K et 290°K tandis que celle mesurée dans la chambre de tranquillisation est de l'ordre de 360°K. Il en résulte des dilatations différentes de chaque partie du montage et des déplacements qui modifient le centrage d'origine.

Pour obtenir des résultats corrects, il eut fallu un montage débouchant à l'ambiante et, de plus, que le mélangeur soit solidaire de la tuyère primaire.

A titre d'exemple, la Figure 12 présente la répartition azimutale de la pression de paroi relevée dans quatre plans de mesure et la Figure 13 compare les relevés radiaux de pression totale  $P_t$  (Il s'agit d'une pression Pitot donc d'une vraie pression totale ou d'une pression totale après choc selon le type d'écoulement rencontré par la sonde) mesurée sur 4 rayons à une distance de 1,2 diamètres du plan de confluence (section de mesure 5). On remarquera que si dans la meilleure configuration géométrique qui a pu être réalisée, la répartition azimutale de pression semble assez uniforme à une grande distance de la section de confluence, d'inévitables distorsions de l'écoulement apparaissent qui rendent difficile une analyse fine de l'écoulement.

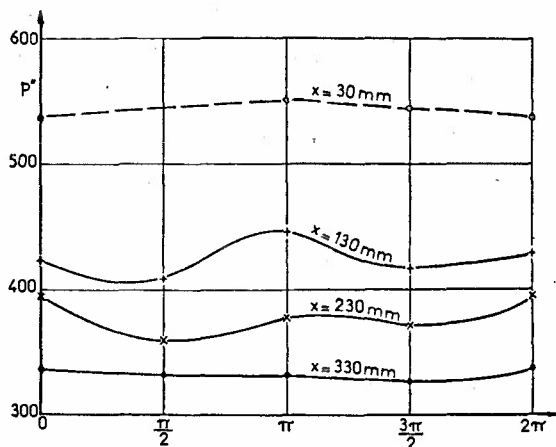


Fig. 12 - Répartition azimutale de la pression de paroi dans différents plans de mesure

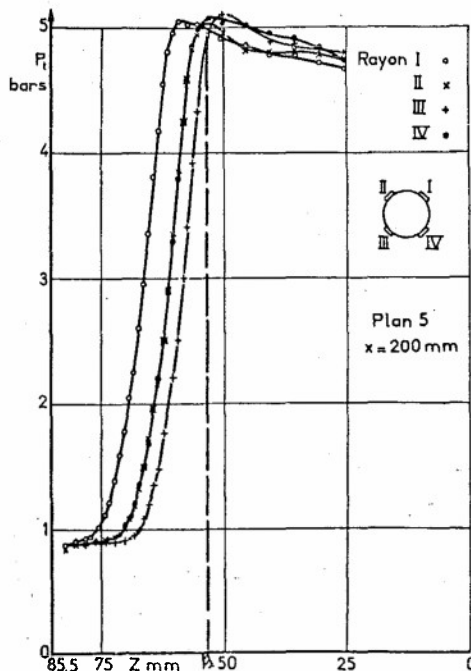
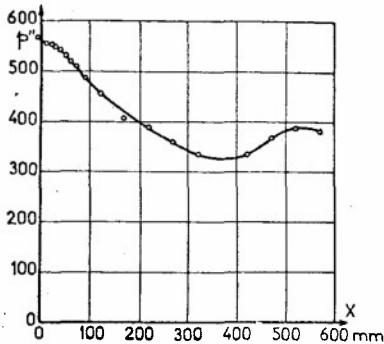


Fig. 13 - Evolution radiale de la pression totale P

#### 4.3. Relevés de pression sur une génératrice du montage.

Bien que les deux écoulements ne soient pas parfaitement concentriques, nous avons relevé l'évolution axiale de la pression de paroi  $P''$  mesurée sur une génératrice du mélangeur.

La répartition présentée sur la Figure 14 donne une idée de l'évolution du flux secondaire et nous verrons par la suite quelle exploitation on peut tirer de ces mesures. Notons simplement que l'allure de cette courbe est très semblable à celle obtenue sur le montage plan.



◀ Fig. 14 - Evolution axiale de la pression sur une génératrice

#### 4.4. Mesures au sein du fluide. Exploration radiale de la voine.

Dans un montage à symétrie de révolution, seule l'exploration radiale de l'écoulement permet de connaître l'évolution de la pression statique (Figure 15). On remarquera ici encore une valeur sensiblement constante de cette pression dans chaque plan de mesure au voisinage de la paroi du mélangeur et une variation plus complexe dès que l'on pénètre dans la zone de mélange.

La pression mesurée à la paroi recoupe bien les indications de la sonde et, d'autre part, les quelques mesures de pression statique au sein du flux primaire et en dehors de la zone de mélange vérifient ou tendent à recouper celles obtenues par le calcul de l'écoulement primaire assimilé à un écoulement de source. Cet écoulement n'est pas influencé par le mauvais centrage du primaire mais par contre celui compris entre la caractéristique de départ issu d'une extrémité de la tuyère et la ligne du jet  $\gamma$  est sensible. Aussi, comme cela était prévisible, l'application de la méthode de calcul du champ de cet écoulement n'a pas donné de résultats probants.

L'étude de la pression totale  $P_t$  (Il s'agit de la pression d'arrêt corrigée lorsque la sonde se trouve dans un écoulement supersonique) portée sur la même figure met en évidence le développement rapide de la zone de mélange et l'on notera, compte tenu du défaut d'alignement des deux flux, que dans le plan VI proche de l'épanouissement maximal du flux primaire, l'écoulement sain secondaire a pratiquement disparu.

De façon générale, sauf dans le plan V, la pression totale mesurée dans le flux primaire, puis corrigée pour tenir compte du choc devant la sonde, recoupe bien la pression totale à l'infini amont. Ce qui montre que les mesures sont correctes dans les zones saines des écoulements.

#### 4.5. Ligne de jet.

Le mauvais centrage des deux flux ne permettant pas un calcul correct de la ligne de jet de l'écoulement primaire, il n'a pas été possible de comparer, comme dans le cas plan, la ligne sonique déduite des mesures avec la position d'épanouissement maximum du jet primaire.

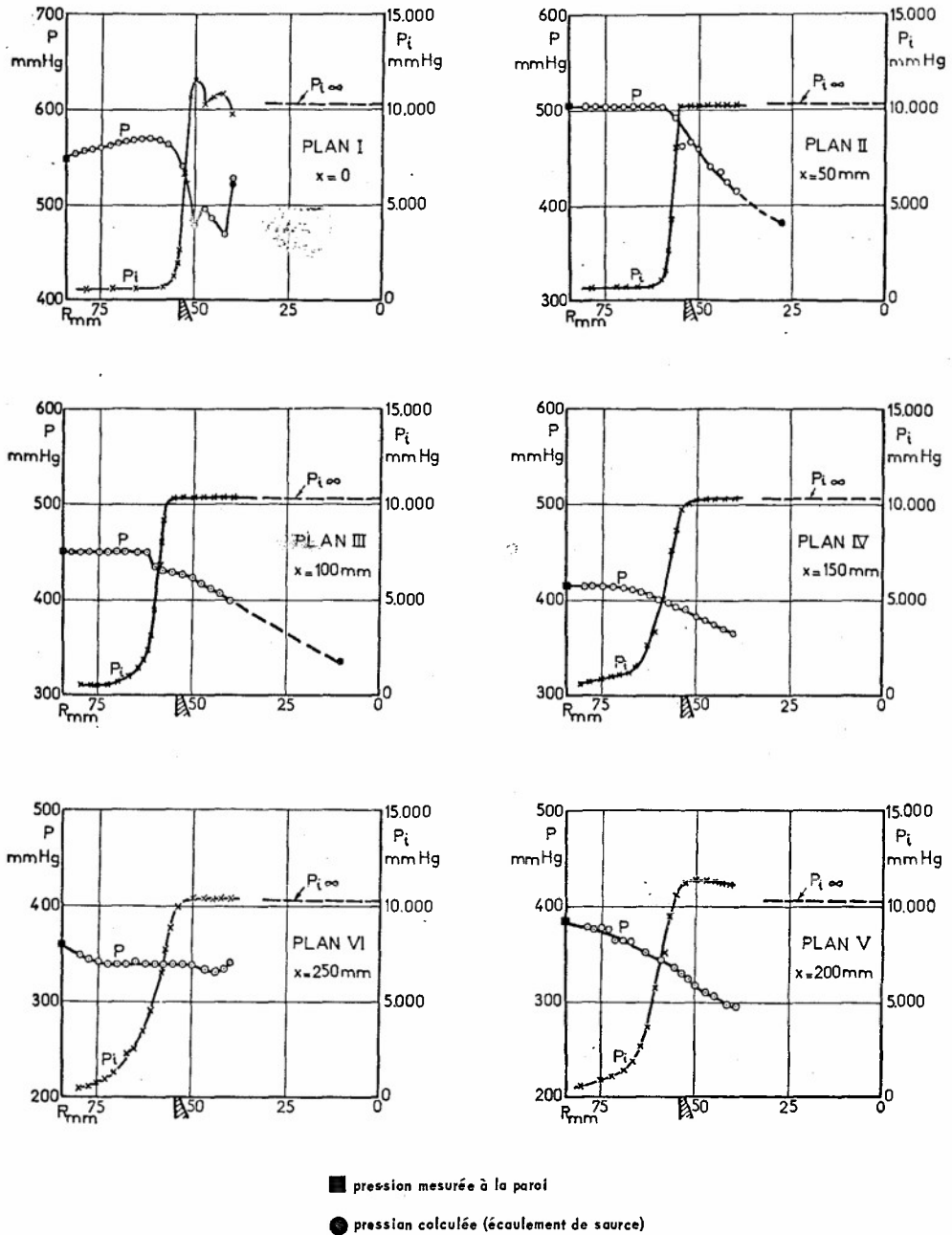
#### 5. CONCLUSION.

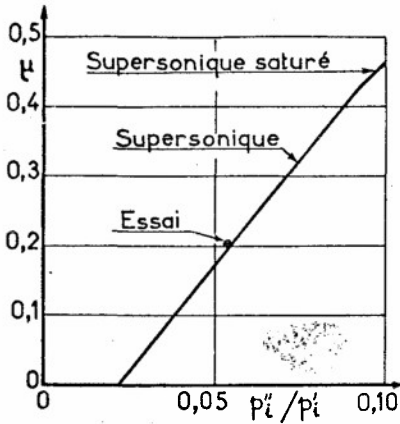
L'analyse comparée d'un mélangeur plan et d'un mélangeur de révolution ayant même lois de section a montré qu'il était possible de réaliser dans les deux montages les mêmes conditions aérodynamiques. Globalement, les performances mesurées restituent avec précision celles que le schéma unidimensionnel permettent de prévoir (Figure 16).

Dans le détail, la répartition des vitesses dans l'écoulement diffère notablement de celle retenue pour le calcul élémentaire [1] ou même plus perfectionné [3] où l'on suppose que l'écoulement secondaire s'effectue par tranches planes.

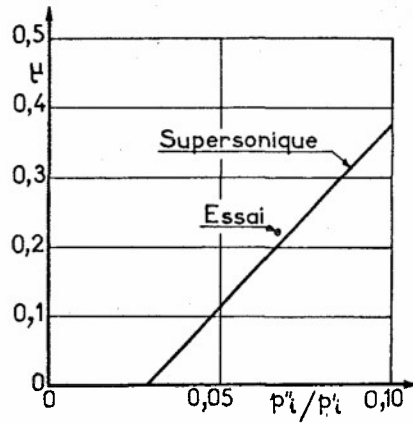
L'importante zone de mélange au contact des deux flux a pu être mise en évidence par striescopia dans le cas du montage plan et les limites de cette zone de transition telles qu'on les déduit des relevés de pression d'arrêt correspondent assez bien avec les limites des zones turbulentes que l'on distingue sur la vue striescopiaque.

On en conclut que la théorie unidimensionnel des mélangeurs à section constante où les deux flux sont supposés non visqueux rend bien compte globalement des performances de ces montages, mais que toute amélioration des schémas de calcul destinée à prévoir le développement longitudinal de l'écoulement devra faire intervenir le mélange visqueux au contact des flux primaire et secondaire.





MONTAGE PLAN



MONTAGE DE RÉVOLUTION

Fig. 16 - Performances globales des deux montages - Comparaison expérience-théorie

#### RÉFÉRENCÉS

- [1] J. FABRI - J. PAULON. Théorie et expérimentation des éjecteurs supersoniques air-air. Note Technique O.N.E.R.A. n° 36 (1956).
- [2] E. LE GRIVES - J. FABRI - J. PAULON. Diagrammes pour le calcul des éjecteurs à flux moteur supersonique. Note Technique O.N.E.R.A. n° 35 (1956).
- [3] J. M. HARDY - J. DELERY. Possibilités actuelles d'étude théorique d'une tuyère supersonique à double flux. AGARDograph n° 103 (1967). Traduction NASA n° TT-F-9870.
- [4] J. PAULON. Etude de la coexistence d'un jet supersonique et d'un jet subsonique dans un canal de section constante. La Recherche Aéronautique n° 1/1971 - T.P. n° 918.
- [5] W.L. CHOW - A.L. ADDY Interaction between primary and secondary streams of supersonic ejector systems and their performance characteristics. AIAA Journal, Vol. II, 4, 1964
- [6] J. PAULON - G. JANSSENS - Y. RIBAUD. La soufflerie de grille d'aubes O.N.E.R.A. - Premiers résultats expérimentaux. La Recherche Aéronautique n° 129 (1969).
- [7] J. FABRI - J. PAULON - G. JANSSENS. Use of supersonic cascades made of blades of simple geometric shapes for cascade wind tunnel performance evaluation. Communication présentée à la Réunion ASME sur les turbines à gaz - Bruxelles 24-28 Mai 1970. ASME Paper n° 70 - GT 110 - T.P. O.N.E.R.A. n° 826.
- [8] R. MICHEL - Calcul pratique de la couche limite turbulente compressible. Principes et Applications. Note Technique O.N.E.R.A. n° 49 (1959).

\*

A NEW CONCEPT OF THE INLET DESIGN AND OF THE THERMODYNAMIC  
CYCLE OF THE TURBOJET ENGINE AT HIGH FLIGHT MACH NUMBERS

by

W. Dettmering and B. Becker  
Institut für Strahlantriebe und Turboarbeitsmaschinen  
Technische Hochschule Aachen  
D 51 Aachen, Templergraben  
Germany

SUMMARY

At high supersonic speeds the efficiency of the inlet strongly depends on the diminution of the Mach number before the normal shock. Theoretical investigations show that this deceleration can be increased by replacing the internal compression in the bladeless channel by a supersonic rotor. Due to the deceleration of the relative flow and the increase of the circumferential velocity from rotor inlet to outlet, a significant augmentation of the static pressure ratio is achieved. Moreover, the Mach number can be decreased by the transfer of mechanical energy to the rotor. After the transition to subsonic velocities in the stator, the energy has to be returned to the flow either by a conventional compressor, or by a second supersonic rotor accelerating the flow between the combustion chamber and the nozzle. Static pressures and temperatures in this turbojet engine, which operates with subsonic combustion, are comparable to those of the supersonic combustion ramjet.

NOTATION

A	cross sectional area
a	sonic velocity
c	absolute velocity
E	exponent
F )	
G )	functions of the Mach number
H )	
h	enthalpy
M	Mach number
$\dot{m}$	mass flow
p	pressure
R	gas constant
s	entropy
T	absolute temperature
u	peripheral speed
w	relative velocity
$\alpha$ )	angles defined in Fig. 2
$\beta$ )	
$\delta$	tip-diameter ratio, rotor outlet to inlet
$\kappa$	ratio of specific heats
$\pi$	pressure ratio
t	temperature ratio

Subscripts

0,1,2..	positions
f	friction
r	relative
t	total
$\hat{\phantom{t}}$	normal shock
'	unstarted flow
"	started flow

The air intake of a jet engine is largely designed to decelerate the air flow approaching at the flight Mach number, with the lowest possible loss, to the subsonic velocity which is determined by the requirements of the subsequent component: compressor or combustion chamber. This deceleration is carried out in a wholly or partly closed diffuser of partly variable geometry, but usually without using rotating parts. The latter possibility will be theoretically examined in the present paper.

In doing so, the problem of material stress caused by high peripheral speeds and high temperatures will be deliberately left aside. On the contrary, the calculations presented depart from the assumption that in future materials, e.g. in the form of composites, will be available which may feasibly reach a multiple of the current strength values.

At Mach numbers of about up to  $M_0 = 3$  it might still be regarded as sufficient if the supersonic flow is first decelerated in the external compression by a steady or un-

steady deflection on a concavely curved wall and subsequently reduced to subsonic velocity in a normal shock. This deflection and the incident nearly isentropic deceleration in the external compression are limited however. Excessive deflection produces separation of the leading edge shocks at the cowl lips. The external drag rises and the inlet efficiency decreases.

Therefore, as the flight Mach number rises, the Mach number before the normal shock increases too. As this would cause also the total pressure loss in the inlet to increase considerably, the attempt is made to produce a further deceleration of the supersonic flow by narrowing the stream tube. This contraction is limited by the Kantrowitz-Donaldson criterion saying that the minimum area of the stream tube must be so large that the mass entering the inlet through a normal shock can be carried through with the maximum mass flow density.

For an ideal gas having constant specific heats, the mass flow may be expressed as a function of the Mach number and of the stagnation condition:

$$\dot{m} = \sqrt{\frac{\kappa}{R}} \left(\frac{T_t}{T}\right)^E M \frac{P_t}{\sqrt{T_t}} A \quad (1)$$

$$\text{with } \frac{T_t}{T} = 1 + \frac{\kappa-1}{2} M^2$$

$$E = \frac{1}{2} - \frac{\kappa}{\kappa-1}$$

The continuity equation for the adiabatic flow ( $T_t = \text{const.}$ ) between the inlet (Subscript 1) and the throat (Subscript 2) results in:

$$\left(\frac{T_t}{T}\right)_1^E M_1 P_{t1} A_1 = \left(\frac{T_t}{T}\right)_2^E M_2 P_{t2} A_2 \quad (2)$$

During the transition from the unstarted ('') to the started (") condition, the inlet Mach number  $M_1$  remains constant. The Mach number in the throat area rises from  $M_{2'} = 1$  into the supersonic range  $M_{2''} > 1$ . With constant geometry ( $A_{2'} = A_{2''}$ ) relations may be derived from Eq (2) for the required area ratio  $A_2/A_1$  and the Mach number  $M_{2''}$ :

$$\frac{A_2}{A_1} = \left[ \frac{1 + \frac{\kappa-1}{2} M_1^2}{1 + \frac{\kappa-1}{2}} \right]^E M_1 \frac{P_{t1}}{P_{t2'}} \quad (3)$$

$$\left(1 + \frac{\kappa-1}{2} M_{2''}^2\right)^E M_{2''} = \left(1 + \frac{\kappa-1}{2}\right)^E \frac{P_{t2'}}{P_{t2''}} \quad (4)$$

In assessing the total pressure loss, often only the total pressure ratio of the normal shock  $\pi_{t1}$  is taken into account. Because of the relatively low compression in the started flow, the friction losses should however not be neglected. The higher wall friction losses produced in the case of supersonic flow by the increased dynamic pressure are opposed in the unstarted flow by additional separation losses caused by the shock-boundary layer interaction. It may therefore be approximately assumed that the sum of friction losses described by the total pressure ratio  $\pi_{tf}$  will remain constant during the starting process.

$$\begin{aligned} P_{t2'} &= \pi_{t1} \pi_{tf} P_{t1} \\ P_{t2''} &= \pi_{tf} P_{t1} \end{aligned} \quad (5)$$

If all factors which are dependent only on  $M_1$  are taken together as one quantity, the influence of friction is clearly revealed:

$$\frac{A_2}{A_1} = \frac{1}{\pi_{tf}} F(M_1)$$

$$M_{2''} = G(M_1)$$

As under the conditions indicated above the Mach number  $M_{2''}$  remains unaffected by friction losses, also the obtainable pressure ratio may be easily calculated:

$$\begin{aligned} \pi &= \frac{P_{t2''}}{P_{t1}} \left[ \frac{1 + \frac{\kappa-1}{2} M_{2''}^2}{1 + \frac{\kappa-1}{2} M_1^2} \right]^{\frac{\kappa}{\kappa-1}} \\ &= \pi_{tf} H(M_1) \end{aligned} \quad (6)$$

Fig. 1 shows the dependence on the Mach number at the channel inlet  $M_1$ . As owing to the preceding external compression this Mach number is much smaller than the flight Mach number  $M_0$ , also this potential deceleration remains small.

Let us assume that the convergent part of the diffuser is replaced by a rotor. The Kantrowitz-Donaldson criterion is now determined by the area ratio of the blade channels as well as by the relative inlet Mach number. Owing to the nondimensional peripheral speed to be vectorially added this Mach number is larger than the absolute inlet Mach number and it may be expected that an increased deceleration will be permissible. In order to pursue this concept further, it is first required that the Kantrowitz-Donaldson criterion be applied to the relative flow in a rotor having a generally inconstant medium radius. The continuity equation for the relative system can be obtained direct from Eq (2) derived for the absolute system, if one replaces:

$$M = \frac{c}{a} \text{ by } M_r = \frac{w}{a}$$

$$P_t \text{ by } P_{tr}$$

$$T_t \text{ by } T_{tr}$$

$$\left(\frac{T_{tr}}{T}\right)^E M_{1r} M_{2r} P_{t1r} A_1 = \left(\frac{T_{tr}}{T}\right)^E M_{2r} P_{t2r} A_2 \quad (7)$$

It should be borne in mind, however, that in formulating the energy equation of the relative flow the peripheral speed must be taken into account.

$$h_{tr} = h + \frac{w^2}{2} - \frac{u^2}{2} = \text{const.}$$

$$\frac{T_{tr}}{T} = \frac{1 + \frac{\kappa-1}{2} M_r^2}{1 + \frac{u^2}{2h_{tr}}} \quad (8)$$

$$= \left(\frac{P_{tr}}{P}\right)^{\frac{\kappa-1}{\kappa}}$$

If only the mass flows in the throat area are compared, the equation is simplified again because during the starting process both the peripheral speed and the total enthalpy of the relative flow remain constant. The result is a relation for the supersonic outlet Mach number in the throat area  $M_{2r}$ , which is completely analogous with Eq (4) which was previously derived for the absolute flow.

$$\left(1 + \frac{\kappa-1}{2} M_{2r}^2\right)^E M_{2r} = \left(1 + \frac{\kappa-1}{2}\right)^E \dot{m}_{t1r} \quad (9)$$

The permissible deceleration  $\Delta M_r$  obtained therefore shows the same dependence on the inlet Mach number  $M_{1r}$ , which was already indicated in Fig. 1. For the subsequent calculation of the rotor flow according to the one-dimensional theory [3], the following parameters defined in Fig. 2 should be varied:

#### 1. Flow angle

The rotor inlet angle  $\beta_1$  determines, with the outlet angle  $\beta_2 = 65^\circ$  being constant, the turning of the relative flow. As there are no inlet guide vanes ( $\alpha_1 = 0^\circ$ ), the non-dimensional inlet triangle is clearly defined by the assumption of  $\beta_1$  and  $M_{1r}$ .

#### 2. Peripheral speed

The mean peripheral Mach number at the rotor inlet is defined by the inlet triangle. The tip-diameter ratio  $\delta$  describes the change in the peripheral speed. As the flow was given a considerable radial component already by the external compression, the peripheral speed must increase.

#### 3. Total pressure loss

With isentropic flow, the total pressure in the relative flow  $p_{tr}$  as defined by Eq (8) remains constant. The total pressure ratio  $\pi_{tr}$  is therefore a standard of the occurring losses. An assessment of the total pressure recovery was however not possible, as so far no sufficient experimental investigations of such supersonic cascades have been conducted. Since, as is shown by the drawing of the blades, the required contraction of the area is reached owing to the turning of the relative flow at nearly constant blade height, wind tunnel experiments on plane cascades would be quite feasible.

The diagrams in Fig. 3 show the influence of the inlet angle with the Mach numbers of the relative flow as a further parameter. Two particularly important points in the course of the total temperature ratio  $\tau_t = T_{t2}/T_{t1}$  were stressed.

Point A is characterised by  $\tau_t = 1$ , i.e. no exchange of total enthalpy and mechanical energy. This became apparent also in the axially directed absolute outlet Mach number ( $\alpha_2 = 0^\circ$ ). The deceleration of the absolute flow has considerably risen as against the bladeless diffuser. The lower diagram shows, as an example, the flow conditions for the outlet Mach number  $M_2 = 1.5$  at which a relatively good compression efficiency may be

expected in the normal shock. The change in Mach number  $M_1 - M_2$  rises from 0.22 without rotor (Fig. 1) to 1.06 with rotor ( $\tau_r = 1$ ). Accordingly, the pressure ratio rises from  $\pi = 1.37$  to 5.10. A comparison of the Mach number triangles of the rotor inlet and outlet shows that the deceleration of the absolute flow is reached both by the deceleration of the relative flow and by the increase of the peripheral speed.

With an increased turning of the relative flow it is possible to further reduce the kinetic energy of the inlet flow by a rotor delivering mechanical energy. At point B ( $\tau_{min}$ ) this delivery of energy reaches its maximum. If the value  $M_2 = 1.5$  is retained, the result is a still greater deceleration of the absolute flow, with considerably reduced relative and peripheral velocities.

The peripheral component is reduced by a following stator which also contains the normal shocks leading to subsonic velocity. Inlet Mach number  $M_2 = 1.5$  and  $\alpha_2 = 40^\circ$  represent very favourable conditions for the application of the tandem cascade which was experimentally examined at the Institute of Jet Propulsion of the Aachen Technical University [2], [3]. The (two-dimensional) cascade reached, under the flow conditions specified, a static pressure ratio of 2.6, with a polytropic compression efficiency of 88 percent.

As is shown in Fig. 3, transition from supersonic to subsonic velocities without any strong shocks may be reached if the parameters are selected accordingly. Fig. 4 shows the influence of the tip-diameter ratio  $\delta$  for the two characteristic points A and B. Variation of the losses in Fig. 5 affects on the whole only the static pressure ratio.

According to the usual definitions, the delivery of energy would characterise the rotor, or the entire stage, as a turbine. Conversely, a considerable increase of pressure is produced by the blading - a typical feature of the compressor. Both effects - delivery of energy and compression - however are utilised to decelerate the air approaching with a high kinetic energy. It may therefore be reasonable to use the terms "deceleration rotor", or "deceleration stage", for this turbine engine.

To improve the efficiency of the engine it is of course imperative that the energy withdrawn from the supersonic flow in the inlet be fed back into the thermodynamic cycle in another place. If one adds to the rotor inlet Mach number  $M_1$  indicated in the numerical example the deceleration reached in the external compression, it will be found that the delivery of mechanical energy is required only at higher flight Mach numbers, e.g. above  $M_0 = 4$ . At this flight Mach number, the ramjet with subsonic combustion has its optimal range of operation. A compression exceeding the pressure increase by complete diffusion is therefore not necessary and owing to the decrease of possible heat transfer in the combustion chamber thereby involved would even lead to a diminished performance.

On the other hand, the ramjet cannot produce a static jet thrust, so that during the starting process and the initial acceleration phase an engine with a compressor will be required. At higher flight Mach numbers, this compressor could be utilised for pressure generation in the inlet. It would then no longer be driven by the turbine, but by the deceleration rotor and at subsonic velocity return the energy withdrawn from the flow in the supersonic stage. To make this possible, there would have to be couplings capable of being engaged and disengaged, or movable flaps.

This case is illustrated in the enthalpy-entropy diagram, shown in Fig. 6. Following the external compression, which leads from point 0 to 1, another compression occurs in the deceleration rotor up to point 2. At the same time, the total enthalpy, which is at first constant during the external compression, diminishes. The h-s diagram shows with particular clarity how the kinetic energy is reduced by the two effects. The further deceleration to subsonic velocity occurs in the stator (point 2 to 3). By means of the compressor included at high flight Mach numbers in the transformation of energy in the inlet, compression is then effected from point 3 to 4, and the total enthalpy again reaches the value  $h_{t0}$ . The thermodynamic cycle is now continued as in the case of the ramjet.

As the maximum static temperature of the thermodynamic cycle is limited, a further increase of the flight Mach number to something like  $M_0 = 6$  will no longer make it appear reasonable to transform the whole kinetic energy of the flow into a corresponding compression. The temperature in the combustion chamber inlet would then be so high that a sufficient temperature increase by combustion could no longer occur. In this case it would therefore seem to be reasonable to increase the share of mechanical energy so as to keep down the temperature rise caused by the compression. It will thus become possible to supply a sufficient quantity of heat at subsonic velocity in a combustion chamber, following the deceleration stage (Fig. 8).

How can the energy withdrawn from the supersonic flow in the inlet and available in the form of mechanical energy be fed back into the thermodynamic cycle? A compression of the hot gas leaving the combustion chamber would involve an impermissible, further rise of temperature. To avoid an undue stress of material it is, on the contrary, advisable to obtain an expansion to supersonic velocity which should be carried up to point 5.

Suppose this acceleration occurred in a stator and the Mach number  $M_5$  corresponded - in an inverse direction, however - to the Mach number  $M_2$  in the deceleration stage. The rotor - again with an inverse sense of motion - could then be used to supply energy to the flow (Fig. 7). At the same time, the enlargement of the blade channels as determined

by the turning would cause the Mach number of the relative flow to rise. Both effects - supply of energy and expansion by enlarging the area - would result in an acceleration of the absolute flow. This is also clearly illustrated in the h-s diagram (Fig. 8). The pressure ratio, which has remained up to the ambient pressure, is eventually expanded in a purely divergent nozzle.

Here again, the terms "compressor" and "turbine" are unsuited to designate this turbine engine, as neither is there any compression nor is any mechanical energy delivered. However, by analogy to the "deceleration stage", the use of the terms "acceleration rotor" or "acceleration stage" suggests itself.

It is known that the other way to avoid total pressure losses in the normal shock and to supply heat at very high flight Mach numbers is the supersonic combustion. If it is assumed that the compression and expansion which precede or follow the supersonic combustion occur with the same efficiency and pressure ratios as in the thermodynamic cycle indicated before and that moreover in both cases a combustion at constant pressure takes place, one obtains a virtually identical course of the static condition.

Although the course of the stagnation condition in the scramjet shows a considerable deviation, one nevertheless obtains the same nozzle outlet velocity, thus making both thermodynamic cycles entirely equal with regard to both efficiency and thrust. For a supersonic combustion at constant pressure it may be inferred from the momentum equation and the continuity equation that the velocity and, as a result, also the kinetic energy remain constant. This corresponds to the equality of the exchanged mechanical energy of the two supersonic rotors. If the fuel mass is neglected, the total enthalpy differences are equal. Also the gasdynamic total pressure loss would be equal in both cases. While in the scramjet the difficulties may be found in the thermodynamic problems of the supersonic combustion, which have so far not been satisfactorily solved, those of the concept suggested here will lie primarily in the high peripheral speed of the rotor blades operated at supersonic velocity.

In conclusion it should again be emphasised that as is suggested by the title only a preliminary concept was to be presented for the application of turbine engines at high flight Mach numbers. Many major problems, such as the adaptation of the supersonic stages to varying flight Mach numbers, problems of material caused by high centrifugal forces and temperatures, or the mechanical difficulties certainly encountered with couplings and flaps in combination engines, had to be left unconsidered.

#### REFERENCES

- 1 W. Dettmering      Entwicklungslinien der luftansaugenden Strahltriebwerke  
Arbeitsgemeinschaft für Forschung des Landes Nordrhein-Westfalen  
Heft 182, 1967
- 2 W. Dettmering      Steps in the Development of a Supersonic Compressor Stage  
B. Becker            AGARD CP No. 34, 1968
- 3 B. Becker            Untersuchungen an stark umlenkenden Überschallverzögerungsgittern  
und deren Einsatzmöglichkeiten in der Axialverdichterstufe  
Diss. T.H. Aachen, 1970

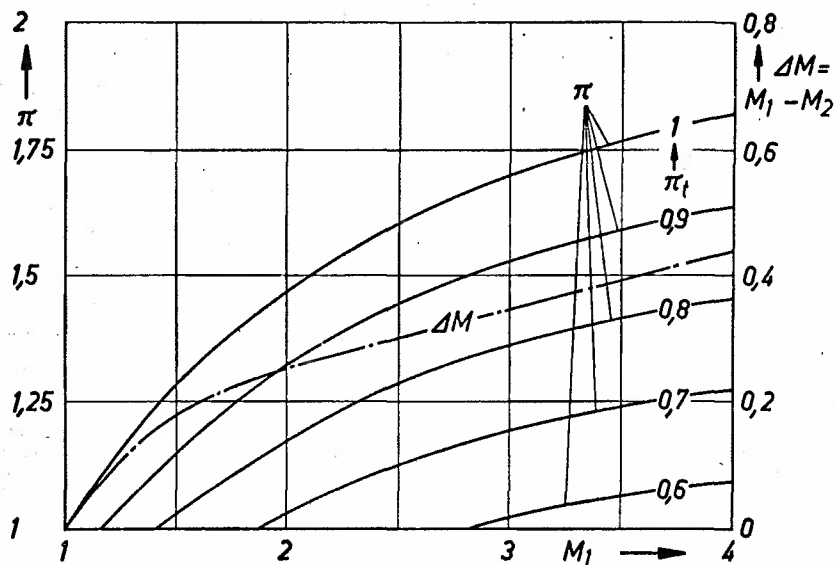


Fig. 1

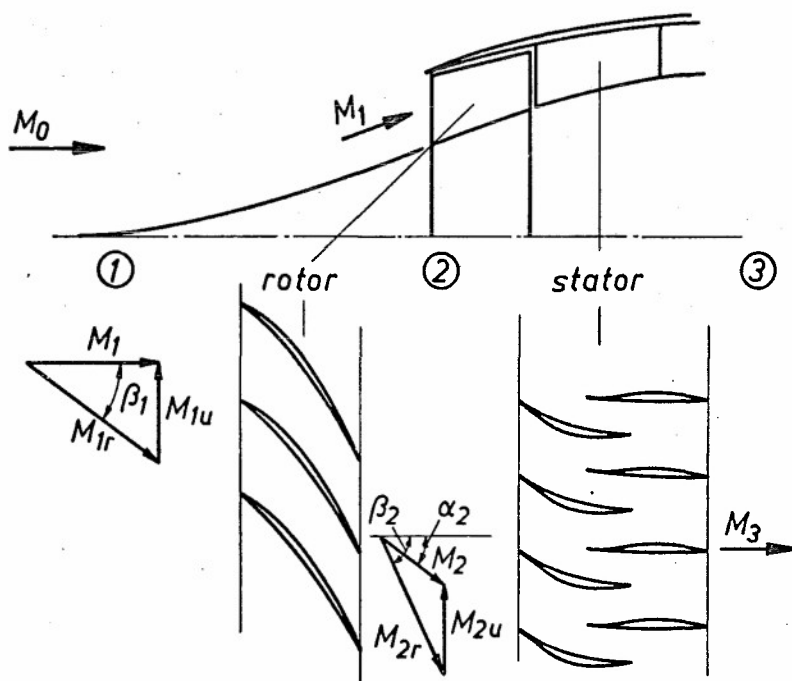


Fig. 2

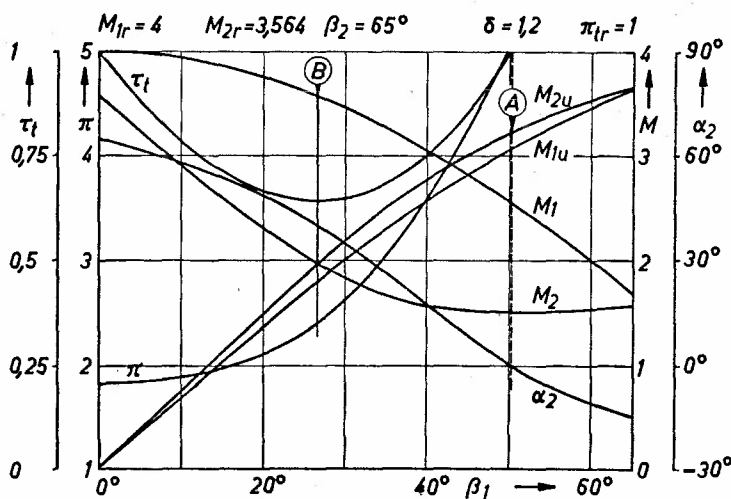
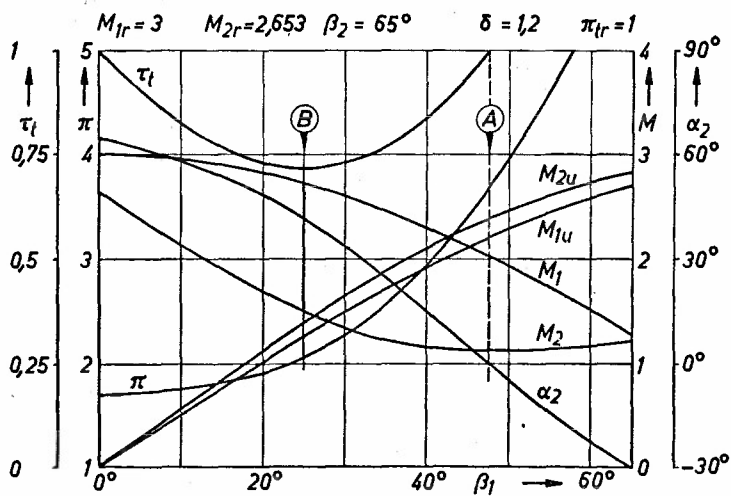
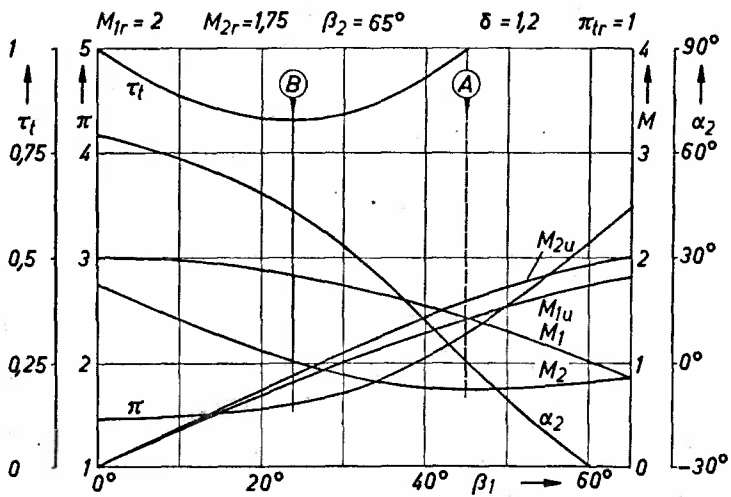


Fig. 3

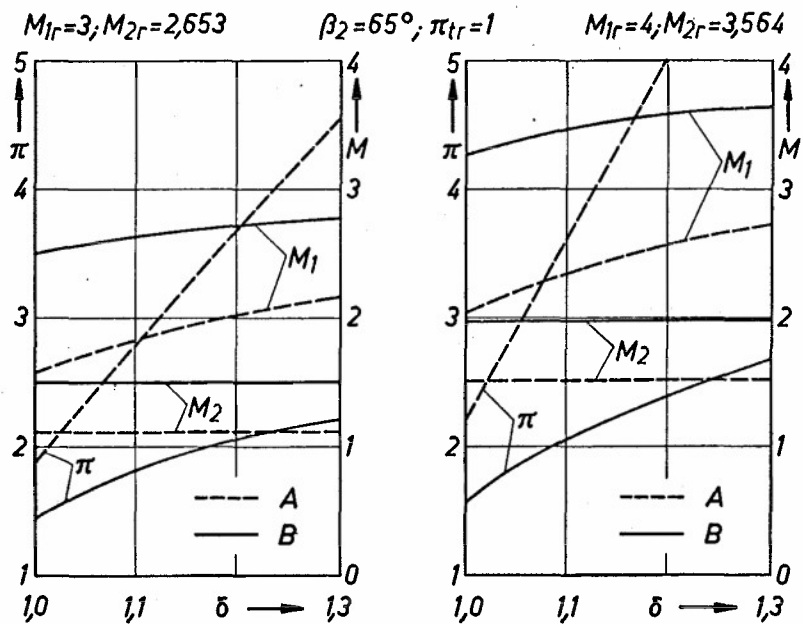


Fig. 4

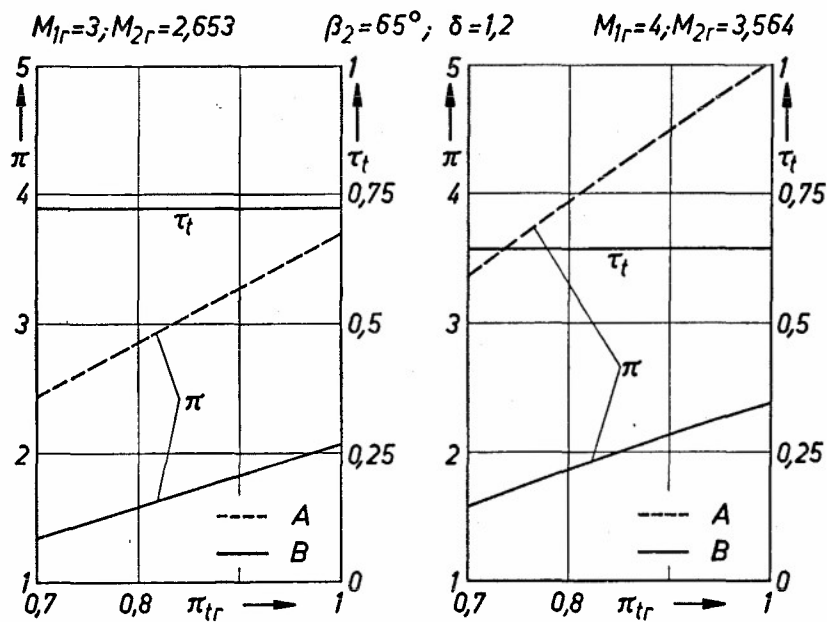


Fig. 5

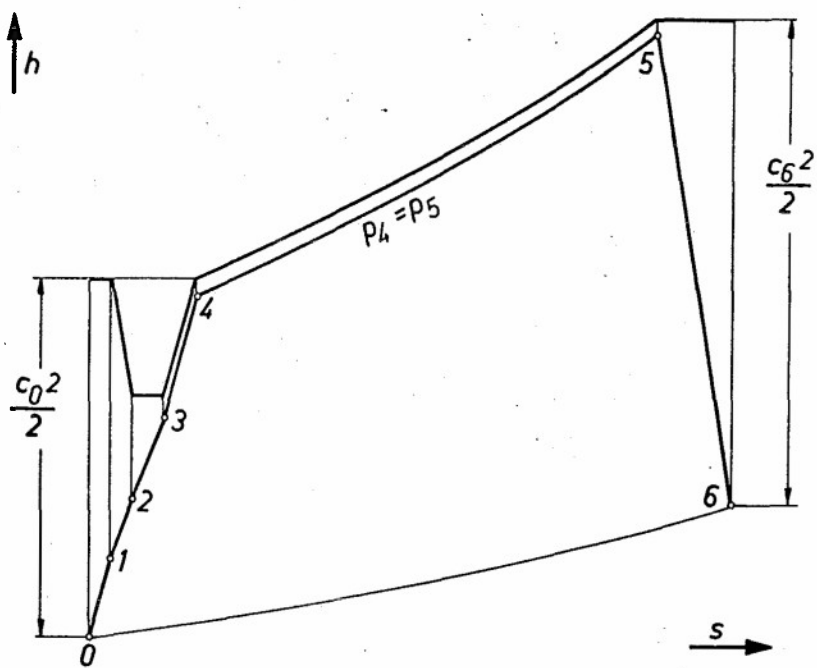


Fig. 6

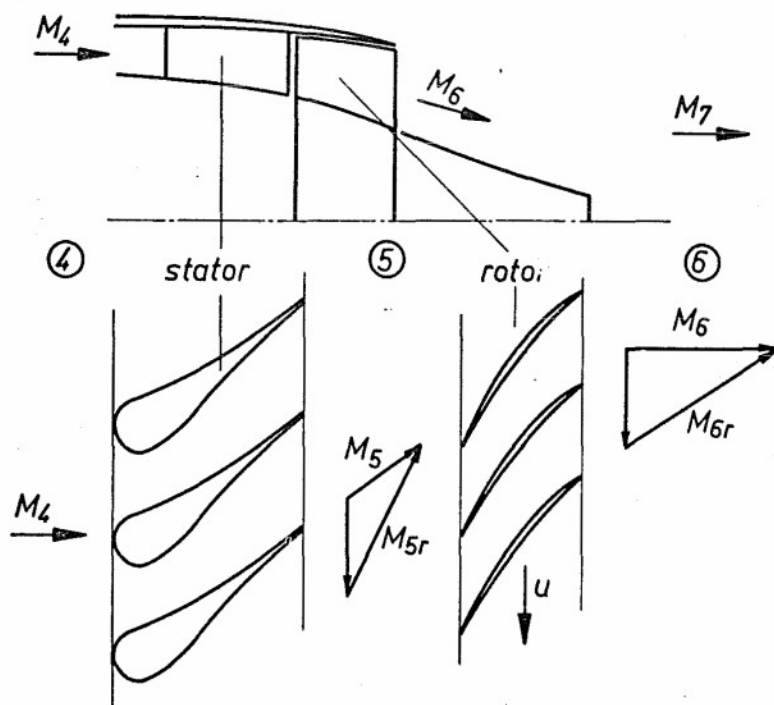


Fig. 7

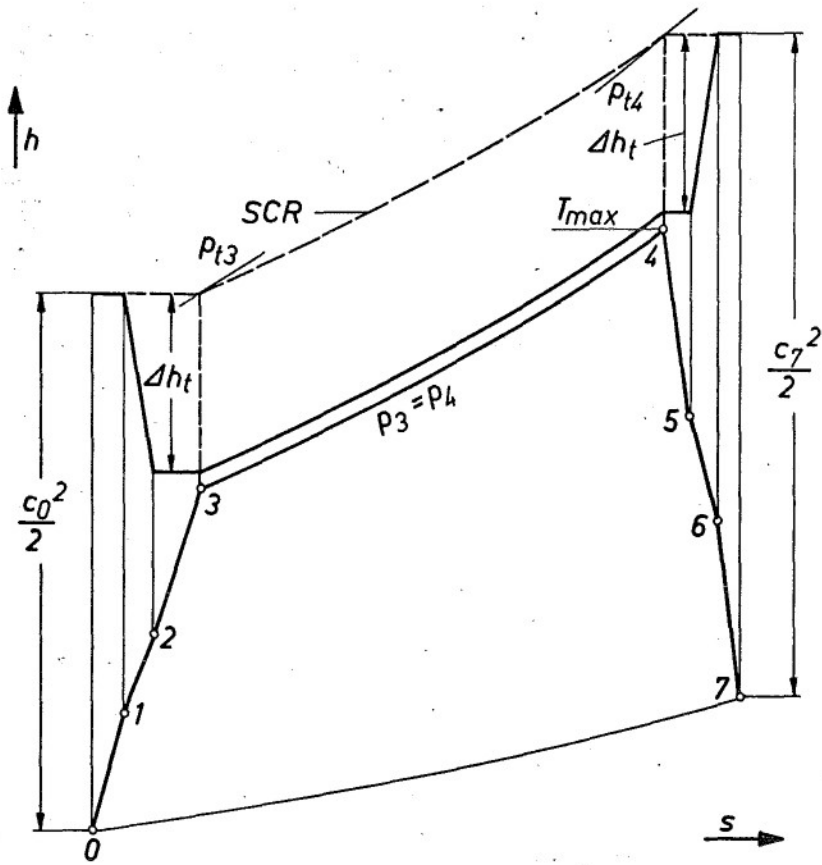


Fig. 8

WIND TUNNEL INVESTIGATIONS OF A SUPERSONIC AIR INTAKE WITH  
VARIOUS AUXILIARY INTAKES AT LOW SPEEDS

Herbert Eibl

Messerschmitt-Bölkow-Blohm GmbH  
Unternehmensbereich Flugzeugentwicklung  
München-Ottobrunn

and

Reinhard Friedrichs

Deutsche Forschungs- und Versuchsanstalt für  
Luft- und Raumfahrt (DFVLR)  
Zentralabteilung Niedergeschwindigkeits-Windkanäle  
Braunschweig, Germany

SUMMARY

Supersonic air intakes require special devices at low flight speeds and particularly under take-off conditions in order to reduce the pressure losses to an acceptable level. This paper deals with some experimental contributions to this design problem. In the low-speed tunnel of the DFVLR Braunschweig model tests were carried out on a twin-engine aircraft configuration with air intakes located on the upper side of the fuselage right next to the trailing edge of the wing.

The measurements mainly refer to the flow field in the compressor inlet area of a supersonic intake at which the influence of auxiliary intakes of different shapes had been investigated.

The results are presented as isobars of the total pressure distribution in the compressor inlet area. Moreover, the pressure loss and distortion parameters are discussed which strongly depend on the inflow incidence and on the intake flow mainstream ratio.

The results allow promising predictions of the favourable geometry and arrangement of auxiliary intakes.

NOTATION

1. Geometric Symbols

D	compressor face diameter (D = 145 mm)
$\varphi$	circumferential coordinate
r	radial coordinate

2. Aerodynamic Symbols \*)

2.1 General

$\alpha$	angle of incidence
$\beta$	angle of sideslip
$\varphi$	angular width of auxiliary intake
s	slot width of auxiliary intake
a	distance of auxiliary intake from compressor face
F	area
p	static pressure
$P_t$	total pressure
q	dynamic pressure
$\rho$	air density
$\nu$	viscosity
v	velocity in the compressor face
$V_\infty$	free stream velocity
M	Mach number
$Re = \frac{\bar{v} \cdot D}{\nu}$	Reynolds number

## 2.2 Pressure Parameters

$$\lambda = \frac{P_{t\infty} - \bar{P}_t}{\bar{q}} \quad \text{total pressure loss}$$

$$\eta = \frac{\bar{P}_t}{P_{t\infty}} \quad \text{total pressure recovery}$$

## 2.3 Flow Distortion Parameters

$$D = \frac{P_{t\infty} - \bar{P}_t}{\bar{q}} \quad \text{local deviation}$$

$$D_{\max} = \frac{P_{t\max} - \bar{P}_t}{\bar{q}} \quad \text{local maximum positive deviation}$$

$$D_{\min} = \frac{P_{t\min} - \bar{P}_t}{\bar{q}} \quad \text{local maximum negative deviation}$$

$$D_{C60} = \frac{(\bar{P}_{t60})_{\min} - \bar{P}_t}{\bar{q}} \quad \text{maximum negative deviation over } 60^\circ\text{-sector}$$

$$I = \frac{P_{t\max} - P_{t\min}}{\bar{P}_t} \quad \text{maximum total pressure difference}$$

$$\Omega = \sqrt{\frac{1}{R \cdot \Phi} \frac{R \cdot \Phi}{D^2}} \quad \text{standard total pressure deviation}$$

} of total pressure from mean value

## 3. Abbreviations and Subscripts

CF	compressor face
$\infty$	conditions in free stream

## 1. INTRODUCTION

Extremely short take-off and landing distances of STOL-aircrafts and high take-off weights of VTOL-aircrafts require the provision of maximum engine thrust at flight speed zero and low subsonic speeds. This, however, can only be achieved, if in every respect satisfactory air supply is guaranteed. As known, the thrust of a jet engine depends to a great extent on the average total pressure in the compressor face, while at the same time low flow distortions have to be achieved to secure the functional reliability of the engine.

Special difficulties in the air supply system in the low subsonic speed range result from inlets which are designed for supersonic flight. In supersonic flight the sharp edged main inlet ensures a proper supply of air to the engine: a system of compression shocks and the following diffuser slow down the incoming air stream to the velocity required by the engine. During subsonic flight, however, the sharp edged peripheral walls of the main inlet, which project into the now sink-like flow field, cause high pressure losses and flow separations along the diffuser walls which jeopardize the efficiency of the engine. Therefore it is necessary to provide the inlet with auxiliary inlets for the low subsonic flight range. Additional openings located at the diffuser and closed during high-speed flight reduce the constricting effects and flow separations by feeding air of higher energy into the inlet tube.

Until now the optimization of the location, size and shape of auxiliary intakes defies all theoretical calculations because of the complexity of the matter. At present only the experimental aerodynamics is able to present solutions.

Within the framework of this report an example of possible auxiliary inlet configuration is given. Different slot shapes and their location shortly ahead of the compressor face have been examined at a diffuser with slight curvature. These tests had been carried out in the low-speed wind tunnel of the DFVLR Braunschweig as a part of a component test program for a VTOL aircraft of MBB Munich.

The results of this report are mainly based on pressure measurements in the compressor face. The most important parameters which are used to judge engine inlet flows had been calculated from the measured pressure distribution. A tabulated compilation of those values contains Fig. 1. The total pressure coefficients are arranged in the left hand column; a selected number of coefficients characterizing the flow distortion are listed in the right hand column.

\* Note: Dashed symbols ( $\bar{P}_t$ ,  $\bar{q}$ ,  $\bar{\lambda}$ ) indicate mean values

It exceeds the scope of this paper to enter into all particular ins and outs of each parameter mentioned. Therefore, only the parameters used in this report shall be discussed. They are marked by shading in Fig. 1:

The average total pressure loss in the compressor face  $\bar{\lambda}$  is based upon the average dynamic pressure in the compressor face  $q$ . Since radial flow distortions have a much more unfavourable influence on the surge line position than circumferential distortions, the parameter  $D_{C60}$  has been chosen to characterize flow distortion. It shows the average total pressure deviation of the worst  $60^\circ$ -sector from the average total pressure in the over-all compressor face based upon  $q$ .

## 2. MODEL AND TESTING EQUIPMENT

As can be seen by the general model view in Fig. 2, the engine inlets are located side by side on top of the aircrafts fuselage next to the trailing edge of the wings. This inlet location seems to be very favourable for jet supported flight near the ground, if cruise engines are also used as lift engines by tilting exit nozzles, since recirculation flows are screened off. The mock-up is confined to those aeroplane parts which might interfere perceptibly with the inflow; this applies to the front and middle section of the fuselage with both engine inlets, and also to the parts of the aerofoils close to the fuselage. The inlet - shown enlarged in the lower part of Fig. 2 - has external compression by oblique compression shocks and a subsonic diffuser, both designed according to commonly used inlet computing methods. The area distribution of the subsonic diffuser  $F_x$  based upon final cross section  $F_D$  is plotted against the diffuser length. The auxiliary inlets are located at the end of the subsonic diffuser just ahead of the compressor face plane. Variations of their axial width ( $s = 0.125 \div 0.7 D$ ), angular width ( $\phi = 90^\circ, 145^\circ, 200^\circ$ ) and their axial and angular location relative to the compressor face had been tested.

Furthermore two auxiliary intake lips had been tested; geometric details can be seen in the upper right part of Fig. 2. In one case the intake openings were furnished with a semicircular lip over the whole circumference, in the other case the lip next to the engine face was slanted.

In place of the real engine, the model has a special built-in component, the so-called test model engine; it is an exact reproduction of the annular inlet cross-section and contains the necessary pressure sensors to determine the local flow field; i.e. six radial rakes with six Pitot tubes each, which could be moved into four optional angular positions by a remotely controlled drive system, thus quadrupling the number of available measuring points. The corresponding pressure lines lead over to a Scanivalve mechanical scanner which converts the local pressures into analogue electrical signals. After being on-line digitalized they are fed into the digital computer.

The inlet flow is generated during the tests by radial vacuum blowers, which were connected with the engine exits by hoses (Fig. 3).

## 3. RESULTS

### 3.1 Auxiliary Inlets with Semicircular Intake Lip

#### 3.1.1 Influence of Axial Slot Width $s$

Pressure loss  $\bar{\lambda}$  and flow distortion  $D_{C60}$  for the intake with auxiliary inlets closed ( $s/D = 0$ ) can be seen in Fig. 4 as a function of velocity ratio  $V_\infty/\bar{v}$  - the ratio of freestream velocity to average velocity in the compressor face plane. The test result for the case of zero flight speed ( $V_\infty/\bar{v} = 0$ ) shows, as expected, high pressure losses which are sharply reduced as the velocity ratio increases and only slightly go up for velocity ratios  $V_\infty/\bar{v} > 1.2$ . A similar tendency applies to the flow distortions  $D_{C60}$ ; for the throttled engine ( $V_\infty/\bar{v} > 1.0$ ), however, they increase more strongly.

Furthermore, Fig. 4 shows, that for small velocity ratios the pressure losses have been decreased very strongly by the auxiliary intake with axial slot width  $s/D = 0.25$ ; the flow distortions, however reach essentially higher values than for the main inlet with closed auxiliary inlet.

Enlarging the axial slot width, leaving the angular width at  $\phi = 145^\circ$ , is not essentially improving either pressure losses or flow distortions, although the auxiliary intake area became three times larger. The diagramme on the right hand side of Fig. 4, where the parameters are plotted against axial slot width, makes it quite obvious.

In addition the test results show, that the efficiency of the auxiliary intakes is limited to the velocity ratio range of  $V_\infty/\bar{v} = 0$  to 0.9.

#### 3.1.2 Influence of Angular Width $\phi$

The results of the auxiliary inlets with semicircular inlet lip and constant slot width, as presented in Fig. 5, show that the pressure losses continually decrease with increasing angular width up to the largest tested angular width of  $\phi = 200^\circ$ , and that for example the pressure losses for the flight speed zero, which was  $\bar{\lambda} = 0.7$  for closed auxiliary inlet, could be reduced to  $\bar{\lambda} = 0.3$ . The flow distortions at low velocity ratios are very strongly influenced by the angular intake width. High flow distortion values, which appear at small angular widths, are essentially improved if the angular width is enlarged. For  $\phi = 200^\circ$  they decrease to values obtained for closed auxiliary inlets.

### 3.2 Modification of the Intake Lip

In order to get a better understanding of the flow field in the compressor face, isobar diagrammes - lines of constant local total pressure deviation,  $D = \text{const}$  - have been drawn, where areas with great losses ( $D > -0.2$ ) have been shaded.

From the isobar diagrammes for the semicircular inlet lip in the upper row of Fig. 6 can be recognized, that heavy total pressure loss areas occur at low velocity ratios, which indicate flow separations behind the intake lip. A possibility for further improvement of the so far achieved results seems to be replacing the previously used intake lip by a new, stream line shaped lip, which is slanted towards the diffuser inside. As can be seen by the isobar diagrammes for the new lip shape there are substantial improvements at low velocity ratios. This results points out that even little modifications of the inlet lip can influence the inlet flow at low velocity ratios. At the high velocity ratio  $V_\infty/\bar{v} = 0.9$  the inlet flow is quite uniform over the compressor face plane for both lip shapes.

Fig. 7 contains the total pressure loss  $\bar{\lambda}$  and the flow distortion  $D_{C60}$  for both lip shapes plotted against the entire velocity ratio range. While the total pressure losses can be improved by the slanted intake lip up to  $V_\infty/\bar{v} = 0.6$ , the flow distortions can only be decreased in the velocity ratio range from  $V_\infty/\bar{v} = 0$  to 0.25.

### 3.3 Auxiliary Intakes with Slanted Lip

Considering the results discussed in paragraph 3.2, it was obvious to repeat the optimization of axial slot widths, angular width and later on examine the influence of axial distance  $a$  of the auxiliary inlet from the compressor face plane.

#### 3.3.1 Influence of Axial Slot Width $s$ and Angular Width $\varphi$

The results of the slanted intake lip, presented in Fig. 8, show the total pressure loss and flow distortions only as a function of the varied geometric parameters: axial slot width  $s/D$  and angular width  $\varphi$ .

Looking at the pressure loss curve, the same tendency can be noticed which was obtained for the semicircular intake lip; as was to be expected the results are more favourable.

As for the flow distortions  $D_{C60}$ , compared to the values of the semicircular lip there is a noteworthy difference. The variation of the axial slot width (Fig. 8, left side) yields in the stationary case a minimum for the smallest tested slot width of  $s/D = 0.125$  with the extremely favourable value of  $D_{C60} = -0.07$ , which is not exceeded up to medium velocity ratios. Is the angular width (Fig. 8, right side) increased, then substantial improvements of the flow distortions can be achieved for  $V_\infty/\bar{v} = 0$  in the range from  $\varphi = 90^\circ$  to  $200^\circ$ . The optimization of the auxiliary intake configuration therefore yielded that, regarding pressure loss and flow distortion, the configuration with the largest angular width  $\varphi = 200^\circ$  and the smallest axial slot width  $s/D = 0.125$  turned out to be the best.

In order to once more clearly present the results, the total pressure distribution in the compressor face plane (isobar diagrammes) have been collated for the velocity ratios  $V_\infty/\bar{v} = 0$  and 0.25 in Fig. 9 for the variation of the axial slot width and in Fig. 10 for the variation of the angular width. It can be clearly seen from these flow patterns that especially for the flight speed zero pressure loss areas develop behind the intake lip with increasing axial slot width (Fig. 9). While with increasing angular width (Fig. 10) the areas of high losses diminish and are completely reduced for the greatest angle  $\varphi = 200^\circ$  except for small fringes near the ends of the auxiliary intake.

#### 3.3.2 Influence of Axial Location of the Auxiliary Intake

The purpose of a further study was to determine the most advantageous distance  $a$  of the auxiliary intake from the compressor face plane. The auxiliary intake configuration with the axial slot width  $s/D = 0.25$  and angular width  $\varphi = 200^\circ$  was tested at distances  $a/D = 0.17$  to 0.53. Fig. 11 shows, that bringing the auxiliary intake closer to the compressor face is further improving pressure loss  $\bar{\lambda}$  and flow distortion  $D_{C60}$  at low velocity ratios.

In addition is to be said that moving an auxiliary intake in circumferential direction does practically not change pressure loss and flow distortion.

### 3.4 Influence of Free Stream Direction

#### 3.4.1 Angle of Incidence

The most favourable auxiliary intake configuration with slanted lip, the narrow slot width  $s/D = 0.125$  and the great angular width  $\varphi = 200^\circ$  has extensively been tested at angles of incidence in the range of  $-10^\circ \leq \alpha \leq 25^\circ$ . The results are presented in Fig. 12.

At low velocity ratios  $V_\infty/\bar{v} = 0.5$  there is, as expected, only a minor influence of the angle of incidence. At greater velocity ratios, however, a clear increase of the pressure losses with increasing angles of attack can be recognized.

The flow distortions are within the entire range of velocity ratios much less sensitive to incidence changes. For the most important range of the velocity ratios, i.e.  $V_\infty/\bar{v} = 0$  to 0.9, the values for all tested angles of incidence are within a relatively narrow margin.

### 3.4.2 Angles of Sideslip

Side slipping test results of the same auxiliary intake configuration for the angles of incidence  $\alpha = 0^\circ$  and  $\alpha = 15^\circ$  can be taken from Fig. 13. At the positive angle of sideslip  $\beta = 10^\circ$  pressure losses and flow distortion of the engine on the windward side are at all velocity ratios only slightly different compared to the straight forward flight. At the negativ angle of sideslip  $\beta = -10^\circ$  pressure losses and flow distortions increase considerably at angle of incidence  $\alpha = 0^\circ$ ; a rising of the angle of incidence, however, causes a substantial drop of pressure losses and flow distortions, since the main intake inflow was quite favourable influenced by the fuselage and aerofoil parts in front.

### 3.5 Variation of Compressor Mass Flow

A characteristic value which is used for power calculations and also to judge inlet flows, is the so called pressure recovery

$$\eta = \frac{\bar{p}_t}{p_{t\infty}}$$

Between pressure loss  $\bar{\lambda}$  used in this report and pressure recovery  $\eta$  there is the following simple relation:

$$\eta = \frac{1}{1 + \bar{\lambda} \cdot \bar{q}/\bar{p}_t}$$

$$\text{with } \bar{q}/\bar{p}_t = \frac{\kappa}{2} M^2 \left(1 + \frac{\kappa-1}{2} M^2\right) \frac{-\kappa}{\kappa-1} = f(M)$$

For an exact determination of the pressure recovery of the full scale inlet, it is therefore necessary to know how the pressure loss coefficient  $\bar{\lambda}$  depends upon Mach number and Reynolds number. These values could not realistically be performed during the described tests, since the engine mass flow was limited by the power of the blowers and the free stream velocity did not cover the entire velocity range.

For the flight speed  $V_\infty = 0$ , a variation of engine mass flow has been carried out with an auxiliary inlet configuration. The results presented in Fig. 14 show that pressure loss and flow distortion decrease with increasing inlet velocities.

## 4. CONCLUSIONS

The most important result of the wind tunnel test to improve inlet flow at take off and landing by additional auxiliary inlets can briefly summarized as follows:

### 1. Variation of auxiliary inlets

While enlarging auxiliary inlet areas by increasing slot width in axial direction proved to be almost ineffective, the total pressure losses and flow distortions decrease substantially, if the angular width is increased. If an auxiliary inlet is moved towards the compressor face plane, small improvements of pressure loss and flow distortion can be achieved at low velocity ratios. No influence can be noticed if auxiliary intakes are moved in circumferential direction.

At low velocity ratios less pressure losses and flow distortions are caused by the slanted intake lip than by the semicircular lip.

### 2. Influence of free stream direction

At high velocity ratios ( $V_\infty/\bar{v} > 0.5$ ) pressure losses increase substantially with increasing angles of incidence; the flow distortions are much less sensitive to changes of incidence angles.

Side slipping has very little influence on the inlet flow of the engine on the windward side compared to the straight forward flight. Whereas the inlet flow of the lee-side engine is very much changed. Small angles of incidence cause deteriorations, a rise of the incidence angle improves the quality of the inlet flow compared to the straight forward flight.

In order to give a better look into the employed test technique, an information film, entitled "Auxiliary air inlet measurements for a VTOL-project", will be projected as part of this report. This film was produced by Messerschmitt-Bölkow-Blöhm and deals with a similar, later tested project.

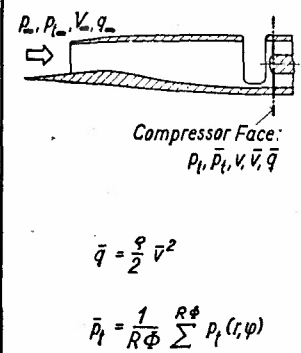
		Pressure Parameters	Flow Distortion Parameters	
 <p>Compressor Face: <math>P_t, \bar{P}_t, V, \bar{V}, \bar{q}</math></p> <p><math>\bar{q} = \frac{\rho}{2} \bar{V}^2</math></p> <p><math>\bar{P}_t = \frac{1}{R\Phi} \sum P_t(r, \phi)</math></p>	1	$\lambda = \frac{P_{t\infty} - P_t}{\bar{q}}$	1	$D_{min} = \frac{P_{tmin} - \bar{P}_t}{\bar{q}}$
	2	$\bar{\lambda} = \frac{P_{t\infty} - \bar{P}_t}{\bar{q}}$	2	$D_{max} = \frac{P_{tmax} - \bar{P}_t}{\bar{q}}$
	3	$\eta = \frac{\bar{P}_t}{P_{t\infty}}$	3	$D_{max} - D_{min} = \frac{P_{tmax} - P_{tmin}}{\bar{q}}$
			4	$I = \frac{P_{tmax} - P_{tmin}}{\bar{P}_t}$
			5	$D_{C60} = \frac{(\bar{P}_{t60^\circ})_{min} - \bar{P}_t}{\bar{q}}$
			6	$\Omega = \sqrt{\frac{1}{R\Phi} \sum D^2}$

Fig. 1 Aerodynamic criterions for engine intakes

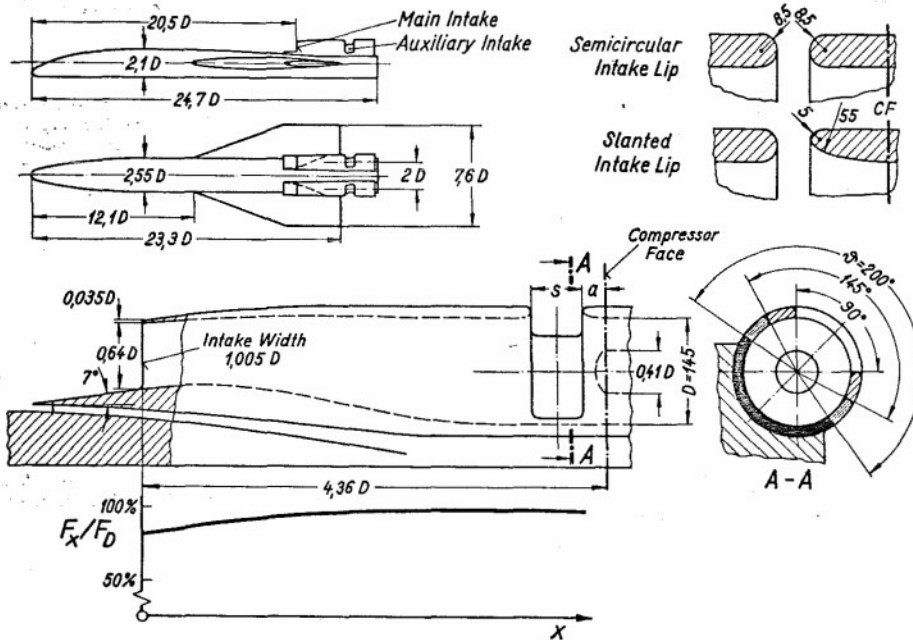
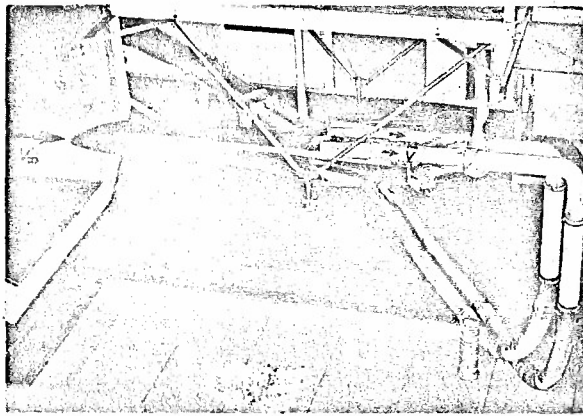
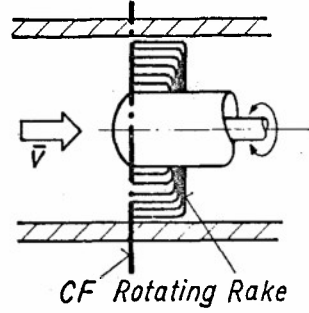


Fig. 2 Model for intake tests



Pressure Probes in the Compressor Face



$V_\infty = 0 \dots 45 \text{ m/s}$     $\bar{v} = 0 \dots 95 \text{ m/s}$

Pitot Probes ( $p_t$ )

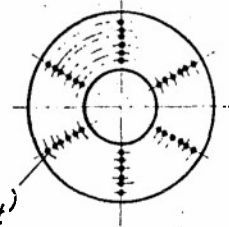


Fig. 3 Model in the DFVLR low-speed tunnel 3,6 m x 2,9 m

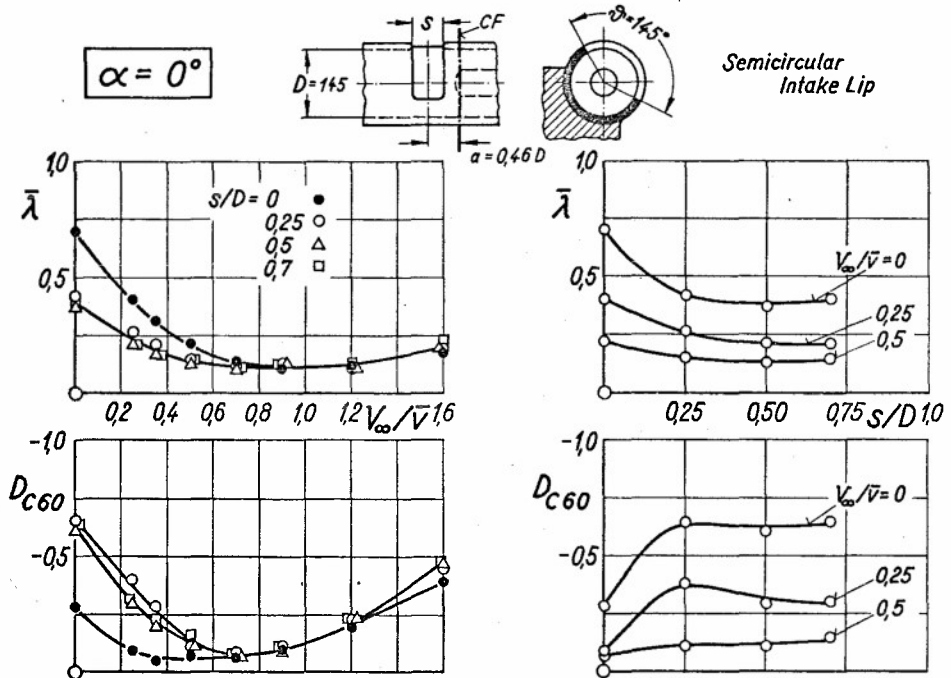


Fig. 4 Total pressure loss and distortion. Influence of axial slot width.  $\beta = 0$ . Semicircular intake lip

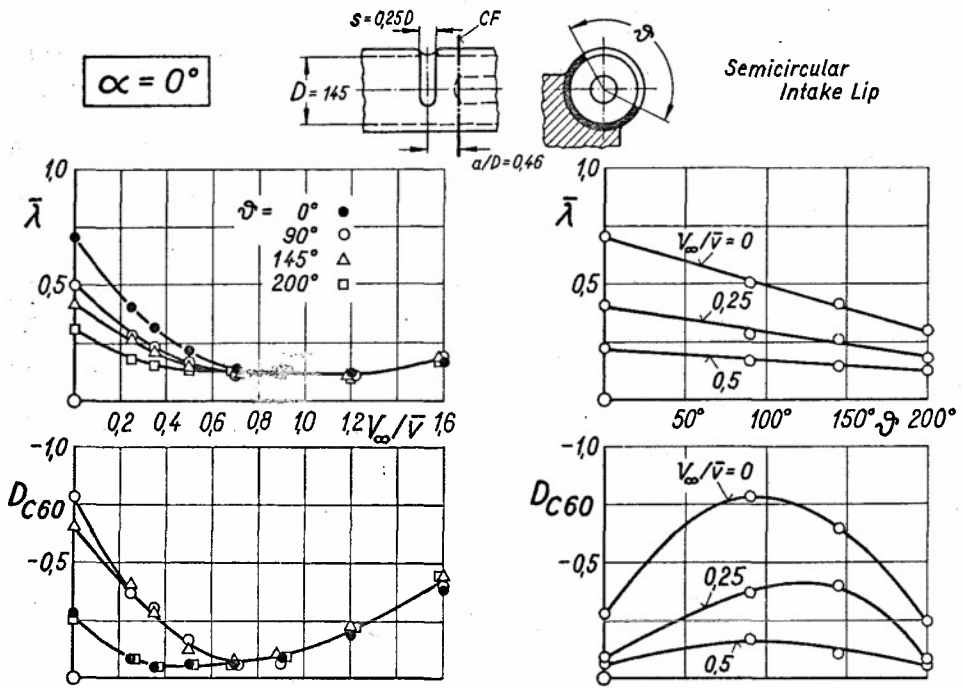


Fig. 5 Total pressure loss and distortion. Influence of angular width.  $\beta = 0$ . Semicircular intake lip

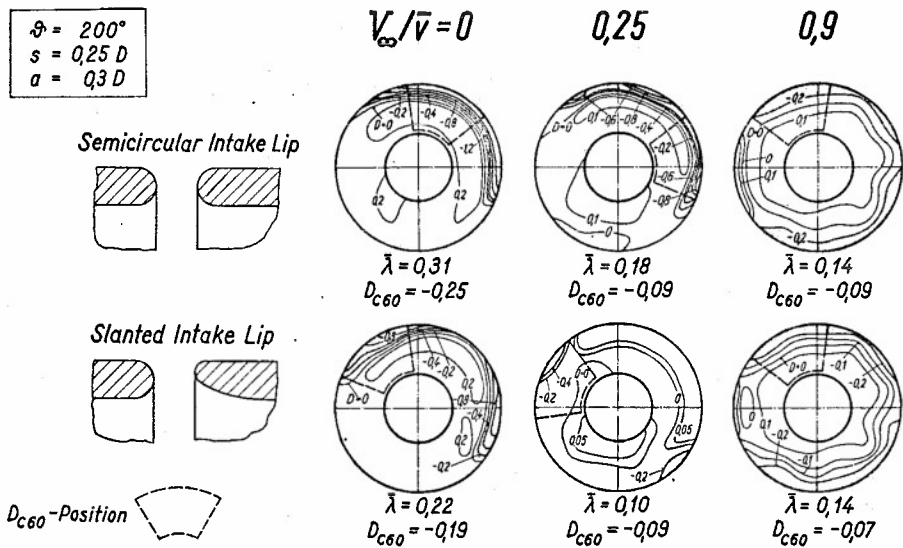


Fig. 6 Total pressure distribution. Influence of lip shape.  $\alpha = 0$ ,  $\beta = 0$ .

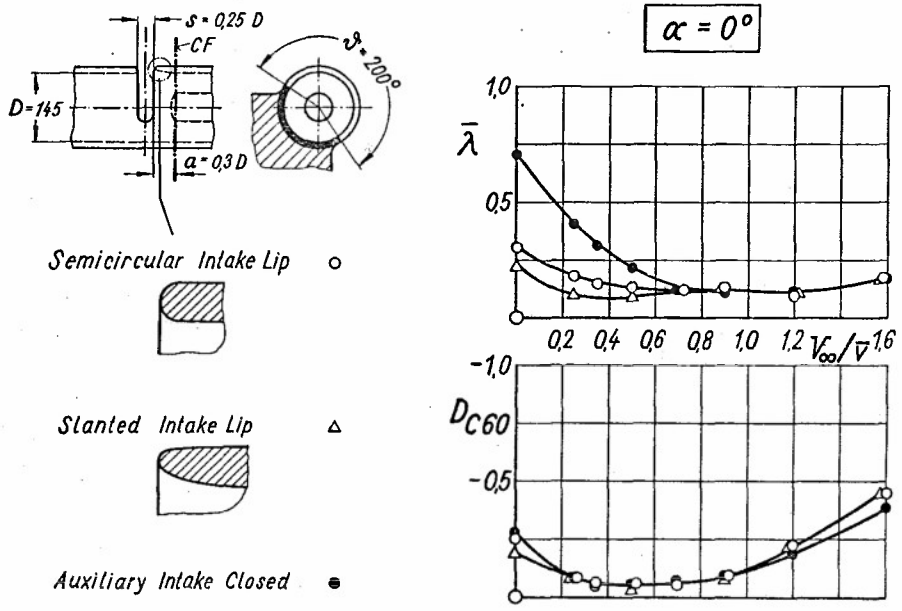


Fig. 7 Total pressure loss and distortion. Influence of lip shape.  $\beta = 0$ .

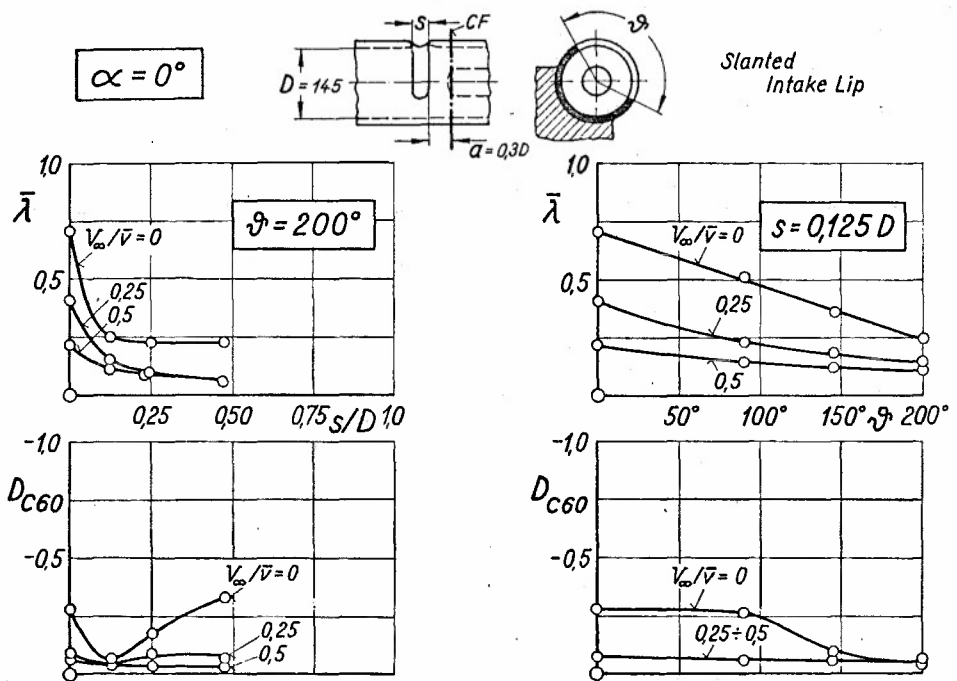


Fig. 8 Total pressure loss and distortion. Influence of axial width and angular width.  $\beta = 0$ . Slanted intake lip

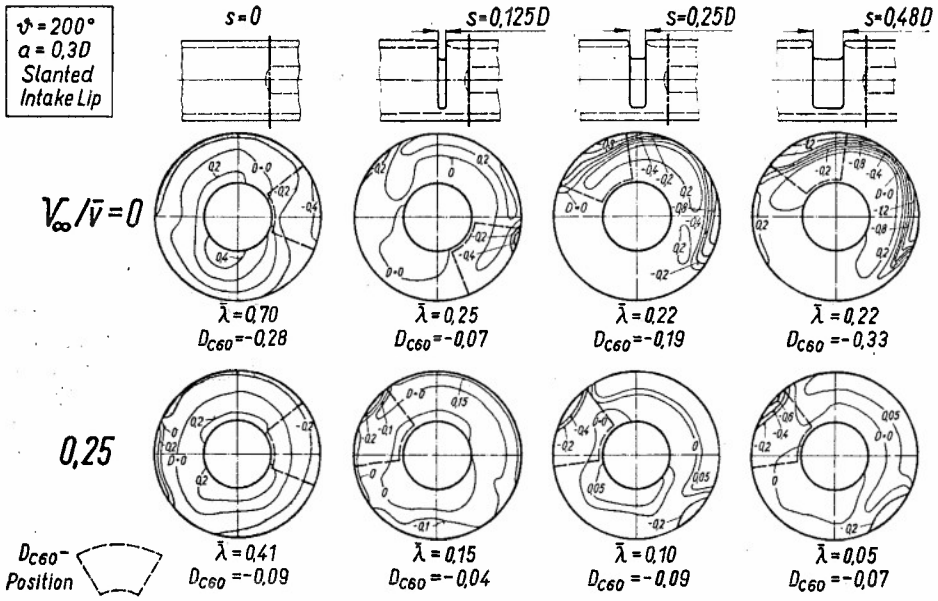


Fig. 9 Total pressure distribution. Influence of axial width.  $\alpha = 0, \beta = 0$ . Slanted intake lip

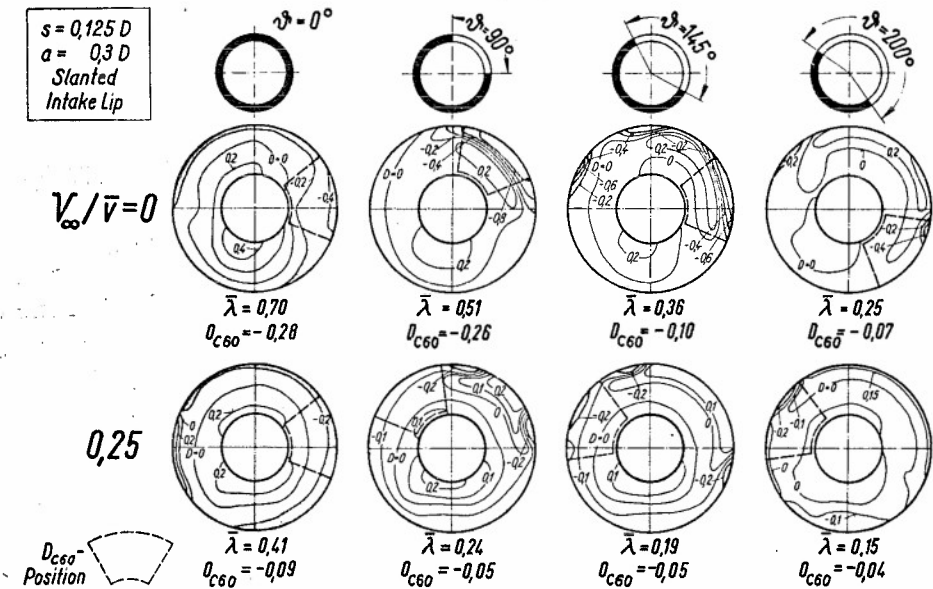


Fig. 10 Total pressure distribution. Influence of angular width.  $\alpha = 0, \beta \neq 0$ . Slanted intake lip

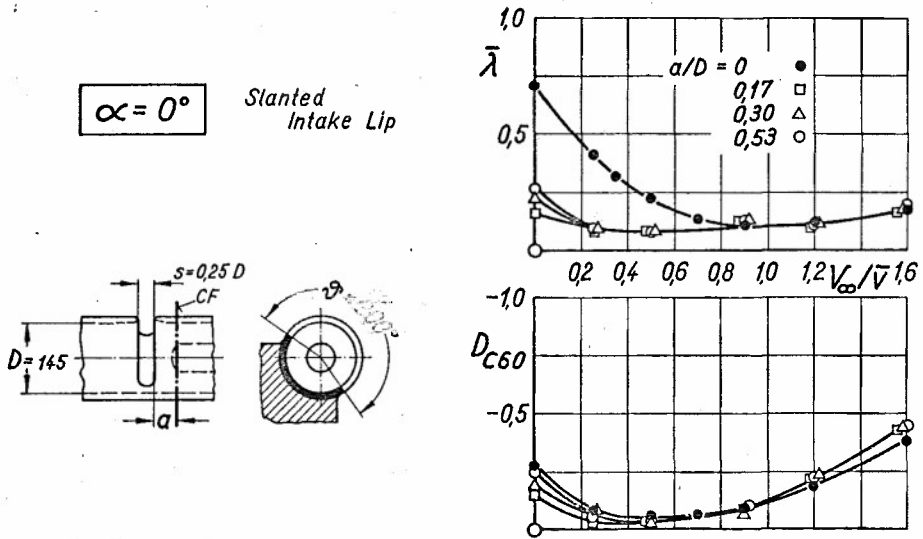


Fig. 11 Total pressure loss and distortion. Influence of distance from compressor face,  $\beta = 0$ . Slanted intake lip

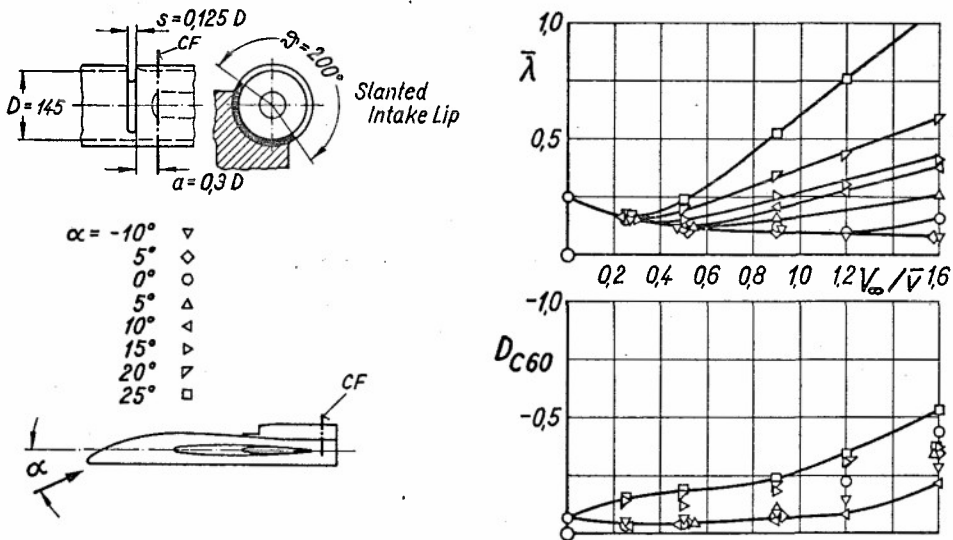


Fig. 12 Total pressure loss and distortion. Influence of incidence,  $\beta = 0$ . Slanted intake lip

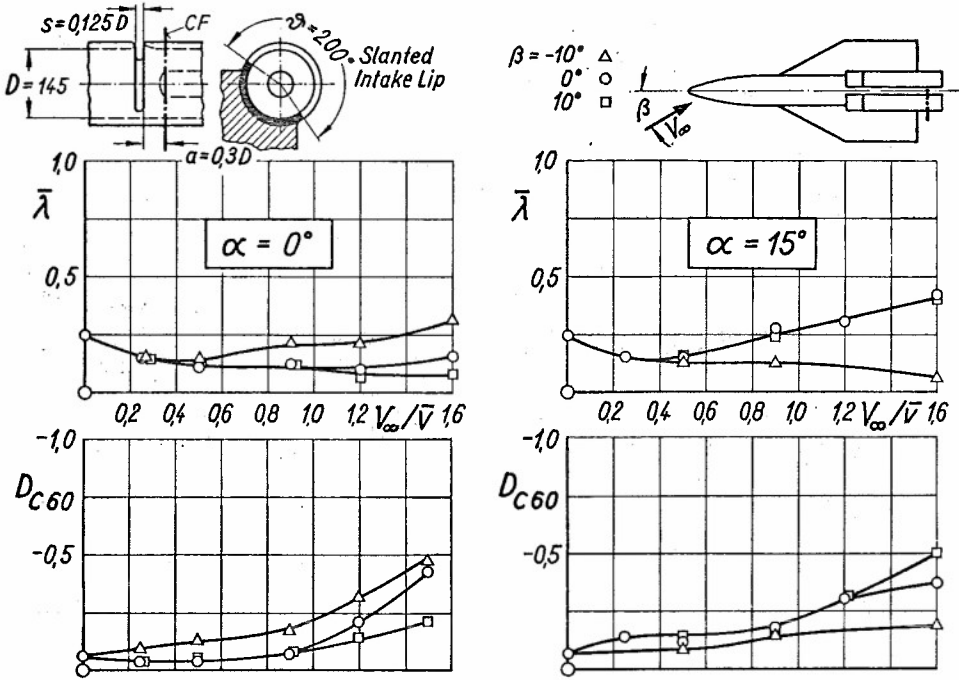


Fig. 13 Total pressure loss and distortion. Influence of sideslip.  $\alpha = 0$  and  $\alpha = 15^\circ$ . Slanted intake lip

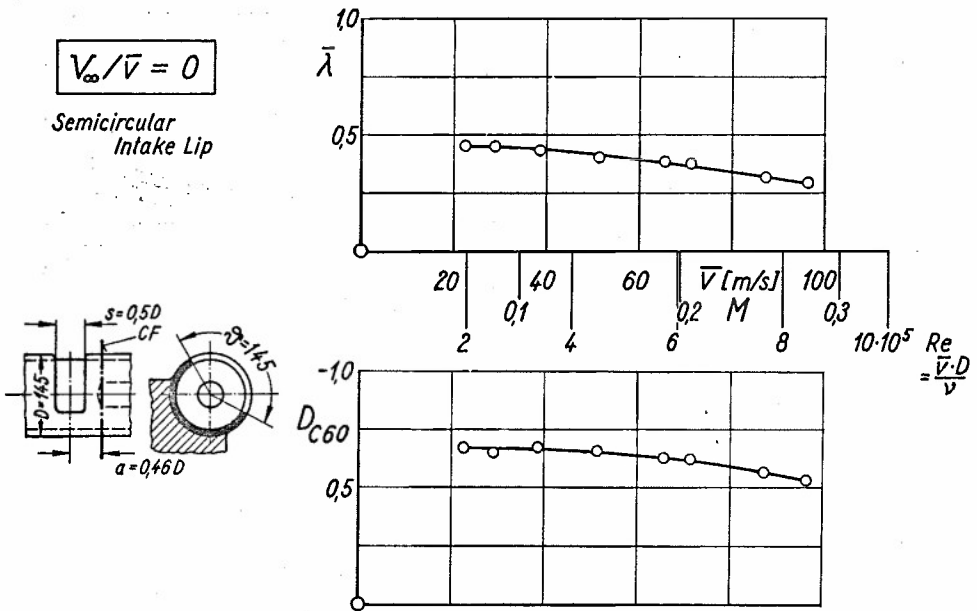


Fig. 14 Total pressure loss and distortion. Influence of mass flow. Semicircular intake lip

## APPENDIX A

## DISCUSSIONS

## LIST OF AUTHORS PRESENT AND COMMENTATORS

This Appendix in principle contains those discussions, following the presentations of papers, for which written texts for incorporation in the Proceedings were furnished by the commentators and responding authors.

Antonatos, P.P.	AF Flight Dynamics Laboratory, Wright-Patterson AFB, Ohio, USA.
Ascough, J.C.	National Gas Turbine Establishment, Pyestock, Farnborough, Hants, UK.
Ashwood, P.F.	National Gas Turbine Establishment, Pyestock, Farnborough, Hants, UK.
Becker, Dr Ing. B.	Technische Hochschule, Aachen, Germany.
Bergnan, D.	General Dynamics Corporation, Fort Worth, Texas, USA.
Bowditch, D.N.	NASA Lewis Research Center, Cleveland, Ohio, USA.
Brown, T.W.	British Aircraft Corporation Ltd, Filton, Bristol, UK.
Burcham Jr, F.W.	NASA Flight Research Center, Edwards, California, USA.
Chesters, C.M.	Rolls-Royce (1971) Ltd, Derby Engine Division, Hucknall, Notts, UK.
Cocheteux, J.B.	Centre d'Essais de Propulseurs de Saclay, Orsay, France.
Dettmering, Prof. Dr Ing. W.	Krupp GmbH, Essen, Germany.
Dunham, Dr J.	National Gas Turbine Establishment, Pyestock, Farnborough, Hants, UK.
Eibl, H.	Messerschmitt-Bölkow-Blohm GmbH, Munich, Germany.
Ellis, S.H.	Pratt & Whitney Aircraft, West Palm Beach, Florida, USA.
Ferri, Prof. A.	Aerospace Laboratory, New York University, NY, USA.
Friedrichs, Dipl. Ing. R.	DFVLR, Braunschweig-Flughafen, Germany.
Friemer, Dipl. Phys. M.	Messerschmitt-Bölkow-Blohm GmbH, Munich, Germany.
Fuhs, Prof. A.E.	Naval Postgraduate School, Monterey, California, USA.
Gallet, P.M.	Von Kármán Institute for Fluid Dynamics, Rhode-St-Genèse, Belgium.
Hardy, J.M.	SNECMA, Centre de Villaroche, Moissy-Cramayel, France.
Hasel, L.E.	NASA Langley Research Center, Hampton, Virginia, USA.
Hengst, J. van	Fokker - VFW, Schiphol-Oost, Netherlands.
Jaarsma, F.	National Aerospace Laboratory, Amsterdam, Netherlands.
James Jr, C.R.	LTV Aerospace Corporation, Dallas, Texas, USA.
Kemp, E.D.G.	Hawker Siddeley Aviation Ltd, Hatfield, Herts, UK.
Lane, R.J.	Rolls-Royce (1971) Ltd, Bristol Engine Division, Filton, UK.
Larsen, H.N.	The Boeing Company, Seattle, Washington, USA.
Ledoux, B.	ONERA, Châtillon-sous-Bagneux, France.
Lewis, W.J.	Rolls-Royce (1971) Ltd, Bristol Engine Division, Filton, UK.
Leynaert, J.	ONERA, Châtillon-sous-Bagneux, France.
Leyman, C.S.	British Aircraft Corporation Ltd, Filton, Bristol, UK.
Lotz, Dr Ing. M.	Dornier AG, Friedrichshafen, Germany.
Macchi, Dr Ing. E.	Istituto di Macchine, Politecnico di Milano, Milan, Italy.
Masure, B.	ONERA, Châtillon-sous-Bagneux, France.
McGregor, I.	Aerodynamics Department, Royal Aircraft Establishment, Bedford, UK.
Milford, C.M.	Hawker Siddeley Aviation Ltd, Kingston, Surrey, UK.
Monti, Prof. R.	Università di Napoli, Naples, Italy.
Osnaghi, Dr Ing. C.	Istituto di Macchine, Politecnico di Milano, Milan, Italy.
Paulon, J.	ONERA, Châtillon-sous-Bagneux, France.
Prechter, Dipl. Phys. H.	MTU München GmbH, Munich, Germany.
Rekos, N.F.	NASA Headquarters, Washington DC, USA.
Ripoll, J.C.	Centre d'Essais de Propulseurs de Saclay, Orsay, France.
Röed, A.E.	Saab-Scania AB, Linköping, Sweden.
Ruýgrok, G.J.J.	Technological University, Delft, Netherlands.
Sawyer, Prof. R.F.	University of California, Berkeley, California, USA.
Schaub, U.W.	Division of Mechanical Engineering, NRC, Ottawa, Ontario, Canada.
Schmitt, Ing. en Chef H.	Société Bertin et Cie, Plaisir, France.
Scholz, Prof. Dr Ing. N.	MTU München GmbH, Munich, Germany.
Schwantes, Dipl. Ing. E.	DFVLR, Braunschweig, Germany.
Smyth, Dipl. Ing. R.	VFW-Fokker GmbH, Bremen, Germany.
Stanley, R.E.	A/S Kongsberg Vapenfabrikk, Kongsberg, Norway.
Stoddart, J.A.P.	British Aircraft Corporation Ltd, Warton Aerodrome, Preston, Lancs, UK.
Surber, L.E.	AF Flight Dynamics Laboratory, Wright-Patterson AFB, Ohio, USA.
Taylor, R.P.	General Electric Co., Aircraft Engine Group, Cincinnati, Ohio, USA.
Tjonneland, E.	The Boeing Aircraft Co., Seattle, Washington, USA.
Tyler, R.A.	Division of Mechanical Engineering, NRC, Ottawa, Ontario, Canada.
Whitley, D.C.	De Havilland Aircraft of Canada Ltd, Downsview, Ontario, Canada.
Williams, D.D.	Rolls-Royce (1971) Ltd, Bristol Engine Division, Filton, UK.
Williamson, R.G.	Division of Mechanical Engineering, NRC, Ottawa, Ontario, Canada.

Discussion on the Paper  
**INLETS-AIRPLANE TESTING IN TRANSONIC WIND TUNNELS**  
 (Paper 2)  
 presented by  
 F.Jaarsma

R.Smyth

With reference to the definition of inlet drag, as shown in the thrust and drag accounting system, Figure 2 of the paper, it appears that the effects of inlet flow are assumed to be concentrated solely at the inlet itself and to have no influence on the rest of the flow around the aircraft model. As there is certainly an effect on the overall drag characteristics of the aircraft, would it not be most useful to measure the total drag of the model and determine the change of this drag due to changing inlet features, such as mass-flow ratio? In the same Figure 2, the afterbody is defined as comprising only a definite portion of the rear end of the model. Here again similar comments apply, because any change in the afterbody, to the geometric shape or the nozzles, has an effect on the pressure distribution of the whole model and thus on the total drag. Would it not be more useful to measure the total drag of the model rather than simply that of a portion?

F.Jaarsma

Of course, the total drag is measured, with the aeroforce model, with flow through nacelles, accounting for sting effects. Usually a variation in mass-flow, representing the actual mass-flow variation in flight, is applied in order to determine the influence of spillage on the total drag. However, since aeroforce models are usually too small for representative bleed, diverter and bypass simulation, due to the thick boundary layers as well as instrumentation problems, special inlet models of larger scale are required to determine the incrementals of the drag components. This technique is not ideal, mainly because of the mismatched afterbodies and necessarily neglected surfaces, but it is presently the best practical method. The shortcomings must always be kept in mind. Checks should be made to make sure that downstream mismatched surfaces do not affect the flow at the inlet, or that the effect can be accounted for, and that spillage, bleed and bypass effects on the afterbody can be determined. There is a need for simple and controllable engine simulators, such as the small turbo-driven fan simulator, to enable such tests to be done. Of course, a similar procedure is desirable for afterbody tests, when the inlets are usually closed.

A.Ferri

Adding to Mr Jaarsma's comments, usually in inlet tests the rear part of the flow field is not simulated, either because the inlet exhaust has a much larger exhaust area than the actual scale model that simulates the airplane or because the engine flow is not correctly simulated. The small variation of drag due to the variation of the mass-flow entering the inlet cannot be predicted correctly by this kind of test. Large variations of drag due to shock formation or shock-induced separation are also possible. However, such variations depend on local flow and boundary layer properties. Such quantities are not correctly simulated in wind tunnel tests, therefore better techniques are required in order to obtain good quantitative information.

D.N.Bowditch

Prof.Ferri made the comment that the variation of bypass ratio on a turbofan engine could affect the measured inlet distortion. Tests have been made at NASA Lewis Research Center utilizing two concentric cold pipes with separate plugs to simulate variation in bypass ratio. The tests were made on a mixed compression, axisymmetric inlet, at Mach numbers from 2 to 2.5. For this case, where the Mach number at the compressor face was about 0.3, negligible effect of bypass ratio was observed for circumferential and radial distortions. Distortion measurements were made about one compressor face radius ahead of the engine.

R.Smyth

How far can theoretical methods such as potential theory be used to account for the interactions mentioned?

F.Jaarsma

In the subcritical régime, especially for inlet tests and inlet fairing determination for afterbody tests, presently available numerical methods for flow-field computations taking into account compressibility can certainly be of great help in determining the effects of non-representative geometries on either upstream or downstream flow fields.

Discussion on the Paper  
**NOZZLE AND EXHAUST TESTING IN TRANSONIC FLIGHT REGIME**  
 (Paper 3)  
 presented by  
 A.E.Fuhs

**C.M.Milford**

Can you tell us how the "actual" full-scale nozzle thrust coefficient of Figure 8 of the paper was defined and measured?

**A.E.Fuhs**

For a discussion on this subject, I would refer you to AGARD Advisory Report AR-36-71 entitled "Report of the AGARD Ad Hoc Committee on Engine-Airplane Interference and Wall Corrections in Transonic Wind Tunnel Tests".

**C.M.Milford**

What progress has been made towards the inclusion of combustion in the supersonic propulsion simulator?

**A.E.Fuhs**

Due to the small size, fast-reacting gas mixtures must be used to ensure combustion within the simulator. Hydrogen burners have been developed. After a later stage, when the supersonic propulsion simulator has been developed with cold flow, there are plans to incorporate hydrogen burners. In wind tunnels, however, hydrogen is particularly dangerous.

**D.D.Williams**

Your paper discusses the work which is being done to account for and simulate the influence of the engine jet on the powerplant external flow field. I would like to ask the reverse question. What work is being done to account for the external flow field - in particular for high bypass podded turbofan engines, upstream effects on the turbomachinery?

**A.E.Fuhs**

There are articles in AIAA publications which indirectly discuss this problem. These include the papers by H.R.Welge and J.R.Orgarato, Journal of Aircraft, July 1971, and D.T.Poland and J.C.Schwanebeck, "Turbofan Thrust Determination for the CSA", AIAA 70-611.

**J.M.Hardy**

Certains expérimentateurs simulent les jets chauds par des mélanges  $H_2$ ,  $O_2$  par exemple. D'autre part, des modèles mathématiques existent en ce qui concerne les écoulements internes et de culots. Que pensez-vous de ces simulations ainsi que des avantages et des inconvénients par rapport au modèle mathématique?

**A.E.Fuhs**

Let's look at Figure 22 to see what parameters are simulated by a hydrogen peroxide exhaust. The ratio of specific heats  $\gamma$  and the ratio  $(RT_T)_j / (RT_T)_\infty$  are well matched. These are important exhaust similarity parameters. For a given nozzle pressure ratio, the Mach number of the jet is simulated. Simulation of the inviscid features of a jet are assured. Aspects, such as Mach angles, wave reflection from shear layer, acceleration from subsonic to supersonic, etc., are correctly simulated. When a viscous, thermally conducting gas is considered, the similarity parameters, such as Prandtl number, are not correctly simulated. Parameters, such as Reynolds number, may or may not be simulated depending on model scale and operating conditions. Mixing between secondary-primary and the exhaust-external streams is largely dominated by turbulent phenomena. One important mismatch is the kinetic energy per unit mass of fluid.

Now to consider the mathematical models. An inviscid model designed to give the skeleton (geometric pattern) of the flow should correctly match either hydrogen peroxide exhausts or kerosene-air exhausts since all pertinent parameters are simulated. Viscous models aimed at predicting flow separation and mixing must of necessity incorporate the similarity parameters, e.g., turbulent Prandtl number and eddy viscosity. If the prediction is for a  $H_2O_2$  jet, then the model must adjust the input data to represent a  $H_2O_2$  jet. An example is the speed of sound, which, for a given Mach number, determines the kinetic energy per unit mass of fluid. Likewise the viscous model needs to use the proper input parameters for an exhaust of kerosene-air combustion products.

Discussion on the Paper  
**PROBLEMES DE MESURE SUR MAQUETTE DE LA POUSSEE D'UN ARRIERE-CORPS  
 D'AVION SUPERSONIQUE - TUYERES DE REFERENCE**

(Paper 4)  
 presented by  
 B.Masure

A.Ferri

The last chart presented indicates that the parameter investigated is  $P_J/P_S$ . However, when  $\frac{\Delta X}{\phi(A_J)}$  is large, then mixing is important. Then the premixing is controlled by  $\frac{\rho_J V_J}{\rho_S V_S}$  and therefore  $T_J/T_S$  becomes an important parameter.

B.Masure

Le problème n'est pas simple. Pour transposer au cas réel les résultats obtenus en gaz froid, on doit tenir compte non seulement des effets de mélange mais aussi de la forme du jet primaire qui est sensible à la valeur de  $\gamma$ . Des éléments de réponse sont donnés dans la communication No.11, planche 15.

Discussion on the Paper  
**INLET-ENGINE-NOZZLE WIND TUNNEL TEST TECHNIQUES**

(Paper 7)  
 presented by  
 D.N.Bowditch

C.M.Milford

Can you explain the differences in Figures 25 and 26? Thus, why is the critical distortion level different in the two cases? Why are the delay times from the occurrence of high instantaneous distortion to the moment of stall, substantially different - 19 msec in one case and 6 msec in the other?

D.N.Bowditch

During distortion testing on the J85 engine, the variation of the exhaust nozzle area was used to force the compressor to operate at different pressure ratios, thereby varying the stall margin at each condition. Therefore, the critical value of the stall margin parameter was different for each operating point. The reason for the different delay times is not known at present.

J.Dunham

The problem of surges induced by dynamic inlet distortions must be cured either by designing the compressor to accept them or by designing the intake not to generate them. As a compressor specialist, I would prefer the latter. Do you regard this as practicable - can an intake be provided with separation-fixing devices to eliminate unsteady distortion? If so, would the resulting steady distortion be an improvement or would the engine still surge?

D.N.Bowditch

The inlet can be modified so that it will provide less dynamic distortion in much the same way that steady-state distortion is improved. However, the improved boundary layer control by bleeding or vortex generators or added inlet length usually have an accompanying penalty of increased weight or drag. The analysis of dynamic distortion primarily provides a tool to determine the necessary inlet improvements with their accompanying penalties required to ensure stable inlet engine operation.

D.D.Williams

Have you derived correlations of loss of surge margin with both steady, time-averaged, spatial distortion and with instantaneous distortion coefficient? If so, are the correlations the same?

D.N.Bowditch

No attempt has been made to correlate separately the instantaneous distortion data. However, as mentioned in the paper, for twelve stall cases studied, ten cases exhibited instantaneous distortions whose distortion parameter exceeded the value required to cause stall under steady-state screen test conditions. Since the compressor could be expected to respond to a distortion in one quarter to a full revolution or a particle transient time, the response time would be expected to be in the one to four millisecond range. Therefore, while the use of a steady-state stall margin parameter may not be the entire answer, it certainly recognizes the major property of the compressor face flow that is ignored in the steady-state or the time-averaged distortion approach.

Discussion on the Paper  
**WIND TUNNEL TESTING OF V/STOL ENGINE MODELS –  
 SOME OBSERVED FLOW INTERACTION AND TUNNEL EFFECTS**  
 (Paper 8)  
 presented by  
 R.G.Williamson

A.E.Fuhs

How much is the data of Figure 7 influenced by the tunnel walls? What are the practical consequences of the vortex illustrated in Figure 6 – would this reduce foreign object damage in the engine?

R.A.Tyler and R.G.Williamson

The data of Figure 7 were obtained with single nozzles located at heights near 10 nozzle diameters above the floor and centred between vertical side walls separated by 15 diameters. In these circumstances neither the floor boundary layer (thickness  $\approx d/2$ ) nor the presence of the side walls is thought to have had significant influence on the stagnation positions plotted in Figure 7, particularly on impingement stagnation position and the special case represented by incipient stagnation. (In the vortex régime, however, the side walls undoubtedly affect the course of the rolled up vorticity, and hence flow conditions at model height.) In particular, the incipient stagnation conditions of Figure 7 should apply reasonably well to aircraft flight at appropriate ground distances, and (in representing the limiting conditions for forward flow, relative to the aircraft, of the ground deflected jet) may have practical bearing on problems relating to engine ingestion of hot gases and jet borne foreign objects.

Discussion on the Paper  
**VECTORED THRUST IN AIR COMBAT**  
(Paper 9)  
presented by  
C.R.James Jr

R.G.Williamson

Do you feel that the full potential of vectored thrust was realized in the simulated combat missions? It seems possible that optimum reactions and tactics might take some time to develop. Thus, was there evidence that the pilots' scores tended to improve during the course of the tests?

C.R.James Jr

Adequate practice and orientation periods were provided so that the pilots were well up on the learning curve prior to beginning the scoring runs. I doubt that additional runs would have produced significantly different results. I do feel, however, that these results warrant further studies to include such factors as thrust losses with deflection angle, engine dynamics, trim changes, and aerodynamic characteristic changes induced by thrust deflection.

R.Monti

How is the thrust vectoring actually accomplished by the pilot? Is there any link or coupling between thrust vectoring control and main stick?

C.R.James Jr

Thrust vectoring is accomplished by moving a control lever adjacent to the throttle, using the left hand. Full aft position gives +100° thrust deflection — nozzle exit down. No coupling between the thrust vector control and the stick was considered in these tests; such a scheme could be readily evaluated in the simulator to establish relative advantages.

J. van Hengst

Is it one of the future objects in this simulator study to investigate to what extent trim changes due to thrust deflection and centre of gravity shift in combat counteract the gain in combat performance due to thrust vectoring? What is the comparison with current fighter aircraft using manoeuvring flaps?

C.R.James Jr

In reply to your first question, these effects would be totally configuration dependent and such tests could be readily performed once the input data on aerodynamic characteristics were determined. These are the sort of tests envisioned in the recommendations section of the paper. To your second question, no comparison has been made with manoeuvring flaps; however, the manned simulator would provide an excellent means for making such comparisons.

R.Smyth

To what extent were the dynamic characteristics of the powerplant simulated, such as acceleration and after-burner schedules which are time-dependent? Were intake pressure losses due to changes in angle of attack and sidewind taken into account?

C.R.James Jr

There was no dynamic simulation of the powerplant and intake. Steady-state engine performance was assumed, with thrust and specific fuel consumption as functions of the throttle angle and flight parameters.

Discussion on the Paper  
**AERODYNAMICS OF THRUST REVERSER DESIGN**  
 (Paper 10)  
 presented by  
 W.J.Lewis

A.E.Fuhs

What is the influence of external flow – was this investigated?

W.J.Lewis and H.Prechter

During the particular series of tests presented in the paper, no study was made with the external flow represented.

R.Smyth

In Figure 15(b) of the paper, showing the nett vertical load as a function of bucket rotation, I am surprised to see a negative vertical load with the bucket in a non-rotated position. Was the configuration asymmetric?

W.J.Lewis and H.Prechter

Yes, there was a difference between the upper and lower buckets in that the lip heights were different.

Discussion on the Paper  
**INFLUENCE DE QUELQUES PARAMETRES CARACTERISTIQUES  
 SUR LES PERFORMANCES DES EJECTEURS**  
 (Paper 11)  
 presented by  
 J.M.Hardy

A.E.Fuhs

Referring to Figure 10 of the paper, does the loss of performance due to eccentricity require special manufacturing tolerances for nozzles?

J.M.Hardy

Dans le cas d'une tuyère primaire convergente et pour des  $\mu > 5\%$ , on peut tolérer des excentrations de l'ordre de 5% du diamètre du convergent. Ces tuyères n'ont donc besoin d'aucune précaution particulière de centrage. Dans le cas d'une tuyère primaire convergente-divergente, Figure 11, nous n'avons aucune expérience sur ce point.

Discussion on the Paper  
**SOME APPLICATIONS OF BOUNDARY-LAYER CONTROL BY  
 BLOWING TO AIR INLETS FOR V/STOL AIRCRAFT**  
 (Paper 12)  
 presented by  
 I.McGregor

R.Friedrichs

How was the local velocity in the compressor face, utilized in the parameter DV, measured? The total pressure probes will give exact values, but static pressure probes are very sensitive to the flow direction, making the determination of the local velocity very difficult.

I.McGregor

I agree that static pressure probes are very sensitive to flow direction. For calculating the velocities, a mean static pressure was used. This was determined from eight static tappings around the periphery of the compressor face. There was very little circumferential variation of static pressure, but the possibility of some radial variation could not be excluded.

P.P.Antonatos

Was the averaging procedure time-weighted or space-weighted?

I.McGregor

An area-weighted procedure was used.

D.N.Bowditch

In the paper, you show results for the effect of blowing on installed thrust. Have you also investigated the effect of blowing on a parameter such as specific fuel consumption?

I.McGregor

This aspect is being investigated by another organization, but I cannot quote any results.

C.M.Milford

In answer to comments, on a straight momentum analysis, it can be shown that both suction and blowing boundary layer control systems are detrimental to installed overall thrust-minus-drag. It would be preferable to let the boundary layer enter the engine. Under some conditions, however, this can result in excessive distortion, rendering some form of boundary layer control necessary. As mentioned in the paper, the effect of spillage drag must be allowed for; with blowing, the inlet airflow is less than the engine airflow, whereas with suction the converse is the case. For a V/STOL airplane, the inlet size may be fixed by the VTO case so that it cannot be optimized for cruise; in such a case, the reduction in spillage drag is sufficient to make the suction boundary layer control system superior to the blowing system in thrust-minus-drag. It should also be pointed out that the suction system described in the paper is not representative of the full-size airplane which has a more complex boundary layer control system and also has multiple auxiliary inlets which operate automatically when required. In addition to permitting the use of increased engine airflow, these modifications substantially reduce the distortion at high angles of attack.

The use of boundary-layer blowing in the air intake of a V/STOL strike fighter was, in fact, proposed by Bore<sup>12,13</sup> and tested by Hawker Siddeley Aviation Ltd, in parallel with the development of the suction bleed system. It is surprising that this earlier work was not referenced by the author in his paper describing the complementary testing at R.A.E.

#### REFERENCES

12. Bore, C.L. *Blowing Quantities Required for Low-Energy Boundary Layer Blowing.* Hawker Siddeley Aviation Ltd, (Kingston), P.O.N. 948 (1965).
13. Bore, C.L. *Boundary Layer Control in the P.1127 Air Intake.* Hawker Siddeley Aviation Ltd, (Kingston), P.O.N. 945 (1965).

D.D.Williams

In response to further comment, the aircraft was originally configured with a boundary layer diverter. However, due to the particular requirements of a single-engine V/STOL installation — thrust centre close to the aircraft centre of gravity and a large intake throat area for high VTO intake efficiency — problems arise due to the relatively high pre-entry flow retardation plus local diffusion on the highly-curved intake duct sidewall. These considerations require that the diverter be pushed forwards and separation tends to occur on the top surface of the diverter splitter. Attempts to increase diverter height/boundary layer thickness ratio aggravate the duct turning problem. Optimization studies led to the selection of a suction bleed system. This development took place before the work on blowing discussed in the present paper.

Discussion on the Paper  
 SOME ASPECTS OF PROPULSION FOR THE AUGMENTOR-WING CONCEPT  
 (Paper 13)  
 presented by  
 D.C. Whittley

H. Schmitt

Les travaux de développement de concepts de portance assistée utilisant des systèmes à dilution, ont, semble-t-il, débuté en Europe.

Il y eut, tout d'abord, la réalisation en Allemagne, en 1943, de l'avion ARADO 232 dans lequel le système d'aspiration — soufflage de la couche limite était alimenté par une trompe à vapeur à haute pression.

Ensuite, l'ONERA (Office National de Recherches Aéronautiques), dès sa fondation en 1945, en France, entreprit des études sur un système d'aspiration — soufflage compact; le dispositif original était alimenté par de l'air comprimé prélevé au refoulement du compresseur d'un turboréacteur, procédé lui aussi utilisé pour la première fois. La Figure 1 représente ces deux principes d'application des trompes au problème de soufflage — aspiration. Description Figure 2. M. Poisson-Quinton faisait état, dès septembre 1948, au Congrès International de Mécanique appliquée, à Londres, les résultats obtenus avec cette aile à volet double aspiré — soufflé: les résultats étaient traduits au moyen d'un coefficient sans dimension original,  $C_{\mu}$ , représentatif de la quantité de mouvement dépensée dans l'opération.

Le dispositif a fait l'objet d'essais sur maquette grandeur de l'avion SO 6020, puis a été appliqué sur l'avion prototype Bréguet Vultur muni d'un turbopropulseur et d'un turboréacteur.

La Figure 3 représente l'avion "Vultur" et la coupe transversale du système installé à l'arrière de la voilure.

L'avion présentait des qualités de vol très intéressantes. Malheureusement le turboréacteur d'appoint qu'il comportait initialement fut supprimé lors de l'évolution du projet et, avec lui, la source d'air comprimé utilisée pour le fonctionnement du système d'aspiration — soufflage.

En 1959, la Société BERTIN proposa le système aile — trompe dont le principe de base va vous être présenté sur la Figure 4.

Le canal formé entre les deux volets mobiles à braquage variable est adapté à la phase de vol à considérer et réalise, en position déployée, le mélangeur — diffuseur de la trompe; l'injecteur est lui-même mobile pour orienter convenablement le jet moteur.

En position normale pour le vol de croisière, les volets rétablissent le profil de l'aile. Toutefois, une fente peut-être ménagée au bord de fuite par laquelle s'échappe le flux moteur alors propulsif. Cette disposition en profil tronqué avec soufflage est favorable du point de vue de la traînée.

Ce dispositif constitue une trompe destinée à augmenter la poussée avec soufflage au bord de fuite d'une quantité de mouvement supérieure à celle du jet moteur; l'aspiration à la cassure du profil a un effet de puits qui augmente l'hypercirculation autour du profil.

La Figure 5 représente des résultats obtenus sur maquettes essayées en 1959 à la Soufflerie de Cannes de l'ONERA.

Le braquage du couple de volets est  $\alpha_v = 30^\circ$ . Pour des angles de braquage plus élevés, la portance continue de croître.

Ces résultats ont permis d'établir des projets d'avions STOL déjà très intéressants en 1959-1960.

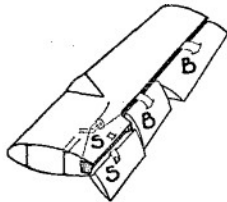
Malheureusement, dans le début des années 60, l'objectif décollage court ayant été écarté par les services officiels en faveur de l'objectif décollage vertical, ce programme fut abandonné.

Il subsistait évidemment des problèmes de canalisation de gaz conduisant à utiliser une pression de soufflage élevée et à limiter le débit de soufflage. Toutefois, grâce aux techniques de dilution développées depuis lors, on peut envisager des progrès sensibles à venir dans un nouveau développement de ce concept.

D.C. Whittley

It is most encouraging to be reminded again of work which has been carried out on other systems which, like the augmentor-wing, also use the principle of "suction by blowing" — that is to say, the generation of a suction source for boundary layer control by means of a propulsive jet. This serves to reinforce the view that it is an important principle. That is why, in my presentation, I took time to describe some of the aerodynamic advantages which result from this, even though this subject matter was not contained in the written paper.

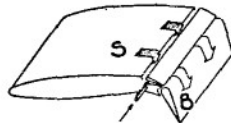
## COMBINED SUCTION AND BLOWING WITH EJECTOR SYSTEMS for boundary-layer control.



ARADO METHOD  
(Wagner. 1943)

Applications :

- \* ARADO 232  
(Walter chemical ejector).
- \* CESSNA 309.
- \* CHASE 123 D.  
(Aspin turbojet)



ONERA METHOD  
(1947)

Patent ONERA/SNCASO  
1952

Applications :

- \* SO.6020 (1949).
- \* BREGUET "VULTUR"  
(Flight: 1956).

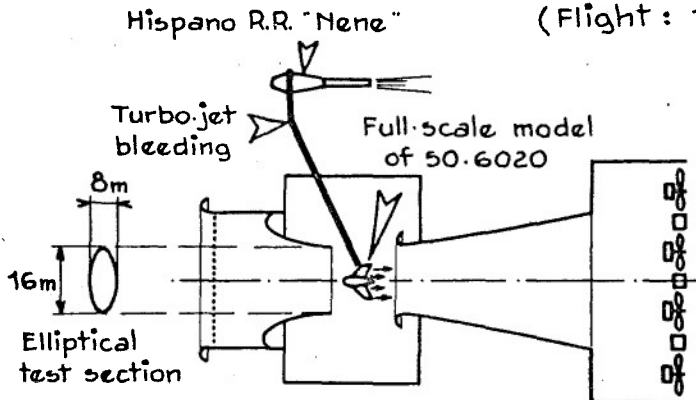


Figure 1

# BREVET D'INVENTION.

Gr. 6. — Cl. 4.

N° 952.926

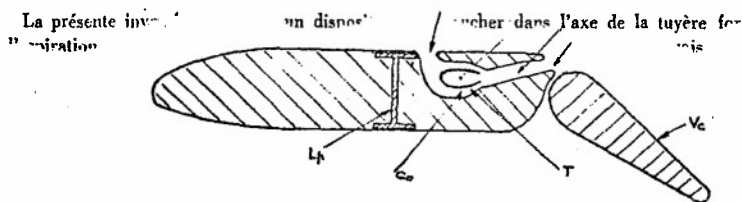
Dispositif d'aspiration et soufflage combinés sur un profil d'aile par l'intermédiaire d'une trompe à induction. (Invention : Philippe Poisson-Quinton.)

OFFICE NATIONAL D'ÉTUDES ET DE RECHERCHES AÉRONAUTIQUES résidant en France (Seine).

Demandé le 31 juillet 1947, à 10<sup>h</sup> 40<sup>m</sup>, à Paris.

Délivré le 16 mai 1949. — Publié le 28 novembre 1949.

[Brevet d'invention dont la délivrance a été ajournée en exécution de l'art. 11, § 7, de la loi du 5 juillet 1844 modifiée par la loi du 7 avril 1902.]



RÉPUBLIQUE FRANÇAISE

MINISTÈRE  
DE L'INDUSTRIE ET DU COMMERCE

SERVICE  
de la PROPRIÉTÉ INDUSTRIELLE

# BREVET D'INVENTION

Gr. 6. — Cl. 4.

N° 969.264

Perfectionnements aux dispositifs d'aspiration et de soufflage combinés sur un profil d'aile par l'intermédiaire d'une trompe à induction. (Invention : Philippe Poisson-Quinton.)

SOCIÉTÉ NATIONALE DE CONSTRUCTIONS AÉRONAUTIQUES DU SUD-OUEST et OFFICE NATIONAL D'ÉTUDES ET DE RECHERCHES AÉRONAUTIQUES résidant en France (Seine).

Demandé le 17 juillet 1948, à 10<sup>h</sup> 40<sup>m</sup>, à Paris.

Délivré le 17 mai 1950. — Publié le 18 décembre 1950.

Il est connu d'augmenter la portance des ailes tant aux dites sections terminales par des déflecteurs, que par des sections secondaires telles que les ailes en sautoir, etc. en

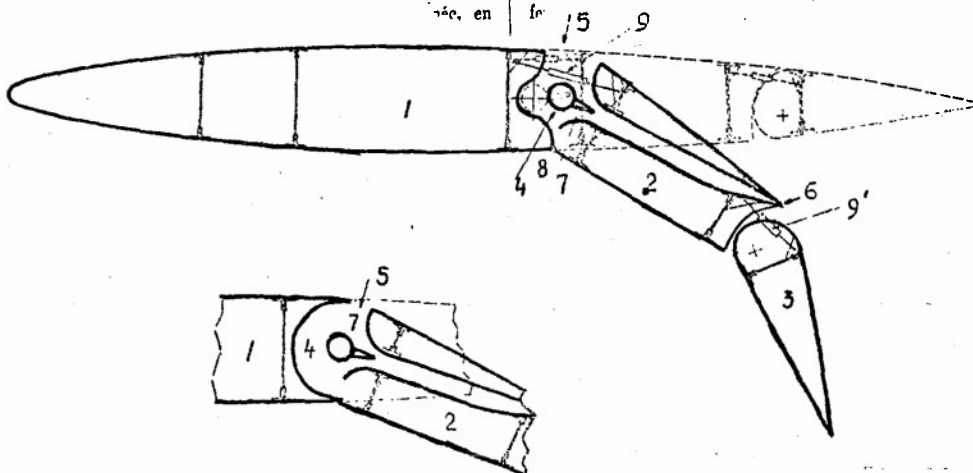


Figure 2

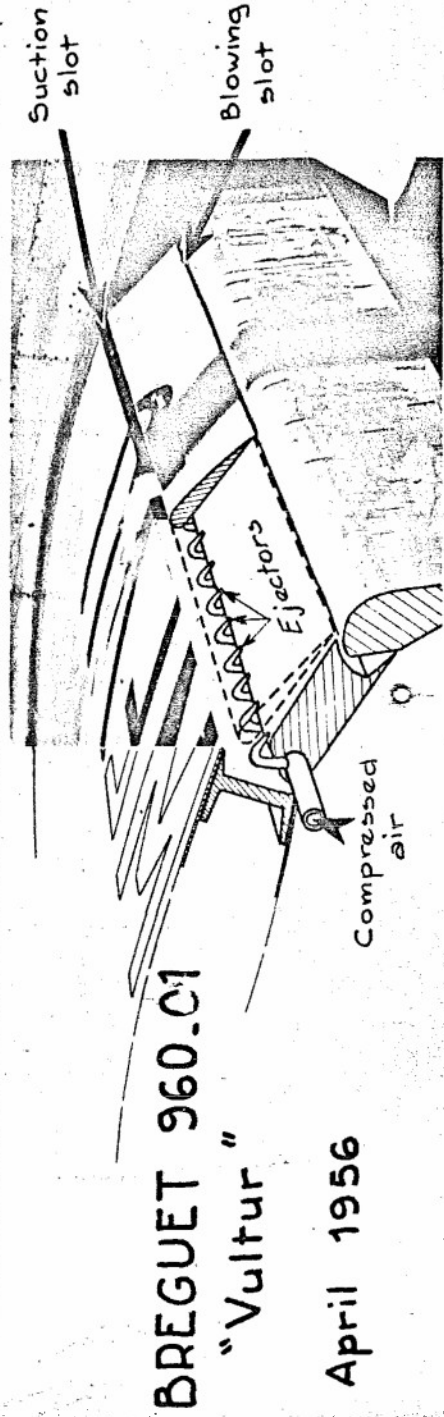
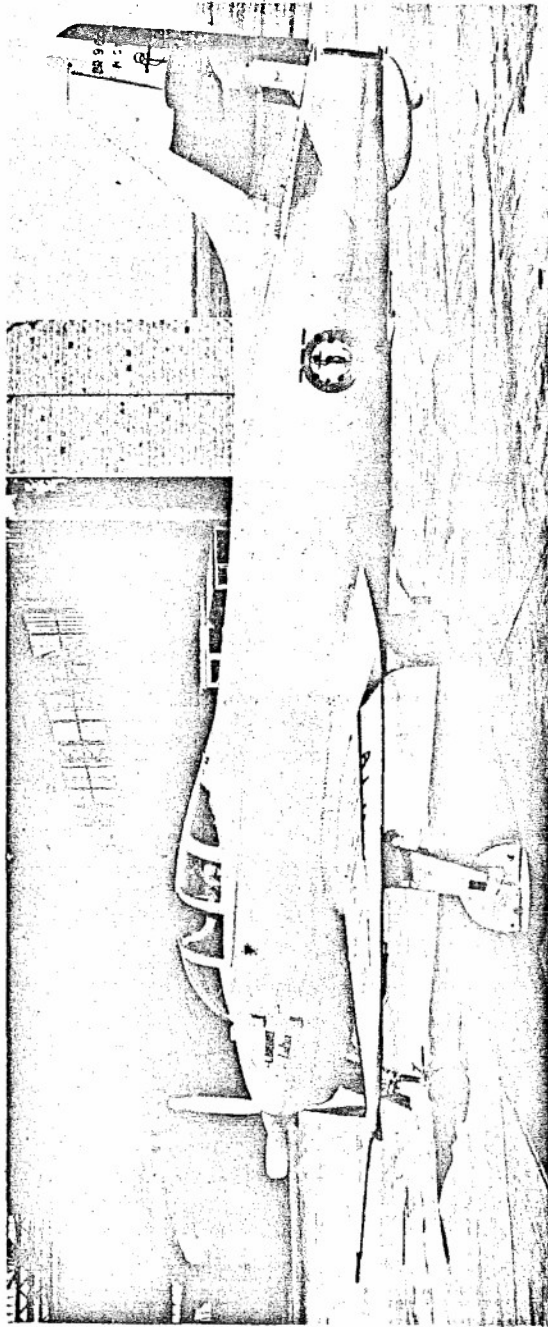


Figure 3

RÉPUBLIQUE FRANÇAISE  
 —  
 MINISTÈRE DE L'INDUSTRIE  
 —  
 SERVICE  
 de la PROPRIÉTÉ INDUSTRIELLE

# BREVET D'INVENTION

P.V. n° 793.209

N° 1.233.014

Classification internationale :

B 24 c

Perfectionnements aux trompes destinées en particulier à la sustentation des aérodynes.

SOCIÉTÉ BERTIN ET C<sup>ie</sup> résidant en France (Seine).

Demandé le 24 avril 1959, à 19 heures, par poste.

Délivré le 2 mai 1960. — Publié le 12 octobre 1960.

(Brevet d'invention dont la délivrance a été ajournée en exécution de l'article 11, § 7, de la loi du 5 juillet 1844 modifiée par la loi du 7 avril 1902.)

Les trompes comportent généralement des diffuseurs formés de parois matérielles divergentes placées autour du ou des jets inducteurs. Il en est ainsi également dans le cas des trompes à divergent

la construction la plus avantageuse des trompes.

La description qui va suivre en regard du dessin annexé, donné à titre d'exemple non limitatif, fera bien comprendre comment l'invention peut être réalisée, les particularités qui ressortent tant que du dessin faisant, bien que de l'invention.

N° 1.233.014

Société Bertin et C<sup>ie</sup>

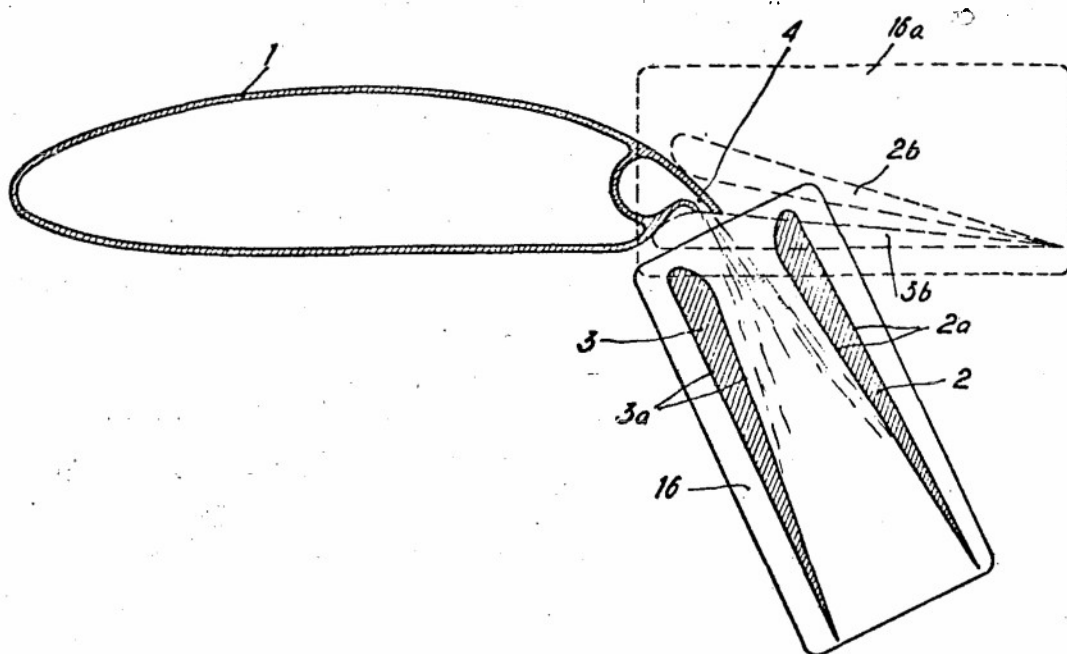


Figure 4

# TWO-DIM TESTS OF BERTIN T.E. EJECTOR in the S<sub>1</sub> Cannes/ONERA wind-tunnel (october 1959)

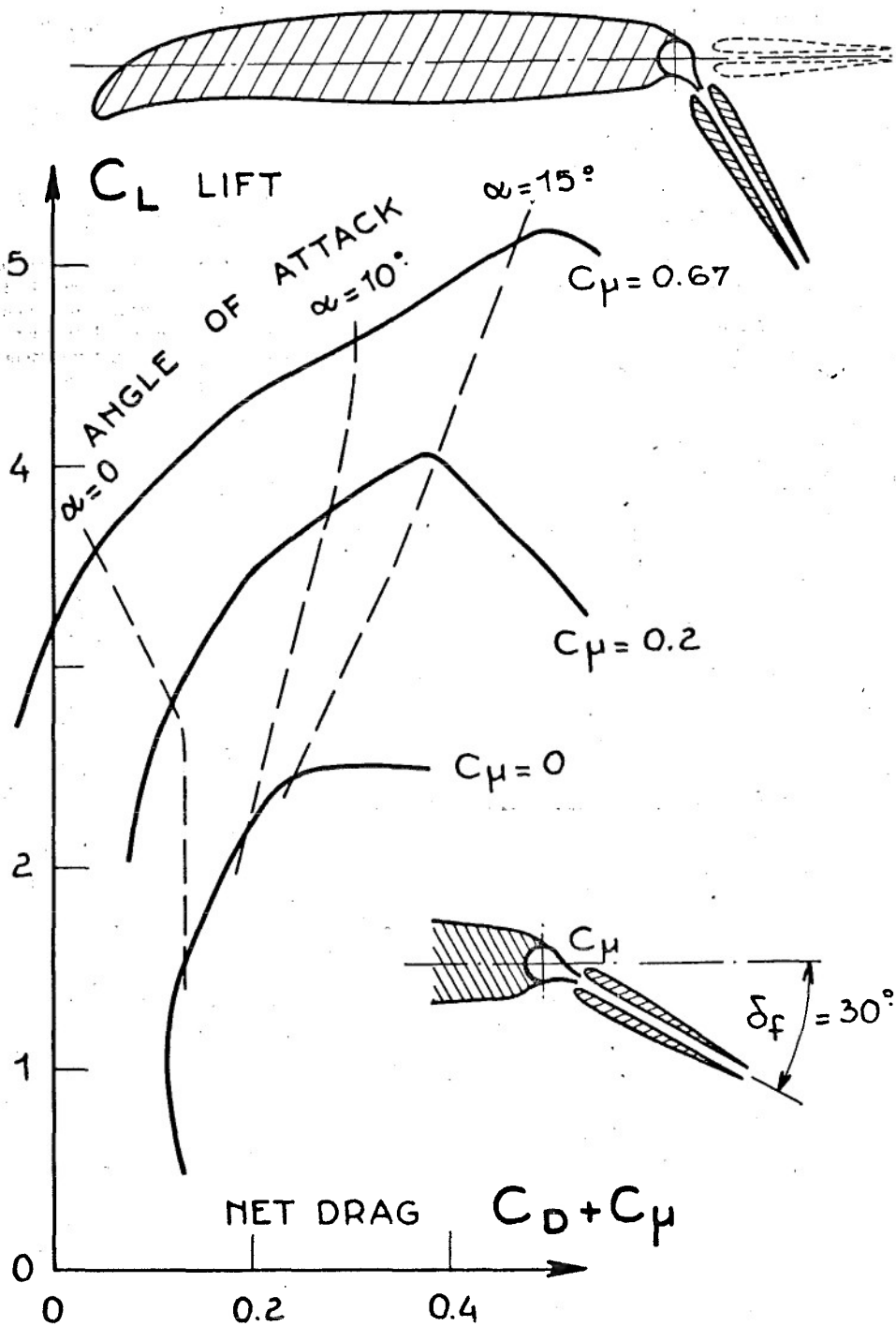


Figure 5

Discussion on the Paper  
**RAPID MIXING NOZZLES FOR V/STOL APPLICATIONS**

(Paper 14)  
 presented by  
 C.M.Chesters

R.Monti

Have you compared a conventional type nozzle plus augmentor tube to the geometry depicted in Figure 11 of your paper?

C.M.Chesters

Yes. The major difference lies in the length of augmentor tube required to achieve a given degree of mixing and hence augmentation. This length is greatly reduced when a rapid mixing nozzle is used, relative to that using a conventional convergent nozzle.

Discussion on the Paper  
**FLOW DISTORTION AND PERFORMANCE MEASUREMENTS  
 ON A 12" FAN-IN-WING MODEL FOR A RANGE OF  
 FORWARD SPEEDS AND ANGLE OF ATTACK SETTINGS**

(Paper 17)  
 presented by  
 U.W.Schaub

E.D.G.Kemp

Transient intake pressure distortions have been shown in preceding papers to be of overriding importance for conventional propulsion engines. Although single-stage low pressure-ratio lift fans are very tolerant to flow distortion, some proposed lift fan engines have their gas generator intakes in the hub of the fan. These gas generator compressors presumably could be sensitive to transient distortions. Have you, therefore, made measurements of transient flow distortions in the intake of your 12" fan?

U.W.Schaub

Some continuous pressure recordings were made, primarily for the purpose of monitoring the behaviour of the leading lip boundary layer under continuously varying simulated transition manoeuvres. However, these data cannot be used to assess possible transient distortion effects since the pressure lines connecting pressure orifices with transducers introduced unknown impedance effects.

The experimental programme was intended to shed light on the fundamental flow distortion problems, as they relate to a typical shallow lifting fan. No attempt has been made so far towards considering more specialized variants of lifting fan installations such as, for example, configurations featuring hub-contained gas generators.

Depending on bypass ratio there is of course some evidence to suggest that the hub-mounted gas generator should really experience a much more favourable inflow environment than it would enjoy if it were not in the fan aligned and accelerated flow field. To start with, there would be much less velocity distortion in the hub-mounted inlet to the gas generator, and there would probably also be much less total pressure distortion. Any transient intake pressure distortions therefore would be less apt to drive the compressor into stall since actually less surge margin is required to accommodate the spatial distortion.

Discussion on the Paper  
**DESIGN, DEVELOPMENT AND TESTING OF A  
 SUPERSONIC TRANSPORT INLET SYSTEM**

(Paper 18)  
 presented by  
 E.Tjonneland

**A.E.Fuhs**

What was the Mach number at the engine face? Did operation unstarted at  $M = 1.6$  give significant drag?

**E.Tjonneland**

At Mach 2.7 cruise, the engine face Mach number was approximately 0.3, while at transonic speed the engine face Mach number increased to about 0.5. At Mach 1.6, unstarted or started recovery was almost the same and very little bypass drag was experienced in either case. Thus, little would be gained by starting the intake at lower Mach numbers. In fact, to do so would only complicate the bleed system and control system design to cover a wider started operating range.

Discussion on the Paper  
**FREE-JET TESTS OF A FULL-SCALE SUPERSONIC  
 INTAKE/ENGINE COMBINATION**

(Paper 19)  
 presented by  
 P.F.Ashwood

**S.H.Ellis**

Figure 10 shows four methods of inducing engine surge. Methods 1, 2 and 4 modify the inlet conditions to increase distortion. Method 3 increases the engine nozzle area. Does method 3 induce surge by driving the inlet supercritical or does it rematch one of the compressors towards the surge line?

**P.F.Ashwood**

Increasing the engine nozzle area whilst maintaining the LP spool speed constant causes the HP spool to run slower so that the running point moves up the LP compressor characteristic until the engine surges. Slight changes in the engine airflow do occur during these excursions into surge, but they are insufficient to result in any significant change in the inlet distortion pattern.

**C.M.Milford**

Figure 12 shows surge points occurring at nearly constant Mach number rather than at constant  $DC_{60}$ . Could this be due to the onset of transient distortions as Mach number increases, and was the instrumentation capable of detecting such transient distortions?

**P.F.Ashwood**

It has been observed that in general the amplitude of the inlet total pressure fluctuations increases with the steady-state distortion index,  $DC_{60}$ . It is likely, therefore, that this was the case in the tests referred to in Figure 12, but the instrumentation fitted at the time the tests were made did not permit this to be confirmed by direct measurement.

Discussion on the Paper  
CONCORDE POWERPLANT DEVELOPMENT  
(Paper 20)  
presented by  
C.S.Leyman

D.N.Bowditch

You mentioned that Concorde had experienced several engine stalls at Mach numbers above 1.7. What happened to the adjacent engine at this time and what was the resulting aircraft manoeuvre?

C.S.Leyman

Above about Mach 1.8, surge will give some degree of interaction on the adjacent engine. This ranges from rough running to surge according to the conditions. Such rough running or surging disappears when the primary cause is removed. It is virtually unknown on Concorde to have engine flame-out as a result of surge. The aircraft response is particularly mild. In the worst case encountered so far, with two engines on the same side in surge, the aircraft manoeuvre was only 2° bank and 1° degree of sideslip. This is indicated in the paper.

Discussion on the Paper  
CONTROL CONCEPT AND WIND TUNNEL TESTING OF  
A SUPERSONIC INTAKE CONTROL SYSTEM  
(Paper 21)  
presented by  
H.N.Larsen

F.W.Burcham Jr

Do you have a rudder interconnect to control yaw in case of an outboard engine unstart?

H.N.Larsen

For normal intake unstart, where the engine continues to operate with the intake in the unstarted - buzz suppression - mode, the answer is no. For an intake unstart which is concurrent with an engine malfunction, such that the engine does not continue to operate and provide thrust during unstarted intake operation, a high sensed airplane lateral acceleration signal coupled with the outboard intake unstart signal is used to initiate opposite outboard intake unstart and corrective rudder movement. This balances the yawing forces on the airplane.

Discussion on the Paper  
JET EFFECTS ON BOATTAIL PRESSURE DRAG AT SUPERSONIC SPEEDS  
(Paper 23)  
presented by  
J.A.P.Stoddart

D.N.Bowditch

The data the correlation is based on is probably from isolated data with uniform well-behaved boundary layers. Have you compared your results with any flight or aircraft configuration data where less uniform boundary layers are present?

J.A.P.Stoddart

No, I have not used any data derived from flight test measurements, but the twin jet installation referred to in the paper had non-uniform onset boundary layers caused by supports and empennage. This data fitted in well with the axisymmetric data.

A.Ferri

I find the work described very interesting, because it represents an approach in which all the basic physical phenomena can be taken into account. The boattail drag is affected by the separation controlled by the boundary layer shock interaction. The data used in the paper are valid only for the case where the outside flow and inside flow have approximately the same stagnation conditions. However, additional experimental information could be generated for the case where these quantities are different. Such an approach could be extended to take into account the effect of boundary layer thickness and hence Reynolds number.

J.A.P.Stoddart

I have tried to produce a rapid method of estimating the effects of a propulsive jet on supersonic pressure drag from some of the available test data. If the phenomenon is judged to be worthy of further study, then more sophistication must be introduced. The principles of doing this type of calculation by interactive, iterative flow field methods are known, but the resulting procedures are quite formidable and, at the present time, are probably no more accurate than the simple methods presented here.

F.Jaarsma

Do you think that for an actual nozzle installation in the aircraft flow field, including boundary layers from the tail-planes and wings, you could arrive at a similar method of predicting afterbody performances by, for example, shifting the  $C_{D\beta AS} - C_{pbc}$  origin in Figure 1(e)?

J.A.P.Stoddart

If the basic flow model is correct, then the short answer to your question is - yes. One of the configurations included is a twin jet model carrying fin and tailplane and the data from this model fits the general correlation as well as any of the other models. This suggests that the effects of a non-uniform boundary layer thickness around the model do not introduce serious discrepancies.

D.D.Williams

In view of the potential importance of the work described, if I understand it correctly, the contention is that designing fully expanded convergent-divergent nozzles for supersonic performance may not be really worthwhile - I would like to ask whether you have made sensitivity calculations around the correlation curve, in order to attempt to account for individual configurations within the scatter band - each of which presumably contributes a result in its own right?

J.A.P.Stoddart

I have made no sensitivity analyses of the type you suggest. However, looking back to the original experimental data sets considered, a very strong impression is formed that convergent nozzles in boattailed afterbodies always produce drag reductions over the range of pressure ratios usually tested. In contrast, convergent-divergent or ejector nozzles produce such benefits only outside the range of pressure ratios of current interest. The effect is primarily a function of the external flow deflection generated by the jet. Indeed, it was this strong impression which led me to perform the analysis in the first place.

Discussion on the Paper  
**FLIGHT INVESTIGATION OF STEADY-STATE AND  
 DYNAMIC PRESSURE PHENOMENA IN THE  
 AIR INLETS OF SUPERSONIC AIRCRAFT**

(Paper 24)  
 presented by  
 F.W.Burcham Jr

**L.Leynaert**

Vous avez mis en évidence un phénomène à Mach 2 entretenu par une structure d'écoulement d'entrée semblant présenter deux états d'équilibre possibles. Avez-vous étudié ce phénomène dans les essais d'entrée d'air en soufflerie, sans moteur?

**F.W.Burcham Jr**

No, we have not, because the wind tunnel model does not have sufficient high-response instrumentation to study this phenomenon. It would, however, be interesting to see if resonance could be found in a scale model.

**A.Ferri**

I am interested in the resonance phenomenon between afterburner and flow. Such an effect indicates an interaction between engine and inlet. Have you attempted any analysis that takes into account the combustion rates and the two-dimensional flow at the compressor face?

**F.W.Burcham Jr**

Other than the simple analysis in the paper, we have not done anything on afterburner combustion. Reference 16 of the paper discusses afterburner combustion instability, but does not consider distortion effects in the incoming flow.

**J.Dunham**

Do instantaneous  $K_D$  measurements on a small-scale intake model, without the engine present, agree with such measurements in flight tests of the complete installation?

**F.W.Burcham Jr**

No instantaneous  $K_D$  measurements have been made on wind tunnel models of the F-111 inlet. However, there has been a program on an RA5-C aircraft, in flight and on 1/4 and 1/8 scale models, which are described in the following paper 25. The results show fair agreement between the flight data and the 1/4 scale results, but poorer agreement between the flight and 1/8 scale results.

**I.McGregor**

Arising from the previous question, in Figure 12 of your paper you show a comparison between flight and tunnel results for the pressure recovery, but only flight results for  $K_D$ . Was there a relatively much greater difference between flight and tunnel results for this factor than for pressure recovery?

**F.W.Burcham Jr**

The wind tunnel distortion data were not presented in the form of the  $K_D$  factor and hence could not be included in Figure 12. There was a significant discrepancy between flight and tunnel distortion factor

$$\frac{P_{t \max} - P_{t \min}}{P_{\text{average}}}$$

because of boundary layer ingestion in the flight test that did not occur on the model.

D.D. Williams

What is the experience regarding the occurrence of turbulence and high instantaneous distortion on subsonic round lip intakes at incidence? How potent is duct length in attenuating intake-induced turbulence and unsteady distortion?

F.W. Burcham Jr

I don't know of any work on turbulence and instantaneous distortion on a truly subsonic inlet, because most subsonic problems have been solved using low-response instrumentation. The separation phenomena occurring at high incidence angles have been studied in our F-111 tests for both the sharp and more rounded cowl lips. The results will be available in the near future. Duct length was a very significant factor in attenuating turbulence in the very long XB-70 duct, as described in Reference 2 of the paper. Mr Gordon C. Oates of Pratt and Whitney Aircraft recently presented an AIAA paper describing the decay of turbulence and this should be a good reference.

H.N. Larsen

I believe that Ross Willoh has shown, in his small perturbation analysis of inlet ducts, that the damping ratio of an inlet duct is a function of the pressure recovery versus mass-flow ratio of the inlet. Have you attempted to correlate the duct resonances measured on the F-111 inlet duct with Willoh's analysis?

F.W. Burcham Jr

No, but it appears that it would be appropriate to do so.

A.E. Fuhs

In the analysis of inlet periodic pressure fluctuations, it is necessary to specify the boundary conditions at the compressor face. In addition, it is necessary to specify shock wave response to pressure waves, including the influence of boundary layer. Your analysis does not recognize phase shifts due to the boundary conditions. In view of the good correlation between theory and experiment that your paper shows, it would appear that precise definition of the boundary conditions at shock and compressor is not necessary — do you agree?

F.W. Burcham Jr

It appears that a simple analysis, neglecting precise definitions of boundary conditions, is suitable for determining the resonant frequency. However, I am sure that the boundary conditions would be important in any amplitude or flow effects calculations.

Discussion on the Paper  
SUPERSONIC INLET PERFORMANCE AND DISTORTION  
DURING MANOEUVRING FLIGHT

(Paper 25)  
presented by  
L.E. Surber

F. Jaarsma

Could you quote figures on repeatability of, for example, steady distortion patterns? What about hysteresis?

L.E. Surber

I have no figures to offer, but repeated tests gave what we considered to be good repeatability of steady-state total pressure recovery, distortion indices, and average RMS levels of turbulence. Basic maps of steady-state distortion were also reproduced reasonably well.

D.D. Williams

Following the recommendations outlined in the paper, might I ask what is the position of Wright-Patterson AFB on the formal need for testing to determine dynamic distortion. Bearing in mind the length of duct, position of intake etc., would you consider that dynamic distortion measurements are required always, or some of the time, or maybe not at all?

L.E. Surber

There has been no formal statement of policy from any organization on Wright-Patterson AFB, but I do believe that the counsel of both the Flight Dynamics and Aero Propulsion Laboratories at Wright-Patterson AFB would be to employ dynamic pressure instrumentation in the development of turbine engine propulsion systems for any supersonic aircraft or near sonic highly manoeuvrable aircraft. Such instrumentation should be sufficient to obtain compressor face total pressure distortion maps at least to the frequency for which engine response may be anticipated.

D.N. Bowditch

In Figure 20 of your paper, you show a basic shift in the distortion pattern with inlet scale. Did you reproduce the subsonic diffuser lines in each inlet, including any duct curvature?

L.E. Surber

Internal contours of the three ducts are exact, scaled replicas, as are the fore bodies ahead of the inlets. Also, the compressor hub geometry and pressure instrumentation locations at the compressor face are identical for all three test articles.

C.M. Milford

Further to the previous comments on Figure 20 of the paper, did the models have sufficient instrumentation to identify where the differences in flow distribution were originating - from the forebody, or within the duct?

L.E. Surber

No. Very little instrumentation was installed in the subsonic duct of the flight test aircraft, making it impossible to make a conclusive judgement. The suggested reasons for the differences in the compressor face total pressure maps seemed the most reasonable explanation consistent with the few forebody and duct static pressure measurements available.

R. Smyth

Do you have any information concerning the distortion levels in the compressor entry plane due to drastic curvatures and flow-area changes of the intake ducts, which are sometimes necessary due to undercarriage space? Were the flow angles at the intake entry plane measured on models with or without the corresponding intakes?

L.E. Surber

Experience in the subsonic diffuser program mentioned in the paper indicated that total pressure recovery performance of diffusers with small offset bends can be comparable to that obtained from straight ducts. On the other hand, offset bends greater than one inlet throat height substantially reduce regions of high pressure at the exit. Pressure loss, flow distortion, and turbulence have been shown to increase with diffusion ratio (engine-to-throat area ratio).

Reference: MacMiller, C.J., "Investigation of Subsonic Duct Distortion", AFFDL TR-69-71, March 1971.

Inviscid flow fields were mapped with a remotely actuated rake of five conical probes. Figures 2 and 5(a) indicate the actual data points in the survey matrix. Due to the size of the rake mechanism, it was not possible to have inlets in position. Also, final inlet design was deferred until the fuselage flow fields had been defined.

Discussion on the Paper  
**INLET-ENGINE COMPATIBILITY ANALYSIS**  
 (Paper 26)  
 presented by  
 S.H.Ellis

H.N.Larsen

Would you please comment on the different distortion indices:  $\Delta P/P$ ,  $K_D$ ,  $DC_{60}$ .

S.H.Ellis

$\Delta P/P$  describes only the pattern intensity. This is not sufficient information for a distortion index unless the pattern shape is also described. For this reason, the distortion index used in this paper has been normalized to a pattern shape of a 180 degree square wave.  $K_D$  is a circumferential distortion index that includes pattern intensity, the extent of the low pressure region and gives more weight to low pressure areas near the hub. I believe  $DC_{60}$  correlates data using the 60 degree segment that has the lowest pressure. Mr Williams of Rolls-Royce can give you a better description of  $DC_{60}$ .

There are many distortion indices, at least one for each engine, each with its own set of units, each correlating data for one engine. Also, successive distortion factors tend to be more complicated because additional terms have been added to correlate new pieces of data. The US Air Force Aero Propulsion Laboratory has recognized that confusion over distortion indices has reached the danger point. They are looking for a distortion factor format which will work for all engines and still be easily understood. We have been supporting them in their studies: progress has been very encouraging and I believe we will see a universal distortion factor in the near future.

H.N.Larsen

Would you please discuss the different filtering techniques – analog versus digital, and the filtering time constants.

S.H.Ellis

For analog filtering we pass the individual inlet pressures through a third order, linear phase, low pass filter with a cut-off frequency corresponding to engine rotor speed. We can obtain the same filter characteristics using digital filtering by averaging the pressures over a time period corresponding to 1/3 of an engine revolution.

After data has been passed through an analog filter, the digitizing rate can be reduced by a factor of five. Consequently it is cheaper to use an analog filter unless the effects of several filter characteristics are being evaluated.

D.D.Williams

As a comment on a question from Mr Larsen (Boeing) the  $DC_{60}$  parameter was derived from correlations of tests of steady distortion on turbomachinery. No direct evidence relating to dynamic distortion on this basis is available at present so that the choice A cut-off frequency in high response data reduction has not arisen.

U.W.Schaub

To what do you attribute the fact that the compressor had so much tolerance to circumferential distortion? Was it because the rotor blades were designed to operate at negative incidence under undistorted flow conditions?

S.H.Ellis

In the example of a stability audit shown on Figure 16, circumferential distortion had a small effect on the compressor because most of the distortion was attenuated by the fan. In this case the rotor was not designed to operate at negative incidence under undistorted flow conditions. As you noted in your question matching lower on the choke side of the compressor characteristic (lowering the rotor incidence) will give better distortion tolerance at the expense of weight and performance.

U.W.Schaub

In view of the fact that compressor blades really cannot react instantaneously to unsteadiness in the main flow what use do you make of high response data away from surge conditions?

S.H.Ellis

High response data measurements at surge conditions are normally taken on an engine or compressor when time variant distortion is produced by an inlet simulator. In these tests the engine inlet data is filtered to account for the fact that the compressor blades cannot react instantaneously to unsteadiness in the main flow. High response instrumentation is also used to identify the stage initiating surge. Other high response measurements, taken at non-surge conditions, are used to evaluate movement of the engine operating line. For example, measurement of the pressure pulse due to augmentor ignition. One very important use for high response instrumentation at nonsurge test conditions is to define the engine-inlet interface during model inlet tests or during combined engine and inlet tests so we can simulate the correct environment during engine testing. From this interface data we use the maximum time variant distortion to determine the effect of distortion on surge line, inphase oscillations to determine the effect of the interface conditions on the transient operating line and the average time variant distortion to determine the effect of distortion on engine rematch and engine performance. It is interesting to note that the average level of time variant distortion is of the order of 10 percent higher than the distortion measured by steady state probes.

J.Dunham

When conducting steady distortion tests on an engine, you have explained that you find that one of the available distortion parameters (e.g.  $\Delta P/P$ ,  $K$ ,  $DC_{50}$ ) correlates the data best. If you now do unsteady distortion tests, do you find the same parameter still correlates the data?

S.H.Ellis

Our data bank contains three engines for which the respective distortion parameters correlate both time variant distortion and distortion produced by inlet screens. We have no cases where we have not obtained the same correlation. However, the data sample is so small that engines should always be checked for tolerance to time variant distortion after a suitable level of distortion tolerance has been developed using inlet screens.

J.Dunham

Is it true that the cure for an unsteady distortion problem in a compressor must necessarily increase the steady-state undistorted surge margin too?

S.H.Ellis

We have always found that an improvement in steady distortion tolerance also improves the tolerance to unsteady distortion; but I do not think the improvements will always be the same magnitude.

J.Dunham

For contractual purposes a target distortion level must be chosen, to which both the inlet designer and the engine designer must work. Have you evolved a philosophy for choosing a "reasonable" target?

S.H.Ellis

My philosophy for choosing a target distortion level is first of all to define adequate interface instrumentation and then to delay choosing a target level until both the inlet and engine people have sufficient information. The inlet information required includes scale model inlet tests, using high response instrumentation, that cover the required range of operating conditions (Mach number, angle of attack, angles of yaw and sideslip and mass flow ratio). Also, if possible, inlet testing should include the effects on performance and distortion of varying inlet bleed, inlet length and inlet location. The engine information should include test data on the sensitivity of components to distortion and Reynolds number, estimates of the effects of transients and component interactions on stability and trade studies between distortion tolerance and performance. This is sufficient information for an airplane system study to choose the best level of distortion for the airplane.

R.J.Lane

I wish to draw attention to the conclusions in Figure 1 of the written paper. These tend to increase the weight and length of engines and reverse recent trends. In order to remain competitive greater emphasis will be placed on high turbine temperatures.

S.H.Ellis

It is true that most of the items that improve stability also increase engine weight and length. Some items, such as low stage loading, also reduce performance. This is also true of the inlet: most approaches to reduce inlet distortion increase inlet length, increase weight or reduce performance. These trades between stability, weight, size and performance add more dimensions to the systems trades which are made during a preliminary design of a new airplane. Fortunately, as noted in your comment, improvements in materials and technology have enabled us to reduce weight and increase performance while satisfying increasingly severe stability requirements.

R.J.Lane

Would you please comment on the best position of bleed from the gas generator:

- (a) for a single spool gas generator,
- (b) for a 2 spool gas generator.

S.H.Ellis

Bleed helps the stability of compression stages in front of the bleed and hurts the stages behind it. For a single spool gas generator the best place to bleed for stability is at the rear of the compressor, the best place for performance is as far forward as possible. The bleed location is therefore a compromise between performance and stability. For a two spool gas generator an inter-spool bleed may be required during transients to prevent back pressuring the low spool due to transient mismatch between high and low rotor speed.

A.E.Fuhs

If you form the following non-dimensional quantity

$$\frac{\left\{ \begin{array}{l} \text{filter} \\ \text{cut-off} \\ \text{frequency} \end{array} \right\} \left\{ \begin{array}{l} \text{blade} \\ \text{chord} \end{array} \right\}}{\left( \begin{array}{l} \text{axial} \\ \text{velocity} \end{array} \right)}$$

what value would this quantity have?

S.H.Ellis

The value of this non-dimensional quantity used in our current analysis of inlet data is 0.44; where the filter cut-off frequency is defined as the 3 db attenuation point.

At the present time we do not change the filter cut-off frequency for either small changes in blade chord or axial velocity, as would be expected from this non-dimensional quantity. Inclusion of the axial velocity term would require filter changes as the inlet flow changed. This would force us from analog filtering to digital filtering and increase our processing cost. It is also interesting to note that the maximum time variant distortion is not very sensitive to filter characteristics: changes in cut-off frequency in the order of 20 percent do not have an appreciable effect on the maximum time variant distortion.

We presently vary filter characteristics with an acoustic scaling law based on engine face diameter. This gives the same scale effect as your non-dimensional quantity for geometrically similar compressors. The blade chord of your non-dimensional quantity may be a more correct dimension.

Discussion on the Paper  
ON THE APPLICATION OF A TIME DEPENDENT TECHNIQUE IN  
TRANSONIC DOUBLE FLOW NOZZLE SOLUTIONS

(Paper 27)  
presented by  
E. Macchi

D.N. Bowditch

In your paper, all the examples have rather shallow angles on the walls. Can you solve the problems with larger wall angles and how would that affect computer time?

E. Macchi

In our method, there are no limitations to wall angles, provided that the computational mesh is spaced closely enough to prevent difficulties in numerical interpolations. Since we found that perturbations on the boundaries must be induced very slowly, the computer time will increase with increasing wall angles, if the initial condition of straight boundary walls is considered.

J.M. Hardy

Combien de temps dure le calcul sur machine pour un cas en double flux?

E. Macchi

As we pointed out in the introduction to our paper, the computing time represents the main obstacle to the application of this method. The computing time exceeded one hour of UNIVAC 1103 for the aforementioned case of a double-flow nozzle. However, we are re-writing the computer program, and we feel that proper modifications will considerably drop the computing time.

Discussion on the Paper  
REPARTITION DES VITESSES A L'ENTREE D'UN  
COMPRESSEUR SUPERSONIQUE

(Paper 28)  
presented by  
B. Ledoux

R. Smyth

Have you tried to make use of the principles of electrical analogy for rotation-symmetrical flows in order to obtain preliminary results for the flow problems?

B. Ledoux

Non, parce que l'analogie électrique ne peut rendre compte correctement des phénomènes de compressibilité intervenant à des nombres de Mach hautement subsoniques.

Discussion on the Paper  
**ETUDE THEORIQUE ET EXPERIMENTALE DE LA CO-EXISTENCE  
 DE DEUX FLUX DANS UN CANAL DE SECTION CONSTANTE**

(Paper 31)  
 presented by  
**J. Paulon**

**D.D. Williams**

One of the problems in ejector design for systems applications is to know the so-called "cut-off pressure ratio" i.e. the conditions governing transition from subcritical to supercritical operations. Not a lot of data appears to be available in the literature. The conditions are in general a function of ejector area ratio, secondary/primary flow and overall pressure ratio. As a result of your work, which I suppose would have to be extended to include regions downstream of the secondary throat, do you consider that theoretical methods can be used for this estimate or do we have to rely on experimental results?

**J. Paulon**

La région en aval du second col est très difficile à étudier car l'écoulement y est extrêmement turbulent.

**J.M. Hardy**

La forme de la ligne sonique que vous présente a une allure conforme à ce qui est pris dans le calcul des éjecteurs. En effet, si dans le calcul en fluide non visqueux le fait de considérer l'écoulement secondaire non-dimensionnel conduit à des surfaces isovitesses planes, la superposition de la correction de viscosité qui fait passer la vitesse dans la zone de mélange de la vitesse de l'écoulement secondaire à la vitesse de l'écoulement primaire quand on passe d'une frontière à l'autre, conduit bien à des surfaces isovitesses non planes en particulier pour la ligne sonique.

Je crois que le recouplement satisfaisant avec la théorie uni-dimensionnelle est dû à l'importance du débit secondaire plus de 20%, pour des débits plus faibles de l'ordre de 5% il serait moins bon.

Le calcul de la position du col sonique que vous nous avez fait suppose que l'écoulement sortant de la tuyère primaire est uniforme — ce qui n'était peut-être pas le cas. L'écart de position trouvé peut-être être imputé à ce fait.

**J. Paulon**

Il est exact que la théorie uni-dimensionnelle marche moins bien pour des débits secondaires très faibles.

En ce qui concerne la position du col sonique, il s'agit d'une interprétation globale qui s'est toujours bien vérifiée. Une analyse plus fine, prenant en compte l'écoulement réel en sortie de tuyère conduirait peut-être à un meilleur recouplement entre l'expérience et la théorie.

**E. Schwantes**

Have you corrected the measurement error due to turbulence in the mixing-zone?

**J. Paulon**

La pression statique mesurée dans la zone de mélange n'a pas été corrigée. Il est précisé dans le texte que cette pression est certainement sujette à caution en raison des importants gradients de pression existants dans cette zone. Une correction serait effectivement nécessaire mais difficile à évaluer.

Discussion on the Paper  
WIND TUNNEL INVESTIGATIONS OF A SUPERSONIC AIR INTAKE  
WITH VARIOUS AUXILIARY INTAKES AT LOW SPEEDS

(Paper 35)

presented by  
R.Friedrichs

R.Smyth

In the investigations described, the maximum intake mean velocity was of the order 95 m/sec, corresponding to a Mach number of about 0.25. The intake Mach number of a jet engine under maximum take-off conditions, however, may be around 0.5. Have you carried out tests to determine the effects of such intake Mach numbers? Do you consider such results would have an influence on the results of the present investigations?

H.Eibl and R.Friedrichs

The tests reported in this paper have been performed only up to intake Mach numbers 0.3 due to the limited performance of the suction system. Just recently a new more powerful vacuum blower has been installed, enabling us to carry out inlet tests at Mach numbers up to 0.5. Some comparable tests performed up to Mach numbers 0.5 showed the same general tendency as those reported in this paper, so that the final results of the first set of investigations remain valid.

Additionally it should be mentioned that the accomplished investigations have to be regarded as comparative tests, mainly to point out the different influences of the various geometries of the auxiliary intakes.

## PROPULSION AND ENERGETICS PANEL

**Chairman:** Professor I. Glassman  
Guggenheim Laboratories  
Princeton University  
Princeton, NJ 08540, USA.

**Deputy Chairman:** Mr F. Jaarsma  
National Aerospace Laboratory (NLR)  
Sloterweg 145  
Amsterdam 17, Netherlands.

## Belgium

Professor J. Chauvin  
Von Kármán Institute for Fluid Dynamics  
72 Chaussée de Waterloo  
1640, Rhode-St-Genèse, Belgium.

Professor J. Ducarme  
Université de Liège  
Institut de Mécanique  
75 rue du Val Benoît  
Liège, Belgium.

Major d'Aviation R. Jacques  
Ecole Royale Militaire  
30 Avenue de la Renaissance  
1040 Bruxelles, Belgium.

Professor A. Jaumotte  
Institut de Mécanique Appliquée  
Université Libre de Bruxelles  
50 Avenue F.D. Roosevelt  
1050 Bruxelles, Belgium.

Professor E. Tits  
Laboratoire de Chimie Appliquée  
Ecole Royale Militaire  
30 Avenue de la Renaissance  
1040 Bruxelles, Belgium.

## Canada

Mr R.A. Reynolds  
Office of Science and Technology  
Department of Industry  
112 Kent Street - Tower B  
Ottawa 4, Ontario, Canada.

Dr R.B. Whyte  
Fuels and Lubricants Laboratory  
Division of Mechanical Engineering  
National Research Council  
Ottawa 7, Ontario, Canada.

## Denmark

Professor Dr Bjørn Qvale  
Laboratoriet for Energiteknik  
Polytekniske Laereanstalt  
Lundtoftevej 100 (Bygning 403B)  
2800 Lyngby, Denmark.

Professor K. Refslund  
Afdelingen for Fluid Mekanik  
Polytekniske Laereanstalt  
Lundtoftevej 100 (Bygning 404)  
2800 Lyngby, Denmark.

## France

Monsieur M.L. Barrere  
ONERA  
29 Avenue de la Division Leclerc  
92 Châtillon-sous-Bagneux, France.

Monsieur J.F. Chevalier  
SNECMA  
Centre d'Essais de Villaroche  
77 Moissy-Cramayel, France.

M. l'Ingénieur en Chef M. Pianko  
Service Technique Aéronautique  
4 Avenue de la Porte d'Issy  
75 Paris 15ème, France.

Monsieur J. Surugue  
Directeur, Energie et Propulsion  
ONERA  
29 Avenue de la Division Leclerc  
92 Châtillon-sous-Bagneux, France.

## Germany

Prof. Dr Ing. W. Dettmering  
Mitglied des Vorstandes der Friedr. Krupp GmbH  
43 Essen  
Altendorf Str. 103, Germany.

Prof. Dr Ing. N. Scholz  
MTU München GmbH  
8 München 50  
Postfach 50 06 40, Germany.

## Greece

Brig. Gen. A. Pavlidis  
State Aircraft Factory  
Old Phaleron  
Athens, Greece.

Lt Colonel C. Sotiropoulos  
Research and Development Directorate (RDD)  
Air Force Command  
Holargos, Athens, Greece.

**Italy**

Professor C.Casci  
Direttore del CNPM  
Piazza Leonardo da Vinci 32  
20133 Milano, Italy.

Professor D.Dini  
Università degli Studi  
Istituto di Macchine  
Via Diotisalvi 3  
56100 Pisa, Italy.

Colonel L.Giorgieri  
Ministero Difesa Aeronautica  
DGAAS - 1° REP 2° Div.  
Viale Università 4  
00100 Roma, Italy.

Dott.Ing.G.Maoli  
Vice Director FIAT  
DA-Uff. Tecnico Motori Avio  
Corso Marche 41  
10100 Torino, Italy

Professor R.Monti  
Via Posillipo 405/b  
Napoli, Italy.

Prof.Dott.G.Salvatore  
Istituto di Propulsione Aerospaziale  
Via Bradano 28/A  
00199 Roma, Italy.

**Netherlands**

Mr. F.Jaarsma  
(See under Deputy Chairman).

**Norway**

Mr S.E.Høst  
NDRE  
Division for Weapons and Equipment  
PO Box 25  
N-2007 Kjeller, Norway.

Mr. T.Krog  
Director  
NDRE  
PO Box 25  
N-2007 Kjeller, Norway.

Mr R.J.Mowill  
Kongsberg Vapenfabrikk  
N-3600 Kongsberg, Norway.

**Turkey**

Major Ibrahim Keskin  
Hava İkmal Bakin Merkezi  
Kayseri, Turkey.

Professor H.Sezgen  
Mechanical Engineering Department  
Orta Doğu Teknik Üniversitesi  
Ankara, Turkey.

**United Kingdom**

Dr J.Dunham  
NGTE  
Pyestock  
Farnborough, Hants  
England

Mr R.J.Lane  
Rolls-Royce (1971) Ltd  
Bristol Engine Division  
PO Box 3, Filton  
Bristol BS12 7QE  
England

**United States**

Mr R.T.Alpaugh  
RD and Eng. Directorate  
US Army Materiel Command  
Department of the Army  
Washington DC 20315, USA.

Professor A.Ferri  
Director, Aerospace Laboratory  
New York University  
177th Street and Harlem River  
Bronx, New York 10453, USA.

Professor A.E.Fuhs  
Department of Aeronautics  
Naval Postgraduate School  
Code 57 Fu, Monterey  
California 93940, USA.

Professor I.Glassman  
(See under Chairman).

Mr Calvin B.Hargis Jr  
Deputy for Development  
Office of the Assistant Secretary of the  
Air Force for R & D  
Washington DC 20330, USA.

Dr H. von Ohain  
Chief Scientist  
Aerospace Research Laboratories (OAR)  
Wright-Patterson AFB  
Ohio 45433, USA.

Mr Nelson F.Rekos  
Acting Deputy Director (Code RL)  
Aeronautical Propulsion Division (OART)  
NASA Headquarters  
Washington DC 20546, USA.

Mr E.C.Simpson  
Chief, Turbine Engine Division  
AF Aero Propulsion Laboratory (TB)  
Wright-Patterson AFB  
Ohio, 45433, USA.

## APPENDIX B

## AGARD PROPULSION AND ENERGETICS PANEL

CATEGORY I PUBLICATIONS — PUBLISHED FOR SALE THROUGH COMMERCIAL OUTLETS: LIMITED NUMBERS OF COPIES PURCHASED BY AGARD AND DISTRIBUTED TO NATIONAL DISTRIBUTION CENTRES LISTED ON BACK COVER.

- No AGARD serial number — "Selected Combustion Problems — Fundamentals and Aeronautical Applications". Combustion Colloquium, Cambridge University, England, December 1953. Butterworths Scientific Publications, London, 1954.
- AGARDograph 4 — "Spontaneous Ignition of Liquid Fuels" by B.P.Mullins. Butterworths Scientific Publications, London, 1955.
- AGARDograph 7 — "Introduction to the Study of Chemical Reactions in Flow Systems" by S.S.Penner. Butterworths Scientific Publications, London, 1955.
- AGARDograph 8 — "Theory of Combustion INstability in Liquid Propellant Rocket Motors" by Luigi Crocco and Sin-I Cheng. Butterworths Scientific Publications, London, 1956.
- AGARDograph 9 — "Combustion Researches and Reviews 1955". Combustion Panel Meetings, Scheveningen, Netherlands, May 1954, and Paris, November 1954. Butterworths Scientific Publications, London, 1955.
- No AGARD serial number — "Selected Combustion Problems II — Transport Phenomena; Ignition; Altitude Behaviour and Scaling of Aeroengines". Combustion Colloquium, Liège, Belgium, December 1955. Butterworths Scientific Publications, London, 1956.
- AGARDograph 15 — "Combustion Researches and Reviews 1957". Butterworths Scientific Publications, London, 1957.
- AGARDograph 27 — "Air Intake Problems in Supersonic Propulsion". 11th AGARD Combustion and Propulsion Panel Meeting, Paris, December 1956. Editor J.Fabri. Pergamon Press, London, 1958.
- No AGARD serial number — "Combustion and Propulsion. Third AGARD Colloquium. Noise — Shock Tubes — Magnetic Effects — Instability and Mixing". Combustion Colloquium, Palermo, Sicily, March 1958. Editors M.W.Thring, J.Fabri, O.Lutz and A.H.Lefebvre. Pergamon Press, London, 1958.
- AGARDograph 31 — "Explosions, Detonations, Flammability and Ignition" by S.S.Penner and B.P.Mullins. Pergamon Press, London, 1959.
- AGARDograph 37 — "Advanced Aero Engine Testing". Joint Meeting of AGARD Combustion and Propulsion and Wind Tunnel and Model Testing Panels, Copenhagen, Denmark, October 1958. Editors A.W.Morley and Jean Fabri. Pergamon Press, London, 1959.
- No AGARD serial number — "The Chemistry of Propellants". Meeting of AGARD Combustion and Propulsion Panel, Paris, June 1959. Editors S.S.Penner and J.Ducarme. Pergamon Press, Oxford, 1960.
- No AGARD serial number — "Combustion and Propulsion. Fourth AGARD Colloquium. High Mach Number Air-Breathing Engines". Milan, April 1960. Editors A.L.Jaumotte, A.H.Lefebvre and A.M.Rothrock. Pergamon Press, Oxford, 1961.
- No AGARD serial number — "Advanced Propulsion Techniques". AGARD Combustion and Propulsion Panel Meeting, Pasadena, California, August 1960. Editor S.S.Penner. Pergamon Press, Oxford, 1961.
- AGARDograph 41 — "Fundamental Data Obtained from Shock-Tube Experiments". Editor A.Ferri. Pergamon Press, Oxford, 1961.

- AGARDograph 47 — "Gas Sampling and Chemical Analysis in Combustion Processes" by G.Tinc. Pergamon Press, Oxford, 1961.
- No AGARD serial number — "Experimental Methods in Combustion Research". Manual. Editor J.Surugue. Pergamon Press, Oxford, 1961.
- No AGARD serial number — "Combustion and Propulsion. Fifth AGARD Colloquium. High Temperature Phenomena". Braunschweig, April 1962. Editors R.P.Hagerty, O.Lutz, A.L.Jaumotte and S.S.Penner. Pergamon Press, Oxford, 1963.
- No AGARD serial number — "Supersonic Flow, Chemical Processes and Radiative Transfer". Editors D.B.Olfe and V.Zakkay. Pergamon Press, Oxford, 1964.
- AGARDograph 75 — "Nonsteady Flame Propagation". Editor George H.Markstein. Pergamon Press, Oxford, 1964.
- AGARDograph 81 — "Combustion and Propulsion. Sixth AGARD Colloquium. Energy Sources and Energy Conversion". Cannes, France, March 1964. Editors H.M.DeGroof, J.Fabri, R.F.Hoglund, T.F.Nagey and M.E.Rumbaugh Jr. Gordon and Breach Science Publishers, New York, 1967.
- AGARDograph 86 — "Low Temperature Oxidation". Editor W.Jost. Gordon and Breach Science Publishers, New York, 1965.
- AGARDograph 88 — "Physics and Technology of Ion Motors". Technical Meeting of Combustion and Propulsion Panel, Athens, Greece, July 1963. Editors Frank E.Marble and Jean Surugue. Gordon and Breach Science Publishers, New York, 1966.
- AGARDograph 96 — "Instrumentation for High Speed Plasma Flow" by A.E.Fuhs. Gordon and Breach Science Publishers, New York, 1965.
- AGARDograph 101 — "Nuclear, Thermal and Electric Rocket Propulsion — Fundamentals, Systems, and Applications". Editors R.A.Willaume, A.Jaumotte and R.W.Bussard. Gordon and Breach Science Publishers, New York, 1967.
- AGARD Conference Proceedings No.1 — "Advances in Tactical Rocket Propulsion". Editor S.S.Penner. Technivision Services, Maidenhead, England, August 1968.
- AGARDograph 116 — "Fundamental Aspects of Solid Propellant Rockets" by F.A.Williams, M.Barrère and N.C.Huang. Technivision Services, Slough, England, October 1969.
- AGARDograph 120 — "Supersonic Turbo-Jet Propulsion Systems and Components". Editor J.Chauvin. Technivision Services, Slough, England, August 1969.
- AGARDograph 129 — "The Performance of Chemical Propellants" by I.Glassman and R.F.Sawyer. Technivision Services, Slough, England, Januar, 1970.
- AGARD Conference Proceedings No.38 — "New Experimental Techniques in Propulsion and Energetics Research". Editors David Andrews and Jean Surugue. Technivision Services, Slough, England, October 1970.

## AGARD PROPULSION AND ENERGETICS PANEL

CATEGORY II PUBLICATIONS – NOT ON COMMERCIAL SALE: FOR AVAILABILITY SEE BACK COVER.

- AGARDograph 89** – “V/STOL Aircraft”. Proceedings of a Meeting held at NATO Headquarters, Paris, September 1964. Part I – UNCLASSIFIED, Part II – CLASSIFIED.
- AGARDograph 98** – “Graphical Methods in Aerothermodynamics” by O.Lutz and G.Stoffers. November 1967.
- AGARDograph 117** – “Behaviour of Supercritical Nozzles under Three-Dimensional Oscillatory Conditions” by L.Crocco and W.A.Sirignano. 1967.
- AGARDograph 122** – “Selected Topics in Electrofluid Dynamic Energy Conversion”. Editors M.Lawson and F.Wattendorf. December 1968.
- Publication Hors-Série (contact AGARD).** – “Properties of Air and Combustion Products with Kerosine and Hydrogen Fuels”. Editor R.W.McIntyre. (13 volumes). 1967.
- Conference Proceedings 8** – “Fundamental Studies of Ions and Plasmas”. Editor H.Dean Wilsted. Proceedings of the PEP 26th Meeting held in Pisa, September 1965. (Two volumes).
- Conference Proceedings 9** – “Gas Turbines”. Papers presented at the PEP 27th Meeting held in Paris, April 1966. (Two volumes).
- Conference Proceedings 12** – “Recent Advances in Aerothermochemistry”. Editor I.Glassman. Selected papers presented at the PEP 28th Meeting (7th Colloquium) held in Oslo, May 1966. (Two volumes).
- Conference Proceedings 21** – “Performance Forecast of Static Energy Conversion Devices”. Editors G.W.Sherman and L.Devol. Proceedings of the PEP 29th Meeting held in Liège, June 1967.
- Conference Proceedings 31** – “Helicopter Propulsion Systems”. Editor R.P.Hagerty. Proceedings of the PEP 31st Meeting held in Ottawa, June 1968.
- Conference Proceedings 34** – “Advanced Components for Turbojet Engines”. Editor R.P.Hagerty. Proceedings of the PEP 32nd Meeting held in Toulouse, September 1968. (Two volumes).
- Conference Proceedings 42** – “Aircraft Engine Noise and Sonic Boom”. Editors R.Barth and R.P.Hagerty. Proceedings of the Joint FDP/PEP (33rd Meeting) held in St.Louis, France, May 1969.
- Advisory Report 22** – “Technical Evaluation Report on AGARD Specialists’ Meeting on Aircraft Engine Noise and Sonic Boom” by W.R.Sears. January 1970. (Primarily treats sonic boom).
- Advisory Report 26** – “Technical Evaluation Report on AGARD Specialists’ Meeting on Aircraft Engine Noise and Sonic Boom” by J.O.Powers and M.Pianko. June 1970. (Primarily treats engine noise).
- AGARDograph 123** – “Space Power Systems”. Editor G.C.Szego. Lecture Series held in October 1967. (Two volumes).
- AGARDograph 135** – “Fluidic Controls Systems for Aerospace Propulsion”. Editor R.J.Reilly. XXXV Lecture Series. September 1969.
- Conference Proceedings 52** – “Reactions between Gases and Solids”. Editor R.P.Hagerty. February 1970. Proceedings of PEP 34th Meeting held in Dayton, Ohio, October 1969.
- Advisory Report 32** – “Technical Evaluation Report on AGARD Propulsion and Energetics Panel’s 34th Meeting (8th Colloquium) on Reactions between Gases and Solids” by S.S.Penner and P.G.Atkinson Jr. February 1971.

- AGARDograph 108 - "Combustibles, Lubrifiants et Fluides Auxiliaires pour l'Aviation Supersonique" by G.J.Souillard, J.Ducarme and T.H. de Menten. June 1970.
- AGARDograph 141 - "Propergols Hautement Energétiques" by P.Tavernier, J.Boisson and B.Crampel. August 1970.
- Lecture Series 39 - "Advanced Compressors". Editor J.Chauvin. August 1970.
- Conference Proceedings 64 - "Advanced Technology for Production of Aerospace Engines". Editor R.P.Hagerty. September 1970. Proceedings of PEP 35th Meeting held in London, England, April 1970.
- Conference Proceedings 73 - "High Temperature Turbines". Editor R.P.Hagerty. January 1971. Proceedings of PEP 36th Meeting held in Florence, Italy, September 1970.
- Advisory Report 29 - "Technical Evaluation Report on AGARD Technical Meeting on High Temperature Turbines" by J.B.Esgar and R.A.Reynolds. February 1971.
- Lecture Series 46 - "Small Gas Turbines for Helicopters and Surface Transport". Editor J.Fabri. May 1971.
- Conference Proceedings 84 - "Aircraft Fuels, Lubricants, and Fire Safety". Editor R.P.Hagerty. September 1971. Proceedings of PEP 37th Meeting held in The Hague, Netherlands, May 1971.
- Advisory Report 36 - "Report of the AGARD Ad Hoc Committee on Engine-Airplane Interference and Wall Corrections in Transonic Wind Tunnel Tests". August 1971. X
- AGARDograph 148 - "Heat Transfer in Rocket Engines" by H.Ziebland and R.C.Parkinson. September 1971.
- Conference Proceedings 91 - "Inlets and Nozzles for Aerospace Engines". Editor R.P.Hagerty. December 1971. Proceedings of PEP 38th Meeting held in Sandefjord, Norway, September 1971.

NATIONAL DISTRIBUTION CENTRES FOR UNCLASSIFIED AGARD PUBLICATIONS

Unclassified AGARD publications are distributed to NATO Member Nations through the unclassified National Distribution Centres listed below

**BELGIUM**

Colonel R. DALLIER  
 Coordinateur  
 Etat-Major F  
 Caserne Prin  
 Place Dailly,

**ITALY**

Aeronautica Militare

National Aeronautics and Space Administration

WASHINGTON, D. C. 20546

OFFICIAL BUSINESS

Penalty For Private Use, \$300.00



POSTAGE AND FEES PAID  
 NATIONAL AERONAUTICS AND  
 SPACE ADMINISTRATION

**CANADA**

Director of  
 Defence Res  
 Department  
 Ottawa, On

**DENMARK**

Danish Defi  
 Østerbrogac  
 Copenhagen

**FRANCE**

O.N.E.R.A.  
 29, Avenue  
 92, Châtilli

**GERMANY**

Zentralstell  
 und Inform.  
 Maria-Theresia Str. 21  
 8 München 27  
 Attn: Dr Ing. H.J.RAUTENBERG

**GREECE**

Hellenic Armed Forces Command  
 D Branch, Athens

**ICELAND**

Director of Aviation  
 c/o Flugrad  
 Reykjavik

004 001 C4 B 06 720127 S00906DS

DEPT OF THE AIR FORCE  
 ARNOLD ENGINEERING DEV CTR

ATTN: AEYSI  
 ARNOLD AF STA TN 37389

ment

**LISBON**

Attn: Brig. General José de Sousa OLIVEIRA

**TURKEY**

Turkish General Staff (ARGE)  
 Ankara

**UNITED KINGDOM**

Defence Research Information Centre  
 Station Square House  
 St. Mary Cray  
 Orpington, Kent BR5 3RE

**UNITED STATES**

National Aeronautics and Space Administration (NASA)  
 Langley Field, Virginia 23365  
 Attn: Report Distribution and Storage Unit

\* \* \*

If copies of the original publication are not available at these centres, the following may be purchased from:

*Microfiche or Photocopy*

National Technical  
 Information Service (NTIS)  
 5285 Port Royal Road  
 Springfield  
 Virginia 22151, USA

*Microfiche*

ESRO/ELDO Space  
 Documentation Service  
 European Space  
 Research Organization  
 114, Avenue de Neuilly  
 92, Neuilly-sur-Seine, France

*Microfiche*

Technology Reports  
 Centre (DTI)  
 Station Square House  
 St. Mary Cray  
 Orpington, Kent BR5 3RE  
 England

The request for microfiche or photocopy of an AGARD document should include the AGARD serial number, title, author or editor, and publication date. Requests to NTIS should include the NASA accession report number.

Full bibliographical references and abstracts of the newly issued AGARD publications are given in the following bi-monthly abstract journals with indexes:

Scientific and Technical Aerospace Reports (STAR)  
 published by NASA,  
 Scientific and Technical Information Facility,  
 P.O. Box 33, College Park,  
 Maryland 20740, USA

United States Government Research and Development  
 Report Index (USGDRI), published by the  
 Clearinghouse for Federal Scientific and Technical  
 Information, Springfield, Virginia 22151, USA

